Lecture Notes in Electrical Engineering 246

Baoju Zhang · Jiasong Mu · Wei Wang
Qilian Liang · Yiming Pi *Editors*

The Proceedings of the Second International Conference on Communications, Signal Processing, and Systems

Springer

For further volumes:
http://www.springer.com/series/7818

Baoju Zhang • Jiasong Mu • Wei Wang •
Qilian Liang • Yiming Pi
Editors

The Proceedings of the Second International Conference on Communications, Signal Processing, and Systems

Springer

Editors
Baoju Zhang
Jiasong Mu
Wei Wang
Tianjin Normal University
Tianjin, China
People's Republic

Qilian Liang
University of Texas at Arlington
Arlington, Texas, USA

Yiming Pi
University of Electronic Science and Technology
Chengdu, China
People's Republic

ISSN 1876-1100 ISSN 1876-1119 (electronic)
ISBN 978-3-319-00535-5 ISBN 978-3-319-00536-2 (eBook)
DOI 10.1007/978-3-319-00536-2
Springer Cham Heidelberg New York Dordrecht London

Library of Congress Control Number: 2013950383

Printed on acid-free paper

Springer is part of Springer Science+Business Media (www.springer.com)

Preface

The Second International Conference on Communications, Signal Processing, and Systems (CSPS) is held in Tianjin during September 1–2, 2013. Tianjin is universally acknowledged for its rich history and cultural development. It is also recognized as a modern international metropolis full of energy and vitality. CSPS 2013 brings together Chinese and international researchers and practitioners in communications, signal processing, and systems together.

The accepted papers of CSPS 2013 are from various regions around the world, which include ten different technical sessions: Wireless Sensor Network and Cognitive Radio System, Image and Video Processing, Circuit Processing System, Millimeter Wave and UWB technology, Radar Signal Processing, Intelligent System and Technology, Wireless Communication and Networks, Localization and Target Detection, Biological Signal Processing, and Sensor and Measuring Network.

The technical program team did an excellent job in soliciting submissions, coordinating the review process, and promoting the technical program. We would like to thank every one of them for taking leadership roles in organizing the various aspects of the technical program.

Also we would like to express our thanks to all members of the organizing committee and all the volunteer reviewers who have been working hard days and nights for this conference. We are grateful to the host institution, Tianjin Normal University, and sponsorships from IEEE Fort Worth Section, University of Texas at Arlington, Beijing University of Posts and Telecommunications, University of Electronic Science & Technology of China (UESTC). Finally, the financial support from the National Science Foundation of China (NSFC), and publication support from Springer are deeply appreciated.

September 2013

Baoju Zhang
Jiasong Mu
Wei Wang
Qilian Liang
Yiming Pi

Welcome Message from the General Chairs

It is our great honor and pleasure to welcome you to Tianjin for the second International Conference on Communications, Signal Processing, and Systems (CSPS) held during September 1–2, 2013. During this conference, scholars and practitioners from all over the world in communications, signal processing, and electronic systems will get together in Tianjin.

Tianjin, a city standing by BoHai Sea, shares a great development of industry. It is famous for its overseas commodities. Additionally, it is the focal point in the country's development of travel and transport, science and technology, and education and communications. It is a remarkable city offering an abundance of ancient and modern architecture, historical relics, churches, assembly halls, natural scenery, temples, museums, commemorative site, and a variety of colorful local flavors and customs.

CSPS 2013 is organized by an international team. The conference features ten technical sessions and two keynote sessions. We invite you to join us by attending the technical and social events held in CSPS 2013.

On behalf of the Organizing Committee, the Technical Program Committee, and all the volunteers who have been working hard for this conference, we warmly welcome you to CSPS 2013 and hope that you will enjoy the conference, and the beautiful city in which it takes place.

Yubao Gao, Tariq S. Durrani, Rabinder N. Madan, Qilian Liang

General Co-Chairs, CSPS 2013

Yubao Gao
Tariq S. Durrani
Rabinder N. Madan
Qilian Liang

Organization

The International Conference on Communications, Signal Processing, and Systems (CSPS) is organized by Tianjin Normal University, University of Texas at Arlington, Beijing University of Posts and Telecommunications, University of Electronic Science and Technology, China.

General Co-Chairs:	Yubao Gao, Tianjin Normal University, China Tariq S. Durrani, University of Strathclyde, UK Rabinder N. Madan, George Washington University, USA Qilian Liang, University of Texas at Arlington, USA
TPC Co-Chairs:	P. P. Vaidyanathan, California Institute of Technology, USA Baoju Zhang, Tianjin Normal University, China Wei Wang, Tianjin Normal University, China Yiming Pi, University of Electronic Science and Technology, China
International Advisory Committee:	Leon Chua, University of California at Berkeley, USA Gene Frantz, Texas Instruments, USA Er Meng Hwa, Nanyang Technological University, Singapore Sanjit Mitra, University of Southern California, USA Zhisheng Niu, Tsinghua University, China Wan-Chi Siu, Hong Kong Polytechnic University, Hong Kong Tieniu Tan, Chinese Academy of Science, China Xiaorong Wu, Tianjin Normal University, China Zheng Zhou, Beijing University of Posts and Telecommunications, China
Keynote Cochairs:	Xiaorong Wu, Tianjin Normal University, China Jean X. Gao, University of Texas at Arlington, USA Chenglin Zhao, Beijing University of Posts and Telecommunications, China
Financial and Local Arrangement Chair:	Ruian Liu, Tianjin Normal University, China Jincheng Wu, Tianjin Normal University, China Guanglin Han, Tianjin Normal University, China

Special Session Co-Chairs:	Jian Ren, Michigan State University, USA Zinan Wang, University of Electronic Science and Technology, China
Publication Co-Chairs:	Jiasong Mu, Tianjin Normal University, China Xin Zhou, Tianjin Normal University, China
Registration Co-Chairs:	Jing Liang, University of Electronic Science and Technology, China Wei Song, Tianjin Normal University, China Xin Yin, Tianjin Normal University, China
Publicity Co-Chairs:	Xiuzhen Cheng, George Washington University, USA Zongjie Cao, University of Electronic Science and Technology, China Yan Li, Tianjin Normal University, China Jin Chen, Tianjin Normal University, China
TPC Members:	Jingfu Bao, University of Electronic Science and Technology, China Zongjie Cao, University of Electronic Science and Technology, China Dechang Chen, Uniformed Services University of Health Sciences, USA, Jin Chen, Tianjin Normal University, China Junjie Chen, University of Texas at Arlington, USA Xiao Chen, Texas State University, USA Ting Cheng, University of Electronic Science and Technology, China Xiuzhen Cheng, George Washington University, USA Junhong Cui, University of Connecticut, USA Luhong Fan, University of Electronic Science and Technology, China Qian He, University of Electronic Science and Technology, China Songbai He, University of Electronic Science and Technology, China Jiyan Huang, University of Electronic Science and Technology, China Ting Jiang, Beijing University of Posts and Telecommunications, China Huiyong Li, University of Electronic Science and Technology, China Liying Li, University of Electronic Science and Technology, China Shenghong Li, Shanghai JiaoTong University, China Shuangtian Li, Institute of Acoustics Academia Sinica, China Tongtong Li, Michigan State University, USA Zhuo Li, University of Texas at Arlington, USA Kuo Liao, University of Electronic Science and Technology, China Ruian Liu, Tianjin Normal University, China Ishrat Maherin, University of Texas at Arlington, USA Yiming Pi, University of Electronic Science and Technology, China Jian Ren, Michigan State University, USA Qingchun Ren, Mircosoft, USA Songlin Sun, Beijing University of Posts and Telecommunications, China Bin Tang, University of Electronic Science and Technology, China Haijiang Wang, University of Electronic Science and Technology, China Lingming Wang, Coherent Logix, USA Wenbo Wang, Beijing University of Posts and Telecommunications, China Wei Wang, Tianjin Normal University, China

Xin Wang, University of Texas at Arlington, USA
Ji Wu, University of Texas at Arlington, USA
Zhengyu Wu, University of Electronic Science and Technology, China
Xinsheng Xia, AT&T, USA
Lei Xu, Broadcom, USA
Xin Yin, Tianjin Normal University, China
Feng Zhao, GuiLin University of Electronic Technology, China
Zhiqin Zhao, University of Electronic Science and Technology, China
Ying Zhang, University of Electronic Science and Technology, China
Daiying Zhou, University of Electronic Science and Technology, China
Xin Zhou, Tianjin Normal University, China
Zheng Zhou, Beijing University of Posts and Telecommunications, China
Hongbo Zhu, Nanjing University of Posts and Telecommunications, China
Jiazu Xie, Tianjin Normal University, China
Jincheng Wu, Tianjin Normal University, China
Jingrui Sun, Tianjin Normal University, China
Na Li, Tianjin Normal University, China
Guanglin Han, Tianjin Normal University, China
Ying Tong, Tianjin Normal University, China
Mingcheng Liu, Tianjin Normal University, China
Bin Liang, Tianjin Normal University, China
Yan Li, Tianjin Normal University, China
Tingting Han, Tianjin Normal University, China
Zhujun Gu, Tianjin Normal University, China
Jiasong Mu, Tianjin Normal University, China
Dongchui Kim, University of Texas at Arlington, USA
Qiong Wu, University of Texas at Arlington, USA
Mingon Kang University of Texas at Arlington, USA
Shuo Li, University of Texas at Arlington, USA

Sponsoring Institutions: Tianjin Normal University
IEEE Fort Worth Section, USA
University of Texas at Arlington
Beijing University of Posts and Telecommunications
University of Electronic Science and Technology, China

Contents

Part III Circuit Processing System

Part IX Biological Signal Processing

Part X Sensor and Measuring Network

Part I
Wireless Sensor Network and Cognitive Radio System

Design of System for Digital Sound Anti-monitoring Based on Wireless Sensor Networks and 3G

Hua Liu, Yong Wei, Ruo-kui Chang, Xuefeng Jin, and Yuan Yuan

Abstract This paper introduces a control system. This system consists of wireless video transmission module, wireless data transmission module, voice and ultrasonic anti-bird module, field of environmental parameters detection and infrared anti-theft alarm module. Host of the system receives the control signal issued by the long-distance computer, controls voice and ultrasonic, and also collects data of video, images, and environmental parameters. 3G network is connected to the host computer. As a result, the system can monitor the information of bird pest, use a variety of modes to scatter birds, also provide remote expert diagnosis with the gathered information about growth of crops.

1 Introduction

With the ecological environment significantly improved, bird populations are sharply increasing, which leads to serious hazard bird damage on agricultural production. Losses due to bird hazard of field crops, especially wheat and paddy rice, are up to 10 %, in several areas even 30 %. In fruit farms, annual loss of fruit is from 5 to 10 %, sometimes above 30 %. It is reported that in Japan, the Ministry of Agriculture, Forestry and Fisheries carries out a study each year. According to the studies, the major pest birds are: two species of crow, the carrion crow and the jungle crow; tree sparrows; ducks; brown-eared bulbuls; grey starlings; and two species of doves and pigeons. As reported by New Zealand Plant Protection Society, among the farmers surveyed, 87 % of them encountered crop damage from birds, which has been a serious problem. In some of these cases, bird hazard

H. Liu (✉) • Y. Wei • R.-k. Chang
School of Electromechanical Engineering, Tianjin Agricultural University, Jinjing Road 22, Tianjin 300384, China
e-mail: tjwqns@tjau.edu.cn; weiytj@sohu.com

X. Jin • Y. Yuan
Tianjin Design & Research Institute of Electric Drive CO. Ltd., Tianjin 300180, China

B. Zhang et al. (eds.), *The Proceedings of the Second International Conference on Communications, Signal Processing, and Systems*, Lecture Notes in Electrical Engineering 246, DOI 10.1007/978-3-319-00536-2_1,

makes the farmers lose 20 % of their total harvest of a year. It is really a large economic blows [1, 2].

This paper proposes and designs a remote monitoring system which is also capable of protecting crops from birds. Some popular industry technologies, including wireless data transmission, 3G, and solar energy, are appropriately combined in the system. Tests have been done to verify effect of the system on avoiding bird damage to crops.

2 Material and Methods

The system consists of host and slave devices. The former receives control signal from the host computer via wireless network [3], and then transmits the collected data of video, images, and environmental parameters. The latter focuses on some auxiliary functions such as voice and ultrasonic anti-bird and detecting environmental parameters. Structure of the remote monitoring system is shown in Fig. 1.

2.1 Structure of Host Device

Figure 2 shows whole structure of the host, consisting of MCU system, power, Wireless video transmission, Wireless data transmission, infrared sensor, PAN/TILT and Sound-light alarm etc. [4]. MCU system receives the control signal and processing them; Wireless video transmission and Wireless data transmission modules accomplish the tasks of transmits data, especially video data; PAN/TILT enlarges the scope and Sound-light alarm aims at theft.

2.2 Audible Bird Scarcer

Figure 3 shows that diagram of audible bird scarcer, including wireless data transmission modules, light intensity detection modules, EPROM, D/A and audio power amplifier etc. The functions of the scarcer include voice select, play pattern, and time interval.

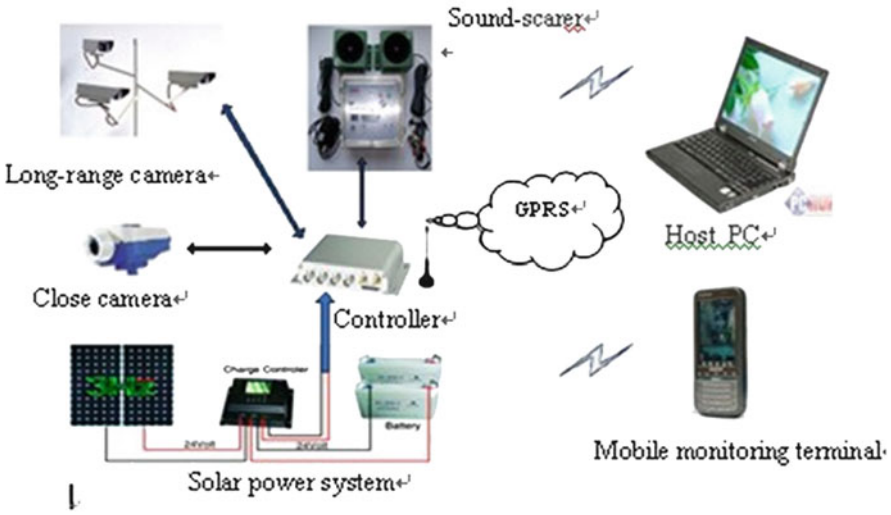

Fig. 1 Structure of remote monitoring system

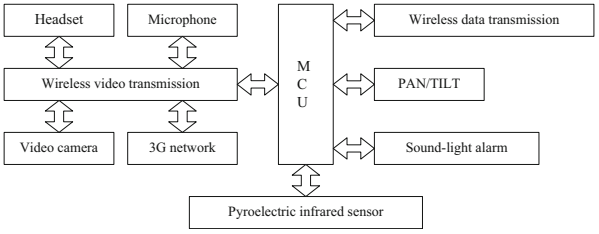

Fig. 2 Structure of host

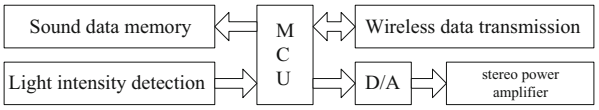

Fig. 3 Diagram of audible bird scarcer

2.3 Function Module

2.3.1 Wireless Video Transmission

Video surveillance as a combination of a traditional video technology and modern communication technology application has aroused more and more attention around the world. A wireless video transmitter is a device with independent

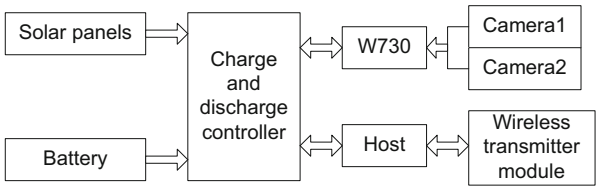

Fig. 4 Flow chart of monitoring host program

monitoring site. Accessing through CDMA/GPRS/EDGE wireless Internet network, the live video image transmission to a remote host computer through Internet network. W730 can not only work independently, but also comes with two serial communications and field equipment connected with the coordination. Flow chart of monitoring host program is shown in Fig. 4.

In the places covered with 3G network, mobile terminal can be used to acquisite and compress field video in real-time way, and transmit it to remote monitoring center. At the same time of video transmission, a two-way voice communications link between the mobile terminal and command center can also be set up. As a result, personnel at command center is able to accomplish remote control. In addition, the video data acquired by command center can also be sent to a network server, which enable personnel at other position to check situation at the site.

2.3.2 Wireless Data Transmission

ZigBee technology is used in wireless data transmission module, especially in serial devices, wireless networking, industry-standard wireless data communication equipment [5].

Due to the enhanced ZigBee wireless technology, wireless communications equipment of the system can be in line with industry standard applications. With the routing capabilities of the relay; the theoretical maximum transfer distance of wireless communication could be 2,000 m. These equipments use 2.4G Direct Sequence Spread Spectrum technology and have anti-jamming capability, with features of transparent data or instruction format transmission, the maximum band rate of 115,200, flexible transmit mode, broadcast or send an optional mode, and network capacity and optional 16-channel, 65536 network ID can be set and performance characteristics.

3 Software Design

3.1 System Software

The software design [6] of the system includes the host monitor and voice bird. Host monitor software design, including the remote host computer to send commands to receive and resolve wireless multiple voice bird with ultrasonic bird control, and monitoring the host's anti-theft protection, receive feedback that the bird will feedback sent to the remote host computer, the data collected by the environment

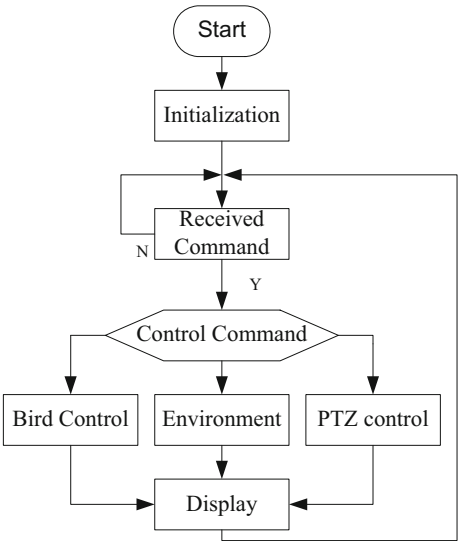

Fig. 5 Flow chart of monitoring host program

parameter module is sent to the remote host computer, PTZ control, voice bird's software design includes voice data of the memory chip read, DA converter, and host monitoring between the wireless communications, and drive the birds device mode settings. The flow chart of overall software design is shown in Fig. 5.

3.2 Wireless Sensor Network

The iterative weighted centroid algorithm can be interpreted as: known node that has positioned and upgraded to the anchor node; unknown node represents not locate the node [7, 8]. Algorithm surrounding anchor nodes greater than three unknown node positioning, the positioning node upgrade as the anchor node; unknown node after the upgrade, re-judge the surrounding anchor nodes, as long as the number of anchor nodes is greater than 3, then the use of centroid localization algorithm. Known node weights in positioning control, and its weight coefficient is set to 0.8, while the anchor node in the right a value of 1.

Experiment in inter-node communication distance of 25 m, the average network connectivity for 18.53. Uniform random distribution of the 10 anchors and 100 unknown node distribution as shown in Fig. 6, indicated with red star anchor node, and the blue dots represent unknown node.

As the anchor node density is not high, and the node communication distance is limited, some nodes around the anchor nodes less than 3, unable to locate. When anchor nodes randomly deployed 10 % node communication distance 25 m, network connectivity for 18.53, the node positioning error of about 20 %. Positioning error is shown in Fig. 7.

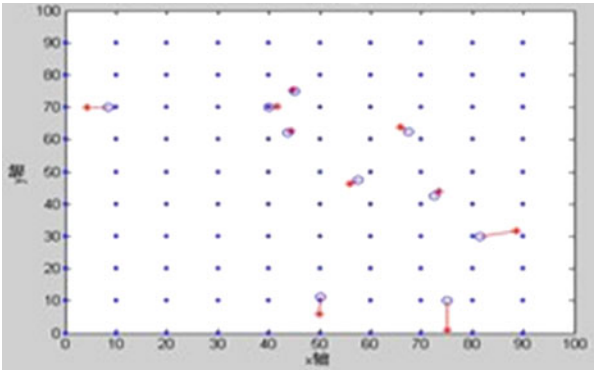

Fig. 6 Node maps

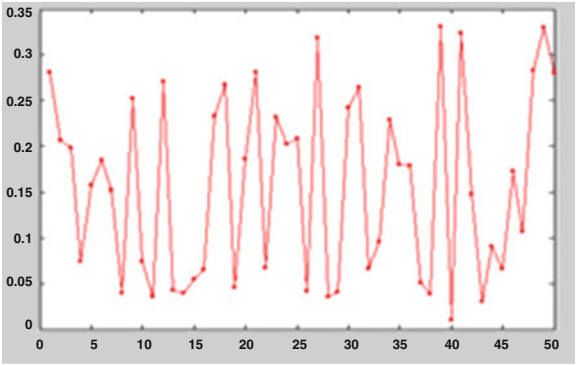

Fig. 7 Corresponding node localization

Loop positioning for more accurate positioning results, the positioning of the nodes of the already upgraded to the anchor node, and then send its own location information to other nodes receive this information nodes as anchor nodes, such nodes are called known nodes. The simulation shows the anchor node weights recorded as 1, a known node weights recorded 0.8 positioning error smaller. The calculated error value is about 16 %, the precision can be improved, as shown in Fig. 8.

The set anchor node number 30, the other parameters are the same, and then iteratively reweighted, the known nodes rights value is still set to 0.8, and node communication radius of 25 m. Positioning accuracy using iterative weighted as shown in Fig. 9. After iterative weighted improve precision, the error value in the 11 % or less.

Analysis of the experimental results, the communication radius of 25 m, the average network connectivity centroid localization algorithm positioning error in 18.53, about 20 %, approximately 16 % of the weighted centroid algorithm error, improve the accuracy of 4 %. Increasing the number of the anchors 30, the positioning error of the weighted centroid algorithm is 13 %, iterative positioning

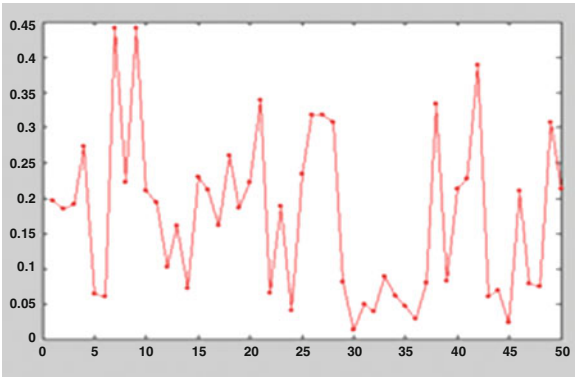

Fig. 8 Improved positioning error

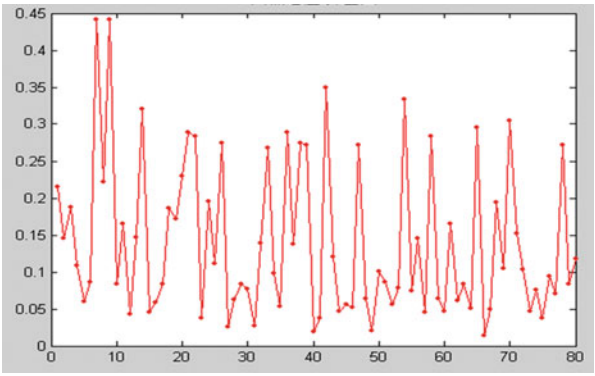

Fig. 9 Iteratively re-weighted positioning error

error of approximately 10 % of the weighted centroid algorithm to improve the accuracy of about 3 %.

4 Debugging

The pattern of scattering away birds is by the W730 wireless video transmission module and the host computer serial port communication software, the switch for remote control and can be collected on-site environmental parameters. When to be collected on-site environmental parameters in the software text box to display the current field of environmental parameters in the PC interface.

Equipments are installed in Baodi District Huangzhuang farm, Tianjin city of China. Figure 10 shows the images of growing rice, which is acquired by the introduced system installed at the farm and transmitted through 3G network.

During the test, it is observed that some birds like flocks of sparrows and magpies are successfully scattered by the audible bird scarcer. As the system combinates sounds of various birds, no local birds familiar with such sounds.

Fig. 10 Site and capture images

From the collected images, the effect of the system on reducing bird damage is significant and satisfying.

5 Conclusion

Digital sound anti-bird monitoring system is not only able to scatter birds to protect crops, but also transmit the crop status information to the expert remote expert diagnosis. It has the following features:

1. Receiving a remote host computer command control on the head.
2. Receiving the instruction of the remote host computer, select the voice the voice of the bird, the mode spacing and random.
3. Environmental parameters collected at the scene to receive the remote host computer instruction to be distributed to users.
4. The host of the Monitor mode, adjustable anti-theft function.

Enough sounds of birds prepared in the system is an effective way to scatter away birds, because it does not produce "immunity". In future work, we are doing researches on bird hazard prevention technology to find more effective scarcing bird methods.

Acknowledgments The work is supported by Tianjin agriculture committee Support Project under Grant (201003060), and in part by Tianjin national college students' innovative entrepreneurial training plan (201310061016).

References

1. Liu P-p, Zhao X-r, Zhang H-j (2010) Research progress on agro-harmful bird and its control in China. Jiangsu Agric Sci 2:139–141
2. Li Y, Wan J-y, Xu L-h (2012) Bird trouble control in orchard. Northern Hortic 3:134–137
3. Bomford M, O'Brien PH (1990) Sonic deterrents in animal damage control: a review of device test and effectiveness. Wildl Soc Bull 4:411–422
4. Liu H, Wang M-h, Wang Y-x (2008) Development of farmland soil moisture and temperature monitoring system based on wireless sensor net work. Jilin Univ Eng Technol Ed 3:605–606
5. Mangas E, Bilas A (2009) FLASH: Fine-grained localization in wireless sensor networks using acoustic sound transmissions and high precision clock synchronization, ICDCS '09: 29th IEEE international conference on distributed computing systems, pp 289–298. Montreal, QC
6. Chen L (2012) The computer monitoring forecasting system of oil refinery. Adv Inform Sci Serv Sci 4:356–362
7. Casadei D, Serra G, Tani K (2007) Implementation of a direct control algorithm for induction motors based on discrete space vector modulation. IEEE Trans Power Electron 4:769–777
8. Shu Yin Chiang, Jin Long Wang (2009) Localization in wireless sensor networks by fuzzy logic system. Department of Information and Telecommunications Engineering, Ming Chuan University, pp. 721–728

Sensing Window Length Optimization in Low-SNR Regime

Liaoyuan Zeng

Abstract For non-coherent detection based cognitive radio (CR), the required length of the spectrum sensing window is inversely proportional to the primary user's (PUs) signal strength. When a CR system's transmission period is fixed, the length of the CR's transmission window can be inadequate to fully utilize the white space if the corresponding PUs operate in low-SNR regime. We propose a sensing window optimization algorithm in this paper aiming at improving the spectral efficiency of the cognitive Ultra Wideband (UWB) radio system. The proposed algorithm can find the optimal tradeoff between the sensing window length and the desired detection probabilities for the UWB based CR system in low-SNR regime. Compared with the conventional sensing algorithms in which the sensing window is fixed, the proposed algorithm can significantly increase the length of the CR-UWB's transmission window so as to use the available spectrum more efficiently while guaranteeing the PUs' operation.

Keywords Spectrum sensing window • Cognitive radio • Ultra wideband • Low-SNR regime

1 Introduction

To implement cognitive radio (CR) [1], one of the ideal candidate technologies is Ultra Wideband (UWB) [2]. UWB operates in 3.1–10.6 GHz with an extremely low power spectrum density (PSD) − 41.3 dBm/MHz [3], which facilitates the underlay spectrum sharing technique to co-exist with the primary users (PUs) that operate within the UWB's wide spectrum band [4]. Generally, to protect the PUs from being harmfully interfered, the CR-UWB's transmit power can be decreased

L. Zeng (✉)
University of Electronic Science and Technology of China, Chengdu, Sichuan, China
e-mail: lyzeng@uestc.edu.cn

B. Zhang et al. (eds.), *The Proceedings of the Second International Conference on Communications, Signal Processing, and Systems*, Lecture Notes in Electrical Engineering 246, DOI 10.1007/978-3-319-00536-2_2,

to a level that is significantly lower than the UWB's regular PSD, which can result in considerably low spectral efficiency for the CR-UWB. By using orthogonal frequency division multiplexing (OFDM) in UWB, the CR-UWB system can adaptively adjust the transmit power of the OFDM subcarriers according to the spectrum sensing results within the interested spectrum segments which are overlapped with the PU's operating bands. The spectral efficiency of the overlapped spectrum is critical to the overall spectral efficiency of the CR-UWB system and is dependent on the performance of the spectrum sensing algorithm.

We assume that the characteristics of the PUs signal are unknown to the CR-UWB. Hence, the non-coherent detection based energy detection technique can be chosen to verify the availability of the overlapped spectrum due to energy detector's use of the Fourier transform (FT) function which is a key in the OFDM based UWB system [5]. To determine the PUs' presence successfully, the length of the CR-UWB's spectrum sensing window shall be adequate which is dependent on the PUs signal's signal to noise ratio (SNR) received at the CR-UWB and the thresholds of the probability of detection/false alarm. Since the length of the sensing window is roughly inversely proportional to the PUs' signal strength, for a CR-UWB system in which the duration of spectrum access is fixed, the length of the CR-UWB's spectrum sensing window can have a critical impact on the finally overall spectral efficiency in a way that the length of the sensing window determines the length of the transmission window, in which an excessive sensing window fulfilling the PUs protection requirement can produce a shortened transmission window which will limit CR-UWB's use of the overlapped spectrum. When PUs operate in a low-SNR regime, i.e., the SNR detected at the CR-UWB's receiver is extremely low, the time required to successfully detect the PUs can be excessively long, which can lead to a considerably short transmission window which in turn can result in a unacceptable spectral efficiency.

In this paper, we propose a spectrum sensing optimization algorithm in low-SNR regime, aiming at improving the CR-UWB's spectral efficiency by finding the tradeoff optimality of the spectrum sensing window length and the spectrum sensing performance. The sensing performance is characterized by the probability of false alarm (PFA) and the probability of detection (PD). By computing the optimal sensing window length, the proportion between the CR-UWB's transmission window length to the duration of the spectrum access can be maximized while guaranteeing the PUs operation, which can facilitate the fully use of the overlapped spectrum by incorporating a high efficient transmission scheme.

The remainder of the paper is organized as follows. Section 2 gives a brief overview of the current spectrum sensing window optimization methods. Section 3 presents the spectrum sensing model and the formulation of the spectrum sensing window optimization problem. The proposed sensing window optimization algorithm is demonstrated in Sect. 4. Then, the numerical results are presented in Sect. 5. Finally, Sect. 6 gives a conclusion to the paper.

2 Literature Review

Stotas et al. and Peh et al. laid the fundamental work for dealing with the spectrum sensing window optimization problem in [6, 7], respectively. The Lagrange dual optimization method was used by Stotas et al. in [6] to optimize the power distribution mechanism and the spectrum sensing scheme by tuning the sensing window length adaptively to optimize the throughput of the CR system. In Stotas's algorithm, the iterations required for identifying the multiple Lagrange multipliers' values is considerable. In [8], Zou et al. used the Taylor approximation to find the relationship of the PFA and PD. The authors then minimized the CR's overall outage probability through optimizing the sensing window length using linear programming technique [9]. However, the performance of Zou's algorithm in low PU SNR regime will be degraded considerably because of the required sensing window length would be excessive.

3 System Model

In the work, we model the spectrum sensing window optimization problem as a convex optimization problem, in which the decision variable is the CR-UWB's sensing window length, and the main constraints consist of the thresholds of CR-UWB's PD and PFA. We deal with the formulated optimization problem by using linear programming. To validate our algorithms performance in term of spectral efficiency enhancement, we combine the proposed sensing window length optimization algorithm with the water-filling based transmission scheme proposed in [10]. We assume the use of the overlay spectrum sharing scheme and the application of an ideal notch filter. Hence, the sideband interference from the CR-UWB system to the PUs can be neglected.

Since the objective of the CR-UWB's spectrum sensing window length is to improve the overall spectral efficiency by increasing the spectral efficiency of the overlapped spectrum, the problem of optimizing the spectrum sensing window length denoted as **P1** can be mapped into the optimization problem of maximizing the overlapped spectrum's spectral efficiency. Thus, **P1** is expressed as:

$$\begin{aligned} \mathbf{P1}\ \arg\max_{\tau_s} S_e &= \frac{\beta}{T_{op}} S(1-P_f)(1-P(\mathcal{H}_1)) \\ \text{s.t.}: \bar{P}_d &\le P_d \le 1 \\ 0 &\le P_f \le \bar{P}_f \\ \tau_s &\ge \frac{2}{\gamma_p^2 f_s}\left(Q^{-1}(\bar{P}_f) - Q^{-1}(\bar{P}_d)\right)^2, \end{aligned} \tag{1}$$

where S_e denotes the spectral efficiency of the overlapped spectrum when the CR-UWB maintains the access to the spectrum while the corresponding PUs cease operating temporarily, S represents the spectral efficiency when the CR-UWB has full access to the overlapped spectrum where no PU is surrounded, $\beta = \frac{(T_{op}-\tau_s)}{T_{op}}$ denotes the ratio between the CR-UWB's transmission window length and the fixed duration of the CR-UWB's access to the overlapped spectrum, T_{op} is the pre-defined length of the spectrum access window, τ_s represents the sensing window length which is determined by the PU's SNR, UWB's sampling frequency and the target PFA/PD, P_f and $\bar{P}_f$ represents the actual PFA and the target PFA respectively, P_d and $\bar{P}_d$ represents the real-time PD and the target PD respectively, and $P(\mathcal{H}_1)$ shows the probability that a PU activates within T_{op}.

We assume that the probability that a PU is activated during T_{op} follows a Poisson process and is expressed as $P(\mathcal{H}_1) = p(x;\lambda t) = \frac{e^{-\lambda t}(\lambda t)^x}{x!}$ [11], where x denotes the expected number of occurrences of PU's activations during the period of t which in our system model $t = T_{op}$.

For the constraints expressed in **P1**, γ_p represents the received PU signals SNR at the CR-UWB receiver, f_s denotes the UWB's sampling rate. Furthermore, $Q(x) = \int_x^{\infty} \frac{1}{\sqrt{2\pi}} exp\left(-\frac{y^2}{2}\right) dy$ is the one-dimensional Gaussian Q-function [12].

By observing that both S and $P(\mathcal{H}_1)$ are independent of τ_s, we can transform the optimization problem shown in **P1** into **P2** which is simpler to tackle as

$$\mathbf{P2}\ arg\ \max_{\tau_s} F_r(\tau_s) = \beta\left[1 - Q\left(\frac{Q^{-1}(P_d)\sqrt{2(2\gamma_p + N)} + \gamma_p}{\sqrt{2N}}\right)\right], \tag{2}$$

where $N = \tau_s f_s$ denotes the number of spectrum sensing samples of CR-UWB's energy detector, and P_f, P_d and τ_s are related by [1]

$$P_f = Q\left(\frac{Q^{-1}(P_d)\sqrt{2(2\gamma_p + N)} + \gamma_p}{\sqrt{2N}}\right) \tag{3}$$

For simplicity and without loss of generality, we assume that there exists a single CR link within the CR-UWB network whose infrastructure is in distributed manner, and there are multiple PUs in the CR-UWB's network and the PUs' operating bandwidth is overlapped with the CR-UWB's. Overlay spectrum sharing is assumed, which indicates that the CR-UWB can access to the overlapped spectrum if and only if the energy detection result shows that the PUs are temporarily absent within the overlapped spectrum.

4 Sensing Window Length Optimization

To show the impact of the variation of the spectrum sensing window length on the CR-UWB's spectral efficiency and that there exists an optimal tradeoff between the sensing window length and the target PD and PFA, we compute the spectral efficiency of the CR-UWB in the overlapped spectrum as a function of the spectrum sensing window length which is measured in μs, as shown in Fig. 1.

At the CR-UWB's receiver, when the PUs' signal strength lies in the low-SNR regime, we observe that the spectral efficiency of the CR-UWB grows exponentially with the increase of τ_s and reaches a peak level when the spectrum sensing window is tuned to a certain value. As the value of τ_s grows beyond the optimal value, the CR-UWB's spectral efficiency decreases monotonically because the transmission window size, $T_{op} - \tau_s$, is shortened. Figure 1 numerically verifies that there exist an optimal τ_s under specific target $\bar{P}_d$, $\bar{P}_f$ and γ_p values.

To compute the optimal spectrum sensing window length for CR-UWB spectral efficiency enhancement under the constrains of $\bar{P}_f$ and $\bar{P}_d$, we use linear programming to calculate the optimized value of τ_s by computing the root for $f_r(\tau_s) = \frac{dF_r(\tau_s)}{d\tau_s} = 0$, where

$$f_r(\tau_s) = -\frac{1}{T_{txop}} - \left[Q'(\tau_s) - \frac{1}{T}(Q(f(\tau_s)) + Q'(f(\tau_s))) \right] = 0, \tag{4}$$

where $f(\tau_s)$ represents a function of τ_s and can be expressed as

$$f(\tau_s) = \frac{Q^{-1}(P_d)\sqrt{2(2\gamma_p + \tau_s f_s)} + \gamma_p}{\sqrt{2\tau_s f_s}} \tag{5}$$

and the $f(\tau_s)'$s first order differentiation is

$$f'(\tau_s) = \frac{Q^{-1}(P_d) f_s}{2\sqrt{(2\gamma_p + \tau_s f_s)\tau_s f_s}} - \frac{\sqrt{2} f_s (Q^{-1}(P_d)\sqrt{(4\gamma_p + 2\tau_s f_s)} + \gamma_p)}{4(\tau_s f_s)^{3/2}} \tag{6}$$

Nevertheless, computing the optimal τ_s in closed form is complex. Hence, exhaustive search method is used to approximately find the optimal spectrum sensing window length.

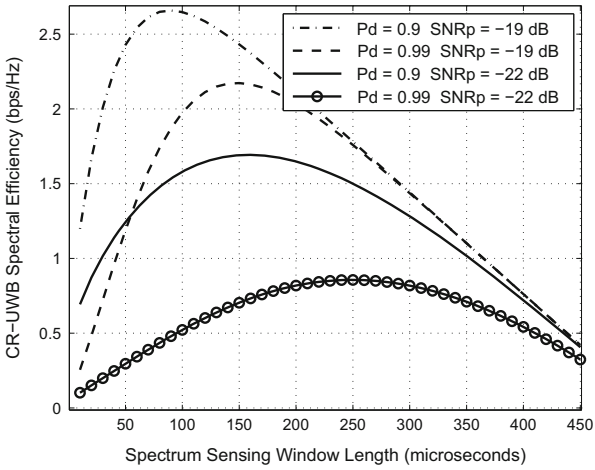

Fig. 1 The spectral efficiency as a function of the spectrum sensing window length

5 Numerical Simulation

In our work, the numerical simulation is implemented within a channel model that is previously specified in the UWB system [3]. The detected spectrum hole is used by an water-filling based algorithm [10] where the parameter settings can be referred to. Furthermore, for the PUs, λ is set to 1,000 per second to represent the random occupance of the PUs in the overlapped spectrum, and the target PD is set to 0.99.

We compare the spectral efficiency achieved by the fixed sensing window length based spectrum sensing method with the proposed sensing window length optimization algorithm, as shown in Fig. 2. It is seen that the proposed algorithm can obviously enhance the CR-UWB's spectral efficiency, especially when the PUs operate in low SNR regime. For instance, the corresponding spectral efficiency achieved by the traditional sensing method approaches zero when the value of γ_p decreases below -19 dB, while the CR-UWBs spectral efficiency achieved by the proposed sensing algorithm is profoundly higher. The spectral efficiency performance of the proposed algorithm is acceptable even when the PUs' SNR decreases below -25 dB. Furthermore, with the increase of the value of γ_p, the two lines gap shrinks in an exponential manner. As a comparison, when the PUs operate in normal or high-SNR regime (e.g., -10 dB), the gap becomes minor because a large value of γ_p can lead to a minor τ_s for a pre-defined threshold of $\bar{P}_f$ and $\bar{P}_d$.

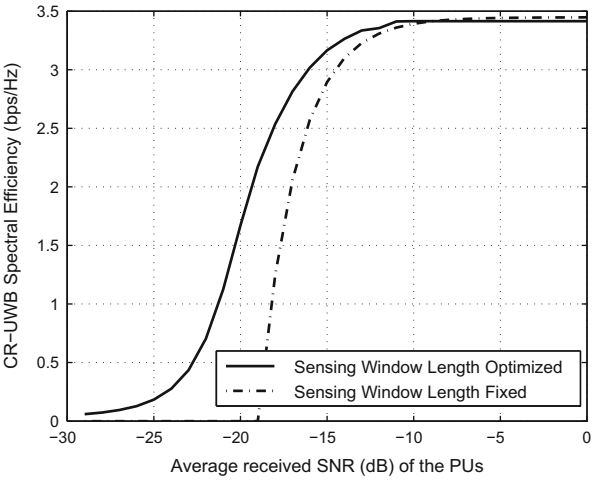

Fig. 2 The peak CR-UWB's spectral efficiency as a function of the PU's SNR received at the CR-UWB's receiver

6 Conclusion

To improve the overall spectral efficiency of the OFDM UWB based CR system when the corresponding PUs' operating power is extremely low, we proposed a novel spectrum sensing window optimization algorithm for the energy detection based CR-UWB system to find the optimal tradeoff between the detection probability and the length of the spectrum sensing window. We showed that our algorithm can identify the optimal length of the sensing window length through numerical method constrained by the target PD and PFA and then significantly prolong the transmission window when the duration of the CR-UWB's access to the overlapped spectrum is fixed. By integrating the spectral sensing window optimization algorithm with the existing spectrum management algorithm, the overall spectral efficiency of the CR-UWB was verified to be significantly increased compared with the traditional window length fixed sensing algorithm, especially in PU's low-SNR regime.

References

1. Mitola III J (1999) Cognitive radio for flexible mobile multimedia communications. In: Proceedings IEEE MoMuC, San Diego, pp 3–10
2. Porcino D, Walter, H (2003) Ultra-wideband radio technology: potential and challenges ahead. IEEE Comm Mag 41:66–74
3. Yang L, Giannakis GB (2004) Ultra-wideband communications: an idea whose time has come. IEEE Signal Process Mag 21:26–54
4. Akyildiz IF, Lee WY, Vuran MC (2006) NeXt generation/dynamic spectrum access/cognitive radio wireless networks: a survey. Comput Netw 50:2127–2159

5. Digham FF, Alouini MS, Simon MK (2007) On the energy detection of unknown signals over fading channels. IEEE Trans Comm 55:21–24
6. Stotas S, Nallanathan A (2011) Optimal sensing time and power allocation in multiband cognitive radio networks. IEEE Trans Comm 59:226–235
7. Peh ECY, Liang YC, Guan YL (2009) Optimization of cooperative sensing in cognitive radio networks: a sensing-throughput tradeoff view. IEEE Trans Veh Technol 58:5294–5299
8. Zou Y, Yao YD, Zheng B (2010) Outage probability analysis of cognitive transmissions: impact of spectrum sensing overhead. IEEE Trans Wireless Comm 9:2676–2688
9. Palomar DP, Cioffi JM, Miguel AL (2003) Joint Tx-Rx beamforming design for multicarrier MIMO channels: a unified framework for convex optimization. IEEE Trans Signal Process 51:2381–2401
10. Zeng LY, McGrath S, Cano E (2009) Rate maximization for multiband OFDM ultra wideband systems using adaptive power and bit loading algorithm. In: Proceedings IARIA AICT, Venice, 369–374
11. Huang S, Liu X, Ding Z (2008) Opportunistic spectrum access in cognitive radio networks. In: Proceedings IEEE INFOCOM, Phoenix 1427–1435
12. Vogel K, Risken H (1989) Determination of quasiprobability distributions in terms of probability distributions for the rotated quadrature phase. Phys Rev 40:2847–2849

Cognitive Group Power Assignment in Low-Power Regime

Liaoyuan Zeng

Abstract To improve the spectrum utilization efficiency by using cognitive radio (CR), the efficient use of power resource is essential. For low-power underlay systems such as ultra wideband (UWB), extremely low transmit power is mandatory for the purpose of primary users' (PU) protection, which however significantly impedes the use of UWB's spectrum. In this paper, for UWB based CR systems, we propose an cognitive group power assignment algorithm to maximize the CR-UWB's spectral efficiency while conforming to the PUs protection requirements. We formulate the spectral efficiency maximization problem as an multidimensional knapsack problem which is generally NP-Hard, and approximate the optimal solution by developing a greedy based algorithm considering the low-power feature of the CR-UWB system. A power grouping technique is derived to limit the proposed algorithm's order-of-growth. Compared with the traditional water-filling based power allocation algorithms, the proposed algorithm can attain the highest spectral efficiency which is close to the optimality in extremely low-power regime.

Keywords Power allocation • Cognitive radio • Low-Power regime

1 Introduction

A key mechanism of cognitive radio (CR) systems is to use the available spectrum as efficient as possible without degrading the overlapped primary users (PUs) performance [1]. Since the amount of data that can be loaded in a specific spectrum is directly correlated to the power assigned, efficient power assignment algorithm designs have been proved to be critical to the CR system's spectral efficiency

L. Zeng (✉)
University of Electronic Science and Technology of China, Chengdu, China
e-mail: lyzeng@uestc.edu.cn

B. Zhang et al. (eds.), *The Proceedings of the Second International Conference on Communications, Signal Processing, and Systems*, Lecture Notes in Electrical Engineering 246, DOI 10.1007/978-3-319-00536-2_3,

enhancement, in addition to the various schemes proposed with respect to spectrum management, sharing and sensing [2].

For the low-power systems, such as ultra wideband (UWB), whose available transmit power range is highly restricted (maximum power spectral density (PSD) cannot exceed $-$ 41.3 dBm/MHz) [3], which allows to use underlay sharing to simultaneously operate with the primary users (PU) in the overlapped spectrum. Nevertheless, it is compulsory for the CR-UWB system to use extremely low power ($\ll -$ 41.3 dBm/MHz) to guarantee the PUs normal operation, which can lead to an unacceptable low spectral efficiency for the CR-UWB. The use of orthogonal frequency division multiplexing (OFDM) technique in UWB facilitates the CR-UWB to adapt the transmit power assigned to the subcarriers according to the behavior of the PUs within the specific overlapped spectrum. The spectral efficiency of the overlapped spectrum is vital to the CR-UWB's overall spectral efficiency and can be significantly enhanced by using smart power assignment algorithms.

In this paper, we propose an cognitive group power assignment algorithm to maximize the OFDM based CR-UWB's spectral efficiency while conforming to the PUs protection requirements. We formulate the spectral efficiency maximization problem as an multidimensional knapsack problem (MKP) with constraints of interference to the PU, CR-UWB's bit error rate (BER) and CR-UWB's peak transmit power. Since the MKP is generally NP-Hard, we derive a greedy based power assignment algorithm to approximate the optimal solution. Furthermore, we present that in low-power regime, the integration of linear and dynamic power assignment techniques can significantly reduce the iteration number of the cognitive group power assignment algorithm while guaranteeing a neglected performance degradation of the proposed algorithm in terms of spectral efficiency enhancement.

The rest of the paper is organized as follows. Section 2 gives a review of the state of the art power assignment algorithms for CR systems. Section 3 presents the CR-UWB system model and the formulation of the spectral maximization problem with CR-UWB's transmit power as the decision variable. The proposed cognitive group power assignment algorithm is demonstrated in Sect 4, and the simulation results are shown in Sect 5. Finally, Sect. 6 concludes our paper.

2 Literature Review

As a specific type of the general assignment problems (GAP), the power assignment problem (PAP) can generally be formulated as an NP-Hard knapsack problem and tackled by linear or dynamic programming based techniques [4]. In [5], Zhang et al. provided an approximate solution by proposing an greedy based algorithm that iteratively assigns power to the OFDM CR system's subcarriers according to the efficiency value which is determined by the residue power of the CR system and the interference margin of the PU. The time complexity of Zhang's algorithm is proportional to the total number of bits and subcarriers.

The sum rate optimization problems studied in [6, 7] are essentially knapsack problem, and were asymptotically solved by the authors' creating linear programming based algorithms. In [6], Chen et al. proposed a round-robin algorithm to find the optimum transmit power for multiple users through iteratively solving the differential equation between rate and power and updating the results. The time complexity of Chen's algorithm is acceptable because only the power limitation is considered as the constraint. Yaacoub et al. constructed a MKP which contains power and subcarriers availability constraints, and the authors provided a solution using an iterative subgradient method [7]. The complexity of Yaacoub's algorithm is proportional to the number of subcarriers and users.

In [8], Xiang et al. presented an approximation solution to remove a CR user according to the power based efficiency value in each iteration in order to maximize the profit and lower the computational complexity which is proportional to the cubic of the number of CR users and PUs. However, the existing power assignment algorithms are generally high-power oriented and encompass high order-of-growth and enormous memory requirement in approaching the optimal spectral efficiency.

3 System Model

For simplicity and without loss of generality, we assume a single CR-UWB link exists in the CR network, where there are multiple PUs operating in the overlapped spectrum. Underlay spectrum sharing is assumed for the CR-UWB system. The CR-UWB's spectral efficiency is defined as the ratio of the usable information transmitted to the spectrum resource consumed for the transmission as

$$S_e = K/(T_s W), \tag{1}$$

where K denotes the number of data bits assigned to the CR-UWB's subcarriers for transmission, T_s is the period of an OFDM symbol, and W shows the corresponding used bandwidth.

3.1 Multiuser Interference

Identifying the interference power generated from the CR-UWB to the PUs is critical to the cognitive group power assignment algorithm, for which the channel model between the multiple CR-UWB systems and the PUs is needed. Assuming that the CR-UWB's channel is linear and time-invariant, since the UWB's multipath gain coefficient can be modeled as a series of independent log-normal random process [3], the total interference introduced by the CR-UWB systems to the PUs $I_j = \sum_{i=1}^{N-1} I_{ij}$ can be modeled as the sum of $N-1$ log-normally distributed signals using Fenton–Wilkinson method [9]. Hence, the superposition of

log-normal variables can be well approximated by a new log-normal distribution, and thus the distribution of the received interference signal amplitude r can be expressed as

$$p(r) = \frac{20/ln10}{r\sigma_z\sqrt{2\pi}} e^{-\frac{(20log(r)-\mu_z)^2}{2\sigma_z^2}}, \tag{2}$$

where the value of μ_z and σ_z^2 can be calculated by [9],

$$\mu_z = \xi^{-1} \cdot \left[\frac{\sigma_{\hat{\xi}}^2 - \sigma_{\hat{z}}^2}{2} + ln\left(\sum_{l=1}^{L} e^{\hat{\mu}_l} \right) \right], \tag{3}$$

$$\sigma_z^2 = \xi^{-2} \cdot \left[ln\left((e^{\sigma_{\hat{\xi}}^2} - 1) \frac{\sum_{l=1}^{L} e^{2\hat{\mu}_l}}{\left(\sum_{l=1}^{L} e^{\hat{\mu}_l}\right)^2} + 1 \right) \right], \tag{4}$$

where $\xi = ln10/20$, $\sigma_{\hat{\xi}}^2 = \xi^2\sigma^2$, and $\hat{\mu}_l = \xi\mu_l$, where μ_l and σ^2 is the mean and variance of the UWB's log-normally distributed multipath gain coefficients [3].

Hence, by manipulating (2), the PUs' average received interference energy $\bar{I}_j = E(r^2)$ can be derived as

$$\bar{I}_j = E(r^2) = exp\left(\frac{\mu_z}{10/ln10} + \frac{\sigma_z^2}{2 \times (10/ln10)^2} \right). \tag{5}$$

3.2 Power Assignment Problem

Since the PAP specified in our paper can be categorized as a GAP, we can formulate the PAP into a MKP. Furthermore, note that the as the objective of solving the PAP is to enhance the CR-UWB's overall spectral efficiency as much as possible, we can formulated the PAP with respect to the spectral efficiency maximization problem as

$$\textbf{P1} \ \arg\max_{P_i} S_e = \frac{1}{T_s W} \sum_{i=1}^{I} \sum_{j=1}^{J} k_{ij} x_{ij} \tag{6}$$

subject to:

$$P_i \le P_m, \tag{7}$$

$$\bar{I}_j \le I_{th}, \tag{8}$$

$$P_e \le \bar{P}_e, \tag{9}$$

where P_i is the power assigned to the CR-UWB's ith subcarrier, $k_{ij} = 1$ represents the value or profit of allocating the j-th bit to the CR-UWB's ith subcarrier, and x_{ij} indicates whether if the CR-UWB's j-th bit can be assigned to the ith subcarrier. The P_m represents the power limitation on each CR-UWB's subcarrier according to FCC's regulation. Furthermore, I_{th} is the interference threshold of the PU. Note that the value of a bit is a unit, and the weight of a bit is the integration of the power needed to assign the bit in a subcarrier and the interference generated to the PUs.

The parameter P_e in (9) denotes the CR-UWB's uncoded average BER, and $\bar{P}_e$ shows the average BER threshold. We assume that the M-ary quadrature amplitude modulation (QAM) is adopted by the CR-UWB, and by assuming the channel state information is perfectly known and the energy of the CR-UWB OFDM symbols transmitted are independent and identically distributed (i.i.d.), P_e of each CR-UWB subcarrier can be approximated as [10]

$$P_e = \frac{2(\sqrt{M}-1)}{\sqrt{M}\log_2 M}\left(1 - \sqrt{\frac{3\bar{\gamma}_b \log_2 M}{2(M-1)+3\bar{\gamma}_b \log_2 M}}\right), \tag{10}$$

where $\bar{\gamma}_b$ represents the average received signal to noise ratio (SNR) per bit as

$$\bar{\gamma}_b = \frac{P_i |H_i|^2}{2\sigma_u^2 \log_2 M}, \tag{11}$$

where H_i represents the frequency response of the CR-UWB's subcarrier, and σ_u^2 represents the variance of the Gaussian noise.

Under a certain value of $\bar{P}_e$, the minimum required transmit power to assign $m = \log_2 M$ bits on a CR-UWB's subcarrier can be given by

$$P_i(m) = \frac{2\sigma_u^2 (M-1)\left(1 - \frac{P_e\sqrt{M}\log_2 M}{2(\sqrt{M}-1)}\right)^2}{3H_i log_2(M)\left[1 - \left(1 - \frac{P_e\sqrt{M}\log_2 M}{2(\sqrt{M}-1)}\right)^2\right]}, \; M = 2, 4, 8 \ldots \tag{12}$$

4 Cognitive Group Power Assignment Algorithm

To tackle the optimization problem defined in **P1** with low time complexity which is a key requirement for the implementation of CR [11], we use heuristic greedy algorithm to develop the cognitive group power assignment algorithm considering the fact that there are unlimited source of bits and **P1** presents the optimal sub-structure features [12]. Based on the two-stage power assignment algorithm proposed in [13], where linear and greedy-based power assignment strategies are combined to lower the time complexity compared with the traditional water-filling

based algorithms, we observe that the complexity of the algorithm proposed in [13] is proportional to $\mathcal{O}(KN_u \log_2 N_u)$, where N_u is the number of the used subcarriers.

Note that a smaller N_u can result in a lower time complexity. Thus, the adjacent CR-UWB subcarriers can be grouped into blocks, and the UWB's multipath selective fading impact on the subcarrier blocks can be neglected if the total bandwidth of the gathered subcarriers is smaller than the UWB's coherence bandwidth. Hence, by evaluating the channel gain of the subcarrier blocks, the power grouping technique can ensure that the cognitive group power assignment algorithm to modulate the same amount of bits to each subcarrier in the block.

The maximum number of subcarriers in a block for is $N_b = \left\lfloor \frac{B_c}{B_{sc}} \right\rfloor$, where B_c is the UWB's coherence bandwidth. Thus, the subcarrier grouping process is performed by $N_g = \left\lceil \frac{N_u}{N_b} \right\rceil$, where N_g is the number of subcarrier blocks after the grouping process. Furthermore, the last subcarrier block in an OFDM symbol consists of $(N_u \;\; N_b)$ subcarriers.

We calculate the equivalent single channel SNR of each subcarrier block as the geometric mean of the SNR of each subcarrier in the block as,

$$SNR_{G_i} = \left(\prod_{j=1}^{N_{block}} SNR_{ij} \right)^{\frac{1}{N_{b_i}}}, \tag{13}$$

where SNR_{G_i} is the equivalent single channel SNR of the ith subcarrier block, and SNR_{ij} represents the channel SNR of the jth subcarrier in the ith subcarrier block, and is given by

$$SNR_{ij} = \varepsilon \cdot |H_{ij}|^2 / \sigma^2 = |H_{ij}|^2 / (B_{sc_{ij}} \sigma^2), \tag{14}$$

where $\varepsilon = 1$ denotes a unit power assignment on each subcarrier, H_{ij} represents the jth subcarrier channel gain in the ith subcarrier block.

The order-of-growth of the cognitive group power assignment algorithm is $\mathcal{O}(KN_g \log_2 N_g)$. Since the complexity of the proposed algorithm take linearithmic time, the reduction of the parameter N in the term $N \cdot \log_2 N$ can significantly lower the complexity of the single subcarrier based power assignment algorithm.

5 Numerical Simulation

In our work, the numerical simulation is implemented within a channel model that is previously specified in the UWB system. The PUs interference threshold is set to 1 mW, and the BER threshold for the CR-UWB is set to 10^{-6} to 10^{-4}. Figure 1 illustrates that the spectral efficiency performance of the cognitive group power

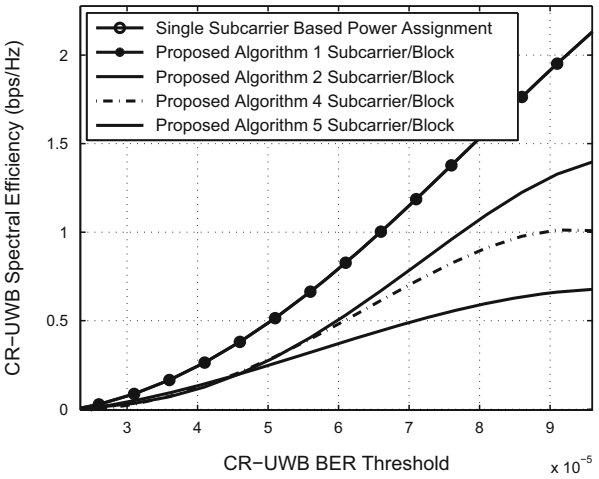

Fig. 1 Spectral efficiency of cognitive group power assignment algorithm

assignment algorithm and the comparison with the traditional water-filling and single subcarrier based power assignment algorithm. It is seen that the spectral efficiency degradation is increased when more subcarriers are included in one subcarrier block. For example, the spectral efficiency reached by the cognitive group power assignment algorithm is 50 % lower than the traditional algorithm when four subcarriers are included in each subcarrier block as the BER threshold approaches 10^{-4}. However, the algorithm complexity is over four times lower in the cognitive group power assignment algorithm than the subcarrier-by-subcarrier based the power assignment algorithm.

6 Conclusion

To improve the spectral efficiency of the low-power OFDM UWB based CR system with limited time complexity, we proposed a greedy based cognitive group power assignment algorithm. We formed the power assignment problem as an NP-Hard MKP, and then provided an approximate solution by developing the power grouping technique based on our previously proposed linear and dynamic power assignment methods. The use of the power grouping technique significantly reduced the time complexity of the proposed algorithm and result in only minor depredation in terms of the maximum spectral efficiency compared with the high-power and water-filling based methods.

References

1. Haykin S (2005) Cognitive radio: brain-empowered wireless communications. IEEE J Select Areas Comm 23:201–220
2. Hossain E, Bhargava V (2007) Cognitive wireless communication networks. Springer, New York
3. Batra A, Balakrishnan J, Aiello G, Foerster J, Dabak A (2004) Design of a multi-band OFDM system for realistic UWB channel environments. IEEE Trans Microwave Theory Tech 52:2123–2138
4. Martello S, Toth P (1990) Knapsack problems: algorithms and computer implementations. Wiley, New York
5. Zhang Y, Leung C (2009) Resource allocation in an OFDM-based cognitive radio system. IEEE Trans Comm 57:1928–1931
6. Chen CS, Shum KW, Sung CW (2011) Round-robin power control for the weighted sum rate maximisation of wireless networks over multiple interfering links. Eur Trans Telecomm 22:458–470
7. Yaacoub E, El-Hajj AM, Dawy Z (2012) Uplink OFDMA resource allocation with discrete rates: optimal solution and suboptimal implementation. Wiley Trans Emerg Telecomm Technol 23:148–162
8. Xiang J, Zhang Y, Skeie T (2010) Admission and power control for cognitive radio cellular networks: a multidimensional knapsack solution. In: Proceedings ACM ISABEL, Roma, 1–5
9. Beaulieu NC, Xie Q (2004) An optimal lognormal approximation to lognormal sum distributions. IEEE Trans Veh Technol 53:479–489
10. Simon MK, Alouini MS (2000) Digital communication over fading channels: a unified approach to performance analysis. Wiley, New York
11. Sahai A, Cabric D (2005) Spectrum sensing: fundamental limits and practical challenges. In: Proceedings IEEE DySPAN, Baltimore
12. Cormen T, Leiserson C, Rivest R, Stein C (2001) Introduction to algorithms, 2nd edn. MIT Press, Boston
13. Zeng L, McGrath S, Cano E (2009) Rate maximization for multiband OFDM ultra wideband systems using adaptive power and bit loading algorithm. In: Proceedings IARIA AICT, 369–374

A Three-Dimensional Space Coverage Algorithm in Wireless Sensor Networks

Meng Tang, Qiang Wan, Jin Li, and Yu Xiang

Abstract Sensor node coverage problem should be considered in 3D-space with the WSN deployed in atmosphere and underwater. In this paper, we focus on the effective coverage algorithm of sensor nodes in 3D networks, the analysis of the space-filling polyhedrons indicated that space-filling based on truncated octahedral is most effective. By the structure characteristics of filling space by Hexagonal Prism, Rhombic Dodecahedron and truncated octahedral, we provided the improved algorithm of cumulating the coordinate of nodes based on 3D mesh and simulated by MATLAB which confirmed there need least nodes by the coverage based on truncated octahedral. Meanwhile, the simulation results shows that the proposed algorithm is faster compared with the traditional calculating coordinate method.

Keywords Three-dimensional networks • Voronoi tessellation • Kelvin's conjecture • Kepler's conjecture • Coverage

1 Introduction

The sensor nodes coverage research mostly focuses on the two-dimensional space cases [1–3]. With the development of the WSN, we should consider how to deploy the sensor nodes in the three-dimensional space. There are some results on how to deploy the sensor nodes in the underwater environment [4–6]. In Ref. [7] it provides a method to calculate the node coordinates one by one which the nodes are deployed by the Voronoi tessellation.

M. Tang (✉) • Q. Wan • J. Li • Y. Xiang
School of Computer Science and Engineering, University of Electronic Science and Technology of China, Chengdu, China
e-mail: tbzeus@gmail.com; 420196217@qq.com; 2433971887@qq.com; jcxiang@uestc.edu.cn

B. Zhang et al. (eds.), *The Proceedings of the Second International Conference on Communications, Signal Processing, and Systems*, Lecture Notes in Electrical Engineering 246, DOI 10.1007/978-3-319-00536-2_4,

In this paper, we focus on the node placement algorithm with 100 % sensing coverage of a 3D space, while minimizing the number of nodes required for surveillance. Meanwhile, the algorithm can calculate the node's coordinates as fast as possible.

Without considering the effect of the border, we call the cells created by Voronoi tessellation of a 3D space as polyhedrons. If the radius of these polyhedrons is fewer than the sensing range R, then to set the nodes in the middle of the polyhedrons can fully cover the sensing area. If the shapes of the Voronoi cells are identical, we call it space-filling polyhedron. In Chap. 2, we will discuss several polyhedrons that can cover the space. In Chap. 3, we will give the effective algorithm guaranteeing 100 % coverage based on truncated octahedral, rhombic dodecahedron, optimal hexagonal prism and cube. In Chap. 4, the simulation results show that our algorithm is better than the traditional algorithm that requires to calculating the nodes' coordinates one by one. In addition, the simulation results also show the algorithm based on the truncated octahedral cells requires the least number of nodes. In Chap. 5, we conclude our work and give the future work plan.

2 Space-Filling Polyhedron

As we know so far, cube, triangular prism, hexagonal prism, truncated octahedral and rhombic dodecahedron are space-filling polyhedron [7].

We define the ratio of the space-filling polyhedron volume to the volume of its circumscribed sphere as volumetric quotient:

$$\frac{V_2}{V_1} = \frac{3V_2}{4\pi R^3} \tag{1}$$

As the definition of the volumetric quotient, when the R is fixed, the bigger the volumetric quotient, the less number of polyhedrons needed to fill the 3D space. Table 1 shows the volumetric quotients of the space-filling polyhedrons.

Now our problem reduces to the problem of finding the space-filling polyhedron has the highest volumetric quotient.

2.1 Truncated Octahedron

Kelvin's conjecture gives a space-filling polyhedron that 14-sided truncated octahedron having a very slight curvature of the hexagonal faces which has the highest isoperimetric quotient [8, 9].

If the volume and the surface area of a structure are V and S, respectively, then in three-dimensions its isoperimetric quotient can be defined as $36\pi V^2/S^3$.

Table 1 Volumetric quotient of the polyhedrons

Polyhedron	Volumetric quotient
Hexagonal prism	0.477
Rhombic dodecahedron	0.477
Truncated octahedral	0.68329
Cube	0.36755

Our problem is to find out the space-filling polyhedron which has the highest volumetric quotient. And the Kelvin's conjecture is essentially the problem of finding a space-filling structure with the highest isoperimetric quotient. Sphere has the highest isoperimetric quotient and the highest volumetric quotient in three-dimensions.

So we may deduce that Kelvin's conjecture and the problem we need to solve is to find a polyhedron that is close to the sphere. Meanwhile, the answer to Kelvin's conjecture is the same to our problem.

Consider the complexity of the calculation and the very slight curvature; we will use the truncated octahedron as the space-filling polyhedron.

2.2 Rhombic Dodecahedron

Kepler's conjecture is the answer to the problem that finds the most efficient way to pack equal-size sphere. And Kepler made a guess that the face-centered cubic lattice was the most efficient of all arguments.

The Voronoi tessellation of the face-centered cubic lattice is rhombic dodecahedron, so will discuss the node coverage base on the face-centered cubic lattice.

2.3 Other Polyhedrons

As the most efficient coverage strategy in two-dimensions is the model based on the regular hexagon, similarly, we will select the hexagonal prism as one of the space-filling polyhedron. We can deduce that the hexagonal prism which the height is $\sqrt{2}$ times of the side length has the largest volumetric quotient. We call this hexagonal prism optimal hexagonal prism. We will use the optimal hexagonal prism as one of the space-filling polyhedrons.

We also choose cube as a selection as a most basic structure.

3 The Nodes' Coverage Algorithm by Using Polyhedron to Fill the Space

3.1 The Nodes' Coverage Algorithm by Using Truncated Octahedron to Fill the Space

Figure 1 indicates the basic structure by using truncated octahedron to divide and fill certain space. There are 8 truncated octahedron cells surrounds another one. The centers of those 8 octahedron cells are located in the vertexes of a cube while the center of the central octahedron is located in the center of the same cube. The Formula (2) shows the relationship between the cube's side length L and the radius of the truncated octahedrons' circumscribed sphere R. R also means the sensing radius of the sensor.

$$l = 4R/\sqrt{5} \tag{2}$$

We can extend the basic structure above to the whole space. The nodes' coverage algorithm by using truncated octahedron to fill the space got the following steps:

1. Start at (xc,yc,zc), let l to be the side length, we can construct the cube lattice inside the coverage space. Then set the nodes of group A in the vertexes of the lattice. The group A nodes' coordinate points are represented as:

$$\begin{aligned}(x_A, y_A, z_A) &= \left(n \times l, m \times l, k \times l\right) \\ &+(xc, yc, zc)\end{aligned} \tag{3}$$

   The n, m, k above are all integers.
2. Every single node of group A can plus vector (0.5l, 0.5l, 0.5l) *to* generate the node of group B. The coordinate points of group B are:

$$\begin{aligned}(x_B, y_B, z_B) = &\left(n \times l, m \times l, k \times l\right) \\ &+ (0.5l + xc, 0.5l + yc, 0.5l + zc)\end{aligned} \tag{4}$$

   The n, m, k above are all integers.
3. The nodes of group A and B have done the space coverage by using truncated octahedron cells.

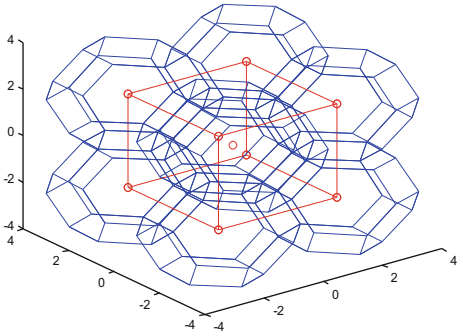

Fig. 1 Voronoi tessellation of 3D space to create truncated octahedral cells

3.2 *The Nodes' Coverage Algorithm by Using Rhombic Dodecahedron to Fill the Space*

In order to solve the Kepler's sphere packing problem, Kepler himself assumed a cube with the side length of 2. The cube has another name is face-centered cubic (FCC) lattice. We can set spheres with radius $\sqrt{2}/2$ at the 8 vertexes and the center points of 6 sides of this cube. These spheres construct the basic cell of FCC is the optimal solution to the sphere packing problem.

According to this Kepler's conjecture above, we can do Voronoi tessellation. The center points of the tessellation should be the spheres' centers. Then we can get the Voronoi cell, it's a rhombic dodecahedron. Its side length is $\sqrt{3}/2$, and the radius of its circumscribed sphere is 1. Figure 2 shows this structure.

We can extend the basic structure formed by FCC lattices in Fig. 2 to fill the whole space. The nodes' coverage algorithm by using rhombic dodecahedron has the following steps:

1. Start at (xc,yc,zc), make $2R$ to be the side length, we can construct the cube grids inside the coverage space. Then set the nodes of group A in the vertexes of the grids. The group A nodes' coordinate points are represented as:

$$\begin{aligned}(x_A, y_A, z_A) &= \big(n \times 2R, m \times 2R, k \times 2R\big) \\ &+(xc, yc, zc)\end{aligned} \tag{5}$$

   The n, m, k above are all integers.
2. Every single node of group A can plus R along x, y, z direction *to* generate the node of group B. The coordinate points of group B can be represented as:

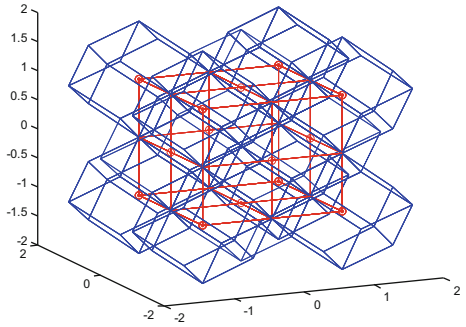

Fig. 2 Voronoi tessellation of 3D space to create rhombic dodecahedron cells

$$\begin{cases} (x_{B1}, y_{B1}, z_{B1}) = (n \times 2R, m \times 2R, k \times 2R) \\ \qquad\qquad + (xc, R + yc, R + zc) \\ (x_{B2}, y_{B2}, z_{B2}) = (n \times 2R, m \times 2R, k \times 2R) \\ \qquad\qquad + (R + xc, yc, R + zc) \\ (x_{B3}, y_{B3}, z_{B3}) = (n \times 2R, m \times 2R, k \times 2R) \\ \qquad\qquad + (R + xc, R + yc, zc) \end{cases} \tag{6}$$

3. The nodes of group A and B have done the space coverage by using rhombic dodecahedron cells.

3.3 The Nodes' Coverage Algorithm by Using Hexagonal Prism to Fill the Space

In the 2D condition, the coverage based on hexagon is the optimal plan. We can know from the calculation above, the hexagonal prism with column height and base length ratio of $\sqrt{2}$ got the best volumetric quotient. This kind of hexagonal prism is called optimal hexagonal prism. In the 3D space (x, y, z coordinate system), we can divide and fill the space by optimal prisms. To set the nodes at every hexagonal prism cell's center, then the nodes are put into two groups. These 2 groups of nodes are all distributed at the vertexes of the cuboid grids, they cross each other to complete the coverage of the whole region.

The nodes' coverage algorithm based on hexagonal prism has following steps:

1. The sensing radius is R, the start coordinate point is (0,0,0).
2. Start at (xc,yc,zc), set the nodes of group A at the vertexes of a cuboids grid. The cuboids grid got the length of $\sqrt{2}R$, width of $4R/\sqrt{6}$, height of $2R/\sqrt{3}$. The coordinate value is:

$$(x_A, y_A, z_A) = \left(n \times \sqrt{2}R, m \times 4R/\sqrt{6}, k \times 2R/\sqrt{3}\right) + (xc, yc, zc) \tag{7}$$

3. Every node in group A, make an offset along $\left(\sqrt{2}R/2, 2R/\sqrt{6}, 0\right)$, then set the nodes of group B there. The coordinate point of group B is:

$$(x_B, y_B, z_B) = \left(x_A, y_A, z_A\right) + \left(\sqrt{2}R/2, 2R/\sqrt{6}, 0\right) \tag{8}$$

4. The nodes of group A and B have done the space coverage by using optimal hexagonal prism cells.

3.4 The Nodes' Coverage Algorithm by Using Cube Cell to Fill the Space

The coverage based on cube cells is the simplest method. To construct cubic cells with the interval value of $l = R/\sqrt{3}$, then set the nodes at the vertexes of these cube cells. After that it has finished the coverage towards the whole space. The coordinate points of nodes can be represented as:

$$(x, y, z) = (n \times l, m \times l, k \times l) + (xc, yc, zc) \tag{9}$$

(xc,yc,zc) is the start point and n, m, k are all integers.

4 Simulations and Performance Comparison

4.1 The Coverage Algorithm Simulation

Assume the sensing radius R is $\sqrt{5}$ m, the target space got the 14 m × 14 m × 14 m size. The simulation based on algorithm by using polyhedron is indicated in Fig. 3.

To cover 6 m × 6 m × 6 m sized space, the nodes' sensing radius R = 1 m. The simulation of algorithm by using hexagonal prism is indicated in Fig. 4.

To cover 12 cm × 12 cm × 12 cm sized space, the nodes' sensing radius R = $\sqrt{6}$ m. The simulation of algorithm by using hexagonal prism is shown in Fig. 5.

To cover 10 m × 10 m × 10 m sized space, the nodes' sensing radius R = $\sqrt{3}$ m. The simulation of algorithm by using cubic cells is shown in Fig. 6.

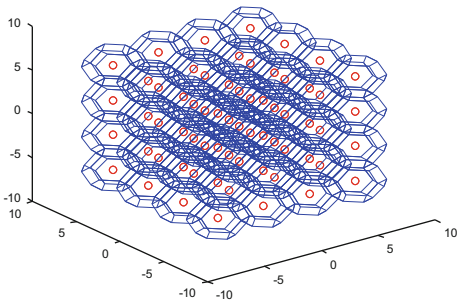

Fig. 3 Truncated octahedron placement strategy

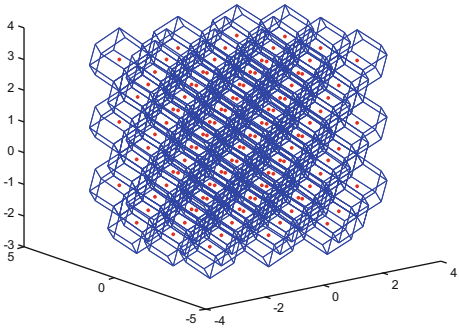

Fig. 4 Rhombic dodecahedron placement strategy

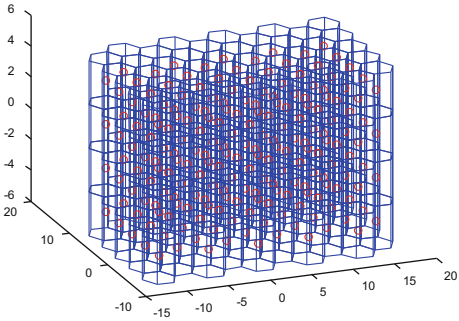

Fig. 5 Hexagonal prism placement strategy

4.2 Comparison of the Number That Algorithm Required Nodes

In Sect. 4.1 we've got the simulation result of the coverage algorithm based on truncated octahedron, rhombic dodecahedron, optimal hexagonal prism and cube cell. Use sensing radius to unitize the coverage region, then to be divided by the

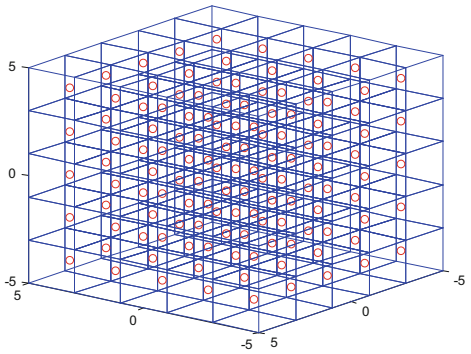

Fig. 6 Cube placement strategy

Table 2 Number of nodes needed in all algorithms

Polyhedron	Truncated octahedron	Rhombic dodecahedron	Optimal hexagonal prism	Cube
Sensing radius	$\sqrt{5}m$	$1m$	$\sqrt{6}m$	$\sqrt{3}m$
Space size	14^3 m^3	6^3 m^3	12^3 m^3	10^3 m^3
Unitized area range	245.4	216	117.5	192.4
Nodes required number	91	108	200	125
Volumetric quotient	0.68329	0.477	0.477	0.36755
Nodes required in unit volume	0.37	0.57	0.58	0.65

nodes number required, we can get the nodes needed number in unit volume Table 2.

As shown in chart 2: the truncated octahedron has the best volumetric quotient, so the coverage algorithm based on it requires the least nodes in unit volume. It also means the coverage algorithm based on it totally needs the least nodes.

4.3 Algorithm Speed Comparison

The reference [7] has mentioned the method to calculate out the coordinate point of polyhedron cells' center which also means the nodes' coordinate points. Before the calculation, truncated octahedron, optimal hexagonal prism and rhombic dodecahedron should be used to divide and fill the space.

This paper has taken the advantage in structure of truncated octahedron, rhombic dodecahedron, and optimal hexagonal prism when they are used in dividing and filling the space. Then we have used cube grid, a very basic structure in 3D space to realize the efficient algorithm to calculate the nodes' coordinate points. It costs less time when to be compared with traditional way.

Shown in Fig. 7, the horizontal axis represents time; the vertical axis means number of nodes which have finished the coordinate point's calculation. The dotted

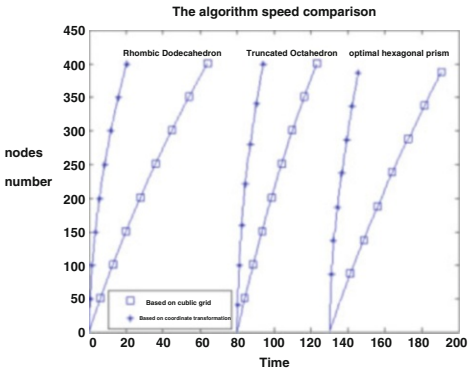

Fig. 7 Nodes' coordinates calculation speed

lines represent the algorithm that use coordinates point transformation while the solid lines represent the efficient algorithm based on using cube grids. The simulation result indicates the latter that is put forward in this paper got a faster speed.

5 Conclusions

In this paper, we analyzed the sensor nodes' coverage issue in 3D space. We compared 4 kinds of available coverage plans, and then found out that the algorithm based on truncated octahedron requires least nodes. Then we put forward the method to use cube grids to realize the efficient algorithm to calculate the nodes' coordinate points because of the structural features of the truncated octahedron, rhombic dodecahedron and optimal hexagonal prism when they are used to divide and fill space. After simulation comparison we can see this cube grids based algorithm has a better speed than the traditional way, the simulation result also certificated the coverage based on truncated octahedron costs least sensor nodes.

This paper has researched how to realize efficient coverage and the fast algorithm to calculate coordinate points. We will make effort on nodes' connection issue in 3D space and backbone network selection algorithm in the future.

References

1. Fan Gao-juan, Wang Ru-chuan, Huang Hai-ping et al (2011) Tolerable coverage area based node scheduling algorithm in wireless sensor networks[J]. Acta Electronica Sinica 39(1):89–94
2. Zhanglihong, Chenshuqian (2011) Simulation of coverage algorithm in wireless sensor networks. Comput Simulat 28(4):119–122
3. Wuyongan, Yinjianping, Limin, Zhuen, Caizhiping (2008) Algorithms for the minimal connected k-coverage set problem under probabilistic sensing models in directional sensor networks. Comput Eng Sci 30(12):19–22

4. Akyildiz IF, Pompili D, Melodia T (2005) Underwater acoustic sensor networks: research challenges. Ad Hoc Networks J 3:257–279
5. John Heidemann, Wei Ye, Jack Wills, Affan Yuan Li (2006) Research challenges and applications for underwater sensor networking. IEEE communications and networking conference. Las Vegas, Nevada, USA
6. Jiejun Kong, Jun-hong Cui, Dapeng Wu, Mario Gerla (2005) Building underwater ad-hoc networks and sensor networks for large scale real-time aquatic applications. IEEE military communications conference (MILCOM'05), 17–20 Oct., Atlantic City, NJ, USA
7. Nazrul Alam SM, Haas ZJ (2006) Coverage and connectivity in three-dimensional networks. MobiCom'06, September 23–29, Los Angeles, California, USA
8. Weyl H (1952) Symmetry. Princeton University Press, Princeton, NJ
9. Thomson, Sir William (Lord Kelvin) (1887) On the division of space with minimum partition area. Philosophical Magazine, 24:503–514. http://zapatopi.net/kelvin/papers/on_the_division_of_space.html

Security Analysis of Distributed Compressive Sensing-Based Wireless Sensor Networks

Ji Wu, Qilian Liang, Baoju Zhang, and Xiaorong Wu

Abstract Due to limited energy and physical size of the sensor nodes, the conventional security mechanisms with high computation complexity are not feasible for wireless sensor networks (WSNs). In this paper, we propose a compressive sensing-based encryption scheme for WSN, which provides both signal compression and encryption guarantees, without the additional computational cost of a separate encryption protocol. We also show that, for proposed WSN, if only a fraction of randomizer bits is stored by an eavesdropper, then he/she cannot obtain any information about the plaintext. WSNs usually are deployed in a hostile environment and left unattended, which could be compromised by the eavesdropper. Numerical results show that there is a trade-off between the number of sensor nodes required to reconstruct the original data and the approximation error in both normal and attack conditions. The approximation error of data decreases when less sensor nodes are compromised by the eavesdropper.

1 Introduction

Sensor nodes in WSNs are inherently resource-constrained. These battery-operated nodes have limited processing capability and very low storage capacity. These limitations are due to limited energy and physical size of the sensor nodes. In most practical situations, the sensor nodes are unattended and even deployed in the hostile environments, which demand careful security consideration in the design of WSN. Because of those constraints, the conventional security mechanisms with

J. Wu (✉) • Q. Liang
Electrical Engineering, University of Texas at Arlington, 416 Yates St, Arlington, TX, 76019, USA
e-mail: wu@wcn.uta.edu; liang@uta.edu

B. Zhang • X. Wu
Physics and Electronic Information, Tianjin Normal University, Tianjin, 300387, China
e-mail: wdxyzbj@mail.tjnu.edu.cn; wu.xiaorong@sohu.com

B. Zhang et al. (eds.), *The Proceedings of the Second International Conference on Communications, Signal Processing, and Systems*, Lecture Notes in Electrical Engineering 246, DOI 10.1007/978-3-319-00536-2_5,

high computation complexity are not feasible for WSNs. In order to design encryption s suitable for WSNs, it is necessary to be aware about the constraints of the sensor nodes such as energy constraint, memory limitations and high latency in communication and synchronization.

In this paper, we exploit the difference in computational capability and energy between sensor nodes and the fusion center in a WSN. We assume that an individual sensor node possesses far less computational power and energy than the fusion center. Then we propose placing the major computations and public key broadcast on the fusion center. On the sensor side, simply compressive sensing-based encryption is deployed, which requires the sensor nodes only active in every s intervals, where s is the sparsity of the measurement matrix. Hence, the energy consumption in sensor nodes is tremendously reduced. In addition, our scheme also supports node addition and revocation due to each sensor node works in a distributed manner.

The remainder of this paper is structured as follows. Section 2 introduces compressive sensing. In Sect. 3, we present our system model and discuss unconditional security of proposed WSN. Section 4 gives numerical results and we draw the conclusion in Sect. 5.

2 Compressive Sensing Overview

Compressive sensing (CS) provides a framework for integrated sensing and compression of discrete-time signals that are sparse or compressible in a known basis or frame. A rich literature has been published to investigate the theoretic bounds [1–3] as well as its applications in radar sensor network and other wireless communication systems [4–13]. Consider a discrete signal $f \in \mathbf{R}^N$ which can be expanded in an orthonormal basis $\Psi = [\psi_1 \psi_2 \ \cdots \psi_n]$ as follows:

$$f(t) = \sum_{i=1}^{N} x_i \psi_i(t), \tag{1}$$

where x is the coefficient sequence of f. We can say the discrete signal f is K-sparse in the domain Ψ, $K << N$, if only K out of N coefficients in the sequence x are nonzero. Sparsity of signal is a fundamental principle used in the compressive sensing.

The new M-length observation vector y can be represented as equation below:

$$y = \Phi f, \tag{2}$$

where Φ is an $M \times N$ measurement matrix. The above equation can be written as

$$y = \Phi \Psi x, \tag{3}$$

With the new observation vector y, the signal f could be recovered using ℓ_1-norm minimization; the proposed reconstruction f^* is given by $f^* = \Psi x^*$, where x^* is the solution to the convex optimization program ($\|x\|_{\ell_1} \equiv \sum_i |x|$)

$$\min_{\tilde{x} \in \mathbf{R}^N} \|\tilde{x}\|_{\ell_1} \quad \text{subject to} \quad y = \Phi\Psi\tilde{x}, \tag{4}$$

That is, among all the objects $\tilde{f} = \Psi\tilde{x}$ consistent with the data, we choose the one whose coefficient sequence has minimal ℓ_1-norm.

3 System Design and Security Analysis

3.1 System Model

Due to the energy constraint and limited computation capability of sensor nodes, our proposed compressive sensing-based encryption scheme for WSNs is quite simple. The system diagram is shown in Fig. 1.

Consider an $n \times n$ sparse measurement matrix Φ'

$$\Phi'_{ij} = \sqrt{s} \begin{cases} +1 & \text{with probability } \dfrac{1}{2s}, \\ 0 & \text{with probability } 1 - \dfrac{1}{s}, \\ -1 & \text{with probability } \dfrac{1}{2s}. \end{cases} \tag{5}$$

We assume entries Φ'_{ij} within each row are four-wise independent, i.e., every subset of size 4 of Φ'_{ij} within each row is independent. Φ'_{ij} across different rows are totally independent. The parameter s indicates sparsity of the random measurement matrix. If $\frac{1}{s} = 1$, the new sparse random measurement matrix Φ' is identical to the conventional measurement matrix Φ in compressive sensing.

Our distributed algorithm is described as follows.

1. Each sensor j generates a set of independent random variables $\{\Phi'_{1j}, \Phi'_{2j}, \ldots, \Phi'_{nj}\}$. If $\Phi'_{ij} \neq 0$, then sensor j stores the product of Φ'_{ij} with received signal x_i. Repeat the process for all $1 \leq j \leq n$.
2. After receiving all x_i, each sensor node simply sends the aggregated data $\sum_{i=1}^{n} \Phi'_{ij} x_i$ to the fusion center, where n is the length of received signal x.

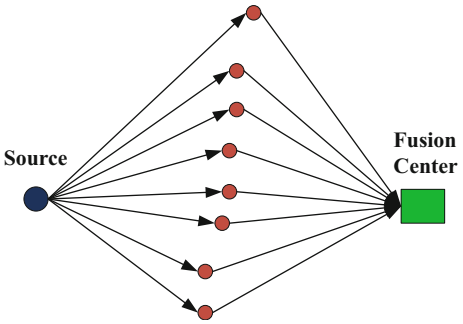

Fig. 1 System model of proposed WSN

3.2 Unconditional Security of Proposed WSN

In our approach, the unconditional security is guaranteed by the limited storage capacity of an eavesdropper. Every sensor node and the fusion center share two short randomly-select secret keys, which are independently chosen by each sensor node. Then, the fusion center broadcasts the randomizer $\mathbf{R}$, which is a burst of random bits over the insecure communication channel prior to the transmission of the actual ciphertext. Hence, the randomizer can be accessed by an eavesdropper as well. The ciphertext is a function of the plaintext, two secret keys, and the randomizer. It can be uniquely determined by the ciphertext, two secret keys, and the randomizer. Without two secret keys it is impossible to obtain any information about the plaintext without examining a very large number of randomizer bits.

Assume for each sensor node, the plaintext $\mathbf{X} = [X_1,\ldots,X_N]$, the ciphertext $\mathbf{Y} = [Y_1,\ldots,Y_N]$ and the keystream $\mathbf{W} = [W_1,\ldots,W_N]$ are sequences of length N. The randomizer matrix $\mathbf{R}$ consists of K rows and T columns and thus has total length $L = KT$ bits and $\mathbf{R} = \{-1,+1\}^{KT}$. Each row is denoted by $R[k,0],\ldots,R[k,T-1]$ $(1 \le k \le K)$. The secret key $Z \in \{0,\ldots,T-1\}$ specifies a position within each row of $\mathbf{R}$, and is chosen to be uniformly distributed over the key space. The other secret key $\mathbf{Z}' = [Z_1,\ldots,Z_{\lceil \frac{N}{s} \rceil}]$, where $Z_k \in \{0,\ldots,N\}$ for $1 \le k \le \lceil \frac{N}{s} \rceil$, specifies $\lceil \frac{N}{s} \rceil$ positions within each row of $\mathbf{R}$, and is chosen to be uniformly distributed over the space $\{1,\ldots,N\}$, where $\lceil X \rceil$ is the largest integer not greater than X.

The keystream $\mathbf{W}$ for kth sensor node is a function of the secret key Z and the randomizer $\mathbf{R}$, i.e., $\mathbf{W}$ is N consecutive bits in the randomizer starting at the position specified by the secret key Z, which can be denoted by

$$W_n^k = R[k, (n-1+Z^k) \mod \mathrm{T}] \qquad 1 \le n \le N$$

The other keystream $\mathbf{W}'$ for kth sensor node can be expressed as

$$W_n'^k = \begin{cases} 1 \text{ if } n \in \mathbf{Z}', 1 < n < N, \\ 0 \text{ otherwise.} \end{cases}$$

Then, our proposed encryption scheme can be decomposed into two steps as follows.

1. For kth sensor node, generate the keystream W_n^k by the secret key Z and the randomizer $\mathbf{R}$. The ciphertext $Y_n^k = W_n^k \cdot X_n^k$ for $1 < n < N$.
2. For kth sensor node, ${Y'_n}^k = Y_n^k$ if $n \in \mathbf{Z}'$,$1 < n < N$; otherwise, ${Y'_n}^k = 0$.

The following theorem states our proposed encryption scheme could achieve perfect secrecy in each sensor node.

Theorem 1. *Let* $\mathbf{W} = \{-1,+1\}^N$, $\mathbf{W}' = \{0,+1\}^N$, $\mathbf{X} = \mathbf{Y} = \{-1,+1\}^{N \log_2 |\mathbf{X}|}$, $\mathbf{Y}' = \{-1,0,+1\}^{N \log_2 |\mathbf{X}|}$, *where* $|\mathbf{X}|$ *denotes the cardinality of* $\mathbf{X}$ *, and let E be the encryption scheme as mentioned above, which can be decomposed into* E_1 *and* E_2*. Then, E is perfectly secret.*

Proof. For encryption E_1: Since $\mathbf{W}$ is constructed by bits from $\mathbf{R}$ whose positions determined by the secret key Z, it is totally independent from $\mathbf{X}$. Then, we have

$$P_{\mathbf{XY}}(X,Y) = P_{\mathbf{XW}}(X,\frac{Y}{X}) = P_{\mathbf{X}}(X) \cdot P_{\mathbf{W}}(\frac{Y}{X}).$$

Since $\mathbf{W}$ is uniformly distributed, then

$$P_{\mathbf{Y}}(Y) = \sum_{X \in \mathbf{X}} P_{\mathbf{XW}}(X,W) = \sum_{X \in \mathbf{X}} P_{\mathbf{X}}(X) \cdot P_{\mathbf{W}}(\frac{Y}{X}) = \sum_{X \in \mathbf{X}} P_{\mathbf{X}}(X) \cdot \frac{1}{2^{N \log_2 |\mathbf{X}|}}$$
$$= \frac{1}{2^{N \log_2 |\mathbf{X}|}}$$

Hence, $\mathbf{Y}$ is also distributed uniformly, and we obtain:

$$P_{\mathbf{X},\mathbf{Y}}(X,Y) = P_{\mathbf{XW}}(X,W) = P_{\mathbf{XW}}(X,\frac{Y}{X}) = P_{\mathbf{X}}(X) \cdot P_{\mathbf{W}}(\frac{Y}{X})$$
$$= P_{\mathbf{X}}(X) \cdot \frac{1}{2^{N \log_2 |\mathbf{X}|}} = P_{\mathbf{X}}(X) \cdot P_{\mathbf{Y}}(Y)$$

Thus, $\mathbf{X}$ and $\mathbf{Y}$ are independent.

Similarly, we can prove for E_2:

$$P_{\mathbf{YY}'}(Y,Y') = P_{\mathbf{YW}'}(Y,\frac{Y'}{Y}) = P_{\mathbf{Y}}(Y) P_{\mathbf{W}'}(\frac{Y'}{Y}).$$

and $P_{\mathbf{Y}'}(Y') = P_{\overline{W}}(\frac{Y'}{X})$ for all $X \in \{-1,+1\}$, where

$$\overline{W}_n = W_n W'_n = \begin{cases} -1 \text{ with prob. } \frac{1}{2s}, \\ 0 \quad \text{with prob. } 1 - \frac{1}{s}, \\ +1 \text{ with prob. } \frac{1}{2s}. \end{cases}$$

Therefore,

$$P_{\mathbf{X}}(X)P_{\mathbf{Y}'}(Y') = P_{\mathbf{X}}(X)P_{\overline{\mathbf{W}}}(\frac{Y'}{X}) = P_{\mathbf{X}\overline{\mathbf{W}}}(X, \frac{Y'}{X}) = P_{\mathbf{X}\mathbf{Y}'}(XY')$$

Then, $\mathbf{X}$ and $\mathbf{Y}'$ are independent and E is perfectly secret.

Although the encryption is perfectly secret for each sensor node. There is still some chance for an eavesdropper to extract the original data. One possible way is to collect the aggregated data $\sum_{i=1}^{n} \overline{W}_{ij} X_i = \sum_{i=1}^{n} Y_i'$ for n sensor nodes, where n is the length of signal X and we can have

$$\overline{\mathbf{W}}\mathbf{X} = \mathbf{Y}'$$

Then, the original ciphertext can be extracted as follows

$$\mathbf{X} = (\overline{\mathbf{W}})^{-1}\mathbf{Y}'$$

The following theorem states that if only a fraction of randomizer bits is stored by an eavesdropper, then the probability that he/she could obtain any information about the plaintext approaches to zero.

Theorem 2. *There exists an event ξ such that, for all possibly probabilistic strategies for examining M bits of randomizer* $\mathbf{R}$*, then*

$$I(\mathbf{X}; \mathbf{Y}'|\mathbf{W}', \xi) = 0 \quad \text{and } P(\xi) > 1 - \sigma^{N^2},$$

where $\sigma = M/NT$ is the fraction of randomizer bits stored by an eavesdropper and n is the length of original signal X.

Proof. Define ξ as the event that at least one bit of $\mathbf{W}$ is not contained in e^M.For each sequence $e^M = [e_1, e_2, \ldots, e_M]$ of length M, we assume m_k randomizer bits are specified by e^M that within the kth column of $\mathbf{R}$, where $1 \leq k \leq T$. Let P_k be the possibility of the secret key $\mathbf{W}^k$ for sensor node k is contained by e^M, then $P_k = \prod_{k=1}^{N} (\frac{m_k}{N})^N$. Under the condition $\sum_{k=1}^{T} m_k = M$, the maximum value of P_k is $(\frac{M}{NT})^N$ if $m_1 = m_2 = \ldots = \frac{M}{T}$.

Since the keystream $\mathbf{W}'$ is unknown by the eavesdropper, then

$$P(\xi) > 1 - (M/NT)^{N^2}$$

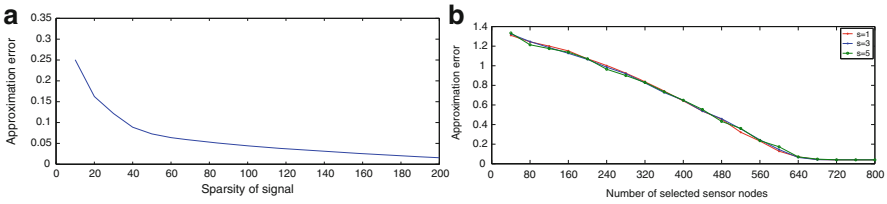

Fig. 2 The approximation error of data $\frac{||u-\tilde{u}||_2^2}{||u||_2^2}$ versus (**a**) the number of sensor nodes queried (**b**) the number of sensor nodes queried and various sparsity of random measurement matrix in normal condition

4 Numerical Results

To understand the behavior of our proposed encryption scheme, we conduct an extensive quantitative study to evaluate its performance. The data used in our study is collected by PulsOn P220 UWB radar. This real-world data is not truly sparse in any transformation domain. However, it can be well-approximated by the optimal k-term approximation. Figure 2a illustrates the relationship between the number of coefficients we kept and the approximation error. We can claim the signal is nearly sparse in DCT domain since only 1/10 of original coefficients are sufficient to represent the original data. Figure 2b compares the approximation error of data versus the number of sensor nodes queried with various sparsity s of random measurement matrix in normal condition (without attack). Note that $\frac{1}{s} = 1$ implies conventional compressive sensing with bernoulli ensemble is employed. The approximation error is comparable to that shown in Fig. 2a if the number of sensor nodes queried is sufficient large. It is also noted that, in our example, the performance is almost the same for sparsity $s = 1$, 3 and 5.

To highlight the effect of compromised sensor nodes on signal reconstruction, Fig. 3 compares the approximation error of the data versus the number of sensor nodes queried with $s = 3$ and various amount of sensor nodes are compromised by the eavesdropper. First, we can observe that the approximation error can increases with the increase of Signal-to-Interference ratio (SIR). For a fixed SIR value, we can see that a increase of the number of sensor nodes queried can significantly reduce the approximation error. The approximation error of data could also decrease when less sensor nodes are compromised by the eavesdropper.

5 Conclusions

We propose a compressive sensing-based encryption scheme for WSN with simple structure. Each sensor node only sends the aggregated data to the fusion center at every n symbol interval, which significantly reduces the overall throughput. Our

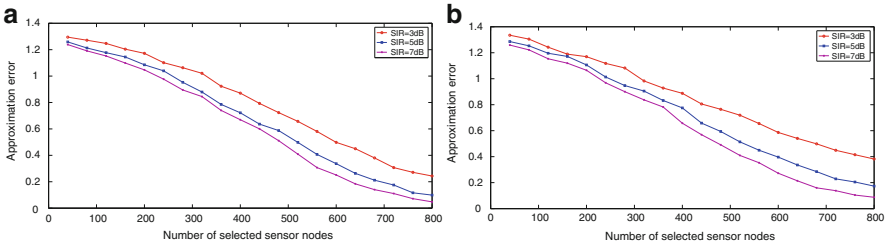

Fig. 3 The approximation error of data $\frac{||u-\hat{u}||_2^2}{||u||_2^2}$ versus the number of sensor nodes queried with (**a**) 10% and (**b**) 30% of sensor nodes are compromised by the eavesdropper

proposed WSN works in a distributed manner and synchronization is not required. We also prove that the encryption is perfectly secret in each sensor node and if only a fraction of randomizer bits is stored by an eavesdropper, the probability that he/she could obtain any information about the plaintext approaches to zero.

There is a trade-off between the number of sensor nodes required to reconstruct the original signal and the approximation error of data in both normal and attack conditions. The approximation error of data could decrease when less sensor nodes are compromised by the eavesdropper in attack condition.

Acknowledgements This work was supported in part by U.S. Office of Naval Research under Grants N00014-13-1-0043, N00014-11-1-0071, N00014-11-1-0865, and U.S. National Science Foundation under Grants CNS-1247848, CNS-1116749, CNS-0964713.

References

1. Chen J, Liang Q (2011) Rate distortion performance analysis of compressive sensing. In: IEEE Global Telecommunications Conference (GLOBECOM), Houston, TX, Dec 2011
2. Chen J, Liang Q, Paden J (2012) Compressive sensing analysis of synthetic aperture radar raw data. In: IEEE international conference on communications, Ottawa, Canada, June 2012
3. Kirachaiwanich D, Liang Q (2011) Compressive sensing: to compress or not to compress. In: Asilomar conference on signals, systems, and computers, Pacific Grove, CA, Nov 2011
4. Xu L, Liang Q (2012) Compressive sensing in radar sensor networks using pulse compression waveforms. In: IEEE international conference on communications, Ottawa, Canada, June 2012
5. Xu L, Liang Q, Cheng X, Chen D (2013) Compressive sensing in distributed radar sensor networks using pulse compression waveforms. EURASIP J Wireless Comm Networking. DOI: 10.1186/1687-1499-2013-36
6. Xu L, Liang Q, Zhang B, Wu X (2012) Compressive sensing in radar sensor networks for target RCS value estimation. In: IEEE Globecom, workshop on radar and sonar networks, Anaheim, CA, Dec 2012
7. Wu J, Wang W, Liang Q, Wu X, Zhang B (2012) Compressive sensing-based signal compression and recovery in UWB wireless communication system. Wiley Wireless Comm Mobile Comput. DOI: 10.1002/ wcm.2228

8. Wu J, Wang W, Liang Q, Zhang B, Wu X (2013) Compressive sensing based data encryption system with application to sense-through-wall UWB noise radar. Wiley Secur Comm Network. DOI: 10.1002/sec.670
9. Wu J, Liang Q, Cheng X, Chen D, Narayanan R (2012) Amplitude based compressive sensing for UWB noise radar signal. In: IEEE Globecom, workshop on radar and sonar networks, Anaheim, CA, Dec 2012
10. Wu J, Liang Q, Kwan C (2012) A novel and comprehensive compressive sensing-based system for data compression. In: IEEE Globecom, workshop on radar and sonar networks, Anaheim, CA, Dec 2012
11. Liang Q, Wu J, Cheng X, Chen D, Liang J (2012) Sparsity and compressive sensing of sense-through-foliage radar signals. In: IEEE international conference on communications, Ottawa, Canada, June 2012.
12. Liang Q (2011) Compressive sensing for synthetic aperture radar in fast-time and slow-time domains. In: Asilomar conference on signals, systems, and computers, Pacific Grove, CA, Nov 2011
13. Liang Q (2010) Compressive sensing for radar sensor networks. IEEE Globecom, Miami, FL, Dec 2010

Simplified Hybrid Routing Protocol in Low Complexity ZigBee Network

Jiasong Mu, Wei Wang, and Baoju Zhang

Abstract The hierarchical routing protocol (HRP) and Z-AODV routing are two options in ZigBee networks. However, the advantages of them, such as the simplicity in HRP and the global shortest path in Z-AODV, are alternative. In this paper, we propose a simplified hybrid routing protocol (SHRP) in low complexity ZigBee networks. The prevailing wisdom regarding the organization of wireless networks assumes unicasting in every hop; however, it is against the nature of broadcasting in wireless channel. Considering the low data rate and node mobility in ZigBee networks, we design a data transmission mechanism which is based on rebroadcasting to achieve the simplification and high efficiency simultaneously. As a cross layer protocol, some modifications have also been made in ZigBee specification. The simulation results show that, compared with original ZigBee routings, SHRP have better performance in lower network load and end to end delay.

Keywords ZigBee routing • Hybrid routing • Rebroadcasting • Cross layer protocol

1 Introduction

ZigBee specification is aiming to be a low cost, low power solution for systems consisting of unsupervised groups of devices in houses, factories and offices [1]. Its attractive properties make it extensively studied and analyzed. And lots of practical deployments are emerging. In the stack of ZigBee specification, great efforts have been made to reduce the energy consumption. As to the routing protocol, the hierarchical tree routing (HRP) and Z-AODV routing are both available to meet the requirements in different applications. However, current network formation and

J. Mu (✉) • W. Wang • B. Zhang
College of Electronic and Communication Engineering, Tianjin Normal University, Tianjin, China
e-mail: mujiasong@aliyun.com

B. Zhang et al. (eds.), *The Proceedings of the Second International Conference on Communications, Signal Processing, and Systems*, Lecture Notes in Electrical Engineering 246, DOI 10.1007/978-3-319-00536-2_6,

routing protocols described in the ZigBee specification do not fully address power consumption issues [2].

As two routing algorithm with different characteristics are supported in ZigBee specification, it is natural thought of designing a hybrid routing methods which could combine the advantages of HRP and Z-AODV. Although some significant works have been done, the improvement is limited [3]. The performance of routing methods seems a compromise of the simplicity and efficiency, which means how much cost in finding a path and how well the path is. To analyze the essential of this contradiction, one can always see at least two separate modes: route discovery/maintenance and the actual forwarding of application packets, with the first mode involving special traffic that does not directly originate at the network's application (for HRP, this course refers to the initialization of ZigBee network) [4]. In routing discovery/maintenance, the command frame is always flooding by broadcasting while the data is always unicast transmitted. The prevailing wisdom regarding the organization of wireless networks assumes point-to-point communication, whereby each node forwarding the packet on its way to the destination sends it to a specific neighbor [5]. Note that the benefits of unicast mechanism tend to be questionable [6] and much more so in sensor networks, where packets tend to be very short. Firstly, the action of announcing the transmission with the handshake may take more bandwidth than the actual transmission; thus, the probability of damage to an unannounced transmission is in fact lower than the one to the announcement. Secondly, the neighbor identifier (the network address in ZigBee) requires room in the packet header and thus incurs extra framing, which significantly inflates the otherwise short packet. So the data transmission which based on broadcasting may achieve better performance by some proper methods to restrain the flooding.

In low complexity ZigBee networks, the topology keeps static or nearly static and the data flows are tend to converge on one or several sink nodes. And the broadcasting is easier to be predicted and controlled. On that basis, a simplified hybrid routing protocol in low complexity ZigBee networks is proposed in this paper. SHRP is based on broadcasting for communication and it could automatically take the global shortest path in packet forwarding without the tradition routing discovery/maintenance procedure.

The rest of this paper is organized as following: Sect. 2 will briefly introduce the related contents in ZigBee specification, the simplified hybrid routing protocol will be proposed in Sect. 3. In Sect. 4, simulation results are presented. Finally, the conclusion is shown in Sect. 5.

2 ZigBee Routing

Based on the IEEE 802.15.4 protocol, the ZigBee specification defines the standard of higher layers. Three device types are defined in ZigBee: ZigBee coordinator (ZC), ZigBee routers (ZR), and ZigBee end devices (ZED). ZC is responsible for starting a new network. ZigBee coordinator and routers are routing capable, while

the ZigBee end devices can't participate in routing and have to rely on their corresponding ZigBee parent routers for that functionality [7].

In ZigBee specification, it is recommended to use Distributed Address Allocation Mechanism (DAAM) for address assignment to form tree structure. The parameter *Cm* represents the largest number of children nodes, *Rm* means the number of children nodes which can be a router and *Lm* decides the most depth in the network. And for the same network, different nodes usually have the constant *Cm* and *Rm*. Every potential parent is provided with a finite sub-block of the address space, which is used to assign network addresses to its children. Given *Cm*, *Lm*, and *Rm*, we can compute the function *Cskip(d)* as the size of the address sub-block distributed by each parent at depth d as (1).

$$Cskip(d) = \begin{cases} 0, & Rm = 0, \\ 1 + Cm \times (Lm - d - 1), & Rm = 1, \\ \left(1 + Cm - Rm - Cm \times R^{Lm-d-1}\right)/(1 - Rm), & Rm > 1. \end{cases} \quad (1)$$

Each ZigBee device maintains a neighbour table which has all the neighbour information in the 1-hop transmission range. Entries in the table are created when the node joins to an existing network. Conversely, the neighbour entry is removed when the neighbour node leaves the network. Since the information on the neighbour table is updated every time a device receives any frame from the some neighbour node, the information of the neighbour table can be said to be up-to-date all the time.

3 Simplified Hybrid Routing Protocol

Simplified Hybrid Routing Protocol in low complexity ZigBee network will be described in this section. Some modifications also have to be made in ZigBee stack. As mentioned before, all the neighbors may receive the frame when a node transmitting a packet, due to the instinct of broadcasting in wireless channel. In the proposing SHRP, this nature is conserved and ruled to achieve better performance in communication. The broadcasting message will flood the whole network without constraint. And it may lead to a broadcast storm which may break down the communication network. So the essential in designing a broadcasting-based routing protocol is to restraint the rebroadcasting. The frames should be able to cover the entire network and the duplicates tend to be as less as possible. By that purpose, a set of rules are proposed in SHRP. In packets broadcasting and rebroadcasting, all the receiving nodes may check each rule and decide whether this frame is to be abandoned or rebroadcasted. This process will be repeated until the data is forwarded to the destination.

The coming question is what information a node needs to know based on the rebroadcasting rules and how to get it with the least cost. In the case of unicast, the

transmission link is decided before delivering the packet and the path is recognized by the nodes address in next hop. In each hop, the receiving node may check the routing method and the destination address to find whether it should drop this packet or not. This process implies that the node has already completed receiving and decoding the frame header. Similarly, the frame header in SHRP should contain the information needed in judging the node behavior. Thus, the frame in broadcasting-based routing mechanism should be unique and the frame header ought to have an identifier to be recognized.

In SHRP, we focus on the following parameters in the transmission. The address of the source, *SA*; the address of destination, *DA*; the session number which implied the sequence of the frame, *SN*; the retired times, *RT*; the hops already took from source, *Hs*; the remaining hops to the destination in estimation, *Hd*; the estimated total hops in transmission, *Ht*, from which it has $Ht = Hs + Hd$; a boolean value indicates whether this frame is required to use HRP, f_{HPR}; a flag implies whether this frame is allowed to be rebroadcasting by other nodes if they are not in the selected path, f_{RB}. With the array of [*SA*, *DA*, *SN*, *RT*], which we called node identity array (NIDA), the frame in the network can be uniquely recognized. The SHRP is based on an assumption that all the transmission links are half-duplex and the path with the least hops from a source to a destination is also the shortest in reverse. Once a packet successfully delivered from node A to B, there should be an entry to A in the routing table of node B. It implies the routing can be used when A tries to send data to B. So the address couple of *SA* and *DA* could identify a routing path. And the array of [*Hs, Ht*] is required in checking the rebroadcasting rules. Thus, only the values of [$SA, DA, SN, RT, Hs, Ht, f_{HPR}, f_{RB}$], which we called packet routing array (PRA), is needed to control and manage the routing in SHRP. The filed name and the size in the frame header are shown in Fig. 1.

Based on the retransmitting mechanism and frame format, the rebroadcasting rules will be described. When a node receives a packet, it may find if it is the destination. If so, the node may decide restore the routing information or not. Owing to the restriction in common ZigBee devices, the routing entries where ZC is the source or destination should be saved by ZC, which always has power supply and sufficient memory. If current node is not the destination, the values in PRA will be extracted and the following rules are going to be examined.

When a node is going to send a frame, as mentioned before, the address of source and destination devices may decide the routings in the network. The communication will decide the NIDA of this frame. If a packet is to be transmitted and its address pair has no corresponding entries in routing table, the transmission path is uncertain and the *Ht* value is set 0, means no reference paths. An example is shown in Fig. 2, ZigBee node A firstly is trying to transmitting a packet to the ZC. As no corresponding routing information, the packet will be broadcasted to all its neighbor devices.

When the f_{HPR} is set *True*, the receiving node may find whether the source node is one of its descendent according to the network address. If so, the current device may store the parameters of this frame and rebroadcast it. By this principle, the packet will be passed along the hierarchical path. Compared with the original HRP,

Field Name	Source Address	Destination Address	Session Number	Retrying Times	Hops from Source	Hops to Destination	HRP enable flag	extra routing flag
Size	16 bits	16 bits	8 bits	4 bit	4 bits	4 bits	1 bit	1 bit

Fig. 1 The routing control field in frame header in SHRP

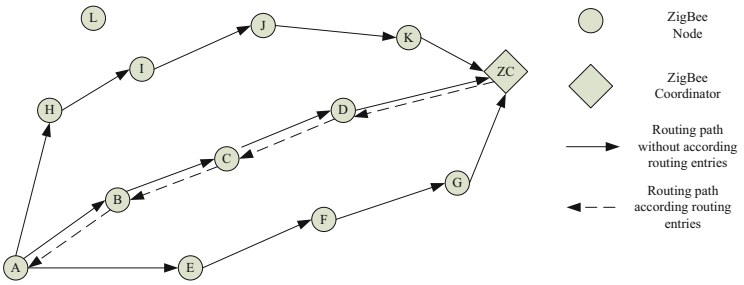

Fig. 2 An example of routing path in SHRP

the receiver address in current hop is not needed in the frame header. When the f_{HPR} is set *False*, the packet may be forwarded by rebroadcasting.

Then, the rebroadcasting mechanism will be described. The source will transmit this frame and each receiving node may rebroadcast it. The packet is able to be delivered to any single node in the network by repeating this procedure. To restraint the unexpected overhead caused by too much duplicated data, some rules are designed. The nodes have the function to record the PRA of each node it received or transmitted. When receiving a packet, the node may find whether this packet is handled before by checking the NIDA. If so, the packet will compare the *Hs*, if the new value is smaller, the node will rebroadcast this packet based on the new *Hs*, which means less hops from source. If it is a new receiving packet, the device may also rebroadcast it. The *Hs* in PRA is plus 1 every time the packet is rebroadcasted.

The packet may be relayed to the destination by intermediate devices. The destination may receive multiple copies from different route and the *Hs* values now represent the total hops they used. In Fig. 2, the available paths include: H-K, B-D and E-G, with the *Hs* values are 5, 4, and 4, respectively. The optimum route with the least hops will be stored. If more than two routings have the same minimum hops, for example, route B-D and E-G are both 4 hops distance, additional principle may be introduced to help judging, such as the link quality. This principle may also apply to the intermediate device to deal with the packets with the same *Hs*. It is assumed the route B-G is the best one and saved by ZC in routing table.

In the case of existing a corresponding entry in routing table for the transmission, such as the packet from ZC to node A after the previous communication mentioned above. The ZC may also broadcast the packet to its neighbors; however, the *Ht* value is set 4 based on the routing table. The receiving node may check the NIDA and it may find the former information related to this source and destination address pair. The node may check the value of *Hd* in current packet and *Hs* in the routing

entries. If the origin *Hs* is no larger than the new *Hd*, the data will be rebroadcasted, otherwise, the device may discard the frame and delete the routing entry with the same address pair.

By the rules introduced above, the multi path problem may occur when there are 2 or more paths with the same least hops. See the B–D and E–G in Fig. 2; it may build 2 reverse paths. This may lead to a waste of bandwidth and even the chaos in communication. To eliminate the unexpected route, we make a modification on rebroadcasting. As the neighbor table is required in ZigBee protocol, each device is asked to look up the destination address in it. If the destination node is one neighbor, the node may rebroadcast the packet along with its own address. If the destination finds more than 1 origin packet received from different paths, it may choose the optimum one based on some standard, such as the best link quality. And it may announce the decision with the sender's address. All the neighbors with different address may delete the corresponding routing information. This procedure guarantee the reverse link is optimum. As to the intermediate node, the rebroadcasting procedure is a little different in reverse link. The *Ht* value is not 0 when the packet is navigated, when a node find a frame with the same NIDA and *Ht*, but larger *Hs*, it may not rebroadcast the packet even it follows all the other rules mentioned above and is going to transmit. By this principle, the reverse transmission path is navigated within the shortest paths, as the routing path form ZC to node A in Fig. 2.

4 Simulations

This section will illustrate the performance of SHRP in low complexity ZigBee network. The simulations were implemented in MATLAB. Some parameters were set as following: time duration was 100 s; node number is 50, *Cm*, *Rm* and *Lm* were set 4, 4 and 5 separately; the data packet size was 100 bits packet interval time was 1 s. The set of source and destination address in transmission imitates the sensor network by make 60 % packets are from sensing device to sink, which means from common ZigBee nodes to ZC, 20 % are from ZC to common nodes as controlling frame and the rest are random chosen as regular communication. The simulations were carried out 100 times and the average results are demonstrated. The results were shown started from 10 s to reduce the impact of network initialization.

Figure 3 shows the network load with different routing algorithms. We may find the SHRP could largely reduce the traffic in the network. This is mainly because the broadcast-based routing algorithm did not have the separate phase to discover/maintain the routing. Besides, the acknowledgement in point-to-point communication is not needed in SHRP. Compared with the cases in which HRP is enabled, the SHRP with *False* f_{HPR} had a high network load at the beginning of the simulation and its performance was better than the one with *True* f_{HPR}. The reason is similar as the one in the phenomenon of HRP and Z-AODV, the routing discovery (the routing without corresponding routing entries in SHRP) may consume extra bandwidth to find shortest path. However, once the optimum link is decided, the coming transmission may benefit from it.

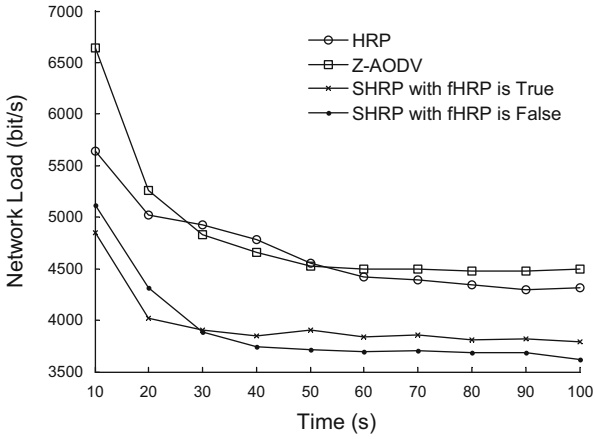

Fig. 3 The average network load in different routing algorithms

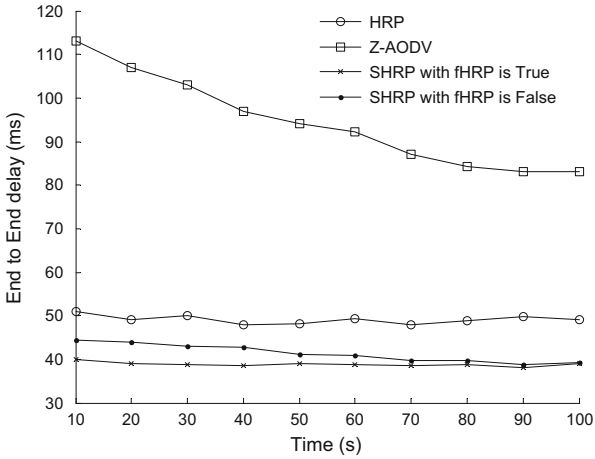

Fig. 4 End to End delay in different routing algorithms

The end to end delay in different is illustrated in Fig. 4, from which; we can see the end to end delay in SHRP is significantly reduced no matter what the value f_{HPR} is. Compared to the origin algorithms, the SHRP did not have the routing discovery which may introduce great latency, nor the acknowledge information in peer to peer communication. This mechanism made the delay is only mainly caused by the operation in intermediate devices.

5 Conclusions

A simplified hybrid routing algorithm in low complexity ZigBee networks is proposed in this paper. SHRP is based on the rebroadcasting, and it may reduce the traffic in ZigBee networks because it does not have the routing discovery/

maintain procedure. The simulation results show it may achieve better performance in lower network load and end to end delay compared with origin routing protocols. For further work, the channel coding and other methods may be introduced to reduce the bit error rate and guarantee the correctness of the packets.

Acknowledgments The work in this paper is funded by Doctoral Scientific Foundation of Tianjin Normal University (52XB1106).

References

1. Tareq AA, Yang SH (2008) A ZigBee-based mobile tracking system through wireless sensor networks. Int J Adv Mechatronic Syst 1(1):63–70
2. Metin T, Ibrahim K (2012) PSAR: power-source-aware routing in ZigBee networks. Wireless Network 18(6):635–651. doi:10.1007/s11276-012-0424-5
3. Han DM, Lim JH (2010) Design and implementation of smart home energy management systems based on zigbee. IEEE Trans Consum Electron 56(3):1417–1425. doi:10.1109/TCE.2010.5606278
4. Gezer C, Buratti C (2011) A ZigBee smart energy implementation for energy efficient buildings. IEEE 73rd vehicular technology conference (VTC Spring), pp 1–5. doi: 10.1109/VETECS.2011.5956726
5. Baronti P, Pillai P, Chook VWC, Chessa S, Gotta A, Hu YF (2007) Wireless sensor networks: A survey on the state of the art and the 802.15.4 and ZigBee standards. Comput Commun. 30(7):1655–1695. doi: 10.1016/j.comcom.2006.12.020
6. Rahman A, Gburzynski P (2006) Hidden problems with the hidden node problem. In Proceedings of 23rd Biennial symposium on communications, Kingston, ON, Canada, June 1, pp 270–273. doi: 10.1109/BSC.2006.1644620.
7. ZigBee standard Organization. ZigBee specification Document 053474r17

Real Time Routing Optimization in ZigBee Hierarchical Networks

Wei Song, Jiasong Mu, Wei Wang, and Baoju Zhang

Abstract ZigBee hierarchical routing protocol (HRP) provides a simple but reliable topology. However, the transmission paths in HRP are always not efficient, and the links keep invariant since they were determined when the network initialized. In this paper, we propose and evaluate a real time routing optimization scheme in ZigBee hierarchical networks. In the improved architecture, the parent node could actively maintain its child links for lower network load. To minimize the energy consumption, all the information needed can be acquired from neighbour table to avoid introducing extra communication. The scheme makes ZigBee hierarchical networks be capable of dynamic maintaining and optimizing the routing paths during lifetime. The simulation results show that the proposing scheme have better performance by obtaining lower average transmission hops and network load.

Keywords ZigBee hierarchical routing • Routing optimization • Neighbour table • Dynamic routing maintaining

1 Introduction

Hierarchical tree routing (HRP) is an active routing method whose routing information was established when the network deployed and kept invariable unless the network structure changed. HRP provides a simple and reliable topology for wireless networks [1]. For each node, if the destination of a data frame is the descendant of itself, it will send the packet to the corresponding child. Otherwise, it will transmit the message to its parent. HRP is efficient from the view of routing acquiring and memory use, but the routing paths in HRP are always inefficient, because the data frames are limited in parent child link [2]. Moreover, the

W. Song • J. Mu (✉) • W. Wang • B. Zhang
College of Electronic and Communication Engineering, Tianjin Normal University, Tianjin, China
e-mail: mujiasong@aliyun.com

B. Zhang et al. (eds.), *The Proceedings of the Second International Conference on Communications, Signal Processing, and Systems*, Lecture Notes in Electrical Engineering 246, DOI 10.1007/978-3-319-00536-2_7,

changeless topology makes it need to rebuild the hierarchical structure when nodes move and limits its performance in network extension [3].

HRP in ZigBee does not need and not allow any communication to maintain the routing path for the purpose of low power consumption. However, due to the broadcasting characteristic of wireless channel, a node may receive frames from its neighbourhood. And some information in transmission is required to be stored according to some functions in the specification, such as updating the neighbour table. On that basis, a real time routing optimization scheme is proposing in this paper. The neighbour table which is required in ZigBee specification is utilized to improve the routing performance, thus the algorithm does not need any extra communication. So far, mostly researches on ZigBee routing were focused on the Z-AODV [4]. The study on HRP was limited [5] and [6] propose two similar routing algorithm for hierarchical topology, the information in neighbour table was used to get to shorter path. However, the links in their methods were still invariable. The real time routing optimization focuses on the maintaining of routing paths. The topology optimization is considered when a node deciding its parent and the links can be changed if there are better options. So the routing performance can be improved during the network lifetime without extra communication.

The rest of this paper is organized as follows: Sect. 2 will briefly introduce the related contents in ZigBee specification, the real time routing optimization will be proposed in Sect. 3. In Sect. 4, simulation results are presented. Finally, the conclusion is shown in Sect. 5.

2 ZigBee Specification and Routing Methods

Based on the IEEE 802.15.4 protocol, the ZigBee specification defines the standard of higher layers. Three device types are defined in ZigBee: ZigBee coordinator (ZC), ZigBee routers (ZR), and ZigBee end devices (ZED). ZC is responsible for starting a new network. ZigBee coordinator and routers are routing capable, while the ZigBee end devices can't participate in routing and have to rely on their corresponding ZigBee parent routers for that functionality [7].

ZigBee network layer (NMK) provides functionality such as dynamic network formation, addressing, routing, and discovering 1 hop neighbours. The network address is recommended to be assigned in a hierarchical tree structure. The deployed ZigBee devices automatically construct the network, and then changes such as joining/leaving of devices are automatically reflected in the network configuration.

ZigBee devices support the function of testing the Link Quality Indication (LQI) measurement every time they receive a frame. The LQI measurement is a characterization of the strength and/or quality of a received packet. The LQI measurement shall be performed for each received packet, and the result shall be reported to the MAC sublayer. The LQI information of every single received packet can be simply

acquired according to the standard with no more extra calculation and communication.

In ZigBee specification, it is recommended to use Distributed Address Allocation Mechanism (DAAM) for address assignment to form tree structure. The parameter *Cm* represents the largest number of children nodes, *Rm* means the number of children nodes which can be a router and *Lm* decides the most depth in the network. And for the same network, different nodes usually have the constant *Cm* and *Rm*. Every potential parent is provided with a finite sub-block of the address space, which is used to assign network addresses to its children. Given *Cm*, *Lm*, and *Rm*, we can compute the function *Cskip(d)* as the size of the address sub-block distributed by each parent at depth d as (1).

$$Cskip(d) = \begin{cases} 0, & Rm = 0, \\ 1 + Cm \times (Lm - d - 1), & Rm = 1, \\ \left(1 + Cm - Rm - Cm \times R^{Lm-d-1}\right)/(1 - Rm), & Rm > 1. \end{cases} \quad (1)$$

Each ZigBee device maintains a neighbour table which has all the neighbour information in the 1-hop transmission range. The contents for a neighbour entry are the network's PAN (Personal Area Network) identifier; node's extended address, network address, device type, relationship, LQI and etc. Optionally, additional information such as depth can be included. Entries in the table are created when the node joins to an existing network. Conversely, the neighbour entry is removed when the neighbour node leaves the network. Since the information on the neighbour table is updated every time a device receives any frame from the some neighbour node, the information of the neighbour table can be said to be up-to-date all the time.

3 Real Time Routing Optimization

The hierarchical tree structure in ZigBee provides a simple and reliable topology for wireless networks. However, as an active routing method, HRP would not update the transmission path as long as the current link is available. In HRP, a node will only try to find new links when current ones are failed by broadcasting rejoining request. In rejoining process, the local node asks all its neighbours to be new parent, and all the neighbours who are able to accept new child will respond the request. The requesting node will choose the neighbour with best link quality as new parent. It can be seen that the node along with all its potential parents may send messages during this course and occupy the wireless channel, and the only info it need, in essential, is the link quality of potential parents. As mentioned in Sect. 2, a node will update its neighbour table when receiving data from neighbours, and the LQ value could be measured by any single packet. In our scheme, we add a one bit long space in NWK frame head to represent whether the node is able to accept new

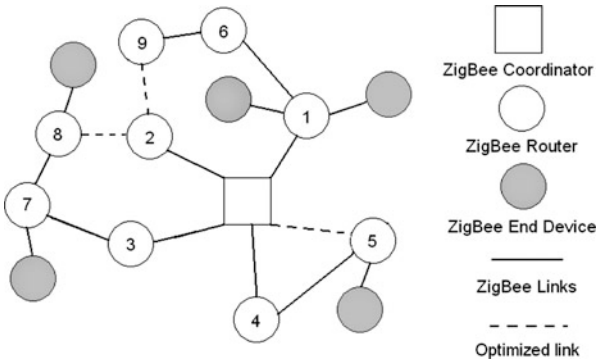

Fig. 1 Example of ZigBee hierarchical topology

children. Thus, all the necessary information needed in rejoining could be acquired in daily neighbour table maintaining. When a node tries to update its parent-child link, it only needs to send a joining request to the proper candidate node directly.

In HRP, the nodes join the network sequentially and the links keep invariant in data transmission. The joining process only choose the node with best LQ to be parent, however, it cannot guarantee it is also the global optimum for the whole network. As shown in Fig. 1, node 8 is the child of node 7 in original ZigBee network. Though it provides better link quality to its parent, the data to coordinator may have 3 hops. As the number of hops in HRP is mainly influenced by the depth of source and target nodes, the node will choose its parent based on the depth along with LQ in proposing routing optimization algorithm. The priority of *i-th* candidate parent node, PPr_i, is calculated as (2):

$$PPr_i = -LQ_i - kD_i \tag{2}$$

Where LQ_i is the link quality value of *i-th* node and D_i is its depth, k is a preset constant to adjust the weight of LQ and depth. A node will choose the candidate with the maximum PPr_i value to be its parent. By above principle, node 8 was the child of node 2 in our method and it improved the global routing performance, since the data transmission from it to ZC only needs two hops.

It is assumed that the maximum number of routing capable children, *Rm*, was 4 in the network shown in Fig. 1. When node 5 tried to join the network, ZC already had four router children, so node 5 cannot be the child of ZC. In proposing scheme, a parent node could maintain and change its children when receiving a joining request from other nodes or a command from upper layer. For a parent node in depth d, its candidate child nodes are all its neighbours, whose depth is more than d. The parent node will choose the new children based on the priority of *i-th* candidate child node, CPr_i, which is shown in (3):

$$CPr_i = LQ_i + \alpha Nd_i + \beta\left(LDP_i - D_{parent}\right) \tag{3}$$

where Nd_i is the number of its descendants, LDP_i is the lowest depth of other

potential parents for candidate node i and D_{parent} represent the depth of the parent node, α and β are 2 constant to adjust the weight of each terms. *Ndi* indicates the importance of the candidate. The more descendants a parent has, the more nodes may benefit from its lower depth. This may lead to less transmission hops for all the nodes in the sub-tree where the parent node is the sub-root. Every router in ZigBee network can sum the number of its children by checking the address allocation and this value is required to be broadcasted as an announcement when it is changing. Thus, the neighbours are able to update their neighbour table. As to ZigBee end device, the *Ndi* is 1. By above principle, the value of *Ndi* can be easily calculated for each node. LDP_i predicts the depth of the candidate's parent if it is rejected by local one. Because the routers may announce if it is able to accept new children in its frame header as we modified in last sub-section, a node may find the lowest depth of potential parents through neighbour entries. The difference between LDP_i and D_{parent} shows the importance of current parent to the *i-th* candidate. When a child may have higher depth with the disconnection to current parent, it should have higher priority to be reserved.

A parent node could maintain its children based on the methods mentioned above. Because the information is acquired by updating neighbour tables and it is not expected to introduce any extra communication to go against the idea of simple and low cost in ZigBee specification. Thus, the improvement may not result in the best option, yet it is good enough and very efficient considering its cost. For example, in Fig. 1, node 5 might definitely be the child of ZC, node 8 was the child of node 2 in proposing scheme, and the network depth and load was reduced.

3.1 Algorithm

Some modifications have been made upon ZigBee specification to achieve routing maintaining, along with the real time routing optimization algorithm, they are listed as following:

- In the header of frames, 1 bit is used to denote whether this source device was able to accept new child nodes. In ZigBee NWK specification, as the 13th–15th bits in format control field are reserved, the 13th is used as the flag.
- When a node tries to rejoin the network, it will send rejoining request and wait for responses. If it receives more than one rejoining confirmations, it chooses the candidate with highest priority to be its new parent based on (3).
- Every ZigBee router, including ZC, is required to announce the number of its children when the value changed by a network status command frame.
- Every ZigBee router, including ZC, is allowed to maintain its children when receiving a joining or rejoining request from other nodes or a command from upper layer.
- In the real time routing optimization algorithm, the following terms were required in neighbor table entries: 16 bit network address, 64 bit IEEE address,

depth, link quality, the lowest depth of other potential parents, device type, relationship for all neighbors; the capability of accepting new children, the number of its descendants for routers and ZC.
- When a router or ZC is maintaining its children, it may decide its new children based on (3), for a parent node in depth d, its candidate child nodes are all its neighbors, including current children, whose depth is more than d.
- In maintaining, if a parent decides a new child, it will send an unsolicited rejoin response command frame to inform the child of the new address and parent; if a parent is going to abandon a related child, it will unicast a network report command to announce the child and make it to rejoin the network.

4 Simulations

The simulation was implemented in Matlab. Some parameters in the simulation were set as following: time duration was 300 s; *Cm*, *Rm* and *Lm* were set 4, 4 and 5 separately; the data packet size was 100 bits packet interval time was 1 s. The source and destination of transmission were randomly chosen. The parameters in routing optimization, k, α and β are set 3, 1, and 3, respectively. The node number in the simulation varied from 10 to 100. We compared the performance of real time routing optimization and origin ZigBee hierarchical routing protocol. Considering ZigBee networks may update the routing by re-initialization, we also took this strategy as a comparative term. In the ZigBee routing with re-initialization, the network might be reset every 100 s. Also, the nodes in the network had a probability to change its position to simulate the unexpected interference in real application. Each node had 10 % chance to move during the simulation and the time it moved was uniformly random. The new position of moving node followed a 2-dimension normal distribution centred with origin coordinates with mean of 5.

Figure 2 shows the average hops in data transmission for different routing schemes. It could be seen that the real time routing optimization could reduce the average hops. ZigBee routing had most hops because it was not able to change its transmission links during the lifetime of network. If the network updated the topology by re-initialization, the average hops may slightly decrease. However, as the re-initialization in not real time, moreover, the parent child links in origin ZigBee networks were only decided based on the link quality, its improvement was limited. On the contrary, the real time routing optimization was near real time, and the information in neighbour table was considered during routing determining. So it had the best performance in our simulations.

As the communication in network may indicate the efficiency of routing methods, the network load for different routing methods is illustrated in Fig. 3. From the chart, we could conclude that the real time routing optimization also improved the efficiency. Initializing the network may introduce a lot of extra frames, thus it had the worst performance. Compared with original ZigBee routing, the proposing method could maintain the routing path and use the knowledge in

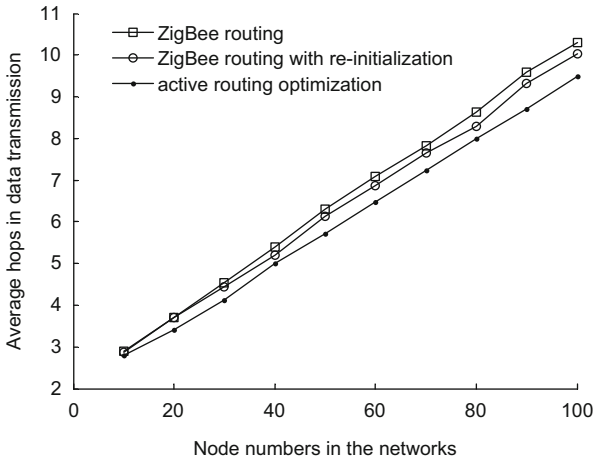

Fig. 2 Average hops in data transmission for different routing schemes

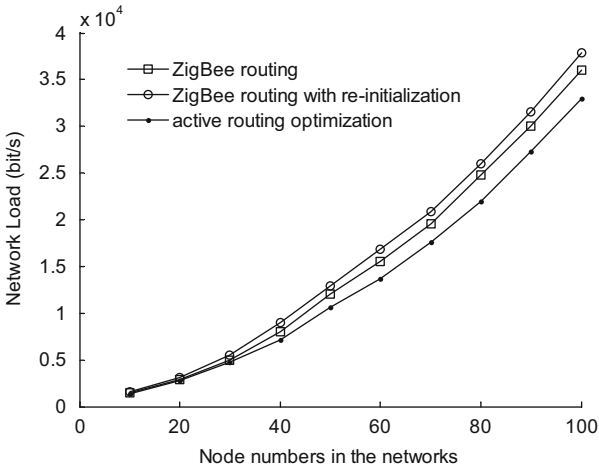

Fig. 3 Network Load for different routing schemes

neighbour table for global optimization, this resulted in the lowest network load from the three approaches.

5 Conclusions

In origin ZigBee hierarchical networks, the parent child links are invariant since the network initialized, and each node may decide the parent only based on the link quality. The global performance is not considered, and the routing paths will not be adjusted in the network life time as long as the related nodes are connected. A real time routing optimization algorithm is proposed in this paper to overcome the

drawbacks mentioned above. As a cross layer optimization scheme, some modifications have to be made in ZigBee stacks. In our method, sub-tree structure and alternative parent are taken in to account. All the information needed can be acquired directly or calculated by the parameters in neighbour table according to ZigBee specifications. The simulation results show that the real time routing algorithm could achieve lower average hops and network load in data transmission. For further work, more simulations are needed to test other parameters in the network, such as end to end delay.

Acknowledgments The work in this paper is funded by Doctoral Scientific Foundation of Tianjin Normal University (52XB1106).

References

1. Ajgaonkar P (2010) Simulation studies on ZigBee communications for home automation and networking. IEEE Autotestcon 1–6
2. Baronti P, Pillai P, Chook VWC, Chessa S, Gotta A, Hu YF (2007) Wireless sensor networks: A survey on the state of the art and the 802.15.4 and ZigBee standards. Comput Commun. 30(7):1655–1695. doi: 10.1016/j.comcom.2006.12.020
3. Tareq AA, Yang SH (2008) A ZigBee-based mobile tracking system through wireless sensor networks. Int J Adv Mechatronic Syst 1(1):63–70
4. Metin T, Ibrahim K (2012) PSAR: power-source-aware routing in ZigBee networks. Wireless Network 18(6):635–651. doi:10.1007/s11276-012-0424-5
5. Ha JY, Park HS, Choi S, Kwon WH (2007) EHRP: enhanced hierarchical routing protocol for ZigBee mesh networks' communications letters. IEEE 11(12):1028–1030. doi: 10.1109/LCOMM.2007.071325
6. Kim T, Kim D, Park N, Yoo SE (2007) Shortcut tree routing in ZigBee networks' 2nd international symposium on wireless pervasive computing, San Juan, Korea, pp 42–47. doi: 10.1109/ISWPC.2007.342571
7. ZigBee standard Organization. ZigBee specification Document 053474r17

Minimal Global Hops Algorithm for Energy Balancing in ZigBee Hierarchical Network

Jiasong Mu, Wei Wang, Baoju Zhang, and Wei Song

Abstract Low power consumption is one of the most significant property and pursuing object for ZigBee networks. Because of the multi-hop mechanism in wireless communication, the nodes are always uneven used from the overall perspective, and some devices may exhaust their power quickly. This will result in the potential network segmentation and badly affect the performance. A minimal global hops (MGH) algorithm for energy balancing in ZigBee hierarchical network is proposed in this paper. When some node has low battery, the network structure will be considered in choosing the substitution device to minimize the transmission paths via modified nodes in MGH. This scheme may reduce the power consumption in low battery nodes, as well as lower the cost of topology changes. The simulation result shows that MGH could effectively preserve the cost in low power nodes.

Keywords ZigBee hierarchical networks • Power balancing • Minimal global hops • Low battery

1 Introduction

One of the primary goals of ZigBee is low power consumption and therefore long-living networks. HRP (hierarchical tree routing) is an active routing method whose routing information was established when the network deployed and kept invariable unless the network structure changed. HRP provides a simple and reliable topology for wireless networks [1]. For each node, if the destination of a data frame is the descendant of itself, it will send the packet to the corresponding child. Otherwise, it will transmit the message to its parent. HRP is efficient from the view of routing

J. Mu (✉) • W. Wang • B. Zhang • W. Song
College of Electronic and Communication Engineering, Tianjin Normal University, Tianjin, China
e-mail: mujiasong@aliyun.com

B. Zhang et al. (eds.), *The Proceedings of the Second International Conference on Communications, Signal Processing, and Systems*, Lecture Notes in Electrical Engineering 246, DOI 10.1007/978-3-319-00536-2_8,

acquiring and memory use, but the routing paths in HRP are always inefficient, because the data frames are limited in parent child link [2].

Although, the devices have a low power cost in ZigBee hierarchical networks, current network formation and routing methods do not fully address power consumption issues [3]. A problem of energy cost in wireless network is the uneven consumption of the nodes. Overall routing methods only guarantee the better average performance. Due to the network structure and node location, some devices may be overused (e.g., the node at the "centre" of network is more likely to receive data and join a routing path.). This may lead to potential network segmentation and shorten the lifetime of whole network, and it is more severe in hierarchical topology [4].

Most researches on energy conserving and balancing algorithms focus on the mesh or hybrid topology, the study in hierarchical structure is little. Moreover, the performance of balanced network is also an important indicator to evaluate the balancing method, it is expected that the changing in topology would effect as little as possible on data transmission [5]. In ZigBee specification, a node may rejoin the network when its connection to the parent is failed. As a consequence, all the descendent of some low power node have to access the rejoining procedure when the ancestor was replaced to conserve its energy. This may lead to more communication and overhead. Moreover, as the HRP could not maintain the routing during network lifetime, the performance of rebuilt network is dubious. This paper is proposing a minimal global hops (MGH) energy balancing algorithm in ZigBee hierarchical networks. The network structure will be considered in choosing the substitution device to minimize the transmission paths via modified nodes. It may reduce the power consumption in low battery nodes, as well as optimize the data transmission in modified network. To avoid extra communication and power consumption, all the information needed in the algorithm can be acquired by updating the neighbour table, which is defined in ZigBee specification.

The rest of this paper is organized as following: Sect. 2 will briefly introduce the related contents in ZigBee specification, the minimal global hops algorithm will be proposed in Sect. 3. In Sect. 4, simulation results are presented. Finally, the conclusion is shown in Sect. 5.

2 ZigBee Specification and Routing Methods

Based on the IEEE 802.15.4 protocol, the ZigBee specification defines the standard of higher layers. Three device types are defined in ZigBee: ZigBee coordinator (ZC), ZigBee routers (ZR), and ZigBee end devices (ZED). ZC is responsible for starting a new network. ZigBee coordinator and routers are routing capable, while the ZigBee end devices can't participate in routing and have to rely on their corresponding ZigBee parent routers for that functionality [6].

ZigBee network layer (NMK) provides functionality such as dynamic network formation, addressing, routing, and discovering 1 hop neighbours. The network

address is recommended to be assigned in a hierarchical tree structure. The deployed ZigBee devices automatically construct the network, and then changes such as joining/leaving of devices are automatically reflected in the network configuration.

In ZigBee specification, it is recommended to use Distributed Address Allocation Mechanism (DAAM) for address assignment to form tree structure. The parameter *Cm* represents the largest number of children nodes, *Rm* means the number of children nodes which can be a router and *Lm* decides the most depth in the network. And for the same network, different nodes usually have the constant *Cm* and *Rm*. Every potential parent is provided with a finite sub-block of the address space, which is used to assign network addresses to its children. Given *Cm*, *Lm*, and *Rm*, we can compute the function *Cskip(d)* as the size of the address sub-block distributed by each parent at depth d as (1).

$$Cskip(d) = \begin{cases} 0, & Rm = 0, \\ 1 + Cm \times (Lm - d - 1), & Rm = 1, \\ \left(1 + Cm - Rm - Cm \times R^{Lm-d-1}\right)/(1 - Rm), & Rm > 1. \end{cases} \quad (1)$$

Each ZigBee device maintains a neighbour table which has all the neighbour information in the 1-hop transmission range. The contents for a neighbour entry are the network's PAN (Personal Area Network) identifier; node's extended address, network address, device type, relationship, LQI and etc. Optionally, additional information such as depth can be included. Entries in the table are created when the node joins to an existing network. Conversely, the neighbour entry is removed when the neighbour node leaves the network. Since the information on the neighbour table is updated every time a device receives any frame from the some neighbour node, the information of the neighbour table can be said to be up-to-date all the time.

3 Algorithms

3.1 Routing Optimization

Energy saving and balancing strategies in wireless network are always cross-layer methods. As an active routing method, HRP would not update the transmission path as long as the current link is available. In HRP, a node will only try to find new links when current ones are failed by broadcasting rejoining request. In rejoining process, the local node asks all its neighbours to be new parent, and all the neighbours who are able to accept new child will respond the request. The joining process only choose the node with best LQ to be parent, however, it cannot guarantee it is also the global optimum for the whole network. To identify the topology in hierarchical network is not difficult; however, we want to eliminate the extra communication. So

we could only estimate the topology based on some parameters in neighbour table and some modifications have to be made in the stacks. As the number of hops in HRP is mainly influenced by the depth of source and target nodes, the node will choose its parent based on the depth along with LQ in proposing routing optimization algorithm. The priority of *i-th* candidate parent node, PPr_i, is calculated as (2):

$$PPr_i = -LQ_i - kD_i \tag{2}$$

Where LQ_i is the link quality value of *i-th* node and D_i is its depth, k is a preset constant to adjust the weight of LQ and depth. A node will choose the candidate with the maximum PPr_i value to be its parent. In proposing scheme, a parent node could maintain and change its children when receiving a joining request from other nodes or a command from upper layer. For a parent node in depth d, its candidate child nodes are all its neighbours, whose depth is more than d. The parent node will choose the new children based on the priority of *i-th* candidate child node, CPr_i, which is shown in (3):

$$CPr_i = LQ_i + \alpha Nd_i + \beta\left(LDP_i - D_{parent}\right) \tag{3}$$

where Nd_i is the number of its descendants, LDP_i is the lowest depth of other potential parents for candidate node i and D_{parent} represent the depth of the parent node, α and β are 2 constant to adjust the weight of each terms. *Ndi* indicates the importance of the candidate. The more descendants a parent has, the more nodes may benefit from its lower depth. This may lead to less transmission hops for all the nodes in the sub-tree where the parent node is the sub-root. Every router in ZigBee network can sum the number of its children by checking the address allocation and this value is required to be broadcasted as an announcement when it is changing. Thus, the neighbours are able to update their neighbour table. As to ZigBee end device, the *Ndi* is 1. By above principle, the value of *Ndi* can be easily calculated for each node. LDP_i predicts the depth of the candidate's parent if it is rejected by local one. Because the routers may announce if it is able to accept new children in its frame header as we modified in last sub-section, a node may find the lowest depth of potential parents through neighbour entries. The difference between LDP_i and D_{parent} shows the importance of current parent to the *i-th* candidate. When a child may have higher depth with the disconnection to current parent, it should have higher priority to be reserved. Because the information is acquired by updating neighbour tables and it is not expected to introduce any extra communication to go against the idea of simple and low cost in ZigBee specification. Thus, the improvement may not result in the best option, yet it is good enough and very efficient considering its cost.

3.2 Modifications in ZigBee Specification

Based on the discussion above, some modifications have been made upon ZigBee specification to achieve the real time routing optimization, they are listed as following:

- In the header of frames, 1 bit is used to denote whether this source device was able to accept new child nodes. In ZigBee NWK specification, as the 13th–15th bits in format control field are reserved, the 13th is used as the flag.
- When a node tries to rejoin the network, it will send rejoining request and wait for responses. If it receives more than one rejoining confirmations, it chooses the candidate with highest priority to be its new parent based on (3).
- Every ZigBee router, including ZC, is required to announce the number of its children when the value changed by a network status command frame.
- Every ZigBee router, including ZC, is allowed to maintain its children when receiving a joining or rejoining request from other nodes or a command from upper layer.
- The following terms were required in neighbor table entries: 16 bit network address, 64 bit IEEE address, depth, the lowest depth of other potential parents, device type, relationship for all neighbors; the capability of accepting new children, the number of its descendants for routers and ZC.
- When a router or ZC is maintaining its children, it may decide its new children based on (3), if a parent decides a new child, it will send an unsolicited rejoin response command frame to inform the child of the new address and parent; if a parent is going to abandon a related child, it will unicast a network report command to announce the child and make it to rejoin the network.

3.3 Minimal Global Hops Energy Balancing

In hierarchical structure, assuming that all the nodes have the same probability to send (and receive) a data frame, for a certain node, the power consumption in communication is only related to (nearly proportional to) the total number of its descendant nodes. So the greater depth a node is at, the less power cost it has in data transmission. The maximum number of descendant nodes in depth d, *Dn(d)*, can be calculated as (4), from which, it may be concluded that as the node depth decrease, the increase of descendants is exponential approximatively.

$$Dn(d) = \begin{cases} Rm^{Lm-d} + \dfrac{Rm^{Lm-d} - 1}{Rm - 1}(Cm - Rm) & , d < Lm \\ 0 & , d = Lm \end{cases} \tag{4}$$

Therefore, based on the battery levels BL_k, the algorithm may limit the minimum

depth $minD_k$ as a router when the low power devices rejoin the network. It is shown as following:

Energy balancing algorithm

```
const BL_k minD_k (0≤k≤Lm),
 N=max messages before rejoining;
array SpareOption[], OptimumOption[];
m=currentbalancinglevel;
while m≤k≤Lm do
 if remainingbattery<BL_k then currentbalancinglevel=k
  if sendingmessage==N or RejoinRequest received then
   sendingmessage=0, rejoin();
On RejoinResponse received do
  if localdepth<minD_m or responsenode.currentbalancinglevel != 0 then
  *SpareOption==*responsenode, *SpareOption++;
 else *OptimumOption==*responsenode, *OptimumOption++;
On MaxResponseTime received do
   if OptimumOption != null then SortwithLQI (OptimumOption),
  ParentNode==OptimumOption[0];
     else SortwithLQI(SpareOption), ParentNode==SpareOption[0];
```

The algorithm begins to function when the node battery drops down to a certain critical value which is pre-set. The while statement decides the balancing level based on remaining power. The first **On** may categorize the response nodes, the ones which could make current device have a qualified depth are in the optimum group and the others are backup to maintain the network structure in case no optimal options were found. The second **On** statement describes the principle of deciding parent node when the response process is over. As this algorithm tries to eliminate the extra communication, the adjustment of depth would wait for rejoining process. At most, the rejoining will be initiated when a pre-set maximum number, N messages have been sent in current topology.

4 Simulations

This section will illustrate the simulation results of the MGH. The simulation was implemented in Matlab. Some parameters were set as following: time duration was 300 s; *Cm*, *Rm* and *Lm* were set 4, 4 and 5 separately; the data packet size was 100 bits packet interval time was 1 s. The source and destination of transmission were randomly chosen. The parameters in routing optimization, k, α and β are set 3, 1, and 3, respectively. The node number in the simulation varied from 10 to 100. Also, the nodes in the network had a probability to change

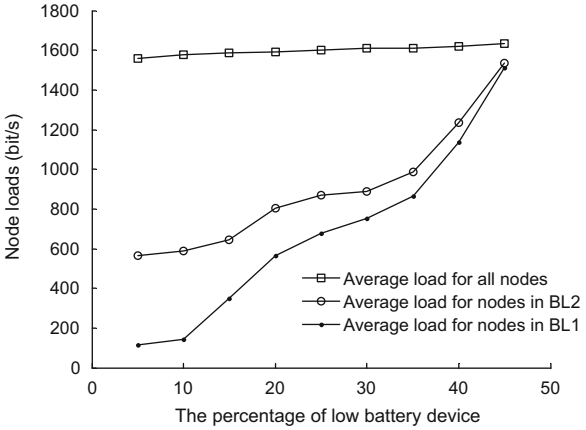

Fig. 1 Average node load of different node types in energy balancing algorithm

its position to simulate the unexpected interference in real application. Each node had 10 % chance to move during the simulation and the time it moved was uniformly random. The new position of moving node followed a 2-dimension normal distribution centred with origin coordinates with mean of 5. *BLi* and *minDi* was set to $BL_1 = 10\ \%$, $minD_1 = 3$ *and* $BL_2 = 30\ \%$ and $minD_2 = 2$. It means if the remaining battery of a certain device was below 30 %, its minimum depth was 2 as a router and if the power was less than 10 %, its depth was no less than 3. Firstly, the balancing performance was tested. The nodes number in the network was fixed 50, the amount of low battery device were changing for different simulations. And the nodes in BL1 and BL2 were equal. As the transmitter power contributes the most of node energy cost, the average load was used to evaluate the performance. The result was shown in Fig. 1. As the percentage of low battery devices added, the average load for all nodes was also slightly increasing. It meant the price of low power for some certain devices was that all the nodes had to take more communication on average. When the rate of low battery devices were 10 % less, the balancing algorithm had best performance, compared with the average load for all nodes, the balanced nodes in BL1 and BL2 only had 9.5 and 37.2 % energy cost on communication separately. However, the rates were added to 40.2 and 51.6 % when there were more than a quarter of low battery nodes. In the proposing algorithm, the balancing was on the basis of the integrity of topology. A node could add the depth only when there was another device which could be use as alternative in the hierarchical structure. Otherwise, it had to keep the current depth even it had inadequate battery. If the percentage of low battery nodes reached 40 %, the nodes in BL1 and BL2 only had 67.9 and 76.1 % node load to the average for all. For the situation of more than half low devices, the effect of energy balancing was very limited. Based on the simulation, it can be concluded that the MGH algorithm was able to limit the power consumption of low power devices when they were less than 10 % to all nodes in the network.

5 Conclusions

The overused of some nodes make them deplete the battery quickly. It also may result in the network segmentation and badly affect the data transmission in wireless network. This paper proposed a minimal global hops algorithm for energy balancing in ZigBee hierarchical network. The MGH algorithm could preserve the power of low battery devices by limiting their depth in network not exceeding a pre-set value. To reduce the cost of the substitution of low power nodes and improve the performance of balanced network, a maintaining scheme is also introduced to minimize the hops in the transmission path via balanced nodes and their origin descendent nodes. The simulation result shows that the MGH could effectively reduce the power consumption in low battery device. For further work, the comparison between MGH and other energy balancing algorithm need to be more investigated and the evaluation of minimal global hops is also need studied.

Acknowledgments The work in this paper is funded by Doctoral Scientific Foundation of Tianjin Normal University (52XB1106).

References

1. Tareq AA, Yang SH (2008) A ZigBee-based mobile tracking system through wireless sensor networks. Int J Adv Mechatronic Syst 1(1):63–70
2. Ajgaonkar P (2010) Simulation studies on ZigBee communications for home automation and networking. IEEE Autotestcon. 1–6
3. Baronti P, Pillai P, Chook VWC, Chessa S, Gotta A, Hu YF (2007) Wireless sensor networks: a survey on the state of the art and the 802.15.4 and ZigBee standards. Comput Commun. 30(7):1655–1695. doi: 10.1016/j.comcom.2006.12.020
4. Han DM, Lim JH (2010) Design and implementation of smart home energy management systems based on ZigBee. IEEE Trans Consum Electron 56(3):1417–1425. doi: 10.1109/TCE.2010.5606278
5. Gezer C, Buratti C (2011) A ZigBee smart energy implementation for energy efficient buildings. IEEE 73rd vehicular technology conference (VTC Spring), pp 1–5. doi: 10.1109/VETECS.2011.5956726
6. ZigBee standard Organization. ZigBee specification Document 053474r17

Research and Design of Real-Time Monitoring Tidal System Based on Internet of Things

Jincheng Wu, Xicheng Yang, Jingrui Sun, and Yanbo Wu

Abstract This paper introduces the embedded NUT/OS operating system and TCP/IP protocol stack in an 8-bit Atmega 128 MCU. It combines RTL8019AS network control chip with the peripheral hardware circuit. It takes the average filtering algorithm by using the digital filtering technology in middle value. The dual function of data processing and Http Web server are now become reality. In the monitoring terminal and based on the Internet of things through the IE browser to login, access and click the embedded in MCU web webpage hyperlink. The remote real-time monitoring can be obtained through both the MCU collection and the tidal dynamic characteristics of processing. Using the embedded operating system to replace the traditional PC as the web server, the utility model has the advantages of lower power consumption, size and cost of the server.

Keywords Embedded system • Digital filtering • Remote monitoring • Tide • The Internet of things

1 Introduction

In both military and civil or in ocean exploitation and engineering, tidal measurements is playing a more and more important role.

J. Wu (✉) • J. Sun
College of Electronic and Communication Engineering, Tianjin Normal University, Tianjin, China
e-mail: wdxywjc@mail.tjnu.edu.cn

X. Yang
Hydrographic Surveys Brigade of Tianjin MSA, Tianjin, China

Y. Wu
College of Computer and Information Engineering, Tianjin Normal University, Tianjin, China

B. Zhang et al. (eds.), *The Proceedings of the Second International Conference on Communications, Signal Processing, and Systems*, Lecture Notes in Electrical Engineering 246, DOI 10.1007/978-3-319-00536-2_9,

The tide is one of the important physical factors in ocean. A ship sailing in the sea or in port affected by the tides. When the tide is low, the ship is easy to run aground and causing the accident; but at high tide the ship can load and upload in time and also improve efficiency. So it is very important to detect the tides [1].

At present, the remote data acquisition, monitoring and transmission mostly adopts the wired and wireless communication mode for data transmission.

With the rapid development of the communication technology, the system application of remote monitoring, data collection and transmission are also increasingly the use of wireless communication network. Therefore, embedded NUT/OS and TCP/IP in the Atmega 128 MCU [2] to obtain tidal acquisition, processing and system monitoring based on the Internet of things. With the combination of RTL8019AS network control chip and the CM6550R CDMA ROUTER wireless communication module, automatic observation, release, prediction and query of tides can be achieved through real-time and network transmission intelligent [3].

2 Working Principle and System Composition

The monitoring terminal system acquisition is signal by MPM4700 intelligent liquid level transmitter and which is transferred for processing. Through the dynamic Web page the advance design is completed, which is stored in the At mega 128 Web page file for real-time display. In a remote monitoring center the IE browser can monitor real-time dynamic tide. Using embedded MCU Ethernet as remote control system is such as shown in Fig. 1.

3 Hardware Design of the Monitoring Terminal System

The monitoring terminal that uses to realize the data processing and network monitoring function block diagram of hardware design is shown in Fig. 2.

Atmega 128 MCU chip uses as the controller of high performance with 128KB Flash, 4KB EEPROM and 4KB SRAM. The rich resources of the chip can run NUT/OS operating system, together with the simple TCP/IP protocol to achieve embedded Web server and data processing purposes, thus saving the high performance gateway and the hardware protocol chip. This is not only simplifies the peripheral circuit but also reduces the cost. It improves the reliability of the system as well.

Network control chip RTL8019AS [4] is a highly integrated Ethernet controller with full duplex data transmission mode of 10 Mbit/s. It is NE2000 compatibility and support 8 bit and 16 bit data bus, so it can be connected with the 8 bit MCU. The A8 to A15 pin (the MCU PC7 output pin of the inverter is connected to the A15 pin) and the A8 to A15 pin of the MCU address bus is connected, D0–D7 data bus with the PA0–PA7 (AD0–AD7) of 8 bit data bus of MCU is connected, pin 29 reads (IORB) and pin 30 writes (IOWB) control pin of port and PG0 (RD\) reads and PG1

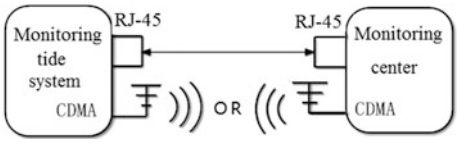

Fig. 1 The control center and the remote monitoring terminal

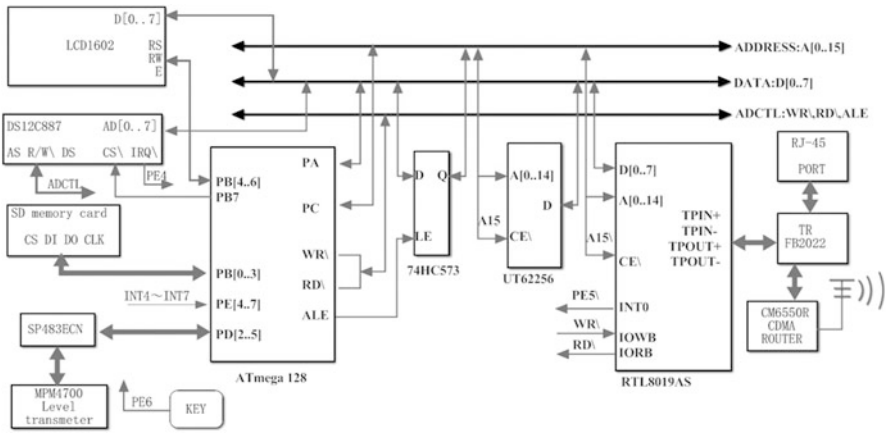

Fig. 2 Monitoring system hardware block diagram

(WR\)writes signal pin of MCU is being connected. The RTL8019AS works in 8 bit bus mode standard.

Extended memory chip UT62256CPC: because the operating system and protocol stack requires high-capacity data storage and Atmega128 MCU internal has only 4K SRAM buffer space, so it cannot complete the data sending and receiving function. If you use the RTL8019AS with the internal 16K RAM, it will affect the data transmission speed of the whole system. The UT62256CPC chip cannot only expand the role of the external RAM, but also can make the input and output buffered serial port. It increases data throughput and improves the performance of the whole system.

In order to collect real-time tidal data, so the calendar clock chip DS12C887 has a 8 bit parallel with real-time clock control register with 4 bytes, 11 bytes of storage time register and a 113 byte RAM. Built-in lithium battery has a power-down self-protection function. In addition, the DS12C887 contains a different interrupt source. It can be programmed by using the interrupt source to the CPU, that is when the DS12C887 IRQ pin is connected to Atmega 128 MCU, the external interrupt INT4 (PE4) pin. Every time it meets the interrupt sources condition, IRQ\ output level is low which will cause INT4 interrupt of Atmega 128 PE4 pin. AD0 to AD7: multiplexing address data bus, the bus adopts time division multiplexing technology. In the bus cycle before half part, appeared on the AD0–AD7 is the address information, it can be used to strobe DS12C887 within

the RAM, the latter part of the bus cycle appears in the AD0–AD7 data. AD0–AD7 is connected to the PA0–PA7 port of the MCU.

AS: address strobe input pin: during read and write operations, the rising edge of AS will latch the address that appears in AD0–AD7 to DS12C887, and the next falling edge will clear AD0–AD7 address information.

CS\: chip selection input is active with lower level, it is connected to the CPU pin with the PB7 control.

LCD 1602 screen: Scrolling display time and tide. Bidirectional three state of I/O Port, so the data of D0–D7 connected to (the data bus) MCU PA port. RS, RW and E are respectively connected to the MCU PB4 to PB6 which are controlled by a MCU.

Intelligent liquid level transmitter MPM4700 with RS-485 interface is connected to Atmega 128 PD2(RO), PD3 (DIHO), PD4 (RE485) and PD5 (DE485) pin by SP483ECN level conversion chip.

When it is connected to the CM6550R CDMA wireless router with RJ45 port, the remote transmission and real-time monitoring tidal dynamic information can be obtained. With the full use of CDMA network "always-online" and at access speed, the characteristics of data flow charging mode has a very high price advantage, it is especially suitable for small data system.

The external key is connected to the CPU PE6 (INT6) pins. It is through the LCD screen and increase the key (PD1) and reduce the key (PD6) and confirmation the key (PD7) to achieve set the time and calibration.

SD card is used to store the real-time tidal data. MCU through the SPI interface (PB0-SS, PB1-SCK, PB2-MOSI, PB3-MISO) and SD (CDDAT3, CLK, CMD, DATO) port connection and writing data to SD card to ensure that the collected data will not loss when the network is busy or under sudden events [5].

4 The Software Design

System software program flow chart is shown in Fig. 3.

After the system is powered on, the Nut/OS operating system automatically calls the entrance to the main( ).

First by calling NutRegisterDevice (&DEV_DEBUG, 0, 0)function, the initialization of UART equipment. Second by calling NutRegisterDevice (& DEV_ETHER, 0, 0) function to register Ethernet controller device. If there is no DHCP in network system or the dynamic configuration fails, then it needs the calling of NutNetIfConfig (DEV_ETHER_NAME, MAC, ip_addr ip_mask) function by using PC dynamic configuration of network card in MAC hardware address, IP address and subnet mask.

By calling the NutRegisterDevice (&MY_FSDEV, 0, 0) function register file system device, block from the EEPROM address 0x00A0 to read the admin user's

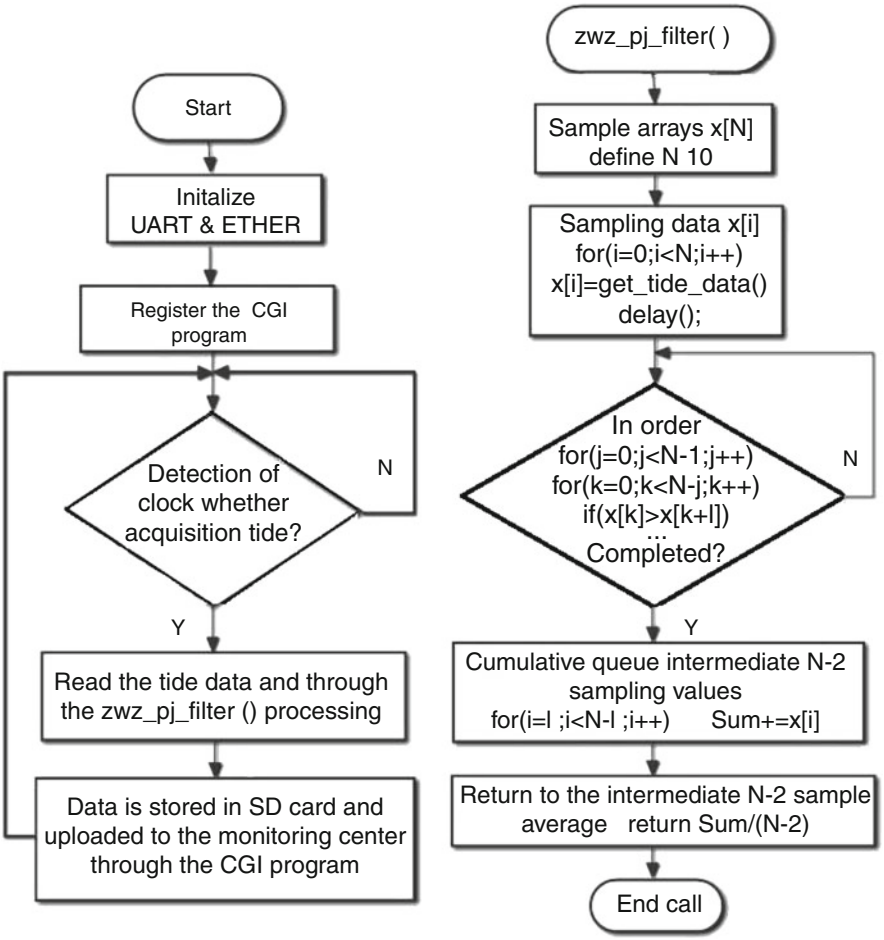

Fig. 3 The main program and subroutine flow chart of data acquisition and processing

initial password, if the first byte is 0x00 or 0xFF, it means no initial password is in the system. The default admin user name and password is root: "123456".

By callingNutRegisterAuth ("admin", admin_password) and NutRegisterCg iBinPath ("cgi-bin /; user /cgi-bin; admin /cgi_bin /") function to protect the program files and to register cgi-bin path under admin /cgi-bin.

By calling the NutRegisterCgi (" MCU_control.Cgi,"MCU_control) functions, the registration of tides and tidal data is obtained, also the cgi programs are under controlled [6].

Create a thread NutThreadCreate (thname, Service, (void *) (uptr_t)i, (HTTPD_ SERVICE_STACK * NUT_THREAD_STACK_MULT) + NUT_THREAD_ STACK_ADD) function; Though Service parameter to call the HTTP service thread (Service, arg) function, the THREAD ( )function creates a socket

NutTcpCreateSocket ( ) and it receives NutTcpAccept ( )function in the 80-port loop where it waits for customer requirements. After receiving the customer request and it is disconnected. NutHttpProcessRequest (stream) function is used to handle http requests.

Tidal status query and processing system functions of mcu_control (FILE * stream, REQUEST * req); When a client requests a cgi-bin/mcu_Control.cgi, it automatically under NutHttpProcessRequest (stream) function call, this function has already been registered by the NutRegisterCgi ( ).

User requests a hyperlink format:

```
admin/mcu_control.cgi? para = GET_TIDE_DATA;
admin/mcu_control.cgi? para = STOP_TIDE_DATA;
```

Read the received parameter names and parameter values:

```
Para_name=NutHttpGetParameterName(req,0)
Para_value=NutHttpGetParameterName(req,0)
 if(!strcmp(para_name,"para")
 {
 if(!strcmp(para_value,"GET_TIDE_DATA")//Get the tidal
data
 {
  zwz_pj_filter( )//Function call after sampling and
processing
 }
else
if (! strcmp (para_value, "GET_TIDE_DATA") / / stop
collecting data
 }
```

By create_status_webpage (stream, tide) function will return samples to the web pages.

if (tide) fprint (stream, html_x [11], "blk_style", "zwz_pj_filter ( )") / / every 5 min collects data and returns to the web page [7].

Each interval of 5 min MCU will collect tidal data for processing, and it is displayed in a web page while stores on the SD card. An hour later the data is sent to the information center. MCU is responsible for recording the latest data and state. Web pages are written in HTML and is stored in binary form of MCU (FLASH). After receiving a user's request to open or to refresh, MCU will find a web page and in accordance with the corresponding character in the corresponding statement into a corresponding value, and then this is sent to the user. Thus, a page refresh is achieved and the user can see the latest data.

During actual tidal data acquisition and processing, in order not only to eliminate the interference pulse caused by the surge and the bad environment but also to obtain the accurate data, the digital filtering techniques is used. Where the median value of the average filtering algorithm data is processed. The principle is to use median filtering algorithm to filter sample values in a pulse interference, and then

Table 1 The real-time measurement data

Number of times	1	2	3	4	5	6	7	8	9	10
Unit (cm)	392	393	394	394	394	395	395	394	394	392
In order	395	395	394	394	394	394	394	393	392	392
Delete max & min	Max	395	394	394	394	394	394	393	392	Min
Average	393									

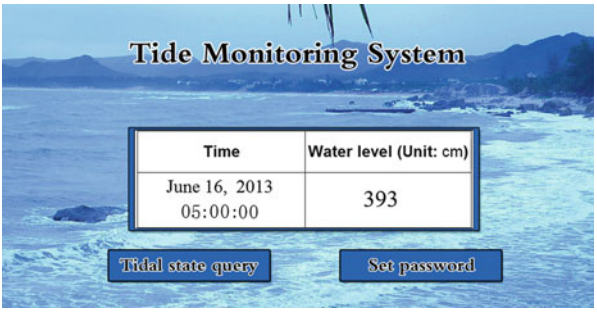

Fig. 4 The tidal dynamic data

average the remaining sampled values filter. It is continuously sampled N times, by sorting excluding its maximum and minimum values, and then seek the remaining N-2, the average of samples. Obviously, this method can suppress random noise, it can filter out the obvious pulse interference. With this algorithm good results are obtained [8]. In June 16, 2013 05:00 AM gathering tidal water of the Tianjin TANGGU, the experimental data is shown in Table 1.

During the acquisition process and through the serial port to get the instantaneous sampling value: get_tide_data ( ) function. The monitoring system uploads every 5 min and it simultaneously stores the data in SD card, later it returns to zwz_pj_filter ( ) function. While waiting for the data to be collected every 5 min, it detects the system. This includes whether the power supply voltage value is accurate or the network is normal. If it is abnormal, at appropriate time and under network normally, the content of transmitted test will be given to the monitoring center via network.

With continuous sampling intervals of 100 ms and after 10 times (N = 10) of data processing, it stores in the SD card, and at the same time it uploads to the monitoring center. To be convenience and accurate in general take $N - 2 =$ 2,4,8,16 as the calculation; often take N = 4,6,10,18.

In the monitoring center, refers to the Fig. 4, the remote tidal dynamic data is under monitoring.

5 Conclusion

This paper describes the working principle of real-time tidal data acquisition system and the software and hardware design. The experiments show that the system is stable, the measurement data is accurate and it meets clients requirements.

References

1. Bo Z, Xiaoming Y (2009) Tide measurement data remote transmission system based on GSM module [J]. Ship Ocean Eng 4(37):107–109
2. Zhang Jianwu, Yan huan (2011) Intelligent home gateway design and application of the Internet of things[J]. Comput Eng 9(37):246–248
3. Ma Feng, Zhang Qingying (2007) Implementation mechanism and improved protocol system of Ethernet based on AVR MCU[J]. J Wuhan Univ Technol 1(29):46–48
4. Yu Fang, Zhang Xin Wang (2009) Design and implementation of GPRS wireless data terminal based on Nut/OS[J]. Micro Comput Inform (25):175–176
5. Rao Zengren Zhao Hao (2009) Realization of multiple MCU and PC communication through RTL8019AS[J]. J Lanzhou Univ 6(45):33–35
6. Xu Xiucheng Hu Shiping (2007) Design of wireless sensor network gateway to access the Internet[J]. Chinese J Sci Instrum 4(28):66–69
7. Zhu Xiaoping Sun Jun (2008) The development and design of DTU module based on NUT/OS [J]. Commun Technol 7(41):89–91
8. Liu Qifang (2008) Algorithms of digital filter in SCM control system [J]. Mech Eng Autom 7 (41):89–91

Research and Application of Building Monitoring Platform Based On the Internet of Things

Jincheng Wu and Jianbo Yu

Abstract Researched the design of building monitoring platform based on the Internet of things, and achieved the function of monitoring real-time information of multiple nodes through a web. Our system uses the STM32F407 as the master chip to complete the conversion of data in different communication protocols. On the user side, the STM32F407, as a Web server, sends the Web page that contains the nodes data to clients; on the nodes side, the STM32F407 achieves the interaction of the nodes through the wireless module nRF24L01. In order to gain good scalability, a specific protocol is used between the microcontroller and nodes. This paper describes architecture and working principle, software and hardware design of the system, illustrates the communication protocol used in this system, analyzes some issues related to the monitoring system and proposes solutions. Related experiments show that the system is stable, the expansion ability of the nodes is powerful and the system meets the needs of most applications of wireless monitoring.

Keywords Embedded server • Intelligent monitoring • The Internet of things • STM32F407 • nRF24L01

1 Introduction

The Internet of things [1] is a new technology that is based on RFID, wireless sensor networks and ubiquitous terminal equipments, which gets communication in a variety way of wired or wireless, and integrates the Internet to achieve data transfer and sharing. Using of cloud computing, high performance computer and other technologies, it can achieve real-time information processing, management and organization. This study is based on the Internet of things to design a building

J. Wu (✉) • J. Yu
College of Electronic and Communication Engineering, Tianjin Normal University, Tianjin, China
e-mail: wdxywjc@mail.tjnu.edu.cn

B. Zhang et al. (eds.), *The Proceedings of the Second International Conference on Communications, Signal Processing, and Systems*, Lecture Notes in Electrical Engineering 246, DOI 10.1007/978-3-319-00536-2_10,

monitoring platform that is efficiency, timeliness and convenience, which merges traditional Internet and new wireless sensor network, using a microcontroller platform as a Web server, to achieve transforming of two different communication protocols. Users could monitor the whole building via the system Web with any network access terminals (e.g., PC, smart phones, etc.), achieving dynamic, convenient building monitoring functions.

2 System Architecture Overview

Shown in Fig. 1, to achieve the embedded Web server function, the system uses the STM32F407 chip with embedded network module as a microcontroller. Users could use any type of network terminal accessing the microcontroller's network, opening its Web page to watch the status of nodes, while the microcontroller obtains information from each node and refresh the pages. Users can get all nodes status at a glance. If users want to change the nodes' status, they can easily achieve the function by page clicking. This system also supports automatic storage of nodes' status and the function of increasing or reducing nodes with convenient operation.

NRF24L01 wireless module [2] provides a 40-bit hardware address (using channel 0), which can be programmed. Considering the operation and security, the microcontroller uses any odd number N as wireless module hardware address, and each node's hardware address of the wireless module is set to (N + 1), so that the system form a point to multipoint broadcast mode. If the node receives data, it indicates that they are in the same system, so that it can be operated, or it cannot receive any data. That ensures the independence of the system.

The capacity of the system is designed to meet the general needs. Firstly, the 40-bit hardware addresses is adequate to the capacity of the system. In certain system, the 8-bit node address indicates the capacity of 255 nodes (0x00 node address is for the micro-controller). Every node could also monitor multiple semaphores simultaneously. If the node hardware resources are sufficient, the number of signals is up to 256 in theory.

3 System Hardware Design

Figure 2 shows the system block diagram. The core part of the controller platform includes supply power part, clock part, reset part, SWD download interface, and connects a serial bus to controlling EEPROM chip 24C64, in order to save user data. And a SPI interface (connecting a wireless module), a network interface, a LCD screen interface and a 232 communication interface are designed in the system.

Physical layer network chip DP83848 is connected to the MAC in STM32F407 through RMII interface, which could complete the network tasks of sending and

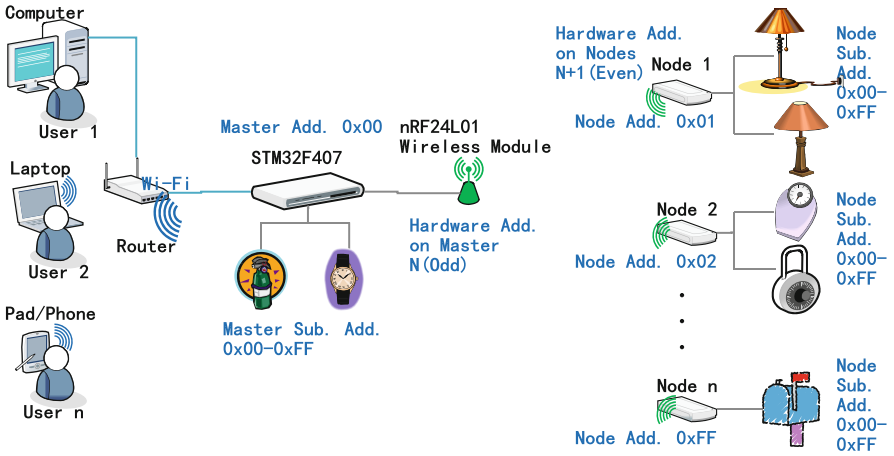

Fig. 1 System architecture

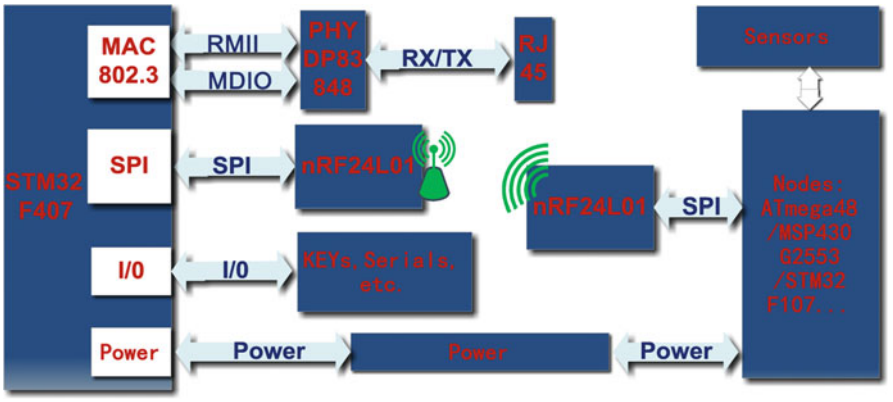

Fig. 2 Hardware schematics

receiving. And wireless module nRF24L01 is connected to the STM32F407 through the SPI bus to achieve the function of communication with nodes.

4 Software Design

4.1 System Workflow

Shown in Fig. 3, after power-on and initialization, the microcontroller shakes hands with saved nodes respectively, and then entering the loop detection. Microcontroller enables wireless module into receive mode, waiting for nodes' data

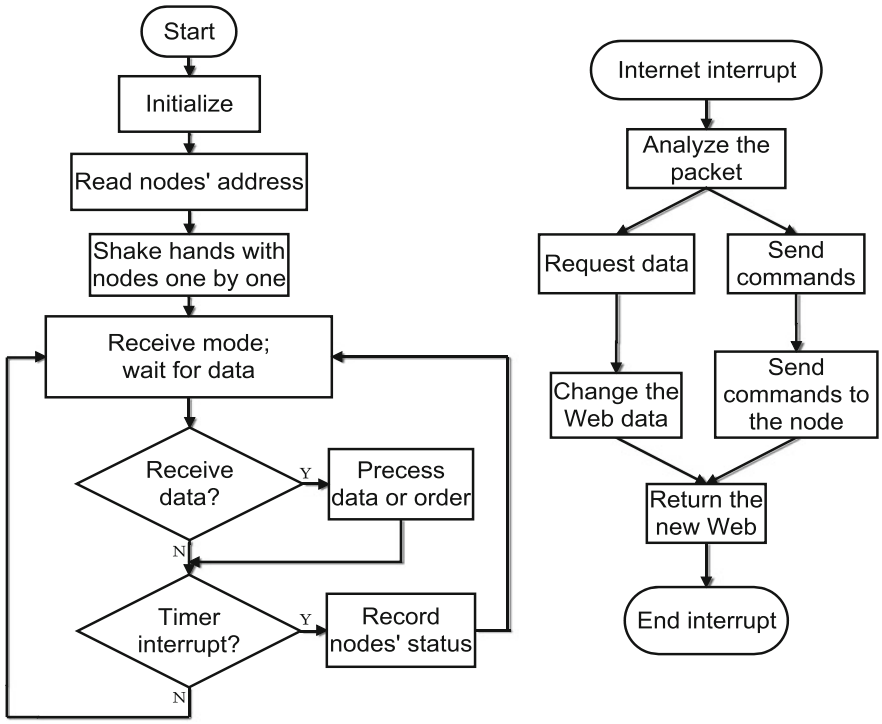

Fig. 3 Software flow chart

reporting. Meanwhile, the network data is occurred in the form of an interrupt, in which microcontroller receives the user's request through TCP/IP protocol [3] stack. The interrupt service program will analyze the contents of the request or the data, and fill the latest state into the corresponding Web pages and send it to users. If users click the page commands to send control commands, the microcontroller will pass a callback CGI to respond to the corresponding command, and send commands to the corresponding node. After the node received the commands and returning the newest data, the microcontroller refreshes client Web page automatically.

Each node uploads new data to the microcontroller every 10 s [4] in different time scales. And microcontroller is responsible for recording the latest data and status of each node. Pages are written in HTML, which are stored in the microcontroller memory (FLASH) in binary form. When received users' opening or refreshing requests, the microcontroller finds the corresponding character in pages and changes its value, and then sends to users, which achieves the function of a Web refresh. Thus users could get the latest data.

For example, if a user would like to see collected voltage data of a certain node, he can open the corresponding web page through a link click. Then the microcontroller receives an HTTP request data and will handle it as follows:

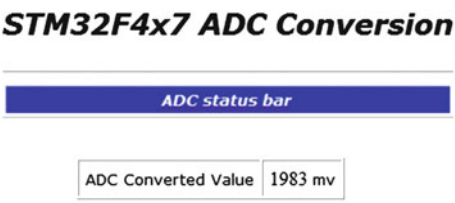

Fig. 4 Show the voltage

/ * Prepare data to be inserted in html * /
* P = (char) (Digit1 +0 x30);
* (p + 1) = (char) (Digit2 +0 x30);
* (p + 2) = (char) (Digit3 +0 x30);
* (p + 3) = (char) (Digit4 +0 x30);

The variable *p* is a pointer that point at the location of voltage data bits in the Web page. *Digit1* to *Digit4* are the uploading voltage data of the node. The microcontroller turns it into ASCII code value (by add 0x30) and then fills it to the voltage Web page, while the names, forms, units (mV) and other formatting information have been saved in the page, and do not need be changed. The microcontroller then transmits the page to the user, who can see the current voltage value on his Internet explorer, as shown in Fig. 4.

And if a user wants to control node's current status, he could complete that just by clicking a button on the page or submitting a form. The page *Action* property makes network service program automatically add form content in the HTTP header of the request packet, which is sent to the microcontroller. After received the packets, the microcontroller goes into a TCP interrupt service routine, in which microcontroller analyzes the packet header to get command contents, and then callbacks a CGI service program to start a wireless module sending program that will send the corresponding command to the corresponding node. the node changes status or value after received the command, and returns data once. And then the microcontroller refresh client page automatically according to the new data. Thus the user can see the consequence of his command.

For example, HTML page contains the following statement:

<form action = "method = get">
<input value = "1" name = "led" type = "checkbox" > LED1
</ form>

If a user checks *LED1* in the selection box and clicks *Send*, the client host will send to the microcontroller an HTTP packet, whose header is as follows:

GET/method = get? Led = 1 HTTP/1.1

In that header, *GET* is an HTTP request command, *method = get* is HTML submitting way controlled by Action property, and *led = 1* is submitting content, followed by the version number. The microcontroller analyzes this information in turn via conditional statements. If any word is same with commands stored in the

Fig. 5 Control LED

memory, the corresponding command will be executed, or it will be given up. Finally, the microcontroller obtains the meaning of opening LED1 by comparing its command, so that it sends a command to the node that controls switch of LED1 lights. Then the node turns on LED1 and returns newest data. After receipted that, the microcontroller changes content of corresponding items in pages (In this situation it's LED1's state), and automatically refreshes the user Web, so that user could view the results of the command execution(Shown in Fig. 5).

4.2 TCP/IP Protocol Stack

To achieve the Internet access, the system uses a realization of TCP/IP protocol stack-LwIP, which is specifically designed for microcontrollers. It is developed to reduce code size and the using percentage of RAM by shrinking the traditional TCP/IP protocol, so that it can be used on resources (especially memory) limited system [5]. The microcontroller used in this study only owns1M program space (Flash), and 192 Kb memories (SRAM). Thus, to complete the function of network server, LwIP is required. In order to minimize the volume of programs, the system does not use any operating systems or any application programming interface (API) provided by LwIP, but directly calls functions in LwIP to complete the embedding of TCP/IP protocol stack.

4.3 Wireless Module Communication Protocol

The system adopts self protocol [6] in the communication between microcontroller and nodes, shown in Tables 1 and 2. The sender transmits 32 bytes every time through the wireless module, which contains the start and stop bytes, command bytes, data bytes, verifiability bytes and other functions bytes, and sets aside enough data extension bytes and encrypted data bytes. As nRF24L01 wireless module has provided hardware address, automatic answer and CRC verifying function, allocation of the relevant bits does not need in this protocol. We only retain the verifying function for the most critical byte (R1), and S is counter R1.

Commands and data transmission should properly select node address and sub address, and send the appropriate commands or data. Transmission data is filled in the protocol from R1 to R6 in order according to the data size, while the insufficient bytes is filled with 0x00, on this situation M (D11) is written with 0x00 to indicate

Table 1 Communication protocol 1

	Num (byte)	D0	D1	D2	D3	D4
Sender	Describe	Start	Sender add	Receive add	Order	Data (R0)
Master	Shake hands	0×A5	0×00	0×01–0×FF	0×25	0×F1
Node		0×5A	0×01–0×FF	0×00	0×52	0×F1
Master	Send order	0×A5	0×00	0×01–0×FF	0×26	Node sub add
Node		0×5A	0×01–0×FF	0×00	0×62	Node sub add
Master	Send data	0×A5	0×00	0×01–0×FF	0×27	Master sub add
Node		0×5A	0×01–0×FF	0×00	0×72	Node sub add
Master	Add node	0×A5	0×00	0×01–0×FF	0×28	0×F1
Node		0×5A	0×01–0×FF	0×00	0×82	Node type
Master	Delete node	0×A5	0×00	0×01–0×FF	0×29	0×F1
Node		0×5A	0×01–0×FF	0×00	0×92	0×F1

Table 2 Communication protocol 2

D5–D10	D11	D12	D13	D14–D30	D31
Data expand (R1–R6)	Grouping num.	Data parity	Encrypt enable	Encrypt data	Stop
Node add (R1–R2)	Reserved	Reserved	Reserved	Reserved	0×B7
Node add (R1–R2)	Reserved	Reserved	Reserved	Reserved	0×7B
Order R1–R6	M	S	K	Encrypt dataY0–Y16	0×B7
Order R1–R6	M	S	K	Encrypt dataY0–Y16	0×7B
Data R1–R6	M	S	K	Encrypt dataY0–Y16	0×B7
Data R1–R6	M	S	K	Encrypt dataY0–Y16	0×7B
Node add R1–R2	Reserved	Reserved	Reserved	Reserved	0×B7
Node add R1–R2	Reserved	Reserved	Reserved	Reserved	0×7B
Node add R1–R2	Reserved	Reserved	Reserved	Reserved	0×B7
Node add R1–R2	Reserved	Reserved	Reserved	Reserved	0×7B

no grouping. Once the amount of data is larger than 6 bytes, grouping is used and M should be written with group number, which starts at 0x01 and arranges sequentially. In the last group M should be written with 0xFF to indicate a packet end.

The protocol sets aside 17 encryption data bytes, K(D13) could enable the encryption bytes. If K is 0x01, the receiver will decrypt the encrypted data, or the encryption data bytes will not be read to save time. The specific encryption method can use some classical algorithms such as DES or AES [7, 8].

5 Conclusion

This study researched a Web-based platform for the building monitoring, which uses STM32F407 microcontroller to communicate with various wireless nodes. The microcontroller obtains data by nodes' uploading and sends it to users through the

Internet, while users could make decisions according to the current information shown on the Web pages, and click the pages to send command. After received the Internet packets, the microcontroller instructs corresponding node to control different signals according to different commands. The system provides users a convenient, efficient and intelligent platform to achieve real-time monitoring capabilities, which could meet the needs of general monitoring occasions, and has broad applications, huge space of development, and wide extending to various areas.

References

1. Zhu Zhongying (2010) Progress and trends of sensor network and internet of things [J]. Microcomput Appl 26(1):1–3
2. Zhu Huiyan, Lin Lin (2012) Design of a wireless network communication system based on high performance microcomputer and nRF24L01[J]. Electronic Sci Technol 25(4):81–83, 91
3. Zhang Qi, Lao Chiyuan (2010) Analysis and improvement of light weight protocol stack LwIP [J]. Comput Eng Design 31(10):2169–2171, 2256
4. Shen Subin, Mao Yanqin, Fan Quli, Zong Ping, Huang Wei (2010) The concept model and architecture of the internet of things[J]. J Nanjing Univ Posts Telecommun (Nat Sci) 30(4):1–8
5. Yan Fan, Yeung Alan KH, Chen Guanrong (2013) A numerical study of energy consumption and time efficiency of sensor networks with different structural topologies and routing methods [J]. Commun Nonlinear Sci Numer Simul 18(9):2515–1526
6. Zhong Ke, Chen Xiangdong (2012) Design on smart home service gateway based on IoT [J]. Commun Technol 45(08):65–67
7. Shen Yongzeng, Yang Liya (2010) Smart home security wireless data transmission[J]. Comput Syst Appl 19(8):221–224
8. Chen Shaoquan, Wang Tao, Fan Hanbo (2012) STM32F407VG digital conversion precise design of the sampling rate[J]. Electronic World 15(08):134–135

A Novel Global Calibration Method for Multi-vision Sensors

Xinghua Li, Jingmei Zhang, and Peifen Chen

Abstract A novel high-precision global calibration method based on structured light and 2D target is proposed for the multiple vision sensors (MVS) measuring system. By capturing a series of feature points on the light plane at the same time, the relative position of local coordinate system and global coordinate system (GCS) can be acquired in the constraint condition of the uniqueness of a world point. The method is simple and low-cost, which is feasible for on-line measurement. The experiment is designed to illustrate the high-precision of the proposed method. The result shows that the average projection error is less than 0.5 pixel, which can meet the accuracy requirement of multiple camera.

Keywords Multi-sensor • Global calibration • Structure light • Local calibration

1 Introduction

Because of its high accuracy, timeliness, and other advantages, vision sensors measurement is widely used in industrial measurement in recent years [1, 2]. MVS measurement technology has obvious advantages in the industrial measurement. In MVS system, each sensor has independent coordinates, which make it impossible for different sensors to describe the scene in consistency, unless a global calibration is achieved.

Researches on the global calibration method of MVS have been done by lots of scholars and various solutions have been proposed. Kumar etc used plane mirror to achieve the global calibration [3]. This method requires a strict restriction for the location of the mirrors and the precision of calibration is not stable. Zhang Guangjun etc suggested the global calibration based on 1D target [4]. It is simple, but only

X. Li (✉) • J. Zhang • P. Chen
State Key Laboratory of Precision Measuring Technology and Instruments, Tianjin University of China, Tianjin, China
e-mail: li.xinghua@126.com; zhangjingmei2009@163.com

B. Zhang et al. (eds.), *The Proceedings of the Second International Conference on Communications, Signal Processing, and Systems*, Lecture Notes in Electrical Engineering 246, DOI 10.1007/978-3-319-00536-2_11,

one feature point can be obtained in each moving of the target and the extracting accuracy of feature point on target cannot be guaranteed. Hu Hao proposed a precise camera calibration method which based on close-range photogrammetry technology [5]. But this technique needs a large target and not portable, so it is inconvenient to use.

This paper proposed a simple and practical method of MVS's global calibration. The system just need a checkerboard which can be printed in lab and a structured light, What's more, this system has a lot of advantages. For example, it can calibrate the relationship of the position of all sensors quickly, the times of coordinate transformation in the proposed method are few. It has a high precision which has been confirmed by experiments.

2 Mathematical Model of Structured Light Vision Sensor

Figure 1 shows the geometrical model [6] of a structured light. The world coordinate frame and the camera coordinate frame $o_c\_x_c y_c z_c$ are the same, and the image plane coordinate are defined as *O-XY*. The relation between the world coordinates and the image coordinates can be illustrated by (1).

$$\begin{cases} \rho \begin{bmatrix} X \\ Y \\ 1 \end{bmatrix} = A \begin{bmatrix} x \\ y \\ z \end{bmatrix} \\ ax + by + cz + d = 0 \end{cases} \tag{1}$$

$A = \begin{bmatrix} \alpha_x & 0 & \mu_0 \\ 0 & \alpha_y & \nu_0 \\ 0 & 0 & 1 \end{bmatrix}$ is the known intrinsic matrix of the camer.ρis a unknown scale. $ax + by + cz + d = 0$ is the function of the light plane in the world coordinate.

3 Global Calibration for Multi-vision Sensors

3.1 Calibration of Single Structured Light Vision Sensor

The process to calibrate a structured light vision sensor includes two parts: camera calibration and projector calibration.

As the camera calibration, we use Zhang's method [7] to get camera intrinsic parameters and distortion factors [8]. In the experiment, we will correct image distortion before processing image.

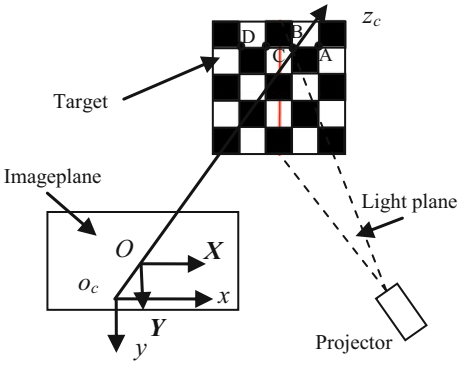

Fig. 1 Geometrical model of a structured light

As the projector calibration method, we use the method in the literature [6] and the method introduction is as follows.

Firstly we will determine the world coordinates of the target feature points. A plane chessboard is selected as the target. Corner points in each line of the chessboard can be seen as a 1D target, such as A B C D shown in Fig. 1. The laser should intersect with the target. The world coordinates of A C D are denoted by (x_A, y_A, z_A), (x_C, y_C, z_C) and (x_D, y_D, z_D). According to the relative positional relationship between the three points, we obtain the following equation:

$$(x_C, y_C, z_C)^T = (x_A, y_A, z_A)^T + h((x_D, y_D, z_D) - (x_A, y_A, z_A))^T \tag{2}$$

Where h is a known parameter. The image coordinates of A, C and D are denoted by (X_A, Y_A), (X_C, Y_C) and (X_D, Y_D), and they can be got from the Chessboard target. Depending on the camera imaging model and (2), we can get (3):

$$\begin{aligned}
&\alpha_x x_A - (X_A - \mu_0) z_A = 0 \\
&\alpha_y y_A - (Y_A - \nu_0) z_A = 0 \\
&\alpha_x x_D - (X_D - \mu_0) z_D = 0 \\
&\alpha_y y_D - (Y_D - \nu_0) z_D = 0 \\
&\alpha_x (1-h) x_A - (1-h)(X_C - \mu_0) z_A + \alpha_x h x_D - h(X_C - \mu_0) z_D = 0 \\
&\alpha_y (1-h) y_A - (1-h)(Y_C - \nu_0) z_A + \alpha_y h y_D - h(Y_C - \nu_0) z_D = 0
\end{aligned} \tag{3}$$

Because the distance L between A and D is known, we can get (4)

$$\|(x_D, y_D, z_D) - (x_A, y_A, z_A)\| = L \tag{4}$$

According to (3) and (4), we can get the world coordinates of the target feature points A and D. Then the world coordinates of point C can be determined by (2).

Secondly we will calculate the world coordinates of light plane feature point. The advantages of using corner points in each line of the chessboard as a 1D target are listed as follows. Firstly, at each position, more than one light plane feature points can be got. Secondly, the image coordinates of feature points in light plane

can be determined by two intersecting lines: one line is fit by the structured light and the other is matched through each row corner points in chessboard, such as corner points A C D shown in Fig. 1. This can improve the accuracy of the image coordinates of light plane feature point. The image coordinates of B is denoted by (X_B, Y_B). According to the camera imaging model, we can get (5).

$$\rho(X_B, Y_B, 1)^T = A(x_B, y_B, z_B)^T \tag{5}$$

The relative positional relationship of A, B and D is described in (6)

$$(x_B, y_B, z_B)^T = (x_A, y_A, z_A)^T + h_x((x_D, y_D, z_D) - (x_A, y_A, z_A))^T \tag{6}$$

Where h_x is unknown. According to (5) and (6), we can get h_x and obtain the world coordinates of point B by (6).

Thirdly we will get light plane coefficients assuming. we freely place the target at n positions within the FOV, light plane feature points denoted as (x_{Bi}, y_{Bi}, z_{Bi}) (i = 1,2,3... kn) can be obtained and k can be determined by the size of the chessboard. According to (1), the following objective function are created:

$$e(t) = \sum_{i=1}^{kn} F(x_{Bi}, y_{Bi}, z_{Bi}) \tag{7}$$

Where $F(x_{Bi}, y_{Bi}, z_{Bi}) = (ax_{Bi} + by_{Bi} + cz_{Bi} + d)^2$. Using the least squares method, light plane coefficients a, b, c and d can be got. Calibration of single structured light vision sensor is finished.

3.2 Global Calibration for MVS

Figure 2 shows the arrangement of MVS system. V_iCF (i = 1,2,3) represented the coordinate system corresponding to each camera respectively. GCS was established in V_1CF, and transformed V_2CF, V_3CF to V1CF coordinate system respectively to complete the global calibration of MVS.

The key to the conversion between two coordinate systems is to obtain the $[R, t]$ matrix that represents a relative positional relationship [9]. Take the solving of $[R_{21}, t_{21}]$ between the local coordinate system V_2CF and the global coordinate system V_1CF as an example, then illustrated the idea of global calibration.

As shown in Fig. 2, the point P on the Light-receiving surface was marked (X_{P1}, Y_{P1}) in the camera 1, and marked (x_{P2}, y_{P2}, z_{P2}) in the camera 2, then the two coordinate must meet (8).

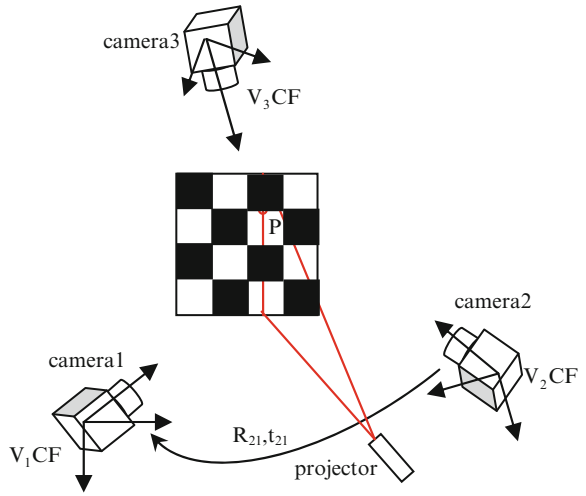

Fig. 2 The arrangement of MVS system

$$\rho \begin{bmatrix} X_{P1} \\ Y_{P1} \\ 1 \end{bmatrix} = A_1[R_{21}, t_{21}] \begin{bmatrix} x_{P2} \\ y_{P2} \\ z_{P2} \\ 1 \end{bmatrix} \tag{8}$$

The matrix A_1 represents the intrinsic parameters matrix of camera 1. $[R_{21}, t_{21}]$ represents the transformation from V_2CF to V_1CF. According to (8), if we get a series of image points in the camera1 and world points in the camera 2, we can obtain the outside parameter matrix $[R_{21}, t_{21}]$.

The following steps are used to complete global calibration:

1. According to Section 2, the positional relationship between the camera 2 and the light plane as shown in Fig. 2 can be determined.
2. Obtain the feature points in light plane by the chessboard. And camera 1 and 2 capture the images at the same time. Calculate the image coordinates (X_{P1}, Y_{P1}) of the feature point P in the camera 1.
3. Calculate the image coordinates (X_{P2}, Y_{P2}) of the feature point P in camera2.
4. According to the calibration results in step 1, calculate the world coordinates (x_{P2}, y_{P2}, z_{P2}) of the feature point P in the camera 2.
5. According to the size of the chessboard, we can get multiple image plane coordinates in camera1and world coordinates in camera 2 at each position. Then by freely moving the target, we can get enough image coordinate points in camera1 and world coordinate points in camera 2. Put the coordinates into (8), using the L-M optimization algorithm [10], we can obtain $[R_{21}, t_{21}]$.Other V_iFC (i = 3,4, ...) coordinate system can be transformed directly or indirectly through the above method. That is the global calibration method we proposed.

4 Experiment Result

The calibration results are shown as follows:

Camera 1: Intrinsic Matrx A_1

$$A_1 = \begin{bmatrix} 1605.638 & 0 & 640.945 \\ 0 & 1616.061 & 509.606 \\ 0 & 0 & 1 \end{bmatrix}$$

The radial and tangent distortion coefficients:
k_1 = -9.77 × 10-2, p_1 = 5.20 × 10-2, k_2 = 1.29 × 10-3, p_2 = -2.67 × 10-3
Camer 2: Intrinsic Matrx A_2

$$A_2 = \begin{bmatrix} 1607.821 & 0 & 674.013 \\ 0 & 1617.634 & 495.395 \\ 0 & 0 & 1 \end{bmatrix}$$

The radial and tangent distortion coefficients
k_1 = -8.65 × 10-2, p_1 = 4.13 × 10-2, k_2 = -2.17 × 10-3, p_2 = 1.16 × 10-3
Camer 3: Intrinsic Matrx A_3

$$A_3 = \begin{bmatrix} 1608.240 & 0 & 592.927 \\ 0 & 1618.168 & 477.667 \\ 0 & 0 & 1 \end{bmatrix}$$

The radial and tangent distortion coefficients:
k_1 = -8.67 × 10-2, p_1 = 8.60 × 10-2, k_2 = -9.17 × 10-3, p_2 = -9.72 × 10-3
The equation of the light plane1 under coordinate V_2CF:

$$x\text{-}0.017y - 0.588z + 293.375 = 0$$

The equation of the light plane2 under coordinate V_3CF:

$$x\text{-}0.002y - 0.692z - 324.375 = 0$$

The Rotation and Translation Matrix [R_{21},t_{21}]from V_2CF to V_1CF is:

$$[R_{21}, \mathrm{t}_{21}] = \begin{bmatrix} 0.561 & \text{-}0.0015 & \text{-}0.828 & 427.411 \\ \text{-}0.002 & 1 & \text{-}0.003 & \text{-}7.136 \\ 0.829 & 0.004 & 0.561 & 228.762 \end{bmatrix}$$

The Rotation and Translation Matrix [*R31*, *t31*] from V3CF to V1CF is:

Table 1 Calibration precision between camer 1 and camera 2

Feature point P	P's image coordinate in camera 1 (pixel)		P's image coordinate from camera 2 to camera 1 (pixel)		Δx	Δy
	X	Y	X`	Y`		
1	477.048	853.892	476.847	854.808	0.201	−0.916
2	462.476	771.734	462.458	772.521	0.018	−0.787
3	462.208	689.678	462.214	690.271	−0.006	−0.593
4	461.942	607.334	461.970	607.752	−0.028	−0.418
5	461.674	525.060	461.726	525.253	−0.052	−0.193
6	461.407	443.111	461.481	442.970	−0.074	0.141
7	461.141	361.185	461.237	360.679	−0.096	0.506
8	460.874	279.586	460.993	278.536	−0.119	1.05
9	479.034	198.497	478.889	196.850	0.145	1.647
10	478.785	844.717	478.634	845.857	0.151	−1.14
Average error					0.014	−0.070

Table 2 Calibration precision between camer 1 and camera 3

Feature point P	P's image coordinate in camera1(pixel)		P's image coordinate from camera 3 to camera 1 (pixel)		Δx	Δy
	X	Y	X`	Y`		
1	618.832	711.188	617.965	710.689	0.867	0.499
2	619.108	636.875	618.386	636.039	0.722	0.836
3	619.385	562.212	618.809	561.259	0.576	0.953
4	619.663	487.515	619.23	486.732	0.433	0.783
5	619.94	412.923	619.649	412.466	0.291	0.457
6	620.217	338.214	620.068	338.241	0.149	0.027
7	620.495	263.548	620.486	264.323	0.009	0.775
8	620.771	189.235	620.9	189.309	0.129	0.074
9	669.176	775.666	668.73	775.679	0.446	0.013
10	669.475	704.014	669.116	703.525	0.359	0.489
Average error					0.398	0.476

$$[R_{31}, t_{31}] = \begin{bmatrix} 0.303 & 0.002 & 0.953 & 427.411 \\ 0.026 & 1 & -0.011 & -11.486 \\ -0.953 & 0.028 & 0.302 & 319.533 \end{bmatrix}$$

An experiment to verify the accuracy of the calibration result is designed. Feature point P on light plane is selected. Camera 1 and 2 capture P at the same time. We can get P's image coordinate (X_{P1}, Y_{P1}) in camera 1.and P's world coordinate(x_{P2}, y_{P2}, z_{P2}) in camera 2 can be calculated according to the calibration result above. Equation (8) can make it possible to translate the coordinate (x_{P2}, y_{P2}, z_{P2}) to camera 1's image coordinate (X_{P1}', Y_{P1}'). The D-value between (X_{P1}, Y_{P1}) and (X_{P1}', Y_{P1}') could illustrate the precision of the calibration result. And the results are shown in Tables 1 and 2.

Ten feature points are obtained from light plane1 and 2. Calibration precision between camer1 and camera 2: the average reproject error in coordinate x is 0.014 pixel and -0.07 pixel in coordinate y. Calibration precision between camer 1 and camera 3: the average reproject error in coordinate x is 0.398 pixel and 0.476 pixel in coordinate y. The results of the experiment show that the method proposed above is feasible as well as high-precision.

5 Conclusions

The novel global calibration method for MVS proposed in this paper, which involved a structured light and plane target, provides a good accuracy. The method makes use of the uniqueness of the feature point to calculate the rotation and translations matrix between MVS. It is easy to use on-site with limited space. The target is easy to make with low-cost. What's more, the real experiment results show a good performance of the proposed methods.

References

1. Senoh M, Kozawa F, Yamada M (2006) Development of shape measurement system using an omnidirectional sensor and light sectioning method with laser beam scanning for hume pipes. J Opt Eng 45(6):064301
2. Chen F, Brown GM, Song M (2000) Overview of the three-dimensional shape measurement using optical methods. J Opt Eng 39(1):10–22
3. Kumar RK, Ilie A, Frahm JM (2008) Simple calibration of non-overlapping cameras with a mirror. Comput Vis Pattern Recogn 2008:1–7
4. Huang BK, Liu Z, Zhang GJ (2011) Global calibration of multi-sensor vision measurement system based on line structured light. J Optoelect Laser 22(12):1816–1820
5. Hu H, LIANG J, Tang ZZ, Shi BQ, Guo X (2012) Global calibration for multi-camera videogrammetric system with large-scale field of view. Optic Precis Eng 20(2):369–378
6. Wei Z, Cao L, Zhang G (2010) A novel 1D target-based calibration method with unknown orientation for structured light vision sensor. Optic Laser Tech 42(4):570–574
7. Zhang ZY (2000) A flexible new technique for camera calibration. J Pattern Anal Mach Intell IEEE Trans 22(11):1330–1344
8. Helferty JP, Zhang C, McLennan G, Higgins WE (2001) Video endoscopic distortion correction and its application to virtual guidance of endoscopy. J IEEE Trans Med Imaging 20 (7):605–617
9. Liu Z, Zhang G, Wei Z (2011) Novel calibration method for non-overlapping multiple vision sensors based on 1D target. Opt Lasers Eng 49(4):570–577
10. More J (1978) The Levenberg-Marquardt algorithm, implementation and theory. Numer Anal Lect Notes Math 630:105–116

Part II
Image and Video Processing

Research on Face Recognition Method Based on Combination of SVM and LDA-PCA

Ruian Liu, Junsheng Zhang, Lei Wang, and Mimi Zhang

Abstract In the face recognition, the nonlinear factors, such as the light, expression and gesture, has great changes, the recognition effect of the PCA algorithm has been seriously influenced. This paper proposes an LDA-PCA algorithm, that merged the idea of LDA (Linear Discriminant Analysis) into PCA algorithm, to obtain the eigen-face subspace and use of the LDA's idea to discriminate and analyze, and then select the feature face vector, mainly reflecting the category difference, to form a new subspace. Then taking use of SVM classifier on the new subspace. The simulation results, on the improved face database, show that the LDA-PCA algorithm can effectively improve the robustness of nonlinear factor and the face recognition rate.

Keywords Principal component analysis (PCA) • Linear discriminant analysis (LDA) • Support vector machine (SVM) • Face recognition

1 Introduction

Principal component analysis (PCA) based on the K-L transformation is a statistical analysis method. It is one of the most widely used methods in facial feature extraction. PCA algorithm also can effectively reduce the dimensions of the face image, and retain most of the main information of original data [1–3]. The methods of PCA algorithm can retain the original image information and extract the feature vectors optimally in the sense of covariance. It transform the face image matrix into one-dimension vector in order to extract the feature vectors. But the one-dimension vectors has transformed are at a disadvantage on the effective feature extraction. At the same time, this would make the algorithm and space complexity higher.

R. Liu (✉) • J. Zhang • L. Wang • M. Zhang
College of Electronic and Communication Engineering, Tianjin Normal University, Tianjin, China
e-mail: ruianliu@sina.com

B. Zhang et al. (eds.), *The Proceedings of the Second International Conference on Communications, Signal Processing, and Systems*, Lecture Notes in Electrical Engineering 246, DOI 10.1007/978-3-319-00536-2_12,

Therefore, Yang and other authors [4] propose the two-dimension PCA (2DPCA) method which is differ from PCA it doesn't require to transform the face image matrix into one-dimension vectors beforehand. The experiments have proved that 2DPCA method simplified the computation, improved the speed of feature extraction and obtained better recognition effect. On the other hand, the draw off of PCA algorithm is the global feature of image. When the conditions, such as light, have changed greatly, the local characteristics are also changed, so the recognition effect will not be ideal. For this reason, Chen and other authors [5] put forward the modular 2DPCA method based on the traditional 2DPCA method. It is able to extract the local features of images so that preferably reflects the differences between the images. After, Zhang [6] proposes a improved modular 2DPCA algorithm. It is a kind of method based on the intra-class adaptive weighted average method. Then Sun and others [7] put forward the modular kernel principal component analysis (MKPCA) method.

PCA method only consider the second order statistics of image data, but ignore the higher order statistics which contain much important information. It cannot be overcome the affection of the performance of recognition when the attitude change, face expression and so on in light condition. Therefore, this article proposes a LDA-PCA algorithm. This method put the linear discriminant analysis (LDA) into the PCA algorithm. Taking advantage of the Wavelet Transform on the face image preprocessing, in order to reduce the dimension and reduce the computational complexity and space complexity. It extracts the effective local information of face images, and removes the image noise. This method selects feature vectors of mainly reflecting the differences inter-classes to construct a new subspace. According to the characteristics of support vector machine (SVM), that can find out the optimal linear classification in the feature space [8], It classify the face images in the new subspace. The LDA-PCA algorithm improves the robustness of the face recognition under the nonlinear factors such as facial expression, illumination conditions, etc.

2 Face Recognition Based on LDA-PCA Algorithm

2.1 Description of LDA-PCA Algorithm

Suppose the face training sample set is $\{T_i | i = 1, \cdots, M\}$, M is the total sample number of the training samples. Taking use of the PCA method, It can obtain the eigenface subspace $U = [u_1, u_2, u_3, \cdots, u_k]$. In order to improve the classification accuracy, it must select the eigenvectors, which mainly reflect the differences between classes, to construct subspace from all the eigenvectors. Suppose c is the class number of the training samples, c_k is part of sample number of the sample of class k. $\overline{m}_k$ is the mean vector of the sample of class k. $\overline{m}$ is the mean vector of all samples. S_W is the subspace projection of the ith eigenvector corresponding to the

intra-class scatter matrix. S_B is the subspace projection of the ith eigenvector corresponding to the inter-class scatter matrix.

$$Var_{\text{inter}}(U_i) = \det(S_B) = \det\left[\sum_{k=1}^{c}\left(U_i^T\overline{m}_k - \overline{m}\right)\left(U_i^T\overline{m}_k - \overline{m}\right)^T\right] \tag{1}$$

$$\begin{aligned} Var_{\text{intra}}(U_i) &= \det(S_W) \\ &= \det\left[\sum_{i=1}^{c}\sum_{t\in c_k}\left(U_i^T T_t - U_i^T\overline{m}_k\right)\left(U_i^T T - U_i^T\overline{m}_k\right)^T\right] \end{aligned} \tag{2}$$

$Var_{\text{int }er}(U_i)$ is the difference of inter-class of the ith eigenvector W_{i}. $Var_{\text{int }ra}(U_i)$ is the difference of intra-class of the ith eigenvector U_i.

$$Q = \max\left(\frac{Var_{\text{inter}}(U_i)}{Var_{\text{intra}}(U_i)}\right) \tag{3}$$

According to the value of Q, It can get the eigenvalues in increasing order of PCA.

$$a = \sum_{i=1}^{q}\lambda_i \Big/ \sum_{i=1}^{M}\lambda_i \tag{4}$$

The new subspace is constructed by selecting q feature vectors that is mainly reflected the difference of inter-class. Linear analysis by the LDA-PCA method is in one-dimensional subspace projection. It avoids the singularity of the intra-class scatter matrix. At the same time, this method solves the problem of small samples in LDA method.

2.2 Face Recognition Based on LDA-PCA Algorithm

As mentioned above, the LDA-PCA method for face recognition adopted by this article contains four steps: First is the image preprocessing; Second is the low-frequency information identification by the wavelet transform; Third is the extracting features by PCA algorithm; The last step is classification by SVM method. Basic steps are as follows:

1. Read-in the face database
   Selecting a set number of images to constitute the training sets from all images of each person in face database, and the remaining images constitute the test sets. It takes the appropriate pretreatment method to preprocess under the same standard.
2. Construction of the eigenface subspace

Taking use of PCA algorithm on the sample sets, It can get p eigenvectors. Recognition of face images by the PCA method doesn't use all eigenvectors to construct the eigenface subspace, but just select. These eigenvectors, containing the main energy of images, belong to the low frequency components, and have the rough shape of face images. They play vital roles in the recognition. For the smaller eigenvectors corresponding to the eigenvalues, they belong to the high-frequency components. They not only contain less energy, but also describe the detail information of face images. These high-frequency components influence the face recognition on the small side, and include some interference noise impacted the results of recognition. As the general method, It would give up these high-frequency components. So the PCA method of face recognition just selects the first k larger eigenvectors corresponding to the eigenvalues to approximately express the face images, and construct the eigenface subspace.

3. Computing $Var_{\text{int } er}(U_i)$ and $Var_{\text{int } ra}(U_i)$

   It selects q feature vectors that mainly reflex the different inter-class to construct subspace U, and project the test images to the subspace U. It projects the preprocessed face images of test set into the eigenface subspace U. It gains a set of coordinate coefficient in the subspace, and shows the exact position of this image in the subspace. It is called the facial feature vector, as identification characteristics of the face image. Different coefficients correspond to different face images, the face images can completely be represent by a set of coefficients of the subspace.

4. SVM classification method for face recognition

   LDA-PCA face recognition algorithm selects the new subspace which mainly reflecting difference of inter-class. According to the characteristic of SVM that can find out the optimal linear classification, LDA-PCA can classify the face images of the new subspace.

3 Results and Analysis

3.1 Choice of the Training Sample Set Impacts on the Recognition Rate

First way of experiments takes a part of the database as the training set, the remains are the test set. The second way of experiments takes a part of the database as the training set, too. But it takes all the database as the test set. The first case selects the face images in the ORL database to be the training samples; the second case uses the ordered ORL face database as the training samples.

It experiments in two different conditions as follow:

Figure 1 is the example of the face images. If it chooses top five pictures of the Fig. 1a as the training sample, it shows that image 1 and image 3 have small differences, and the image variation range doesn't contain the condition of image

Fig. 1 Part of the face image in ORL face database. (**a**) is the ten images of original database. (**b**) is the ten images of ordered database

9. So it only needs to choose one of the image 1 and 3 as the training sample, taking the image 9 as the test sample. The images are adjusted the order as shown in Fig. 1b. In the Fig. 1b, the top five images basically cover the images that are different rotation angles from left to right and from top to bottom, etc. The range of rotation angles are on the small side.

Figures 2 and 3 show the experimental results about the ordered or disordered face database, and the choice of test sets. It takes image 1–9 of the ORL and ordered face database as the training set, respectively they are 40, 80, 120, 160, 200, 240, 280, 320 and 360. The rest of the images as the test sets, which respectively are 360, 320, 280, 240, 200, 160, 120, 80 and 40. It uses PCA algorithm to extract features and SVM to classify and recognise. Figure 2 shows the recognition rate of the test sets are the part of the ORL database.

It takes image 1–9 of the ORL and ordered face database as the training sets, respectively they are 40, 80, 120, 160, 200, 240, 280, 320 and 360. All the face image as the test sets, which respectively are 400. It uses PCA algorithm to extract features and SVM to classify and recognise. Figure 3 shows the recognition rate of the test sets are all the ORL database.

The experimental result shows that there are differences between recognition results in both cases of the training sample. When the disordered face images are the training sample, the same kinds of samples are similar in illumination, pose, expression. It cannot contain the range of other images. So the recognition effect is poorer. After sorting, the difference of the training images is larger. It can contain different changes more widely in illumination, pose, expression. So the recognition effect is better, and the recognition time is the same, the complexity of the calculation doesn't increase.

3.2 Number of Principal Components and Different Classifiers Impact on Recognition

The choice of the number of principal components in the PCA algorithm is a very critical problem. To more accurate approximation of the original face image, the

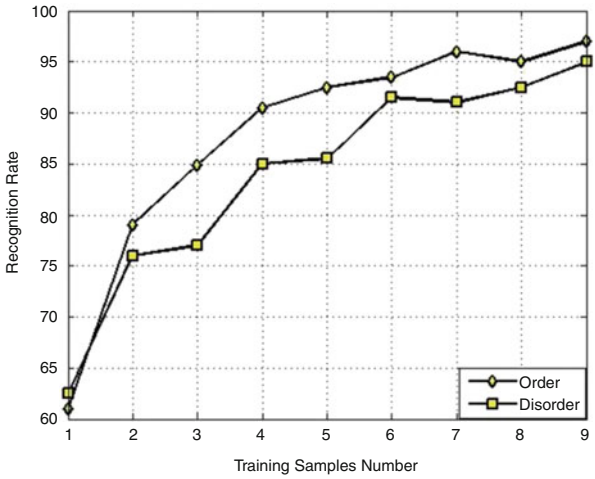

Fig. 2 Remaining test sets as the training sets

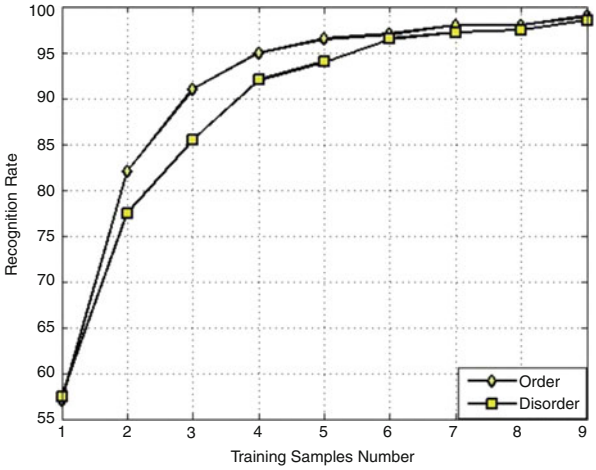

Fig. 3 All database as the test sets

selected principal components are the more the better. But choose the principal components too many, on the one hand, will increase the complexity of the calculation, thereby prolong time, and greatly reduce the real-time performance of image recognition. On the other hand, the smaller eigenvectors corresponding to the eigenvalues contain the less image information, and it may introduce the noise or the factors of interference identification. But if the selected principal components too small, it can loss some main information in favor of the classification. So according to the variance contribution rate, it selects the top k eigenvectors.

This experiment adopts the improved ORL face image database of face image. The top five of each type is the training sample set, after five is the test sample set. In the experiments, the images are preprocessed by the histogram equalization and wavelet transform, extracted of the feature by PCA. The classification method takes

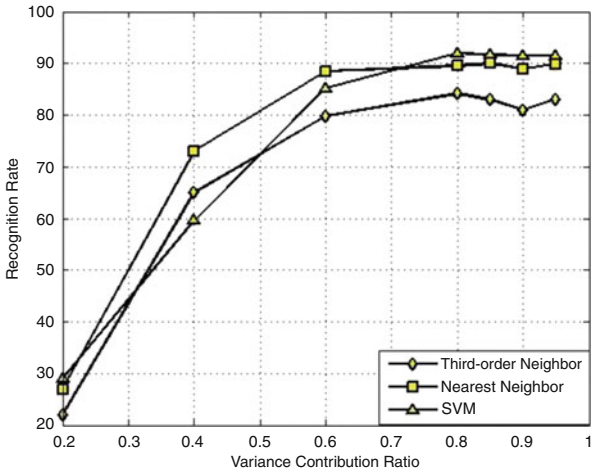

Fig. 4 Three kinds of classification methods

the third-order neighbor, nearest neighbor, and the SVM to classify the test samples. Recognition rate is as shown in Fig. 4:

Experiment results show that selecting the different number of components can influence the function of classifier for recognition. When the contribution rate is 0.7, the recognition rate of SVM and the nearest neighbor method can reach 90 %. As the principal components are more, the effect of SVM classifier is more remarkable.

3.3 Recognition Rate Comparing Based on Different Face Recognition Methods

Figure 5 is the comparison of the recognition rate of face recognition by the LDA, PCA, 2DPCA, NMF and LDA-PCA, etc methods. It shows that when the training samples are big enough, the LDA-PCA method can obtain very good recognition effect.

Experiment results show that the LDA-PCA method for human face recognition rate changes with the change of training samples. When the training sample reaches a certain degree, the recognition rate will change no longer significantly. It is only when the training samples are partial smaller, it has the particularly evident change. This is because the eigenvectors, which can best represent the difference of inter-class, are in the front.

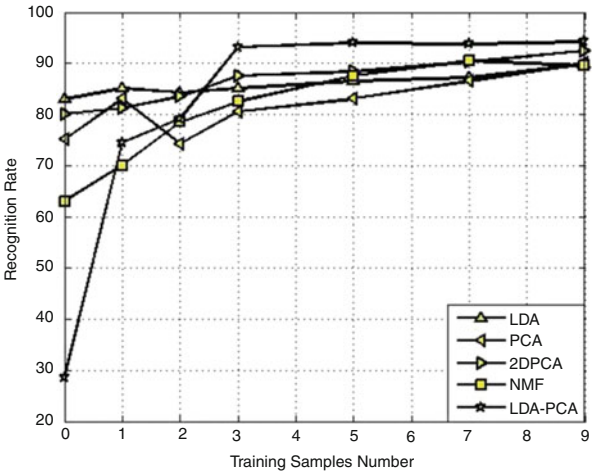

Fig. 5 The image recognition rate of various face recognition methods

4 Conclusion

In the process of face recognition, there will be a part of the face image deviates from the class, leading to an error identification. Therefore a LDA-PCA method is put forward. It puts the linear discriminant analysis (LDA) into PCA algorithm, and selects feature vectors of mainly reflecting the differences inter-classes to construct a new subspace. Linear analysis by the LDA-PCA method is in one-dimensional subspace projection. It avoids the singularity of the intra-class scatter matrix. At the same time, this method solves the problem of small samples in LDA method. Simulation experiments, on the improved ORL face database, prove that the LDA-PCA algorithm can effectively improve the recognition rate of face recognition, and increase the robustness of the algorithm to a certain degree.

Acknowledgment This research was supported by the Tianjin natural science Fund (13JCYBJC15800).

References

1. Pantic M, Rothkrantz LJM (2000) Automatic analysis of facial expressions: the state of the art. IEEE Trans Pattern Anal Mach Intell 22(12):1424–1445
2. Peng H, Zhang C, Rong G et al (1997) Research of automated face recognition based on K-L transform. J Tsinghua Univ (Sci Tech) 3:67–70
3. Sun D, Li L, Wu L (2001) Face recognition feature space optimization method. Signal Process 17(6):510–514
4. Yang J, Zhang D, Frangi A et al (2004) Two-dimensional PCA: a new approach to appearance based face representation and recognition. IEEE Trans Pattern Anal Mach Intell 26(1):131–137
5. Chen F, Chen X, Zhang S et al (2006) A human face recognition method based on modular 2DPCA. J Image Graph 11(4):580–585

6. Zhang L (2010) Face recognition method using improved modular 2DPCA. Comput Eng Appl 46(13):147–150
7. Sun Z, Wang F, Wu X (2012) Face recognition based on modular Kernel principal component analysis. Comput Digit Eng 40(8):119–121
8. Bian Z, Zhang X (2007) Pattern recognition. Tsinghua University, Beijing, pp 87–91, 222–226

Adaptive Retinex Tone Mapping for Image Enhancement under Nature Light

Yunfeng Sui

Abstract A novel image enhancement approach is proposed for images acquired under dynamic nature light illuminations using a single image. It has satisfactory performance in both global light compression and local tone mapping. Our method is based on multi-scale retinex, which provides a reliable, but not accurate on details, estimation of the global illumination. The contribution of our approach is first to apply edge-preserving filters to preserve details, reduce halo artifacts and increase image quality on edges. Second, a light channel is introduced in our approach for fast light estimation and color restoration. From experimental results, we show that our method provides satisfactory results under dynamic nature light illuminations, and demonstrate the performance improvements over multi-scale retinex method.

1 Introduction

A common problem in generating images (or video sequences) is that the captured images are often different from what is seen though human eyes, especially under dynamic light range. In most of these situations, images rendered are poor compared to human observations. Regions in shadows are often under-exposed while regions under direct illumination are often over-exposed. The advantage of human observation is significantly contributed by the color constancy feature of color perception system, which ensures that the perceived energy of light stays relatively constant under varying illumination conditions.

Reducing the impact of dynamic light source and enhancing the quality of the image is highly desired in both consumer/computational photography and computer vision applications. First, most computer vision algorithms assume the input image

Y. Sui (✉)
The second research institute of CAAC, Chengdu, China
e-mail: yunfengsui@gmail.com

B. Zhang et al. (eds.), *The Proceedings of the Second International Conference on Communications, Signal Processing, and Systems*, Lecture Notes in Electrical Engineering 246, DOI 10.1007/978-3-319-00536-2_13,

is the scene radiance under uniform illumination within normal range. The performance of these algorithms will inevitably suffer from high dynamic illumination. Second, since both human visual recognition system and recognition algorithms are heavily depended on local contrast. When the dynamic range of illumination exceeds the dynamic range of a scene, there is an irrevocable loss of information considering the limits of the recording medium. Compressing the difference between dark and bright regions and increasing the difference of scene radiance provides more accurate information for both human and computer vision algorithm.

However, reducing the impact of dynamic light source and enhancing the quality of the image is a challenge problem. The image signal received by the sensor is a combinational effect of light source, scene radiance and light transmission. The problem is under-constrained with only one observed image. Many methods [2, 9, 16] has been proposed to solve this issue. In general, these approaches are referred to as tone mapping. One long-studied and competitive category of methods is retinex [6] based. Adapted from human vision and recognition system, retinex-based methods bridge the gap between color images and human observation of the scene [7, 12, 15].

In this paper, we proposed a novel approach to enhance image quality under dynamic illumination condition based on the concept of retinex. Over years, retinex based approaches evolved from a random walk computation to single kernel operation, then to multiple kernels. There are three major drawbacks on the latest approaches [1, 10, 13]: (1) the choice of kernel sizes is related to the image contents, (2) halo artifacts on the edges between light and shadow, and (3) difficult for true color restoration. Our approach is targeted for these drawbacks. An edge preserving filter is applied to solve the first and second drawbacks in one shoot. While a light channel based illumination estimation is proposed to solve the third one and to provide guidance information for edge preserving filter.

Our method provides an approach to reproduce images that are similar to what a person observes the scene. It is able to enhance the quality of the image especially under dynamic illuminations with high performance both in dynamic range compression and detail preserving. First, edge preserving filter works equivalently in adaptively modifying the kernel size based on the image contents. It works even better in removing the halo artifacts, and makes the image sharp and clear. Second, the light channel provides a reliable information source for estimating the illumination. In addition, it solves the color restoration issue fast and accurately. The assumption limits the algorithm to white light scene. But it is assumption is valid for a large number of situations.

The remainder of this paper is organized as follows. Section 2 introduces the evolution of retinex based approaches and the drawbacks of current approaches. Our approach to solve these drawbacks is proposed in Sect. 3. The performance of our approach is demonstrated in Sect. 4. Finally Sect. 5 concludes our work.

2 Background

Inspired by human color perception system, Land proposed the concept of retinex [6], a combination of retina and cortex. Over years, Land and McCann developed the algorithm in a form similar to the neurophysiological functions of individual neurons in the primate retina, lateral geniculate nucleus, and cerebral cortex. It describes the formation of an image, simple but widely used, as follow:

$$I(x,y) = L(x,y)R(x,y)$$

Where $I(x,y)$ is the observed intensity, $R(x,y)$ is the scene radiance, $L(x,y)$ is the illumination and (x,y) are the pixel coordinates in image. The scene radiance $R(x,y)$ is what we are interested. However, the observation $I(x,y)$ is severely impacted by dynamic illumination $L(x,y)$. The goal of image enhancement is to recover $R(x,y)$ and remove $L(x,y)$ from $I(x,y)$:

$$log(R(x,y)) = log(I(x,y)) - log(L(x,y))$$

For estimating the illumination $L(x,y)$, Land's algorithms evolved from a random walk computation to a center spatially opponent operation [7, 8]:

$$log(R_i(x,y)) = log(I_i(x,y)) - log(F(x,y) * I_i(x,y))$$

Where $*$ denotes 2D convolution, i is the index for each color spectral band ($i = 1,2,3$ for red, green and blue), and $F(x,y)$ is a Gaussian surround function:

$$F(x,y) = K \exp(-(x^2 + y^2)/c^2)$$

where c is the Gaussian surround space constant, and K is the normalization factor such that $\int\int F(x,y)dxdy = 1$. Initially, it was proposed for general purpose automatic image enhancement. Later feedbacks indicate that it works well for dynamic illumination problems. But it is not able to use a fixed kernel that works well for universal images.

More recently, Rahman, Jobson and Woodwell improved the retinex algorithm from single center spatially opponent operation, which is often referred to as single-scale retinex (SSR), to multiple kernels (multi-scale retinex, MSR) [5, 12, 13]:

$$R_{MSR_i} = \sum_{n=1}^{N} \omega_n R_{n_i}$$

where N is the number of scales, ω_i is the weight associated with the nth scale, R_{n_i} is the ith component of the nth scale, and R_{MSR_i} is the ith spectral component of the MSR output. The only difference is that at each scale, $R_n(x,y)$ has unique kernel size.

The choice of kernel operator size is a major limitation on the robustness of the algorithm. A kernel of smaller size emphasizes details and works well for high frequency illumination variances. While a bigger size one has more reliable estimation of illumination and works well for low frequency illumination variances. By using multiple kernels, MSR achieves a balance between dynamic range compression and tonal rendition. However, it is not able to adaptively modify the weights and sizes of different cores based on the contents of the image.

For the purpose of having accurate local illumination estimation and fine local toning, latest research on retinex focuses on adaptive approaches. NASA Langley research center developed an automatic approach for images enhancement, which took adaptive algorithms and parameters for image enhancement using the overall evaluation feedbacks from visual servo [15]. Bertalmio [1] proposed an anti-symmetric retinex algorithm with emphasis on both under-exposed and over-exposed image regions. Meylan [10] introduced an adaptive filter and a sigmoid function to generate better local tone. However, none of these approaches solve the halo problems introduced by kernels and the local tone performance is poor.

3 Adaptive Retinex Tone Mapping Model

3.1 Estimating the Illumination Using Light Channel

We assume the source of illumination is white light, which is valid for a large number of scenes, such as nature light. In most situations, the objects in the scene only absorb a certain band(s) of the light spectrum. The light outside the absorption band(s) is reflected at large. In our case, L_r, L_g and L_b are equal for the illumination. During the image formation, part of the energy is absorbed that makes $I_r \leq L_r, I_g \leq L_g$ and $I_b \leq L_b$. The maximum value of I_r, I_g and I_b is closest to the true value of illumination intensity at a particular pixel location. Since some object reflect more energy than others. The maximum reflection over a small image patch represents the illumination over this area more accurately. As a result, we estimate the local illumination intensity in the following form:

$$J(x,y) = \max_{(x',y')\in\Omega(x,y)} \left(\max_{i\in\{r,g,b\}} (I_i(x',y')) \right)$$

where $\Omega(x,y)$ is a local patch centered at (x,y). $J(x,y)$ is referred to as light channel in the remaining of this paper. In short, the light channel $J(x,y)$ is computed by finding the maximum value from all color channels in a small local patch. And the global illumination is estimated as follow:

$$L_g(x,y) = \sum_{n=1}^{N} log(F_n(x,y) * J(x,y))$$

3.2 *Edge Preserving Filter*

The process of light estimation is very similar to image noise removal filtering in terms of smoothing away noise while maintaining sharp edges. Many edge-preserving smoothing operators [3, 11, 14] have been proposed for a variety of applications, such as high dynamic range compression, image stitching, and image matting. In our approach, a guided image filter algorithm [4] is applied, which generates the filtering output by considering the content of a guidance image. It has better behavior near the edges, and it has a fast and non-approximate linear-time computation complexity.

Edge preserving filter is used to remove halo artifacts after steps taken in Sect. 3.1. It refines the local light estimation without modifying the kernel sizes. The light channel image $J(x,y)$ is taken as the guidance image to refine the global illumination estimation $L_g(x,y)$. Our experiments indicate that using light channel as guidance image has better performance than using original color or grey image. The output of this step $L'(x,y)$ is taken as the final illumination to recover the scene radiance:

$$log(R_i(x,y)) = log(I_i(x,y)) - log(L'(x,y))$$

followed by an exponential operation and a linear intensity stretching operation that converts image intensities into normal range.

4 Experimental Result

A large number of experiments have been conducted to test our approach against MSR under a variety of scenes. We set constant parameters in all of these experiments to evaluate the robustness of our approach. All experiments indicate this set of parameter works well regardless of the contents of the image.

Figure 1 demonstrates the different illumination estimation results. Clearly, our method works well in removing the halo artifacts. Meanwhile, the illumination intensity estimation result is more accurate. As we can see from Figs. 2 and 3, our method generates better quality results both in the very dark and very bright regions. More results are provided in Fig. 4 to demostate fine local tone mapping of our approach as well.

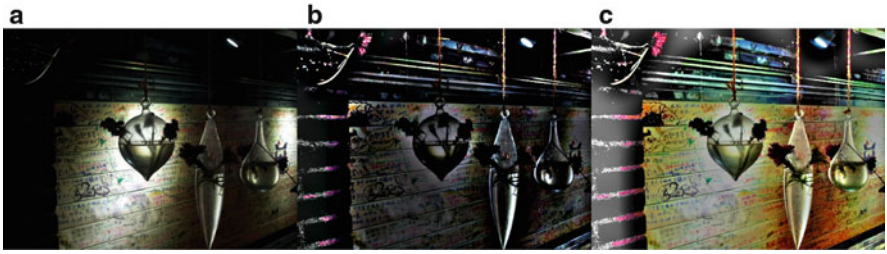

Fig. 1 (**a**) An image captured under high dynamic range illumination. (**b**) The estimated illumination using MSR (**C**) The estimated illumination using our approach (output in step Sect. 3.2)

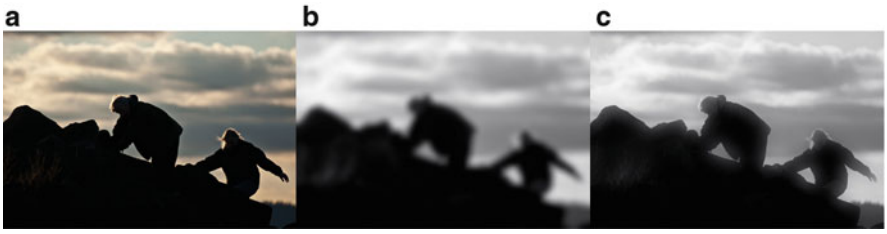

Fig. 2 High dynamic range compression and image enhancement using a single image under white light. (**a**) input image. (**b**) output of multi-scale retinex method. (**c**) output of our approach

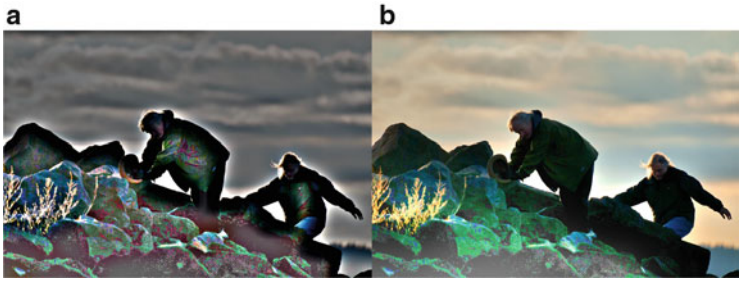

Fig. 3 The recovered result using MSR (**a**) and our approach (**b**) for image given in Fig. 1

5 Conclusion

In this paper, we have proposed a novel approach for image tone mapping under high dynamic range illumination. Our approach is based on multi-scale retinex model combined with light channel estimation and edge preserving filter. A light channel model is proposed against color restoration issue for fast and accurate estimation of light globally. Edge preserving filter is applied to refine the local light estimation, which removes the halo artifacts and provides more accurate estimation in details. This approach is able to enhance image quality by high dynamic range

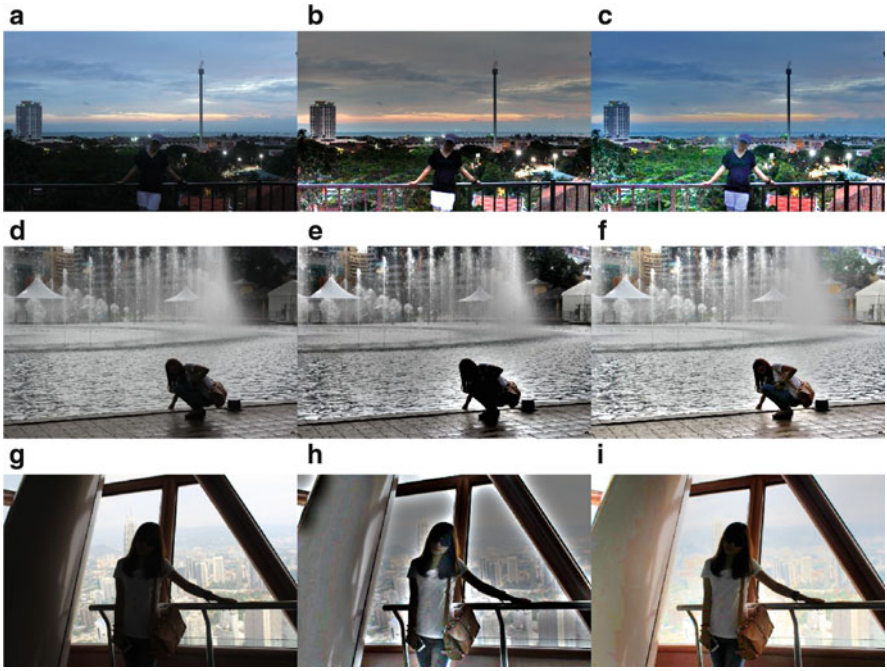

Fig. 4 Two more sets of experimental results. Figures in left column are the original images (**a**, **d**, and **g**). Figures in middle column are the results of MSR method (**b**, **e**, and **h**). Figures in the right column are the results of our method (**c**, **f**, and **i**)

compression. It also solves the color consistency and tonal rendition very well, which are often the side effects of HDR compression. Experimental results also demonstrate the improvement of performance over MSR.

Acknowledgements This work is partially supported by the National Natural Science foundation of China (No. 61139003). The authors would like to thank the anonymous reviewers and editors for their helpful comments and suggestions.

References

1. Bertalmio M, Caselles V, Provenzi E (2009) Issues about retinex theory and contrast enhancement. Int J Comput Vis 83(1):101–119
2. Devlin K (2002) A review of tone reproduction techniques. Technical report, Dept. Comput. Sci., Univ. Bristol, Bristol, U.K., 2002
3. Durand F, Dorsey J (2002) Digital photography with flash and no-flash image pairs. In: ACM SIGGRAPH, pp 257–266, 2002
4. He K, Sun J, Tang X (2010) Guided image filtering. In: European conference on computer vision, pp 1–14, 2010

5. Jobson D, Rahman Z, Woodell G (1997) A multiscale retinex for bridging the gap between color images and the human observation of scenes. IEEE Trans Image Process 6:965–976
6. Land E (1964) The retinex. Am Sci 291–306
7. Land E (1986) Recent advances in retinex theory. Vis Res 26(1):7–21
8. Land E, McCann JJ (1971) Lightness and retinex theory. Vis Res 61(1):1–11
9. Larson GW, Rushmeier H, Piatko C (1997) A visibility matching tone reproduction operator for high dynamic range scenes. IEEE Trans Visual Comput Graph 3(4):291–306
10. Meylan L, Susstrunk S (2006) High dynamic range image rendering with a retinex-based adaptive filter. IEEE Trans Image Process 15(9):2820–2830
11. Petschnigg G, Szeliski R, Agrawala M, Cohen M, Hoppe H, Toyama K (2004) Digital photography with flash and no-flash image pairs. In: ACM SIGGRAPH, pp 664–672, 2004
12. Rahman Z, Jobson D, Woodell G (1996) Multiscale retinex for color image enhancement. IEEE Int. Conf. Image Process 3:1003–1006
13. Rahman Z, Jobson D, Woodell G (2004) Retinex processing for automatic image enhancement. J Electron Imag 13(1):100–110
14. Tomasi C (1998) Bilateral filtering for gray and color images. In: Internation conference on computer vision, pp 839–846, 1998
15. Woodell G, Jobson D, Rahman Z (2005) Enhancement of imagery in poor visibility conditions. In: SPIE, sensors, and command, control, communications, and intelligence technologies for homeland security and homeland defense, vol 5778, pp 1–11, 2005
16. Xiong Y, Saenko K, Darrell T, Zickler T (2012) From pixels to physics: Probabilistic color de-rendering. In: IEEE intl. conf. on computer vision and pattern recognition, pp 1–8, 2012

True-Error Detection of Compressed Video: Temporal Exploration

Xudong Zhao, Shenghong Li, Chenglin Zhao, and Shilin Wang

Abstract In this paper, we propose a novel error detection method in the temporal domain for H.264/AVC encoded video streams. The corrupted macro blocks (MBs) are detected by exploiting the correlations between MBs in the neighboring two frames. Correlation coefficient and mean of residual block are introduced to quantify the correlations in the temporal domain. A supervised classifier based on probability density functions of proposed features is designed for error detection and expectation maximum algorithm is employed to find the optimal parameters of the classifier. Eight corrupted H.264/AVC encoded video sequences are used in our experimental work for test, and experimental results show that the proposed error detection method can detect the corrupted MBs effectively.

Keywords H.264/AVC • Error detection • Expectation maximum algorithm

1 Introduction

H.264/AVC encoded streams are vulnerable to transmission errors because of the use of predictive coding and variable-length coding (VLC) [1, 2]. Therefore, error resilience techniques are essential in video communications. Much research effort has been made to investigate how to conceal corrupted areas due to data loss within video streams. Unfortunately, it is sometimes too late because decoders might concatenate neighboring bits of the true error into some code word in the code table. In convenience, let false-match be such wrong but decodable bit concatenation in video decoding and no-match be a non-decodable code-word in the sense of

X. Zhao (✉) • S. Li • S. Wang
Department of Electronic Engineering, Shanghai Jiao Tong University, Shanghai, China
e-mail: zxd_1220@sjtu.edu.cn

C. Zhao
School of Information and Communication Engineering, Beijing University of Posts and Telecommunications, Beijing, China

B. Zhang et al. (eds.), *The Proceedings of the Second International Conference on Communications, Signal Processing, and Systems*, Lecture Notes in Electrical Engineering 246, DOI 10.1007/978-3-319-00536-2_14,

syntax and/or semantics of video standards. An error would not be detected until such false-match deteriorates into no-match. All analysis thus far started the thinking about efficient true-error detection algorithms. Without loss of generality, it is assumed true-error detection consists of two steps: first, error detection has been done by no-match in video decoders and all the corrupted areas of current picture would be recorded before decoding the following picture; second, error detection would then identify the true beginning position of corrupted MBs and which is our concern in this paper.

In the past few years, several methods have been proposed for error detection. In [2], syntax analysis based method exploiting the code words as well as range and significance of the H.264/AVC information elements was proposed to detect the errors in H.264/AVC encoded video streams. Experimental results of this method showed that about 57 % of the corrupted MBs were detected. Image content based detection methods were proposed in [3, 4], and corrupted MBs were detected in the pixel domain using different features. However, thresholds of all these methods were set heuristically which limits their applications. Two-class classifier based methods were also proposed to detect visually corrupted MBs; Farrugia in [5], and [6], employed probability neural network and support vector machine (SVM) respectively to detect visually distorted MBs in the compressed video streams. However for the two-class classifier based methods, the detection results are affected greatly by the training samples, i.e., inappropriately selected training set could degrade the detection performance, which limits their applications.

In this paper we propose a one-class classifier based method to detect corrupted MBs in the temporal domain, that is, image contents based features are extracted in the neighboring two frames, which are treated as discriminative features for classification. A simple and effective scheme is designed for error detection. Experimental results show that the proposed detector can achieve a relatively high detection rate with low false positive rate. The rest of this paper is organized as follows. Feature extraction method in temporal domain is introduced in Sect. 2. Section 3 describes the classifier design approach and the parameter estimation method. Experimental results and performance analysis are given in Sect. 4. Finally, conclusions are drawn in Sect. 5.

2 Feature Extraction

H.264/AVC consists of two encoding strategies: intra (I) frames and inter predicted (P) frames. I frames are encoded using spatial correlations in a frame, while P frames are encoded by exploiting the temporal correlations between neighboring frames. Corrupted MBs are likely to destroy the correlations in temporal domain, which could be treated as evidence for error detection.

2.1 Correlation Coefficients of MBs

The n-th MB in the (f + 1)-th frame denoted as $MB_{f+1}(n)$ can be predicted by $MB_f(m)$ and the Motion Vector (MV) information stored in the f-th frame. $MB_{f+1}(n)$ can be formulated as

$$MB_{f+1}(n) = MB_f(m) + \xi'_f(m) \tag{1}$$

where $\xi'_f(m)$ is the residual between $MB_{f+1}(n)$ and $MB_f(m)$. For normal video frames, $\xi'_f(m)$ is a 16×16 matrix with small elements. Correlation coefficient is therefore introduced in our work to describe the correlation between $MB_{f+1}(n)$ and $MB_f(m)$. Damaged MBs are with random appearances, they may appear normal in one color channel while abnormal in another one. Thus, color channel information should also be considered. Based on the above reasons, correlation coefficient feature $\rho_f(m)$ is given as

$$\rho_f(m) = \left(\rho_{f,R}(m) + \rho_{f,G}(m) + \rho_{f,B}(m)\right)/3 \tag{2}$$

where

$$\rho_{f,C}(m) = \frac{\mathrm{cov}\left(MB_{f+1,C}(n), MB_{f,C}(m)\right)}{\sqrt{\mathrm{var}\left(MB_{f+1,C}(n)\right)\mathrm{var}\left(MB_{f,C}(m)\right)}} \tag{3}$$

where $C \in \{R,G,B\}$, cov and var denote covariance and variance respectively. The distribution of ρ extracted from video sequence *foreman* is presented in Fig. 1 (left part), from which we can see that most MBs in the neighboring two frames are highly correlated. Corrupted MBs destroy the correlations in the temporal domain and do not obey the distribution of normal ρ; therefore ρ can be employed as a distinguished feature for detection.

2.2 MB Residuals

Mean of MB residuals defined in (4) is proposed as the second feature

$$\xi_f(m) = E\left(\xi'_{f,R}(m) + \xi'_{f,G}(m) + \xi'_{f,B}(m)\right), \tag{4}$$

where $\xi'_{f,C}(m)$ is the MB residual of $MB_f(m)$ in C channel ($C \in \{R,G,B\}$) and $\xi_f(m)$ is the mean value of $\xi'_{f,C}(m)$. Since MBs in the neighboring two frames are highly correlated, $\xi_f(m)$ would be small. The distribution of $\xi_f(m)$ extracted from 300 frames of *foreman* is given in Fig. 1 (right part). It can be observed that most

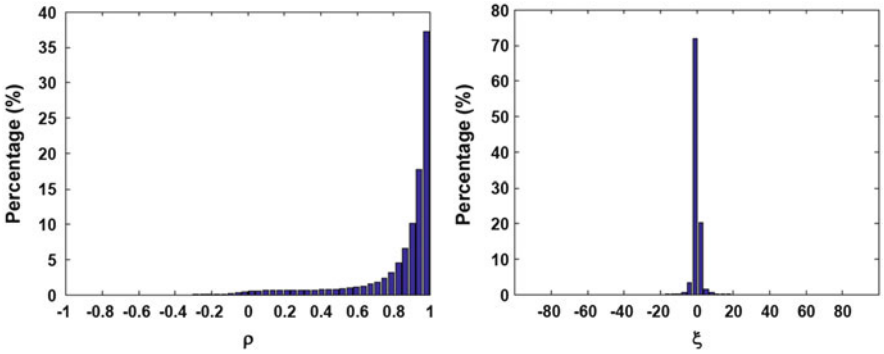

Fig. 1 Statistical histograms of ρ and ξ

$\xi_f(m)$ are concentrated around zero due to the strong correlations existing in neighboring frames. It is reasonable to assume that $\xi_f(m)$ between corrupted MB and normal MB would deviate from 0.

3 Classifier Design

We design a supervised one-class classifier for error detection. The classifier is trained via normal samples, and the corrupted MBs are detected by mismatching the probability density functions (PDFs) of the proposed features.

3.1 Classifier Design and Parameter Estimation

Let $p_\rho(\rho;\ \theta_\rho)$ be the PDF of ρ with parameter θ_ρ, $p_\xi(\xi;\ \theta_\xi)$ be the PDF of ξ with parameter θ_ξ. For new features (ρ_{new} and ξ_{new}) extracted from unknown MBs, if ρ_{new} (or ξ_{new}) obeys the $p_\rho(\rho;\ \theta_\rho)$ (or $p_\xi(\xi;\ \theta_\xi)$) no less than certain probability, then it can be predicted as normal MB, otherwise it is regarded as a corrupted MB. This process can be formulated as:

$$\begin{cases} \text{Normal}, & p_\rho(\rho;\theta_\rho)p_\xi(\xi;\theta_\xi) \geq \text{threshold} \\ \text{Damaged}, & \text{otherwise} \end{cases}. \tag{5}$$

According to Fig. 1, we find that the PDF of ρ is similar to exponential distribution while ξ is similar to Gaussian distribution. Mixture probability models are therefore employed to fit the PDFs of proposed features. Specifically, M-component exponential mixture model and M-component Gaussian mixture model which are given in (6)–(7) are employed to fit the probability density functions of ρ and ξ.

$$p_\rho(\rho;\theta_\rho)=\sum_{k=1}^{M} p_k(\rho;\theta_\rho^k)P_\rho^k,\quad p_\xi(\xi;\theta_\xi)=\sum_{k=1}^{M} p_k(\xi;\theta_\xi^k)P_\xi^k \tag{6}$$

$$p_k(\rho;\theta_\rho^k)=\begin{cases}\lambda_k e^{\lambda_k(\rho-1)}, & |\rho|\le 1\\ 0, & \text{otherwise}\end{cases},\quad p_k(\xi;\theta_\xi^k)=\frac{1}{\sqrt{2\pi}}e^{-\frac{(\xi-\mu_k)^2}{2\sigma_k^2}} \tag{7}$$

Expectation maximization (EM) algorithm [7] is employed to estimate the unknown parameters of PDFs. EM algorithm maximizes the expectation of the log likelihood function which is conditioned on the training samples and current iteration estimate of parameters. Two steps are involved to estimate the unknown parameters (ρ is employed here for illustration and the parameter estimation of ξ is similar to ρ):

(a) E-step: Expectation of log-likelihood function,

$$E\left(\sum_{l=1}^{N}\ln p_\rho\left(\rho_l|k;\theta_\rho^k\right)P_k\right)=\sum_{l=1}^{N}\sum_{k=1}^{M}P(k|\rho_l;\Theta(t))\ln p_\rho\left(\rho_l|k;\theta_\rho^k\right)P_k, \tag{8}$$

(b) M-step: Maximizing above formula with parameter θ_ρ^k, i.e.

$$\frac{\partial E\left(\sum_{l=1}^{N}\ln p_\rho\left(\rho_l|k;\theta_\rho^k\right)P_k\right)}{\partial\theta_\rho^k}=0. \tag{9}$$

We can get $P(k|\rho_l;\Theta(t))$ by

$$P(k|\rho_l;\Theta(t))=\frac{p_\rho(\rho_l|k;\theta_\rho^k(t))P_k(t)}{\sum_{k=1}^{M}p_\rho(\rho_l|k;\theta_\rho^k(t))P_k(t)}. \tag{10}$$

The EM algorithm starts from initial value $\Theta(0)=[\theta_\rho^i(0), P_i(0)]^T$ and iterations are terminated if $|\Theta(t+1)-\Theta(t)|<\varepsilon$, ε is a preset small positive value.

3.2 Adaptability of the Proposed Method

Since the corrupted MBs may be caused by various reasons and errors in the frames are in quite different forms, the parameters for the classifier are probably different from each other for different video sequences. Therefore, the adaptability of the

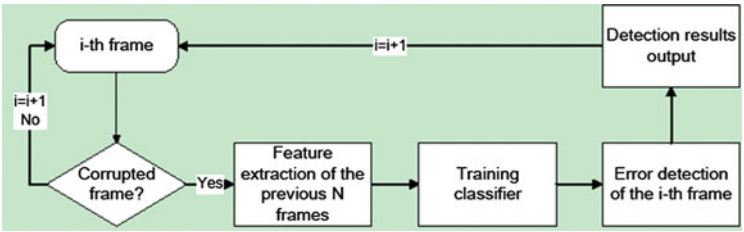

Fig. 2 Diagram of the adaptive error detection method

proposed method should be considered in the practical applications. We propose an adaptive framework for error detection and the diagram is given in Fig. 2. For a given video clip: (a) Check whether the current frame (e.g., i-th frame) contains corrupted segments or not by no-match in video decoders. If no, let $i = i + 1$ and continue, else, go to step (b); (b) The previous N normal frames (i.e. $[i - 1, i - 2, \ldots, i - N]$) are treated as training set to train the classifier according to (6)–(10). N can be set according to specific problems; (c) Detect the unknown MBs in the i-th frame according to (5); (d) The detection results are recorded, let $i = i + 1$, go to step (a).

4 Experimental Results and Discussions

To evaluate the performance of proposed method, eight corrupted H.264 video sequences, i.e. *flower*, *container*, *akiyo*, *foreman*, *hall*, *mother-daughter* (*m-d* in short), *stefan* and *coastguard*, are employed in our experimental work. The proposed method is integrated within the JM Software [8]. The sequences are encoded in baseline profile and the size of selected group of picture (GOP) is 10. Corrupted video sequences are encoded as follows: (a) Randomly selected a frame in every GOP; (b) Randomly selected a byte of the frame and change the byte in one of the three ways: (1) deleting the byte, (2) adding a byte and (3) replacing the byte by another byte. The corrupted video sequences are detected according to the scheme described in Sect. 3.2. Some of the detection results are given in Fig. 3 in which the detected errors are marked by red squares.

The final detection results of the eight corrupted video sequences are given in Table 1 where TPR denotes the rate of normal MBs classified as normal ones and TNR denotes the rate of corrupted MBs detected as corrupted ones. It can be observed from Table 1 that:

1. For single feature (ρ or ξ), the TPR of which is lower than that combine features (i.e. $\rho + \xi$). The combined features could decrease the false alarms.
2. TNRs of combined features are lower than that of single feature. Single feature detects the corrupted MBs effectively at the cost of higher false alarms.

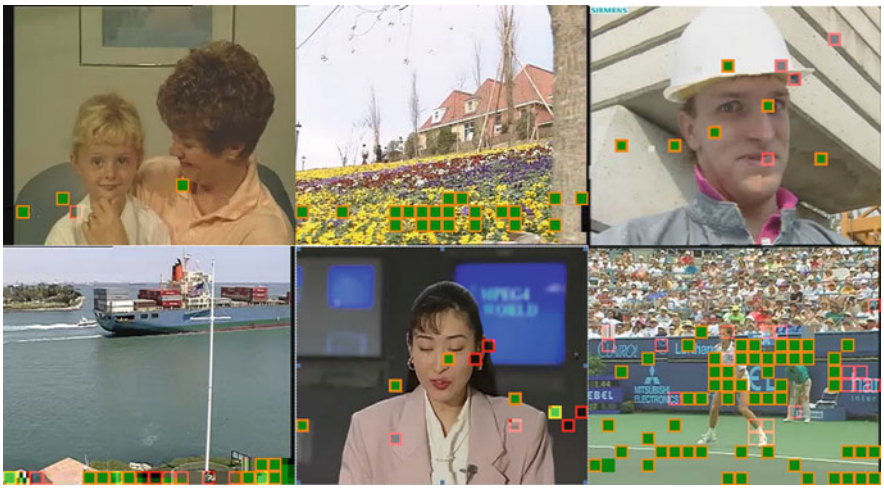

Fig. 3 Some of the detection results. The detected errors are marked by *red squares*

Table 1 Detection results

		Flower	Container	Akiyo	Foreman	Hall	Coastguard	Stefan	m-d
TPR	ρ	93.1 %	97.1 %	88.9 %	91.6 %	99.1 %	95.9 %	91.7 %	97.8 %
	ξ	96.9 %	98.6 %	97.0 %	85.7 %	96.8 %	93.2 %	86.3 %	97.3 %
	$\rho + \xi$	99.3 %	99.7 %	99.7 %	98.6 %	99.8 %	98.5 %	94.9 %	99.8 %
TNR	ρ	96.1 %	78.6 %	87.2 %	74.9 %	75.0 %	92.9 %	96.1 %	74.5 %
	ξ	93.1 %	87.8 %	96.8 %	89.9 %	90.1 %	96.5 %	98.7 %	92.4 %
	$\rho + \xi$	91.4 %	70.1 %	85.1 %	68.7 %	76.1 %	88.6 %	93.5 %	62.1 %

3. The combined features can achieve the TPR at about 98 %, which is higher than that of either feature. Therefore, ρ and ξ could compensate for each other.

5 Conclusions

Detecting corrupted MBs is a fundamental step for the concealment of corrupted video bit-streams. Although we may know the occurrence of corrupted MBs by analyzing the decoder, we can't locate the exact positions of them. In this paper, instead of analyzing the bit-streams by semantics method, we proposed a temporal detection method to locate the exact positions of corrupted MBs. Correlation coefficients and MB residuals based features are proposed to discriminate corrupted MBs from normal ones. A simple and effective classifier based on the PDFs of proposed features is designed as the detector. To evaluate the effectiveness of proposed method, ten different video sequences are employed in our experimental work and the experimental results have shown that most of the normal MBs are detected as normal ones and the corrupted MBs are classified as corrupted ones with

the accuracy of 80.2 % on average. In the future, we would further improve our method by introducing more discriminative features in different domains (e.g. DCT, spatial and wavelet) for error detection of video streams.

Acknowledgments This work is funded by National Science Foundation of China (61271316, 61071152), 973 Program (2010CB731403, 2010CB731406, 2013CB329605) of China, Chinese National "Twelfth Five-Year" Plan for Science & Technology Support (2012BAH38 B04), Key Laboratory for Shanghai Integrated Information Security Management Technology Research, and Chinese National Engineering Laboratory for Information Content Analysis Technology.

References

1. Gao Y, Wang J, Chen X, Zhang D, Yang X, Wang J (2006) Object geometry based error resilient video coding. In: IEEE International Conference on Image Processing, Atlanta, GA, 8–11 October, 2006, pp. 789–792
2. Superiori L, Nemethova O, Rupp M (2006) Performance of a H.264/AVC error detection algorithm based on syntax analysis. In: International Conference on Advances in Mobile Computing and Multimedia, 4–6 December, 2006, Yogyakarta, Indonesia, pp. 1–10
3. Superiori L, Nemethova O, Rupp M (2007) Detection of visual impairments in the pixel domain of corrupted h.264/avc packets. In: IEEE International Picture Coding Symposium, Lisbon, Portugal, November, 2007, pp. 7–9
4. Ye S, Lin X, Sun Q (2003) Content based error detection and concealment for image transmission over wireless channel. In: IEEE International Symposium on Circuits and Systems, Thailand, May 2003, vol. 2, pp. 368–371
5. Farrugia RA, Debono CJ (2007) Enhancing error resilience in wireless transmitted compressed video sequences through a probabilistic neural network core. In: IEEE International Picture Coding Symposium, Lisbon, Portugal, November, 2007
6. Farrugia RA, Debono CJ (2008) A robust error detection mechanism for h.264/avc coded video sequences based on support vector machines. IEEE Trans Circ Syst Video Techn 18:1766–70
7. Dempster A, Laird N, Rubin D (1977) Maximum likelihood from incomplete data via the em algorithm. J Roy Stat Soc 99:1–38
8. Ver. 18.2, J.S.: H.264/avc software coordination. In: http://iphome.hhi.de/suehring/tml/

Image Splicing Detection Based on Improved Markov Model

Su Bo, Yuan Quan-qiao, Wang Shi-lin, Zhao Cheng-lin, and Li Shen-ghong

Abstract Digital image splicing detection is a new and important subject in image forensics. Research shows that Discrete Cosine Transform (DCT) and Discrete Wavelet Transform (DWT) based Markov features are effective for image splicing detection. However, the state selection in the traditional Markov model was simply rounding the parameters and taking threshold value, which has not exploited the parameter distribute information. In this paper, a novel Markov state selection method is proposed. The approach matches states with parameters evenly according to fixed ratio calculated by pre-set state numbers. Experiments show that the improved Markov model achieves higher recognition accuracy rate compared with the traditional Markov model with the same feature dimension.

Keywords DCT • DWT • Markov model • State selection • Image splicing detection

1 Introduction

With the digital image equipment and processing software springing up, tampering a digital image has becomes easy and convenient. When photos as a record of what have happened cannot be trusted, it is a great threat to our society especially in news media, military, and legal arguments.

To verify the originality of photos, many methods have been proposed. Watermarking is an effective active detection approach, which is widely used in

S. Bo (✉) • Y. Quan-qiao • W. Shi-lin • L. Shen-ghong
School of electronic information and electrical engineering, Shanghai Jiao Tong University, Shanghai City 200240, China
e-mail: subo@sjtu.edu.cn

Z. Cheng-lin
Information and Communication Engineering, Beijing University of Posts and Telecommunications, Beijing City 100876, China

B. Zhang et al. (eds.), *The Proceedings of the Second International Conference on Communications, Signal Processing, and Systems*, Lecture Notes in Electrical Engineering 246, DOI 10.1007/978-3-319-00536-2_15,

copyright protection and digital image authentication [1]. Watermark method detects the tampered images by checking the embedded information which is inserted during imaging [2]. However, most digital cameras do not have that function owe to the cost and imaging quality, making the approach not universal in application. More over all active detection methods need prior information, which is not available for third party. So they are not suitable for many practical applications. In contrast, passive or blind approaches for image tamper detection demand no prior information and only exploit the knowledge of the image itself. The wide and practical application prospect makes them gain much attention.

Many passive image tampering detection methods have been proposed in recent years and a brief survey is given in [3]. In [4], a nature image model for splicing detection is proposed, which consists of statistical features including characteristic function moments of wavelet sub-bands and Markov transition probabilities of block DCT coefficients. The method achieves a detection accuracy rate of 91.8 % over [5]. Chen et al. put forward a blind image splicing detection method in [6]. It is based on 2-D phase congruency and statistical moments of characteristic functions of wavelet sub-bands, which gains a detection rate of 82.32 %. Dong et al. [7] proposes an approach extracting statistical features from image run-length representation and image edge statistics. The method makes a balance between detection accuracy and computational complexity. Zhao et al. [8] came up with a method exploiting gray level run-length run-number vectors from de-correlated chroma channels to detect image splicing. In [9], He et al. extended the Markov features in [4] to DWT domain and combine them with features on block DCT coefficients, and achieves a detection accuracy rate of 93.55 % on [5].

After comparing the detecting results of these methods, Markov features in transform domain displays a better performance. Markov feature extraction is comprised of two steps, that is, the state selection and state transform probability calculation. Both the state selection methods in [4] and [9] are rounding and threshold, which is not sufficient to employ the distribution of coefficients for splicing detection. In this paper, we will analyze the distribution in detail and propose our state selection method.

The rest of this paper is organized as follows. The proposed Markov model is given in Sect. 2. In Sect. 3, we conduct the experiments and analyze the results. Conclusion is given in Sect. 4.

2 The Proposed Markov Model

2.1 Procedure of Markov Model

As presented in [4], the Markov based method in the transformed domain is depicted as follows: firstly, block discrete cosine transformation or discrete wavelet transformation is performed on source images; secondly, differencing operation is

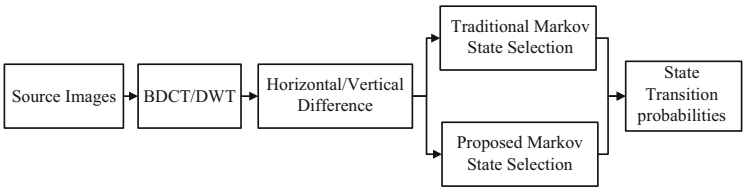

Fig. 1 Flow diagram of Markov model

made; thirdly, select the state and map them with coefficients (i.e. states); finally, calculate the state transform probabilities. The brief flow diagram is given in Fig. 1.

2.2 The Traditional Markov State Selection Method

The Markov state selection method in [4] and [9] rounds coefficients to integer and then thresholds them with a preset threshold T. We operate BDCT or DWT and differencing operation on images in [5], and then conduct the Markov state selection method on coefficients. We calculate the ratio of coefficients in range [-T, T] and that of coefficients mapped to Markov state zero. Results are recorded in Tables 1, 2 and 3 and we get two problems based on inference from them, which are described as follows:

1) Rounding operation makes big part of parameters mapped to Markov state 0. From Table 1, we see that the ratio of coefficients between -0.5 and 0.5 is over 30 %. And from Table 2, the ratio is 46.5 %, which means the number of state 0 is the same as all the other states.
2) There are a lot of parameters greater than threshold. As Tables 1 and 2 show, the ratio of BDCT coefficients over threshold $T = 3$ after horizontal and vertical difference is 42.7 % and 42.8 %. And Table 3 shows that the ratio of DWT coefficients over $T = 3$ at H2 sub-band after vertical difference reach up to 57.5 %.

State transition probabilities are only able to catch relational features among different states. Therefore, in the two situations above, mapping large scale coefficients to one state is not appropriate. Generally speaking, the purpose of Markov state selection is to calculate state transition probabilities only. So the lost information during this progress may be valuable to splicing detection and worth of preservation. In the following, we will give our proposed state selection method for Markov model which better deals with the problems mentioned above.

Table 1 The coefficients distribute situation after BDCT and differencing operation with Threshold T = 3 or T = 4

	Horizontal difference			Vertical Difference		
Threshold	In range [-T,T]	Out of range [-T,T]	Ratio of state 0	In range [-T,T]	Out of range [-T,T]	Ratio of state 0
T = 3	57.3 %	42.7 %	30.3 %	57.2 %	42.8 %	30.3 %
T = 4	62.2 %	37.8 %	30.3 %	62.4 %	37.6 %	30.3 %

Table 2 The 2-level sub-band coefficients distribute situation after DWT and differencing operation with Threshold T = 3

	Horizontal difference			Vertical difference		
Sub-band	In range [-T,T]	Out of range [-T,T]	Ratio of state 0	In range [-T,T]	Out of range [-T,T]	Ratio of state 0
H1	71.2 %	28.8 %	29.4 %	69.2 %	30.8 %	28.5 %
V1	69.3 %	30.7 %	27.3 %	71.5 %	28.5 %	28.3 %
D1	85.2 %	14.8 %	45.4 %	86.3 %	13.7 %	46.2 %
H2	44.2 %	55.8 %	17.6 %	44.1 %	55.9 %	13.4 %
V2	43.6 %	56.4 %	12.2 %	42.5 %	57.5 %	11.3 %
D2	54.4 %	46.6 %	13.6 %	53.3 %	46.7 %	17.2 %

Table 3 The 2-level sub-band coefficients distribute situation after DWT and differencing operation with Threshold T = 4

T = 4	Horizontal difference			Vertical difference		
Sub-band	In range [-T,T]	Out of range [-T,T]	Ratio of state 0	In range [-T,T]	Out of range [-T,T]	Ratio of state 0
H1	77.4 %	22.6 %	29.2 %	24.9 %	75.1 %	28.6 %
V1	75.3 %	24.7 %	27.3 %	22.5 %	77.5 %	28.1 %
D1	89.1 %	10.9 %	45.2 %	9.8 %	90.2 %	46.5 %
H2	51.7 %	48.3 %	17.4 %	49.7 %	50.3 %	13.2 %
V2	49.5 %	50.5 %	12.1 %	50.4 %	49.6 %	11.5 %
D2	60.1 %	39.9 %	13.5 %	39.7 %	60.3 %	17.4 %

2.3 The Improved Markov State Selection Method

We operate transformation and differencing on source images, put all the coefficients together and then extract their histogram, showed below in Figs. 2 and 3. The range is set to [-30, 30] with minimal interval 0.1 according to experience. Figure 2 is the histogram of coefficients after BDCT and horizontal and vertical difference operations. Figures show that majority of coefficients are in [-10, 10] and the most is near zero. Since the two histograms are very similar, we only consider horizontal direction afterwards. Figure 3 are histograms of coefficients after DWT and horizontal difference. The figures show that 1-level sub-bands are similar to BDCT, most coefficients in [-10, 10] and centering on zero.

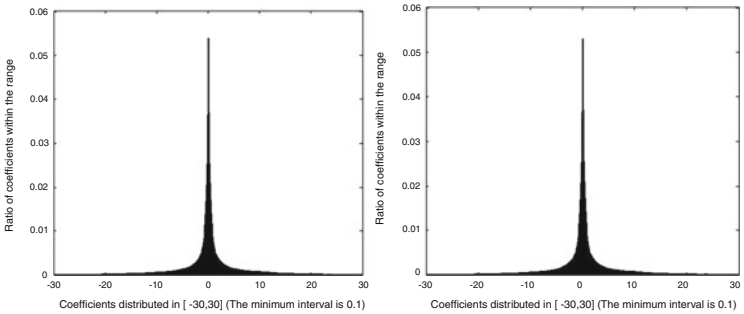

Fig. 2 Histogram of coefficients in range [-30, 30], minimum interval 0.1, after BDCT and horizontal difference (*left*) and vertical difference (*right*)

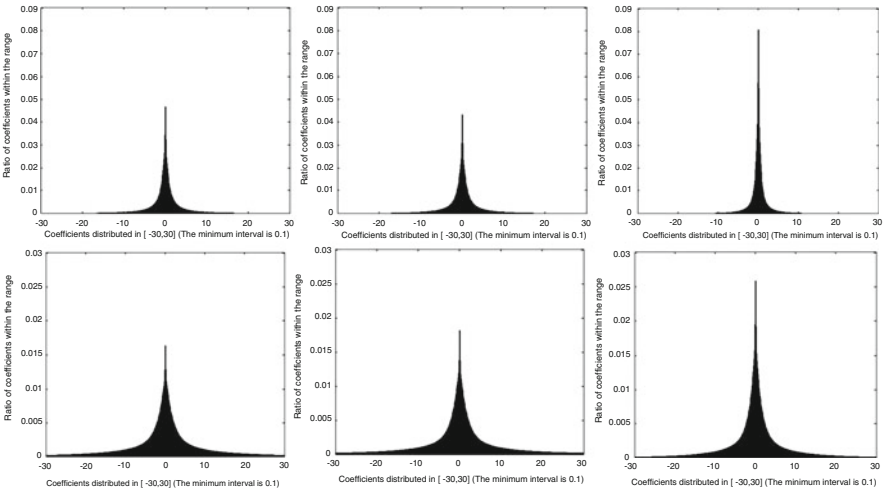

Fig. 3 Histogram of coefficients in range [-30, 30], minimum interval 0.1, after DWT and difference operation, 1-level sub-bands are in the *up* with horizontal, vertical and diagonal direction in order from *left* to *right*, and 2-level sub-bands are in the *bottom*

While in the 2-level, coefficients have larger range and energy out of [-10, 10] is still strong.

The purpose of Markov state selection is to map coefficients with finite states. The method we give is to map states evenly with the coefficients: that is, we first set the state number N, and then calculate the percentage of each state as 1/N; finally we map coefficients of this ratio with a Markov state. In this way, Markov states will describe coefficients in different range evenly. The two problems caused by traditional state selection method are resolved. From Figs. 2 and 3, we get that coefficients approximately distribute about $X = 0$ symmetry. So when calculating

coefficient energy, we shine the negative part upon positive. For example, suppose state number N to be 7, and states, represented by S, will be -3, -2, -1, 0, -1, -2, -3, with each state having a probability of 1/7. We distribute the coefficients to 7 different intervals $(-\infty, -T_3)$, $(-T_3, -T_2)$, $(-T_2, -T_1)$, $(-T_1, T_1)$, (T_1, T_2), (T_2, T_3), $(T_3, +\infty)$, and then map each interval to a Markov state S.

Without losing generality, with an odd state number N, there are M = (N-1)/2 marginal values, $T_1, T_2, \ldots, T_M$, that should be calculated. The algorithm is designed as follows:

1) Suppose the initial interval to be $[T_s, T_e]$, set $T_s = 0$, and $T_e = 0.1$;
2) Calculate the percentage of coefficients in $[-T_e, -T_s)$ and $(T_s, T_e]$, if not above 1/M, then $T_e = T_e + 0.1$;
3) Repeat 2), if the percentage is above 1/M, then end the loop, return T_e, set $T_s = T_e$ and $T_e = T_e + 0.1$;
4) Repeat 2) and 3), if the loop number is above M or T_e is above or equal to the maximum of coefficients, then end the loop.

Finally, we get $T_1, T_2, \ldots, T_M$ in order from the return in each loop.

3 Experiment and Results

3.1 The Image Dataset

The Columbia Image Splicing Detection Evaluation Dataset [5] is widely used to evaluate the effect of image splicing detecting algorithm. The database consists of 933 real images and 912 splicing images. Real images are taken by one camera and splicing images are generated from two real images, only the splicing operation and no post dispose, which makes for splicing detection particularly (Fig. 4).

3.2 Classifier and Detection Results

Support vector machine (SVM) is wide used in classification and we employ LIBSVM by Prof Lin [10] as the classifier, with Radial Basis Function (RBF) as kernel function. Grid searching algorithm is used to find best parameters C and G for classification. Images are divided into two parts randomly, i.e. training set and testing set, and it is repeated 50 times for each parameter group (C, G). Then the performance is measured by the average classification result.

Tables 4 and 5 show the detection results of traditional Markov model and proposed Markov model in BDCT domain. AC stands for average detection accuracy rate, TP for detection accuracy rate of real images, TN for that of splicing images, and variance is right below the detection accuracy rate. The data shows that

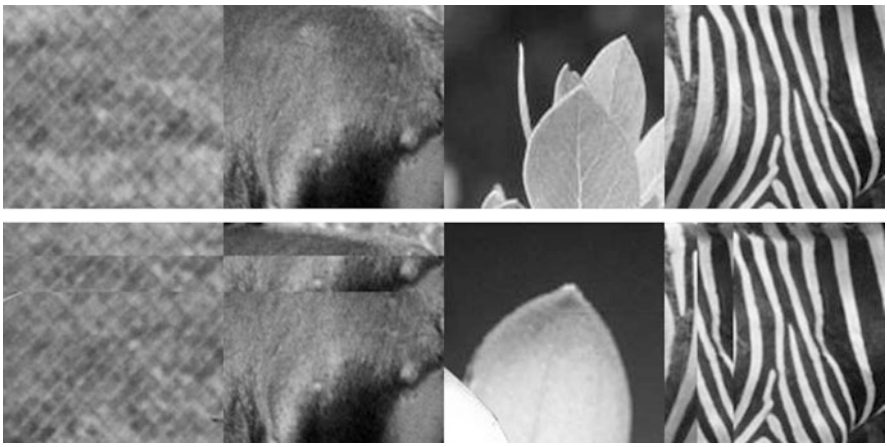

Fig. 4 Image samples in the database, the up two are Authentic and bottom ones are Splicing

Table 4 Comparison of detection results of Markov features with traditional state selection and proposed state selection on BDCT domain (N = 7)

	Traditional state selection			Proposed state selection		
BDCT (N = 7)	AC	TP	TN	AC	TP	TN
Horizontal difference	85.3 %	85.1 %	85.6 %	87.2 %	87.2 %	87.3 %
	0.9 %	2.0 %	1.7 %	1.0 %	1.7 %	1.1 %
Vertical difference	85.0 %	84.6 %	85.5 %	87.2 %	86.4 %	88.1 %
	1.3 %	1.5 %	2.6 %	1.2 %	1.9 %	2.0 %

Table 5 Comparison of detection results of Markov features with traditional state selection and proposed state selection on BDCT domain (N = 9)

	Traditional state selection			Proposed state selection		
BDCT (N = 9)	AC	TP	TN	AC	TP	TN
Horizontal difference	87.2 %	86.2 %	88.3 %	88 %	87.3 %	88.8 %
	0.7 %	1.6 %	1.5 %	0.8 %	1.7 %	1.7 %
Vertical difference	86.3 %	84.7	87.9 %	87.6 %	87.4 %	87.9 %
	1.0 %	1.7 %	2.2 %	1.0 %	1.5 %	1.7 %

the proposed method boosts the detection accuracy rate by one to two percent with the same feature dimension for each individual feature. He et al. combined BDCT and DWT Markov features together and increased the detection accuracy rate from 91.87 % in [4] to 93.55 % in [9]. But the sacrifice is to enlarge feature dimension from 266 to 7,290, which lead to that feature selection method like SVM-RFE (support vector machine recursive feature elimination) must be used before classification in order to avoid overfitting.

Table 6 Comparison of detection results of Markov features with traditional state selection and proposed state selection on DWT domain (N = 7)

	Traditional state selection			Proposed state selection		
DWT (N = 7)	AC	TP	TN	AC	TP	TN
1-level sub-band	81.6 %	82.5 %	80.7 %	83.3 %	82.9 %	83.7 %
	1.1 %	2.2 %	2.4 %	0.9 %	2.0 %	1.9 %
2-level sub-band	70.0 %	68.2 %	71.9 %	71.4 %	66.7 %	76.2 %
	1.2 %	2.9 %	3.3 %	1.3 %	3.2 %	3.7 %

Table 7 Comparison of detection results of Markov features with traditional state selection and proposed state selection on DWT domain (N = 9)

	Traditional state selection			Proposed state selection		
DWT (N = 9)	AC	TP	TN	AC	TP	TN
1-level sub-band	82.0 %	83.0 %	80.9 %	83.2 %	83.3 %	83 %
	1.0 %	2.8 %	3.0 %	1.0 %	1.7 %	1.8 %
2-level sub-band	70.7 %	65.0 %	76.6 %	72.3 %	68.9 %	75.9 %
	1.2 %	3.3 %	3.2 %	1.2 %	3.3 %	3.4 %

The DWT Markov model in [9] employs position, scale and direction features together. Among these three features, position contributes the most and the detection accuracy rate of direction or scale feature alone is less than 75 %. Even incorporating them with position features, the accuracy gain is insignificant. So we only compare the detection results of the position features. Tables 6 and 7 show that proposed model will improve the detection accuracy rate by 1 % or more.

4 Conclusion

This paper improves the Markov state selection method in [4] and [9], enhancing the Markov model's ability for image splicing detection. The improved method maps states evenly with coefficients and employs coefficients of distribute efficiently. The proposed model increases the detecting accuracy rate of each individual feature by more than 1 % in average with the same feature dimension.

Acknowledgments This work is funded by National Science Foundation of China (61271316, 61071152), 973 Program (2010CB731403, 2010CB731406, 2013CB329605) of China, Chinese National "Twelfth Five-Year" Plan for Science & Technology Support (2012BAH38 B04), Key Laboratory for Shanghai Integrated Information Security Management Technology Research, and Chinese National Engineering Laboratory for Information Content Analysis Technology.

References

1. Nikolaidis N, Pitas I (1996) Copyright protection of images using robust digital signatures. In: Reeves SJ (ed) Proceeding on international conference on acoustics, speech, and signal processing. IEEE Press, Atlanta, GA, pp 216–217
2. Cox IJ, Kilian J, Leighton FT et al (1997) Secure spread spectrum watermarking for multimedia. IEEE Trans Image Process 6(12):1673–1687
3. Farid H (2009) A survey of image forgery detection. IEEE Signal Process Mag 26(2):16–25
4. Shi YQ, Chen C, Chen W (2007) A natural image model approach to splicing detection. In: Deepa K, Balakrishnan P (eds) 9th workshop on multimedia and security. ACM, New York, NY, pp 51–62
5. Columbia DVMM Research Lab (2004) Columbia image splicing detection evaluation dataset, http://www.ee.columbia.edu/ln/dvmm/downloads/authsplcuncmp.
6. Chen W, Shi, Y (2007) Image splicing detection using 2D phase congruency and statistical moments of characteristic function, In: Proc. SPIE, electronic imaging, security, steganography, watermarking of multimedia contents IX, San Jose, CA, 29 January–1 February, 2007, vol. 6505, pp. 0R–0S
7. Dong J, Wang W, Tan T, Shi Y (2008) Run-length and edge statistics based approach for image splicing detection. In: Digital watermarking, 7th international workshop, IWDW 2008, Busan, Korea, 10–12 November, 2008, pp. 76–87
8. Xudong Zhao, Jianhua Li, Shenghong Li and Shilin Wang (2010) Detecting digital image splicing in chroma spaces. International workshop on digital watermarking, Seoul, Korea, 1–3 October, 2010, LNCS, vol. 6526, pp. 12–22
9. He Z, Lu W, Sun W et al (2012) Digital image splicing detection based on Markov features in DCT and DWT domain. Pattern Recogn 45(12):4292–4299
10. Chang C-C, Lin C-J (2011) LIBSVM: a library for support vector machines. ACM Trans Intell Syst Technol 2(27):1–27. Software available at http://www.csie.ntu.edu.tw/~cjlin/libsvm

Image Fusion Based on Compressed Sensing

Xin Zhou, Wei Wang, and Rui-an Liu

Abstract Compressive sensing (CS) has received a lot of interest due to its compression capability and lack of complexity on the sensor side. This paper presented a new image fusion based on compressed sensing. The method decomposes two or more original images using directionlet transform, and gets the sparse matrix by the directionlet coefficients sparse representation, and fuses the sparse matrices with the coefficients absolute value maximum scheme. The compressed sample can be received through randomly observed. The fused image is recovered from the reduced samples by solving the optimization. The study demonstrates that CS-based image fusion has a number of perceived advantages in comparison with image fusion in the infrared image domain. The simulations show that the proposed CS-based image fusion algorithm has the advantages of simple structure and easy implementation, and also can achieve a better fusion performance.

Keywords Image fusion • Compressive sensing • Directionlet transform

1 Introduction

The main goal of image fusion is to extract all the important features from all input images and integrate them to form a fused image which is more informative and suitable for human visual perception or computer processing.

Image fusion is mainly divided into three levels, namely the pixel level fusion, feature fusion and decision level fusion [1]. This article only focuses on the pixel level fusion. There are a number of pixel-level image fusion methods, including the weighted average method [2], the pyramid transform method [3], principal component analysis (Principal Component Analysis, PCA) method [4] as well as fusion

X. Zhou (✉) • W. Wang • R.-a. Liu
College of Electronic and Communication Engineering, Tianjin Normal University, Tianjin, China
e-mail: zhouxintjnu@126.com

B. Zhang et al. (eds.), *The Proceedings of the Second International Conference on Communications, Signal Processing, and Systems*, Lecture Notes in Electrical Engineering 246, DOI 10.1007/978-3-319-00536-2_16,

based on wavelet transform methods. The wavelet transform has become an important tool in image fusion method for its excellent feature of time frequency analysis [5]. However, wavelet bases are isotropy and of limited directions and fail to represent high anisotropic edges and contours in images well. For the drawbacks of the wavelet transform, directionlet transform is anisotropic transform proposed by Vladan, which is based on integer lattice. The directionlet still use the one-dimensional filter group, but with the base function of multi-directional anisotropy, the directionlet have a detachable filter and critical structure, and are able to be fully reconstructed, thus, theoretically it has more advantages than the general wavelet transform, and the other second generation wavelet transform [6].

In recent years, inspired by the ideas of "sparse" approximation, a novel theory called compressed sensing (CS) has been developed [7–9]. The CS principle claims that if a signal is compressive or "sparse" in a certain transform domain, it can be projected onto a low-dimensional space using a measurement matrix which is irrelevant with transform basis while still enabling reconstructed at high probability from these small number of random linear measurements via solving an optimization problem. Therefore, it is expected to provide a new idea for image fusion by combined directionlet with CS.

This article proposes a new scheme for image fusion. Directionlet transform first decomposes each source image into two components, i.e., dense and sparse components; then the dense components are fused by the selection method according to the manifestations of defocus while the sparse components are fused under the frame of CS via fussing a few linear measurements by solving the problem of l_1 norm minimization which is based on two-step iterative shrinkage reconstruction algorithm. The proposed fusion scheme is applied to infrared and visible image fusion experiments, and the performance is evaluated in terms of computational efficiency, visual quality and quantitative criterion.

2 Directionlet Transform

The directionlet transform proposed by German researchers Vladan is the multi-directional anisotropy based upon the integer lattice [10–12]. It adopts multi-directional anisotropy basis functions, therefore, it has more advantages in expressing the image than the average wavelet transform. At the same time, it only uses the one-dimensional filter banks with separable filtering and critical structures, and can be reconstructed totally, thus, as far as the computational complexity is concerned, it has more advantage than other second generation wavelet transform. The directionlet transform is a new multi-scale analysis tools.

When using one-dimensional filter banks to conduct multi-directional two-dimensional separable wavelet transform, we select any two rational slope $r_1 = b_1/a_1$ and $r_2 = b_2/a_2$'s digital line direction to filtering and down-sampling, however, When the critical sampling is enhanced, Two digital lines will have the issue of direction of mutual inductance, that is, along the slope r_1 and r_2, the concept

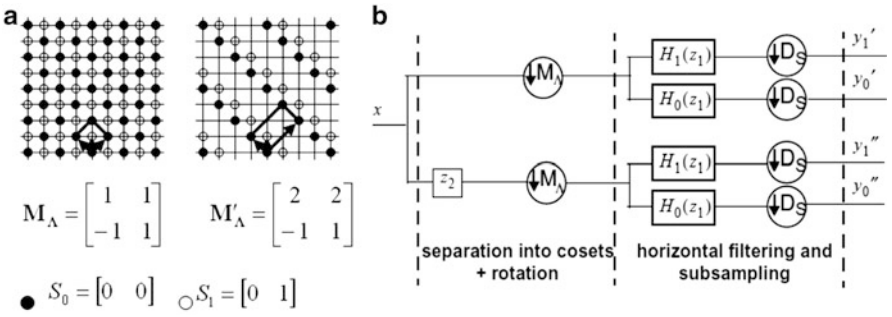

Fig. 1 Based on the integer lattice's filtering and down sampling. (**a**) expressed with the generator matrix, (**b**) two-dimensional dual-channel filter

of the digital line can't provide a systematic rule for the down-sampling of the repeated filtering and repeat sampling.

Therefore, Vlada has proposed the multi-directional filtering and down-sampling which are based on lattice. First, chose any two reasonable slopes $r_1 = b_1/a_1$ $r_2 = b_2/a_2$'s directions in grid space z^2, expressed in matrix as:

$$\mathbf{M}_\Lambda = \begin{bmatrix} a_1 & b_1 \\ a_2 & b_2 \end{bmatrix} = \begin{bmatrix} d_1 \\ d_2 \end{bmatrix}, a_1, a_2, b_1, b_2 \in Z, n_1 \neq n_2 \tag{1}$$

The direction along the slope r_1 of the vector r_1 is called the change of direction; the direction along the slope r_2 of the vector d_2 is called the queue direction. Along the skewed collinear transform of the transformation of the lattice in the queue application, it has n_1 and n_2 ($n_1 \neq n_2$) transformation in an iterative steps along the transform direction and queue direction. Marked as $S - AWT(\mathbf{M}_\Lambda, n_1, n_2)$. From $\mathbf{M}_\Lambda$, the integer lattice Λ can be ascertained. According to the case theory, z^2 has been divided into the | det $\mathbf{M}_\Lambda$|'s co-set which is about the entire integer lattice Λ. The filtering and down-sampling has been conducted in every co-set, and then the remaining pixels belong to the lattice Λ' of integer lattice Λ, the matrix $\mathbf{M}'_\Lambda$ generated accordingly. There out, sparse representation of the anisotropic object on the direction of the image can be obtained. The principle is shown as in Fig. 1 (the change of direction in the figure is 45°).

The image which has gone through the above mentioned directionlet transform has a very sparse coefficient, and then can obtain more directional information, which can be better used to describe the edge contour of the infrared image.

3 Compressive Sensing and Image Fusion

Compressive sensing enables a sparse or compressible signal to be reconstructed from a small number of non-adaptive linear projections, thus significantly reducing the sampling and computation costs [13]. CS has many promising applications in

signal acquisition, compression and medical imaging. In this paper, we investigate its potential application in the image fusion.

As far as a real-valued finite-length one-dimensional discrete-time signal x is concerned, it can be viewed as a R^N space N × 1dimensional column vector, and the element is $x[n]$, n = 1,2,· · ·,n. If the signal is sparse K, it can be shown as the following formula:

$$x = \psi s \tag{2}$$

ψ is the $N \times N$ matrix, s is the coefficient component column vector of dimension N × 1.

When the signal x in the base of ψ has only non-zero coefficients of K ≪ N (or greater than zero coefficients), ψ is called the sparse base of the signal x.

The CS theory indicates that if the signal x's (the length is N) transform coefficient which is at a orthogonal basis ψ is sparse (That is, only a small number of non-zero coefficients can be obtained.) if these coefficients are projected into the measurement basic ϕ which is irrelevant to the sparse base ψ, The $M \times 1$ dimensional measurement signal y can be get. By this approach, the signal x's compressed sampling can be realized. The expression can be expressed as:

$$y = \phi x = \phi\psi s = \Theta s \tag{3}$$

ϕ is the measurement matrix of $M \times N$, and $\Theta = \phi\psi$ is the $M \times N$ matrix, and it is called the projection matrix. y is the measurement value of the projection matrix Θ, which is relevant to the sparse signal s. Only when the orthogonal basis ψ is irrelevant to the measurement matrix ϕ, that is to say, the projection matrix can satisfy the requirement of Restricted Isometry Property(RIP), the signal x can be accurately recovered via these measured value by solving (3) in the best optimized way. The block diagram derived from the CS theory for the field of image processing is shown in Fig. 1.

$$\min_s \|s\|_{l1} \quad \text{s.t.} \quad y = \phi\psi s \tag{4}$$

The advantage that the CS theory has is that the data obtained via the projection measurement is much smaller than the conventional sampling methods, breaking the bottleneck of the Shannon sampling theorem, so that the high-resolution signal acquisition becomes possible. The attraction of CS theory is that it is for applications in many fields of science and engineering and has important implications and practical significance, such as statistics, information theory, coding theory, computer science theory and other theories.

Compared with the traditional fusion algorithms, the CS-based image fusion algorithm theory has shown significant superiority: the image fusion can be conducted in the non-sampling condition of the image with the CS technique; the quality of image fusion can be improved by increasing the number of measurements; this algorithm can save storage space and reduce the computational

complexity. The main ideas of the CS-based image fusion algorithm theory are: first of all, the two images which need to deal with should undergo the directionlet transform; the sparse matrix can be obtained after the directionlet coefficients processed with sparse treatment; and then determine the fusion rules for sparse matrix integration; obtaining compressive sampling through random sampling matrix; finally, the fused image can be obtained in the best optimized way.

The practical function of wavelet transform is the signal de-correlation, and all the information of the signal is concentrated into the wavelet coefficients with large amplitude. These large wavelet coefficients contain far more energy than that contained in small coefficient, so that in the reconstruction of the signal, a large coefficient is more important than the smaller one.

This paper adopted the fusion rule which concentrated on the larger absolute value, comparing two wavelet coefficients of the same location in two images, the absolute value which is greater are selected as fusion wavelet coefficients. The expression is as follows:

$$D_f = D_M, \quad \text{and} \quad M = \arg\max_{i=1,2,\cdots,I}(|D_i|) \tag{5}$$

The D_f is the fusion wavelet coefficient; D_M is the wavelet coefficient whose absolute value is the largest of the wavelet coefficients in the same location in different images; I is the number of the source image.

The directionlet transform is used to deal with the source image; directionlet coefficients obtained sparse treatment: small coefficient (or coefficient of close to zero) is set to zero, to obtain an approximate sparse coefficient matrix.

When the source image is conducted via sparse transformation, the wavelet is used as the sparse basis To make the image can be reconstructed with less measurement value the reconstruction, we must ensure the sparse basis ψ and the measurement matrix ϕ is irrelevant, because any random sparse matrix has superiority that it is irrelevant to any sparse basis. That is the reason why it can be used as a measurement measure matrix.

The concrete realization of image fusion algorithm which is based on CS theory is as follows:

1. For each $m \times n$ pixel image conducts directionlet transform to obtain the directionlet coefficients matrix.
2. The directionlet coefficients are processed with sparse treatment, and then the directionlet coefficients are fused according to the larger absolute value rule.
3. For the fused directionlet coefficients, the random matrix is selected as the measurement matrix ϕ, after the measuring, the measured value y can be obtained.
4. By solving the linear programming of the l_1 norm, the approximate solution $\hat{x}$ can be acquired.
5. Conducting the inverse transform to the obtained directionlet coefficients, and thus the fusion image can be acquired.

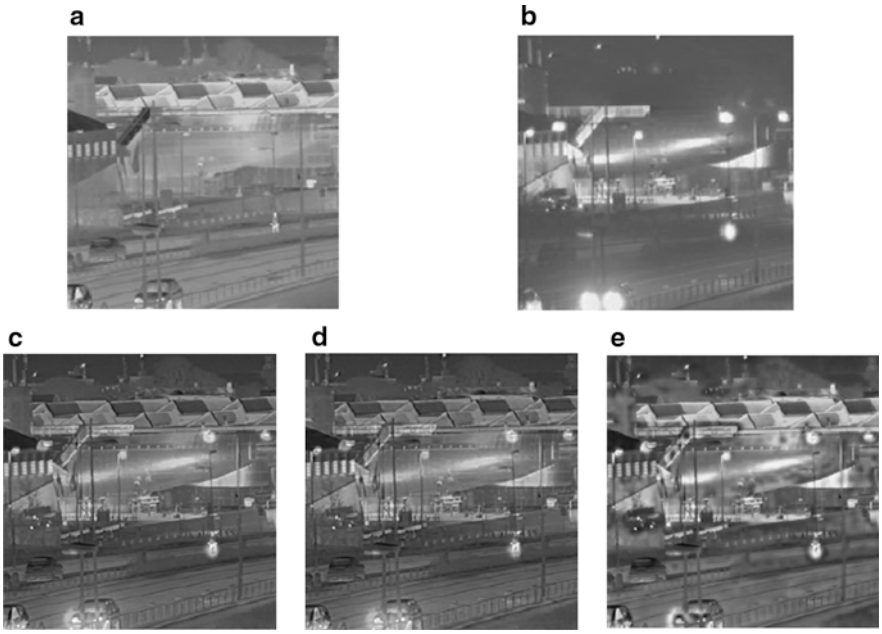

Fig. 2 Fusion experiment. (**a**) Infrared image (**b**) Visible image (**c**) LP (**d**) DWT (**e**) CS

Table 1 Comparison of statistical parameters about fusion results according to different fusion rules

	Entropy	Cross entropy	Standard deviation	Average gradient
LP	12.551	0.708	14.112	28.410
DWT	12.689	0.917	14.978	28.341
CS	12.974	0.961	15.201	29.134

4 Experimental Results and Analysis

The experiments selected the infrared and visible registration images to conduct the fusion experiment with different approaches. Figure 2 shows image (a) and image (b) respectively represent the infrared and visible images of the airfield, and the two images contain much detail and texture information; the image (c) represents the fusion result based on the Laplacian pyramid (LP) transform; the image (d) the fusion result based on the fusion of the discrete wavelet transform(DWT); the image (e) represents the fusion results based on CS. As can be seen from the figure, the images (c) and (d) have different degrees of blur. Compared to (c) and (d), the image (e) is clearer as far as the visual effect is concerned.

Table 1 is an objective evaluation towards the quality of the images in this set of experiments. As can be seen from the table, the standard deviation and the average gradient of the image (e) are the highest, which demonstrate that the image

(e) having better contrast and sharpness, and therefore is consistent with the subjective evaluation results.

5 Conclusions

The paper put forward an infrared and visible fusion algorithm based on the compressed sensing. Compared with the traditional wavelet transform, the proposed CS-based image fusion algorithm can preserve the infrared and visible image's feature information, enhance the fused image's space detail representation ability, and improve the fused image's information. The experiment proves that the approach in this paper is better than the discrete wavelet transform and Laplace pyramid decomposition, etc.

Acknowledgment The authors are grateful to the anonymous referees for constructive comments. This study was funded by the Tianjin Normal University Doctoral Fund (52X09008).

References

1. Zhou Xin, Liu Rui-An, Chen Jin (2009) Infrared and visible image fusion enhancement technology based on multi-scale directional analysis. In: Image and Signal Processing, 17–19 October, 2009, pp. 1–3
2. Hall DL, Linas J (1997) An introduction to multisensor data fusion. Proc IEEE 85(10):6–23
3. Toet A, Ruyven LV, Velaton J (1989) Merging thermal and visual images by a contrast pyramid. Opt Eng 28(7):789–792
4. Yonghong J (1998) Fusion of landsat TM and SAR image based on principal component analysis. Rem Sens Tech Appl 13(1):4649–4654
5. Yu-chi L, Qi-hai L (2010) An image fusion algorithm based on directionlet transform. Nanotech Precis Eng 8(6):565–568
6. Velisavljevic V, Beferull-Lozano B, Vetterli M (2006) Directionlets: anisotropic multi-directional representation with separable filtering. IEEE Trans Image Process 15 (7):1916–1933
7. Jin Wei F, Ran-di YM (2011) Multi-focus fusion using dual-tree contourlet and compressed sensing. Opto-Electron Eng 38(4):87–94
8. Candes E, Wakin MB (2008) An introduction to compressive sampling. IEEE Signal Process Mag 48(4):21–30 (S1053-5888)
9. Provost F, Lesage F (2009) The application of compressed sensing for photo-acoustic tomography. IEEE Trans Med Imag 28(4):585–594 (S0278-0062)
10. Velisavljevic V (2009) Low-complexity iris coding and recognition based on directionlets. IEEE Trans Inform Forensics Secur 4(3):410–417
11. Velisavljevic V, Beferull-Lozano B, Vetterli M (2007) Space-frequency quantization for image compression with directionlets. IEEE Trans Image Process 16(7):1761–1773
12. Velisavljevic V, Beferull-Lozano B, Vetterli M (2007) Efficient image compression using directionlets. 6th international conference on information, communications & signal processing, Singapore, 1–13 December, 2007, pp. 1–5
13. Tao Wan, Nishan Canagarajah, Alin Achim. Compressive image fusion. IEEE international conference image process, San Diego, CA, 12–15 October, 2008, pp. 1308–11

Freight Status Classification in Real-World Images Using SIFT and KNN Model

Dongyang Wang, Dahai Yu, Junwei Han, and Shujun Li

Abstract This paper proposes a unified image classification framework to label railway freights status that includes the Scale-Invariant Feature Transform (SIFT) description through a robust optimization approach. The developed model consists of several computational stages: (a) the SIFT descriptors in each image are extracted; (b) the training features are optimized by using K-Affinity Propagation (K-AP) algorithm; (c) construction of the Expectation-Maximization Principal Component Analysis (EMPCA) is applied for feature compression into low dimensional space; and finally (d) k-nearest neighbor (KNN) is used to register each image to trained classifiers. In this paper we are particularly interested to evaluate the classification performance of proposed algorithm on a diverse dataset of 600 real-world freights images. The experimental results show the effectiveness of proposed feature optimization technique when compared with the performance offered by the same classification schema with different feature descriptors.

Keywords Image classification • Freights status classification • SIFT • K-AP • EMPCA • KNN

D. Wang • J. Han
School of Automation, Northwestern Poly-technical University, Xi'an, China

D. Yu (✉)
School of Automation, Northwestern Poly-technical University, Xi'an, China

Tianjin Optical Electrical GaoSi Communication Engineering Technology Co., Ltd, Tianjin, China
e-mail: yudahai_dublin@hotmail.com

S. Li
Tianjin Optical Electrical GaoSi Communication Engineering Technology Co., Ltd, Tianjin, China

B. Zhang et al. (eds.), *The Proceedings of the Second International Conference on Communications, Signal Processing, and Systems*, Lecture Notes in Electrical Engineering 246, DOI 10.1007/978-3-319-00536-2_17,

1 Introduction

In last decade, railway transportation plays very important role in modern logistics. In order to guarantee the safety of transportation, every freight train has to be pattern analysis. One way of doing this is manually, but this manner is expensive and unreliable. Actually machine vision technologies have been widely employed in logistic industries instead of human work [1]. In this technique, automatic image classification becomes a focal point in image analysis. In this paper, we focus on classifying loaded status of metal freights into different categories, which is a crucial task for railway inspection system and many other transportation applications. However this task is a complex problem because the image of railway scenes is very dynamic, plus the system requires fast processing speed.

Review previous works, it is very worth to emphasize that, most of standard image classification algorithms can be formulated in two categories: discriminative and generative [2, 3]. Generative algorithms such as Hidden Markov model Bayesian Hierarchical model etc., is generating joint probability distribution over observations. Discriminative algorithms such as Spatial Pyramid Matching (SPM), SVM, k-nearest neighbor (KNN) [4] etc. is generating conditional probability distribution. To address the object classification problem, both kinds of algorithms often extract local features such as Scale-Invariant Feature Transform (SIFT) [5], Speeded Up Robust Features (SURF) [6] that used to directly represent whole picture for image classification. This is appropriate for the simple object which is shown on an image, but not suitable for the variance in appearance of objects within the same class remains. For instance, metal freights can be horizontally loaded on the car with different quantities. Although they are belonging to the same state class, but each group of metal object shows different appearance and loaded status. This fact can be observed in Fig. 1.

We motivate this paper by the requirement of categorizing freight images for video surveillance of rail transportation system. For this regard, each image consists of several contents such as train, freights, track, but the category of image can only be registered based on one object of interest (OOI). In real streaming environment, the underlying OOI distribution changes over time. The traditional classification techniques are capable of recognizing novel instances based on ensemble technique of clustering or classification on feature evaluation technique. The goal of feature evaluation technique is selecting the correct points of data grouping. For proper selection of features, we introduced a novel method based on KNN from which SIFT features are optimized by K-Affinity Propagation (K-AP) algorithm and Expectation-Maximization Principal Component Analysis (EMPCA) projection. In the experiments, we collected a challenge dataset with a total of 600 images. We demonstrate our algorithm with image classification tasks for freights status. The results show that its accuracy is comparable to classification without proper features optimization, while requiring significantly less computation time. The rest of the paper is organized as follows. In Sect. 2, proposed algorithm model is described in details. Then Sect. 3 presents the experiment setting and their results

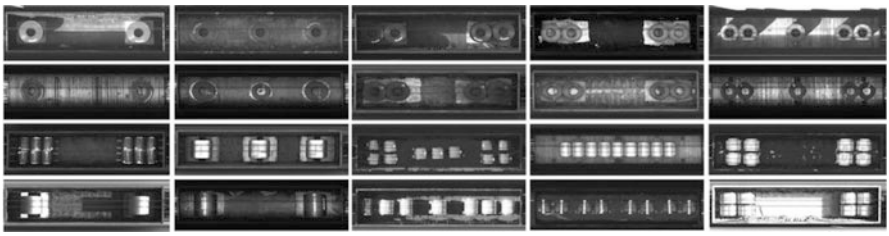

Fig. 1 Real-time examples of railway freights. Note that row 1 and 2 are belonging to the same state class; row 3 and 4 are belonging to another state class

are described. Concluding remarks and discussions on the future work are provided in Sect. 4.

2 Proposed Algorithm

The proposed algorithm is based on KNN algorithm, which has been used for years by many applications such as Magnetic Resonance Imaging [7], Visual Speech Recognition [8] due to its good stability conditions. It is a non-parametric supervised pattern classification technique where input data is classified according to the distance to the nearest neighbor from pre-known classes. However, we also notice that it is essential to extract the features of the images efficiently for KNN, without losing important local information, and reduce redundant features. In order to achieve this goal, we propose a novel framework that consists of two stages, the block diagram of the proposed system is depicted in Fig. 2.

On training stage:

(1) In the first step, key-points of freight are extracted from training images by SIFT feature extraction.
(2) The aim of the second component is to filter a large number of feature points by using K-AP algorithm.
(3) The role of third step is to project filtered feature vectors from high dimensional feature space to low dimensional EMPCA space. The low-dimensional EMPCA feature vectors are registered to the particular classifiers.

On testing stage:

(4) The test image is projected to the low-dimensional EMPCA representation in same feature space of training data and considered as a feature vector for classification. The KNN classifier is used to identify which class to assign the test image to.

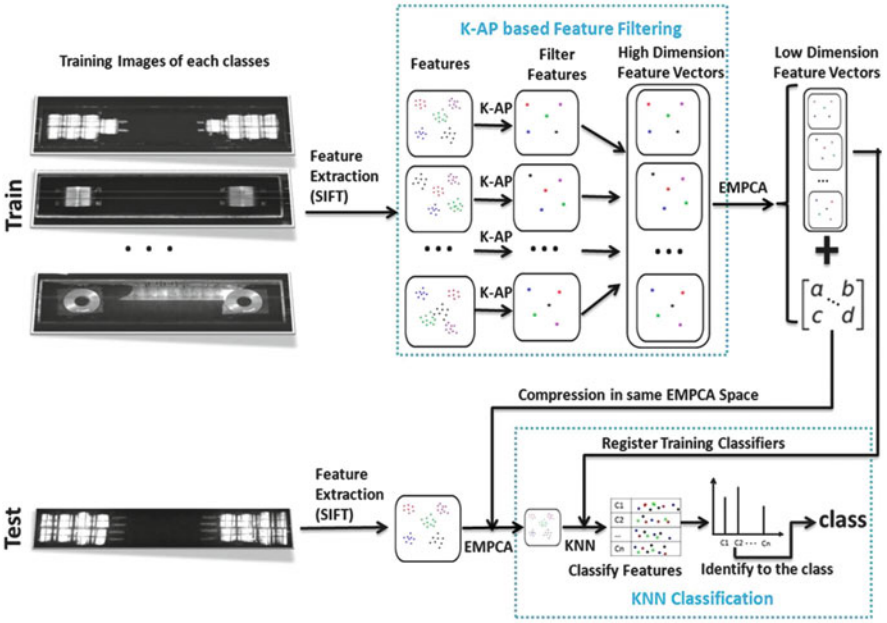

Fig. 2 Illustration of our two stages method based on KNN Model

2.1 SIFT Feature Extraction

Successful extract characteristics that describe the images by suitable algorithms are important for classification. To achieve this, firstly we extract key points and their descriptors of image from training dataset. Key point is stable local information under protean appearance in the image domain, such as affine transformations, scale changes and rotation. Learning from the state-of-the-arts, we notice that many key point descriptors including SURF, FSAT (Features from Accelerated Segment Test) [9], ORB (Oriented FAST and Rotated BRIEF) [10] and SIFT providing very fascinating results. In our implementation, we use SIFT due to its stability in most of experiments comparing to other methods [11].

SIFT detector has four main stages: scale space extrema detection, key-point localization, orientation computation and key-point descriptor extraction [5]. The difference of Gaussian (DOG) function is applied to identify potential interest points, which were invariant to scale and orientation. And hessian matrix was used to compute the principal curvatures and eliminate the key-points that have a ratio between the principal curvatures greater than the ratio [5]. According to our experiments, the best results were achieved with a 128 dimensions SIFT descriptor. We select 40 images and extract their feature points as training data for each category, and totally get 28,007 feature points for training data.

Although SIFT descriptor can robustness extract key-points under perturbed activities in the image, but the computation for classifying is still expensive because of its large amount of data points. In order to reduce the processing time, meanwhile remain the accuracy as directly SIFT matching on our tasks, we used K-AP and EMPCA for feature optimization.

2.2 K-AP Algorithm Based Feature Filtering

Affinity Propagation (AP) is a clustering algorithm that is first introduced by Frey et al. [13]. AP takes as input a collection of real-valued similarities between data point, where the similarity $s(i, k)$ indicates how well the data point with index k is suited to be the exemplar for data point i. It can be briefly described as following:

$$s(i,k) = -||X_d - X_k|| \tag{1}$$

$$r(i,k) \leftarrow s(i,k) - \max\left\{a\left(i,k^{'}\right) + s\left(i,k^{'}\right)\right\} \tag{2}$$

$$a(i,k) \leftarrow \min\left\{0, r(k,k) + \sum_{i^{'} \neq i, i^{'} \neq k} \max\left\{0, r\left(i^{'},k\right)\right\}\right\} \tag{3}$$

The responsibility $r(i, k)$ reflects the accumulated evidence for how appropriate feature k is the exemplar of feature i, considering other potential exemplars of feature i. Availability $a(i, k)$ reflects the accumulated evidence for how appropriate it would be for feature i to choose feature k as its exemplar, considering the support from other feature vectors that feature k should be an exemplar. When the preference $s(k, k)$ grows big, each node tends to select itself as the exemplar, then the number of clusters will increase.

Many literatures have indicated that AP algorithm can provide more accuracy rate than other traditional clustering algorithm [14, 15]. Based on this fact, AP algorithm is further implemented to optimize training data [16]. Despite AP's efficient clustering performance, it does not allow directly specifying the number of clusters. Instead, the number of clusters produced by AP is implicitly controlled by a user-defined parameter. Frey and Dueck [15] have suggested repeating launch AP many times with different parameters setting searched by bisection method until the desired number of clusters are found. As AP suffering from the quadratic computational complexity, repeating launching AP to obtain a given number of clusters will greatly increases the computational complexity.

In order to generate specified K clusters, Zhang [17] introduce a constraint of limiting the number of clusters to be K for automatically adapting the message passing call K-AP. The proposed K-AP method offers the same guarantee of optimality of AP and generates user-specified number K of clusters for negligible computational cost overhead compared to AP.

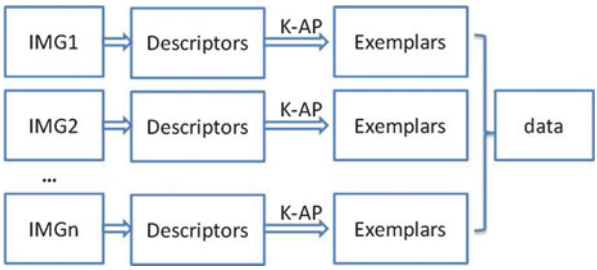

Fig. 3 K-AP feature optimization

In this paper, we use experience of K-AP for feature optimization. Instead of dealing with all images at same time, we apply K-AP to filter SIFT features (see Sect. 2.2) for each image separately, and then integrate all exemplar results into training data set. According to our experiments, we select 50 exemplars for each image, this process can be observed in Fig. 3. Note that SIFT feature descriptors are filtered by K-AP algorithm, the 50 exemplar results of each image are gathered into training data set. In this result we totally have 6,000 feature points for training set, while the total of feature points is 28,007 in original set before K-AP.

2.3 EMPCA

From last section, we obtain 2,000 feature points for each category. So, there are 2,000 dimensional feature vectors for each class. For further feature optimization of both qualities and quantities, we analysis the principal components of feature vectors by using EMPCA algorithm.

EMPCA [12] is an extension of the standard PCA by incorporating the advantages of the EM algorithm in terms of estimating the maximum likelihood values for missing information. The main advantage of this technique over standard PCA is the fact that it is more appropriate to handle large datasets especially when dealing with sparse training sets. The EMPCA procedure can be defined as follows:

E-step: $W = (V^T V)^{-1} V^{-1} A$; M-step: $V_{new} = AW^T (WW^T)^{-1}$

where 'W' is the matrix of unknown states, 'V' is the test data vector, 'A' is the observation data, and 'T' defines the transpose operator.

In our implementation, EMPCA is applied to linearly-project high dimensional SIFT feature vectors into a low dimensional feature space. The motivation of this step is to remove unrelated or less related features and reduce the classification time. We also note that the size of EMPCA feature space can be varied practically. In our experiments, we select three different sizes from 5 to 100 to evaluate the performance of proposed model.

2.4 KNN Classification

KNN algorithm is an efficient classification schema where the testing data is registered based on distance to the nearest neighbor from some previously known classes [18]. If we have a testing image, KNN is used to classify each image with respect to the multiple classes. If feature points in testing image are classified to more than one class, the image will be assigned to the class that is projected with the maximum numbers of feature points.

3 Experimental Results

The dataset is a collection of 600 real-world freight images and contains three classes including freight upright style 1 (S), horizontal style 1(L1) and horizontal style 1(L2). These images are acquired by real-time rail transportation inspection system. In this paper, we are particularly interested in two evaluations. The first is to provide the comparison of proposed algorithm with same classification schema based on different feature descriptors. In addition to the first test, it is to demonstrate the competitive running-time performance of proposed algorithm. The second test is to indicate the impacts of classification when the number of EMPCA dimensions is in a series of different options.

Our testing is implemented by MATLAB R2011a on personal PC with Intel i5 CPU, 3G memory and running under windows XP application.

3.1 Experiment 1

In the first experiment, we evaluated the performance based on three classes: Up1, Up2 and Hor. The example images can be viewed from Fig. 4. The experiment was repeated with following different features descriptors: SIFT only (KNN), SIFT + K-AP only (KNN + K), SIFT + EMPCA only (KNN + E), proposed algorithm (KNN + K + E) and SURF only. All of classifications are based on KNN schema. The motivation of this test is trying to evaluate the proper feature optimization approach and to demonstrate the improvement of proposed feature evaluation process.

The accuracy rate and the processing time are shown in Fig. 5a. The results indicate that the proposed method can achieve efficient classification accuracy while the running time is significant lower than other approaches. We also note that the correct identification of the freight status in images drops significantly with the increase of the number of classes in the database for SURF only classification. Conversely, the recognition rate of proposed algorithm (KNN + K + E) presents stability with 92 % in average.

Fig. 4 Real-world Images of three status classes

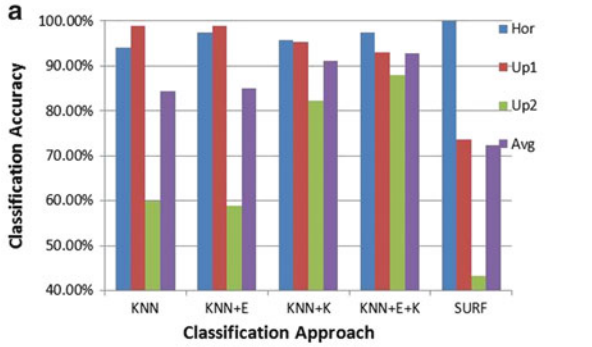

	KNN	KNN+E	KNN+K	KNN+E+K	SURF
Hor	94.12%	97.48%	95.80%	97.48%	100.00%
Up1	98.83%	98.83%	95.32%	92.98%	73.68%
Up2	60.00%	58.89%	82.22%	88.00%	43.33%
Avg	84.32%	85.07%	91.11%	92.82%	72.34%
Time(s)	6.0689	2.9042	1.4487	0.9565	2.85371

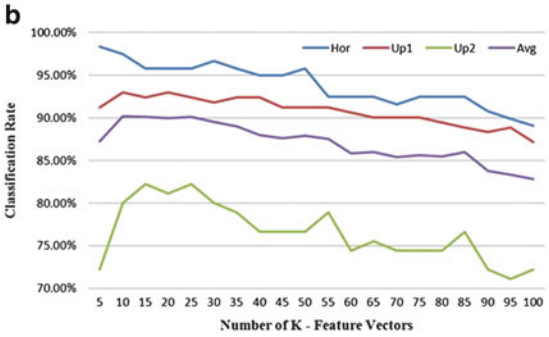

Fig. 5 Classification Results. (**a**) Classification accuracy and running time; (**b**) Classification accuracy in different number of K features vectors

3.2 Experiment 2

In this test, we evaluate the classification impacts with different number of principal features in EMPCA space. Due to the capability of EMPCA procedure is leading to overall classification performance, the aim of this test is trying to find the optimization number for EMPCA representation. From Fig. 5b, we can observe that the classification accuracy is robust when the number is selected between 10 and 25.

4 Conclusion

In this paper, we have proposed a fast and robust image classification algorithm based on SIFT features descriptors. The features are optimized by K-AP algorithm and compressed by EM-PCA to low dimensional feature space. KNN method is used to classify three template of railway freights status in the image. The experimental results were encouraging and indicate that our method is efficient to group the image into distinct class while the computation complexity is further reduced to meet real-time requirements. In additional to this, the implementation of proposed algorithm is feasible for railway inspection system based on its evaluation results on real-world images. Also during experimentation, we notice that there is a variation result in the different number of principal feature vectors. We intend to further develop the approach presented in this paper in order to improve the classification result by increasing the number of classes that are used to present the real-world rail object status.

References

1. Yu DH, Han JF (2011) The application of digital image processing in freight wagon inspection system. Third Int Conf Comput Tech Dev 3(1):319–327
2. Dong D, Dinh TB, Dinh T, Duc D (2012) Sports video classification using bag of words model. Intelligent information and database systems, vol 7198. Springer, Heidelberg, pp 316–325
3. Grauman K, Darrel T (2005) The pyramid match kernel: discriminative classification with sets of image features. Proc. IEEE Int. Conf. Computer Vision (ICCV), Beijing, 17–21 October, 2005, pp. 1458–1465
4. Duda R, Hart P (1973) Pattern classification and scene analysis. Wiley, New York, NY
5. Lowe DG (2004) Distinctive image features from scale-invariant keypoints. Int J Comput Vis 60(2):91–110
6. Bay H et al (2006) Surf: speeded up robust features. Computer Vision–ECCV, 7–13 May, Graz, Austria, 2006, pp. 404–417
7. Clarke L, Velthuizen R et al (1993) MRI: stability of three supervised segmentation techniques. Magn Reson Imaging 11(1):95–106
8. Yu DH, Ghita O, Sutherland A, Whelan PF (2006) Dictionary based lip reading classification. In: China-Ireland international conference on information and communications technologies, Hangzhou, China, 18–19 October, 2006, pp. 226–229
9. Rosten E, Drummond T (2006) Machine learning for high-speed corner detection. Computer Vision–ECCV, 7–13 May, Graz, Austria, 2006, pp. 430–443
10. Rublee E et al (2011) ORB: an efficient alternative to SIFT or SURF. Proc. IEEE Int. Conf. Computer Vision (ICCV), Barcelona, 6–13 November, 2011, pp. 2564–2571
11. Juan L, Gwun O (2009) A comparison of SIFT, PCA-SIFT and SURF. Int J Image Process 65:143–152
12. Roweis S (1998) EM algorithm for PCA and SPCA. Adv Neural Inform Process Syst 10:626–632
13. Frey BJ, Dueck D (2007) Clustering by passing messages between data points. Science 315:972–976

14. Dueck D. and Frey BJ. (2007). Non-metric affinity propagation for unsupervised image categorization. Proc. IEEE Int. Conf. Computer Vision (ICCV), Rio de Janeiro, 14–21 October, 2007, pp. 1–8
15. Lv G et al (2010) Optimization of training samples with affinity propagation algorithm for multi-class SVM classification. Adv Neural Network 2010:33–41
16. Yang D, Guo P (2009) Improvement of image modeling with affinity propagation algorithm for semantic image annotation. Proceedings of international conference on neural information processing, Bangkok, Thailand, 1–5 December, 2009, pp. 778–787
17. Zhang X et al (2010) K-AP: generating specified k clusters by efficient affinity propagation. Proc. IEEE Int. Conf. data mining (ICDM), Sydney, Australia, 14–17 December, 2010, pp. 1187–1192
18. Sim J, Kim SY, Lee J (2005) Prediction of protein solvent accessibility using fuzzy k-nearest neighbor method. Bioinformatics 21(12):2844–2849

Weakly Supervised Learning for Airplane Detection in Remote Sensing Images

Dingwen Zhang, Jianfeng Han, Dahai Yu, and Junwei Han

Abstract In contrast to the conventional approaches to learn geo-target classifier using fully supervised learning techniques which heavily rely on the artificial annotation in the training set of remote sensing images (RSIs), this paper attempts to develop a weakly supervised learning (WSL) approach for airplane detection in RSIs with cluttered background. The framework includes a novel WSL method to train airplane classifier using the training images with weak labels and an efficient detection scheme to localize the airplanes. The proposed WSL mainly consists of three components: the negative mining based training set initialization, the updating process for both the positive and negative training set, and the classifier evaluation mechanism that can efficiently terminate the updating process for the best performance. Comprehensive experiments on a large number of RSIs and comparisons with state-of-the-art fully supervised models demonstrate the effectiveness and efficiency of the proposed work.

Keywords Weakly supervised learning • Negative mining • Airplane detection

D. Zhang • J. Han
School of Automation, Northwestern Polytechnical University, Xi'an, China

J. Han (✉)
Computer Department, Information Engineering School, Tianjin University of Commerce, Tianjin, China
e-mail: hjf1208@sohu.com

D. Yu
School of Automation, Northwestern Polytechnical University, Xi'an, China

Tianjin Optical Electrical GaoSi Communication Engineering Technology Co., Ltd, Tianjin, China

B. Zhang et al. (eds.), *The Proceedings of the Second International Conference on Communications, Signal Processing, and Systems*, Lecture Notes in Electrical Engineering 246, DOI 10.1007/978-3-319-00536-2_18,

1 Introduction

The advance of remote sensing technology leads to the dramatic growth of geospatial images in the amount and quantity. The high spatial resolution images can provide abundant spatial and contextual information for certain targets on the earth [1], which has necessitated the research into automatic analysis and understanding of RSIs. Nowadays, recent researches about target detection and recognition in high-resolution RSIs have become one of the most fundamental challenging tasks in this field. Typically, fully-supervised classifiers are used to fulfill the target detection task. However, a high-resolution RSI always contains complex textures that are hard for manually annotation. Since the target in RSIs only takes size between 1 and 5 % of the whole image area, people can hardly focus their attention on such small regions for detailed annotation. Moreover, since some special geo-targets are occluded or camouflaged, the artificial annotations to these targets become to be less precision and unreliable. Overall of above discussion, the manual annotation of geo-targets' locations is the most important part in fully-supervised detector training process which is tedious, time-consuming and inaccuracy. In order to solve this problem, it is essentially necessary to train target classifiers by weakly supervised methods [2–5].

In the process of weakly supervised learning (WSL) of target classifier, each image in the training set is annotated with a weak label which only indicates whether the image contains certain targets or not whereas locations and sizes are not necessarily provided. In this certain circumstance, a target model is training by using WSL that attempts to address two sub-problems simultaneously: localizing the targets in each positive training image (automated annotation) and training a model based on the automated annotation results (detector learning) [6]. To overcome these challenges and apply WSL method for airplane detection in RSIs, a novel framework is proposed as shown in Fig. 1. It includes a novel WSL method to train airplane classifier using the training images with weak label and an efficient detection scheme to localize the airplanes in RSIs. The WSL training process that is the most challenging task in this work consists of three major components. The first component is a negative mining based training set initialization which we can get from an initial training set. The second component is an updating process for both the positive and negative training set. In this process, our target classifier can improve its precision and accuracy gradually. The third component is a classifier evaluation mechanism that can efficiently terminate the updating process for the best performance.

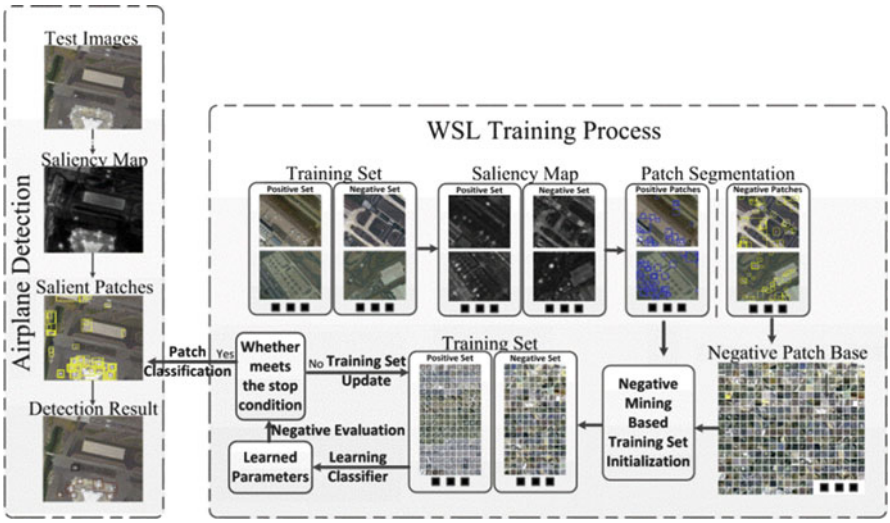

Fig. 1 Framework of the proposed algorithm

2 Training Set Initialization

In the training set initialization process, we use a novel saliency computation model to obtain the saliency maps of training images, and then apply a self-adaptive multi-threshold segmentation to obtain both positive and negative patch bases. Finally, we adopt negative mining to generate initial training set.

2.1 Saliency Model

Inspired by the characteristic of visual attention mechanism, different computational models [7, 8] have been proposed to detect salient object. In this paper, we propose a salient feature fusion process. For each RSI, the low- and mid-level features are extracted for every pixel of down-sampled image and they are used to generate the final saliency map like [9]. The low-level features are local contrast of intensity, orientation and color, color value in each channel, and global color contrast [9]. The mid-level features are SR [7], GBVS [8], FT [6], WSCR [10], and SDS [11]. All of these silent features have already been demonstrated by previous works to correlate with visual saliency or be biological plausible. For the weakly labeled training set, we do not know the locations of the targets. Duo to this reason, we cannot use artificial annotation to train a set of coefficients to fuse the salient features in our salient computation model. For this regard, we treat the weight of each salient feature equally which means that if a pixel is salient in most

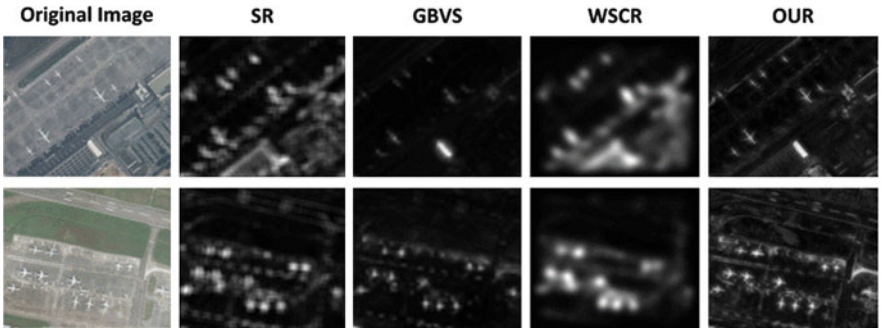

Fig. 2 Saliency map comparison

salient features, it is salient in the final saliency map. Figure 2 shows that our salient computation model can outperform most state-of-the-art methods.

2.2 Self-Adaptive Segmentation

Saliency model can calculate a salient value for each pixel in every RSI. Then, the next step is to obtain candidate patches which may contain certain targets based on the saliency map. An efficient way is to segment the saliency map by one or more adaptive threshold as (1) in [6].

$$thresh = \frac{k}{W \times H} \times \sum_{x=0}^{W-1} \sum_{y=0}^{H-1} S(x, y) = k \times mean(S) \tag{1}$$

where W and H are the width and height of the saliency map in pixels respectively, and $S(x, y)$ is the saliency value of the pixel at position (x, y), k is a parameter set manually.

Afterwards, the candidate patches will be re-cropped to obtain the patch which should be the similar size as one target rather than some approximate region including large areas such as background. To achieve this goal, we prefer to use the technique in [4] by finding the area enclosing majority of its edge energy. Finally we obtain the external rectangle of certain area as one candidate or salient patch. In this paper we set $k = 1.5$ and 3 to acquire the refined patches which are stable for the next process.

2.3 Negative Training Set Initialization

Negative training set is the salient patches in negative RSIs. As we mentioned before, the negative RSIs are weakly labeled RSIs without any targets. In order to generate the negative patch base, we calculate their saliency map and use our self-adaptive segmentation method to obtain salient patches. Afterwards, we randomly select negative patches with the same number of patches in the positive training set to form the negative training set.

2.4 Positive Training Set Initialization

Positive training set is obtained from the positive RSIs. After getting positive patch base by using our saliency model and self-adaptive segmentation method, we need to adopt negative mining to select several positive patches with highest probability of containing the targets to form the positive training set.

As described in [12], negative mining is an approach of mining the nearest negative patches. Unlike [3, 5], it relies on the abundance of known negative patches and does not require optimization of intra-class cost function. The training image set consists of a set of positive images I_i^+ that contain the object of interest and a set of negative images I_i^- which do not. We consider a set of positive patches $x_{i,j=1..n}$ in each image i. Each patch $x_{i,j}$ is represented by a bag-of-words (BOW) histogram. The goal of this step is to score every patch in each positive image I^+ and select some highest scored patches as the initial positive training set. The negative mining algorithm accomplishes this by selecting the patches with large distance to the nearest neighbor in the negative patch base [see (2)] where $\|\cdot\|_1$ is the L_1 norm and $N(x_{i,j}^+)$ refers to the negative nearest neighbor of $x_{i,j}^+$.

$$Dist\left(x_{i,j}^+\right) = ||x_{i,j}^+ - N\left(x_{i,j}^+\right)||_1 \tag{2}$$

3 Training Set Updating

In order to implement the target detection task precisely, a training set updating process is applied to train the classifier iteratively. The motivation of this process is to achieve a strong classifier ultimately that can improve the performance of the classifier. It is important to notice that we use BOW features to train the target classifier because it is invariant to the target rotation, shape and size variation. After training the BOW classifier by using the initial training set, the obtained target classifier is then run on each positive image. Next, a set of patches with highest classification score are selected as the new positive training set. We then randomly select the same number of negative patches from the negative patch base to generate

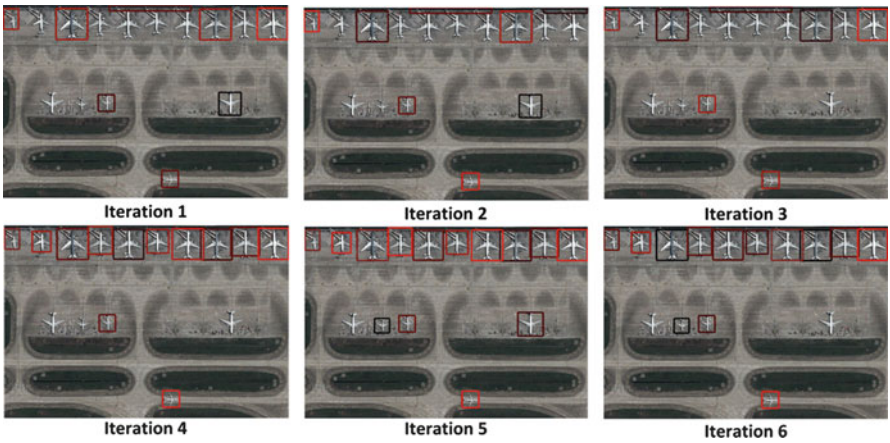

Fig. 3 Performance of training set updating

Table 1 Performance of negative evaluation

	Iteration 1	Iteration 2	Iteration 3	Iteration 4	Iteration 5	Iteration 6
F-measure	0.7361	0.7452	0.7441	0.7650	0.7741	0.7699
False rate	0.1412	0.0619	0.0387	0.0295	0.0290	0.0348

the new negative training set. Figure 3 shows the gradually improvement of the target classifier in each iteration and achieve the best performance in iteration 5.

4 Classifier Evaluations

Evaluating trained target classifier in each iteration using weakly labeled data is difficult because we don't know what the target looks like and where the exact target locations are in positive images? To solve this problem, we propose to use a negative evaluation mechanism to measure the effectiveness of current classifier in iteration since negative instances do not contain any target. Specifically we use the classifier to classify each negative patch in negative patch base and calculate the false rate in iteration. Continually, the false rate decreases in the first several iterations and then begins to increase. Therefore, we setup the iteration with the local minimal false rate is the stop iteration, and the target classifier trained in this iteration will be selected as the final classifier which is preferred as the best performance in the updating process. This intuitive measure is proved base on the performance of the trained classifier in our experiments evaluation (see Table. 1). From Table. 1, we can observe that the local minimal false rate locates in iteration

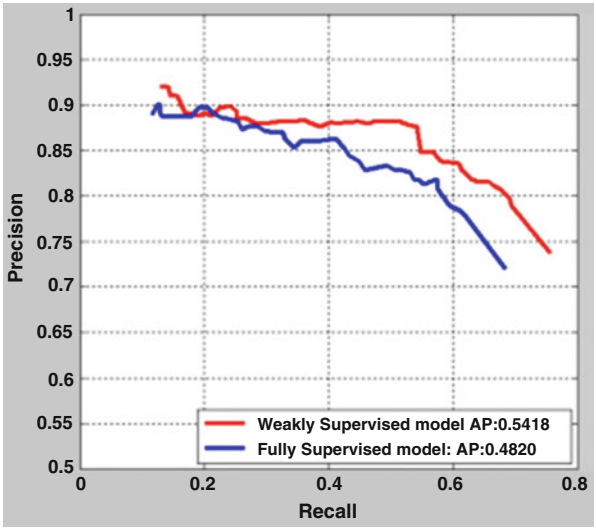

Fig. 4 Precision-recall curve

5 and the F-measure which is popularly used in object annotation evaluation increases to the maximum.

5 Airplane Detection

For the airplane detection, a salient patch based target detection scheme is adopted (see Fig. 1). We calculate the saliency maps of RSIs at first, and use our self-adaptive segmentation method to get their salient patches. Because our approach is robust to get salient patches which would contain the airplane targets in the entire test images, it appears to be more efficient to detect targets by classifying the salient patches in one RSI instead of the sliding windows. In this regard we use the classifier trained by our WSL method to accomplish the weakly supervised airplane detection.

6 Experimental Results

For this experiment, we collect 120 high resolution RSIs from ten different airports in different countries on Google Earth. The resolution of them is about 0.5 m per pixel, the scale of an image is about 1,000 by 800 pixels, and the size of an airplane target is from 700 pixels to 25,488 pixels. Hence, the result of our experiment can demonstrate that our algorithm is able to deal with multi-size target in large scale RSIs with cluttered background.

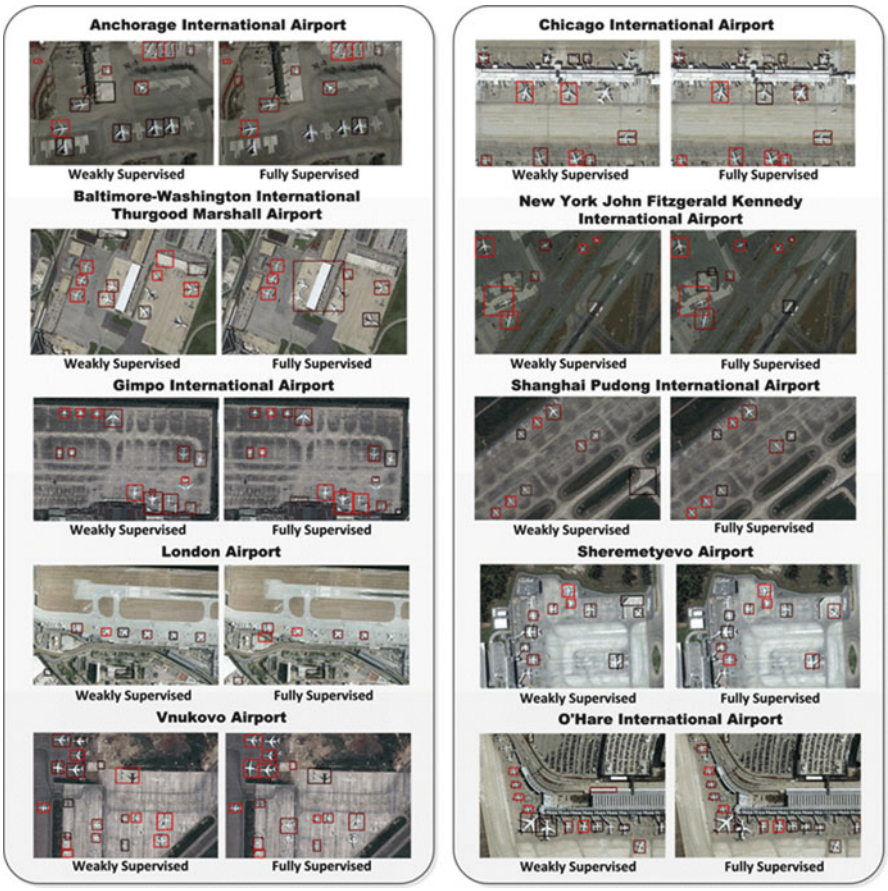

Fig. 5 Examples of detection results

In this evaluation we separate all RSIs into three sets: 50 of them as test set, 50 of them as positive training set, and 20 of them as negative training set. The training set is used to train airplane classifier by our WSL method, and the test set is used to compare the performance of the trained classifier by using proposed method and the classifier trained by fully supervised method.

In additional to demonstrate the airplane detection accuracy based on proposed WSL trained airplane classifier among the test data, we present the Precision-Recall curve (see Fig. 4) and several detection result examples (see Fig. 5). Both figures demonstrate that the proposed WSL method can achieve higher detection precision in more test RSIs and a mean AP of 0.5418 superior to a mean AP of 0.4820 of the FS approach. The mean AP has been proved to be the most accurate approximation to average precision and the most robust measure in the presence of incomplete detection. Note that the weakly supervised method is the proposed approach in this

paper and the fully supervised method is the classifier trained by artificial annotation with BOW feature to detect target in the same test image set.

7 Conclusions

In this paper, we present a framework for the challenging task of detecting airplane with classifier trained by WSL method in large scale RSIs with clustered background. The framework includes a novel WSL method to train airplane classifier using the training images with weak label and an efficient detection scheme to localize the airplanes in RSIs. The experimental results demonstrate that WSL method in remote sensing target detection is an efficient approach since weakly supervised learning target classifier can achieve better detection accuracy compared with a fully supervised classifier.

Acknowledgments This work is supported by graduate starting seed fund of Northwestern Polytechnical University under grant Z2013105.

References

1. Tuia D, Pacifici F, Kanevski M, Emery WJ (2009) Classification of very high spatial resolution imagery using mathematical morphology and support vector machines. IEEE Trans Geosci Rem Sens 47(11):3866–3879
2. Deselaers T, Alexe B, Ferrari V (2012) Weakly supervised localization and learning with generic knowledge. Int J Comput Vis 100(3):275–293
3. Deselaers T, Alexe B, Ferrari V (2010) Localizing objects while learning their appearance. ECCV Part IV. LNCS 6314:452–466
4. Pandey M, Lazebnik S (2011) Scene recognition and weakly supervised object localization with deformable part-based model. ICCV, Barcelona, 6–13 November, 2011, pp. 1307–1314
5. Siva P, Xiang T (2011) Weakly supervised object detector learning with model drift detection. ICCV, Barcelona, 6–13 November, 2011, pp. 343–350
6. Achanta R, Hemami S et al (2009) Frequency-tuned salient region detection. IEEE conference on computer vision and pattern recognition, Miami, FL, 20–25 June, 2009, pp. 1597–1604
7. Hou X, Zhang L (2007) Saliency detection: a spectral residual approach. IEEE conference on computer vision and pattern recognition, Minneapolis, MN, 17–22 June, 2007, pp. 1–8
8. Harel J, Koch C, Perona P (2007) Graph-based visual saliency. Advances in neural information processing systems. MIT Press, Cambridge, MA, pp 545–552
9. Judd T, Ehinger K, Durand F, Torralba A (2009) Learning to predict where humans look. Proc. IEEE 12th international conference on computer vision, Kyoto, 29 September–2 October, 2009, pp. 2106–2133.
10. Han B, Zhu H, Ding Y. (2011) Bottom-up saliency based on weighted sparse coding residual. ACM International Conference on Multimedia, Scottsdale, Arizona, pp. 1117–1120
11. Achanta R, Estrada F, Wils P, Süsstrunk S (2008) Salient region detection and segmentation. Int Conf Comput Vis Syst 5008:66–75
12. Siva P, Chris R, Tao X (2012) In defence of negative mining for annotating weakly labelled data. In ECCV. Springer, Berlin, pp 594–608

Measurement of Rice Growth Based on the Remote Video Images

Ruokui Chang, Hua Liu, YuanHong Wang, Yong Wei, and Nan Wang

Abstract Rice is one of the major crops in our country. Tracking the growth of rice in time with remote monitoring equipment can provide safeguard for production forecast and disease control of the rice. Adopting wireless video transmission module W730 to realize remote video monitoring on rice growth, the experiment could obtain the growth of rice information, and thus will lay a foundation for forecasting rice yield by collecting growth images of rice at different times, preprocessing real-time image data with the MATLAB image processing module, making segmentation of the image with finite difference method, and marking the median-filtered image.

1 Introduction

Rice is one of the major food crops in China and its production accounts for about half of the total grain output. Monitoring and predicting rice growth conditions timely and accurately is remarkably significant for planting industry structure adjustment and grain policy making. Compared with big errors resulted from traditional methods such as artificial observation for rice growth change and yield prediction, the experiment, employing computer remote control technology, realizes real-time monitoring on the rice growth conditions, which lays a foundation for accurate forecasting of plant diseases and insect pests at the production level.

R. Chang • H. Liu • Y. Wei • N. Wang
School of Electromechanical Engineering, Tianjin Agricultural University, Jinjing Road 22, 300384 Tianjin, China
e-mail: changrk@163.com

Y. Wang (✉)
School of horticulture, Tianjin Agricultural University, Jinjing Road 22, 300384 Tianjin, China
e-mail: wangyh@tjau.edu.cn

B. Zhang et al. (eds.), *The Proceedings of the Second International Conference on Communications, Signal Processing, and Systems*, Lecture Notes in Electrical Engineering 246, DOI 10.1007/978-3-319-00536-2_19,

2 Material and Methods

Remote monitoring system is composed of several big modules such as single chip microcomputer system (MCU), power supplies, wireless video transmission module, wireless data transmission module, pyroelectric infrared sensor module, cloud terrace (PAN/TILT), and Sound-light alarm. Among them, the single chip microcomputer system is mainly responsible for controlling command parsing and other modules to complete the corresponding functions; Adopting W730 wireless video transmitter, wireless video transmission module works in coordination with the microcontroller through the serial port communication to transmit video data and controlling commands between the system and the remote PC; Wireless data transmission module's main function is data transmission between the host and environment parameter detection module; PAN/TILT enlarges the video scope by changing the angle of the camera and Sound-light alarm aims at warning of theft. The system structure is shown in Fig. 1.

By receiving remote control signal from the PC, host transmits the collected data of video, images, and environmental parameters to the remote PC through 3G network, which provides experts with crop growth status information and thus realizes the remote expert diagnosis function.

3 Measurement of Rice Growth

Rice growth image processing is the key to measure the growth via image processing method. After acquiring images for the growth of rice, Matlab software was applied for image processing and analysis. Working flow chart for rice growth forecast is shown in Fig. 2. Firstly, the original image was preprocessed (such as getting rid of the shadow and adjusting the size); Secondly, RGB(red, green, blue) image was converted to a grayscale image; then image segmentation was conducted to make binary value transformation; and then, the accurate difference of rice growth was obtained through the edge detection; finally, forecast data of rice growth could be gotten by calculating the pixel number gotten through morphological image processing, median filtering, marking and the like.

3.1 Video Preprocessing

First of all, the size of original image got adjusted by the written MATLAB program since image from video capture is very big (3,264 $\times$ 2,448). After adjustment, the size of the image became small and suitable for image processing (652 $\times$ 490). As a kind of important means of image enhancement, gray-scale transformation increases the dynamic range of the image, extends the image

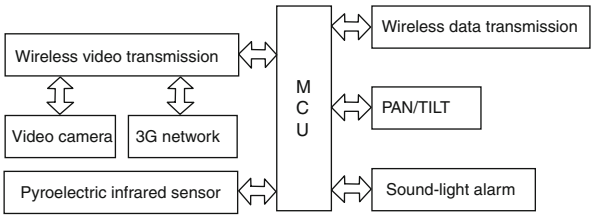

Fig. 1 Structure of host

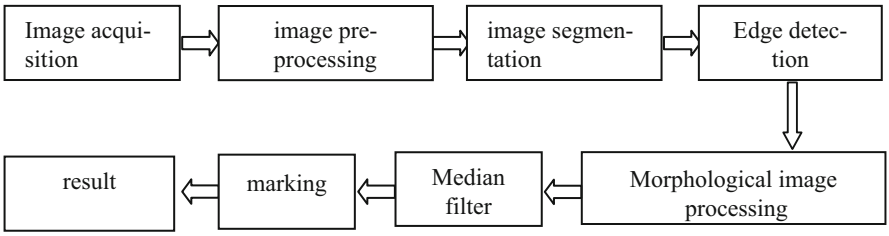

Fig. 2 The flow chart of rice growth forecasts

contrast, enables image clearer and features more obvious. Therefore, true color image (RGB format) would be converted to grayscale images in the experiment.

3.2 Image Segmentation

In the experiment image segmentation was conducted via the finite difference method which is a method of image processing usually for detecting image transforming and moving objects [1, 2]. With the reference image as a background image, the finite difference skill gains the moving target area through subtraction between the current frame image and the background image [3]. The basic idea of background difference method is as shown in Fig. 3.

Among them, $f_k(x, y)$ is on behalf of the current frame, $B_k(x, y)$ represents the background frame, $D_k(x, y)$ represents the difference of binary image, th is on behalf of the set threshold. Based on (1), binary image $D_k(x, y)$ is obtained though binarization processing of the difference image.

$$D_k(x,y) = \begin{cases} 1 & if\,|f_k(x,y) - B_k(x,y)| > th \\ 0 & if\,|f_k(x,y) - B_k(x,y)| < th \end{cases} \quad (1)$$

In the Matlab, with imsubtract functions the pixel values of one input image gets subtracted from the corresponding pixel values of another input image, then the result will be as the Output image pixel values. The procedure is as follows:

```
image = imread(image_name);
image1 = imread ('Background.jpg');
```

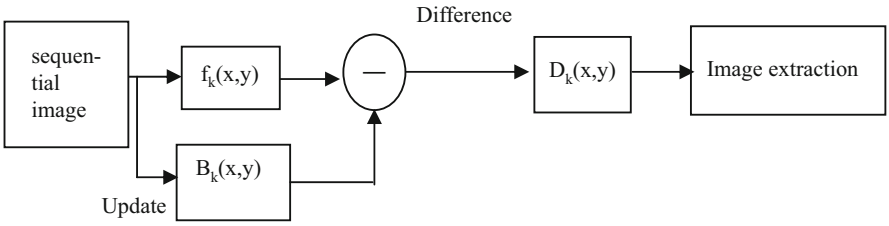

Fig. 3 The basic principle diagram of background difference method

```
grayscale = rgb2gray (image);
grayscale1 = rgb2gray (image1);
subtract = imsubtract (grayscale1,grayscale);
figure, imshow (subtract);
```

In order to eliminate the edge effect in the image, the imclearb border command also needs to be used. Command format is as follows:

```
noborder = imclearborder(image,coon);
```

Coon means connectivity. A fully connected path formed by elements of a set exists between any two pixels in a connectivity. And removing the background of the image is based on the concept of connectivity among pixels to determine which pixels and edge pixels connect so as to remove this part of the background object. Procedure is as follows:

```
R = imclearborder(subtract,8);
figure,imshow(R).
```

3.3 Image Filtering

Image enhancement is one of digital image processing methods which improves the appearance of the image or convert the image into another form more suitable for the human eye observation and analysis of the machine. The image enhancement methods mainly include average filtering and median filtering method. Experimental comparison proves the median filtering is a better method to remove the noise [4–7]. Hence, this method was applied for image denoising processing.

Median filter is widely used as it will not make the image boundaries fuzzy in the attenuation of noise at the same time. The effect to remove noise with median filter relies on two factors: space range in the field and pixel number involved in the median calculation. In general, the bright and dark objects whose size is smaller than half size of the filter area will be filtered, whereas larger objects remain intact. Therefore, the space size of median filter must be adjusted according to the existing problems, whose basic principle is to adopt the median value of pixel gray value within the neighborhood as the grey value of postprocessed pixels. The images contrast before and after filtering is shown in Fig. 4.

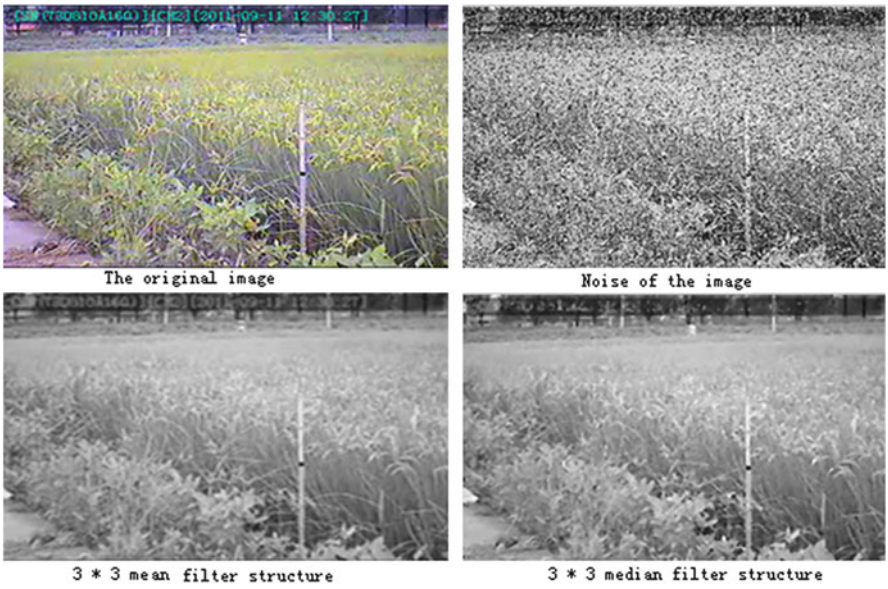

Fig. 4 The image contrast before and after filtering

3.4 Marking

First, the target object in the image was determined and then marked clearly with a unique number by finding connected components with bwlabel function which could accept a binary image and specify connectivity value of the respective target object (4 or 8, said 4 or 8 connected) as input variables. In order to verify the digital image processing prediction of rice growth, the experiment analyzed pictures of rice plant height from different growth periods and compared the analysis result with actual measuring data. The comparison is shown in Fig. 5, from which it can be seen the increment data gotten from the Matlab image processing method is very close to the actual test data, the average relative error being only 3.05 %.

4 Conclusion

Putting forward rice growth forecast method based on video image processing, the experiment realizes the image processing of the rice growth and synchronized forecasts based on Matlab platform. Employing machine vision to track the rice growth improves the experiment efficiency by reducing much time owing to repeated measurement, and thus helps the results more reliable and accurate.

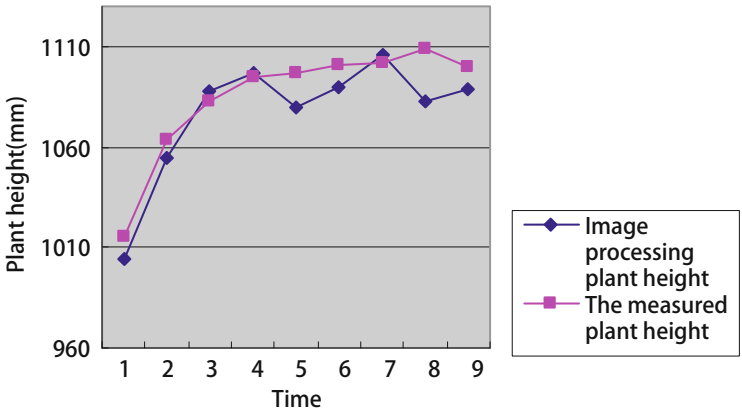

Fig. 5 Comparison graph for experiment and actual measurement of plant height

Acknowledgments This work is supported in part by Tianjin agriculture committee Support Project (201003060),The State Science and Technology Commission Spark Program projects (10ZHXHNCO8300).

References

1. Wenchuan Guo, Xinhua Zhu (2002) Research progress of machine vision technology in grains identification and classification. Cereal & feed industry (6):50–51
2. Rei JF et al (1991) Computer vision sensing of stress cracks in corn kernels. Trans ASAE 34 (5):2226–2244
3. Majumdar S et al (1999) Classification of bulk samples of cereal grain using machine vision. Agric Eng Res 73:35–47
4. Tianzhen L, Baiqing Z (2005) Research on rice-quality inspection basing on computer vision technology. Cereal Food Indus 12(4):50–53
5. Xuemei W, Chengyao Z, Longqin W (2005) Tomato identification technique based on computer vision using MATLAB. Agri Equip Tech 31(4):15–17
6. Ming S, Yun L, Yiming W (2002) Computer vision based rice chalkiness detection using MATLAB. Trans CSAE 18(4):146–148
7. Caiyun H, Oshita S, Seo Y, Kawagoe Y, Torii T, Kudoh K, Higuchi T, Do G (2001) Application of 3D-microslicing image processing system in rice quality evaluation. Trans CSAE 17 (3):92–95

Image Measurement Strategy for Extreme Circumstances

Xiong Zhang, Xiaoli Yang, Ruizhu Yang, Jingxiong Huang, and Yelong Zheng

Abstract A new strategy of image measurement in an extreme circumstance was proposed, according to the high-accuracy measuring requirements in high-low temperature. A camera imaging model was chosen and analyzed. A precise vision measurement system was designed based on a comprehensive analysis of the ambient influences on the system. The system utilized camera temperature control device, high-intensity light source, telecentric lens and vibration isolation platform to ensure imaging quality, such as low distortion, high contrast and stability. A quartz standard part with very low coefficient of linear expansion was chosen, combined with sub-pixel feature extraction algorithm, so as to realize a real-time calibration of the measurement system errors. Through a continuous 60 h and three temperature cycle measurement experiment in an extreme circumstance, the results show that the system can work stably for a long period and can achieve high measurement accuracy.

Keywords High-low temperature • Image measurement • Real-time calibration • Sub-pixel

1 Introduction

Aerospace devices are operated under extreme circumstance with a dramatic temperature variance. The large temperature gradient due to insufficient thermal convection causes dimensional changes in the components. Thus, the overall safety and reliability of the device will be compromised. Therefore, dimensional

X. Zhang • R. Yang • J. Huang • Y. Zheng (✉)
State Key Laboratory of Precision Measuring Technology and Instruments, Tianjin University, Tianjin, China
e-mail: zhengyelong_tju@126.com

X. Yang
China Petroleum Technology & Development Corporation, Beijing, China

B. Zhang et al. (eds.), *The Proceedings of the Second International Conference on Communications, Signal Processing, and Systems*, Lecture Notes in Electrical Engineering 246, DOI 10.1007/978-3-319-00536-2_20,

measurement experiments under extreme circumstance must be considered during aerospace device testing. The extreme circumstance experiment is usually conducted in the environment where pressure is below 10^3 Pa and temperature ranges from -35 to 65 °C, with random electromagnetic interference existing around. Moreover, aerospace devices are commonly presented with irregular surfaces which composed of metallic materials such as copper aluminum alloy, together with nonmetallic insulating materials. Therefore, traditional methods have significant limitations in dimensional measurement under extreme circumstance. Various effective methods have already been done for measurement under this environment, including strain gauge method [1], electronic speckle pattern interferometry method [2], holographic method [3], digital speckle correlation method [4], and the method based on the phase shift principle [5]. However, such methods are still limited, such as the strain gauge method, which could inevitably affect the tested objects because of contact, and the other methods that are relatively sophisticated and expensive to realize.

Recent advances in computer vision and image sensing technology offer vision measurement as a promising method for dimensional measurement under extreme circumstance because of its high accuracy, non-contract feature, and wide adaptability. Recent studies by NASA, MCSE, and IGP mostly focus on solutions in vision measuring methods, with the results already been put into practice [6–8]. Domestic research on vision measurement methods under extreme circumstance mainly focuses on aerospace field, such as the photogrammetric system for detecting antenna distortion [9, 10].

This paper analyzes the influences of extreme circumstance on the measurement system. According to the high-accuracy requirements of 2-D size measurement of the components, a special system that can work properly in extreme circumstance is designed. High brightness LED light sources and telecentric lenses are adopted to enhance the imaging clarity under extreme circumstance. Temperature control devices are utilized to ensure the safety of cameras, and a vibration isolation platform is employed to improve stability. Effects on image quality and measurement accuracy caused by the environment are eliminated through exposure compensation and real-time calibration, respectively. The validity of this system is proved by the experiments under extreme circumstance.

2 Principle of Vision Measurement

Vision measurement, based on the perspective geometric theory, is a method used to obtain geometric parameters of the tested object through images taken by camera. The 2-D vision measurement model is applicable for testing coplanar dimensional parameters (the object plane is parallel to the image plane, and both the object plane and the image plane are perpendicular to the optical axis of the imaging system). Neglecting lens distortion, the pinhole model is chosen to fit the single-camera imaging system. Four coordinate systems are established, namely,

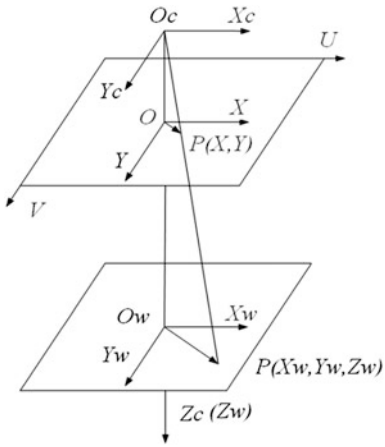

Fig. 1 2-D planar imaging model of a single camera

world coordinate system $O_wX_wY_wZ_w$, camera coordinate system $O_cX_cY_cZ_c$, image coordinate system OXY, and pixel coordinate system OUV, as shown in Fig. 1.

The object and the image are in accordance with the central projection transformation. Therefore, the similarity of image point $P(x, y)$ in the image coordinate system with P (x_w, y_w, z_w) in the world coordinate system can be expressed as follows:

$$\begin{cases} x = \dfrac{x_w Z_w}{f} \\ y = \dfrac{y_w Z_w}{f} \end{cases}. \tag{1}$$

When the manufacturing errors of the CCD photosensitive arrays can be ignored, the relationship between pixel coordinate (u,v) and image point $P(x, y)$ can be described as follows:

$$\begin{cases} u = u_0 + \dfrac{x}{dX} \\ v = v_0 + \dfrac{y}{dY} \end{cases}. \tag{2}$$

In (1), f represents the effective focal length. In (2), dX and dY stand for the physical size of each pixel in the X axis and the Y axis, respectively. (u_0,v_0) is the coordinate of point o in the coordinate system u,v. Combining (1) and (2) gives

$$\begin{cases} \Delta u = u_1 - u_2 = \dfrac{Z_w}{fdX}\Delta x_w \\ \Delta v = v_1 - v_2 = \dfrac{Z_w}{fdY}\Delta y_w \end{cases}, \tag{3}$$

where Δx_w and Δy_w represent the horizontal and vertical components of the real distance between two points in the object, respectively. Δu and Δv stand for the number of pixels arraying on the horizontal and vertical intervals in the image, respectively. As long as the pixel coordinate parameters are extracted from the image and multiplied by a proportionality factor called the pixel equivalent value, actual geometric dimension of the objects can be acquired [11].

3 Vision Dimensional Measurement Method Under Extreme Circumstance

3.1 Measurement System Components

As shown in Fig. 2, the vision measurement system mentioned herein is composed of a CCD camera, optical lens, light source, vibration isolation platform, temperature control device, image capturing card, computer, and measurement software. Two sets of imaging systems are used for carrying out two sets of dimensional measurements simultaneously to improve efficiency because of the long duration of the extreme circumstance experiment.

An industrial-level digital CCD camera (Baumer TXG50) with 2,448 × 2,050 pixel resolution is used. The image capturing frame rate is up to 15 fps, and the transmission distance can reach 100 m, meeting the remote real-time measurement requirement. The camera supports software parameter settings, and the range of exposure time can be set from 4×10^7 to 6×10^7 μs. A built-in temperature sensor can access the internal temperature in real-time. The telecentric lens used (Computar TEC-M55) has a fixed focal length of 55 mm, a large depth of field ranging from 3.5 to 6.0 mm, and a small distortion. The optical system can provide high measurement accuracy under a constant field-angle to ensure clear imaging under extreme circumstance. High-brightness LED light sources are chosen to provide high-intensity, stable, and uniform illumination. Both side-light reflection and back-light transmission lighting are applied to enhance the contrast of the complex component edges. Measurement software consists of several modules, including image capturing, image processing and control modules.

The temperature control device of the camera is composed of a semiconductor cooling equipment and a water cycling machine. The semiconductor cooling equipment compares the real-time camera surface temperature with the preset temperature and regulates the current through the cooling chip, thus maintaining

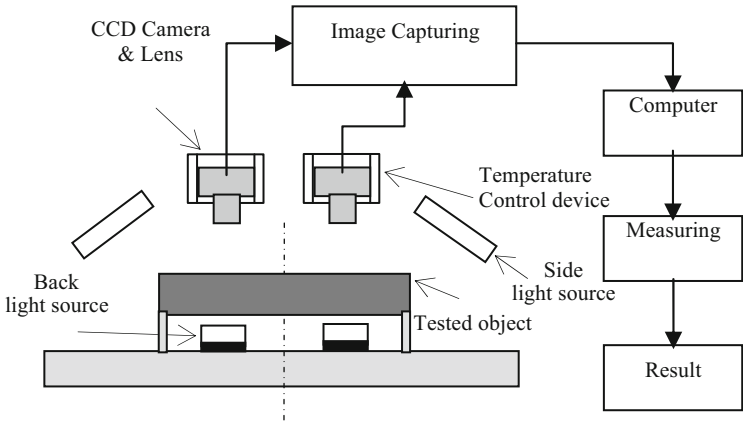

Fig. 2 Schematic diagram of the vision measurement system

a normal range of temperature. Fluorocarbon oil is used as the circulating fluid for the cycling machine because of its stability, thermal conductivity, and adaptability for temperature ranging from -80 to 300 °C. Circulating fluid pipes are connected to the hot surface of the semiconductor chip, enabling redundant heat to be sent out through the water cycling machine.

3.2 Real-Time Calibration Method

Vision measurement calibration is generally performed prior to measurement. A dimensional reference is used to calibrate the system so that a corresponding pixel-object relationship can be established. The reference is removed afterward, and the tested object is then put in. The changes in temperature and pressure affecting the measurement system also cause the calibration to vary under extreme circumstance. Therefore, a real-time calibration method based on the pixel equivalent value [12] is adopted in this environment. As shown in Fig. 3, the reference component is made of transparent quartz whose linear expansion coefficient is 5.5×10^{-7}/ °C, which has a good thermal stability. The known high-precision size of the black rectangle carved on a surface by photolithography is set as the measuring reference feature. During the measurement, the reference component should be placed in the imaging field at the same height with the measured surface of the tested object. Pixel equivalent value can be obtained by calculating the ratio of the actual distance between the two parallel lines with the number of pixels. This real-time calibration aims to improve the measurement accuracy by reducing the influences of ambient changes in the measurement system.

Sub-pixel subdivision algorithm is adopted to improve the calibration accuracy. First, the pixel coordinates of each point on two opposite edge lines are extracted

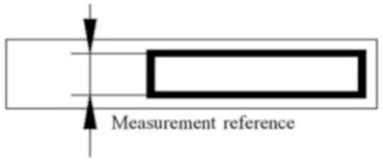

Fig. 3 Reference component used for real-time calibration

through edge detection in the calibrated region. These pixel coordinates are used for selecting the gray-level sequence of the edges from the original gray-scale images, thus determining the edge points at the sub-pixel precision level. The least squares method is applied to realize the centerline fitting, and the number of pixels in the distance between the two centerlines of the opposite edges can be obtained. Finally, the pixel equivalent value can be acquired by calculating the ratio of the actual distance to the number of pixels.

4 Experimental Results

A vacuum container serves as the extreme circumstance simulator system. The vision measurement system is divided into two parts, namely, the internal and the external parts, connected by a vacuum flange cable. Ambient pressure ranges from 1.0×10^{5} to 1.3×10^{-3} Pa, and the temperature varies from -35 to 65 °C, with changing speed of 10–15 °C per h. The 60 h measurement experiment undergoes three cyclic processes. Experimental data are recorded by the measurement software during the process. L is the dimension being measured, as Fig. 4 shows.

The tested object is a 2-D aerospace device whose size changes under extreme circumstance can be monitored by the measurement experiment. In the experiment, the imaging quality is stable, and the fluctuation range of AGV remains less than 1. The measurement results at each temperature point hold stably. The extreme circumstance can alter the component dimension. The maximum standard deviation value is smaller than 0.02 mm.

5 Conclusion

The influences of extreme circumstance on the vision measurement system are analyzed, and a method for 2-D vision measurement under this environment is proposed. Trial results show that the system can work stably under extreme circumstance for a long duration without producing pollutions in the experimental devices and the tested objects. Moreover, it does not affect the temperature and vacuum degree of the experimental environment. The exposure compensation method can reduce the effects of light intensity changes on image quality, and real-time calibration can decrease the effects of the varying ambient parameters in measurement

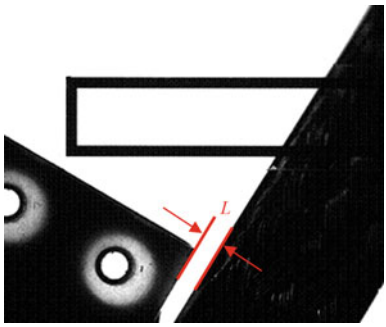

Fig. 4 Measuring image in extreme circumstance

accuracy. Theoretically and practically, this research provides a novel dimensional measuring solution for aerospace devices under extreme circumstance. A reasonable structural design is necessary to ensure the dimensional stability of parts in a spatial environment. Materials with a small thermal distortion rate (i.e., α/λ) should be adopted. If various materials are introduced into the same component, their values of α should be matched, and the environmental control should be considered to reduce the effects of ambient environmental factors.

Acknowledgements This work was supported by National Natural Science Foundation (No. 51175377) and Tianjin Natural Science Foundation (No.12JCQNJC02700).

References

1. Liang JS, Wu WQ, Huang T et al (2010) Design of measurement and control system in space camera test based on LabVIEW. Chin J Opt Appl Opt 3(2):133–139
2. Yang XN, Gong J (2008) A feasibility study for strain measurement of two antennas in thermal vacuum environment at the same time. Spacecraft Environ Eng 25(4):334–337
3. Mongan TR (2007) Holography and non-locality in a closed vacuum-dominated universe. Int J Theor Phys 46(2):399–404
4. Chmid U, Grosser M (2009) Electrical performance of ti/pt thin films on glass-ceramic substrates after high temperature loading. Appl Phys Mater Sci Process 96(4):921–932
5. Nomura T (2010) Single-exposure digital holography by a generalized wave-splitting phase-shifting method. 9th Euro-American workshop on information optics, Helsinki, 12–16 July, 2010, pp. 1–3
6. Littel JD (2010) Large field photogrammetry techniques in aircraft and spacecraft impact testing. Soc Exp Mech SEM Annu Conf Expos Exp Appl Mech 1:305–317
7. Beauvivre S (2008) Micro-cameras for space applications. Proc SPIE Int Soc Opt Eng 6960:69600S-1–69600S-9
8. Parian JA, Cozzani A, Appolloni M et al (2009) New developments with design and construction of a thermal/vacuum qualified photogrammetric system. J Photogram Rem Sens 64 (3):317–327
9. Jiang SP, Yang LH, Yu J (2010) A high accuracy CCD photogrammetry system used in the vacuum cryogenic environment. Spacecraft Environ Eng 27(3):361–363
10. Lu CJ, Huang GP, Li GY (2008) Deformation measurement of antenna reflector using photogrammetry in thermal-vacuum. Proc SPIE Int Soc Opt Eng 7130:713039–713046

11. Wang GT, Xue XD, Wu LM (2006) Study on the micro width measurement method for graphics wafer. Chin J Scient Instr 27(9):1138–1140
12. Tao L, Lin YC, Song L (2012) Study on the calibration method of dual dimensions size vision measurement in thermal vacuum environment. Laser Infrared 42(1):63–66

Blind Forensics of Median Filtering Based on Markov Statistics in Median-Filtered Residual Domain

Yujin Zhang, Chenglin Zhao, Feng Zhao, and Shenghong Li

Abstract Revealing the processing history of a digital image has received a great deal of attention from forensic analyzers in recent years. Median filtering is a non-linear operation and has been used widely for noise removal and image enhancement. Therefore, exposing the traces introduced by such operation is helpful to forensic analyzers. In this paper, a passive forensic method to detect median filtering in digital images is proposed. Since overlapped window filtering introduces the correlation among the elements of the median-filtered residual (MFR) which is referred to as the difference between a test image and its corresponding median-filtered version, the transition probability matrices along the horizontal, vertical, main diagonal and minor diagonal directions are calculated from the MFR to characterize the correlation among the elements of the MFR. All elements of these transition probability matrices are served as discriminative features for median filtering detection. Experiment results demonstrate the effectiveness of the proposed method.

Keywords Image forensics • Median filtering • Median-filtered residual

Y. Zhang • S. Li (✉)
Department of Electronic Engineering, Shanghai Jiao Tong University, Shanghai 200240, China
e-mail: yjzhang82@sjtu.edu.cn; shli@sjtu.edu.cn

C. Zhao
School of Information and Communication Engineering, Beijing University of Posts and Telecommunications, Beijing 100876, China
e-mail: clzhao@bupt.edu.cn

F. Zhao
Department of Science and Technology, Guilin University of Electronic Technology, Guilin 541004, China
e-mail: zhaofeng@guet.edu.cn

B. Zhang et al. (eds.), *The Proceedings of the Second International Conference on Communications, Signal Processing, and Systems*, Lecture Notes in Electrical Engineering 246, DOI 10.1007/978-3-319-00536-2_21,

1 Introduction

Nowadays, with the rapid development of smart image acquisition devices and image processing tools with friendly interface, forensic analyzers pay more and more attention to the authenticity of digital images. Existing approaches for digital image forensics can be roughly divided into two categories: active [1] and passive [2]. The active approaches mainly insert watermarks or signatures to digital images at the time of recording. Compared with the active methods, the passive ones only need the intrinsic characteristics of digital images rather than any watermarks or signatures, making them more practical. There are many promising passive forensic methods for the detection of malicious forgeries [3]. However, the subtle traces of tampering may be diminished by using some content-preserved manipulations, such as median filtering, blurring and contrast enhancement, which do not change the image content in general, but may decrease the reliability of forensics techniques [4]. Therefore, detecting such operations is helpful to forensic analyzers. We focus on the forensics of median filtering in this paper because it has been used widely for noise removal and image enhancement.

Recently, some passive techniques for detecting median filtering have been developed. In [5], Kirchner and Fridrich employed the ratio of histogram bins h_0 and h_1, and subtractive pixel adjacency matrix (SPAM) features in the first-order difference domain to capture the median filtering artifacts for the uncompressed and JPEG post-compressed images, respectively. In [6], Cao *et al*. used the probability of zero values on the first-order difference image in textured regions as statistical fingerprint to distinguish the median-filtered images from the non-median-filtered images. Yuan in [7] constructed the median filtering forensics (MFF) and scalar merged features to detect median filtering based on the observation that median filtering significantly affects either the order or the quantity of the gray levels contained in the image area encompassed by the filter window. Chen *et al*. in [8] formed the distinguishing fingerprints by combining global probability features with correlation features in the difference domain for median filtering detection. Kang *et al*. in [9] stated that overlapped window filtering introduces the correlation among the elements of the median filtered residual (MFR) and used the autoregressive model to model the MFR for identifying median filtering, achieving better performance than the methods in [5] and [7] in the JPEG post-compressed scenario.

It has been shown in [3, 5] that Markov transition probability matrix (TPM) can be used to model the correlation between the adjacent elements effectively. The above discussion motivates us to investigate the effectiveness of Markov features in the MFR domain for median filtering detection. We use transition probability matrices along the horizontal, vertical, main diagonal and minor diagonal directions generated from the MFR to characterize the correlation among the elements of the MFR to capture the traces introduced by median filtering in this paper.

The rest of this paper is organized as follows. The proposed method is described in Sect. 2. The Experimental results are reported in Sect. 3. Finally, the conclusions are drawn in Sect. 4.

2 Measuring the Median Filtering Artifacts Using Markov Statistics of the Median Filtered Residual

The main idea of the median filter is to sort the gray levels encompassed by the filter window and replace the value of the center pixel with the median of the gray levels. The most extensively used median filters are with the square windows of odd sizes (i.e. 3×3, 5×5, $\cdots$). Therefore, we concentrate on these forms of median filtering in this paper.

It is nonlinearity of median filtering that makes the theoretical analysis of general relationship between input and output distributions of median filter complicated [10]. Therefore, the forensics of median filtering is mainly focused on specific features extraction [5–9]. The first-order difference has been proven to be effective in capturing median filtering artifacts [5]. However, the performance of statistical features derived from the first-order difference domain is susceptible to the interference of the image content. It has been shown in [9] that the median filtered residual (MFR) can reduce the effects caused by the diversity of image content effectively. This motivates us to further investigate the statistical characteristics of the MFR. We first crop 1,000 images with size 256×256 from NRCS database [11] and convert them to the 8-bit grayscale images. Then, we perform 3×3 and 5×5 median filtering on these images to obtain their corresponding median-filtered versions, respectively. Figure 1 shows the arithmetic average of the histograms ranging from -20 to 20 calculated from the MFRs of the original images and their corresponding median-filtered versions, respectively.

From Fig. 1, it is observed that the elements of the MFRs are concentrated around zeros and quickly fall off. In addition, the distribution of the elements of the MFRs generated from the median-filtered images has a sharper peak than that generated from the original images. This means that overlapped window filtering introduces the correlation among the elements of the MFR. Markov transition probability matrix (TPM) [3, 5] has also been proven to be effective in characterizing the correlation among the elements. Motivated by the Markov TPM, the proposed discriminative features for median filtering detection are constructed as follows:

1) Calculate the difference between the given image with size $M \times N$ and its corresponding 3×3 median-filtered version to obtain the MFR array E similar to that in [9].
2) Calculate the transition probability matrices along the horizontal, vertical, main diagonal and minor diagonal directions of the MFR array E in the range $[-T,T]$ using

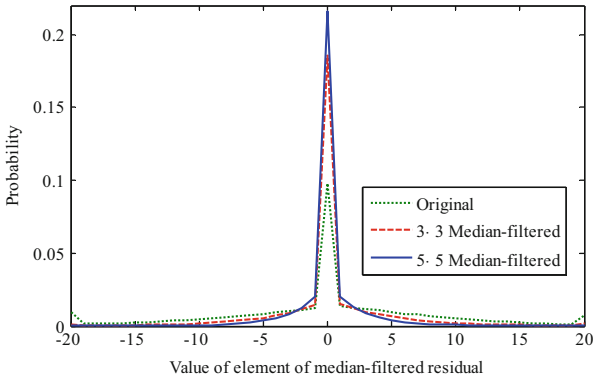

Fig. 1 The arithmetic average of the histograms ranging from -20 to 20 calculated from the MFRs of 1,000 original images and their corresponding median-filtered versions, respectively

$$
\begin{aligned}
P_h(u,v) &= \frac{\sum_{i=0}^{M-2N-2}\sum_{j=0}\delta(E(i,j)-u)\delta(E(i+1,j)-v)}{\sum_{i=0}^{M-2N-2}\sum_{j=0}\delta(E(i,j)-u)} \\
P_v(u,v) &= \frac{\sum_{i=0}^{M-2N-2}\sum_{j=0}\delta(E(i,j)-u)\delta(E(i,j+1)-v)}{\sum_{i=0}^{M-2N-2}\sum_{j=0}\delta(E(i,j)-u)} \\
P_d(u,v) &= \frac{\sum_{i=0}^{M-2N-2}\sum_{j=0}\delta(E(i,j)-u)\delta(E(i+1,j+1)-v)}{\sum_{i=0}^{M-2N-2}\sum_{j=0}\delta(E(i,j)-u)} \\
P_m(u,v) &= \frac{\sum_{i=0}^{M-2N-2}\sum_{j=0}\delta(E(i+1,j)-u)\delta(E(i,j+1)-v)}{\sum_{i=0}^{M-2N-2}\sum_{j=0}\delta(E(i+1,j)-u)}
\end{aligned}
\tag{1}
$$

where the subscripts h, v, d, and m denote the horizontal, vertical, main diagonal and minor diagonal directions, respectively; $u, v \in \{-T, -T+1, \cdots, 0, \cdots, T\}$ and

$$
\delta(n-n_0) = \begin{cases} 1, & n = n_0 \\ 0, & n \neq n_0 \end{cases} \tag{2}
$$

By doing so, each of the transition probability matrices is of size $(2T+1) \times (2T+1)$.

3) Average P_h and P_v, and then P_d and P_m to form the matrices P_1 and P_2 as

$$P_1 = (P_h + P_v)/2; \quad P_2 = (P_d + P_m)/2 \tag{3}$$

4) Take all elements of the matrices P_1 and P_2 as discriminative features for median filtering detection.

Note that since the mask of the median filtering is symmetric about the origin, the averaging procedure reduces the feature dimension without affecting the detection performance of the proposed method. Based on the experimental dataset prepared in Sect. 3.1, we empirically choose the threshold $T = 7$ for a compromise between the detection performance and computing complexity when constructing the transition probability matrices. Therefore, there are $2(2T + 1)^2 = 450$ elements in the developed feature set for the given image.

3 Experiments and Results

3.1 Image Database

In our experiments, NRCS image database [11] is used to evaluate the performance of the propose method. The original color images in above database are of size 1,500 × 2,100 in general. We first pick out 1,000 images in TIFF formats from the above database randomly and convert them to the 8-bit grayscale images. Then, to investigate the performance of the proposed method for the varying image size, we crop 1,000 image blocks with size 256 × 256, 128 × 128 and 64 × 64 from central region of each grayscale image to construct three sizes of the image databases, respectively. After that, for each of three sizes of the image databases prepared above, nine training-testing pairs are constructed similar to that in [7] as follows:

1) Perform 3 × 3 and 5 × 5 median filtering, 3 × 3 average filtering, 3 × 3 Gaussian low-pass filtering with the standard deviation $\sigma = 0.5$, and rescale operation which is randomly generated by nearest or bilinear interpolation and scaling factors 1.1 on all images in the original database, denoted as S^{ORI}, to obtain the corresponding databases S^{MF3}, S^{MF5}, S^{AVE}, S^{GAU} and S^{RES}, respectively.
2) Build eight training-testing pairs using the image databases S^{MF3}, S^{MF5}, S^{ORI}, S^{GAU}, S^{RES} and S^{AVE}, i.e. MF3 versus ORI, MF5 versus ORI, MF3 versus GAU, MF5 versus GAU, MF3 versus RES, MF5 versus RES, MF3 versus AVE, and MF5 versus AVE.
3) Group each 50 % (randomly selected) of the median-filtered databases S^{MF3} and S^{MF5} into the database S^{MF35}, and group each 25 % (randomly selected) of the non-median-filtered databases S^{ORI}, S^{GAU}, S^{RES} and S^{AVE} into the database

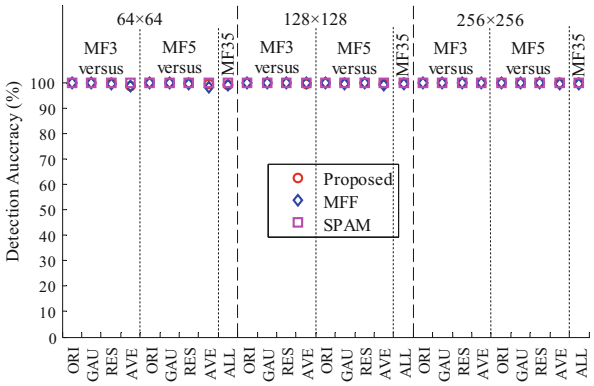

Fig. 2 Detection accuracies achieved by using the proposed, SPAM-based, and MFF-based methods for varying training-testing pairs built in Sect. 3.1

S^{ALL}. Build one training-testing pair using the databases S^{MF35} and S^{ALL}, i.e. MF35 versus ALL.

3.2 Classification

LIBSVM [12] is used as the classifier in our experiments. The RBF kernel function is selected for classification. For each of training-testing pairs constructed above, 2/5 of the positive samples and 2/5 of the negative ones are randomly picked out to train the SVM classifier, and the remaining 3/5 of the positive samples and 3/5 of the negative ones are used to test the trained SVM classifier. Note that all the median-filtered images are considered as the positive samples, while all the non-median-filtered images are defined as negative samples. The optimal parameters (C,γ) for the SVM classifier are achieved in the multiplicative grid $(C,\gamma)\in\{(2^i,2^j)|i\in\{0,0.5,\ldots,8\}, j\in\{-5,-4.5,\ldots,5\}\}$ by a fivefold cross-validation on the training set. The above procedure is repeated thirty times for reducing the effect of randomness caused by image selection for training and testing. The detection accuracy, which is the arithmetic average of true positive rate (TPR) and true negative rate (TNR), is averaged over thirty times random experiments.

3.3 Detection of Median Filtering

To evaluate the effectiveness of the proposed method, a series of experiments are carried out. Two state-of-the-art methods (i.e. the SPAM-based [5] and MFF-based methods [7]) have also been investigated for comparison on the same dataset. For the SPAM detector, the threshold T in [5] is set to 3, which leads to the 686-D SPAM features. Figure 2 shows the detection performance of the proposed, SPAM-based, and MFF-based methods for varying training-testing pairs built in Sect. 3.1. As seen in Fig. 2, all these three methods perform well in detecting median filtering

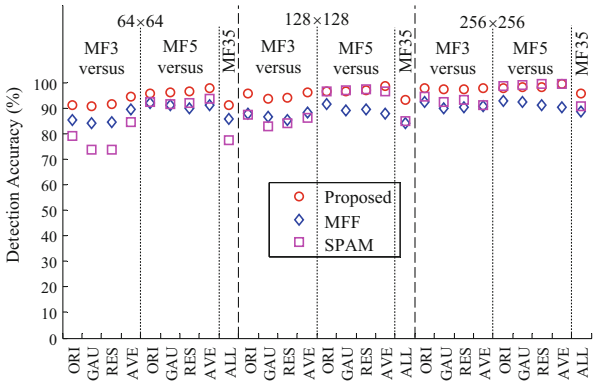

Fig. 3 Detection accuracies achieved by using the proposed, SPAM-based, and MFF-based methods for varying training-testing pairs with the quality factor $Q = 90$

even when the test images are small (i.e. 64×64). In addition, it is easily observed that the SPAM detector achieves nearly perfect detection performance for all the training-testing pairs built in Sect. 3.1.

JPEG is one of the most widely used formats in many digital devices and image processing software. It is expected that a forensic scheme is robust against JPEG compression to certain extent. To assess the robustness of the proposed method against JPEG compression, we use the JPEG versions of the training-testing pairs constructed in Sect. 3.1 with the JPEG quality factor $Q = 90$, resulting in $9 \times 3 = 27$ training-testing pairs. Figure 3 shows the classification performance of the proposed, SPAM, and MFF detectors for JPEG post-compressed training-testing pairs with the quality factor $Q = 90$. From Fig. 3, it is observed that the proposed detector is more robust than the MFF and SPAM detectors in general. Besides, The MFF detector performs better than the SPAM detector in distinguishing the 3×3 median-filtered images from the non-median-filtered ones for lower image resolution (i.e. 128×128 and 64×64), whereas the SPAM detector achieves better performance than the MFF detector for 5×5 median filtering detection.

4 Conclusions

In this paper, Markov statistics in median-filtered residual domain have been investigated for median filtering detection. Overlapped window filtering introduces the correlation among the elements of the MFR, leaving detectable traces. The transition probability matrices along the horizontal, vertical, main diagonal and minor diagonal directions are calculated from the MFR to characterize the correlation among the elements of the MFR. All elements of these transition probability matrices are utilized as discriminative features for median filtering detection. Experiment results have shown that the proposed method can detect the median filtering effectively and perform better than several state-of-the-art methods. Future

work will be devoted to performance improvement of the proposed method and localization of the median-filtered regions in image forgeries.

Acknowledgments This work is funded by National Science Foundation of China (61271316, 61071152, and 61271180), 973 Program (2010CB731403, 2010CB731406, and 2013CB329605) of China, Chinese National "Twelfth Five-Year" Plan for Science & Technology Support (2012BAH38 B04), Key Laboratory for Shanghai Integrated Information Security Management Technology Research, and Chinese National Engineering Laboratory for Information Content Analysis Technology. We would like to thank Prof. Yuan for his kindness by providing us with the code of the MFF scheme in [7].

References

1. Cox IJ, Kilian J, Leighton FT, Shamoon T (1997) Secure spread spectrum watermarking for multimedia. IEEE Trans Image Process 6(12):1673–1687
2. Luo W, Huang J, Qiu G (2010) JPEG error analysis and its applications to digital image forensics. IEEE Trans Inform Forensics Secur 5(3):480–491
3. Shi YQ, Chen C, Chen W (2007) A natural image model approach to splicing detection. In: Proceedings of ACM Multimedia and Security Workshop, Dallas, TX, 20–21 September, 2007, pp. 51–62
4. Kirchner M, Böhme RJ (2008) Hiding traces of resampling in digital images. IEEE Trans Inform Forensics Secur 3(4):582–592
5. Kirchner M, Fridrich J (2010) On detection of median filtering in digital images. Proc SPIE Electron Imag Med Forensics Secur II 7541:1–12
6. Cao G, Zhao Y, Ni R, Yu L, Tian H (2010) Forensic detection of median filtering in digital images. In: Proceedings of the 2010 I.E. international conference on multimedia and expo, Suntec City, 19–23 July, 2010, pp. 89–94
7. Yuan HD (2011) Blind forensics of median filtering in digital images. IEEE Trans Inform Forensics Secur 6(4):1335–1345
8. Chen C, Ni J, Huang R, Huang J (2013) Blind median filtering detection using statistics in difference domain. In: Proceedings of 14th information hiding. LNCS 7692:1–15
9. Kang X, Stamm MC, Peng A, Liu KJR (2012) Robust median filtering forensics based on the autoregressive model of median filtered residual. In: Proceedings of signal & information processing association annual summit and conference, Hollywood, CA, 3–6 December, 2012, pp. 1–9
10. Bovik AC (1987) Streaking in median filtered images. IEEE Trans Acous Speech Signal Process 35(4):493–503
11. NRCS Photo Gallery [Online]: http://photogallery.nrcs.usda.gov/res/sites/photogallery/
12. Chang CC, Lin CJ (2001) LIBSVM: a library for support vector machines [Online]. http://www.csie.ntu.edu.tw/cjlin/libsvm

Research on the Influence of Backlight Parameters on the Display Device Color Restoration Ability

Yan Li, Na Li, Jing Wang, and Guiling Li

Abstract This paper measures chromaticity parameters for Cold Cathode Fluorescent Lamp-Liquid Crystal Display (CCFL-LCD) and Light-Emitting Diode-Liquid Crystal Display (LED-LCD) display devices. The results show that using the LED as a backlight can improve effectively color restore ability of display device, the difference of the two color gamut coverage rates is 0.5 %, and the difference of three-dimensional color gamut volume is 0.15×10^5. The difference of intensity of the backlight source can change accordingly brightness of the white, red, green and blue, but it has no obvious impacts for color gamut of the displays. The result shows that in order to achieve wide color gamut, it is feasible to select a backlight, which has a better color reduction performance, a high luminous efficiency.

Keywords Backlight • LED-LCD • CCFL-LCD • Color gamut

1 Introduction

Photoelectric parameters of video display device directly affect the color restoration ability of equipment. This paper studies the influence of backlight type and backlight intensity on brightness and chroma of displays based on colorimetry experiment. The Result shows selecting LED as backlight will get a better color display effect compared with CCFL; While the intensity of backlight only affects the brightness of the device, there is no obvious influence on 2D, 3D color gamut.

Y. Li • N. Li (✉) • J. Wang
College of Electronic and Communication Engineering, Tianjin Normal University, Tianjin, China
e-mail: 514860658@qq.com

G. Li
Tianjin University, Tianjin, China

B. Zhang et al. (eds.), *The Proceedings of the Second International Conference on Communications, Signal Processing, and Systems*, Lecture Notes in Electrical Engineering 246, DOI 10.1007/978-3-319-00536-2_22,

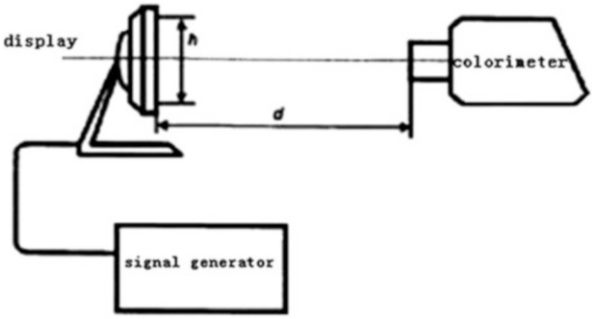

Fig. 1 Experimental equipment diagram

2 Measure Experiment

Experimental instrument consists of three parts: signal generator, the monitor to be tested and colorimeter. Experimental equipments are set up according to Fig. 1, and the optical axis of colorimeter and central area of the display should be tested orthogonal, where h is an effective and visual height of the display to be tested, d refers to the horizontal distance between colorimeter lens and the display to be tested, Moreover the test distance should be three times as large as the effective visual height of the screen (HDTV), or four times (SDTV).

According to the relevant provisions of the HDTV test signal standard GY/T 155-2000 [1], the measure environment of this paper is as follows:

ambient temperature: 15 – 35 °C, preference to 20 °C;
relative humidity: 25 – 75 %;
the atmospheric pressure: 86 – 106 kPa;
ambient intensity of illumination $\leq$11 lx.

Experimental measurements were conducted in the darkroom [2], in order to ensure that the feature of display does not significantly change over time, all experimental apparatus needs to be preheated for more than 30 min before the experiment.

3 Experimental Analysis of the Influence of Backlight Parameters on the Color Restoration Ability

Liquid Crystal Display (LCD) is a passive light emitting display. Its itself can not glow, so the backlight that provides all light sources for LCD display modules is very important. Backlight is used to supply light source, which has full brightness and uniform distribution to make LCD panel display images normally. So the brightness, the color and the power consumption of the display, are very dependent on the backlight performance [3]. The main backlight types: Cold Cathode

Fluorescent Lamp (CCFL) and Light Emitting Diode (LED), etc. The market occupancy rate of LED increases year by year. This paper firstly conducts the experiment in terms of the influence of the two kinds of backlights on the device color restoration ability.

3.1 Different Types of Backlights

Choose two displays that have different backlights, CCFL-LCD and LED-LCD. Using the experimental method proposed by this paper to test chromaticity characteristics of the displays, the main chromaticity parameters tested are listed in Table 1. According to the data from Table 1, a CIE-u' v' chromaticity diagram is drawn, and 2D color gamut features of the two monitors can be got, as shown in Fig. 2.

From Fig. 2, LED-LCD, the saturation of the red primary color is higher than that of CCFL-LCD, so for the Light Emitting Diode display, the red and the colors around red present better, more gorgeous subjectively. The saturation of CCFL-LCD in the range of blue color and blue - green is higher than LED-LCD, but the display effect is not as good as LED in the area of blue - red color. For the display effect of green color, the two displays are mainly the same. Shown in Table 1, the color gamut coverage of Cold Cathode Fluorescent Lamp tube display is 33.61 %, while the color gamut coverage of Light Emitting Diode display is 34.12 %, so the difference of both color coverage is 0.5 %.

Figure 3 is made by experimental data, and it shows 3D color gamut model of the two displays in the CIELAB color space. Where the gray entity refers to 3D color gamut range of CCFL-LCD, the dotted line refers to the color gamut that LED-LCD can reproduce. Figure 3 clearly indicates that color gamut range of LED-LCD is larger than that of the CCFL-LCD. Especially in the high brightness and yellow area, this advantage is more obvious. According to the calculation method of the reference [4], get color gamut volume of CCFL-LCD and LED-LCD is 7.76×10^5, 7.91×10^5 respectively. The color restoration ability of LED backlight is obvious.

3.2 Influence of Backlight Intensity on the Color Gamut of the Displays

This article selects the display whose backlight intensity is adjustable as a test object, and analyzes the influence of backlight intensity of displays on the chromaticity characteristics of the displays. Close the dynamic backlight adjustment function of the display to be tested before the experiment [5], adjust the backlight intensity of the display, to make backlight intensity of the display 0, 30, 70, 100 (relative) respectively for measuring chromaticity parameters of monitor.

Table 1 Chromaticity coordinates and color gamut coverages of different backlight displays

	Coordinates			
	CCFL-LCD		LED	
Primary colors	u′	v′	u′	v′
Red	0.4465	0.5221	0.4389	0.5274
Green	0.1137	0.5582	0.1143	0.5637
Blue	0.1695	0.158	0.1696	0.1470
White	0.2274	0.4192	0.1890	0.4375
Color gamut coverages (%)	33.61		34.12	

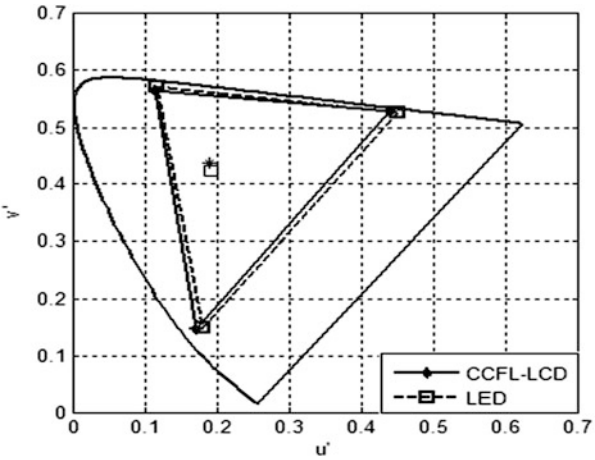

Fig. 2 The influence of different backlights on 2D color gamut of the displays

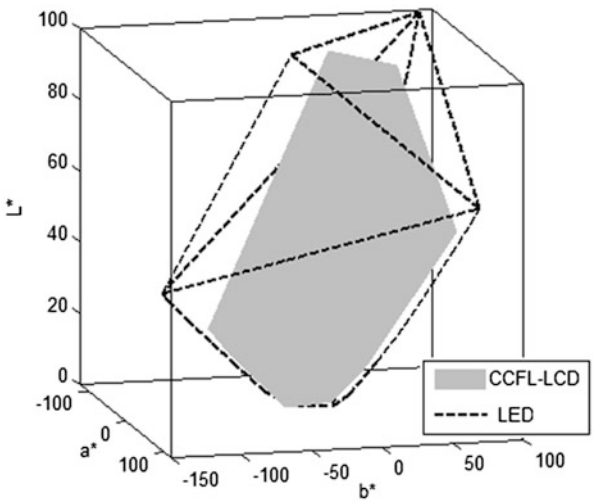

Fig. 3 The influence of different backlights on 3D color gamut of the displays

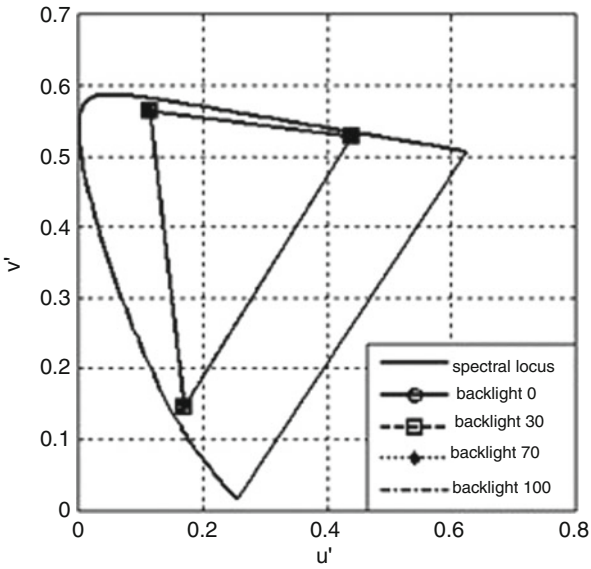

Fig. 4 The influence of backlight intensity on 2D color gamut of the display

The data from the experiment were drawn in CIE-u' v' chromaticity diagram, shown in Fig. 4. Meanwhile they were drawn in the CIE-LAB,which is a three dimensional chromaticity diagram [6], showed in Fig. 5. In CIE-u' v' space, the primary colors—Red, Green, Blue do not change basically with the backlight intensity increasing, and the color gamut of the display is about the same under the four kinds of backlight intensities. That is to say that it has no effect for 2 D chrominance features of the display to adjust the backlight intensity of the display. According to the formula to calculate the $L^*a^*b^*$, it is known that the $L^*a^*b^*$ are normalized by $X_nY_nZ_n$, so the maximum value of L^* is 100. In $L^*a^*b^*$ 3D color space, with the strength of the backlight, 3D coordinates of the display is basically the same, that is, it does not affect three dimensional chromaticity characteristics of the display to adjust the backlight intensity.

3.3 Influence of Backlight Intensity on the Brightness of the Displays

Backlight intensity directly affects the brightness of the display, so this paper studies the impact of the backlight intensity on the brightness of the three primary colors of the display.

A figure is made for the relationship between the backlight intensity and the brightness of three primary colors of the display, shown in Fig. 6. As backlight intensity increases, the brightness of the green primary color improves most, about 240 lx; then red primary color, its brightness increases 60 lx; Blue primary color, minimum brightness change, its brightness increases around 25 lx. This is mainly

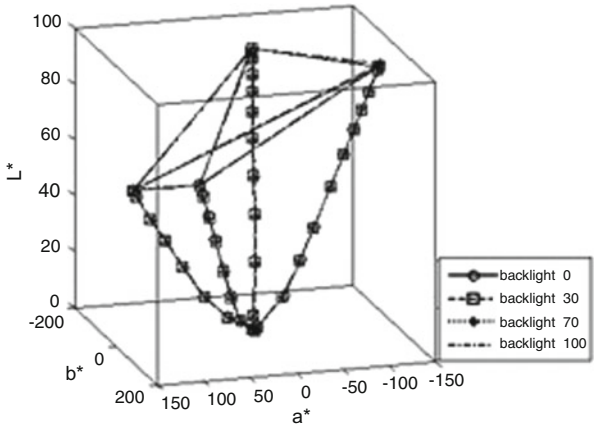

Fig. 5 The influence of backlight intensity on 3D color gamut of the display

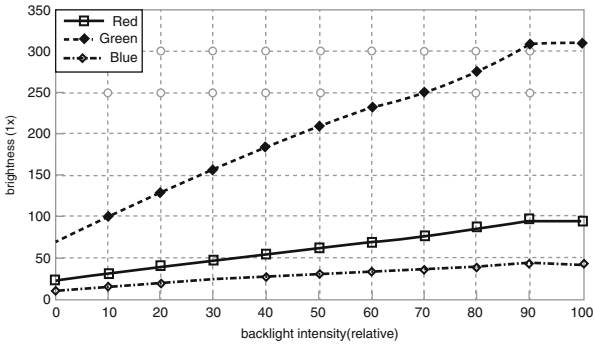

Fig. 6 The impact of the backlight intensity on the brightness of the three primary colors of the display

because the display color mechanism is the additive mixing color principle [7]. In the three primary colors, the brightness of the green primary color makes is the highest, then red primary color takes second place, the brightness of the blue primary color is the lowest, so the brightness of the green primary color makes a significant contribution to the brightness of the display. The increasement of backlight intensity of the display makes the overall brightness of monitor improve. According to the proportion of red, green and blue primary colors in the brightness equation, the backlight intensity mainly affects the brightness of the green primary color of the display.

3.4 Analysis of the Test Result on the Backlight Adjustment Function and Brightness Adjustment Function of LCD

Monitors usually have the backlight adjustment and brightness adjustment functions, so the paper measures and analyzes the two functions. Firstly, restore

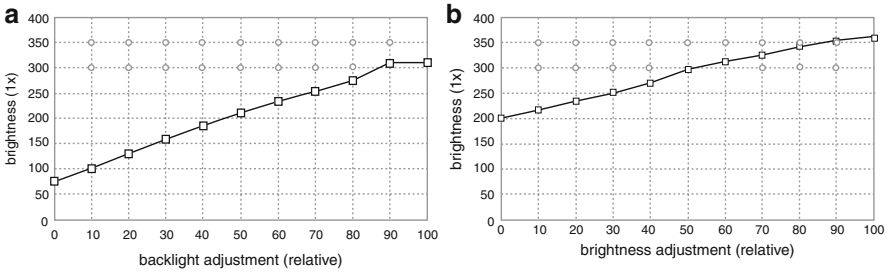

Fig. 7 (**a**) influence of backlight adjustment on white field signal brightness of the display (**b**) influence of brightness adjustment on white field signal brightness of the display

the brightness adjustment function of the display to factory Settings 30 (relative), to test the influence of the backlight adjustment function of the display on the white field signal brightness, shown in Fig. 7a. Secondly, restore the backlight adjustment function of the display to factory Settings 70 (relative), to test the influence of the brightness adjustment function of the display on the white field signal brightness, shown in Fig. 7b.

With the increase of backlight intensity, the white field signal brightness changes from 75 to 310 lx, while the brightness adjustment function makes the white field signal brightness of the display increase from 200 to 360 lx. It shows that the backlight adjustment makes more contribution to the brightness adjustment of the display, compared with the brightness adjustment function. This may be due to their different action principles. The backlight adjustment controls the luminous intensity of backlight tube, while the brightness adjustment is used to fine tune after selecting the basic standard, in the case that the backlight intensity is confirmed.

4 Conclusions

The performance ability of the display device for images is directly related to the backlight. In the paper, through experiment measurement, the research results show that the back light intensity could significantly enhance the brightness of the green primary color, thus can improve the brightness of the display device. But the backlight intensity adjustment cannot improve the color gamut coverage and the color gamut volume of the equipment, thereby, the type of backlight is the only way to improve color restoration ability.

Acknowledgments This paper is subsidized by the Dr Fund of Tianjin Normal University (52XB1006).

References

1. State administration of radio, film and television (2000) Video parameter values for HDTV standard for production and programme exchange, GY/T 155-2000
2. A darkroom measurement
3. Zhonglian Qiao, Dongsheng Yang, Fei Liu (2010) The application and development of Medium-Large size display backlight modules. The modern display
4. Kim M-C (2008) Comparative color gamut analysis of xvYCC standard. Displays 29:376–385
5. Chang N, Choi I, Shim H (2004) DLS: dynamic backlight luminance scaling of liquid crystal display. IEEE Trans VLSI Syst 12(8):837–846
6. Weijie H, Tang S, Zhu Z (2007) Modern color science and application. Beijing Institute of Technology Press, Beijing
7. National radio and television products quality supervision and inspection center (2010) TCL multimedia technology holdings limited company, GPC r&d center, colorimetry in the digital TV and flat TV. Post & Telecom Press, Beijing

The Development and Application of Video's Color Gamut Test Sequence

Yan Li, Na Li, Jing Wang, Guiling Li, Weihua Wu, and Mo Li

Abstract This article develops a color gamut sequence which is used for measuring the video's three-dimensional color gamut. According to the relevant video measurement standards, considering the actual measurement needs, this paper develops five test cards. Then the completeness of test data and the scientific nature of test card's design are demonstrated by this paper. Color gamut test sequence has been put into use, the practice proved that the design of sequence is reasonable and can be used easily. It provides the reliable data for the research of reconstructing video's 3D color gamut and cross-media gamut mapping.

Keywords Color gamut • Color measurement • Test sequence • Principle of color mixing

Y. Li
College of Electronic and Communication Engineering, Tianjin Normal University, Tianjin, China

Tianjin University, Tianjin, China

N. Li (✉) • J. Wang
College of Electronic and Communication Engineering, Tianjin Normal University, Tianjin, China
e-mail: 514860658@qq.com

G. Li
Tianjin University, Tianjin, China

W. Wu • M. Li
National radio and television products quality supervision and inspection center, Beijing, China

B. Zhang et al. (eds.), *The Proceedings of the Second International Conference on Communications, Signal Processing, and Systems*, Lecture Notes in Electrical Engineering 246, DOI 10.1007/978-3-319-00536-2_23,

1 Introduction

Considering TV system and the compatibility of equipment, the conventional analog and digital TV systems are still using Cathode Ray Tube (CRT) features to select part of photoelectric and colorimetric parameters of TV system, color signal encoding and decoding, and transmission method is also compatible with the original TV system. It makes color range that the system can transfer and reproduce (gamut) limited. It means that human's visions can percept part of the colors which exist in nature, which can be synthetized by humans or computer, but the current TV system cannot realize the transmission and display. The researches indicate that gamut coverage rate of the current TV signal only is about 1/3 of that the visions can percept [1].

With the rapid development of modern science technology and industry, many kinds of new display devices and display technologies emerge in recent years. In addition to the traditional Cathode Ray Tube (CRT), Liquid Crystal Display(LCD), Plasma Display Panel(PDP), Digital Light Processor(DLP), Liquid Crystal on Silicon (LCoS), LED back light Liquid Crystal Display(LED-LCD)multi-color display which is more than four colors has been used or has been developed. In the aspect of display mode, in addition to the direct type, front projection, rear projection, laser projection and multiple color projection have also been put into practice. These new display devices and display based on different principles, different structures, use the different materials, devices and technology, so the color rendering properties have been improved obviously, the color gamut are expanded [2–4]. Some of the "future" display device and display method will emerge.

In order to achieve the gamut mapping between different color gamut signals and different display devices or display mode such as expending the narrow gamut TV signal. It displays narrow color gamut images or video images with wide color gamut display devices or wide color gamut display mode and makes narrow color gamut images or video images more saturated. This is used to improve the visual effect. This is called color gamut mapping or gamut matching, and these studies will need to video test data as the basis and premise.

Two-dimensional test pattern with certain intensity (lightness) is usually used for the chroma test. For example, when the relevant standards were used to test "color gamut coverage" [5], the chromaticity parameters of three kinds of 100 % of red, green and blue were tested to calculate the ratio between the chromaticity range that three primary colors limited and the chromaticity range of visible light. In effect, the color gamut of the different display devices or a different way has a big difference under the different luminance (brightness) [6], such as LCD, PDP and other flat panel display, when the luminance (brightness) is improved, the color range narrowed greatly. This means that these display devices can't display the high color saturation in high luminance (brightness) with the existing technology.

Therefore, based on color mixing principle of three primary colors [7], this article designs a new test method for video color gamut, including the way that

the test sequence diagram generated by computer, test scheme, the post-processing methods of test data, and so on. All of these will be used to determinate the luminance (brightness), hue and saturation of the video display, make all kinds of display mode match the transmitted signal's chromaticity characteristics, and achieve the color gamut mapping between different media in order to give full play to the potential of reproduction gamut for different types of display devices and display mode, improving the color vision effect.

2 The Design of Colorimetric Parameters

2.1 Color Mixing Principle of Three Primary Colors

RGB color cube is shown in Fig. 1, and its color matching law follows (1). When the three primary colors choose different tristimulus values R, G, B, chromaticity parameters of synthetic colors are different, thus the image will present different subjective colors. Therefore, theoretically, as

$$C = R[Re] + G[Ge] + B[Be] \tag{1}$$

long as traverse tristimulus values of the three primary colors within 0 – 1, using to (1) to combine respectively, you can get all the color cube surface and internal colors. If you want to test maximum gamut of a display device, only select RGB color cube surface colors.

2.2 The Selection of Colors

When choosing the color in the test sequence, this paper considers the distributed situation of the color point in the color space, accuracy requirement and the workload of the test, selects the 866 colors as the test object to be tested. Specific plan is as described below.

Each edge of the RGB cube is quantized by 8 bit, so the range of RGB cube's each edge is [0,255] after quantized. Then approximate evenly selects 13 points in the range of 0–255 to get 12 equal parts, the quantized values were shown in Table 1. A total of 866 color points are obtained after the recombination of these RGB values. There are 469 saturated color points among them. These colors are in the surface of RGB three-dimensional color gamut, so the gamut range limited by these color points is the maximum gamut of video system. The above design has the test completeness.

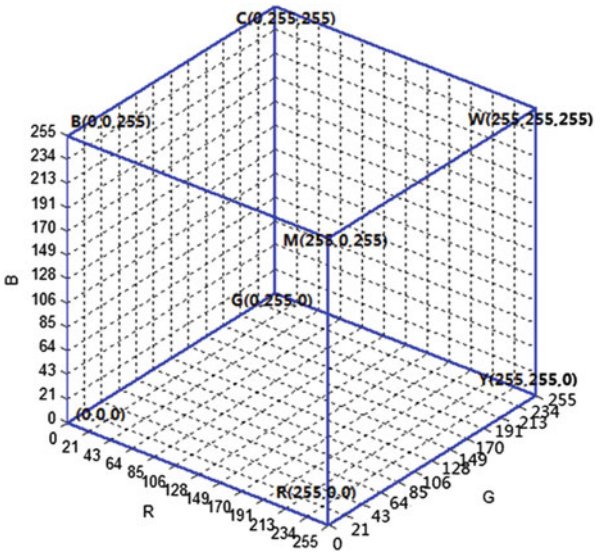

Fig. 1 RGB color cube

Table 1 The 13 level uniform distribution values after 8 bit quantization for digital test pattern

Quantitative level	0	1	2	3	4	5	6	7	8	9	10	11	12
Quantized values	0	21	43	64	85	106	128	149	170	191	213	234	255

2.3 Selection of Gray Scale

A total of 13 gray-scale color piece were chosen from black (R = G = B = 0) to white (R = B = G = 1). Using gray order can show the performance ability of monochrome picture that the display device can be displayed.

3 Test Pattern Layout

Due to the different working mechanism or process defects, etc., the images displayed by all kinds of display devices or display usage are often uneven [8], especially the edge of the screen and the middle of screen, the chromaticity characteristics often have differences, while the vision or video screen is more concerned about the middle of image. In order to reduce the influence of uneven picture for chromaticity measurement, and make the test pattern sequence suitable for the chromaticity parameters testing for all kinds of display device and display usage, the effective test area of test pattern sequence proposed by this paper removes the area around the picture as shown in Fig. 2. Figure 2 removes 1/9 of the height up and down, 1/9 of the width of the screen [9]. The ineffective measurement section was

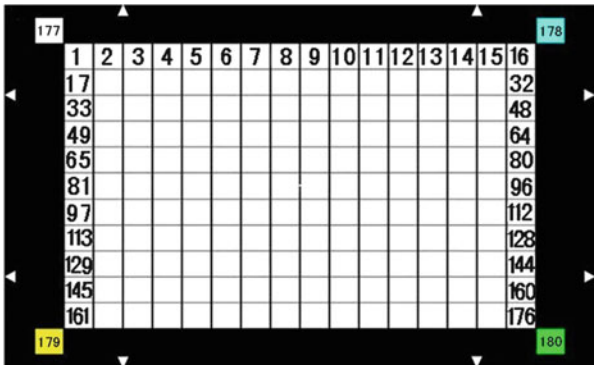

Fig. 2 Test pattern layout

filled with black to reduce the influence that comes from the edge of test image, the light of the ineffective measurement area has influence on the measurement result. For locating the relative position between the colorimeter and the test pattern, full pictures of logo are set with white triangle at the edges of test pattern, and the sign of test pattern center is also set in the middle of the test pattern.

In order to make colorimeter to collect the data of multiple color pieces at a time, improve the efficiency of measurement, the effective testing region of test pattern is divided into small color pieces with a number of columns and lines. Each color piece contains enough pixels (at least 500 pixels) so that colorimeter can collect chromaticity data of multiple pixels, and use their mean value as the measured results of this color piece, improving the reliability of the measured results. In Fig. 2, there is enough distance (pixels) between the columns and rows to reduce the influence that comes from the light of adjacent color pieces when measuring the color piece chromaticity parameters, and filled the distance with black.

Four auxiliary colors in each of the test pattern are used for maintaining the consistency of the measurement condition when using multiple test pattern to measure three dimensional chromaticity parameters. The position and size of auxiliary colors in each test pattern are relatively fixed, colorimetric parameters are also corresponding (for example, the bright white, blue, yellow and color saturation green is in turn).

The test pattern sequence designed in this article is arranged as the configuration of Fig. 2, so there are five test sequence diagram generated. In order to make the time that colorimeter collects color piece's data in each test diagram the same, the luminance (brightness) should be divided equally, and the similar luminance (brightness) should be classified into the same test diagram. For example, the luminance (brightness) are divided into five grades, the 176 color pieces in the different grades should be placed at the corresponding test diagram. Figure 3 is the highest luminance (brightness) picture in the test diagram.

It should be pointed out that the commonly used TV monitor or projector screen aspect ratio is 4:3 and 16:9. In this paper, the test sequence designed by this paper is applicable for both of them, but the test diagram need to be modified according to the test requirement.

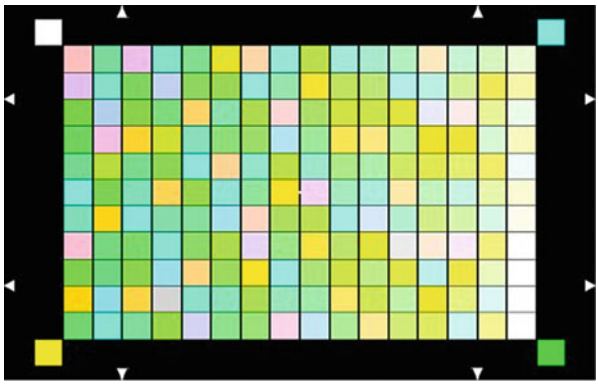

Fig. 3 The highest luminance (*brightness*) picture in the test diagram

4 Application Example

Five computer bitmaps of test sequences were generated based on matlab, and they were displayed on the tested monitor separately. Measurement is made from top to bottom, from left to right. Firstly colorimeter should be aimed at the center of the color piece of the first row and column, and start to measure after working state of images and colorimeter is stable. After completion of measurement, the system automatically removes the test pattern towards left, making the colorimeter aimed at the color piece of the first row and the second column. Likewise, when the working state of images and colorimeter is stable, the second color piece is tested. Like this, all color pieces are tested, a total of 176 plus 4 color pieces to be measured.

Figure 4 shows the scatter plots of a LCD digital TV in the 3D color gamut, which are got by the method proposed by this article, where * point presents test data. By observing the distribution of color gamut of Fig. 4 in the 3D color space, you can get a changing rule that the reproduction ability of the digital television follows the brightness, and know the expressive ability in different hues. In addition, the test data obtained by the method of this paper also can achieve the entity fitting of the 3D color gamut and the calculation of the three-dimensional color gamut volume, which are the quantitative index to evaluate color gamut reproduction of display device.

Using the measured data to calculate the 3D color gamut volume of LCD, the result is 8.58×10^5 color gamut cubes. At last, this article also calculates 3D color gamut volume of the current international video system ITU-R BT.709, the result is 7.6×10^5 color gamut cubes. Obviously the reproduction color gamut of this LCD is greater than the conventional color gamut. The follow-up study can use the 3D data got from this paper to realize cross-media gamut mapping.

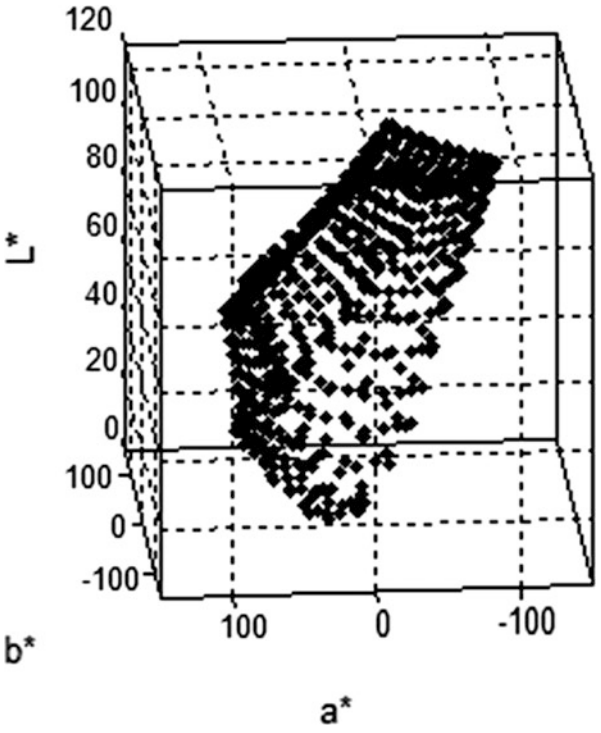

Fig. 4 The test result of LCD

Acknowledgments This paper is subsidized by Dr Fund of Tianjin Normal University (52XB1006).

References

1. Yan X, Yan L, Yong-cheng A, Gui-ling L (2009) Analysis and comparison of extended color gamut for video system in ITU-R BT.1361 and IEC61966–2–4. Video Eng 33(3):92–94
2. Zheng G, Wang B, Fang T, Cheng H, Qi Y, Wang YW, Yan BX, Bi Y, Wang Y, Chu SW, Wu TJ, Xu JK, Min HT, Yan SP, Ye CW, Jia ZD (2008) Laser digital cinema projector. Disp Tech 4 (3):314–318
3. Lai Y-K, Lee S-M (2013) Wide color-gamut improvement with skin protection using content-based analysis for display systems. Disp Tech 9(3):146–153
4. Sugiura H, Kagawa S, Kaneko H, Ozawa M, Tanizoe H, Kimura T, Ueno H (2005) Wide color gamut displays using LED backlight - signal processing circuits, color calibration system and multi-primaries, ICIP2005, vol. II,, 11–14 September, 2005, pp. 9–12
5. Quan-en L (2004) Color domain and color domain coverage ratio. Video Eng 269(11):49–51
6. Matsumoto T (2006) xvYCC: a new standard for video systems using extended-gamut YCC color space. SID Symp Dig Tech 37:1130–1133
7. Weijie H, Tang S, Zhu Z (2007) Modern color science and application. Beijing Institute of Technology Press, Beijing
8. Chaji GR, Jaffari J (2012) Generic low-cost characterization of VTH and mobility variations in LTPS TFTs for non-uniformity calibration of active-matrix OLED displays, Design Automation Conference (DAC), 49th ACM/EDAC/IEEE, San Francisco, CA, 2012
9. Methods of measurement for digital television flat panel displays. SJ/T11348-2006

Error and Artifact Detection in Video Decoding: A Temporal Method

Daqing Zhang, Shenghong Li, Kongjin Yang, and Yuchun Jing

Abstract Video communication via error-prone networks suffers from visibility of data impairment. Lots of research effort has been made to investigate error concealment algorithms, which almost always assume that all errors have been detected successfully. However, this assumption is not always the fact. As widely used, syntax and semantics analysis (SSA), cannot guarantee complete error detection. Furthermore, an error detected by SSA should not be inevitably concealed unless it is a visual artifact. On the other hand, temporal concealment, using motion vector recovery (MVR) and copying, has been recognized simple and effective. This paper proposes an MVR based error and artifact detection (EAD) algorithm, abbreviated by MVR-EAD, which compares a risk area with its temporal counterpart in the reference frame and decides if an artifact occurs. MVR-EAD gains attractive detection accuracy, an increase from 7.8 to 73.87 % demonstrated by extensive experiments. Accordingly, this incurs 0.09 to 1.88 dB in PSNR improvement with the error concealment strategy embedded within JM18.0.

1 Introduction

Compressed video streams are very vulnerable to transmission errors because of the use of predictive coding and variable-length coding (VLC). Therefore, error resilient techniques are essential in video transmission via error prone channels.

Much effort has been made to research how to conceal damaged areas of compressed videos and resulted in a lot of error concealment algorithms [1]. Underlying these, it is assumed that all damaged macro-blocks (MBs) should have been detected successfully. However, this assumption is not always true. As a widely adopted method, most decoders detect errors in terms of syntax and semantics

D. Zhang (✉) • S. Li • K. Yang • Y. Jing
Department of Electronic Engineering, Shanghai Jiao Tong University, Shanghai, China
e-mail: charles_zhang_cn@163.com

B. Zhang et al. (eds.), *The Proceedings of the Second International Conference on Communications, Signal Processing, and Systems*, Lecture Notes in Electrical Engineering 246, DOI 10.1007/978-3-319-00536-2_24,

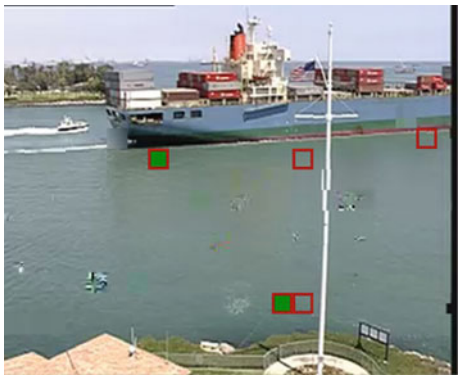

Fig. 1 Examples of error and artifact detection failure of SSA. All errors detected by SSA have been labeled by a *red bold hollow square*

violations or analysis, namely SSA. Unfortunately, SSA cannot guarantee complete error detection. For example, if damaged bits happen to become other legal codeword according to the coding standard, SSA would not be able to detect such an error. It is reported a 57 % detection success rate by syntax tests [2].

Comparatively, only a small number of literary publications focus on error detection of corrupted coded video streams. In [3], an iterative solution was used to identify corrupted areas. This method is computation intensive and does not distinguish visually annoying artifacts and imperceptible errors. In [4], once an MB is flagged as potentially corrupted, a set of features of surrounding areas are extracted and fed to a support vector machine (SVM). On the one hand, such feature extraction is computation intensive. On the other hand, for example in Fig. 1, it is not reasonable to apply feature factors of the tanker area to error detection in the flagpole area.

As shown in Fig. 1, an error detected by SSA does not inevitably need concealed unless it is a perceivable artifact. A decoder should only conceal perceivable artifacts while leave imperceptible error MBs so as to save its computation and memory resources especially in real time applications. That is, a desirable detection algorithm should be able to differentiate visibly annoying artifacts. This has be mentioned in [4, 5]. However, The solutions by [4, 5] mainly consider the spatial dissimilarity metrics. In other words, the temporal redundancy has not been fully explored. Using motion vector recovery (MVR) and copying, temporal concealment has been proven simple and effective. This paper proposes an MVR based error and artifact detection (EAD) algorithm, abbreviated by MVR-EAD. MVR-EAD decides if an artifact occurs by comparing the risk area with its temporal counterpart in the reference frame. It consists of three steps. The first step is to identify risk MBs (RMB), including error MBs by SSA and some of their neighboring MBs. As the second step, it is proposed to find their error concealment candidate areas (ECCA) by MVR. In the third step, if the ECCA and neighboring areas are similar while the ECCA is different from the current RMB, it should be reasonable to conclude the RMB as an artifact.

The rest of this paper is organized as follows. Section 2 describes the proposed algorithm, MVR-EAD. In Sect. 3, we present experiment results. Conclusions are drawn in Sect. 4.

2 MVR-EAD

The proposed MVR-EAD includes three steps as shown in Fig. 2, i.e., (1) SSA-RMB; (2) Feasibility of MVR and (3) Perceptibility.

2.1 SSA-RMB

Three types of detection failure of SSA can be observed, i.e.,

- An error has been reported. But the MB and even its neighboring MBs look all right.
- An error has been reported. But visual artifacts occur as well in front of it.
- A perceivable damaged MB has not been detected.

This paper will focus on the first two types of failure. Studies on the third type are left for future work.

As for the first type, it is denoted as "false detection" in this paper. A bit error does not inevitably result in a visible artifact. If not perceptible, it should not be concealed. As a possible reason of the second type of SSA failure, error bits might happen to become another decodable code-word. The wrong but legal code-word might deviate a decoder from the right decompression path. It is late when the propagated error is detected by SSA. Therefore, once an error has been detected by SSA, some previous MBs should be examined. In summary, a notion of "risk MBs (RMB)" is proposed and consists of error MBs reported by SSA and a number of previous MBs. The number, for convenience, named by "risk number" and denoted as n, should be selected according to the specific scenario and resources available.

2.1.1 Feasibility

The second step checks the feasibility of MVR-EAD. The temporal concealment of MVR algorithm in [1] is adopted to find temporal error concealment candidate areas (ECCAs) for all RMBs as if they are to be concealed. The MVR outperforms rival interpolation algorithms in two aspects. On the one hand, it incurs little computation cost thus keep the proposed MVR-EAD simple. On the other hand, if feasible, it can keep content details as much as possible. The more similar an ECCA is to the original area, the more accurate MVR-EAD should be.

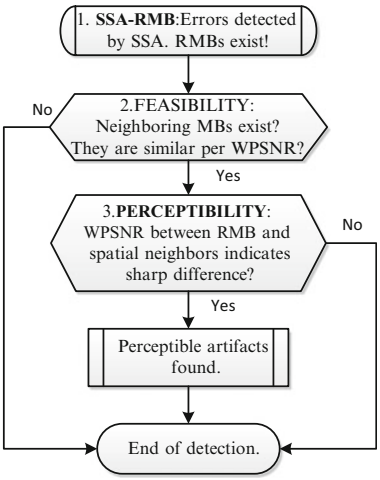

Fig. 2 Diagram of the proposed MVR-EAD

Table 1 Feasibility decision of MVR-EAD basing on coding modes of top and bottom MBs

		Top MB	
MVR-EAD feasibility decision of MB		Intra	Inter
Bottom MB	Intra	NOT feasible	Warning
	Inter	Warning	Feasible

Table 2 Feasibility decision of MVR-EAD basing on coding modes of left, right, top and bottom MBs

MVR-EAD feasibility decision of MB	Sum of four MBs' score	Feasibility
where Intra_MB scores "0";	4	Feasible
	3	
Inter_MB scores "1".	2	Warning
	1	NOT feasible
	0	

Therefore, it is necessary to check whether MVR is suitable for the current RMB. If not, MVR-EAD should not be applied. Motivated by Fig. 10 of [1] and for completeness, we give more detailed design in two cases and further discussion in terms of specific applications as below.

In a simple case where only top and bottom MBs are available, we propose to use a simple feasibility scheme shown in Table 1 where "NOT feasible" indicates no ECCA and "feasible" means existence of ECCA.

In another common case where flexible MB ordering (FMO) is used and neighboring MBs exist in four directions, i.e., top, bottom, left and right, an advanced feasibility decision scheme is proposed as Table 2. For each neighboring

inter-coded MB, it scores "1". For each intra-coded MB, it scores "0". Options of "feasible" and "NOT feasible" share the same meaning with Table 1. Feasibility decision of MVR basing on coding modes of left, right, top and bottom MBs. The option "warning" is not specified because many factors should be taken in account, such as the video content complexity, the spatial resolution of the video and the tolerance to artifacts. It is left open to specific applications and scenarios.

2.1.2 Perceptibility

The sum of absolute difference (SAD) is chosen to characterize the content similarity between MBs in the third step. Assume SAD between the RMB and its ECCA is much bigger than those of neighboring MBs, the RMB should be concluded as a perceptible artifact. Otherwise, it should not be concealed.

Let the pixel values of the reconstructed frame n be denoted by $P(x,y,n)$, where (x,y) is the spatial coordinate. Suppose an MB at frame n is an RMB. We denote the estimate MV by d, and its x,y components by d_x and d_y respectively. The SAD between the RMB and its ECCA is then

$$SAD_e(x,y) = \sum_{i,j\in[0,15]} |P(x+i, y+j, n) - P(x+i+d_x, y+j+d_y, n-1)| \quad (1)$$

where (x,y) is the upper left coordinate of the RMB.

Without losing generosity, assume four neighboring MBs and MVs exist. Let d_t, d_b, d_l and d_r be MVs of top, bottom, left and right MBs. Then there are SAD_t, SAD_b, SAD_l and SAD_r similarly defined by Eq. (1) for four neighbors, as shown in Fig. 3a. Using these MVs as estimate for the RMB respectively, we get SAD_{et}, SAD_{eb}, SAD_{el} and SAD_{er} as Fig. 3b.

Following notations are defined,

$$SAD_{max} = max\{SAD_t, SAD_b, SAD_r, SAD_l\} \quad (2)$$
$$SAD_{min} = min\{SAD_t, SAD_b, SAD_r, SAD_l\} \quad (3)$$
$$T_{diff} = SAD_{max} - SAD_{min} \quad (4)$$
$$SAD_{emax} = max\{SAD_{et}, SAD_{eb}, SAD_{er}, SAD_{el}\} \quad (5)$$
$$SAD_{emin} = min\{SAD_{et}, SAD_{eb}, SAD_{er}, SAD_{el}\} \quad (6)$$
$$T_{ediff} = SAD_{emax} - min\{SAD_{emin}, SAD_{min}\} \quad (7)$$

Assume MVs are sufficiently accurate, SAD_{max} and SAD_{min} should correspond to the maximal and minimal discontinuity around the RMB area between two consecutive pictures. T_{diff} measures the fluctuation amplitude of such discontinuity.

If T_{diff} is small while T_{ediff} is very large, it should be reasonable to conclude the RMB as a perceptible artifact. Mathematically, the condition is defined as

$$artifact := T_{ediff} > k * T_{diff} \quad (8)$$

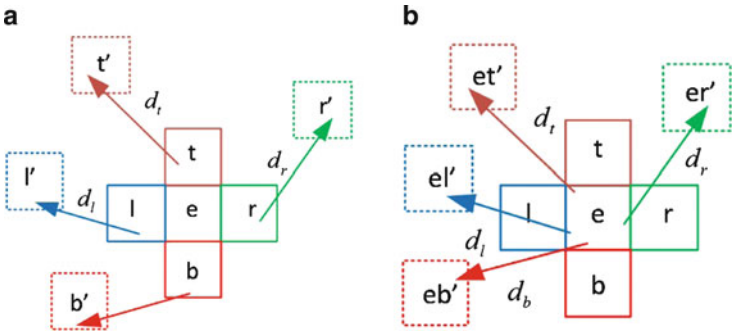

Fig. 3 SADs of MVR-EAD. (**a**) SADs of neighbors, (**b**) SADs of RMB

where k denotes the threshold factor and plays a key role in the artifact perceptibility step. According to our experiments, Eq. (8) achieves the best detection accuracy when k is around 1.5. The bigger k is, the more conservative MVR-EAD would be. In a case where MVR-EAD feasibility is "warning" as in Tables 1 or 2, it is recommended to choose a bigger k because the RMB may be a new object or a strange aspect of existing objects.

3 Experimental Results

The proposed MVR-EAD is integrated within the joint model (JM) software version 18.0. Sixteen video sequences in QCIF resolution are encoded. Each I frame is followed by 12 P-frames. Packet loss rates from 5 to 10 % are used to simulate streaming error patterns of the Internet backbone and wireless channels [6].

The risk number n is set to cover all previous MBs of the error detected by SSA in the same slice. Experimental results are summarized in Table 3. The column "artifacts" lists the number of perceptible error MBs within each video sequence. Columns "$B \rightarrow B$" and "$G \rightarrow B$" give numbers of artifacts detected. The former means true detection, i.e., a perceivable artifact is detected. The latter denotes false detection, corresponding to the case where an MB looks good and is reported as an artifact. The true detection rate is provided in the "success" column. The basic error concealment scheme in [7] is applied and the resulting PSNRs are provided. Figure 4 lists the PSNR comparison of these video sequences.

Table 3 Experimental results of SSA and MVR-EAD

		SSA				MVR-EAD				Improvement	
Videos	Number of artifacts	B → B	G → B	Success (%)	PSNR (dB)	B → B	G → B	Success (%)	PSNR (dB)	△ success (%)	△ PSNR (dB)
Akiyo	179	92	2	51.40	38.75	145	4	81.01	39.29	29.61	0.54
Bus	671	71	0	10.58	29.98	551	10	82.12	31.24	71.54	1.26
Coastguard	256	120	2	46.88	32.87	214	1	83.59	33.40	36.71	0.53
Container	304	124	5	40.79	34.62	257	10	84.54	35.64	43.75	1.02
Flower	762	69	0	9.06	29.34	644	0	84.51	30.78	75.45	1.44
Football	929	101	0	10.87	31.37	748	165	63.38	31.78	52.51	0.41
Foreman	733	72	0	9.82	32.72	526	24	71.76	33.53	61.94	0.81
Hall	470	125	2	33.07	35.61	378	29	80.43	36.51	47.36	0.90
Mobile	314	178	1	56.69	28.94	253	0	80.57	30.15	23.88	1.21
Mother-Daughter	231	54	0	23.38	37.60	172	7	74.46	38.18	51.08	0.58
News	441	144	0	32.65	35.70	337	28	76.43	36.76	43.78	1.06
Silent	310	102	0	32.90	34.57	224	12	72.26	34.91	39.36	0.34
Stefan	407	59	0	14.50	31.22	336	3	82.56	32.26	68.06	1.04
Tempete	141	82	0	58.16	32.36	93	8	65.96	32.45	7.80	0.09
Vectra	639	39	0	6.10	28.84	511	4	79.97	30.72	73.87	1.88
Waterfall	96	43	0	44.79	33.96	66	0	68.75	34.30	23.96	0.34

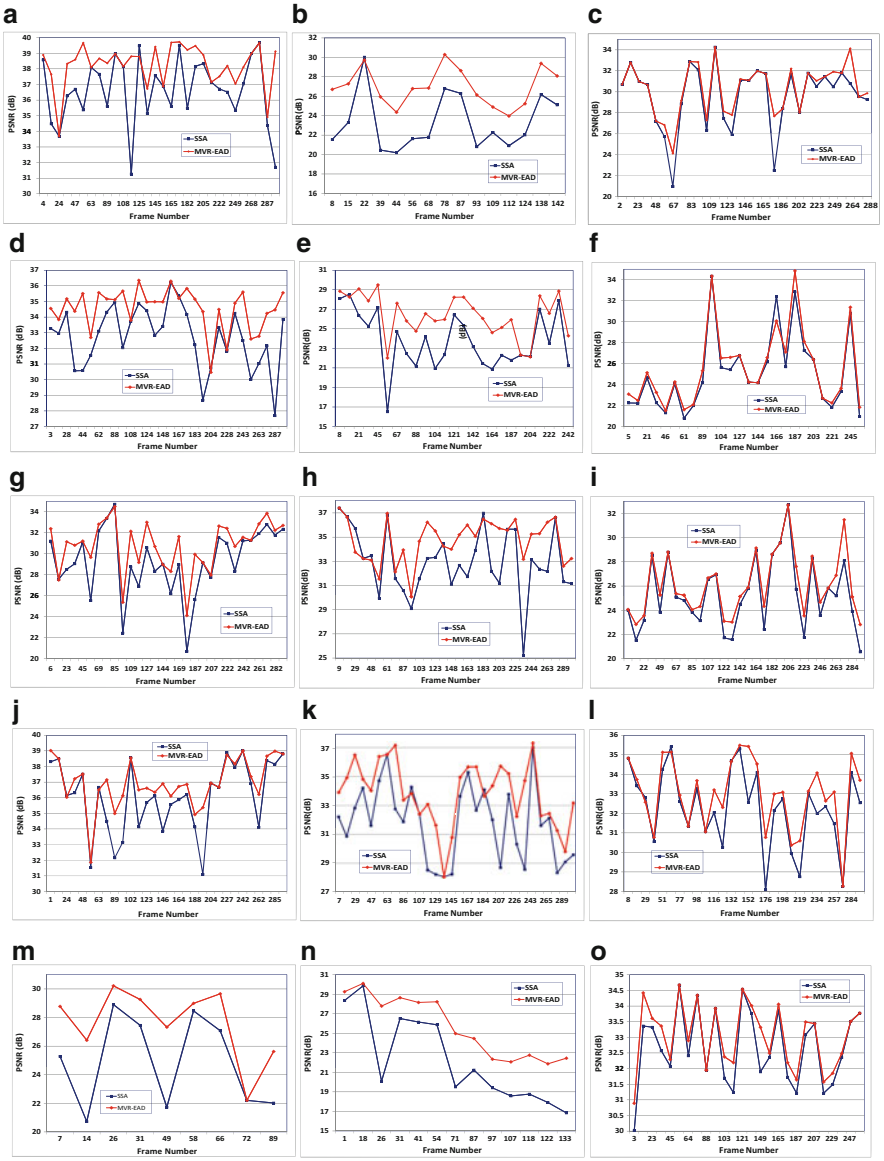

Fig. 4 PSNR vs. frame number using SSA and MVR-EAD with the basic error concealment scheme [7] in JM18.0. (**a**) akiyo, △ PSNR = 0.54 dB, (**b**) bus, △ PSNR = 1.26 dB, (**c**) coastguard, △ PSNR = 0.53 dB, (**d**) container, △ PSNR = 1.02 dB, (**e**) flower, △ PSNR = 1.44 dB, (**f**) football, △ PSNR = 0.41 dB, (**g**) foreman, △ PSNR = 0.81 dB, (**h**) hall, △ PSNR = 0.90 dB, (**i**) mobile, △ PSNR = 1.21 dB, (**j**) mother–daughter, △ PSNR = 0.58 dB, (**k**) news, △ PSNR = 1.06 dB, (**l**) Silent, △ PSNR = 0.34 dB, (**m**) stefan, △ PSNR = 1.04 dB, (**n**) vectra, △ PSNR = 1.88 dB, (**o**) waterfall, △ PSNR = 0.34 dB

4 Discussions and Conclusions

This paper presents an error and artifact detection algorithm which uses temporal concealment to find the corresponding area in the reference frame for the risk MB. It is assumed that the similarity of a small area between two frames does not fluctuate much. Once only the similarity of the risk MB varies suddenly from those of its neighbors, it should be detected as an artifact.

It is worth mentioning that when temporal concealment works poorly, the false detection rate will increase. For example, in the sequence of "football" which contains fast and complex motion, the similarity distribution tends to be inconsistent. Although a conservative k in the Eq. (8) is selected, MVR-EAD outputs the highest false detection rate and the lowest detection success rate. This indicates the future research direction of this work.

The proposed MVR-EAD gains attractive detection accuracy, an increase from 7.8 to 73.87 % demonstrated by extensive experiments. As a result, it incurs 0.09–1.88 dB on average in PSNR improvement with the error concealment strategy within JM18.0. The fact that at most eight times of SAD calculation are incurred ensures the simplicity of MVR-EAD and its excellent applicability for real-time low-bit rate applications.

References

1. Wang Y, Zhu Q.-F (1998) Error control and concealment for video communication: a review. In: Proceedings of the IEEE
2. Superiori L, Nemethova O, Rupp M (2006) Performance of a H.264/AVC error detection algorithm based on syntax analysis. In: Proceedings of the 4th international conference on advances mobile computing and multimedia
3. Khan E, Lehmann S, Gunji H, Chanbari M (2004) Iterative error detection and correction of H.263 coded video for wireless networks. IEEE Circ Syst Video Technol 14(12):1294–1307
4. Farrugia R, Debono C (2010) A hybrid error control and artifact detection mechanism for robust decoding of H.264/AVC video sequences. IEEE Circ Syst Video Technol 20(5):756–762
5. Ye S, Lin X, Sun Q (2003) Content based error detection and concealment for image transmission over wireless channel. In: Proceedings of the IEEE international symposium circuits and systems, Bangkok, pp 368–371
6. Wang Y-K, Wenger S, Hannuksela M (2005) Common conditions for SVC error resilience testing. Joint Video Team (JVT) of ISO/IEC MPEG & ITU-T VCEG (ISO/IEC JTC1/SC29/WG11 and ITU-T SG16 Q.6) 16th Meeting, July, 2005
7. Wang Y-K, Hannuksela M, Varsa V, Hourunranta A, Gabbouj M (2002) The error concealment feature in the H.26L test model. In: Proceedings of ICIP

A Novel Fractional Fourier Domain Filter Design Based on Time–Frequency Image Edge Detection

Jiexiao Yu, Kaihua Liu, Xiangdong Huang, and Ge Yan

Abstract To realize the lossless recovery of non-stationary signal in complicated noise environment, a novel design method of fractional Fourier domain filter is proposed assisted by time–frequency image edge detection. The time–frequency distribution of observed signal is obtained by Gabor-Wigner transform, and based on technique of image edge detection and selection algorithm, adjacent edge information of the different regions of in the time–frequency plane are obtained, which can be used to build support vector machine (SVM) training set. Respectively, for the two cases of linearly separable and inseparable signal and noise distribution, the separating line is drawn by the SVM separating algorithm and then the parameters of filter can be determined by the parameters of separating line. Simulation results show that without any prior knowledge of signal and noise, the design process can ensure the optimal performance of the filter and higher signal noise ratio is reached. Furthermore, an undistorted signal recovery is achieved even in the case of strong coupling between signal and noise, which proves the reliability, versatility and effectiveness of our filter design.

Keywords Time–frequency filtering • Fractional Fourier transform • Gabor-Wigner transform • Image edge detection • Support vector machine

1 Introduction

Fractional Fourier transform(FRFT), as a rotated operator in the time–frequency plane [1], can analyze the signal in the unified time–frequency domain and therefore it can be adopted in the time–frequency filter design in order to achieve the parameter estimation and signal recovery [2]. Some fractional Fourier domain

J. Yu (✉) • K. Liu • X. Huang • G. Yan
School of Electronic Information Engineering, Tianjin University, Tianjin, China
e-mail: yjx@tju.edu.cn

B. Zhang et al. (eds.), *The Proceedings of the Second International Conference on Communications, Signal Processing, and Systems*, Lecture Notes in Electrical Engineering 246, DOI 10.1007/978-3-319-00536-2_25,

optimal filtering algorithms based on minimum mean square error are presented in [3] and [4], which need the prior statistical knowledge of signal and noise and simply be limited to a single rotation angle. Erden achieved an iterative filtering algorithm in consecutive fractional Fourier domains, which complexity is very high and the iterative process cannot guarantee that the result is convergence to the global optimal solution [5]. Reference [6] presents a novel idea to convert the fractional Fourier domain filter to a separating line in the time–frequency plane, though no specific design is proposed. In this paper, edge detection and selection algorithms are used to construct SVM training sets in order to get the optimal separating line, which is the key of the filter design in fractional Fourier domain.

2 Principal of Fractional Filter Design

2.1 Fractional Fourier Transform

The pth FRFT of signal $x(t)$ is defined as a linear integral transform with kernel $K_p(u,t)$:

$$X_p(u) = \int_{-\infty}^{\infty} K_p(u,t)x(t)dt \tag{1}$$

where $K_p(u,t) = \sqrt{1-j\cot\alpha}\,\exp[j\pi(u^2\cot\alpha - 2ut\csc\alpha + t^2\cot\alpha)], \alpha = p\pi/2$, $p \neq 2n$, $K_{4n}(u,t) = \delta(u - t)$ and $K_{4n\pm 2}(u,t) = \delta(u + t)$ The u domain is generally known as the fractional Fourier domain.

Many types of discrete fractional Fourier transform (DFRFT), the discrete counterpart of continuous FRFT, have been derived and are useful for signal processing applications. In this paper, Pei sampling fast algorithm is adopted, which is unitary, reversible, and flexible, in addition, the closed-form analytic expression can be obtained. It can be efficiently calculated by FFT, which is satisfied the general application requirement [7].

2.2 Fractional Filter Design

Assume that the input signal is

$$x(t) = s(t) + n(t) \tag{2}$$

where $s(t)$ is the useful non-stationary signal and $n(t)$ is the additive noise.

The time–frequency distribution of $x(t)$ is shown in Fig. 1a and it is obvious that the useful signal and the noise are mutually coupled both in the time domain and

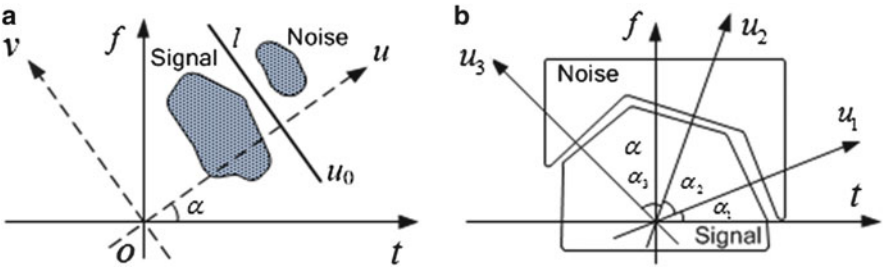

Fig. 1 Signal-noise separation. (**a**) In single u domain (**b**) In multi-u domain

frequency domain and the noise cannot be filtered out completely through the time or frequency domain filtering individually, which could be obtained by an u domain filter after rotating the coordinate axis to the right angle by FRFT and the expression of the filter in u domain is:

$$r(t) = F^{-p}\{F^{p}[x(t)]H(u)\} \tag{3}$$

where, $r(t)$ is the recovered signal and $H(u)$ is the time–frequency filter transfer function.

The time–frequency filter as showed in (3) is equivalent to a separating line in the time–frequency plane, which could separate the useful signal and noise completely. For more general signal distribution, series of rotation of the time–frequency plane are needed to eliminate the signal-noise coupling. At this point, the single-order filter could be extended to a filter bank with continuously changing order, as Fig. 1b shows. It is obviously that the option of the separating line is non- uniqueness, hence how to find an optimal solution is the key to the filter design.

3 Fractional Fourier Domain Filter Based on Edge Detection

Frame diagram of the fractional Fourier domain filter is shown in Fig. 2

Main steps of the design are summarized as follows:

(a) The observed signal is transformed in the time–frequency plane in order to obtain the time–frequency distribution image of signal and noise;
(b) Image edge detection technique is used to separate the time–frequency image, and different edges of signal or noise are labeled differently;
(c) After selecting the edge points of signal and noise region as a training sample set of the classifier with the edge selection algorithms, the optimal time–frequency classified line between signal and noise is obtained by training the sample set with SVM algorithm;

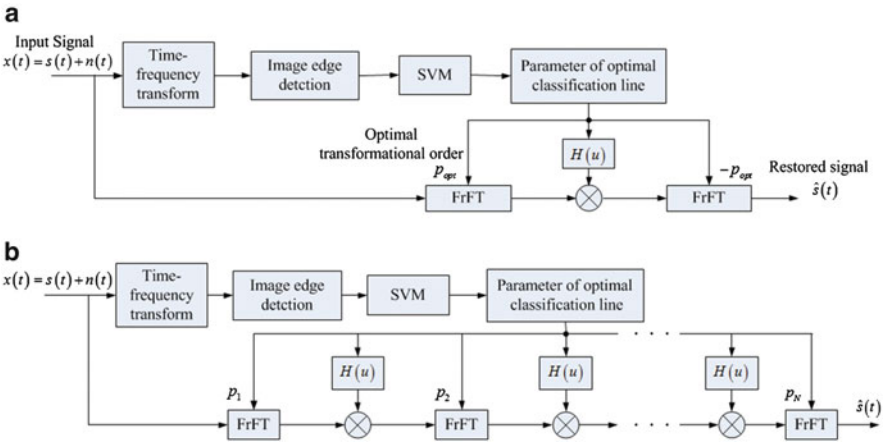

Fig. 2 The design frame diagram of the FRFT filter. (**a**) 1-D filter; (**b**) Multi-order filter

(d) In the case of linear separability between signal and noise, the optimal transform order and transfer function of 1-D filter is determined by the parameters of the optimal classified line directly, however the least-square piecewise linear fitting algorithm was used to divided the optimal classified line into segments and the parameters of multi-order filter bank are determined by each segment in the case of linear inseparability;
(e) According to the parameters of filter (bank) determined by (d), the signal recovery and the noise filtering could be achieved by the fractional Fourier domain filters.

3.1 Time–Frequency Image Representations

The time–frequency transform selected in this paper should suppress cross-term interference effectively and be a high-resolution one in order to reduce the number of SVM training set. Therefore, Gabor-Winger transform (GWT) is used which form is as follows:

$$C_s(t,f) = G_s^{2.6}(t,f)W_s^{0.6}(t,f) \tag{4}$$

where $G_s\,(t,f)$ is the Gabor transform and $W_s\,(t,f)$ is Wigner distribution, and

$$G_s(t,f) = \int_{-\infty}^{\infty} e^{-(\tau-t)^2/2} e^{-j2\pi f\tau} s(\tau) d\tau \tag{5}$$

$$W_s(t,f) = \int_{-\infty}^{+\infty} x(t+\tau/2) x^*\left(t-\tau/2\right) e^{-j2\pi f\tau} d\tau \tag{6}$$

Obtaining the time–frequency distribution of the signal, we can apply an image processing technique for the construction of training set of SVM in order to solve separating line equation parameters because of the equivalence of each time–frequency point and the pixel in the image based on the inherent similarity between the time–frequency plane and the two-dimensional image.

3.2 Edge Detection and Selection in Time–Frequency Domain

The image edge detection algorithm is adopted to construct the training-set of SVM, which mainly includes three parts, which are edge detection, edge labeling and the edge selection.

(a) Edge detection: multi discrete highlight energy concentration areas are in the time–frequency image as several signal components exist simultaneously. One of the most direct and effective way of separating these components is according to the edge of these highlight areas. In this paper, Canny operator [8] is adopted, which is one of the best operators to detect the step edge and still work well when the difference between the strength of signal and noise is extremely.
(b) Edge labeling: label all the pixels in the binary image which is obtained from the edge detection with integer number, followed by an 8-domain connectivity labeling algorithm for the edge label. However, there are no contacts among these labels of different edges though they are same in every signal edge. Arrange these labels in sequential order and replace them by the sequence number in order to facilitate the edge selection.
(c) Edge selection: calculate the length of each x-axis projection of the edge line and sort them in descending order, as shown in Fig. 3a. Select previous four edges and calculate each y-value of the selected edge corresponds to the center point of the intersection of the abscissa of these four edges. After sorting the y values in ascending order, select two edges, which correspond to the two intermediate points of y values, as the training-set of SVM, as shown in Fig. 3b.

Considering the two-component separation problem, the separating lines are located within two inside edges and the signal energy is concentrated in areas between the upper two edges and the lower two edges.

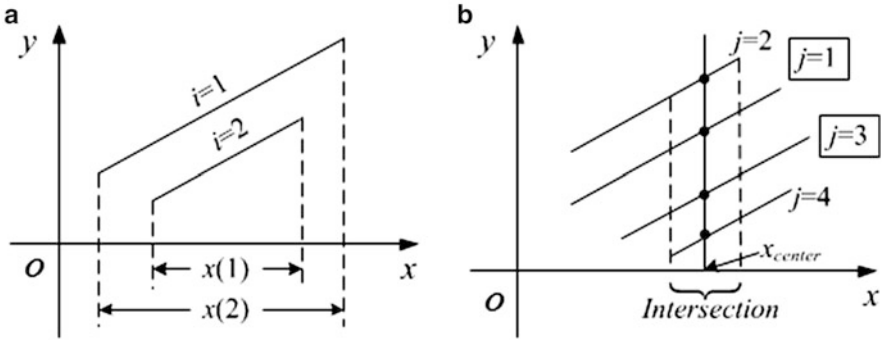

Fig. 3 Edge selection. (**a**) x-axis projection of the edge line; (**b**) selecting the training-set

3.3 Determination of the Optimal Separating Line by SVM

In this paper, the learning mechanism of SVM [9] is used to determine optimal separating line equation between the edges of the signal and noise, which is the basis for reasonable setting of time–frequency filter parameter. The training set of SVM classifier is a following set of points:

$$E = \left\{(\boldsymbol{x}_i, c_i)\middle|\boldsymbol{x}_i \in \boldsymbol{R}^2, c_i \in \{1, -1\}\right\}, \quad i = 1, 2, \cdots, N \tag{7}$$

where x_i is a 2-D position vector representing the edge pixels in time–frequency image obtained from the edge detection algorithm and the interval of c_i, the category identifier value of x_i, is 1 or -1, which indicates that the vector belongs to the edge of signal or noise. N support vector $\{d_i\}$ and coefficients $\{a_i\}$, which is used to classify the two edges of the training set, can obtain from the SVM training and then, we can use them to build the optimal support vector separating line equation.

In the case of linearly separable signal and noise distribution, the optimal separating line is straight and defined by the following equation:

$$f(x) = \sum_{i=1}^{n} c_i a_i (x_i x) + w_0{}' \tag{8}$$

where $(x_i \cdot x)$ is the dot product operation and $w_0{}'$ is the separating threshold.

In the case of linearly inseparable situation, the inner production $K(x,x')$ of the support vector machine is needed instead of the dot product and Gaussian radial basis function is select as the inner production in this paper so that the optimal separating line is a curve and the equation is:

$$f(x) = \sum_{i=1}^{n} c_i a_i K(x_i, x) + w_0' \tag{9}$$

3.4 Construction of Fractional Fourier Domain Filter

After getting the optimal separating line parameters, the fractional domain filter can be constructed, while the transform order p is determined by the slope k of the separating line and the cutoff frequency u_0 equal the distance from the origin of the separating line. Assuming the linear separating line equation in time–frequency domain is l: $f = kt + f_0$, the coordinate transformation formula can be obtained:

$$p = -\frac{2}{\pi} arc\cot(k); u_0 = 2\pi f_0 \sin\left(\frac{\pi}{2}p\right) \tag{10}$$

In the case of linearly separable signal and noise distribution, using (8), the equation of SVM separating line, can determine the parameters of the time–frequency filter directly, and then achieve the recovery of useful signal and the filter of noise according to (3).

In the case of linearly inseparable signal and noise distribution, with the proper choice of SVM kernel function, an optimal separating curve is obtained which can not assisted FRFT filter design directly so that a piecewise linear fitting algorithm is used under a global least-square error criterion and the multi-order filter bank is designed by the parameters of each segment. In order to avoid introducing the discrete errors repeatedly and reduce algorithm complexity, the above serial filter bank may be converted into the parallel structure in practice, that is, filter each fitting segment $x_n(t)$ separately and superimpose the output as the ultimate recovered signal $r(t)$,

$$r(t) = \sum_{n=1}^{N} F^{-p_n}\{F^{-p_n}[x_n(t)]H_n(u)\} \tag{11}$$

4 Simulation

4.1 Case 1: Linearly Separable Signal and Noise Distribution

We consider a Gaussian amplitude modulated LFM signal $s(t) = e^{-t^2/4} e^{j\pi(2t^2+60t)}$ with the additive noise $n(t) = e^{-t^2/4} e^{j\pi(5t^2+40t)}$. The observation time is from -2 s to 2 s and the sampling rate f_s is 100 Hz. The GWT time–frequency distribution of the observed signal $x(t) = s(t) + n(t)$ is shown in Fig. 4a and signal and noise are present coupling either in the time domain or frequency domain. Figure 4b shows the labeled edges after using Canny operator to detect the time–frequency image edge. Through the edge filtering algorithm,the edges of signal and noise can be

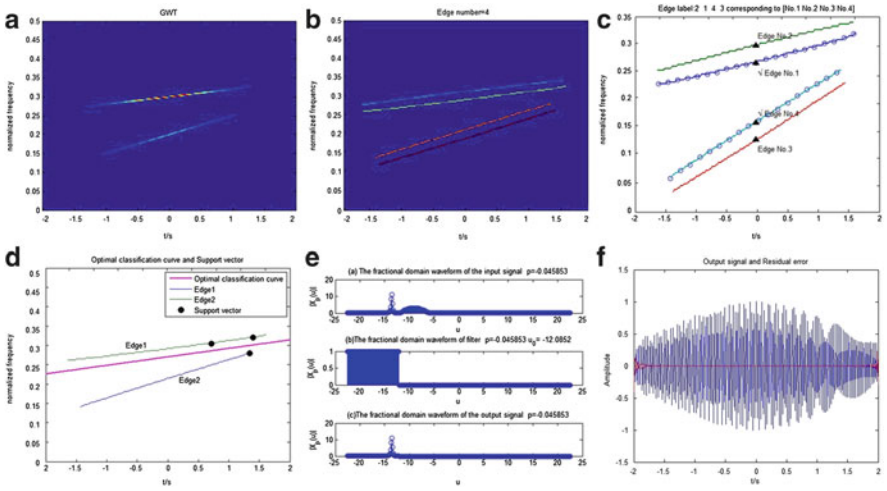

Fig. 4 Filtering experiments in the case of linearly separable distribution. (**a**) GWT of x(t); (**b**) the time–frequency distribution after edge detection and labeling; (**c**) SVM training set after edge selection; (**d**) optimal separating line and support vector; (**e**) filtering in fractional domain; (**f**) recovered signal and recovered error

selected which is the SVM training set, as shown in Fig. 4c. Based on these edges, the optimal separating line and support vector are obtained, as Fig. 4d shows, and the separating line equation is, l: $f(x) = 2.2059x + 26.7279$. Figure 4e shows the process of filter in u domain and the recovered signal and recover error are shown in Fig. 4f.

Evaluate the time–frequency filter from the SNR improvement factor IF $= SNR_{out}/SNR_{in}$, mean square error (MSE) of recovered signal MSE $= \int |r(t) - s(t)|^2 dt / \int |s(t)|^2 dt$ and the number of training set samples. Figure 5 shows the relationships between the sampling rate and IF, MSE and the number of samples. As can be seen, a high SNR improvement and a small amount of sample number in training set is obtained and when the sampling rate is increased, the sample number shows an upward tendency, then the edge is more accurate and the separating results of optimal classifier line is better. However, the algorithm complexity increases, therefore, the sampling rate should be selected according to the actual application.

Figure 6 shows the relationship between input SNR and IF, MSE and output SNR. As can be seen SNR improvement factor with the decrease of SNR_{in}, other words, as long as the edges of signal and noise can be detected, the lower the input SNR is, the better the IF is. MSE of the recovered signal reduces with the growing of SNR_{in} in the beginning and nearly flat in a small value after the strength of signal is greater than it of noise, that means the SNR_{out} has a little change when SNR_{in} is larger than 0 dB and it explains why IF raises when the strength of noise increases on the other hand.

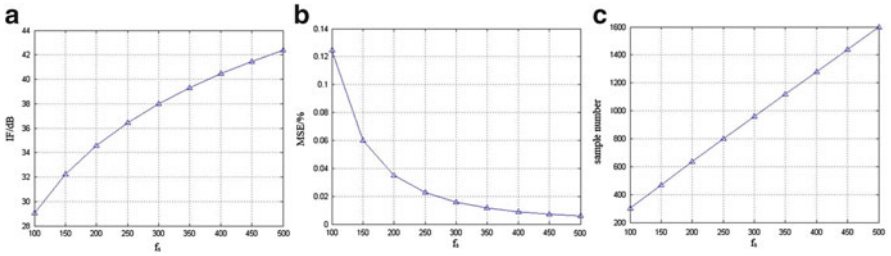

Fig. 5 The influence of sample rate. (**a**) the relationships between sampling rate and IF; (**b**) the relationships between sampling rate and MSE; (**c**) the relationships between sampling rate and sample number in training set

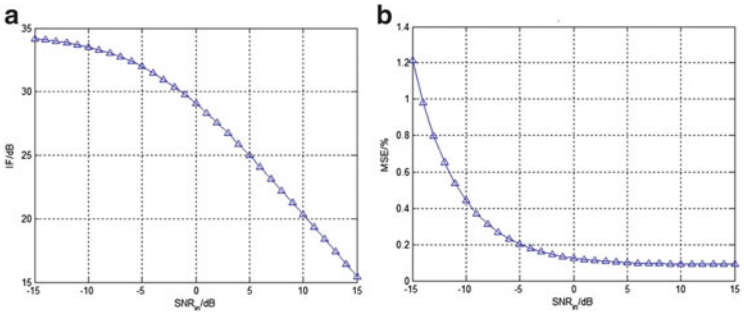

Fig. 6 The influence of input SNR_{in}. (**a**) the relationship between SNR_{in} and IF; (**b**) the relationship between SNR_{in} and MSE

4.2 Case 2: Linearly Inseparable Signal and Noise Distribution

In the case of signal and noise non-linear separability, the expressions of signal and noise are $s(t) = \mathrm{e}^{-t^2/100}\mathrm{e}^{j\cdot 2\pi\left(0.01t^3+4.5t\right)}$ and $n(t) = \mathrm{e}^{-t^2/100}\mathrm{e}^{j\cdot 2\pi\left(0.01t^3+2t\right)}$. Signal observation time is from -10 s to 10 s and the sampling rate f_s is 30 Hz. Figure 7 (a) shows the The GWT time–frequency distribution of the observed signal $x(t) = s(t) + n(t)$ and the third order fitting of SVM separating line is showed in Fig. 7(b), which is enough to our experiments, however higher order fitting can be adopted to achieve more accurate approximation. The fitting equation is:

$$f(x) = \begin{cases} -0.32972x + 2.5141 & x < -2.534 \\ -8.7609\mathrm{e}-005x + 3.3393 & -2.534 \le x < 2.466 \\ 0.32879x + 2.5208 & x \ge 2.466 \end{cases} \tag{12}$$

Calculate IF and MSE, and the result is IF $=$ 23.0251 dB, MSE $=$ 0.1483 %. As can be seen from the above results, the proposed algorithm still achieves an

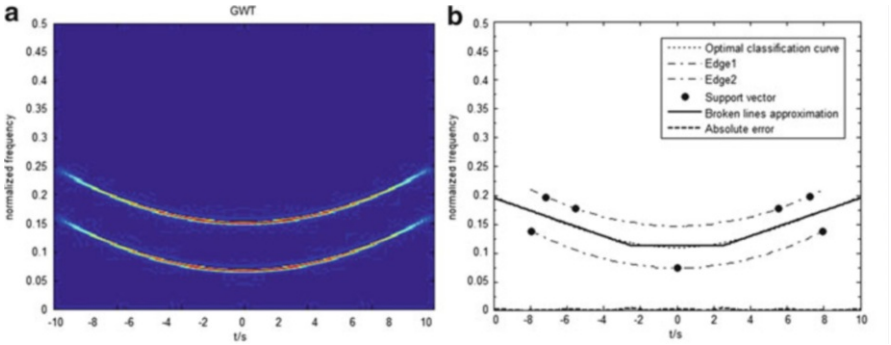

Fig. 7 Filtering experiments in the case of linearly inseparability. (**a**) GWT of x(t); (**b**) third order fitting of SVM separating line

effective noise filter for the case of linearly inseparable signal and noise distribution. However, compared with the case of linearly separability, the performance degradation cannot be helped caused by the errors of piecewise linear fitting and the discrete multi-order filter bank.

5 Conclusion

To recover the non-stationary signal in complicated noise environment without distortion, a novel general design of fractional domain filter is proposed, which can automatically obtain the optimal separating lines and determine the filter parameters combining with time–frequency transform, image edge detection, support vector machines and other technology. This design is reliability and versatility and can ensure the optimal performance of the filter without any statistic priori knowledge or other information such as form, strength or distribution of signal and noise. Simulation results show that the small number of sampling set and the high signal noise ratio can be obtained and it still work well even in the case of strong coupling between the signal and noise.

Acknowledgments This work is supported by the National Natural Science Fund of China (61271069).

References

1. Almeida LB (1994) The fractional Fourier transform and time-frequency representations. IEEE Trans Signal Process 42(11):3084–3091
2. Suba RS, Bingo WL, Apostolos G (2012) Filtering in Rotated Time-Frequency domains with unknown noise statistics. IEEE Trans Signal Process 60(1):489–493

3. Zalevsky Z, Mendlovic D (1996) Fractional Wiener filter. Appl Opt 35(20):3930–3936
4. Kutay MA, Ozaktas HM, Onural L et al (1997) Optimal filtering in fractional Fourier domains. IEEE Trans Signal Process 45(5):1129–1143
5. Erden MF, Kutay MA, Ozaktas HM (1999) Repeated filtering in consecutive fractional Fourier domains and its application to signal restoration. IEEE Trans Signal Process 47(5):1458–1462
6. Pei SC, Ding JJ (2007) Relations between Gabor transforms and fractional Fourier transforms and their applications for signal processing. IEEE Trans Signal Process 55(10):4839–4850
7. Pei SC, DING JJ (2000) Closed-form discrete fractional and affine Fourier transforms. IEEE Trans Signal Process 48(5):1338–1353
8. Ding L, Goshtasby A (2001) On the Canny edge detector. Pattern Recognit 34(3):721–725
9. Cortes C, Vapni C (1995) Support-vector networks. Mach Learn 20(3):273–297

A Novel 3D Video Format Identification Algorithm

Sheng Su and Zhuo Chen

Abstract More and more 3D videos are uploaded on the web. It becomes very difficult to find an expected 3D video from online videos because search engineering identifies 2D and 3D format according to the text description of each video currently. In this paper, a novel 3D video format identification algorithm CM is proposed. The frame extraction and L&R image matching are analyzed. CM combines the gray histogram matching (GHM) and the SIFT feature matching (SFM). It can obtain high identification accuracy up to 99.5 % at the price of low computational time. Compared to GHM and SFM, it shows better comprehensive performance.

Keywords 3D video • Automatically format identification • Search engineering

1 Introduction

The 3D video is becoming more and more popular because of the great success of 3D films in recent years. A large number of 3D videos are uploaded on the web and mixed into the sea of 2D videos. It is the key to identify whether a video is 3D video or not before a 3D compatible video player can play a 3D video from the web. The easiest way is to embed 3D format information into the 3D video [4]. Many video encoding standards, such as DVB, SMPTE and MPEG, are seeking to define 3D standards to address the issue [3]. However, it should take long time to find a final solution of 3D video standards. Currently, most of 3D videos on the web do not contain the 3D format information. Thus, other way should be explored to achieve the goal of 3D video identification. In this paper, we proposed a 3D video

S. Su (✉) • Z. Chen
School of Computer Science and Engineering, University of Electronic Science and Technology of China, Sichuan, China
e-mail: susheng@uestc.edu.cn; ladjzero@163.com

B. Zhang et al. (eds.), *The Proceedings of the Second International Conference on Communications, Signal Processing, and Systems*, Lecture Notes in Electrical Engineering 246, DOI 10.1007/978-3-319-00536-2_26,

identification technique to distinguish automatically whether a video is 3D video or not and the 3D formation of the video.

2 3D Formation Detection

2.1 3D Format Classification

In general, the 3D format is the 2D compatible format or Multiview Video Coding (MVC) format. The 2D compatible format uses AVC standard which is a 2D video coding standard. MVC is an amendment to AVC and designed for 3D video coding.

The compatible format includes time multiplexed format and space multiplexed format. The time multiplexed format, also named as Frame Sequential format, uses double frame rate to storage Left Eye and Right Eye Images (L&R images) respectively. The advantage of this format is resolution lossless. However, some old displayers with low refresh rate could not support this format. The space multiplexed format merges L&R images into a single frame. Since the frame compatible format has perfect compatibility with 2DTV device, it is the most popular 3D format on the web.

2.2 3D Video Identification Framework

Let G_i ($i = 1,\ldots,k$) be the all known 3D formats. A video has a 3D format of G_i if the format of n frames in the video is the format G_i. Figure 1a shows the process of the 3D format identification for a given video. As shown in Fig. 1a, the first step is to extract n frames of the video. Then, the formats of the n frames are detected and the distribution statistics of 3D format frame is analyzed. Based on the results of the analysis and a given threshold value, the video can be classified into of the 3D video or the 2D video.

The key of the 2D/3D format identification of a video is the format detection of 3D frame in the video. According to the methodology in the paper [3], Fig. 1b shows the format detection process of a frame.

For a given frame, all frame formats need to be identified until a frame format or no frame format is matched. In order to verify a frame format G_i (i $= 1,\ldots,k$), L&R images are extracted from the frame. If the L&R images satisfy the requirement of binocular images, this frame could be considered as the format G_i. Otherwise, the same steps are repeated for the next format until all formats were tested. The frame is judged as 2D format if no 3D format is matched.

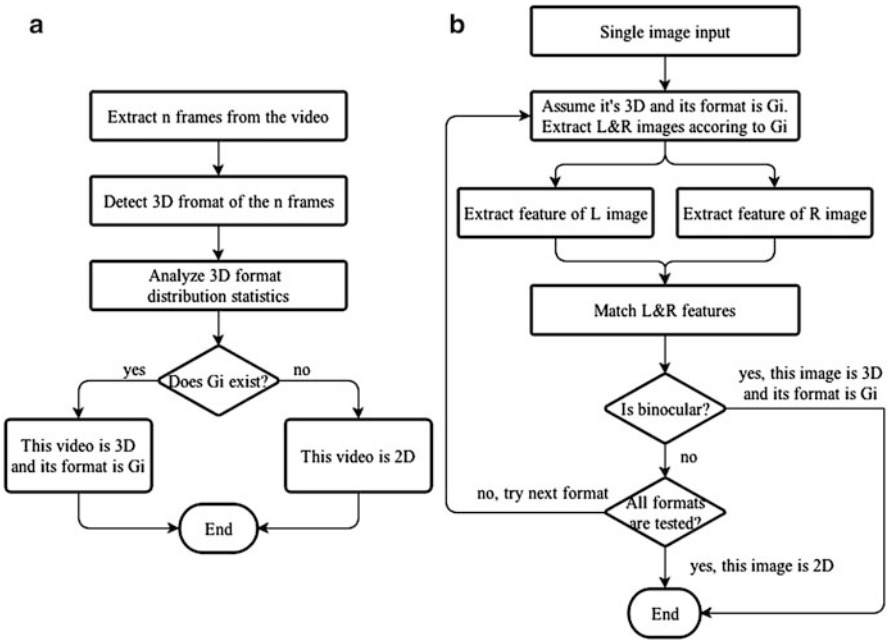

Fig. 1 (**a**) Process of 3D video format detection. (**b**) Process of 3D frame format detection

2.3 Frame Extraction

It is inefficient to test all frames in a video because a video contains a large number of frames. Moreover, time-adjacent frames are always highly similar in content. In order to achieve an effective and efficient 3D recognition, the selection of the video frame should follow the following three rules:

1. Select video frames with large variances in color, texture and shape. Because rich color, texture and shape help to find enough feature points for binocular matching.
2. Select key frames. Key frames have better image quality than prediction frames. A key frame is always the first frame of one scene, so that two adjacent key frames differ from each other to a large extent. It helps to improve the diversity of frame samples.
3. Frames should be extracted from the whole time range of video. Too many frames in a narrow time range may lead to the mistake in the format recognition.

2.4 L&R Images Extraction

The extraction method of L&R images should be defined for every specific 3D format. For instance, a Side-by-Side format L&R images can be divided into left and right half. For a frame image with horizontal interlaced format, L and R images can be extracted from odd and even line, respectively. In addition, the frames with oven index are L image and its next neighbor frame is R image for the frame image with sequential format.

2.5 L&R Images Match

The image matching is the process of matching and superimposing between two or more images, which are from a same scene and captured in different time, perspective and sensors [5]. The literature [2] defined four elements for image matching. They are feature space, the similarity measurement, geometry transformation, and transformation parameters. It shows that the major way of image matching is to find out feature points from two views and match them, and then calculate the geometry transformation.

In order to achieve high quality of stereo viewing experience, the L&R images are filmed synchronously by two same cameras. The distance between binocular cameras' optical centers is close to the span of two eyes of a person. The parallax of L&R images is small. Based on these characteristics of the 3D video, feature points matching and gray-scale histogram matching are feasible to address the L&R images matching.

2.5.1 Gray Histogram Matching (GHM)

The global gray histogram is an h (the size of histogram) dimensional feature vector without any location information. No location information leads to a high risk of false judgments. To overcome the drawback, a cross is made within the image to divide it into four smaller parts. A 16 dimensional histogram is extracted for every part. Thus, a 64 dimensional feature vector can be built for each image. In this paper, histogram intersection distance is used to measure the similarity of two histograms.

2.5.2 SIFT Feature Matching (SFM)

SIFT was proposed by David Lowe in 1999 and improved in 2004 [1]. Let *Lrect* be the projection rectangle of L image on the left view. The projection *Rrect* of *Lrect* on the right view can be obtained through the homography transform matrix.

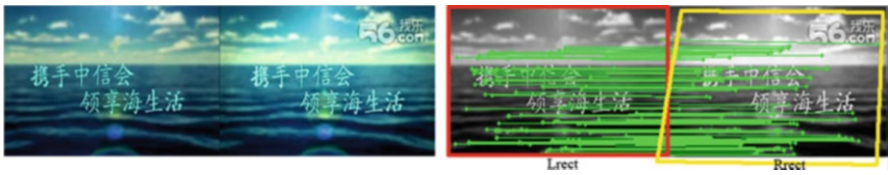

Fig. 2 An instance of SIFT feature matching

Assume the four vertexes of *Lrect* are (x_0,y_0), (x_1,y_1), (x_2,y_2), (x_3,y_3), respectively, and the four vertexes of *Rrect* are (x'_0,y'_0), (x'_1,y'_1), (x'_2,y'_2), (x'_3,y'_3), respectively. The distance between *Lrect* and *Rrect* can be defined as the (1).

$$Distance = \sum_{i=0}^{3} \sqrt{(x_i - x'_i)^2 + (y_i - y'_i)^2} \tag{1}$$

Figure 2 shows an instance of the point correspondences and projections. The left part is an original 3D format images. The right part is the matched L&R images. The start point and end point of each line are SIFT feature point correspondences in the right part. The whole L image is represented as Lrect. The projection Rrect of Lrect is a quadrangle which has similar size with Lrect and heels to the left.

2.5.3 Comprehensive Matching (CM)

GHM can extract features and execute matching easily and efficiently. However, it has little information on location and is sensitivity to light changing. SFM overcomes the drawbacks of GHM, but it is computationally expensive and has weak ability to find key points of the image with smooth edge or monotonous content.

Based on the following experiments, we proposed a CM algorithm. A similarity range for GHM is set in the algorithm. GHM has big probability to make wrong identification if the similarity of L&R images falls into the range. To avoid the false identification, SFM is called.

2.5.4 Threshold Evaluation

Sample training is used to determine the threshold for both the GHM and SFM. Let A be the statement that the image is 3D. B is the statement that the image is 2D. a denotes the judgement that the image is evaluated as 3D. b denotes the judgement that the image is evaluated as 2D. The posterior probability of misjudgment $P(b/A)$ and $P(a/B)$ can be estimated through experiments. Assume $P(A) = P(B)$ in the initial condition. The probability of misjudgment can be defined by (2).

$$P_{mis} = P(A)\left[P\left(b\middle|A\right) + P\left(a\middle|B\right)\right]. \quad (2)$$

As shown in (2), the chosen threshold should minimize the value of $P(b|A) + P(a|B)$ in order to obtain minimum probability of misjudgment.

3 Experiments Results and Analysis

The experiment was divided into two parts: image format identification test and video format identification test. 2,000 3D images and 2,000 2D images are chosen for image test. 200 3D videos and 200 2D videos are chosen for video test. All 3D images and videos are Side-by-Side format. L&R images were extracted according to this format. In SFM, the size of *Lrect* is set to (320 × 240). Ten key frames are extracted from each video for video format identification test.

3.1 Image Format Identification Test

Figure 3 shows the distribution of similarity of all tested images based on the GHM. The threshold of GHM is set to 0.82. Images, of which L&R histogram similarity is greater than 0.82, are considered as 3D.

The L&R histogram similarities of 2D images approximately follow Gaussian distributions ($\mu = 0.5$, $\sigma = 0.1$). The similarities of 3D images approximately follow a left skewed distribution with a peak at 0.96. In the range from 0.7 to 0.9, it is easy to make a wrong judge.

Figure 4 shows the identification results of SFM. In order to draw the distance chart easily, 100 biggest distances from 3D image test and 1,000 smallest from 2D test are selected. They are sorted by descending order and ascending order respectively in this chart. As shown in Fig. 4, the threshold of SFM is set to 450. Images, of which *Lrect* and *Rrect* distances are greater than 450 or cannot be obtained, are considered as 2D images.

According to the results of GHM and SFM, CM set a threshold range from 0.7 to 0.9 for GHM. Images whose GHM similarities locates in the range will be identified by SFM. The threshold of SFM is also set as 450.

Table 1 summarizes the identification accuracies and time consumption of the three algorithms.. GHM is most efficient, but its accuracy is a bit low. SFM and CM reaches high accuracy rate, and CM is much more efficient.

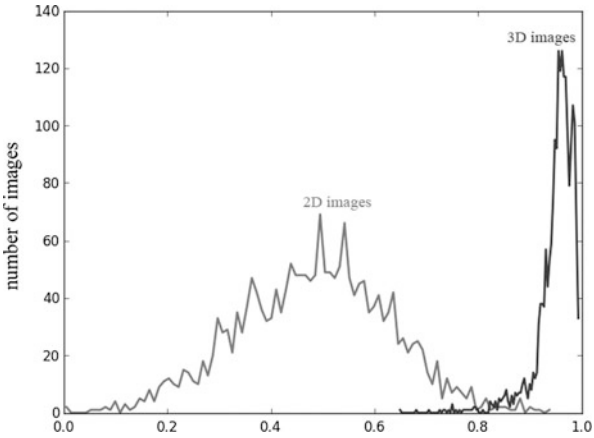

Fig. 3 The distribution of L&R images similarity measured by GHM

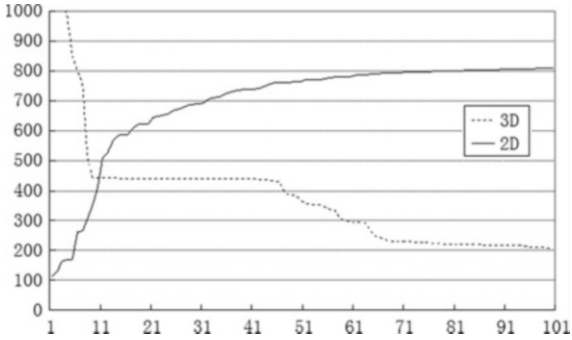

Fig. 4 Distances of L&R images measured by SFM. Distances of 3D image test is in a descending order (*dotted*) and distances of 2D images test is in an ascending order (*solid*)

Table 1 Image test of three algorithms

	Identification of 3D images		Identification of 2D images	
Matching	Accuracy (%)	Time (s)	Accuracy (%)	Time (s)
GHM	98.9	28.1	98.7	17.6
SFM	99.6	4,012.8	99.5	1,844.5
CM	99.6	113.4	99.55	171.8

3.2 Video Format Identification Test

The number of false judgments is shown in Table 2, and the optimal threshold can be determined easily from this table. The optimal thresholds of the three algorithms are determined as 7, 5 and 6 (the index of number underlined in Table 2).

Table 3 summarizes the accuracies and computational times for all three matching methods. As shown in Table 3, CM has best accuracies and computational efficiency. It can obtain high identification accuracy up to 99.5 %. Though SFM has

Table 2 Number of false judgments of different thresholds

	Number of false judgments of different thresholds										
Matching	0	1	2	3	4	5	6	7	8	9	10
GHM	200	111	62	38	28	23	16	14	15	14	40
SFM	200	18	5	4	3	2	4	7	19	49	95
CM	200	76	35	18	7	5	2	4	2	6	35

Table 3 Accuracy and computational time of the three algorithms

Matching	Accuracy (%)	Time (s)
GHM	96.5	59.05
SFM	99.5	1,230.2
CM	99.5	101.19

the same identification accuracy as CM, it spends over ten times computational time than CM. GHM is most efficient and can finish identification in 59.05 s. However, it shows worst identification accuracy. Thus, we argue that CM is the best matching method for 2D/3D format identification of videos.

4 Conclusions

A widely accepted 3D video standard is not available at present. 3D formats are so confused that 3D format detection is necessary. We analyzed many kinds of 3D formats and proposed a method of 3D format detection. The designed CM 3D format identification algorithm archives good comprehensive performance on identification accuracy and computational efficiency. We further analyzed the cases of false identification. Some experiences are obtained. It includes the follows. (1) GHM cannot cope with the frame image with flat color and different illumination. (2) SFM cannot work well for the frame image with insufficient texture. (3) SFM is prone to fail for the identification of the frame image with too much repetitive texture.

References

1. Lowe DG (2004) Distinctive image features from scale-invariant keypoints. Int J Comput Vis 60(2):91–110
2. Yanjun, Wang Hongmei Zhang Ke Li (2004) Research progress on image matching. Comput Eng Appl 19:012
3. Zhang T, Wang Z, Zhai J et al (2011) Automatic 3D video format detection. In: IS&T/SPIE electronic imaging. International Society for Optics and Photonics, pp 78631H–78631H
4. Zheng G, Jiang X (2012) Introduction of delivery system for frame compatible stereoscopic 3DTV. Video Eng 36(18):36–40
5. Zitova B, Flusser J (2003) Image registration methods: a survey. Image Vis Comput 21 (11):977–1000

Research on HD Video Wireless Transmission System Based on Mesh Network

Ruian Liu, Daxi Liu, Junsheng Zhang, and Lei Wang

Abstract The technology of high-definition(HD) video wireless transmission enables users to get rid of the shackles of cable, displaying real-time video information through PC and other intelligent terminal. In this paper, it is focused on analyzing the characteristics and key technology on mesh network as well as the methods of guaranteeing the quality of HD video. Using TMS320DM368 processors as a core processing chip, and video acceleration coprocessors to complete H.264 video coding. Real Time Streaming Protocol packages the compressed video stream, EMAC module composes mesh network with multiple Wi-Fi AP, which achieve the work of wireless transmission for 720P HD video.

Keywords HD video • Wireless transmission • Mesh network

1 Introduction

Currently, many video transmission systems rely on 3G to spread. In the area covered by 3G signal, transmission distance is not limited, but the high cost and serious delay, besides, the theoretical maximum uplink rate of video upload are 5.4 Mbps in 3G modules, the usual approach is to improve the 3G communication modules with a plurality of parallel transmission link to increase the bandwidth, which can also augment the cost of systems and consumption of power. The common standard of Wi-Fi is IEEE802.11n, including the 2.4 and 5.8 GHz frequency bands, which maintains 802.11b/g/a backward compatibility, the transmission rate is 320–600 Mbps through the technology of MIMO (Multiple Input Multiple Output) and OFDM (Orthogonal Frequency Division Multiplexing) currently [1]. In transmission system of point to point, it will lead to paralysis of the

R. Liu (✉) • D. Liu • J. Zhang • L. Wang
College of Electronic and Communication Engineering, Tianjin Normal University, Tianjin, China
e-mail: ruianliu@sina.com

B. Zhang et al. (eds.), *The Proceedings of the Second International Conference on Communications, Signal Processing, and Systems*, Lecture Notes in Electrical Engineering 246, DOI 10.1007/978-3-319-00536-2_27,

entire transmission system if a node cannot work. Wireless Mesh Network (also known as “multi-hop” network), is a new structure of wireless network, integrate WLAN (Wireless Local Area Network) and mobile Ad-hoc network, and has the advantages of a high-capacity and high-rate, which is the wireless version of the Internet.

2 The Characteristics of Wireless Mesh Network

WMN (Wireless Mesh Network) has the following advantages: WMN adopts a multi-hop access methods, expands network coverage by increasing the number of user node, increases reliability of data transmission. The anti-jamming capability is enhanced as the design simplification of wireless link. This short-range radio link allows data transmission success rate and costs are reduced, the interference has been raised between nodes, which is a more secure and reliable network. Flexible network structure, easy maintenance. As WMN has self forming, self-healing and self-organizing ability, necessary wireless devices are used where needed. WMN Routing with selection characteristics can process locally and maintain without affecting the operation of the entire network, when an interrupt occurs and other links fail, network flexibility and feasibility have been greatly improved. Network has good compatibility. WMN is a new network technology based on traditional technology, the compatibility and interoperability are better than traditional wireless networks. Meanwhile, WMN avoids the issues of traffic aggregation, central network congestion and single point of failure, enhances network reliability largely. WMN has advantages in scalability, automatic configuration and wide range of applications. The architecture of WMN will gradually be applied between the base station and the base station, with the communication systems developing.

Since the data stream needs multi-hop in the WMN, it will induce a series of issues, such as bandwidth reduction, radio interference and network delay.

Bandwidth reduction: The multi-hop causes serious problem of bandwidth reduction [2, 3] when backhaul is shared in the single-frequency and dual-frequency solutions. It is illustrated in Fig. 1 that throughput lowered about 802.11a/g and 802.11b solutions with single frequency in the best case. It is obviously spotted from the Fig. 1 that the loss of bandwidth is unacceptable if used in medium and large-scale multi-hop transmission, even in the best case.

Radio interference: radio interference is a very important issue that it will affect the performance of wireless network. In today’s wireless network, Most wireless mesh deployment uses 802.11b as a wireless backhaul infrastructure, the backhaul bandwidth is disturbed from the neighboring devices in the same frequency bands of radio.

Network delay: The data is multi-hop via intermediate nodes in the WMN, each hop leads to the decline of transmission rate, and causes the delay, with the expansion of WMN, the more hop the more total accumulated delay [4]. However

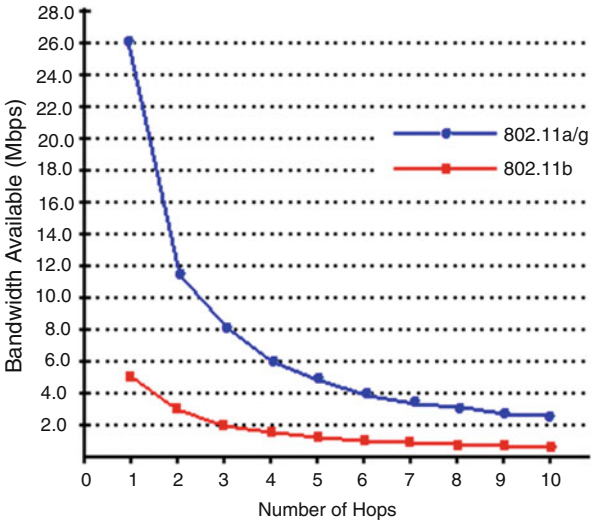

Fig. 1 Single radio throughput degradation (in best case)

it requires the network to be just a small delay and jitter in the high-definition video transmission.

3 The Key Technologies of WMN

For WMN, its reliability involves many aspects, including the reliability of network's own software and hardware design reliability, network architecture design, and the protocol layers, as well as the need to meet the operating system and other auxiliary means reliability. In addition, business with the WMN has asynchronous, distributed and random characteristics, the network operating environment and failure process is dynamic.

WMN adjacent nodes need the duplex mode to support two-way information transfer, There is a significant influence to the radio resource allocation due to selecting FDD (Frequency Division Duplex) or TDD (Time Division Duplex). FDD is appropriate for the bidirectional symmetric information case on the link, while in WMN, more information transmission is asymmetric from the gateway node to the user node. TDD system is selected because it adapts to asymmetric information transmission.

QDMA (Orthogonal Division Multiple Access) technology is designed for wide area network communications and WMN. QDMA technology provides a high-performance RF front-end, which includes the fairness algorithm to overcome the rapidly changing RF environment. QDMA provides a stronger capability of error correction in a wide range of mobile communications, as well as enhances the ability of interference and sensitivity of signal.

The technologies of self-discovery, self-organizing, self-healing: WMN AP can eliminate impact on the bugs of single points on the business and provide redundant paths as its auto discovery and dynamic routing connectivity. The AP can automatically access the wired network through other AP if a link is broken for wired access root AP. Once the wired link breaks down, it automatically turns off its radio link, to make other connections to the root AP nodes automatically select other wired access points, which ensure the normal operation of the network.

Routing Optimization: WMN Routing protocol is the most important technology. The support for network fault tolerance and robustness is provided by the WMN routing protocol, which can quickly select an alternate link to avoid the interruption of service provision while a wireless link fails, the routing protocol be able to take advantage of traffic engineering technology, balancing load for multiple paths, to maximize the use of system resources.

QoS (Quality of Service) assurance mechanism: With all the different types of business applications in the mesh network, especially in the Mesh hops case, which needs to guarantee the demands of access, delay and fairness for various services, also needs to coordinate the access QoS policy of mesh network [5] and the QoS policy of wired network interconnection consistency, so as to provide end to end business Qos guarantee.

Mesh Security: The security risks are further amplified in a multi-hop Mesh network than traditional network. Currently, there are two kinds of security solutions in Mesh Networks, is a multi-layered security architecture, which provides WEP and WPA protection to the client, and encrypts the data of AP by 64/128 bit WEP or 128 bit AES; while using a VPN to enhance overall security at the network layer. Other solution is establishing encrypted IPSec tunnels between the AP, to securely transmit data service, internal signaling processing and management information for all users. In a word all data transmitted between the AP are in protection of IPSec.

4 The Assurance Method of HD Video Quality Based On Terminal System

Compared with the traditional approach based on the transmission network, the QoS policy based on end-system is a viable approach. In order to provide end to end QoS in wireless environment, the video application layer should be able to perceive and adapt the change of network conditions [6], which includes network adaptation and media adaptation. Network adaptation refers to how many network resources (such as bandwidth) can be used, and designs an adaptive transport protocol for video transmission. Media adaptation can control bit rate of the video stream based on predicted bandwidth, adjust errors and energy control according to changing radio conditions. The framework of QoS guarantee is shown in Fig. 2.

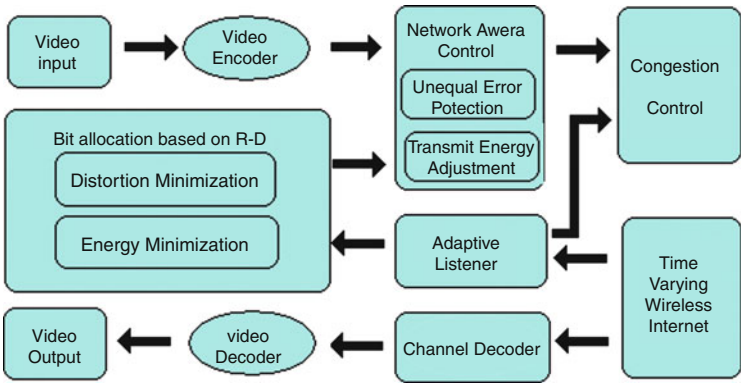

Fig. 2 The framework of QoS guarantee based on terminal system

End to end video transmission protocol to complete dynamic detection and estimation of network environment by congestion control and adaptive network monitor. The congestion control module adjusts the transmission rate according to the feedback condition, and solves the network adaptability. Considering the characteristics of high-definition video streaming, unequal error protection measures are adopted, the bit allocation module based on rate-distortion completes the adaptive control of the media. Taking the ways of Rate Control, Rate-adaptive Video Encoding and Rate Shaping to reduce packet loss and delay when congestion is detected.

Error Control, The lost of packet is intolerable for text type of data, but accept the existence of certain delay is accepted, channel coding to correct or retransmission restore is adopted when a packet is lost. In real-time video services, new error control mechanism is introduced against the characteristics high requirements for the delay, such as FEC (Forward Error Correction), the retransmission and Error Resilience at the sending end and receiving end, Adopted the way of Error Concealment at the receiving end, which can guarantee the quality of HD video.

5 Construction of HD Video Wireless Transmission System

An excellent video transmission system has high performance requirements for wireless data transmission link: high transmission speed, high real-time, the smaller jitter of the screen and high reliability. In coverage of directional Wi-Fi signal, for wireless video transmission systems, the farther between server and receiving end of the transmission distance, the more limited of network bandwidth for video transmission, the lower of its transfer video resolution. However the RTSP can take advantage little bandwidth to transmit streaming media, and adapt to various of

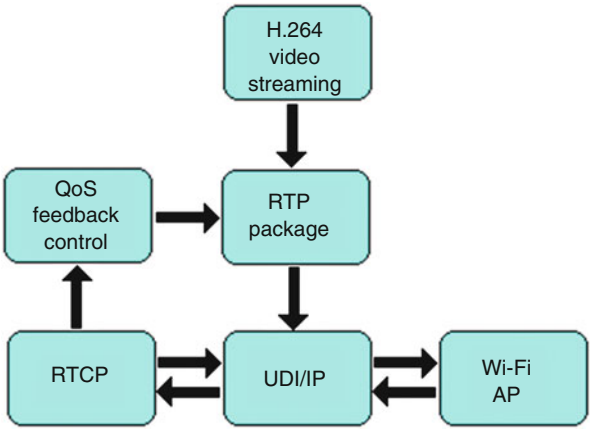

Fig. 3 Based on RTP/UDP H.264 video transmission function block diagram

complex network transmission environment, the video transmission system can achieve longer transmission distance in the limited network bandwidth. Therefore, the design introduces RTSP based on the low-power directional Wi-Fi antenna technology, by constructing an H.264 video server, and the PC client with Wi-Fi AP to access the server to achieve the wireless transmission of video data via RTSP.

In the procedure of H.264 video transmission using RTSP: The compressed H.264 video streams are packed by RTP encapsulation module. QoS feedback control module adjusts dynamically sending rate of RTCP packets according to the received feedback information packets RR. Transmit buffer module sends RTP and RTCP packets, UDP communicates directly with the Ethernet physical layer for transmission of the video RTP packet. Its function is as shown in Fig. 3.

The RTP packet of the video data is transmitted to the wireless channel in the 5.8 GHz band in the system with Wi-Fi AP, AP broadcasts SSID packets once per 0.1 s via beacons, beacons packet transmission rate is 1 Mbps, and the packet length is shorter, the operation of entire broadcast has less impact on network performance, which ensures that the client PC's Wi-Fi network card can receive the SSID broadcast packets. When connection is established, it constitutes a temporary formation of non-central distributed control network between server and PC client in wireless video transmission system, a video packet is transmitted according to PC instruction.

When the video server is out of communication range with client PC, the multi-hop communication is completed using the other AP transfer the video stream as a relay point [7], owing to mesh network is constructed. During the data transmission, when a Wi-Fi AP node fails, the system can select a nearby node for communication. As the presence of Wi-Fi AP, it plays the role of the relay amplification for the wireless signal, and exerts the virtue of mesh network.

In conventional wireless video transmission, in order to reduce costs, the WMN system arrays multiple AP single-frequency in linear, and sets up the structure of single-frequency mesh [8] the most efficient communication flows as shown in

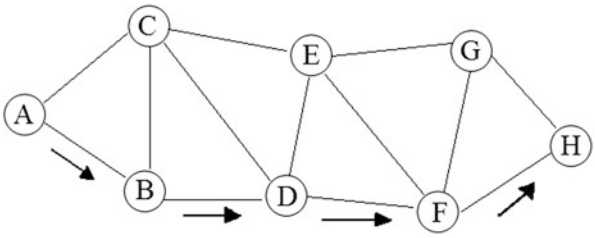

Fig. 4 Single-frequency wireless mesh structure

Fig. 4, where A is the Wi-Fi AP node of the video server, H is the Wi-Fi AP node of video browsing software end.

The applications of mesh network can further expand the transmission distance of wireless video transmission system, when the Wi-Fi antenna is directional well and channel is stable, the resolution of transmission video is improved.

WMN is very sensitive for phenomenon of radio interference and network delay, bandwidth reduction is particularly affected owing to large-scale multi-hop. For example, directly jumping from point B to point D, the video transmission rate is almost cut in half. For calculation of transmission rate in the multi-hop, the final velocity of transmission is reduced to 1/n of the transmitter (where n is the number of hops) in the best case and $1/2^{n} - 1$ in the worst case, the maximum number of nodes $n_{\max}$ is calculated as shown in formula (1).

$$n_{\max} = \sqrt{\frac{V_{\max}}{V_{\text{avg}}}} + 1 \tag{1}$$

In the case of external and open environment, for routine application of Wi-Fi AP, the single-hop transmission rate $V_{\max}$ is 54 Mbps in the 5.8 GHz ISM band, the H.264 video streams of 720P is above 2 Mbps generally, so the maximum number of multi-hop $n_{\max}$ is 5, in the worst case.

Learned from the previous experimental tests, in the case, system transmitter chooses directional antenna and increases the transmit power, the effective transmission distance is 5 km for Single-hop, so the maximum effective transmission distance is 25 km for the system. But it is not limited to these, we can improve the initial transmission rate and increase the distance of the video by upgrading Wi-Fi AP equipment of system video server.

6 Conclusion

This paper analyzes the characteristics and key technology on mesh network as well as the methods of guaranteeing the quality of HD video, with DM368 as the core chip, RTSP and WMN to achieve the design of a stable HD video wireless

transmission system. It is proved that the feasibility of HD video wireless transmission based on mesh network. The delay is 330 ms between display screen and collection in the test of system. For the delay phenomenon of video screen, the subsequent research will focus on the optimization design of algorithm and system.

Acknowledgments This research was supported by the Tianjin natural science fund (13JCYBJC15800).

References

1. Foschini GJ, Gans MJ (1998) On limits of wireless communications in a fading environment when using multiple antennas. Wireless Pers Comm 6(3):311–335
2. Hung Quoc Vo, Choong Seon Hong (2008) Hop-count based congestion-aware multi-path routing in wireless mesh network. Inform Network 1–5. doi: 10.1109/ICOIN.2008.4472752
3. Lee Jangh-Wan, Yoon Hyun-Soo, Yeom Ik-Jun (2010) Distributed fairs scheduling for wireless mesh networks using IEEE 802.11. IEEE Trans Veh Tech 59(9):4467–4475
4. Pérez-Bellido AM, Salcedo-Sanz S, Ortiz-Garcl'a EG et al (2009) A dandelion-encoded evolutionary algorithm for the delay-constrained capacitated minimum spanning tree problem. Comput Comm 32(1):154–158
5. Tehuang Liu, Wanjiun Liao (2009) Interference-aware QoS routing for multi-rate multi-radio multi-channel IEEE 802.11 wireless mesh networks. IEEE Trans Wireless Comm 8, iio. K:166–175
6. Lamia Romdhani, Christian Bonnet (2008) Cross-layer QoS routing framework for wireless mesh networks. Wireless Mobile Comm 382–388. doi: 10.1109/ICWMC.2008.70
7. Xua S, Saadawi T (2002) Revealing the problems with 802.11 medium access control protocol in multi-hop wireless ad hoc networks. Comput Networks 38(4):531–538
8. Ochiai H, Nakayama M, Esaki H (2011) Hop-by-hop reliable, parallel message propagation for intermittently-connected mesh networks. IEEE International Symposium on WoW-MoM. Lucca, Italy

FPGA-Based Single-Phase Photovoltaic Inverter Design

Bin Liang, Jun Shi, and Mingcheng Liu

Abstract Based XC3S500E FPGA chip as its control core, structuring SOPC system through embedding 32-bit MicroBlaze soft core processor, so that 1KW image acquisition system is implemented. Its main circuit topology consists of DC/DC push–pull converters, DC/AC full-bridge inverters and LC filters. Its sampling circuit consists of ADS1115 A/D converters and associated sensors, realizing the sampling of the PV arrays, DC/DC booster circuits, the voltage and current of inverter circuits. It completes the controller loop design, realizing the I^2C interfaces of A/D converters, the PWM generator controlled by MPPT, the SPWM generator controlled by PID and the interactive user interface. The results of the test show that the design of the inverter is reasonable and reliable, and meets the requirements of the power output. Not only its inversion efficiency can be up to 92 %, but also its power factor can be close to 1.

Keywords FPGA • SOPC • PV • Inverter

1 Introduction

In the global background, the environmental pollution is growing more seriously and the energy consumption is becoming more scarcely. The solar, a kind of large-scale developed and available clean energy, has been used widely in the form of photovoltaic power. The PV inverter is the core equipment of photovoltaic power, its performance directly determines the energy efficiency. This article puts forward the design of miniaturization PV inverter which is based on the SOPC system of FPGA chip.

B. Liang (✉) • J. Shi • M. Liu
College of Electronic and Communication Engineering, Tianjin Normal University, Tianjin, China
e-mail: wdxylb@mail.tjnu.edu.cn

B. Zhang et al. (eds.), *The Proceedings of the Second International Conference on Communications, Signal Processing, and Systems*, Lecture Notes in Electrical Engineering 246, DOI 10.1007/978-3-319-00536-2_28,

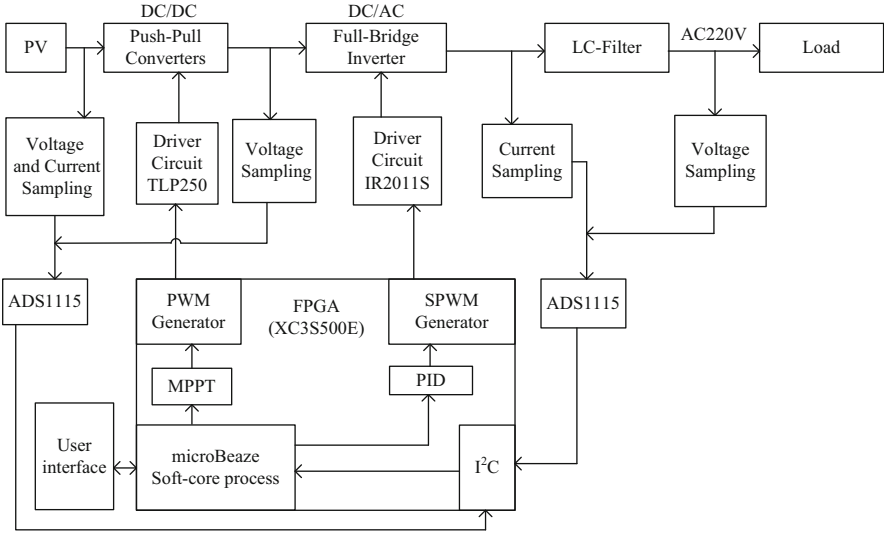

Fig. 1 System architecture diagram

2 Design of System

As Fig. 1 shown, it is the overall framework of the system. The main circuit of this design consists of DC/DC push–pull converter circuit, DC/AC full-bridge inverter circuit and LC filter circuit [1]. Its sampling circuit consists of ADS1115 A/D converters and associated sensors, realizing the sample of the PV arrays, DC/DC booster circuits, the voltage and current of inverter circuits. It completes the controller loop design, realizing the I2C interfaces of A/D converters, the PWM generator controlled by MPPT, the SPWM generator controlled by PID and the interactive user interface.

It's DC/DC push–pull converter circuit can raise the output voltage of the PV arrays to 400 V or so. FPGA takes sample of the voltage-current characteristics of PV and the voltage after rising separately by A/D converters. Also it uses MPPT algorithms to control the duty cycle of the push–pull converter circuit [2], so that it can regulate the maximum power output of the voltage finally. On the other hand, FPGA take sample of the output current of the full-bridge inverter circuit and the output voltage of LC filters by another ADS1115 chip, it uses PID algorithms to control the SPWM generator [3, 4, 5], so that it can realize the closed-loop control of full-bridge inverter circuit.

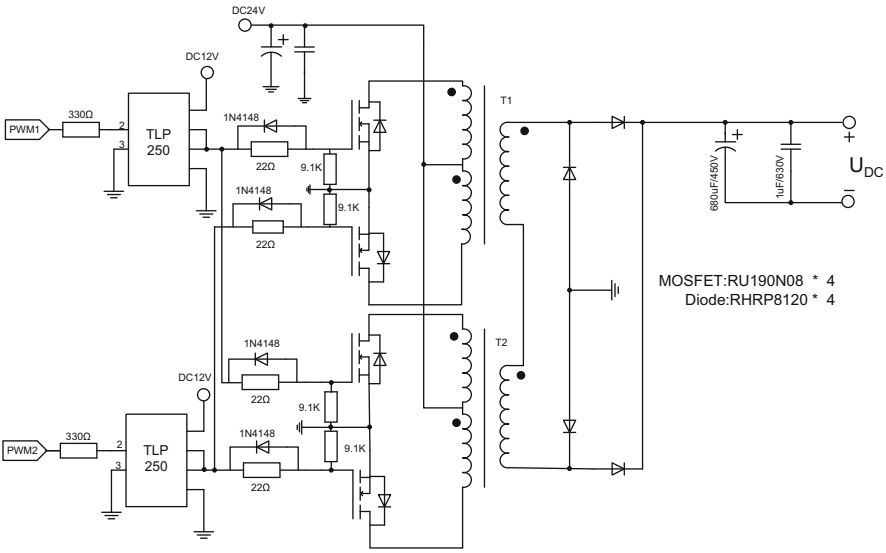

Fig. 2 Push–pull converter circuit schematics

3 The Design of Functional Circuit

3.1 Push–Pull Converter Circuit

Push–pull converter circuit is equivalent to a combination of two forward converter. Complementary work by turns, and two windings with a center tap at one side of the transformer work with each connection of the switch tube conduction by turns. It is particularly suitable for low input voltage DC / DC converter and can power up to 1KW or more.

In actual design, the circuit structure as shown in Fig. 2 is a combination of two sets of push–pull transform circuit. So that each transducer only need for the power of 500 W, which lower the index of volume of a transformer and requirements of the switch tube standards effectively. The transformer choose two EC49 core winding, which are primary parallel and secondary series, and their power is 500 W. The switch tube choose MOSFET and models for RU190N08 with the characteristics of withstand voltage 80 V and maximum current 190A. The switching diode choose RHRP8120 whose reverse voltage is 1,200 V and working current is 8A.

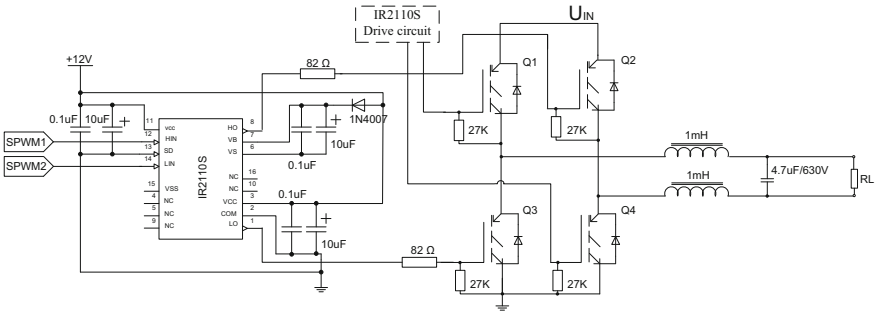

Fig. 3 Full-bridge inverter circuit schematics

3.2 *Full Bridge Inverter Circuit*

Full bridge inverter circuit is shown in Fig. 3,the SPWM1 and SPWM2 driving signal control the power switch Q4, Q1 and the open and shut off of the Q2, Q3 respectively. When the Q4 and Q1 is on and the Q2 and Q3 is off, the voltage of the load on both ends is +UIN. When the Q2 and Q3 is on and the Q4 and Q1 is off, the voltage of the load on both ends is -UIN. The Q1–Q4 as the power switch tube of IGBT, choose GW39NC60VD model. Its withstand voltage is 600 V, maximum current is 40A and the collector to emitter saturation voltage is 1.8 V. Driving circuit with the bootstrap floating power supply selects two IR2110S half bridge driver chips, in which the driving current is 2A.

3.3 *Sampling Circuit*

As is shown in the Fig. 4, the core of sampling circuit adopts two slices of interconnected Analog-digital Converter called ADS1115 based on I^2C-bus. It's a high-speed 16-bit converter, integrated an internal reference voltage source, and can achieve single-ended and difference sampling. It disposes the Voltage and Current Signal converted in the sampling and quantitative main circuit.

The voltage and current signal outputed from PV Cell Array is cut down by Resistance Voltage-division network, and gets converted when flowing through Hall Current Sensor SW4T50C50V6. Just as the output of PV Cell Array, the output voltage of Push–Pull Converter is reduced by Resistance Voltage-division network, and then, enters ADC. The output current of Inverter gets converted through Hall Current Sensor ACS712-30A. Voltage Mutual Inductor takes sample of the output AV filtered via LC Filter, and after this, the signal will flow into ADC.

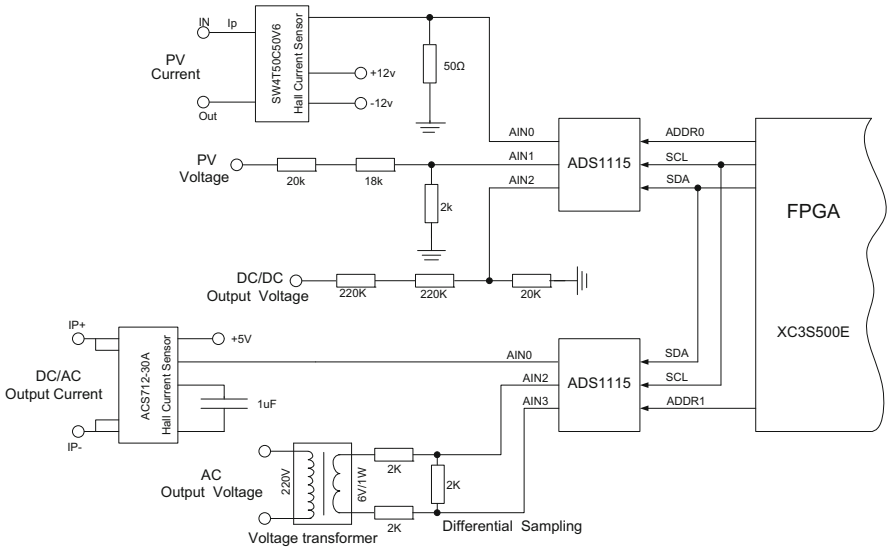

Fig. 4 Sampling circuit schematics

Table 1 With load power test data

Number	Load	Input vottage (v)	Input current (A)	Power input (W)	Bus vottage (V)	Bus current (A)	Power output (W)	Efficiency %
1	100 Ω	24.5	13.4	330.7	369	0.86	318.3	96.3
2	200 Ω	24.4	27.1	660.8	362	1.74	629.4	96.2
3	300 Ω	24.3	40.7	988.2	350	2.63	918.8	93
4	400 Ω	24.3	52.4	1,272.4	339	3.44	1,165.2	91.6

4 Testing Data

In the testing process, it takes use of resistive load to complete the test of power ranged from 300 W to 1KW, and the testing data is depicted in the Table 1. It shows that Inverter works steadily, and that its efficiency is expected to 96 % under the circumstances of low load, to 91 % in a full load condition, which matches the design's requirements.

5 Conclusion

This article takes XC3S500E FPGA chips as the core, embeds 32-bit MicroBlaze soft core processor in it, structures SOPC system, and implements 1KW image acquisition system. It introduces hardware circuit architecture, the working

principles and parts selection of the inverter system. It shows the associated experiments results and data through the practical operation and test. The inverters' efficiency can be up to 92 %, and the power factor can be close to 1. Not only its harmonic content of the inverters is low, but also it has the function of over-current and under-voltage protection.

Acknowledgment This research was supported by the Tianjin natural science fund (13JCYBJC15800).

References

1. Zhou L, Zhang L et al (2012) Single-phase photovoltaic inverter control technology. Power System Technol 9:25–29
2. Junjuan Wu, Yida Jiang et al (2012) An improved control algorithm MPPT PV systems. Acta Energiae Solaris Sinica (3):478–483
3. Jingwei Yang, Gang Luet al.(2012) Based on SPWM inverter control design and simulation. Drive and Control (9):63–65
4. Shunfeng Han, Min Du et al. (2013) A new digital SPWM signal design and implementation. Modern Electron Tech(3):133–138
5. Leilei Lu, Yaohua Luo (2012) Single-phase photovoltaic grid-connected inverter control strategy and design.Telecom Power Technol(1):14–16

The Design and Implementation of Linear Array Image Acquisition System

Baoju Zhang, Xiang Tong, Wei Wang, and Jiazu Xie

Abstract The theory of Compressive Sensing is briefly introduced and the design of the linear array image acquisition system which is based on the Compressive Sensing is deduced. The system design includes two aspects: the hardware design and the software design. The core components of the system and the structure of the circuit are introduced. The image acquisition program which can construct the measurement matrix of Compressive Sensing and process the image signal is devised. Numerical simulations have verified that the linear array image acquisition system has good performance in linear array image acquisition and reconstruction.

Keywords Compressive sensing • Linear array image acquisition system • Core components • Measurement matrix

1 Introduction

The compressive sensing theory in signal processing provides a new approach to data acquisition which overwhelms the common Nyquist sampling theory [1]. Consider a signal that is sparse in some basis (often using a wavelet-based transform coding scheme), the basic idea of compressive sensing is projecting the high dimensional signal onto a measurement matrix, which is incoherent with the sparsifying basis, resulting to a low dimensional sensed sequence. Then with a relatively small number of appropriately designed projection measurements, the underlying signal may be recovered exactly. In contrast to the common framework of collecting as much data as possible at first and then discarding the redundant data by digital compression techniques, CS seeks to minimize the collection of redundant data in the acquisition step. Because of the special advantage of compressive

B. Zhang (✉) • X. Tong • W. Wang • J. Xie
College of Electronic and Communication, Tianjin Normal University, Tianjin, China
e-mail: wdxyzbj@163.com; xt2858@163.com; wangweivip@tju.edu.cn; veryaz@foxmail.com

B. Zhang et al. (eds.), *The Proceedings of the Second International Conference on Communications, Signal Processing, and Systems*, Lecture Notes in Electrical Engineering 246, DOI 10.1007/978-3-319-00536-2_29,

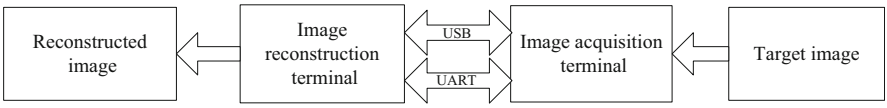

Fig. 1 Linear array image acquisition system diagram

sensing, many data compressing and reconstruction methods based on CS have been researched [2].

Linear array image acquisition system based on compressive sensing theory has two parts:image acquisition terminal and image reconstruction terminal. Due to the large amount of calculation of image reconstruction and the need for PC operating system function library, the part of the image reconstruction will be completed by PC. In this research, we only introduce the design of image acquisition hardware circuit and the related function program [3].

The image acquisition terminal samples the linear array image signal according to the measurement matrix, and then sends the sampling signal and the related parameters to the image reconstruction terminal through the RS232/USB [4]. The Image reconstruction terminal reconstructs the image according to the sampling measurements and the parameters. The process is shown in Fig. 1.

2 Image Acquisition Terminal Hardware Circuit Design

We select the XC3S400 of Xilinx company as the logic control device in image acquisition terminal, which mainly completes the construction of the measurement matrix, linear array image sensor reading, and communications with the image reconstruction terminal. In this system, the linear array image sensor is DLIS-2K of Panavision company. Because the XC3S400 needs to create a large array when constructing the measurement matrix, so we extended the RAM. Considering that the current mainstream computer has no RS232 interface, so USB interface is used in this system to enhance generality. Because XC3S400 logic controller does not have the USB interface, so we need to choose a USB interface transition chip. In this system, we choose the FT245BM which is the parallel interface to USB interface conversion chip. Because asynchronous serial interfaces of PC is usually RS232 level, the system also needs to convert the TTL level to RS232 interface level to communicate between the asynchronous serial interface and the upper machine [5]. Due to the core voltage of logical processor XC3S400 is different with the external I/O voltage requirement, so the system needs to provide different voltages to ensure that the system is stable. The structure of image acquisition terminal is shown in Fig. 2.

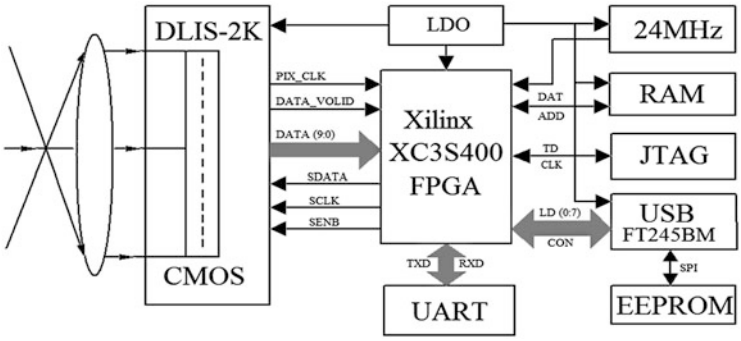

Fig. 2 The diagram of the image acquisition terminal

2.1 Linear Array Image Sensor Hardware Circuit Design

This system adopts the CMOS sensor DLIS-2K of Panavision company, which is a widely used chip in linear array image acquisition. DLIS-2K linear image sensor consists of four lines of pixels, each pixel contains 2,065 optical pixels and 16 dark pixels. The first line consists of rectangle pixels of 4 μm × 32 μm size, the last three lines consists of square pixels of 4 μm × 32 μm size. Each line of pixels can be arbitrarily chosen to read, control and reset separately.

2.2 XC3S400 Logic Controller and Peripheral Circuit Design

System image acquisition terminal selects the XC3S400 chip of XILINX company as the logic processor. The chip is XILINX SPARTAN3 series 400,000 level FPGA, 8,064 logical blocks internal integrated, with7 k bytes of RAM. In this circuit, XC3S400 mainly completes the measurement matrix construction, control and read of the image sensor and the communication of the upper machine.

This circuit chooses IS42S16400N chip as the extended RAM. The RAM size is 64 MBIT with DC3.3V power supplied. The highest clock frequency is 166 MHz so it meets the operation need of XC3S400.

Voltage regulator chip MIC29372A can output the minimum voltage DC1.24V as the XC3S400 processor core voltage.

Image acquisition terminal communicates with the computer in the two ways, namely the asynchronous serial interface and USB. Due to the asynchronous serial port of the computer is RS232 level, so we need the MAX3221 chip to convert the TTL level to RS232 level in image acquisition terminal.

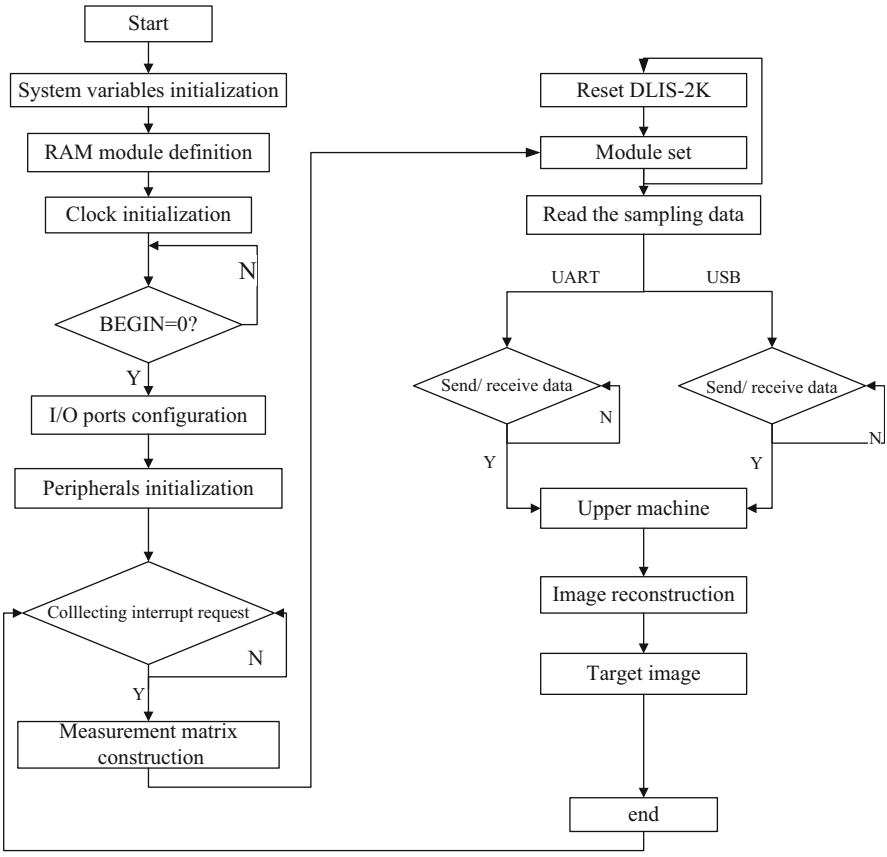

Fig. 3 The diagram of linear array image acquisition system program design

3 Image Acquisition Program Design

The program of image acquisition mainly completes the following functions: compressive sensing measurement matrix construction, DLIS-2K linear array image sensor control, serial data communication, etc. [6]. The diagram of linear array image acquisition system program design is shown in Fig. 3.

3.1 The Design of CS Measurement Matrix Construction Program

The construction program design is based on Kronecker product measurement matrix, which has better performance in storage space, construction time, and

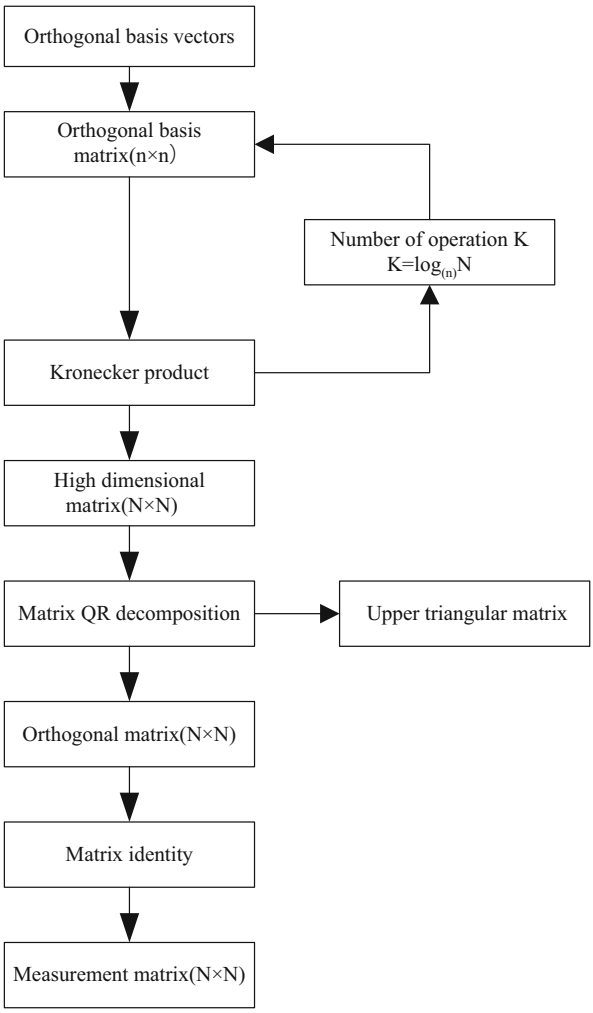

Fig. 4 The construction process of Kronecker product measurement matrix

image reconstruction effect when compared with commonly used matrices in compressive sensing. What's more, the Kronecker product measurement matrix offers great potential for hardware implementation of compressive sensing [7]. The construction process is as shown in Fig. 4.

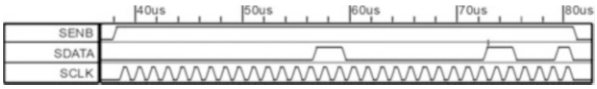

Fig. 5 The write operation sequence of DLIS-2K

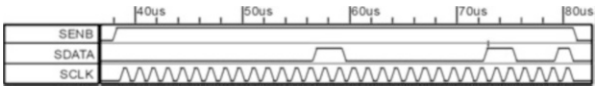

Fig. 6 The read operation sequence of DLIS-2K

3.2 The Design of CS DLIS-2K Line Array Sensor Control Reading Program

XC3S400 processor controls the DLIS-2K linear array image sensor by the line buses. Before the control operation of the DLIS-2K, the electricity initialization is needed. XC3S400 offers stable clock frequency square wave for DLIS-2K [8].

The write operation sequence of DLIS-2K is shown in Fig. 5.

The read operation sequence of DLIS-2K is shown in Fig. 6.

The read operation is initiated by the bus line SENB. Firstly, sending 15 the addresses, and then data line sets 1which means the read operation [9]. The data is read in on the falling edge of the SCLK clock line. Every time a 16-bit data is read in, the enabling line turns into low-level which means a read operation is completed [10].

4 Debugging and Results

The linear array image acquisition circuit board is shown in Fig. 7. The linear array CMOS image sensor is equipped with a lens which is used for adjusting the focus and broaden the horizons [11].

In the test experiment, we choose ordinary bar code as the test image. Under the premise of enough light, we fix the distance between the bar and linear array image sensor in 20–25 cm, and ensure that the bar code line are vertical with the sensor array.

The Fig. 8 shows the different reconstruction effect of different compression ratio, the compression ratio [12]. We can see that the reconstruction image quality drops obviously when the compression ratio below 0.4.

5 Conclusion

In this research, firstly we introduce linear array image acquisition terminal based on compression sensing which realizes the compression and acquisition of linear array image. Secondly the devices and chips which are used in this research and the

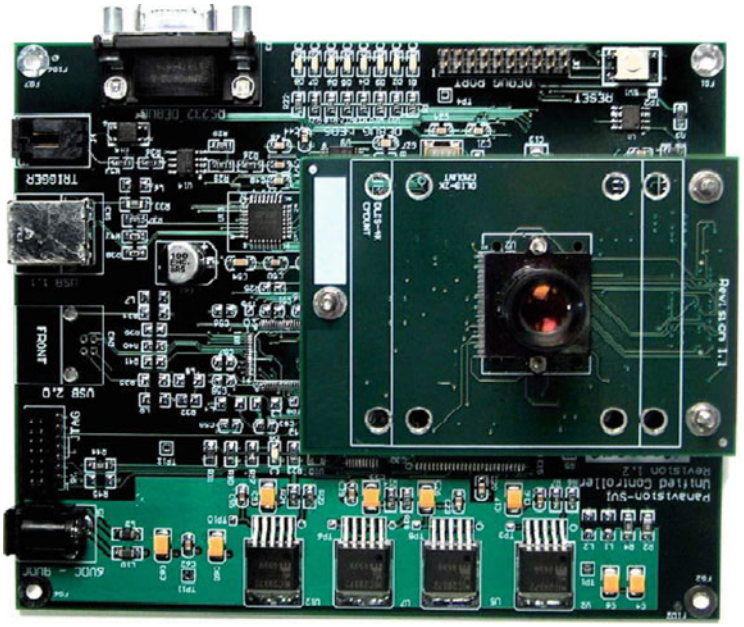

Fig. 7 The linear array image acquisition circuit board

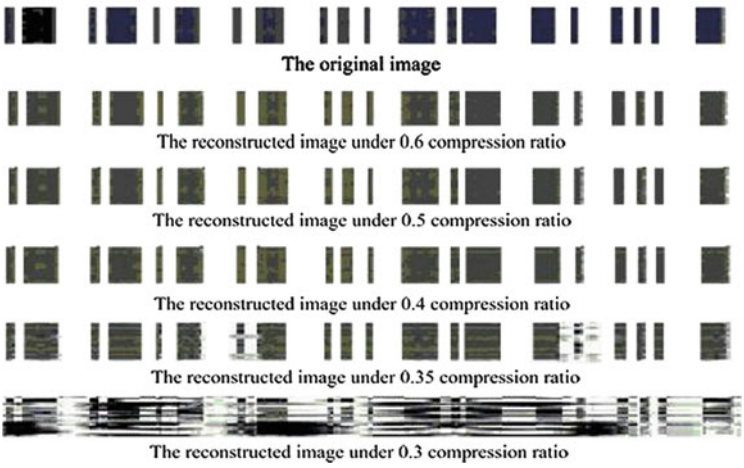

Fig. 8 The contrast of reconstructed image under different sampling compression ratio

structure of linear array image acquisition terminal have been introduced and described. Thirdly, we have shown the program design of each part of our system, and analyzed the implement process. At last, the linear array image acquisition terminal circuit board is shown.

Through the experiment of image acquisition and reconstruction, we have deduced that when the compression ratio is above 0.4, the system performs well in the quality of the reconstructed image.

Acknowledgment This research was supported by the Tianjin Younger Natural Science Foundation(12JCQNJC00400). National Science Foundation of China: 61271411.

References

1. Rivenson Y, Stern A (2009) Compressed imaging with a separable sensing operator. IEEE Signal Process Lett 16(6):449–452
2. He L, Carin L (2009) Exploiting structure in wavelet-based Bayesian compressive sensing. IEEE Trans Signal Process 57(9):3488–3497
3. Lustig M, Donoho DL, Pauly JM (2007) Sparse MRI: the application of compressed sensing for rapid MR imaging. Magn Reson Med 58(6):1182–1195
4. Yoon-Chul Kim, Narayanan SS et al (2009) Accelerated three-dimensional upper airway. MRI using compressed sensing. Magn Reson Med 61:1434–1440
5. Xie Xiao-Chun, Zhang Yun-Hua (2010) High-resolution imaging of moving train by ground-based radar with compressive sensing. Electron Lett 46(7):529–531
6. Budillon A, Evangelista A, Schirinzi G (2011) Three-dimensional SAR focusing from multipass signals using compressive sampling. IEEE Trans Geosci Rem Sens 49:488–499
7. Wai Lam Chan, Kriti Charan, Dharmpal Takhar et al (2008) A single-pixel terahertz imaging system based on compressed sensing. Appl Phys Lett 93, 121105:1–3
8. Amir Averbuch, Shai Dekel, Shay Deutsch (2012) Adaptive compressed image sensing using dictionaries. SIAM J Imag Sci 5:57–89
9. Marcia RF, Willett RM (2008) Compressive coded aperture video reconstruction. Proceedings of 16th European signal processing conference, Lausanne, Switzerland, pp 918–923
10. Stern A, Yair Rivenson, Bahram Javidi (2008) Single exposure optically compressed imaging and visualization using random aperture coding. J Phys Conf Ser 139:1–10
11. Fergus R, Torralba A, Freeman WT (2006) Random lens imaging. MIT Comput Sci Artif Intell Lab Rep 9:111–118
12. Ji Wu, Wei Wang, Qilian Liang, Xiaorong Wu, Baoju Zhang (2012) Compressive sensing-based signal compression and recovery in UWB wireless communication system, Wiley wireless communications and mobile computing, DOI: 10.1002/wcm.2228

Experimental Study of Torque Measurement Based On FBG

Shengnan Fu, Yinguo Huang, and Xinghua Li

Abstract This paper discusses a method of torque measurement based on the fiber Bragg grating (FBG) sensor, and introduces the FBG's application for torque measurement in a rotating shaft with four same planes. With external torsion applied to the shaft, the data obtained by finite element analysis verified the rationality, reliability and strain sensitivity of this design. One end of the shaft is fixed, while the other is connected to a device providing a particular value of torsion with a full scale of 100 Nm. Two parallel gratings FBG1 and FBG2 are bonded on the purposefully machined planes on the shaft symmetrically. Considering the differential-mode wavelength of the dual-grating torsion sensor, the result shows a low temperature sensitivity and a high torsion sensitivity. The sensitivity of the torque measurement system is 14.5 pm/Nm, and has a high linearity and linear correlation.

Keywords Torque measurement • Fiber Bragg grating • Finite element analysis • Optical fiber sensors

1 Introduction

Torque sensing is very important in industrial production and is widely needed in the field of ship and aviation, aerospace especially in special applications in harsh environments where torque measurement is often presented as technical bottlenecks. Optical fiber sensors are paid great attention because of many desirable properties such as immunity to electromagnetic interference, their multiplexing capability and small size [1]. Tian X.M. et al. proposed a fiber sensor using a single fiber Bragg grating that is bonded to a shaft at the appropriate angle [2]. As the

S. Fu (✉) • Y. Huang • X. Li
State Key Laboratory of Precision Measuring Technology and Instruments, Tianjin University, Tianjin 300072, China
e-mail: fsn666@163.com

B. Zhang et al. (eds.), *The Proceedings of the Second International Conference on Communications, Signal Processing, and Systems*, Lecture Notes in Electrical Engineering 246, DOI 10.1007/978-3-319-00536-2_30,

deviation caused by temperature cannot be eliminated, the accuracy of the fiber sensor remains to be improved. In 2003, Zhang W.G. in Nankai University designed a linear torsion sensor with very little temperature dependence, the torque sensor sensitivity is as high as 2.076 nm/Nm, with torsion angle changing in ±40° [3]. But the device is not suited to any application especially in the industry because of its unusual structure and the weak mechanical strength of the organic material shaft. Kruger et al. researched that a fiber sensor comprised of two cascaded Bragg gratings with distinct resonance wavelengths showed if the FBGs are mounted at angles of +45° and −45° with respect to the longitudinal axis of the shaft, the differential-mode wavelength will be proportional to torsion with very little temperature dependence [4].

2 Background Theory

According to fiber grating coupled mode theory, central wavelength of reflectance spectrum satisfy the following conditions: $\lambda_B = 2n_{eff}\Lambda$ [5], where λ_B is Bragg central wavelength, n_{eff} is the effective index of refraction of the core mode, Λ is the period of the grating. It is apparent that central wavelength will change following the change of n_{eff} and Λ, which leads shift of FBG center wavelength $\Delta\lambda_B$ is function of strain ε and temperature T. So the equitation can be written as:

$$\frac{\Delta\lambda_B}{\lambda_B} = \left[\frac{1}{n_{eff}}\frac{\partial n_{eff}}{\partial \varepsilon} + \frac{1}{\Lambda}\frac{\partial \Lambda}{\partial \varepsilon}\right]\Delta\varepsilon + \left[\frac{1}{n_{eff}}\frac{\partial n_{eff}}{\partial T} + \frac{1}{\Lambda}\frac{\partial \Lambda}{\partial T}\right]\Delta T = (\alpha_f + \xi)\Delta T + (1 - p_e)\Delta\varepsilon \tag{1}$$

where α_f is the coefficient of thermal expansion of the fiber, representing the period of the grating varies with temperature; ξ is the thermo-optical coefficient of fiber material, representing the index of refraction varies with temperature and p_e is the elasto-optical coefficient of fiber material, representing the refractive index varies with strain.

When a static torque applied to the shaft having a radius of r, the elastic deformation should produces a shear strain, assuming that the deformation is too small to alter the length and cross-section of the shaft. The total shear is given by:

$$M = \frac{\tau \cdot G \cdot I}{r} \tag{2}$$

where M is the torsion, τ is the shear, G is the shear modulus of the material and I is the polar moment of inertia of the shaft.

As shown in Fig. 1, the shaft, with its length $L = 180$ mm and radius $r = 20$ mm, is shaved into four planes between the axis of the cylindrical portion in the middle to bond fiber grating and increase the axis's sensitivity. Supposing the FBGs are

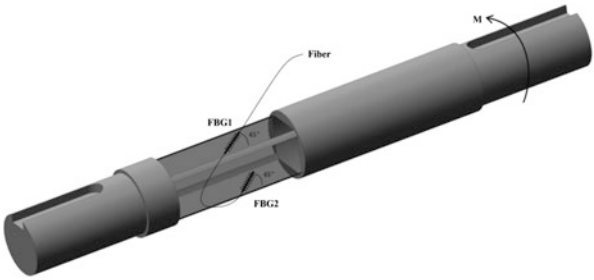

Fig. 1 The design of the shaft and situation of FBGs bonded on the planes

mounted on the two symmetrical planes at angles α and $-\alpha$ with respect to the cross section of the shaft, FBG's strain is given by:

$$\Delta\varepsilon_s = \frac{r\sin 2\alpha}{2GI}M \tag{3}$$

It is well known that the gratings will experience principal strains of the same magnitude but opposite in sign, if the shaft is subjected to pure torsion. As following equitant shows:

$$\begin{cases}\Delta\lambda_1=(1-p_e)\lambda_1\\ \Delta\lambda_2=-(1-p_e)\lambda_2\end{cases} \tag{4}$$

$\Delta\lambda_1$, $\Delta\lambda_2$ are the changes in the resonant wavelengths of the gratings FBG1 and FBG2 respectively. We define the differential-mode wavelengths of these two gratings as follows:

$$\Delta\lambda = \Delta\lambda_1 - \Delta\lambda_2 = (1-p_e)\cdot\Delta\varepsilon_s\cdot(\lambda_1+\lambda_2) \tag{5}$$

As gratings' common-mode wavelengths $\lambda_{cm} = {}^1\!/_2(\lambda_1+\lambda_2)$ always remain unchanged, the strain sensitivity of the gratings is given by: $K_\varepsilon = 1 - p_e$. The relationship between the change of central wavelength $\Delta\lambda$ and the torque M can be described as:

$$\Delta\lambda = \frac{\lambda_m\cdot K_\varepsilon\cdot r\sin 2\alpha}{GI}\cdot M \tag{6}$$

Differential-mode wavelength of the FBGs remains for the most part unaffected by temperature [6], we can use this method to obtain the desired precision in torque measurement.

3 Finite Element Analysis and Simulation

Finite element analysis can shorten the cycle of design and analysis, make a better solution of product design, reduce the material consumption or cost, and discover potential problems of product manufacture or engineering construction in advance. The virtual prototype effect of CAE design has largely replaced physical prototype based design and verification process with huge resource consumption in conventional design. It can predict the product reliability throughout the whole lifecycle, and ensure the rationality of product design.

Firstly, the material of the shaft is defined as solid187 element with 10-nodes tetrahedral structure, which can simulate the situation of bending moment and torque. The element also has plasticity, hyper elasticity, creep, stress stiffening, large deflection, and large strain capabilities. Create a single node on the centerline out of the shaft, and define it as mass21 element, which is structural mass with six degrees of freedom. A different mass and rotary inertia may be assigned to each coordinate direction. The element coordinate system hardly rotates with the nodal coordinate rotations during a small deflection analysis. And due to small deflection of the shaft in this experiment, the 3-D mass will obtain moment of inertia by setting KEYOPT(3) = 0, which leads to six degrees of freedom of the node.

Secondly, import geometric model of the shaft to the ANSYS software, and the meshing will be applied to this geometry. A rigid connection is coupled between the major node and all the nodes of end face via "cerig" order. Due to the transitivity of torque, the torque will pass to the entire shaft, when loaded on the major node, which can also avoid the phenomenon of stress concentration caused by the torque loaded directly on the end face.

Finally, Constraints and loads are applied to the shaft, and the result will be displayed by the solver. The software will give the data of strain, deformation, shear force and stress distribution diagrams of the shaft under a torque of 100 Nm, from which the value computed by finite element analysis is to be compared with material mechanical properties to judge whether the material meets the requirements and whether the design is rational.

The material selected in this experiment is quenched and tempered steel of 40CR. Its shear modulus $G = 80.8$ GPa, Poisson's ratio $\mu = 0.31$, the yield limit is 800 MPa, the allowable stress is 400 MPa, and the allowable stress in shear is 280 MPa. The distribution diagrams of deformation, shear stress, and equivalent stress intensity for a torque of 100 Nm is showed in Fig. 2. All the values computed are in acceptable range of material, meeting the requirements absolutely. Strain distribution of the shaft as shown in Fig. 3, indicates that the planes have a better strain sensitivity than other parts of the shaft.

Sensor sensitivity is related to the length, both inside and outside diameter and material properties of the shaft, so it's feasible to obtain a higher sensitivity by optimizing the shaft's relevant parameters. The determination of the measuring range (including temperature variation range) should follow the principle of avoiding destroying the fiber gratings and ability to keep shaft's elasticity.

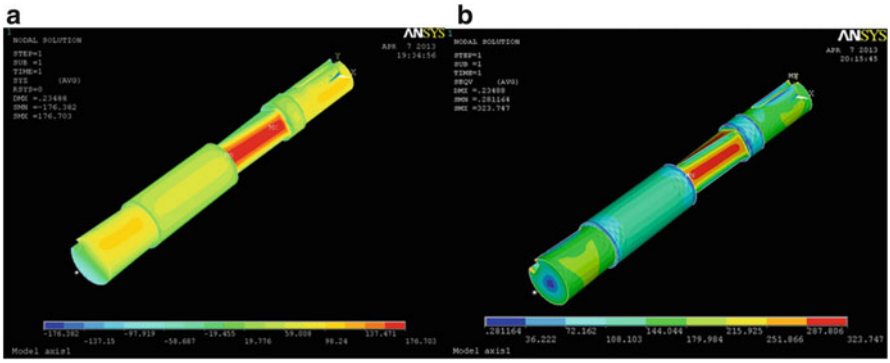

Fig. 2 Simulation result. (**a**) Shear stress distribution of the shaft in SYZ direction, (**b**) equivalent stress distribution of the shaft based on the fourth strength theory

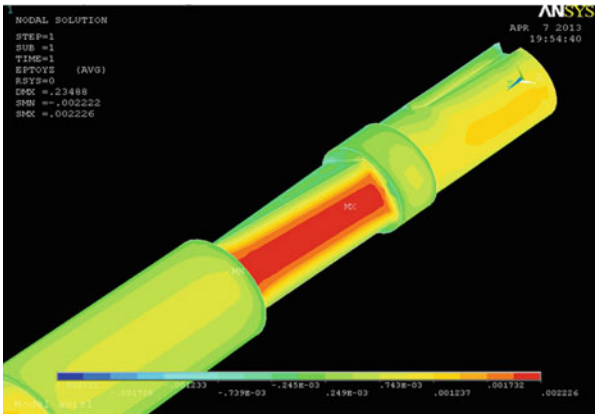

Fig. 3 Strain distribution of the plane

4 Experiment and Results

Experimental apparatus is composed of fixed platform, torque loading device, shaft, FBG interrogator and the host computer. Torque loading device can provide a particular value of torque with a full scale of 100 Nm; the real-time data processing, display and other correlation manipulations are run by the host computer, which is connected to the FBG interrogator through the TCP/IP port.

The torque is applied to one end of the shaft, while the other is fixed. And then strain can be reflected by the FBG sensors. According to the photosensitivity of FBG, we can obtain the wavelength shift by the FBG interrogator, and thus calculate the torque value of the shaft.

Experimental data and its fitting curve of FBG1 and FBG2 are showed in Fig. 4 respectively. As for FBG1, the determination coefficient is equal to $R^2 = 0.9997$,

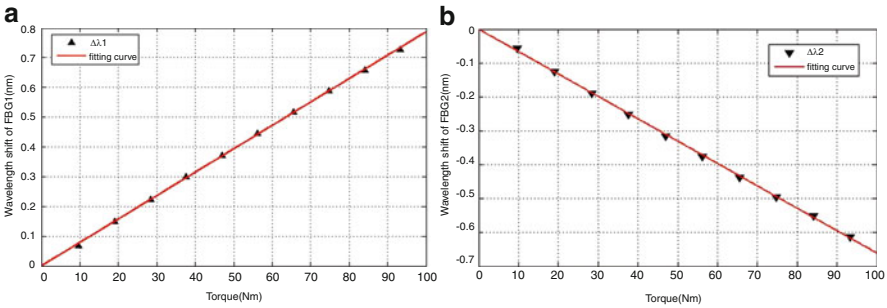

Fig. 4 Experimental data of FBG1 and FBG2. (**a**) Wavelength shift of FBG1 as a function of torque, (**b**) wavelength shift of FBG1 as a function of torque

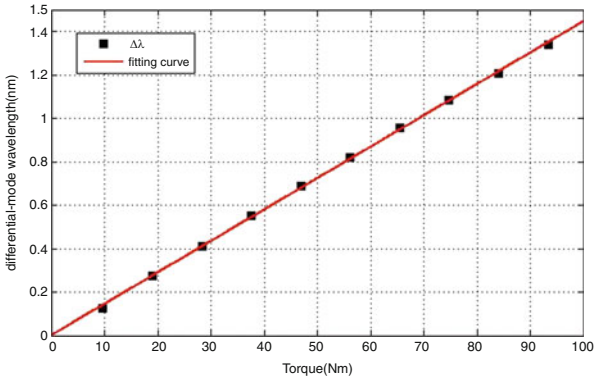

Fig. 5 Differential-mode wavelength of the two FBGs as a function of torque

the square sum of error $SSE = 0.000154$ and the root mean square error $RMSE = 0.004388$, while for FBG2 $R^2 = 0.9994$, $SSE = 0.0001776$, $RMSE = 0.004712$. The result indicates that FBG in tensile state has a more ideal linearity than that in compression state.

The relationship between the change of differential-mode wavelength as a function of torque and its fitting curve are shown in Fig. 5, with key indexes of $R^2 = 0.9996$, $SSE = 0.0006519$, $RMSE = 0.009027$. Although linearity compared with FBG1 falls slightly, the sensitivity is double, with value of 14.5 pm/Nm and linear correlation coefficient is 0.99978, suggesting that the accuracy of this structure is relatively good.

5 Conclusion

Torque measurement technology based on fiber gratings has incomparable advantages for many desirable characteristics of fiber grating, such as insulation, anti-electromagnetic interference. This paper analyzes a method using two fiber gratings to measure torque with lower temperature affect. The shaft is elaborately designed in purpose of mounting fiber gratings in a more user-friendly way and optimizing its sensitivity. By finite element analysis we have verified its safety, rationality, stability of the mechanical structure, and got further understanding of the relevant characteristics of the shaft. The experimental apparatus has a torque sensitivity with value of 14.5 pm/Nm and high linearity, having laid the theoretical and experimental basis for large torque measurement and distributed measurement in the future.

References

1. Kersey AD, Davis MA, Patrick HJ, LeBlanc M, Koo KP, Askins CG, Putnam MA, Friebele EJ (1997) Fiber grating sensors: fiber gratings, photosensitivity, and poling. J Lightwave Technol 15(8):1442–1463
2. Tian XG, Tao XM (2000) Torsion measurement by using FBG sensors. Proc SPIE 4077:154–164
3. Zhang WG, Kai GY, Dong X, Yuan S, Zhao Q (2002) Temperature-independent FBG-type torsion sensor based on combinatorial torsion beam. Photon Technol Lett IEEE 14 (8):1154–1156
4. Kruger L, Swart PL, Chtcherbakov AA, van Wyk AJ (2004) Non-contact torsion sensor using fibre Bragg gratings. Meas Sci Technol 15(8):1448–1452
5. Othonos A, Kalli K (1999) Fiber Bragg gratings: fundamentals and applications in telecommunications and sensing. Artech House, Boston
6. Swart PL, Chtcherbakov AA, van Wyk AJ (2005) Bragg grating sensor for torsion and temperature measurements in rotating machinery. Proc SPIE 5634:353–360

Face Detection Based on Cost-Gentle Adaboost Algorithm

Jian Cheng, Haijun Liu, Jian Wang, and Hongsheng Li

Abstract With the development of information technology, the research on face detection has been an important topic in computer vision. In this paper, a novel method is proposed for face detection based on Cost-Gentle Adaboost algorithm. The main differences between our method and the traditional Gentle Adaboost are that the cost factors have been introduced into the training process: the higher the value, the more important of this class samples. In the new training process, the selected classifiers can more effectively focus on the face samples than the traditional Gentle Adaboost algorithm. The face detector trained by our method can achieve higher detection rate at appropriate false positive rates. Experimental results also show that our method is effective.

Keywords Face detection • Cost factors • Gentle Adaboost algorithm

1 Introduction

In recent years, face detection has been driven by a wide spectrum of promising application areas such as face recognition, human-computer interactions. Many excellent methods have been introduced for face detection, such as neural networks, support vector machines (SVM), skin detection, etc. These methods find the relevant characteristics of face and non-face patterns with the techniques of statistical analysis and machine learning.

Recently, Paul Viola proposed a new method for face detection based on Discrete Adaboost algorithm [1, 2]. In this system, small best weak classifiers are selected from the huge number of the weak classifiers, and then unite them to strong classifiers. Finally, the strong classifiers form the cascade classifier. The Adaboost

J. Cheng (✉) • H. Liu • J. Wang • H. Li
School of Electronic Engineering, University of Electronic Science and Technology of China, 2006 Xiyuan Avenue, Chengdu 611731, China
e-mail: pami.cheng@gmail.com

B. Zhang et al. (eds.), *The Proceedings of the Second International Conference on Communications, Signal Processing, and Systems*, Lecture Notes in Electrical Engineering 246, DOI 10.1007/978-3-319-00536-2_31,

algorithm are proposed by Freund and Schapire [3, 4], and its three variants have been used in face detection: Discrete Adaboost, Real Adaboost, Gentle Adaboost. They all have one problem in the training process following the Adaboost algorithm which chooses the best weak classifier with minimum mean square error under the weight distribution, but face and non-face samples are treated same. In practical application the influence of missing face is larger than missing non-face. In order to solve this problem, some methods have been proposed. Paul proposed a new variant of Real Adaboost algorithm as a mechanism for training the simple classifiers used in cascade [5]. Yang presented a variant of Discrete Adaboost algorithm, called Cost-Sensitive Adaboost (CS-Adaboost) algorithm [6] which focuses on modifying the weight of those misclassified face samples. In order to gain better results, Hou changed the least error expression to select better classifiers [7]. Xue [10] proposed a two-stage face detection method using skin color segmentation and heuristics-structured adaptive to detection AdaBoost (HAD-AdaBoost) algorithms, which can obtain good results with fewer weak classifiers. These variant algorithms all achieved good results. But there is no one based on Gentle Adaboost algorithm.

In this paper, we proposed a new variant method based on the Gentle Adaboost algorithm, named as Cost-Gentle Adaboost, to construct a strong face detection system with better weak classifiers. In new algorithm, false positive and false negative are treated differently so that the weak classifier with better acceptance ability could be selected. Experiments demonstrate that our face detector can achieve higher detection rate with appropriate false positive rates.

2 Cost-Gentle Adaboost Algorithm

In traditional Adaboost algorithm, samples from different classes are treated equally. However, in practical applications the misclassified face samples produce larger impact than misclassified non-face samples. So our goal is to find new weighting update strategy to distinguish samples from different classes, and boost more weights on those samples associated with higher identification importance.

2.1 Modification Weight Update Strategy

To show the different importance of samples, on each weight update round, every sample is associated with a cost value C, the higher the value, the more important of this class samples. In the weight update process, the weight of misclassified face samples are increased more than the misclassified non-face samples. So the weight of face sample will possess bigger proportion in the weight distribution. For this case, there are three ways to introduce cost value into the weight update process, outside the exponent function, inside the exponent function, and both inside and outside the exponent function. Three modifications are showing as follows,

Modification 1:

$$w_i \leftarrow C_i \cdot w_i \cdot \exp(-y_i \cdot h_t(\mathbf{x}_i)) \tag{1}$$

Modification 2:

$$w_i \leftarrow w_i \cdot \exp(-C_i \cdot y_i \cdot h_t(\mathbf{x}_i)) \tag{2}$$

Modification 3:

$$w_i \leftarrow C_i \cdot w_i \cdot \exp(-C_i \cdot y_i \cdot h_t(\mathbf{x}_i)) \tag{3}$$

where $\mathbf{x}_i$ and y_i are the i-th sample and the corresponding class label(face = 1 or non-face = −1), respectively. C_i and w_i are the cost factor and weight for i-th sample, respectively. $h_t(\mathbf{x}_i)$ is weak classifier. The modified methods can be taken as three new Adaboost algorithms named as: C-AdaC1, C-AdaC2, C-AdaC3.

When the cost value is introduced into the weight update process, the weight distribution is affected by cost value. After each update round, weights on those samples associated with higher identification importance will occupy a larger proportion in the weight distribution. Because of the modification of the weight update, the weak classifier $h(\mathbf{x})$ is also changed. In [8], it has been shown that Adaboost is equivalent to forward stage-wise additive modeling using exponential loss function, and the Gentle Adaboost algorithm uses Newton steps for minimizing the exponential loss function.

Here we introduce the weak classifier $h(\mathbf{x})$ for C-AdaC2 algorithm as follows. For the m-th round, we have $F_{m-1}(\mathbf{x})$ and seek an improved estimation $F_m(\mathbf{x}) = F_{m-1}(\mathbf{x}) + h_m(\mathbf{x})$, where $F_t(\mathbf{x}) = \sum_{j=1}^{t} h_j(\mathbf{x})$. Therefore, the new Gentle Adaboost can be derived from minimizing the cost function,

$$\begin{aligned} J_{asy}\big(F_m(\mathbf{x})\big) &= J_{asy}\big(F_{m-1}(\mathbf{x}) + h_m(\mathbf{x})\big) = E\big[e^{-yC(F_{m-1}(\mathbf{x})+h_m(\mathbf{x}))}\big] \\ &= E\big(e^{-yCF_{m-1}(\mathbf{x})} \cdot e^{-yCh_m(\mathbf{x})}\big) \\ &= E_w\big(I\big(y=1\big|\mathbf{x}\big) \cdot e^{-C_1 h_m(\mathbf{x})}\big) + E_w\big(I\big(y=-1\big|\mathbf{x}\big) \cdot e^{C_2 h_m(\mathbf{x})}\big) \\ &= P_w\big(y=1\big|\mathbf{x}\big) \cdot e^{-C_1 h_m(\mathbf{x})} + P_w\big(y=-1\big|\mathbf{x}\big) \cdot e^{C_2 h_m(\mathbf{x})} \end{aligned} \tag{4}$$

where $w = w_{m-1}(\mathbf{x}, y) = e^{-yCF_{m-1}(\mathbf{x})}$, C is the cost factor, $C = C_1$ if $y = 1$, $C = C_2$ if $y = -1$, and $C_1 > C_2$. $E_w[\cdot]$ is the weighted expectation defined as $E_w(g(\mathbf{x}, y)) = \frac{E(w(\mathbf{x},y)g(\mathbf{x},y))}{E(w(\mathbf{x},y))}$.

Then the optimal weak hypothesis of the C-AdaC2 can be obtained using Newton steps by minimizing (4) and described as follows:

$$h(\mathbf{x}) = \frac{C_1 P_w(y=1|\mathbf{x}) - C_2 P_w(y=-1|\mathbf{x})}{C_1^2 P_w(y=1|\mathbf{x}) + C_2^2 P_w(y=-1|\mathbf{x})} \tag{5}$$

Finally, we get the whole C-AdaC2 algorithm. But when we use the new method to train the cascade classifier, a new problem happened. If the cost factor C is not appropriate, the sign of the result of the optimal weak classifier $h(\mathbf{x})$ may be the same. In next part, we will introduce a modification method to solve this problem.

2.2 The Modification of the C-AdaC2 Algorithm

Supposing the feature values of the samples are sorted from small to large as $f(\mathbf{x}_1), \ldots, f(\mathbf{x}_N)$, the weights of the samples are $w_1, \ldots, w_N$, the number of the samples is N. The weak classifier $h(\mathbf{x})$ is rewritten as follows

$$h(\mathbf{x}) = \begin{cases} \dfrac{C_1 PWSUM[j] - C_2 NPSUM[j]}{\sum_{i=1}^{j} C_1^2 w_i + \sum_{i=1}^{j} C_2^2 w_i} & f(\mathbf{x}) < \theta \\ \dfrac{C_1(PWSUM[N] - PWSUM[j]) - C_2(NPWSUM[N] - NPWSUM[j])}{\sum_{i=j+1}^{N} C_1^2 w_i + \sum_{i=j+1}^{N} C_2^2 w_i} & otherwise \end{cases} \tag{6}$$

where $PWSUM[j] = \sum_{i=1}^{j} w_i \cdot 1_{[y_i=1]}$, $NPWSUM[j] = \sum_{i=1}^{j} w_i \cdot 1_{[y_1=-1]}$, and $\theta = f(\mathbf{x}_j)$ is the threshold of the weak classifier. $PWSUM[j]$ denotes the cumulative weight value of the j-th face samples, $NPWSUM[j]$ denotes the cumulative weight value of the j-th non-face samples. Because of the feature values have been sorted increasingly, the feature values of those data sorted in front of the j-th data are all smaller than the threshold $\theta = f(\mathbf{x}_j)$.

From formula (6), we can see the sign of the $h(\mathbf{x})$ is relate to the subtraction value of $C_1 PWSUM[j] - C_2 NPWSUM[j]$. If the subtraction value satisfies the formula (7), $h(\mathbf{x})$ will be only have on sign, and in this case, we can't give the discriminate result.

$$\begin{aligned} C_1 PWSUM[j] - C_2 NPWSUM[j] &= C_1\big(PWSUM[N] - PWSUM[j]\big) \\ &\quad - C_2\big(NPWSUM[N] - NPWSUM[j]\big) = \delta \end{aligned} \tag{7}$$

To solve this problem, we normalize the weight for the face samples and non-face samples respectively in order to make the sum value of the weight of face samples equal to the sum value of the weight of non-face samples. The method is described as follows

For the face samples:

$$\begin{aligned} &for \;\; i = 1 : numPos \\ &\qquad w_i \leftarrow \frac{C_2}{C_1 + C_2} w_i / PosSumW \end{aligned} \tag{8}$$

For the non-face samples:

$$\begin{aligned} &for \;\; i = 1 : numNeg \\ &\qquad w_i \leftarrow \frac{C_1}{C_1 + C_2} w_i / NegSumW \end{aligned} \tag{9}$$

where *PosSumW* is the sum weight value of all the face samples, *NegSumW* is the sum weight value of all the non-face samples.

Then through the above method, the output results of the weak classifier are strictly distinguished with zero for the boundary. And here if we adopt C-AdaC1 or C-AdaC3 modification algorithm, the cost factor outside the exponent is balanced out. So we adopt the C-AdaC2 as our weight update strategy.

Using the C-AdaC2 will produces another problem, each round the selected weak classifier is not the optimal classifier. In the traditional Gentle Adaboost algorithm, each round the algorithm selects the optimal classifier which minimizing the mean square error under the current weight distribution. When we adopt C-AdaC2 algorithm, the domain of the $h(\mathbf{x})$ is $[-1/C_2, 1/C_1]$. But in the traditional Gentle Adaboost algorithm the domain of the $h(\mathbf{x})$ is $[-1, 1]$. If we adopt the original formula to calculate the mean square error, the selected classifier is not the optimal classifier.

Supposing the cost factor values are $C_1 = 1, C_2 = 0.8$, then the domain of weak classifier is $h(\mathbf{x}) \in [-1.25, 1]$. To a non-face sample ($y_i = -1$), when $h(\mathbf{x}_i) = -1.25$, the sample is classified the non-face sample completely, and the mean square error of this sample is zero in theory. But when adopting the original formula, the mean square error of this sample is $\sum 0.25^2 \cdot w_i$, it is contradiction. Simultaneously, when $h(\mathbf{x}_i) = -0.75$, the mean square error of this sample is also $\sum 0.25^2 \cdot w_i$. According to the definition of the weak classifier, the higher value of the $h(\mathbf{x})$, the lower value of the mean square error. So we modify the mean square error expression. The new expression is described as follows,

$$\varepsilon = \sum_{i=1}^{N} w_i (y' - h(\mathbf{x}_i))^2 \tag{10}$$

where $y' = 1/C_1$ if $y_i = 1$, $y' = -1/C_2$ if $y_i = -1$. Here the modification C-AdaC2 algorithms are named as Cost-Gentle Adaboost.

Above all, there are two places have been modified in the C-AdaC2, the normalization weighted process and the expression of the mean square error. In

the next part, some experiments are demonstrated to evaluate our new algorithm Cost-Gentle Adaboost.

3 Experimental Results

In this section, we set up some experiments to investigate the performance of the algorithms, Gentle Adaboost (original method) and our proposed Cost-Gentle Adaboost in the domain of frontal face detection.

In the first experiment, the size of training and testing set for face and non-face samples is fixed to 24×24. There are 2000 face samples and 2000 non-face samples in training dataset. And test dataset also consists of 2000 faces and 2000 non-faces. The face samples are manually cropped from the web images and basic face database (CAS-PEAL). The non-face samples are randomly collection from web images without contain any faces.

Gentle Adaboost and Cost-Gentle Adaboost are used to train classifiers (every classifier is a strong classifier) with 13 features like in [9]. The ROC curves on this test data are shown in Fig. 1. Here we only change the cost factor of the face samples. For example, we set the cost factor $C_2 = 1.0$, then change the cost factor C_1. Figure 1 shows that in the same training and testing set, if the cost factor is taken proper value, to the single strong classifier, the detection rate is improved by the Cost-Gentle Adaboost algorithm at the same false positive rate. If the cost factor is big, the weight of the misclassified face samples will be continuously increased more than other samples. The selected weak classifier maybe focus on these difficult misclassified samples, thus the selected weak classifier have not gain the good classification ability for the whole samples, such as $C_1 = 1.05$.

In the second experiment, two different complete cascade face detectors are trained with Gentle Adaboost and Cost-Gentle Adaboost. Here the performance of each detector is investigated for the real world images which contain some faces.

In the cascade training process, the training set of the non-face samples for the later stage need to be verified by the previous stages. So the selection of non-faces used to train later stages are relate to the performance of earlier stages. As a result, different sets of non-face samples and the same set of face samples (used in the first experiment) are used to train two different complete cascade face detectors with Gentle Adaboost and Cost-Gentle Adaboost algorithm.

The two cascade face detectors respectively contain 19 layers. The minimum detection rate and maximum false positive rate for one strong classifier are respectively the same for the two algorithms. Thirteen features [9] are used for the two algorithms. Here we choose the NewTest set in MIT+CMU test sets as our final test set. The NewTest set consists of 64 images with 170 frontal faces. At the same time another dataset with the selection web images are used to test the comparison performance. It is the Football set consisting of 19 football team images with 229 frontal faces.

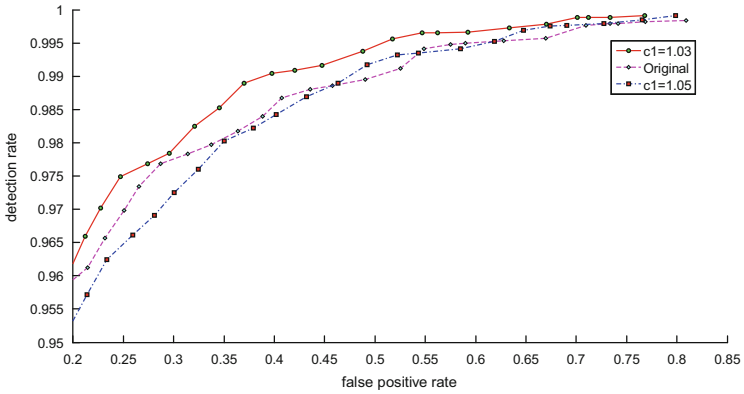

Fig. 1 The ROC curves with different parameterizations of three basic strong classifiers

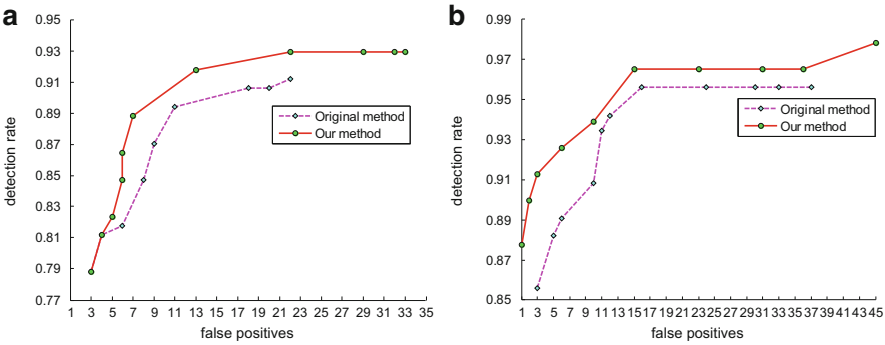

Fig. 2 The ROC curves of different complete cascade face detectors, (**a**) on NewTest set, (**b**) on Football set

The ROC curves on the two test set are shown in Fig. 2. The key result is that the performance of the cascade face detectors with the Cost-Gentle Adaboost algorithm is better. Namely, our proposed method can gain the higher detection rate at the same false positive rate.

4 Conclusion

In this paper, a novel cost-Gentle Adaboost algorithm has been presented. In our method, the cost factor is introduced into the weight update process. The weak classifiers selected by our proposed method achieve the better capability of accepting the face samples than one selected by the Gentle Adaboost algorithm. Comparative results on different test sets demonstrate our method is effective, and

the performance of the cascade face detector with our method is better than traditional Gentle Adaboost algorithm.

Acknowledgments This work is supported by the National Natural Science Foundation of China under Projects 61201271 and Specialized Research Fund for the Doctoral Program of Higher Education 20100185120021.

References

1. Viola P, Jones MJ (2004) Robust real-time face detection. Int J Comput Vis 57(2):137–154
2. Viola P, Jones M (2001) Rapid object detection using a boosted cascade of simple features. IEEE Comput Soc Conf Comput Vis Pattern Recogn 1:511–518
3. Freund Y, Schapire RE (1997) A decision-theoretic generalization of on-line learning and an application to boosting. J Comp Syst Sci 55(1):119–139
4. Freund Y, Schapire RE (1996) Experiments with a new boosting algorithm. In: Int Conf Mach Learn., pp 148–156
5. Viola P, Jones M (2001) Fast and robust classification using asymmetric adaboost and a detector cascade. Adv Neural Inform Process Syst 14
6. Ma Y, Ding X (2003) Robust real-time face detection based on cost-sensitive adaboost method. In: Proceeding of the IEEE international conference on multimedia and expo, vol 1. pp 465–468
7. Hou X, Liu CL, Tan T (2006) Learning boosted asymmetric classifiers for object detection. In: Proceeding of the IEEE conference on computer vision and pattern recognition, vol 1. pp 330–338
8. Friedman J, Hastie T, Tibshirani R (2000) Additive logistic regression: a statistical view of boosting. Ann Stat 28(2):337–407
9. Lienhart R, Maydt J (2002) An extended set of haar-like features for rapid object detection. In: Proceeding of the international conference on image processing, vol 1. pp 900–903
10. Xue L, Liu Z (2012) Using skin color and HAD-AdaBoost algorithm for face detection in color images. Proceedings of the 2012 National Conference on Information Technology and Computer Science

The Uncertainty Assessment of Vehicle Speed Measurement Based on Laser Switch

Li Li and Hong He

Abstract This paper presents a vehicle speed measurement method based on laser switch, due to the effects of laser switch emission frequency and mechanical structure, it exists large error for measured speed. To ensure the measuring system meet accuracy requirements, for example a fixed length of 10 m, the uncertainty of laser switch speedometer was effective analyzed. Through making the effects of laser switch frequency distance and mechanical error averaged, the influence from switch frequency, mechanical error and other aspects was evaluated. Selected laser switch of 10 kHz and debugged various parameters, experiment shows that speed measuring system can achieve accuracy ± 0.2 km/h to ± 0.3 km/h, which can meet the required accuracy to provide a vehicle speed basis for relevant departments.

Keywords Laser switch • Speed measurement • Uncertainty assessment

1 Introduction

Speeding is the more prominent reason in accidents, so the traffic control department has taken some appropriate limiting means. Using advanced vehicle speed measuring device is one of the effective management tool, which can take appropriate punishments to speeding. Therefore, research of vehicle speed measuring method has great significance for urban transport modernization and sustainable development.

Radar detection accuracy is usually up to ± 1 km/h, but the detection distance is relatively short and easily detected by the target, thus its shortcoming is inevitable to avoid or disturb speed measurement [1, 2]. In order to accurately measuring vehicle speed, a vehicle measuring speed method based on laser switch was

L. Li (✉) • H. He
Tianjin Key Laboratory for Control Theory & Applications in Complicated Systems, Tianjin University of Technology, Tianjin, China
e-mail: green_linda@163.com; heho604300@126.com

B. Zhang et al. (eds.), *The Proceedings of the Second International Conference on Communications, Signal Processing, and Systems*, Lecture Notes in Electrical Engineering 246, DOI 10.1007/978-3-319-00536-2_32,

proposed in this paper, whose measuring precision can reach other radar speedometer 3–5 times.

However, due to laser switch emission frequency, the mechanical structure errors and other issues, if not analyzing the uncertainty of the amount of influence, the device will be difficult to achieve accurate speed requirements. In order to achieve equipment installation and commissioning basis with specific parameters, save costs to achieve the desired target speed, therefore, the device uncertainty must be analyzed.

2 Measuring Principle

Measuring principle based on laser switch is: it consists of two laser switch and two standard rods. Along the road on both sides, each group standard rods mounted a set of laser switches, emitting laser beam of two mutually parallel and perpendicular to the vehicle traveling direction, respectively, two laser switch successively generates an electrical signal when passing through the target vehicle speed range, time counter is transferred to IPC for processing target vehicle speed [3].

The system set up three sampling points, each sampling point placed a laser switch, the sampling points were fixed intervals, when the car reaches the first sampling point, and the first laser switch will produce a rising edge pulse signal, which would be transmitted to the camera. Then some information was captured such as vehicle license, and the signal is transmitted to the counter.

When the car reaches the second sampling points, the second rising edge pulse also generates signal and transmits the signal to the counter. After receiving two signals, the counter calculated time interval of two samples, then make the result to the computer for final processing (distance divided by known transmission time, that is speed). Set two laser distance sensors in the next the first and second rod respectively, that the distance signal is transmitted to the IPC in order to identify vehicles lane and target number. The vehicle speed range and the distance between laser switch have detected, which can effectively prevent false positives.

3 Error Analysis

Machining accuracy of laser switch is: As the production process constraints, two connecting rods between the laser switch would inevitably produce a certain amount of error, the production error of connecting rod can be controlled within ± 1 mm.

Two laser switch calibration accuracy: In the field, two laser switches is connected by two connecting rods, the fixed length of the laser switches mounted on both sides of road, the laser switches need to be calibrated. Its calibration

accuracy is determined by the accuracy of laser calibrator, the error can be controlled within the range within ±1 range.

The laser switch should be perfectly parallel to the road surface in theory, but the actual road roughness is difficult to achieve the desired level state, laser speedometer is also required calibrator adjustment in actual use [4].

The uncertainty of laser switch is dominated by its emission frequency. Though the laser has high frequency, there are slight changes in time, only the laser switch is rising, it can emitting laser, the measuring system would work when laser hit the tested vehicle. When the car enters the first laser light, assuming the laser is switched to finished state of previous signal, that is low, and the second is the same, the error caused by laser speed system would the greatest. The system uses laser switching frequency 10 kHz, a period of 0.1 ms, the maximum traveling speed of 180 km/h, and fixed length 10 m for analysis.

4 The Uncertainty Assessment

Let δ_t is evenly distributed; half-width A is a 0. 05 ms, including factor $k = \sqrt{3}$, its standard uncertainty is:

$$u(t) = \frac{a}{k} = \frac{0.05}{\sqrt{3}} \approx 0.028868ms \tag{1}$$

The sensitivity coefficient C is, then

$$c = \frac{\partial V}{\partial T} = \frac{L}{T^2} \tag{2}$$

And its actual measuring distance L is 10 m, the time interval of two sensor signals T is 200 ms. The corresponding uncertainty component is:

$$u(T) = C \cdot u(t) = \frac{10000mm}{(200ms)^2} \times 0.028868 = 0.007217Km/h \tag{3}$$

Estimate $u(T)$ relative uncertainty is 10 %, then the freedom $v(T) = 50$

The standard uncertainty of $u(L)$:Δl_1 caused by laser emission direction is not perpendicular to the connecting rod between laser switch, that is standard uncertainty $u(l_1)$, the other is the standard uncertainty $u(l_2)$ caused by the size error Δl_2 of double pole axis distance. B-type uncertainty can be used for evaluation method to analysis uncertainty [5, 6].

Three sets of laser emission direction when switching is not perpendicular to the connecting rod error Δl_1 standard uncertainty caused by breakdown of $u(l_1)$, Theoretically, we require the emission direction must be perpendicular to the

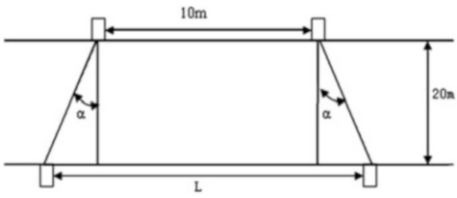

Fig. 1 Laser emission direction deviation schematic

connecting rod, but the laser emission direction inevitably inclined at an angle α with the connecting rod, then actually traveling distance of target vehicle is:

$$L_\alpha = 10 \pm 2L^{'} \bullet \tan\alpha \tag{4}$$

Where L' is the road width. We chose the side of road width 20 m, which result in $L_\alpha \neq L$, that the measured speed is not accurate. Required α control within ± 0.1 degree, the maximum error for the first group to one side 0.1 degree while the second group tends to the other side 0.1 degree.

Laser emission direction deviation schematic is shown in Fig. 1.

Set 10 m as fixed length of laser switch, the actual driving distance is:

$$L_\alpha = 10 + 2L^{'} \bullet \tan\alpha \tag{5}$$

When two switches deviated toward the center, the actual distance is:

$$L_\alpha = 10 - 2L^{'} \bullet \tan\alpha \tag{6}$$

Measurement error Δl_1 is generated, that is 69.8 mm. Let Δl_1 is uniform distribution, half-width A is a $\Delta l_1/2$ containing factor $k = \sqrt{6}$, then

$$u(l_1) = \frac{a}{k} = \frac{34.9}{\sqrt{6}} = 14.2479mm \tag{7}$$

Estimate $u(l_1)$ relative uncertainty of 10 %, the degree of freedom $v(l_1) = 50$.

Standard uncertainty $u(l_2)$ caused by dimension error Δl_2. Although this error is inevitable for laser alignment, the distance between the axis of rods is 1,000 cm; the size of the error Δl_2 is ± 2 cm. The distance between the axes is known (1,000 − 2, 1,000 + 2), whose probability near the center is larger than probability of the boundary. Δl_2 is estimated at ± 2 cm range with triangular distribution, a half width of a is 1 cm, including factors $k = \sqrt{6}$, then

$$u(l_2) = \frac{a}{k} = \frac{10}{\sqrt{6}} = 4.0825mm \tag{8}$$

Estimate $u(l_2)$ relative uncertainty of 10 %, the degree of freedom $v(l_2) = 50$.

The standard uncertainty $u(l)$ is calculated

$$u(l) = \sqrt{u(l_1)^2 + u(l_2)^2} \approx 14.82124mm \tag{9}$$

The sensitivity coefficient C1 is:

$$C_1 = \frac{\partial V}{\partial L} = \frac{1}{T} \tag{10}$$

Therefore, the corresponding uncertainty components as follows:

$$u(L) = C_1 \cdot u(l) = \frac{1}{T} \cdot u(l) \tag{11}$$

When T is 200 ms,

$$u(L) = \frac{14.82124}{200} = 0.0741062km/h \tag{12}$$

$$v(L) = \frac{u^4(l)}{\frac{u^4(l_1)}{v(l_1)} + \frac{u^4(l_2)}{v(l_2)}} = 58 \tag{13}$$

There is no correlation between two uncertainties, according to the propagation law of uncertainty; the combined standard uncertainty $U(V)$ is calculated [7]. Let velocity V = 180 km/h, the time interval of two sensor signals T = 0.1 ms, then

$$U(V) = \sqrt{\sum_{i=1}^{N} \left(\frac{\partial V}{\partial x_i}\right)^2 U^2(x_i)} = \sqrt{0.007217^2 \times 0.0741062^2}$$

$$= 0.07451 \ \ km/h \tag{14}$$

$$v_{eff} = \frac{u^4(V)}{\sum_{i=1}^{2} \frac{u^4(x_i)}{v(x_i)}} \approx 59 \tag{15}$$

The expanded uncertainty $U(p) = Kpu(V) = t_p u(V)$, take confidence probability $P = 0.95$, lookup table to obtain distribution containing factor, then k_{95} (59) =2.00,

$$U = K_{95} \cdot u(V) = 2.00 \times 0.07451 = 0.14902km/h \tag{16}$$

5 Conclusion

In order to verify the measuring accuracy can meet design requirements, using high precision sense coil speedometer as a benchmark, a common radar guns was be used to do comparison.

Table 1 Experiment data

Number	Sense coil ($kmh^{-1)}$	Radar ($kmh^{-1)}$	Laser switch ($kmh^{-1)}$	Absolute error		Relative error	
				Radar	Laser switch	Radar	Laser switch
1	26.2	26	26.203	−0.2	0.003	−0.0077	0.00145
2	38.6	39.0	38.710	0.4	0.110	0.01040	0.00285
3	46.4	47.2	46.520	0.8	0.120	0.01724	0.00258
4	59.6	59.6	59.450	1.0	−0.150	0.01678	−0.00251
5	67.8	67.0	68.010	−0.8	0.210	−0.01179	0.00309
6	78.3	79.5	78.035	1.2	−0.265	0.01532	−0.00338
7	92.5	91.1	92.806	−1.4	0.306	−0.01514	0.00331
8	104.0	106.1	104.335	2.1	0.335	0.02019	0.00322
9	112.3	114.5	112.703	2.2	0.403	0.01959	0.00359
10	124.6	127.5	125.090	2.9	0.490	0.02327	0.00393
Mean				0.82	0.1562	0.00882	0.00181

Speedometer based on laser switch and radar guns were installed on both sides of the road. For different grade highway, speed limiting requirements is different, each 10 km/h for the test in 20–130 km/h interval respectively. Each experiment was performed ten times in order to detect speeds equipment accuracy in different conditions.

Experimental data show: compared with the radar, laser switch speedometer can reach higher detection accuracy 3–5 times (Table 1).

This paper presents a speed measuring method based on laser switch, the laser speed measurement uncertainty is analyzed, which make the mechanical error averaged, determine accuracy of the laser switch detector and save development costs.

In summary, the result is obtained by calculating. We selected laser switch frequency of 10 kHz, machined the connecting rod in laboratory conditions, that can guarantee its length in (1,000 ± 2 cm) range. When the laser switch is installed in the field calibration, its deviation angle can controlled within ±1 degree by using laser alignment. The speed accuracy can meet ±0.2 km/h to ±0.3 km/h requirements in the above conditions [3].

By adjusting the parameters, measurement accuracy can meet standard requirements. Thus it can better use to velocity measurement system of road traffic authorities for the improvement of vehicle safety.

Acknowledgments This paper is supported by Tianjin Social Development Fund Project (09ZCGYSF00300) "Research of Speed Secure Real-time monitoring system for measuring traceable calibration standards". And thanks Tianjin Key Laboratory for Control Theory and Application in Complicated Systems, Tianjin University of Technology, Tianjin 300191, and China.

References

1. Feng L, YueBing S (2009) Research on motor vehicle radar system errors. Sci Technol Inf 14:61–61
2. Yong X (2009) License plate recognition and radar speeding on the highway surveillance system application. Intell Transport 11:188–190
3. Xiong S (2005) Laser speedmeter. Optics and Fine Mechanics 2:9–10
4. Sheng YC, Dong J, Liang C (2009) Vehicle remote video radar speed measurement system. Control Automat 18:143–145
5. Ming B (2009) The uncertainty analysis of vehicle radar measurement results. Meas Technol 3:46–47
6. HaiMing X (2009) Disturbance factors machining accuracy and error analysis. Technol Aspect 5:37–39
7. YeTai F (2002) Error theory and data processing. Machinery Industry Press, Beijing

Adaptive Threshold Nonlinear Image Enhancement Algorithm Based on NSCT Transform

Ying Tong, Meirong Zhao, and Zilong Wei

Abstract A nonlinear image enhancement algorithm based on nonsubsampled contourlet transform (NSCT) is proposed. The image is decomposed into coefficients of different scales and directions through nonsubsampled contourlet transform. Thresholds of the nonlinear enhancement function are determined according to the coefficients of each scale. The two parameters of the function, among which one is used to control the range of enhancement and the other can determine the strength of enhancement, are obtained by solving nonlinear equations. The coefficients processed by the enhancement function are used to reconstruct the image. The simulation results on Matlab platform show that the algorithm has good effect of enhancing the detail of images and suppressing the noise signals meanwhile.

1 Introduction

In the image acquisition process, due to the effects of environment, system noise and other factors, images captured by cameras are often hardly to meet the demands of image processing. As a common image pre-processing technique, image enhancement plays an important role in improving the quality and visual effect of digital images.

Enhancement algorithms based on transform domain are more common in wavelet transform, contourlet transform and so on. But these algorithms lack the

Y. Tong (✉)
Sate Key Laboratory of Precision Measuring Technology & Instruments, Tianjin University, Tianjin, China

College of Electronic and Communication Engineering, Tianjin Normal University, Tianjin, China
e-mail: tongying2334@163.com

M. Zhao • Z. Wei
Sate Key Laboratory of Precision Measuring Technology & Instruments, Tianjin University, Tianjin, China

B. Zhang et al. (eds.), *The Proceedings of the Second International Conference on Communications, Signal Processing, and Systems*, Lecture Notes in Electrical Engineering 246, DOI 10.1007/978-3-319-00536-2_33,

shift invariance property. They are possible to cause pseudo-Gibbs phenomena at the edges of the processed image. Nonsubsampled contourlet transform (NSCT for short) which has the translation-invariant feature was proposed by Arthur L Cunha et al. on the foundation of contourlet transform. The algorithm has showed good performance in image denoising and enhancement. This paper proposes an adaptive nonlinear enhancement algorithm based on NSCT transform. The experiments show that the algorithm has good effect of enhancement. The image quality has been significantly improved.

2 Introduction of NSCT

Contourlet Transform is a two-dimensional representation of an image proposed by Do and Vetterli et al. in 2005 [1]. It not only has the multi-resolution feature of wavelet transform, but also has the superiority of anisotropy, which means that the algorithm has a good grasp of the geometry of the image. However contourlet transform itself is not shift-invariant, due to downsamplers and upsamplers, so it tends to show the problem of the pseudo-Gibbs distortion, which affects the image processing effects.

The basic idea of NSCT is to use the nonsubsampled pyramid decomposition to decompose the image into multiple scales. And then through the nonsubsampled directional filter bank, the signals of each scale are decomposed into different directional sub bands. The number of sub bands in each scale can be any power of 2. NSCT has no down-sampling process in the two-step decomposition, so it has the feature of translation invariant [2].

3 Nonlinear Enhancement Model

3.1 Nonlinear Function

The information contained in an image can be divided into several types: Edges and details, approximate trends and noise signals. And the edges of image can be subdivided into strong edges and fuzzy edges. In the process of image enhancement, these types of information need to be treated differently. That is, the strong edges should be preserved; the fuzzy edges need to be enhanced; while the noise signals must be suppressed. Thus, using a non-linear function as an enhancement model is a better choice. The selected enhancement function herein is presented in 1996 by Laine [3]. Since then, many scholars have achieved good results in applying it to image enhancement [4–6]. The function is as follows:

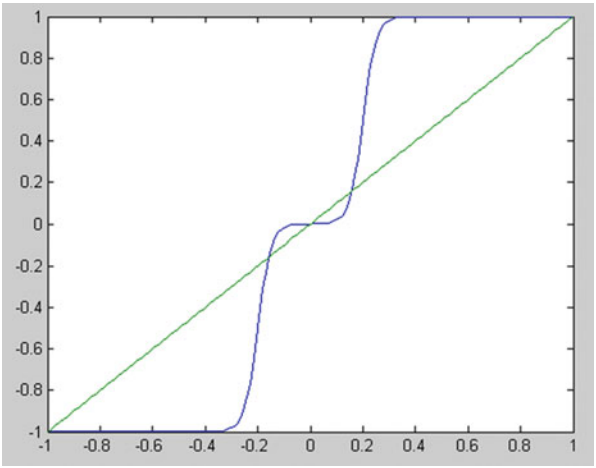

Fig. 1 *f(x)* for b = 0.25 and c = 40

$$f(x) = a[sigm(c(x-b)) - sigm(-c(x+b))] \tag{1}$$

where a is defined as $a = \frac{1}{sigm(c(1-b))-sigm(-c(1+b))}$, *sigm* is defined as $sigm(x) = \frac{1}{1+e^{-x}}$.

There are b and c two parameters in this function, Where b is used to control the scope of enhancement, its value is in the range of (0, 1). And c is used to control the enhancement strength. It is usually used as a fixed value taken between 20 and 50. The blue curve in Fig. 1 shows the image of *f(x)*, in this picture, b is set to be 0.25, while c is 40.

Order to see the feature of the function clearly, Fig. 2 illustrates the first-order derivative of the function shown in Fig. 1.

It can be seen from the two figures above that after processed by *f(x)*, within the range of (−b, b), the original coefficients are suppressed, while in the range of [(−1, −b) and (b, 1)], they are enhanced notability. The values of the first derivative of *f(x)* reach the maximum when the coefficients are in the points of b and −b, and then monotonically decrease. The derivative approaches zero near the point of $x = \frac{9}{c} + b$ [6]. These key points can be a reference to select the enhancement threshold.

3.2 Selection of Threshold

By analyzing the characteristics of the enhancement function, it can be seen that (taking the positive direction of horizontal axis as an example), when the value of x equals b, it reaches the point that can distinguish the coefficients between enhancement area and inhibition area. And after the point of $x = \frac{9}{c} + b$, the values of the enhancement function are almost 1. So the interval of $\left(b, \frac{9}{c} + b\right)$ is the range of monotonically increasing. Thus the span of the coordinates of the two points can

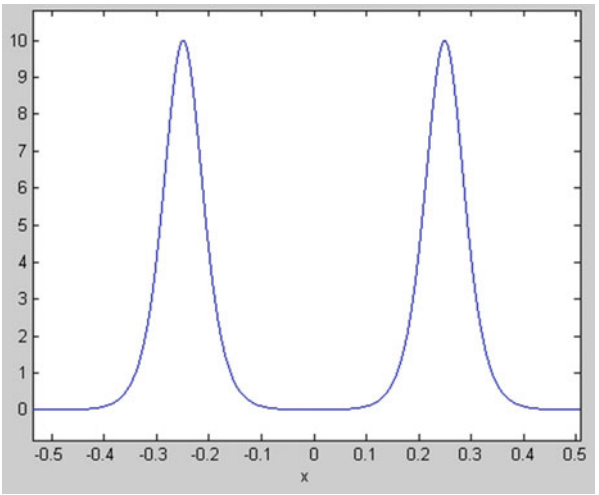

Fig. 2 The first-order derivative of *f(x)*

determine the dynamic range of grayscale contrast of the enhanced image. Based on the above analysis, we take two key points in the curve to fix the enhancement function and form the enhancement model. Set two thresholds as T^l_{klow} and T^l_{khigh}. T^l_{klow} is the threshold to distinguish coefficients from enhancement and suppression. It is supposed to be proportional to the standard deviation of decomposition coefficients, and it can be calculated by (2). It is the value of the enhancement function when the value of coefficient equals b. T^l_{khigh} is used to adjust the range of coefficients that belongs to the increasing enhancement area. It is the value of *f(x)* when $x = \frac{9}{c} + b$. It is supposed that T^l_{khigh} is proportional to T^l_{klow}. They meet the equation of $T^l_{khigh} = kT^l_{klow}$, k is a proportional coefficient.

$$T^l_{klow} = \frac{1}{2}\sqrt{\frac{1}{MN}\sum_{m=1}^{M}\sum_{n=1}^{N}\left(c^l_{\mathrm{k}}(m,n) - mean_c\right)^2} \tag{2}$$

3.3 The Parameters of the Nonlinear Function

As shown in (1), the enhancement function proposed by A.F. Laine has two parameters b and c. Some papers used this function to enhance images and achieved good results. But the values of b and c were taken as fixed values. It meant that the enhancement model was formed definitively. So coefficients of different scales or directions were processed in the same way, the advantages of multi-resolution analysis were not fully embodied in the model. The paper proposes to calculate the values of b and c adaptively according to the characteristics of coefficients in different scales and directions. Owing to obtain the values of b and c, nonlinear

equations should be solved. The two thresholds of the enhancement function have been determined according to the standard deviation of the coefficients of NSCT decomposition. So the equations can be formed as follows:

$$\begin{cases} f\left(T^l_{klow}\right) = T^l_{klow} \\ T^l_{khigh} = \dfrac{9}{c} + b \end{cases} \tag{3}$$

where $T^l_{khigh} = kT^l_{klow}$ and k is a constant between 1.5 and 3.

By solving the equations, it is possible to obtain the parameters b and c in different scales and directions. So the coefficients of different resolution are enhanced by varying model adaptively. It can bring the advantages of multi-resolution analysis into full play.

4 Experimental and Simulation

4.1 Comparison and Analysis of Enhanced Results

In order to test the enhancement effect of the proposed algorithm, we selected a test image and enhanced it using the proposed algorithm, NSCT enhancement algorithm with b and c taken as fixed values and NSCT enhancement algorithm with c as a fixed value but selected b adaptively. The enhancement results are shown in Fig. 3.

It can be seen that according to our subjective feelings, the enhancement effects of Fig. 3(c) and Fig. 3(d) have obviously differences, though they just use different way to set the value of b, as Fig. 3(c) sets b to a fixed value while Fig. 3(d) uses an adaptively selected value to substitute b. Thus, it is supposed that to calculate the thresholds of the enhancement model according to the coefficients of NSCT decomposition and then find the values of b and c of different scales and directions adaptively is an effective way to enhance images. The result of the proposed algorithm shown in Fig. 3(b) verifies the above judgment well. The details of the image processed by our algorithm have been well enhanced, while the background of the original image is well preserved and the contrast of the processed image is sprightlier.

4.2 Objective Evaluation of Enhancement Effect

In order to evaluate the effect of image enhancement objectively, it is necessary to select some evaluation parameters to do quantitative analysis. Different papers

Fig. 3 Contrast of enhancement effect of lena image. (**a**) Original image; (**b**) The proposed algorithm; (**c**) b = 0.1,c = 40; (**d**) c = 40,b selected adaptively

select various parameters and the discrimination criteria are not quite similar [7–10]. Our purpose is to examine whether the algorithm can effectively enhance the details and meanwhile suppress noise and maintain the background parts of the image. So we divide the pixels of the image into two kinds: background pixels and detail pixels. These two kinds of the pixels are evaluated separately. We define a parameter named Vr to compute the ratio of the variance of the detail pixels and variance of the background pixels. The relative value of original image's Vr and enhanced image's Vr can measure the effect of image enhancement. The greater the relative value, the stronger the enhanced level of detail compared to the background.

The evaluation parameters are calculated as follows:

1. Calculate the local variance value for each pixel in the original image.
2. Select the appropriate local variance threshold to distinguish between the background pixels and details pixels. Calculate the mean value of details pixels' local variance as DV1 and the mean value of background pixels' local variance as BV1. Compute the ratio of DV1 and DV2 as Vr1.

Table 1 Comparison of enhancement objective evaluation parameters

	b = 0.1, c = 40	b selected adaptively, c = 40	The proposed algorithm
Er	1.1170	1.1774	1.2332

3. According to the enhanced image, calculate the mean value of details pixels' local variance as DV2 and mean value of background pixels' local variance as BV2. Compute the ratio of DV2 and DV2 as Vr2.
4. Calculate the relative value of Vr1 and Vr2 as Er, and it can also be calculated directly by the following equation:

$$E_r = \frac{DV_1}{BV_1} : \frac{DV_2}{BV_2} \tag{4}$$

Through the above analysis we can see, the greater the ratio of DV and BV, the sharper the details to the background. If the value of Er is greater, it means the enhancement effect is more ideal. Table 1 shows the comparison of Er values of the algorithms using different way to define the value of b and c. Er of the proposed algorithm is larger, it means that it highlights the image details better.

5 Conclusion

This paper implements an adaptive nonlinear enhancement algorithm based on NSCT transform. Two thresholds of the nonlinear function are selected in accordance with the NSCT decomposition coefficients of the image, so the parameters of the function that determine the enhancement strength and range can be calculate adaptively in different scales and directions. The enhancement results simulated on matlab platform show that the proposed algorithm can enhance images obviously and stretch the image contrast. A new evaluation parameter of enhancement effect is defined to measure the enhancement strength of the details compared to the background of image. By objective evaluation, it can be seen that the proposed algorithm has better effect on stressing image details while effectively suppressing background noise and the background information is preserved well.

References

1. Do MN, Vetterli M (2005) The contourlet transform: an efficient directional multiresolution image representation. IEEE Trans Image Process 14(12):2091–2106
2. da Cunha AL, Zhou J, Minh ND (2006) The nonsubsampled contourlet transform: theory, design, and applications. IEEE Trans Image Process 15(10):3089–3100
3. Laine AF, Schuler S, Fan J, Huda W (1994) Mammographic feature enhancement by multi scale analysis. IEEE Trans Med Imag 13(14):725–740

4. Zong X, Laine AF, Geiser EA (1998) Speckle reduction and contrast enhancement of echocardiograms via multiscale nonlinear processing. IEEE Trans Med Imag 17(4):532–540
5. Dong L, Bing Y, Mei Y (2008) Image enhancement based on the nonsubsampled contourlet transform and adaptive threshold. Acta Electronica Sinica 36(3):527–530
6. Gang W, Liang X, Anzhi H (2007) Algorithm research of adaptive fuzzy image enhancement in ridgelet transform domain. Acta Optica Sinica 27(7):1183–1190
7. Panetta K, Agaian S, Zhou Y (2011) Parameterized logarithmic framework for image enhancement. IEEE Trans Syst Man Cybernet 41(2):460–473
8. Tang J, Liu X, Sun Q (2009) A direct image contrast enhancement algorithm in the wavelet domain for screening mammograms. IEEE J Sel Top Signal Process 3(1):74–80
9. Hong J-H, Cho S-B, Cho U-K (2009) A novel evolutionary approach to image enhancement filter design: method and applications. IEEE Trans Syst Man Cybernet 39(6):1446–1457
10. Jingbo X, Xiuqin S, Tao L (2009) Image enhancement based on the contourlet transform and mathematical morphology. Acta Optica Sinica 38(1):224–227

Sub-pixel Edge Detection Algorithm Based on the Fitting of Gray Gradient and Hyperbolic Tangent Function

Zilong Wei, Meirong Zhao, and Ying Tong

Abstract It is important for visual accuracy to position the edge of the image precisely. There proposed a new kind of sub-pixel edge detection algorithm which is based on the fitting of gray gradient and hyperbolic tangent function. Firstly, the Sobel operator is used to extract the edge of the input image crudely. And the gray gradient direction is struck point by point by using the preliminary extracted edge pixels. Then the sub-pixel edge position is obtained through the least squares method using the fitting of the hyperbolic tangent function on the gray gradient of the edge of the image.

1 Introduction

With the development of the image measurement technology, the applied research of vision measurement in various fields is becoming more and more concerned and attracted widespread attentions. The measuring principle of vision measurement system is that the geometrical parameters are obtained through processing the image of the edge of the object. There are some pixel edge detection methods such as the Sobel operator, the Laplacian operator and the Robert operator. They are in the form of a little simple and easy to implement, but the positioning accuracy is poor [1, 2]. Since the requirements of the measurement accuracy have increased, the pixel extraction cannot meet the needs of the actual measurement. A more

Z. Wei (✉) • M. Zhao
Sate Key Laboratory of Precision Measuring Technology & Instruments, Tianjin University, Tianjin, China
e-mail: zil000002@163.com

Y. Tong
Sate Key Laboratory of Precision Measuring Technology & Instruments, Tianjin University, Tianjin, China

College of Electronic and Communication Engineering, Tianjin Normal University, Tianjin, China

B. Zhang et al. (eds.), *The Proceedings of the Second International Conference on Communications, Signal Processing, and Systems*, Lecture Notes in Electrical Engineering 246, DOI 10.1007/978-3-319-00536-2_34,

precise edge extraction method which is named sub-pixel detection method is needed. To solve this problem, since the 1970s many experts have raised some valid sub-pixel methods. The domestic and international research on sub-pixel edge detection theory and technology can be summarized as interpolation [3], fitting [4], and moment method [5] in mathematics. There proposed a new kind of sub-pixel edge detection algorithm which is based on the fitting of gray gradient and hyperbolic tangent function. The coordinate system is established with gradation of image and the gradient direction. The pixel gray values of the pixel edge detection windows is processed through least squares fit using the hyperbolic tangent function in order that the sub-pixel edge detection can be achieved.

2 Fundamentals

2.1 Edge Detection Algorithm of Sobel

Sobel operator is a derivative of the edge detection operator. The core of the edge detection operator is the 3 × 3 horizontal and vertical Sobel operator which is made convolution with the selected image window in the same size for each pixel [6]. Calculate the horizontal and vertical gradient value. Then calculate a gradient according to the corresponding algorithms with the horizontal and vertical gradient. At last, the calculated gradient will be made a comparison with the threshold value which was set previously. The Sobel operator is defined to be:

$$\begin{aligned} s(i,j) &= |\Delta_x f| + |\Delta_y f| \\ &= |(f(i-1,j-1) + 2f(i-1,j) + f(i-1,j+1)) - (f(i+1,j-1) + \\ &\quad 2f(i+1,j) + f(i+1,j+1))| + |(f(i-1,j-1) + 2f(i,j-1) + \\ &\quad f(i+1,j-1)) - (f(i-1,j+1) + 2f(i,j+1) + f(i+1,j+1))| \end{aligned} \tag{1}$$

The following judgments can be made through selecting a appropriate threshold TH.

$$s(i,j) > TH$$

Then (i,j) is the step-like edge point and $s(i,j)$ is the edge image [7].

2.2 Fundamentals of the Fitting Operator

Firstly, the pixel level edge of the input image is extracted crudely using the Sobel operator. The gray gradient direction of the edge pixels which are extracted out preliminarily are struck point by point. And the directions are sorted into eight kinds

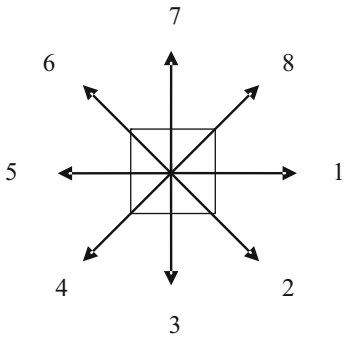

Fig. 1 Eight gray gradient of the crudely extracted edge pixel

of situations as shown in Fig. 1. For examples, when the results of a pixel gray gradient direction is given in the shaded area as shown in Fig. 2, it will be included in the gradient direction of the case 8.

Since the eight selected gradient directions and the eight neighborhood directions of pixel are in the same direction. The regular gradient direction is called "eight neighborhood gradient directions". The pixel gray gradient direction shows the gray-scale variation direction around the pixel which changes the most. So the tangent which is located around the edges of the pixel might be perpendicular to the gradient direction. According to this kind of consideration, the coordinate axes are established whose positive direction is the gradient direction based on the eight neighborhood gradient direction according to the edge point for the pixel and the pixel is the origin. Some numbers of pixels are selected on each side of the origin adding to the edge of the detection windows as shown in Fig. 3.

The red box is considered to be the edge pixel which is extracted through the Sobel operator. The coordinate of the pixel on the gradient direction represents for x-axis and the gray-scale of the selected pixel represents for y-axis. As the images collected in the project whose edge characteristics are significantly and most of the edges are step-edges, the pixel gray values of the pixel edge detection windows is processed through least squares fit using the hyperbolic tangent function as shown in Fig. 4.

The hyperbolic tangent function expression is defined to be

$$y(x) = -\frac{k}{2}\{\tanh[p(x-R)]\} + H \tag{2}$$

p is considered to be the fuzzy factor.

$$H = h + \frac{k}{2} \tag{3}$$

After the optimized solution, the parameter R is calculated. R is considered to be the offset of the position of sub-pixel edge and the axis origin of the gradient orientation. For example, the edge detection window is the one which is shown in

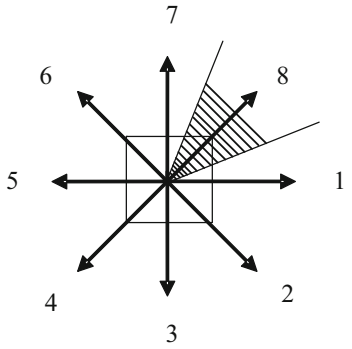

Fig. 2 The instance of structured gradient direction

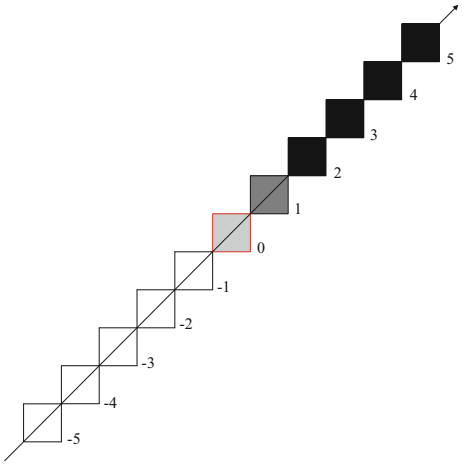

Fig. 3 Edge detection windows

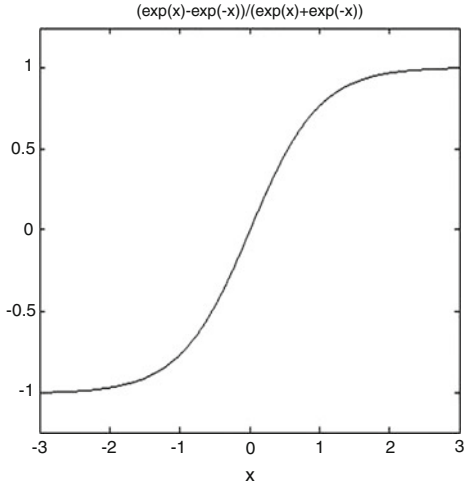

Fig. 4 Hyperbolic tangent function

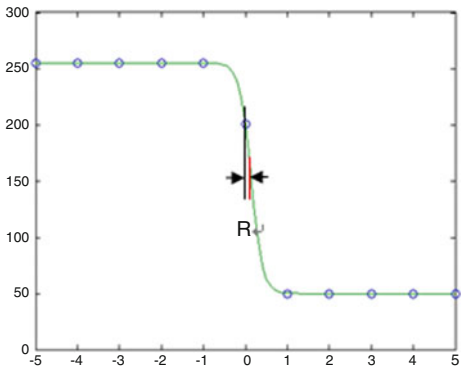

Fig. 5 The offset of the position of sub-pixel edge and the axis origin of the gradient orientation

Fig. 3. The value of R is calculated to be 0.1315 by fitting of the function as shown in Fig. 5.

3 Experiment and Result Analysis

3.1 Detection of Vertical Edges

In order to verify the stability and accuracy of the algorithm, industrial CCD camera is used to take photos of the checkerboard target in the experiment as shown in Fig. 6.

The size of each cell is designed to be the same. After measuring the dimensions of each cell through the image measuring instrument, the maximum error if less than 0.01 mm and it can meet the experimental needs. By imaging the target, a few cells in the center of the view are intercepted to be the experimental subjects in order to avoid the error caused by the presence of an imaging lens distortion near the edge of vision. The pixel-level edge shown in Fig. 7 is extracted by Sobel operator.

The three adjacent grids in the center of the view are selected to be the edge extraction subject among which the first grid and the third grid are black and the second one is white. The longitudinal edges are taken as the research objectives and the sub-pixel coordinate of the pixel coordinates extracted through Sobel operator are all extracted by means of the original image sub-pixel edge detection. The coordinates are shown in Table 1.

Since the edges extracted through this algorithm are sub-pixel-level edges and the smallest unit the computer can show is pixel when the pictures are displayed, sub-pixel edge detection results cannot be visualized by means of pictures shown directly. In order to show the extraction effects indirectly the sub-pixel edge positions are rounded to a whole pixel as shown Fig. 8.

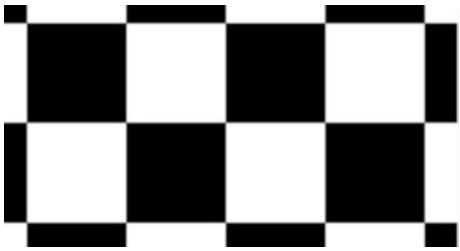

Fig. 6 The origin picture of the checkerboard

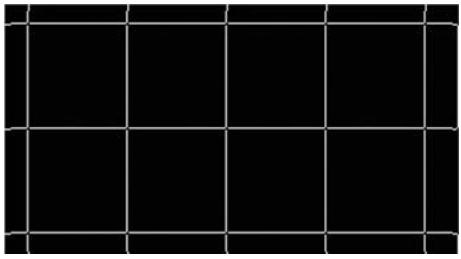

Fig. 7 Pixel-level result processed by Sobel operator

Table 1 The comparison between the average value of pixel-level edge position extracted by Sobel operator and the average value of sub-pixel-level edge position extracted by the operator in this paper

	1	2	3	4	5
The average value of pixel-level edge position extracted by Sobel operator	20	100	180	260	340
The average value of sub-pixel-level edge position extracted by the operator in this paper	19.4916	99.4916	179.4920	259.4920	339.4920

Fig. 8 Sub-pixel result structured to pixels

By comparison with pixel edge calculated by Sobel operator, the location calculated by sub-pixel algorithm of this article was similar to that calculated by Sobel operators. After cal calculating the difference between the adjacent edges, we got pixels of four adjacent cells and the width of each cell are80, 80.0004, 80 and80. The maximal relative error is 5×10^{-6} which can meet the accuracy requirements of sub-pixel edge detection.

Fig. 9 The rotated image

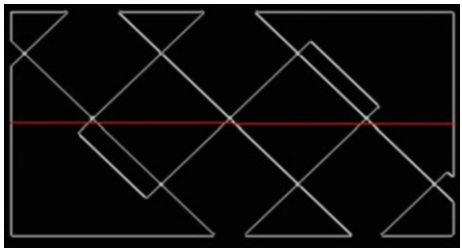

Fig. 10 Fig. 8 sub-pixel result structured to pixels

Table 2 The average value of pixel-level edge position extracted by Sobel operator

Pixel coordinate y	130	130	130
Pixel coordinate x	144	257	370

Table 3 The average value of sub-pixel-level edge position extracted by the operator in this paper

Sub-pixel coordinate y	129.492	129.154	130.085
Sub-pixel coordinate x	143.652	256.914	370.085

3.2 Edge Detection Direction of 45°

In the experiment above the width of the vertical edge is measured. In order to test if it is accurate when positioning a non-vertical edge the following experiment is processed. Firstly, rotate the origin image about 45°and the origin image will be like the image shown in Fig. 9. Secondly, extract the pixel edge of the rotated image using Sobel operator. Furthermore, extract the sub-pixel edge through the sub-pixel algorithm. Finally, the sub-pixel edge positions are rounded to a whole pixel as shown Fig. 10. Regard the two squares crossed by the red line as the research object. The coordinates of the intersections of the red line and the edges extracted separately through sub-pixel edge detection operator and the Sobel operator are listed in Tables 2 and 3.

The horizontal coordinate difference between two adjacent intersections is $\sqrt{2}$ times of the grid width. We can achieve that the width calculated through the Sobel operator are 80 and which calculated through sub-pixel detection operator are 80.001 and 80.004 the maximal relative error is 0.0005. Above all, the accuracy can satisfy the requirement.

4 Conclusions

There proposed a new kind of sub-pixel edge detection algorithm which is based on the fitting of gray gradient and hyperbolic tangent function in the paper. The first step is the crude extraction of gray image with the traditional edge extraction method. The second step is the construction of coordinate system with the axis of the gray gradient value and gray value on this base, then making least-squares fitting of data which is in the windows of pixel gray of pixel edge detection by the method of the hyperbolic tangent function, so as to achieve sub-pixel edge extraction. This calculation method is simple and rapid. The sub-pixel edge extraction has a high precision and meets the sub-pixel edge extraction accuracy requirements. Experiments show this algorithm has better stability properties of sub-pixel edge extraction and accuracy with a certain practical value.

References

1. Zou F, Li Z (2008) Performance comparison of image edge detection algorithms [J]. Comput Appl 28(1):215–219
2. Eiter T, Icz TL, Schindlauer R et al (2004) Proceedings of the ninth international conference on principles of knowledge representation and reasoning. American Association for Artificial Intelligence, Vienna, Austria, pp 141–151
3. Coleman SA, Scontney BW, Hwrron MG (2007) A validated edge model technique for the empirical performance evaluation of discrete zero-crossing methods. Image Vision Comput 25 (6):1315–1328
4. Angela C, Alfredo C, Remo S et al (2009) Hyperbolic tangent algorithm for periodic effect cancellation in sub-pixel resolution edge displacement measurement. Measurement 42 (4):1226–1232
5. Zhao P, Qiang G, Bang PZ (2009) Simultaneous perimeter measurement for multiple planar objects [J]. Opt Laser Technol 41(5):186–192
6. Yao L (2011) An improved Sobel edge detection operator. GuangXi Light Industry (05): 59–60
7. Chun-lan Y, Zong-long X (2009) Study of infrared image edge detection based on Sobel operator [J]. Laser Infrared (01):85–87

Self-Adaptive Image Transfer with Unequal Protection by Prioritized LT Code

YaXian Wang and Ting Jiang

Abstract The degree distribution of a fountain code is a key evaluation point. Good fountain codes should have low average degrees and fine performance. This paper suggests a way of allocating the source code based on the Robust Soliton Distribution. Input source codes firstly will have wavelet transformation, and then be encoded using unequal error protection (UEP) method with the improved prioritized LT code. Furthermore, a self-adaptive system is mentioned in the paper for saving system resource and a better decode effect.

Keywords Fountain codes • LT code • UEP • Degree distribution • Self-adaptive system

1 Introduction

The society requires tremendous and frequent information communications nowadays, and the media transmission on wireless channels is becoming hot research direction. M. Luby gave the paper which proposed LT code on 2002. This kind of fountain code is adaptive to a lot of kind of channel situations, such as deep space communication and multicast [7]. The LT code especially plays well when facing the BEC (Binary Erasure channel) channel, for it is a rateless packet oriented FEC (forward error correction) code with easy decode method. The decode process can start quickly after receiving several encoded codes that is just a little more than the original inputs. The BEC channel always performs its way on the application layer

Y.X. Wang (✉) • T. Jiang
Key Laboratory of Universal Wireless Communication, Ministry of Education, University of Posts and Telecommunications, Beijing, China
e-mail: cluster_wyx@163.com

B. Zhang et al. (eds.), *The Proceedings of the Second International Conference on Communications, Signal Processing, and Systems*, Lecture Notes in Electrical Engineering 246, DOI 10.1007/978-3-319-00536-2_35,

and transport layer, in where the data are always deleted because of congestion and loss.

The UEP (unequal error protection) method aims at giving extra protection to important data during transmission [3]. The method is widely used in media stream, such as H.264 formation video transmission. Its P and B frame carrying the key information of the video hence need more protect. As for the images, progressive images are sensitive to the channel environment, a little mistake leads to big errors, transporting effective and robust images is a big challenge [6], if we use the one-dimensional wavelet decomposition, the whole image will be differentiated into many parts; the top ones are low-frequency component, then comes the low-frequency part of the high-frequency component, and so on. The quantum of the components depends on scale of the wavelet. The low-frequency part carries more important messages than the high part.

Now there are many ways of improvements for LT code. Such like the way mentioned in literature [4] for Raptor Codes and literature [2] for prioritized UEP LT code. This passage have similar considers to literature [2], but the way of allocating codes is improved. This paper propose an idea that we can assure the transport of the important part by formulating the mean value of this part, and before its transport some of the unnecessary data should be abandoned, so we will get a stair-step UEP level shape while do not change the structure of original degree distribution function. The paper gives out a detailed description of this method in Sect. 2, and theoretical analysis about it in Sect. 3. Section 4 provides the simulation results and comparison between results of the theory and simulation.

2 Improved UEP LT Code and the Self-Adaptive System

2.1 The Robust Soliton Distribution of the LT Code

The literature [1] has detailed description of the Ideal Soliton Distribution and Robust Soliton Distribution of the LT code. This paper is related with the Robust Soliton Distribution and its expression is as below:

For $\forall\ i = 1, 2, \ldots, k$, there are:

$$\mu(i) = \frac{\rho(i) + \tau(i)}{\beta} \tag{1}$$

Here, $\beta = \Sigma_{i=1}^{k} \rho(i) + \tau(i)$, ρ(i) is the Ideal Soliton Distribution, and k is the amount of the encode element:

$$\rho(i) = \begin{cases} \frac{1}{k}, i = 1 \\ \frac{1}{i(i+1)}, i = 2, 3, \ldots, k \end{cases} \tag{2}$$

We define $R = c\ln(\frac{k}{\delta})\sqrt{k}$, in where c is a constant that is greater than 0. δ represents the fail probability of decoding. Then the final expression is:

$$\tau(i) = \begin{cases} \frac{R}{ik}, i = 1, 2, \ldots, \frac{k}{R} - 1 \\ \frac{Rln\frac{R}{\delta}}{k}, i = \frac{k}{R} \\ 0, others \end{cases} \tag{3}$$

For fountain codes, the degree distribution function decides its way of encoding and the proportion of the encode elements belongs to different degrees. The quantity of d1 and d2 codes stand an important role and always decide the performance of the whole code. Too much d1 codes slow down the process, while too little d1 codes may break it. The same principle works for d2 codes. For detailed way of making codes please refer to literature [1].

2.2 The Improved UEP Prioritized LT Codes

The idea is similar to literature [2] that we can change the protect strength by changing the allocation method of degrees of the important data area into another special one. What's different is this paper suggest that we use a sequential allocate in important data area, so there is no way to get loose to a source code nor send the repeated ones. During the process, we sort the data according to the structure of the Robust Soliton Distribution so that we do not change the structure of the function. There will always be enough data ripples for decoding.

This paper uses an image source that has 4-level wavelet decomposition. The data will be parted into four parts as decomposed: the most important data $\{S_{(H,H)}\}$, corresponding to the lowest frequency part; less important data$\{S_{(H,L)}\}$, corresponding to the higher frequency part beside the $\{S_{(H,H)}\}$; normal data $\{S_{(L,H)}\}$, the higher level of the front ones and unnecessary data $\{S_{(L,L)}\}$, the highest frequency ones. The structure is shown as Fig. 1.

The detailed process is as follows:

Firstly we discard a part of data in the $\{S_{(L,L)}\}$. E_ξ, the mean times of appearance of $S_{(H,H)}$ symbols, should be set according to the channel condition.

When $d = 1$, we select code from $\{S_{(H,H)}\}$ by sequence to make the d1 code. For a specified sized image, the quantity of $\{S_{(H,H)}\}$ symbols is identified. We also can adjust the Robust Soliton Distribution by modifying δ and c to make the proportion

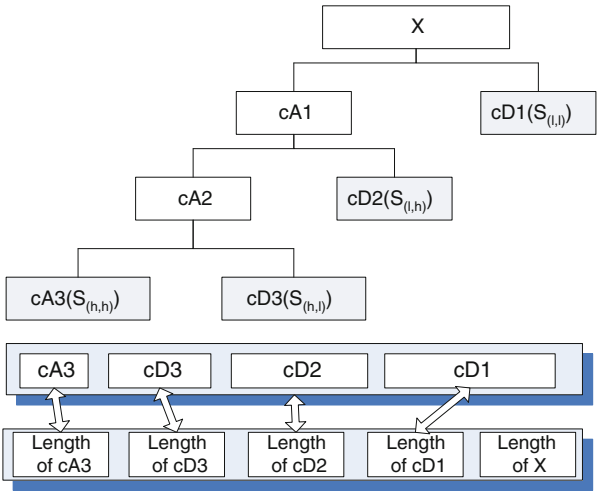

Fig. 1 Structure of the four level wavelet decomposition

of d1 codes close to the proportion of $\{S_{(H,H)}\}$' s. For example, the 256 × 256 image has the property as below:

$$u_{S_{(H,H)}} \approx 0.06$$

$$u_{A=} \frac{1+R}{k \cdot \beta}$$

But there're always a little more $\{S_{(H,H)}\}$ than d1 codes. So we have to assort a part of d2 codes for the rest of $\{S_{(H,H)}\}$ and still the process is by sequence, and the other symbols used to make one d2 code are selected randomly from the whole dataset $\{S\}$. Then we choose $(E_\xi - 1)\xi$ symbols from $\{S_{(H,H)}\}$ randomly, and mark it as $\{\Delta S_{(H,H)}\}$. We start the d2 encoding with $\{\Delta S_{(H,L)}\}$ and $\{\Delta S_{(H,H)}\}$, after the $\{\Delta S_{(H,H)}\}$ have been used up, we turn to use $\{S\}$ randomly again with the rest $\{S_{(H,L)}\}$ to make other d2 codes. These processes are all done in sequence. The trace work will follow the normal way of Robust Soliton Distribution. The flow chart.

2.3 The Self-Adaptive System

The wireless channel condition changes frequently and shows a non-stable property, the error rate changes from good to bad, so we need a system that can perform differently as the situation turns. We can say that the fountain codes will always decode every symbol by 0 % error rate when there are enough resources. The enough resource means the amount of symbols that the system can receive is not limited (Fig. 2).

The unlimited system lead to lots of resource waste when we don't ask for a 100 % correct image. This is because the fountain code can start decoding when it

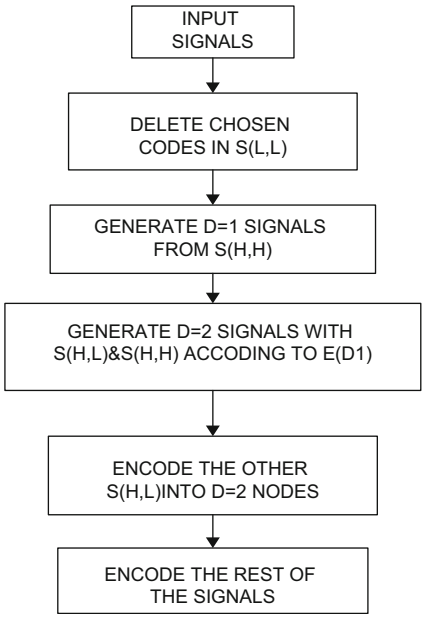

Fig. 2 Flow chart of PLT codes

receives encoded codes a little more than source codes, and the decode speed arise rapidly when the receive amount enters the tornado area [5]. When more and more codes are received, the process slows down, in the end when there are little code to decode, the proportion of receiving codes and the code to be decoded will become too large to waste the system resource. Also, it's not realistic to make the unlimited system. So we should adjust the number of received encoded codes (N) to takes control of the quality of images. We can collect the channel's erase rate during periods and change N to adapt it. The flow chart is shown in Fig. 3.

3 Analysis of the PLT code

3.1 Error Rate Analysis

The error may appear in two kind of situations when there are enough codes for decoding: the channel's error and the miss of source code when encoding. We suppose the channel is BEC, and the erasure rate is e_w. Because we randomly XOR the codes together from the $\{S_n\}$ to make the encoded codes $\{K_n\}$, so there are possibilities to miss several $\{S_n\}$ codes, which means there are some $\{S_n\}$ codes that are not chosen to participate in encoding process. Let us set this possibility as δ. If there are $\xi\ S_{(H,H)}$ code, and $\xi_{HL}\ S_{(H,L)}$ code, and the directly deleted S_d codes. Then we get $S_\Delta = S - \xi - \xi_{HL} - S_d$ and $\Delta S = S - S_d$. For the PLT coding, we don't

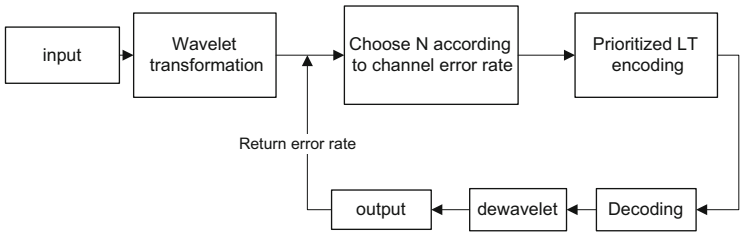

Fig. 3 Flow chart of the whole system

miss source code among $\{S_{(H,H)}\}$ and $\{S_{(H,L)}\}$ codes when encoding. Set the N_Δ to be the number of the unprotected data:

$$N_\Delta = N - E_\xi - [\xi_{HL} - (E_\xi - 1)\xi] \tag{4}$$

Error rate of the unprotected part { $S_{(L,H)}$+$S_{(L,L)}$}:

$$E_1 = \frac{N_\Delta}{N} e_w \cdot \left(1 - \frac{1}{\Delta S}\right)^{N_\Delta} + \frac{S_\Delta}{\Delta S} \cdot \left(1 - \frac{1}{S_\Delta}\right)^{N_\Delta} \tag{5}$$

Error rate of the special protected part $\{S_{(H,H)}\}$:

$$E_2 = \left(\frac{\xi \cdot e_w}{\Delta S}\right) \cdot \left(1 - \frac{1}{\Delta S}\right)^{N_\Delta} \cdot \left[\frac{(E_\xi - 1)}{E_\xi} + \frac{1}{E_\xi}\right] \tag{6}$$

Error rate of the normal protected$\{S_{(H,L)}\}$:

$$E_3 = \frac{\xi_{HL}}{\Delta S} \cdot e_w \cdot \left(1 - \frac{1}{\Delta S}\right)^{N_\Delta} \tag{7}$$

Then we can get:

$$e_{pLT} = E_1 + E_2 + E_3 \tag{8}$$

We'll have a contrast with the LT code:

$$e_{LT} = (e_w + 1) * \left(1 - \frac{1}{S}\right)^{N} \tag{9}$$

Seeing d and e, the different error rate of unprotected part and $\{S_{(H,L)}\}$ part in LT and PLT code reflects in ΔS and ΔN. The $\{S_{(H,H)}\}$ part have an extra coefficient, and the coefficient is a monotone decreasing function by increasing of E_ξ and it's value is always beneath 1. So it's easy to know that d $<$ e. For further derivation we

can find that the $\{S_{(H,H)}\}$ part has an error rate that is $\frac{1-e_w}{E_\xi}$ times less than its corresponding part in LT codes.

3.2 Self-Adaptive System Analysis

When N is big enough, if we want to limit the error rate to $e_r < \varepsilon_0$ beneath the channel with e_w erasure rate, there are:

$$E_1 + E_2 + E_3 < e_r \tag{10}$$

But if N is not big as we respected, the $\left(1 - \frac{1}{\Delta S}\right)^{N_\Delta}$ (set as ε) part in (4)–(6) equation should be replaced by the fail possibility φ. Error rate increases greatly in this stage. So the whole distribution function of error rate is decided by N:

$$\varphi = \begin{cases} f(\varepsilon), N > N_0 \\ g(\varphi), N > N_0 \end{cases} \tag{11}$$

Here, N_0 is the threshold of the amount needed to satisfy the decoding need. It is related with e_w. It's easy to know that when e_w is large, N_0 is large, assuming that the other situations remain stable. So the system should choose different N with different e_w to reach the best coding effect. The rule between N and e_w can be got by simulation.

4 Simulate and Result

This paper use a 256 × 256 lena image for simulation. The error rate verifies from 0.01 to 0.1. Firstly we assume that the resource is limited and cannot reach N_0. Set $N = 1.4S$. Set $\delta = 0.05$.

As we can see in the simulation result in Fig. 4, when $e_w > 0.04$, $N < N_0$, the N is not large enough for decoding process and error rate arise rapidly. The PLT code has a little better performance than the LT code for the total data area.

When it comes to the protected part, the $\{S_{(H,H)}\}$ area, we can see that the PLT code obviously works out a better performance than LT code in Fig. 5. With the same e_w, the error rate of LT code is almost two times higher than the PLT code. This proved that the PLT code can give extra protection to the important data.

When the other condition maintains same as usual, for different e_w, the N needed for successfully decoding also changes. Figure 6 shows the proportion of $\frac{E(N)}{S}$ the PLT code needs to be decoded under different e_w. We run 100 times simulation for N under every e_w from 0.01 to 0.1 and obtain the mean value of N, $E(N)$. It can be seen that the $E(N)$ increases with the rise of e_w.

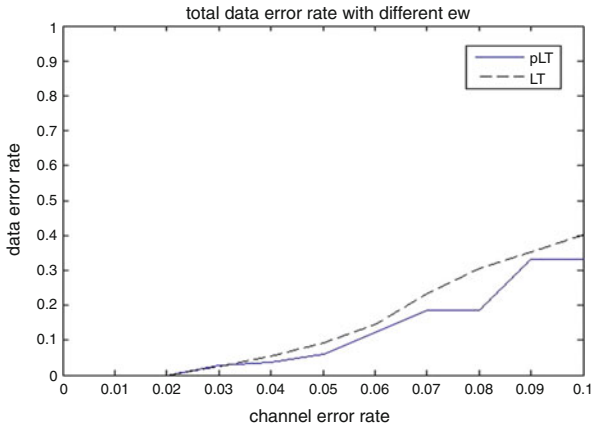

Fig. 4 Total data error rate with e_w

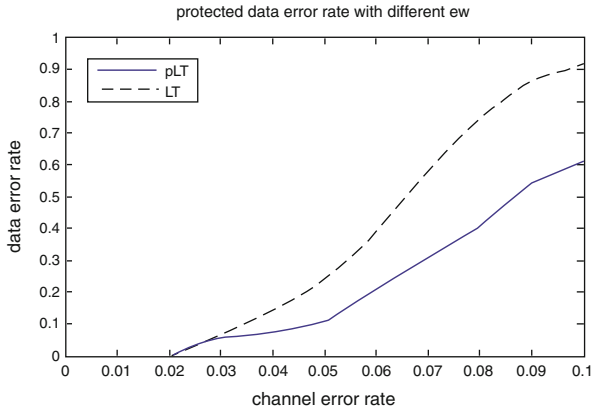

Fig. 5 Protected data error rate with e_w

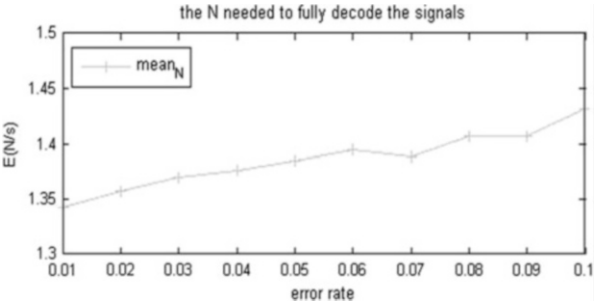

Fig. 6 $\frac{E(N)}{S}$ needed to fully decode the signals

Therefore, when we get different e_w feedback of the system, we change the most suitable N to finish the whole process, so that we can get the best image transport effect with least codes amount.

Fig. 7 LT and PLT image when N = 315 × 256

What's more, for the PLT code abandons a part of unnecessary data, the real N needed is much smaller than LT code. Figure 7 shows the images we can receive by LT and PLT code when N=315 × 256.

It's clearly that the LT code can hardly decode out the image with 315 × 256 decoding bit while the PLT code works well with some noise line that do not affect the whole image.

5 Conclusions

We can see that the PLT code gives rank higher protection for important data, and need less encoded codes to reorganize the original image. The performance is good especially in a bad channel condition such like wireless channel condition. So this improvement is available with better error correct feature for special data part and has a lower complexity in decoding process.

Acknowledgment This work was supported by Important National Scenes & Technology Specific Projects (2010ZX03006-006) and NSFC (61171176).

References

1. Luby M (2002) LT codes. In: Proceedings of the 43rd annual IEEE symposium on foundations of computer science (FOCS), Vancouver, BC, Canada, 2002, pp 271–280
2. Woo SS, Cheng MK (2008) Prioritized LT codes. Information sciences and systems, (CISS 2008), 42nd, pp 568–573
3. Rahnavard N, Vellambi BN, Fekri F (2007) Rateless codes with unequal error protection property. Proc IEEE Trans Inf Theory 53(4):1521–1532
4. Shokrollahi A et al (2007) Raptor codes. IEEE T Inf Theory 580:2551–2567

5. Lin Guang Rong, Lin Xin rong, Yi Na, Jin Ye, Liang Qin lin (2008) Digital fountain base on LDPC code. J Electron Inform Technol 30(4):822–825
6. Zhao-kai, Cui Hui-juan, Tang-kun (2012) Joint source-channel coding of progressive images for complicated wireless channel environments. J Tsinghua Univ (sci & Tech) 52(3): 25–27
7. Li Shan (2008) Research on the combination and optimization of digital fountain code and superposition code in wireless multicast systems, D. Wu Han University 13–15

Part III
Circuit Processing System

Detection Accuracy Comparison Between the High Frequency and Low Frequency SSVEP-Based BCIs

Zhenghua Wu and Sheng Su

Abstract Steady-state visually evoked potential (SSVEP) based brain-computer interface (BCI) is frequently discussed in recent years for its potential benefits to the disabled person, and some works using high frequency stimulus have been launched for the past few years. In these works, only one or a few special electrodes were selected as the signal electrode. In this work, all electrodes are used as the signal electrode, and it is found that, although the absolute amplitude of high frequency SSVEP is weaker than that of low frequency SSVEP, there is no significant difference of the relative amplitude between the high frequency and low frequency SSVEP, which leads to a similar detection accuracy of them.

Keywords Steady-state visually evoked potential (SSVEP) • Brain-computer interface (BCI) • High frequency stimulus • Low frequency stimulus

1 Introduction

SSVEP-based BCI systems have been widely discussed in recent years for it can bring benefits to the disabled person [1–4]. These systems have two important features compared to other BCIs [5, 6]. The first is its high signal/noise ratio (SNR)

Z. Wu (✉)
School of Computer Science and Engineering, University of Electronic Science and Technology of China, ChengDu 610054, China

Key Laboratory for NeuroInformation of Ministry of Education, School of Life Science and Technology, University of Electronic Science and Technology of China, ChengDu 610054, China

Department of Biomedical Engineering, University of Florida, Gainesville, FL 32611, USA
e-mail: wzhzxwz@sina.com

S. Su
School of Computer Science and Engineering, University of Electronic Science and Technology of China, ChengDu 610054, China

B. Zhang et al. (eds.), *The Proceedings of the Second International Conference on Communications, Signal Processing, and Systems*, Lecture Notes in Electrical Engineering 246, DOI 10.1007/978-3-319-00536-2_36,

and the second is its high transfer rate. This is because many stimulating frequencies can be applied in the same system, and SSVEP of each frequency can be extracted from a short period such as 2–3 s with a high accuracy. According to the formula of computing transfer rate, a relatively high transfer rate can be achieved [7].

In these SSVEP-based BCIs, the stimulating frequencies were almost located at the low frequency band [2–4, 8]. A widely quoted work used frequencies from 6 to 14 Hz as stimuli [2], and another new work with two targets used 8 Hz and 13 Hz as stimuli [4]. However, flicker with low frequency is harmful to person's eyes, it can lead to dizziness and fatigue, and it can probably induce epilepsy for some persons [6, 9].

Only a few works have used the high frequency stimulus [6, 9]. In these works, normally one or a few special electrodes were selected as the signal electrode and the reference electrode, and were used under any frequency stimulus, and 35–45 Hz stimulus around were proved to be valid both at the detection accuracy and decreasing the feeling of flickering. In one of these works [9], one optimum reference was selected first for each stimulating frequency, and then one optimum signal electrode was selected, the results showed the SNR of SSVEP had a similar curve to SSVEP amplitude in different frequency bands.

In this work, all electrodes were looked as the signal electrodes, Cz was selected as the reference, the SSVEPs in high β band were compared to that in α band and θ band, the results showed the absolute amplitude of high frequency SSVEP is smaller than that of low frequency SSVEP, but there was no significant difference between the relative amplitudes. And the result about the relative amplitude was absolutely different from the previous work in which the relative amplitude had a property of three SSVEP subsystems [9]. When using the sum of relative power as an indicator of SSVEP, there was no significant difference between the detection accuracies of different frequency SSVEPs.

2 Methodology

2.1 Data Acquirement

Eleven subjects with normal sight or corrected normal sight took part in this experiment. They were seated 60 cm from the stimulator in front of them. EEG was collected by a EGI system with 129 electrodes, and Cz (No.129) electrode was selected as the reference. 40 s length spontaneous EEG data were collected first, then 40 s length SSVEP data were collected for each stimulating frequency. There were totally six frequencies used as the stimulus, i.e. 33.33, 25, 16.67, 12.5, 8.33, and 6.25 Hz.

2.2 SSVEP Gain

Because SSVEP was relative immunity to noise such as the eyes movement or body movement, no other pre-process was applied on SSVEP data.

FFT was applied on 40 s spontaneous EEG. The power corresponding to each stimulating frequency was divided by the average power of the band ± 1 Hz around the stimulating frequency to get the relative power of this frequency, and the sum of relative power at each electrode was used as a threshold for the corresponding frequency SSVEP.

Then FFT was applied on 40 s SSVEP, the same method as above was adopted to get the sum of SSVEP relative power, and this relative power was divided by the corresponding threshold to get SSVEP gain. This SSVEP gain can be used to judge whether EEG included SSVEP. On the other hand, the SSVEP gain of different frequency was compared to each other. The comparison results can be used to evaluate the evoking effectiveness of high frequency and low frequency stimulus.

2.3 SSVEP Detection Accuracy

The spontaneous EEG and SSVEP were both divided into 2 s length segments, and FFT was applied on these segments. The same method as that in Sect. 2.2 was applied on each segment. For spontaneous EEG segment, the relative power of all frequencies were computed. Then the relative power of each frequency were averaged across all the segments to get the corresponding threshold of that frequency. For each SSVEP segment, the relative power of all frequencies were computed. These relative powers in each segment were used to judge whether this segment included SSVEP.

In order to check the difference significance between different frequencies, the one way analysis of variance (ANOVA) was applied, and the significance level was set to 0.05.

3 Result

3.1 SSVEP Power Comparison Under Different Frequency Stimulus

The absolute power of high frequency SSVEP was smaller than that of low frequency SSVEP, significantly. The relative power of 12.5 Hz was significantly bigger than that of other frequencies, for example, the ANOVA result was ($F(1,20) = 9.23, p = 0.006$) between 25 and 12.5 Hz. While there was no significant

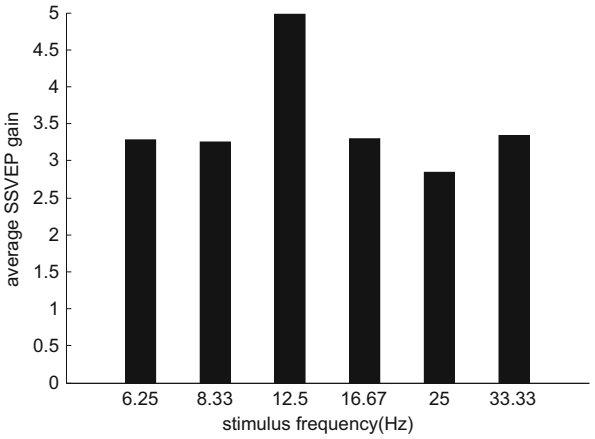

Fig. 1 Mean SSVEP gain for all subjects under different stimulating frequency

difference between the relative power of other frequencies, for example, the ANOVA result was ($F(1,20) = 0.64$, $p = 0.43$) between 33.33 and 25 Hz. The average SSVEP gain for all subjects under each frequency was shown in Fig. 1.

3.2 Detection Accuracy Under Different Stimulating Frequency

Except the 25 Hz detection accuracy was significantly lower than that of 8.33 Hz ($F(1,20) = 7.2$, $p = 0.01$), there were no significant difference between the other detection accuracies. For example, the ANOVA result was ($F(1,20) = 0.15$, $p = 0.7$) between 33.33 and 16.67 Hz, ($F(1,20) = 1.77$, $p = 0.2$) between 33.33 and 12.5 Hz. Figure 2 shows the average detection accuracy for all subjects at all stimulating frequencies.

4 Discussion

The power of background EEG in high frequency band decreases dramatically, so the SNR of SSVEP in high frequency holds at the similar level as that in low frequency. This result is consistent with Wang's work to some extent, but there are some important differences [9]. Although only six frequencies were checked, it is clear that the result is completely not consistent with the three SSVEP subsystem curves in Wang's work.

From Fig. 1, it can be found there indeed was some difference between the detection accuracy of different frequencies. Generally, the detection accuracy in high frequency band was a little lower than that of low frequency band, but not

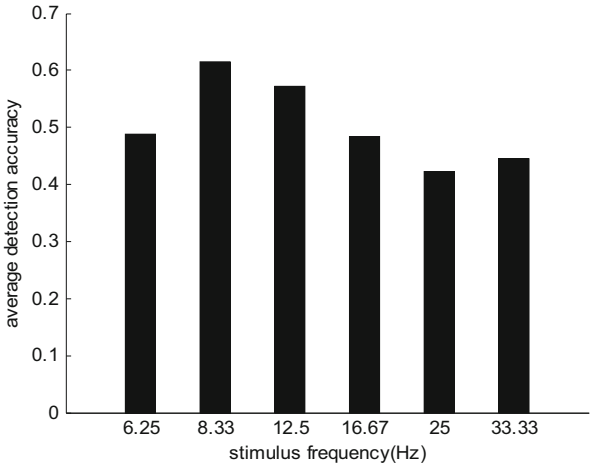

Fig. 2 The mean SSVEP detection accuracy for all 11 subjects at 6 stimulating frequencies

significantly. As for the low accuracy of 25 Hz, it can be because the second harmonic has not been taken into account for sake of power frequency. Compared to decreasing the feeling of flickering, the price of a little decreasing accuracy using high frequency stimulus can be acceptable. So high frequency SSVEP-based BCI is promising.

Selecting all the electrodes as the signal electrode has a great benefit compared to selecting only one or a few electrodes as the signal electrode. First, the optimum electrode may be different for each subject for the inter-subject difference of SSVEP. Second, for the travelling property of SSVEP [10], the optimum electrode for different stimulus frequency may be different. For high frequency stimulus, although the relative SSVEP amplitude in the occipital area can be smaller than that of low frequency SSVEP, the sum relative power on the whole scalp was similar to each other, so a similar detection accuracy can be gotten.

5 Conclusion

This work has proved that if using the whole electrodes around the scalp as the signal electrode, a high SNR of the high frequency SSVEP can be gotten, then a similar detection accuracy to the low frequency stimulus can be resulted.

Acknowledgements The work was supported by Science and Technology Bureau of Sichuan Province (#2013GZ0017).

References

1. Bin G, Gao XR, Yan Z et al (2009) A nonline multi-channel SSVEP-based brain–computer interface using a canonical correlation analysis method. J Neural Eng 6:1–6
2. Cheng M, Gao XR, Gao SK et al (2002) Design and implementation of a brain-computer interface with high transfer rates. IEEE Trans Biomed Eng 49(10):1181–1186
3. Luo A, Sullivan TJ (2010) A user-friendly SSVEP-based brain–computer interface using a time-domain classifier. J Neural Eng 7:1–10
4. Ortner R, Allison BZ, Korisek G et al (2011) An SSVEP BCI to control a hand orthosis for persons with tetraplegia. IEEE Trans Neural Syst Rehabil Eng 19(1):1–5
5. Friman O, Volosyak I, Graser A (2007) Multiple channel detection of steady-state visual evoked potentials for brain-computer interfaces. IEEE Trans Biomed Eng 54(4):742–750
6. Volosyak I (2011) SSVEP-based Bremen-BCI interface-boosting information transfer rates. J Neural Eng 8:1–11
7. Shanon CE, Weaver W (1964) The mathematical theory of communication. University of Illinois Press, Urbana, IL
8. Cheng M, Gao XR, Gao SK et al (2005) Stimulation frequency extraction in SSVEP-based brain-computer interface 2005. First international conference on neural interface and control proceeding, p 64–67
9. Jun WY, Ping WR, Gao XR et al (2005) Brain-computer interface based on high-frequency steady-state visual evoked potential. 2005 First international conference on neural interface and control
10. Burkitt GR, Silberstein RB, Cadusch PJ et al (2000) Steady-state visual evoked potentials and travelling waves. Clin Neurophysiol 111:246–258

A New Simulated Floating Inductor Synthesized by Nodal Admittance Matrix Expansion

Lingling Tan, Xin Guan, Jianfu Teng, and Kaihua Liu

Abstract This paper demonstrates the method of symbolic circuit design using nodal admittance matrix (NAM) expansion. A new simulated inductor synthesized by NAM expansion is applied in the design of seventh-order Butterworth LC lowpass filter, the simulation results by Spice verify the effectiveness of the proposed circuit design method.

1 Introduction

The pathological elements, that are the nullator, the norator, the voltage mirror and the current mirror [1], have extremely enriched the theory of active network synthesis. The popularity of their usage is for their ability to construct behavioral model [2] and the simplicity to implement nodal analysis (NA) [3] method. Characteristic investigation of the pathological elements [4] demonstrates their possibility to be applied in circuit analysis [5] and circuit synthesis [6], while circuit synthesis is the reverse process of circuit analysis. Method of nodal admittance matrix (NAM) expansion [7] has been proposed and provided us with a new approach to circuit design [8], which is a method different from the conventional generation methods.

In actual circuit design, LC network has been widely applied to the realization of transfer function with conjugated poles in s plane, which makes the frequency response characteristics of the circuit have excellent selectivity. However, realization of the simulated inductor [9] has been investigated to conquer the hard integration of the inductive element in the low frequency for its big volume and low Q.

L. Tan • X. Guan (✉) • J. Teng • K. Liu
School of Electronic Information Engineering, Tianjin University, Tianjin, China
e-mail: guanxin@tju.edu.cn

B. Zhang et al. (eds.), *The Proceedings of the Second International Conference on Communications, Signal Processing, and Systems*, Lecture Notes in Electrical Engineering 246, DOI 10.1007/978-3-319-00536-2_37,

This paper proposed a new simulated inductor synthesized by the theory of NAM expansion, operational amplifier realization of the floating three-terminal nullor in reference [10] is used to simulate the inductor.

2 A Synthesized Simulated Inductor Using NAM Expansion

2.1 Method of NAM Expansion

Gaussian elimination can be implemented on line-by-line basis by performing combinations of element-by-element operations, as illustrated in (1). However, pivotal expansion, as illustrated in (2), is the reverse process of Gaussian elimination, which is the tool of NAM expansion [11]. That is, a $p \times p$-port admittance matrix can be expanded to an $n \times n$-port nodal admittance matrix by pivotal expansion, for which, the dimension of the original matrix is increased.

$$\left[\begin{array}{cc:c} a & e & -b \\ \hdashline -c & -f & \boxed{d} \end{array}\right] \rightarrow \left[\begin{array}{cc} a-\frac{b\times c}{d} & e-\frac{b\times f}{d} \end{array}\right] \tag{1}$$

$$\left[t+\frac{rq}{s}\right] \rightarrow \left[\begin{array}{cc} t+\frac{rq}{s} & 0 \\ 0 & 0 \end{array}\right] \rightarrow \left[\begin{array}{cc} t & \mp q \\ \pm r & \pm s \end{array}\right] \tag{2}$$

The element of nullor [12] is introduced to a matrix after adding rows and columns with zeros without affecting the terminal characteristics of the original port matrix [13]. That means, a norator can be connected between node n and an arbitrary node m (including the port node and the reference node), for input current $I_n = 0$, and a nullator can be connected between node k and an arbitrary node j (including the port node and the reference node), which made the voltage of k is equal to the voltage of node j, as shown in matrix (3). Based on the elements shift theory, elements in the rows connected by a norator can shift between the two rows but in the same column, also elements in the columns connected by a nullator can shift between the two columns but in the same row.

$$\begin{bmatrix} y_{11} & y_{12} & \cdots & y_{1j} & \cdots & y_{1k} & \cdots & y_{1N} \\ y_{21} & y_{22} & \cdots & y_{2j} & \cdots & y_{2k} & \cdots & y_{2N} \\ \vdots & \vdots & \cdots & \vdots & \cdots & \vdots & \cdots & \vdots \\ y_{m1} & y_{m2} & \cdots & y_{mj} & \cdots & y_{mk} & \cdots & y_{mN} \\ \vdots & \vdots & \cdots & \vdots & \cdots & \vdots & \cdots & \vdots \\ y_{n1} & y_{n2} & \cdots & y_{nj} & \cdots & y_{nk} & \cdots & y_{nN} \\ \vdots & \vdots & \cdots & \vdots & \cdots & \vdots & \cdots & \vdots \\ y_{N1} & y_{N2} & \cdots & y_{Nj} & \cdots & y_{Nk} & \cdots & y_{NN} \end{bmatrix} \tag{3}$$

2.2 A Synthesized Simulated Inductor

A 2-port admittance matrix representing a floating inductor with value $L_{eq} = CR_1R_2$ is in the left form of matrices (4). Assume a capacitor and two resistors are used to synthesize the inductor. After once pivotal expansion, the 2-port admittance matrix is expanded to a 3 × 3 matrix.

$$\begin{bmatrix} \frac{1}{sL} & -\frac{1}{sL} \\ -\frac{1}{sL} & \frac{1}{sL} \end{bmatrix} \rightarrow \begin{bmatrix} \frac{G_1G_2}{sC} & -\frac{G_1G_2}{sC} \\ -\frac{G_1G_2}{sC} & \frac{G_1G_2}{sC} \end{bmatrix} \rightarrow \left[\begin{array}{cc:c} 0 & 0 & G_2 \\ 0 & 0 & -G_2 \\ \hdashline -G_1 & G_1 & sC \end{array}\right] \tag{4}$$

Expand the right matrix of (4) through node adding, nullor adding and the element shift theory in Sect. 2.1. By two adding nullators, -G_1 and G_1 are moved to the fourth and the fifth column respectively, then by an adding norator, -G_1 and G_1 are moved from the third row to the fifth row, another norator is used to move G_1 and -G_1 from the zero row to the fourth row. Similarly, element G_2 is processed as element G_1 to appear in the form of floating. Based on the operation above, matrix (5) describing a circuit with four nullors and three passive elements is deduced, while the circuit topology containing nullors is shown in Fig. 1.

$$\left[\begin{array}{cc:ccccc} 0 & 0 & 0 & 0 & 0 & 0 & 0 \\ 0 & 0 & 0 & 0 & 0 & 0 & 0 \\ \hdashline 0 & 0 & sC & 0 & 0 & 0 & 0 \\ 0 & 0 & 0 & G_1 & -G_1 & 0 & 0 \\ 0 & 0 & 0 & -G_1 & G_1 & 0 & 0 \\ 0 & 0 & 0 & 0 & 0 & G_2 & -G_2 \\ 0 & 0 & 0 & 0 & 0 & -G_2 & G_2 \end{array}\right] \tag{5}$$

2.3 Circuit Realization of the Simulated Inductor

Nullor has been widely applied in circuit analysis [14, 15] and synthesis [16] for its popularity and capacity in behavioral modeling [17] of the active blocks. The combination of a nullator and a norator with a common node, as shown in Fig. 2

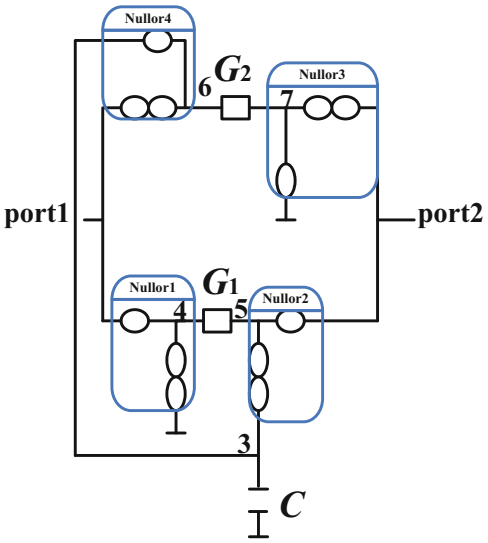

Fig. 1 The synthesized circuit topology of the simulated inductor

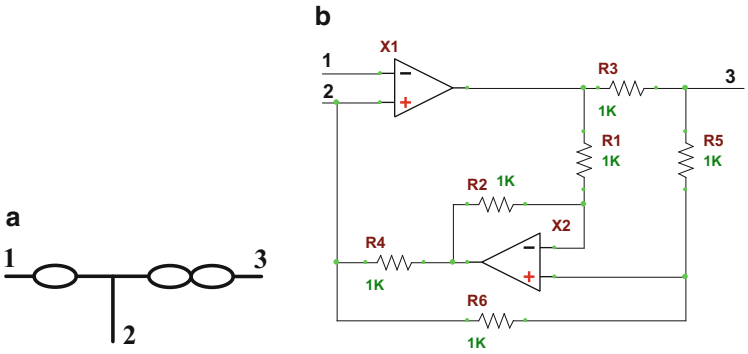

Fig. 2 (**a**) The floating three-terminal nullor (**b**) Operational-amplifier realization of floating three-terminal nullor in reference [10]

(a), names the floating three-terminal nullor, which can model the ideal transistor [18]. However, the ideal transistor with trans-conductance G_m approaching to infinity can not be realized in practical circuit design. It is desirable to construct the floating three-terminal nullor for simulation and measurement of practical designed circuit. So nullor 2, 3, 4 in Fig. 1 can be replaced with its realization of the operational amplifiers in reference [10], as shown in Fig. 2b. While the combination of a nullator and a norator connected with the ground can be represented by the operational amplifiers [6], which means the nullor 1 in Fig. 1

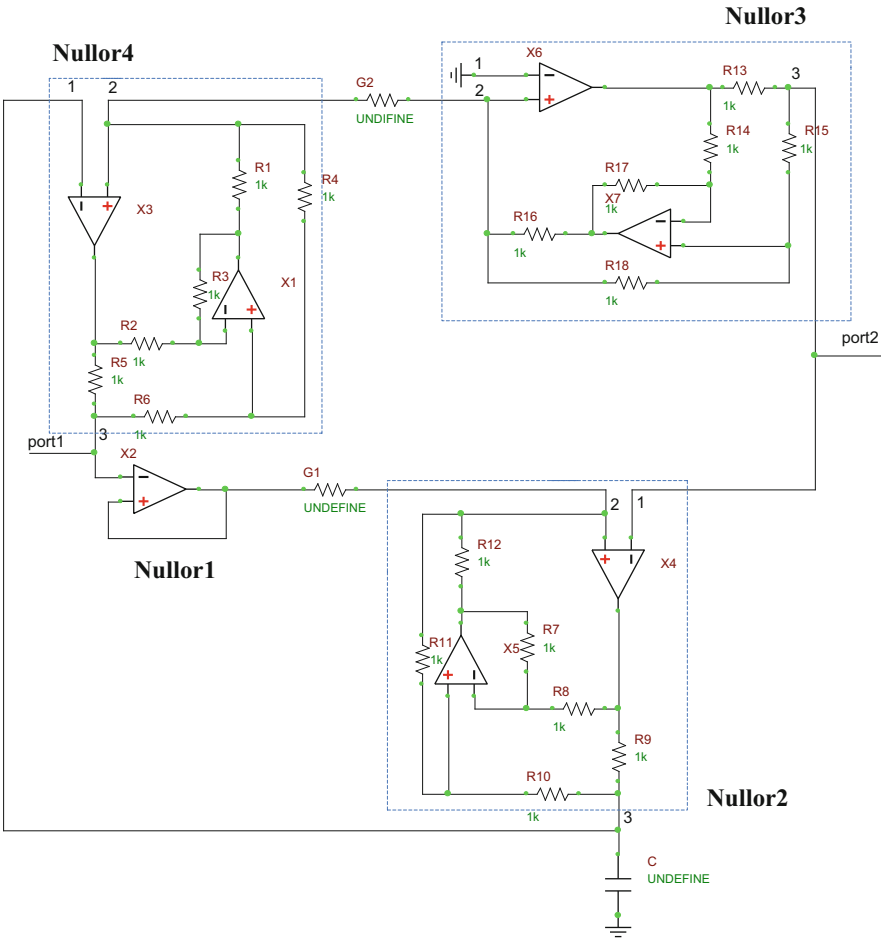

Fig. 3 The synthesized inductor

can be replaced by an operational amplifier. Then the synthesized inductor can be constructed with operational amplifiers and passive elements, as shown in Fig. 3. The values of element G_1, G_2 and C are defined according to the desired value of the synthesized inductor, all the other resistors in Fig. 3 are set to 1 kΩ.

3 Application Example

In this section, we take the designed simulated inductor into the Butterworth LC lowpass filter design with the following parameters: the passband edge frequency $f_p = 10$ kHz; the maximum attenuation in passband $A_{max} = 0.044$ dB; the stopband

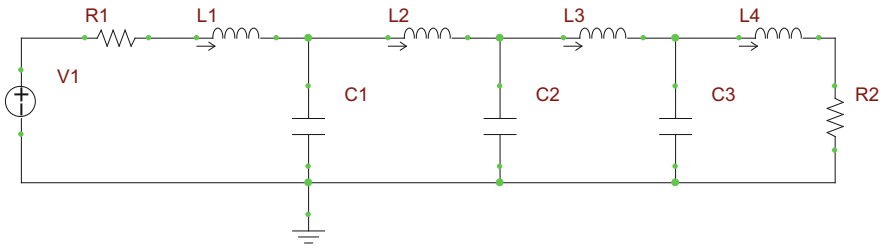

Fig. 4 The seventh-order Butterworth LC lowpass filter

Table 1 Values of the components

R1 = R2 = 600 Ω	L1 = 3.062508 mH	C1 = 23.835998 nF	L2 = 12.399664 mH
C2 = 38.229412 nF	L3 = 12.399664 mH	C3 = 23.835998 nF	L4 = 3.062508 mH

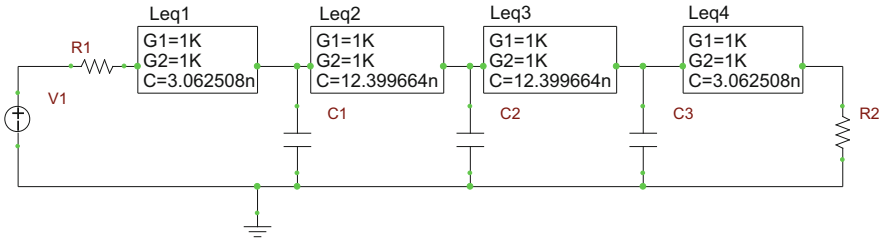

Fig. 5 The equivalent filter constructed by the simulated inductor

edge frequency $f_s = 20$ kHz and the minimum attenuation in stopband $A_{min} = 20$ dB.

According to the filter design theory [19], the seventh-order Butterworth, as shown in Fig. 4, can satisfy the requirement. The values of all the components are listed in Table 1.

Then substitute all the inductors in Fig. 4 with the designed simulated inductor in Fig. 3. For all the simulated inductor, the values are defined as shown in Fig. 5

The input voltage is set to 1 V. Simulation results of the performances of the original and the simulated seventh-order Butterworth LC Lowpass filter using Spice is shown in Fig. 6, where the blue line corresponds to the simulation result of Fig. 4 and the red line to the simulation result of Fig. 5. The comparison diagram shows the designed filter using the simulated inductor can satisfy the requirements at the frequency less than 20 kHz. However, the difference is mainly due to the effect of non-ideal characteristic of operational amplifiers.

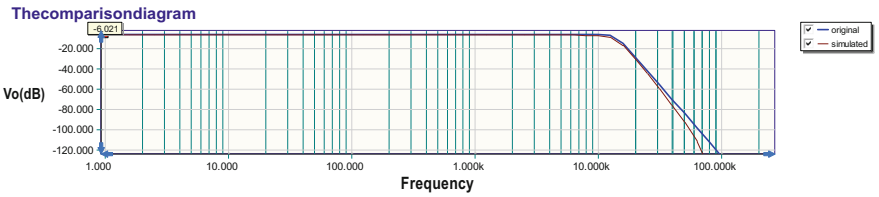

Fig. 6 The comparison diagram of the original and the simulated filter

4 Conclusions

This paper proposed a simulated inductor synthesized by the systematic circuit design method, which is the method of nodal admittance matrix expansion. The floating three-terminal nullor is constructed by the operational amplifiers, which makes it feasible to realize in practical circuit design. The simulated inductor is applied in the seventh-order Butterworth LC Lowpass filter design. The simulation results by Spice demonstrate that the method of nodal admittance matrix expansion can be extended to novel active circuit design.

Acknowledgments This research is supported by National Natural Science Foundation of China under grants 60802049, 61101225 and by the Innovation Foundation of Tianjin University under Grants 60302015.

References

1. Awad IA, Soliman AM (2002) On the voltage mirrors and the current mirrors. Analog Integr Circ Signal Process 32(1):79–81
2. Sanchez-Lopez C, Fernandez FV, Tlelo-Cuautle E, Tan SX-D (2011) Pathological element-based active device models and their application to symbolic analysis. IEEE Trans Circ Syst I 99:1
3. Wang H-Y, Huang W-C, Chiang N-H (2010) Symbolic nodal analysis of circuits using pathological elements. IEEE Trans Circ Syst II 57(11):874–877
4. Wang HY, Lee CT, Huang CY (2005) Characteristic investigation of new pathological elements. Analog Integr Circ Signal Process 44(1):95–102
5. Asenova I (2011) Calculation of second-order symbolic sensitivity by using nullor model and modified coates flow graph. International Symposium of Mixed Design of Integrated Circuits and Systems, MIXDES, Gliwice, Poland, June, 2011, Vol. I, pp 587–591
6. Haigh DG (2006) A method of transformation from symbolic transfer function to active-RC circuit by admittance matrix expansion. IEEE Trans Circ Syst I 53(12):2715–2728
7. Haigh DG, Radmore P et al (2004) Systematic synthesis method for analogue circuits - Part I Notation and synthesis toolbox. International symposium of Circuit and System, ISCAS, May, 2004, Vol. I, pp 701–704
8. Soliman AM (2011) Generation of current mode filters using NAM expansion. Int J Circ Theor Appl 19:1087–1103

9. Tangsrirat W, Dumawipata T, Unhavanich S, Surakampontorn W (2004) Simulation of electronically tunable lossless floating inductor using current-controlled differential current voltage conveyors. International Symposium of Communications and Information Technology, ISCAIT, October, 2004, Vol. I, pp 39–42
10. Cox N, Su K, Woodward R (1971) A floating three-terminal nullor and the universal impedance converter. IEEE Trans Circ Theor 18(3):399–400
11. Haigh DG, Tan FQ, Papavassiliou C (2005) Systematic synthesis of active-RC circuit building-blocks. Analog Integr Circ Signal Process 43(3):297–315
12. Davies AC (1967) The significance of nullators norators and nullors in active network theory. Radio Electron Eng 34:259–267
13. Lingling Tan Y, Bai JT, Liu K, Meng W (2013) Trans-impedance filter synthesis based on nodal admittance matrix expansion. Circ Syst Signal Process 32:1467–1476. doi:10.1007/s00034-012-9514-y
14. Sánchez-López C, Tlelo-Cuautle E, Martínez-Romero E (2011) Symbolic analysis of OTRAs-based circuits. J Appl Res Tech 9(1):69–80
15. Tlelo-Cuautle E, Sánchez-López C, Moro-Frías D (2010) Symbolic analysis of (MO)(I)CCI (II)(III)-based analog circuits. Int J Circ Theor Appl 38(6):649–659
16. Sánchez-López C, Fernández FV, Tlelo-Cuautle E (2010) Generalized admittance matrix models of OTRAs and COAs. Microelectron J 41(8):502–505
17. Tan L, Kaihua Liu Y, Bai JT (2013) Construction of CDBA and CDTA behavioral models and the applications in current-mode symbolic circuits analysis. Analog Integ Circ Signal Process 75:517–523. doi:10.1007/s10470-013-0065-3
18. Haigh DG (2004) Systematic synthesis method for analogue circuits - Part III all-transistor circuit synthesis. International symposium of Circuit and System, ISCAS, 23–26 May, 2004, Vol. I, pp 709–712
19. Sedra AS, Brackett PO (1978) Filter theory and design: active and passive. Matrix, Beaverton, Champaign, IL

Design of C8051F340 USB Communication System Based on USBXpress

Yuan Lu, Xiaoli Lu, Zhenchao Wang, and Xiaoou Song

Abstract A USB (Universal Serial Bus) communication system based on C8051F340 is developed in this paper. The system can be used to solve the problems of the communication between MCU serial RS-232 and computer. This article describes the features of C8051F340 and designs the hardware circuit according to these characteristics. It makes the application of USB host and the firmware of USB device simple by using the USBXpress development software provided by the silicon company. The communication system uses Keil uVision4 to develop the firmware and Microsoft Visual Studio 2010 to develop the application. This article verifies the feasibility of the circuit, and then provides a simple method of interface test, which has high practical value in system development and design.

Keywords C8051F340 • USB • Application • USBXpress

1 Introduction

The traditional communication interface of data acquisition equipment generally use the RS232 and RS422 standards, but the signal level of these interfaces is higher so that the circuit chips are easily damaged, because it is not compatible with the TTL level, a level switching circuit should be used to make it connect with the TTL circuit; transmission rate is lower; the noise resistance is weak; the transmission distance is limited. Thus, the current device communication interface mostly uses the USB standard [1]. As a new serial communication standard, the product based on USB interface has the characteristics of high transmission rate, good scalability, the bus power supply, supporting hot-plugging and so on. In recent years, the USB

Y. Lu (✉) • X. Lu • Z. Wang • X. Song
College of Electronic and Information Engineering, Hebei University, Baoding, China
e-mail: 916320450@qq.com

B. Zhang et al. (eds.), *The Proceedings of the Second International Conference on Communications, Signal Processing, and Systems*, Lecture Notes in Electrical Engineering 246, DOI 10.1007/978-3-319-00536-2_38,

interface is developing very fast, and it has the trend of replacing the above standard completely.

2 Hardware Design of System

With the USB technology is developing rapidly, its peripherals have been used more and more widely, the chips based on USB communication interface are more and more diverse [2]. Choose the microcontroller with USB controller can not only make the hardware circuit be simplified and reduce the peripheral volume, but also can improve the reliability of the product, so it has become the first choice of external device design [3].

According to the design demand, the chip of C8051F340 microcontroller has been emerged. It integrates with the USB 2.0 controller. Its main features are as follows:

1. High-speed pipelined 8051-compatible microcontroller core (up to 48 MIPS).
2. In-system, full-speed, non-intrusive debug interface (on-chip).
3. True 10-bit 200 ksps differential/single-ended ADC with analog multiplexer.
4. On-chip Voltage Reference and Temperature Sensor.
5. On-chip Voltage Comparators (2).
6. Internal low-frequency oscillator for additional power savings [3].
7. Up to 64 kB of on-chip flash memory.
8. Up to 4352 Bytes of on-chip RAM (256 + 4 kB).
9. USB function controller, compliant with the USB specification version 2.0, integrated clock recovery circuit, eliminating the need for an external crystal; endpoint supports 8; 1KBUSB cache; integrated transceiver, eliminating the need for external resistors [3].

In Hardware, a USB communication system contains USB host and USB device. The C8051F340chip has obvious advantages in device design and development. The USB host is the computer in the system [4].

Because of the advantages of C8051F340 in the USB interface, the design of hardware interface has become very simple, data transmission and control can achieve with no need to add other electronic devices. The connected graph of 51F340 interface is shown in Fig. 1.

3 Software Design of System

The software design of system can be divided into two parts: firmware and application. The USB device provides firmware, while the USB host provides application and driver. Firmware is mainly responsible for its initialization and

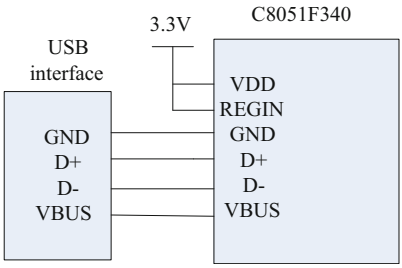

Fig. 1 Connecting circuit of USB interface

communication to the USB host, and application is responsible for calling the order of firmware, so that the data transmission can be realized.

The software design uses USBXpress [5] package of Silicon Laboratories Company, which covers all the functions of the host and device and supports USB communication of C8051F32X, C8051F34X and CP210X. The USBXPress package contains t device driver, device installation driver, dynamic link library (DLL) of the host and the function library file of the device. API function which can support USB communication of C8051F32X and C8051F34X is provided by the device function library files. These functions can be compiled by Keil uVision4. The related files should be added in the project before compiling.

The communication diagram of firmware and application is shown in Fig. 2. In USBXpress software package, the SiUSBXp.dll is called in dynamic link library file of USB host; USB_API.h is applied to header files, USBX_F34X.LIB is chosen in firmware library file, and SiUSBXp.sys is used to drive program.

3.1 Firmware Design [6]

The reason why USB device chooses Keil uVision 4 to develop is that the C8051F340 support system debugging (ISP), which greatly simplifies the development and debugging process [7]. In the process, USB_API.h header files and USBX_F34X.LIB library files should be called, and device interface function meets the requirements for API applications. The device interface functions mainly used are as follows:

USB_Clock_Start ( )	Initialize the USB clock
USB_Init ( )	Enable USB interface
Block_Write ( )	Write data to the computer through USB
Block_Read ( )	Read data from the computer through USB
Get_Interrupt_Source ( )	Get the type of API interrupt
USB_Int_Enable ( )	Enable API interrupt
USB_Int_Disable ( )	Disable API interrupt

The USB API interrupt vector entrance address 0x008B (interrupt 17) must be specified in the firmware, because API works in interrupt-drive mode. Note: in

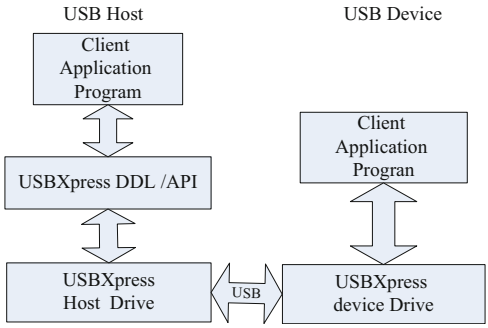

Fig. 2 USB communication principle diagram of MCU and PC

C8051F340, the USB API interrupt 17 is a virtual interrupt, which is produced by the USBXpress firmware library and triggered by specific events, the vector entrance address of hardware interrupt is 0x0043 (interrupt 8). The type of the event is got by the function Get_Interrupt_Source (). The USB communication process of the firmware is shown in Fig. 3.

USB API interrupt function a call of form as follows:

```
void USB_API_ISR (void) interrupt17
{
BYTEINTVAL=Get_Interrupt_Source ();/*Get the type of interrupt*/
If (INTVAL&TX_COMPLETE)/*Finish the data transmission*/
{
Block_Write (In_Packet, ...);/* Write data to send buffer */
}
If (INTVAL&RX_COMPLETE)/*Data received*/
{
Block_Read (Out_Packet, ...);/* Read data into receive buffer */
}
...../*other type of interrupt*/
}
```

3.2 Design of Application

The application [6] is developed in the Microsoft Visual Studio 2010 by using C# [8]. Visual Studio 2010 is a development environment launched by Microsoft, it can be used to create Windows applications under the Windows platform. Microsoft Visual Studio 2010 which uses pull-type to complete the software development, can simply generate an interface. The towed interface should also have a corresponding

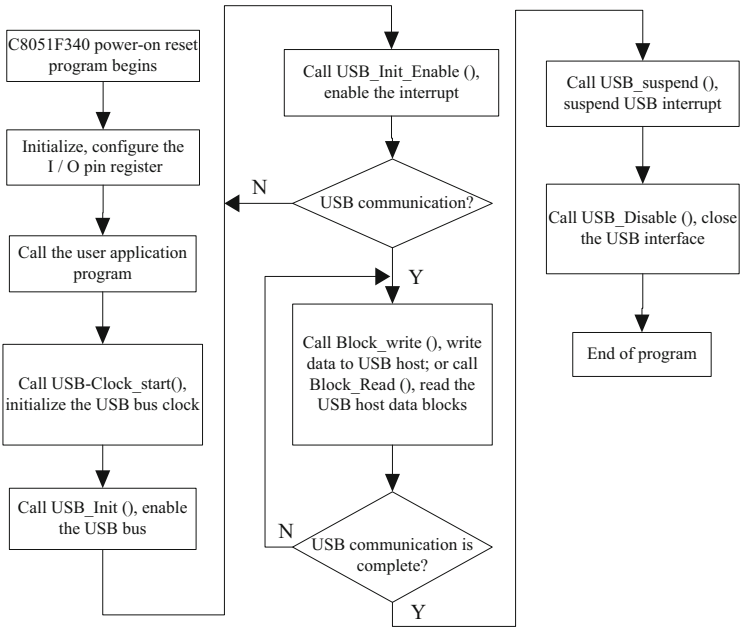

Fig. 3 USB communication flow chart of the firmware

code to implement the function, the Microsoft Visual Studio 2010 which supports C#, C++ and VB can quickly implement function.

The dynamic link library file SiUSBXp.dll is called by API function of USB host, to enable the communication between application and device driver to complete the data communication between the USB device and the USB host. The USB communication process of the application is shown in Fig. 4.

The host functions mainly used are as follows:

SI_GetNumDevices ( )	the number of return USB devices connected with host
SI_GetProductString ( )	return the descriptor of USB device
SI_Open ( )	turn on the USB device
SI_Close ( )	turn off the USB device
SI_Read ( )	reading device
SI_Write ( )	writing device

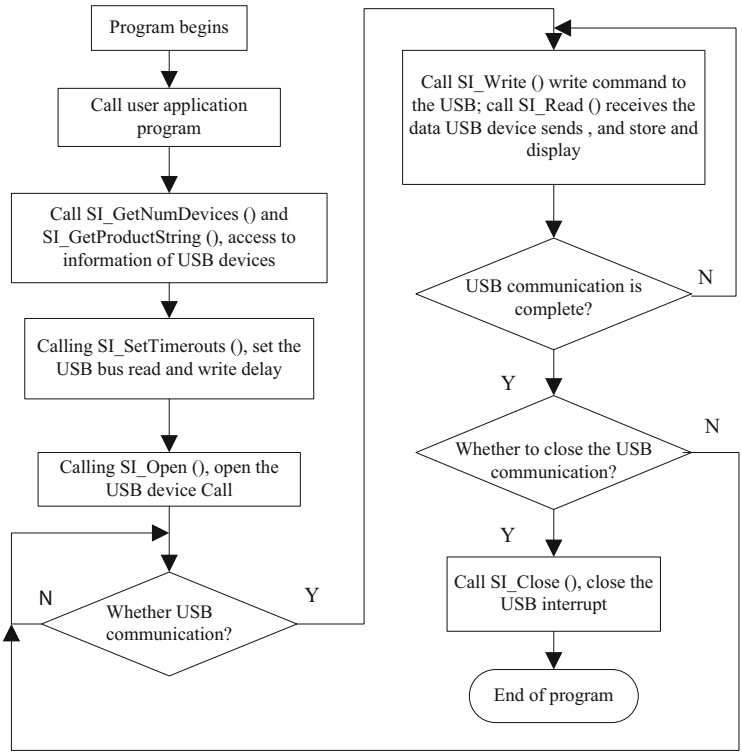

Fig. 4 USB communication flow chart of the application

4 Debugging

Figure 5 is the USB communication debugging block diagram, which illustrates that when the firmware of USB device is finished, it can be burned into the USB device through a JTAG port, and then through USB interface debugs the firmware via debugging assistant.

USB communication is a dynamic process, there are time-sensitive in each transmission process of USB, when the waiting time is too long, the communication process is aborted. Therefore, the serial debugging tools are used to aid USB communication module to complete the communication between computer and MCU. In this way, it requires a serial port RS232 level conversion chip on the hardware. Serial debugging tools can simplify the process of sending data and recording the received data. When using serial debugging tool, the baud rate should be set to 115200, the serial port is corresponding to the serial device manager serial port, the stop bit is 1 bit, the data length is 8 bit, send the 2-byte hexadecimal data into the send box, and click Send. Then observe the receive box until the 8-bit data from MCU has been successfully received by computer. Then repeat some times, and confirm that the received data is correct every time. In order to further confirm

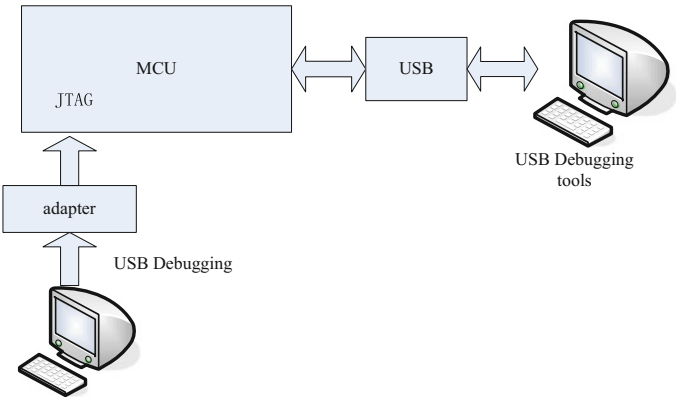

Fig. 5 USB communication debugging block diagram

the stability of the system, the USB communication module can be unplugged and then reinserted, the PC can automatically identify the serial port, and turn on the serial port debug tool again, sending and receiving data is still correct, that is to say, the system is stable. Therefore, the stability of the USB system and the accuracy of the data communication module are verified.

5 Conclusion

With the rapid development of USB technology, USB peripherals are widely used in more and more occasions. Many computers and devices no longer use the serial interface as a basic configuration, even some only have USB interface, and thus, MCU engineer should master the USB communication. In this paper, the USB interface communication technology based on C8051F340 is researched, the hardware circuits between C8051F340 and computer are designed, and the application programs of MCU and computer are introduced. Experiment results show that the data communication between MCU and computer can be achieved, and this design can improve the transmission speed of the system data, and enhance the accuracy of data transmission.

References

1. Xiao S-w, Song Y-q (2007) USB 2.0 Hardware Design. Tsinghua University Press, Beijing
2. Li Y-w (2007) USB2.0 principle and project development. National Defence Industry Press, Beijing
3. Silicon Laboratories (2006) C8051F340 Data Sheet[DB/OL]. http://www.silabs.com

4. Zhang Y-x, Lei W, Yao J-b (2005) C8051F MCU principle and application. National Defence Industry Press, Beijing
5. Silicon Laboratories (2008) USBXpress Programmer's Guide[EB/OL]. http://www.silabs.com/AN169_USBXpress_Programmers_Guide.pdf
6. Yan-bo Liu, Shi-qing zheng (2004) Firmware design of USB device. Journal of Information Engineering University, Zhengzhou, vol 5, pp 5269–5272
7. Ma Z-m, Ji S-x, Zhang K (2007) Microcontroller C language application design. Beihang University Press, Beijing
8. Cooper JW, Ye B (2011) C# design patterns. Science Press, Beijing

Speeding Up Colon CAD Using KD-Tree

Zhangjing Wang and Junhai Luo

Abstract This paper proposes an efficient technique to speed up our colon CAD software for flat lesion recognition in colon CT images. The proposed technique uses KD-tree to speed up the neighbor searching part in the software. We test our method under Linux system with intel(R) Xeon(R) 2.66 GHz CPU X5355, 12 G memory. Experiments on 50 computed tomographic colonography (CTC) scan database demonstrate the performance of our speeding up method based on KD-tree. It significantly reduces the average processing time from 6,134 s down to 514 s for each CTC scan.

1 Introduction

CTC is a rapidly evolving technique for screening colon cancer, but the interpretation of the data sets is still time-consuming. It is desirable to speed up CAD for CTC using all kinds of techniques [1]. In our laboratory, a new method for flat lesion detection in CTC has been developed [2]. It achieves high sensitivity of flat lesions compare to other methods [3, 4], but a large amount of time (6,134 s for each dataset) is needed to finish the whole recognition process. It is well known that KD-tree can be widely used to reduce computation burden in large scale data processing [5, 6]. In our method we utilize KD-tree to reduce the computation load. The total time has been decreased from 6,134 to 514 s. Hence the time efficiency of our CAD software is superior to radiologists who normally take more than 20 min for each scan dataset [1].

Z. Wang • J. Luo (✉)
School of Electronic Engineering, University of Electronic Science and Technology of China, Chengdu 611731, China
e-mail: 1310466336@qq.com; junhai_luo@uestc.edu.cn

B. Zhang et al. (eds.), *The Proceedings of the Second International Conference on Communications, Signal Processing, and Systems*, Lecture Notes in Electrical Engineering 246, DOI 10.1007/978-3-319-00536-2_39,

Fig. 1 Segmentation and reconstruction illustration: (**a**) original slice; (**b**) segmented colon area; (**c**) reconstructed colon

Flat lesion detection method: Our CAD scheme consists of three stages: colon segmentation, detection of polyp candidate voxels using spinning tangent line approach, and a density-based clustering of polyp candidate voxels into final candidates. More details can be found in [2]. Three representative pictures are given to illustrate the process from original CT slices to segmented ones and reconstructed colon in Fig. 1.

Although our method achieves higher accuracy of detecting flat lesions on colon than other methods [4, 5], a large amount of time (6,134 s) is needed to check one scan dataset. We tested the software and found that most of the time is spent in searching for neighborhood of each vertex among millions of vertices of reconstructed colon surface. To solve the time efficiency problem encountered in our method, we propose to use KD-tree technique. We first review KD-tree in the following section.

2 Proposed Method

2.1 Introduction of KD-Tree

A KD-tree is a data structure for storing a finite set of points from a k-dimensional space [7]. The KD-tree is a binary tree in which every node is a k-dimensional point. For example, given a data set (2,3), (5,4), (9,6), (4,7), (8,1), The tree generated is shown in Fig. 2. More details on KD-tree construction, adding elements, removing elements and neighborhood searching are available in [7].

Finding the nearest point is an O(logN) operation in the case of randomly distributed points. The worst case searching time for a k-dimensional KD tree containing N nodes is given by the following equation:

However, a completely exhaustive nearest neighbor searching has time complexity O(N), where N is the size of point set. It can be concluded that the difference of time efficiency is large between KD-tree based nearest neighbor searching method and naive nearest neighbor finding approach when the size, N, of point set is huge. In fact, in our colon CAD the number of vertices for each colon surface is over one million in average. Hence, it can be expected that naive nearest neighbor

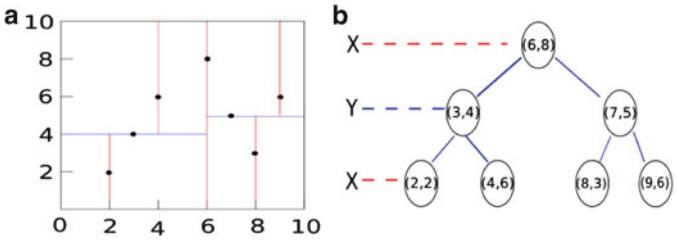

Fig. 2 KD-tree: (**a**) data point distribution; (**b**) KD-tree

searching in our colon CAD is extremely time-consuming. We use KD-tree based method to solve this problem.

2.2 Speeding Up Flat Lesion Detection

In our flat lesion detection method, we need to find the spherical neighborhood with radius 5 (empirically set) for each vertex among millions of vertices from reconstructed colon surface. In the original version of the implementation of the flat lesion detection method, we used naive neighborhood searching algorithm. It makes our software run very slowly. The time spent in checking each scanned colon by the software is 6,134 s.

Here, we use KD-tree to reorganize the point set composed of millions of vertices. With this tree structure, we have enhanced the efficiency of finding neighborhood process in our software. The whole time in examining each scanned colon has been reduced from 6,134 to 514 s. It makes time efficiency of our software comparable to radiologist when interpreting CT colonography.

3 Experiment

The database we used consists of 50 CTC scans obtained from the Rockey nation-wide clinical trial. Each patient was scanned in the supine and prone positions with a multi-detector-row CT system with collimations of 1.0–2.5 mm and reconstruction intervals of 1.0–2.5 mm. Further details on this dataset can be found in [3].

We test our algorithm in this paper on the above database and get 82 % sensitivity (23 polyps/28 polyps) under Linux system with intel(R) Xeon (R) 2.66 GHz CPU X5355, 12 G memory. The sensitivity of our method is superior to that of other methods [4, 5]. And the time spent in examining one colon is 514 s in average. To illustrate the time efficiency of our proposed KD-tree based method, one histogram of time taken to check one colon by our two methods with or without

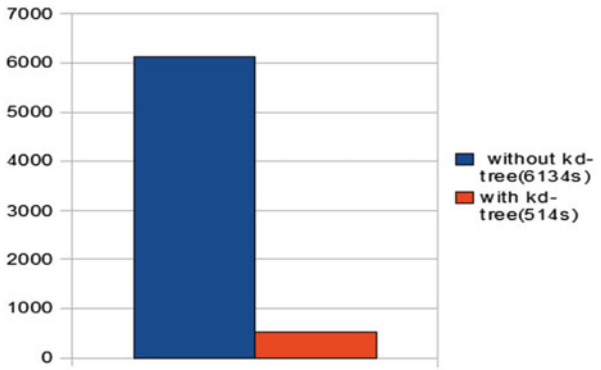

Fig. 3 Histograms of time spent in methods with and without KD-tree

KD-tree is given below in Fig. 3. It shows how much KD-tree affects the speed of our colon CAD software.

4 Conclusion

In this paper, we propose to use KD-tree to speed up our flat lesion detection method. The experiments demonstrate that our method is sufficiently efficient and the speed of improved method is fast.

However, the speed of our software can be enhanced further by using multi-thread programming technique. It can also be real time if utilizing GPU technology. In the future, we will focus on the real time implementation of our flat lesion detection method.

Acknowledgements Supported by the National Natural Science Foundation of China under Grant No.61001086 and the Fundamental Research Funds for the Central Universities Grant No. ZYGX2011X004.

References

1. Dachman AH (2003) Atlas of virtual colonoscopy. Springer, New York
2. Ferraro F, Kawaler E, Suzuki K (2011) A spinning tangent based CAD system for detection of flat lesions in CT colonography. In: Proceedings of ISBI2011, pp 156–159
3. Suzuki K, Rockey DC, Dachman AH (2010) CT colonography: advanced computer-aided detection scheme utilizing MTANNs for detection of "missed" polyps in a multicenter clinical trial. Med Phys 37:12–21
4. Ravesteijn VFV, Wijk CV, Vos FM, Truyen R, Peters JF, Stoker J, Vliet LJV (2010) Computer-aided detection of polyps in CT colonography using logistic regression. IEEE Trans Med Imag 29:120–131
5. Omohundro SM (1987) Efficient algorithms with neural network behavior. Complex Syst 1:273–347

6. Sanger TD (1991) A tree-structured algorithm for reducing computation in networks with separable basis functions. Neural Comput 3:67–78
7. Moore AW (1991) An introductory tutorial on kd-trees. Technical Report No. 29, Computer Laboratory, Univeristy of Cambridge, pp 1–20

Low-Power Design of Hybrid Instruction Cache Based on Branch Prediction and Drowsy Cache

Li Wei and Xiao Jian-qing

Abstract In the design of modern high-performance embedded processors, Branch prediction and larger capacity instruction cache greatly improves the performance of processors. They also consume a larger proportion of total power consumption of processors at the same time. There are many methods to reduce their power consumption. However, there is few method of combining them to reduce the power consumption. Based on these two technologies having a similar structure, this paper presents a hybrid cache structure of combining them to a new structure named B-Cache. By the method, we reduce the number of Comparisons of tag or PC. And based on spatial locality of instruction cache, we propose the method to reduce the number of tag comparison of instruction cache. By the experiments, we found this method compared with the common method of two-port BTB used to wake up cache line on demand can significantly improve the performance and reduce the power consumption of processors.

Keywords Branch prediction • Instruction • Cache • B-Cache • Tag

1 Introduction

In the design of high-performance embedded processors, most of processors use deep pipeline in order to improve the performance. But the target address of branch instruction is just known in the execution of pipeline that causes a decrease of throughout of pipeline. When the level of pipeline reach 7–8, the performance dropped by more than 30 % [1]. So now, in the design of embedded processors, it is very important to use branch prediction techniques to improve the performance.

L. Wei (✉) • X. Jian-qing
Xi'an Microelectronics Technology Institute, Xian, Shaanxi, China
e-mail: lw@stu.xjtu.edu.cn

B. Zhang et al. (eds.), *The Proceedings of the Second International Conference on Communications, Signal Processing, and Systems*, Lecture Notes in Electrical Engineering 246, DOI 10.1007/978-3-319-00536-2_40,

Nowadays, most of embedded processors use the branch prediction to improve the performance such as BTB (Branch target buffer), BHT (Branch history table) or PHT (Pattern history table). The BTB is used to predict the target address of branch. BHT or PHT is used to predict the direction of branch. Adoption of this technique greatly improves the performance of processors. However, power consumption is also one of serious problems that designers have to face. Firstly, the number of BTB entries directly determines the prediction accuracy. Secondly, the fetch of pipeline cannot know whether current instruction is a branch instruction, so it is necessary to access the BTB every cycle. The experimental results show that the instructions of branch take up 20–30 % of total. That means 80–70 % of power consumption of BTB waste [2, 3]. BTB has a similar structure with instruction cache, both use set associative structure. So there are some overlapping functions that waste the energy. Therefore, this paper presents a hybrid structure of BTB and instruction cache that are integrated one unit called B-Cache (BTB-Cache). There are no needs to compare PC of BTB and tag of instruction Cache both. There is only one comparison for both prediction of target address and tag match of instruction Cache. It is well known that sequential instructions take up most of total. Instruction Cache checks the tag bits when it accesses the different cache line regardless of whether there is a sequential feature of instruction flow. Further, based on the hybrid structure, this paper shows a method of tag-less of instruction cache to reduce the power consumption of processors.

2 Instruction Cache and BTB

2.1 Typical Structure of Instruction Cache and BTB

Figure 1 shows a typical structure of 2-way set-associated BTB and instruction cache. As the figure shown, instruction cache and BTB have a similar structure. The difference of them is that BTB stores the target address and instruction cache stores the instructions.

When the pipeline issues PC, the BTB checks the PC to obtain the target address of branch at first. Then it predicts the direction based on the information of BHT. According to the result of predictions, BTB sends the address to cache to obtain the instruction. Regardless of whether the instruction is a branch and whether the branch is valid, BTB have to compare the current PC with recorded PC.

2.2 Low-Power Strategy for BTB and Cache

The ways of research can be basically divided into two techniques. The first one is to wake up the line of drowsy cache on demand [4]. And the rest of cache lines are

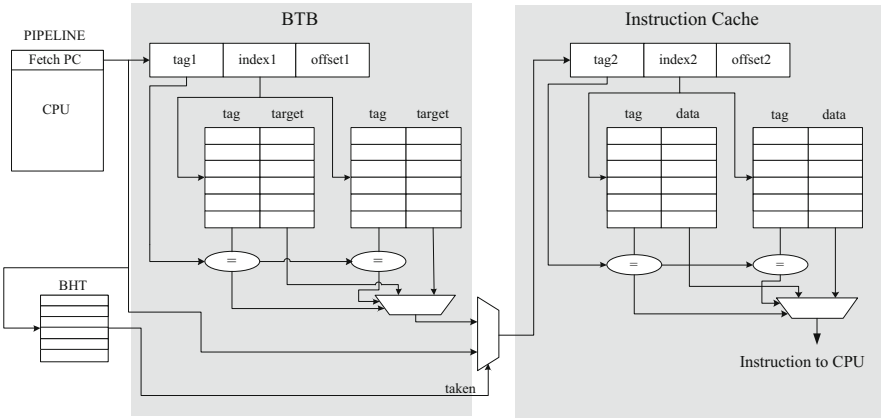

Fig. 1 Typical structure of two set-associated BTB and cache

switched to drowsy mode to reduce the leakage power consumption. Therefore, the quality of predicted algorithm determines the power consumption and performance of processors. These algorithm is general based on spatial locality to predict the next cache line accessed in next access such as wake-up sequence set [5], wake-up sequence block[6, 7], JITA[8] and sub-blocked cache[9].

Another one is based on a technique of cache decay [10]. That is based on historical information of cache access. The last accessed cache lines hold the active state. When the cache lines are not accessed after a period of time, they are switched to drowsy mode. The difference with on-demand wake-up is the technique is based on the temporal locality.

In order to improve the prediction accuracy of the branch instruction, the processors generally use the technique of BTB and BHT to predict the target address of branch. Since sequential and branch instructions account for the vast majority of the total instructions, and BTB have the feature of predicting address of next instruction. Therefore BTB is often used to wake up the cache line in the drowsy mode on demand. In ref. 11, there is a method that the modified BTB had two ports that used to send two addresses. The one is the target address of branch like classic BTB. The anther was the address used to switch the cache line from the drowsy mode to normal mode. This technique is called two-port BTB. However, the BTB has the set-associated structure. The power consumption cannot be ignored. In ref. 12, the paper presented a method used to reduce the dynamic power consumption of BTB.

2.3 Strategy of B-Cache

Although, there are many effective strategies for reducing the power consumption of Cache and BTB, there are few methods considering the two parts as a unit for reducing the power consumption. We compared the two structures, and founded the

structure has a similar feature. Therefore, we designed a hybrid cache including information of BTB and instruction cache. The two parts were integrated one unit. Firstly, the match of BTB and tag no longer performed separately. Secondly, the entry of sequential instructions was recorded in order to further reduce the number of tag comparisons. There is only one comparison of tag for sequential instructions. Since the entry of sequential instructions and target of branch was recorded, it is very convenient to adopt the drowsy technique for the instruction cache. In order to eliminate the extra 1- to 2-cycle overhead of drowsy cache, an instruction queue is added in B-Cache. Prefetching the instructions not only rely on the PC, but also rely on the predicted address of B-Cache. The prefetching the instructions do not stop until the queue is full.

3 Implementation of B-Cache

3.1 Structure of B-Cache

As the Fig. 2 shown, the paper presents a 2-way set-associated B-Cache. The difference with classical structure as Fig. 1 shown is that there are a description instead of target in BTB and instruction in cache. The description includes TType (terminated type), SIL (sequential instruction length), V (valid), S (subsequence) and way. TType indicates the type of instruction that terminate the sequential instructions. SIL is the number of sequential instructions. V is the valid bit of cache line. S is the valid bit used to indicate whether this cache line stores the subsequent sequential instructions. Way is used to indicted to in which set the next valid cache line is. The instructions and targets of branch are stored in the dependent SRAM. The lines or entries can be adjusted based on the application. In this paper, the size of instruction SRAM is 32 Kb, the number of entries of target SRM is 128. The instruction queue is used to store the perfetched instruction. The perfecting instruction is based on the bits of SIL, V and S. That means B-Cache only checks the entry of instructions and sends the address to instruction SRAM. If there is no branch or jump instruction and underflow of SIL, the instructions are sent to queue until queue is full. If there a branch or jump instruction, the address decided by BHT or PHT also sent to instruction SRAM. The target address of branch or jump is as an entry of anther sequential instructions.

3.2 Implementation of Control

For an instruction snippet that have never been executed or been replaced, B-Cache index the cache line based on PC at first. When the instruction is written into the

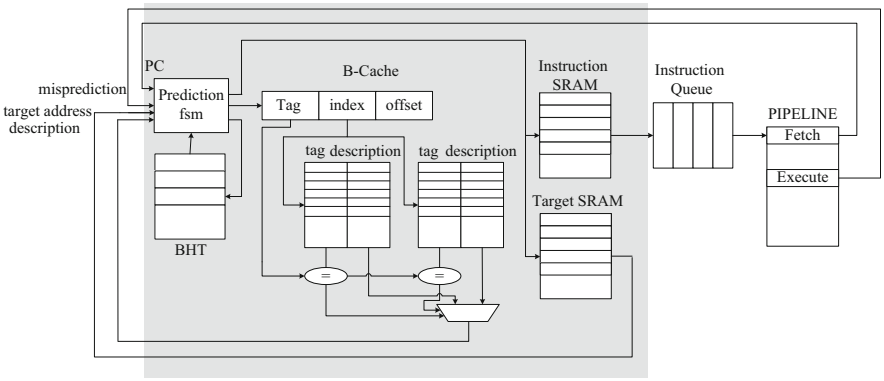

Fig. 2 Implement of 2-way set-associated B-Cache

instruction SRAM from L2 cache or main memory, the information of description is also written into the cache line based on the situation of execution.

The Fig. 3 shows the checking flow of B-Cache. When the tag of B-Cache matches the PC, B-Cache enters into the current state. If the offset of address from the address of entry is smaller than the recorded SIL, B-Cache no needs to compare tag and just check the bits of V and H. The instruction from instruction SRAM is sent to queue until the bits of V and H is invalid. When the offset is equal with the SIL, B-Cache sends the SPC (Speculative PC) based on prediction of B-Cache to instruction SRAM. Then it continues to send the instruction to the queue. When the pipeline sends the signal of misprediction to the B-Cache, it flushes the queue and re-enters into a new entry based on CPC (Current PC) sent from pipeline. If the bit of H is invalid that means the instructions in the current matched cache line was replaced by new instructions and the stream of sequential instructions is broken. So B-Cache misses.

4 Experiments

4.1 Experiments Setup

In the paper, hot-leakage toolsets based on the engine of simple-scalar is used to model a single-issue processor with a two-level cache hierarchy that is used to evaluate the power consumption and performance. The simulation parameters roughly correspond to PXA270 is listed in Table 1.

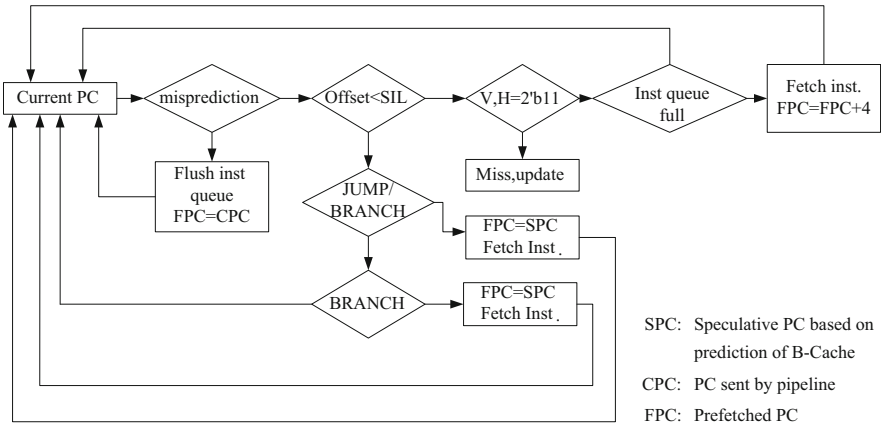

Fig. 3 The checking flow of B-Cache

Table 1 Simulated parameters for three different policies

Parameters	Value for no-drowsy	Value for BTB	B-Cache
Fetch/issue/ decode/ commit	1 instruction		
Fetch queue/ speed	1 instruction/1×		
Branch prediction	Bimodal, 2 k		
Interger ALUs/ multi-dives	1/1	1/1	1/1
Floating point ALUs/mul-div	1/1	1/1	1/1
Memory bus width/ latency	4B/30-cycle latency		
Inst./data TLBs	16-entry/32-entry, page size is 4 Kb, 2-set, LRU, 30-cycle latency		
BTB	32-/64-/128-entry, 1-/2-/4-set		–
RAS	4-entry		
L1 cache	32 K, 32B block, 1-/2-/ 4-set, LRU, 1-cylce latency	32 K, 32B block, 1-/2-/ 4-set, LRU, 2-cylce latency	–
B-cache	–		32 K, 32B block, 1-/2-/4-set, LRU, 2-cylce latency, 128-entry target
L2 unified cache	256 K, 2-set, 64B block, LRU, 8-cycle latency		

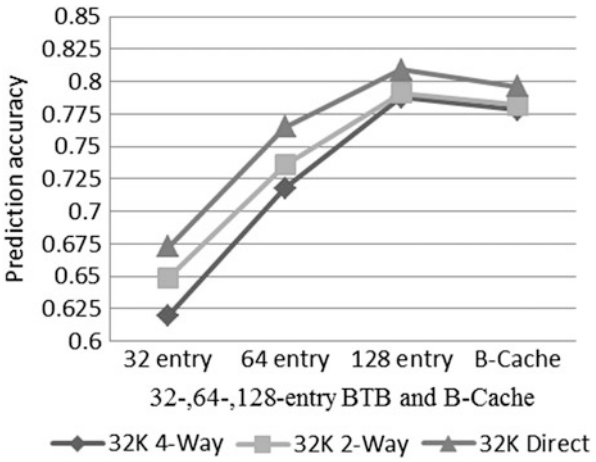

Fig. 4 Prediction accuracies using different polices

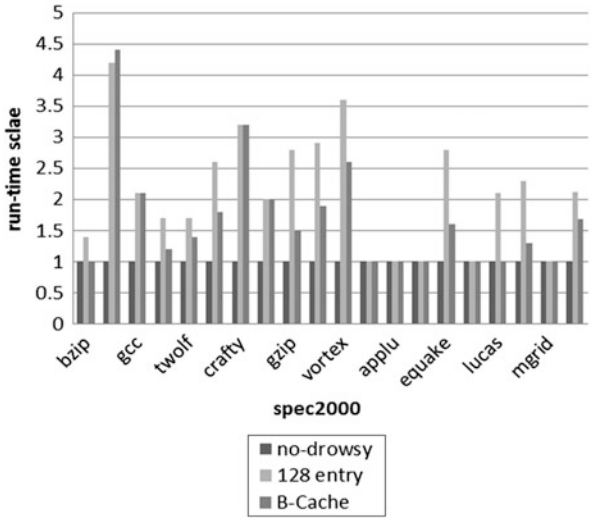

Fig. 5 Run-time scale using the three different policies

4.2 Results and Analysis

The structure of BTB is modified to two-port BTB used to adopt the drowsy cache as the ref. 13. Because the run-time of test program is positively correlated with the prediction accuracy, we first compare the prediction accuracies of the two different structures.

As Fig. 4 shown, the prediction accuracies are roughly equal between the BTB-Cache with 128 entries and the two-port BTB with also 128 entries.

Figure 5 shows the comparison of the execution time. As the figure shown, the run time of processor used the B-Cache is less than the run time of processor used the two- port BTB. We analysis this situation, the reason is the B-Cache contains an

instruction queue and send the instructions to queue ahead of PC. That can reduce the number of cycles for adoption of drowsy cache. As 68 % of the executed sequential blocks include four instructions or less [14] and the prediction accuracy is about 78 %, B-Cache cannot completely eliminate the loss of performance caused by drowsy cache. But it is better than the method using the two-port BTB prediction. Compared to no-drowsy and 2-port BTB prediction, the EDP of B-Cache reduces the 85 and 45 %.

5 Conclusions

Based on the similarities of BTB and instruction cache in structure and the spatial locality, this paper proposes a structure of B-Cache that integrates the BTB and instruction cache as a unit. It is significant to reduce the number of tag comparisons, so that it is very effective to reduce the dynamic power consumption of BTB. By using the spatial locality of instructions to design a tagless structure of cache for sequential instructions, this structure can also reduce the dynamic power consumption of instruction cache. B-Cache adopts the instruction queue and predictors at the same time, so that the prefetching instructions can be send to queue ahead of PC given by pipeline. This method can compensate for the loss of performance caused by using the techniques of phased cache and drowsy cache. Experiments show this method can reduce more the dynamic power consumption and improve the performance compared with the method using two-port BTB prediction.

References

1. Zheng W-m, Tang z-z (1998) Computer architecture, 2nd edn. Tsinghua University Press, Beijing, In Chinese
2. Chang YJ (2006) Lazy BTB: reducing BTB energy consumption using dynamic profiling. Proceedings of conference on Asia South Pacific design automation, Yokohama, 2006, 917–922. doi: 10.1109/ASPDAC.2006.1594803
3. Deris KJ, Baniasadi A (2006) Branchless cycle prediction for embedded processors. Proceedings of ACM symposium on applied computing, Dijon, 2006, 928–932. doi: 10.1145/1141277.1141492
4. K Flautner, Kim NS et al. (2002) Drowsy caches: simple techniques for reducing leakage power. In: SIGARCH proceedings of the 29th annual international symposium on computer architecture. IEEE Computer Society, Washington, 148–157. doi: 10.1109/ISCA.2002
5. Zhang C, Zhou HW et al. (2006) Architectural leakage power reduction method for instruction cache in ultra deep submicron microprocessors. In: The 11th Asia-Pacific computer systems architecture conference. Springer, Heidelberg, 588–594. doi: 10.1007/11859802_62
6. Hu J et al. (2003) Exploiting program hotspots and code sequentiality for instruction cache leakage management. In: International symposium on low power electronics and design (ISLPED'03). Springer, Heidelberg, 25–27. doi:10.1109/LPE.2003.1231936

7. Chung SW, Skadron K (2006) Using branch prediction information for near-optimal I-Cache leakage. In: The 11th Asia-Pacific computer systems architecture conference. Springer, Heidelberg, 24–37. doi: 10.1007/11859802_4
8. Kim NS, Flautner K et al. (2004) Single-VDD and single-VT super-drowsy techniques for low-leakage high performance instruction caches. In: International symposium on low power electronics and design (ISLPED'04). Springer, Heidelberg, 54–57. doi: 10.1145/1013235.1013254
9. Kim NS et al. (2002) Drowsy instruction caches. Leakage power reduction using dynamic voltage scaling and cache sub-bank prediction. In: 35th Annual IEEE/ACM international symposium on microarchitecture (MICRO'02), Istanbul, Turkey. Springer, 219–230. doi:10.1109/MICRO.2002.1176252
10. Kim NS, Flautner K et al (2004) Circuit and microarchitectural techniques for reducing cache leakage power. IEEE T VLSI Syst 12(2):167–184. doi:10.1109/TVLSI.2003.821550
11. Hong-wei Z, Min-xuan Z (2008) The research on power controlling policies for instruction cache with architecture level methods. Acta Ectronica Sinica 36(11):2107–2112, In Chinese
12. Mingyan Y, Xiangjian Z, Bing Y (2010) Low power branch target buffer design based on hopping access. Journal of Computer-Aided Design & Computer Graphics 22(4):695–702, In Chinese
13. Zmily A, Kozyrakis C (2005) Energy-efficient and high-performance instruction fetch using a block-aware ISA. In: International symposium on low power electronics and design. Springer, Heidelberg, 36–41. doi: 10.1145/1077603.1077614

Simple and Efficient Algorithm for Automatic Modulation Recognition for Analogue and Digital Signals

Badreldeen Ismail Dahap, Liao HongShu, and Mohammed Ramadan

Abstract In this paper we propose new analogue and digital recognition algorithm to discriminate between 15 signals (amplitude modulation (AM), frequency modulation (FM), double sideband modulation (DSB), lower sideband modulation (LSB), upper sideband modulation (USB), vestigial sideband (VSB), combined (AM–FM), carrier wave (CW), Noise, binary amplitude shift keying (ASK2), ASK4, binary phase shift keying (PSK2), PSK4, binary frequency shift keying (FSK2) and FSK4). Six key features extracted from instantaneous information (amplitude and phase) and signal spectral, are used to fulfill the requirement of this algorithm. Computer simulations for the signals of interest corrupted by band limited Gaussian noise was performed, the simulation results show that the overall recognition rate can reach 99.6 % when the signal to noise ratio (SNR) = 3 dB. This algorithm uses a lesser number of features compared with most of the existing automatic analogue and digital modulation recognition algorithms, thus leading to lower computational load.

Keywords Features • Instantaneous information • Modulation recognition and algorithm

B.I. Dahap (✉) • M. Ramadan
Department of Electronics and Computer science, Collage of Engineering, Karary University, Omdurman, Sudan
e-mail: bader_6dahap@hotmail.com; nopatia@gmail.com

L. HongShu
School of Electronic Engineering, University of Electronic Science and Technology of China, Chengdu, Sichuan 610054, P. R of China
e-mail: hsliao@uestc.edu.cn

B. Zhang et al. (eds.), *The Proceedings of the Second International Conference on Communications, Signal Processing, and Systems*, Lecture Notes in Electrical Engineering 246, DOI 10.1007/978-3-319-00536-2_41,

1 Introduction

Generally, automatic modulation recognition algorithms can be classified into three groups depending on the signals used. The first group deals with analogue communication signals only. The second group deals with digital communication signals only. While the third group deals with both analogue and digital communication signals; this third group is preferred in the practical automatic modulation recognition algorithms.

Nandi and Azzouz in [1–3] developed three algorithms for analogue and digital modulation recognition to discriminate between thirteen signals (AM, FM, DSB, LSB, USB, VSB, combined (AM–FM), ASK2, ASK4, PSK2, PSK4, FSK2 and FSK4). The overall recognition rate of these algorithms reached 94 % when SNR = 15 dB. The overall recognition rate was enhanced by using artificial neural networks (ANN), though, still less than 98 % when SNR = 15 dB.

Several other automatic modulation recognition algorithms have been established in the last few years to discriminate both analogue and digital communication signals. Cheol-Sun et al. [4] proposed algorithm to discriminate between nine signals using neural network and support vector machine the overall recognition rate reached 96 % when SNR = 5 dB. Jie Yang et al. [5] suggested algorithm to discriminate between nine signals the overall recognition rate reached 95 % when SNR = 7 dB. Xudong Liu et al. [6] proposed algorithm to discriminate between eleven signals the overall recognition rate reached 95 % when SNR $\geq$10 dB. Chisheng Li et al. [7] developed algorithm to discriminate between eleven signals the overall recognition rate reached 98 % when SNR $\geq$3 dB.

All the algorithms proposed in [4–7] have good performance at low SNR. But none of these algorithms contain VSB and Combined (AM–FM) signals .Also some of these algorithms reduce the analogue or digital signals to get better recognition rate. While the algorithms proposed by Azzouz and Nandi do not have acceptable performance (effective at high SNR).

Our paper aims at the development of a new algorithm for the automatic modulation recognition of analogue and digital signals, using six features extracted from instantaneous information (amplitude and phase) and spectra of the intercepted signal, to discriminate between fifteen signals same as in [1–3], in addition to carrier wave (CW) and Noise signals at low SNR. This algorithm not only achieves a better recognition rate but also extends the number of analogue signals and reduces the computational loads.

This paper is organized as follows: Sect. 2 presents the key features used to fulfill the requirements of this algorithm. In Sect. 3, Computer simulations including the determination of thresholds, the flowchart and the simulation results are presented. Finally, the paper concludes in Sect. 4.

2 Feature Extraction

To discriminate the analogue and digitally modulated signals, six features extracted from instantaneous information (amplitude and phase) and spectra of the intercepted signals are used.

(1) The first feature (**P**); is used for the measuring the spectrum symmetry around the carrier frequency, and it is based on the spectral powers for the lower and upper sideband of the RF signal.
(2) The second feature ($\boldsymbol{\sigma_{dp}}$); is the standard deviation of the centered non-linear component of the direct instantaneous phase, evaluated over the non-weak interval of signal segment.
(3) The third feature ($\boldsymbol{\gamma_{max}}$); is the maximum value of the spectral power density of the normalized-centered instantaneous amplitude of the intercepted signal.
(4) The fourth feature ($\boldsymbol{\mu_a}$); mean of instantaneous amplitude squared.
(5) The fifth feature ($\boldsymbol{\mu_{aa}}$); the mean of normalized-centered instantaneous amplitude squared.
(6) The sixth feature ($\mathbf{V_{phs}}$); the variance of a non-linear component of the instantaneous phase squared.

The features P, $\boldsymbol{\gamma_{max}}$ and $\boldsymbol{\sigma_{dp}}$ were proposed by Nandi and Azzouz in [1]. While the mean of instantaneous amplitude squared (μ_a) was proposed by Jaspal Bagga and Neeta Tripathi in [8]. μ_{aa} and V_{phs} are the two newly features.

The first new feature μ_{aa} is defined as

$$\boldsymbol{\mu_{aa}} = E\left(a_{cn}^2(i)\right) \tag{1}$$

$$a_{cn}(i) = \frac{(a(i) - E(a(i)))}{E(a(i))} \tag{2}$$

Where $a(i)$ the instantaneous amplitude and μ_{aa} the mean of normalized-centered instantaneous amplitude squared. This feature is used to discriminate between signals with constant amplitude (MPSK, MFSK and FM) and signals with no constant amplitude (DSB, MASK, COM and Noise). Also, it is used to discriminate the ASK2 from ASK4.

The second new feature, V_{phs}, is modified from V_{ph} proposed in [9] to discriminate between large types of the signals and defined as:

$$V_{phs} = \frac{1}{c}\sum_{Ø(i)<2_t}^{c} Ø^4(i) - \left(\frac{1}{c}\sum_{Ø(i)<2_t}^{c} Ø^2(i)\right)^2 \tag{3}$$

where c is the number of samples less than the threshold a_t, the value of a_t used equal $3\pi/2$. Ø is the non-linear component of the instantaneous phase at time instants $t = i/f_s$.

This feature leads to a complete classification of five modulated signal types, separating them into five regions simultaneously. Among the five sets, the first set

consists of the FM signal and the second set consists of the PSK2 signal. The third set consists of the FSK2 signal and the fourth set consists of the FSK4 signal and the last set consists of PSK4 signal. This separation stage requires four proper threshold values of V_{phs} such as $t1_{(Vphs)}$, $t2_{(Vphs)}$, $t3_{(Vphs)}$ and $t4_{(Vphs)}$ and is performed by following procedure.

$V_{phs} < t1_{(Vphs)}$ first set: FM signal.
$t1_{(Vphs)} < V_{phs} < t2_{(Vphs)}$ second set: PSK2 signal.
$t2_{(Vphs)} < V_{phs} < t3_{(Vphs)}$ third set: FSK2 signal.
$t3_{(Vphs)} < V_{phs} < t4_{(Vphs)}$ fourth set: FSK4 signal.
$V_{ph} > t4_{(Vphs)}$ fifth set: PSK4 signal.

3 Computer Simulation

The software used is Matlab R2011b and the simulation parameters (carrier frequency (f_c), sampling frequency (f_s) and symbol rate (f_b)) are the same as mentioned in [1].

3.1 Thresholds Determinations

The thresholds for all features are shown in the Figs. 1–11, and the specific values are shown in Table 1.

Figure 1 shows that LSB, USB and VSB can be discriminated from others at SNR $\geq$3 dB by the threshold (t1).

Figure 2 shows that LSB can be discriminated from USB and VSB at SNR $\geq$ 0 dB by the threshold.

From Fig. 3, it can be observed that ASK2, ASK4, AM and CW can be discriminated from others at SNR $\geq$1 dB by the threshold (t2).

Similarly, from Fig. 4 it can be observed that USB can be discriminated from VSB at SNR $\geq$0 dB by the threshold (t3).

Figure 5 shows that DSB can be discriminated from COM and noise at SNR $\geq$0 dB by the threshold (t4).

Figure 6 shows that MPSK, MFSK and FM can be discriminated from DSB, COM and noise at SNR $\geq$2 dB by the threshold (t5).

Figure 7 shows that ASK2 can be discriminated from ASK4 at SNR $\geq$0 dB by the threshold (t6).

From Fig. 8 it can be observed that CW can be discriminated from ASK2, ASK4 and AM at SNR $\geq$0 dB by the threshold (t7).

Figure 9 shows that COM can be discriminated from Noise at SNR $\geq$0 dB by the threshold (t8).

From Fig. 10 it can be observed that AM can be discriminated from ASK2 and ASK4 signals at SNR $\geq$1 dB by the threshold (t9).

Figure 11 shows that FM, PSK2, PSK4, FSK2 and FSK4 signals can be discriminated from one another at SNR $\geq$3 dB by the four different thresholds (t10, t11, t12 and t13).

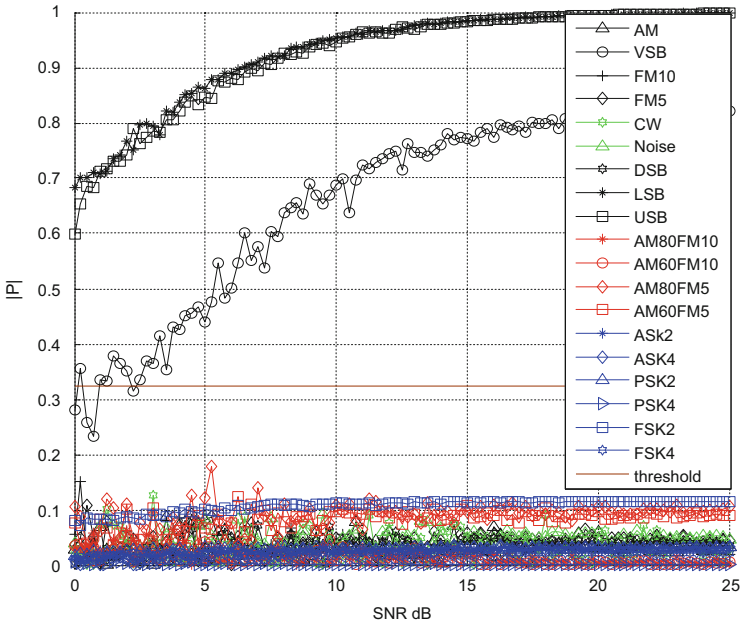

Fig. 1 Using feature |p| to discriminate SSB and VSB from other signals

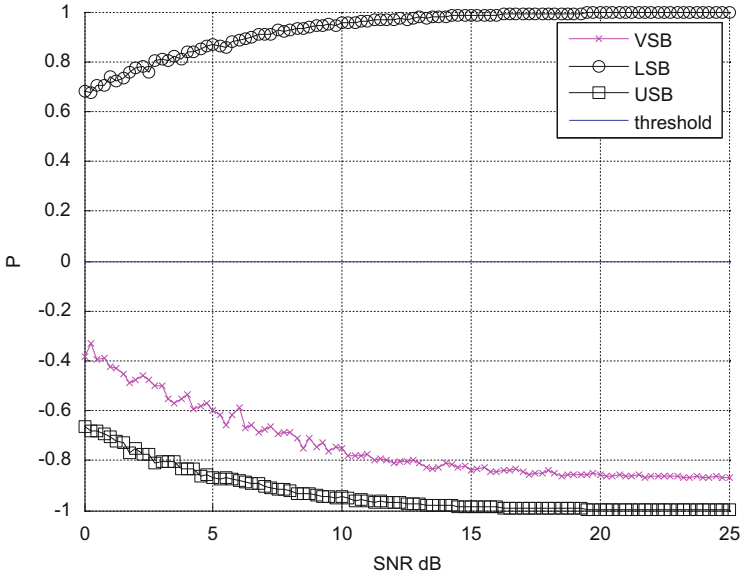

Fig. 2 Using feature P to discriminate LSB from USB and VSB

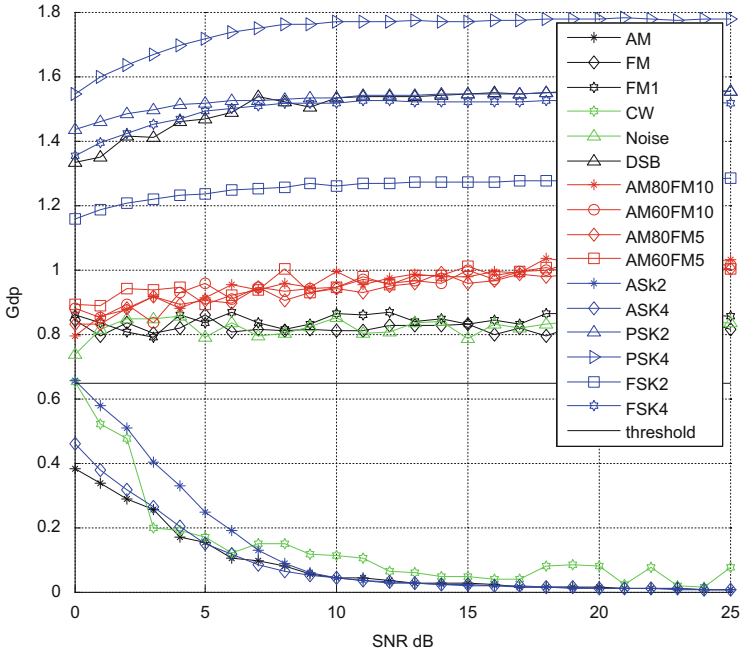

Fig. 3 Using feature $\boldsymbol{\sigma_{dp}}$ to discriminate MASK, AM and CW from other signals

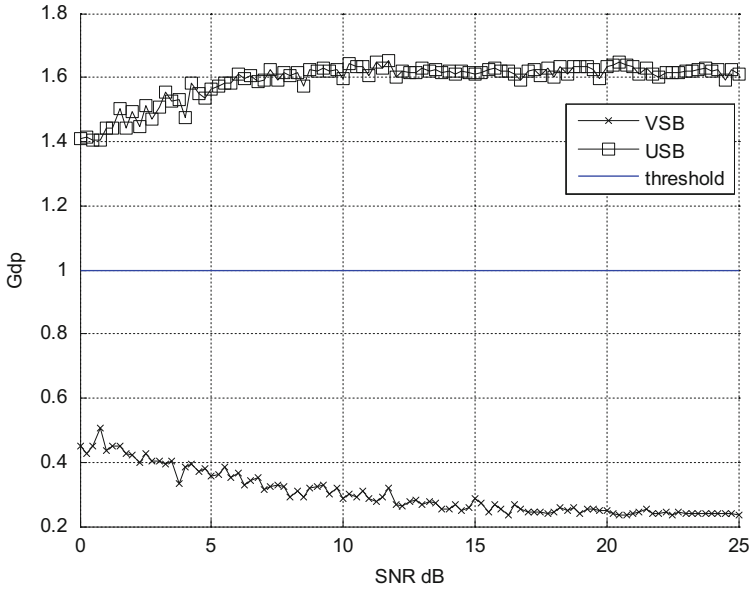

Fig. 4 Using feature $\boldsymbol{\sigma_{dp}}$ to discriminate USB from VSB signals

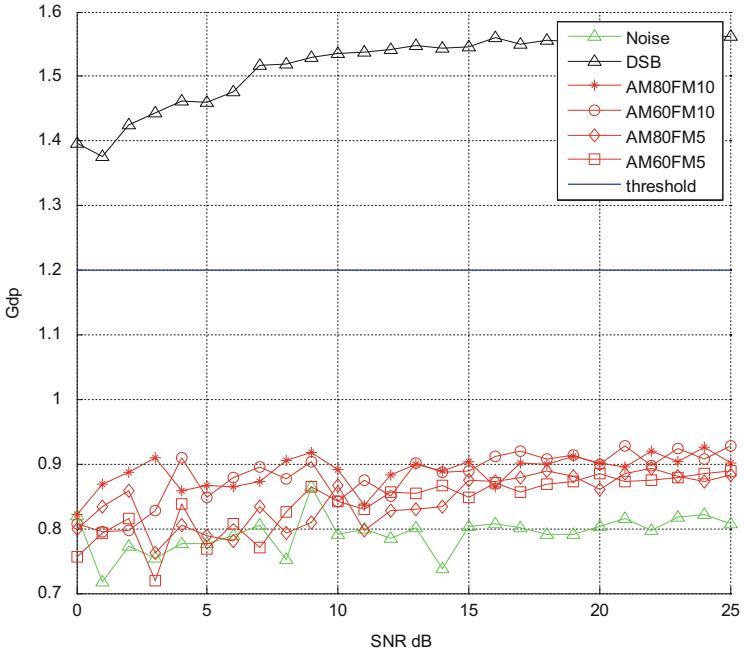

Fig. 5 Using feature $\boldsymbol{\sigma_{dp}}$ to discriminate USB COM and noise from DSB signals

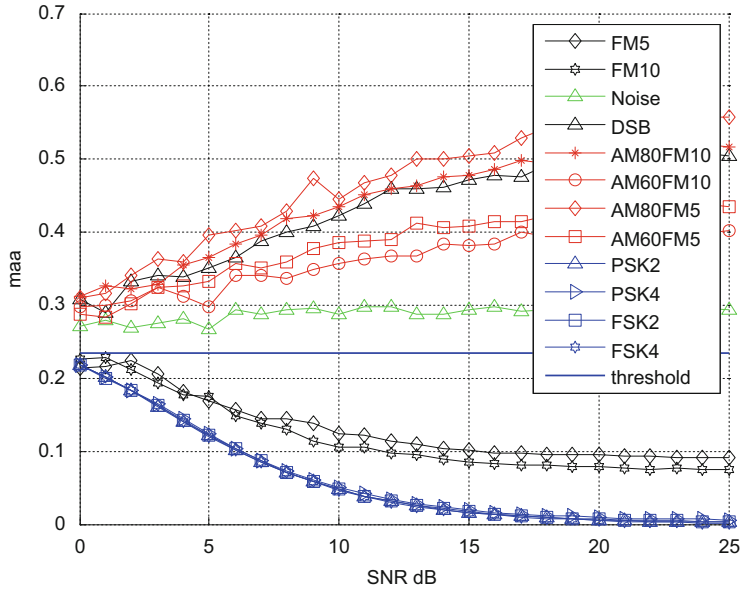

Fig. 6 Using feature $\boldsymbol{\mu_{aa}}$ to discriminate MPSK, MFSK and FM from other signals

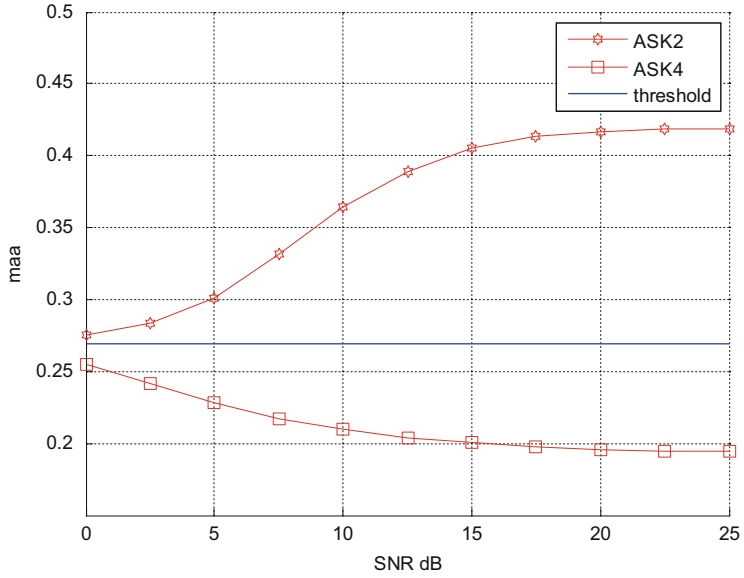

Fig. 7 Using feature μ_{aa} to discriminate ASK2 from ASK4 signals

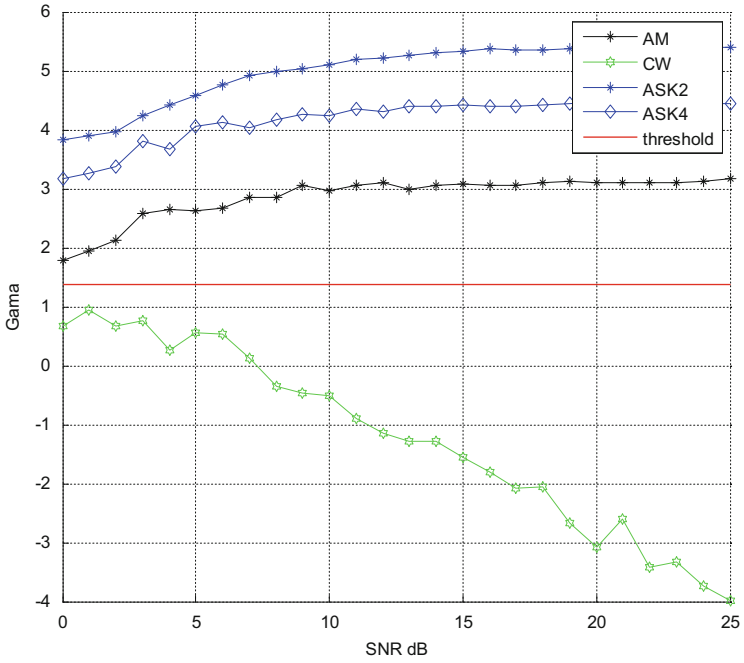

Fig. 8 Using feature γ_{max} to discriminate CW from MASK and AM signals. (The logarithm is used to make the different between two groups clear)

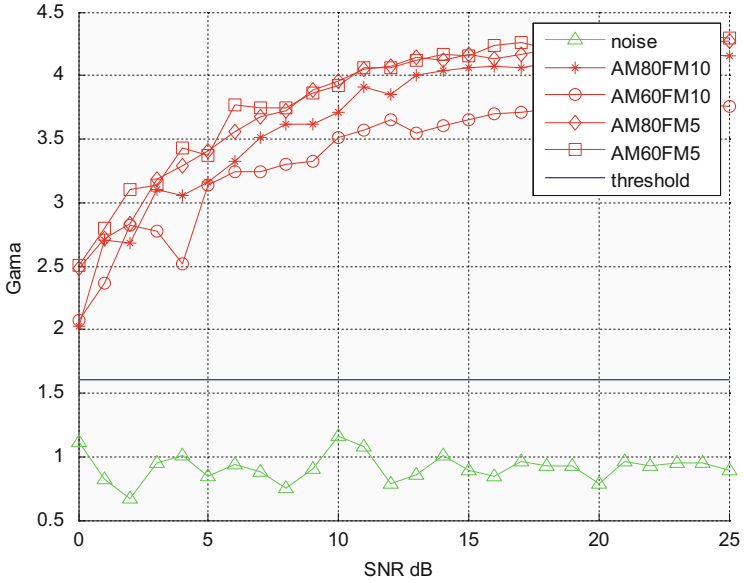

Fig. 9 Using feature $\boldsymbol{\gamma_{max}}$ to discriminate COM from Noise signal. (The logarithm is used to make the different between two groups clear)

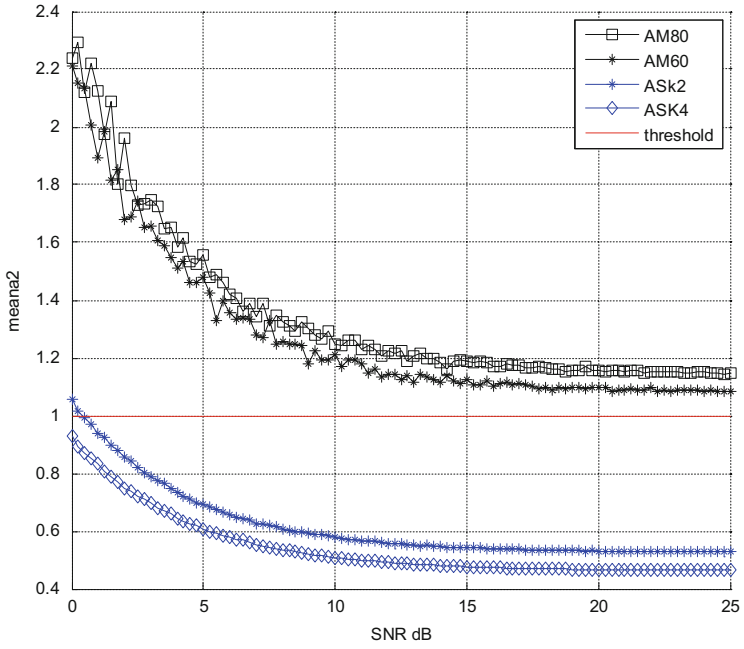

Fig. 10 Using feature $\boldsymbol{\mu_a}$ to discriminate AM from ASK2 and ASK4 signals

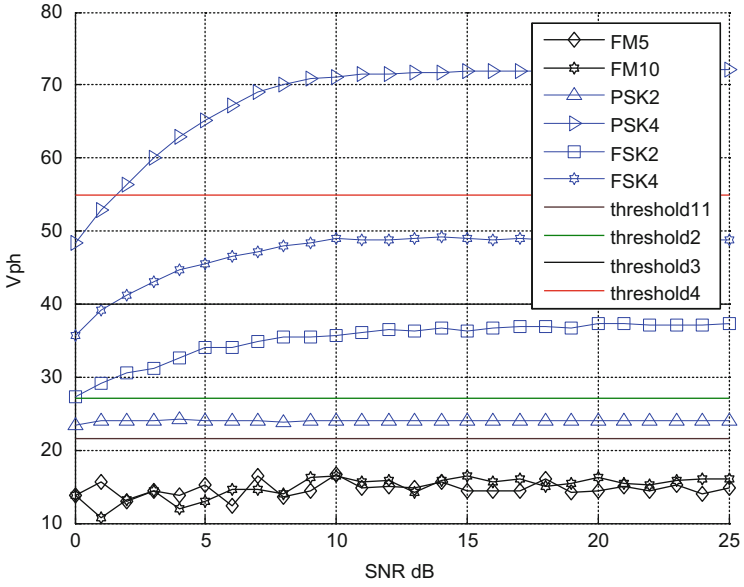

Fig. 11 Using feature $\mathbf{V_{phs}}$ to discriminate MPSK, FM and MFSK from one another

Table 1 The threshold values

Feature	Threshold	Function	Figures
$\mathbf{\lvert P \rvert}$	t1 = 0.325	Discriminate LSB, VSB, USB from AM, DSB, VSB, FM, FSK2, FSK4, ASK2, ASK4, PSK2, PSK4, COM, CW, Noise	Fig. 1
P	0	Discriminate LSB from USB and VSB	Fig. 2
$\boldsymbol{\sigma_{dp}}$	t2 = 0.7	Discriminate AM, ASK2, ASK4, CW from DSB, FM, FSK2, FSK4, PSK2, PSK4, COM and Noise	Fig. 3
	t3 = 1	Discriminate VSB from USB	Fig. 4
	t4 = 1.2	Discriminate DSB from COM and Noise	Fig.5
$\boldsymbol{\mu_{aa}}$	t5 = 0.235	Discriminate DSB, Noise and COM from PSK2, PSK4, FM, FSK2 and FSK4	Fig. 6
	t6 = 0.265	Discriminate ASK2 from ASK4	Fig. 7
$\boldsymbol{\gamma_{max}}$	t7 = 5	Discriminate COM from Noise	Fig. 8
	t8 = 4	Discriminate CW from AM, ASK2 and ASK4	Fig. 9
$\boldsymbol{\mu_a}$	t9 = 0.97	Discriminate AM from ASK2 and ASK4	Fig. 10
$\mathbf{V_{phs}}$	t10 = 22.5	Discriminate FM from PSK2, PSK4, FSK2and FSK4	Fig. 11
	t11 = 25	Discriminate PSK2 from PSK4, FSK2 and FSK4	
	t12 = 40	Discriminate FSK2 from PSK4and FSK4	
	t13 = 55	Discriminate FSK4 from PSK4	

3.2 Flowchart of Automatic Recognition of Analogue and Digital Signals

Figure 12 shows that the sequence order of selecting the features to discriminate between signals of interest.

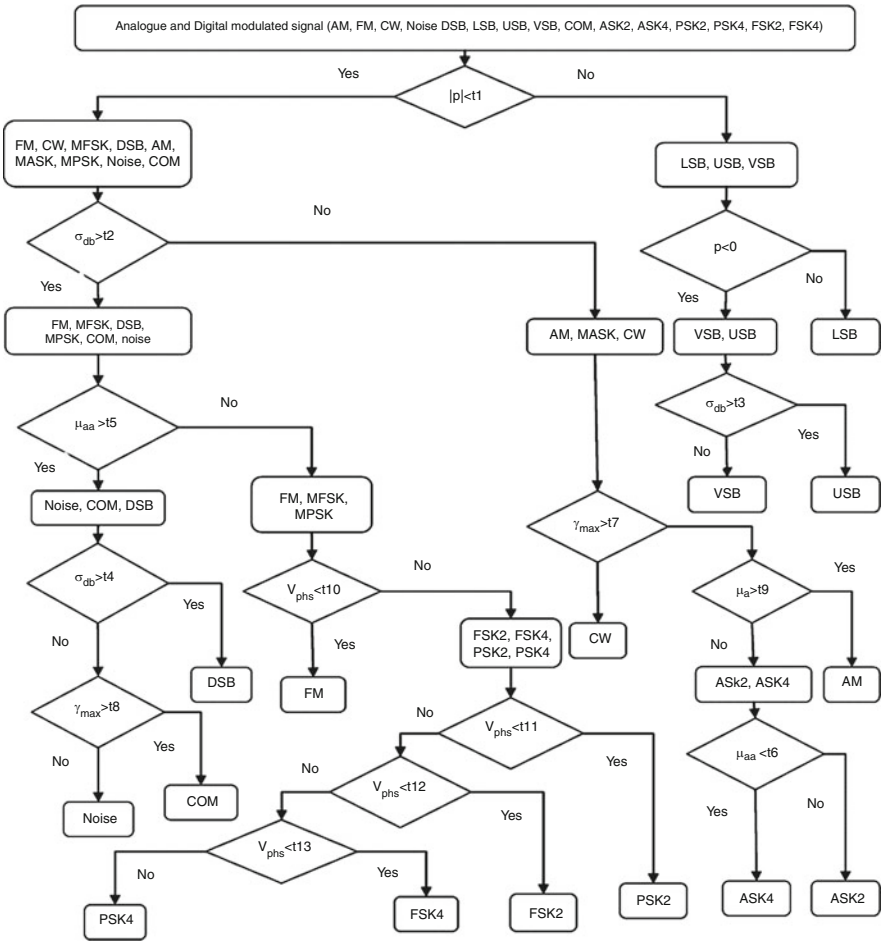

Fig. 12 Functional flowchart of automatic recognition algorithm

3.3 Simulation Results and Analysis

500 iterations are used to get the recognition rates in Tables 2 and 3.

Table 2 shows that, by using $\boldsymbol{\mu_{aa}}$ to discriminate ASK2 from ASK4 the average recognition rate can reach 98 % when SNR $= -2$ dB. Also to discriminate constant amplitude signals from non-constant amplitude signals the average recognition rate can reach 99.9%, when SNR $= 2$ dB.

Table 3 shows that, by using V_{phs} to discriminate PSK2, PSK4, FM, FSK2 and FSK4 signals from one another, the average recognition rate can reach 98.3 % when SNR $= 2$dB.

By using these six features, an average recognition rate not less than 99.6 % can be achieved when SNR $= 3$ dB, as shown in Fig. 13 which is much better than those in [1–7] and [9].

Table 2 The results of feature μ_{aa}

SNR/dB	−4 (%)	−3 (%)	−2 (%)	≥0 (%)	SNR/dB	0 (%)	2 (%)	≥3 (%)
ASK2	100	100	100	100	DSB, COM and Noise	100	100	100
ASK4	6.2	50.4	96	100	Constant amplitude signals	41.2	99.8	100
Average recognition	53.1	75.2	98	100	Average recognition rate	70.6	99.9	100

Table 3 The results of feature V_{phs}

SNR/dB	0(%)	2(%)	≥3(%)
PSK2	100	100	100
PSK4	0	93.6	100
FSK2	100	100	100
FSK4	0	97.8	100
FM	100	100	100
Average recognition rate	60	98.3	100

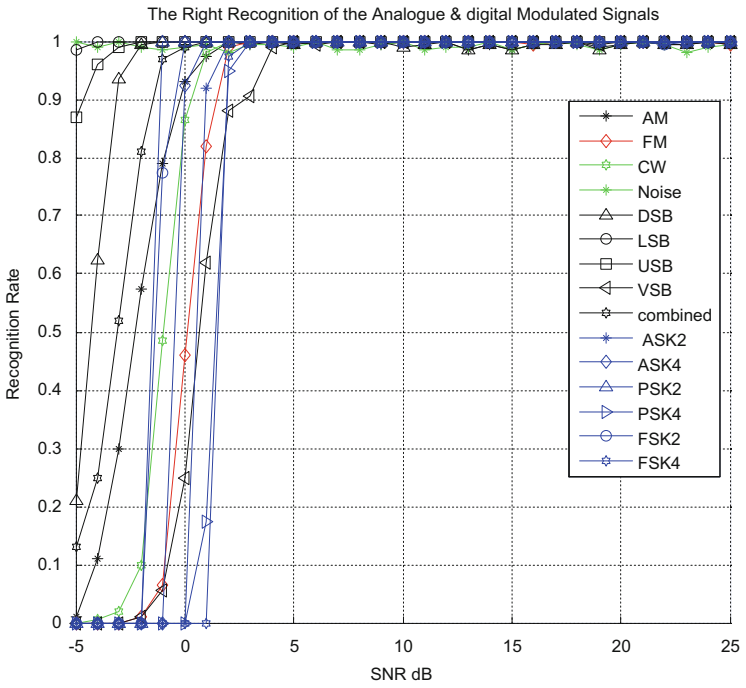

Fig. 13 The overall performance of the algorithm

4 Conclusion

In this paper we propose two new features based on the instantaneous amplitude and phase. By using these two new features, along with four other previously proposed features, an average recognition rate not less than 99.6 % can be achieved when SNR = 3 dB. This algorithm not only gives a better recognition rate, compared to existing algorithms, but it is also easier to compute. The simulation results also show that only one feature can be used to discriminate the FM, MPSK and MFSK signals from one another. This is more feasible in practical scenarios.

Acknowledgement The authors would like to acknowledge Sarafadeen of UESTC for his support and contributions towards the accomplishment of this paper. This work was supported in part by the National Natural Science Foundation of China under Grant 11176005.

References

1. Azzouz EE, Nandi AK (1996) Automatic modulation recognition of communications signals. Kluwer Academic, Netherlands
2. Azzouz EE, Nandi AK (1996) Procedure for automatic recognition of analogue and digital modulations. Communications – IEEE Proceedin 143(5):259–266
3. Nandi AK, Azzouz EE (1998) Algorithms for automatic modulation recognition of communication signals. IEEE T Commun 46(4):431–436
4. Cheol-Sun Park, Dae Young Kim (2007) A modulation classification of analog and digital signals using neural network and support vector machine. ISNN 2007, Part III, LNCS 4493, p. 368–373
5. Jie Yang, Xumeng Wang, Hongli Wu (2009) Modified automatic modulation recognition algorithm. Wireless Communications, Networking and Mobile Computing, p. 1–4, Dec 2009.
6. Xudong Liu, Jinzhao Su, Wei Wu (2010) A modulation recognition method based on carrier frequency estimation and decision theory. Communications (APCC), 2010 16th Asia-Pacific conference, p. 6–11, Nov 2010
7. Chisheng Li, ShuliangXu, GuofengZha (2010) An efficient recognition algorithm between analog and digital signals at low SNR. IEEE Intelligent Computation Technology and Automation (ICICTA), (1)505–508
8. Jaspal Bagga, Neeta Tripathi (2011) Analysis of digitally modulated signals using instantaneous and stochastic features for classification. International Journal of Soft Computing and Engineering (IJSCE) 1(2) ISSN: 2231–2307
9. Dahap B, Liao H (2013) Simple and efficient algorithm for automatic digital modulation recognition. (sent to an international conference on communications signals processing and system —CSPS2013), "accepted"

Control System by Laser Positioning Based on Free Pendulum

Liguo Hao, Xueling Zhao, and Shengbin Liang

Abstract The system is designed on the basis of Question B from 2011 National Undergraduate Electronic Design Contest-plate control system based on free pendulum. The system measures the angle change of the pendulum using the rotary encoder to control the motor mounted on the end of the pendulum in order to make the plate fixed on the motor shaft stable, ensuring that coins on the plate are stable. According to the trigonometric relation among the angle and direction of pendulum, the angle of the plate, and the distance between the pendulum and the light point from the laser pen fixed on the plate, the system controls the angle of the plate and makes the laser pen irradiate on the central line. When the pendulum swings freely, the system uses the PID algorithm to control the angle of the plate, so that the laser pen always irradiates on the central line. The experimental data show that the angle error is less than 5° during the rotation of the plate, and eight coins on the plate can keep in the stacked state when the pendulum swings freely within the range of ±60°, and the offset between the light point and the target is less than 3 cm during the free swing of the pendulum. The system won the national first prize in National Undergraduate Electronic Design Contest of China.

Keywords Free pendulum • Laser positioning • Servo motor • Rotary encoder

L. Hao (✉)
Engineering Training Center, Tianjin University of Technology and Education, Tianjin, China
e-mail: ivy.lou@163.com

X. Zhao • S. Liang
Join Lab of Information Sensing and Intelligent Controlling, Tianjin University of Technology and Education, Tianjin, China

B. Zhang et al. (eds.), *The Proceedings of the Second International Conference on Communications, Signal Processing, and Systems*, Lecture Notes in Electrical Engineering 246, DOI 10.1007/978-3-319-00536-2_42,

1 Introduction

With the rapid development of the modern detection and control technology, the microcomputer is employed as the main body of the measurement and control system, instead of the conventional electronic circuits of the traditional measurement and control system, which forms a new generation of Computerized Measurement and Control System [1, 2]. National Undergraduate Electronic Design Contest of China almost has the control subject every time, and universities across the country pay attention to the study of the subject, which shows that the study is of great significance [3].

The control system of the plate based on free pendulum is the experimental installation designed for teaching experiments of basic control courses, such as Principle of Automatic Control. It is a classic experimental subject in the control field, and can build a good experimental platform for the teaching, experiment and research on automatic control theory [4]. The system uses the microcontroller, AVR128, to control the servo motor, the keyboard, the LCD (Liquid Crystal Display), the rotary encoder collecting the data, the pneumatic device and the voice circuit.

2 Overall Design

The system belonging to the Motion Control System includes constant value control and following control, and consists of the detection unit, the control unit, the execution unit and the human machine interface. The block diagram for the system is shown in Fig. 1.

The detection unit serves to detect the moving angle of the pendulum rod and between the plate and the pendulum rod. The angle sensor, the rotary encoder, the potentiometer and gyroscope are generally available in the angle detection [5–8]. The system uses the rotary encoder to measure the moving angle of the pendulum and the plate.

The control unit acquires the system information and transforms into the control instruction according to which the execution unit controls the moving angle of the plate and displays the related information. The keyboard input, the LCD and the voice output are used to make the system user-friendly and easy to operate in the system of the human-machine interface.

The execution unit mainly controls the angle of the plate. The controlled parameters include the angle and the angular velocity. The system requires higher real-time, therefore, the DC servo motor is used in the system [9, 10].

Because the system is a typical motion control system, the classic control method, PID, is adopted in the system. The coefficients of the proportion, the differential and the integral are constantly modified through theoretical calculations and experiments [11–13].

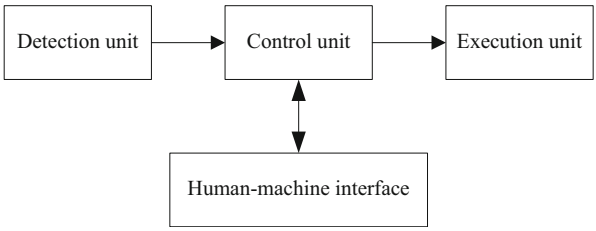

Fig. 1 Block diagram of the system

3 Theoretical Analysis and Computing

The swing process of the free pendulum in the control system is studied primarily, so the free pendulum is regarded as the rigid body with the most basic motion form, the translation and the movement around a fixed axis. The movement of free pendulum is analyzed using the model for the rigid body as follows.

3.1 Control of the Plate

The angle of the plate is adjusted according to that of the pendulum movement. When the pendulum swings a cycle, the plate must rotate proportionally a cycle. The structure of the system is shown in Fig. 2, in which R is the length of the pendulum, a and b are the maximum angle between the pendulum and the vertical line respectively when the pendulum swinging. The angle change between the plate and the pendulum is written as

$$\varphi = \frac{360}{2(a+b)}\theta \tag{1}$$

where φ and θ are the angle change of the plate and the pendulum respectively.

The pendulum rod is pulled left or right to an angle of a or b (30°–45°) and the plate is parallel to the ground. Then a coin is placed stably in the center of the plate. After the system starting, the pendulum is released and swings freely. During the swinging, the coin does not fall from the plate. The stress for the coin is shown in Fig. 3. The coin is subject to the gravity G, the support N and the friction F1. When the component force of G in the plane direction, F, is greater than F1, the coin will move along the direction of F with the acceleration of $a = \frac{F-F_1}{m}$. To avoid the relative motion between the coin and the plate, it is necessary to control the plate to keep the same acceleration as the coin in the direction of F. The acceleration of the coin is along the circumferential tangential direction. As long as the plate is still perpendicular to the pendulum rod during the movement, the plate can keep the same acceleration as the coin.

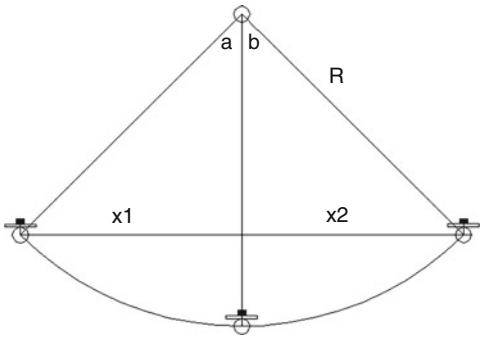

Fig. 2 Motion schematic diagram of pendulum bar

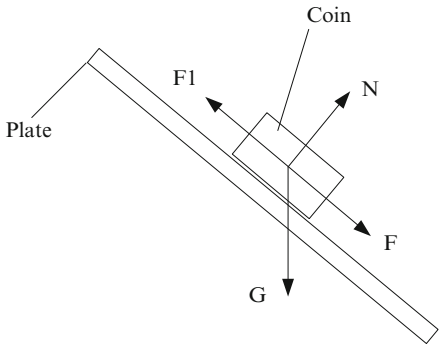

Fig. 3 Stress of the coin

3.2 Positioning of the Laser

The laser pen fixed on the plate irradiates on the vertical target at a distance of 150 cm from the pendulum. When the pendulum is vertical and static, and the plate is in the horizontal direction, the height of the target is adjusted to make the light point from the laser pen on any one line of the paper pasted on the target, and then this line denotes the central line, as shown in Fig. 4, in which R is the length of the pendulum.

If a is the swing angle of the pendulum, $\times 1$ is the projection of the pendulum on the *x*-axis, and y1 is the projection of the pendulum on the *y*-axis, h1 is the difference between y1 and R, and L1 is the distance between the plate and the baffle. If b is the swing angle of the pendulum, *x*2 is the projection of the pendulum on the *x*-axis, and y2 is the projection of the pendulum on the *y*-axis, h2 is the difference between y2 and R, and L2 is the distance between the plate and the baffle.

After the pendulum is pulled left or right to the angle of a or b (30°–60°) and the system is started, the system controls the plate to make the light point on the central line in 15 s, and uses the LED as the indicator, as shown in Fig. 5.

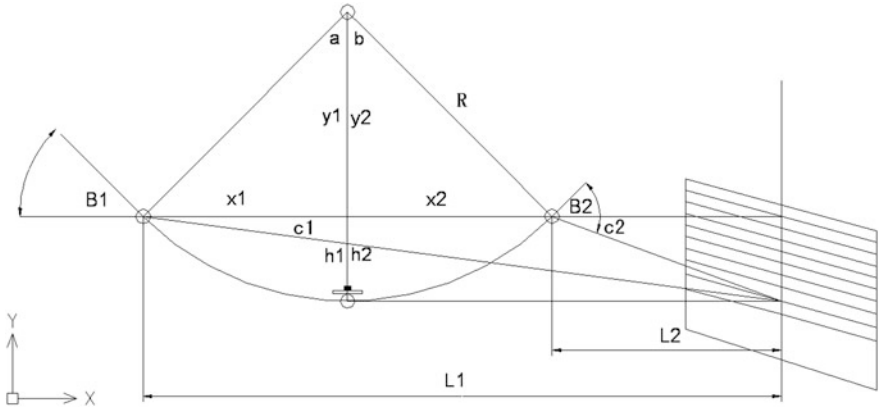

Fig. 4 Analysis on the light point

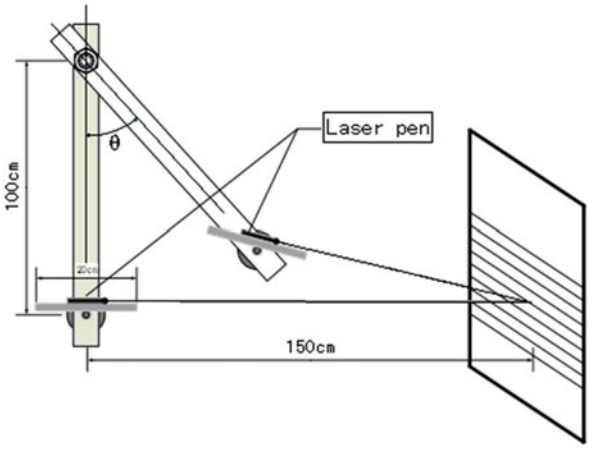

Fig. 5 Schematic diagram of laser pen irradiation

In Fig. 4, when the pendulum swings left at the angle of a or b, c1 or c2 is the angle between the plate and the horizontal plane, and R is the length of the pendulum. The relationship between c1and a is written as

$$c_1 = a - \arctan\frac{R - R\cos a}{1.5 + R\sin a} \tag{2}$$

The relationship between c2 and b is written as

Table 1 Stacking state of the coin

Times	Swing angle	Stacking number	Falling number	Deviating position (cm)
1	45°	0	6	1
	60°	0	7	4
2	45°	2	4	3
	60°	4	2	2
3	45°	1	1	2~4
	60°	2	1	2~4
4	45°	6	0	1
	60°	6	0	2
5	45°	8	0	2~3
	60°	8	1	2~3
6	45°	8	0	0.5
	60°	8	0	0.5

$$c_2 = b - \arctan\frac{R - R\cos b}{1.5 - R\sin b} \tag{3}$$

During the swing of the pendulum, the angle of the plate is controlled to make the light point of the laser pen on the central line of the target.

In order to improve the operating speed of the system, the method of look-up table will be used to calculate trigonometric functions in the equations (2) and (3).

4 Experimental Results and Analysis

4.1 Control Testing the Plate

Eight coins are stacked on the plate center, the pendulum is pulled slowly to the angle of 45°–60°, and whether the coins fall from the plate is observed, and the testing is repeated. Then, the pendulum is pulled to the angle of 45°–60°, eight coins are stacked on the center of the plate keeping horizontal, and then the pendulum is released and swings freely, and whether the coins fall from the plate is observed, and the testing is repeated. The experimental results are shown in Table 1.

The results show that the coins do not fall from the plate and keep the stacking state in five swing cycles by controlling the plate.

4.2 Positioning Testing of the Laser

The laser pen is placed in parallel on the plate and irradiates on one of the target lines in vertical state, and the line is marked. Then, the pendulum is pulled to the angle of 30°–60° and is released and swings freely, the distance between the light

Table 2 Off-centered distance of the light point (cm)

Swing angle			
Times	30°	45°	60°
1	Fail		
2	Fail		
3	8	10	10
4	4	4	3
5	6	5	6
6	3	2	2
7	0.5	0.5	0.5

point and the central line is observed, and the testing is repeated. The data from the experiment is shown in Table 2.

The experimental results show that the light point from the laser pen is near the central line in 2 s (less than 3 cm).

5 Conclusion

The absolute value of the error produced by the plate rotating a circle is less than 5° in one swing cycle of the pendulum. During the swing of the pendulum pulled to the angle of 40°–60°, the coins do not fall from the plate in five swing cycles of the pendulum, and keep the stacking state. After the pendulum is pulled to the angle of 30°–60°, the system can control the plate within 2 s to make the light point about 3 cm apart from the central line. The system was awarded the first in the 2011 National Undergraduate Electronic Design Contest.

References

1. Bo W, Wenchang H, Zhichao W et al (2012) Analysis and design of a free pendulum flat-panel control system. Electron Technol 8:43–46
2. Zhanlin C, Xiaosuo W (2012) The dynamical equilibrium control system for free swing of a plate. Automation & Instrumentation 3:179–180
3. Jiuyuan G, Yuyang B, Jiahui L (2011) The flat control system based on the free pendulum–2011 National undergraduate electronic design contest B of undergraduate group. Electronics World 15:10–12
4. Zhen L, Yubing Z, Jingjing H et al (2012) Panel control system based on the free pendulum. Sensor World 1:13–16
5. Yulong G (2012) Design of flat-panel control system of free pendulum. Physics Experimentation 32(6):40–46
6. Ming W, Yanji H, Junhua W et al (2007) Application of incremental revolving encoder in impulse measurement with compound pendulum. Chinese Journal of Scientific Instrument 28(1):140–144

7. Hongjun B (2011) The development of the nonlinear wire-wound potentiometers. University of Electronic Science and Technology of China, 4–17
8. Ning W, Zhuolin D, Ye Z (2012) Panel control system based on the free pendulum. Electr Eng 4:87–91
9. Yang Z, Lei W, Tao Z (2010) Control-oriented correlation analysis identification for servo systems with friction. Journal of Electronic Measurement and Instrument 24(9):814–818
10. Wei H, Jian R, Sheng L et al (2012) Dual-loop control system of DC servo motor based on DSP. Journal of Mechanical & Electrical Engineering 29(1):70–73
11. Qiyuan W, Xiaogang R (2012) Dual loop nonlinear PID control of single-wheeled robot. Control and Decision 27(4):593–597
12. Ping H, Zhanxia Z, Weihua M (2012) Design and simulation of servo system based on self-adaptive fuzzy PID control. Computer Simulation 29(1):138–142
13. Xiyin L, Jianping L, Xiujuan D et al (2012) Design of free place flat control system based on the ARM9. Microcomputer & Its Applications 31(8):81–83

Humanoid Robot Design

Xueling Zhao, Shouquan Bian, Liguo Hao, and Peng Zhao

Abstract The paper introduces the design process of the mini-type humanoid robot. According to the human morphological characteristics and the principle of bionics, the robot structure close to the proportion of human body size is designed. And the DOF (Degree of Freedom) configuration scheme in accordance with functional requirements of the robot is designed by using the principle of least DOF. The controller of the steering engine is designed to cooperate with the PC in order to control the humanoid robot, and it can transform the commands transmitted by the PC into signals controlling the steering engine. The experimental results show that the humanoid robot is able to complete the corresponding action and realize the dancing demonstration.

Keywords Humanoid robot • Steering engine • AVR

1 Introduction

The research on humanoid robot with human characteristics and behavior integrates multi-science and is an important indicator of a country's high-tech development [1]. A lot of work has been done in the development of humanoid robot by the researchers from the United States, Japan, South Korea, the United Kingdom and other countries, and has achieved a breakthrough [2]. In this regard, China also made a lot of work. For example, National University of Defense Technology, Harbin Institute of Technology, Shanghai Jiao Tong University and other developed a biped walking robot [3], Beijing University of Aeronautics and Astronautics,

X. Zhao (✉) • S. Bian • P. Zhao
Join Lab of Information Sensing and Intelligent Controlling, Tianjin University of Technology and Education, Tianjin, China
e-mail: 756525358@qq.com

L. Hao
Engineering Training Center, Tianjin University of Technology and Education, Tianjin, China

B. Zhang et al. (eds.), *The Proceedings of the Second International Conference on Communications, Signal Processing, and Systems*, Lecture Notes in Electrical Engineering 246, DOI 10.1007/978-3-319-00536-2_43,

Harbin Institute of Technology, Beijing University of Science and Technology developed a multi-fingered dexterous hand [4], Chinese Academy of Sciences, Hefei Institute of Substances developed intelligent feet [5].

A low-cost small humanoid robot meeting the basic requirements of the biped robot is developed with the most basic motion function. With reference to the proportion of actual limb of the human body, trunk, limbs and head of the robot are built with aluminum extruded sections, each active joint uses a steering engine, and the driver is designed to control steering engines to achieve each joint action. The control software of steering engines is programmed to control the robot motion by VB. Experiments show that the humanoid robot is able to complete the required combination of dance movement.

2 System Design

The system mainly consists of the mechanical structure, the control circuit and the PC control software, as shown in Fig. 1. The mechanical structure is built based on of limbs of a real person, and is close to the actual proportion of the human body as much as possible, and the activities of the joint is achieved through the steering engine. The control circuit is used to control each steering engine and makes the system imitate the body movements. PC control software is to schedule the robot dance, and calculates the movement angle of corresponding joint for every action.

According to dance movements done by the system, the motion range of each joint and sequencing are scheduled, and enter the PC software which is to transmit one by one action instructions to the controller installed with the battery in the robot body by serial communication interface. After receiving instructions, CPU in the controller will control the steering engine driving the joint to move and reaching the specified position. Thus, the system can imitate a variety of body movements.

3 Structural Design

The mechanical structure is basis of the robot making a variety of imitating action [6]. The system wants to imitate lifelike human action, the number of joints and the degree of freedom should be as much as possible because of very complex human joints [7]. But the increase in the number of joints and the degree of freedom will make the robot more difficult control, raising the cost of hardware [8]. It is found by observing the performance of the dancers that the movements of the dancer's arms, legs and head will bring better visual effect, while the action of fingers and other parts is generally not clear. Therefore, the mechanical structure uses only limbs and joints with apparent movement, while such as fingers, spine and other joints are ignored, which will reduce its degree of freedom.

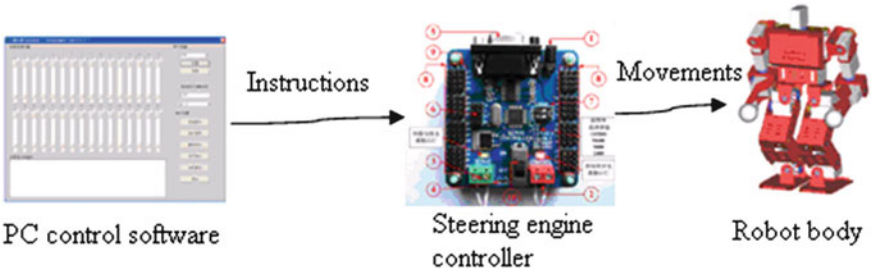

Fig. 1 System structure

3.1 Degree of Freedom Configuration

The mechanical structure mainly consists of head, trunk, upper limbs and lower limbs, as shown in Fig. 2. The head and the trunk are connected by a neck joint with only one rotation degree of freedom. The upper limbs are connected to the trunk by the shoulder joint with 2° of freedom, and can make side swing arm and front and rear swing arm. The big arm and the forearm are connected together by the elbow joint with one bending degree of freedom. The lower limbs are connected to the trunk by the hip joint with 2° of freedom, and can make the side leg lift and the front and rear leg. The thigh and the crus are connected together by the knee joint, and can make the bending action. The crus and the foot are connected together by the ankle joint, and can make the bending action. The system includes 11 joints with a total of 15° of freedom.

3.2 Body Design

The system selects the aluminum extruded sections as the body, which ensures the mechanical strength, simplifies the mechanism and reduces the weight of the system. In Fig. 3, (a) is the trunk made of aluminum sheet, its hollow portion is used to mount the circuit and the battery, and (b) is the basic shape of the upper and lower limbs with the U-shaped aluminum. According to the mounting position, its size can be adjusted to fix the steering engines.

3.3 Body Connection

The body is connected in accordance with the corresponding position, thus the mechanical structure is built basically. In order to simplify the mechanism, the body is directly connected by output shafts of steering engines, the rotation angle of which corresponds to the flexion angle of the joint. For shoulder and hip joints with

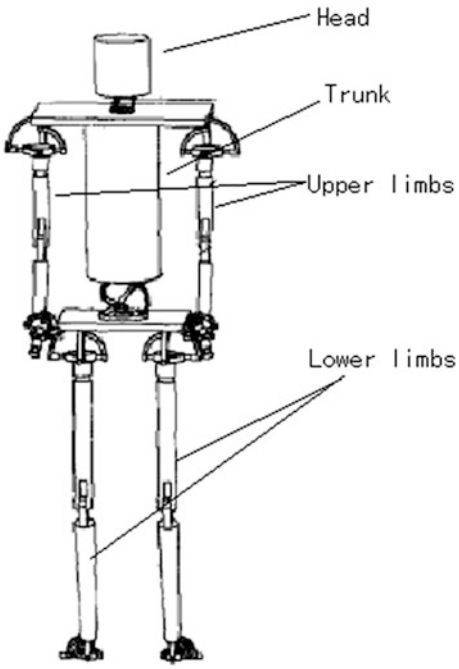

Fig. 2 Body structure of humanoid robot

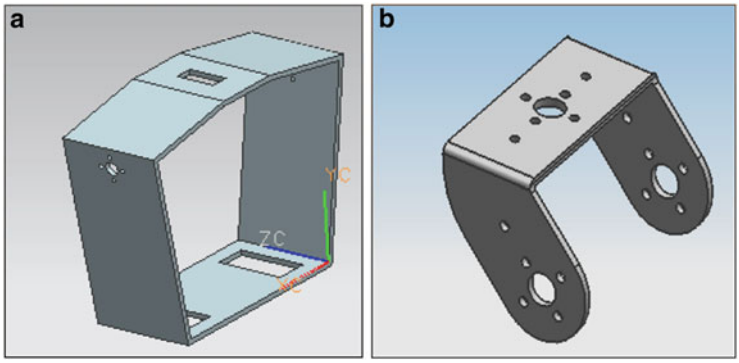

Fig. 3 Body outline

2° of freedom, the system uses two steering engines orthogonal connection. Figure 4 shows the overall structure of the system.

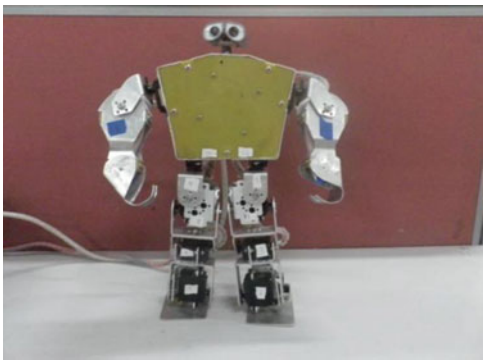

Fig. 4 Overall structure

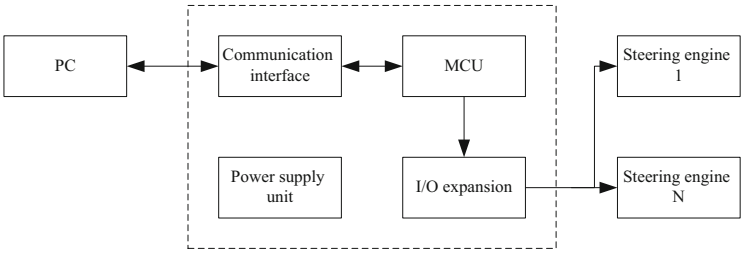

Fig. 5 Control circuit structure

4 Control Circuit Design

The control circuit serves to control the rotation angle of the output shaft for the steering engine according to the dance movement scheduled, thus making the joints bend for a variety of body movements. The control circuit controls the output angle of the steering engines by changing the duty ratio of the square wave of 50 Hz, and mainly includes MCU, power supply unit, communication interface, I/O expansion, as shown in Fig. 5.

4.1 MCU and Interface Unit

The system uses AVR series of 8-bit microcontroller, ATmega48, as MCU. The serial communication is used between the ATmega48 and PC by the MAX232 chip converting TTL to RS232 level. The I/O ports are expanded by four serial-in parallel-out chips of 74HC595, presenting 32-channel square waves in output and simultaneously controlling 32 steering engines at most. For preventing the control delay too long, four chips of 74HC595 are divided into two groups controlled by two groups of I/O ports respectively. SMD(Surface Mounted Devices) are used in the circuit to reduce the volume of the system.

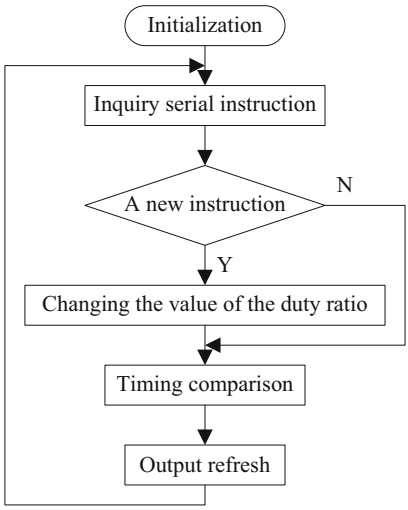

Fig. 6 The flowchart of MCU

4.2 MCU Programming

The main function of the MCU program is to control the corresponding I/O port to generate the square wave output with different duty ratio according to the instructions from PC. The program mainly includes the communication subroutine, the timing subroutine, and the I/O output subroutine. The flowchart of the program is shown in Fig. 6. The system initializes firstly after provided by electricity, and controls the steering engines from different joints to present the square-wave output with different duty ratio for making the system upright. The system starts to enter the main loop after initialization. The loop mainly consists of the following steps: inquiry serial instruction, changing the value of the duty ratio, timing comparison, and output refresh.

The instructions which the serial interface receives are two consecutive frames of data with each frame of 16 bytes. The system uses MG599 from Shenghui Co. Ltd. as the steering engine controlled by the pulse width modulated signal of 20 ms changing linearly with a pulse width of 0.5–2.5 ms and the corresponding position of 0°–180° for the steering wheel in the steering engine. Each byte represents the pulse width of one square-wave output (0.1 ms) for reducing microcontroller's program computation. After receiving the serial data, the system will refresh the array for the values of the pulse width.

The timer brings the time base interrupt of 0.1 ms, the timing variable accumulated in the interrupt handling function is compared one by one with the data in the array for the values of the pulse width in the loop body of the main program. If the values are equal, the I/O port corresponding to the element in the array presents

the low level in output. When the timing reaches 20 ms, all I/O port will have the output of high level and the timing variable will be zero clearing.

5 Software Design

The software for scheduling the dance movements is designed by VB. The dance movements arranged by the operator are broken into changes in the angle of the steering engine entered into the control interface according to the action sequence. The control interface includes the channel setting, the serial setting, and the operation setting. The serial setting is used to set the baud rate and the data format for communication. The dance movements can be scheduled after the serial setting completed.

According to the number of the steering engines used in the system, the corresponding control channel is selected and activated. The progress bar for each channel is dragged to control the corresponding steering engine after the dance movement decomposition. After the setting for all the joints are completed in decomposition and the adding command is clicked, the movement will be stored in the instruction sequence. By this method, all dance movements can be set. When the running instruction is clicked, the PC will transmit the instruction sequence to MCU at setting interval in turn, then, the system can achieve the specified dance movements.

6 Experimental Result

The function and reliability of the system are verified by experiments including single joint testing and the multi-joint associated debugging, after the system completed.

The single joint testing serves to determine the scope and direction of its rotation angle and the initial position. The value of each channel can be changed through the control interface in the PC, and thus the movement of the corresponding joint can be observed. Table 1 shows the initial position for each joint when the system is static.

The single joint testing shows that this system can imitate the basic movements of the human. While the human actions need multiple joints to exercise jointly, so the multi-joint testing should be carried out.

With the simple squat as an example, the action needs the hip, the knee and the ankle joints to exercise jointly, which ensures that the position of the center of gravity will not shift and the system will not fall. The system can complete the squat and keep balance by continuously adjusting the angle, the speed and the context of the placement of the relevant joints.

Table 1 The initial position for each joint when the system is static

Channel	Joint	Pulse width (mS)
1	Neck	1.5
2	Lateral left shoulder	1.0
3	Radial left shoulder	1.5
4	Left elbow	0.5
5	Lateral right shoulder	1.0
6	Radial right shoulder	1.5
7	Right elbow	0.5
8	Lateral left hip	0.5
9	Radial left hip	1.5
10	Left knee	2.5
11	Left ankle	1.5
12	Lateral right hip	0.5
13	Radial right hip	1.5
14	Right knee	2.5
15	Right ankle	1.5

7 Conclusion

This paper describes the design process of the humanoid robot. The system designed according to the structure proportion of the human body uses 15 steering engines to complete the movement of every joint with 15° of freedom, provided with an integrated controller for the steering engines which can control multi-way steering engines by communicating with the PC in a coordinated fashion. The experiments show that the design of the system is reasonable and the system achieves all dance movements.

Acknowledgements This work was supported by Tianjin University of Technology and Education Foundation (No.KYQD10004).

References

1. Maochuan Z, Wei Y, Lili L (2010) Overview of humanoid robot theoretical research. Machinery Design & Manufacture 4:166–168
2. Jing L (2012) Current situation of the development and prospect of humanoid robot. Science & Technology Information 21:42–43
3. Jindong H, Guodong L (2011) Whole-body online modification of biped robot walking pattern. J Comp Appl 31(1):286–288, 292
4. Intelligent robot dexterous fingers hand successfully developed (2010). Robot Technique and Application 6:45
5. 'intelligent foot' of China robot will not afraid bumpy road, Silicon Valley (2012). The People's Daily 10:1
6. Ming J, Zhao S, Kangsheng Q et al (2009) Study on serial-parallel mechanisms. Manufacturing Automation 31(1):61–65

7. Yulin Z, Feng G (2006) Mechanism architecture of humanoid robot. Chinese J Mech Eng 42 (11):66–70
8. Qinglin A, Shunjiang Z, Fang X (2012) Review of kinematics and singularity of parallel manipulator. Journal of Zhejiang University (Engineering Science) 46(8):134–135
9. Dongchao Y, Mingguo Z, Ken C et al (2003) DOF analysis for a humanoid robot. Chinese J Mech Eng 14(6):453–456

Comparative Study on the Textbooks of Classic "Electric Circuits Analysis"

Guanglin Han and Xiaoyang Song

Abstract "Circuit analysis" course is an important basic course of electrical and related professional, is the foundation of the follow-up courses for students learning. This article from the relationship between the content of teaching philosophy and teaching materials, methods and circuit design of the circuit analysis, the relationship between knowledge structure and cognition of the students, the "circuit analysis" to compare the textbook. To explore more suitable for Chinese students, the introduction of foreign excellent achievements in teaching and teaching methods, enrich and perfect our country University "circuit analysis" course teaching.

1 Introduction

"Circuit analysis" curriculum theory, logic is strong, wide application, to cultivate the students seriously rigorous science attitude, theory and practice ability, thinking ability, analysis of experimental ability and scientific ability, computation ability to have the vital role. In-depth understanding of domestic and foreign classic "circuit analysis" the content of the teaching material and differences, to learn the successful experience and reference of foreign materials, according to the current situation and development trend of domestic teaching materials, summed up the more suitable for Chinese students cognitive style of teaching contents, to build with Chinese characteristics "circuit analysis" teaching material system.

G. Han (✉) • X. Song
Department of Physics and Electronic Information, Tianjin Normal University, Tianjin, China
e-mail: hgltj@163.com

B. Zhang et al. (eds.), *The Proceedings of the Second International Conference on Communications, Signal Processing, and Systems*, Lecture Notes in Electrical Engineering 246, DOI 10.1007/978-3-319-00536-2_44,

2 Relationship Between the Content of Teaching and Textbook Author

Teaching philosophy is a textbook of the soul, is the core of the overall architecture material. The study found the "circuit analysis" material initial part will explain the author's own teaching philosophy. The content of teaching materials and the teaching idea gradually, to express the author's teaching philosophy. Because every one of the author's teaching experience, the experience and the different focus, the formation of teaching philosophy is different, so different. Reflected in the teaching content of the presentation, basic knowledge of the theory of knowledge, the emphasis of auxiliary materials, supporting, appendix design with personality and characteristics of the author's unique, forming a diversity of materials. Make the reader different textbooks, on the same theory and experience different feeling, to obtain the most direct knowledge and ideas.

"J. David Irwin Basic Engineering Circuit Analysis" a book that: circuit analysis has been in more extensive field reflects its importance, so the circuit analysis teaching design goal should be to provide a more effective environment for students as much as possible to understand the circuit principle analysis with the circuit analysis, master skills, understand circuit relevant design ideas [1]. Due to the development scale and the development needs of the different universities, considering the objective restrictions reduce hours, coupled with the impact of individual differences in learning habit of students, "design of circuit analysis" to emphasize learning design details, do not only provide detailed materials about the theoretical knowledge, but also to provide the learning methods and learning for the skills. The textbook compilation thoughts, the teaching material content and structure layout and attention to details are required, try to do: clear and concise interpretation, the basic theory is easy to read; provide a lot of help, meet the students' individual difference, make it quickly master the teaching content; to provide a large number of able to solve the definitive answer examples, exercises and test project, give readers ample opportunity to understand the content of teaching materials, teaching knowledge digestion. The textbook is actually reflect the rich teaching experience and practice experience, author of circuit analysis course reflection and experience.

China's "circuit analysis" teaching textbooks written by the team, in the purpose of creation is often discussed in textbook compiling team work. Emphasis circuit materials is the basis of teaching materials for electrical majors, basic theory focuses on the circuit and the commonly used analysis methods, this compilation of the textbook content more logical and tight, but it is hard to explain, teaching his experience and practice experience, easy to cause the same textbook, no characteristics. To prepare the team have sufficient practical experience can be created for the outstanding student textbooks in china.

Mr. Qiu Guanyuan pointed out, now the basic content and the scope of our circuit courses have been largely stable, the content of textbooks focus on basic knowledge, provides important theoretical foundation for the following study. In order to meet the objective fact hours reduced, material cut too strict and profound

knowledge about; increase the exercise type, reducing the number of exercises are too simple, the extensive type of exercises; the addition of a small amount of new knowledge, develop the basic ability of students' thinking and responding to market demand [2]. Our textbook has been absorbing advantages of excellent foreign teaching materials, but the extent is still not enough. The basic idea of the teaching material to add new content, on one hand, open up horizons of students, let the students know their future development direction of professional; on the other hand, presents a new circuit world to students, increase the learning interest.

3 Science History Plays an Important Role in the Teaching of Circuit Analysis

Foreign open thought influence teaching contents, the author put circuit phenomena attributed to natural science. That knowledge is the charge circuit and results from the interaction between. Master the related knowledge of the need to understand the history of electrical circuit theory. To understand the characteristics of the development trend of modern engineering technology and method as well as the new century circuit engineering, but also to understand the basic circuit theory origin, development and maturation process. Therefore, most textbooks of circuit theory the important historical figures and experiment to do a simple introduction. Some textbooks is described in detail in the text and pictures of typical experiment. Let the students see the development process of classic experiment.

"Introduction to Electric Circuits" in the first chapter introduces the history of electricity scientists Guerlcke, Benjamin, Volta, Ampere, Joule, Maxwell and their contributions to the theory of electricity, and attach the important schedule from 1600 to 1995 in electrical engineering. Each chapter in respectively introduces the electricity class specialized historical figures, historical figures and all the experiments and all attached to the photo [3]. Some textbooks not only describes the research experience and experiment process circuit history have made outstanding contributions to the scholars, and introduces their entrepreneurial history. The author believes that this is not necessary, the role is: to enable students to understand the development process of circuit theory, increase the learning interest; let the students know more in-depth electrical theory, see how theory is developed and improved in practice.

Circuit Textbooks in China rarely introduced important figures in the development of electricity. Textbooks in China compared to the theory, so that the students in the learning process to be boring. The author make the practice example to us. The history of a landmark event, to raise the level of science and technology has made great contributions to the history of the characters introduced to students. Use the example of the scientific progress and development is hard work and sweat of the scholars. Combine theory with practice. Students got the innovative education and quality education.

4 The Relationship Between Method and Circuit Design of Circuit Analysis

Because of the influence of foreign culture, students' abilities of attention. Circuit analysis of the author attaches great importance to the circuit design, the circuit analysis and circuit design in the equally important position, the design of organic combination of the process and the actual circuit problem of circuit analysis, that is to let the learning method of circuit materials to circuit analysis to solve practical problems for circuit design.

"Electric Circuits" this book will make a case at the beginning of each chapter and the end of circuit analysis, the application of knowledge to solve practical problems in life, explains the research process of electronic products from the idea to the specific product. With the design of practical engineering makes theory and practice together in the circuit in the textbook, let students have a preliminary understanding of electrical applications, to have a better understanding of their future occupation. The teaching of theoretical knowledge and practical application together, let the students have a good understanding of the importance of the basic theory of in the textbook. To attract, stimulate the curiosity of the learners, active imagination and desire to succeed in the electricity class specialized work. The successful completion of a project from design to finished product, give students a sense of achievement.

Our textbooks are mainly circuit analysis skills, very few specific issues related to circuit design, put forward the importance of design and rarely on the circuit analysis is an important feedback, it is easy to cause the students fuzzy circuit analysis, the analysis method of become rigid experience, the theory and practice. This point we should foreign circuit analysis teaching, the circuit design into the circuitry neatly analysis. The need for such a textbook author has rich practical experience in engineering circuit.

5 Part of the Experiment Teaching Materials to the Status of Circuit Analysis

Circuit analysis course is set up on the foundation of experiment. The circuit analysis experiment focus is to let the students for the actual project design. In the process of finishing the project, theory and practice are combined. Let the students strengthen capacity according to the theory of practical process. Design experimental project and working process is to make students aware of their own in the course of the experiment, which is easy to make mistakes, to avoid in the future study. The author thinks that the foreign teaching material is the carrier of knowledge, is the basis for preparation of the experiment; but our author thought experiment is the circuit analysis theory verification method, is the students deepen process of theoretical knowledge in practical process of impression.

Our experimental analysis of key circuit is verified classical circuit theory. The students' learning process theory in the process of the experiment, enhance mutual understanding and memory theory. Separate from the majority of university curriculum theory and practice of courses, respectively. Because of our universities in circuit teaching by the few hours, site equipment limitations, students can acquire knowledge from teacher to most verbal description in the experimental part. From the current settings of each college courses, this situation is easing. Circuit experiment was also pay attention gradually. Such as: Undergraduate Electronic Design Contest and other forms of attention; all kinds of advanced experimental equipment into China; social experiment project in gradually into the university. All these prove that our circuit teaching receive recognition. The students are trying to improve their learning ability and practical ability.

6 The Relationship Between Knowledge Structure and Cognition of the Students

The circuit analysis teaching attaches importance to teaching methods, teaching ideas and practical experience. The textbook is an important carrier of the teaching process, it provides the contributions made by a circuit of scientific development platform for the author. Foreign materials with full respect for the teaching ideas and teaching ideas of the author's personal experience, according to the author's own teaching experience and industrial project design, on the basis of the cognitive level of students to meet the reasonable arrangement of teaching material, the layout. Students are the main body of learning activity, the preparation of teaching materials should pay attention to the student's cognitive level and cognitive style. The author firstly have an overall mastery of knowledge difficulty, then according to the knowledge of the difficulty of knowledge order, let the students in reading materials can master the basic knowledge, so that students do not feel the content of textbooks to understand, without logic. The intellectual content of the set to grab the attention of the fundamental, from simple to difficult, not only in accordance with the textbook architecture thinking order to knowledge points sequence analysis, but in the overall level of students' cognitive level. Considering the students psychological fear, foreign materials at the beginning part more often than domestic teaching is easy to understand. Foreign materials will make simple symbols corresponding marked in some after-school exercises, students can see the corresponding symbols to understand the type and the level of exercise, if students do exercises difficult, according to the corresponding symbols can be returned to the relevant examples and the corresponding knowledge points [4].

Circuit in China focuses on the analysis of textbook knowledge theory and circuit analysis method, the classification and knowledge structure according to knowledge, and is in accordance with the students' cognitive level of classification and arrangement of knowledge. Although not completely sorted according to the

knowledge of the depth, but let the students have a overall cognition to the circuit knowledge, have overcome the difficulties of the circuit knowledge prepared psychologically, to avoid students because the knowledge difficulty caused by too large abandonment. In order to meet different levels of students, with the teaching of different colleges and universities, circuit analysis teaching material of our country as the circuit theory of classic textbook at the front half part, give full consideration to the influence of psychology on the primacy effect and effect on students' learning to produce, as far as possible to make the students master the most important knowledge in the most efficient stage [5].

7 Conclusions

In order to maintain its long-term vitality of an excellent circuit analysis teaching, as learners in important assistant learning career, in a complete and detailed knowledge system, learning habits and learning methods but also suitable for different level students, each class conforms to the law of students' cognitive development, the most important thing is to keep pace with the times. The development trend in the future so the circuit analysis teaching is to grasp the pulse of the times, keep pace with the times, in the premise of basic knowledge of circuit analysis, meet the cognitive level of modern students, for students to provide the most suitable circuit analysis.

References

1. David Irwin J (2001) Basic engineering circuit analysis, 7th edn
2. Guanyuan Q (1999) A circuit, 5th edn. Higher Education Press, Beijing
3. Dorf RC, Svoboda JA (2006) Introduction to electric circuits, 7th edn
4. Nilsson JW (2009) Electric circuits. 8th edn
5. Jin Bo (2008) The exploration of three-dimensional teaching material construction foundation. Circuit Analysis, Journal of Yangtze University (natural science edition) 3(5)

MIMO System Based on UWB Transmitter Channel Transmission Matrix Optimization

Guanglin Han and Tingting Wang

Abstract This study is based on UWB (Ultra Wide Band) MIMO (Multiple Input Multiple Output) intelligent receiver. To optimize the use of PSO (Particle Swarm Optimization) transmitter channel transmission matrix. Completed the design of an intelligent receiver model. Simulation and test on it. The calculated results, UWB can improve the quality of communication system.

1 Introduction

With the development of communication technology and parallel technology, proposed the MIMO based on UWB technology, changing the traditional technologies can not make full use of the channel status, improve the quality of UWB communication equipment. The first design of channel model of MIMO system based on UWB, and then through the calculation of the optimal scheduling and channel transmission matrix transmitter MIMO system based on UWB using the PSO algorithm, using SVM (Support Vector Machine) design of intelligent receiver, signal optimization of MIMO system based on UWB.

2 MIMO System Channel

The UWB system has high transmission rate, single antenna transmission system can not meet the requirements of IEEE. The principle of the information theory by Shannon: can be expressed in $y(t) = \alpha \bullet x(t) + n(t)$ single input channel and single

G. Han (✉) • T. Wang
College of Electronic and Communication Engineering, Tianjin Normal University, Tianjin, China
e-mail: hgltj@163.com

B. Zhang et al. (eds.), *The Proceedings of the Second International Conference on Communications, Signal Processing, and Systems*, Lecture Notes in Electrical Engineering 246, DOI 10.1007/978-3-319-00536-2_45,

output signal $y(t)$ and signal transmission in $x(t)$, the relationship between α and channel noise gain of $n(t)$, maximum channel capacity of C system:

$$C = \log_2\left(1 + \frac{P}{\sigma^2}\left|\alpha^2\right|\right) \tag{1}$$

Type (1), the transmit signal power to noise power P, mean square value is σ^2, the gain is α [1].

If the use of power P emission signal or increase the transmitting and receiving gain way of α channel capacity to increase signal transmission, will increase the cost of physical realization. In order to improve the efficiency and the communication performance of emission, using the MIMO UWB system design [2].

To represent the channel model of UWB system using multipath channel model is proposed by the IEEE802.15.3a working group. The multipath channel model of MIMO, as shown in Fig. 1.

The user in the system are assumed to K, the transmitting station number is T, each of the transmitting station for M number of transmit antennas, antenna number allocation for each user is p, in order to simplify, using l (l =1) said the number of multipath channel. Each user data stream into a constant rate of G data flow, then G is integer times of M, assuming that the data stream and transmitting antenna number equal to. Insert a isolated bits in each user Q bits of information behind the sending end (empty bits) at the receiver, each of length $(Q + 1)T_b$ bits. And the transmitted symbol energy transmitting antenna was normalized, that is multiplied by $\frac{1}{\sqrt{M}}$, to keep constant the total average transmit energy can be in the same symbol intervals [3].

3 MIMO Transmitter Channel Transmission Matrix Optimization

3.1 Channel Reuse Model MIMO

Transmitted signals are processed by a computer to multiple antenna transmitter antenna receiver, after receiving the signal, then through computer processing. MIMO includes open-loop spatial multiplexing and closed-loop spatial multiplexing. Fig. 2 is the whole process of sending and receiving transmitter.

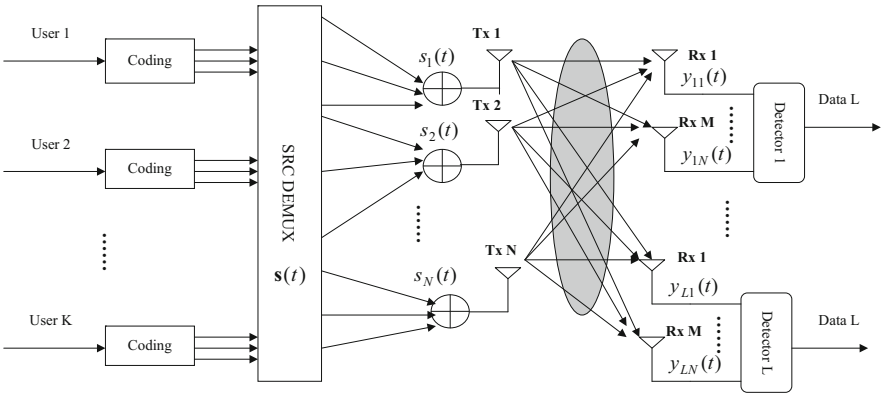

Fig. 1 Channel model of MIMO system

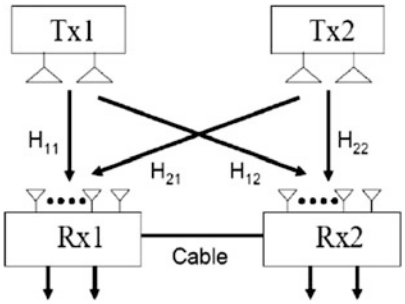

Fig. 2 Two transmitters and two receivers whole multiple transmitters receivers

3.2 The MIMO Transmitter Channel Transmission Matrix Optimization

UWB high frequency, wide spectrum, to avoid interference, must meet the following conditions: when and only when the transmitter is received by a receiver to broadcast. A transmitter is not at the same time broadcasting a plurality of receivers of information. A receiver cannot receive a plurality of transmitters at the same time information [1].

Transmission planning channel matrix can be used to represent the formula (2), is one of the optimal scheduling scheme. TDMA scheduling matrix to be optimized is expressed by matrix A. The set of positive integers Z^+, if $N_{TS}, N_{GT}, N_S \in Z^+$ are used to denote the total number of time periods, receiver and transmitter. Time, receiver and transmitter domain can use $GT = \{x | x \in Z^+, x \leq N_{GT}\}$, $TS = \{x | x \in Z^+, x \leq N_{TS}\}$ and $S = \{x | x \in Z^+, x \leq N_S\}$ to say. The number of transmitters need time domain as a collection of $R = [r_1, r_2, r_3, \cdots r_{N_S}]$, the number of communication time transmitter 1, 2, 3... N_S needs were $r_1, r_2, r_3, \cdots r_{N_S}$. $S^* = S \cup \{0\}$ said transmitter range. If the transmitter and receiver in the allocation of time not communication counterpart, with value of 0 represents. If the corresponding

transmitter receiver in a communication time distribution and the corresponding, with 0 sets of non. The definition of a N_S is composed of the columns of the matrix vector, said transmitter if and only if it can be the receiver receives broadcasting, with $N_S \times N_{GT}$ rows and N_{TS} columns with matrix to express:

$$A = \begin{bmatrix} A_1 \\ A_2 \\ \vdots \\ A_{N_S} \end{bmatrix} = \begin{bmatrix} a_{111} & a_{112} & \cdots\cdots & a_{11N_{TS}} \\ \vdots & \vdots & & \vdots \\ a_{1N_{GT}1} & a_{1N_{GT}2} & \cdots\cdots & a_{1N_{GT}N_{TS}} \\ \vdots & \vdots & & \vdots \\ a_{N_SN_{GT}1} & a_{N_SN_{GT}2} & \cdots\cdots & a_{N_SN_{GT}N_{TS}} \end{bmatrix} \tag{2}$$

A matrix $N_{GT} \times N_{TS}$ is denoted by A_i, $a_{ijk} \in A_i$ as the constraints associated with the i, is the constraint relationship between the transmitter and the receiver, the range was defined as the a_{ijk}:

$$a_{ijk} = \begin{cases} 1, \text{If the transmitter } i \text{ at the time of the } k \text{ can be } j \text{ receiver} \\ 0, \text{else} \end{cases} \tag{3}$$

Use a constrained matrix optimization problem to represent the MIMO communication scheduling problem. A matrix to be optimized for the P:

$$P = \begin{bmatrix} p_{11} & \cdots\cdots & p_{1N_{TS}} \\ \vdots & p_{ik} & \vdots \\ p_{N_{GT}1} & \cdots\cdots & p_{N_{GT}N_{TS}} \end{bmatrix} \tag{4}$$

Among them, a collection of S^* represents the elements of the domain [4]. Remove the matrix column number from TS element is arranged in order, also from GT remove the row matrix and in accordance with the order of arrangement. Let $i, j \in GT$, $k \in TS$, the matrix elements of the constraint domain: each element value matrix are determined and only. Any matrix P of the two elements of P_{ik}, P_{jk}, if $i \neq j$, then $P_{ik} \neq P_{jk}$; if $P_{ik} = i$, $i \in S$, then $a_{ijk} \cdot P_{jk} > 0$. The provisions of these constraints and communication planning phase matching, minimum gap as the objective function to be optimized, and its value for the matrix values in the number 0 or 1 elements and the value corresponding to the demand quantity of the absolute value of the difference. Physically speaking, said right limit emission time each transmitter segment number for time demand number.

Using PSO of matrix operations are optimized, the following four steps:

1. Coding and generation of initial population

Particle matrix population by operational rules, the solution space (matrix satisfying the constraints set). Represented by the matrix elements of P_{jk}, there are:

$$S_{nm}^{i} = \begin{cases} 1, if P_{nm} = i \\ 0, else \end{cases}, S_i = \sum_{m}^{TS} \sum_{n}^{GT} s_{nm}^{i} \tag{5}$$

The elements of the matrix are the initial population, according to the order from small to large order. If:

$$S^{jk} = \left\{ i \middle| i \in S, a_{ijk} = 1, \sum_{m=0}^{k-1} \sum_{n=0}^{GT} s_{nm}^{i} \prec r_i, i \neq P_{tk}, t = 0, 1, \cdots, j-1 \right\} \tag{6}$$

Is not empty, then AA BB can be used in an arbitrary elements to represent; otherwise, CC 0. For nonempty set, S^{jk} can be used in an arbitrary elements to represent P_{jk}; otherwise, $P_{jk} = 0$. Auxiliary transmitter matrix using S_i and S^{jk} to say, convenient assignment of P_{jk}, m rows and n columns of the elements in a S_i are denoted by s_{nm}^{i}. If the communication segment time distribution, the total number of small, can make the initial population is easy to produce the best individual, algorithm can fast convergence and solving speed.

2. Selection of fitness function

According to the definition of fitness function system:

$$f = \sum_{i=1}^{N_S} f_i \tag{7}$$

$$f_i = \begin{cases} 2 \times S_i, if S_i \leq r_i \\ 2 \times r_i - 3 \times (S_i - r_i), if S_i > r_i and 2 \times r_i - 3 \times \left(S_i - r\right) > 0 \\ 0, else \end{cases} \tag{8}$$

3. The particle velocity and position update

To improve the speed of convergence, it should be appropriate to improve the probability of evolution, can be in when the number of time allocated to a receiver over the required time period when the number of repair particle matrix, the diversity of population space is also improved.

Matrix of single elements of evolution, the maximum of each column specified probability set probability of evolution and population matrix, evolution and not judge. If:

$$S_o^{jk} = \left\{ i \middle| i \in S, a_{ijk} = 1, \sum_{m \neq k} \sum_{n=0}^{GT} s_{nm}^{i} \prec r_i, i \neq P_{tk}, t = 0, 1, \cdots, j-1 \right\} \tag{9}$$

Is not empty, you can use any S_o^{jk} in a elements to represent; otherwise, $P_{jk} = 0$.

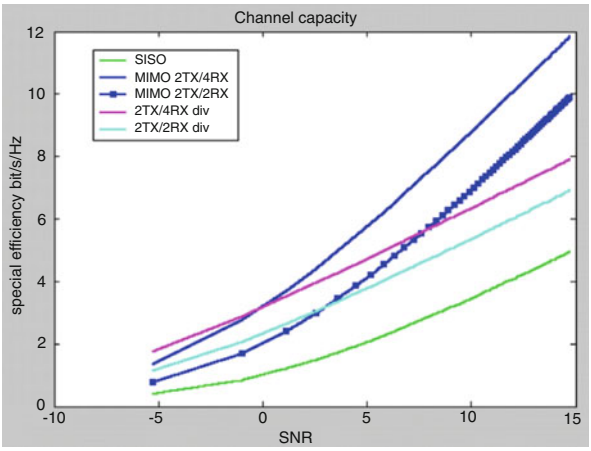

Fig. 3 Comparison of channel capacity between optimized UWB MIMO system and traditional UWB system

So the new generated particles under constraint conditions. Progeny many continue to multiply and iteration, forming a plurality of population.

4. Iterative and termination conditions

In evolution, the forming process of the new species could be used each iteration of PSO algorithm to represent. After several numerical evolution, if evolutionary generation equals to the presets value, or relative error and father population and population, termination of evolutionary operation. The relative error:

$$E(k+1) = \frac{f_{\max}^{k+1} - f_{\max}^{k}}{f_{\max}^{k}} \leq \varepsilon \tag{10}$$

In the formula, $f_{\max}^{k}$ and $f_{\max}^{k+1}$ are fitness, by type (7) and (8) available, k and adaptive $(k + 1)$ times the maximum degree of evolution. Terminate parameter for ε.

4 Simulation and Test of MIMO

The bit error rate performance index is as distinguishing different planning transmission index. The PS parameter setting of experiment, the evolutionary probability single-point random evolution operator probability of evolution and matrix were 0.5 separate evolutionary operators. Fig. 3 is the signal-to-noise ratio is 16–41 dB, compare the channel capacity of UWB system MIMO system UWB with traditional optimization based on.

From the experimental results, the distributed transmission mechanism than the overall transmission performance is better; and PSO algorithm used to optimize reuse mechanism and planning, the bit error rate is greatly reduced, performance

significantly, the channel capacity increase. However, the interference is larger, the optimization effect is not too obvious.

5 Conclusions

This paper has conducted the research and the simulation test on the theory of UWB based on MIMO technology. Conclusion: the multiplex channel model can effectively realize the MIMO system based on UWB, and there exists an optimal scheme. To optimize the scheduling command channel transmission matrix MIMO system based on UWB using PSO, the transmitter communication can be carried out according to the optimized scheme, effectively improving the utilization rate of the channel.

References

1. Nanping L (2011) Computational intelligence UWB system based on the emission and detection technology research. Hebei University of Technology, Hebei
2. Zhang Yi (2008) Related technology research on super channel and receiver for wideband wireless communication, Master thesis. Nanjing University of Posts and Telecommunications, Nanjing
3. Zhao Chun (2006) Research on some key technologies of ultra-wideband impulse radio receiver based on _UWB_, Doctoral dissertation. Beijing University of Posts and Telecommunications, Beijing
4. Zhang Jing, Li Haitao, Zhang Ping (2001) High technology and development, broadband wireless communication. Chengdu University of Electronic Science and technology

Research of Fine Control Technology About the Tire Rubber Production Line Auxiliary Machine

Jin Chen, Rong-rong Zhang, Mao-lin Ji, Feng-cai Fang, Qing Wang, and Ying Tong

Abstract Smelting auxiliary machine is an equipment which provide rubber matrix for tire rubber production. This paper describes a technology which's core are sigma-delta ADC, impact aloft component extraction model weighed algorithm and the structure of the double helix, solved the current involute spiral and electronic scale's problem that emerge from powder state materials weighing automatic device on tire rubber production line. It can effectively control the double spiral conveyor, enhance weighing accuracy of smelting auxiliary machine, and improve the mixing efficiency and benefit.

1 Introduction

With the rapid development of the automotive industry, tire industry is rapid developing and continuous optimizing. Rubber tire market continues to increase, and consumers also have the high standard of the tire. The high efficiency, high standards of production system, which become very important to the rubber tire manufacturers. Therefore, high-quality, high-precision control equipment become extensive in rubber tire manufacturing industry. Smelting auxiliary machine is indispensable on tire rubber production line. Powder, carbon black's feeding, weighing and feeding accuracy, are all have a influence on the speed and the efficient of tire rubber production directly. Today, smelting auxiliary machine weighing rubber on tire rubber production, are all deliver powder state materials in high precision spiral transmitter. However, the weighing time of smelting

J. Chen • R.-r. Zhang • M.-l. Ji • Q. Wang • Y. Tong (✉)
College of Electronic and Communication Engineering, Tianjin Normal University, Tianjin 300380, China
e-mail: tongying2334@163.com

F.-c. Fang
College of Physics and Electronics Information, Guangxi Normal College, Guangxi 530023, China

B. Zhang et al. (eds.), *The Proceedings of the Second International Conference on Communications, Signal Processing, and Systems*, Lecture Notes in Electrical Engineering 246, DOI 10.1007/978-3-319-00536-2_46,

auxiliary machine is so long during the weighing that the production efficiency is limited, and outstripping weighing error easily when weighing, which causes rubber weighing failure and decrease the production efficiency. This paper support a way which's core technology are sigma-delta ADC, impact aloft component extraction model weighed algorithm and the structure of the double helix, that used to auto weighing powder state materials. That way can overcome defects in power state material automatic weighing, also made the weighing of materials procedure more efficient, accurate, not only save raw materials effectively but reduce costs.

2 Tire Rubber Auxiliaries Machine Survey

Smelting auxiliary machine is an equipment that feed, weight, prepare, transport, storage natural rubber, carbon black, additives, accelerators, oil and etc. Despite various businesses' smelting auxiliary equipment is different, which generally contains oil weighing, storage, transportation and fuel injection systems, the carbon black feeding, weighing, transportation, storage systems and materials' feeding, let-off, the weighing system, auto control system and dust removal system [1].

Auto control system is mainly adopt the upper-lower level, it composed by the microcomputer control system and PLC (Programmable Logic Controller) control system. Microcomputer control as the host computer system, its function are collect and organize data, dynamically monitor the production process, supervise the production formula and print production report. PLC control system as the slave computer system, establish the remote workstation [1] by using bus control. Remote workstation is divided into oil, sizing system workstations and powder workstations. Each workstation will pass data and signals collected by themselves back to the PLC system. PLC system uniform and analyzed all data and signal.

The main advantages of the smelting auxiliary machine are: First of all, due to the improvement of the process of production machinery, get rid of the original scattered on the condition of a thick layer of dust near the rubber mixer. Second, the feeding of the carbon black, oil, sizing and other step that can be done automatically except for the weighing of unvulcanized rubber that need to manual handling to material scale. This made smelting auxiliary machine automation and mechanization of unity [2], and the mixing efficiency has been greatly improved. At the rate of 40–60 r/min on banburying auxiliary equipment, the feeding of the raw material can be finished in 10–20 s, the carbon black feeding can be completed in 15–40 s, while the oil feeding takes about 10–20 s to finish [3]. Furthermore, employees often caused the drop of the material in the feed at past, affect the accuracy of the compound formula seriously. Also feeding time duration is long or short, that can not be fixed, and affecting the implementation of the mixing process procedures seriously. After the improvement of the auxiliary machine, the quality of banburying mixer is improved in contrast to mixed by employees.

3 The Pandect of the Auxiliary Machine Fine Control

At present, there are a lot of problems between the weighing system and feeding system on the tire rubber production line. For example, the slow speed feeding and poor accuracy when feeding. This seriously affected the mixing quality and efficiency, but also the tire rubber production efficiency. So, the weighing system and feeding system of the smelting auxiliary machine need to improve.

3.1 Design Idea

First, the double helix differential quantitative control device includes a major control unit, load cell, human-computer interaction (HCI) device, switch input and output modules, main screw driver and vice screwdriver. HCI adopting operation display panel to achieve setting and displaying the information of weight and weighing accuracy. Weighing sensor is installed in the electronic scales for collecting information on the weight of the material. Switch input and output modules adopt PLC control modules to control switching capacity collect and output data, the main control unit controlled main drive motor and vice spiral coil motor via the main screw driver and vice screw driver. When operator input information of the weight and weighing accuracy through the human-computer interaction, the double helix differential quantitative control device according to the operator's command to start the primary and secondary helix spiral rotating and feeding the material through the screw conveyor outlet into the electronic scales, double helix differential quantitative control device collecting information sent by the weight sensor, compared to the setting weight values constantly, and judge the material handling state information of the main spiral and vice spiral helix, and then control both of them to feeding material through the double helix differential quantitative control device (Fig. 1).

Second, the data acquisition. It adopt spiral data acquisition and control device, whose main cores are Σ-ΔADC (sigma-delta Analog-to-Digital Converter) and impact aloft component extraction model weighed algorithm. Its input is connected to the weighing sensor, rapid acquisition of the weighing data. Its output can be connected to the PLC system which controls the helix to manipulate the screw conveyor start and stop. Specific device has a simple structure, but the analog signal susceptible to field work environment, so we adopt a digital filter, electromagnetic shielding to modify the error.

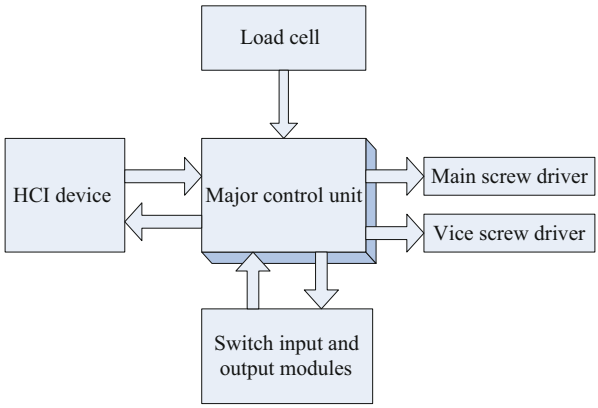

Fig. 1 The double helix differential quantitative control device

3.2 Key Technologies

The key technology of the entire program is how to collect, control, handle weight information, that is perform data acquisition control device of the embedding program to control the dual auger feeding process. This selection of model is ADS1246 sigma -delta ADC, as smelting auxiliary machine main control section, in combination with impact aloft component extraction model weighed algorithm, manipulate the double helix conveyor. Its overall structure is shown in Fig. 2.

First of all, judge the specific location of the double helix conveyor before acquisition and control device running, and then obtain the value of the preset target weight information by the PLC system communication interface, the weight of the collected information as the control target value. Then start double screw conveyor, at the same time, recording start time and work time, also the rotational speed of double helix conveyor. At this point, the acquisition and control device acquest the load cell weight values, and record. When select weighed start, collect the weight values of the second and third. Using these two values, generate 2 s weight map. And then to establish the weight information model associated to double helix conveyor. And make digital filtering and analysis to the value of the weight, then extract the weight and impulse information, but also the estimated aloft weight verification. Filtered off the impact introduced from the decrease of the powder state material in the extraction of information by weight, that is impulse information extracted in the information model. Then add the previously estimated aloft weight value, and make up the estimated aloft weight value. Finally, according to the results of the calculated weight value compared with a preset target weight values, to control the start and stop of screw conveyor and the mechanical structure of the precession speed, so as to achieve high-precision double auger quantitative conveyance of plastic material.

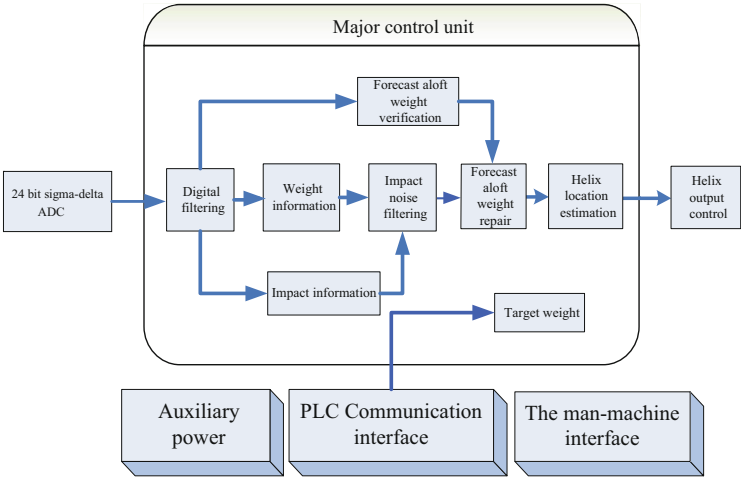

Fig. 2 Double helix data acquisition-control technology

4 The Weight of the High-Resolution Information Collection

4.1 The Selection of AD Converter

Sigma-delta ADC is one of the existing analog-to-digital converter used in this paper [4]. Sigma-Delta ADC is widely used among over-sampling ADC. The main components of the sigma-delta ADC are the digital section and analog section. The digital portion is used to extract the signal and using digital filter noise. While the analog section is the signal modulator for modulating completed. The important principle of sigma-delta modulator is the spectrum shaping and over-sampling, the quantization noise in the band use the spectral shaping function to debilitating, while the band quantization noise can be sampled using digital filter to eliminating, so that the overall of the quantization noise is drastically reduced, by increasing the spectral shaping function and the order number of the over-sampling ratio [5], the precision of sigma-delta ADC can reach over 20 bit [6].

4.2 High Resolution Analog-to-Digital Conversion Circuit

In data acquisition and control device, the 24 -bit analog-to-digital converter ADS1246 is used. It is a highly integrated [7], high-resolution and low-noise, low-power analog-to-digital converter. ADS1246 analog-to-digital converter including ultra-low-noise high-impedance programmable gain amplifier PGA (Programmable Gain Amplifier), the internal oscillator with adjustable single cycle of

high-resolution sigma-delta digital filter [8], and a simple but flexible SPI-compatible serial interface.

Collected analog signal through multiple collector [9], enlarge collected signal by PGA. Then enter the third order Sigma- delta modulator to modulate. the signal. After that, put the modulated signal to the incoming adjustable digital filter, in which filter out the signal-to-noise component. Finally, make the signal which has filtered out the noise output from the serial port to reach the external circuit control.

4.3 Ultra-Low Noise Signal Conditioning

Collected signal generally contain noise. If we want to filter out the noise, we can use the method of signal processing technology to eliminate the noise signal generally, if can not, we must make the noise signal attenuation. A lot of noise signal are considered to be additively, that means it can be superimposed. Accordingly, the noise signal can be separated from the useful signal by linear filtering techniques.

For the ADS1246 ADC used in smelting auxiliary machine, it including an adjustable single-cycle set high resolution sigma-delta digital filter. Its use a finite impulse response digital filter which has a linear phase, therefore, it can adjust the type of the output data rate. And it's always fixed in a single cycle, can be used for the fast channel recycle, input multiplexer and supports data rates up to 2 kSPS. And when the rate is 20 sps or less, the filter is giving a better refuse for 50 Hz and 60 Hz.

5 Fine Control Signal Extraction and Threshold Selection

5.1 The Weight Information Model Analysis

According to collected weight information's chronological order, establish the double helix conveyor weight information model. Equation (1) as follows:

$$\mathrm{X}(n) = a\mathrm{x}_1(n) + \mathrm{b}x_2(n+k) - \mathrm{c}x_3(n) - \Delta\mathrm{x}(n) \tag{1}$$

$ax_1(n)$ is the output weight information of the double helix conveyor, $bx_2(n + k)$ is the estimation aloft weight, $cx_3(n)$ is the impact caused when power state material descending, $\Delta x(n)$ is the environmental component of the system noise.

Add the collected weight information output by double screw conveyor to estimated aloft weight value, and then subtracting corresponding impact and system noise introduced from the decrease of the powder state material so as to get the final weight information to manipulate feeding process of double screw conveyor.

5.2 The Extraction of the Control Signal

To deal with analog signals is to extract useful information, and to remove the noise, if it is possible. Its main purpose is to remove noise, or to improve the signal-to-noise ratio [10]. We can use the technology of frequency domain, adaptive digital filter, digital filter and the matched filtering detection theory, remove noise from signal.

In most cases, the working principle of analog signal processing system is to make the system reacting the signal, output and deal with the voltage, then reconstruct the original signal analog form [11]. Signals are not complete the square wave or sine wave in the actual situation, they are often a kind of complex broadband functions which is performed as weak periodic short pulse signal that lost in noise signal component [10]. This need repair tiny signal waveform that annihilated in noise signal component through the integrator.

The analog integrator and analog adder sampling the analog signal, control noise. The output signal as shown in formula (2):

$$V_{out} = -\frac{1}{RC}\int_0^T V_{in}dt + \frac{R_f}{R_1}V_{in} \tag{2}$$

6 Results and Discussion

6.1 Experimental Data

1. Data map of linearity testing for stabilized voltage supply static various points: From Fig. 3, we can see with the increase of weight, the value of the stabilized voltage supply increases, although there is error, it still shows good linearity. The sensor analog circuit has a good linearity within the scope of work.
2. Gathering switching power supply, dynamic non-jog ADC output data. Waveform diagram is shown in Fig. 4.

When switching power supply provides energy, gathering dynamic ADC output data, left is the original data map, right is data graph after filtering. We can see by the comparison of the two figures, left noise is filtered obviously, in $0.5*10^4$ point collected impact component is filtered obviously, and in $3.5*10^4$ point jog filtered.

6.2 Results and Discussion

It can be concluded by the above data and waveform:

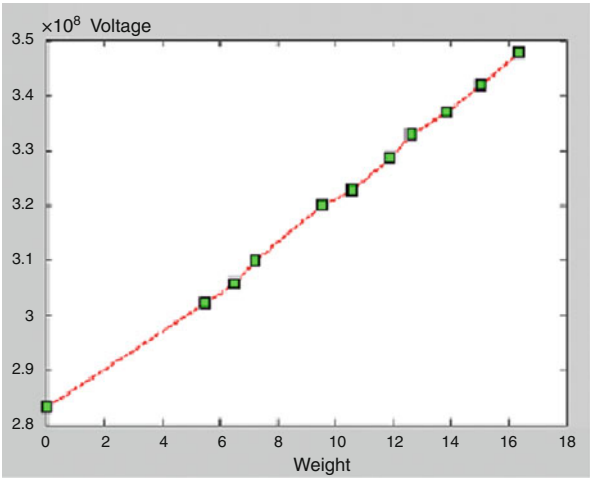

Fig. 3 Stabilized voltage supply static various points linear analysis diagram

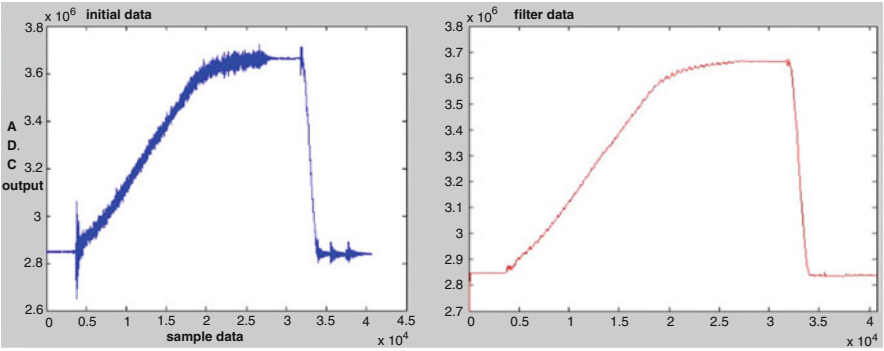

Fig. 4 Switching power supply dynamic global time and frequency domain waveform

1. From Fig. 3, the linearity of the sensor and analog circuits within the scope of work is good, although there is still a static error, it nearly showed a good linearity.
2. From Fig. 4, adopt switching power supply provides energy, the ripple is rose, since it has a greater impact on the signal-to-noise ratio, that compared to stabilized voltage supply. And the signal through an adjustable single-cycle set high resolution sigma-delta digital filter, which make the noise signal filtered well.
3. Using technique of high-resolution ADC as the auxiliary machine's main control unit, impact aloft component extraction model weighed algorithm and double helix conveyor mechanical structure, there is feasibility in specific manipulate engineering.

References

1. Li Y (2003) Development and progress in up-stream equipment of mixer. Special Purpose Rubber Products 24(6):51–55. doi:10.3969/j.issn.1005-4030.2003.06.017
2. Zhu B (2006) Optimization of the mixer upstream equipment control system. China Rubber/Plastics Technology and Equipment 32(9):52–54. doi:10.3969/j.issn.1009-797X.2006.09.012
3. Wu MS, Chen WX, Chen XZ (2008) Influence on NR processing and mechanical property from carbon black granulation. China Rubber 24(23):38–40
4. Norsworthy SR, Schreier R, Temes GC (1997) Delta-sigma data converters. IEEE Press, Piscataway, NJ
5. Candy JC, Temes GC (1992) Over-sampling delta-sigma data converters. IEEE Press, New York
6. Hao ZG, Yang HG, Zhang C, Wu QS, Yin T (2010) An improved digital decimation filter for sigma-delta ADC. Journal of Electronics and Information Technology 4(32):1012–1016. doi:10.3724/SP.J.1146.2009.00247
7. Piao XL, Xiong JJ, Shen SS (2008) Design of a high-speed data acquisition system based on FPGA. Control and Automation 24(2):209–211. doi:10.3969/j.issn.1008-0570.2008.02.085
8. Li QB (2011) Research on high-resolution AD converter. Instrument Technique and Sensor 10 (10):93–95. doi:10.3969/j.issn.1002-1841.2011.10.034
9. Li BG, Ma DW (2012) Research of application of FPGA in data acquisition system. Computer Measurement and Control 20(4):1138–1141
10. Xia JH (2012) FPGA signal processing algorithm implementation. Information and Communication 117(1):108–109. doi:10.3969/j.issn.1673-1131.2012.01.059
11. Aziz PM, Sorensen VDS (1996) An overview of sigma-delta converters. IEEE Signal Processing Magazine 1996:61–84

The PLL Amplifier Design Based on Analog Multiplier

Lei Fan, Feng-cai Fang, Heng Quan, Qiang Li, Hui Wang, Yue-yang Cui, and Jin Chen

Abstract The weak signal is referred to the amplitude of the useful signal with respect to the amplitude of the noise signal is very weak, i.e. the useful signal is drowned in noise. The weak signal detection use the issuance of electronic technology and signal processing to extract the useful signal from the noise. The key lies in the weak signal detection process noise suppression, recovery and extract useful signal. This article from the signal processing methods to improve the signal-to-noise ratio discussed weak signal detection theory, this paper focuses on the detection method and application of the principle of weak signal detection method to detect weak signal amplitude and phase-locked loop amplifier.

1 Introduction

Weak signal is the amplitude of the useful signal related to the amplitude of the noise is very small that the useful signal drowned by noise. Weak signal detection and signal detection generally differed by conventional methods and techniques in the noise signal cannot be detected in the amount of weakness .According to the causing of the noise signal and its variation and correlation with the measured signal, a range of solutions have been proposed, which improve the signal to noise ratio and suppress noise becomes weak signal detection key. Currently, the weak signal detection theory and methods of transportation in many areas and become an indispensable means of detection of weak signal detection has become a hot spot of

L. Fan • H. Quan • Q. Li • H. Wang • Y.-y. Cui • J. Chen (✉)
College of Electronic and Communication Engineering, Tianjin Normal University, Tianjin 300380, China
e-mail: jinchen76@tju.edu.cn

F.-c. Fang
College of Physics and Electronics Information, Guangxi Normal College, Guangxi 530023, China

B. Zhang et al. (eds.), *The Proceedings of the Second International Conference on Communications, Signal Processing, and Systems*, Lecture Notes in Electrical Engineering 246, DOI 10.1007/978-3-319-00536-2_47,

many scientific fields, and use the phase-locked loop amplifier detects weak signals is a common methods.

2 Principles and Methods of Weak Signal Detection

Weak signal detection technique is used to study the noise and the useful signal laws and characteristics, according to the different characteristics of the noise and the signal given weak signal detection methods, so as to achieving the detection of weak signals from the noise purposes [1]. In weak signal detection process is the most important of the useful signal noise suppression effect, and to recover as much as possible and extract useful signal, that is, maximizing the system to improve the signal to noise ratio (SNIR) [2].

Here by the signal processing to improve the signal to noise ratio improvement perspective simply discusses the principle of weak signal detection. If the noise power spectral density in the entire frequency domain is evenly distributed, saying this noise is white noise, if the noise power spectral density is known, then the noise power can be expressed as:

$$P_n = V_{no}^2 = \int_0^\infty Sn(f)df \tag{1}$$

Equivalent noise broadband $B_e = \int_0^\infty K_{vo}df$, among $K_{vo} = \frac{V_o}{V_s}$.

A system is provided for the input noise is white noise, the signal processing system, the signal input voltage is V_{si}, the signal output voltage is V_{so}, input noise voltage is V_{mi}, output noise voltage is V_{mo}, bandwidth of the input noise is white noise, the noise bandwidth B_i,noise power spectral density S_{ni},the mean square value of the input noise $V_{ni}^2 = S_{ni} \times B_i$, if the system voltage gain with $K_v(f)$ representation, system noise equivalent broadband use B_e Representation, the output noise of meaning square value:

$$V_{no}^2 = \int_0^\infty S_{ni}K_v^2(f)df = S_{ni}\int_0^\infty K_v^2(f)df = S_{ni} \times B_e \times K_{vo} \tag{2}$$

In the formula, $K_{vo} = V_{so}/V_{si}$.

Obviously SNIR available systems are:

$$SNIR = \frac{\left(V_{so}^2/V_{no}^2\right)}{\left(V_{si}^2/V_{ni}^2\right)} = \frac{K_{vo}S_{ni}B_i}{K_{vo}S_{ni}B_e} = \frac{B_i}{B_e} \tag{3}$$

By the (3), we know: input noise bandwidth of the system noise equivalent bandwidth ratio of the signal processing system to improve the signal to noise ratio

by (3), we know just reduce system noise equivalent bandwidth of the system can be improved the output signal to noise ratio [3].

2.1 Narrowband Filtering

Narrowband filtering method is a commonly used method of weak signal detection, the principle is to use the narrowband filter to filter out the noise signal, retaining the useful signal [4]. White noise signal above has been carried out a detailed analysis of the following key $1/f$ noise. Let upper cut-off frequency of the narrowband filter is f_2, lower cut-off frequency is f_1, bandwidth $B = f_1 - f_2$, $1/f$ After a narrow band filter noise power spectral density $K_0 \times 1/f$, The mean square value of the output voltage can be expressed as:

$$\begin{aligned} E_{no}^2 &= \int_{f_1}^{f_2} K_v^2 \left[K_0 \times \frac{1}{f} \right] df = K_v^2 K_0 \int_{f_1}^{f_2} \frac{1}{f} df \\ &= K_v^2 K_0 \ln[(f_2 - f_1 + f_1)/f_1] = K_v^2 K_0 \ln\left(1 + B/f_1\right) \end{aligned} \tag{4}$$

By the formula (4) shows that the smaller the mean square value of the output voltage is smaller, stronger inhibition of noise sound capability. The above shows that narrowband filtering method can reduce the impact of noise on the useful signal. The disadvantage is unstable, since the filter center frequency, with a limited range.

2.2 Dual Noise-Cancellation

Since the signal and noise with completely different properties and characteristics, in general, the variation of the signal is known, the variation of the noise is unknown, but which satisfies the statistical law. According to this feature, you can propose a dual-noising method, the principle as shown in Fig. 1. When the random noise signals from the two channels into the adder, since the road noise, the two opposite polarity, the adder in each addition operation can disappear. This can eliminate a lot of noise of only a few strong noise from entering the threshold circuit, the threshold circuit for counting the noise, according to known statistical laws, the background count when a longer time constant. This can be achieved by strong noise background count first measure it, and then subtracted from the total number of the measured noise signal counts can achieve the purpose of the detection signal. However, this method has its drawback is that only detect the existence of weak signal sinusoidal signal, the signal waveform and not be able to restore it.

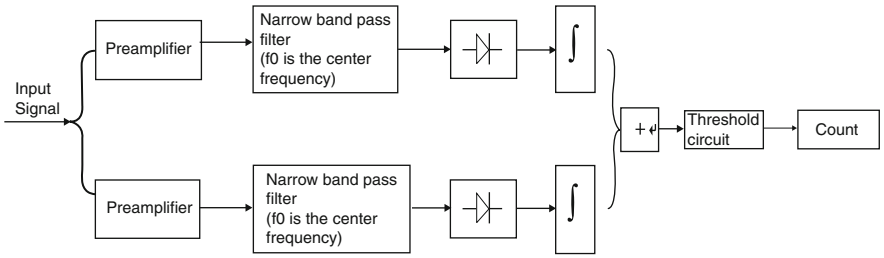

Fig. 1 Dual noise canceling hair schematic

2.3 Synchronous Accumulation Method

As the useful signal is regular, repetitive changes in the noise is random, if the cumulative number of times the signal can be improved SNIR, but this method requires time-consuming [5]. Here's a detailed description of this method. After several repeated cumulative noise and output signals, respectively:

Noise:

$$V_{no}^2 = \sum_{i=1}^{n} V_{ni}^2 \Rightarrow V_{no} = \sqrt{\sum_{i=1}^{n} V_{ni}^2} = \sqrt{n/n\left(V_{n1}^2 + V_{n2}^2 + \cdots + V_{nn}^2\right)}$$
$$= \sqrt{n\overline{V}_n^2} = \sqrt{n} \times \sqrt{\overline{V}_n^2} = \sqrt{n} \times E_n \tag{5}$$

Signal:

$$V_{so} = \sum_{i=1}^{n} V_{si} = n \times \frac{1}{n}\left(V_{s1} + V_{s2} + \cdots + V_{sn}\right) = n\overline{V}_s \tag{6}$$

Then $SNIR = \left(V_{so}^2/V_{no}^2\right)/\left(\overline{V}_s^2/\overline{V}_n^2\right) = n.$

By the formula (5) and (6) shows that the greater the number n of total, SNIR, the larger the can to improve the signal to noise ratio improvement purposes.

2.4 Correlation Detection Method

2.4.1 Since the Correlation Detection

Said autocorrelation function signal $f(t)$ and the signal after delay τ $f(t - \tau)$ correlation can be expressed as:

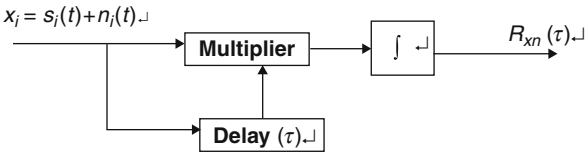

Fig. 2 Since the correlation detection schematic

$$R(t) = \lim_{t\to\infty} \int_0^T f(t)f(t-\tau)\,dt \tag{7}$$

Formula (7) can be expressed by the following diagram autocorrelation principle (Fig. 2):

Let the noise signal mix with $x_i(t) = s_i(t) = n_i(t)$, where $s_i(t)$ is the useful signal, $n_i(t)$ is the noise signal, a weak signal is input to the relevant receiver, the signal is divided by two aspects, where all the way into the delay device, the signal delay time τ, the delayed signal $x_i(t - \tau)$ and non-the delayed signal $x_i(t)$ is supplied to a multiplying circuit for multiplying, for the subsequent integration of their product, and taking the average. This allows to obtain the correlation function as a parameter τ, which is obtained from the correlation output:

$$R_{xx} = \lim_{T\to\infty} \frac{1}{T}\int_0^T x_i(t)x_i(t-\tau)dt = R_{ss}(\tau) + R_{sn}(\tau) + R_{ns}(\tau) + R_{nn}(\tau) \tag{8}$$

2.4.2 Correlation Detection

Cross-correlation function describes two different random variables $f(t)$ and $F(t)$ the correlation between, which is defined as follows:

$$R_{f.F} = \lim_{T\to\infty} \frac{1}{T}\int_0^T f(t)F(t-\tau)dt \tag{9}$$

When the cross-correlation function $R_{f.\,F}$ equal to zero, then $f(t)$ an $F(t)$ is independent of no correlation; cross-correlation function $R_{f.\,F}$ if not zero, then $f(t)$ and $F(t)$ is not certain correlation. Let the noise signal is mixed with: $x(t) = s(t) + n(t)$, where $s(t)$ is the measured signal, $n(t)$ is the noise signal, the map of the $y(t)$ is the known reference signal, wherein $y(t)$ with the test signal $s(t)$ correlated with the noise $n(t)$ no correlation. The $y(t)$ via a delay τ delay, and then through the multiplier for multiplication, integration may R_{xy} is:

$$R_{xy} = \lim_{T\to\infty} \frac{1}{T}\int_0^T x(t)y(t-\tau)dt = R_{sy}(\tau) + R_{ny}(\tau) + R_{sn}(\tau) + R_{ns}(\tau) \tag{10}$$

Since the reference signal $y(t)$ and noise $n(t)$ no correlation, so $R_{ny} = 0$; also because the test signal $s(t)$ and noise $n(t)$ no correlation, so $R_{sn}(\tau) = R_{ns}(\tau) = 0$ In

summary: Final $R_{xy}(\tau) = R_{sy}(\tau)$ Obviously $R_{sy}(\tau)$ test signal contains $s(t)$, which can be measured signal $s(t)$ detected.

Phase-locked loop amplifier is a universal testing instrument, people often use it to detect weak signals, because it not only has a frequency selective amplifier selected frequency characteristics, but also the phase of the signal can be locked. Phase-locked loop amplifier equivalent noise bandwidth is very narrow, much smaller than the selected frequency bandwidth of the amplifier, in addition, phase-locked loop amplifier also has an output stable and can be a good ability to suppress noise, so generally used in phase-locked loop amplifier detect weak signals.

3 System Overall Scheme

This system is mainly used MPS430, LM393, AD8034, CD4066, OPA2134, such as chips, through the adder circuit integrates the signal to get mixed signals, and then get through the attenuated signal attenuation network weak signal, and then filtered and amplified by amplifying the signal, the amplified signal is then sequentially through the lock phase loop amplification, low-pass filtering, we need to get a detectable signal.

Test signal and the reference signal correlation is obtained by the multiplier and low pass filter to achieve, usually in the lock-in amplifier usually used in switch-mode multiplier [6, 7].

In the signal detection process, the noise is an interference signal in the detection process has been interference detection results, and the noise and shielding measures cannot be shielded, so try to suppress noise, reduce the noise of the useful signal interference, you can use a low pass filter to filter some narrowband noise to improve the signal to noise ratio of the system. Accordance with the relevant principles of the signal can be multiplication and integral calculation that the correlation operation, filter out the noise of the useful signal interference.

4 Unit Circuit Design and Numerical Analysis

4.1 Adder Circuit and Attenuation Network

Sine wave signal source and the noise source through the blocking capacitor, into the band-limited composed by AD8034 adder, the source generating a signal mixed with the noise signal to produce an output signal and then enter the resistive divider constituted by the attenuation network, signal attenuation, the attenuation of the signal fed into the next unit circuit. The circuit unit using the same to the adder, the

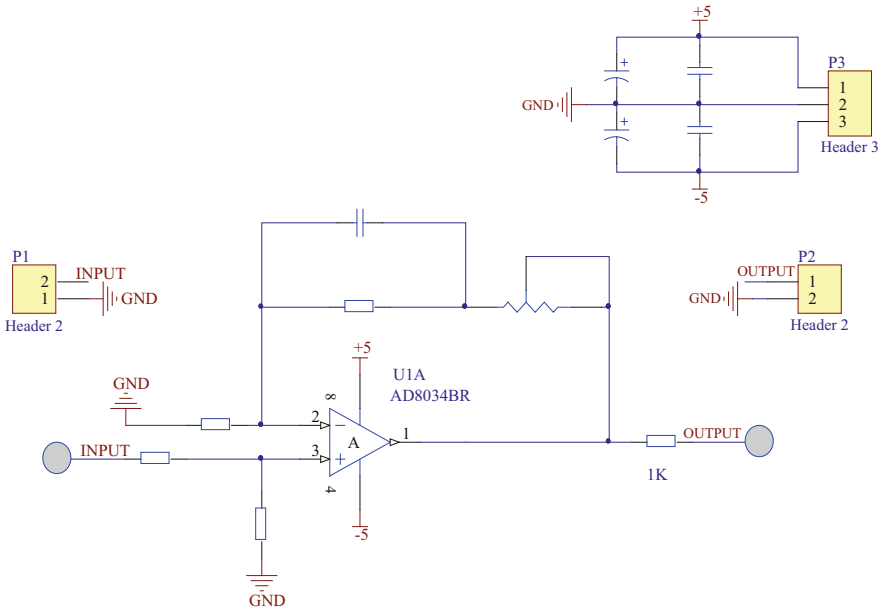

Fig. 3 In-phase cascade amplification circuit

input impedance is large, to meet the general demands of the weak signal of the input impedance is greater than equals to 1M requirements.

4.2 In-Phase Cascade Amplification Circuit

Since the signal out from the attenuation network is weaker, they through cascade circuit, increased the voltage gain, the signal is amplified (Fig. 3).

4.3 Filter Circuit

Band -pass filter is used to eliminate the interference, the amplified signal input filters and filtered to give pure DC signal. Band -pass filter allows a certain frequency band signal can be masked by other frequency bands. At the same time a signal simplest and the most common is a band-pass filter RLC oscillation circuit, RLC oscillation circuit can make it within the band-limited signals, while the frequency band the signal can be a lot of external filter. RLC oscillation circuit can make within the band-limited signals, while signals outside the frequency band of the filter can be a lot.

4.4 Phase Lock Amplifying Circuit

PLL amplifier consists of four main components, namely, the reference channel, low pass filter, phase-sensitive detector, the signal channels. With the frequency of the input signal and the reference signal into the phase-locked loop amplifier can filter out most of the correlation operation noise, the signal then enters a low-pass filter is a DC signal can be obtained, and then the AD sampling, to measure the weak signal.

In the lock-in amplifier of the reference signal and the test signal must be synchronized square wave. Lock-in amplifier is usually used to detect a sine or square wave signal, if the measured signal is a direct current, to be cut is generally used to convert the first DC square wave signal amplitude after the measurement.

Sine wave signal and noise sources simultaneously blocking after entering the adder, mixed-signal source output to meet the strong noise requirements of weak signals extracted by the attenuation coefficient of attenuation network to meet the actual requirements, eliminating high-frequency low-pass miscellaneous the interference wave, sine wave signal and into another path of the amplifier can be adjusted to raise the voltage magnification factor enters phase shifter, the shift signal from the switch control enters a comparator, the output signal is low-pass filtered output signal at the same view into the multiplication the phase detector, the output from the multiplier phase signal into the lower cutoff frequency of the low-pass filter circuit, the filtered signal through the DC amplification, the amplified signal after AD conversion, the MPS430G2553 displayed on the LCD screen.

In the phase-locked loop amplifier circuits requires the use of multipliers, generally can be divided into analog multiplier, multirole multiplier and switch, since the analog multiplier is fast but not stable enough, what's more in communication with the microprocessor when the need for conversion circuit; switching multiplier generally used for high-speed ADC aim to sampling of the signal, and using some of more complex operations carried out lock, so we chose switching multipliers.

4.5 Numerical Analysis

1. Circuit according to each unit, using the function signal generator, oscilloscope, etc. The following signal values measured by the instrument
   (1) Measure the sine wave signal source $V_s(A)$
   (2) Measurement of the noise source $V_n(B)$
   (3) Measure the signal source and the noise source through the mixed signal adder source $V_c(c)$.
   (4) Measuring the attenuation of the signal source $V_i(D)$
   (5) Measure the amplified filtered signal source $V_\circ(E)$.
2. Oscilloscope displays waveform (Fig. 4)

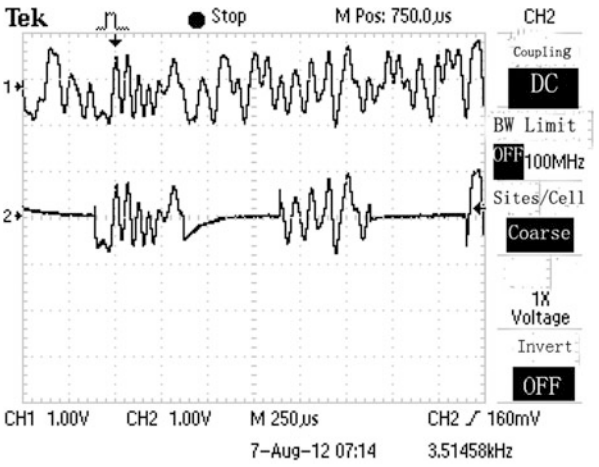

Fig. 4 Lock-in amplifier output waveforms

5 Conclusion

With the increasing development of science and technology, weak signal detection as an emerging technology applications continue to expand, at the same time, weak signal detection technology also received continuous development and innovation, people have also made some better detection methods. The above are just describing several commonly used methods, and focus on the use of phase-locked loop amplifier for weak signal detection, in practical application, should be mastery learning, depending on the signal and different requirements, different characteristics and laws of the appropriate choice of method, in order to truly achieve the weak signal detection purposes.

References

1. Gao JZ (2004) Weak signal detection. Tsinghua University, Beijing
2. Chen ZT (2006) Weak signal correlation detection technology overview. Technology Square 07:488–490. doi:1671-4792-(2006)7-0070-02
3. Zeng QY (2004) Weak signal detection, 2nd edn. Zhejiang University, Hangzhou
4. Chen JG (1987) Weak signal detection. China Central Radio and TV University, Beijing
5. Ye JX (1997) Photovoltaic systems and signal processing. Science, Beijing, an edition
6. Wang FP, Jing B et al (2001) Strong chaos interference in the harmonic signal extraction. Physics 50(6):119–123
7. Wang DS, Cao L (1995) Chaos fractal and its application. State University of Science and Technology, Hefei

Part IV
Millimeter Wave and UWB Technology

Rain Attenuation Prediction Models of 60GHz Based on Neural Network and Least Squares-Support Vector Machine

Lina Zhao, Long Zhao, Qizhu Song, Chenglin Zhao, and Bin Li

Abstract Although 60 GHz mmWave (millimeter-wave) has attractive features and promising applications, it is affected seriously by rain attenuation. Based on the neural networks and SVM (support vector machine), two novel rain attenuation prediction models for 60 GHz millimeter-wave are proposed in this paper. We respectively applied the BP (back-propagation) neural network and LS-SVM (least squares-support vector machine) to simulate the non-linear relationship between rainfall intensity and rain attenuation, then the two models are compared with general ITU-R model. Experimental results showed that both of the proposed prediction models are indeed superior to the existing ITU-R model for rain attenuation prediction in the sense of both accuracy and stability while LS-SVM is the most promising model for the prediction of rain attenuation.

Keywords 60 GHz mmWave • Back-propagation neural network • Least squares-support vector machine • Rain attenuation

1 Introduction

With attractive features and broad unlicensed bandwidth, 60 GHz mmWave is becoming one of the most promising candidates for multigigabit wireless communication system. Despite of advantages of 60 GHz mmWave, a lot of technical challenges still need to be overcome before its fully deployed. Rain attenuation effect, one of technical challenges, limits the practical use of 60 GHz mmWave for longer terrestrial links and Earth-space urban communication [1].

Rain attenuation effect [2] is caused by the absorption and scattering of raindrops and it can result in attenuation and depolarization of electromagnetic wave. In 2003,

L. Zhao (✉) • L. Zhao • Q. Song • C. Zhao • B. Li
Beijing University of Posts and Telecommunications, Beijing, China
e-mail: zhaoln@bupt.edu.cn; zhaolongbupt@gmail.com; 15810538403@163.com; clzhao@bupt.edu.cn; 632071612@qq.com

B. Zhang et al. (eds.), *The Proceedings of the Second International Conference on Communications, Signal Processing, and Systems*, Lecture Notes in Electrical Engineering 246, DOI 10.1007/978-3-319-00536-2_48,

a study was performed by QinetiQ to investigate bastatic scattering at 60 GHz. This study concluded that even for modest rainfall rates r ($r < 10$ mm/h), rain attenuation is often evident [3]. The study also highlighted the need for the development of theoretical models.

In order to predict rain attenuation of 60 GHz mmWave according to the rainfall intensity, ITU-R recommended a popular model which established a non-linear relationship between rain attenuation factor γ_R and rain intensity R (mm/h). The ITU-R model [4] can be described $\gamma_R = k \times R^{\alpha}$, where k and α are correlation coefficients that depend on the raindrop size, frequency, electromagnetic wave polarization and can be estimated by statistical regression and curving fitting.

Despite the ITU-R model has been widely used for calculating rain attenuation, some problems still exist and attract widespread attention. On one hand, the traditional ITU-R model can only satisfy accuracy requirement when frequency is below 55 GHz, but it can not fully meet the high accuracy requirement of 60 GHz mmWave. On the other hand, rain attenuation coefficients depend on complex factors such as radio parameters which are difficult to be evaluated accurately. Therefore, it is natural to find the evident difference between measured values of rain attenuation and the ITU-R calculated ones.

Motivated by the considerations above, we utilize two efficient and robust models for rain attenuation prediction inspired by the promising BP neural network [5] and the LS-SVM [6] algorithm. Experimental results show that both of the proposed prediction models are indeed superior to the existing ITU-R model for rain attenuation prediction in the sense of both accuracy and stability.

The rest of this paper is structured as follows. The principles of BP neural network and LS-SVM algorithm are depicted in Sects. 2 and 3, respectively. Subsequently, two kinds of rain attenuation models are established according to the measured rainfall intensity samples in Sect. 4. In Sect. 5, we compare the performance of ITU-R model, BP neural network model and LS-SVM model in the sense of accuracy and stability. Finally, we conclude the whole investigation in Sect. 6.

2 BP Neural Network [5]

Artificial neural network (ANN) is a large-scale parallelism nonlinear dynamical system, consisting of a series of simple nodes and the links between nodes. Neural network processes the input knowledge by learning and analyzing samples parallelly and possesses characteristic of high speed calculation, abundant association, great robustness, potentiality of self-adaptive, self-organization and self-learning.

BP neural network, a type of article neural network, is a multilayer feed-forward neural network based on back propagation algorithm. It has been proven by CHENT to be able to approximate continuous nonlinear function which makes

the neural network widely-used in nonlinear system modeling. A typical BP neural network is given as Fig. 1 shows.

We suppose a BP neural network composed of M layers and N nodes. The sum input and output of the j-th neuron of M-th layer are expressed as I_{jk}^{M}, O_{jk}^{M} which can be calculated as formulas (1) and (2). In these formulas, W_{ij} represents the weight between the i-th neuron of $(M-1)$-th layer and the j-th neuron of M-th layer.

$$I_{jk}^{M} = \sum_{i=1}^{n} W_{ij} O_{jk}^{M-1} \tag{1}$$

$$O_{jk}^{M} = f(I_{jk}^{M}) \tag{2}$$

When it comes to back propagation, we define E_k as object function which represents the error between expected output d_k and actual output y_k by the formula (3). Then, the overall error value of these S samples can be calculated as formula (4).

$$E_k = \frac{1}{2} \sum_{j=1}^{m} (d_{jk} - y_{jk})^2 \tag{3}$$

$$E = \frac{1}{2S} \sum_{k=1}^{S} E_k \tag{4}$$

The learning processing of BP neural network is equivalent to unconstrained optimization problem. By optimizing the weights between nodes continuously, the overall error value E will drop below some pre-determined threshold. After the learning process, the "well enough" BP neural network can be applied to predict the output according to input data.

3 LS-SVM Algorithm [6]

Standard SVM algorithm can convert an original sample space into a higher-dimension or even infinite-dimension space through nonlinear mapping. By the conversion, the nonlinear problems can be solved through the linear learning machine in higher-dimension feature space. Compared with the SVM algorithm, Suykens proposed LS-SVM algorithm. LS-SVM is the least squares version of support vector machines (SVM), which is a set of related supervised learning methods that analyze data and recognize patterns, and is used for classification and regression analysis widely. By LS-SVM, we can find the solution by solving a set of linear equations instead of a convex quadratic programming (QP) problem for classical SVMs.

For a given set of training data set $S = \{(x_1, y_1), (x_2, y_2), \ldots, (x_n, y_n)\} \in R_n \times R_n$, regression analysis is to find a function f after training. Then, if we give a new

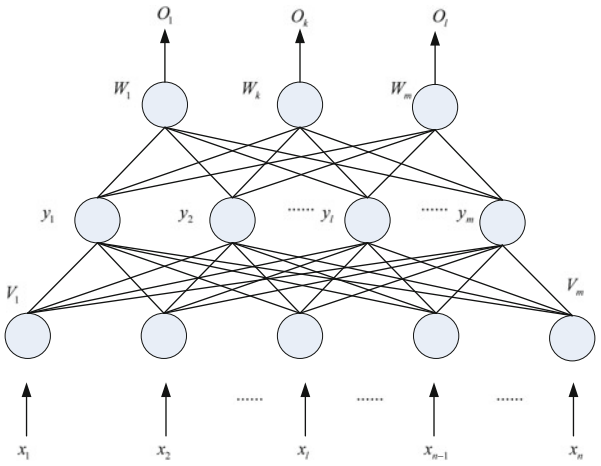

Fig. 1 BP neural network topology diagram. The BP neural network includes input layer, hidden layer and output layer. *X* represents the input data while the *O* represents the output data

sample, we can get a corresponding output which has the minimum deviation from the true value according to the trained function. According to the LS-SVM algorithm, we can map the sample set into a higher-dimension feature space by the following linear function:

$$f(x) = \mu^T \phi(x) + t \tag{5}$$

In the above formula, $\phi(x)$ represents the nonlinear mapping results from original feature space to higher-dimension feature space, μ is the coefficient vector in feature space while t is the offset. According to the structural risk minimization principle, the risk bound is minimized by the following minimization problem:

$$min\{\frac{1}{2}\mu^T\mu + \frac{\lambda}{2}\sum_{i=1}^{l} e_i^2\} \tag{6}$$

Subject to the equality constraints:

$$y_i = \mu^T \phi(x_i) + t + e_i \qquad i = (1 \sim l) \tag{7}$$

Hence, the solution of LS-SVM regressor will be obtained after we construct the Lagrangian function:

$$L = \frac{1}{2}\mu^T\mu + \frac{\lambda}{2}\sum_{i=1}^{l} \alpha_i[\mu^T \phi(x_i + t) + e_i - y_i] \tag{8}$$

where $\alpha_i \in R$ are the Lagrange multipliers and the conditions for optimality are:

$$\begin{cases} \dfrac{\partial L}{\partial \mu} = 0 \quad \longrightarrow \quad \mu = \sum_{i=1}^{l} \alpha_i \phi(x_i) \\ \dfrac{\partial L}{\partial t} = 0 \quad \longrightarrow \quad \sum_{i=1}^{l} \alpha_i = 0 \\ \dfrac{\partial L}{\partial e_i} = 0 \quad \longrightarrow \quad \alpha_i = \gamma e_i \\ \dfrac{\partial L}{\partial \alpha_i} = 0 \quad \longrightarrow \quad \mu^T phi(x_i) + e_i + t - y_i = 0. \end{cases} \tag{9}$$

Elimination of μ and e_i will yield a linear system instead of a quadratic programming problem:

$$\begin{bmatrix} 0 & e_i^T \\ e_i & Q + I/\gamma \end{bmatrix} \begin{bmatrix} t \\ \alpha \end{bmatrix} = \begin{bmatrix} 0 \\ y \end{bmatrix} \tag{10}$$

with $e_i = [1, \ldots, l]^T$, $\alpha = [\alpha_1, \ldots, \alpha_l]^T$, $y = [y_1, \ldots, y_l]^T$, $Q = \phi(x_i)^T \phi(x_i)$.

Radial basis function are chosen as kernel function, then LS-SVM regression function can be obtained based on the least square method:

$$f(x) = \sum_{i=1}^{l} k(x_i, x_j) + t \tag{11}$$

Seen from the above formulas, the optimization problems can be converted to linear equation according to the LS-SVM algorithm. Meanwhile, LS-SVM accelerates the speed of modeling by reducing the search dimension.

4 Two Kinds Rain Attenuation Models

In order to study the external factors which affect the rain attenuation model in 60 GHz, Vaclav Kvicera and Martin experimented in Prague for 5 years. The experimental results show that the factors which affect the rain attenuation model include the distance s between transmitter and receiver, frequency f, rainfall intensity r, raindrop temperature t, humidity n, pressure P, wind velocity v, wind direction d and visibility k [7]. Therefore, the prediction function of rain attenuation model can be summarized as:

$$A = f(s, f, r, t, n, P, v, d, k) \tag{12}$$

However, rain intensity is the key factor which has greatest influence on rain attenuation. Over a 5-year period, cumulative distributions of rain intensity and rain attenuation were measured exactly and the experimental samples proved to be helpful as reference for further study. In this paper, we select the experimental samples randomly from their experimental results and establish the model between rain intensity r and rain attenuation A without considering the other factors by the formula (13)

$$A = kf(r) \tag{13}$$

4.1 BP Neural Network Model

In order to establish BP neural network model which represents the relationship between rain intensity r and rain attenuation A, learning process should be conducted first. In this paper, 78 samples of rain intensity are selected randomly as example cases and the learning process works in small iterative steps. Firstly, one of rain intensity samples is applied to network, and the network produces the corresponding rain attenuation value based on the current state of its synaptic weights. Then the mean-squared error signal is calculated. Next the error value is propagated backwards through the network, and small changes are made to the weights to reduce the error signals in each layer. The whole process is repeated for each of the 78 example cases, then back to the first case again, and so on. The cycle is repeated until the overall error value drops below pre-determined threshold. Through several simulations, we choose to establish a "well enough" BP neural network which composes the input layer with one node, a single hidden layer with 13 nodes and the output layer with one node. The selected transfer function of hidden layer and output layer is "logsig" and "purelin", respectively.

4.2 LS-SVM Model

Similarly, we can set up the LS-SVM model between rain intensity r and rain attenuation A basing on the nonlinear combination principle of LS-SVM. Supposing 78 samples of rain intensity and rain attenuation values constitute the LS-SVM training model $\{(X_t, Y_t), X_t \in R^m\}_{t=1}^{l}$, then the optimal linear regression function can be obtained in higher-dimension feature space according to the formula (5).

After setting up mapping relationship, the problem of solving combinatorial prediction function by LS-SVM is equivalent to constrained optimization problem. Through several mathematical formula transformations, we can establish the fitting function successfully. In order to get the function which can represent the mapping between rain intensity and rain attenuation, we adopt Python27 for optimization, while the optimized parameter is c = 4,096, g = 1, p = 1.

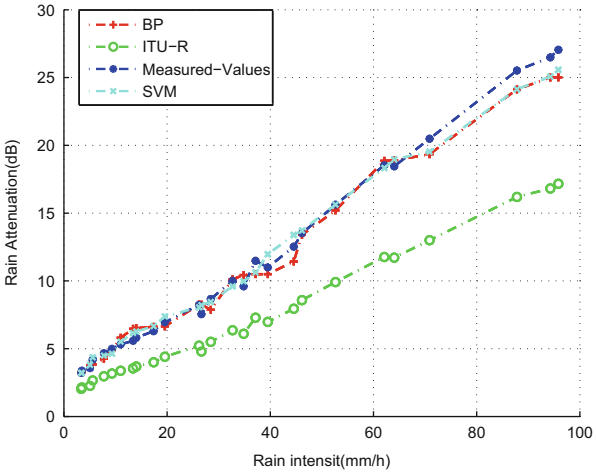

Fig. 2 Predictive values of different models. The predictive values based on BP neural networks model and LS-SVM model have smaller deviations from actual measurement whereas the ITU-R model can not always get the correct prediction

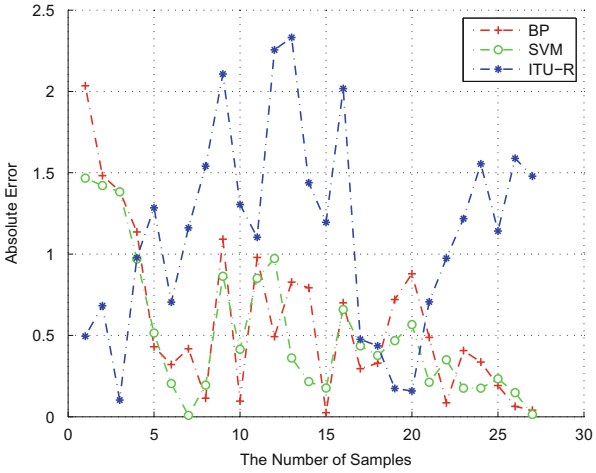

Fig. 3 Absolute error of different models. The absolute errors of proposed models are apparently smaller than ITU-R model

5 Performance Comparison

In accordance with the principles above, BP neural network model and LS-SVM model for the prediction of rain attenuation have been set up successfully. To examine the performance of models, 27 rain intensity samples are selected as test samples which can be used to get the corresponding rain attenuation values based on BP neural network model, LS-SVM model and ITU-R model. Figure 2 shows the contrast between the predictive values and the measured values. In parallel, Figs. 3 and 4 give the absolute error and square error, respectively.

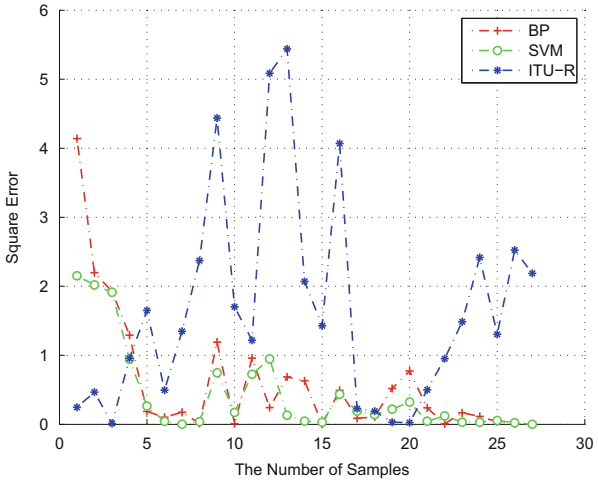

Fig. 4 Square errors of different models. The square errors of our proposed models are apparently smaller than ITU-R model

Table 1 MAE, MSE, MAX of different models

Prediction models	MAE	MSE	MAX
ITU-R model	1.1337	1.6605	2.3320
BP model	0.5988	0.6036	2.0348
LS-SVM model	0.5123	0.4362	1.4668

In order to evaluate the performance of these models fully, the following three indicators including mean absolute error (*MAE*), maximum error (*MAX*) and mean square error (*MSE*) are adopted to compare the performance of models in this paper just by the formulas (14)–(16), where t_i represents predictive value of the three models, k_i represents the measured value and N is the number of test samples.

$$MAE = \sum_{i=1}^{N} \frac{t_i - k_i}{N} \tag{14}$$

$$MAX = max(|t_i - k_i|) \tag{15}$$

$$MSE = \sum_{i=1}^{N} \frac{(t_i - k_i)^2}{N} \tag{16}$$

According to the formulas, we calculate MAE, MSE and MAX of the three rain attenuation models just as Table 1 shows.

In summary, BP neural network model and LS-SVM model are indeed superior to the existing ITU-R model in the sense of both accuracy and stability. In addition, because of LS-SVM model based on the principle of structural risk minimization, it has the unique global optimum solution. So it is superior to the BP model.

6 Conclusion

Comparing with the popular model recommended by ITU-R, we proposed two novel rain attenuation prediction models for 60 GHz mmWave based on the BP neural networks and LS-SVM algorithm in this article. The experimental results show that BP neural networks model is superior to the popular ITU-R model in the sense of accuracy and stability. Meanwhile, LS-SVM model can predict the rain attenuation with a better performance regardless of accuracy or stability compared with the other models and that make it an ideal and promising model for rain attenuation prediction at 60 GHz.

Acknowledgements This work was supported by Nation Natural Science Foundation of China (61271180).

References

1. Yong SK (2005) Multi gigabit wireless through millimeter wave in 60 GHz band. In: Proceedings of wireless conference Asia, Singapore, November 2005
2. Asen W, Gibbins CJ (2002) A comparison of rain attenuation and drop size distributions measured in Chilbolton and Singapore. Radio Sci 37(3):1–15, June 2002
3. Swindell RM, Fraser DJ (2003) Improving spectrum utilisation at 58–66GHz through an accurate assessment of rain scatter interference phase 1 report, QinetiQ/03/00084, 2003, unpublished
4. **Recommendation ITU-R** P.838-2 (2005) Specific attenuation model for rain for use in prediction methods. ITU-R P Sers., March 2005
5. Hagan MT, Demuth HB, Beale MH (2002) Neural net-work design[M]. Translated by DAI Kui, Beijing: China Machine Press, 2002
6. Suykens JAK, Vandewalle J (1999) Least squares support vector machine classifiers. (03)
7. Kvicera V, Grabner M (2007) Rain attenuation at 58 GHz: Prediction versus long-term trial results. 2007:7. Article ID 46083

The Received Signal Characteristics-Based TOA Estimation in UWB Dense Multipath Channels

Xinyue Fan, Wei Lu, and Fei Zhou

Abstract In impulse radio ultra wideband (IR-UWB) dense multipath environment, the time of arrival (TOA) based on energy detection (ED) estimation algorithms are usually used as the ranging methods, in which the signal's first path (FP) detection is very challenging. In ED receiver, threshold-crossing (TC) algorithms are used frequently. The choice of threshold becomes a key part of TC algorithms, or else the false detection probability will be high. The paper sets the threshold according to the skewness and the maximum slope of the received signal, and then because of the fixity of the FP and the randomness of TC noise samples, detects the FP by calculating the frequencies of TC energy samples in certain frames. The performance of several approaches is compared via Monte Carlo simulations using the CM3 channel model of the standard IEEE 802.15.4a. Simulation results show that the TOA estimation algorithm in the paper outperforms others.

Keywords UWB • Time of arrival • Energy receiver • Threshold

1 Introduction

In recent years, with the development of near field communication and mobile technology, location-based services (LBS) have got much attention in indoor environment. Many fields need accurate positioning information, such as hospital, airport and storage. Because IR-UWB technology owns the advantages of high time resolution, high data rate and strong penetration, it is very applicable and typically intended for precise ranging and location. Classic UWB ranging method is to detect the first arrival path. However, under the influence of noise, multipath and

X. Fan (✉) • W. Lu • F. Zhou
Chongqing Key Lab of Mobile Communications Technology, Chongqing University of Posts and Telecommunications, Chongqing 400065, P. R. China
e-mail: fanxy@cqupt.edu.cn

B. Zhang et al. (eds.), *The Proceedings of the Second International Conference on Communications, Signal Processing, and Systems*, Lecture Notes in Electrical Engineering 246, DOI 10.1007/978-3-319-00536-2_49,

non-line-of-sight (NLOS), the first arrival path is mostly not the strongest. This makes TOA estimation challenging [1].

Conventional matched filter (MF) algorithm [2], such as RAKE receiver and correlator, can be employed to TOA estimation in UWB systems. As the MF algorithm needs apriori channel information and high sampling rate, it is not practical in many applications. The maximum likelihood (ML) algorithm [3, 4] has the similar disadvantages. On the other hand, the ED-based algorithm with low complexity at sub-Nyquist sampling rate is studied widely. One simple method is maximum energy selection (MES) algorithm [2] which directly selects the strongest energy sample of ED output as the FP path. But in multipath or NLOS case, the FP is always not the strongest path. Another method called TC algorithm is most frequently used. It compares each energy sample to an appropriate threshold. Therefore, the choice of threshold becomes a key factor that affects the estimation accuracy.

In [5], the authors proposed the optimal threshold algorithm. It can achieve high accuracy, while the cost of calculation is too large. In [6], cell averaging constant false alarm rate (CA-CFAR) algorithm was used to set an adaptive threshold. In [7, 8, 10], the authors approached TOA estimation according to the characteristics of the received signal. Reference [9] defined the threshold as a function of delay. In [11], the paper focused on weighted non-coherent receiver for IR-UWB systems.

In this paper, the threshold is set based on the skewness and the maximum slope of the received signal. Then by calculating the frequencies of TC energy samples, a new threshold is obtained to consider TOA. The algorithm improves the estimation accuracy especially in the case of low signal-to-noise ratio (SNR). The paper is organized as follows. Section 2 describes the system model. Section 3 introduces the implementation of the algorithm. Section 4 presents the simulation results. Section 5 gives a conclusion to the paper.

2 System Model

2.1 Signal Model

The transmission signal in IR-UWB systems can be expressed as

$$s(t) = \sqrt{E_s} \sum_{j=-\infty}^{\infty} a_j p\left(t - jT_f - c_j T_c\right) \tag{1}$$

where E_s is the energy of pulses; $p(t)$ is UWB pulse waveform; T_f and T_c are the frame duration and chip duration respectively; N_p is the number of chips in a frame. $a_j \in \{-1, 1\}$ and $c_j \in \{0,1, \ldots,N_p\}$ represent time hopping code and polar code respectively. Note that T_p, the pulse duration, is smaller than T_c. One transmission signal symbol consists of a number N_f of frames, and every frame has one pulse.

Transmitted in a multipath channel, the received signal is given by

$$\widetilde{r}(t) = \sum_{l=1}^{L} \alpha_l s(t - \tau_l) \tag{2}$$

where l represents each multipath; τ_l is the delay of the l - th multipath component, among these delays, τ_1 is the TOA to be estimated and uniformly distributed in (0, T_b]. And α_l denote the channel gains.

Without loss of generality, perfect synchronization between the transmitter and the receiver is assumed here, and no modulation is considered. The paper adopts a single user strategy, i.e. $c_j = 0$, $a_j = 1$. Then the received signal can be rearranged as

$$r(t) = \sqrt{E_s} \sum_{j=0}^{N-1} p\left(t - jT_f\right) * h(t) + n(t) \tag{3}$$

where N is the number of frames; $n(t)$ is the additive white Gaussian noise (AWGN) with zero mean and two sided power spectral density $N_0/2$.

2.2 System Model

The typical receiver model of TC estimator is shown in Fig. 1.

The signal passes through a band-pass filter (BPF), is processed with a square law device, and enters an integrator before sampling as indicated in Fig. 1. The integrator output samples are

$$Z_{n,k}^{ED} = \int_{(n-1)T_f + (k-1)T_{\text{int}}}^{(n-1)T_f + k*T_{\text{int}}} \left| r_{bpf} \right|^2 dt \tag{4}$$

where $n = 1, 2, \ldots, N$, $k = 1, 2, \ldots, \lfloor T_f/T_{\text{int}} \rfloor$; N is the number of frames; $Z_{n,k}^{ED}$ represents the k - th energy sample value in n - th frame. r_{bpf} is the output of BPF, and T_{int} is the size of integral interval. The paper assumes that the FP completely falls within its corresponding energy sample after integration.

3 Algorithm Implementation

In order to select the FP, the problem changes into choosing the first energy sample exceeding the threshold. In dense multipath environment, TOA estimation is not a pure parameter estimation problem, but rather a joint detection-estimation problem

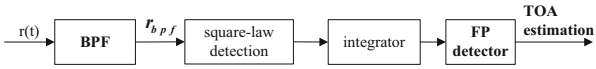

Fig. 1 The TC receiver mode

[5]. The choice of threshold becomes significant. If the threshold is set too low, it will lead to a high false alarm probability. This kind of error is called large error. On the other hand, if the threshold is set too large, it will arouse a low probability of detecting the FP and a high probability of detecting an erroneous path. This kind of error is called the small error [10]. In the presence of noise, the big error dominates in TC algorithms. Therefore, by reducing the false alarm probability, estimation accuracy can be greatly improved. As the optimal threshold is needed, but it is hard to get, the paper keeps away from setting threshold to reach optimal threshold, but sets it according to the skewness and the maximum slope of the received signal. Then based on the randomness of TC noise samples and the fixity of the FP, the frequencies of TC energy samples are employed to estimate TOA. The estimation procedures are shown in Fig. 2.

In the observation time, it is can be assumed that the channel is time invariant. In addition, the noise in different frame is statistic independent. Specific procedures are as follows:

1. Calculate the output $Z_{n,k}^{ED}$ of integrator in each frame using (4);
2. Because the threshold in this procedure directly influences the results of frequencies of TC energy samples, the skewness and the maximum slope of integrator output are employed to set the threshold. By considering the characteristics of received signal, estimation accuracy will be improved.

In the statistics, skewness is used to measure the asymmetry of real random variable probability distribution. The value of skewness can be positive or negative. Its computation formula can be given by:

$$S = \frac{1}{(N_b - 1)\sigma^3} \sum_{i=1}^{N_b} (x_i - \overline{x})^3 \tag{5}$$

where $\overline{x}$ and σ is the mean value and standard deviation of integrator output respectively. Specifically, for noise only, low SNR or large freedom of chi-squares distribution cases, $S = 0$.

As time delay or transmission time is not taken into account by skewness, the maximum slope of integrator output is regarded as another measure value. The calculation of the maximum slope is as follows: there has a number N_b of data. The data is divided into a number $(N_b - M_b + 1)$ of groups. Then the slope of every group is obtained by using the least squares line fit algorithm. Hence, the maximum value can be selected.

The relationship between skewness, the maximum slope and SNR respectively is shown in Fig. 3. From Fig. 3, it shows that skewness increases as SNR increases. On the contrary, the maximum slope increases as SNR decreases. Moreover, the

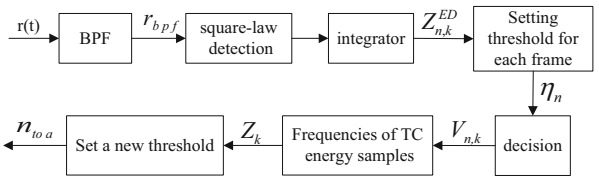

Fig. 2 The estimation procedure

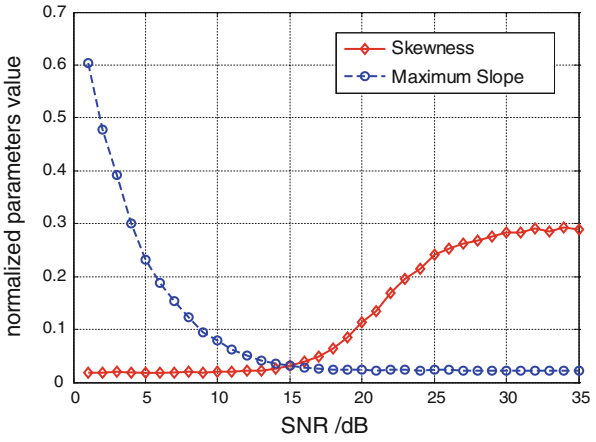

Fig. 3 The relationship between skewness, maximum slope and SNR

skewness changes slowly compared with the maximum slope when SNR is under 15 dB. The situation is contrary when SNR is more than 15 dB. Therefore, a single parameter can not reflect the characteristics of the received signal in a wide range of SNR. So the skewness and the maximum slope are combined as (6) to set the threshold.

$$J = S - M \tag{6}$$

The relationship between J and SNR can be seen in Fig. 4. From Fig. 4, it can be seen that J is a monotone increasing function in a wide range of SNR.

In order to obtain the threshold, the relation between RMSE and threshold coefficient is considered first. By 1,000 CM3 channel realizations, the relationship of RMSE, J and threshold coefficient is obtained in Fig. 5. As indicated in Fig. 5, the threshold coefficient corresponding to the least value of RMSE is regarded as optimal threshold coefficient ξ_{best}. As J increases, ξ_{best} becomes smaller. By choosing ξ_{best}, the relationship between J and ξ_{best} is shown in Fig. 6. The red curve is fitting curve according to the known data.

The optimal threshold coefficient approaches 0.1 when J is more than 10. And it reaches 0.7 from 0.8 when J is less than 5, so J is taken as mean value 0.75. By combining Fig. 6, the relationship between J and ξ_{best} is gotten as follows:

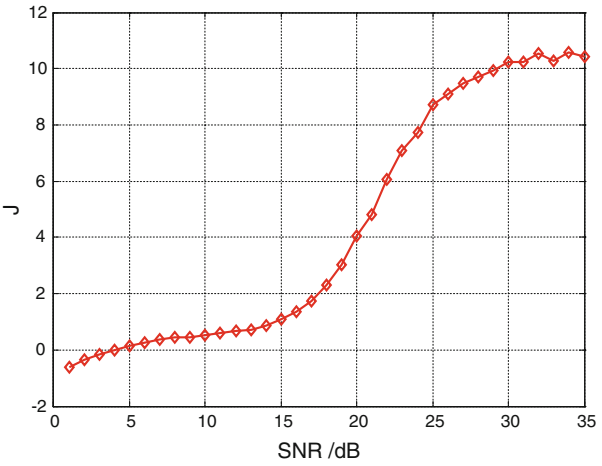

Fig. 4 The relationship between J and SNR

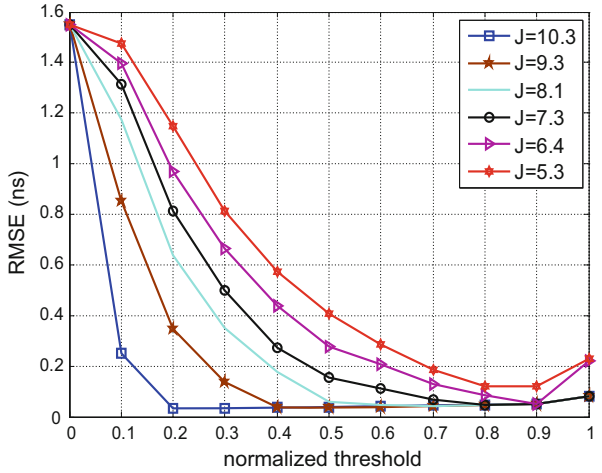

Fig. 5 The relation of RMSE, J and threshold coefficient

$$\xi_{best} = \begin{cases} 0.75 & J < 5 \\ -0.03137 * J * J + 0.3436 * J - 0.029 & 5 \leq J \leq 10 \\ 0.1 & else \end{cases} \tag{7}$$

So the threshold can be expressed as:

$$\eta_n = \xi_{best}(\max(Z_k) - \min(Z_k)) + \min(Z_k) \tag{8}$$

3. The output of integrator $Z_{n,k}^{ED}$ is compared to η_n. Then a new sequence $V_{n,k}$ can be obtained by using (9).

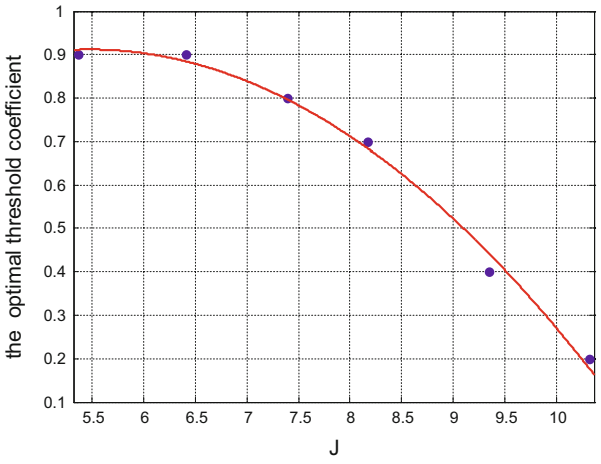

Fig. 6 The relation between J and optimal threshold coefficient

$$V_{n,k} = \begin{cases} 1 & if\ Z_{n,k}^{ED} > \eta_n \\ 0 & else \end{cases} \tag{9}$$

where P is the number of energy samples in a frame.

4. By using (10), add $V_{n,k}$ of all frames to get Z_k. It represents the frequencies of each TC energy sample in N frames.

$$Z_k = \sum_{n=1}^{N} V_{n,k} \tag{10}$$

5. Set a new threshold to detect FP. As the noise samples are uniformly distributed in noise region, the probability that two TC noise samples in different frames have the same index is very small. Moreover, FP is always not the strongest path in the presence of NLOS and noise, so the frequencies of TC FP may not reach N sometimes. It works well when η is not more than $9N/10$ or not lower than $N/2$ [10]. In this paper, the new threshold η is set to be $2/3 \times \max(Z_k)$.

   Z_k are compared to η. And the desired index is the index k when Z_k first reaches η.

$$n_{toa} = First\left(k \middle| Z_k >= \eta\right) \tag{11}$$

   Then TOA can be expressed as follows:

$$\tau_{toa} = (n_{toa} - 1)T_{\text{int}} + T_{\text{int}}/2 \tag{12}$$

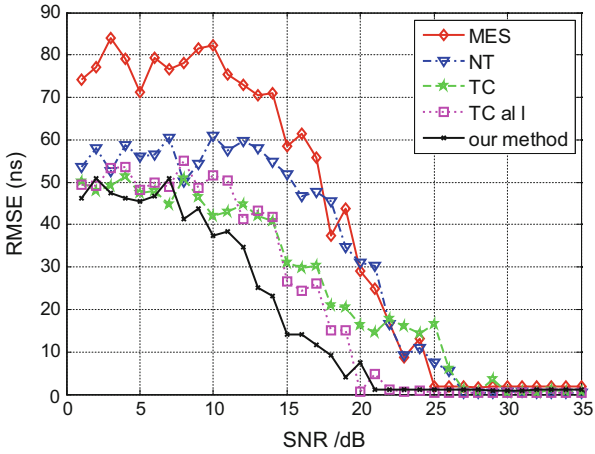

Fig. 7 RMSE of different methods. "TC" means using threshold in [7]. "TC all" means using threshold in [10]

4 Simulation Results

The simulation parameters used are set as follows.

$\theta = 0.4 \times 10^{-9}$, $T_f = 200ns$, $T_p = 1ns$, $t_{\text{int}} = 1ns$, $T_b = 100ns$, $B = 3GHz$. With 1,000 I.E. 802.15.4a CM3 (office LOS) channel realizations generating for each algorithm, the root mean square error (RMSE) is examined for different algorithms. The simulation results are shown in Fig. 7.

In the simulation, the normalization coefficient of normalized threshold (NT) algorithm is 0.3. The false detection probability is 0.08. And the algorithm "TC all" based on the characteristics of received signal is simulated by using (7).

As indicated in Fig. 7, it shows that the estimation errors of all algorithms are large under 20 dB, and the performance is unstable. As the noise becomes weakened when SNR is more than 20 dB, the performance of all algorithms tends to be stable gradually, and the estimation error reaches 0.5 ns approximately at last. Because FP is mostly not the strongest path in real situation, the estimation error of MES algorithm is large. When the threshold is smaller than the amplitude of FP, the NT algorithm can achieve good estimation accuracy. The algorithm based on the characteristics of received signal relies on the received signal much. Its estimation accuracy is better than the first two algorithms from 10 to 20 dB. As the influence of noise is reduced, the algorithm based on frequencies improved the estimation accuracy much, especially from 15 to 25 dB. Our method considers the skewness and the maximum slope of the received signal. Moreover, by calculating the frequencies of TC energy samples, the early detection probability can be reduced effectively. As indicated in Fig. 7, it shows that our approach has the best performance. Especially in low SNR range, it improves estimation accuracy obviously.

5 Conclusion

The paper focuses on TC algorithms of UWB ED receiver. First the threshold is set according to the skewness and the maximum slope of received signal. Because of the randomness of TC noise samples and the fixity of FP, the frequencies of TC energy samples are calculated to consider TOA. This algorithm is easy to implement. And simulation results show that it can improve estimation accuracy in low SNR range.

Acknowledgments This work was supported by the special fund of Chongqing key laboratory (CSTC) and by the project of Chongqing Municipal Education Commission (Kjzh11206) and National Science & Technology Major Program (2011ZX03006-003 (7)) and by Fundamental and Frontier Research Project of Chongqing (cstc2013jcyjA40034).

References

1. D'Amico AA et al (2008) Energy-based TOA estimation. IEEE Trans Commun 7(3):838–847. doi:10. 1109/TWC. 2008. 060545
2. Stoica L et al (2006) A low-complexity noncoherent IR-UWB transceiver architecture with TOA estimation. IEEE Trans Microw Theory Tech 54(4):1637–1646. doi:10. 1109/TMTT. 2006. 872056
3. Gezici S et al (2005) Localization via ultra-wideband radios: a look at positioning aspects for future sensor networks. IEEE Signal Processing Mag 22(4):70–84. doi:10. 1109/MSP. 2005. 1458289
4. Soganci H et al (2011) Accurate positioning in ultra-wideband systems. IEEE Wireless Commun 18(2):19–27. doi:10. 1109/MWC. 2011. 5751292
5. Dardari D et al (2008) Threshold-based time of arrival estimators in UWB dense multipath channels. IEEE Trans Commun 56(8):1366–1378. doi:10. 1109/TCOMM. 2008. 050551
6. Maali A et al (2009) Adaptive CA-CEAR threshold for Non-coherent IR-UWB energy detector receivers. IEEE Commun Lett 13(12):959–961. doi:10. 1109/LCOMM. 2009. 12. 091579
7. Hao Z et al (2012) Threshold selection for TOA estimation based on skewness and slope in ultra-wideband sensor networks. J Netw 7(7):1038–1045. doi:10.4304/JNW.7.7
8. Guvenc I, Sahinoglu Z (2005) Threshold selection for UWB TOA estimation based on kurtosis analysis. IEEE Commun Lett 9(12):1025–1027. doi:10. 1109/LCOMM. 2005. 1576576
9. Chi X, Law CL (2008) Delay-dependent threshold selection for UWB TOA estimation. IEEE Commun Lett 12(5):380–382. doi:10. 1109/LCOMM. 2008. 080015
10. Wenyan L et al (2012) TOA estimation in IR UWB ranging with energy detection receiver using received signal characteristics. IEEE Commun Lett 16(5):738–741. doi:10. 1109/LCOMM. 2012. 030912. 112445
11. Feng W et al (2011) Weighted energy detection for non-coherent ultra-wideband receiver design. IEEE Trans Wireless Commun 10(2):710–720. doi:10. 1109/TWC. 2010. 120310. 101390

A Method of Object Identification Based on Gabor-Network and UWB

Kang Liu and Ting Jiang

Abstract UWB communication has obvious advantages in the aspect of transmission rate, power consumption and price cost. Therefore, it has become the focus of the academia and industry. For the low power consumption, high multipath resolution and strong penetrating power, UWB radar has great potential in person positioning, object detection and obstacle recognition. This paper takes the advantage of UWB radar's environmental perception ability and combines it with Gabor transform in the scenes with different obstacle such as los, human body and metal barrier. We extract the UWB radar signal's Gabor coefficients and combine them with neural network to identify categories and locations.

Keywords UWB • Gabor • Neural network • Identification

1 Introduction

For UWB radar's low power consumption, high multipath resolution, strong concealment and penetrating power, it is mainly applied in radar target detection, imaging, complex environment detection and positioning for person [1]. In this paper we research UWB radar's ability of perceiving transmission environment by extracting its Gabor transform coefficients.

Gabor transform is a time-frequency method for signal analysis and Gabor transform is a kind of integral formula based on Gabor transform coefficients [2]. Now, Gabor transform and Gabor transform are known as one of the best ways in communication and signal processing. Gabor transform can be used for signal's feature extraction [3].

K. Liu (✉) • T. Jiang
Key Lab of Universal Wireless Communication, MOE, Beijing University of Posts and Telecommunications, Beijing, China
e-mail: lkang0305@163.com; Tjiang@bupt.edu.cn

B. Zhang et al. (eds.), *The Proceedings of the Second International Conference on Communications, Signal Processing, and Systems*, Lecture Notes in Electrical Engineering 246, DOI 10.1007/978-3-319-00536-2_50,

In this paper, we extract the Gabor transform coefficients of the received UWB radar's signal in some kinds of outdoor transmission environment with different obstacles such as LOS, metal barrier and human body. Further we use neural network, a kind of pattern recognition method, to realize the purpose of determining the current transmission environment type according to the received UWB signal. We call the neural network combined with Gabor coefficients as Gabor-network.

The paper is organized as follows: we do some introduction of Gabor transform, including the Gabor transform principle and method in part 2. In part 3 we combine UWB signal's Gabor coefficients with neural network to realize the obstacle's location and type identification. Finally, the conclusions are given according to the simulation results in part 4.

2 Gabor Transform and Neural Network

2.1 Using Gabor Transform to Extract Signal Features

The most basic question in Gabor transform is how to choose the Gabor primary function and how to calculate the Gabor transform coefficients, which means how to realize the Gabor transform [4]. Before the introduction of discrete Gabor transform of dimensional signal, we draw out the concept of continuous Gabor transform first.

2.1.1 Continuous Gabor Transform of Dimensional Signal

Assume that $\varphi(t,\omega)$ is a continuous dimensional signal. We define the Gabor transform as follows:

$$\varphi(t) = \sum_{m=-\infty}^{\infty} \sum_{n=-\infty}^{\infty} a_{mn}(t) g_{mn}(t) \tag{1}$$

The following three functions:

$$g_{mn}(t) = g_{mn}(t - mT) e^{jn\Omega t} \tag{2}$$

$$a_{mn} = \int \varphi(t) \gamma^*_{mn}(t) dt \tag{3}$$

$$\gamma_{mn}(t) = \gamma(t - mT) e^{jn\Omega t} \tag{4}$$

is called Gabor primary function, Gabor coefficients and dual Gabor primary function respectively [5] T and Ω show the sampling interval of time and frequency. Critical sampling happens when $T\Omega = 2\Pi$, undersampling happens when $T\Omega > 2\Pi$

and oversampling happens when $T\Omega < 2\Pi$. Gabor transform exist only when $T\Omega \leq 2\Pi$. Function (4) is known as Gabor transform. To completely reconstruct the original signal, $g(t)$ and $\gamma(t)$ must satisfy the following conditions:

$$\sum_{m=-\infty}^{\infty} \sum_{n=-\infty}^{\infty} \gamma_{mn}^{*}(t') g_{mn}(t) = \delta(t - t') \tag{5}$$

Function (8)is called completely reconstruction formula. $g_{mn}(t)$ and $\gamma(t)$ which satisfy the conditions above is described as complete. The more practical function is :

$$\int_{-\infty}^{\infty} \gamma(t) g^{*}(t - mT)\, e^{-jn\Omega t} dt = \delta_m \delta_n \tag{6}$$

which is called biorthogonality relation. $\gamma(t)$ and $g(t)$ are orthogonality just when m and n are not zero at the same time. Therefore we say $\gamma(t)$ is the biorthogonality function of window function g(t).

It is worthy emphasizing that biorthogonality relation still stand when $\gamma(t)$ and g(t) are exchanged, which means Gabor transform and Gabor coefficients can be described as:

$$\begin{aligned} \varphi(t) &= \sum_{m=-\infty}^{\infty} \sum_{n=-\infty}^{\infty} a_{mn}(t) \gamma(t - mT) e^{jn\Omega t} \\ &= \sum_{m=-\infty}^{\infty} \sum_{n=-\infty}^{\infty} a_{mn}(t) \gamma_{mn}(t) \end{aligned} \tag{7}$$

$$\begin{aligned} a_{mn} &= \int_{-\infty}^{\infty} \varphi(t) g^{*}(t - mT)\, e^{jn\Omega t} dt \\ &= \int_{-\infty}^{\infty} \varphi(t) g_{mn}^{*}(t) dt \end{aligned} \tag{8}$$

When coefficients calculation method is selected, the following question is the choice of basis functions, because a more appropriate basis function can make the Gabor transform have a better localization performance in the aspect of time and frequency [6].The most commonly used basis function is gaussian function.

2.1.2 Discrete Gabor Transform of Dimensional Signal

Considering the UWB receiver's signal is discrete on the time axis, in order to extract the Gabor coefficients, we need to use discrete Gabor transform.

$\varphi(k)$ is a finite discrete time signal whose length is L_s, window function g(k) has a length of L_g,we prolongate $\varphi(k)$ and g(k) respectively to generate two sequence $\hat{\varphi}(k)$ and $\hat{g}(k)$ whose period is $L = L_s + L_g$

Supposing time and frequency sampling interval is respectively ΔM and ΔN. Define M = L/ΔM, N = L/ΔN, we will get:

$$\hat{\varphi}(k) = \sum_{m=-\frac{L_S}{\Delta M}}^{\frac{L_S}{\Delta M}-1} \sum_{n=0}^{N-1} a_{mn} \hat{g}_{mn}(k) \tag{9}$$

where

$$a_{mn} = \sum_{k=0}^{L_S-1} \hat{\varphi}(k) \hat{\gamma}^*_{mn}(k) \tag{10}$$

$$\hat{g}_{mn}(k) = \hat{g}(k - m\Delta M) W_N^{nk}, W_N = e^{j\frac{2\pi}{N}} \tag{11}$$

$$\hat{\gamma}_{mn}(k) = \hat{\gamma}(k - m\Delta M) W_N^{nk} \tag{12}$$

The conditions for completely signal reconstruction is:

$$\Delta M * \Delta N \leq L \tag{13}$$

Which means $\hat{g}(k)$ and $\hat{\gamma}(k)$ should satisfy:

$$\begin{gathered} \sum_{k=0}^{L-1} \hat{g}(k + mN) W_{\Delta M}^{-nk} \hat{\gamma}^*(k) = \delta_m \\ \delta_n, 0 \leq m \leq \frac{1}{N}, 0 \leq n < \Delta M \end{gathered} \tag{14}$$

Gabor transform coefficients a_{mn} can be calculated by FFT:

$$a_{mn} \sum_{k=0}^{L_S-1} \varphi(i + m\Delta M) \gamma^*(i) W_N^{-n(i+m\Delta M)} \tag{15}$$

When extracting the Gabor coefficients, Gabor transform for obvious fluctuating part of the signal is enough, it can reduce redundancy. We select eight time scale, fifteen frequency scale so we can get 120 Gabor coefficients as the input vector of neural network. At the same time, identification result of target classification is the output vector of the neural network.

After training the network with training sample is done, we input test data to realize target recognition.

2.2 Neural Network Recognition Mode

Neural network model consists of input layer, hidden layer and output layer. Each layer contains several neurons node which is used to process information. Neurons in different layer is linked together [7]. Neurons in the same layer has no connections.

Neural network information dissemination process in one layer to another layer by neurons to neurons, this kind of operation is called positive-propagation of information. In contrast, the error's dissemination is called back-propagation in neural network [8].

Specific, neural network's basic implementation process is disseminating information from the input layer to the output layer and disseminating the error between the expected value and actual value from the output layer to the input layer. The neural network will adjust the weights and thresholds at the same time.

The information's positive-propagation and error's back- propagation will be repeated again and again until the error of the output layer is less than a given value or the number of iterations has reached the maximum value. After the learning procedure, the neural network will have the ability of identification.

3 Application in Target Recognition

3.1 Test Scene

The test scenarios used in this article is shown in Fig. 1 below:

The distance between transmitter and receiver is 21.3 m, data collection is done in a small forest. Figure 1 shows the four different locations of obstacles.

When we start testing, the same obstacles will be placed in different locations or different obstacles will be placed in the same location respectively.

3.2 Test Procedures

Using the Gabor coefficients to realize object's type recognition is carried out as following: the different obstacles like metal cabinet, LOS conditions and human are placed in position No.3, then we establish training sample sets and testing sample sets respectively. At last we do the Gabor transform for each sample set to extract the Gabor coefficients.

Using the Gabor coefficients to identify the location is carried out by establishting training sample sets and testing sample sets respectively with obstacles (human) at position No. 1, 2, 3, 4 respectively.

Fig. 1 Test scene

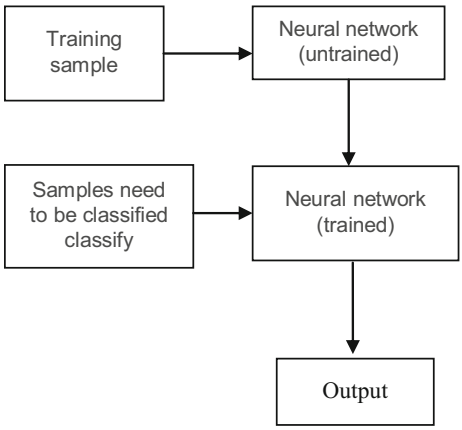

Fig. 2 Algorithm flow

After getting sample of each set, we extract the Gabor coefficients and make them as the input vector for the Neural network. The algorithm flow is shown in Fig. 2.

In order to confirm that the extracted Gabor coefficients can describe the character of received signal completely, we can use the Gabor coefficients to reconstruct the signal and compare the reconstructed signal with original signal's waveform, if the waveform are the same, then we can confirm the Gabor coefficients is effective.

Taking the scene in which there is one person at position No. 2 for example, Fig. 3 shows the original signal and reconstructed signal. Red signal represents the original signals and blue signal is the signal reconstructed by the Gabor coefficients of original signal.

Through the observation, the reconstructed signal has no distortion, which means the Gabor coefficients can represent the original signal correctly.

To show the distribution of the Gabor coefficients derived from the received signal intuitively, taking the scene in which there is one person at position No. 2 for example again.

The Gabor coefficients of received signal is shown in the 3D coordinate vector diagram in Fig. 4, the x coordinate is frequency domain scales, y is the time scale, z coordinates is the Gabor coefficients after normalizing.

Joining the Gabor coefficients matrix in the time - frequency domain together according to the row vector, we can get a training sample.

The training sample set is sent into the neural network to train it. Finally we send test sample set into neural network to identify the obstacle and statistical accuracy.

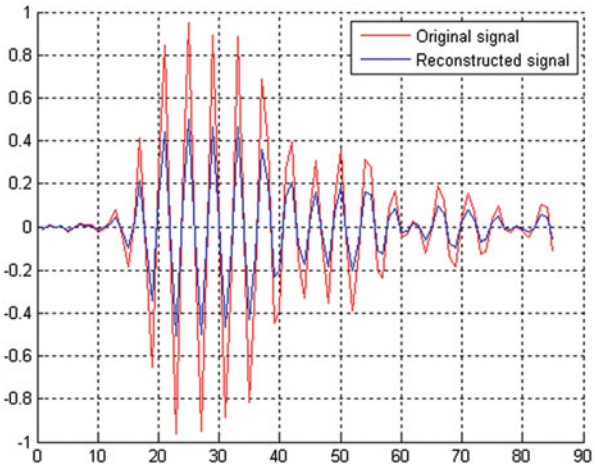

Fig. 3 Original signal and reconstructed signal

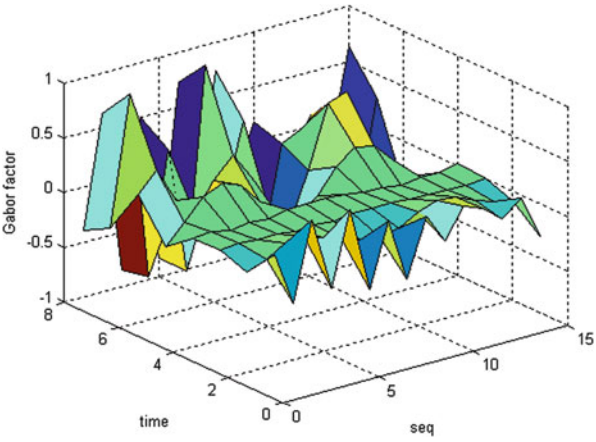

Fig. 4 Gabor coefficients of the received signal

We select 450 groups of data under each scenes, 225 sets of which is used for training and learning, the rest of the 225 groups of data is used to test the identification effect.

We set the error of the neural network as 0.01, the stride length as 3000 steps and select the BP training algorithm. The neural networks will be trained until it reach the training error of the large step.

3.3 Test Result

Through simulation calculation, the recognition statistical rate of obstacles classification and the obstacle position identification are shown in Tables 1 and 2.

Table 1 Accuracy of identify obstacles classification

Obstacles classification	Total test samples number	Correct classification number	Classification accuracy (%)
Los	225	224	99.5556
Metal	225	222	98.6667
Human	225	222	98.6667

Table 2 Accuracy of identify obstacles position

Obstacles position	Total test samples number	Correct classification number	Classification accuracy (%)
1	225	224	99.5556
2	225	225	100
3	225	222	98.6667
4	225	220	97.7778

By the test results, the different locations and different types of obstacles can be well identified by using the Gabor-network.

4 Conclusion

In this paper we study the ability of perceiving different transmission environment of UWB communication process by using the Gabor coefficients of UWB signals and combining them with the neural network's learning and classification ability. We can achieve the goal of classification when we send Gabor coefficients of signals into the neural network as the input vector.

Acknowledgment This work was supported by NSFC (61171176).

References

1. Maherin I, Liang Q (2011) An entropy based approach for sense-through foliage target detection using uwb radar. WASA 6843:180–189
2. Yanfei S (2009) Combined neural network and PCA for complicated damage detection of bridge. Nat Comput 2:524–528
3. Yan BF, Miyamotoa A, Bruhwilerb E (2006) Wavelet transform-based modal parameter identification considering uncertainty. J Sound Vib 291:285–301
4. Kong AW-K (2010) "An alternative gabor filtering scheme image processing". 2010 17th IEEE international conference on digital object identifier. p 1925–1928
5. Dolu O, Kirtac K, Gokmen M (2009) "Ensembled gabor nearest neighbor classifier for face recognition". Comput Inform Sci, p 99–104
6. Lagae A, Lefebvre S, Dutre P (2011) Improving gabor noise. IEEE Trans Vis Comput Graph 17:1096–1107

7. Lajevardi SM, Lech M (2008) “Facial expression recognition using neural networks and log-gabor filters”. Digital image computing: techniques and applications (DICTA), p 77–83
8. Areekul V, Watchareeruetai U, Suppasriwasuseth K, Tantaratana S (2005) “Separable Gabor filter realization for fast fingerprint enhancement”. Image Processing, 2005. ICIP 2005, vol 3, p III-253–256

A Method of Target Detection and Identification Based on UWB and PSO-WNN

Feng Gao and Ting Jiang

Abstract UWB radar is widely used in target detection and identification because of its spectrum in range of GHz. A novel method of target detection based on Particle Swarm Optimization-based Wavelet Neural Network (PSO-WNN) and UWB is proposed. Using this method, we extract and analyze the characteristic parameters of the received signals and channel impulse responses in the communication systems from the view of UWB communications, then apply PSO-WNN to identify the target. According to the obtained results, this method is quite effective for target identification.

Keywords UWB • PSO • Wavelet neural network (WNN) • Target identification • Channel characteristic parameters

1 Introduction

In recent years, wavelet neural network (WNN) is widely used in pattern recognition as a new artificial neural network (ANN). WNN combines feed forward neural networks with wavelet theory. As a result, compared with classical neural networks, WNN has a better generalization property and is more appropriate for the modeling of high frequency signals. In the learning algorithm of WNN, Back Propagation (BP) and its improved algorithms are most widely used. While BP algorithm is essentially a gradient descent learning algorithm, the complexity in the actual application often makes it have some shortcomings such as long training time, low precision, local minimum and so on [1]. PSO algorithm, which has some advantages of simple structure, parallel processing, few adjustment parameters and stronger global convergence [2], is a good alternative to optimize the WNN.

F. Gao (✉) • T. Jiang
Key Laboratory of Universal Wireless Communication, Ministry of Education, Beijing University of Posts and Telecommunications, Beijing, China
e-mail: fengg0708@163.com

B. Zhang et al. (eds.), *The Proceedings of the Second International Conference on Communications, Signal Processing, and Systems*, Lecture Notes in Electrical Engineering 246, DOI 10.1007/978-3-319-00536-2_51,

In the UWB communication technologies, the received signals change when placing different obstacles between the UWB-IR transmitter (TX) and UWB-IR receiver (RX). Thus, we can identify target by analyzing the forward received signal. On the basis of this idea, a method based on selected bispectra and radial-basis function (RBF) was successfully applied to identify obstacle by You Minglei [3] while a method based on the ROROP (resilient back-propagation) and the channel characteristic parameters was proposed to detect and classify the target by He Junqin [4]. Although these methods succeed, they have some shortcomings. The data they use is from simulated channel model and the capacity of approximate and robust is not doughty. On the basis of previous research results, we design the whole procedure as follows: First, we can obtain the Channel Impulse Response (CIR) from received signals by CLEAN algorithm. Second, we use the UWB channel parameters (e.g. channel energy, excess delay) which are obtained from CIR as the features of targets. Finally apply the designed PSO-WNN to identify target in the real scenario.

The paper is organized as follows. In Sect. 2 characteristic parameters used as feature vector are introduced. In Sect. 3 we introduce Particle Swarm Optimization and Wavelet Neural Network, whose feature vector for the target recognition is built based on the characteristic parameters of the UWB channel, then PSO-WNN is proposed. In Sect. 4 we get raw test data from the real scenarios of different targets and PSO-WNN is applied to identify different targets. Finally, according to the test results, the conclusions are given in Sect. 5.

2 The Selection of Feature Vector for WNN

By analyzing the signals, we can find that the waveform of signals received in different communication environments is slightly different. These differences contain the essential information called characteristic parameters for us to identify the special target. So extracting characteristic parameters to distinguish targets is critical. These parameters are selected mainly from the view of channel based on the following considerations: (1) the main parameters such as the delay and the number of multipath are used to describe multipath channel; (2) if targets are placed between TX and RX, signals are considerably more weakened and have smaller energy and amplitude due to reflections or obstructions; (3) the root mean-square (RMS) delay spread, is larger if targets placed between TX and RX. Besides we also consider other parameters that described in the literature. Taking all these considerations into account, characteristic parameters in use are as follows:

1. Maximum amplitude of the received signal:

$$A_{\max} = \max_{t} |r(t)| \tag{1}$$

2. The mean excess delay:

$$\tau_{excess} = \frac{\int_{-\infty}^{+\infty} t|r(t)|^2 dt}{\int_{-\infty}^{+\infty} |r(t)|^2 dt} \tag{2}$$

3. The number of MPCs that contain 85 % of the received energy:

$$NP\_E85 = \min_{n} \left(\sum_{t=1}^{n} |r(t)|^2 > 0.85E_r \right) \tag{3}$$

4. The number of the MPCs within 10 dB of the strongest path for each received signal:

$$NP\_10dB = \sum_{t} \left(|r(t)| > 10^{-A\max} \right) \tag{4}$$

5. Energy of received signal:

$$G_r = \int_{-\infty}^{+\infty} |r(t)|^2 dt \tag{5}$$

6. Variance of received signal:

$$\sigma_{|r|}^2 = \frac{1}{T} \int_{T} \left[|r(t)| - \mu_{|r|} \right]^2 dt \tag{6}$$

where $\mu_{|r|} = \frac{1}{T} \int_{T} [|r(t)|] dt$

7. Kurtosis:

$$K = \frac{1}{\sigma_{|r|}^4 T} \int_T \left[\left| r(t) - \mu_{|r|} \right| \right]^4 dt \tag{7}$$

8. Skewness:

$$S = \frac{\frac{1}{T} \int_T \left[r(t) - \mu_{|r|} \right]^3 dt}{\left[\sqrt{\frac{1}{T} \int_T \left[r(t) - \mu_{|r|} \right]^2 dt} \right]^3} \tag{8}$$

Besides, these characteristic parameters will be used as feature vector of WNN.

3 Fundamentals of PSO-WNN

3.1 Fundamentals of WNN

The WNNs have been successfully applied in the field of function learning, nonlinear system identification [5], and time series predictions [6]. The core of wavelet neural network is wavelet transform. In general, the wavelet transform of time series signal $f(t)$ is defined as follows:

$$WT(a,b) = \frac{1}{\sqrt{a}} \int_{-\infty}^{\infty} f(t) \psi \left(\frac{t-b}{a} \right) dt \tag{9}$$

Where ψ(t) is the mother wavelet, and a and b are the scale and time-shift parameters, respectively. The WNN can be considered as a special case of neural network. The difference is that the transfer function of the hidden nodes take nonlinear mother wavelet function instead of classical Sigmod function. Because it combines the function of time-frequency localization by wavelet transform and self-studying by neural network, the network possesses doughty capacity of approximate and robust. The structure of WNN is shown as Fig. 1.

In this paper, the activation function of the hidden neurons is Mexican Hat mother wavelet, whose function is shown as follows:

$$\psi(\mathrm{x}) = e^{-x^2/2} \left(1 - x^2\right) \tag{10}$$

While the activation function of the output layer is Sigmoid function, shown as follows:

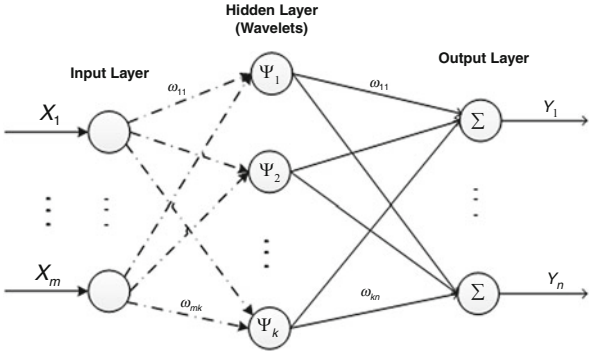

Fig. 1 The structure of Wavelet Neural Network

$$\sigma(\mathrm{u}) = \frac{1}{1+e^{-u}} \tag{11}$$

As shown in the Fig. 1, WNN is made up of three layers: input layer, hidden layer and output layer.

1. Input layer: the input vector is made up of the characteristic parameters, which is expressed as follows:

$$X = [X_1 \quad X_2 \quad \cdots \quad X_m] \tag{12}$$

In this formula, m represents the number of characteristic parameters. Besides the number of nodes in the input layer is determined by that of characteristic parameters. As described in Sect. 2, the number of characteristic parameters is eight.

2. Output layer: the output vector is the target to be classified and can be expressed as follows:

$$Y = [Y_1 \quad Y_2 \quad \cdots \quad Y_n] \tag{13}$$

In this paper, there are three targets: LOS, woods and iron cabinet. Thus, the number of output layer is three.

3. Hidden layer: the number of nodes of hidden layer is determined by the empirical formula.
4. Error function: the error function uses the principle of minimum mean square error (MSE).

$$Y_i = \sigma(\mathrm{u}_i) = \sigma\left[\sum_{k=1}^{K} w_{k,i}\psi_{a_k,b_k}\left(\sum_{m=1}^{M} w_{m,k}x_m\right)\right] \quad i = 1, 2, \cdots, N \tag{14}$$

$$E(N) = \frac{1}{N}\sum_{i=1}^{N}(D_i - Y_i)^2 \tag{15}$$

Where D is the desired output vector, Y is the actual output vector, K is the number of iterations, N is the number of nodes of output layer.

From the structure of Fig. 1, the key of making up a proper WNN is how to calculate the parameters $\{w_{mk}, a_k, b_k, w_{kn}\}$ in the net.

3.2 Fundamentals of PSO

PSO stemmed from the research on the prey behavior of a swarm of bird [7]. As one of the evolutionary computation techniques, PSO imitates the process of a flock of birds searching food. Instead of crossover and mutation in Genetic Algorithm (GA), PSO follows the principle that particles follow the best one to search for the best. In PSO, each potential solution is represented as a particle in a population (called swarm), which is initialized with a random position and search velocity. Each particle has its fitness value determined by the optimized function and its velocity that determined its flight course and distance. A particle updates itself by following two essential values: *pbest* and *gbest* in each iteration. *pbest* is the best solution obtained by itself while *gbest* is the best solution found by all the particles. Besides the produce of updating itself is accomplished by the two formulas:

$$X_i(k+1) = X_i(k) + v_i(k+1)\Delta t \tag{16}$$

$$\mathrm{v}_i(k+1) = wv_i(k) + c_1 r_1[P_i - X_i(k)]/\Delta t + c_2 r_2[P_s - X_i(k)]/\Delta t \tag{17}$$

where X_i represents the position of the particle i, P_i represents the best previous position of particle i, P_s represents the best position among all particles in the population X, k is the algebra of evolutionary iteration, w is the internal weight coefficient, c_1 and c_2 are the learning efficiencies, r_1 and r_2 are the random real numbers in the range of [0,1], Δt represents the space length of the particle in iteration, v_i represents the velocity of the particle, and in the range of [0.1].

Thus, particles communicate with each other and share their information among each other during their search. The search don't stop until the given max iteration frequency or fitness value meets the requirement.

3.3 Process of PSO-WNN

In this article, PSO is used to optimize wavelet neural network to avoid the curse of dimensionality and enhance the learning capability as well as the training efficiency. Associated with previous analysis on WNN, the parameters to be global

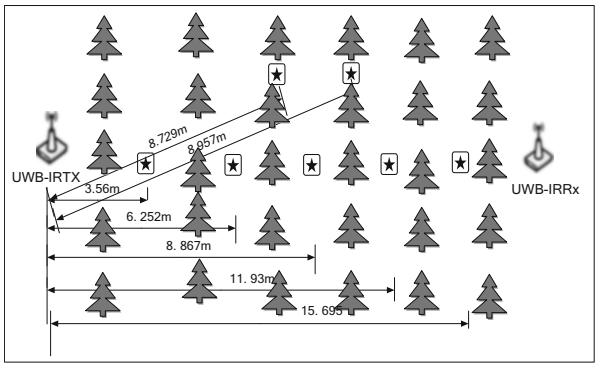

Fig. 2 The curve of fitness function in the process of optimization

optimized are $\{w_{mk},a_k,b_k,w_{kn}\}$. At the same time, he fitness value can be calculated by formula (15).

Considering all these, the process of PSO-WNN is represented as follows:

Step 1: Normalize the given input variables and expected output.
Step 2: Define the element of position vector function X of particle swarm as structure of the wavelet neural network, including the number of the hidden layer neurons and give termination condition.
Step 3: Initialize particle swarm.
Step 4: For all particles of the swarm, the following steps are taken:

1. Using the global best *gbest* and local best of each particle *pbest*, each particle's velocity and position are updated according to formulas (16) and (17);
2. Evaluate the fitness of each particle and compare the evaluated fitness value of each particle with its *pbest*. If current value is better than *pbest*, then *pbest* is updated with current position;
3. If current value is better than *gbest*, *gbest* is updated with current position.

Step 6: This procedure proceeds until termination condition is satisfied, and then the global optimum values are obtained. Otherwise, loop to step 4.
Step 7: Initialize WNN with the optimum $\{\omega_{m,k},a_k,b_k,\omega_{k,n}\}$.

4 Application of PSO-WNN Model to UWB Target Identification

4.1 Measurement Setup and Environments

The measurements were taken using PulsON 400 (P400) RCM by the Time Domain Co, Ltd. The P400 RCM operating band is from 3.1 to 5.3 GHz, with center frequency 4.2 GHz. Time Domain Broadspec toroidal dipole antennas are used

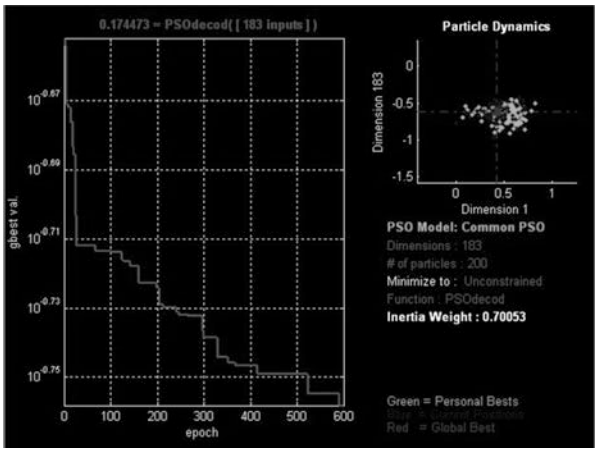

Fig. 3 The topology of foliage environment and measurement antennas deployment and target position

Table 1 Comparison of target identification results between WNN and PSO-WNN

Class	LOS (%)	Wood board (%)	Iron cabinet (%)
WNN	93.1429	96.8571	76.8571
PSO-WNN	94.8571	100	90.8571

for transmitting and receiving antennas. The gain of the antenna is about 3 dbi. The P400 RCM is controlled by a PC and data are recorded digitally. Our measurements have been conducted in foliage. As shown in Fig. 2, the UWB-IR transmitter (TX) and UWB-IR receiver (RX) were placed at fixed position, while the height of both TX and RX were fixed at 1.5 m from the floor and the distance is 19.136 m. Then two objects: wood board and small iron cabinet were placed between Tx and Rx to build different scenarios.

As shown in Fig. 2, we set seven different spots for each target to enhance the reliability of results. And in each spot we conducted 100 times measurements for each scenario. So there are three scenarios in our measurement: LOS, woods and iron cabinet. Thus in total we got 2,100 times data, which are divided equally into two pieces: for training and testing. Give 15 as the number of nodes in hidden layer. Give 200 as the number in the swarm, $c_1 = 2$, $c_2 = 2$ is given as the initialized parameters in PSO. Give 1,000 iteration steps or 0.001 exactness ratio as the precondition to terminate the training of the network learning.

4.2 Results of Identification and Analysis

The data and figures obtained in the process are shown as follows.

Figure 3 shows the result of PSO optimization. Green spots represent *pbest*, red ones represent *gbest* and blue ones represent the position of the particle. After every iteration, the position is gradually approaching the *gbest*.

Table 1 shows comparison of target identification results between WNN and PSO-WNN. The results show that the recognition rate of PSO-WNN is higher than 90 % and the targets are effectively identified. From the comparison, it is obvious that PSO can enhance the performance of WNN in target identification based on UWB.

5 Conclusions

In this paper, we build three scenarios in foliage. The channel characteristic parameters are extracted to be feature vector. PSO-WNN is used to identify targets. The results of measurement demonstrate that the method proposed in this paper based on PSO-WNN and UWB is efficient for target identification.

Acknowledgment This work was supported by NSFC (61171176).

References

1. Zhang Q, Benveniste A (Jul. 1992) Wavelet networks. IEEE Trans Neural Netw 3(6):889–898
2. Kenedy J, Eberhart RC (1995) "A new optimizer using particle swarm theory". In Proceedings of the 6th international symposium on micro machine and human science, IEEE Service Center, Piscataway, p 39–43, Oct 1995
3. You Minglei (2012) "A method of obstacle identification based on UWB and selected bispectra", lecture notes in electrical engineering, communications, signal processing, and systems: the 2012 Proceedings of the international conference on communications, signal processing, and systems, p 373–382
4. He Junqin (2012) "A method of target detection and identification based on RPROP and UWB channel characteristic parameters", 2012 I.E. Globecom Workshops, GC Workshop 2012, p 1460–1463
5. Billings SA, Wei H-L (2005) A new class of wavelet networks for nonlinear system identification. IEEE Trans Neural Netw 16(4):862–874
6. Iyengar SS, Cho EC, Phoha VV (2002) "Foundation of wavelet networks and applications", Chapman & Hall/CRC, p 178–179
7. Huang K, Chen SF, Yuan X, Zhou ZG (2004) "Neural network optimal design based on orthogonal experiment method", systems engineering theory methodology applications, p 272–275

A New UWB Target Detection and Identification Method Based on Extreme Learning Machine

Hao Shen and Ting Jiang

Abstract UWB is a short-range wireless communication technology with strong resolution, detection and anti-jamming capability. UWB radar has been widely used in the transportation detection, bridge detection [1], medical detection [2], etc. However traditional UWB radar is used for target detection and identification by analyzing the echo signals. It cannot content the requirement of accomplishing communication and target detection at the same time which is significant in individual combat and intrusion detection. In this paper, we propose a novel target detection and recognition method which is different from the traditional UWB radar to content the above requirement. This method extracts the characteristic parameters of the received signals instead of the echo signals, and employ the extreme learning machine (ELM) to identify target. According to Matlab simulation result, the new method is quite fast and effective in target identification.

Keywords UWB • ELM • Channel characteristic parameters • Target identification

1 Introduction

UWB possess not only a good performance in communication, but also the capabilities of environment detecting. When UWB signals transmit across the target obstacle, the signals will reflect, diffract, scatter and transmit, etc. UWB receiver will receive different signals through different target obstacle. It is possible to analyze the characteristic parameters of the received signals instead of the echo signals to identify target obstacle. There are some studies, in which UWB radar is

H. Shen (✉) • T. Jiang
Key Lab of Universal Wireless Communication, Beijing University of Posts & Telecommunications, Beijing, China
e-mail: mouse19900311@163.com

B. Zhang et al. (eds.), *The Proceedings of the Second International Conference on Communications, Signal Processing, and Systems*, Lecture Notes in Electrical Engineering 246, DOI 10.1007/978-3-319-00536-2_52,

used for target detection and identification by analyzing the received signals in the target recognition literature [3].

The past studies in the field have shown there is a major disadvantage that the learning speed of neural networks is much slower than practical required. To resolve these disadvantages of neural networks, in this paper we suggested a new learning algorithm called extreme learning machine for single-hidden layer feedforward neural networks (SLFNs) which randomly choose hidden nodes and analytically determines the output weights of SLFNs. In theory, this algorithm tends to provide good generalization performance at extremely fast learning speed [4, 5]. To verify the effectiveness of the method, we apply the method to three UWB outdoor communication scenes with different types of target obstacles and the simulation results demonstrate that this method can identify the target extremely fast and precisely.

The paper is organized as follows: In Sect. 2, we discuss the characteristic parameters of the UWB channel, in Sect. 3, the extreme learning machine algorithm is introduced, in Sect. 4, we apply the method in UWB outdoor communication scenes and analyze the simulation result, in Sect. 5, the conclusions are given.

2 Extracting the Characteristic Parameters of UWB Channel

In general, the characteristic of signals is analyzed by their energy, amplitude, delay, number of multipath, waveform. The delay and the number of multipath are the key parameters in UWB channel. So in this section, we focus on these two parameters. In the delay, we consider the excess delay which describes the delay of the arriving time of the multipath signal relative to time zero and the RMS delay spread which is the standard deviation of the mean delay.

2.1 The Excess Delay

$$\tau_{excess} = \frac{\int_{-\infty}^{+\infty} t\left|r(t)\right|^2 dt}{\int_{-\infty}^{+\infty} \left|r(t)\right|^2 dt} \tag{1}$$

2.2 The RMS Delay

$$\tau_{RMS} = \sqrt{\frac{\sum_{K} (\tau_K - \tau_m)^2 P(\tau_K)}{\sum_{K} P(\tau_K)}} \tag{2}$$

Where, τ_K is the delay of the kth multipath, τ_m is the mean excess delay, $P(\tau_K)$ is the power delay distribution.

2.3 The Number of Significant Paths Within 10 dB of Peak

In the number of multipath, we use the number of significant paths (NSP) within 10 dB of peak which is the paths whose energy is in the 10 dB dynamic range compared with the largest peak path.

$$NP\_10dB = \sum_{t} \left(\left| r(t) \right| > 10^{-A_{\max}} \right) \tag{3}$$

Where, A_{max} is the maximum amplitude of the received signal.

In addition, we choose the maximum amplitude of the received signal, the total energy of the received signal, the number of paths that contain 85 % of the total energy, the variance of the received signal, the Kurtosis coefficient and the Skewness coefficient as supplements of the characteristic parameters. Channel characteristic parameters are different and these parameters are used as the input vector of extreme learning machine and the target objects can be classified and identified.

3 The Extreme Learning Machine Algorithm

Extreme learning machine is a new learning algorithm for single-hidden layer feedforward neural networks (SLFNs). The output of SLFNs with L hidden nodes and activation function $g(x)$ as on (4):

$$f_L(x) = \sum_{i=1}^{L} \beta_i G(a_i, b_i, x) = t_i \tag{4}$$

Where a_i and b_i are the learning parameters of ith hidden nodes, β_i is the weight vector connecting the ith hidden node and the input nodes.

$$\beta_i = [\beta_{i1}, \beta_{i2}, \ldots, \beta_{im}]^T \tag{5}$$

Given any small positive value $\varepsilon>0$ and activation function g which is infinitely differentiable in any interval, there exists $K \leq Q$ such that for Q arbitrary distinct samples (x_i t_i), where $x_i \in R^m$ and $t_i \in R^n$ for any w_i and b_i randomly chosen from any intervals of R^n and R, according to any continuous probability distribution, then with probability one,

$$\left|\left|H_{N\times m}\beta_{M\times m} - T^{'}\right|\right| < \varepsilon \tag{6}$$

The weight vector connecting the hidden nodes and the output nodes can be obtained by the least squares solutions of the linear equations. The weight vector as on (7):

$$\hat{\beta} = H^{+} \times T \tag{7}$$

For single-hidden layer feedforward neural networks, ELM learning algorithm is available for any infinitely differentiable activation functions [6, 7]. Traditional activation functions include Sigmoidal function, Sine function, Hardlim function, etc. In this paper we choose Sigmoidal function as activation function of ELM. The readers can find more information about the SLFNs in references [8, 9].

4 Simulate and Analyze

4.1 Outdoor Communication Scene

The outdoor communication scene is a forest in the west of Beijing University of Posts & Telecommunications. To verify this method can identify the target at any position, we set seven positions for each target obstacle as Fig. 1 shown. In Fig. 1, the R_X and T_X indicate the transmit device and receive device. The distance between two devices is 19.136 m. Every star indicates the position target obstacles may be placed and each position we set three kinds of obstacles which are no obstacles (LOS), wood block (WB), iron cupboard (IC). Every scene for each position we collect 1,000 date.

In the outdoor communication scenes, the received signal is mixed with noise. After denoising, we extract the characteristic parameters from the received signals. Figure 2 shows the variance and the total energy of the received signals under three scenes. Figure 3 shows the RMS delay spread and the number of significant paths within 10 dB of peak of the received signals. The characteristic parameters change with the different targets. It is obvious the received signals change in different scene.

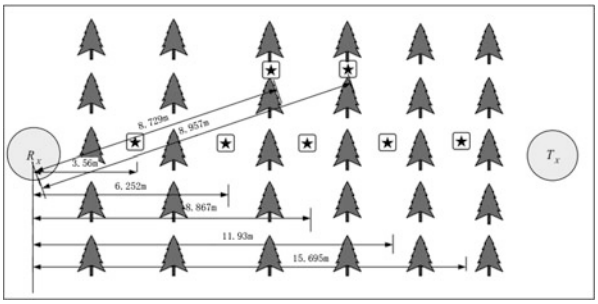

Fig. 1 The target distribution in outdoor communication scene

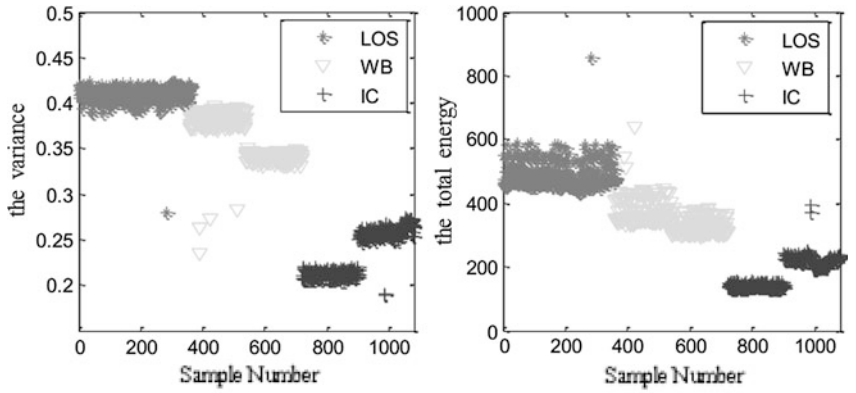

Fig. 2 The distribution of the variance and the total energy of the received signals

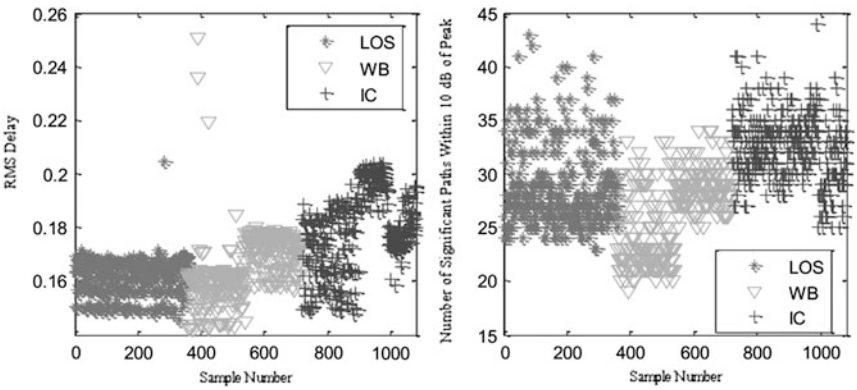

Fig. 3 The distribution of RMS delay spread and the NSP within 10 dB of peak

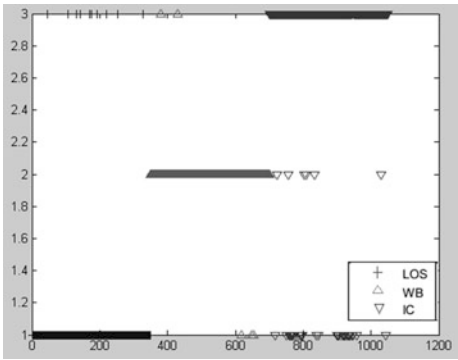

Fig. 4 The recognition result of simulation

Table 1 The performance comparing results of ELM method with BP method

Algorithms	LOS (%)	WB (%)	IC (%)	Training Time (s)
ELM	96	98.5714	87.1492	0.39063
BP	96.8571	88.8571	71.7143	15.3438

4.2 Analysis of the Simulation Result

In these experimental studies, 100 received signals in each position are used for each of the target obstacle. So, the total number of the acquired received signals is $100 \times 7 \times 3 = 2{,}100$. In order to facilitate the training and recognition, we separate half of the received signals for training and half of the received signals for recognition. The characteristic parameters extracted from received signals are used as the input vector of extreme learning machine and the result of recognition and identification is the output.

Figure 4 shows the recognition results, different shapes represent different classes. By counting the number of errors, we get the recognition rate. The results of testing experimental studies of ELM method for UWB target recognition can be shown in Table 1. The performance of the proposed ELM learning algorithm is compared with the popular algorithms of feedforward neural networks like the BP algorithm by using same input vector. All the experimental studies for the BP and ELM algorithms are carried out in MATLAB2012a. environment running in a PC has dual-core 3.0 GHz CPU and 2 GB RAM. In Table 1, The performance comparing results of ELM method with BP method are given as below. Table 1 shows the recognition rate of ELM method is better than BP method. The recognition rate increase 10 and 15 % in the case of WB and IC. Moreover, the training time of ELM method is only 2.5 % of BP method.

5 Conclusions

In this paper, we suggested a new UWB target detection and identification method based on ELM. The UWB channel characteristic parameters are extracted from received signals, and ELM is selected to detect targets. The simulation results demonstrate that the ELM method can produce a higher recognition rate and can learn thousands of times faster than traditional BP method. The new ELM method will have a board application prospect in UWB target detection and identification.

Acknowledgement This work was supported by NSFC (61171176).

References

1. Yanfei S (2009) Combined neural network and PCA for complicate d damage detection of bridge. Nat Comput 2:524–528
2. Young Hoon Choi, Yoon Hyun Kim (2012) "Novel transmission algorithm of UWB signals for WBAN applications", Consumer Electronics, p 374–375
3. Junqin He, Ting Jiang, Zhihao Xing (2012) A method of target detection and identification based on RPROP and UWB channel characteristic parameters. 2012 I.E. Globecom Workshop: Radar and Sonar Networks—RSN. 12, p 1460–1463
4. Huang G-B, Zhu Q-Y, Siew C-K (2004) Extreme learning machine: a new learning scheme of feedforward neural networks. In 2004 international joint conference on neural networks (IJCNN'2004), Budapest, Hungary, 25–29 Jul 2004
5. Huang G-B, Chen L, Siew C-K (2006) Universal approximation using incremental constructive feedforward networks with random hidden nodes. IEEE Trans Neural Netw 17(4):879–892
6. Huang G-B, Siew C-K (2004) Extreme learning machine: RBF network case. In Proceedings of the 8th international conference on control, automation, robotics and vision (ICARCV'2004), Kunming, China, 6–9 Dec 2004
7. Huang G-B, Zhu Q-Y, Siew C-K (2006) Extreme learning machine: theory and applications. Neurocomputing 70:489–501
8. Huang G-B, Ding X, Zhou H (2010) Optimization method based extreme learning machine for classification. Neurocomputing 74:155–163
9. Huang G-B, Zhou H, Ding X, Zhang R (2012) Extreme learning machine for regression and multiclass classification. IEEE Trans Syst Man Cybern B Cybern 42(2):513–529

Target Detection and Classification by UWB Communication Signal Based on Third-Order Cumulants

Yi Zhong, Zheng Zhou, and Ting Jiang

Abstract We have taken an experimental study about a novel method of the feasibility of ultra-wideband (UWB) communication system to concealed obstacles detection and classification. The recognition of target can be achieved by received UWB-IR signals from the UWB communication system which is different from traditional method using UWB radar echoes. In this paper, we propose a third-order statistic method to extract features that are representative of the target types from the received signals. Then, support vector machine (SVM) is used to realize the obstacle identification. The detection performance is compared with that of feature extraction method based on statistical characteristics of received signal (Ru Ying et al., Globecom Workshops (GC Wkshps), 2012 IEEE;1389–1393, 2012; Junqin He et al., Globecom Workshops (GC Wkshps), 2012 IEEE, 1460–1463, 2012). According to the experiment based on real data collected by the received signals of UWB communication, the results indicate that the detection method based on third-order cumulant shows better noise immunity than that based on statistical characteristics.

Keywords UWB communication • Target detection • Third-order cumulant • Support vector machine

1 Introdution

In recent years, UWB radar-based detection and identification of concealed targets in a strong clutter background, such as foliage, soil cover or building has been well studied. In their studies, all the objects are identified by analyzing echo data [1, 2]. In this paper, a new target detection and recognition method from the view of

Y. Zhong (✉) • Z. Zhou • T. Jiang
Key Laboratory of Universal Wireless Communication, Ministry of Education, Beijing University of Posts and Telecommunications, Beijing, China
e-mail: zhongyim2m@gmail.com

B. Zhang et al. (eds.), *The Proceedings of the Second International Conference on Communications, Signal Processing, and Systems*, Lecture Notes in Electrical Engineering 246, DOI 10.1007/978-3-319-00536-2_53,

UWB communications is proposed, which is different from the recognition principle of the traditional UWB radar. The system is completely using received UWB communication signals to achieve the objective that the identification and perception will be done simultaneously during the communication procedure. The method extracts features that are representative of the target from these received signals, then employs machine learning techniques to identify target.

Two points are important in establishing our approach: the first is that we concentrate on the obscured targets recognition through foliage based on the real data collected by received signals of UWB communication system. It has been theoretically demonstrated that the effectiveness of the proposed UWB communication system used for target identification based on simulated data of ultra-wideband indoor obstacle scenes modeled by Finite Difference Time Domain (FDTD) in [3, 4]. However, it has been shown that theoretical simulation methods have many deficiencies, such as: (1) upper frequency of UWB signals below 2 GHz due to limited amount of computer memory, (2) the more obvious differences of extract features compared to real scenarios related to the calculation error based on FDTD, (3) different targets identification on the same position with simulation model. Contrapose this phenomenon, we investigate the feasibility of classifying the real measured data using UWB wireless commutation in this paper.

The second key point of our approach is that we consider to decrease the noise effect and to enhance the detection performances. Because Gaussian noise can be completely inhibited by higher-order cumulant (HOC) and characteristics can be very rich after any HOC, this paper presents a simple, very low complexity, robust method based on third-order cumulant that can easily be applied to classify various targets in the proposed UWB communication system. This feature extraction method can be better utilized and suppress the Gaussian noise comparing to the statistical characteristics.

The paper is organized as follows. In Sect. 2, a brief introduction of data measurement and collection in real scenarios is provided. In Sect. 3, third-order cumulant classification approach using SVM is explained. The obtained experimental results are illustrated in Sect. 4. Finally, conclusions are given in Sect. 5.

2 Data Measurement Using UWB Radar

We selected a forest to take the targets penetration measurement in September 2012. Our work is based on the received UWB-IR signals from the UWB communication system.

We placed the UWB-IR transmitter (TX) and UWB-IR receiver (RX) at fixed positions. Four scenarios are measured, one scenario is the LOS and others are NLOS scenarios. Targets of human, wood board and small iron cabinet are placed separately to build different penetration scenarios. For the LOS scenarios, the penetration measurement was taken without target placed between TX and RX. For the NLOS scenarios, considering the uncertainty in target position, we

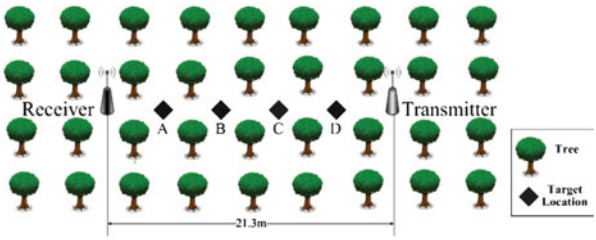

Fig. 1 The topology of forest environment and measurement antennas deployment and target location

selected four points within a region between the TX and RX to ensure the method can effectively detect and classify the concealed obstacle in the monitoring area. The topology is shown in Fig. 1, in which the deployment of the measurement equipment and target positions are illustrated. More than 500 penetration measurement data were collected when a target placed at each position.

3 Method of Target of Recognition

The target recognition process block diagram of UWB communication is shown in Fig. 2 and consists of three steps: sense through foliage data collection, feature extraction, and target classification and recognition. In Sect. 2, we have discussed the data collection in real scene. The proposed method consists of two procedures—the generation of feature extraction, and the classification of obstacle.

3.1 Proposed Feature Extraction

1) *Higher order basis*

High order statistics, especially the general third-order cumulant, which is mostly used in the practical engineering field, concerned us here is the capability of HOS to alleviate the effect of Gaussian noise.

Let $\{x(t)\}$ be a zero-mean *kth*-order stationary random process. The *kth*-order cumulant of this process, denoted $C_{kx}(\tau_1,\tau_2, \cdots,\tau_{k-1})$, is defined as the joint *kth*-order cumulant of the random variables $x(t)$, $x(t+\tau_1)$, $\cdots$, $x(t+\tau_{k-1})$, i.e.,

$$\begin{aligned} &C_{kx}(\tau_1,\tau_2,\cdots,\tau_{k-1}) \\ &\quad = cum(x(t),x(t+\tau_1),\cdots,x(t+\tau_{k-1})) \end{aligned} \tag{1}$$

The second-, and third-order cumulant of zero-mean $x(t)$ are,

Fig. 2 Block diagram of UWB communication target recognition

$$C_{2x}(\tau) = E\{x(t)x(t+\tau)\} \tag{2}$$

$$C_{3x}(\tau) = E\{x(t)x(t+\tau_1)x(t)x(t+\tau_2)\} \tag{3}$$

where E denotes the expection operater.

A non Gaussian signal can be decomposed into its higher order cumulant functions where each one of them may contain different information about the signals. This can be very useful in signal classification problems where distinct classification features can be extracted from higher order domain [5].

Suppose $x(t)$ is interfered by a independent additive Gaussian noise $e(t)$, and we have $y(t) = x(t) + e(t)$; then

$$\begin{aligned} &C_{ky}(\tau_1, \tau_2, \cdots, \tau_{k-1}) \\ &\quad = C_{kx}(\tau_1, \tau_2, \cdots, \tau_{k-1}) + C_{ke}(\tau_1, \tau_2, \cdots, \tau_{k-1}) \end{aligned} \tag{4}$$

Since $e(t)$ is Gaussian and $k \geq 3$ then, $C_{ky}(\tau_1,\tau_2, \cdots,\tau_{k\ -\ 1}) = C_{kx}(\tau_1,\tau_2, \cdots,\tau_{k\ -\ 1})$, whereas $C_{2y}(\tau) = C_{2x}(\tau) + C_{ke}(\tau)$. This makes the HOC of Gaussian process and even the colored Gaussian process constantly zero. In essence, cumulants can draw non-Gaussian signals out of Gaussian noise, thereby boosting their signal-to-noise ratios[6].

2) *Feature extraction based on third-order cumulant*

If a random process is symmetrically distributed, then its third-order cumulant equals zero. In fact, to avoid the computation complexity of the third-order cumulant, 1-D slices of the third-order cumulant is usually applied in signal processing.

A 1-D slice of the kth-order cumulant is obtained by freezing (k-2) of its k-1 indexes. Many types of 1-D slices are possible, including radial, vertical, horizontal, diagonal, and offset-diagonal. All these 1-D slices are very useful in applications of cumulants in signal processing [7].

Third-order cumulant diagonal slice has following three properties:

- The diagonal slice of the third-order cumulant retains all the useful signal characteristics.
- Additionally, 1-D higher order cumulants slice of Gaussian processes are zero.
- Further, since only 1-D slice of the cumulant are used, the computational burden is still modest.

Because of those inherent advantages, we propose an extraction method based on 1-D diagonal slice of third-order cumulant. In this paper, we select 1-D third-order cumulant diagonal slice as the effective features of the received UWB communication signals.

If $x(t)$ is a real-valued, zero-mean and stationary random process, suppose $\tau_1 = \tau_2 = \tau$ in (4), its third-order cumulant diagonal slice can be consistently estimated using

$$\begin{aligned} C_{3x}(\tau) &= E\{x(t)x(t+\tau)x(t+\tau)\} \\ &= E\left\{x(t)x^2(t+\tau)\right\} \end{aligned} \tag{5}$$

3.2 Classification Using Support Vector Machine

We use an SVM as a classification algorithm because of its some superior properties [8]:

- The optimization problem for constructing an SVM has a unique solution.
- The learning process for constructing an SVM is rather fast.
- Simultaneously with constructing the decision rule, one obtains the set of support vectors.
- Implementation of a new set of decision functions can be done by changing only one function (kernel $K(x_i,x)$), which defines the dot product in Z-space.

As SVM is a binary classifier, we detect and classify the target sense through foliage in four scenarios by incorporate multi- classification techniques. In this paper, we choose one-versus-one method and classify the scenarios based upon majority vote. This method process is rather fast and exhibit higher accuracy compared with other methods [8].

The data recorded were separated into two sets for processing, training set and validation set respectively. The training set is used as the basis for training of SVM, and the validation set is used to test the accuracy of the classification algorithm. To maintain a more realistic investigation of this classification technique, the training and testing sets do not include any overlap in data or any same position feature samples selected as the processing sets.

We use LibSVM, a freely available SVM library implemented by Chang and Lin [9]. In the SVM training process, the radial basis function (RBF) kernel function is selected because it is the most commonly used kernel for its powerful performance. The penalty parameter c of the SVM and the RBF kernel function width g is searched exhaustively by grid search parameter optimization approach to minimize average classification error for each SVM.

4 Experimental Results

4.1 Database Description and Experimental Design

The dataset used in our experiments is a penetration measurement of four scenes through foliage taken over in a forest by the UWB communication system in

autumn 2012. From the 500 samples acquired by the extraction features of UWB communication received signals through each targets, 200 samples were selected randomly in each four location. The database were used to generate a random set of 600 training samples (used for learning the classifiers), and 200 test samples (exploited for assessing their accuracies).

The experimental analysis was organized into two main experiments. The first aims at analyzing the feasibility of detecting and classifying target sense through foliage using UWB communication system based on proposed 1-D third-order cumulant slice extraction method. In the second experiment, proposed method of 1-D third-order cumulant slice is compared with the statistical characteristics adopted for the detection and classification statistic under various levels of added Gaussian white noise.

4.2 Results of Experiment 1: Classification in the Original Scenarios

In this part, proposed 1-D third-order cumulant diagonal slice is employed to detect and classify the different target types by using classifier SVM. The performance of the proposed method was examined using a Monte Carlo simulation 100 times with best related parameters c and g.

The results in terms of classification accuracy provided by the proposed method are summarized in Table 1. In order to assess the stability of each classifier, we derived some statistics by looking at the overall accuracy (OA). The results reported in Table 1 confirm the feasibility of the UWB communication detection system in terms of all the four targets, with accuracy 100.00 % for "wood board", 99.46 % for "no target", 91.00 % for "small iron cabinet", 89.50 % for "human". Furthermore we can conclude that, the proposed method is effective in detecting and classifying the concealed obstacles with overall accuracy higher than 94 % for all the four classifiers.

4.3 Results of Experiment 2: Classification in Additive Gaussian Noise

At last, we perform classification for a range of signal-to-noise ratios (SNRs) to demonstrate the robustness of the proposed method based on classifier SVM. And the results are compared with that of statistical characteristics method. For the statistical characteristics, we select energy of received signal E_r, RMS delay spread τ_{RMS} and mean excess delay τ_{excess} these three parameters as the effective features. White Gaussian noise is added to the received UWB communication signals and

Table 1 Classification accuracy of third-order cumulant and statistical characteristics

Class	No target	Wood board	Small iron cabinet	Human	OA
Accuracy (%)	99.46	100.00	91.00	89.50	94.99

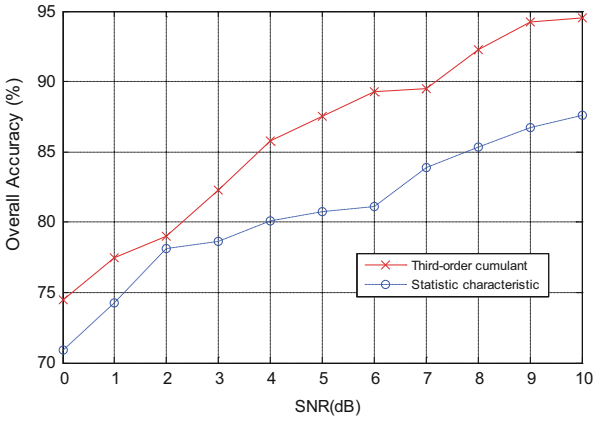

Fig. 3 The performance of third-order cumulant and statistical characteristics with SVM classifier

features are extracted using the two methods. The comparison between the performances of the above mentioned methods is given in Fig. 3.

From Fig. 3, we can see that the detection effect of third-order cumulant is extremely better than that of statistical characteristics at all the SNRs. For SNR = 3 dB, the third-order cumulant method still exhibited an acceptable accuracy (higher than 82 %), whereas a worse accuracy (lower than 80 %) was obtained by the method of statistical characteristics. From the obtained experimental results, it can easily be inferred that the method based on third-order cumulant achieves very good recognition rates even in the presence of large amount of Gaussian noise, whereas the statistical characteristics verified to be very sensitive to Gaussian noise. Therefore, we can say that the statistical characteristics method is not suitable in the target detection with additive Gaussian white noise.

5 Conclusions

In this paper, we have assessed the potential of the novel UWB communication system in the problem of recognizing and classifying targets obscured by foliage in a forest. Using two feature extraction methods based on statistical characteristics and third-order cumulant, we demonstrated that characteristic features of the targets from their UWB received signals can be classified by using classifier SVM. As shown by the comparison with statistical characteristics feature extraction method, it appears that proposed 1-D third-order cumulant diagonal slice can be effectively trained at all the circumstance, even if the signals with additive Gaussian white

noise(over 94 % correct on average for 10 dB SNR). However, the average accuracy of statistical characteristics with varying level of noise is not conclusive (only 85 % correct on average for 10 dB SNR). Therefore, we can conclude that proposed 1-D third-order cumulant diagonal slice shows extremely better effectiveness and robustness of the novel UWB communication recognition system.

Acknowledgment This work was supported by NSFC (61171176).

References

1. Zhang Z et al (2013) Human-target detection and surrounding structure estimation under a simulated rubble via UWB radar. IEEE Geosci Remote Sens Lett 10(2):328–331
2. Liang J, Liang Q, Samn SW (2008) Foliage clutter modeling using the UWB radar. IEEE Int. Conf. on Communications 2008 (ICC'08) Rec., 2008, pp 1937–1941
3. Ru Ying, Ting Jiang, Zhihao Xing (2012) Classification of transmission environment in UWB communication using a support vector machine. Globecom workshops (GC Wkshps), IEEE, December 2012, pp 1389–1393
4. Junqin He, Ting Jiang, Zhihao Xing (2012) A method of target detection and identification based on RPROP and UWB channel characteristic parameters. Globecom workshops (GC Wkshps), IEEE, December 2012, pp 1460–1463
5. El-Khamy SE, Elsayed HA, Rizk MRM (2012) Neural network for classification of multi-user chirp modulation signals using wavelet higher order statistics features. Int J Emerg Technol Adv Eng 2(8):520–533
6. Mendel JM (1991) Tutorial on higher-order statistics (spectra) in signal processing and system theory: theoretical results and some applications. Proc IEEE 79(3):278–305
7. Vapnik VN (1999) An overview of statistical learning theory. IEEE Trans Neural Netw 10(5):988–999
8. Abe S (2010) Support vector machines for pattern classification, 2nd edn. Springer, Heidelberg
9. Chih-Chung Chang, Chih-Jen Lin (2011) LIBSVM: a library for support vector machines. ACM Trans Intell Syst Technol 2(3):1–27

A New Method of Target Identification in UWB Communication System Based on Smooth Pseudo Wigner Ville Distribution and Semi-supervised Clustering

Qiqi Tang and Ting Jiang

Abstract Ultra Wideband (UWB) technology has been widely used for target identification with its strong penetrability, high resolution and good anti-interference ability. This paper proposes a new method to detect and classify target surrounded by foliage based on the real data collected from the UWB communication system. Different targets between the transmitter and receiver affect the signal differently, so the received signal contains lots of information about the target. We use smooth pseudo Wigner Ville (SPWVD) distribution to extract the feature vector of the signal and apply the semi-supervised method to realize the target identification. The experimental result shows that this method is very effective. It provides a potential way of target identification in normal UWB communication system.

Keywords UWB technology • Target identification • Smooth pseudo Wigner Ville distribution • Semi-supervised clustering

1 Introduction

The identification of target hidden in the foliage is always a research hotspot and of great significance. It has many applications both in the military and civilian field such as border violations, jungle combat, mountain rescue and fight against illegal poaching [1]. Since the target is all or partly covered by the foliage, it is hard to "see" them with normal methods.

The signal whose relative bandwidth is greater than 20 % is called Ultra Wideband (UWB) signal [2]. The spectrum of UWB is in range of GHz, therefore it is widely used to identify target for its strong penetrability, high resolution and good anti-interference ability [3]. In recent years, the study about target

Q. Tang (✉) • T. Jiang
Key Lab of Universal Wireless Communication, Beijing University of Posts & Telecommunications, Beijing, China
e-mail: tangqiqiinbupt@126.com

B. Zhang et al. (eds.), *The Proceedings of the Second International Conference on Communications, Signal Processing, and Systems*, Lecture Notes in Electrical Engineering 246, DOI 10.1007/978-3-319-00536-2_54,

identification using UWB has made a lot of progress. Most of them achieve the goal by using UWB radar and analyzing the reflected signal [4]. Liu Dong Hong proposed a way to identify target by using UWB radar based on waveform matching; Fang Xue Li successfully detected and classified the target in the foliage with UWB-SAR (Ultra Wide Band Synthetic Aperture Radar). In those models, the target identification and communication are totally two independent processes.

As we all know, the shape of received signal's waveform is greatly influenced by the communication channel. So we can combine target identification and communication together. We can identify target in normal wireless communication system by analyzing the forward received signal. Based on this idea, Minglei You successfully identified whether there is a target or not in the transmitting channel by using selected bispectra and radial-basis function (RBF) [5]. Junqin He studied the channel characteristic parameters and applied the ROROP (resilient back-propagation) to detect and classify the target [6]. Although these methods successfully identified the target, they have some shortages. The data they use is from simulated channel model and the ability of noise immunity is not good. Besides they need a lot of data to train the classification machine so as to classify the target.

To overcome these shortages and identify target in real environment, we propose a new target identification method. It can detect whether there is a target between the transmitting channel and identify what kind the target is with a few previous sample data. It extracts the time-frequency feature of the received signal as the feature vector and uses semi-supervised clustering [7, 8] to identify the type of the target. All the data is collected from real outdoor experiments. The result shows this method is very effective and maybe can be used into real application.

This paper is organized as follows. Section 2 describes the main idea of the method, the time margin distribution of smooth pseudo Wigner-Ville distribution [9] and K-means algorithm. The time margin distribution of smooth pseudo Wigner-Ville distribution (SPWVD) is used to extract the feature vector of the signal. The K-means algorithm is one method of semi-supervised clustering and is used to classify the targets. The method is applied in four scenes in Sect. 3. In Sect. 4, we get the result and analyze it. Finally, we make a conclusion in Sect. 5.

2 The Basic Idea

The received signal will be greatly affected by the obstacle between the transmitter and the receiver. Therefore, the time frequency distribution is various. We extract the time margin distribution of the smooth pseudo Wigner-Ville distribution as the feature vector of the target and use it as the input of the K-means [10] Clustering which is used to classify the target.

2.1 The Marginal Distribution of the Smooth Pseudo Wigner-Ville Distribution

The smooth pseudo Wigner-Ville distribution is an important kind of time frequency distribution. It shows the time-frequency (t-f) signature [11] of the signal and provides combined information of the time domain and frequency domain. The form is as follows:

$$W(t,f) = \int_{-\infty}^{+\infty} \int_{-\infty}^{+\infty} z\left(t + \frac{\tau}{2}\right) z * \left(t - \frac{\tau}{2}\right) e^{-2\pi\tau f} h(\tau) g(\mu) d_\tau d_\mu \tag{1}$$

The g and h are real symmetric window and $h(0) = g(0) = 0$ [12].

In order to extract the time frequency feature of the signal, we calculate the time margin distribution of smooth pseudo Wigner-Ville distribution. It shows the real-time energy of the signal and the definition is as follows:

$$m_f(t) = \int_{-\infty}^{+\infty} tW(t,f) d_f \tag{2}$$

2.2 K-Means Clustering

The semi-supervised clustering analysis is one of pattern recognition method and can be used to classify the target. It divides the data into different groups by the feature and can identify the type with some marked sample data.

The K-means clustering is an important kind of semi-supervised clustering. It has been employed in different applications of data analysis and can achieve the goal that the distance of the data in the same kind is small while the distance in different kind is large. It can divide the data effectively and correctly. The principal is as follows:

1. Choose K data as the center of the clustering. Each data represents the center of a kind. Assume that the center is $C = \{x_1, x_2, x_3 \ldots x_k\}$;
2. Calculate every data's distance D to every data in C and find the smallest distance D_i $(1 <= i <= k)$. We think this data is of the same kind with X_i.
3. Modify C. Xi equals the mean of all of data in kind i.
4. Return to step 2.Do the process of calculating distance, judging kind and modifying center again until the new distance to center equal the last time's distance. Then finish the clustering process [13].

3 Experimental Activities

3.1 Experiment Process

The experiment is performed in a forest. The measurements are made using two UWB radios named P400 RCM (product of Time Domain) which operating frequency is 3.1–5.3 GHz with center frequency of 4.2 GHz. The UWB signal transmitter (RX) and receiver (TX) is set at the fixed position and the distance between them is 19.136 m. The target is between RX and TX. Three kinds of target including wooden door, iron cabinet and human beings is applied in this experiment. Besides, we get the data without targets as to judge whether there is a target or not. For each kind of target, concerned the randomness of the target's position between the two radios, we measured seven positions in our experiment. In each position, we measured 500 times and got 500 digitalized received signals. The positions and surrounding of the target is shown in Fig. 1. The stars represent the target and the target is surrounded by trees.

3.2 Data Processing

In this experiment, four scenes (no target, wooden door, iron cabinet, human beings) are made. After collecting data, we process the data and get the result. The steps are as follows:

1. For each scene, randomly extract 30 sample data from the position which is the nearest position to the line between TX and RX among all the positions. Mark these sample data. They form the sample dataset.
2. For each scene, randomly select 270 data. Combine these data as the test dataset. Disturb the order of the test dataset.
3. Calculate clustering center. For each scene, calculate the mean of the sample data's time margin of SPWVD distribution. Use these four records as the initial center of the K-means clustering.
4. Combine these sample data and test dataset as the data to be clustered. Calculate their time margin of SPWVD, and then conduct K-means clustering.
5. Identify the target. If a data in test dataset is in the same group with certain marked sample dataset, then we can know which kind of target the data belongs to. In that way, the target is identified.

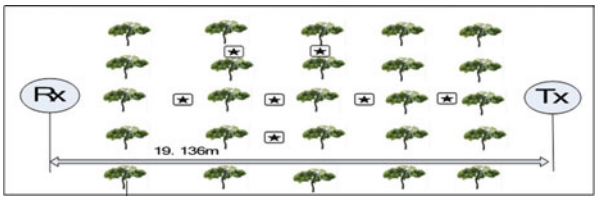

Fig. 1 The positions and surrounding of the target in our experiment

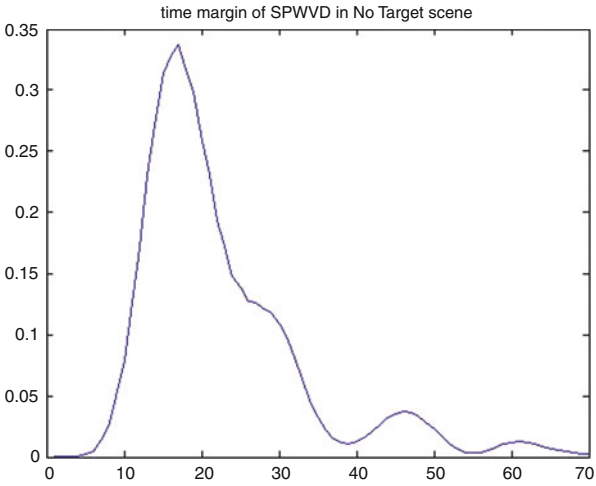

Fig. 2 Time margin of SPWVD in the scene of no target

4 Results and Analysis

Figures 2, 3, 4, and 5 shows received signal's time margin of SPWVD in different scene respectively. It represents the change of instantaneous energy over time. From those figures, we can see in different scenes, because of the target, the signal's instantaneous energy changes differently. We can identify the target with this feature.

We count the error numbers and calculate the recognition rate to see the effectiveness of the method. The test use only 10 % of the whole data as the sample data and the other 90 % are test data. The average recognition rate is shown in Table 1.

To study the noise immunity of the method, we add noise to the test data and applied two different methods to identify target. Figure 6 shows average recognition rate in the situation of different SNR (Signal to Noise Ratio) [14]. From this figure we can see the method using SPWVD and K-means has better noise immunity than the method using channel characteristic parameters and RPROP proposed by Junqin He. Especially, when the SNR is between 4 and 7 db, the recognition rate of the method using SPWVD can be above 85 %, while the other one is below 70 %. Besides, the number of sample data we need to use in K-means is smaller than in

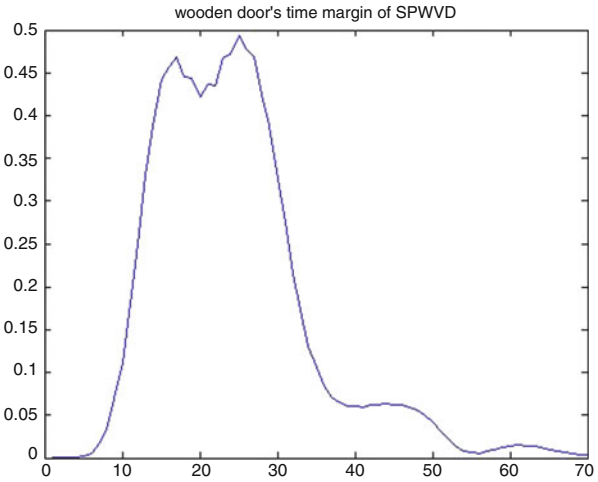

Fig. 3 Time margin of SPWVD in the scene of wooden door

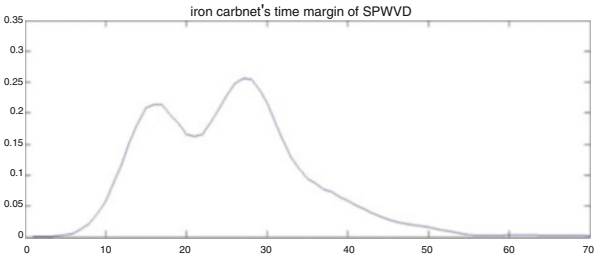

Fig. 4 Time margin of SPWVD in the scene of iron cabinet

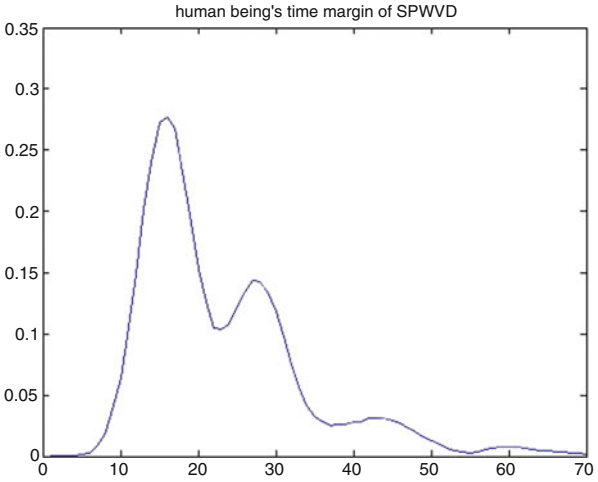

Fig. 5 Time margin of SPWVD in the scene of human being

Table 1 Recognition rate using SPWVD

Class	No target (%)	Wooden door (%)	Iron cabinet (%)	Human being (%)
Recognition rate	100	97.9	94.6	92.3

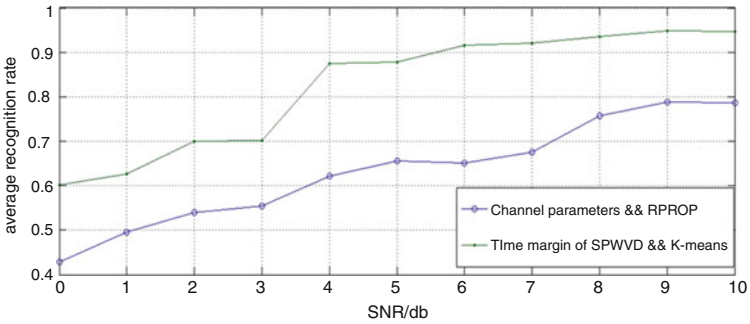

Fig. 6 The comparison of the two methods in the situation of different SNR

RPROP. In our experiment, the time for classifying target in ROROP is about five times longer than semi-supervised K-means. So, the method of using SPWVD and semi-supervised K-means has better performance than the one using channel characteristic parameters and RPROP.

5 Conclusion

In this paper, we propose a new method for target identification. It is different from traditional radar which is usually used to identify target with back reflected signal. It uses the forward received signal in UWB communication system. The data is collected from real experiment. The result shows the average recognition rate is more than 90 %.With very few previous sample data, we can detect and classify the target at a high rate. This method enable us combine normal wireless communication with target identification together. However, the experiment only studies the identification of the still target. It can't identify the moving targets. In the future studies about it will be made to realize that goal.

Acknowledgement This work was supported by NSFC (61171176).

References

1. Cao Qiu Sheng, Liu He Jun (2012) UAV systems analysis for jungle target identification based on UWB radar. Journal of China Academy of Electronics and Information Technology 8(4)
2. Editorial Committee of Journal on communication ,The UWB technology Journal on communication, Journal on communication ,2005.10(26)

3. Huang Qiu,Wu ShiYou (2011) The imaging algorithm of moving body target tracking based on UWB radar. Chinese Journal of Electronics 3(3)
4. S.Venkatesh,R.M.Buehrer (2007) "Non-line-of-sight identification in ultra-wide band System based on received signal statistics", Microwaves, Antennas & Propagation, IET, vol 1
5. Minglei You (2012) A method of obstacle identification based on UWB and selected bispectra, lecture notes in electrical engineering, communications, signal processing, and systems: the 2012 Proceedings of the international conference on communications, signal processing, and systems, p 373–382
6. Junqin He (2012) A method of target detection and identification based on RPROP and UWB channel characteristic parameters, 2012 I.E. Globecom Workshops, GC Workshop 2012, p 1460–1463
7. Chang C-C (2012) Semi-supervised clustering with discriminative random fields. Pattern Recognition, 45(12)
8. Xiao Y, Yu J (2008) Semi-supervised clustering based on affinity propagation algorithm. Journal of Software 9(11):2803–2813
9. Zhou HongXing, Zhou XiaoBo, LI Yan Da (2009) Time frequency analysis: backtracking and Prospects. Chinese Journal of Electronics 9(9)
10. David P. Casasent, Tien-Hsin Chao (2007) Object detection in hyperspectral imagery by using K-means clustering algorithm with preprocessing Alam M.S. Optical Pattern Recognition XVIII, Orlando, Florida, USA
11. Jing Guo, Xiao Ping Zeng (2010) A time-frequency algorithm for noisy BSS model, 2010 international conference on signal and information processing 1
12. Yue Ye Qing, Xu Zheng (2008) The appliance of smooth pseudo Wigner Ville distribution in detecting Harmonics and voltage change in power system, Relay 8
13. Yang Shu Ying (2011) Pattern recognition and intelligent computing: realization with matlab, Publishing House of Electronics Industry, p 247, 8
14. Atapattu, Saman (2011) Spectrum sensing via energy detector in low SNR, IEEE International conference on communications, 2011 I.E. international conference on communications, ICC 2011

Part V
Radar Signal Processing

A SVD-Based Visual Attention Detection Algorithm of SAR Image

Shuo Liu, Zongjie Cao, and Jin Li

Abstract This paper proposes a new method based on visual attention and singular value decompositions (SVD) for target detection in SAR image. SAR image is confronted with many difficulties such as complicated environment and scarcity of target information. To solve these problems, we proposed the method that combined the pyramid model with singular value decomposition to simulate human retina. The human retina collected information in Non-uniform way. Experimental results validate a effect performance of the method in improving both the efficiency and the accuracy of target detection in complicated environment and weak target condition.

Keywords Singular value decomposition (SVD) • Visual attention • Target detection • SAR image

1 Introduction

Visual attention of human visual system makes human focus on the interest areas rapidly and make a decision on them [1]. So the visual attention greatly improved the ability of human visual system to deal with the complicated environment image. Obviously, there is a positive effect to introduce the visual attention into target detection in SAR image.

Current visual attention model are generally using gauss pyramid model proposed by Burt and Crouely to simulate a feature of human retina [2]. The feature can be described as that center of the retina has smaller receptive field, otherwise the receptive field in periphery of the retina is much bigger [3]. So the feature can be concluded as that sampling density and visual resolution of a position become

S. Liu • Z. Cao (✉) • J. Li
School of Electronic Engineering, University of Electronic Science and Technology of China, Chengdu, China
e-mail: zjcao@uestc.edu.cn

B. Zhang et al. (eds.), *The Proceedings of the Second International Conference on Communications, Signal Processing, and Systems*, Lecture Notes in Electrical Engineering 246, DOI 10.1007/978-3-319-00536-2_55,

smaller with the increase of the distance between the position and the center of the human retina, a large number of information in periphery were compressed [4]. After building a gauss pyramid model, visual attention system would guide the attention to an interest area according to some feature of a target such as shapes, color and intensity [5]. But with the continuous development of military technology, the situation of target detection in SAR image became more difficult, the environment around target became more complicated and information of target became less [6]. Current visual attention method is not suit to the target detection in complicated environment and condition of weak target.

In this paper, a new visual attention algorithm for target detection is proposed. Because the gauss pyramid model of visual attention was hard to compress a SAR image which concludes weak targets effective. But the singular value decomposition method can keep the important information of a SAR image when the image was compress [7]. So combining the SVD with gauss pyramid model and produce images with different compression ratio. This makes the images keep target information and obscure environment information well. Then achieve the purpose of efficient target detection in the case of complicated environment and weak target.

2 Visual Attention Model Based on Pyramid

The model of Itti is a classic visual attention model and the algorithm proposed in this paper is improved on the basis of the Itti. In this part, we describe the details about building the pyramid model. The details of Itti model can be found in literature [6].

Visual attention model adopt multi-scale spatial to simulate non-uniform sampling mechanism of human retina. Burt and Crouely proposed the pyramid structure from summary of the non-uniform sampling mechanism. One pyramid structure of an image is show in Fig. 1.

The establishment of pyramid structure includes two steps: one is smoothing, another is down-sampling. Itti model adopt linear discrete guass filter to do smoothing and down-sampling in the horizontal and vertical directions of the input image respectively and formed eight different resolution sub-image. Including the original image, there are nine images to build up the gauss pyramid structure. The smoothing filter is [1 4 6 4 1] and down-sampling is achieved by a convolution with a filter [1 1]/2. Using the two filters to achieve the aim, which take the average value of every two pixels in the previous image as one pixel value in the next image. The two steps can be combined into a convolution with a filter K = [1 4 6 4 1]*[1 1]/2 in the horizontal and vertical directions respectively.

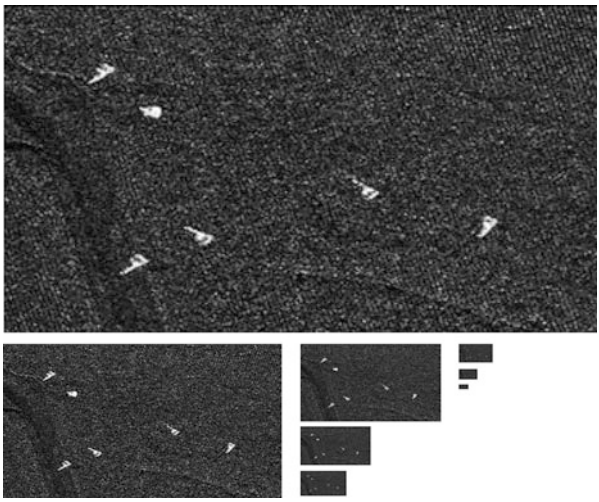

Fig. 1 Pyramid structure of an image

3 Visual Attention Model Based on SVD

Singular value decomposition has the characteristics of energy aggregation for an image. This makes it to be a popular technology in the area of image compression. This algorithm extracted the algebraic feature from an image. The feature react the essential characteristics of an image, so the SVD algorithm has the advantages of insensitive to a noise and complexity of an image.

3.1 The SVD Algorithm

The SVD algorithm is defined as follows: A is a matrix of m $\times$ m dimension. It can be computed as three matrices U, S and V which can be expressed as

$$A = U \cdot S \cdot V^T \tag{1}$$

Where S is a matrix of m $\times$ n dimension (same as A) and U and V are matrices of m $\times$ m and n $\times$ n dimension respectively. The singular value decomposition of matrix A is equal to solve eigenvalues and corresponding eigenvectors of AA^H and A^HA. The singular value of matrix A is the square root of the eigenvalues of the matrix AA^H or A^HA. The matrix S is a diagonal matrix that can be expressed as followed diag(S) = (σ_1, σ_2, σ_3, $\cdot \cdot$, σ_k). The diagonal elements can be constituted by the singular value of A and has been ordered according to value by descending. So matrix A can be approximated by matrix B and the rank of matrix B is k.

$$B = \sum_{i=1}^{k} \left(\sqrt{s_i} u_i\right)\left(\sqrt{s_i} v_i^H\right) \tag{2}$$

Where u_i and v_i are the column vectors of matrix U and V respectively. s_i is the i-th singular value. According to the energy aggregation characteristics of Singular value decomposition, we can discard the smaller proportion eigenvalues, corresponding eigenvectors and retain the bigger proportion part.

3.2 SVD Combined with the Pyramid Model

In order to make the visual attention model adjust to the target detection in complicated environment SAR image, we combine SVD with pyramid model. The information about targets was retained and about environment was obscured in these images with different compression rate. This let the center-surrounding module find the saliency point more effectively and optimize the detection results in complicated environment.

The major steps of the proposed SVD-Pyramid model method are listed as follows.

Step (1) Perform the SVD to original SAR image I to extract one diagonal matrix S and two orthogonal matrices U, V.
Step (2) Compute the number of non-zero elements in matrix S and assigned to k. These k elements in descending order constitute a vector q.
Step (3) Discard the minimum of m elements in q and the remaining elements constitute a vector q1. m = k*0.6.
Step (4) Use the elements in the vector q1 to be the diagonal elements in a new diagonal matrix S1.
Step (5) Perform the formula (2) to extract a new compressed image I1.
Step (6) Repeat steps 1–5 until m < k*0.02.

3.3 Processing Steps

Based on the SVD algorithm mentioned above and visual attention model-Itti model, the flowchart about visual attention based on SVD algorithm is presented in Fig. 2.

Because the algorithm in this paper is based on Itti model, the detailed steps of the algorithm will not be listed. In feature extraction module, we use features including intensity, color, orientation, consistency. In center-surround difference module, the images of No. 2,3,4 are selected as center-image and the numbers of surround-image are 2,3,4 add 3,4.

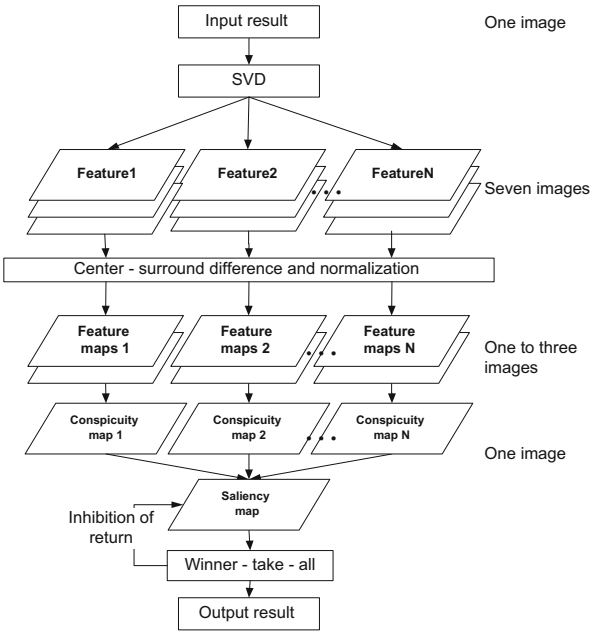

Fig. 2 Flowchart of visual attention based on SVD

4 Simulations

In order to validate the feasible of the proposed algorithm, several simulations have been performed. The simulation data are divided into two types. One type data concludes 20 images. The size of each image is 384 × 256. These images are in the simple environment and conspicuous target condition. The targets are tanks and in the glassland environment. The other type data are images of complicated environment and weak targets. The size of each image is 2406 × 512. The targets are tanks and in the glassland and jungle environment.

The simulation compares the algorithm of Itti model with the visual attention based on SVD method. Figures 3 and 4 are the test image in the first type data and second type data respectively.

In the simulation, compare the Fig. 5 with Fig. 6, two methods get six FOA areas and six areas cover the targets well. So, for an SAR image of simple environment and conspicuous target, the Itti model and visual attention based SVD method have a good effect. The size of FOA in SVD method is smaller.

In order to verify the performance of visual attention based SVD algorithm in complicated environment condition, we make another simulation by second type data. Figures 7 and 8 are the simulation result of one image in the data. In this simulation, the FOA area is shown by the yellow line area. Comparing the Fig. 7 with the Fig. 8 (contain the front six FOA), the seven FOA areas obtained by Itti model method only have three of them covered targets, others covered the shadow areas and empty areas. Otherwise, all the seven FOA areas obtained by the

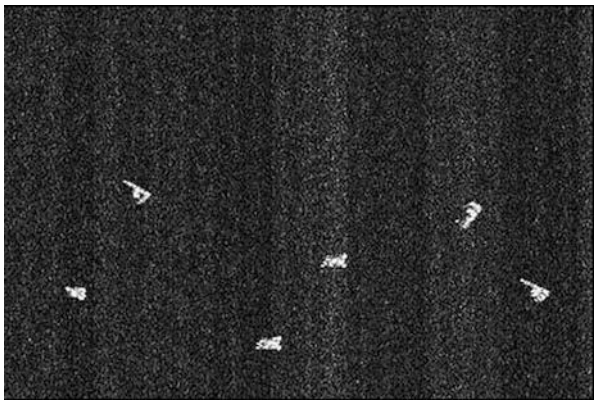

Fig. 3 The test image of simple environment

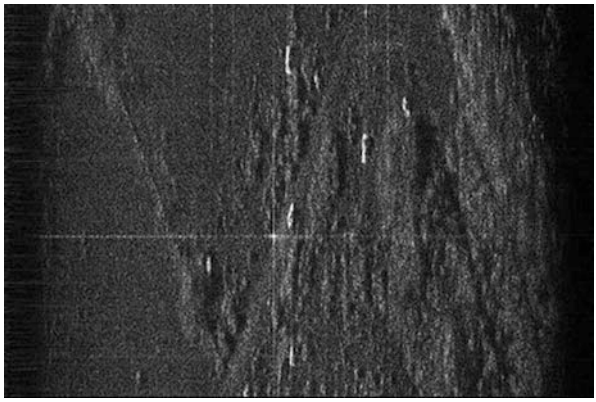

Fig. 4 The test image of complicated environment

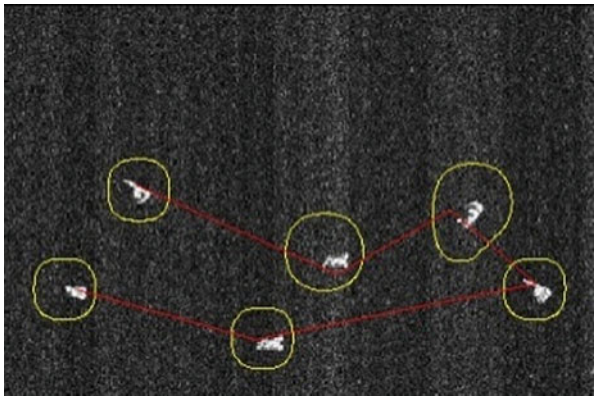

Fig. 5 The result of Itti model algorithm in simple environment

algorithm proposed in this paper covered targets exactly. The visual attention based SVD algorithm can adapt to the condition of complicated environment and weak target.

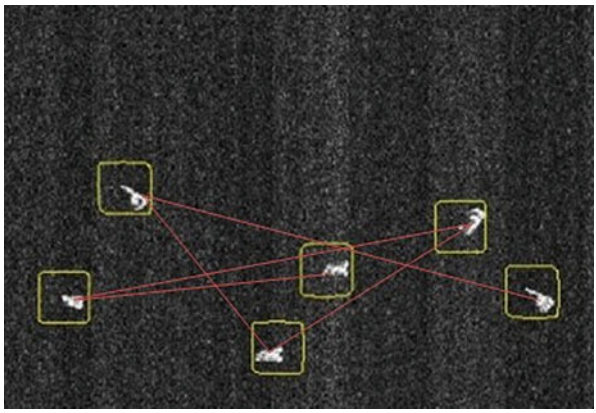

Fig. 6 The result of VA-SVD algorithm with simple environment

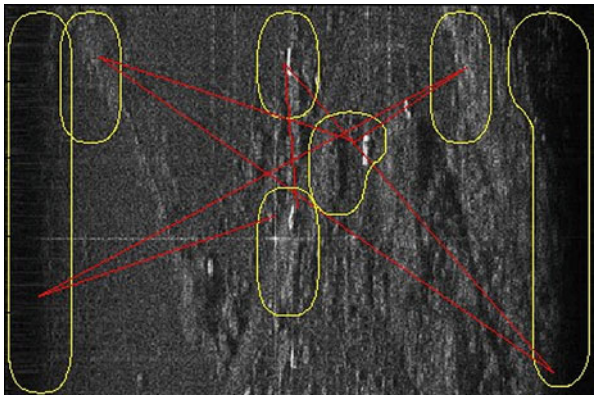

Fig. 7 The result of Itti model algorithm in complicated environment

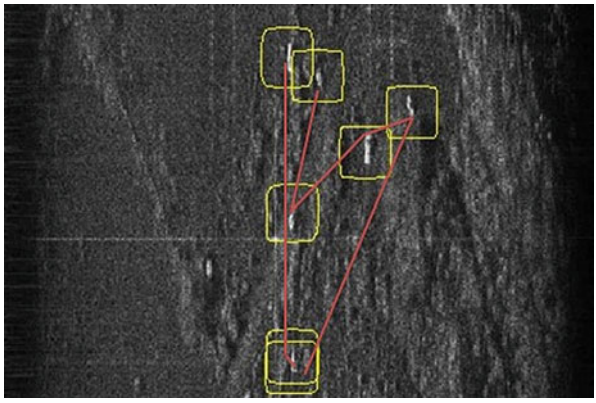

Fig. 8 The result of VA-SVD algorithm in complicated environment

5 Conclusion

In this paper, a visual attention based SVD algorithm adapted to SAR image target detection in complicated environment and weak target condition has been developed. The method of combining singular value decomposition with pyramid model has been introduced in detail. To validate the performance of the method, some simulations have been performed. These results show the feasibility of visual attention based SVD algorithm to SAR image target detection in complicated environment condition.

Acknowledgement This work is supported by the National Natural Science Foundation of China (Grant No. 61271287).

References

1. Dirk B. Walther, Christof Koch (2007) Attention in hierarchical models of object recognition, DB Walther, C Koch: Progress in brain research
2. Itti L, Koch C, Niebur EA (1998) Model of saliency-based visual attention for rapid scene analysis. IEEE Trans Pattern Anal Mach Intell 20(11):1254–1259
3. Dirk Walther (2006) Interactions of visual attention and object recognition: computational modeling, algorithms, and psychophysics. PhD thesis, California Institute of Technology, Pasadena, CA, 23 Feb 2006
4. Rigas I, Economou G, Fotopoulos S (2013) Low-level visual saliency with application on aerial imagery, geoscience and remote sensing letters, IEEE
5. Navalpakkam V,Itti L (2006) An integrated model of top-down and bottom-upattention for optimal object detection. Proc. IEEE conference on computer vision and pattern recognition (CVPR). New York, NY, p 2049–2056
6. Jilan Feng, Zognjie Cao, Yiming Pi (2013) Multiphase SAR image segmentation with G0 statistical model based active contours. IEEE Trans GRS 51(7)
7. Rybak IA, Gusakova VI, Golovan AV et al (1998) A model of attention-guided visual perception and recognition. Vision Res 38:2387–2400

SAR Target Recognition via Sparsity Preserving Projections

Lan Li, Jian Cheng, and Haijun Liu

Abstract Feature extraction is critical in Synthetic Aperture Radar (SAR) target recognition. Principle Component Analysis (PCA) which preserves global structure and Locality Preserving Projections (LPP) which captures local structure are two typical feature extraction methods in SAR target recognition. But they both keep only one kind of space structure. To combine these two structures, a method of SAR target recognition via Sparsity Preserving Projections (SPP) is proposed in this paper. First, SPP is employed to extract features. It preserves sparse reconstruction information which contains both global and local structure. Natural discriminative information is also kept in sparse reconstruction coefficients without prior knowledge. Then, Sparse Representation based Classification (SRC) is utilized in classification because of its robustness to noise. Experimental results on MSTAR datasets demonstrate effectiveness of our method.

Keywords SAR target recognition • Feature extraction • Sparse representation • Sparsity preserving projections

1 Introduction

Synthetic Aperture Radar (SAR) target recognition has become an important research topic due to its imaging advantages. Target scatter information could be obtained regardless of weather situations, working periods and environmental conditions. Therefore, it is widely used in national defense especially in real-time battlefield. But the unique imaging mechanism causes lots of speckle noises distributing on whole image, and it's hard to estimate poses of SAR targets. Those make SAR target recognition a tough task.

L. Li • J. Cheng • H. Liu (✉)
School of Electronic Engineering, University of Electronic Science and Technology of China, 2006 Xiyuan Ave., Chengdu 611731, China
e-mail: lilan2007021090@gmail.com; pami.cheng@gmail.com; haijunliu518128@gmail.com

B. Zhang et al. (eds.), *The Proceedings of the Second International Conference on Communications, Signal Processing, and Systems*, Lecture Notes in Electrical Engineering 246, DOI 10.1007/978-3-319-00536-2_56,

Sparse Representation (SR) has become a hot issue recently and been used in many areas [1–3]. SR is robust to noise, and natural discriminating information can be kept without prior information. It also saves trouble of pose estimating in SAR target recognition [4, 5]. Thiagarajan [2] combined random projection with SR to realize SAR target recognition. The advantages of SR in SAR target recognition are well stated. Zhang [4] proposed Joint Sparse Representation (JSR) to fully exploit SAR images under multi-views. The training data without feature extraction is deployed as dictionary atoms directly. Nevertheless, these papers didn't focus on feature extraction. Wright [6] pointed out that if sparsity in face recognition problem is properly harnessed, the choice of feature extraction is no longer critical. However, in SAR target recognition problem, training samples and testing samples are both polluted by speckle noises, hence, feature extraction method plays an important role. Principal Component Analysis (PCA) [7] and Locality Preserving Projection (LPP) [8] are two typical feature extraction methods. The former captures global information and the latter preserves local information. These two kinds of information are both useful for recognition while no precedent of their combination is employed in SAR target recognition.

To settle this issue, a Sparsity Preserving Projections (SPP) based feature extraction method is used in our paper. SPP is a new feature extraction method which preserves sparse reconstructive relationship [9]. Natural discriminating information is kept without prior knowledge due to application of SR in process. Global and local structure can be both preserved well. Furthermore, unlike general feature extraction methods of local information preserving, local information in SPP is robust to noise. Experiments on MSTAR datasets demonstrate the effectiveness of our method.

2 SAR Target Recognition via SPP

2.1 Sparse Representation (SR) and Sparse Representation Based Classification (SRC)

Given a signal $\mathbf{y} \in \mathbf{R}^m$, a matrix $\mathbf{D} = [\mathbf{d}_1, \mathbf{d}_2, \cdots, \mathbf{d}_n] \in \mathbf{R}^{m \times n}$ and SR coefficient vector $\mathbf{a} \in \mathbf{R}^n$. $\mathbf{D}$ is a dictionary whose each column denotes a dictionary atom and usually composed of training images in SAR target recognition, and n is the number of dictionary atoms. SR aims to seek a linear combination of dictionary atoms to represent $\mathbf{y}$ by imposing a sparse restriction on representation coefficient vector $\mathbf{a}$ which also could be called sparse reconstructive weight, i.e.

$$\min_{\mathbf{a}} \|\mathbf{a}\|_0 \quad s.t. \quad \mathbf{y} = \mathbf{D}\mathbf{a} \tag{1}$$

where $\| \bullet \|_p$ refers to ℓ_p norm. However, (1) is NP-hard. There are two ways to solve this thorny problem.

1. Greedy algorithm. The representative algorithm is Orthogonal Matching Pursuit (OMP).
2. Convex relaxation. The objective function after convex relaxation is as follows:

$$\min_{\mathbf{a}} \|\mathbf{a}\|_1 \quad s.t. \quad \mathbf{y} = \mathbf{D}\mathbf{a} \tag{2}$$

In reality, (1) and (2) also take noise into consideration [6]. Wright [6] proposed SRC to perform classification in SR. SRC gives a signal label by evaluate how well the SR coefficients associated with each class in reconstructing. Therefore, we rewrite $\mathbf{D} = [\mathbf{D}_1, \cdots, \mathbf{D}_i, \cdots, \mathbf{D}_K]$ and $\mathbf{a} = [\mathbf{a}_1; \cdots; \mathbf{a}_i; \cdots; \mathbf{a}_K]$ where K is the number of classes. $\mathbf{D}_i$ and $\mathbf{a}_i$ are dictionary and SR coefficient vector associated with the i th class training samples, respectively. So reconstruction of $\mathbf{y}$ on each class could be represented as:

$$\widehat{\mathbf{y}}_i = \mathbf{D}_i \mathbf{a}_i, i = 1, \cdots, K \tag{3}$$

We then classify $\mathbf{y}$ based on these reconstructions by assigning it to the object class that minimizes the residual between $\mathbf{y}$ and $\widehat{\mathbf{y}}_i$:

$$class(\mathbf{y}) = \min_i \left\| \mathbf{y} - \widehat{\mathbf{y}}_i \right\|_2 \tag{4}$$

2.2 Sparsity Preserving Projections (SPP) and Analysis of Its Application on SAR Target Recognition

SPP explores projections to preserve sparse reconstructive weights. It uses a modified sparse representation framework to acquire sparse representation of each training data on subspace of all training data except itself. Given training data matrix $\mathbf{X} = [\mathbf{x}_1, \mathbf{x}_2, \cdots, \mathbf{x}_n] \in \mathbf{R}^{m \times n}$. The modified sparse representation framework is:

$$\min_{\mathbf{v}_i} \|\mathbf{v}_i\|_1 \quad s.t. \quad \mathbf{x}_i = \mathbf{X}\mathbf{v}_i, 1 = \mathbf{e}^{\mathrm{T}}\mathbf{v}_i, i = 1, \cdots, n \tag{5}$$

where $\mathbf{v}_i = [v_{i1}, \cdots, v_{i,i-1}, 0, v_{i,i+1}, \cdots, v_{in}]^{\mathrm{T}}$ is a n-dimensional vector whose ith element is zero, and $\mathbf{e}$ is a vector of all ones.

Sparse reconstructive weight vector $\mathbf{v}_i$ reflect intrinsic geometric properties of data in some sense. Natural discriminating information is contained owing to the application of sparse representation in weight construction. Then an objective function is defined to obtain projection $\mathbf{w}$ which best preserves the optimal sparse weights:

$$\begin{aligned} &\min_{\mathbf{w}} \sum_{i=1}^{n} \left\| \mathbf{w}^{\mathrm{T}} \mathbf{x}_i - \mathbf{w}^{\mathrm{T}} \mathbf{X} \mathbf{v}_i \right\|^2 \\ &= \min_{\mathbf{w}} \mathbf{w}^{\mathrm{T}} \mathbf{X} \left(\mathbf{I} - \mathbf{V} - \mathbf{V}^{\mathrm{T}} + \mathbf{V}^{\mathrm{T}} \mathbf{V} \right) \mathbf{X}^{\mathrm{T}} \mathbf{w} \end{aligned} \tag{6}$$

where $\mathbf{V} = [\mathbf{v}_1, \mathbf{v}_2, \cdots, \mathbf{v}_n]$. To avoid degenerate solutions, a constraint $\mathbf{w}^{\mathrm{T}} \mathbf{X} \mathbf{X}^{\mathrm{T}} \mathbf{w} = 1$ is added to (6), and then the minimization problem is further transformed to a maximization problem for compact expression and more numerically stable solution [9]:

$$\max_{\mathbf{w}} \frac{\mathbf{w}^{\mathrm{T}} \mathbf{X} \mathbf{V}_{\beta} \mathbf{X}^{\mathrm{T}} \mathbf{w}}{\mathbf{w}^{\mathrm{T}} \mathbf{X} \mathbf{X}^{\mathrm{T}} \mathbf{w}} \tag{7}$$

where $\mathbf{V}_{\beta} = \mathbf{V} + \mathbf{V}^{\mathrm{T}} - \mathbf{V}^{\mathrm{T}} \mathbf{V}$, then the optimal problem could recast to solve a generalized eigenvalue problem.

Data's SR coefficients can be seen as data's sparse character. It is well-known that SR reveals natural discriminative information without prior knowledge. Therefore, SPP becomes discriminative by means of retaining data's sparse character. SPP is a global feature extraction method from the view of objective function. Furthermore, the dictionary atoms automatically chosen to reconstruct data reside in same subspace with data. Therefore, SPP preserves local structure as well.

To avoid sacrifice of original image information, complex noise suppression isn't adopted. In this case, the local structure seized by LPP is easily affected by noise, while local structure in SPP is robust to noise thanks to SR's robustness. Though global feature extraction is effective in resisting interference of noise in low dimension space, it is underperforming in high dimension space. SPP maintains merits of global and local feature extraction. Therefore, it's quite potential to utilize SPP as feature extraction in SAR target recognition.

The algorithmic procedure of SAR target recognition via SPP with SRC is given:

1. Input: a test sample $\mathbf{y}$, a matrix of K classes training samples $\mathbf{X} = [\mathbf{X}_1, \cdots, \mathbf{X}_i, \cdots, \mathbf{X}_K] \in \mathbf{R}^{m \times n}$, where $\mathbf{X}_i = [\mathbf{x}_{i,1}, \mathbf{x}_{i,2}, \cdots, \mathbf{x}_{i,l_i}]$ indicates the ith class training data and $n = \sum_{i=1}^{K} l_i$ indicates the number of all training data;
2. Normalize the columns of $\mathbf{X}$;
3. Feature extraction using SPP. So the dictionary could be expressed as $\mathbf{D} = \mathbf{W}^{\mathrm{T}} \mathbf{X} = [\mathbf{D}_1, \mathbf{D}_2, \cdots, \mathbf{D}_K]$ and $\mathbf{y}$ could be represented as $\widetilde{\mathbf{y}}$;
4. Solve ℓ_1 norm problem: $\widehat{\mathbf{a}} = \min_{\mathbf{a}} \|\mathbf{a}\|_1 \quad s.t. \quad \mathbf{D}\mathbf{a} = \widetilde{\mathbf{y}}$;
5. Output: $class(\mathbf{y}) = \min_i \left\| \widetilde{\mathbf{y}} - \mathbf{D}_i \widehat{\mathbf{a}}_i \right\|_2$, $\widehat{\mathbf{a}} = \left[\widehat{\mathbf{a}}_1; \cdots; \widehat{\mathbf{a}}_K \right], i = 1, \cdots, K.$

Table 1 Training and testing datasets from MSTAR

	Type	Depression angle	Size
Training set	BMP2-c21	17°	233
	BTR70-c71	17°	233
	T72-132	17°	232
Testing set	BMP2-c21	15°	196
	BMP2-9563	15°	195
	BMP2-9566	15°	196
	BTR70-c71	15°	196
	T72-132	15°	196
	T72-812	15°	195
	T72-s7	15°	191

3 Experiments

The proposed SAR target recognition method is tested on the MSTAR (Moving and Stationary Target Acquisition and Recognition) database provided by DARPA/AFRL America. The information of targets for training and testing is given in Table 1. All the images are 128 × 128 pixels and the resolution is 0.3 m × 0.3 m. The azimuth of the target lies between 0°and 360°.

3.1 SAR Image Preprocessing

As large area of the background noise and the non-uniform scattering will affect the performance of recognition rate dramatically, we exclude the redundant background and adjust the amplitude of images firstly:

1. Turn multiplicative noise to additive noise through logarithm transformation;
2. Exclude the redundant background by crop original image to the size of 50 × 50 pixels with the target at the center.

Examples of original image and preprocessed images are shown in Table 2.

3.2 Experimental Results and Analysis

Our method is compared with four approaches: (1) PCA for feature extraction and SRC for classification, (2) PCA for feature extraction and K-Nearest Neighbor (KNN) for classification, (3) LPP for feature extraction and SRC for classification, (4) LPP for feature extraction and KNN for classification. The result is shown in Fig. 1. And a comparison of best performance is given in Table 3.

It can be seen in Table 3 and Fig. 1 that SPP + SRC outperforms other approaches. LPP performs poorly both under KNN and SRC, and PCA based

Table 2 SAR image preprocessing

Original image	After step 1	After step 2
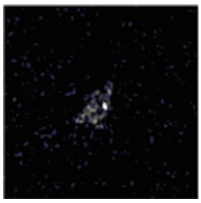	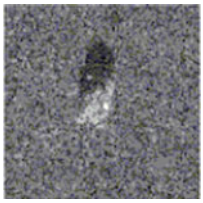	

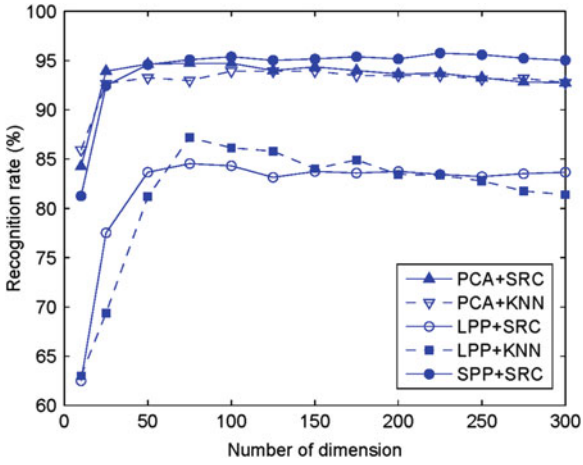

Fig. 1 Recognition performance with increasing dimension numbers

Table 3 Comparison on best recognition rate

Method	Recognition rate	Dimensionality
PCA + SRC	0.9447	100
PCA + KNN	0.9392	125
LPP + SRC	0.8454	75
LPP + KNN	0.8718	75
SPP + SRC(Our method)	0.9575	225

methods achieve good performance in low dimension but doesn't continue as the dimension of feature increases while SPP dose.

As LPP captures local structure by keeping neighborhood relationships which are measured by Euclidean distance, the local structure is easily influenced by noise which is inevitable in SAR target recognition and manually chosen parameters such as number of neighbors. This results in LPP an inappropriate feature extraction method in SAR target recognition task. As PCA reconstructs data by retaining as much of the variability in the data as possible, it's quite useful in weakening noise in low dimension. That makes PCA a good feature extraction method in low dimension as shown in Fig. 1, whereas data in low dimension means insufficient target information. This causes that the best recognition of PCA based methods which occurs in dimensionality of 100 fails to exceed SPP. The best recognition

Table 4 Best recognition rates of SPP + SRC on testing data

Type	BMP2-c21	BMP2-9563	BMP2-9566	BTR70-c71	T72-132	T72-812	T72-s7
Recognition Rate	1	0.9077	0.8980	1	1	0.9436	0.9529

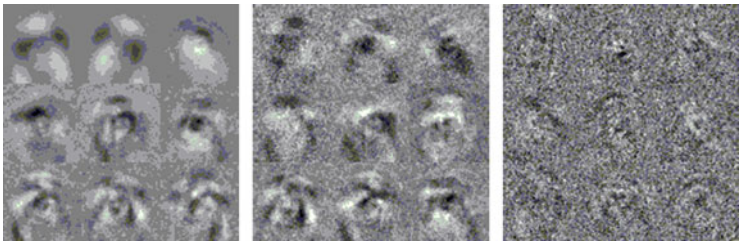

Fig. 2 Nine "eigentargets" of PCA (*left*), SPP (*middle*) and LPP (*right*)

result of SPP + SRC occurs when the number of dimension is 225, and Table 4 gives specific corresponding recognition rates of seven types. The sparse character of targets representation indicates latent recognition information and less affected by noise. And it's integrated into SPP by means of retaining SR coefficients.

Another evidence of SPP's effectiveness is shown in Fig. 2 by comparing "eigentargets" associated with 9 largest eigenvalues in PCA, SPP and LPP. Apparently, the "eigentargets" of LPP is seriously polluted by noise and fail to well describe target information. In spite of the nine "eigentargets" of PCA barely comprised of noise, they contain inadequate target information. And as the dimension of feature increases, more noise information is added in to mislead recognition as incremental number of eigenvectors is kept in PCA. Though the "eigentargets" of SPP preserve both target information and noise information, target discriminative information is leading in "eigentargets" of SPP. As Table 4 shows, recognition rates on seven types are pretty high, and specifically, recognition rates on BMP-c21, T72-132 and BTR70-c71 are 100, 100 and 100 %, respectively. This illustrates that the sparse character preserved is beneficial to recognition in noise condition especially when the testing sample has the same type with training samples, and preserving of noises makes less sacrificing of original image information. Therefore, this kind of mixture of target and noise is beneficial for classification.

4 Conclusion

This paper proposes a SAR target recognition method via SPP. SPP is employed as feature extraction and SRC is utilized as classifier. SPP preserves sparse reconstruction information which captures both global and local structures. What's better is that it maintains more discriminative target information under acceptable noise. The effectiveness and advantages of our method are demonstrated in experiments.

Acknowledgments This work is supported by the National Natural Science Foundation of China under Projects 61201271 and Specialized Research Fund for the Doctoral Program of Higher Education 20100185120021.

References

1. Guha T, Ward RK (2012) IEEE Trans Pattern Anal Mach Intell 34(8):1576–1588
2. Thiagarajan JJ, Ramamurthy KN, Knee P, Spanias A, Berisha V (2010) Sparse representations for automatic target classification in SAR images. 2010 4th international symposium on communications, control and signal processing (ISCCSP), 1–4
3. Pillai JK, Patel VM, Chellappa R, Ratha NK (2011) Secure and robust iris recognition using random projections and sparse representations. IEEE Trans Pattern Anal Mach Intell 33 (9):1877–1893
4. Zhang HC, Nasrabadi NM, Zhang YN, Huang TS (2012) Multi-view automatic target recognition using joint sparse representation. IEEE Trans Aerosp Electron Syst 48(3):2481–2497
5. Knee P, Thiagarajan JJ, Ramamurthy KN, Spanias A (2011) SAR target classification using sparse representations and spatial pyramids. 2011 I.E. Radar Conference (RADAR), 294–298
6. Wright J, Yang A, Ganesh A, Sastry S, Ma Y (2009) Robust face recognition via sparse representation. IEEE Trans Pattern Anal Mach Intell 31(2):210–227
7. He ZG, Lu J, Kuang G (2007) A fast SAR target recognition approach using PCA features. 2007 4th international conference on image and graphics, 580–585
8. Liu M, Wu Y, Zhao Q, Gan L (2011) SAR target configuration recognition using Locality Preserving Projections. IEEE CIE Int Conf Radar 1:740–743
9. Qiao L, Chen S, Tan X (2010) Sparsity preserving projections with applications to face recognition. Pattern Recognition 43(1):331–341

Comparing Spectral Analysis Methods of the Wind Profiling Radar Echoes

Mingbao Hu, Hongbing He, Weihua Ai, and Miaoying Li

Abstract In order to know the feasibility of the modern spectrum methods being applied in the wind profiling radar, direct transform based on Fast Fourier Translate (FFT), the wavelet technology and maximum entropy method (MEM) are contrasted by using simulated and real data respectively. The results show: when the radar echo is strong, the effect of three methods are equivalent, but when the echo is weak, the MEM spectra is better than others; the MEM can powerfully remove the ground clutter, and the effect of wavelet technology isn't obvious; the MEM has smoother spectrum and can be used to suppress white noise.

1 Introduction

It has been a long time that direct transform based on Fast Fourier Translate(FFT) is used in spectral analysis of the wind profiling radar(hereinafter referred to as profiler) signals [1], after getting the power spectrum, via DC removal, integration, cancellation and filtering, noise and clutter can be restrained. Because the noise and clutter spectrum often mix with the signal spectrum, it's difficult to remove them. The signal detected by the profiler is weaker, and is more susceptible to interference of the noise and clutter. Thus FFT's effort is finite in many cases. In order to improve quality of data, wavelet transform was used to remove the noise and ground clutter from the profiler echoes, but the wavelet transform's effort is subjected to an appropriate choice of the wavelet basis [2]. As one of the modern spectrum methods, Maximum entropy method (MEM) is early used for power spectrum estimation of the weather signals [3]. In this paper, using simulated and real profiler signals, FFT, the wavelet technology and MEM are contrasted respectively, and better method for improving spectral analysis is discussed.

M. Hu • H. He (✉) • W. Ai • M. Li
Institute of Meteorology and Oceanography, PLA University of Science & Technology, Nanjing, China
e-mail: hehongbing1969@163.net

B. Zhang et al. (eds.), *The Proceedings of the Second International Conference on Communications, Signal Processing, and Systems*, Lecture Notes in Electrical Engineering 246, DOI 10.1007/978-3-319-00536-2_57,

2 Analysis Methods

2.1 Wavelet Transform

After wavelet transform has been done for profiler echoes using discrete and orthonormal wavelet, because noise is spread over all scales of wavelet coefficients, but signal distributed in large wavelet coefficients, and the ground clutter lies in the several maximum of the lowest frequency coefficients in the wavelet domain. Thus the wavelet coefficients' magnitude of the signal is larger than that of the noise, and smaller than that of the ground clutter. By means of cutting, nulling, thresholding and other processing to the wavelet coefficients, noise and clutter are removed from the echoes, the useful signal is reconstructed by the inverse wavelet transform.

Assumption that $w_{i,j}$ is the lowest frequency coefficients, λ_1 is the threshold of rejecting the clutter, K is the adjustment factor which is relative to the weather. $w_{i,j}$ is given by

$$w_{i,j} = \begin{cases} sign\left(w_{i,j}\right)\left(K\lambda_1\right) & \left|w_{i,j}\right| \geq \lambda_1 \\ w_{i,j} & \left|w_{i,j}\right| < \lambda_1 \end{cases} \tag{1}$$

Where $sign(w)$ is sign function, and give out the sign of w.

De-noising is different from rejecting the clutter. Noise is random, and distributed over the whole wavelet domain, and corresponded to wavelet coefficients of small value. After wavelet decomposition, because the amplitude of the wavelet coefficient of signal is usually larger than that of noise, wavelet coefficients having rejected the ground clutter can be further processed. De-noising uses the threshold λ_2, that is, the wavelet coefficients being larger than λ_2 are reserved, and that being smaller than λ_2 is being reduced to zero. λ_2 is determined by [4]

$$\lambda_2 = \sigma * \sqrt{2\log(N)} \tag{2}$$

Where σ is the standard deviation of noise, N is signal length. σ is unknown in the actual situation and can be estimated by the wavelet coefficients as follows

$$\hat{\sigma} = \frac{Median|x|}{0.6745} \tag{3}$$

Where Median $|x|$ is the medium value of the wavelet decomposition coefficient in (1).

2.2 Maximum Entropy Method

When MEM is used for spectral analysis of the profiler echoes, it corresponds to a predicted error filter with minimum phase [5]. The power spectrum density $s(f)$ of input data $\{X(n)\}$ that is determined jointly by the filter coefficients $a(1,K)$, $a(2,K)$, …, $a(K,K)$ and its output power P_k can be written as

$$S(f) = \frac{P_K \Delta t}{\left| 1 - \sum_{k=1}^{K} a(k,K) \exp(-j2\pi f k \Delta t) \right|^2} \tag{4}$$

With minimizing the energy sum of the predicted error of the forward and backward filter as constrains, Burg had given out the recursive algorithm of the filter coefficients [6]. The recursive formulas are as follows

$$f_K(n) = f_{K-1}(n+1) - a(K,K) b_{K-1}(n) \tag{5}$$

$$b_K(n) = b_{K-1}(n) - a^*(K,K) f_{K-1}(n+1) \tag{6}$$

$$a(k,K) = a(k,K-1) - a(K,K) a^*(K-1,K-1) \tag{7}$$

$$a(K,K) = \frac{2 \sum_{n=0}^{N-1-K} b_{K-1}^*(n) f_{K-1}(n+1)}{\sum_{n=0}^{N-1-K} \left(|b_{K-1}(n)|^2 + |f_{K-1}(n+1)|^2 \right)} \tag{8}$$

Where $K = 1,2,\ldots$; M. $k = 1,2,\ldots,K-1$. And assumption $f_0(n) = b_0(n) = X(n)$.

The filter coefficients can be given recursively under K is increased up to appropriate from 1 using (5)–(8), then power spectrum can be computed using (4).

3 Simulated Test

In order to objectively evaluate these methods, the comparative analysis is made using the simulated signals. The power spectrum and its corresponding time signals are simulated by Sirmans method [7], that is, Gaussian spectrum having known spectral width is given firstly, next it is quantized, and is added random white noise of a certain amplitude in the end. By this time, the discrete spectrum called the simulated spectrum which is relatively in accordance with the practice has been gotten. The simulated time signal is gotten by applying inverse FFT to the simulated spectrum.

Using the simulated I, Q signals, the results of the three methods are shown in Fig. 1. In the figure, the rows are the results of that there in turns from top to bottom

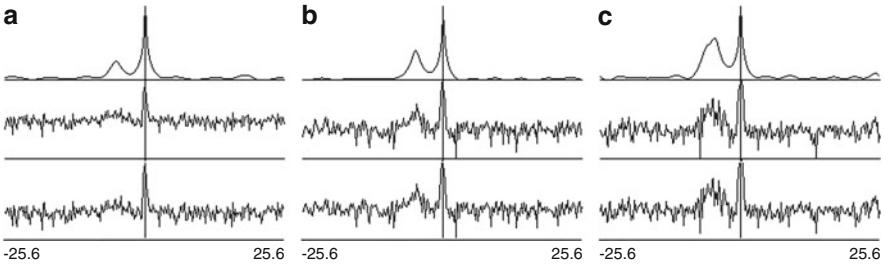

Fig. 1 Comparing the simulated results of the three methods using different signals. (**a**) −5 dB; (**b**) 0 dB; (**c**) 5 dB

are MEM, the wavelet-based technique and FFT. Fig. 1a–c give the processing results of −5, 0, 5 dB (signal/noise—SNR) respectively. From the figure, we can get: when signal is strong(SNR is larger than 0 dB), the three methods all give out signal peaks normally; but when signal is weak(SNR is about −5 dB), the effect that the MEM resolve signal peak is better than the other methods. In the same time, the smoothly spectrum can be given out in MEM, that indicates MEM can also suppress the random white noise to the some extent.

4 Real Data Analysis

The comparative analysis of the three methods (FFT, wavelet-based technique and MEM) is also made using the I, Q signal measured by the profiler. A typical result is shown in Fig. 2. In the figure, the horizontal axis is Doppler velocity, which maximum value is 10.0 m/s; vertical axis is height in metres.

Figure 2a shows the results of FFT, obvious peaks can be found in many layers, but signal peak isn't obvious between 3,150 and 4,350 m. Figure 2b shows the results of the wavelet-based technique, DC are suppressed in all layers, and signals positioned near zero frequency are also suppressed in 2,850, 4,800 and 4,950 m, and peaks between 3,150 and 4,350 m cannot be found availably. Figure 2c shows the results of MEM, obvious peaks and its continuity in height are easily seen, and spectrum is obviously improved between 3,150 and 4,350 m, this indicates the MEM is superior to the other methods.

5 Conclusions

Via having analysed the FFT, wavelet-based technique and the MEM using simulated and real I, Q signals respectively, we can get:

When signal is strong, the three methods have little difference on resolving signal peak, and when signal is weak, the MEM is better than the other methods;

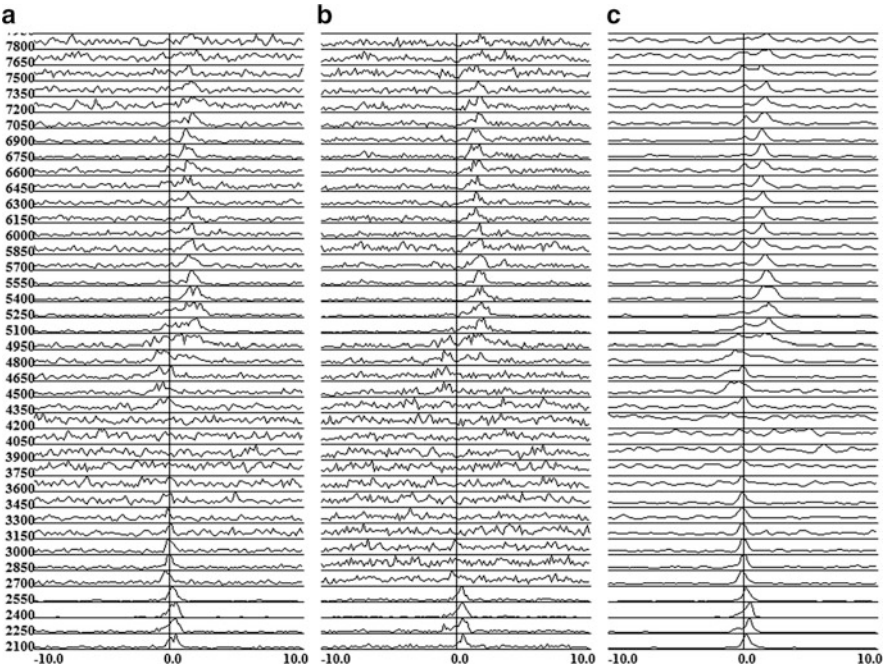

Fig. 2 Comparing the real results of the three methods. (**a**) FFT; (**b**) the wavelet-based technique; (**c**) MEM

MEM can suppress the ground clutter and the random white noise to the some extent and gives out a smoothly spectrum.

Acknowledgments This work was supported by the National Science Foundation of China under the grant number of No. 41005018. The authors would like to thank 23rd Research Institute of China Changfeng Mechanics and Electronics Technology Academy to provide real profiler data for this paper.

References

1. Endlice RM, Singleton RC, Kaufman JW (1969) Spectral analysis of detailed vertical wind speed profiles. J Atmos Sci 26(5):1030–1040
2. Jordan JR, Lataitis RJ, Carter DA (1997) Removing ground and intermittent clutter contamination from wind profiler signals using wavelet transforms. J Atmo Oceanic Technol 14 (6):1280–1297
3. Urban B (1995) Humidity profile retrieval using a maximum entropy principle. Mon Wea Rev 123(4):1185–1196
4. Donoho DL (1995) De-noising by soft thresholding. IEEE Trans IT 41(3):613–627
5. Burg JP (1972) The relationship between maximum entropy and maximum likelihood spectra. Geophysics 37(2):375–376

6. Burg JP (1975) Maximum entropy spectral analysis. Ph.D. dissertation, Department of Geophysics, Stanford University, CA
7. Sirmans D, Bumagarner B (1975) Numerical comparison of five mean frequency estimators. J Appl Met 14(6):991–1003

Improved Multi-Channel Reconstruction Algorithm for High Resolution Wide Swath Imaging with Squint Stripmap SAR

Weihua Zuo and Rui Min

Abstract The multi-channel reconstruction algorithm was proposed to reconstruct the down-sampled azimuth echo in the side-looking stripmap SAR with displaced phase center multiple azimuth beam antenna configuration. It is an effective algorithm for high resolution wide swath imaging. But when it is applied in squint mode directly, the de-focus phenomena appear in azimuth direction. The reason responsible for that lies in the non-zero doppler center frequency. In this paper, we improve the original multi-channel reconstruction algorithm, in which the aliased doppler center frequency is compensated in the preprocessing step and the reconstruction filter for each channel is adjusted. The analysis is given in details. The simulations verify the validity of the proposed method.

Keywords Synthetic aperture radar • Squint mode • Multi-channel reconstruction algorithm

W. Zuo (✉)
School of Electronic Engineering, University of Electronic Science and Technology of China (UESTC), No. 2006, XiYuan Avenue, West High-Tech Zone, Chengdu, People's Republic of China

Department of Physics and Information Engineering, Huaihua University, Hunan, People's Republic of China
e-mail: kingso801021@163.com

R. Min
School of Electronic Engineering, University of Electronic Science and Technology of China (UESTC), No. 2006, XiYuan Avenue, West High-Tech Zone, Chengdu, People's Republic of China
e-mail: minrui@uestc.edu.cn

B. Zhang et al. (eds.), *The Proceedings of the Second International Conference on Communications, Signal Processing, and Systems*, Lecture Notes in Electrical Engineering 246, DOI 10.1007/978-3-319-00536-2_58,

1 Introduction

High resolution wide swath (HRWS) imaging is required in many SAR applications such as map acquisition, disaster evaluation and ocean observation etc [1, 2]. Unfortunately high resolution and wide swath imaging give contradicting requirements to SAR system design. This contradiction can be reflected by the selection of the pulse repetition frequency (PRF). In traditional SAR system, *PRF* should satisfy the condition described in (1), in which ρ_a is the azimuth resolution, W_g is the swath width, θ_f is the far incident angle and c is the speed of light.

$$\frac{V}{\rho_a} \leq PRF \leq \frac{c}{2W_g sin\theta_f}, \tag{1}$$

High azimuth resolution ρ_a requires large *PRF* to ensure the left part of (1), while wide swath requires small *PRF* to ensure the right part of (1).

In order to conquer the contradiction, several solutions were proposed. Currie [3] proposed the multiple elevation beam (MEB) and multiple azimuth beam (MAB) imaging modes. The shortcoming of the MAB lies in the discontinuous swath. The MAB mode has two configurations called single phase center MAB (SPC MAB) and displaced phase center MAB (DPC MAB). All the followed proposed methods for HRWS imaging are based on the researches of [3]. Callaghan [4] combined the MEB and MAB to form a Quad-element array. The proper null steering technologies were proposed to suppress the range and azimuth ambiguities. Suess [5] proposed the HRWS mode. In HRWS mode the scan on receiver (SCORE) technology based on digital beam-forming (DBF) in elevation was combined with MAB to compensate the transmitter gain loss in elevation direction. Nicolas [6] and Xu [7] combined MAB or MEB with the scan mode or the terrain observation by progressive scans (TOPS) mode to get super-wide swath image. The multi-dimension waveform encoding (MWE) technology was proposed by Krieger [8] to improve the ambiguity suppression ability for HRWS imaging. The literature [9, 10] gave the realization of MWE in details.

As for the imaging algorithm for HRWS imaging, the multi-channel reconstruction algorithm was proposed in [11] and [6] for the DPC MAB configuration. It reconstructs the azimuth spectrum from down-sampled azimuth echoes of multiple azimuth channels. And the nonuniform sampling caused by the platform movement is considered and compensated. Thus it is an effective imaging algorithm for HRWS imaging with DPC MAB. But it is proposed for side-looking stripmap mode. When it is applied in squint mode directly, because of the non-zero doppler center frequency, the de-focus phenomenon occurs in azimuth direction [12]. In this paper, it will be improved to make it applicable for squint stripmap mode.

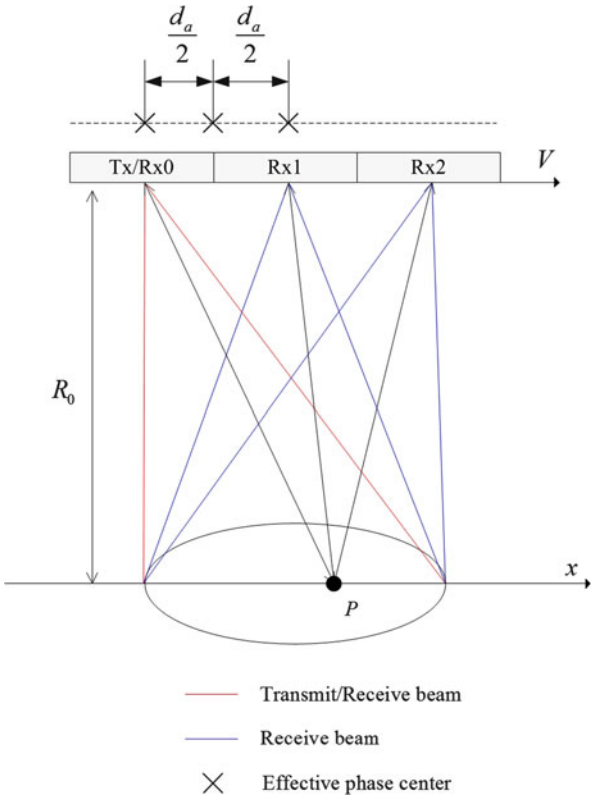

Fig. 1 The DPC MAB antenna configuration in side-looking stripmap SAR mode

2 The Improved Multi-channel Reconstruction Algorithm

2.1 The Original Multi-channel Reconstruction Algorithm

Before discussing the multi-channel reconstruction algorithm, the DPC MAB antenna configuration is given in Fig. 1, in which there are one transmit antenna and three receive antennae along azimuth direction. The dimension of each antenna in azimuth direction is d_a. The effective phase centers are shown as crosses. The distance between them is $d_a/2$.

Set the azimuth return of point target P in the k_{th} receive antenna is $S_{ak}(t)$ as (2), in which λ is the wavelength, R_0 is the shortest slant range of P.

$$S_{ak}(t) = \exp\left[-j\frac{4\pi R_{xk}(t)}{\lambda}\right], k = 0, 1, 2 \tag{2}$$

In (2), $R_{xk}(t)$ is:

$$R_{xk}(t) = \left[\sqrt{R_0^2 + V^2 t^2} + \sqrt{R_0^2 + V^2\left(t - \frac{kd_a}{V}\right)^2}\right]/2, k = 0, 1, 2 \tag{3}$$

In traditional SAR, the azimuth return in the k_{th} effective phase center is $S_{tr,ak}$ as:

$$S_{tr,ak}(t) = \exp\left[-j\frac{4\pi R_{tr,xk}(t)}{\lambda}\right] \tag{4}$$

In (4), $R_{tr,xk}(t)$ is:

$$R_{tr,xk}(t) = \sqrt{R_0^2 + V^2\left(t - \frac{kd_a}{2V}\right)^2} \tag{5}$$

Based on the approximations in side-looking mode: $\sqrt{R_0^2 + V^2 t^2} \approx R_0 + \frac{V^2 t^2}{2R_0}$, $\sqrt{R_0^2 + V^2\left(t - \frac{kd_a}{2V}\right)^2} \approx R_0 + \frac{V^2}{2R_0}\left(t - \frac{kd_a}{2V}\right)^2$ and $\sqrt{R_0^2 + V^2\left(t - \frac{kd_a}{2V}\right)^2} \approx R_0 + \frac{V^2}{2R_0}\left(t - \frac{kd_a}{2V}\right)^2$, the relationship between $S_{ak}(t)$ and $S_{tr,ak}(t)$ is as:

$$S_{ak}(t) = S_{tr,xk}(t)\exp\left[-j\frac{\pi(kd_a)^2}{2\lambda R_0}\right] \tag{6}$$

Set the azimuth return in traditional stripmap SAR be $S(t)$. Then the relationship between $S(t)$ and $S_{tr,xk}(t)$ is $S_{tr,xk}(t) = S\left(t - \frac{kd_a}{2V}\right)$. Combining it with (6), we can get (7).

$$S_{ak}(t) = S\left(t - \frac{kd_a}{2V}\right)\exp\left[-j\frac{\pi(kd_a)^2}{2\lambda R_0}\right] \tag{7}$$

Converting (7) to the doppler frequency domain, (8) is obtained, in which B_d is doppler band. From (8), it is found the echo of the k_{th} channel is the time-shift version of the correct echo by $\Delta t = \frac{kd_a}{2V}$, and an additional phase term $\exp\left[-j\frac{\pi(kd_a)^2}{2\lambda R_0}\right]$ is added, which in fact can be omitted because $kd_a \ll R_0$.

$$S_{ak}(f_a) = S(f_a)\exp(-j\frac{\pi k d_a}{V}f_a)\exp\left[-j\frac{\pi(kd_a)^2}{2\lambda R_0}\right],\ f_a \in [-\frac{B_d}{2}, \frac{B_d}{2}] \tag{8}$$

When SAR works with $PRF = \frac{B_d}{N_a}$ (N_a is the number of the displaced antenna along azimuth direction), although the azimuth echo is down-sampled by N_a in each single channel, the total azimuth echo or spectrum can be reconstructed from all the echoes of displaced azimuth channels. The reconstruction is accomplished by the

filtering to each channel and the summarization of all the filtered echoes. For simplicity, the filters for a two-channel DPCA configuration are given as follows.

For the 0_{th} channel, the filter is as (9).

$$F_0(f_a) = \begin{cases} \dfrac{1}{1-\exp(j\frac{\pi d_a}{V}PRF)}, & -PRF < f_a < 0 \\ \dfrac{1}{1-\exp(-j\frac{\pi d_a}{V}PRF)}, & 0 < f_a < PRF \end{cases} \tag{9}$$

For the 1_{th} channel, the filter is as (10).

$$F_1(f_a) = \begin{cases} \dfrac{1}{\exp(-j\frac{\pi d_a}{V}f_a) - \exp(-j\frac{\pi d_a}{V}(f_a+PRF))}, & -PRF < f_a < 0 \\ \dfrac{1}{\exp(-j\frac{\pi d_a}{V}f_a) - \exp(-j\frac{\pi d_a}{V}(f_a-PRF))}, & 0 < f_a < PRF \end{cases} \tag{10}$$

2.2 *The Improved Multi-channel Reconstruction Algorithm*

The original multi-channel reconstruction algorithm was proposed in side-looking mode. In this subsection we will discuss the situation when SAR works with moderate or high squint angle.

The most important difference between the side-looking and the squint mode is the doppler frequency center f_{dc}. In side-looking mode, the doppler band is in base band $[-\frac{B_d}{2}, \frac{B_d}{2}]$. In the squint mode, the doppler frequency band is not in base band any longer, but in a pass-band as $[f_{dc} - \frac{B_d}{2}, f_{dc} + \frac{B_d}{2}]$, in which $f_{dc} \neq 0$. When the azimuth echo is down-sampled with $PRF = \frac{B_d}{N_a}$, the azimuth spectrum will be not only aliased but also be folded in $[-\frac{PRF}{2}, \frac{PRF}{2}]$. If the original multi-channel reconstruction algorithm is applied, the de-focus phenomenon appears in azimuth direction. In order to reconstruct the azimuth spectrum correctly, some revisions must be made to the original multi-channel reconstruction algorithm. In the following parts, we take two receive azimuth channels for example to analyze.

2.2.1 Preprocessing Step

The azimuth spectrum aliasing and folding phenomena in squint mode are shown in Fig. 2. After FFT operation, the observed spectrum is in $[-\frac{PRF}{2}, \frac{PRF}{2}]$, shown as the red-mapped area. Because normally f_{dc} is not an integer times of the PRF, the observed spectrum is not alike that in the pass-band $f_{dc} + [-\frac{PRF}{2}, \frac{PRF}{2}]$, shown as

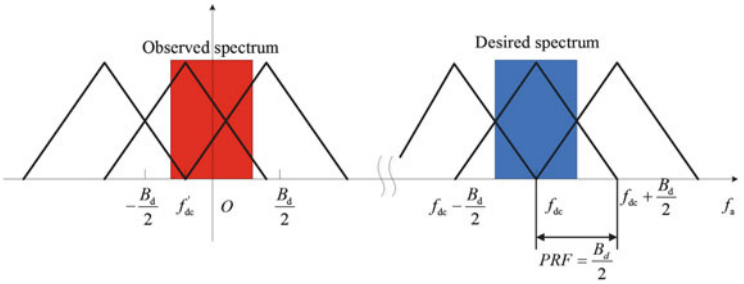

Fig. 2 The aliased and folded spectrum in each channel

the blue-mapped area, which is the desired spectrum for reconstruction. The f_{dc} will be folded in the base band as f'_{dc}. The relationship between them can be described as $f'_{dc} = f_{dc} - \lfloor \frac{f_{dc}}{PRF} \rfloor \times PRF$. The aliased doppler center frequency should be compensated to obtain the desired spectrum for the followed reconstruction. It can be accomplished by the phase term as (11).

$$H_{alpc} = \exp(-j2\pi f'_{dc} t) \tag{11}$$

The compensation is implemented before the reconstruction and imaging steps, so we can call it a preprocessing step. Though after the phase compensation, the obtained spectrum is still aliased and folded, it is alike that in $f_{dc} + [-\frac{PRF}{2}, \frac{PRF}{2}]$. Thus it can be used for the spectrum reconstruction.

2.2.2 Multi-channel Reconstruction Filters for Squint Mode

The original multi-channel reconstruction algorithm was proposed based on the multi-channel sampling theory of the low-pass signals [13]. In [13], the limited band $[-\frac{B_d}{2}, \frac{B_d}{2}]$ is divided into N_a sub-band. The reconstruction filter for each channel is calculated in the first sub-interval $I_1 = [-\frac{B_d}{2}, -\frac{B_d}{2} + PRF]$. The first sub-interval in squint mode should be $I_1 = f_{dc} + [-\frac{B_d}{2}, -\frac{B_d}{2} + PRF]$. All the followed derivation is alike that of the original multiple channel reconstruction algorithm. Based on the preprocessing step and the analysis, the improved reconstruction filters for the k_{th} channel should be as follows.

For the 0_{th} channel, the filter is as (12).

$$F_0(f_a) = \begin{cases} \dfrac{1}{1-\exp(j\frac{\pi d_a}{V}PRF)}, & -PRF < f_a < 0 \\ \dfrac{1}{1-\exp(-j\frac{\pi d_a}{V}PRF)}, & 0 < f_a < PRF \end{cases} \tag{12}$$

For the 1_{th} channel, the filter is as (13).

$$F_1(f_a) = \begin{cases} \dfrac{1}{\exp(-j\frac{\pi d_a}{V}(f_a+f_{dc}))-\exp(-j\frac{\pi d_a}{V}(f_a+f_{dc}+PRF))}, & -PRF < f_a < 0 \\ \dfrac{1}{\exp(-j\frac{\pi d_a}{V}(f_a+f_{dc}))-\exp(-j\frac{\pi d_a}{V}(f_a+f_{dc}-PRF))}, & 0 < f_a < PRF \end{cases} \tag{13}$$

2.2.3 Imaging Processing

After the preprocessing step and the reconstruction filtering, the azimuth spectrum is obtained, which can be used for imaging. We take advantage of the nonlinear chirp scaling algorithm (NCSA) [14] for the followed imaging processing.

3 Simulation Results

In this section, some simulation results are provided. The system parameters for simulation are listed in Table 1. Nine point targets are selected for the imaging. The echo of them will be processed by the method proposed in HRWS [5], the original multi-channel reconstruction algorithm [6, 11] and the proposed method respectively. The simulation results are shown in Fig. 3. The comparison between the imaging results is provided as follows.

The left image in Fig. 3 is obtained by the method proposed in HRWS system. The azimuth data of all channels are interleaved with the sequent order of the effective phase centers, while no other processing steps are implemented. From the imaging result, it is found that in the azimuth direction there are two other "Ghost" shades except for the desired imaging result. This is because in HRWS method, each channel is down-sampled by $N_a = 2$. Without the azimuth spectrum reconstruction, the azimuth spectrum will be aliased and folded in $[-\frac{PRF}{2}, \frac{PRF}{2}]$. The discontinuous and folded spectrum makes errors in the range walk correction, which result in the "Ghost" shades.

Table 1 The parameters for simulation

Parameter	Value	Parameter	Value
Carrier frequency	2 GHz	Squint angle	5°
Platform height	10,000 m	Platform velocity	200 m/s
Antenna azimuth dimension	4 m	Azimuth channel number	2

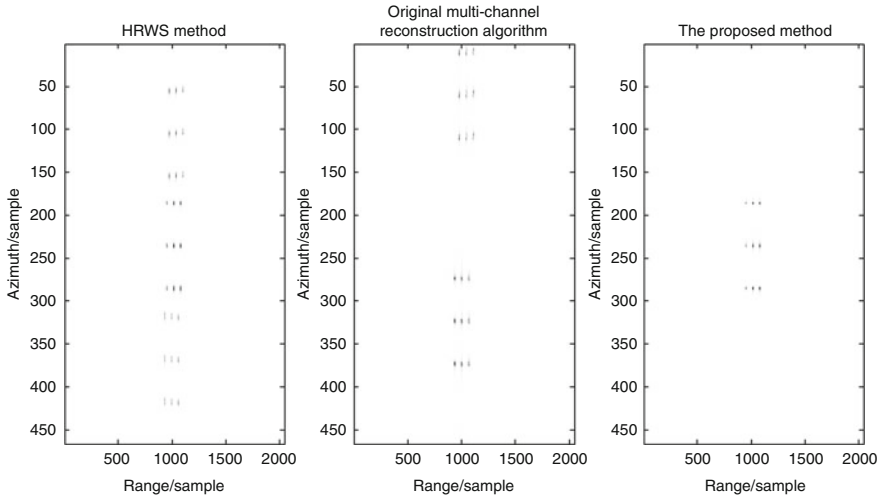

Fig. 3 The imaging results obtained by (*left*) HRWS method, (*middle*) original multi-channel reconstruction algorithm, (*right*) the proposed method

The middle image in Fig. 3 is obtained by the original multi-channel reconstruction algorithm. It is found that there are two images of each point target. And the position of each point target is wrong. This can be explained as follows. Although the azimuth data of each channel is filtered by the corresponding reconstruction filter, it does not consider the non-zero doppler frequency. The filter's phase, moreover, is incorrect because of the incorrect doppler frequency interval. Thus the azimuth spectrum is not reconstructed correctly actually, which results in errors in followed imaging steps such as range walk correction.

The right image in Fig. 3 is obtained by the proposed method of this paper. It is found all the targets are in the correct positions. The de-focus phenomenon in azimuth direction disappears. This is because before the reconstruction, the folded doppler center frequency f'_{dc} is compensated to obtain the desired spectrum. The reconstruction filter, moreover, is revised to the correct value. Then the reconstruction is implemented perfectly. After the imaging processing steps, the correct image is obtained.

4 Conclusions

In this paper, the multi-channel reconstruction algorithm is improved based on the research of the spectrum structure in squint stripmap mode with DPCA configuration. The simulation results comparison between the HRWS method, the original multi-channel reconstruction algorithm and the proposed method verifies the validity of the proposed method.

References

1. Cao Z, Chen, L (2012) Security in application layer of radar sensor networks: detect friends or foe. Secur Comm Netw 1:35–40
2. Xu J, Pi Y, Cao Z (2012) Bayesian compressive sensing in synthetic aperture radar imaging. IET Radar Sonar Navig 6(1):2–8
3. Currie A, Brown MA (1992) Wide-swath SAR. IEE Proc Inst Electr Eng F 139(2):122–135
4. Callaghan GD, Longstaff ID (1992) Wide swath spaceborne SAR using a quad element array. IEE Proc Radar Sonar Navig 139(2):122–135
5. Suess M, Grafmueller B, Zahn R (2001) A novel high resolution, wide swath SAR system. In: Proceedings of IEEE International Geoscience and Remote Sensing Symposium, Sydney, pp 1013–1015
6. Nicolas G, Gebert N, Moreim A (2010) Multichannel Azimuth processing in ScanSAR and TOPS mode operation. IEEE Trans Geosci Remote Sens 48(7):2994–3008
7. Xu W, Huang PP, Deng YK (2011) Multi-channel SPCMB-TOPS SAR for high-resolution wide-swath imaging. Prog Electromagn Res 116:533–551
8. Krieger G, Gebert N, Moreira A (2008) Multidimensional waveform encoding: a new digital beamforming technique for synthetic aperture radar remote sensing. IEEE Trans Geosci Remote Sens 46(1):31–46
9. Feng F, Li S, Yu W, Wang S (2012) Study on the processing scheme for space-time waveform encoding SAR system based on two-dimensional digital beamforming. IEEE Trans Geosci Remote Sens 50(3):910–932
10. Feng F, Li S, Yu W, Huang P, Xu W (2012) Echo separation in multidimensional waveform encoding SAR remote sensing using an advanced null-steering beamformer. IEEE Trans Geosci Remote Sens 50(10):4157–4172
11. Krieger G, Gebert N, Moreira A (2004) Unambiguous SAR signal reconstruction from nonuniform displaced phase center sampling. IEEE GRS Lett 1(4):260–264
12. Zuo W, Pi Y, Min R (2013) An extended frequency scaling algorithm for high squint spotlight airborne SAR. Prog Electromagn Res 138:41–63
13. Brown JL (1981) Multi-channel sampling of low-pass signals. IEEE Trans Circ Syst CAS-28 (2):101–106
14. Davidson GW, Cumming IG, Ito MR (1996) A chirp scaling approach for processing squint mode SAR data. IEEE Trans AES 32:121–133

Design and Implementation of 0.28 THz Terahertz Radar System with Ranging Capabilities

Kun Tian, Jin Li, and Gang Yao

Abstract This Terahertz radar system has ranging capabilities with high precision. By frequency modulating the K-band supplied by Agilent E8257D PSG analog signal generators, we have achieved a range resolution of approximately 8 cm for targets at a range of several meters. This work demonstrates the feasibility of high-resolution terahertz radar based on an all solid-state approach. This system has great potentiality in bandwidth improving. We could obtain a sub-cm resolution from it by some improvement.

1 Introduction

Terahertz band is the type of electromagnetic wave that the frequency range is from 100 GHz to 10 THz, which is between millimeter wave and infrared. Because of its high frequency and wide bandwidth, the spatial resolution and range resolution of terahertz radar system could be higher than conventional radar system working in X-band. This advantage makes it prospectable in the domain of radar target imaging, environment monitoring, safety inspection and anti-terrorism detection. For example, we could use it in secure communication among satellites and imaging radar system, such as airship detection at High Altitude Platform Station (HAPS) and ballistic missile imaging in midcourse.

Compared to traditional millimeter-wave radar system, the advantages of terahertz radar system is as below. First of all, the shorter wave length could be convenient for providing wider bandwidth, which causes higher precision of imaging. Second, the narrower antenna beam in terahertz band could not only obtain higher antenna gain in radar LOS for improving the ability of multi-target discrimination and recognition, but also reduce the opportunity of main lobe jamming. The

K. Tian • J. Li (✉) • G. Yao
School of Electronic Engineering, University of Electronic Science and Technology of China, Chengdu, Sichuan, China
e-mail: lijin@uestc.edu.cn

B. Zhang et al. (eds.), *The Proceedings of the Second International Conference on Communications, Signal Processing, and Systems*, Lecture Notes in Electrical Engineering 246, DOI 10.1007/978-3-319-00536-2_59,

higher gain of main lobe may also suppress the side lobe interference [1, 2]. When we contrast between terahertz radar and laser radar, the advantages are also in two aspects. On one hand, the beam width of terahertz radar is wider than lidar, which causes a larger visual field and better searching ability. On the other hand, sub-millimeter wave has good fog penetration capability than laser. Thus, the terahertz detector is more effective than photodetector under a terrible weather condition. At the present time, the experimental terahertz radar systems are 580 GHz imaging radar system in Jet Propulsion Laboratory (JPL) in US [3–7] and 220 GHz COBRA Inverse Synthetic Aperture Radar (ISAR) imaging system in Research Establishment for Applied Science (FGAN) in Germany [8]. In this paper, the frequency of radar system is 0.28 THz, and we can use this system ranging and distinguish targets with a range resolution of approximately 8 cm.

2 Radar System Design

This radar system adopts LFMCW waveform with two independent channels for transmitting and receiving. The bandwidth of LFMCW is 2.4 GHz, and the frequency sweep period is 10 ms, so the chirp rate is 240 GHz/s. The timing diagram for signal transmitting and receiving is below (Fig. 1).

The block diagram of this terahertz radar system is as follow (Fig. 2).

By 12 times frequency multiplied the K-band supplied by Agilent E8257D PSG analog signal generator by power amplifier modules and frequency multiplier chains consisting of doublers and triplers, we obtain the terahertz wave at about 0.28 THz. In transmitting channel, the signal generator supplies signal at 21.5 GHz, and turns into 23.5–23.7 GHz after modulates by a VCO with bandwidth 200 MHz at 2–2.2 GHz. When transmitting, we achieve the frequency at 282–284.4 GHz and the bandwidth is 2.4 GHz. The receiving channel is the same as transmitting channel except the initial frequency is at 21.4 GHz and the final frequency is at 140.4–141.6 GHz because of a subharmonically mixer.

From the diagram, we can see that the initial frequency at transmitting channel is 100 MHz higher than it at receiving channel. We obtain the 100 MHz IF signal by mixing the two initial signals and 12 times frequency multiplied it. The transmitted signal is downconverted and deramped by subharmonically mixer with LO at 140 GHz. The final IF signal of ~1.2 GHz is orthogonal two-channel zero-IF processing by ADL5382 and we use FFT algorithm to obtain the frequency caused by range.

3 Experiment Results

Integration of transmitting, receiving, signal processing and display systems we acquire the terahertz radar system as below. Figure 3 is the photo of the radar system and transmitting-receiving system.

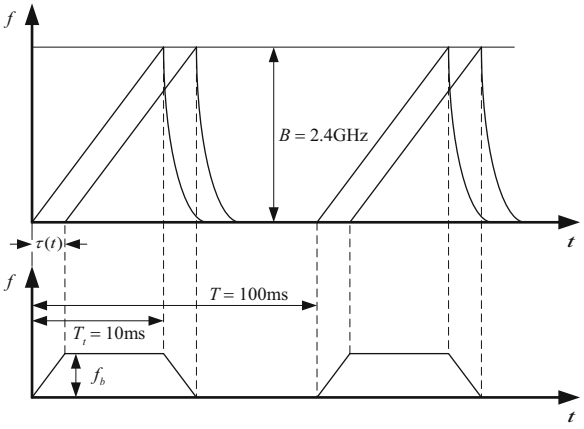

Fig. 1 The timing diagram for signal transmitting and receiving. $\tau(t)$ represents time delay by the range of target, and f_b is proportional to the range of target

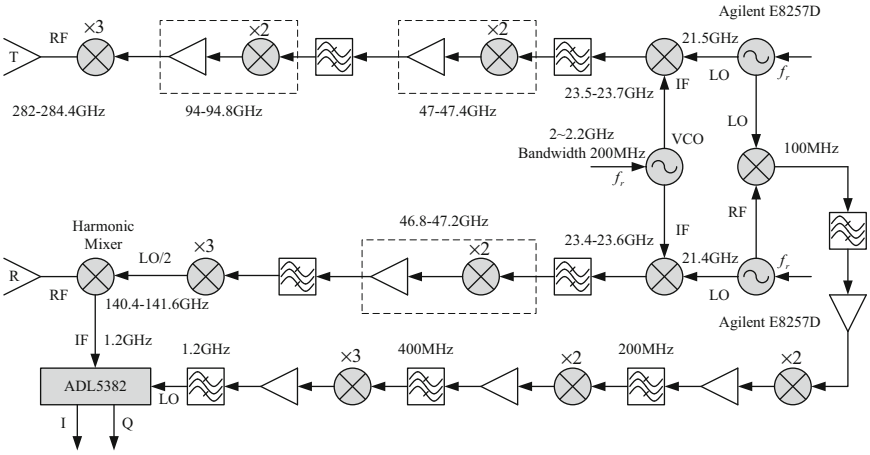

Fig. 2 Block diagram of radar system

Figure 4 is the result of ranging experiment (1). In this experiment, the distance between radar system and target is 1.04 m, and the IF signal is 1,312 Hz that corresponding to the range of 0.82 m. The error is 0.22 m.

Figure 5 is the result of ranging experiment (2). In this experiment, the distance between radar system and target is 2.70 m, and the IF signal is 3,905 Hz that corresponding to the range of 2.44 m. The error is 0.26 m.

Table 1 is the data of range experiments. From these experiments, we could get the conclusion that the errors are always existent and is about -0.24 m after averaging. In this system, the error is caused by the lager delay of receiving channel due to more MMIC chips used in it.

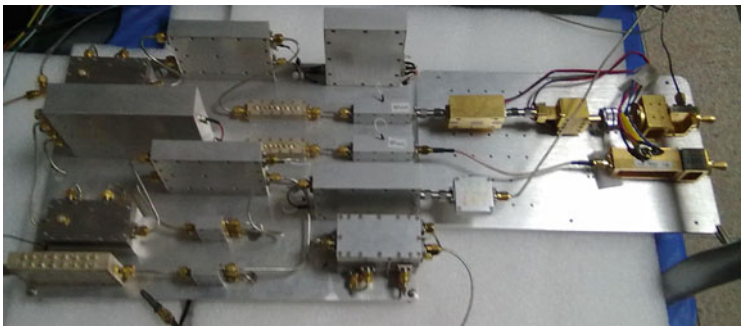

Fig. 3 Terahertz radar system

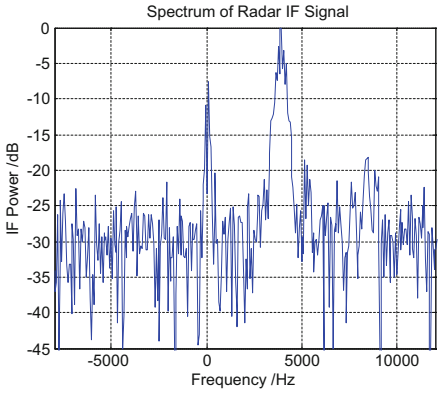

Fig. 4 The result of ranging experiment (1)

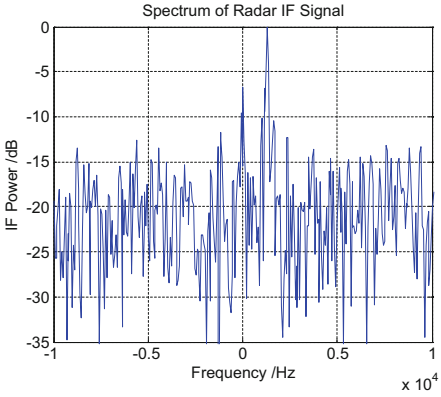

Fig. 5 The result of ranging experiment (2)

Table 1 Data of ranging experiments

IF (Hz)	Measurement range (m)	Real range (m)	Error(cm)
1,312	0.82	0.104	-0.22
1,608	0.100	0.123	-0.23
2,087	0.130	0.157	-0.27
3,150	0.197	0.218	-0.21
3,905	0.244	0.270	-0.26
4,430	0.277	0.302	-0.25
4,839	0.302	0.326	-0.24
5,368	0.336	0.359	-0.23

From Fig. 6, we can see that the transmitting and receiving channels are out of step, which leads to a fixed additional frequency added to the IF signal caused by real distance. The fixed error is corresponding to the fixed frequency, which is decided by the response time of two channels. In this system, the ranging error is about -0.24 m. That is to say, the additional frequency is about 384 Hz. So, the response time of receiving channel is 1.6 ns delayed by transmitting channel according to the 240 GHz/s chirp rate. We can use this value to compensation the measurement result.

The result of ranging resolution is shown in Fig. 6. There are three peaks in the IF spectrum, 1,862, 1,983 and 2,533 Hz, which are corresponding to 1.40, 1.48 and 1.82 m after compensation. It is accord with the truth, and moreover, this system can distinguish the targets in the range of about 8 cm (1.40 and 1.48 m). This is the bandwidth-limited range resolution of the 2.4 GHz LFMCW radar measurement by $\Delta R = c/2B$.

4 Conclusion

This paper introduces the terahertz radar system we established by frequency multiplication method. Range resolution of 8 cm was achieved by ramping the transmit signal over a bandwidth of 2.4 GHz in 10 ms and these results demonstrate the feasibility of high-resolution terahertz radar based on an all solid-state approach. In this system, the bandwidth of transmitted signal can be improved to about 15 GHz easily by increasing the VCO's bandwidth, and then, we could acquire sub-cm resolution.

Acknowledgement This work has been supported by the Fundamental Research Funds for the Central Universities (ZYGX2011J020).

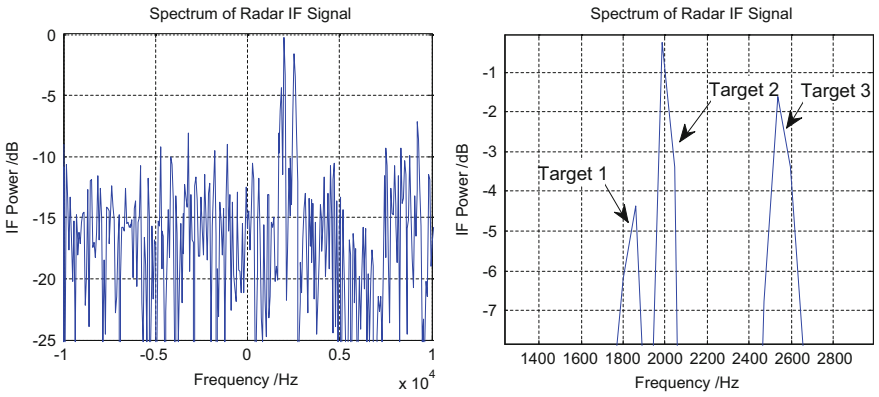

Fig. 6 The result of ranging resolution

References

1. Sanchez AR, Zhang X (2008) Terahertz science and technology trends. IEEE J Sel Top Quant Electron 14(2):260–269
2. Li J, Pi YM (2010) Micro-doppler signature feature analysis in terahertz band. J Infrared Millim Thz Wave 31(3):319–328
3. Dengler RJ, Maiwald F, Siegel PH (2006) A compact 600 Ghz electronically tunable vector measurement system for submillimeter wave imaging, IEEE MTT-S Int. Digest, San Francisco, June, 2006, pp. 1923–1926
4. Dengler RJ, Cooper KB, Chattopadhyay G, Mehdi I, Schlecht E, Skalare A, Chen C, Siegel PH (2007) 600 Ghz imaging radar with 2cm range resolution, IEEE MTT-S Int. Digest, Honolulu, June, 2007, pp. 1371–1374
5. Cooper KB, Dengler RJ, Chattopadhyay G, Schlecht E, Gill J, Skalare A, Mehdi I, Siegel PH (2008) A high-resolution imaging radar at 580 GHz. IEEE Microw Wireless Compon Lett 18 (1):64–66
6. Weg CA, Spiegela WV, Hennebergerb R (2009) Fast active Thz camera with range detection by frequency modulation, terahertz technology and applications II, Proceeding of SPIE, Vol. 7215, Orlando, 2009.
7. Weg CA, Spiegel WV, Henneberger R et al (2009) Fast active THz cameras with ranging capabilities. J Infrared Millim THz Wave 30(8):1281–1296
8. Essen H, Wahlen A, Sommer R et al (2007) High-bandwidth 220 GHz experimental radar. Electron Lett 43(20):1114–1116

The Impact Analysis of the Array Elements Number on the Beam Direction in the Presence of Amplitude and Phase Errors

Xu Wang, Huiyong Li, and Julan Xie

Abstract The digital beamforming is able to improve the performance of the radar system. The amplitude and phase errors are the unavoidable non-ideal factors in the real system. As a matter of course, such errors would lead to the deterioration of the performance of the antenna array. In this paper, the impact analysis of the amplitude and phase errors on the beam direction for different elements numbers is analyzed. A relationship between the number of elements and the beam direction in the presence of amplitude and phase errors is deduced. The analysis reveals that the real beam direction in the presence of amplitude and phase errors can approximate to the ideal one by increase the number of elements. The simulations show that the real results follow the trend of the deduced ones.

Keywords Amplitude and phase errors • Beam direction • Number of elements • Pointing deviation

1 Introduction

In modern warfare, various jamming, stealth target, low altitude penetration, anti-radiation missile and saturation attack are becoming the mainly threats and challenges to the radar system. The application of the phased array radar has reduced many difficulties faced by radar systems. Especially the digital beamforming (DBF) technique has effectively improved the performance of radar systems. Comparing with analog beamforming, the digital beamforming has many advantages. For example, digital beamforming is much easier to reduce sidelobe level and to form particular beam pattern. For such reasons, digital beamforming has been gaining

X. Wang (✉) • H. Li • J. Xie
School of Electronic Engineering, University of Electronic Science and Technology of China, Chengdu, Sichuan 611731, P.R.China
e-mail: alienfrog@163.com

B. Zhang et al. (eds.), *The Proceedings of the Second International Conference on Communications, Signal Processing, and Systems*, Lecture Notes in Electrical Engineering 246, DOI 10.1007/978-3-319-00536-2_60,

popularity in the fields of mobile communication, satellite communication and radar.

However, the amplitude and phase errors among RF channels will lead to the deterioration of the performance of the antenna array. A considerable amount of work has been done to analyze the effect of amplitude and phase errors on the performance of the antenna array [1–3]. Generally, it will lead to the beam sidelobe rising and the beam direction mismatching. In tradition, many algorithms of the calibration of amplitude and phase errors have been applied to solve these problems [4–6]. In this paper we analyze the effect of the amplitude and phase errors from a different point of view. The impact of the number of elements on the beam direction in the presence of the amplitude and phase errors has been analyzed. The analysis results show that the performance of the antenna array can be improved by increasing the number of the array elements.

This paper is organized as follows. In Sect. 2, a uniform linear array model has been presented. And in Sect. 3, the impact of the number of the array elements on the beam direction in the presence of the amplitude and phase errors has been analyzed. In Sect. 4, MATLAB simulation has been shown. In Sect. 5, the conclusion has been presented.

2 Problem Formulation

Consider a signal source impinging on an N-element uniform linear array (ULA). Ideally, the beam pattern is given by

$$F_o(x) = \sum_{n=1}^{N} a_n e^{j(n-1)x} \tag{1}$$

where a_i is the amplitude weighting of element i.

$$x = 2\pi d(\sin\theta - \sin\theta_0)/\lambda \tag{2}$$

where θ_0 is the desired beam direction. When the presence of the amplitude and phase errors is considered, the beam pattern becomes

$$F(x) = \sum_{n=1}^{N} (a_n + \Delta a_n) e^{j\Delta\varphi_n} e^{j(n-1)x} \tag{3}$$

where Δa_i and $\Delta\varphi_i$ are two zero mean random variables and independent with each other. Their variances is σ_a and σ_φ, respectively. Obviously, we can get the maximum value of $F(x)$ when $x = 0$, if there are no amplitude and phase errors.

The antenna power pattern can be written as

$$P(x) = |F(x)|^2 = F(x) \cdot F^*(x)$$
$$= \sum_{n=1}^{N} (a_n + \Delta a_n) e^{j\Delta\varphi_n} e^{j(n-1)x} \cdot \sum_{t=1}^{N} (a_t + \Delta a_t) e^{-j\Delta\varphi_t} e^{-j(t-1)x}$$
$$= \sum_{n=1}^{N} \sum_{\substack{t \neq n \\ t=1}}^{N} (a_n + \Delta a_n)(a_t + \Delta a_t) e^{j(\Delta\varphi_n - \Delta\varphi_t)} e^{j(n-t)x} + \sum_{n=1}^{N} (a_n + \Delta a_n)^2. \quad (4)$$

We can get the beam direction by analyzing $P(x)$.

3 Problem Analysis

In this section, the impact of the array elements on the beam direction in the presence of the amplitude and phase errors will be analyzed. Assuming that $a_i = 1$ $i = 1, 2, \cdots, N$, (4) can be written as

$$P(x) = \sum_{n=1}^{N} (1 + a_n^2) + (1 + \Delta a_1)\{(1 + \Delta a_2) e^{j(\Delta\varphi_1 - \Delta\varphi_2 - x)} + \cdots + (1 + \Delta a_N) \bullet$$
$$e^{j(\Delta\varphi_1 - \Delta\varphi_N + (1-N)x)}\} + (1 + \Delta a_2)\{(1 + \Delta a_1) e^{j(\Delta\varphi_2 - \Delta\varphi_1 + x)} + (1 + \Delta a_3) \bullet$$
$$e^{j(\Delta\varphi_2 - \Delta\varphi_3 - x)} + \cdots + (1 + \Delta a_N) e^{j(\Delta\varphi_2 - \Delta\varphi_N + (2-N)x)}\} + \cdots + (1 + \Delta a_N)\{(1 + \Delta a_1) \bullet$$
$$e^{j(\Delta\varphi_N - \Delta\varphi_1 + (N-1)x)} + (1 + \Delta a_2) e^{j(\Delta\varphi_N - \Delta\varphi_2 + (N-2)x)}$$
$$+ \cdots + (1 + \Delta a_{N-1}) e^{j(\Delta\varphi_N - \Delta\varphi_{N-1} + x)}\}. \quad (5)$$

Equation (5) can be transformed as follow

$$P(x) = 2(1 + \Delta a_1)\{(1 + \Delta a_2)\cos(\Delta\varphi_1 - \Delta\varphi_2 - x) + \cdots + (1 + \Delta a_N) \bullet$$
$$\cos[\Delta\varphi_1 - \Delta\varphi_N + (1-N)x]\} + 2(1 + \Delta a_2) \bullet \{(1 + \Delta a_3) \bullet$$
$$\cos(\Delta\varphi_2 - \Delta\varphi_3 - x) + \cdots + (1 + \Delta a_N) \bullet \cos[\Delta\varphi_2 - \Delta\varphi_N + (2-N)x]\}$$
$$+ \cdots + 2(1 + \Delta a_{N-1})(1 + \Delta a_N)\cos(\Delta\varphi_{N-1} - \Delta\varphi_N - x) + \sum_{n=1}^{N} (1 + a_n^2). \quad (6)$$

The maximum value of $P(x)$ has been evaluated based on the formula of $dP(x)/dx = 0$.

Apparently, we can get the maximum value of $P(x)$ when $x = 0$, if there are no amplitude and phase errors. Since $\Delta\varphi_m - \Delta\varphi_n + (m - n)x$ is comparatively small, we can get

$$dP(x)/dx = 2\big(1 + \Delta a_1\big)\big\{\big(1 + \Delta a_2\big)\big(\Delta\varphi_1 - \Delta\varphi_2 - x\big) + \cdots + \big(N - 1\big)\bullet$$
$$\big(1 + \Delta a_N\big)\big[\Delta\varphi_1 - \Delta\varphi_N + \big(1 - N\big)x\big]\big\} + 2\big(1 + \Delta a_2\big)\big\{\big(1 + \Delta a_3\big)\bullet$$
$$\big(\Delta\varphi_2 - \Delta\varphi_3 - x\big) + \cdots + \big(N - 2\big)\big(1 + \Delta a_N\big)\big[\Delta\varphi_2 - \Delta\varphi_N + \big(2 - N\big)x\big]\big\}$$
$$+\cdots + 2(1 + \Delta a_{N-1})\big(1 + \Delta a_N\big)\big(\Delta\varphi_{N-1} - \Delta\varphi_N - x\big) = 0. \tag{7}$$

Substituting (2) into (7) and solving (7), the beam direction in the presence of the amplitude and phase errors can be expressed as follow

$$\theta = \arcsin[f(N, \Delta a_m, \Delta\varphi_m)/g(N, \Delta a_m) + \sin\theta_0] \tag{8}$$

where

$$f(N, \Delta a_m, \Delta\varphi_m)/g\big(N, \Delta a_m\big) = \frac{\lambda}{2\pi d}\left\{\sum_{m=1}^{N}(1 + \Delta a_m)\bullet\right.$$
$$\left.\left[\sum_{t=1}^{N}(t - m)(1 + \Delta a_t)\right]\Delta\varphi_m/\left[\sum_{n=1}^{N-1}n^2\sum_{t=1}^{N-n}(1 + \Delta a_t)(1 + \Delta a_{t+n})\right]\right\}. \tag{9}$$

The relationship has been established between the number of elements and the beam direction. It is clearly shown that the amplitude errors have little impact on the beam direction. If $\Delta\varphi_m = 0$, in other words, there are only amplitude errors, (8) can be transformed as follow

$$\theta = \arcsin\{0 + \sin\theta_0\} = \theta_0. \tag{10}$$

Equation (10) shows that the actual beam direction is equal to the desired value that we want. This result has been proved in the numerical simulation later in Sect. 4 by Fig. 1. It is straightforward to prove that the order about N of the function $f(N, \Delta a_m, \Delta\varphi_m)$ is greater than that of the function $g(N, \Delta a_m)$. Consequently, we can get

$$\lim_{N\to\infty}[f(N, \Delta a_m, \Delta\varphi_m)/g(N, \Delta a_m)] = 0. \tag{11}$$

This result has also been proved in the numerical simulation by Figs. 3 and 4.

Because the amplitude errors have little impact on the beam direction, it is necessary to analyze the impact of the phase errors alone. Without loss of generality, an assume has been made, that is $\Delta a_i = 0$. Equation (8) can be written as follows if there are no amplitude errors

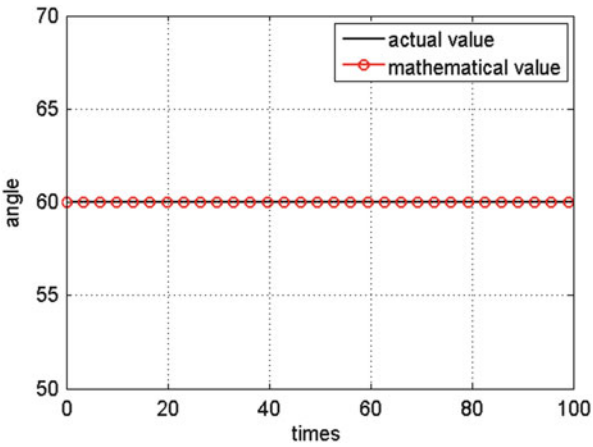

Fig. 1 Comparison of the mathematical beam direction and the actual value in the presence of amplitude only

$$\theta = \arcsin[A + \sin\theta_0]. \tag{12}$$

Considering A as the directing offset, we can express it as

$$\widetilde{A} = A/60 = \frac{\left(N^2+N\right)\sum_{m=1}^{N}(\Delta\varphi_m/\pi) - 2N\sum_{m=1}^{N} m(\Delta\varphi_m/\pi)}{2N^5+5N^4-5N^2-2N}. \tag{13}$$

Calculating the absolute value of (13), we can get an inequation as follow

$$0 \le \left|\widetilde{A}\right| \le \frac{\left(N^2+N\right)\sum_{m=1}^{N}|\Delta\varphi_m/\pi| + 2N\sum_{m=1}^{N} m|\Delta\varphi_m/\pi|}{2N^5+5N^4-5N^2-2N}. \tag{14}$$

Extending (14), the upper limit of $\left|\widetilde{A}\right|$ can also be transformed as

$$0 \le \left|\widetilde{A}\right| \le \frac{\left(N^2+N+2N^2\right)\sum_{m=1}^{N}|\Delta\varphi_m/\pi|}{2N^5+5N^4-5N^2-2N}. \tag{15}$$

Since $\Delta\varphi_m$ is assumed to be the random variable followed the uniform distribution of $(-90°, 90°)$, the maximum value of $|\Delta\varphi_m/\pi|$ can be defined as 1/2. Moreover, the non-zero minimum value of $|\Delta\varphi_m/\pi|$ is assumed to be $\Delta\delta$. Calculating the

limitation of $\left|\widetilde{A}\right|$ while N tends to infinity, an equation is obtained and shown as follow

$$\begin{aligned}
&\lim_{N\to\infty}\left\{\frac{\left(N^2+N+2N^2\right)\sum_{m=1}^{N}|\Delta\varphi_m/\pi|}{2N^5+5N^4-5N^2-2N}\right\}\geq\lim_{N\to\infty}\left\{\frac{\left(N^2+N+2N^2\right)N\Delta\delta}{2N^5+5N^4-5N^2-2N}\right\}=0\\
&\lim_{N\to\infty}\left\{\frac{\left(N^2+N+2N^2\right)\sum_{m=1}^{N}|\Delta\varphi_m/\pi|}{2N^5+5N^4-5N^2-2N}\right\}\leq\lim_{N\to\infty}\left\{\frac{\left(N^2+N+2N^2\right)N/2}{2N^5+5N^4-5N^2-2N}\right\}=0.
\end{aligned}\tag{16}$$

Combining (13) with (16), the limitation of $|A|$ can be achieved when the number of elements tends to infinity based on *the approximation theorem*:

$$\lim_{N\to\infty}|A|=0\Rightarrow\lim_{N\to\infty}\theta=\theta_0.\tag{17}$$

Equation (17) shows that the directing deviation in the presence of the phase errors tends to zero when the number of elements tends to infinity. Consequently, the actual beam direction is equal to the ideal value.

In fact, the optimum value of beam direction can be obtained as long as the number of elements is large amount.

4 Numerical Simulation

A ULA with elements ranged from 10 to 100 and inter-element spacing $d = 0.5\lambda$ is used in the simulations. To consider the worst case, it is assumed that the amplitude errors follow the Gaussian Distribution with variance of 0.09 and the phase errors follow the Uniform Distribution from -90° to 90°. To prove the result (10), 100 times independent repeat trials have been made. From Fig. 1, we can see that the actual beam direction is always equal to the ideal one. Actually, the amplitude errors have little impact on the beam direction.

Since approximation exits in the derivation, there must be deviation between the actual beam direction in the presence of amplitude and phase errors and the mathematical value calculated from (8) and (12). To make comparison, both of

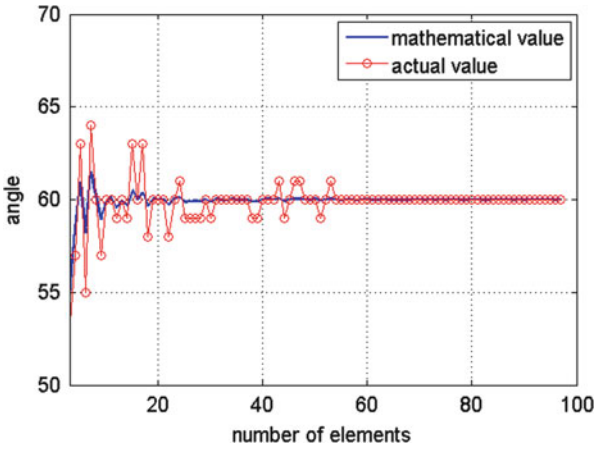

Fig. 2 Comparison of the mathematical beam direction and the actual value in the presence of only phase errors

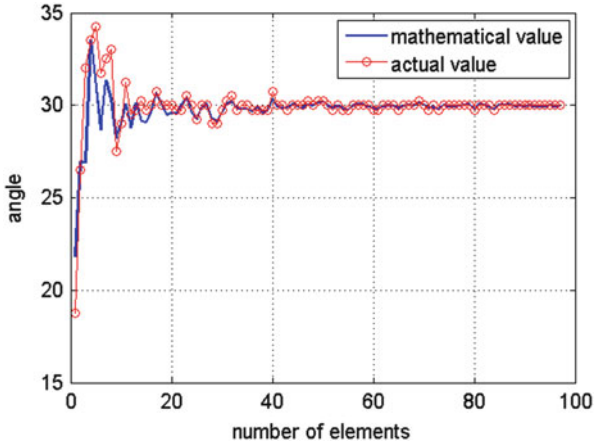

Fig. 3 Comparison of the mathematical beam direction and the actual value in the presence of both amplitude and phase errors and the ideal beam direction is 30°

them have been simulated. It is shown from Fig. 2, apparently, that small deviation exits between the mathematical value and the actual one in the presence of phase errors only. Both of them tend to the ideal beam direction as long as the number of elements is more than 60.

Moreover, the case that both the amplitude and phase errors are considered is simulated. Figures 3 and 4 show that the beam deviation is larger than the case in Fig. 2. This is caused by the amplitude errors. However, the directing deviation tends to be zero as long as the number of elements is large enough. This phenomena is the same with the one in Fig. 2.

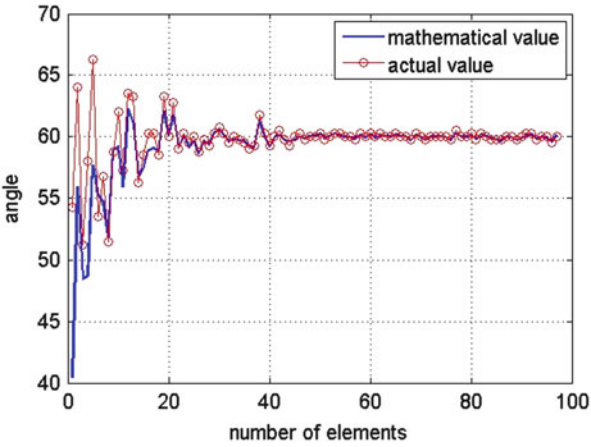

Fig. 4 Comparison of the mathematical beam direction and the actual value in the presence of both amplitude and phase errors and the ideal beam direction is 60°

5 Conclusion

The relationship between the number of elements and the pointing direction has been presented in the presence of amplitude and phase errors. It has been proved mathematically that the offset of beam direction in the presence of phase errors tends to zero with the number of elements increasing to infinity. Simulations have been done and verified the mathematical derivation. The actual pointing direction, it is shown in the presence of not only phase errors but amplitude and phase errors, can be ideal with the number of elements more than 60.

References

1. Li Y, Huang X, Zhimin Z (2005) Effect of amplitude and phase errors on the performance of uniform circular array. Rad Sci Tech 3(2):123–127
2. Zhang S, Ding S, Sun G, Liu Z (2008) Effect of amplitude-phase errors on digital beamforming system. Mod Electron Tech 2008:7–10
3. Chen S, Deng W, Dan Q, Wang X (1996) The effect of the phase deviation of array elements beam direction in active antenna array. J Harbin Inst Tech 28(4):63–66
4. Hongfeng Qin, Jianguo Huang, Qunfei Zhang (2001) An array calibration method for amplitude and phase errors based on the subspace approaches, Computer Engineering and Applications, DOI: 1002-8331-(2001)19-0055-03
5. Jinghua Gu, Guang Liang, Jinpei Yu, Wenbin Gong (2009) Channel calibration of amplitude-phase error of DBF transmitter based on maximum likelihood estimation, International Conference on Networks Security, Wireless Communications and Trusted Computing, Wuhan, Hubei, 25–26 April, 2009.
6. Wang D, Ye G, Li C, Ying W (2009) A calibration algorithm for amplitude and phase errors in uniform linear array. Rad Sci Tech 4:289–295

Virtual Transmitting-Receiving Beamforming Approach to Achieving Narrower Mainlobe for MIMO Radar by Tapering

Yubing Jiang, Wei Zhang, Huiyong Li, and Cheng Luo

Abstract An innovative approach is introduced to form narrower mainlobe of virtual transmitting-receiving beamforming by transmitting orthogonal coding waveforms from the antenna elements and digitally processing of their echoes at the receiver. The benefits such as increased angle resolution and increased Doppler resolution of MIMO radar mainly depend on the sparse arrays without the adverse effects of sidelobes. However, due to the actual limitation, such as room limitation for airborne, cost or other factors, we have to set the array in dense arrays configuration. With the proposed amplitude taper approach, a narrower main beam can be achieved with dense arrays configuration after virtual transmitting-receiving beamforming which can improve the performance of detecting slow moving target. The signal-to-noise ratio (SNR) loss of tapering is also discussed.

Keywords MIMO radar • Narrower mainlobe • Beamforming

1 Introduction

Multiple-input and multiple-output (MIMO) radar has been a very active area for several years. In recent literatures [1–5], MIMO radars have been shown to provide a number of potential benefits as compared with conventional radar, such as increased angle resolution, increased Doppler resolution, sharper airborne radar clutter notches, etc. MIMO radars emit orthogonal signals, the orthogonal signals can be extracted at the receiver by a matched filterbank, and the extracted signals can be used to improve the spatial resolution for clutter. The phase differences caused by different transmitting antennas along with the phase differences caused by different receiving antenna can form a new virtual array steering vector. With

Y. Jiang (✉) • W. Zhang • H. Li • C. Luo
School of Electronic Engineering, University of Electronic Science and Technology of China, Chengdu, Sichuan 611731, P. R. China
e-mail: jiangyubing.eva@163.com

B. Zhang et al. (eds.), *The Proceedings of the Second International Conference on Communications, Signal Processing, and Systems*, Lecture Notes in Electrical Engineering 246, DOI 10.1007/978-3-319-00536-2_61,

judiciously designed antenna positions, one can create a very long, critically sampled, array steering vector at a small number of antennas [6]. Just as pointed in [7], the fundamental advantage of coherent MIMO radars is that they enable the use of sparse arrays without the adverse effects of sidelobes.

However, due to room limitation, there is no enough room for sparse arrays configuration, especially for airborne radar application. Secondly, with sparse arrays configuration, the array elements can't be used by the transmitting array and receiving array at the same time, so the cost will rise. In this paper, we only consider the dense arrays configuration, i.e., the transmitting array and receiving array use the same antennas, the spacing between the transmitting antennas and receiving antennas are half of wavelength. The goal of our work is achieving narrower mainlobe than traditional beamforming [8].

The rest of the paper is organized as follows. In Sect 2, the concept of MIMO radar will be briefly reviewed. In Sect. 3, firstly, the beamforming technique and traditional MIMO radar synthesized beamforming will be briefly reviewed. Then, we formulate narrower beamforming approach of the MIMO radar with dense packed array; the signal-to-noise ratio (SNR) loss is also discussed. Finally, Sect. 4 concludes the paper.

2 MIMO Radar Signal Mode

The assumed MIMO radar system geometry is shown in Fig. 1.

As illustrated in Fig. 1, the transmitting antennas are the same with the receiving antennas, such as azimuth angle θ and elevation angle φ. There are N_T transmitting elements with uniform space d_T, and N_R receiving elements with uniform space d_R. The receiving antennas are collocated with transmitting antennas meaning that monostatic MIMO radar configuration is used. At each transmitter, a coherent processing interval consists of L pulses, and the signals are assumed to be orthogonal to each other. The radar platform travels at velocity v. In this paper, we assume $N_R = N_T = N$, $d_T = d_R = d = \lambda/2$, where λ is the wavelength. In each pulse repetition interval (PRI) T_r, the system will transmit a waveform set.

$$\mathbf{s}(t) = [s_1(t), s_2(t), \ldots, s_{N_T}(t)]^T \tag{1}$$

$s_{n_t}(t)$ ($n_t = 1, 2, \ldots, N_T$) is the transmitting signal from the n_tth element, they are orthogonal to each other. We define the transmitting steering vector, receiving steering vector and Doppler vector in (2), respectively.

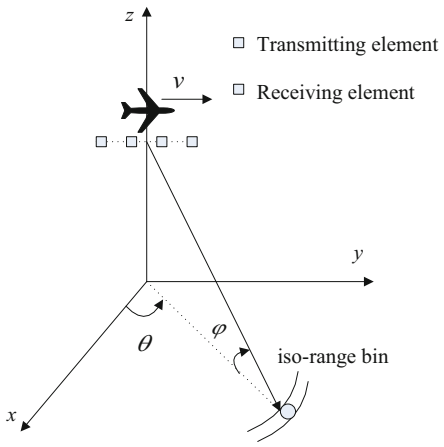

Fig. 1 MIMO radar geometry

$$\begin{aligned}\mathbf{v}_T(\theta) &= \left[1, e^{j2\pi\gamma f_s}, \ldots, e^{j2\pi\gamma(N_T-1)f_s}\right]^T \\ \mathbf{v}_R(\theta) &= \left[1, e^{j2\pi f_s}, \ldots, e^{j2\pi(N_R-1)f_s}\right]^T \\ \mathbf{v}_D &= \left[1, e^{j2\pi f_d}, \ldots, e^{j2\pi(L-1)f_d}\right]^T\end{aligned} \tag{2}$$

Each received signal is processed for all of the transmitted waveforms, we employ $\mathbf{s}^H$ as the filter bank in the receivers, and if the iso-range ring is divided in the cross-range dimension into $N_C (N_C \gg N_T N_R L)$ clutter patches, then the discrete form of the clutter data from the lth pulse is

$$\mathbf{x}_l = stack(\mathbf{X}_l) = stack\left(\mathbf{Y}_l \mathbf{s}^H\right) = \sum_{i=1}^{N_C} \xi(\theta_i) e^{j2\pi(l-1)f_{d,i}} \mathbf{v}_R(\theta_i) \bigotimes \mathbf{v}_T(\theta_i) \tag{3}$$

Where $\mathbf{Y}_l = \sum_{i=1}^{N_C} \xi(\theta_i) e^{j2\pi(l-1)f_{d,i}} \mathbf{v}_R(\theta_i) \mathbf{v}_T^T(\theta_i)\mathbf{s}$, and $\bigotimes$ means Kronecker product. With $f_{d,i} = 2vT_r \sin\theta_i \cos\varphi/\lambda$, and $f_{s,i} = d_R \sin\theta_i \cos\varphi/\lambda$. Generally, $\xi(\theta_i)$ can be modeled as a zero-mean independent complex Gaussian random variable with the variance of σ_i^2. Then we can stack the total clutter snapshot of the pulses in a vector form:

$$\mathbf{x} = stack(\mathbf{X}) = \sum_{i=1}^{N_C} \xi(\theta_i) \mathbf{v}_D(\theta_i) \bigotimes \mathbf{v}_R(\theta_i) \bigotimes \mathbf{v}_T(\theta_i) \in C^{N_T N_R L \times 1} \tag{4}$$

3 Narrower Mainlobe Beamforming Approach

The orthogonal signals of MIMO radar can be extracted at the receiver by a matched filterbank, the extracted signals can be used to improve the spatial resolution for clutter. The $N_T N_R$-length array steering vectors are equivalent to the steering vectors that would result from a spatial convolution of the transmitting and receiving phase centers providing an augmentation of the conventional array steering vectors.

Without losing generality, we assume that only an equally-spaced linear array is considered for beamforming. The digital filter coefficient vector $\mathbf{w}$ is selected as

$$\begin{aligned}\mathbf{w} &= \kappa \mathbf{s}_0^* = \kappa\left(\mathbf{v}_R(\theta_0) \bigotimes \mathbf{v}_T(\theta_0)\right)^* = \left(\kappa_1 \mathbf{v}_R^*(\theta_0)\right) \bigotimes \left(\kappa_2 \mathbf{v}_T^*(\theta_0)\right) \\ &= \mathbf{w}_R \bigotimes \mathbf{w}_T \end{aligned} \tag{5}$$

Where $\kappa = \kappa_1 \kappa_2$, they are all constants, $\mathbf{w}_T$ is the digital filter coefficient vector of virtually transmitting beamforming, and $\mathbf{w}_R$ is the weighting of receiving beamforming. With the optimum filter in (5), we can get the virtual antenna gain through the virtual transmitting-receiving beamforming

$$\begin{aligned}|G(\theta, \theta_0)| &= |\mathbf{w}^T(\theta_0)\mathbf{s}(\theta)| = \left|(\mathbf{w}_R \bigotimes \mathbf{w}_T)^T (\mathbf{v}_R(\theta) \bigotimes \mathbf{v}_T(\theta))\right| \\ &= \kappa \left| \sum_{n=1}^{N_R} e^{-j2\pi f_{s,0}} \mathrm{e}^{j2\pi f_{s,i}} \right| \left| \sum_{n=1}^{N_T} e^{-j2\pi\gamma f_{s,0}} \mathrm{e}^{j2\pi\gamma f_{s,i}} \right| \end{aligned} \tag{6}$$

Which has the form of a discrete Fourier transform (DFT), and ^{H} denotes the Hermitian operation. The virtual transmitting-receiving beamforming of MIMO radar can be viewed as the product of DFT of two square waveforms. From Fourier theory, the main lobe of the transform is widened. To make it clear, we rewrite the signal after matched filter in MIMO radar receiver as a matrix as

$$\mathbf{v}_R \bigotimes \mathbf{v}_T^T = \begin{bmatrix} 1 & e^{jf_s} & \cdots & e^{j(N-1)f_s} \\ e^{jf_s} & e^{j2f_s} & & e^{jNf_s} \\ \cdots & \cdots & & \cdots \\ e^{j(N-1)f_s} & e^{jNf_s} & \cdots & e^{j(2N-1)f_s} \end{bmatrix} \tag{7}$$

Where $\gamma = d_T/d_R = 1$, For the example we considered in this paper, i.e., dense array configuration.

From the properties of DFT, the main lobe of square waveform is narrower than the triangle waveform with the same length. Intuitively, we can set an inverse-weight process.

The inverse-weighting matrix corresponding to (7) is given by

$$\mathbf{D} = \begin{bmatrix} N & \cdots & \frac{N}{N-1} & 1 \\ \cdots & \cdots & \cdots & \cdots \\ \frac{N}{N-1} & \cdots & \frac{N}{3} & \frac{N}{2} \\ 1 & \cdots & \frac{N}{2} & N \end{bmatrix} \tag{8}$$

Define $\mathbf{d} = stack\ (\mathbf{D})$, where $stack\ (\cdot)$ is the stacking operator. Then the total digital filter coefficients vector corresponding to the virtual transmitting-receiving beamforming is $\mathbf{w}_{new} = \mathbf{w} \bigodot \mathbf{d}$. If a taper or windows is employed, there is a loss in SNR since the weight vector $\mathbf{w}_{new}$ is no longer perfectly matched to the expected signal $\mathbf{s}$.

It is straightforward to calculate this loss in SNR as follows. We define the virtual transmitting-receiving taper efficiency ratio, η_{eff}, as the ratio of the tapered output SNR (SNR_{tap}) to the optimal SNR (SNR_{opt}). For the tapered case, $\mathbf{w}_{new} = \mathbf{s}_0^* \bigodot \mathbf{d}$, where to insure the unity gain constrain $\mathbf{w}_{new}^H \mathbf{w}_{new} = 1$, $vec(\mathbf{t})$ must satisfy

$$\mathbf{w}_{new}^{'} \mathbf{w}_{new} = \left(\mathbf{s}_0 \bigodot \mathbf{s}_0^*\right)^H \left(\mathbf{d}^* \bigodot \mathbf{d}\right) = [\,1 \quad \ldots \quad 1\,]\left(\mathbf{d}^* \bigodot \mathbf{d}\right) = \|\mathbf{d}\|_2^2 = 1 \tag{9}$$

Where $\|\mathbf{d}\|_2$ denotes the usual Euclidean vector norm. The definition of η_{eff} is given as the following:

$$\eta_{eff} = \frac{SNR_{tap}}{SNR_{opt}} = \frac{\left|\mathbf{w}_{new}^T \mathbf{s}_0\right|^2}{N^2} = \frac{\left|\left(\mathbf{s}_0^* \bigodot \mathbf{s}_0\right)^H \mathbf{d}\right|^2}{N^2} = \frac{\|\mathbf{d}\|_1^2}{N^2} \tag{10}$$

Where $\mathbf{s}_0$ is the expected signal, $\|\mathbf{d}\|_1^2$ denotes the -norm.

For the 4-element virtual transmitting-receiving beamforming, $\|\mathbf{d}\|_1 = 3.537$, which when substituted into (10) yields $\eta_{eff} = 0.7819$ (-1.0685 dB). We note that with the number of elements increase, η_{eff} will degrade, this is illustrated in Fig. 2.

From Fig. 2, we note that with number increase, the degrading rate of η_{eff} will slow down. There is a tradeoff between the benefits from narrow mainlobe and SNR gain loss. The narrow beam can be used to improve angle resolution, increased Doppler resolution, weak the clutter from mainlobe competes with target. We can still use the Dolph-Chebyshev window function as

$$\mathbf{w}_{new} = \mathbf{w} \bigodot \mathbf{d} \bigodot \left(\mathbf{w}_{ch,N} \bigotimes \mathbf{w}_{ch,N}\right) \tag{11}$$

We named (11) as Method1. We can make a change of Dolph-Chebyshev window function which can be well suppressed the sidelobe. $\mathbf{w}_{ch,2N-1}$ is the weights of Dolph-Chebyshev window function with $2N - 1$ points, then extend it

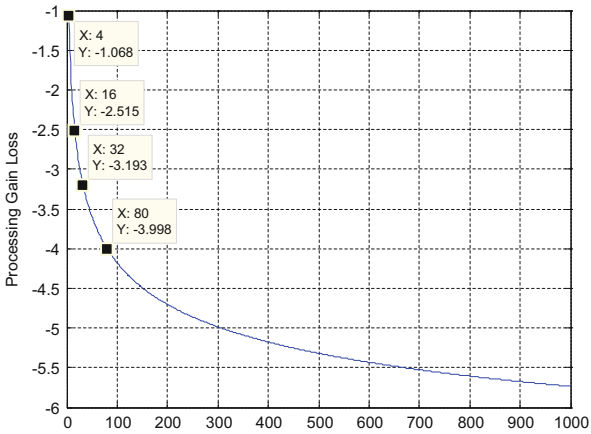

Fig. 2 Illustration of η_{eff} egrades with the number of transmitting or receiving elements increase

to N^2 points, the output of matched filter with the same phase will have the same weight of Dolph-Chebyshev window function.

$$\mathbf{w}_{ch,N^2} = \left[\mathbf{w}_{ch,2N-1}(1), \cdots, \mathbf{w}_{ch,2N-1}(N), \cdots, \mathbf{w}_{ch,2N-1}(N), \cdots, \mathbf{w}_{ch,2N-1}(2N-1)\right]^T \tag{12}$$

We named (12) as Method2. Then Method1 can be given as

$$\mathbf{w}_{new} = \mathbf{w} \bigodot \mathbf{d} \bigodot \mathbf{w}_{ch,N^2} \tag{13}$$

Where $\mathbf{w}$ is defined in (4). We can get the virtual antenna gain as

$$|G(\theta, \theta_0)| = \left|\mathbf{w}_{new}^T(\theta_0)\mathbf{s}(\theta)\right| \tag{14}$$

The narrower mainlobe which we would get through using the proposed Taper method may bring superiorities, such as improved angular resolution, increased Doppler resolution, sharper airborne radar clutter notches.

4 Simulated Results

Consider a four-element array is used in transmitter and receiver, i.e., $N_T = N_R = N = 8$, $d_T = d_R = d = \lambda/2$, θ_0 =0o. The carrier frequency f_0 is 1.2 GHz, pulse repeat frequency (**PRF**) is 2,000 Hz. $M = 64$ pulses will be transmitted in one coherent processing interval (CPI). The radar travels at $v = 125$ m/s. The input SNR for one antenna and one pulse is -5 dB, CNR is 45 dB. The beampattern

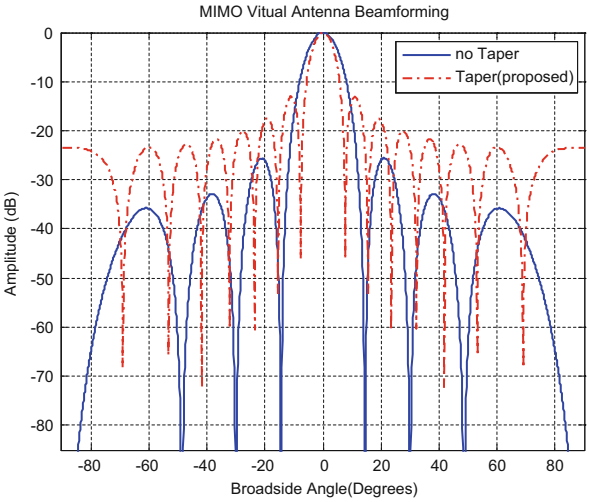

Fig. 3 The beampattern comparison with the proposed Taper method and without proposed Taper

without Dolph-Chebyshev window is showed in Fig. 3. For convenience, the outputs of beamforming are normalized.

From Fig. 3, it can be seen that, through the amplitude taper, the mainlobe is narrower than the virtual transmitting-receiving beamforming without amplitude taper.

We will make a comparison among the three transmitting-receiving beampatterns corresponding to two kinds of generating weights of Dolph-Chebyshev window in (13), (11) and the Phased Array(PA) radar which uses Dolph-Chebyshev window only in receiving beamforming. The beampattern comparison for Dolph-Chebyshev window methods corresponding to (13), (11) and the PA radar with 30-dB Dolph-Chebyshev window is showed in Fig. 4.

From Fig. 4, it is worth to note that the sidelobe of Dolph-Chebyshev window is not being suppressed effectively, this is due to the shape of window function has been change. We can also see that the sidelobe of Dolph-Chebyshev window Method2 has been suppressed effectively. Due to the virtual transmitting-receiving, the sidelobe has been well suppressed. For PA radar, due to the consideration of maximal power transmitting, the Dolph-Chebyshev window is only used in receiving beamforming, the sidelobe is well suppressed but has wider mainlobe width.

5 Summary and Conclusions

We propose an amplitude taper approach which can get narrower mainlobe, improve the detection performance for slow moving target which is an important aspect of modern airborne radar. Such weighting may improve the clutter suppression performance to a remarkable degree. The proposed virtual transmitting-

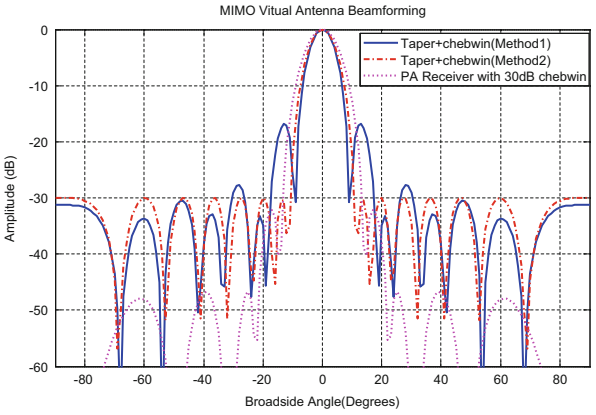

Fig. 4 The beampattern comparison for Dolph-Chebyshev window function Method1, Method2 and Phased Array

receiving beamforming with tapering approach can also be used other beamspace STAP algorithms.

Acknowledgment The authors would like to thank the anonymous reviewers and the associate editor for the insightful comments and suggestions. This work was supported partly by the China Postdoctoral Science Foundation under Contract number 2012M520077, and by the Fundamental Research Funds for the Central Universities of China under Contract number ZYGX2012J018.

References

1. Bliss DW, Forsythe KW (2003) Multiple-input multiple-output (MIMO) radar and imaging: degrees of freedom and resolution. Proc Asilom Conf Signal Syst Comput 1:54–59
2. Forsythe KW, Bliss DW (2005) Waveform correlation and optimization issues for MIMO radar. Proc Asilom Conf Signal Syst Comput 1:1306–1310
3. Rabideau DJ, Parker P (2003) Ubiquitous MIMO multifunction digital array radar. Proc Asilom Conf Signal Syst Comput 1:1057–1064
4. Rabideau DJ (2009) Non-adaptive multiple-input, multiple-output radar techniques for reducing clutter. IET Rad Son Navig 3(4):304–313
5. Fuhrmann DR, San Antonio G (2008) Transmit beamforming for MIMO radar systems using signal cross-correlation. IEEE Trans Aerospace Electron Syst 43(3):171–186
6. Chun-Yang Chen, Vaidyanathan PP (2006) Beamforming issues in modern MIMO Radars with Doppler. Signals, Systems and Computers, 2006. ACSSC '06, pp: 41–45.
7. Forsythe KW, Bliss DW (2009) MIMO radar: concepts, performance enhancements, and applications. In: Li J, Stoica P (eds) MIMO radar signal processing. Wiley, New York, NY
8. Deng H, Himed B (2009) A virtual antenna beamforming (VAB) approach for radar systems by using orthogonal coding waveforms. IEEE Trans Antenn Propag 57(2):425–435

CFAR Detection Method in Multi-target Environments for Foreign Object Debris Surveillance Radar

Jing Wu, Hong Wang, Xuelian Yu, Xuegang Wang, and Meng Zhao

Abstract Detection of weak targets in heavy ground clutter is the key issue for Foreign Object Debris (FOD) surveillance radar on airport runways. Since of "target-masking" effect, traditional CFAR detection algorithms cannot detect FOD in multi-target environments effectively. To solve these problems, a trimmed-mean clutter-map CFAR method based on order-statistics is proposed in this paper. First, multi-target echo model of Frequency Modulation Continue Wave (FMCW) radar on airport runways is established. Then, several of the largest samples in reference window are discarded and the remaining ones are averaged as the clutter-level estimation to tolerate interfering targets. In order to obtain a stationary detection threshold to reduce false alarm probability, clutter-map cells are updated scan-by-scan in time domain. At last, simulations verify effectiveness of this proposed method.

1 Introduction

FOD (Foreign Object Debris) usually refers to a fixed small object located on airport runways that has capacity to damage aircraft. The FOD surveillance system mainly uses radar monitoring technology to detect and locate targets [1]. SCR (Signal-to-Clutter Rate) of FOD surveillance radar lower than others, because the length of runway is generally about 3,000 m while FOD is only between 3 and 20 cm and erection height of antennas (typically 2 m) is limited due to airport security requirements [2], FOD surveillance radar should detect weak targets in heavy clutter effectively. The "target-masking" effect occurs when there are several interfering targets in adjacent range units. In this paper, we focus on CFAR (Constant False Alarm Rate) detection in multi-target environments.

J. Wu (✉) • H. Wang • X. Yu • X. Wang • M. Zhao
Department of Electronic Engineering, University of Electronic Science and Technology of China, Chengdu 611731, P. R. China
e-mail: dingqing19880225@sina.com

B. Zhang et al. (eds.), *The Proceedings of the Second International Conference on Communications, Signal Processing, and Systems*, Lecture Notes in Electrical Engineering 246, DOI 10.1007/978-3-319-00536-2_62,

CFAR is used to achieve stable detection threshold in spite of intensity fluctuation of clutter and interfering targets. Either Cell-Averaging CFAR or Ordered-Statistics CFAR is only appropriate to situations that clutter fluctuates smoothly in adjacent range cells [3,4]. Traditional Nitzberg clutter-map CFAR uses a digital filter to update background level estimation at each scan; however, it will result in a sharp increase of detection threshold so that "target-masking" effect occurs in multi-target environments [5,6]. To solve these problems, this paper proposes a Trimmed-Mean Clutter-Map CFAR (TM-CM-CFAR) method based on order-statistics. In this case, several of the largest samples in a reference window needed to be trimmed to tolerate interfering targets and average of remaining ones is the clutter-level estimation.

2 Principle of FOD Surveillance Radar

In order to detect FOD in heavy clutter effectively, FMCW (Frequency Modulation Constant Wave) radar system has been used to obtain high range resolution. The principle block diagram of FOD surveillance radar is provided in Fig. 1.

The transmitted signal from FM generator is

$$S_T(t) = A\cos\left[2\pi\left(f_0 t + \frac{1}{2}\mu t^2\right) + \phi\right] \quad \left(-\frac{T}{2} < t < \frac{T}{2}\right) \tag{1}$$

Where, ϕ is an initial phase, f_0 is the center frequency, B is the signal bandwidth, T is the time period and $\mu = B/T$ represents the slope of frequency modulation. Normally, we can assume that there are I FOD targets, radial distance of each FOD is $R_i (i = 1, 2, \cdots, I)$, delay of each echo is τ_i and $\tau_i = 2R_i/c$, where c is the speed of light. Thus, the total target echo is sum of a number of sinusoidal signals and can be expressed as

$$S_R(t) = \sum_{i=1}^{I} B_i \cos\left\{2\pi\left[f_0(t-\tau_i) + \frac{1}{2}\mu(t-\tau_i)^2\right] + \phi + \Delta\varphi_i\right\} \tag{2}$$

Where, $\Delta\varphi_i$ is the phase shift of each echo. As shown in Fig. 1, $S_T(t)$ is the local oscillation signal and $S_R(t)$ enters the mixer too. After band-pass filtering of the mixer's output, a beat signal is achieved as

$$S_B(t) = \sum_{i=1}^{I} C_i \cos\left[2\pi\left(\mu\tau_i t + f_0\tau_i - \frac{1}{2}\mu{\tau_i}^2\right) - \Delta\varphi_i\right] \tag{3}$$

Obviously, each frequency component of beat signal is $f_i = \mu\tau_i = (B/T) \cdot (2R_i/c)$. Deal with Fourier transformation, different spectrum positions corresponding to

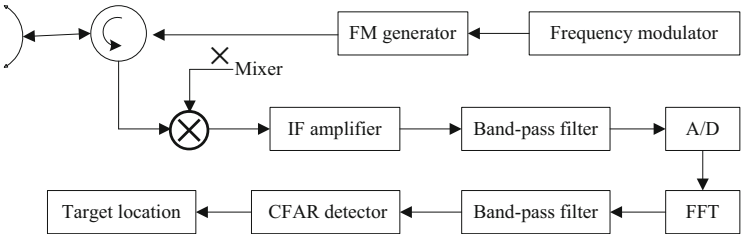

Fig. 1 Structure of FOD surveillance radar

different frequency components of the beat signal are used to estimate distance of FOD targets. However, FOD target is small and the intensity distribution of each target is not uniform, hence, CFAR is needed to locate FOD targets in heavy clutter accurately. That's to say, a target will be declared present if the amplitude of spectrum exceeds its estimation which is yielded by a CFAR detector and absent otherwise. If a target is detected, we can take its frequency in the spectrum and calculate its range.

3 TM-CM-CFAR Algorithm Based on FOD Detection

The statistical characteristics of clutter in different ground environments for Millimeter Wave (MMW) radar had been analyzed in paper [7], and the envelope distribution of backscattering signals can be approximated by Rayleigh law if scatters are enough. Moreover, for FOD surveillance radar, land clutter fluctuates dramatically in spatial domain while more smoothly in time domain [8]. Therefore, clutter level should be estimated by clutter-map and updated scan-by-scan to realize CFAR detection. The architecture of TM-CM-CFAR detector is shown in Fig. 2.

Where, $t_l(i,j)$ is the sample of the (i,j)th azimuth-range unit in clutter map cells and also the input of CFAR detector at the lth scanning period while $z_l(i,j)$ is output of the square law detector. If $t_l(i,j)$ only contains clutter without target signal, $z_l(i,j)$ is subjected to exponential distributed. Steps of TM-CM-CFAR are as follows.

Step 1. The clutter map cells are divided by a rectangular sliding reference window and the tested unit is not involved in clutter level estimation. There are M units in the reference window and are fed into a ranker which outputs are in ascending order according to amplitude. The largest m samples are removed and the remaining $M - m$ samples are sorted as

$$v_l^1(i,j) \le v_l^2(i,j) \le \cdots v_l^k(i,j) \le \cdots \le v_l^{M-m}(i,j) \tag{4}$$

Clearly, $\{v_l^k(i,j)\}$ doesn't satisfy the requirement of IID (Independent and Identically Distributed) each other so that a linear transformation is needed.

Step 2. Linear transformation is used to make $\{v_l^k(i,j)\}$ meet IID, just as

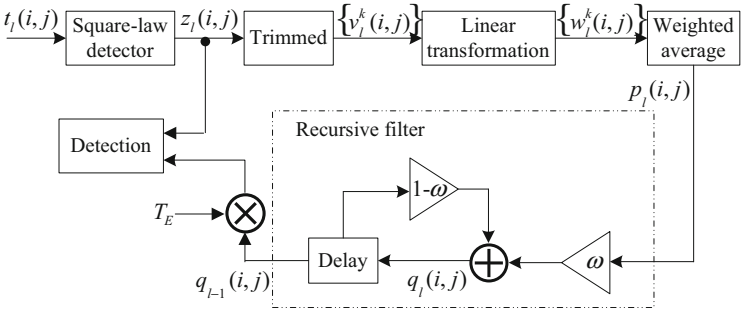

Fig. 2 Architecture of TM-CM-CFAR detector

$$\begin{aligned} w_l^1(i,j) &= M\left[v_l^1(i,j)\text{-}v_l^0(i,j)\right] \\ w_l^2(i,j) &= (M-1)\left[v_l^2(i,j)\text{-}v_l^1(i,j)\right] \\ &\vdots \quad\quad \vdots \quad\quad \vdots \\ w_l^{M-m}(i,j) &= (m+1)\left[v_l^{M-m}(i,j) - v_l^{M-m-1}(i,j)\right] \end{aligned} \tag{5}$$

Where, $v_l^0(i,j) \equiv 0$ and $\{w_l^k(i,j),\ k = 1, 2, \cdots, M - m\}$ are statistically IID and also exponentially distributed. We can define the clutter power is λ, so the probability distribution function of $\{w_l^k(i,j)\}$ is

$$f(w) = \frac{1}{\lambda}\exp\left(-\frac{w}{\lambda}\right) \tag{6}$$

Step 3. When the largest samples are been trimmed, the weighted average of others is the clutter power estimation of the tested unit. The weighted coefficients are defined as

$$\eta_k = \begin{cases} \dfrac{1}{M} & (k=1) \\ \dfrac{M-m-k+1}{(M-m)\cdot(M-k+1)} & (k \neq 1) \end{cases} \tag{7}$$

Thus, we can achieve the estimation of $z_l(i,j)$ is

$$p_l(i,j) = \frac{1}{M-m}\sum_{k=1}^{M-m} v_l^k(i,j) = \sum_{k=1}^{M-m} \eta_k w_l^k(i,j) \tag{8}$$

Step 4. Since the land clutter from runways changed with the scanning of antennas,

a recursive filter is designed to obtain stable detection threshold to control false alarm. As shown in Fig. 2, ω is a recursive factor and output of the filter is

$$\begin{aligned} q_l(i,j) &= \omega p_l(i,j) + (1-\omega) q_{l-1}(i,j) \\ &= \omega p_l(i,j) + \omega(1-\omega) p_{l-1}(i,j) + \cdots + \omega(1\text{-}\omega)^{l-1} p_1(i,j) \\ &= \omega \sum_{n=0}^{l-1} (1-\omega)^n p_{l-n}(i,j) \end{aligned} \tag{9}$$

Natural of MGF (Moment Generating Function) shows that the MGF of multiple IID random variables shall be equal to the product of each other. Hence, the MGF of $q_l(i,j)$ is

$$\begin{aligned} M_q(u) &= \prod_{n=0}^{l-1} M_p[\omega(1-\omega)^n u] = \prod_{n=0}^{l-1} \prod_{k=1}^{M-m} M_w[\omega(1-\omega)^n \eta_k u] \\ &= \prod_{n=0}^{l-1} \prod_{k=1}^{M-m} [1 + \eta_k \omega(1-\omega)^n \lambda u]^{-1} \end{aligned} \tag{10}$$

Step 5. Decision criteria of TM-CM-CFAR detector is

$$z_l(i,j) \underset{H_0}{\overset{H_1}{\gtrless}} T_E q_{l-1}(i,j) \tag{11}$$

Where, $z_l(i,j)$ is the tested statistic, T_E is a threshold factor and $T_E q_{l-1}(i,j)$ is the detection threshold. It represents by H_1 when a target is detected and by H_0 otherwise. Since $T_E q_{l-1}(i,j)$ is a random variable, the false alarm probability is

$$P_f = E_q\{P[z_l(i,j) \geq T_E q_{l-1}(i,j) | H_0]\} = M_q(u)\Big|_{u=\frac{T_E}{\lambda}}$$

$$= \prod_{n=0}^{l-1} \left\{ \left[1 + \frac{1}{M} T_E \omega (1-\omega)^n \right]^{-1} \times \prod_{k=2}^{M-m} \left[1 + \frac{M-m-k+1}{(M-m)\cdot(M-k+1)} T_E \omega (1-\omega)^n \right]^{-1} \right\} \tag{12}$$

In fact, TM-CM-CFAR can be equivalent to Nitzberg clutter-map CFAR when $m = 0$. Figure 3 gives the computed T_E with various iteration factors and the number of trimmed cells when $P_f = 10^{-5}$.

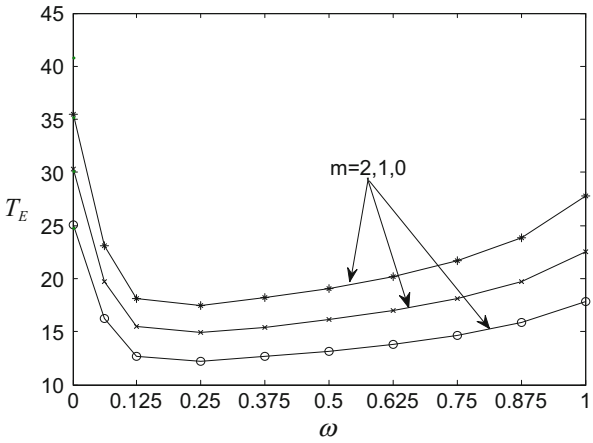

Fig. 3 Threshold factor versus iteration factors

4 Analysis of Simulation

To verify effectiveness of the proposed CFAR algorithm for FOD detection, we carry out simulation in this section with two interfering targets. Since it is difficult to obtain a close-form expression of the amplitude distribution of echoes in multi-target situations, Monte-Carlo simulation has been used to obtain detection probability with different simulation parameters. Relevant parameters of FMCW radar are listed in Table 1.

The range resolution is $\Delta R = c/2B \approx 55.6cm$. Hence, the total number of azimuth-units and range-units are 60 and 540 respectively. The simulation parameters of targets are listed in Table 2.

To better observe simulation results, Fig. 4a only gives a partial enlarged view of detection results of the 15th azimuth-unit which is the orientation of targets when $P_f = 10^{-5}$, $M = 32$, $L = 20$, $\omega = 0.2$ (where, L is the number of scanning cycle times in a loop). The solid line with circles is samples of echo, the dashed line is the detection threshold for the number of trimmed samples is 0 and the solid line is the threshold for the number of trimmed samples is 2. Obviously, if there are two interfering targets in the reference window, detection of two censored samples can be better than ones or zero censored samples, where the threshold in the vicinity of the target range-unit has a raised and cannot detect low power targets accurately.

Figure 4b indicates the detection probability for $M = 32$, $L = 20$, $\omega = 0.25$. Obviously, if there are two interfering targets in reference window, the best performance of detector only in the case that the number of trimmed samples is equal to the number of interfering targets. Figure 4c shows that different iteration factor corresponding to different detection probability. P_d will be reduced with increase of ω. In fact, it is clearly from Fig. 4, when $\omega < 0.125$, threshold coefficient T_E has a drastic increase and P_d increases naturally. Moreover, the smaller ω is, the longer accumulation time is. So ω usually be set between 0.125 with 0.25. Figure 4d indicates that P_d will be increased with L only when $L < 10$.

Table 1 Relevant parameters of FMCW radar

Center frequency	10 GHz	Scanning angle	(-30°,30°)
Bandwidth	100 MHz	Sampling frequency	4 MHz
Width of runway	300 m	Modulation frequency	1 ms

Table 2 Simulation parameters of targets

	Main target	Interfering target 1	Interfering target 2
Distance of target	125 m	123 m	127 m
Coordinate position	(15,225)	(15,220)	(15,230)
SCR	10 dB	12 dB	8 dB

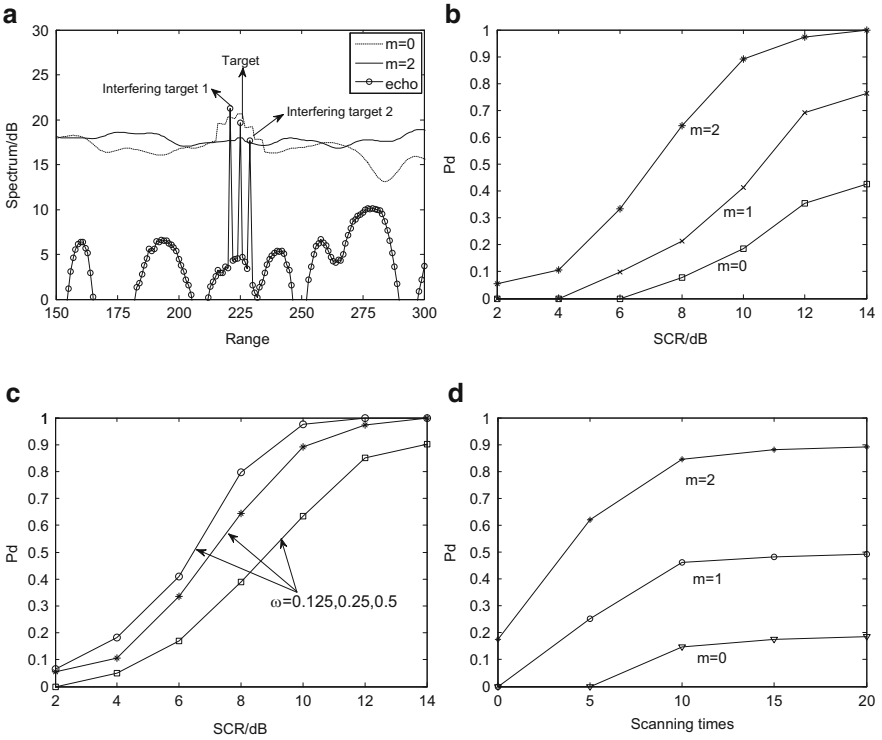

Fig. 4 Simulations of detection performance with different parameters. (**a**) A larger view of figure for target detection (**b**) P_d with $L = 20$, $\omega = 0.25$ for different m. (**c**) P_d with $L = 20$, $m = 2$ for different ω (**d**) P_d with $\omega = 0.25$, $SCR = 10dB$ for different L

Therefore, in order to obtain a stable threshold and the detection time as little as possible, L can be limited between 10 with 20.

5 Conclusions

In order to overcome the "target-masking" effect and detect FOD target effectively, the trimmed-mean clutter-map CFAR has been discussed. In the sliding reference window, several of the biggest samples are trimmed and others are averaged as clutter-level estimation. This detector reduces the probability of interfering targets involve the clutter-level estimation to improve the detection probability. Besides, the recursive filter is used to achieve stable detection threshold. Compared with conventional CFAR algorithm, TM-CM-CFAR not only has better anti-interference performance, but can also achieve higher detection probability with low SCR in multi-target environments. It has important significance for FOD detection on airport runways.

Acknowledgments The authors are very thankful to the anonymous referees for their careful reading, helpful comments and constructive suggestions of this paper. This work was supported by the Key Program of National Natural Science Foundation of China under Grant No. 61139003, the National Key Technology Research and Development Program of the Ministry of Science and Technology of China under Grant No. 2011BAH24B05 and the Fundamental Research Funds for the Central Universities under Grant No. ZYGX2012J027.

References

1. Civil Aviation Administration of China (2009) FOD prevention manual. CAAC, Beijing
2. Wang H, Wang X (2011) Key technologies of radar for foreign objects debris detection on runways. Chin J Telecomm Eng 51(2):7–10
3. Tom A, Viswanathan R (2008) Switched order statistics CFAR test for target detection. 2008 I. E. radar conference, Rome, Italy, 26–30 May, 2008. Inst. of Elec. and Elec. Eng. Computer Society, US, pp 1–5
4. Zattonta B, Farrouki A, Barkat M (2007) Automatic censoring detection using binary clutter-map estimation for non-gaussian environments. IEEE International Conference on Signal Processing and Communications, Dubai, United Arab Emirates, 24–27 November, 2007. Inst. of Elec. and Elec. Eng. Computer Society, US, pp 205–208
5. Nitzberg R (1986) Clutter-map CFAR analysis. J IEEE Trans AES 22:419–421
6. He Y, Guan J (2011) Radar target detection and CFAR processing. Tsinghua University Press, Beijing, pp 36–67
7. Kulemin GP, Tarnavsky EV, Goroshk EA (2004) Land backscattering for millimeter wave radar. Proceedings of International Conference on Modern Problems of Radio Engineering Telecommunication and Computer Science, Lviv-Slavsko, Ukraine, February 24–28, 2004. Lvivska Polytechnica, Ukraine, p 138–141
8. Chen M, Xie J, Zhang W (2008) Study on simulation on signal processing system of space surveillance radar. Proceedings of the International Conference on Radar, Adelaide, SA, Australia, 2–5 September, 2008. Inst. of Elec. and Elec. Eng. Computer Society, US, pp 474–477

Time-Shifted Synchronization Applied into the Low-Cost Chaos Radar

Lianjun Sun, Jinfeng Hu, Cheng Luo, and Zishu He

Abstract In this paper we firstly report a design of time-shifted synchronization aimed at the low-cost chaos radar. Based on the theory by Voss (Phys Rev E 61(5): 5115–5119, 2000), we adopt the first-order Taylor formula to make the delay parameter correspond to the system parameters which are resistors and capacitors of the chaotic circuit. So we can control time delay by adjusting the resistors and capacitors of chaotic system. And we prove that it is feasible to realize the time delay in analog domain of chaotic signal generated by the low-cost chaos radar without a variable delay line. It is so significant in taking the place of the delay devices in the engineering filed that the cost of ultra-wideband chaotic beam-forming radar can be decreased. The simulation results suggest that generalized synchronization is maintained over the entire chain length. Compared with the traditional methods bringing about the time delay by the phase shifter, this article's way only leads to a little attenuation. And the time delay can be controlled by adjusting the size of coupling parameters and the number of slave systems.

Keywords Chaos radar • Time-shifted synchronization • Wideband beam-forming

1 Introduction

The low-cost chaos radar with coherent reception was proposed in 2010. This radar uses chaotic signals with a matched filter which can work as a coherent receiver. It can be achieved by a simple RLC circuit. Several papers have proved this chaotic radar can measure range and velocity [1–4]. So it is a new milestone in the development of chaotic radar. If we can directly realize the time-delay of chaotic

L. Sun (✉) • J. Hu • C. Luo • Z. He
School of Electronic Engineering, University of Electronic Science and Technology of China, Chengdu 611731, China
e-mail: slj2007028@163.com

B. Zhang et al. (eds.), *The Proceedings of the Second International Conference on Communications, Signal Processing, and Systems*, Lecture Notes in Electrical Engineering 246, DOI 10.1007/978-3-319-00536-2_63,

signal in analog domain utilizing the synchronization character of chaos, doesn't it have a profound significance in ultra-wideband beam forming?

There are several conventional solutions which realize the time delay, such as the random signal radar [5] of the Pennsylvania University utilizes the delay lines, some phased array radars [6] put to use the phase shifter. Among these solutions there is a common shortcoming that these devices are expensive and complicated, and the phase shifter is just suitable for narrow-band signal.

In our work, we firstly report the time-shifted synchronization aimed at the low-cost chaos radar. We adopt the first-order Taylor formula to make the delay parameter correspond to the system parameters which are resistors and capacitors of the chaotic circuit. The simulation results show that it is feasible to directly realize the time delay in analog domain without a variable delay line. It's only a little attenuations compared with the phase-shifter way.

This paper is organized as follows: Sect. 2 introduces the principle of the low-cost chaos radar. Section 3 proposes the time-shifted synchronization theory [7] into the low-cost chaos radar. Section 4 presents the simulation results. Finally, conclusions are given in Sect. 5.

2 The Principle of the Low-Cost Chaos Radar

2.1 Signal Generation

The chaos signal with a matched filter can be generated by (1)

$$\begin{cases} \ddot{x} - 2\beta\dot{x} + \left(\omega^2 + \beta^2\right)(x - s) = 0 \\ \dot{x}(t) = 0 \Rightarrow s(t) = \mathrm{sgn}(x(t)) \end{cases} \tag{1}$$

where $\omega = 2\pi$, $\beta = \ln(1.9)$, and $\mathrm{sgn}(x) = \begin{cases} +1, x \geq 0 \\ -1, x < 0 \end{cases}$.

Figure 1a shows a typical waveform generated by (1). Figure 1b shows the corresponding phase-space projection.

2.2 Coherent Reception Using a Matched Filter

The echo signal $r(t) = x(t - \tau) + v(t)$ is a sequence of basis pulses, where $v(t)$ is the additive noise. A matched filter for $r(t)$ is defined as (2)

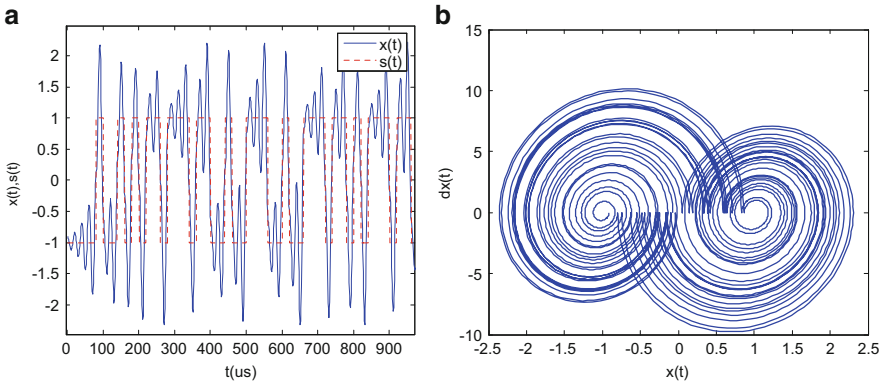

Fig. 1 (**a**) Typical waveforms of and obtained from (1). (**b**) Phase-space projection obtained from (1)

$$\begin{cases} \dot{z}(t) = \sum_{m=0}^{N-1} s_m \cdot \{r(t+m+1) - r(t+m)\} \\ \ddot{y}(t) + 2\beta\dot{y}(t) + \left(\omega^2 + \beta^2\right)\left(y(t) - z(t)\right) = 0 \end{cases} \tag{2}$$

where $y(t)$ is the matched filter output, $\omega = 2\pi$, $\beta = \ln(1.9)$, s_m is the polarity of each basis pulse and N is the number of basis pulses in $r(t)$.

The impulse response of the system with (2) is $h(t) = x(-t)$,so it is a matched filter for signals given by (1). The output of $x(t)$ via its matched filter is

$$y(t) = \int_{-\infty}^{+\infty} h(u)x(t-u)du = \int_{-\infty}^{+\infty} x(-u)x(t-u)du = R_{xx}(t) \tag{3}$$

As shown in (3), a signal's matched filter output is equivalent to its autocorrelation function in mathematical formula. So the system in (3) is a matched filter for $x(t)$ that can be used to achieve coherent reception.

3 The Time-Shifted Synchronization Theory Aimed at the Low-Cost Chaos Radar

In this section, we firstly apply the time-shifted synchronization theory into the low-cost chaos radar. Based on the theory by Voss, we adopt the first-order Taylor formula to make the delay parameter correspond to the system parameters which are resistors and capacitors of the chaotic circuit. So the two systems from Voss's theory, a "master" and a "slave," which are unidirectionally coupled via an easily controlled time-delay feedback in such a manner that the slave system predicts the

behavior of the master system. The contiguous systems are cascaded by coupling vectors.

According to (1) the chaotic signal generator, let's restate as follows:

$$\ddot{x} - 2\beta\dot{x} + \left(\omega^2 + \beta^2\right)(x - s) = 0 \tag{4}$$

where assume $\mathbf{x} = [x,x']^{\mathrm{T}} = [x_1,x_2]^{\mathrm{T}}$, (4) is equivalent to (5), it is the mathematical of the master system.

$$\begin{cases} \mathrm{d}x_1/\mathrm{d}t = x_2 \\ \mathrm{d}x_2/\mathrm{d}t = 2\beta x_2 - \left(\omega^2 + \beta^2\right)x_1 + \left(\omega^2 + \beta^2\right)s. \end{cases} \tag{5}$$

Assume $\mathbf{y}^1 = [y^1\ y^{1\prime}]^{\mathrm{T}} = [y_1^1,y_2^1]^{\mathrm{T}}$, according to the first-order Taylor formula a delay signal $y(t - \lambda) \approx y(t) - \lambda\dot{y}(t)$, so the mathematical of the slave system set as follows:

$$\begin{cases} \mathrm{d}y_1^1/\mathrm{d}t = y_2^1 + \mathbf{k_1}\left(\mathbf{x} - \mathbf{y}^1 + \lambda\dot{\mathbf{y}}^1\right) \\ \mathrm{d}y_2^1/\mathrm{d}t = 2\beta y_2^1\text{-}\left(\omega^2 + \beta^2\right)y_1^1 + \left(\omega^2 + \beta^2\right)s + \mathbf{k_2}\left(\mathbf{x} - \mathbf{y}^1 + \lambda\dot{\mathbf{y}}^1\right) \end{cases} \tag{6}$$

where $\mathbf{k}_1 = [k_{11},k_{12}]$, $\mathbf{k_2} = [k_{21},k_{22}]$ are the coupling vectors, λ is a tunable system parameter controlling delay time.

To simplify (6), set the parameter $k_{12} = k_{21} = 0$, so (6) is reduction to (7)

$$\begin{cases} \mathrm{d}y_1^1/\mathrm{d}t = y_2^1 + k_{11}\left(x_1 - y_1^1 + \lambda\dot{y}_1^1\right) \\ \mathrm{d}y_2^1/\mathrm{d}t = 2\beta y_2^1\text{-}\left(\omega^2 + \beta^2\right)y_1^1 + \left(\omega^2 + \beta^2\right)s + k_{22}\left(x_2 - y_2^1 + \lambda\dot{y}_2^1\right) \end{cases}. \tag{7}$$

The (7) is the truly slaver system, where system parameter $\omega = 2\pi, \beta = \ln(1.9)$, s is the sign function defined as (8)

$$\dot{y}^1(t) = 0 \Rightarrow s(t) = \mathrm{sgn}\left(y^1(t)\right) \tag{8}$$

To increase the time delay, we can also construct several slave systems which are cascaded one another by the coupling vector such as (9)

$$\begin{cases} \mathrm{d}y_1^m/\mathrm{d}t = y_2^m + k_{11}\left(y_1^{m-1} - y_1^m + \lambda\dot{y}_1^m\right) \\ \mathrm{d}y_2^m/\mathrm{d}t = 2\beta y_2^m\text{-}\left(\omega^2 + \beta^2\right)y_1^m + \left(\omega^2 + \beta^2\right)s + k_{22}\left(y_2^{m-1} - y_2^m + \lambda\dot{y}_2^m\right) \end{cases} \tag{9}$$

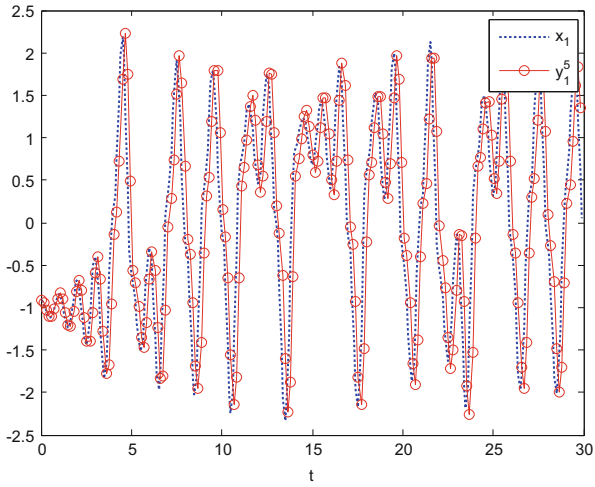

Fig. 2 The contrast of the master system's output (*blue dotted line*) and the fifth slave system's output (*red line* (labeled 'o'))

where the parameters ω and β are the same as (1), $m = 1, 2, 3, \cdots, M$, M is the number of slave systems, the sign function s is defined as (10)

$$\dot{y}^m(t) = 0 \Rightarrow s(t) = \mathrm{sgn}(y^m(t)) \tag{10}$$

4 Numerical Simulation Results

In order to verify the correctness and validity of the delay system model, this section gives the results from the numerical simulation by Matlab.

Set the Matlab parameters as follows:

The time step is $t = 0.01$;the delay time parameter $\lambda = -0.03$ ($\lambda < 0$, all the slave systems lag the master system); the initial value of the various systems are $[-0.9123, 0]^{\mathrm{T}}$;the coupling parameters $k_{11} = 2.1$, $k_{22} = 0.9$; the number of slave systems is $M = 5$.We do the simulation by the fourth order Runge-Kutta algorithm from Matlab and combining with (5) and (9).

Figure 2 shows that generalized time-shifted synchronization is maintained over the entire chain length despite several attenuations between the output of master system and the fifth slave system.

Figure 3 shows that phase-space projection of the fifth slave system, suggesting that the output is still chaotic. It is homologous with the master system's phase-space projection presenting by Fig. 1b.

Figure 4 shows that an enlarged view of the output of the master system with five slave systems, the master system's output anticipates the other systems. Each of the slave systems lags the preceding system by a bit of time units. Thus, y_1^1 follows x_1, y_1^2 follows y_1^1, etc. The chaotic waveform of all system's output are resemble but a little distortion in the form of amplitude. The error that the fifth slave system output's peak of wave exceeds the peak of the master system is about 0.2. In short, we can control the time delay by designing the number of slave systems.

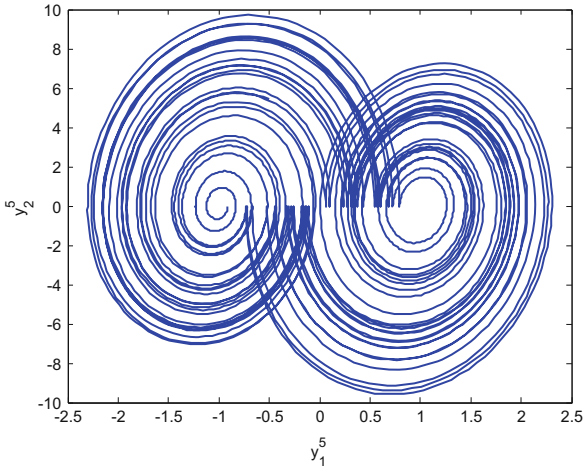

Fig. 3 The phase-space projection of the fifth slave system

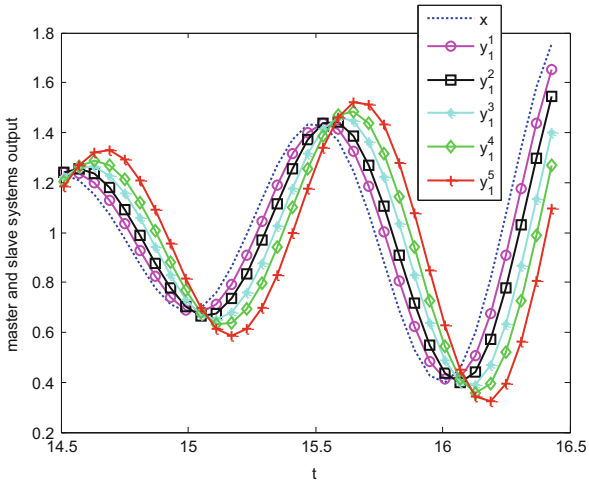

Fig. 4 The master system's output $x_1(t)$ (*blue dotted line*) and the other five slave systems' output y_1^m (the other formed *solid lines*)

Figure 5 shows that an enlarged view of the output waveforms of the fifth slave system in different values of λ, the output lags each other with the increasing of the absolute of λ. So we can also control the time delay by adjusting λ.

Figure 6 gives a distinct contrast about showing the same delay time, we separately employ the traditional solution which depends the phase shifter and the method of this article. We can obviously comprehend that the traditional

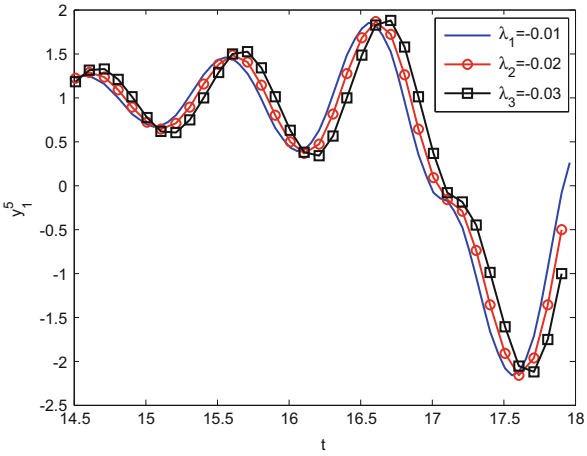

Fig. 5 The fifth slave system's output for $\lambda = -0.01$ (*blue line*), $\lambda = -0.02$ (*red line* (labeled 'o')), $\lambda = -0.03$ (*black line* (labeled *square*))

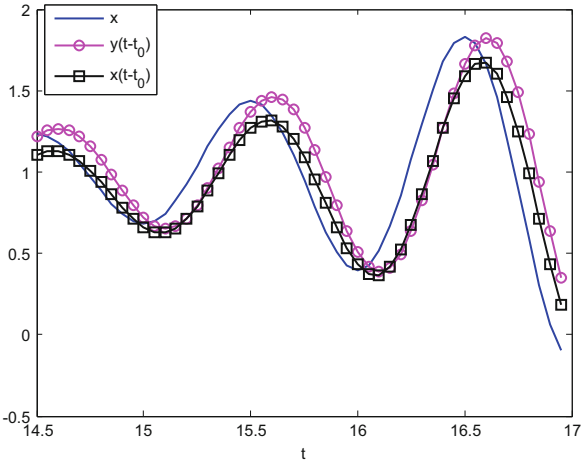

Fig. 6 The master system's output x (*blue line*) and the slave system' output $y(t - t_0)$ (*pink line* (labeled 'o')) between output $x(t - t_0)$ of the same delay time by phase shifter (*black line* (labeled *square*))

solution achieves the delay time by means of changing the phase of signal which leads to the bigger distortion of amplitude. The performance is far behind the method of this paper. It just may be suitable for narrow-band signal.

5 Conclusions

In this paper we firstly report the time-shifted synchronization aimed at the low-cost chaos radar. This way which realizes the time delay by the synchronization character of chaos is useful where a time delay or memory is needed but variable delay line technologies are expensive or impractical to the broadband signal. As a result, an adjustable lag or anticipation effect can be easily achieved, making the method simpler and more economical to implement in ultra-wideband beam forming.

Acknowledgements This work is supported by the National Natural Science Foundation of China (Grant Nos. 61101172, 61032010).

References

1. Corron NJ, Blakely JN, Stahl MT (2010) A matched filter for chaos. Chaos 20:023123
2. Blakely JN, Corron NJ (2010) Concept for low-cost chaos radar using coherent reception, Proc. of SPIE, Vol. 80211H-1, DOI: 10.1117/12.884688
3. Corron NJ, Stahl MT, Blakely JN (2010) Exactly solvable chaotic circuit, ISCAS Proc of IEEE, pp. 1356–1359, DOI: 10.1109/ISCAS.2010.5536943
4. Corron NJ, Blakely JN, Stahl MT (2010) A matched filter for communicating with Chaos. AIP Conf Proc 1339:25–35
5. ZhiXi L, Narayanan RM (2006) Doppler visibility of coherent ultraband random noise radar systems. IEEE Trans Aerospace Electron Syst 42(3):904–916. doi:10.1109/TAES.2006.248211
6. Dolfi D, Joffre P, Huignard JP et al (1996) Experimental demonstration of a phased-array antenna optically controlled with phase and time delays. Appl Opt 35(26):5293–5300
7. Corron NJ, Blakely JN, Pethel SD (2005) Lag and anticipating synchronization without time-delay coupling. Chaos 15:023110

High Squint SAR Imaging Using the Modified Range-Doppler Algorithm

Zhihao Mei, Youxin Lv, Jing Wu, and Meng Zhao

Abstract Based on the imaging geometry of squint mode, the characteristics of echoes based on four order approximate expressions in slow time domain in squint mode are analyzed in this paper. The conclusion that the influence of range walk is much larger than range bending in high squint mode is drawn. The traditional Range-Doppler algorithm is no longer suitable for high squint SAR imaging. Based on the conclusion a modified Range-Doppler algorithm suitable for high squint SAR imaging is derived in this paper. At first range walk is corrected in range frequency domain to make the coupling between range and azimuth small. After that, range compression, secondary range compression, azimuth compression and higher order phase correction are presented in the modified algorithm. Compared with the traditional Range-Doppler algorithm, the imaging results of simulation are presented to demonstrate the accuracy and validity of the proposed algorithms in high squint SAR imaging.

Keywords Synthetic aperture radar • High squint mode • Modified range-Doppler algorithm • Range walk

1 Introduction

Synthetic Aperture Radar is a kind of two-dimensional imaging sensor. Compared with the traditional range imaging sensor and the infrared imaging sensor, SAR has a huge advantage. It can work all-time, all-weather, gain high resolution image of the ground target similar to optical photograph in low-visibility weather conditions. Based on the orientation of azimuth beam, SAR has two kind of geometric model-positive mode and squint mode. The positive mode is relative simple and the

Z. Mei (✉) • Y. Lv • J. Wu • M. Zhao
University of Electronic Science and Technology of China (UESTC), Qingshuihe Campus, 2006 Xi Yuan Avenue, Western Hi-tech Zone, Chengdu 611731, P. R. China
e-mail: meizhihao@163.com

B. Zhang et al. (eds.), *The Proceedings of the Second International Conference on Communications, Signal Processing, and Systems*, Lecture Notes in Electrical Engineering 246, DOI 10.1007/978-3-319-00536-2_64,

complete algorithm like Range-Doppler algorithm and Chirp Scaling algorithm [1–3] are almost suitable for this mode. Squint mode is more complex than positive mode and the traditional algorithm is no longer suitable for this mode. We need to improve the traditional algorithm.

SAR obtains the two-dimensional signals of range and azimuth. Range cell migration correction is the most important part in high squint SAR imaging. The range cell migration concludes the range walk and range bending. In the positive mode, there is only the part of range bending. But there are two parts in squint mode. In high squint SAR imaging, range walk is much larger than range bending and range walk makes the coupling between range and azimuth seriously. That can lead to the defocusing and fuzzy of targets. So, correcting the range cell migration to realize the decoupling of two-dimensional signals is the key part in high squint SAR imaging [4–6].

2 Signal Analysis in Squint SAR Mode

The geometry of squint SAR is shown in Fig. 1. We assuming that platform fly along the X axis and the speed is v.Q is the point target in this geometry, its azimuth coordinate is X, r is the slant distance from the platform to the beam center on the ground, $R(t_a;r)$ is the instantaneous slant distance from the point target to the platform, θ is the squint angle.

$R(t_a;r)$ is instantaneous slant distance between ground targets and platform:

$$R(t_a;r) = \sqrt{r^2 + (vt_a - X)^2 - 2r(vt_a - X)\sin\theta} \tag{1}$$

Through Taylor series expansion, with fourth-order kept, we can get

$$R(t_a;r) = r - (vt_a - X)\sin\theta + \frac{\cos^2\theta}{2r}(vt_a - X)^2 + \frac{\sin\theta\cos^2\theta}{2r^2}(vt_a - X)^3 - \frac{\cos^2\theta(1 - 5\sin^2\theta)}{8r^3}(vt_a - X)^4 \tag{2}$$

$R_{RCM}(t_a)$ is the Range cell migration and we can know from (2) that

$$R_{RCM}(t_a) = -(vt_a - X)\sin\theta + \frac{\cos^2\theta}{2r}(vt_a - X)^2 + \frac{\sin\theta\cos^2\theta}{2r^2}(vt_a - X)^3 - \frac{\cos^2\theta(1 - 5\sin^2\theta)}{8r^3}(vt_a - X)^4 \tag{3}$$

$s(\tau)$ is the linear frequency modulation signal that radar transmits.

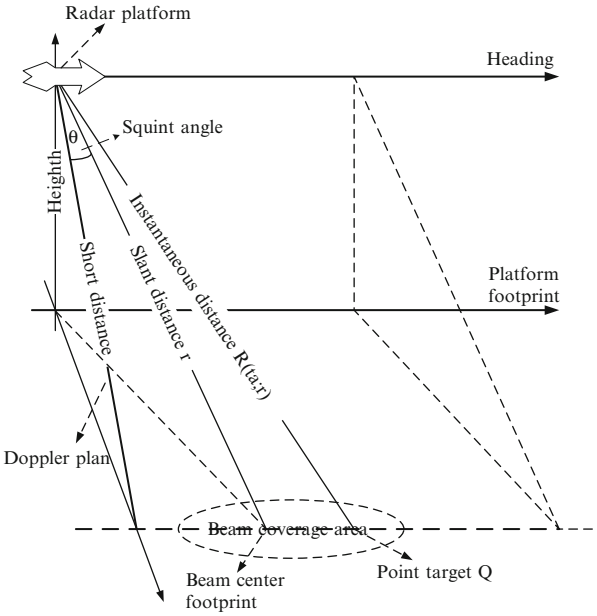

Fig. 1 Imaging geometry of squint mode

$$s(\tau) = A_0(\tau)\exp\left\{j2\pi f_c\tau + j\pi K_r\tau^2\right\} \tag{4}$$

The raw signal is backscattered by the ground targets to receiver and we can get the baseband echo signal.

$$s_r(\tau;t_a) = A_0\left(\tau - \frac{2R(t_a;r)}{C}\right)A_a(t_a)\exp\left\{-j\frac{4\pi}{\lambda}R(t_a;r)\right\}\exp\left\{j\pi K_r\left(\tau - \frac{2R(t_a;r)}{C}\right)^2\right\} \tag{5}$$

From (5), we can know that the variation of $R(t_a;r)$ can not only influence the phase of echo signal, but can also cause the coupling between range and azimuth.

3 Modified Range-Doppler Algorithm

The basic principle of traditional RD algorithm and modified RD algorithm is the same. It is to decompose the two-dimensional imaging into two one-dimensional. The processing diagram of modified Range-Doppler algorithm is shown in Fig. 2. The procedure concludes five steps: range walk correction; range compression; secondary range compression; azimuth compression and higher-order phase correction.

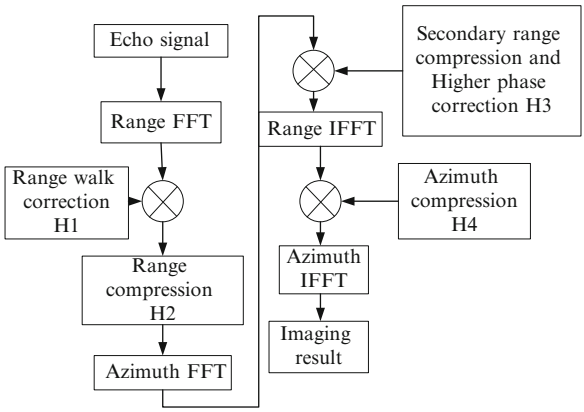

Fig. 2 Processing diagram of modified range-Doppler

The frequency signal in range domain can be obtained by performing FFT over the fast time.

$$s_1(f_r;t_a) = \exp\left\{-j\frac{4\pi}{C}(f_c+f_r)R(t_a;r)\right\}\exp\left\{-j\pi\frac{f_r^2}{K_r}\right\} \tag{6}$$

From (6), we can get the function expression of range walk correction.

$$H_1(f_r;t_a) = \exp\left\{j\frac{4\pi}{C}(f_r+f_c)\Delta R(t_a)\right\} \tag{7}$$

Wherein $\Delta R(t_a) = -vt_a \sin\theta$, the function of $H_1(f_r;t_a)$ is to offset the component of $vt_a \sin\theta$. Through this procedure, we can get the corrected represents of echo signal.

$$s_2(f_r;\bar{t}_a) = \exp\left\{-j\pi\frac{f_r^2}{K_r}\right\}\exp\left\{-j\frac{4\pi}{C}(f_r+f_c)R_1(\bar{t}_a)\right\} \tag{8}$$

$$R_1(\bar{t}_a) = r + X\sin\theta + \frac{v^2\cos^2\theta}{2r}\bar{t}_a{}^2 + \frac{v^3\sin\theta\cos^2\theta}{2r^2}\bar{t}_a{}^3 - \frac{v^4\cos^2\theta(1-5\sin^2\theta)}{8r^3}\bar{t}_a{}^4 \tag{9}$$

Given $\bar{t}_a = t_a - X/v$.

The range compression of modified algorithm is carried out through pulse compression. In fact, it is a problem of matched filtering. To make the calculation easy, we usually carry out this operation in frequency domain. From the represents (6), we can get the function expression of range compression.

$$H_2(f_r;\bar{t}_a) = \exp\left\{j\pi\frac{f_r^2}{K_r}\right\} \tag{10}$$

Through the operation of range compression and range walk correction, we can get the new represents of signal.

$$s_3(f_r;\bar{t}_a) = \exp\left\{-j\frac{4\pi}{C}(f_r + f_c)R_1(\bar{t}_a)\right\} \tag{11}$$

We can get the expression of 2-D frequency domain performing FFT over the slow time.

$$s_4(f_r;f_a) = \int s_3(f_r;\bar{t}_a)\exp\{-j2\pi f_a \bar{t}_a\}d\bar{t}_a \tag{12}$$

Using the principle of POSP [7], we can easily get the accurate expression of $s_4(f_r;f_a)$

$$s_4(f_r;f_a) = \exp\left\{j\left[\phi_0(f_a) + \phi_1(f_r;f_a)f_r + \phi_2(f_r;f_a)f_r^2\right]\right\} \tag{13}$$

Given

$$\phi_0(f_a) = -\frac{4\pi}{\lambda}r - \frac{4\pi X\sin\theta}{\lambda} - 2\pi\frac{X}{v}f_a + \frac{2\pi r}{\lambda f_{aa}^2}f_a^2 + \frac{4\pi v\sin\theta r}{\lambda^2 f_{aa}^4}f_a^3$$

$$\phi_1(f_r;f_a) = -\frac{4\pi r}{C} - \frac{4\pi X\sin\theta}{C} - \frac{2\pi r}{C f_{aa}^2}f_a^2 - \frac{8\pi v\sin\theta r}{\lambda C f_{aa}^4}f_a^3$$

$$\phi_2(f_r;f_a) = \frac{4\pi v r(\cos\theta f_{aa} + 3\sin\theta f_a)}{C^2 f_{aa}^4}f_a^2$$

$$f_{aa} = \frac{2v\cos\theta}{\lambda}$$

The expression of secondary range compression and higher order phase correction are

$$H_3(f_r;f_a) = \exp\left\{j\phi_2(f_r;f_a)f_r^2 + j\phi_{11}(f_r;f_a)f_r\right\} \tag{14}$$

$$\phi_{11}(f_r;f_a) = \frac{2\pi r}{C f_{aa}^2}f_a^2 + \frac{8\pi v\sin\theta r}{\lambda C f_{aa}^4}f_a^3 \tag{15}$$

Then performing IFFT over the range frequency domain and we can get the signal in Range-Doppler domain.

$$s_5(\tau;f_a) = \sin c\left\{\Delta f\left[\tau - \frac{2(r + X\sin\theta)}{C}\right]\right\}\exp\{j\phi_0(f_a)\} \tag{16}$$

Wherein Δf is the bandwidth of transmitted pulse.

The matched filtering function of azimuth can be expressed as

$$H_4(\tau;f_a) = \exp\left\{-j\left[\frac{2\pi r}{\lambda f_{aa}^2}f_a^2 + \frac{4\pi v\sin\theta r}{\lambda^2 f_{aa}^4}f_a^3 - \frac{4\pi r}{\lambda}\right]\right\} \tag{17}$$

Table 1 Radar simulation parameters

Signal bandwidth/MHz	33.3
Pulse width τ/μs	2.6
Center distance/m	5,000
Wavelength λ/m	0.03
Platform speed/m/s	200
Carrier frequency f_c/GHz	10

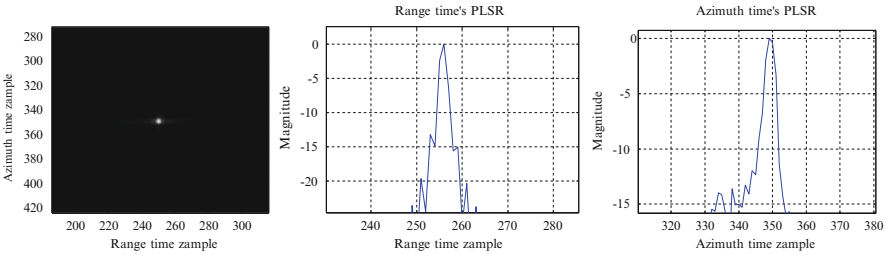

Fig. 3 The results of traditional RD algorithm of 10°

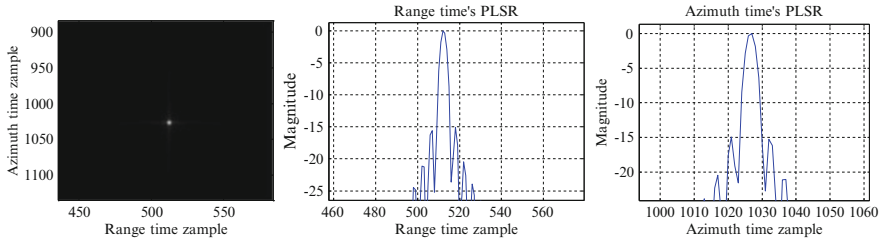

Fig. 4 The results of modified RD algorithm of 10°

After that, performing IFFT over the slow time can get the final signal expression in 2-D time domain. (Wherein Δf_a is the Doppler bandwidth.)

$$s_6(\tau;t_a)=\sin c\left\{\Delta f\left(\tau-\frac{2(r+X\sin\theta)}{C}\right)\right\}\sin c\left\{\Delta f_a\left(t_a-\frac{X}{v}\right)\right\}\exp\left\{-j\frac{4\pi}{\lambda}X\sin\theta\right\} \tag{18}$$

4 Simulation Results

In this section, the algorithm proposed in this paper is compared with the traditional algorithm. The radar parameters are given in Table 1.

The simulation results are shown as followed. Figure 3 shows the imaging result of traditional RD algorithm when the squint angle is 10. Figure 4 shows the imaging result of modified RD algorithm when the squint angle is 10. Figure 5 shows the imaging result of modified RD algorithm when squint angle is 50. Figure 6 shows the simulation results of four targets with modified RD algorithm.

The results indicate that the algorithm proposed in this paper works better than traditional algorithm when squint angle is large.

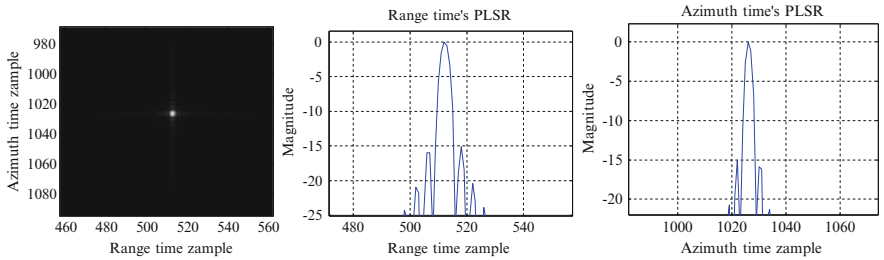

Fig. 5 The results of modified RD algorithm of 50°

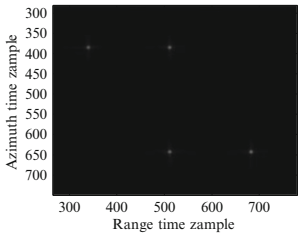

Fig. 6 The simulation results of four targets with modified RD algorithm

5 Conclusion

In this paper an efficient SAR imaging algorithm suitable for high squint is shown The proposed algorithm firstly constructs range walk correction function in range frequency domain to make the coupling small. Then range compression, secondary range compression, range bending correction and higher order phase correction are constructed in 2-dimension frequency domain. The point target simulation and processing results are presented to demonstrate the accuracy and validity of the proposed algorithm.

Acknowledgments The author thanks Pro. LV for his constant support. The discussions with his classmates were very important for his research.

References

1. Li Y (2008) The imaging techniques of Missile-borne synthetic aperture radar. NUDT, Changsha
2. Sun XB, Yeo TS (1999) Time-varying step-transform algorithm for high squint SAR imaging. IEEE Trans GRS 37(6):2668–2677
3. Han C, Wang J, Chen Z (2002) An algorithm for squint SAR imaging. J Electron Inform Tech 24(6):816–819
4. Bao Z, Xing M, Wang T (2005) Radar imaging technology. Electronic industry press, Beijing

5. Jing W, Zhang L, Xing M (2009) Algorithm for wide-swath spotlight SAR data processing. ACTA Electron Signal 37(3):470–475
6. Liu G, Liang D (2004) A suitable study of chirp scaling algorithm. Mod Rad 26(3):50–53
7. Neo YL, Wong FH, Cumming IG (2007) A two-dimensional spectrum for bistatic SAR processing using series reversion. IEEE Geosci Rem Sens Lett 4(1):93–96

A Two-Stage Target Detection Method for High-Resolution SAR Images

Yuchen Ge, Zongjie Cao, and Jilan Feng

Abstract Since that traditional CFAR is not suitable for high resolution target detection of SAR images, in this paper, a new two-stage target detection method is proposed. On the first stage, we extract ROIs from the SAR image based on the variance weighted information entropy (WIE). The rough ROIs are further processed with a series of methods, including false alarm exclusion, rectangular-completing and centroid alignment. On the second stage, for each ROI, we adopt a variational segmentation algorithm to accurately extract the target. In our experiment, in particular, we test the proposed method on a real SAR image, and its effectiveness is successfully demonstrated.

1 Introduction

Among applications of SAR images, the Automatic Target Recognition (ATR) system is of great importance. The target detection of SAR images, serving as the first stage of ATR systems, provides a basis for the validity of subsequent recognition.

By now, the most widely used detection algorithm is constant false alarm detection (CFAR). CFAR algorithms detect targets by pixel-wise threshold operation, in which the threshold is adaptively computed for each pixel according to the statistical property of pixels within a local window.

For Mean Level (ML) CFAR, some common used detectors are cell average (CA) [1], greatest of (GO), and smallest of (SO)-CFAR [2]. In order to improve the performance of the of ML class in the detection for multi-target situation, Rohling proposed order statistic (OS) CFAR [3], which brings derivatives like Generalized order statistics CFAR [4], Linearly Combined Order Statistics CFAR [5] and so

Y. Ge • Z. Cao (✉) • J. Feng
School of electronic engineering, University of Electronic Science and Technology of China, Chengdu, China
e-mail: zjcao@uestc.edu.cn

B. Zhang et al. (eds.), *The Proceedings of the Second International Conference on Communications, Signal Processing, and Systems*, Lecture Notes in Electrical Engineering 246, DOI 10.1007/978-3-319-00536-2_65,

on. When it comes to adaptive CFAR detection, we have Variably Trimmed Mean [6] Excision-CFAR Approach [7], etc.

However, since that CFAR is a kind of pixel level methods of target detection, it is not suitable for SAR images of high resolution in reality. First of all, the impact of speckle of high resolution SAR image is serious, which increases the probability of false alarm. Secondly, in high resolution SAR images, a target often occupies a lot of resolution cells, and is with multiple number of independent strong scattering. After CFAR detection, a target is likely to be composed of a plurality of distributed pixels that cannot form a connected region, which increases the probability of false alarm and the loss of information of structure and shape.

To overcome the problems of traditional CFAR algorithm, this paper proposes a target extraction algorithm of high-resolution SAR image based on 'location-segmentation' stages, importing the variance weighted information entropy (WIE) concept from infrared image to the detection stage of high resolution SAR image. This particular concept serves to measure the non-uniformity of infrared image. On first step, ROIs are obtained through an iterative algorithm based on WIE. Subsequently, we refine the ROI regions and filter out false alarms. At the second stage, the variational SAR image segmentation method is utilized to get ROI pieces. In the experiment part, we test this new algorithm with a real high resolution SAR image and a composed SAR image with transcendental position information and get result which confirms the validity.

The rest of the paper is organized as follows. Section 2 introduces SAR image positioning based on the variance weighted information entropy. In Sect. 3, the detailed steps of each detection stages are introduced and the variational segmentation method is introduced in Sect. 3.4. Section 4 is devoted to experimental results for SAR target extraction with the proposed techniques. Conclusions are drawn in Sect. 5.

2 SAR Image Positioning Based on the Variance Weighted Information Entropy

Graph entropy is a statistical form of characteristics, which reflects the average information of a figure. After getting the probability distribution of each gray level from an image, suppose that Pi represents the proportion of the gray value of pixel i. Then the one-dimensional graph entropy can be expressed as:

$$H = \sum_{i=0}^{255} pi\log pi \tag{1}$$

Although, one-dimensional graph entropy can depict the accumulation characteristics of gray level distribution, it can only represent global information rather

than the property of its spatial relationships [8, 9]. Hence, the variance WIE is introduced in this paper to deal with location processing.

2.1 The Variance Weighted Information Entropy (WIE)

The variance WIE was first applied to the detection of infrared images. Due to the fact that infrared objects with different radiation usually appear to have distinct gray value in real images, the variance WIE which has been proved to be a simple and effective quantitative description index for the complex degree of infrared image background [10], is introduced:

$$H(s) = -\sum_{s=0}^{255} (s-\overline{s})^2 \, Ps\log(Ps) \tag{2}$$

Where Ps is the probability of the gray-levels in the infrared image, and $\overline{s}$ is the mean intensity of the infrared image. Especially, When ps = 0, let Ps log (ps) = 0;

Considered that SAR images are also non-uniformed, in this paper, we import WIE to the detection stage of SAR images. We test the value of WIE from a real SAR image in its uniform area, area including the ups and downs, and area which contains the target. The result is shown in the picture below, which preliminary verified the conjecture (Fig. 1).

Analogous to the infrared image, the variance WIE of SAR images can be expressed as:

$$H(s) = -\sum_{s=0}^{255} (s-\overline{s})^2 \, Ps\log(Ps) \tag{3}$$

Where Ps is the probability of the gray-levels in the SAR image, and $\overline{s}$ is the mean intensity of the SAR image. Especially, When ps = 0, let Ps log (ps) = 0;

3 Target Extraction by Using a Location-Segmentation Strategy

Briefly, this average WIE algorithm based on 'positioning - segmentation' is reflected in a 'rough-refine' structure: First of all, extract block pieces which may contain the target though ROIs [11]. Then, refine the ROIs and conduct the variational segmentation. In fact, both rough extraction and refine adjustment process involve multiple iteration and image updating.

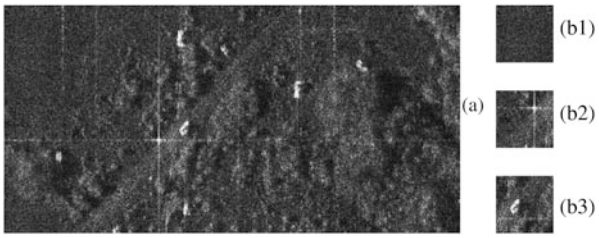

Fig. 1 The WIE value of a real SAR image in different areas (**a**): the original image; (**b1**): an uniform area, WIE = 0.58; (**b2**): an area including the ups and downs, WIE = 0.76; (**b3**): an area which contains the target, WIE = 0.82; the size of (**b1**), (**b2**), (**b3**) are all 100 × 100 pixels

As it mentioned before, one-dimensional graph entropy can only represent global information rather than the property of its spatial relationships. In order to obtain the target position information in the SAR image, we divide image into pieces, using global WIE as well as local WIE to reflect both information. Figure 2 shows the consolidated flowchart of the whole algorithm.

3.1 Pretreatment

Firstly, measure the size of the input image F and denote it by X × Y. Due to the fact that averaging segmentation method is proposed to the subsequent stage of ROI rough extractions which demands for the size of the image, we must intercept or expand the image boundary.

Suppose the closest power of 2 item for X is 2^M and closest power of 2 item for Y is 2^N, then we intercept or expand the image boundary into $2^M \times 2^N$.

After that, we get the global WIE from the pretreated image F through (3).

According to the conjecture of SAR images preliminary verified before, areas which contain target have a higher WIE value, so we divide the SAR image into blocks with certain size. Serving as potential blocks for ROIs, the seed block can be gained through getting its local WIE and a given threshold.

For images that contain multiple objectives, in order to get the complete ROIs through iteration. We need to set a global threshold Th:

$$Th = k \times meanEntropy \tag{4}$$

Where meanEntropy is the mean value of the variance WIE of the whole image, and k is a constant which defines the number of detected target. An inappropriate value of k will cause the phenomenon of false alarm or missed alarm. The experience range of k is [0.5, 3].

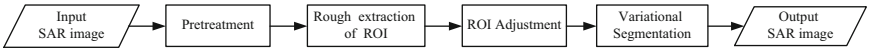

Fig. 2 Consolidated flowchart of the whole algorithm

3.2 Rough Extraction

After pretreatment, the size of the image F has been adjusted to $2^M \times 2^N$.

Step 1: Evenly divide image F into four Sub-regions of $2^{M-1} \times 2^{N-1}$.
Step 2: For sub-regions from 1 to 4, calculate their WIE value respectively.
Step 3: Label the sub-region with maximum WIE value, and denote its value into Hmax.
Step 4: Get the mean μ, and the standard deviation σ of the labeled sub-region in Step 3, so the sub-threshold Ht of it is measured as follows:

$$Ht = \mu + \alpha \times \sigma \tag{5}$$

Where α is a constant which defines the size of the seed block. If the value of α is too small, it may result in too small size ROIs, which cannot contain the entire targets, and a too big α may lead to too big size ROIs, which contains too much background. The experience range of α is [0.5, 3].

Step 5: Judge whether Hmax is greater than Ht, if Hmax $\geq$ Ht, then the labeled area in Step 3 is a seed block; if Hmax $<$ Ht, let m $=$ m/2, n $=$ n/2 and repeat Step 1–Step 4, until the maximal value in the variance weighted information SAR image satisfies Hmax $\geq$ Ht or m $=$ 2 or n $=$ 2.
Step 6: Judge the seed block attended by Step 5 again, if Hmax $>$ Th, the seed block is truly a ROI and then go to Step 7, otherwise, the ROI detection stops.
Step 7: The gray values of the pixels in the ROI are set to the mean gray value, and then go back Step 1 using the updated image.

3.3 ROI Adjustment

The averaging segmentation based on mean WIE can roughly determine the location of ROIs. However, due to the restrictions of itself, targets are often not completely included in the ROI or are not completely in the center of the ROI. To get an effective segmentation in next stages, this paper proposes a series of processing methods, including false alarm exclusion algorithm, rectangular-completing algorithm of ROI and centroid alignment algorithm to adjust the ROI.

First of all, a false-alarm exclusion algorithm based on the knowledge of target size is applied to all ROIs in the image. Among ROIs, whose area less than the setting value LEVEL will be ruled out. Next, we conduct a rectangular-completing algorithm of ROIs, adjusting ROI with irregular shape to a rectangle. Finally, let the

geometric center of the ROIs be aligned with the centroid of the corresponding area on the Image F.

In a 2-dimensional space the coordinate formula of the centroid is expressed particularly as:

$$r_m = \frac{\sum m_i r_i}{\sum m_i} \tag{6}$$

Where r $\in$ [x,y]; m_i denotes the weighting of pixel i and r_i denotes the coordinate of pixel i;

Let r_g be the geometric center of a piece of ROI, then the displacement distance v is as follow:

$$\mathrm{v} = r_m - r_g \tag{7}$$

Repeat the steps above until that v is less than a certain standard (2 units for instance).

3.4 Segmentation

Due to the impact of speckle noise, SAR image segmentation is known to be difficult. In this paper, we address this problem with a variational SAR image segmentation approach.

The variational image segmentation approach based on statistical model has shown its effectiveness in SAR image segmentation. It formulates the problem of SAR image segmentation as energy minimization. To deal with the effect of spackle noise, statistical models are often used to define the energy functional. In this paper, the Gamma model is used [12]. Hence, the statistical models of spackle noise is defined with mean μ_k and a number of looks l.

$$P_{\mathrm{k}}(u(x,y)) = \frac{l^{\mathrm{l}}}{\mu_k \Gamma(l)} \left(\frac{u(x,y)}{\mu_k}\right)^{l-1} e - \frac{lu(x,y)}{\mu_k}, k \in (i,b) \tag{8}$$

According to the Gamma model, the energy for ROI segmentation is defined as follows:

Let u: $\Omega \rightarrow$ R be the intensity SAR image, defined on $\Omega \subset \mathrm{R}^2$. u is assumed to be composed of target, denoted by Ω_i and background, denoted by Ω_b. That is $\Omega = \Omega_{\mathrm{i}} \cup \Omega_{\mathrm{b}}$. Both Ω_i and Ω_b is homogeneous regions that follow the Gamma distribution. The image data is therefore modeled by a mixed Gamma distribution.

The likelihood function of the probability model is:

$$L(\mathrm{u}\ (x,y)) = \prod_{(x,y)\in\Omega_i} p_i(u(x,y)) \prod_{(x,y)\in\Omega_i} p_t(u(x,y)) \tag{9}$$

Based on maximum likelihood criterion, we can realize the regional segmentation of Ω_i and Ω_b through the maximization of the likelihood function. And the maximization of likelihood function L equals to the minimization of −log (L). Therefore, we can take advantage of the statistical model of coherent speckle noise and define the energy functional as follows:

$$E_R(\Phi) = -\log(L) = -\sum_{k\in(i,b)} \sum_{(x,y)\in\Omega_k} (\log(p_k(u(x,y)))) \tag{10}$$

Utilizing the statistical model of an image, energy functional can make full use of the area information and the influence of coherent speckle noise which has high anti-noise performance. Meanwhile, since that image edge is the most intuitive criterion to distinguish the different parts of the image. We add image gradient part in the energy functional models to define the constraints of energy so as to improve the accuracy of boundary location:

$$E_B = \oint_c g(|\nabla u|)ds \tag{11}$$

Where ∇ denotes the gradient operator, and g(|∇u|) is a monotone decreasing function of image gradient

Thus, consolidate E_R and E_B, we can define the following energy functional model:

$$E = E_R + \lambda E_B \tag{12}$$

After the energy functional has been established, the segmentation of a ROI is obtained by solving the energy minimization problem. Here, the Split-Bregman algorithm is used [13].

4 Experiments and Results

In this paper, we conduct one experiment to test the performance of this algorithm.

Figure 3 shows a group of tanks in the wild which contains trees, grass, road, tanks, military facilities and other complex objects types. Picture (a) defines the original SAR image of 512*1,024 pixels. Yellow lines in picture (b) sketches the outline of ROI that has deformity shapes after rough extraction. Picture (c) includes two types of lines which are red and green, the former type shows the outline of ROIs after the rectangular-completing stages and the latter one sketches the outline of ROIs after the centroid alignment stages. The obvious changes between picture (b) and picture (c) verified the effectiveness of ROI adjustment. The last picture in

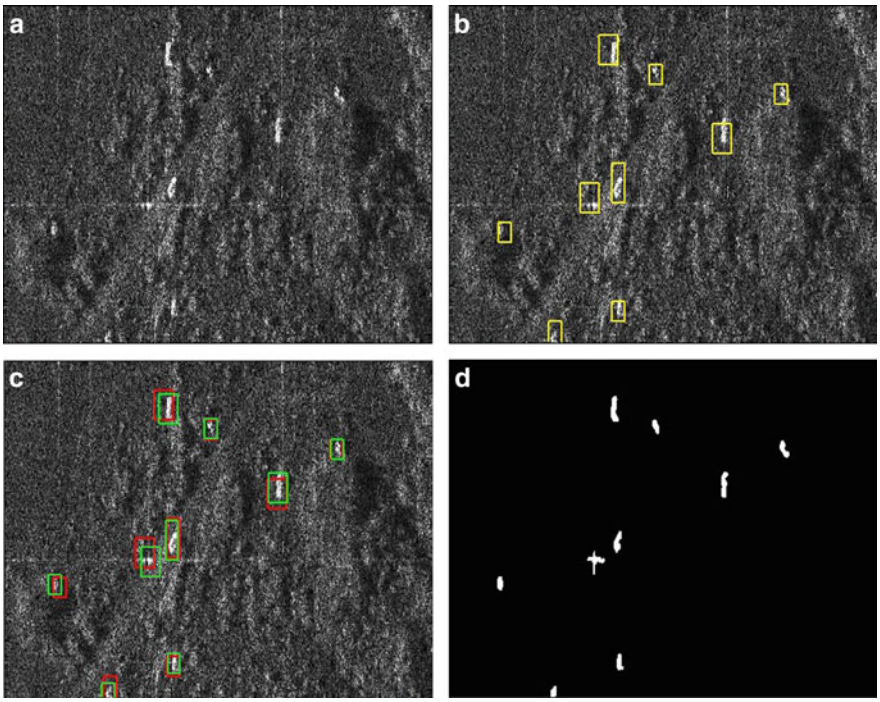

Fig. 3 Experiment and results. (**a**) the original SAR image; (**b**) ROIs after rough extraction; (**c**) ROIs adjustment; (**d**) variational segmentation

Fig. 3 shows the output image after variational segmentation. The whole program takes 6.93 s in this

5 Conclusions

A Two-stage Target Detection Method for High-resolution SAR images is proposed. The ROIs are first roughly detected by the variance WIE. And then the adjustment method which includes three parts is introduced to improve the location of ROIs. At last, the targets are accurately extracted by variational segmentations Experiments show very promising results for our method.

Acknowledgments This work is supported by the National Natural Science Foundation of China (Grant No.61271287).

References

1. Finn HM, Johnson RS (1968) Adaptive detection mode with threshold control as a function of spatially sampled clutter level estimates. RCA Rev 29(3):414–464
2. Barkat M, Himonas SD, Varshney PK (1989) CFAR detection for multiple target situations. IEE Proc F 136(5):193–209
3. Rohling H (1983) Radar CFAR thresholding in clutter and multiple target situation. IEEE Trans AES 19(3):608–621
4. Kim CJ, Han DS, Lee HS (1993) Generalized OS CFAR detector with noncoherent integration. Signal Process 31(1):43–56
5. Nagle DT, Saniie J (1995) Performance analysis of linearly combined order statistic CFAR detectors. IEEE Trans AES 31(2):522–533
6. Ozgunes I, Gandhi PP, Kassam SA (1992) A variably trimmed mean CFAR radar detector. IEEE Trans AES 28(4):1002–1014
7. Goldman H (1990) Performance of the excision CFAR detector in the presence of interferers. IEE Proc F 137(3):163–171
8. Yang L, Yang J (2004) Adaptive detection for infrared small target under sea-sky complex background. Electron Lett 40(17):1083–1085
9. Yang L, Yang J, Ling J (2005) New criterion to evaluate the complex degree of sea-sky infrared background. Opt Eng 44(12):126401–126406
10. Yang L, Zhou Y, Yang J et al (2006) Variance WIE based infrared images processing. Electron Lett 42(15):857–859
11. Li Y, Mao X, Feng D et al (2011) Fast and accuracy extraction of infrared target based on Markov random field. Signal Process 91(5):1216–1223
12. Cao ZJ, Pang LL, Pi YM (2007) A variational level set approach for automatic target extraction of SAR images. Synthetic Aperture Radar, 2007. APSAR 2007. 1st Asian and Pacific Conference on IEEE, 5–9 November, 2007, Huangshan, pp 375–378
13. Goldstein T, Osher S (2009) The split Bregman method for L1-regularized problems. SIAM J Imag Sci 2(2):323–343

Bistatic ISAR Imaging Algorithm Based on Compressed Sensing

Lin Dong, Fan Luhong, and Jin Li

Abstract Compressed sensing (CS) theory can be used to extract target scattering characteristics and frequency characteristics from the partially missed bistatic ISAR(Bi-ISAR) echo directly to achieve high-resolution imaging. In this paper, based on the analysis of sparse property of BI-ISAR signal, sparse basis matrix and the observation matrix which is irrelevant to the sparse base matrix are constructed to get the observed signal. Provided that l_1 norm of original signal coefficients based on sparse base is minimum, gradient projection method is used to reconstruct the target signal with high precision, and then bistatic ISAR imaging algorithm based on CS is given. Computer simulations using frequency stepped signal are given to verify the effectiveness of the proposed method.

Keywords Bistatic inverse synthetic aperture radar • Compressed sensing • Stepped-frequency signal • High-resolution imaging

1 Introduction

Compared with traditional ISAR [1], Bi-ISAR [2] has larger operating distance and better security, anti-interference and anti-interception performance. Bi-ISAR is of great importance in military and civilian fields. However, imaging targets of Bi-ISAR are usually non-cooperative. Affected by actual situation, the received echo signal may be partially missing. Moreover, because of the existence of bistatic included angle, range resolution gets lower as bistatic included angle gets larger, which eventually causes range resolution of Bi-ISAR to be far lower than that of monostatic radar with equivalent bandwidth [3]. Transmitting signal bandwidth is increased by traditional solutions usually to raise range resolution, and linear

L. Dong (✉) • F. Luhong • J. Li
School of Electronic Engineering, University of Electronic Science and Technology of China, Chengdu, China
e-mail: 306345432@qq.com

B. Zhang et al. (eds.), *The Proceedings of the Second International Conference on Communications, Signal Processing, and Systems*, Lecture Notes in Electrical Engineering 246, DOI 10.1007/978-3-319-00536-2_66,

interpolation [4, 5] and all-pole model matching algorithm [6] in sparse part of signal are utilized. Nevertheless, when the sparse degree of the signal is too large, this kind of methods will result in large errors, thus the quality of Bi-ISAR imaging is affected. With the increasing requirement of ISAR imaging precision, traditional method cannot meet the demand of high resolution imaging in the case of large sparse extent. It has become a research hot spot about how to carry out high resolution imaging of target using sparse signal.

Donoho et al. proposed CS theory in 2004 [7, 8], and proved that as long as the signal is sparse in an orthogonal space, lower frequency sampling can be used to get sparse signal and then the signal is reconstructed with high probability. Bi-ISAR target scattering points usually occupies a small space in the imaging projection plane, thus the Bi-ISAR signal is sparse, and this is in line with the basic requirements of the CS theory. So according to the CS theory framework, in Bi-ISAR target signal sparse condition, high-resolution ISAR target image is got through few observed sample combined with sparse optimization algorithm, at the same time the burden of data sampled and stored are greatly reduced. In the algorithm, simulation of stepped frequency signal [9] is used, and ISAR turntable imaging model [10] is constructed to get target echo signal. Then combining signal sparse characteristics on timer axis with compressive sensing theory, a suitable sparse basis is built. The signal is projected onto the substrate to do low-frequency sampling, then in signal recovery using the gradient projection algorithm based on the l_1 norm sparsity constraint [11, 12], finally target scattering characteristic and Doppler information with high-precision is extracted and high-resolution image is got. In the end of this paper, the feasibility and effectiveness of the algorithm is verified by simulation.

2 Compressed Sensing Theory

In the signal processing, said coefficient of signal X with length of $N \times 1$ is sparse on a set of orthogonal basis Ψ, so linear observation of coefficient signal vector can be done by a observation matrix unrelated to transform basis Ψ: $\Phi : M \times N(M << N)$, and observation collection $Y : M \times 1$ is got. Optimization algorithm can be used to reconstruct original signal X from observation collection Y with high accuracy. This is the basic concept of CS theory. The approximate steps of CS signal processing are:

First, if signal $X \in R^N$ is sparse on a certain orthogonal basis, work out transformation coefficient $\Theta = \Psi^T X$, and Θ is equivalent or approximate sparse representation of Ψ; second, design a steady $M \times N$-dimensional observation matrix unrelated to transform basis Ψ, and observe Θ to get observation collection $Y = \Phi\Theta = \Phi\Psi^T X$, finally, because of stability and uniqueness of the minimum 1-norm solution, use optimization problem under the 1-norm to solve $\hat{X}s$ exact value or approximation. That is to solve the following problem:

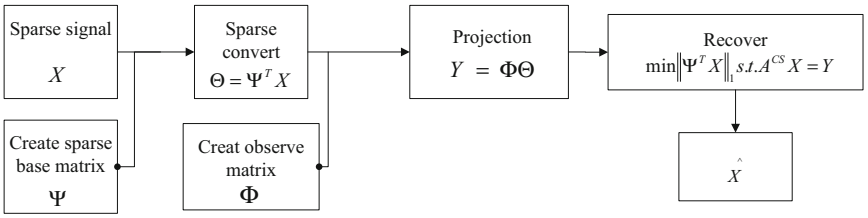

Fig. 1 CS theoretical frame

$$\min\left\|\Psi^T X\right\|_{l_1} \quad s.t. \quad A^{CS}X = \Phi\Psi^T X = Y \tag{1}$$

The compression sampling process shown in Fig. 1:

3 Bi-ISAR Imaging Algorithm Based on CS

3.1 Sparse Representation of the Echo

In the sparse representation process, if using a linear FM signal, in order to meet the requirement of sparse representation in CS theory, a step of neglecting higher order term is needed to go through and the imaging precision is affected to a certain extent. Compared with linear FM signal, the phase and the time of the stepped frequency signal is linear relation not quadratic power relationship, and the signal sparse representation can be got accurately. Therefore, the stepped frequency signal is used as transmitted signal in this algorithm. Launched stepped frequency signal can be described as:

$$s(t) = \sum_{n=1}^{N}\sum_{m=1}^{M} rect\left(\frac{t - t_{mn}}{T_P}\right)\exp[-j2\pi f_m t] \tag{2}$$

Based on (2), scattering point's echo on target in nth sequence and mth pulse is:

$$s(n,m) = A \cdot \text{rect}\left(\frac{t - t_{(p)}}{T_p}\right)\exp\left[-j2\pi f_{m-K+1}\left(t - t_{(p)}\right)\right] \tag{3}$$

A is amplitude, $n = 1, 2, 3 \ldots N$, $m = 1, 2, 3 \ldots M + k(n)$, carrier frequency $f_{m-K+1} = f_0 + (m - K) \cdot \Delta f$. The entire target's echoes are obtained by adding the echoes of individual scattering points:

$$s_R(n,m) = \sum_{i}^{I} A_i \cdot \mathrm{rect}\left(\frac{t - t_{i(p)}}{T_p}\right) \exp\left[-j2\pi f_{m-K+1}\left(t - t_{i(p)}\right)\right] \tag{4}$$

Making $s_{(0)}(t) = A_i rect\left(\frac{t}{T_P}\right) \exp\left[-j2\pi f_{m-k+1}(t)\right]$, echo can be expressed as:

$$s_R(n,m) = \sum_{i=1}^{I} s_0(t - t_i(p)) \tag{5}$$

Now, construct sparse basis $\Phi = [s_0(t), s_0(t - t_0), s_0(t - 2t_0), s_0(t - 3t_0 \ldots)]$, where t_0 is equivalent delay time unit which is set based on the demand of imaging resolution. As long as t_0 is small enough, delay time $t_i(p)$ of any target scattering point can be approximately equal to integral multiple of t_0, so target echo can be represented by some points in this sparse basis. If the echo's sparse said coefficient on the basis Φ is $\theta^T = [\theta_{c1}\theta_{c2}\theta_{c3} \ldots \theta_{cL}]_{1 \times L}$, the original signal on this sparse basis can be expressed as:

$$s_R(n,m) = \Phi\theta \tag{6}$$

θ is sparse projection coefficient. Furthermore, the target only takes up a very small part in imaging region, so echo signal can be represented by a very small part of Φ, that is $s_r(,\hat{t}, t_m)$ is sparse in space Φ.

3.2 Structure of Observation Matrix

Fourier basis is the most direct and effective basis on Bi-ISAR imaging, and is widely used in various sparse representation algorithm. Here Fourier basis is used to construct the observation matrix Ψ:

$$\begin{bmatrix} e^{-j\omega_0 t_0} & e^{-j\omega_1 t_0} & \cdots & e^{-j\omega_{M-1} t_0} \\ e^{-j\omega_0 t_1} & e^{-j\omega_1 t_1} & \cdots & e^{-j\omega_{M-1} t_1} \\ \vdots & \vdots & \ddots & \vdots \\ e^{-j\omega_0 t_{N-1}} & e^{-j\omega_1 t_{N-1}} & \cdots & e^{-j\omega_{M-1} t_{N-1}} \end{bmatrix} \tag{7}$$

In the formula, $\omega_m = 2\pi f_m$ represents frequency and t_n represents azimuth sampling time. Observed sample $Y = \Psi\Phi\theta$ can be got by combining this observation basis and (7).

3.3 Recovery of Original Signal

Based on CS theory, the problem of estimating sparse coefficient θ from observed signal Y can be described as

$$\hat{\theta} = \text{argmin}\|\theta\|_{l_1} \quad s.t. \quad Y = \Theta\theta \tag{8}$$

$\Theta = \Psi\Phi$ is known matrix. Solving formula is a NP difficult problem. Convex optimal problem can be solved by solving a linear programming problem, which also be called Basis Pursuit. If considering the errors in process of reconstruction, the above problem can be described as:

$$\hat{\theta} = \text{argmin}\|\theta\|_{l_1} \quad s.t. \quad \|Y - \Theta\theta\|_{l_2} \leq \varepsilon \tag{9}$$

This problem can be solved by using Gradient Projection for Sparse Reconstruction (GPSR) [12] which is one of LP problem solving method. The first step of GPSR: (9) can be described as:

$$\min_{\theta} \frac{1}{2}\|Y - \Theta\theta\|_{l_2}^2 + \tau\|\theta\|_{l_1} \tag{10}$$

In (10), $\theta \in R^N$, $Y \in R^N$,and Θ is $M \times N$ matrix, and τ is non-negative parameter. Let $\theta = u - v$, in which u, v are non-negatives. So (9) is described as: $\min_\theta \frac{1}{2}\|Y - \Theta(u - v)\|_{l_2}^2 + \tau 1_n^T u + \tau 1_n^T v$, in which $1_n = [1,1,\ldots,1]^T$. Then let $z = \begin{bmatrix} u \\ v \end{bmatrix}$, $b = \Theta^T Y$, $c = \tau 1_{2n} + \begin{bmatrix} -b \\ b \end{bmatrix}$, $B = \begin{bmatrix} \Theta^T\Theta & -\Theta^T\Theta \\ -\Theta^T\Theta & \Theta^T\Theta \end{bmatrix}$, so the expression is further written:

$$\min c^T z + \frac{1}{2} z^T B z \equiv F(z), \quad z \geq 0 \tag{11}$$

The gradient of (11) is $\nabla F(z) = c + Bz$.To solve (11), there are four steps pretreatment needed to go through:

1) Iterative process of $z^{(k)}$ to $z^{(k+1)}$, set $w^{(k)} = (z^{(k)} - a^{(k)}\nabla F(z^{(k)}))_+$
2) Select the parameter $\lambda^{(k)} \in [0,1]$, set $z^{(k+1)} = z^{(k)} + \lambda(w^{(k)} - z^{(k)})$
3) In iteration $z^{(k)}$, along the negative gradient $-\nabla F(z^{(k)})$ to search, define $g^{(k)}$ as:

$$g_i^{(k)} = \begin{cases} \left(\nabla F\left(z^{(k)}\right)\right)_i, & z_i^{(k)} > 0 \,\|\, \left(\nabla F\left(z^{(k)}\right)\right)_i < 0 \\ 0, & other \end{cases}$$

4) Select initial value is $\alpha_0 = \arg\min_{\alpha} F(z^{(k)} - \alpha g^{(k)})$, so the accurate formula is:

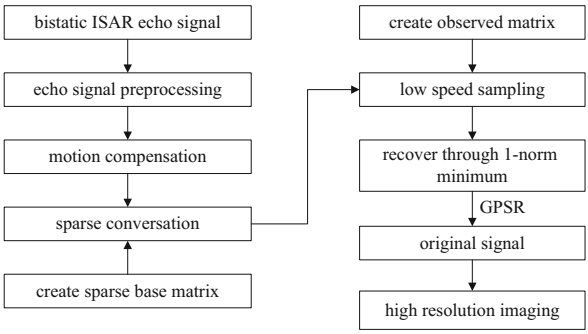

Fig. 2 The Bi-ISAR imaging algorithm based on CS

$$\alpha_0 = \frac{\left(g^{(k)}\right)^T g^{(k)}}{\left(g^{(k)}\right)^T B g^{(k)}} \tag{12}$$

Now, do a iteration to get estimated value of α_0 to recover the original echo, then get the imaging result.

In sum, Bi-ISAR imaging method based on CS can be described as following steps: (Fig. 2)

4 Verification of Simulation Experiment

To verify correctness of imaging method in this paper, Bi-ISAR imaging two-dimensional geometry model is constructed as shown in Fig. 3a. To facilitate analysis, the entire imaging model is projected on the same plane. Radar transmitter is placed in position R_L, receiver is placed in position R_R, and assuming the distance of transmitter and target is L, the distance of receiver and target is R.

The model of imaging target scattering points is shown in Fig. 3b. Radar's transmitting signal is stepped frequency signal.

Radar parameters are shown in Table 1. It launches 64 stepped pulse groups and every pulse group includes 128 pulses.

The simulation result is shown in Fig. 4. Partial deletion of original echo data is shown in Fig. 4a. The simulation result of complete echo data RD imaging algorithm is shown in Fig. 4b, and every point target is clearly visible. Imaging result of sparse signal is shown in Fig. 4c–e. Sparse aperture all-pole RD imaging is used in Fig. 4c, and the error is larger. The method used by Fig. 4d is direct-zero padding imaging for sparse echo, and its side lobe is higher and imaging point is

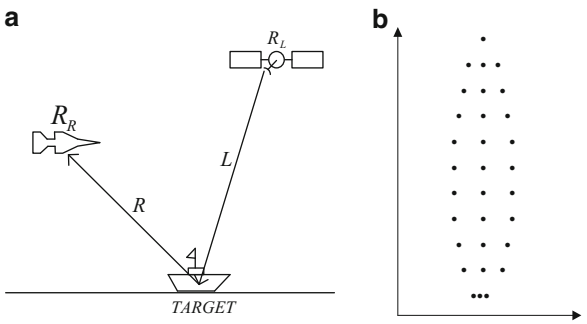

Fig. 3 (**a**) The Bi-ISAR imaging geometry model, (**b**) the imaging target scattering points model

Table 1 Bi-ISAR imaging simulation parameters

Parameters	Variable name	Variable value	Parameters	Variable name	Variable value
Carrier frequency	f_0	10 GHz	Bandwidth	B	1 GHz
Pulse repetition frequency	PRF	400 Hz	Observation time	CPI	2.5 s
Stepped frequency	∇f	10 MHz	Distance	R_0	10 km

blurry. The result of method mentioned in this paper is shown in Fig. 4e. Every point target is clear and imaging result is without side lobe clutter. It's the most ideal method.

5 Conclusion

In the Bi-ISAR echo sparse situation, linear prediction or parametric model interpolation estimated by power spectrum is used to estimate full aperture data in traditional methods, then traditional Range-Doppler algorithm is used to achieve imaging. Ideal image can be obtained by this method when signal sparse degree is small, but a serious distortion will be caught as sparse degree reaches certain extent.

As it mentioned in this paper, Bi-ISAR signal sparse imaging method based on CS is irrelevant to signal sampling method because of different signal representation. Since the characteristics of range and Doppler information are directly distracted, imaging results of the proposed method has no side-lobe clutter. When data are partially missing, imaging quality of the proposed method is far superior to other imaging algorithms. Simulations of multiple point targets are conducted to verify and the effectiveness of the proposed method.

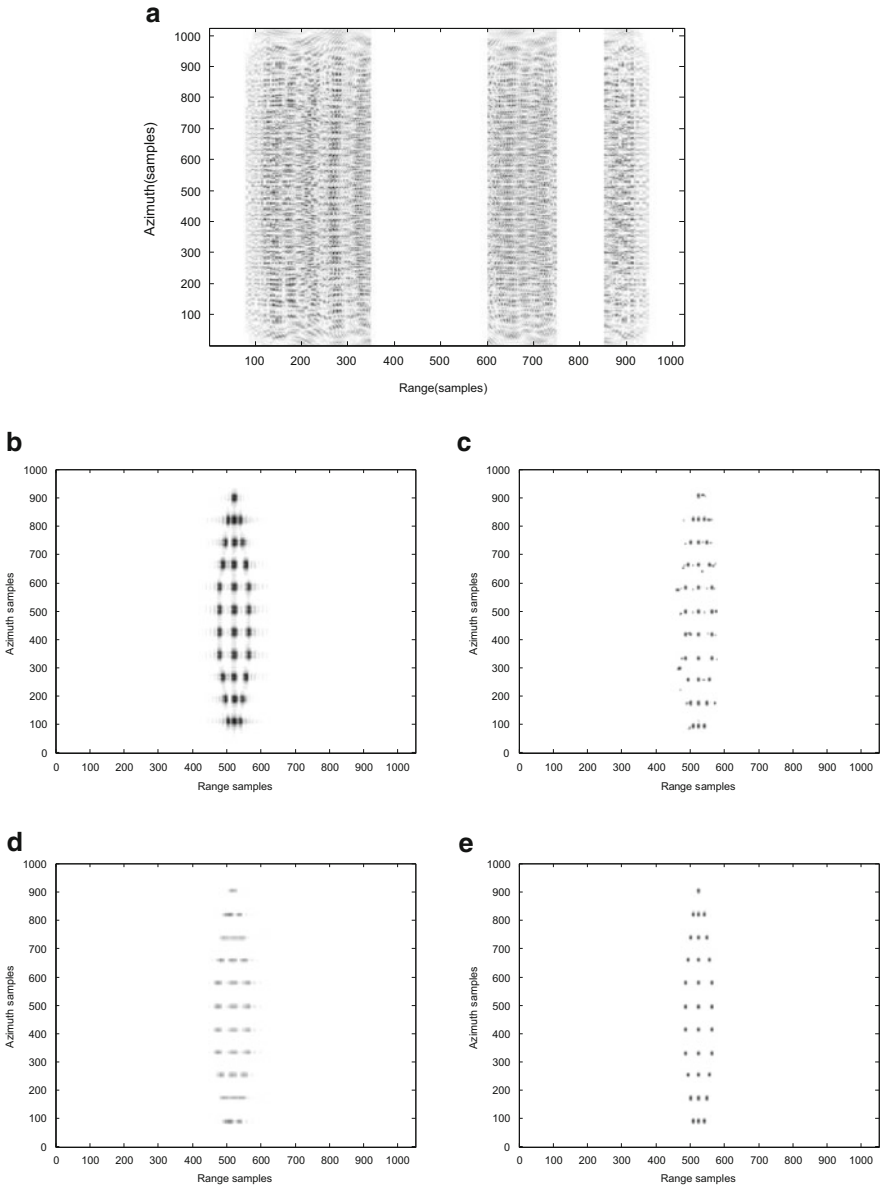

Fig. 4 (**a**) Original echo; (**b**) the complete echo data RD imaging; (**c**) the sparse aperture all-pole RD imaging; (**d**) the Sparse direct zero-padding imaging; (**e**) the result based on CS

References

1. Martorella M, Palmer J, Homer J et al (2007) On bistatic inverse synthetic aperture radar. IEEE Trans Aerospace Electron Syst 3:1125–1134
2. Simon MP, Schuh MJ, Woo AC (1995) Bistatic ISAR images from a time-domain code. IEEE Antenn Propag Mag 37(5):25–32
3. Skolnik MI (2001) Introduction to radar systems. McGraw-Hill, New York
4. Cuomo KM, Piou JE, Mayhan JT (1999) Ultra wide-band coherent processing. IEEE Trans Antenn Propag 47(6):1094–1107
5. Potter LC, Arun KS (1989) Energy concentration in band-limited extrapolation. IEEE Trans Acoust Speech Signal Process 37(7):1027–1041
6. Li HJ, Farhat N, Shen Y (1987) A new iterative algorithm for extrapolation of data available in multiple restricted regions with application to radar imaging. IEEE Trans AP 35(5):581–588
7. Tsaig Y, Donoho DL (2006) Extensions of CS. Signal Process 86(3):549–571
8. Donoho DL (2006) CS. IEEE Trans Inform Theory 52(4):1289–1306
9. Varshney KR, Cetin M, Fisher JW et al (2008) Sparse representation in structured dictionaries with application to synthetic aperture radar. IEEE Trans Signal Process 56(8):3548–3561
10. Ya-biao Z, Zhen-bo Z, Zi-yue T et al (2006) Bistatic inverse synthetic aperture radar image formation. J Electron Inform Tech 28(6):969–972
11. Jalal Fadili M, Starck J-L, Moudden Y et al (2010) Image decomposition and separation using sparse representations: an overview. Proc IEEE 98(6):983–994
12. Figueiredo Mario AT, Nowak RD, Wright SJ (2007) Gradient projection for sparse reconstruction: application to compressed sensing and other inverse problems. IEEE J Sel Top Signal Process 1(4):586–597

Continuous Potts Model Based SAR Image Segmentation by Using Dictionary-Based Mixture Model

Yadan Yu, Zongjie Cao, and Jilan Feng

Abstract In this paper, Potts model based on the dictionary-based mixture model (DMM) is proposed to make image classification. Potts model is used for SAR image segmentation by minimizing energy functional, which is a weighted sum of data fidelity and the length of the boundaries of the regions. However, it needs prior information such as the number of regions and the probability density function of image. In this paper, we overcome this problem by using the dictionary-based mixture model, which can compute the optimal number of segments automatically and the probability density function of complex SAR image. Experiments on several real SAR images show that Potts model based on DMM has better performance in SAR image segmentation than that with sole distribution.

1 Introduction

The classification of SAR images is a crucial problem. Traditionally classification methods are easy to be affected by speckle noise. Therefore, it will lose message of targets and edge while it is processing image, which makes the classification results bad. We take advantage of variational classification method (Potts model) [1]. It can attain accurate classification results without speckle noise, which has been proved in the reference [2–4]. However, statistical model based on variational methods usually requires prior information such as the number of regions and initial conditions, which could be unpleasant in real applications. Therefore, it is desired to develop variational SAR image segmentation methods that require less supervised information.

Recently, a novel SAR image statistical modeling method called Dictionary-based mixture model (DMM) [5] has been proposed to describe the statistical

Y. Yu • Z. Cao (✉) • J. Feng
School of electronic engineering, University of Electronic Science and Technology of China, Chengdu, China
e-mail: zjcao@uestc.edu.cn

B. Zhang et al. (eds.), *The Proceedings of the Second International Conference on Communications, Signal Processing, and Systems*, Lecture Notes in Electrical Engineering 246, DOI 10.1007/978-3-319-00536-2_67,

property of complex SAR scene. As finite mixture models are widely used to fit data with complex distribution, DMM is different from them by using SAR statistical models as its component models. Dictionary includes Log-Normal distribution, Nakagami distribution, generalized Gaussian Rayleigh (GGR) distribution, symmetric α-stable distribution (SαSGR), Weibull distribution and k-root distribution. Log-normal distribution is fit to urban [6]. Nakagami distribution is applied to the multi-look data and non-textured image areas [6, 7]. GGR distribution is always used to single-look SAR image data [6]. SαSGR distribution can make better results in the urban areas [8, 9]. Weibull distribution is successfully applied to land, sea and sea-ice [6]. K distribution can well describe uneven region. Different distribution owns different advantages. Put gray values divided into segments. Then, the six distributions are used to every segment to estimate PDF. The maximum likelihood criterion is presented to choose the best model for every segment. The whole image PDF is the sum of production of the segment probability and its optimal model. We get the optimal number of segments by comparing the correlation coefficient between histogram and estimated PDF of the whole image. As a result, DMM can automatically compute the optimal number of classification segments and get the optimal PDF of image.

In this paper, a novel variational SAR image segmentation approach is presented by taking advantage of DMM. Note that the DMM can model complex SAR images by learning component models as well as the optimal component number. Therefore it can be taken as a good initialization of variational SAR segmentation models. We combine the DMM with the continuous Potts model, which leads to a fully unsupervised variational SAR image segmentation approach.

The continuous Potts model is introduced in Sect. 2. In Sect. 3, we describe dictionary-based mixture model and give the algorithm. Section 4 reports the classification results. A conclusion is drawn in Sect. 5.

2 The Continuous Potts Model

In this article, we assume that the labels of the segments are $\{l_1, l_2, \ldots, l_n\}$. Then, the every pixel in the image will be classified to some corresponding label by Potts model.

The whole image is represented by Ω, while $\{\Omega\}_{i=1}^{n}$ is n disjoint subdomains.

The Potts Model is:

$$\min_{(\Omega_i)_{i=1}^{n}} \sum_{i=1}^{n} \int_{\Omega} f_i(x)\mathrm{d}x + \alpha \sum_{i=1}^{n} |\partial\Omega_i| \tag{1}$$

Subject to: $U_{i=1}^{n}\Omega_i = \Omega,\ \ \Omega_k \cap \Omega_l = \varnothing,,\ \forall\ k \neq 1,$

Where $|\partial\Omega_i|$ is the length of boundary of i^{th} subdomain Ω_i. The function $f_i(x)$ is the probability density function of the SAR image background. In the Potts model, the subdomains are disjoint.

In order to compute the optimal labels, we define characteristic function $U_i(x)$, i = 1, 2, ..., n, to delegate the characteristic functions of disjoint domains.

$$U_i(x) = I_{\Omega_i(x)} := \begin{cases} 1, x \in \Omega_i \\ 0, x \notin \Omega_i \end{cases}, \quad \mathrm{i} = 1, \ldots \mathrm{n} \tag{2}$$

The length of boundaries of disjoint domain:

$$|\partial \Omega_i| = \int_{\Omega} |\nabla U_i(x)| \mathrm{dx}, \mathrm{i} = 1, \ldots, \mathrm{n} \tag{3}$$

Let (2) and (3) substitute to (1). Then, we can attain another different style of the Potts model:

$$\min_{U_i(x) \in \{0,1\}} \sum_{i=1}^{n} \int_{\Omega} U_i(x) f_i(x) dx + \alpha \sum_{i=1}^{n} \int_{\Omega} |\nabla U_i(x)| dx \tag{4}$$

Subject to: $\sum_{i=1}^{n} U_i(x) = 1, \forall\, x \in \Omega$

From above formulation, we can find that the Potts model is binary configuration. And it is typically formulated as the minimization of an energy function which mathematically encodes all the information needed for the imaging and vision task. Lower energy solutions are regarded as better posteriori estimates. In the Potts model, the number of the labels n and the probability density function f_i(x) is needed to be defined. In this paper, we adopt the dictionary-based mixture model to determine n and probability density function f_i(x). Thus, the dictionary-based mixture model is the initialization of the Potts model.

In this paper, we compare the segmentation results based on DMM with that based on gamma distribution. To clear the paper structure, we give the following algorithm flow chart (Fig. 1).

As far as we know, the gamma model is usually used and well-known. We don't repeat it. Next, let's introduce the DMM.

3 The Dictionary-Based Mixture Model for SAR Amplitude Probability Density Function Estimation

To take the heterogeneous scenario into account, when several distinct land-cover typologies presents in the same SAR image, a DMM for the distribution of grey levels is assumed. All the gray values of the image will be assigned to one of K segments, where K_{max} is equal to 10 based on experience. Therefore, all the gray values will be divided into K segments. Then, every distribution in dictionary will model every segment in the image. The maximum likelihood criterion is used to judge which distribution is best of the segment. The PDF of the all SAR image is the

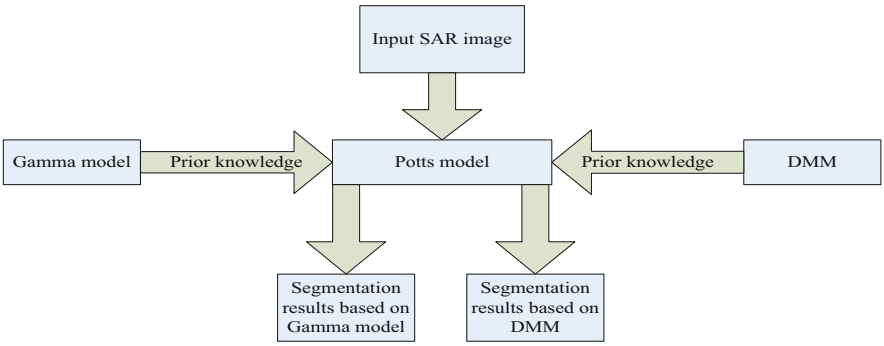

Fig. 1 The flow chart of DSEM algorithm

sum of the production of the corresponding distribution of the segment and its probability.

$$p_z(z|\theta) = \sum_{i=1}^{k} P_i p_i(z|\theta_i), z \geq 0 \tag{11}$$

Where $p_i(z|\theta_i)$ is the best distribution of the segment. And z is the gray value of the segment, while P_i is the probability of i^{th} segment. The letter i is the number of segments. And:

$$\sum_{i=1}^{k} P_i = 1, 0 < P_i < 1 \tag{12}$$

Parameter spaces: $\Phi = \{\theta : \sum_{j=1}^{k} P_j = 1, \theta_i \in \Phi_i, 0 \leq P_i \leq 1, i = 1, \ldots, K$, where parameter θ_i is estimated of i^{th} segment by the Mellin transform in this paper, since it brings smaller calculation and more accurate estimation than current estimation and maximum likelihood estimation. The PDFS and estimation equations of the distributions are in the dictionary in Table 1.

Then, we make use of an algorithm to gain the result of fitting with image, called Dictionary Stochastic Expectation Maximization (DSEM) algorithm. t^{th} DSEM iteration as follows:

E-step: Compute the posterior probability $T_i^t(z)$ of every gray value to redistribute gray value to the K segments.

$$T_i^t(z) = \frac{P_i^t p_i^t(z)}{p^t(z)}, p^t(z) = \sum_{j=1}^{k} P_j^t p_j^t(z) \tag{13}$$

Where, $z = 1, \ldots Z$ is the gray value and $i = 1, \ldots K$ is the number of segments.

Table I MoLC equations for all the parameteric families included in the adopted dictionary

Parametric family		MoLC equation
f_1	Log-Normal	$\kappa_1 = \mu$ $\kappa_2 = \sigma^2$
f_2	Nakagami	$2\kappa_1 = \text{In}\ \mu + \Psi(L) - \text{In}\ L$ $4\kappa_2 = \Psi\ (1, L)$
f_3	GGR	$\kappa_1 = \lambda\Psi\ (2\lambda) - \text{In}\ \gamma - \lambda G_1(\lambda)G_0(\lambda)^{-1}$ $\kappa_1 = \lambda^2\ \Psi\ (1, 2\lambda) + \lambda^2 G_2(\lambda)G_0(\lambda)^{-1} - \lambda^2\ G_1(\lambda)^2 G_0(\lambda)^{-2}$
f_4	SαSGR	$\alpha\kappa_1 = \Psi\ (1)(\alpha - 1) + \alpha\ \text{In}\ 2 + \text{In}\ \gamma$ $\kappa_2 = \Psi\ (1, 1)\alpha^{-2}$
f_5	Weibull	$\kappa_1 = \text{In}\mu + \Psi\ (1)\eta^{-1}$ $\kappa_2 = \Psi\ (1, 1)\eta^{-2}$
f_6	K-root	$2\kappa_1 = \text{In}\mu + \Psi\ (L) - \text{In}\ L + \Psi\ (M) - \text{In}\ M$ $4\kappa_2 = \Psi\ (1, L) + \Psi\ (1, M)$ $8\kappa_3 = \Psi\ (2, L) + \Psi\ (2, M)$

S-Step: According to the posterior probability $T_i^t(z)$, we sample a segment σ_i for the gray value z. The category label of segments is $\{\sigma_i, \text{i} = 1, \ldots, \text{K}\}$.

MoLC-step: Compute the t^{th} iteration probability P_i^t of every segment and the t^{th} iteration first three logarithmic accumulations K_{1i}^t, K_{2i}^t, K_{3i}^t to estimate the parameters of segments by the method-of-log-cumulants (MoLC) [7].

$$P_i^{t+1} = \frac{\sum_{z \in Q_i^t} h(z)\text{ln}z}{\sum_{z=0}^{Z-1} h(z)} \tag{14}$$

$$K_{1i}^t = \frac{\sum_{z \in Q_i^t} h(z)\text{ln}z}{\sum_{z \in Q_i^t} h(z)} \tag{15}$$

$$K_{2i}^t = \frac{\sum_{z \in Q_i^t} h(z)\left(\text{ln}z - K_{1i}^t\right)^2}{\sum_{z \in Q_i^t} h(z)} \tag{16}$$

Where $Q_i^t = \{\text{z} : S^t(\text{z}) = \sigma_i\}$, $S^t(z)$ is sampling result σ_i of the gray value z in the i^{th} iteration. The label σ_i is the i^{th} segment of the image. We will take use of the prior information of the image histogram to compute the first three logarithmic accumulations of every segment to attain distributions $f_j(\diagup \xi_j)$ parameters ξ_{ij}^t ($i = 1, 2, \ldots$ K, j = 1, 2, ..., M) by Table 1. The letter M is the number of the distributions in the dictionary.

MS-step: Calculate the t^{th} iteration log-likelihood values L_{ij}^t of the estimated probability density functions $f_j(\diagup \xi_{ij}^t)$ of every distribution in the dictionary of every segment.

$$L_{ij}^t = \sum_{z \in Q_i^t} h(z)\text{ln}f_j\left(z/\xi_{ij}^t\right) \tag{17}$$

Where h(z) is the image histogram, z = 0,1,...,N-1, the letter N is the maximum gray value. When log-likelihood value $L_{ij}^t(i = 1, 2, \ldots, \text{K}, \text{j} = 1, 2,, \ldots, \text{M})$ in the

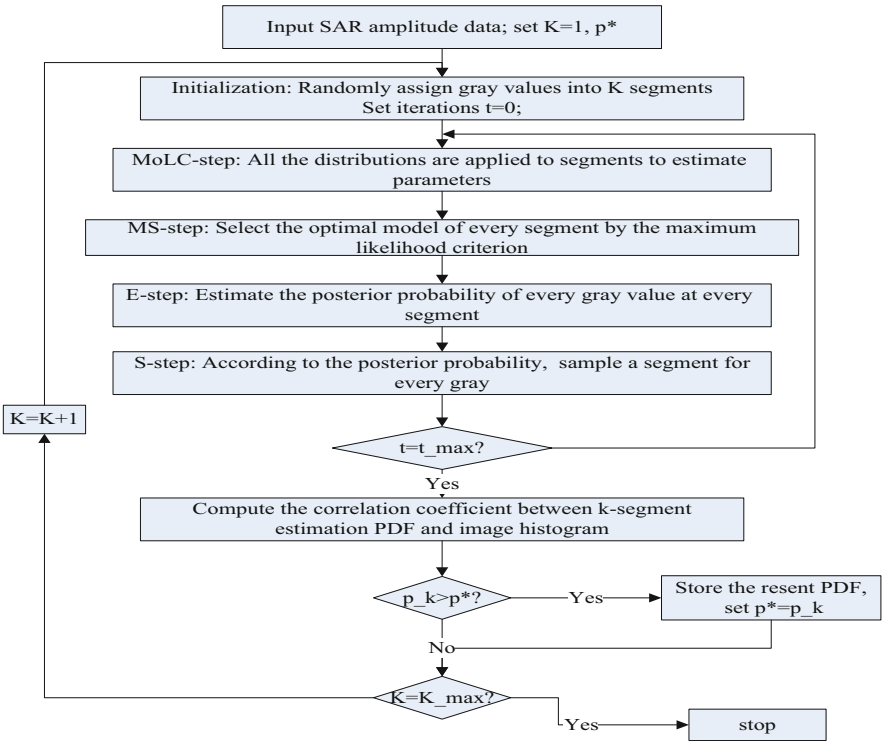

Fig. 2 The flow chart of DSEM algorithm

segment is the maximum, the corresponding PDF is the best estimation. The iteration is stopped, until log-likelihood is stable. At last, we compute the correlation coefficient ρ_K between histogram and K-segment PDF estimation. The number K of the max correlation coefficient ρ^* is the optimal number K^* of segments. The initialized probabilities of segments are same and equal to the value $\frac{1}{K}$, while the initialized gray values in every segment are randomly assigned.

From above description of DSEM algorithm, we can get the following flow chart (see Fig. 2).

We can attain the mixture model probability density function $f_i(x)$ and the optimal number K^* of segments which is the n in the Potts model. Of course, the results of DSEM algorithm is substituted to the Potts model as the input.

4 The Classification Results

In this paper, we make use of the following SAR data to verify the performance of the proposed approach for SAR image classification:

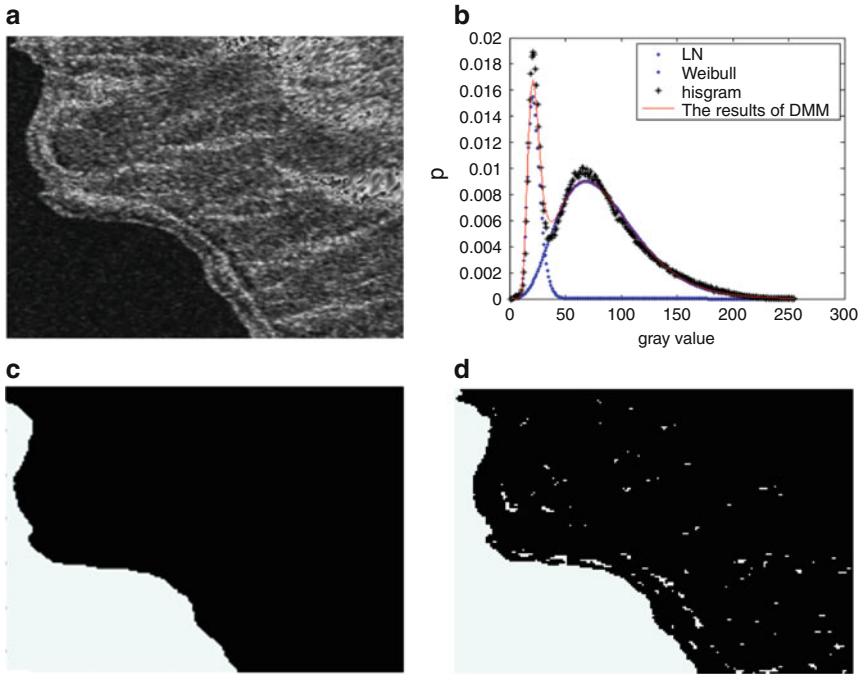

Fig. 3 The fitting and classification results of TSX1. (**a**) The original image of the TSX1 (**b**) The result of DSEM. (**c**) The classification result based on DSEM (**d**) The classification result based on Gamma

Two-look TerraSAR-X, Stripmap, approximately 6-m resolution, HH-polarized image. We present the experiments with three portions, TSX1and TSX2 (see Figs. 2 and 3).

The original SAR images, estimated results and classification results are described in the following figures. We also proposed a contrast classification method, which is the Potts model only based on gamma model and the number of segment is assumed.

The DSEM method has been used in the TerraSAR images (See Figs. 3 and 4). The top right images of the three figures are the estimated results. In Figs. 3 and 4, the correlation coefficients are 0.986, 0.979. And the corresponding optimal number of segments is 2 in the two figures, while the corresponding optimal model of each segment is: Weibull model and Log-Normal model, Log-Normal model and GGR. The correlation coefficients between the resulting estimated PDFs and the image histograms are so high for all images considered, thus demonstrating the effectiveness of the proposed method in terms of estimation accuracy. As we all know, the estimated results are more accurate, the classification result is better.

From the above two figures, we can easily find that the classification results of Potts model based on DMM model is more accurate than that of Potts model based on gamma model. The classification result of gamma model is fuzzy, while that based on DMM model is clear and obvious.

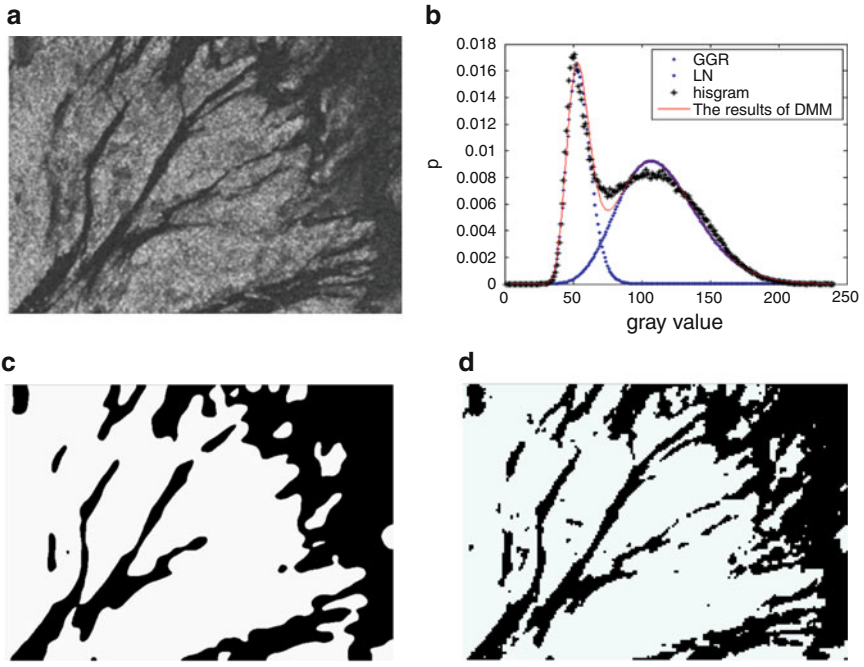

Fig. 4 The fitting and classification results of TSX2. (**a**) The original image of the TSX2 (**b**) The result of DSEM. (**c**) The classification result based on DSEM (**d**) The classification result based on Gamma

5 Conclusion

In this letter, we combine the Potts model with dictionary-based mixture model to classify the SAR image. Moreover, Potts model needs prior information such as the number of regions and the probability density function of image, which is available in the DMM. In the DMM, a set of theoretical or empirically models for SAR amplitude data have been adopted as a dictionary. It can automatically choose the optimal number of segments and get the optimal model of each segment.

The report results of the application method to several real SAR sensors have suggested that the Potts model based on the dictionary-based mixture model is more efficient, from the viewpoint of a visual comparison between the below left figure and corresponding below right figure of the above figures. Moreover, we can find that the DSEM algorithm is an attractive method for PDF modeling in the complex SAR images.

Acknowledgments This work is supported by the National Natural Science Foundation of China under Projects 61271287.

References

1. Bae E, Yuan J, Tai X-C (2011) Global minimization for continuous multiphase partitioning problems using a dual approach. Int J Comput Vis 92:112–129
2. Galland F, Bertaux N, Refregier P (2003) Minimum description length synthetic aperture radar image segmentation. IEEE Trans Imag Process 12(9):995–1006
3. Ayed IB, Vazquez C, Mitiche A et al (2004) SAR image segmentation with active contours and level sets. IEEE Int Conf Imag Process 4:2717–2720
4. Ayed IB, Mitiche A, Belhadj Z (2005) Multiregion level set partitioning of synthetic aperture radar images. IEEE Trans Pattern Anal Mach Intell 27(5):793–800
5. Gabriele M, Josiane Z, Sebastiano B (2006) Dictionary-based stochastic expectation–maximization for SAR amplitude probability density function estimation. IEEE Trans Geosci Rem Sens 44(1):188–200
6. Oliver C, Quegan S (1998) Understanding synthetic aperture radar images. Artech House, Norwood
7. Tison C, Nicolas J-M, Tupin F, Maitre H (2004) A new statistical model for Markovian classification of urban areas in high-resolution SAR images. IEEE Trans Geosci Rem Sens 42 (10):2046–2057
8. Kuruoglu EE (2001) Density parameter estimation of skewed alpha-stable distributions. IEEE Trans Signal Process 49(10):2192–2201
9. Kuruoglu EE, Zerubia J (2003) Skewed-stable distributions for modeling textures. Pattern Recog Lett 24:339–348

A High-Resolution Terahertz LFMCW Experimental Radar

Yao Gang, Zhang Biao, and Min Rui

Abstract A summary of UESTC's Terahertz (THz) imaging radar is presented, with an emphasis on some key design aspects. By using of the linear frequency modulated continuous-wave (LFMCW) radar technique with a 4.8 GHz bandwidth, nearly 3 cm range resolution is achieved. Some measures are taken for correcting the signal error in the intermediate frequency receiver to optimize the radar's range resolution. High dynamic range detection comes from the radar's system structure, low-noise LMF source. And the radar image can be acquired in ISAR imaging mode.

Keywords Terahertz • LFMCW radar • Error correction • ISAR

1 Introduction

Terahertz frequency band is a very important research and valuable undeveloped frequency resource, which especially has a great potential for development of high-resolution imaging radar. Compared to the traditional microwave radar, the advantages of terahertz radar system are as follows. First of all, the shorter wave length is favorable toward provide a wider bandwidth, which could benefit higher precision of imaging. Secondly, the narrow antenna beam in terahertz band could not only obtain higher antenna gain in radar LOS, improving the ability of multi-target discrimination and recognition, but also reduce the opportunity of main lobe jamming. Terahertz radar detection system is an important direction of terahertz technology in domestic and overseas.

LFMCW radar has advantages of high range resolution; low transmit power, high receiver sensitivity and simple structure etc. There is no distance blind area,

Y. Gang (✉) • Z. Biao • M. Rui
School of Electronic Engineering, University of Electronic Science and Technology of China, Chengdu, China
e-mail: yaog@vip.sina.com

B. Zhang et al. (eds.), *The Proceedings of the Second International Conference on Communications, Signal Processing, and Systems*, Lecture Notes in Electrical Engineering 246, DOI 10.1007/978-3-319-00536-2_68,

better anti-stealth ability than pulse radar, anti-background clutter and anti-jamming characteristics, and it's particularly suitable for near range applications. Terahertz wave has great bandwidth itself, so making use of the LFMCW radar structure can obtain very high range resolution; the emission power of terahertz wave is still very low at present, and LFMCW radar has lower emission power than pulse radar, so using LFMCW radar system can reduce the transmitter power requirements. In consideration of the great bandwidth of terahertz waves and the high range resolution of LFMCW radar, the terahertz LFMCW radar can obtain high range resolution.

Currently, the international research institutions with terahertz radar experimental systems are the Jet Propulsion Laboratory (JPL) 0.6 THz radar imaging system [1], the German Institute of Applied Science (Forschungs gesellschaftfür Angewandte Naturwissenschaften, FGAN) High Frequency Physics and Radar Techniques(FHR) 0.22 THz COBRA ISAR imaging system [2]. In 2006, Dengler et al. of JPL, have successfully developed the first high-resolution terahertz imaging system of 2 cm range resolution, this system introduced frequency modulation continuous wave (FMCW) radar technology into the imaging system, processed the waveform distortion compensation by software, obtained 2 cm range resolution internal 4 m [3]. In 2008, Cooper et al. of the 0.6 THz radar imaging system have successfully developed 0.58 THz high-resolution three-dimensional imaging radar system based on the further 0.6 THz radar imaging system [4]. The imaging system used to the ISAR imaging can obtain sub centimeter resolution. In 2007, Essen et al. of German Institute of Applied Science (FGAN) High Frequency Physics and Radar Technology (FHR) Laboratory, have successfully developed a 220 GHz terahertz imaging radar system COBRA-220 [5]. The system is also based on LFMCW radar system, which FM bandwidth is 8 GHz, successfully achieved the 1.8 cm range resolution in 200 m distance.

In this paper, we present an overview of the THz imaging radar technology. The radar is currently a portable laboratory prototype system operating in a linear frequency-modulated continuous-wave (LFMCW) mode over a 4.8 GHz bandwidth in UESTC. The remainder of this paper is organized as follows. Section 2 describes LFMCW signal model. In Sect. 3, a dual-source structure model for intermediate frequency receiver in the THz radar is developed. This is followed by Sect. 4 in which a detailed analysis of the signal and correcting method are presented. In Sect. 5, the experiment results for the LMFCW THz radar are shown. We conclude the paper in Sect. 6.

2 LFMCW Signal Analysis

In ideal conditions, LFMCW radar's transmitting and receiving signal frequency can be shown in Fig. 1. The transmitting signal is expressed as

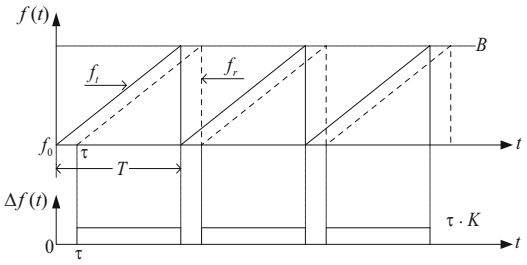

Fig. 1 Time-frequency of transmitting signal (f_t), receiving signal (f_r) and beat signal ($\Delta f(t)$)

$$S_t(t) = \exp\left\{2\pi f_0 t + \pi K t^2 + \theta_0\right\}, 0 \le t \le T \tag{1}$$

Where f_0 is the carrier frequency, t is the time variable, K is the frequency modulation slope, and T is the duration of signal, θ_0 is the initial phase.

If τ is the time delay of a stationary target at the range R, then the received signal can be expressed as:

$$\begin{aligned} S_r(t) &= S_t(t-\tau) \\ &= \exp\left\{2\pi f_0(t-\tau) + \pi K(t-\tau)^2 + \theta_0\right\}, \tau \le t \le T \end{aligned} \tag{2}$$

Where $\tau = 2R/c$,and c is the speed of light.

In order to reduce sampling rate, the beat signal can be obtained in intermediate frequency after mixing the transmitting signal and received echo signal.

$$\begin{aligned} S_b(t) &= S_t(t) \times S_r{}^*(t) \\ &= \exp\left\{2\pi f_0 \tau + 2\pi K \tau t - \pi K \tau^2\right\}, \tau \le t \le T \end{aligned} \tag{3}$$

The beat frequency can be calculated which is the derivative of the beat signal phase.

$$f_b(t) = \frac{1}{2\pi} \times \frac{d\Phi_b(t)}{dt} = K\tau = K\frac{2R}{c} \tag{4}$$

It is obvious that the beat frequency is a fixed value, only related to the distance and frequency modulation slope. Then the range of target is expressed as:

$$R = \frac{f_b c}{2K} = \frac{cT}{2B} f_b \tag{5}$$

So the frequency of the beat signal is the identification to the target range. After sampling was carried out on the beat signal of LFMCW radar, the beat frequency signal's frequency spectrum can be obtained by the discrete Fourier transform (DFT). In the spectrum the peak lines is corresponding to the beat frequency and static target's range.

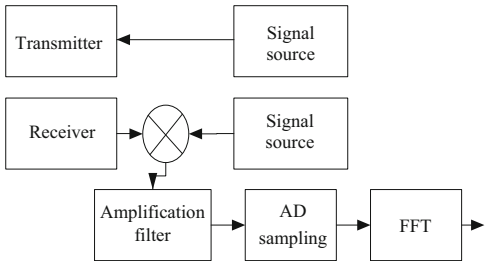

Fig. 2 The conventional LFMCW radar system structure

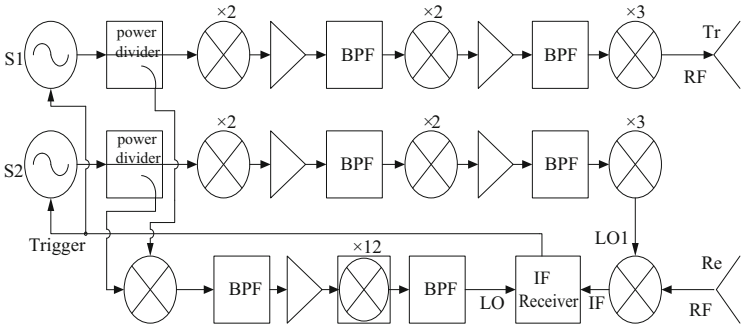

Fig. 3 THz LFMCW radar system structure

3 Intermediate-Frequency Receiver

Figure 2 can show the conventional LFMCW radar's system structure which signal model is analyzed in previous chapters. The power of signal source is limited by apparatus in THz wave band. The single frequency source has difficulty to drive transmitting and mixing at the same time. If two independent frequency sources are employed in radar system, it may lead to the issue of phase out of sync.

The "non-coherent dual-source implementing coherence" way is applied in the THz LFMCW radar system. The coherent system structure can be shown in Fig. 3. Mixing twice need to be used in order to realize coherent system. The intermediate frequency receiver is designed after the first mixing of the received THz band frequency signal. The second mixing, I/Q demodulation, signal correction and some other processing are involved in the intermediate frequency receiver.

Signal source S1 and S2, two low frequency linear frequency modulation signal, are used to produce transmitting signal and the local oscillator (LO) signal respectively. They can be respectively represented as:

$$S_1(t) = A_1 \exp\left\{2\pi f_{C1} t + \pi K_{S1} t^2\right) + \phi_1\right\} \tag{6}$$

$$S_2(t) = A_2 \exp\left\{2\pi f_{C2} t + \pi K_{S2} t^2 + \phi_2\right\} \tag{6}$$

Where f_{c1} and f_{c2} are the carrier frequency, t is the time variable, K_{s1} and K_{s2} are the frequency modulation slope, ϕ_1 and ϕ_1 are the initial phase.

Transmitting signal can be generated from the source S1 by means of × 12 frequency multiplication (× 2 twice and × 3 once), band-pass filtering and amplification. Then it can be represented as:

$$S_T(t) = A_T \exp\left\{2\pi \cdot 12 f_{C1} t + \pi \cdot 12 K_0 t^2 + 12\phi_1\right\} \tag{7}$$

where A_T is the signal amplitude. It is supposed that $R(t)$ is the range of target and $\tau(t) = 2R(t)/c$ is echo signal time delay. The received echo signal can be expressed as:

$$S_R(t) = K A_T \exp\left\{2\pi \cdot 12 f_{C1}(t - \tau(t)) + \pi \cdot 12 K_0 (t - \tau(t))^2 + 12\phi_1\right\} \tag{8}$$

LO signal in THz band can come from the source S2 by the same procedure as transmitting signal. It can be expressed as:

$$S_{LO1}(t) = A_{LO1} \exp\left\{2\pi \cdot 12 f_{C2} t + \pi \cdot 12 K_0 t^2 + 12\phi_2\right\} \tag{9}$$

where A_{LO1} is the amplitude of the LO signal. The first mixing is realized between received echo signal ($S_R(t)$) and the LO signal ($S_{Lo1}(t)$). So the obtained intermediate signal is:

$$\begin{aligned} &S_{IF}(t) = \\ &A_{IF} \exp\left\{2\pi\left[12(f_{C2} - f_{C1})t + 12 f_{C1}\tau(t) + \mu\tau t(t) - \mu\tau(t)^2/2\right] + 12\Delta\phi\right\} \end{aligned} \tag{10}$$

where A_{IF} is the amplitude of the intermediate frequency signal, $\mu = 12K_0$ is the frequency modulation sloop, $\Delta\phi = \phi_2 - \phi_1$ is the difference of initial phases.

The other LO signal is acquired through the procedure—mixing S1 and S2, × 12 frequency multiplication, amplifying and filtering. It can be represented as:

$$S_{LO}(t) = A_{LO} \exp\{2\pi \cdot 12(f_{C2} - f_{C1})t + 12\Delta\phi\} \tag{11}$$

In the end, the result of mixing intermediate frequency signal $S_{IF}(t)$ and LO signal $S_{LO}(t)$ is:

$$\begin{aligned} S_B(t) &= S_{IF}(t) \times S_{LO}^*(t) \\ &= A_B \exp\left[2\pi\left(\mu\tau(t)t + 12 f_{C1}\tau(t) - \mu\tau(t)^2/2\right)\right] \end{aligned} \tag{12}$$

The results show that the initial phase difference is offset through taking advantage of the dual-source system structure. The results are consistent with the

traditional single source LFMCW radar system structure. Thereby, the problem about dual-source's non-sync can be solved effectively.

4 Error Analysis and Correction

If the radar tone is measured for the time Δt, the Fourier-limited single-target spectral width will be $\delta f_{b\min} = \frac{1}{\Delta t}$. In according to (5), the minimum range resolution can become:

$$\delta_{r\min} = \frac{c}{2K_0}\delta f_{b\min} = \frac{c}{2K_0}\frac{1}{\Delta t} = \frac{c}{2\Delta F} \tag{13}$$

It means that range resolution only depends on the total swept bandwidth. The inverse relationship between range resolution and bandwidth is similar to the ordinary pulsed radar. With a bandwidth of 4.8 GHz, the theoretical range resolution of our THz radar is 3.1 cm, however this theoretical value is only achieved if unwanted modulation in the LFM waveform is compensated for.

Now the amplitude an phase error would be discussed in detail, which will deteriorate severely range resolution. Suppose a modulation in phase or amplitude of the LFM waveform can be modeled as perturbations $\varphi(t)$ and $A(t)$ in the transmitted and LO signals which are not flat in the total bandwidth. Besides, a direct current or low frequency component $S_L(t)$ will bring owing to sampling in our practical THz radar system. Thus (12) becomes:

$$\begin{aligned} &S_B(t) = A_B \exp\left\{2\pi(\mu\tau t + 12 f_{C1}\tau(t) - \mu\tau^2/2)\right\} \\ &\cdot A(t)\cdot \exp\left\{\Delta\varphi(t)\right\} + S_L(t) \end{aligned} \tag{14}$$

Where $A(t) = A_{LO}(t)\cdot A_T(t-\tau)$, $\Delta\varphi(t) = \varphi_{LO}(t) - \varphi_T(t-\tau)$.

In order to compensate for this degradation, some steps are taken in signal processing.

Firstly, a smoothing low-pass filter is applied to remove the low frequency component $S_L(t)$.

Secondly, a calibration signal is acquired as reference using a typical bright target at a range R0 in the radar's operating range, and the referent IF signal is recorded.

$$S_{ref}(t) = \exp\{2\pi(\mu\tau_0 t)\}\cdot A_{R0}(t)\cdot \exp\{\Delta\varphi_{R0}(t)\} \tag{15}$$

Finally, some other subsequent signals are divided by this calibration reference before spectral analysis, so the detected IF signal will be modified as:

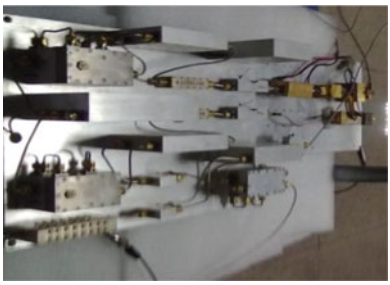

Fig. 4 The real product photo of the THz LFMCW radar

$$S_B(t) = S_B(t) \cdot \exp\{-\Delta\varphi_{R0}(t)\}_{A_{R0}(t)} \tag{16}$$

The signal spectrum will also be shifted by a known amount $\Delta f = \mu\tau_0 = \mu\frac{2R_0}{c}$ which can be added back easily. The resolution can improve significantly as long as the compensated amplitude approaches unity and the phase approaches zero.

5 Experimental Result

The LFMCW radar prototyping system working in the THz waveband has been developed in the Radar Imaging Laboratory of UESTC. The transmitting signal bandwidth is 4.8 G. Some experiments have been conducted and the results will be shown as follows. Figure 4 is the picture of the radar system, Fig. 5 shows a testing metal ball range detecting experiment results with the range 1.25 m, and three metal ball detection can been seen in Fig. 6. Finally, eight metal rods are arrayed in the platform which can rotate at a constant speed controlled by servos system, their image can be obtained by ISAR imaging method, shown in Fig. 7.

6 Conclusions

It is feasible to use LMFCW radar in THz waveband to obtain high range resolution and high quality images. Some measures taken for correcting the signal error are valid in the intermediate frequency receiver to optimize the radar's range resolution. The radar's system structure, low-noise LMF source can do the trick. In short, the THz LFMCW radar is an effective tool for range detection and imaging.

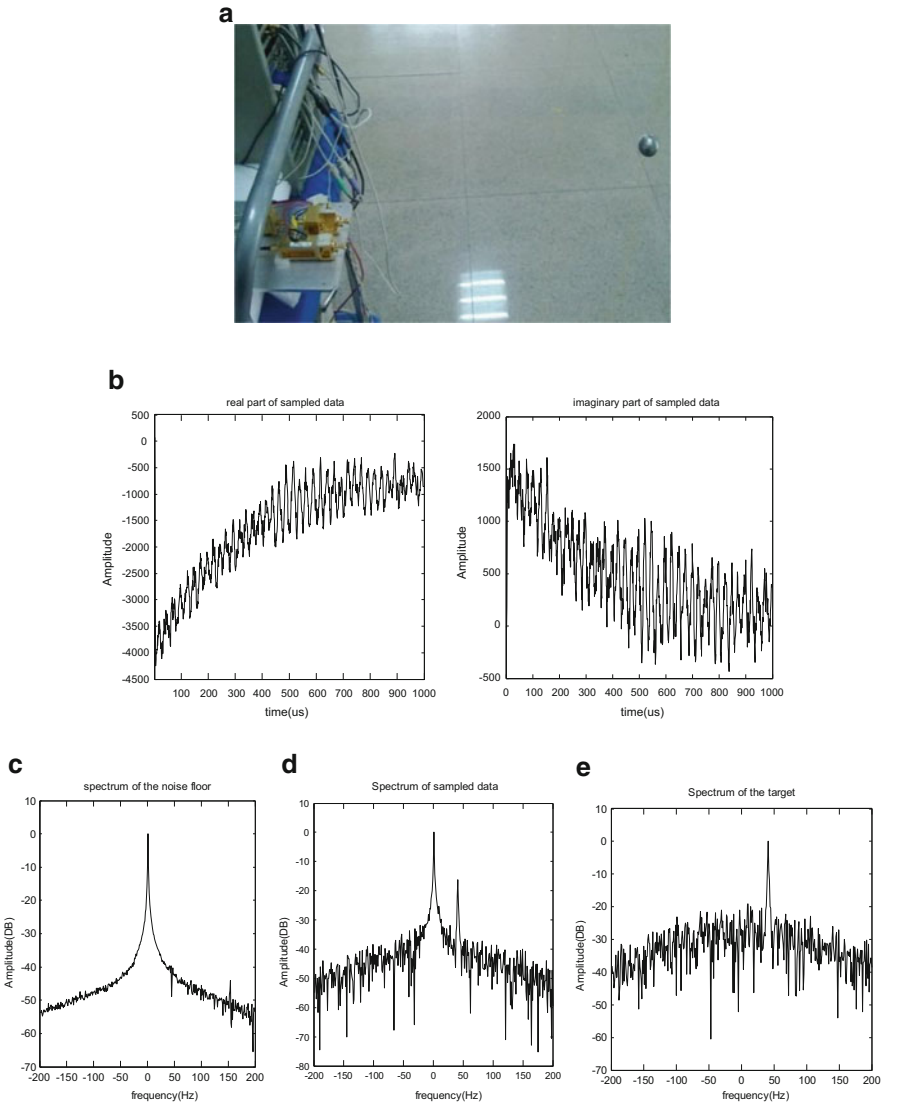

Fig. 5 (**a**) Single metal ball testing scene. (**b**) The sampled data (real and imaginary part). (**c**) Spectrum of signal noise floor detected. (**d**) Range detect without error correction; (**e**) Range detection after error correction (range 1.25 m, frequency 40 Hz)

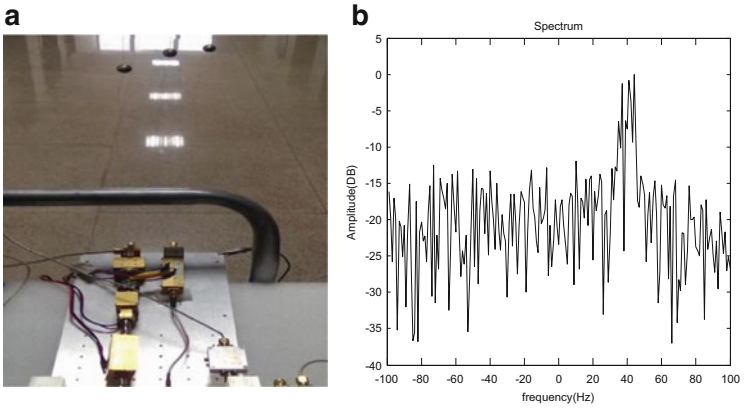

Fig. 6 (**a**) Three metal balls testing scene; (**b**) the spectrum of sampled data for rang detection

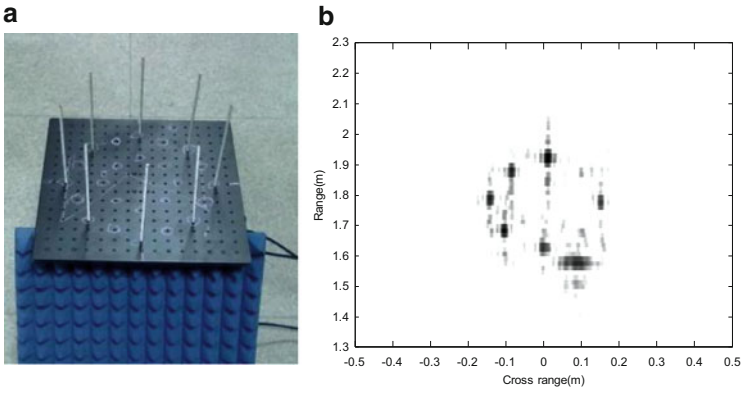

Fig. 7 ISAR imaging for eight metal rods

References

1. Dengler RJ, Maiwald F, Siegel PH (2006) A compact 600 Ghz electronically tunable vector measurement system for submillimeter wave imaging, IEEE MTT-S Int. Digest, San, Francisco, 2006, pp 1923–1926
2. Essen H, Wahlen A, Sommer R et al (2007) High-bandwidth 220GHz experimental radar. Electron Lett 43(20):1114–1116
3. Dengler RJ, Cooper KB, Chattopadhyay G, Mehdi I, Schlecht E, Skalare A, Chen C, Siegel PH (2007) 600 Ghz imaging radar with 2cm range resolution, IEEE MTT-S Int. Digest, Honolulu, 2007, pp 1371–1374
4. Cooper KB, Dengler RJ, Chattopadhyay G et al (2008) A high-resolution imaging radar at 580 GHz. IEEE Microw Wireless Compon Lett 18(1):64–66
5. Essen H, Stanko S, Sommer R et al (2008) A high performance 200-GHz broadband experimental radar. IEEE 33rd International Conference on Infrared, Millimeter and Terahertz Waves, IRMMW-THz, Pasadena, CA, 2008, Vol. 2, pp. 527-528

A Spatial Regularity Constrained Active Contour Model for PolSAR Image Segmentation

Zongjie Cao and Ying Tan

Abstract A variational active contour model based on the statistical model and local information of PolSAR images is proposed for PolSAR image segmentation. The energy functional of the proposed model consists of two parts: the likelihood data term, and the regularization term. We introduce a spatial regularization term which imposes a regional homogeneity effect on the segmentation results. The contours are evolved by minimizing the functional using fuzzy region competition method. With the above two modification, the proposed method can lead to more accurate and efficient PolSAR image segmentation algorithm than method based on standard level set method. Experimental results on both synthetic and real PolSAR images are shown. Performance evaluation and comparison with another method are also given.

Keywords Polarimetric aperture radar • Image segmentation • Variational method • Spatial regularization

1 Introduction

Polarimetric synthetic aperture radar (PolSAR) provides more information about the investigated objects by measure complex scattering matrix with full-polarization, thus improving the ability for us to automatic interpreting the observed scenes. Segmentation is a crucial step for understanding PolSAR image [1]. But due to the presence of strong speckle noise and the complexity of data, segmentation of PolSAR image is a difficult task. Much effort has been made on trying to solve this problem. In recent years, there have been many works in applying the variational active contour model [2, 3] in SAR and PolSAR image

Z. Cao (✉) • Y. Tan
School of Electronic Engineering, University of Electronic Science and Technology of China, Chengdu, China
e-mail: zjcao@uestc.edu.cn

B. Zhang et al. (eds.), *The Proceedings of the Second International Conference on Communications, Signal Processing, and Systems*, Lecture Notes in Electrical Engineering 246, DOI 10.1007/978-3-319-00536-2_69,

segmentation problems. In [4], active contour model is used to segment the SAR images, and a multiregion representation model is proposed. In [5], the active contour method is used to separate the water and land region in SAR images, and then the segmentation results are used for flood monitoring. The curve evolution problems in both [4] and [5] are solved with standard level set method [6]. Although the level set method is flexible with topological change, it may result in unexpected state since the energy function has local minimum. The standard level set method is also computational inefficient as it needs re-initializing steps. In [7], this disadvantage of level set method is overcome by designing a new energy functional which has a global minimum. All those methods mentioned above are developed for intensity SAR images, but not for fully polarimetric SAR images. For active contour method applied in PolSAR image segmentation, we refer to [8] and [9]. In [8], a B-spline snake model is used for boundary detection in PolSAR images. In [9], Ayed et al. extended their work in [4] to polarimetric images. However, like all classical snake models, the B-spline snake suffers the difficult of topological change. As the active contour model in [9] is implemented via standard level set method, it shares the same disadvantages of the method in [4] such as local minimum and computational inefficient, just as [7] point out. Besides, all energy functionals in aforementioned works are composed of two parts: a likelihood data term and a regularization term. The regularization term is used to introduce prior information about the images into the energy functional. In those works, the regularization term are simply chosen as the Euclidean length of the contour, which will ensures the contour to be smooth. Nevertheless, no more prior information is introduced. However, works show that by incorporating proper prior information, better segmentation results can be obtained [10, 11].

To overcome those limitations, we propose an active contour model for PolSAR image segmentation with spatial regularity constraint. The segmentation of PolSAR images is formulated as a maximum a posterior probability problem. Assuming that each statistical homogenous region is independent, the conditional probability for each region is modeled by complex Wishart distribution. A prior that considers the neighborhood correlation is introduced in the form of prior probability for each pixel. The segmentation is performed by minimizing energy functional derived from maximum a posterior probability principle. Like in [7], to avoid the disadvantages of standard level set method, the energy functional is modified to be convex. The effect of this modification is twofold. On one hand, the energy functional is convex means that a global minimum can be achieved, which ensures a unique segmentation result. On the other hand, this modification also enables us to adopt the fast fuzzy region competition method to execute the minimization. So the algorithm becomes more computational efficient.

The rest of this paper is organized as follows. Section 2 addresses the proposed active contour model, in which the prior information term is introduced and discussed. Section 3 introduces the minimization scheme. Experiment results are demonstrated in Sect. 4 and finally the paper is concluded.

2 The Proposed Model

Assuming that Ω be the image domain, and $T(x)$ is the complex PolSAR data at each pixel x. The PolSAR image is assumed to be composed of N regions. The goal of segmentation is to derive a partition of the image domain, i.e. $\Omega = \cup_k \Omega_k$, $\Omega_i \cap \Omega_j = \varnothing$, $i \neq j$. Denote the conditional probability of $T(x)$ belongs to region Ω_k as $p(T(x)|\Omega_k)$, and the prior probability for each region Ω_k is $p(\Omega_k)$, then by assuming each region is statistical independent, the segmentation of PolSAR image into N region can be modeled as a maximum a posterior probability problem:

$$\begin{aligned}\{\Omega_k\}_{k=1}^N &= \underset{\{\Omega_k\}_{k=1}^N}{\operatorname{argmax}} \prod_{k=1}^N \prod_{x\in\Omega_k} p\big(\Omega_k \big| T(x)\big) \\ &= \underset{\{\Omega_k\}_{k=1}^N}{\operatorname{argmax}} \prod_{k=1}^N \prod_{x\in\Omega_k} p(\Omega_k) p\big(T(x)\big|\Omega_k\big)\end{aligned} \tag{1}$$

By logarithm operation, we can derive the energy functional to be minimized, that is:

$$\begin{aligned}E &= -\log\left[\prod_{k=1}^N \prod_{x\in\Omega_k} p(\Omega_k) p\big(T(x)\big|\Omega_k\big)\right] \\ &= \sum_{k=1}^N \int_{x\in\Omega_k} -\log p\big(T(x)\big|\Omega_k\big) - \log p(\Omega_k)\end{aligned} \tag{2}$$

The probability distribution function of the PolSAR matrix data is often assumed to be Gaussian-Wishart distribution. More specifically, it is often assuming that mono-look PolSAR data follows complex Gaussian distribution and multi-look PolSAR data follows complex Wishart distribution. For simplifying the flow of the reasoning, we just assume that the PolSAR data is multi-look (The mono-look case can be treated by the same flow with complex Gaussian model). For multi-look case, the polarimetric covariance matrix is often used to represent the PolSAR data. The probability density function of the covariance matrix $T(x)$ in each region Ω_k can be written as:

$$p\big(T(x)\big|\Omega_k\big) = \frac{det(T(x))^{L-n}\exp\big(-L\cdot tr\big(\boldsymbol{C}_k^{-1}T(x)\big)\big)}{K(L,n)det(\boldsymbol{C}_k)^L} \tag{3}$$

where $K(L,n) = \pi^{\frac{n(n-1)}{2}}\Gamma(L)\Gamma(L-n+1)$, L is the number of looks, and n is the dimension of the data, $\boldsymbol{C}_k$ is the mean covariance matrix of the data in region Ω_k.

In [9], the prior term $\log\, p(\Omega_k)$ is chosen as a classic boundary length term which imposes a smooth effect on the contour. This term considers the interaction of

points on the contour. However, the correlation between adjacent pixels is ignored. Therefore, unsatisfying results can be obtained when the background disturbance is strong. For inhomogeneous regions, the contours tend to be very fragmental. Furthermore, at the boundary of two adjacent regions, the transition area can be classified as regions with intermediate property, which leads to the appearing of line-like misclassified areas.

We propose to solve those problems by adding a regional regularization term, which introduces a prior information that considers the neighborhood correlation of pixels. The assumption is simple but reasonable: the more pixels in the neighborhood of one pixel belong to a specific region, the higher the probability of this pixel belongs to this specific region is. Obviously, this assumption encourages the adjacent pixels to be classified into a same region, and thus enhance the ability of contours to resist the effect of the area inhomogeneity and background disturbance. For each pixel x with neighborhood area $N(x)$, the prior probability can be estimated by:

$$p(x \in \Omega_k) = \frac{1}{G} \exp\left(-\sigma \left(\frac{M(x)}{M_k(x)} - 1 \right) \right), k = 1, 2 \cdots N \tag{4}$$

where G is the normalization coefficient, $M(x)$ is the total number of pixels in $N(x)$, and $M_k(x)$ is the number of pixels in $N(x)$ that belongs to region Ω_k,the parameter σ controls the increasing speed of the prior probability from 0 to 1. It can be easy observed that the probability is higher with bigger $M_k(x)$. By multiplying this prior probability, the local region information is introduced to increase or decrease the posterior probability of one pixel belongs to a specific region.

By substituting (3) and (4) into (2), with some algebraic manipulations and removing terms independent with segmentation [9], we can yield:

$$E = \sum_{k=1}^{N} \int_{x \in \Omega_k} \log(det(\boldsymbol{C}_k)) + \sigma \left(\frac{M(x)}{M_k(x)} - 1 \right) dx \tag{5}$$

We also add the classic regular term related to the boundary length:

$$E_r = \sum_{k=1}^{N} \int_{\Gamma_k} ds \tag{6}$$

where ds is the Euclidean arc-length. Then we can obtain the new maximum a posterior probability energy functional with a weighting coefficient β:

$$E = \sum_{k=1}^{N} \int_{x \in \Omega_k} \log(det(\boldsymbol{C}_k)) + \sigma\left(\frac{M(x)}{M_k(x)} - 1\right) dx + \beta \sum_{k=1}^{N} \int_{\Gamma_k} ds \tag{7}$$

3 Minimization Energy Functional by Fuzzy Region Competition

With level set representation and multi-region scheme, minimizing the energy functional leads to the segmentation of PolSAR images. But the traditional level set methods is computational inefficient as it often needs the re-initialization step, which is time consuming, to keep the level set function to be signed distance function[12]. Moreover, the existence of local minimum of the energy functional (7) may make the evolving contours to stop at undesired positions [12]. At last, as [7] point out, the utilizing of signed distance function makes it's difficult to set an appropriate terminate criterion. Recently, many efforts have been devoted to find global minimizer of active contour model and many efficient algorithms [13, 14] have been proposed. We adopt the multiphase fuzzy region competition methods in [14] to implement the minimizing of energy functional (7) to obtain the segmentation of PolSAR images.

Following the idea in [14], firstly we introduce the fuzzy membership functions $u_i \in BV_{[0,1]}(\Omega)$, $\sum_{i=1}^{N} u_i = 1$ to represent the regions. Note that $BV_{[0,1]}(\Omega)$ is the set of bounded variation functions valued between 0 and 1. The bigger the value of $u_i(x)$ is, the more likely the pixel x belongs to region Ω_i. The representation is natural, and with the set of membership functions $\mathbf{U} = \{u_k\}_{k=1}^{N}$, the pixel x is decided to belong to region Ω_k if:

$$k = \underset{i}{\operatorname{argmin}} \left\{ i \middle| u_i(x) = \max\left(u_j(x), j = 1, 2 \cdots N\right) \right\} \tag{8}$$

Using (8), each pixel can be assigned a unique label which corresponds to a segmented region. Then set $\lambda = 1/\beta$, the fuzzy region competition energy functional corresponding to (7) is:

$$E = \sum_{k=1}^{N} \int_{\Omega} |\nabla u_k| dx + \sum_{k=1}^{N} \lambda \int_{\Omega} u_k \left[\log(\det(\boldsymbol{C}_k)) + \sigma\left(\frac{M(x)}{M_k(x)} - 1\right) \right] dx \tag{9}$$

where $\|$ is the L1 norm, ∇u_k is the gradient of u_k and the first term is the boundary length. Note that:

$$\xi_k = \log(\det(\boldsymbol{C}_k)) + \sigma\left(\frac{M(x)}{M_k(x)} - 1\right) \tag{10}$$

The direct minimizing of (9) based on a PDE is slow [13]. For efficiently

minimizing of energy (9), based on [13–15], we use a convex regularization of the variational model:

$$E = \sum_{k=1}^{N} \left(\int_{\Omega} |\nabla v_k| dx + \frac{1}{2\theta} \int_{\Omega} (v_k - u_k)^2 dx + \lambda \int_{\Omega} u_k \xi_k dx \right) \tag{11}$$

where $\mathbf{V} = \{v_k\}_{k=1}^{N}$ is the auxiliary variable set. Each $v_k \in \mathbf{V}$ is called the dual variables of $u_k \in \mathbf{U}$. And θ is chosen small enough to make sure that u_k and v_k are almost identical with respect to L^2 norm.

The value of energy function E is decided by three sets $\mathbf{U}$, $\mathbf{V}$ and $\mathbf{\Xi} = \{\xi_k\}_{k=1}^{N}$. Based on [13, 15], it easy to verify that (11) is convex with respect to u_k and v_k respectively when $\mathbf{\Xi}$ is fixed. So with $\mathbf{\Xi}$ fixed, the minimization can be executed with respect to u_k and v_k separately, and to iterate until convergence. Firstly fix $\mathbf{V}$, minimizing (11) with respect to each $u_k \in \mathbf{U}$. For $u_N = 1 - \sum_{k=1}^{N-1} u_k$, only u_k, $k = 1, 2, \cdots N-1$ need to be solved, Let $\partial E / \partial u_k = 0$ yield:

$$\widetilde{u}_k = v_k - \lambda\theta(\xi_k - \xi_N), k = 1, 2, \cdots N-1 \tag{12}$$

To satisfy the condition of $u_i \in BV_{[0,1]}(\Omega)$, we project $\widetilde{u}_k$ on [0,1], that is:

$$\widetilde{u}_k = \min\{\max(\widetilde{u}_k, 0), 1\}, k = 1, 2, \cdots N-1 \tag{13}$$

Secondly, fix $\mathbf{U}$, minimizing (11) with respect to each $v_k \in \mathbf{V}$, which yields the following solution:

$$v_k = u_k - \theta div(w_k), k = 1, 2, \cdots N-1 \tag{14}$$

where w_k is given by:

$$\nabla(\theta div(w_k) - v_k) - |\nabla(\theta div(w_k) - v_k)| w = 0 \tag{15}$$

Equation (15) comes from solving the dual formulation of (11) respect to v_k, and w_k is the auxiliary variable. We refer [13, 15] for the details of mathematic derivation. w_k can be updated by fix point method with initialization condition $w_k^0 = \mathbf{0}$:

$$w_k^{n+1} = \frac{w_k^n + \tau \nabla\left(div\left(w_k^n\right) - u_k/\theta\right)}{1 + \tau \left| \nabla\left(div\left(w_k^n\right) - u_k/\theta\right) \right|} \tag{16}$$

The time step is set as $\tau < 1/8$ to ensure converge stably [15].

After updating the membership functional, each $\xi_k \in \mathbf{\Xi}$ is updated by using (10). The prior probability is updated with (4), and $\boldsymbol{C}_k$ is updated by:

$$\boldsymbol{C}_k = \frac{\int_{\Omega} u_k T(x) dx}{\int_{\Omega} u_k dx}, , k = 1, 2, \cdots N - 1 \tag{17}$$

Finally, the label for each pixel is obtained according to:

$$L(x) = \underset{i}{\operatorname{argmin}} \left\{ i \middle| u_i(x) = \max\left(u_j(x), j = 1, 2 \cdots N\right) \right\} \tag{18}$$

With the three steps, the energy functional can be minimized efficiently, and the algorithm can be summarized as:

Step 1: Initializing the membership functions u_k, $k = 1, 2 \cdots N$;

Step 2: using (17) and (10) to compute ξ_k for $k = 1, 2 \cdots N$;

Step 3: updating v_k, $k = 1, 2 \cdots N - 1$ by (16) and (14);

Step 4: updating u_k, $k = 1, 2 \cdots N - 1$ by (12) and (13), and $u_N = 1 - \sum_{k=1}^{N-1} u_k$.

Repeat steps 2–4 until the convergence condition $\sum_{k=1}^{N} \|u_k^{n+1} - u_k^n\| < \varepsilon$ is satisfied.

4 Experiment Results

We set the parameters in the experiments as follows. The neighborhood area of pixel x is set as a square window, and the size is generally chosen to be 5×5. Bigger size means more local information is used, but also more computational burden is added. $M(\boldsymbol{x})$ is equal to 25 for all images, $M_k(x)$ can be computed by convolution the label map with the window. In the experiments, the parameter σ ranges from 0.02 to 2, in which the probability arises with a moderate velocity. The parameters used in the fast minimization scheme are chosen to be $\theta = 1.5$, $\lambda = 0.3$, $\tau = 1/8$, which are suitable for a wild range of PolSAR images. For better segmentation results, the parameter θ and λ can be decided by the following principle: bigger θ and smaller λ should be used for obtaining smoother segmentation result, and vice versa. The stopping parameter ε is set as a function of the image size (N_x,N_y) and the number of regions N. It is chosen as $\varepsilon = 0.03 \times N_x \times N_y \times N$ in our experiments.

Firstly, the proposed method is tested on a synthetic 8-look PolSAR image. The image is composed of three regions as shown in Fig. 1a. Figure 1b is the image with initial contours. To show the advantage of the proposed method over method in [9], we demonstrate the segmentation results of two methods in Fig. 1c, d. With the method in [9], spurious regions are presented at the boundary of two regions, as shown in Fig. 1d, which are in the white rectangle. However, the spurious regions are absent in Fig. 1c, which is obtained by the proposed method. It shows that by introducing the local prior information, the proposed spatial regularity constrained

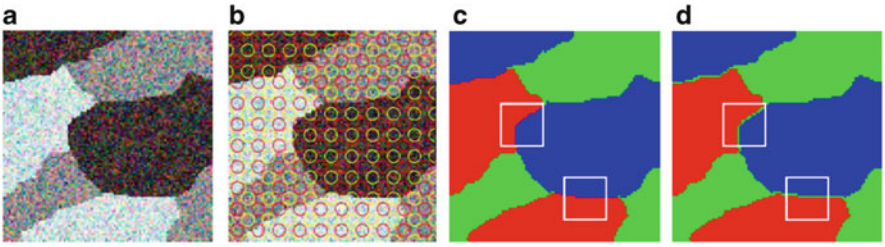

Fig. 1 Segmentation of a synthetic PolSAR image. (**a**) The synthetic PolSAR image; (**b**) Initial contours; (**c**) Segmentation result of the proposed method; (**d**) Segmentation result of methods in [9]

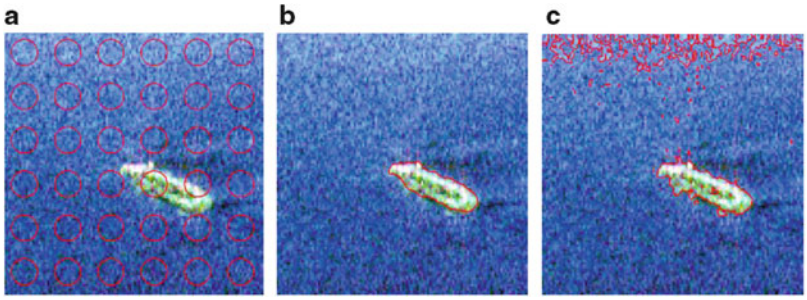

Fig. 2 Segmentation of an AIRSAR PolSAR image. (**a**) Initial contour; (**b**) Final contour of the proposed method; (**c**) Final contour of the method in [9]

active contour method can lead to more accurate segmentation result than the maximum likelihood method in [9].

In Fig. 2, we show one experimental result on a real L-Band 4-look AirSAR PolSAR image in San Francisco Bay. In the middle of the image is an island. We segment the image with the proposed method and the method in [9]. Again, the proposed method gets satisfied results in Fig. 2b, and the comparing method produces many fragmental regions in Fig. 2c. That is because the proposed method uses the local prior information, and thus has stronger ability to resist the effect of area inhomogeneity and background disturbance.

The method in [9] is implemented with traditional level set method, which converges slowly and is time consuming. As we adopt the fast fuzzy region competition method, both iteration numbers and consumption time decrease dramatically, which means the proposed method is much more practical.

5 Conclusion

We present a maximum a posterior probability active contour model for PolSAR image segmentation. By introducing the local prior information into the energy functional, the proposed method is more applicable for PolSAR image segmentation

than current ones. Because of using the fuzzy region competition method, the method is also computational efficient. Experiments on both synthetic and real SAR images demonstrate the superior performance of the proposed methods. The future work includes exploring more appropriate prior models and investigating techniques to decide the number of regions automatically.

References

1. Beaulieu J-M, Touzi R (2004) Segmentation of textured polarimetric SAR scenes by likelihood approximation. IEEE Trans Geosci Rem Sens 42(10):2063–2072
2. Kass M, Witkin A, Terzopoulos D (1987) Snakes: active contour models. Int J Comput Vis 1 (4):321–331
3. Chan TF, Vese LA (2001) Active contours without edges. IEEE Trans Imag Process 10 (2):266–277
4. Ayed IB, Mitiche A, Belhadj Z (2005) Multiregion level-set partitioning of synthetic aperture radar images. IEEE Trans Pattern Anal Mach Intell 27(5):793–800
5. Silverira M, Heleno S (2009) Separation between water and land in SAR images using region-based level sets. IEEE Geosci Rem Sens Lett 6(3):471–475
6. Malladi R, Sethian JA, Vemuri BC (1995) Shape modeling with front propagation: a level set approach. IEEE Trans Pattern Anal Mach Intell 17(2):158–175
7. Shuai NY, Sun H, Xu G (2008) SAR image segmentation based on level set with stationary global minimum. IEEE Geosci Rem Sens Lett 5(4):644–648
8. Frery AC, J-berlles J, Gambini J, Mejail ME (2010) Polarimetric SAR image segmentation with B-Splines and a new statistical model. Multidim Syst Sign Process 21:319–324
9. Ayed IB, Mitiche A, Belhadj Z (2006) Polarimetric image segmentation via maximum-likelihood approximation and efficient multiphase level-sets. IEEE Trans Pattern Anal Mach Intell 28(9):1493–1500
10. Chen Y, Tagare H, Thiruvenkadam S et al (2002) Using shape priors in geometric active contours in a variational framework. Int J Comput Vis 50(3):315–328
11. Cremers D, Sochen N, Schnorr C (2006) A multiphase dynamic labeling model for variational recognition-driven image segmentation. Int J Comput Vis 66(1):67–81
12. Li C, Xu C, Gui C (2005) Level set evolution without re-initialization: a new variational formulation. In: Proc IEEE CVPR, San Diego, CA, 2005, pp 430–436
13. Bresson X, Esedoglu S, Vandergheynst P et al (2007) Fast global minimum of the active contour/snake model. J Math Imag Vis 28(1):151–167
14. Li F, Ng MK, Zeng TY, Shen C (2010) A multiphase image segmentation method based on fuzzy region competition. SIAM J Imag Sci 3(3):277–299
15. Chambolle A (2004) An algorithm for total variation minimization and application. J Math Imag Vis 20(1–2):89–97

The Research on Fuzzy Ontology Modeling Method and Its Application on Intelligent Household Security

Huang Lin, Yongheng Wang, and Xiaoming Zhang

Abstract Currently the ontology based context modeling technology has got a wide application. Semantic information which includes vague information and user's preference brings huge challenge to ontology modeling, because the existing ontology model can't deal with the large information from semantic context with fuzziness and uncertainty so that we can't provide satisfying intelligent information service for the user. In this paper, we propose a sharing fuzzy ontology modeling method based on fuzzy theory to solve this problem, by establishing a fuzzy ontology conceptual model which includes the fuzzy membership function and the fuzzy limited concept. Finally a intelligent household security fuzzy ontology is demonstrated to prove the feasibility of the proposed approach.

Keywords Fuzzy ontology conceptual model • Fuzzy membership function • Fuzzy limited concept • Intelligent household security

1 Introduction

The service model of the future convergence network is transforming from "network-centered" and "content-centered" to "user-centered." Whether the service can sense the user context and adapt according to the user's requirement and preference will be pivotal to the success the future convergence service [1]. Context modeling based on the ontology is widely applied [2].

The ontology technology plays an important role on semantic information organization, semantic information access and semantic information processing [3]. Human win the high intelligent fuzzy logic thinking ability, and can deal with fuzzy information in the process of development. In the application of web

H. Lin (✉) • Y. Wang • X. Zhang
School of Information Science and Engineering, Hunan University, Changsha, China
e-mail: 871958107@qq.com

B. Zhang et al. (eds.), *The Proceedings of the Second International Conference on Communications, Signal Processing, and Systems*, Lecture Notes in Electrical Engineering 246, DOI 10.1007/978-3-319-00536-2_70,

service, the fuzzy ontology little considers user's preference and application scenarios so that it can't provide user with more satisfied service, meanwhile it doesn't make full use of the fuzzy membership degree and fuzzy reasoning to support decision service for the user [4]. The current fuzzy ontology research primarily focuses on domain ontology modeling of specific areas, and only applies the obfuscation of semantic in specific areas instead of establishing general sharing fuzzy ontology which can apply fuzzy ontology to different areas and tasks [5]. This paper describes the fuzzy set and the fuzzy relation by using fuzzy membership degree, puts forward to two kinds of fuzzy concepts which are the extend fuzzy limited concept and the range fuzzy limited concept, establishes a fuzzy ontology conceptual model, and conducts the OWL semantic description on fuzzy membership function and fuzzy limited concept. At the same time based on this model a fuzzy ontology of household security is established.

2 Related Concept

2.1 Fuzzy Ontology

Ontology is composed of entity, attribute, relationship and axiom. With the help of ontology user and system can communicate with each other. But the ontology based context model can't handle the fuzzy context information and their uncertainty reasoning. So we propose to use the fuzzy ontology [5] to address this issue. Several fuzzy ontology descriptions have been proposed, a fuzzy ontology is a quintuple defined as $F = < I, C, R, F, A >$. I is the individual set. C is all the concepts of the domain. E is all the objects that involved in the interaction between the user and the service, which has the same attributes. And it can be defined as $E = C \cup U$. F is the fuzzy taxonomic relationship. R is fuzzy non-taxonomic relationship. A is axioms that expressed in a logical language.

2.2 Fuzzy Set

There is a mapping relation: $\mu_A : U \rightarrow [0,1]$; $\mu \rightarrow \mu_A(u) \in [0,1]$. Fuzzy set is defined as A; the theory of the domain is defined as U; the subset of U is defined as u. if $\forall\ u \in U$ is set up, a certain value of $\mu_A(u)$ is restricted to [0,1]. $\mu_A(u)$ is the membership degree, in other words $\mu_A(u)$ is the membership degree of the fuzzy set (A) when the element u is from theory of the domain(U). When the value of $\mu_A(u)$ is 0 or 1, the set is a precise set.

2.3 Fuzzy Membership Function

For the fuzzy set, when it need to reflect each element to the membership degree of a fuzzy set, Membership Function [6] is applicable to describe the fuzzy set which exists in the theory of domain (U).

When it is necessary to process the fuzzy information by using fuzzy theory, the first thing is to define the membership function. There are some usually used membership functions which are Trapezoidal Function, Left Semi-Trapezoidal Function, Right Semi-Trapezoidal Function, Normal Function, and Triangular function. When U values [k1, k2], Trapezoidal Function and Normal Function are defined as follows:

$$Trapezoidal(u; k_1, k_2; a, b, c, d) = \begin{cases} 0 & u \le a \\ \dfrac{u-a}{b-a} & a < u \le b \\ 1 & b < u \le c \\ \dfrac{d-u}{d-c} & c < u \le d \end{cases} \tag{1}$$

$$Normal(u; k_1, k_2; a, b) = \begin{cases} e^{-\pi(u-v)2} & |u-v| \le \dfrac{b-a}{2} \\ 0 & |u-v| > \dfrac{b-a}{2} \end{cases} \tag{2}$$

2.4 Fuzzy Limited Concept

Fuzzy limited concept is used as the prefix for the accurate concept or the fuzzy concept. Fuzzy limit concept mainly includes the extend fuzzy limited concept and the range fuzzy limited concept.

Extend fuzzy limited concept is used to modify information so that we can strengthen the tone or abate tone. Extend fuzzy limited concept is defined as follows:

$$\mu_{M_\lambda A}(\mu) = [\mu_\lambda(u)]^\lambda = \mu_M{}^\lambda(\mu) \tag{3}$$

λ which is positive real number is the degree of operator, when it is greater than 1, M_λ is the degree of operator that strengthens the tone; when it is less than 1, M_λ is the degree of operator that abates the tone. The degree of the extend fuzzy limited concept can be said the power set of "$\mu_\lambda(u)$" and "λ." Extend fuzzy limited concept only works on the fuzzy concept and the fuzzy relationship, and doesn't work on the precise concept and the common relationship.

Range fuzzy limited concept is used to modify information so that we can blur the semantic information. Its main roles in the following two aspects: 1. It can

obscure clear semantic information; 2. It can make the fuzzy concepts and fuzzy relations more blurred. Range fuzzy limited concept is defined as follows:

$$\mu_N(u) = \mu_A(u) \times \mu_E(\nu, u) \tag{4}$$

The fuzzy set is defined as $N = A \cup E$, E which is fuzzy relations with U is range fuzzy limited concept, and this relationship is generally similar relationship. One of the range fuzzy limited concept can meet the Normal distribution. Fuzzy relations (E) can show in (2).

The precise concept "177 cm" after modified by range fuzzy limited concept "about" is fuzzy information "about 177 cm" that can express:

$$\mu_{about}(u) = A_{177}(u) \times E(177, u) = E(177, u) \tag{5}$$

3 Implementation

To achieve fuzzy ontology model, we follow the latter approach, based on the ontology definition and formalization, by combining the fuzzy concept and fuzzy relation in the fuzzy theory, by solving the uncertainty and fuzziness of the concept and relation through the fuzzy membership degree. At the same time, for uncertainty of the thing boundary scope fuzziness, it is necessary to add fuzzy limited concept before the described concept and relationship so that we can fully extend the fuzziness for specific domain ontology. After part of the chapter, the OWL semantic description of fuzzy membership function and fuzzy limited concept is described; the sharing fuzzy ontology model including fuzzy membership function semantic model and fuzzy limited concept semantic model is designed.

3.1 Fuzzy Membership Function OWL Semantic

The OWL semantic description [7] of Normal Function is the following, and it is mainly described about function data types, parameters and variables. Pseudo codes are firstly described.

```
  Define float variable "u" as ID, as an input from Normal
Distribution Function whose domain is "#Normal".
  Define float datatypes "k1". "k2". as ID, resulting from
Normal Distribution Function whose domain is "#Normal".
  Define float parameters "a". "b" "degree" as ID, resulting
from Normal Distribution Function whose domain is "#Normal".
  <owl:DatatypeProperty rdf:ID = "u"."k1"."k2"."b"."degree">
  <rdfs:range rdf:resource = "XMLSchema#float"/>
  <rdfs:domain rdf:resource = "#Normal"/>
</owl:DatatypeProperty>
```

```
<owl:DatatypeProperty rdf:ID = "a">
  <rdfs:comment rdf:datatype = "XMLSchema#float"/>
  <rdfs:domain rdf:resource = "#Normal"/>
</owl:DatatypeProperty>
```

Above the OWL describes the variable "u," datatypes"k1" and "k2," parameters "a" and "b" and the degree which all belong to Normal Function. By using the same way, we can describe the ontology semantic of other functions by using OWL.

3.2 Fuzzy Limited Concept OWL Semantic

Fuzzy limited concept is made of the extend fuzzy limited concept and the range fuzzy limited concept. There are described below that are a extend fuzzy limited concept "extremely" and a range fuzzy limited concept "about."

```
Define float 4.0 as "extremely", resulting from extend fuzzy
limited concept.
Define float 10.0 as "about", resulting from range fuzzy
limited concept.
<owl:AllDifferent>
  <owl:distinctMembers rdf:parseType = "Collection">
    <ExtendLimited rdf:ID = "EM_extremely">
    <limited rdf:datatype = "XMLSchema#string"> extremely
</limited>
    <lambda rdf:datatype = "XMLSchema#float" > 4.0</lambda>
</ExtendLimited>
    <RangeLimited rdf:ID = "RM_about">
    <limited      rdf:datatype = "XMLSchema#string" > about</
limited>
    <delta rdf:datatype = "XMLSchema#float" > 10.0</delta>
</RangeLimited>
```

3.3 Conceptual Model of Sharing Fuzzy Ontology

Ontology is a conceptual model [8]. When we need to establish a big situation by using the ontology tool, it is usually divided into some parts. According to the above research, a ontology may contain the precise concept, the accurate relation, the fuzzy concept or the fuzzy relation. So the precise ontology of a big ontology must be the precise concept or the precise concept with the accurate relation. And the fuzzy ontology may be the fuzzy relation with the precise concept, the fuzzy concept or the fuzzy relation with the fuzzy concept. So the conceptual model of sharing fuzzy ontology is showed in Fig. 1.

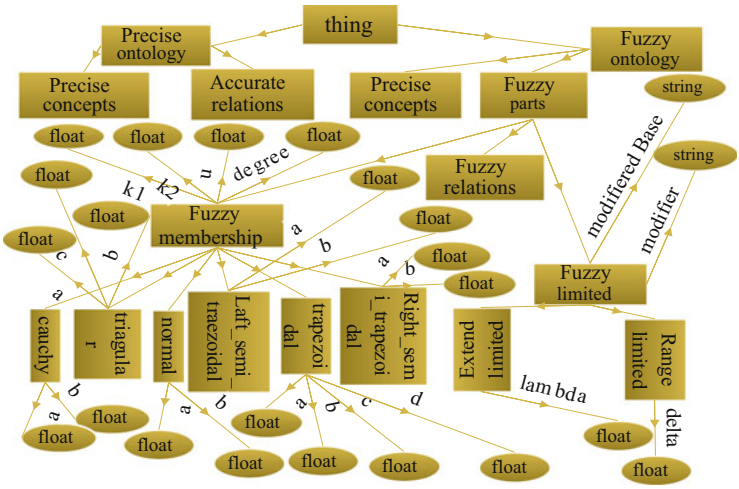

Fig. 1 The conceptual model of sharing fuzzy ontology

3.4 Implementation of the Sharing Fuzzy Ontology

Based on the conceptual model, we can visually build the sharing fuzzy ontology using the popular ontology editor tool of Protégé_4.2. The main concepts and their hierarchies of the sharing fuzzy ontology as shown from Protégé_4.2 are presented in Fig. 2.

The fifth layer displays most subclasses of the fuzzy membership and the fuzzy limited concept, and the sixth layer displays some exact concept respectively belonging to the extend fuzzy limited and the range fuzzy limited concept.

3.5 Model of Intelligent Household Security

After creating the concept and the relation of intelligent household security according the above model, we can define attributes of concepts, create axioms of concepts and attributes, and add instances and axioms into intelligent household security according to the domain knowledge and application requirement. In Fig. 3 the third layer is three concepts which are user, device and environment; the sixth layer is some attributes and instances about security. The model is simple but it can be extended. And we can find the process of modeling is not unambiguous but also straightforward.

Example: We may define data types *Age*: $U_{Age} = [120,200] \rightarrow [0,1]$, denoting the degree of a person being short, middle and high, as: $R_{Yong}(u;20,100;40,50)$;

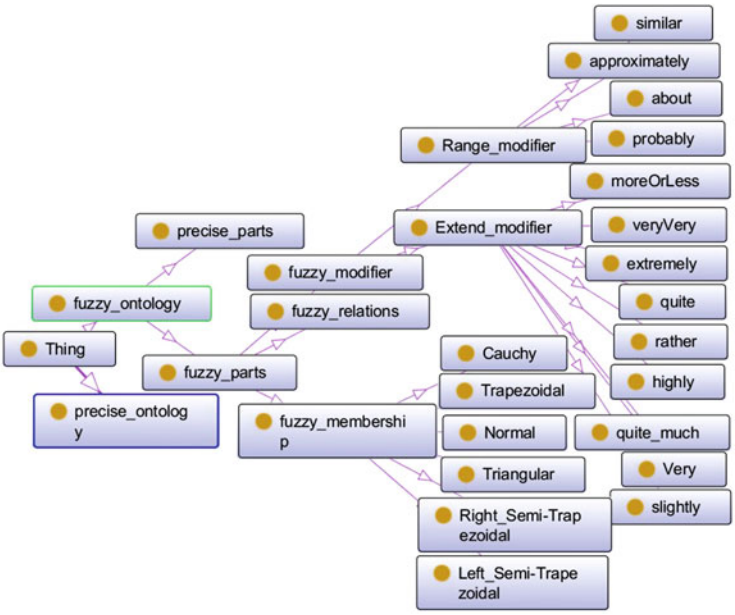

Fig. 2 Implementation of the sharing fuzzy ontology

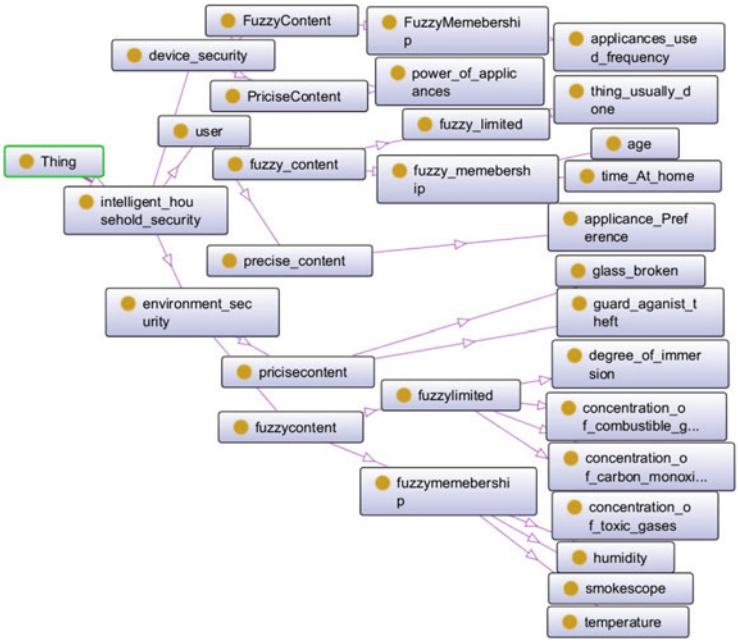

Fig. 3 Model of intelligent household security

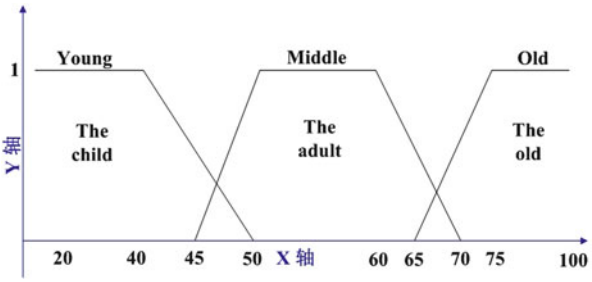

Fig. 4 The membership function of age from model of intelligent household security

$R_{Middle}(u;20,100;45,50,60,70);$. $R_{Old}(u;20,100;65,75)$. The age of the people from the household can be reflected in Fig. 4.

4 Conclusion

The paper has done the research on the fuzzy membership function and the fuzzy limited concept, then conducts the OWL semantic description about the two concepts, sets up a conceptual model of the sharing fuzzy ontology and implements it by using the ontology editor tool of Protégé_4.2. Finally a intelligent household security fuzzy ontology is demonstrated to prove the feasibility of the proposed approach.

In the future work, there are a large amount of uncertain information and knowledge in the real application, so we will resolve the problem of uncertainty reasoning of fuzzy context by using fuzzy reasoning theory. Meanwhile, we will compare the fuzzy reasoning theory with the other reasoning theories to optimize the reasoning.

Acknowledgments Project is supported by Hunan Provincial Natural Science Foundation of China "Context-aware and proactive complex event processing for large scale internet of things (13JJ3046)" and is supported by the "complex event processing in large scale internet of things (K120326-11)" project of Changsha technological plan.

References

1. Yanna L, Xiuquan Q, Xiaofeng L (2010) An uncertain context ontology modeling and reasoning approach based on D-S. J Electron Inform Tech Theor 32(8):1806–1811
2. Cai Y, Yeung CA, Leung H (2012) Fuzzy computational ontologies in contexts. Higher education press, Beijing
3. Singh A, Juneja D, Sharma AK (2011) A fuzzy integrated ontology model to manage uncertainty in semantic web: the FIOM. Int J Comput Sci Eng 3:1057–1062
4. Jun-min L, Yu-yun W, Bin W (2011) Research on the fuzzy ontology and its evolution. Microelectron Comput 28(5):140–143

5. Li G, Zou H, Yang F (2011) Fuzzy ontology and fuzzy D-S evidence theory based context modeling and uncertainty reasoning. J Converg Inform Tech 6:185–193
6. Dazhou K, Baowen X, Jianjiang L (2006) Description logics for fuzzy ontologies on semantic web. J SE Univ 22(3):343–347
7. Fernando Bobillo, Umberto Straccia (2010) Fuzzy ontology representation using OWL2. In: Proceedings of the 19th IEEE International Conference on Fuzzy Systems (FUZZ-IEEE), Taipei, Taiwan, June 2011, pp 1727–1734
8. Yan-hui LB, Zong-Min MA, Zhang F (2009) An approach to fuzzy ontology framing based on fuzzy conceptual model. J NE Univ (Nat Sci) 30(9):1262–1265

Wideband Radar Target Detection Based on the Probability Distance of Empirical Cumulative Distribution Function

Guishan Lin, Zhiming He, Jing Wu, Meng Zhao, and Zhihao Mei

Abstract The broadband radar technology has attracted much attention in the field of modern radar. Wideband radar target detection is the important part of broadband radar integration systems, in which there are still many technical problems to be solved Wehner DR (1995) High-resolution radar, 2nd edn. Artech House, Boston, MA, pp 12–18; Wei Z (2009) Research on the techniques of radar constant false alarm rate detection under complex clutter. University of Aeronautics and Astronautics, Nanjing. The significant broaden of radar bandwidth makes that many preconditions in the narrow-band radar theoretical systems are no longer applicable, which also results in a series of new theory and technical issues with broadband radar. In this paper, I proposed new target detection algorithms based on the probability distance of empirical cumulative distribution function (ECDF), on which four detectors were designed. And also analyze the detection performance of these detectors through comparative simulation.

1 Introduction

Cumulative distribution function(CDF) as a real probability distribution of random variables of a complete description, has certain advantages of measure the difference in statistical properties. The target detection algorithm based ECDF main draw goodness of fit test. Use the "distance" between the empirical cumulative distribution function of sample data and the experience of the target echo data to sentence if the target is present [1].

The sequence of Empirical Cumulative Distribution Function can be calculated as follows.

G. Lin (✉) • Z. He • J. Wu • M. Zhao • Z. Mei
Qingshuihe Campus, University of Electronic Science and Technology of China (UESTC), 2006 XiYuan Avenue, Western Hi-tech Zone, Chengdu 611731, P. R. China
e-mail: sunny-linguishan@sohu.com; 451279571@qq.com

B. Zhang et al. (eds.), *The Proceedings of the Second International Conference on Communications, Signal Processing, and Systems*, Lecture Notes in Electrical Engineering 246, DOI 10.1007/978-3-319-00536-2_71,

Suppose (x1, x2, …, xN) is the observed random variable X to get sample sequence, first by ascending order of the sample data, the ordered ascending (x (1), x (2), …, x (N)), define the real number domain function.

$$\widetilde{F}(x) = \begin{cases} 0, & x < x_{(1)} \\ \dfrac{k}{N}, & x_{(k)} \le x < {}_{(k+1)}, k = 1, 2, \cdots, N-1 \\ 1, & x \ge x_{(N)} \end{cases} \tag{1}$$

$\widetilde{F}(x)$ is called empirical cumulative distribution function (ECDF). According to Glivenko Theorem, the random variable X is the cumulative distribution function $\widetilde{F}(x)$ and the empirical cumulative distribution function of the sample has the following relationship:

$$P\left\{\lim_{N\to\infty} \sup_{-\infty<x<+\infty} \left|\widetilde{F}(x) - F(x)\right| = 0\right\} = 1 \tag{2}$$

That is, when the sample data is more than enough, by the sample estimate the cumulative distribution function and the theoretical values in the statistical sense is equivalent replacement.

2 Goodness of Fit Test Criteria

Represented by KS test based on the empirical cumulative distribution function (ECDF) goodness of fit test mainly has KS test, CVM test and AD test [2].

KS test statistic above infimum empirical cumulative distribution function to measure the difference between the value and the theoretical. Basic statistics expression:

$$d_{ks} = \sup_{-\infty<x<\infty} |F(x) - F_X(x)| \tag{3}$$

CVM test statistic is based on secondary statistics to measure the difference between empirical cumulative distribution function and theoretical value. Basic statistics expression:

$$Q = N\int_{-\infty}^{+\infty} \left[\widetilde{F}(x) - F(x)\right]^2 \varphi(x) dF(x) \tag{4}$$

Where, N is the sample length of the sequence, the weighting function. When $\varphi(x) = 1$, (4) is converted to CVM classical statistics, the basic expression:

$$W^2 = N\int_{-\infty}^{+\infty} \left[\widetilde{F}(x) - F(x)\right]^2 dF(x) \tag{5}$$

When $\varphi(x) = \{F(x)[1 - F(x)]\}^{-1}$, (5) is converted to AD test statistic.

Basic statistics expression:

$$A^2 = N\int_{-\infty}^{+\infty} \frac{\left[\widetilde{F}(x) - F(x)\right]^2}{F(x)[1 - F(x)]} dF(x) \tag{6}$$

In practical applications, the amount of calculation of the statistics are larger, to simplify the operation, and suitable for engineering applications, it must be discrete simplified. Observed statistic expression, the key of optimize is to simplify the $\widetilde{F}(x) - F(x)$ calculations.

Continuous random variable X is the cumulative distribution function $F(X)$ subject to uniform distribution on the interval the [0,1], that is:

$$Z = F(X) \sim U(0, 1) \tag{7}$$

Definition $z_i = F(x_i)$ is a sequence of samples after the change of probability integral data sequence, it is empirical cumulative distribution function of this data, Then the $\widetilde{F}(x) - F(x)$ can be calculated instead of $\widetilde{F}_Z(z) - F_Z(z)$ to calculate the distance between the empirical cumulative distribution function and the theoretical cumulative distribution function. that is:

$$\widetilde{F}(x) - F(x) = \widetilde{F}_Z(z) - F_Z(z) = \widetilde{F}_Z(z) - z \tag{8}$$

Formula (8) into (5), and discrete treatment, gets:

$$M^2 = \frac{1}{12N} + \sum_{i=1}^{N} \left|\widetilde{F}_Z(z_i) - \frac{2i - 1}{2N}\right|^2 \tag{9}$$

Formula (9) into (6), and discrete treatment, gets:

$$A^2 = -N - \frac{1}{N}\sum_{i=1}^{N} [(2i - 1)\ln z_i + (2N + 1 - 2i)\ln(1 - z_i)] \tag{10}$$

3 Algorithm Description

The key point of the target detection algorithm based ECDF is to estimate the difference of empirical cumulative distribution function between the current echo signal and clutter signal, mainly draws the ideas of clutter map and goodness of fit. Accordingly, designing ECDF differences estimation methods refer to different goodness of fit test criteria [3]. In other word it is to design and deduce test statistic which can be measured the "distance" of empirical cumulative distribution function between current echo and clutter [4].

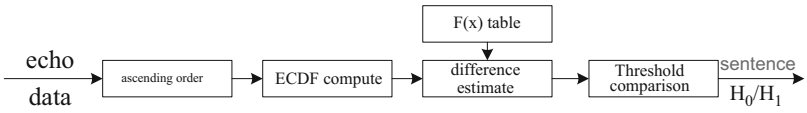

Fig. 1 Basic processing block diagram based ECDF

Real-time target detection algorithm has certain requirements in the actual radar work. Therefore, the detection statistic calculations must balance contradiction between complexity and precision. Select clutter sample of sufficient length to fit for clutter empirical cumulative distribution function $F(X)$ then produce the corresponding $F(X)$ table for practical engineering applications to reduce the amount of computation and improve the detection efficiency. Basic processing block diagram as Fig. 1:

Similar to the KS test, you can design one statistic to quantify and estimate the different ECDF and two detectors can be designed.

1. The maximum detector based on probability distance, its expression is:

$$T_{Max} = \max\left\{\left|\widetilde{F}(x_i) - F(x_i)\right|\right\}, \quad T_{Max} \underset{H_0}{\overset{H_1}{\gtrless}} \eta, \quad i = 1, 2, \cdots, N \tag{11}$$

2. The summing detector based on probability distance, its expression is:

$$T_{Sum} = \sum_{i=1}^{N} \left|\widetilde{F}(x_i) - F(x_i)\right|, \quad T_{Sum} \underset{H_0}{\overset{H_1}{\gtrless}} \eta \tag{12}$$

Where $\widetilde{F}(\cdot)$ is the cumulative distribution function of current echo signal and $F(\cdot)$ is the cumulative distribution function of current clutter signal.

Similar to the CVM test, you can design secondary statistics to quantify and estimate the different ECDF and detectors can be designed as follow:

1. The SVM detector based on probability distance, its expression is:

$$T_{SVM} = \sum_{i=1}^{N} \left[\widetilde{F}(x_i) - F(x_i)\right]^2, \quad T_{SVM} \underset{H_0}{\overset{H_1}{\gtrless}} \eta \tag{13}$$

Similar to the AD test, you can design AD test statistic to quantify and estimate the different ECDF and detectors can be designed as follow:

$$T_{AD} = \sum_{i=1}^{N} \frac{\left[\widetilde{F}(x_i) - F(x_i)\right]^2}{F(x_i)[1 - F(x_i)]}, \quad T_{AD} \underset{H_0}{\overset{H_1}{\gtrless}} \eta \tag{14}$$

In practical engineering, real-time computing the empirical cumulative distribution function of current echo signal is very difficult. Therefore, we must simplify the four detectors. For (7), the probability distance between echo empirical cumulative distribution function and clutter empirical cumulative distribution function can be converted into the distance between echo integral change empirical cumulative distribution function Integral change and uniform distribution cumulative distribution function. As (8), the above four types of detectors can be simplified to:

1. KS maximum detector, its expression is:

$$T_{Max} = \max\left\{\left|z'_i - i/N\right|\right\}, \quad T_{Max} \gtrless_{H_0}^{H_1} \eta, \quad i = 1, 2, \cdots, N \tag{15}$$

2. KS summing detector, its expression is:

$$T_{Sum} = \sum_{i=1}^{N} \left|z'_i - i/N\right|, \quad T_{Sum} \gtrless_{H_0}^{H_1} \eta \tag{16}$$

3. CVM detector, its expression is:

$$T_{CVM} = \sum_{i=1}^{N} \left(z'_i - i/N\right)^2, \quad T_{CVM} \gtrless_{H_0}^{H_1} \eta \tag{17}$$

4. AD detector, its expression is:

$$T_{AD} = \sum_{i=1}^{N-1} \frac{\left(Nz'_i - i\right)^2}{i(N-i)}, \quad T_{AD} \gtrless_{H_0}^{H_1} \eta \tag{18}$$

Where $\{z'_i\}$ is $\{z_i = F(x_i)\}$ array in ascending order, let $\mathbf{Z} = [z'_1 - 1/N, z'_2 - 2/N, \cdots, z'_N - 1]^T$ then (17) can be written in vector form:

$$T_{CVM} = \mathbf{Z}^T\mathbf{Z} \tag{19}$$

Formula (18) vector form:

$$T_{AD} = \mathbf{Z}^T HZ \tag{20}$$

Where $H = N^2 \cdot diag[(N-1)^{-1}, (2N-4)^{-1}, \cdots, (Ni - i^2)^{-1}, \cdots, (N-1)^{-1}]$

Processing block diagram as follow (Fig. 2):

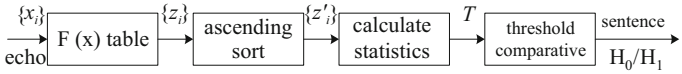

Fig. 2 Improved target detection algorithm based on ECDF processing block diagram

4 Simulation Performance Analysis

Compare and analyses the four detectors (Max detector, Sum detector, CVM detector, AD detector) detection performance simulation through Monte Carlo simulation method. Minimize the simulation computation and improve the efficiency of detection algorithm without prejudice to the detection performance of target detection algorithm [5].

This section of the basic parameters of the simulation is set as follows:

1. Transmitting signals: transmit signals using linear FM signal (LFM), FM pulse width 40 μs, and bandwidth of 300 MHz;
2. Target model: The target is assumed to be stationary or slow moving target goals, with eight scattering centers, the relative position of the scattering point (m) and amplitude RCS respectively [10, 6, 17, 20, 22, 28, 30, 40], and [0.8, 0.3, 0.2, 0.6, 0.4, 0.3, 0.5, 0.9], ignoring phase effect;
3. Clutter distribution parameter settings:
   Rayleigh distribution: a = 1, b = 2, v = 1;
   Weibull distribution: a = 1, b = 1.5, v = 1;
   K distribution: a = 1, b1 = 2, b2 = 2, v1 = 1, v2 = 2;
   Generalized compound distribution: a = 1, b1 = 1, b2 = 1.5, v1 = 3, v2 = 2;
4. Detection distance window: N = 50 m;
5. False alarm probability: $p_f = 10^{-2}$;
6. Monte Carlo: simulation times. Num = $100/p_f = 10^4$;

Performance compares between Max, Sum, CVM and AD detector detection.

Different clutter distribution models of max detectors, Sum detector, CVM detector and AD detector r detection performance SCR-pf curve in Fig. 3a–b:

It can be seen from the simulation results, the four detectors detect differences in performance of the merits comparison in different clutter, but relatively stable. AD detector detection performance is better than the other three detectors and with good stability in various clutters. The detection performance of Sum detector and CVM detector are center. The performance of these two detectors has advantages and disadvantages in a different clutter. And relatively speaking, Max detection performance of four detectors is biased disadvantage. This is because the echo sequences of Max detector deviate from clutter to the maximum extent are with greater randomness. Sum detector and CVM detector respectively a statistics and secondary statistic assess the global gap, but the weighting function does not express a different local feature differences. The AD detector is more accurate characterization of the probability of each point deviation using the weighting

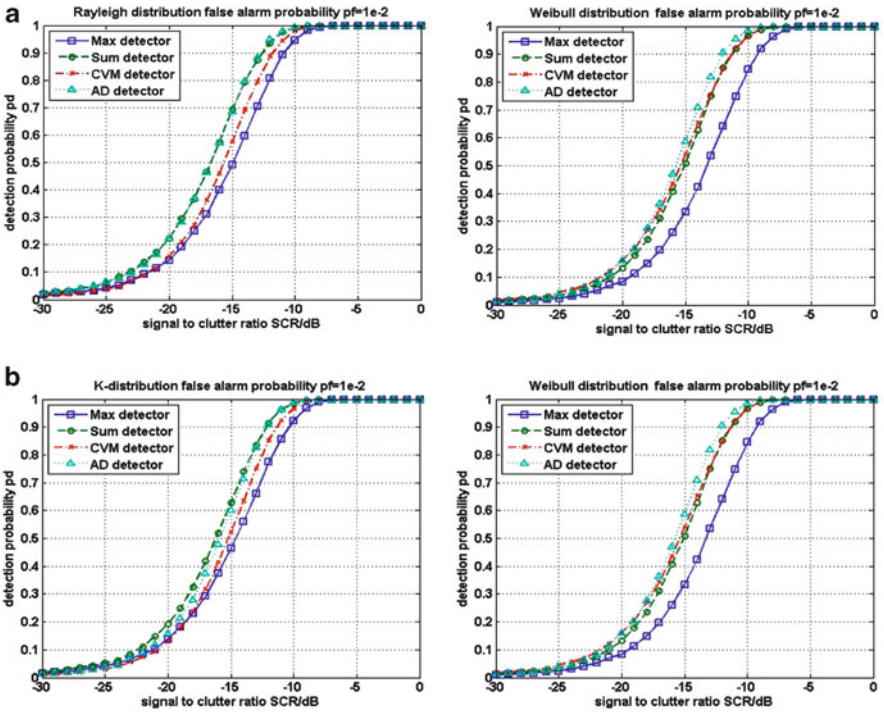

Fig. 3 (**a**) Rayleigh distribution and Weibull distribution. (**b**) K-distribution and Generalized compound distribution

function $\varphi(x) = \{F(x)[1 - F(x)]\}^{-1}$. So that weighted mean square distance can be more stable and more accurate measure the difference between current echo empirical cumulative distribution function and clutter empirical cumulative distribution function.

References

1. Cong-ana X, Taoa J et al (2012) CFAR detector based on Anderson-Darling test. Comput Eng 38(9):231–233
2. Aggarwal M, Ahuja N (2004) Split aperture imaging for high dynamic range. Int J Comput Vis 58(1):1–17
3. Debevec PE, Malik J (1997) Recovering high dynamic range radiance maps from photographs. Proc of ACM SIGGRAPH'97. ACM Press, Los Angeles, CA
4. Mitsunaga T, Nayar SK (1999) Radiometric self calibration. Proc of IEEE Conference on Computer Vision and Pattern Recognition. IEEE Press, Fort Collins, CO
5. Fattal R, Lischinski D (2011) Gradient domain high dynamic range compression. Proc of the 29th Annual Conference on Computer Graphics and Interactive Techniques, Vancouver, Canada, 7–11 August, 2011

Study of Illuminated Area and Doppler Characteristics of Airborne Pulse Radar Based on Vector Analysis

Haijiang wang

Abstract In this paper, using vector analysis tool, the illuminated area and the Doppler frequency distribution are studied. Through coordinate transform, the relationship between the radar antenna's frame and the ground frame under aircraft's motion attitude is derived. By space-time analysis, the overlap area of the radar beam's footprint and the pulse's illuminated area is obtained, and the Doppler frequency expression is deduced and the Doppler frequency distribution is plotted.

1 Introduction

In a certain radar system, we always want to describe the time-space relation as clear as we can. Radar geometry study is very important for the deduction of radar echo signal. For example, in airborne radar, if we want to write out the radar echo equation, even obtain the illuminated area and Doppler characteristics, the geometry relation among the airplane, the antenna, and the ground must be analyzed intensively.

Some researchers have done some study on the illumination characteristics of radar. In [1], Korkmaz and van Genderen measured the footprint of stepped frequency CW radar using a probe antenna, but they used little geometry and time-space analysis. In [2], for airborne radar, the attitude changes and their influences on the echo's Doppler spectrum were analyzed, but the time-space analysis was little and the illuminated area was not obtained. In [3], the radar pulse's wave field on the ground was calculated with pseudospectral time domain method. This article is written on the hypothesis that the antenna's shape is known

H. wang (✉)
CMA. Key Laboratory of Atmospheric Sounding, Chengdu University of Information Technology, Chengdu 610225, Sichuan, China

College of Electronic Engineering, Chengdu University of Information Technology, Chengdu 610225, Sichuan, China
e-mail: whjpost6@126.com

B. Zhang et al. (eds.), *The Proceedings of the Second International Conference on Communications, Signal Processing, and Systems*, Lecture Notes in Electrical Engineering 246, DOI 10.1007/978-3-319-00536-2_72,

and its position is fixed and there is no any discussion of the radar platform's motion and attitude changes.

In this paper, we will use vector analysis tool to study the geometry configuration of airborne pulse radar. In Sect. 2, under the hypothesis of the airplane's attitude we deduce the relationship between antenna coordinate frame and ground coordinate frame. In Sect. 3, through the analysis of transmitted and received signal's paths of the radar, according to the vector differential equation, a complete expression of the radar echo is obtained. In Sect. 4, the echo area of the airborne pulse radar and the echo's Doppler distribution on the ground are calculated. Section 5 is the conclusion.

2 Coordinate Frame Relationship

Suppose that ground frame is formed by unit vectors $\hat{\mathbf{X}}$, $\hat{\mathbf{Y}}$ and $\hat{\mathbf{Z}}$. $\hat{\mathbf{X}}$ and $\hat{\mathbf{Y}}$ are parallel to ground level and $\hat{\mathbf{Z}}$ is perpendicular to it.

$$\hat{\mathbf{Z}} = \hat{\mathbf{X}} \times \hat{\mathbf{Y}} \tag{1}$$

Suppose the aerocraft frame is formed by unit vectors $\hat{\mathbf{F}}$ (along fuselage direction), $\hat{\mathbf{W}}$ (along wing direction) and $\hat{\mathbf{T}}$ (along top direction), and they satisfy:

$$\hat{\mathbf{T}} = \hat{\mathbf{F}} \times \hat{\mathbf{W}} \tag{2}$$

Suppose the initial attitude of the aircraft is:

$$\begin{bmatrix} \hat{\mathbf{F}}' \\ \hat{\mathbf{W}}' \\ \hat{\mathbf{T}}' \end{bmatrix} = \begin{bmatrix} 1 & 0 & 0 \\ 0 & 1 & 0 \\ 0 & 0 & 1 \end{bmatrix} \begin{bmatrix} \hat{\mathbf{X}} \\ \hat{\mathbf{Y}} \\ \hat{\mathbf{Z}} \end{bmatrix} \tag{3}$$

Then suppose the aircraft rotates along the top axis $\hat{\mathbf{T}}$ by an angle ψ, which is called the azimuth angle. Through vector calculation, the new attitude is:

$$\begin{bmatrix} \hat{\mathbf{F}}'' \\ \hat{\mathbf{W}}'' \\ \hat{\mathbf{T}}'' \end{bmatrix} = \begin{bmatrix} \cos\psi & \sin\psi & 0 \\ -\sin\psi & \cos\psi & 0 \\ 0 & 0 & 1 \end{bmatrix} \begin{bmatrix} \hat{\mathbf{F}}' \\ \hat{\mathbf{W}}' \\ \hat{\mathbf{T}}' \end{bmatrix} = P(\psi) \begin{bmatrix} \hat{\mathbf{X}} \\ \hat{\mathbf{Y}} \\ \hat{\mathbf{Z}} \end{bmatrix} \tag{4}$$

On this basis, let suppose the aircraft rotates along the new wing axis $\hat{\mathbf{W}}''$ by an angle α, which is called the elevation angle, then the attitude of the aircraft becomes to:

$$\begin{bmatrix} \hat{\mathbf{F}}''' \\ \hat{\mathbf{W}}''' \\ \hat{\mathbf{T}}''' \end{bmatrix} = \begin{bmatrix} \cos\alpha & 0 & \sin\alpha \\ 0 & 1 & 0 \\ -\sin\alpha & 0 & \cos\alpha \end{bmatrix} \begin{bmatrix} \hat{\mathbf{F}}'' \\ \hat{\mathbf{W}}'' \\ \hat{\mathbf{T}}'' \end{bmatrix} = A(\alpha)P(\psi) \begin{bmatrix} \hat{\mathbf{X}} \\ \hat{\mathbf{Y}} \\ \hat{\mathbf{Z}} \end{bmatrix} \tag{5}$$

On the basis of the above two-time rotation, suppose the aircraft rotates ones more along the fuselage axis by an angle β, which is called the rolling angle, then the attitude is:

$$\begin{bmatrix} \hat{\mathbf{F}} \\ \hat{\mathbf{W}} \\ \hat{\mathbf{T}} \end{bmatrix} = \begin{bmatrix} 1 & 0 & 0 \\ 0 & \cos\beta & -\sin\beta \\ 0 & \sin\beta & \cos\beta \end{bmatrix} \begin{bmatrix} \hat{\mathbf{F}}''' \\ \hat{\mathbf{W}}''' \\ \hat{\mathbf{T}}''' \end{bmatrix} = B(\beta)A(\alpha)P(\psi) \begin{bmatrix} \hat{\mathbf{X}} \\ \hat{\mathbf{Y}} \\ \hat{\mathbf{Z}} \end{bmatrix} \tag{6}$$

For the angles above, the range of elevation angle α is $[0\pi)$, the range of azimuth angle ψ and rolling angle β are both $[0\ 2\pi)$. These three angles cover all possible attitudes of the aircraft.

The antenna frame can be derived from the aircraft frame:

$$\begin{aligned} \begin{bmatrix} \hat{\mathbf{x}} \\ \hat{\mathbf{y}} \\ \hat{\mathbf{z}} \end{bmatrix} &= \begin{bmatrix} 1 & 0 & 0 \\ 0 & \cos\left(\gamma+\frac{\pi}{2}\right) & -\sin\left(\gamma+\frac{\pi}{2}\right) \\ 0 & \sin\left(\gamma+\frac{\pi}{2}\right) & \cos\left(\gamma+\frac{\pi}{2}\right) \end{bmatrix} \begin{bmatrix} \hat{\mathbf{F}} \\ \hat{\mathbf{W}} \\ \hat{\mathbf{T}} \end{bmatrix} = \begin{bmatrix} 1 & 0 & 0 \\ 0 & -\sin\gamma & -\cos\gamma \\ 0 & \cos\gamma & -\sin\gamma \end{bmatrix} \begin{bmatrix} \hat{\mathbf{F}} \\ \hat{\mathbf{W}} \\ \hat{\mathbf{T}} \end{bmatrix} \\ &= Q(\gamma) \begin{bmatrix} \hat{\mathbf{F}} \\ \hat{\mathbf{W}} \\ \hat{\mathbf{T}} \end{bmatrix} \end{aligned} \tag{7}$$

Where γ is the depression angle of the antenna's main-lobe, $\hat{\mathbf{z}}$ represent the direction of the main-lobe's center line, $\hat{\mathbf{x}} = \hat{\mathbf{F}}$ is along the fuselage direction and $\hat{\mathbf{y}} = \hat{\mathbf{z}} \times \hat{\mathbf{x}}$. So the antenna frame is obtained by rotating the aircraft frame by $\gamma + \frac{\pi}{2}$ along the fuselage direction.

From above discussion, the relationship between antenna frame and ground frame can be written as:

$$\begin{bmatrix} \hat{\mathbf{x}} \\ \hat{\mathbf{y}} \\ \hat{\mathbf{z}} \end{bmatrix} = Q(\gamma)B(\beta)A(\alpha)P(\psi) \begin{bmatrix} \hat{\mathbf{X}} \\ \hat{\mathbf{Y}} \\ \hat{\mathbf{Z}} \end{bmatrix} = \Pi(\alpha,\beta,\gamma,\psi) \begin{bmatrix} \hat{\mathbf{X}} \\ \hat{\mathbf{Y}} \\ \hat{\mathbf{Z}} \end{bmatrix} \tag{8}$$

It is obviously that:

$$Q(0) = B(0) = A(0) = P(0) = \widetilde{\mathbf{I}} = \begin{bmatrix} 1 & 0 & 0 \\ 0 & 1 & 0 \\ 0 & 0 & 1 \end{bmatrix} \tag{9}$$

Through algebra calculation it can be easily obtained that:

$$Q(\gamma)B(\beta) = \begin{bmatrix} 1 & 0 & 0 \\ 0 & \sin(\beta-\gamma) & -\cos(\beta-\gamma) \\ 0 & \cos(\beta-\gamma) & \sin(\beta-\gamma) \end{bmatrix} = C(\beta-\gamma) \tag{10}$$

Without loss of generality, let's assume the azimuth angle $\psi = 0$, then:

$$\begin{aligned} \Pi(\alpha,\beta,\gamma,0) &= Q(\gamma)B(\beta)A(\alpha) = C(\beta-\gamma)A(\alpha) \\ &= \begin{bmatrix} \cos\alpha & 0 & \sin\alpha \\ \cos(\beta-\gamma)\sin\alpha & \sin(\beta-\gamma) & -\cos(\beta-\gamma)\cos\alpha \\ -\sin(\beta-\gamma)\sin\alpha & \cos(\beta-\gamma) & \sin(\beta-\gamma)\cos\alpha \end{bmatrix} \end{aligned} \tag{11}$$

3 Expression of the Airborne Pulse Radar's Echo Signal

Before considering the expression of the airborne pulse radar's echo signal, let's deduce a formula for the differential of a vector's magnitude.

For any vector **a**:

$$|\mathbf{a}|^2 = \mathbf{a} \cdot \mathbf{a} \tag{12}$$

Conduct differential operation on both sides of the above equation, we have:

$$2|\mathbf{a}|\, d|\mathbf{a}| = 2\mathbf{a} \cdot d\,\mathbf{a} \tag{13}$$

So,

$$d|\mathbf{a}| = \frac{\mathbf{a}}{|\mathbf{a}|} \cdot d\,\mathbf{a} = \hat{\mathbf{a}} \cdot d\,\mathbf{a} \tag{14}$$

This result is very important and we will use it in the later soon.

Suppose the position vector of the aircraft is:

$$\mathbf{R}(t) = \mathbf{R}_0 + t\,\mathbf{v} \tag{15}$$

Where **v** is the velocity vector.

Assume that a ray in the radar beam is transmitted at time zero and reaches the ground point, the length of the ray is:

$$l_1 = |\mathbf{r}| = |\mathbf{r}_s - \mathbf{R}(0)| \tag{16}$$

If the reflected signal arrived to the radar at time t, then the distance that the reflected signal traverses is:

$$l_2 = |\mathbf{r}_s - \mathbf{R}(t)| \tag{17}$$

Suppose the transmitted pulse signal of the airborne radar is:

$$S(t) = A_m(t)e^{j\omega t} \tag{18}$$

Where

$$A_m(t) = \begin{cases} 1 & 0 \le t \le \tau \\ 0 & elsewhere \end{cases} \tag{19}$$

The time delay between the received signal and the transmitted signal is:

$$t_d(t) = \frac{l_1 + l_2}{c} = \frac{1}{c}\left[|\mathbf{r}_s - \mathbf{R}(0)| + |\mathbf{r}_s - \mathbf{R}(t)|\right] \tag{20}$$

For the radar's motion, l_1, l_2 and t_d are functions of t. According to (11), the differential coefficient of t_d is:

$$\frac{dt_d}{dt} = -\frac{1}{c}\left[\frac{[\mathbf{r}_s - \mathbf{R}(0)]}{|\mathbf{r}_s - \mathbf{R}(0)|} + \frac{[\mathbf{r}_s - \mathbf{R}(t)]}{|\mathbf{r}_s - \mathbf{R}(t)|}\right] \cdot \mathbf{v} \tag{21}$$

It is obviously that:

$$t_d(0) = \frac{2r}{c}; \quad \left.\frac{dt_d}{dt}\right|_{t=0} = -\frac{2}{c}\hat{\mathbf{r}} \cdot \mathbf{v} = -\frac{2v_r}{c} \tag{22}$$

So the one-order expansion of t_d can be obtained:

$$t_d(t) \approx \frac{2r}{c} - \frac{2v_r}{c}t \tag{23}$$

The second item in the above equation is much smaller than the first item, so in the amplitude expression, it can be neglected:

$$A_m(t - t_d) = A_m\left(t - \frac{2r}{c}\right) \tag{24}$$

But in the phase expression the second item in (23) cant be neglected because

after multiplied by ω it can also reached to the magnitude order of π. So the following expression of the airborne pulse radar's echo signal can be obtained:

$$s(t) = \iint_{\Sigma} \frac{A_m\left(t - \frac{2r}{c}\right)G^2(\phi,\theta)\Lambda(\mathbf{r}_s)\exp\left[j\omega\left(1 + \frac{2v_r}{c}\right)t - \frac{2r}{c}\right)\Big]}{r^2} d\Sigma \tag{25}$$

4 The Airborne Pulse Radar's Illuminated Area and the Doppler Characteristic Distribution

Expressing with the radar's antenna frame, the vector $\hat{\mathbf{r}}$ is:

$$\hat{\mathbf{r}} = \sin\theta\cos\phi\ \hat{\mathbf{x}} + \sin\theta\sin\phi\ \hat{\mathbf{y}} + \cos\theta\ \hat{\mathbf{z}} \tag{26}$$

Because $\mathbf{r}_s = \mathbf{R}(0) + \mathbf{r}$ and $\mathbf{r}_s \cdot \hat{\mathbf{Z}} = 0$, so $[\mathbf{R}(0) + \mathbf{r}] \cdot \hat{\mathbf{Z}} = \mathbf{0}$. Suppose $\mathbf{R}(0) = H\hat{\mathbf{Z}}$, then $\mathbf{r} \cdot \hat{\mathbf{Z}} = r\hat{\mathbf{r}} \cdot \hat{\mathbf{Z}} = -\mathbf{R}(0) \cdot \hat{\mathbf{Z}} = -H$. Basing (26) we can obtained:

$$\begin{aligned} r &= -\frac{H}{\hat{\mathbf{r}} \cdot \hat{\mathbf{Z}}} \\ &= \frac{-H}{\sin\theta\cos\phi\sin\alpha - \sin\theta\sin\phi\cos\alpha\cos(\beta-\gamma) + \cos\theta\cos\alpha\sin(\beta-\gamma)} \end{aligned} \tag{27}$$

At the same time, it is easily to determine the coordinate position of the ground reflecting point:

$$\begin{aligned} X &= \mathbf{r}_s \cdot \hat{\mathbf{X}} = \mathbf{r} \cdot \hat{\mathbf{X}} = r\hat{\mathbf{r}} \cdot \hat{\mathbf{X}} \\ &= \frac{-H[\sin\theta\cos\phi\cos\alpha + \sin\theta\sin\phi\sin\alpha\cos(\beta-\gamma) - \cos\theta\sin\alpha\sin(\beta-\gamma)]}{\sin\theta\cos\phi\sin\alpha - \sin\theta\sin\phi\cos\alpha\cos(\beta-\gamma) + \cos\theta\cos\alpha\sin(\beta-\gamma)} \\ Y &= \mathbf{r}_s \cdot \hat{\mathbf{Y}} = \mathbf{r} \cdot \hat{\mathbf{Y}} = r\hat{\mathbf{r}} \cdot \hat{\mathbf{Y}} \\ &= \frac{-H[\sin\theta\sin\phi\sin(\beta-\gamma) + \cos\theta\cos(\beta-\gamma)]}{\sin\theta\cos\phi\sin\alpha - \sin\theta\sin\phi\cos\alpha\cos(\beta-\gamma) + \cos\theta\cos\alpha\sin(\beta-\gamma)} \end{aligned} \tag{28}$$

For the antenna's beam, Guassian model can be used:

$$G(\phi,\theta) = G_0\exp\left[-\frac{\theta^2}{2}\left(\frac{\cos^2\phi}{\sigma_x^2} + \frac{\sin^2\phi}{\sigma_y^2}\right)\right] \tag{29}$$

Define the half-power area:

$$G(\phi,\theta)=\frac{G_0}{\sqrt{2}} \tag{30}$$

From (29), we can obtain:

$$\exp\left[-\frac{\theta^2}{2}\left(\frac{\cos^2\phi}{\sigma_x^2}+\frac{\sin^2\phi}{\sigma_y^2}\right)\right]=\frac{1}{\sqrt{2}} \tag{31}$$

So,

$$\frac{\theta^2}{2}\left(\frac{\cos^2\phi}{\sigma_x^2}+\frac{\sin^2\phi}{\sigma_y^2}\right)=\frac{\log 2}{2} \tag{32}$$

Expressing θ with ϕ:

$$\theta=\sqrt{\frac{\sigma_x^2\sigma_y^2\log 2}{\sigma_y^2\cos^2\phi+\sigma_x^2\sin^2\phi}} \tag{33}$$

The above equation denotes the relationship between θ and ϕ and the beam edge can be obtained from it.

Let ϕ vary in the range [0, 2π) and substituting (33) into (28), the beam outline on the ground can be obtained. The area inside the outline can expressed as:

$$G(\phi,\theta)\geq\frac{G_0}{\sqrt{2}} \tag{34}$$

According to (19), $A_m\left(t-\frac{2r}{c}\right)$ is not zero only under the following condition:

$$0\leq t-\frac{2r}{c}\leq\tau \tag{35}$$

So,

$$\frac{c(t-\tau)}{2}\leq r\leq\frac{ct}{2} \tag{36}$$

Let $\rho=\sqrt{X^2+Y^2}=\sqrt{r^2-H^2}$, so the above equation becomes:

$$\sqrt{\left[\frac{c(t-\tau)}{2}\right]^2-H^2}\leq\rho\leq\sqrt{\left(\frac{ct}{2}\right)^2-H^2} \tag{37}$$

Equation (34) represents a area like a long ellipse and (37) represents an ring

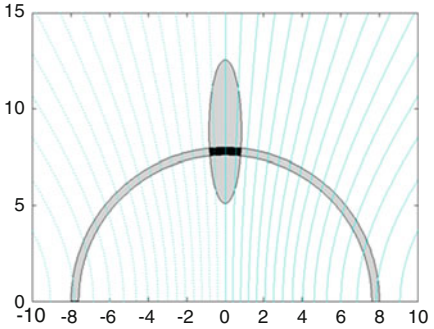

Fig. 1 The Doppler Distribution in a = 0 network

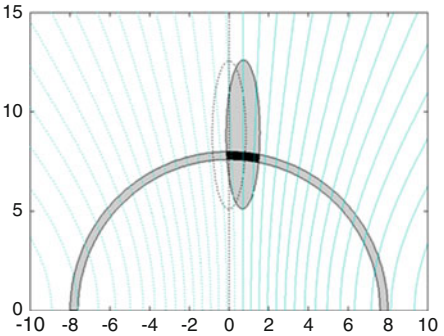

Fig. 2 The Doppler Distribution in a = 5 network

area. These two area overlap to an area, which is shown in Figs. 1 and 2 and denoted by black color.

There is Doppler frequency in the echo signal expression of (25):

$$f_d = \frac{2\omega v_r}{2\pi c} = \frac{4\pi f v_r}{2\pi c} = \frac{2v_r}{\lambda} = \frac{2v}{\lambda}(\hat{\mathbf{r}} \cdot \hat{\mathbf{x}}) \tag{38}$$

In Figs. 1 and 2, $\hat{\mathbf{r}} \cdot \hat{\mathbf{x}}$, namely Doppler distribution, is plotted.

$$\alpha = 0;\ \ \beta = 0;\ \ \gamma = 45^0;\ \ \sigma_x = 5^0;\ \ \sigma_y = 15^0;\ \ H = 5km$$
$$\alpha = 5^0;\ \ \beta = 0;\ \ \gamma = 45^0;\ \ \sigma_x = 5^0;\ \ \sigma_y = 15^0;\ \ H = 5km$$

5 Conclusion

Figures 1 and 2 show that the illuminated area of a radar pulse at an instant can be obtained precisely, and the Doppler frequency distribution is plotted clearly. This result can be used in SAR imaging, especially in synchronization [4] and motion compensation.

References

1. Korkmaz E, van Genderen P (2004) Antenna footprint measurements of stepped frequency CW radar on the air_ground interface, IEE Antenna Measurements and SAR, 2004. AMS 2004, 25–26 May, 2004, Loughborough, pp 87–91
2. Justin WG, Todd BH, Michael AT, John TB (2006) Incorporating pulse-to-pulse motion effects into side-looking array radar models, Fourth IEEE Workshop on Sensor Array and Multichannel Processing, Waltham, MA, 12–14 July, 2006, pp 580–585
3. Lanbo L, Steven AA (2004) Near-surface radar pulse propagation in complex terrain environments: preliminary results, 10th International Conference on Ground Penetrating Radar, Delft, The Netherlands, 21–24 June, 2004, pp 21–24.
4. Yonghong Y, Yiming P, Ran L (2006) Considerations for non-cooperative bistatic SAR with spaceborne radar illuminating, CIE '06, Shanghai, 16–19 October, 2006, pp 1–4

Part VI
Intelligent System and Technology

FOD Detection on Airport Runway with an Adaptive CFAR Technique

Weidong Liu, Zhongjin Zhang, and Xuelian Yu

Abstract Cell averaging CFAR (CA-CFAR) detection method is usually applied to homogeneous clutter background environment. However, when the background is complex or non-homogeneous, the performance of CA-CFAR may decline greatly. In this paper, focusing on the effective detection of FOD (foreign object debris) targets on airport runway, an adaptive cell averaging CFAR technique (ACA-CFAR) is used to obtain relatively good detection performance, especially when targets exist in the clutter edge or multi-targets interference environment. Experimental results show the effectiveness of the ACA-CFAR detector in the complex airport runway environment.

Keywords FOD detection • Adaptive • CFAR technique

1 Introduction

Airport runway foreign object debris (FOD) may cause damages or disasters to aircrafts. The crash of a Concorde jet in France in 2000 is an example of disasters due to FOD. Moreover, a lot of money is spent each year by airlines in repairing the damages caused by FODs to aircrafts. Consequently, some FOD detection systems have been developed and tested on airports recently, such as Tarsier system, FODetect, iFerret, and etc. Most of them are based on millimeter-wave radar and optical sensors [1].

One of the key problems of FOD detection is how to find small target under relatively strong clutter background. The clutter situation on airport runway faced

W. Liu (✉) • Z. Zhang
The Second Research Institute of CAAC, Chengdu, China
e-mail: atmlwd@163.com; jinsbm@163.com

X. Yu
University of Electronic Science & Technology of China, Chengdu, China
e-mail: iceyu23@126.com

B. Zhang et al. (eds.), *The Proceedings of the Second International Conference on Communications, Signal Processing, and Systems*, Lecture Notes in Electrical Engineering 246, DOI 10.1007/978-3-319-00536-2_73,

by the FOD detection radar is rather complex. So it is necessary to use the constant false alarm rate (CFAR) technique to obtain a satisfactory detection performance.

Cell averaging CFAR (CA-CFAR) detection method has good detection performance in homogeneous clutter background environment. But in Multi-targets interference environment, when one or more interferences exist in the reference unit of main target, the detection performance will become worse as the strength and number of interference increased [2]. Moreover, if airport runway FOD targets exist nearby grass or edge lights, the threshold will be elevated by strong interference, which may cause detection rate decline.

In this paper, aiming at effective FOD detection on airport runway, an adaptive CFAR technique, called adaptive cell averaging CFAR (ACA-CFAR), which is proposed by Li et al. [3], is used. In ACA-CFAR, the reference window is first divided into several sub-windows with the same length, and the reference background will be approximately homogeneous by removing the non-homogeneous clutter by judging the clutter power of each sub-window, and then the classical CA-CFAR detection method is used to finish the FOD target detection.

The rest of the paper is organized as follows. In Sect. 2, the principle of ACA-CFAR detector is introduced. In Sect. 3, the simulation experiment is conducted on airport runway FOD detection and the performance of ACA-CFAR is verified in both multi-targets interference and clutter edge environment, respectively. Finally, conclusions are drawn in Sect. 4.

2 ACA-CFAR

2.1 Principle

The principle block diagram of ACA-CFAR detection method is shown in Fig. 1, where I/Q dual-channel data are input to a linear detector to construct the detection statistics $D(v)$ [3]. In Fig. 1, T is the scale factor, Z is the estimated value of the background clutter power, D is detecting unit, $x_i(i = 1, 2, \cdots, qM)$ are reference units, which are divided into q sub-windows, each with the same length of M, and the population mean E is defined as the mean of all distance units in one repeated radar cycle.

The mean of the p-th sub-window is defined as:

$$m_p = \frac{1}{M} \sum_{(p-1)M+1}^{pM} x_i, p = 1, 2 \ldots q \tag{1}$$

Then, the ratio between the mean of each sub-window and the population mean can be defined as:

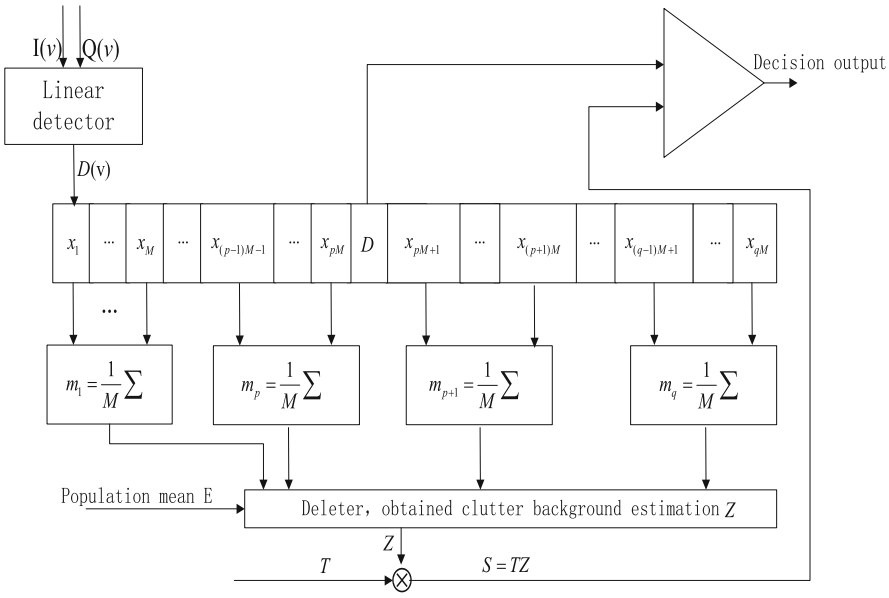

Fig. 1 Functional block diagram of ACA-CFAR detection

$$C = \frac{m_p}{E} \tag{2}$$

The value of C shows how much a sub-window mean is deviated from the population mean. Specifically, if there is no interference existing in the sub-window, its mean will be close to the population mean, while the value of C will increase if some interference exists. Therefore, the ratio of C can be used to judge the degree of clutter power changing in each sub-window.

Some experiment results found that C has a relatively steady and robust maximum value A in homogeneous clutter environment, which is named delete factor. If $C < A$, it indicates the sub-window is in homogeneous clutter environment and this sub-window will be selected. Otherwise, it should be removed if $C > A$. Consequently, K sub-windows which approximate homogeneous clutter environment are selected to estimate the background clutter adaptively, and get the clutter statistics Z:

$$Z = \frac{1}{K}\sum_{K} m_K, m_K \in \{m_p\} p = 1, 2 \ldots q \tag{3}$$

Let $S = TZ$ be the detection threshold, then the ACA-CFAR judging criteria can be expressed as

$$D \underset{H_0}{\overset{H_1}{\gtrless}} TZ \tag{4}$$

2.2 Determination of the Delete Factor A

It's clear that the delete factor does direct effect on the performance of the ACA-CFAR detection. Because the delete factor is a function jointly determined by the clutter distribution type and parameters, it is difficult to obtain the expression of the function in variety type of clutter. As a result, we use the Monte Carlo simulation to determine the delete factor of different distribution types of clutter approximately. The distribution function of A in homogeneous clutter environment is:

$$F(c) = p\left\{C = \frac{m}{E} \leq c\right\} \tag{5}$$

In order to determine whether the clutter in sub-windows is homogeneous, select value c when $F(c) \approx 1$ as the value of delete factor A. In this paper, 300 points Rayleigh clutter data with $\lambda = 1.0$ is generated and divided into 30 sub-windows. Probability density transform test method [4] is used to obtain probability distribution function F(c) by 100,000 simulations according to (2), which is shown in Fig. 2. It can be seen from Fig. 2 that c is about 1.18 when $F(c) \approx 1$, So the corresponding delete factor A is set to be 1.18 in the following experiments.

3 Experiments and Results

3.1 Rayleigh Clutter

Rayleigh clutter is suitable for the description of clutter background in airport runway environment. ACA-CFAR is an improved detection method based on the classic CA-CFAR method, so first given the CA-CFAR detection expression of Rayleigh clutter model in linear square-law detector. When the echo that envelope obey of the Rayleigh distribution through the square-law detector, the sampling of each detection unit obey exponential distribution, the probability density function is [5]

$$f_D(x) = \frac{1}{\lambda}\exp\left(-\frac{x}{\lambda}\right), \quad x \geq 0 \tag{6}$$

False alarm probability can be calculated by formula (7)

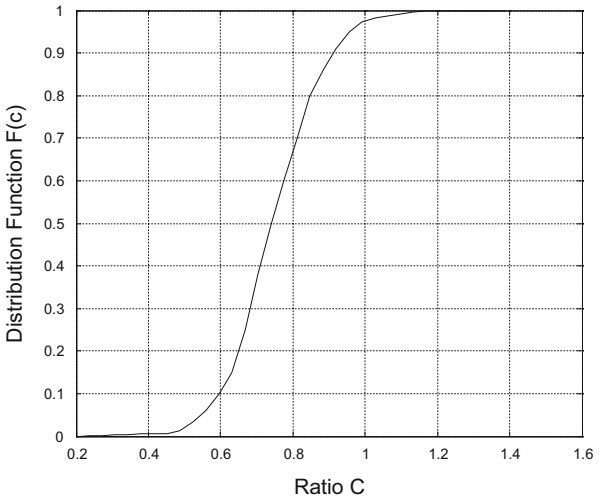

Fig. 2 Probability distribution function F(c) of Rayleigh clutter

$$P_{fa} = E_Z[P[D(v) > TZ|H_0]] = \int_0^\infty f_z(Z)\int_{TZ}^\infty \frac{1}{\lambda}\exp\left(-\frac{y}{\lambda}\right)dydz = M_z(\phi)\big|_{\phi=T/\lambda} \quad (7)$$

Where $f_z(Z)$ is probability density function of Z, $M_z(\cdot)$ is moment generating function (MGF) of Z.

3.2 Target Detect in Multi-targets Interference Environment

In this experiment, we will simulate the FOD target detection with multi-targets interference in homogeneous clutter environment.

When one or more interference targets exist in the reference window of the detection target, the total level of clutter power is elevated such that the main target may be shadowed and cannot be detected effectively [6]. That is, target shadowing effect may occur. And this is the truth when two or more FOD targets lie closely on the runway.

In the simulation, Rayleigh distribution clutter sequences are generated with 20 dB-power. Let target 1 with 35 dB-power and target 2 with 40 dB-power be two FOD targets to be detected, located in 100th and 91th distance unit, respectively. Assuming the probability of false alarm is $P_{fa} = 10^{-3}$, the delete factor A is 1.18, and the sliding window before and after detecting unit contain two protection units and ten reference units. Both the CA-CAFA and ACA-CFAR are used to conduct the target detection. The Simulation results are shown in Fig. 3a, b.

It can be seen from Fig. 3 that target 1 cannot be detected by using CA-CFAR detector, but it is detected distinctly by using ACA-CFAR detector. The reason is

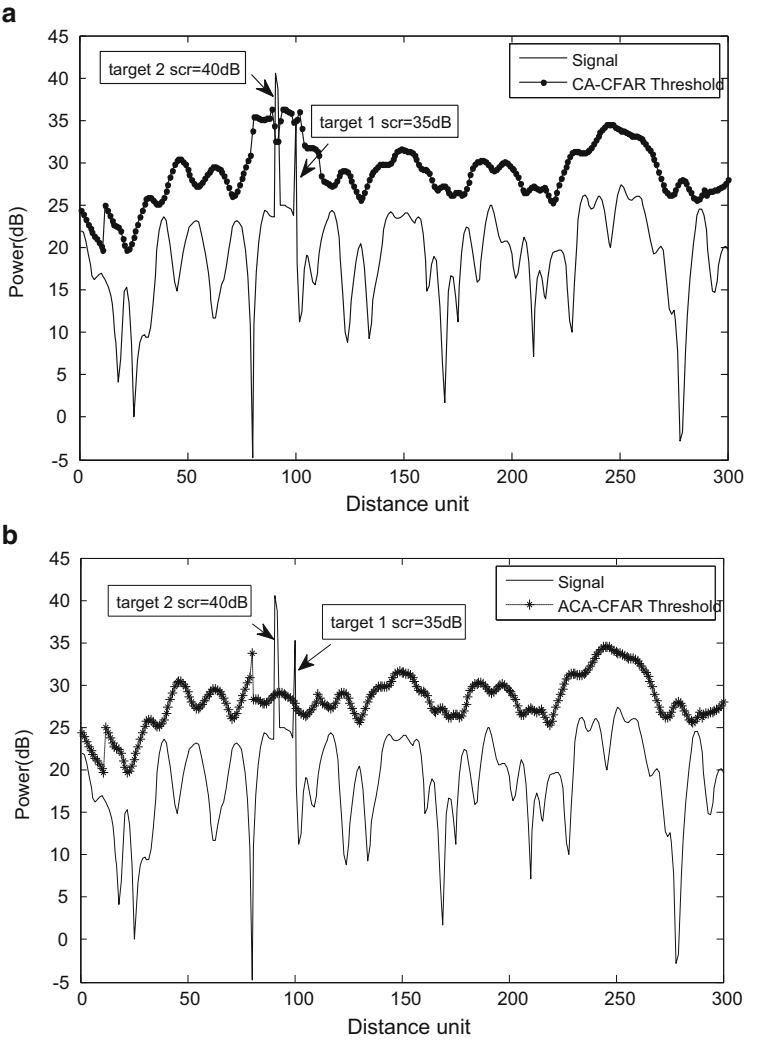

Fig. 3 Target detection in Multi-targets interference environment. (**a**) Detection result by CA-CFAR detector. (**b**) Detection result by ACA-CFAR detector

clear. In CA-CFAR detector, when target 1 is located in the detecting unit, target 2 is located in the reference sliding window, and its higher power of target 2 increases the estimated value of the background power, so the threshold of CA-CFAR detector is raised and as a result, target 1 is not detected. While in ACA-CFAR detector, the sub-window in which target 2 lies is removed and only the remained sub-windows are used to estimate the background power, which is

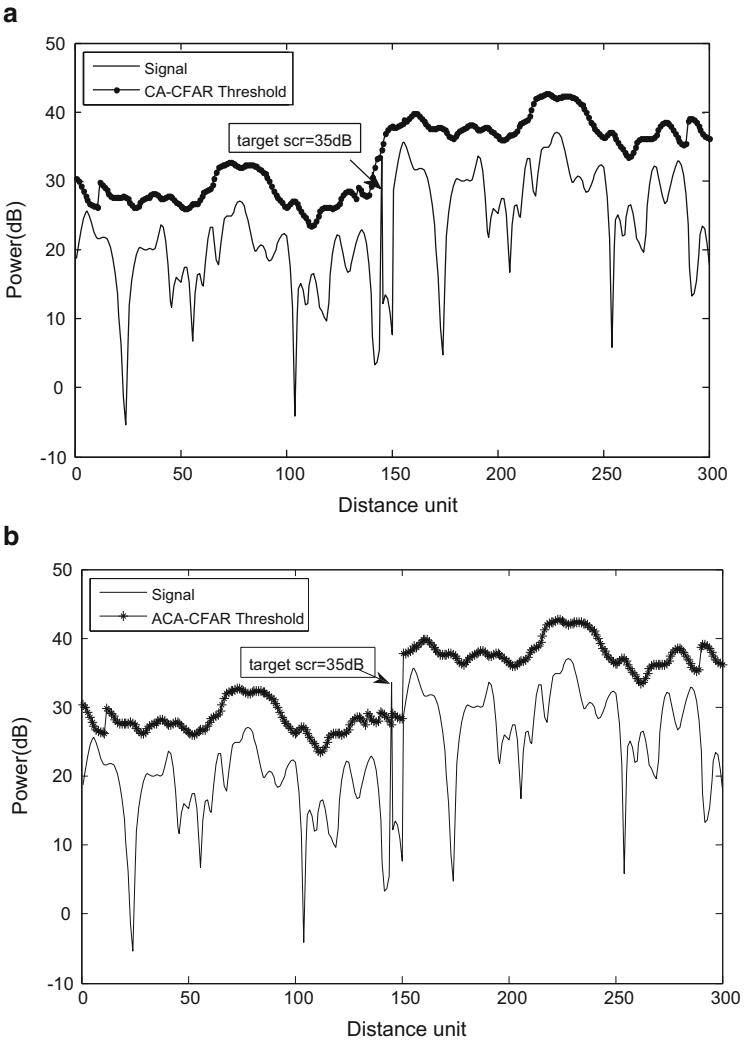

Fig. 4 Target detection in clutter edge environment. (**a**) Detection result by CA-CFAR detector. (**b**) Detection result by ACA-CFAR detector

obviously lower than that of CA-CFAR detector and is almost agreed with the true background power level.

The above analysis is the same with target 2, but due to its high signal-to-clutter ratio (SCR), target 2 can be detected obviously by both ACA-CFAR detector and CA-CFAR detector, unaffected by target 1.

3.3 Target Detect in Clutter Edge Environment

In practical FOD detection, the radar beam radiation area could include part of airport runway ground and part of the grass ground, so the clutter often is non-homogeneous. When the detecting unit is located near the boundary of two different reflectance zones, the reference sliding window in CFAR processing will contain clutter edge, which may result in the target with low power being missed. This is the truth if a FOD target lies on the edge of runway and nearby grass ground.

In this simulation, the average power of Rayleigh clutter of the first 150 distance units is 20 dB and is up to 30 dB in the follow 150 distance units. Assuming one FOD target is located in the 145th distance unit with 35 dB-power. Other conditions are the same as the first simulation. The detection results are shown in Fig. 4a, b.

Similarly, the FOD target is missed by using CA-CFAR detector, because the detection threshold is elevated relatively by those clutter units from the high reflectance zone in its reference sliding window. While ACA-CFAR detector removes the sub-window from high reflectance zone adaptively and estimates the total clutter level appropriately, and thus the FOD target located on clutter edge can be detected correctly.

4 Conclusions

The basic task of FOD detection is how to find small target in complex airport runway environment. The ACA-CFAR detector is very suitable to both multi-targets interference and clutter edge environment. The method divides the reference window into several sub-windows and removes the non-homogeneous clutter by judging the clutter power of each sub-window, so as to estimate a relatively appropriate clutter power level. Experimental results show that the ACA-CFAR detector is very suitable to the task of FOD detection on airport runway and some good detection performance is obtained by selecting reference units adaptively.

Acknowledgments This work is partially supported by the National Natural Science foundation of China (No. 61139003) and the Fundamental Research Funds for the Central Universities (No. ZYGX2010J022). The authors would like to thank the anonymous reviewers and editors for their helpful comments and suggestions.

References

1. Mazouni K, Kohmura A (2010). 77GHz FMCW Radar for FODs detection. Proc. 7th European Radar Conf. Paris, France: EuMA, pp. 451–454
2. Gandhi PP, Kassam SA (l988) Analysis of CFAR processor in nonhomogeneous. IEEE Trans Aerosp Electron Syst 24(4):427–445

3. Li J, Wang S, Hu W (2005) Adaptive CA-CFAR detection for multi-class clutter distribution model. J Air Force Radar Acad 19(3):4–7
4. Wang S, Liu J, Wang Y (2005) CFAR detection for multi-class clutter distribution based on airborne radar. Chin J Electron 33(3):484–487
5. He Y (2001) The review of radar automatic detection and CFAR processing methods. J Syst Eng Electron 11:9–15
6. Roling H (1983) Radar CFAR thresholding in clutter and multiple target situations. IEEE Trans Aerosp Electron Syst 219(4):608–612

Complex Event Processing Over Uncertain Event Stream

Xinlong Zhang, Yongheng Wang, Xiaoming Zhang, and Xinhui Zhu

Abstract In the practical application of the Internet of things, due to noise, sensor error, wireless communication techniques and other reasons, uncertain complex event processing has become very important. In order to deal with the large-scale probabilistic stream, we propose an improved method to not only process large volumes of real-time event stream effectively but also calculate the probability of outputs of compound events. It is based on an existing stream processing engine RFID Complex Event Detection Algorithm (RECDA), and we extend its evaluation model to a new type of matching tree in order to process the historical probabilistic event. In the design of matching tree, we consider optimizations to reduce the multi-query cost with Related Query Table. The experiment shows that the method is effective in handling multi-query uncertain event stream applications.

Keywords Internet of things • Complex event processing • Uncertain event streams

1 Introduction

Complex event processing has been studied widely in active database. The conventional methods are based on a fixed data structure, such as finite automaton [1], Petri nets [2], Graph [3], Tree [4]. RCEDA is a graph-based RFID complex event processing algorithm. It constructs an event graph with leaf nodes representing primitive events, internal nodes presenting complex events. However, this method

X. Zhang (✉) • Y. Wang • X. Zhang
College of Information Science and Engineering, Hunan University, Changsha, China
e-mail: mysileng@gmail.com

X. Zhu
College of Science, Hunan Agricultural University, Changsha, China

B. Zhang et al. (eds.), *The Proceedings of the Second International Conference on Communications, Signal Processing, and Systems*, Lecture Notes in Electrical Engineering 246, DOI 10.1007/978-3-319-00536-2_74,

only considers single complex event detection, without considering the sharing of intermediate results between the multiple complex events.

There are two main challenges based on uncertain event stream complex event processing: one is how to detect complex events satisfying query requirements from a large number of possible worlds in high-speed and real-time; the other is how to calculate the probability of complex event aggregated from correlated uncertain events. Aiming at the two challenges, this paper proposes a Uncertain Stream Complex Event Processing (USCEP). USCEP based on the RCEDA address the improvement of probabilistic computational efficiency. Our main contributions consist of: first, extension of RCEDA to support historical simple event processing over uncertain data stream; second, a foundation of probability model: event probabilistic model; third, optimization for a large number of registered query.

2 Event Probabilistic Model and Query Language

Definition 1 simple probabilistic event: simple probabilistic event is represented as : <RID, A, T, Pro> where RID is RFID tag and A is the area of RFID reader location. T is the timestamp that the event occurs. Pro is the concrete probability value used to present the occurrence probability of the event.

Definition 2 complex probabilistic event: Complex event is a combination of primitive events or complex events by some rules. A complex probabilistic event is represented as <E, R, Ts, Pr> where E represents the elements that compose the complex event, R represents the rule of the combination, Ts represents the time span of the complex event and Pr is the probability.

The query language structure of USCEP is defined as:

```
IN <event area>
SELECT <event pattern>
WHERE <qualification>
WITHIN <time window>
```

<event area> clause is the area of RFID reader location that is involved in the <event pattern>; <event pattern> clause declares the structure of a pattern that consists of event operators; <qualification> is the limit of the query; <time window> is the limit of complex probabilistic event timestamp.

In fact, calculation of the complex probabilistic events can be divided into two sets: Set I contains the independent primitive events while set D contains one or more Markov chain. The probability can be computed as follows:

$$Pro(E) = \prod_{e \in I} Pro(e) \bullet \prod_{di \subseteq D} \left(Pro(e_1) \bullet \prod_{n=1}^{|di|-1} Pro(e_{n+1} | e_n) \right) \tag{1}$$

Where d_i is one Markov chain of dependent set D, e_1 represents the first event in

Table 1 RID conditional probabilistic table

RID	
Conditional event	Probability
B|A	0.9
C|B	0.8
...	...

the Markov chain, $Pro(e_{n+1}|e_n)$ represents continuous events are related, it is calculated as follows:

$$Pro(en, en+1) = Pro(en) \bullet Pro\left(en+1\middle|en\right) \tag{2}$$

We get the probability of $Pro(e_{n+1}|e_n)$ by the conditional probabilistic table. Shown in Table 1, it is the conditional probabilistic table of a specific RID. Each conditional probabilistic table can learn and change by itself according to the input stream.

Figure 1 shows the framework of learning:

Different RFID readers put their probabilistic event into the RID classifier which uses for event classification. Then different id streams output from classifier, conditional probabilistic graph can transform every input stream into historical event graph, that can provide support to conditional probabilistic table.

Conditional probabilistic graph is a weighted directed graph, shown in Fig. 2. Node represents the area's event. Directed edge <X,Y> represents the node Y occurs after X. When system detects the two events that occur in a clear time sequence, it will add the probability of the latter event to the edge, which represents the latter event has been integrated into the probability graph.

Tuple of the conditional probabilistic table is calculated as follows:

$$Pro\left(B\middle|A\right) = value(< A, B >)/\sum_{X \in N} value(A, X) \tag{3}$$

<A,B> is a weighted directed edge with starting point A and ending point B. We can use Value () operator to extract value of edge. Set N is a ending points collection, and each point of the collection is a part of directed edge that is started from point A. For example, Fig. 2 shows the calculation of Pro(C|B): Pro(C|B) = 12.5/(4.9 + 12.5 + 3.8) = 0.59

The input to event processing system is a simple uncertain event stream with infinite sequence of probabilistic events. Each probabilistic event from input has a concrete probability value used to present the occurrence probability of this event (Fig. 3). The output of USCEP system is also a probabilistic stream of event. In Table 2, this example of output ignores the time interval that we may doesn't care. Two main attributes remain: the matched sequences and corresponding probability. The first tuple depicts that we can obtain the query result string $A_0B_1C_3$ from the USCEP system and their probability (0.78).

Fig. 1 Learning framework

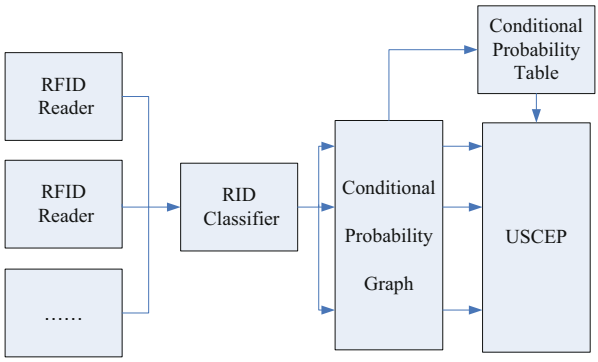

Fig. 2 Conditional probabilistic graph

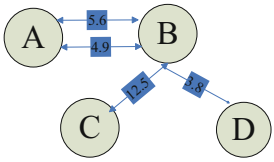

Fig. 3 Input probabilistic stream

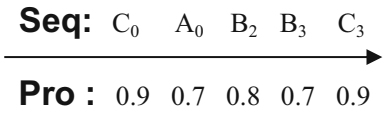

Table 2 Output probabilistic stream

Sequence	Probability
$A_0\ B_1\ C_3$	0.78
$A_0\ B_2\ C_3$	0.504

Moreover, we give a example of the complex probabilistic event query. In event instances Query 1 (Fig. 4), event type A, B and C mean the RFID readers detect vehicle in area A_A, A_B and A_c, and the vehicle passes A_A, A_B and A_c in sequence. The time span between A and B must be limited to 1–3. Exactly, Query 1 describes an RFID-based vehicle trajectory. It requires max span of different events within the timestamp of 30, and the probability of all events should exceed 0.5.

3 Uncertain Event Stream Complex Event Processing

3.1 System Architecture

USCEP system architecture is shown in Fig. 5.

Fig. 4 Query 1

```
IN       A,B,C
SELECT   SEQ(TSEQ(A,B;1,3),C)
WHERE    A.RID=B.RID=C.RID
         AND Conf(*)>0.5
WHTHIN   30
```

Fig. 5 System architecture

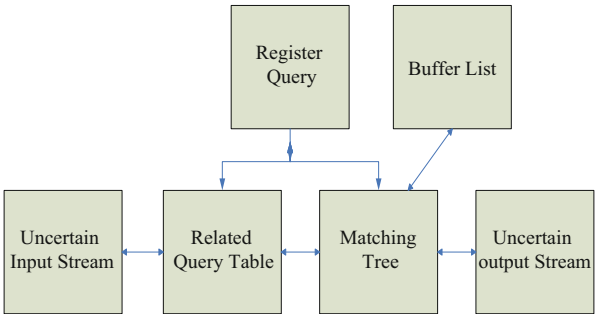

Table 3 Related query table

Area	Related query
A	Query1
B	Query1
	Query2
C	Query1
D	NULL
...	...

When a user submits a query by query language, complex event query will be registered. It is assigned with a matching tree and is stored as a query index into Related Query Table (Table 3). Related Query Table is used to determine the relationship between physical area and a specific registered query. When an event occurs in monitored area, system can use the Related Query Table to determine the area that is associated with registered query quickly, rather than the way for polling to access total registered query.

3.2 USCEP Algorithm

USCEP Algorithm shown in Algorithm 1:

Algorithm 1. USCEP(PS, QTree)

Input: PS is the simple probabilistic stream, QTree is matching tree of query

Output: SC is an instance collection of the complex probabilistic events

```
Method:
for each incoming event E
do query[i] ← RELATEDTABLE(E.A,E.RID)
for each query in query[i]
do qtree ← INITQTREE(query)
for each qtree's Area Node
do if E.A is in this Area
then ADDTOLIST(E)
SENDUPDATE()
while node N received updated notice
do if MATCH(N.children)
then ADDTOLIST(N)
SENDUPDATE()
if qtree's root list size >0
then SC ← RETRIOUTPUT(qtree)
Return SC
```

We first register query. When a event comes, we find its related query sets from Related Query Table. After that, we transport simple event to matching tree. For a matching tree, it is matched by the way of bottom-up. If the current node matches successfully, it will add a successful matched record to the node's buffer list, and then send updated message to the parent node. If parent node receives an updated message, it will check its children's buffer list to determine whether the match is successful. If the match is successful, it would continue to add the record and send message to superior. So iterations until there are no nodes receive updated message again. Finally, take a view on the root node buffer list, top-down output process can be triggered if there is a successful matched record in list, and then system would return the result set.

3.3 USCEP Algorithm Instance

Algorithm instance uses query 1 (Fig. 4). Figure 3 shows input stream of instance. Firstly, query will be registered. Then it runs USCEP algorithm with Table 1:

1. C_0 arrives; we know from the Related Query Table, Query1 is only related query with the C Area, so we enter the matching tree qtree1.
2. Matching stage of matching tree. It finds c leaf node can be matched from all leaf nodes, and adds successful matched record of C_0 to the buffer list, then node will send updated message to its parent node. Parent node "SEQ" checks buffer lists of all the children according to SEQ's matching rule, and Observes whether there are records that meet rule. if success, it will insert a record into buffer list and send message again. But actually it is fail now, so end of the matching stage (Fig. 6).

Fig. 6 C_0 process

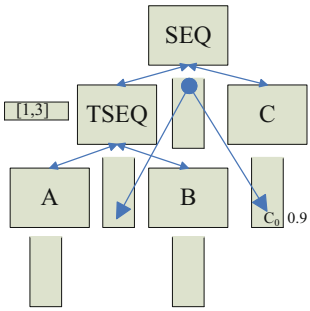

3. A_0 arrives (same procedure as Step 1). It is easy to find that the buffer list of node B is empty, which is not satisfying the rule. It's end.
4. B_2 arrives. System adds successful matched record of B_2 to the buffer list. After a while, "TSEQ" node receives the updated message. It finds that there is a pair of records that include A_0 and B_2 meet the matching rule, and then generates a successful matched record of "TSEQ"(Record has two pointers that pointer to A_0 and B_2, they are used for output retrieval). Record also contains a new composite probability: $pro(T_2) = pro(A_0) * pro(B|A) = 0.63$. After that, "TSEQ" node also sends updated message to "SEQ" node. Though it is found that the buffer list of "SEQ" and C node both have records exists, but they does not meet the rule (T_2 is older than C_0), so it's end (Fig. 7).
5. B_3 arrives. The same process is similar to B_2. After we ignore that event B_3 has a weak effect on conditional probability table, the probability values of T_2 and T_3 will be regarded as almost the same.
6. C_3 arrives. After the same inserted processing to the node C's buffer list, node C will send message to "SEQ" node. Message calls "SEQ" node's Match function. It shows that there is a pair of records, i.e. $TSEQ_2$ and C_3, meets the matching rule. So, system inserts successful matching record into list and calculates the new probability, $pro(S_3) = pro(T_2)*pro(C|B) = 0.504$. Because the current node is the root node, it doesn't have parent node to send message again. Instead, it will trigger a complex event generation process. In this process, all probability values of related records are going to meet the CONF statement. If one of related records less than 0.5, the record of the root node is marked invalid. On the contrary, it will use the top-down way to track the sequence of complex events and output (Fig. 8). Result shows in the second tuple of Table 2.

4 Experimental Evaluations

We have developed a car-based NetLogo network emulator, it can automatically generate a variety of RFID and sensor events by different device configurations. The experiment uses a Founder desktop with 2 GB memory and the Intel G630 processor. The operating system is Window XP SP3. The experimental system was developed by Java.

Fig. 7 B_2 process

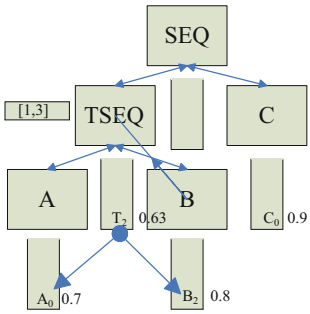

Fig. 8 C_3 process

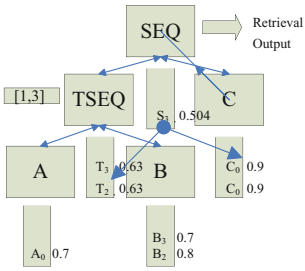

Fig. 9 Output numbers of complex events

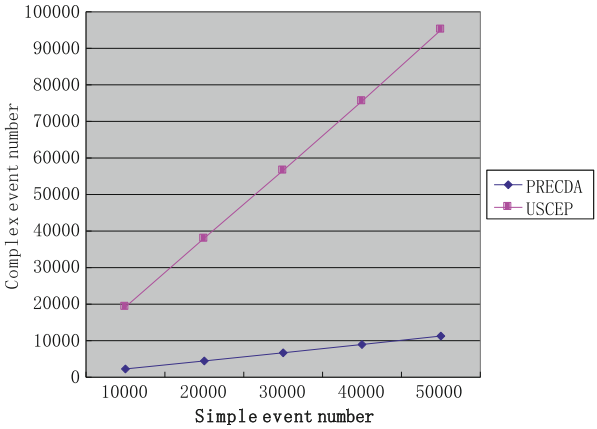

Currently we have not found other method has the same function with ours. Therefore we compare our method with a "PRCEDA". The PRCEDA extends the classic RCEDA method directly to support probabilistic SEQ event processing like the work of our approach. We assume that all registered queries are binary tree and tree's depth less than 3 layers.

Figure 9 shows that the output numbers of complex events with same registration and input. As we can see, when simple event number is large, the USCEP has more complex event to generate than PRECDA. Because the system buffers many

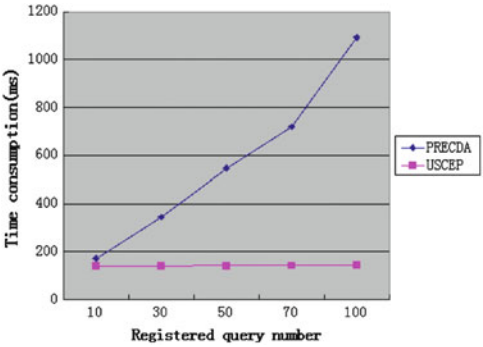

Fig. 10 Time consumption

successful matching records under specified time window, so output numbers of complex events increased significantly. In next experiment, we study the performance of same input stream with different registered queries. From Fig. 10 we can see the performance of USCEP is better than the PRECDA. When the number of registered queries becomes larger, PRECDA has rapid growth, but USCEP maintains stable time consumption for the reason Related Query Table brings almost constant processing efficiency rather than constantly polling.

5 Discussion and Conclusion

This paper describes an effective uncertain event stream complex event processing. In order to resolve the uncertainty of the event, this method uses the event probabilistic model and USCEP query language for modeling and custom queries. USCEP would transfer the event of specific area to the corresponding query, and then transform the different simple events to complex events with the combination of matching tree and node's buffer list. Experiments show that the method is effective in handling multi-query uncertain event stream applications

Acknowledgments This project is sponsored by the "Context-aware and proactive complex event processing for large scale internet of things (13JJ3046)" project of Hunan Province Natural Science Fund and the "complex event processing in large scale internet of things (K120326-11)" project of Changsha technological plan, the national science and technology plan "compositive information service technology project for Internet of things for rural area (2012BAD35B07)."

References

1. Eugene Wu, Yanlei Diao, Shariq Rizvi (2006) High-performance complex event processing over streams. Proceedings of the 2006 ACM SIGMOD international conference on Management of data, p 407–418, 10.1145/1142473.1142520

2. Wenhui Hu, Wei Ye, Yu Huang, Shikun Zhang (2008) Complex event processing in rfid middleware: a three layer perspective. Proceedings of the 3rd international conference on in convergence and hybrid information technology, vol 1, p 1121–1125
3. Fusheng Wang, Shaorong Liu, Peiya Liu, Yijian Bai (2006) Bridging physical and virtual worlds: complex event processing for rfid data streams. Proceedings of the 10th international conference on extending database technology, p 588–607, 10.1007/11687238_36.
4. Hongying Liu, Satoshi Goto, Junhuai Li (2009) The study and application of tree-based rfid complex event detection algorithm. Proceedings of the 2nd international symposium on electronic commerce and security, p 520–524

The Application of Speech Synthesis in Car Warning System

Jianli Liu and Jinying Chen

Abstract By introducing the theory of SPCE061A, Wyt software, Total Recorder software and SunAudiorV103 software, we can discuss the process of speech synthesis. Through the combination of the automotive anti-collision system which composed by sensors and speech synthesis, we can get a early warning system with voice service function, which can make the car terminal more humanized and intelligent , can improve drivers safety coefficient in driving.

1 Introduction

With the highly development of industrialization in modern society, transportation security question has already become a big problem that needed to be solved urgently to all countries. Speech synthesis technology has undergone a gradual development, from the parameters synthesis to splicing synthetic parameters, and then to the gradual combination. People's cognitive level and demand is the power of development. And the voice alarm way is easier for human to accept, compared with the traditional warning lights or just in the reverse a "reverse please note" simple speech broadcast way, the design of the speech broadcast makes the language more selectivity, alarm type more diversified. Not only suitable for reversing alarm, the design can also play a role in the prison door or pedestrians, vehicles, obstructions close to the body, or some dangerous situations occurs. In this paper, the vehicle collision avoidance system, which installed in the car with the antennas of multiple sensors, microprocessors and digital signal processors, controls different directions SPCE061A for corresponding broadcast, prompts the driver to take emergency measures to cope with the special danger to avoid losses.

J. Liu (✉) • J. Chen
College of Information Science and Technology, Chengdu University of Technology, Chengdu, China
e-mail: 2437306780@qq.com

B. Zhang et al. (eds.), *The Proceedings of the Second International Conference on Communications, Signal Processing, and Systems*, Lecture Notes in Electrical Engineering 246, DOI 10.1007/978-3-319-00536-2_75,

2 SPCE061A and Speech Softwares

Single-chip microcomputer speech processing technology becomes more and more widely used in different kinds of processing control and motion situations, compared to the similar products, sunplus SPCE061A uses unique hardware design and software algorithms, makes use of its audio processing peripheral devices to reduce program designed to simplify, a small voice processing environment seems more applicable.

(1) SPCE061A is a 16-bit microcomputer developed by SUNPLUS Technology Company, with 16-bit latest processors, high-speed processing performance makes it easier to quickly handle complex digital signals, so SPCE061A widely used in digital audio processing and speech recognition field. SPCE061A applies on various occasions with the voltage of 2.4–3.6 V and a frequency of 0.32–49.152 MHz, and memory capacity includes 32 KB Flash program memory and 2 KB SRAM. Other features such as 32 programmable multi-function I/O ports, two16-bit timer/counter, 32768Hz real-time clock, low voltage reset/monitoring, seven AD converter channels and one channel audio AD converter channel (with automatic gain controller built-in microphone amplifier), 10-bit DAC output ports, built-in online simulation interface, etc. SPCE061A can be applied in speech recognition products, intelligent interactive session toys, senior learning toys, children's learning products, general speech synthesizer, duration of language products, recording/playback product and other application fields. The SACMv41dx voice library is created by Sunplus Technology for SPCE061A to voice recording and playback solutions. The broadcast principle is shown in Fig. 1. It includes SACM_A1600, SACM_DVR1600, SACM_S720, SACM_MS01 four voice encoding software packages, suitable for speech broadcast, music player and other purposes.

    This is the SACM_S720, 4.8 Kbps, which can compress the"8 KHz, 16 bit" documents into 26.7:1 for coding. For SACM_S720, only can be used to playback the compressed voice resources, rather than with real-time compression encoding (recording) functions. With SunAudior software, *.Wav format file can be compressed into the voice of SACM_S720 which can broadcast speech resources. The speech broadcast has three kinds of compression ratio: SACM-A2000, SACM-S480, SACM-S240, each compression ratio has different voice quality. The compression ratio of SACM-S480 is 80:3 and 80:4.5 combined with the advantages of waveform coding and parametric coding.

(2) Wyt is a powerful document reading software, can read the common document formats (such as Doc, TXT and Html, etc.) in a clear, natural, smooth voice. The program runs initialize and loads the service automatically, supports gb2312\GBK\BIG5, can realize the synthesis and "real-time preview mode" at the same time.

Total Recorder is excellent recording software of High Criteria Company, has powerful and extremely rich sources. It can record almost all the sound through the

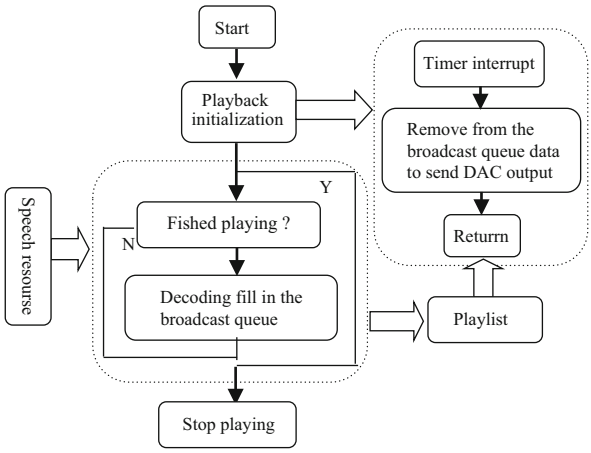

Fig 1 Speech broadcast principle

sound card and software, including the sounds from the Internet, audio CD, microphone, games and IP telephones. The working principle of Total Recorder is to use a virtual "sound card" to capture the output voice of other programs, and then transfer to physical sound card, the whole process is completely digital recording, so won't appear any distortion in theory. The software is divided into: the Standard Edition, Professional Edition, designed specifically for developers, advanced user version. The use of Total Recorder Professional Edition.

3 The Principle and Process of Early Warning System in Speech Synthesis

When the vehicle sensors detect a target, SPCE061A will give an alarm signal to the driver. While the microprocessor can finish and integrate the unprocessed signal of sensors, and optimize the sensitivity of detecting incident signal and identification process. The digital signal processor has the function of control, self-calibration, output and fault diagnosis.

3.1 Generate Speech Data

(1) Record Through wyt2.0_pj can get a recording on a PC. The wyt2.0_pj can directly convert the WORD documents into sounds, add a corresponding statement, for example: "The obstacle to attention" etc. But can not generate a sound file, audio file generated by Total Recorder software. Set the audio recording source to software (W), set the quality to 8,000 Hz, otherwise will not support the SunAudior compressed files, save and generate *.Wav file. This

method makes recording, cutting together, data property is an uncompressed PCM format, sampling rate is 8,454 Hz, 16-bit coding, mono.

(2) Generate single-chip microcomputer voice file. The voice file which is available for single-chip microcomputer radio is a synthetic voice encoded file. It is converted from uncompressed PCM encoded files by Sunplus SunAudiorV103 software, the file format is .S48. The *.Wav file can be compressed into SACM_S480 corresponding voice data, you can use SACM-LIB library to process these datas.

The library makes the A/D, encoding, decoding, storage and D/A into corresponding modules, each module has its application programming interface of API functions, call the corresponding function can be realized to their respective functions with voice compression and playback API function, to constitute a complete voice applications system.

4 Speech Broadcast Working Process

Speech synthesis principle is based on the result of the modeling rhythm, get the original speech library from the voice primitive, use specific speech synthesis technology to adjust and modify voice-based, and synthesize realistic voice ultimately. Here we use the u'nSP IDE integrated development environment for programming. U'nSP IDE integrated developed environment set the functions of procedures, compiled, links, debugging and simulation and so on as one, the software simulation functions can unconnect to the emulation board to simulate the function of the hardware debugger.

step 1 Establish a project. Open u'nSP IDE integrated development environment, select the File/ New menu item, create a new project.

step 2 Copy speech resources and SACMv41dx relevant documents to the project folder. Will be compressed and exported by SunAudior voice files and copied to the folder of the project. In SACMv41dx Files folder, S72 related documents, including SACMv 41dx_061A.l, SACM_S72.asm, SACM _S720 _User_ C_C. c, S720.h and S720.inc, also copied to the engineering in the folder.

step 3 Add speech resources to the project. Operate u'nSP IDE software, in the IDE "Project" menu, select "Add to Project/Resource", choose to play the speech of the resources in the popup dialog box.

step 4 Add SACMv41dx_061A.lib to the project. Choose "Setting" of "Project" menu item, select "Link" tab in the popup dialog box, click "Library Modules" to save the project.

step 5 Add S720 program files to the project. Related program files include SACM_ S720.asm and SACM_ S720_User_C.c, choose "Add To Project/File" in the menu of "Project".

step 6 Write speech broadcast program. In the engineering, create a C program file, write a speech broadcast function. During the loop playback, the program

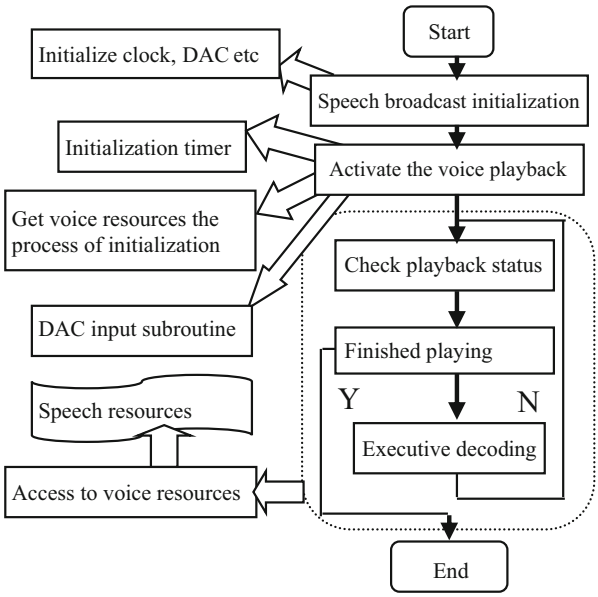

Fig 2 Speech broadcast program diagram (1)

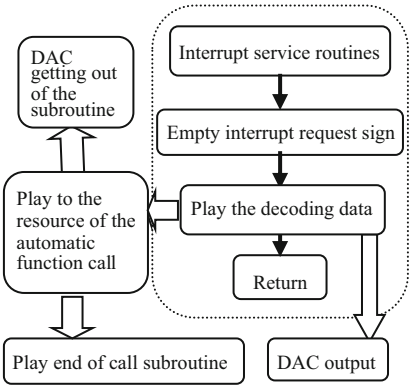

Fig 3 Speech broadcast program diagram (2)

constantly to decode voice resources, and fill in the playback queue, the decoded data will be playbacked by DAC in the timer interrupt service routine. Voice player schematic diagram is shown in Figs. 2 and 3.

step 7 Modify the access to procedures. The function for S720 to access the voice resource is defined in SACM_S720_User_C.c, USER_S720_GetResource_Init and USER_ S720_GetResource included.

step 8 Build the engineering and download runs. Implementation the "Build" menu "Rebuild All", If there are no syntax errors, can be download to SPCE061A. Then can achieve speech broadcast.

5 Conclusion

Vehicle terminal which based on the SPCE061A speech synthesis technology can be widely used in navigation systems, vehicle scheduling, vehicle monitoring etc, can improve the intelligence of Car terminal, the drivers safety and comfort, make the users using it more convenient, more user-friendly. With the rapid increase of the voice interface requirements which has high performance and high stability in the consumer electronics products, SCM voice processing technology is also developing rapidly. The in-depth research and development of such products has a far-reaching practical significance.

Null Space Pursuit Algorithm Based on a Fourth-Order Differential Operator

Weiwei Xiao and Shuying Zhang

Abstract The null space pursuit (NSP) algorithm based on a fourth-order differential operator is a method of signal processing. The NSP algorithm uses an adaptive operator to separate a signal into additive subcomponents. Furthermore, it is possible to design different operators to fit different signal models. In this paper, we propose a new type of a differential operator. We theoretically derive the new differential operator and then test the proposed method using simulated signals.

1 Introduction

Single-channel signal separation and estimation has attracted considerable attention in recent years. The most widely used approach models a signal as a superposition of additive coherent basic signals. The methods used to separate signals vary because different subcomponents are used to construct the signals. For example, in the empirical mode decomposition (EMD) approach [1, 2], an oscillatory signal is decomposed into a sum of intrinsic mode functions. In the matching pursuit (MP) approach [3], a signal is decomposed into a sum of time-frequency atoms. In all methods of signal separation, the null space pursuit algorithm based on a differential operator is of particular interest to us.

The null space pursuit (NSP) algorithm based on a differential operator was proposed by Silong Peng and Wen-Liang Hwang [4] in 2008, and they further improved it in 2010 [5]. This method makes use of an adoptive operator to separate a signal into a sum of simpler signals, and these simple signals belong to the null space in the above. The important processes include estimating the adaptive

W. Xiao • S. Zhang (✉)
North China University of Technology, Beijing 100144, China
e-mail: yujinxiang.1986@163.com

B. Zhang et al. (eds.), *The Proceedings of the Second International Conference on Communications, Signal Processing, and Systems*, Lecture Notes in Electrical Engineering 246, DOI 10.1007/978-3-319-00536-2_76,

operator T_s from the signal S and separating it into U and R, where U is the extracted signal, set $T_s(U) = 0$, and R is the residual signal.

In [5], the form of the operator is $T_s = d^2/dt^2 + \omega^2(t)$, which can annihilate the FM signal $\cos(\phi(t))$, where $\phi(t)$ is a local linear function defined as $\omega(t) = d\phi(t)/dt$, and $\omega(t)$ is the IF of the signal at t.

In 2011, Xiyuan Hu [6] improved the null space pursuit algorithm and then further expanded the scope of signals that could be decomposed. The operator he proposed is $T_s = d^2/dt^2 + P(t)(d/dt) + Q(t)$, which can annihilate an AM-FM signal.

In this paper, we improve the algorithms in [5, 6] to use a fourth-order differential operator. The proposed algorithm can annihilate the signal $s(t) = A(t)\cos(\phi(t))$, where $A(t)$ is a cubic polynomial.

2 Annihilation Operators for Continuous Signals

To expand the scope of signals that can be decomposed, we propose another differential operator that can annihilate signal $s(t) = A(t)\cos(\phi(t))$. The original form of the differential operator is not applicable to the signal model; thus, we propose the following fourth-order differential operator:

$$T_s = \frac{d^4}{dt^4} + \omega_2(t)\frac{d^2}{dt^2} + \omega_0(t) \tag{1}$$

When we substitute signal $s(t) = A(t)\cos(\phi(t))$ into (1) and set the result to zero, we obtain

$$\left(\frac{d^4}{dt^4} + \omega_2(t)\frac{d^2}{dt^2} + \omega_0(t)\right)A(t)\cos\left(\phi(t)\right) = 0 \tag{2}$$

By using calculations to solve the ordinary differential equation in (2), we obtain the following equation set:

$$-2A^{(3)}(t)\phi^{'}(t) + 2A^{'}(t)\phi^{'}(t)^3 - \omega_2(t)A^{'}(t)\phi^{'}(t) = 0, \text{ and} \tag{3}$$

$$-6A^{''}(t)\phi^{'}(t)^2 + A(t)\phi^{'}(t)^4 + \omega_2(t)a^{''}(t) - A(t)\omega_2(t)\phi^{'}(t)^2 + \omega_0(t)A(t) = 0 \tag{4}$$

We obtain $\omega_0(t)$ and $\omega_2(t)$ from the above equation set:

$$\omega_0(t) = \phi^{'}(t)^4 + 4\frac{A^{''}(t)\phi^{'}(t)^2}{A(t)} + 2\frac{A^{(3)}(t)A^{''}(t)}{A(t)A^{'}(t)} - 2\phi^{'}(t)^2\frac{\phi^{(3)}(t)}{\phi^{'}(t)} \tag{5}$$

$$\omega_2(t) = 2\phi^{'}(t)^2 - 2\frac{A^{(3)}(t)}{A^{'}(t)} \tag{6}$$

After substituting $\omega_0(t)$ and $\omega_2(t)$ into (1), we obtain the proposed operator:

$$\begin{aligned} T_s = \frac{d^4}{dt^4} + \left(2\phi^{'}(t)^2 - 2\frac{A^{(3)}(t)}{A^{'}(t)}\right)\frac{d^2}{dt^2} + \phi^{'}(t)^4 + 4\frac{A^{''}(t)\phi^{'}(t)^2}{A(t)} \\ + 2\frac{A^{(3)}(t)A^{''}(t)}{A(t)A^{'}(t)} - 2\phi^{'}(t)^2\frac{\phi^{(3)}(t)}{\phi^{'}(t)} \end{aligned} \tag{7}$$

When the signal is fit to the signal model, it is separated by (7). However, most real-life signals are discrete signals, and the method described in this section is not applicable. Thus, we need to find another method that applies to discrete signals.

3 Null Space Pursuit Algorithms for Discrete Signals

We use the NSP algorithm to separate discrete signals, and the form of the operator remains as

$$T_s = \frac{d^4}{dt^4} + \omega_2(t)\frac{d^2}{dt^2} + \omega_0(t) = D_4 + \omega_2(t)D_2 + \omega_0(t)$$

However, all the parameters are replaced by the corresponding matrix forms described in the following algorithm. We now use the NSP algorithm to search for $\hat{P}(t)$, $\hat{Q}(t)$, and $\hat{R}(t)$ that minimize the equation:

$$\begin{aligned} \|T_S(S(t) - R(t))\|^2 + \lambda_1\left(\|R(t)\|^2 + \gamma\|S(t) - R(t)\|^2\right. \\ \left. + \lambda_2\left(\|D_4\omega_2(t)\|^2 + \|D_4\omega_0(t)\|^2\right)\right) \end{aligned} \tag{8}$$

where λ_1 and λ_2 are Lagrange parameters, and γ is the leakage parameter that determines the amount of information retained in $S(t) - R(t)$ in the null space of T_S. The terms following λ_2 represent the regulation of the parameters of the AM-FM operator.

To minimize (11), we adopt the smooth variations of $D_4W_2(t)$,which is the weighted sum of the squares of **IF** and the small squared instantaneous bandwidth $W_0(t)$. The NSP algorithm can estimate λ_1 and γ adaptively; however, λ_2 is insensitive,so we set λ_2 as a constant in our implementation.

For ease of presentation in the discrete representation, we use bold upper case, e.g., **A**, to represent matrices and bold lower case, e.g., **a**, to represent vectors. Matrix **Ax** denotes a diagonal matrix in which the elements are equal to vectors **x**.

In the discrete case, $S(t)$, $R(t)$, $\omega_2(t)$ and $\omega_0(t)$ can be represented as the column vectors $\mathbf{s}$, $\mathbf{r}$, $\mathrm{W}_2(t)$, and $\mathrm{W}_0(t)$, respectively. Further, D_2 and D_4 can be represented as matrices of the second- and fourth-order differences, D_2 and D_4, respectively. Equation (8) is then rewritten as

$$\begin{aligned} F(\mathbf{p},\mathbf{q},\mathbf{r}) = \|(\mathbf{D}_4 + \mathbf{A}_{\mathrm{W}_2}\mathbf{D}_2 + \mathbf{A}_{\mathrm{W}_0})(\mathbf{s}\text{-}\mathbf{r})\|^2 + \lambda_1\left(\|\mathbf{r}\|^2 + \gamma\|\mathbf{s}\text{-}\mathbf{r}\|^2\right) \\ + \lambda_2\left(\|\mathbf{D}_4\mathrm{W}_2(t)\|^2 + \|\mathbf{D}_4\mathrm{W}_0(t)\|^2\right) \end{aligned} \tag{9}$$

We let Φ be the vector that contains all the parameters of the operator $\Phi = [\mathrm{W}_2{}^T, \mathrm{W}_0{}^T]^T$. Then, (9) becomes

$$\begin{aligned} \mathbf{F}(\Phi,,\mathbf{r}) = \|(\mathbf{D}_4 + \mathbf{B}_\Phi\mathbf{M}_1)(\mathbf{s}\text{-}\mathbf{r})\|^2 + \lambda_1\left(\|\mathbf{r}\|^2 + \gamma\|\mathbf{s}\text{-}\mathbf{r}\|^2\right) \\ + \lambda_2\left(\|\mathbf{M}_2\Phi\|^2\right) \end{aligned} \tag{10}$$

where $\mathbf{B}_\Phi = [\mathbf{A}_{\mathrm{W}_2}\ \mathbf{A}_{\mathrm{W}_0}]$, $\mathbf{M}_1 = [\mathbf{D}_2^T\ \mathbf{E}^T]^T$, and $\mathbf{M}_2 = \begin{bmatrix} \mathbf{D}_4 & \\ & \mathbf{D}_4 \end{bmatrix}$, in which $\mathbf{E}$ is the identity matrix.

$$\begin{aligned} (\mathbf{D}_4 + \mathbf{B}_\Phi\mathbf{M}_1)(\mathbf{s}\text{-}\mathbf{r}) &= \mathbf{D}_4(\mathbf{s}\text{-}\mathbf{r}) + [\mathbf{A}_{\mathrm{W}_2}\ \mathbf{A}_{\mathrm{W}_0}](\mathbf{M}_1(\mathbf{s}\text{-}\mathbf{r})) \\ &= \mathbf{D}_4(\mathbf{s}\text{-}\mathbf{r}) + \mathbf{A}_{\mathbf{D}_2(\mathbf{s}\text{-}\mathbf{r})}\mathrm{W}_2 + \mathbf{A}_{(\mathbf{s}\text{-}\mathbf{r})}\mathrm{W}_0 \\ &= \mathbf{D}_4(\mathbf{s}\text{-}\mathbf{r}) + \mathbf{A}\Phi \end{aligned} \tag{11}$$

In (11), $\mathbf{A} = \left[\mathbf{A}_{\mathbf{D}_2(\mathbf{s}\text{-}\mathbf{r})}\ \mathbf{A}_{(\mathbf{s}\text{-}\mathbf{r})}\right]$. By taking the partial derivative of $\mathbf{F}$ with respect to Φ and setting the result equal to zero, we obtain $\frac{\partial \mathbf{F}}{\partial \Phi} = 0$. Then,

$$\hat{\Phi} = -\left(\mathbf{A}^T\mathbf{A} + \lambda_2\mathbf{M}_2^T\mathbf{M}_2\right)^{-1}\mathbf{A}^T\mathbf{D}_4(\mathbf{s}\text{-}\mathbf{r}) \tag{12}$$

Similarly, we use $\frac{\partial \mathbf{F}}{\partial \mathbf{r}}\Big|_{\Phi=\hat{\Phi}} = 0$ to estimate $\hat{\mathbf{r}}$ and obtain

$$\hat{\mathbf{r}} = \left(\mathbf{T}^T\mathbf{T} + (1+\gamma)\lambda_1\mathbf{E}\right)^{-1}\left(\mathbf{T}^T\mathbf{T}\mathbf{s} + \lambda_1\gamma\mathbf{s}\right) \tag{13}$$

where $\mathbf{T} = \mathbf{D}_4 + \mathbf{B}_{\hat{\Phi}}\mathbf{M}_1$.

For the NSP algorithm, parameters λ_1 and γ can be calculated as follows:

$$\lambda_1 = \frac{1}{1+\hat{\gamma}}\,\frac{\mathbf{s}^T\mathbf{M}(\lambda_1,\hat{\gamma},\hat{T})^T\mathbf{s}}{\mathbf{s}^T\mathbf{M}(\lambda_1,\hat{\gamma},\hat{T})^T\mathbf{M}(\lambda_1,\hat{\gamma},\hat{T})\mathbf{s}} \tag{14}$$

where $\mathbf{M}(\lambda_1,\hat{\gamma},\hat{T}) = \left(\hat{\mathbf{T}}^T\hat{\mathbf{T}} + (1+\hat{\gamma})\lambda_1\mathbf{E}\right)^{-1}$, $\hat{\mathbf{T}} = \mathbf{D}_4 + \mathbf{B}_{\hat{\Phi}}\mathbf{M}_1$, and

$$\frac{(\mathbf{s}-\hat{\mathbf{r}})^T\mathbf{s}}{\|\mathbf{s}-\hat{\mathbf{r}}\|^2}-1=\gamma \tag{15}$$

Based on (12)–(15), we use the NSP algorithm to separate the signal. The optimal solution of λ_2 is unable to be estimated by using the above process. However, we instead numerically estimate λ_2 and choose the optimal solution according to the result. In our implementations of the NSP algorithm, we find the optimal solution of (9) is insensitive to λ_2, so we assign it a fixed value.

Algorithm The NSP algorithm using a fourth-order differential operator:

1. Input signal **s** and parameter λ_2 and choose a stopping threshold ε and the values of λ_1^0 and γ^0.
2. Set $j \leftarrow 0, \hat{\mathbf{r}}_j \leftarrow 0, \lambda_1^j \leftarrow \lambda_1^0 \text{and} \gamma^j \leftarrow \gamma^0$, and repeat.
3. Compute Φ_j to obtain $\overset{\wedge}{\mathrm{W}}_2^j$ and $\overset{\wedge}{\mathrm{W}}_0^j$ and according to (12) using $\hat{\mathbf{r}}_j$.
4. Compute λ_1^{j+1} according to (14) using $\mathbf{M}(\lambda_1, \hat{\gamma}, \hat{T})$.
5. Compute $\hat{\mathbf{r}}_{j+1}$ according to (13) using γ^j, $\overset{\wedge}{\mathrm{W}}_2^j, \overset{\wedge}{\mathrm{W}}_0^j$, and λ_1^{j+1}.
6. Compute γ^{j+1} according to (15) using $\hat{\mathbf{r}}_{j+1}$ and set $j = j + 1$.
7. Repeat until $\left\|\hat{\mathbf{r}}_{j+1} - \hat{\mathbf{r}}_j\right\|^2 < \varepsilon$.
8. Return the extracted $\hat{\mathbf{u}} = (1+\gamma^j)(\mathbf{s}-\hat{\mathbf{r}}_j)$ and the residual signal $\hat{\mathbf{r}} = \mathbf{s} - \hat{\mathbf{u}}$.

By executing the algorithm, we can separate $\mathbf{u}_1$ from **s** and obtain the residual **s** - $\mathbf{u}_1$. The residual signal can be used as the input for the algorithm to extract $\mathbf{u}_2$ and the residual **s** - $\mathbf{u}_2$. Thus, by repeating the process N times, the signal **s** is decomposed into a sum of N signals as $\mathbf{s}=\sum_{i=1}^{M}\mathbf{u}_i+\mathbf{r}_M$.

4 Simulation and Results

4.1 Simulation Details

In step 4 of the algorithm in Sect. 3, we use (10) to estimate all values of W_2 and W_0 of the signal simultaneously in each iteration. Because there are two parameters $\mathrm{W}_2(t)$ and $\mathrm{W}_0(t)$ to estimate at each t, (9) is an underdetermined system, and matrix $\mathbf{A}^T\mathbf{A}$ in (10) is a singular matrix. Thus, at each point t_0, we select a neighborhood B_{t_0} and set the values of $\mathrm{W}_2(t)$ and $\mathrm{W}_0(t)$ equal to $\mathrm{W}_2(t_0)$ and $\mathrm{W}_0(t_0)$, respectively, with $[t_0 - \Delta t, t_0 + \Delta t]$. Then, the parameters at t_0 are estimated by

$$\left[\hat{\mathbf{W}}_2(t_0), \hat{\mathbf{W}}_0(t_0)\right]^T = \left(\mathbf{A}_{t_0}^T \mathbf{A}_{t_0} + \lambda_2 \mathbf{E}_2\right)^{-1} \mathbf{A}_{t_0}^T \mathbf{D}_4(\mathbf{s}_{t_0} - \mathbf{r}_{t_0}),$$

where $\mathbf{A}_{t_0}$ has the form of matrix $\mathbf{A}$, as defined in (9), but it is restricted to the data point in the neighborhood B_{t_0} of t_0. Similarly, $\mathbf{s}_{t_0}$ and $\mathbf{r}_{t_0}$ are the corresponding data points restricted in B_{t_0}. Matrix $\mathbf{E}_2$ is a 2×2 identity matrix. After estimating $\hat{\mathbf{W}}_2(t)$ and $\hat{\mathbf{W}}_0(t)$, we use a low-pass filter to smooth the values of the two functions. Note that this is an approximation of applying $\mathbf{M}_2$ to the estimation of the parameters.

4.2 Results and Analysis

In the first simulated example, we aim to demonstrate the accuracy and robustness of the proposed algorithm to remove the noise from a noisy signal. Figure 1 shows the input signal $s(t) = (0.01t^3 - 0.03t^2 - 9t + 1)\cos(5t + 3)$ with added Gaussian random noise. By executing a Matlab program, we obtain the PSNR of the input signal as 0.6814 dB, and the PSNR of the extracted signal is 9.9954 dB. Our proposed algorithm exhibits better results for signal denoising.

In the second example, we aim to demonstrate the advantages of our proposed algorithm by using it to separate a signal. Figure 2 shows the input signal $s = (0.01t^3 - 2t^2 + 2t)\cos(20t) + (0.01t^3 - 2t^2 + 9t + 1)\cos(5t + 3)$. The results after

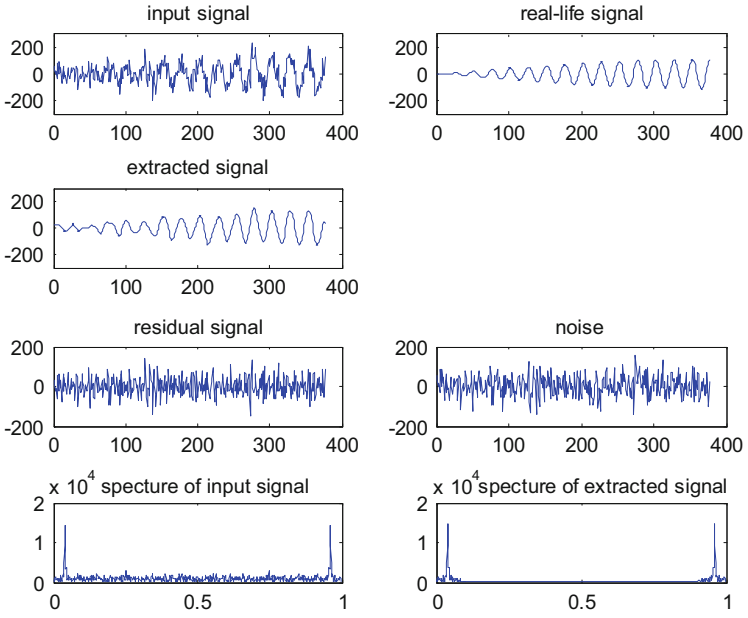

Fig. 1 Signal denoising

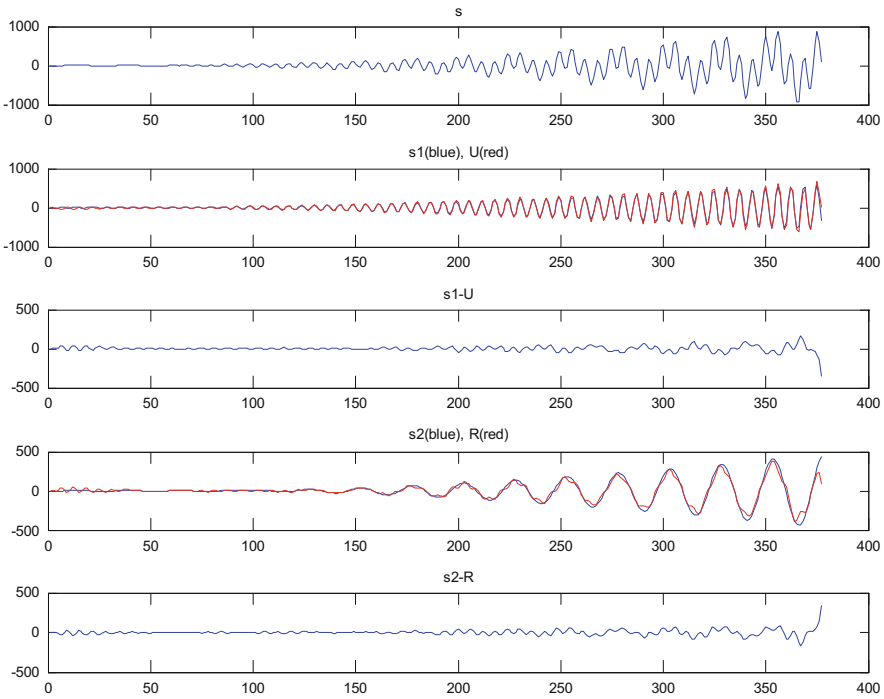

Fig. 2 Signal separation

separation are illustrated in Fig. 2, where the extracted signal is U, and the residual signal is R. From this figure, U approximates the original signal $s_1 = (0.01t^3 - 2t^2 + 2t)\cos(20t)$. The residual signal R approximates $s_2 = (0.01t^3 - 2t^2 + 9t + 1)\cos(5t + 3)$. We now let $\gamma^0 = 1$, $\lambda_2 = 1e - 2$, $\lambda_1 = 1e - 2$, and $\varepsilon = 1e - 4$.

5 Conclusion

In this paper, we proposed an NSP algorithm based on a fourth-order differential operator. Compared to previous NSP algorithms, we expanded the scope of the algorithm for decomposing signals and presented some of the proposed algorithm for a signal model. As can be seen from the simulations, we successfully used the NSP algorithm to denoise and decompose signals.

Acknowledgments This work was supported by National Natural Science Foundation of China (11126140,11201007); Beijing Talents Training Program (2011D005002000006); Science and Technology Development Plan Project of Beijing Education Commission (KM201210009013); Scientific Research Personnel Promotion Plan of North China University of Technology(BJRC201309).

References

1. Rilling G, Flandrin P (2008) One or two frequencies? the empirical mode decomposition answers. IEEE Trans Signal Process 56(1):85–95
2. Wu Z, Huang NE (2004) A study of the characteristics of white noise using the empirical mode decomposition method. Proceedings of the royal society of London (series A) 460: 1597–1611
3. Mallat S, Zhang Z (1993) Matching pursuits with time-frequency dictionaries. IEEE Trans Signal Process 41(12):3397–3415
4. Peng SL, Hwang WL (2008) Adaptive signal decomposition based on local narrow band signals. IEEE Trans Signal Process 56(7):2669–2676
5. Peng SL, Hwang WL (2010) Null space pursuit: an operator-based approach to adaptive signal separation. IEEE Trans Signal Process 58(5):2475–2483
6. Xiyuan Hu (2011) Adaptive signal and image separation and its applications. Dissertation for the degree of doctor of philosophy, Institute of Automation Chinese Academy of Sciences, Beijing

High Efficient Complex Event Processing Based on Storm

Shengjian Liu, Yongheng Wang, Shuguang Peng, and Xinlong Zhang

Abstract In recent years there is a huge increase in real-time data, which cannot be processed efficiently. Complex event processing has become a very important method to get meaningful information. However, supporting complex event detection in multiple sources environments is a challenging problem. To allow for inferring high level information from vast amounts of continuous arriving data. In this paper, we present a complex event processing system based on a novel distributed computing platform Storm, which goes further than distributing queries and achieves better scalability by parallelizing event detection, and also higher efficiency through the use of some optimizations. The experimental shows that the event processing system is effective and better scalability.

Keywords Complex event processing • Event detection • Distributed processing

1 Introduction

In recent years there has been a huge increase in the data produced on the Internet, effectively doubling in size every year. In many cases, the data is continuously produced by software applications in quantities that are not examinable manually. Complex event processing (CEP) is a set of techniques to address such classes of problems [1]. CEP targets applications that both require the processing of large amounts of data and low processing latencies. One application scenario for such systems is when too much data is generated, but only a fraction of the data can be stored.

Historically, the common approach for such applications was to store the generated data in databases or logs, and process it afterwards in batch processing

S. Liu (✉) • Y. Wang • S. Peng • X. Zhang
College of Information Science and Engineering, Hunan University, Changsha, China
e-mail: phosic@sina.cn

B. Zhang et al. (eds.), *The Proceedings of the Second International Conference on Communications, Signal Processing, and Systems*, Lecture Notes in Electrical Engineering 246, DOI 10.1007/978-3-319-00536-2_77,

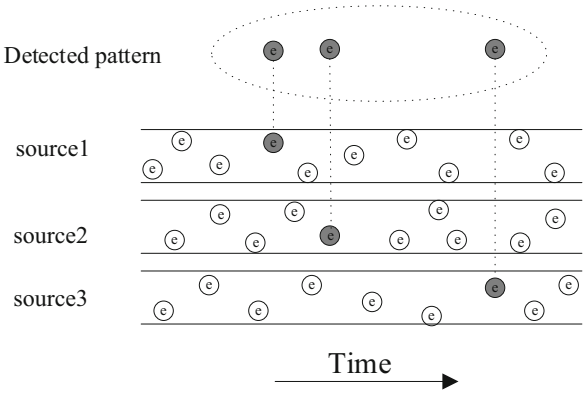

Fig. 1 Example of event pattern detection from three different streams

jobs, leveraging distributed frameworks such as Hadoop. However, it is becoming increasingly inefficient to store all the data in its whole entirety. Many businesses also require answers as soon as the data becomes available. Furthermore, the businesses are not primarily interested in raw data, but rather in the high-level intelligence that can be extracted from it. As a response, systems were developed that can filter, aggregate and correlate data, and notify interested parties about its results, abnormalities, or interesting facts.

The latest advance in such systems is the development of high performance complex event processing engines that are capable of detecting patterns of activity from continuously arriving data. As illustrated in Fig. 1, CEP systems receive continuous streams of events from multiple data sources over underlying network, they discover patterns of interest among the events, and notify the users.

In this paper, we focused on distributing complex event processing to achieve better scalability. We design a CEP system that explores the possibilities of parallelizing complex event detection, and also achieves higher throughput, while retaining low detection latency. Furthermore, the implementation would try to obtain a balance between CPU, memory and available network usage, and also explore some optimizations, which could be applied to event detection for higher performance.

The rest of the paper is organized as follows: Sect. 2 introduces the related work of this research; Sect. 3 introduce Event and temporal model; Architecture design and implementation issues will be described in Sects. 4 and 5 describes the evaluation of the system; Sect. 6 concludes this paper.

2 Related Work

CEP has been extensively studied in active database [2]. These works focused on evaluation of complex patterns in traditional databases which cannot accommodate real time and streaming requirements of current applications. In [3], a declarative

event language-SASE is proposed to define, filter, aggregate and correlate events from stream data. However, NFA (non-deterministic finite automata) implementation of SASE event queries can't work efficiently when domain size in event definition is large and event objects of the same type are considered, as it focuses mainly on RFID applications. CEDR [4] is an event streaming system with a declarative query language which cannot define multiple object-oriented event queries. Distributed detection of pattern has been first explored in [5], with a very simple language. An important contribution comes from [6], where the authors study how patterns can be rewritten for efficient distribution. Cayuga [7] is a centralized general purpose event processing system that allows event detection through a small number of well-defined operators. It is developed from a pub/sub system which is focused on common sub-expressions searching amongst multiple patterns. In Cayuga, a SQL-style event definition language is proposed. Objects involved in Cayuga event queries are single object-oriented. SAMOS [8] is a petri Nets based systems which are able to support concurrency but are very complex to express and evaluate. Plan based CEP across distributed sources has been studied by Mert [9]. The STREAM system [10] from Stanford University uses the CQL [11] query language for relational style queries. The STREAM system uses adaptive algorithms for ordering of pipelined operators, to minimize processing cost.

3 Event and Temporal Model

Event in our system are triples $< p, t_0, t_1 >$ that continuously arrive from external sources at some specified mean event arrival rates. Throughout the paper we refer to these events as to external or primitive events. Here p corresponds to event's payload, which contains values that correspond to event's attributes, as specified in an event schema. The values are populated by an input source and their types and order of occurrence must be the same as declared in the event schema.

Apart from the payload, each event carries a pair of timestamps t_0 and t_1. These are arbitrary integer values representing respectively the start timestamp and the end timestamp of the event, where timestamps follow logical time (i.e. they do not need to correspond to system time). We require that start timestamp is smaller or equal to the end timestamp, i.e. $t_0 \leq t_1$. Furthermore, we require all events on the same input stream to be ordered by their end timestamps. Since events include two timestamps, some care has to be taken when defining their ordering. To specify the semantics of various operators, we need to make this clear. First, let us specify the set of all possible external events as:

$$\mathrm{E} = \{< p, t_0, t_1 > \wedge\, t_0, t_1 \in \wedge\, t_0 \leq t_1\} \tag{1}$$

Then we can define an ordering on events $\prec$ as a tuple, where $<$ is the usual ordering on natural numbers and:

$$\forall e, e' \in E. e \prec e' \Leftrightarrow t_1 < t_0' \text{ where } e = < p, t_0, t_1 > \text{ and } e' = < p', t_0', t_1' > \quad (2)$$

This means that an event e precedes another event e' only if the end timestamp of e is smaller than the start timestamp of e'.

4 Event Processing Framework

In this section we will describe the Step (Storm Complex Event Processing) system. To implement a distributed complex event processing system that works over streams, we use the Storm stream processing framework. This section describes the Storm framework, event streams and event processing topology.

4.1 Storm Framework

Storm [11, 12] is a distributed real-time stream processing platform that can be used to assemble and execute stream processing elements. The applications that run on top of Storm cluster are called topologies.

A topology in Storm is a data flow graph of computation, which consists of elements called Bolts and Spouts, connected together with streams. Streams are unbounded sequences of tuples, and a tuple is a list of values of any type. The sources of streams are Spouts, which read data from an external source, for example stock exchange, sensors or program logs. The streams are consumed by Bolts, which do some processing and possibly emit new streams that can be consumed by further Bolts. The processing done at Bolt can be anything, from filtering or aggregation, to saving tuples to a database. An example of a topology can be seen in Fig. 2.

At runtime, each component of a topology will run within a number of tasks, which are specified by a parallelism of that component. Every task for the same component executes the same blueprint code, but is a different instance and runs in a separate thread of execution. A task receives a tuple on its input queue, processes it and may emit new tuples to its output streams. Streams are divided between multiple tasks depending on specified stream grouping. Available stream groupings include shuffling stream in round robin fashion, replicating stream to all tasks, or shuffling stream depending on tuple attributes. An illustration of component tasks communicating over streams can be seen in Fig. 3.

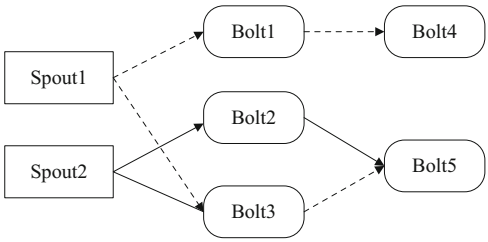

Fig. 2 A storm topology

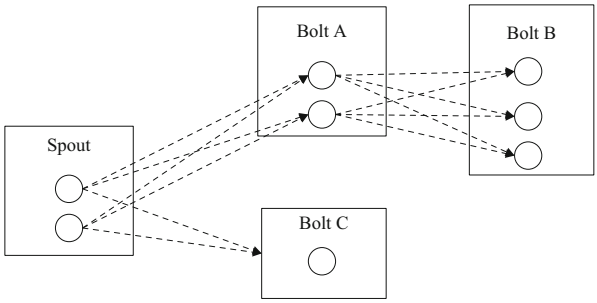

Fig. 3 Component tasks communicating over streams

4.2 Event Input Streams

Events to our CEP system arrive on continuous input streams from input adapters and detected events are consumed by output adapters. We will now briefly discuss the stream input, output streams.

The input to the system is handled by Storm components called Spouts. As seen in Fig. 4, Spouts receive events from external sources by means of input adapters, and distribute them to different Bolts corresponding to operators detecting events. A single Spout may emit input events to multiple Bolts.

Input adapters are user defined, enabling data to arrive from a variety of sources, for example sensors supplying measurements, databases providing historical data. Note that to handle high event rate, we require input adapters to be parallelizable. This is because for high input event rates more than one task for a Spout will be spawned, such that input can be consumed in parallel.

4.3 Event Output Streams

After a complex event was detected, it will be reported by a projection operator to the corresponding event sink adapter, as seen in Fig. 4. Similarly to input adapters, event sinks cannot be single objects, but should be designed to run in multiple instances. This is because for high event rates projection operators will be parallelized, and each projection task will instantiate its own sink adapter.

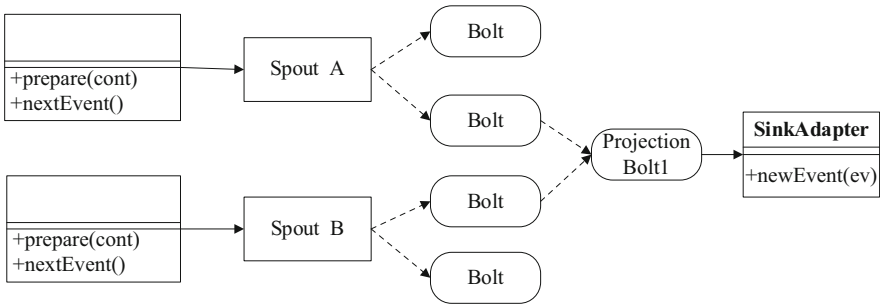

Fig. 4 The input and output of Step runtime framework

This will also be the case when different projection operators (queries) report to the same sink adapter class. Thus, it may happen that different adapter instances will run on different physical nodes. Since detected events consist of multiple external events, each having their own fields, the reporting format is different from external event format. An output complex event contains start and end timestamps, and a list of fields. A field is described by its name, value, and a name of an external event stream, from which the value originates.

4.4 Event Processing Method

The event detection happens on data-flow graphs, which is a method also used by some DSMS systems (e.g. Borealis). Data-flow graphs consist of boxes connected by streams, where each box performs some computation over its input streams and may emit some events to its output streams. It can be seen that data-flow graphs exactly resemble the Storm topology paradigm, and hence are the best design choice when using Storm as an underlying framework. From now on we will refer to event detection graphs as Step topologies.

Step topologies consist of Spouts and Bolts connected by streams with a specified grouping. We already know that one of the responsibilities of Spouts is to handle event input and projection Bolts handle event output. In fact, each topology component (whether Bolt or Spout) corresponds to some operator in the Step language and performs its function. For example, Spouts are implementations of the external operator and projection Bolts of the projection operator. An illustration of a general topology built from operators can be seen in Fig. 5.

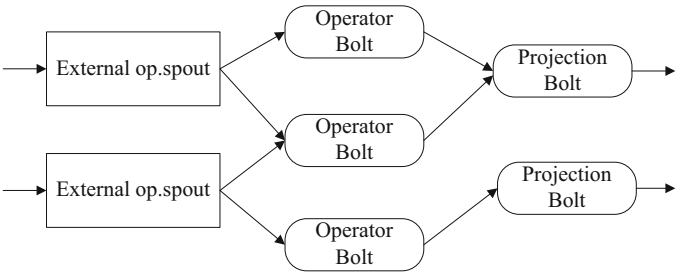

Fig. 5 A Step topology containing components that correspond to operators in the Step

5 Performance Evaluation

Our goal was to develop an efficient, scalable and fast system for complex event detection. In this section, we evaluate our Event processing framework. Our experiments were executed on PC with 4 GB memory and two Intel Core 2 Duo processors. The operating system is Ubuntu 9.1.

We will measure the number of events that the Bolt can receive per second and the network usage. The measurements of sending throughput and network utilization for different batch sizes can be seen in Fig. 6. Note that the experiment was performed over 1 Gbps LAN network. The throughput rises in a logarithmic curve, radically up to the event batch of size 100 and then increases at a slow steady rate. The corresponding network usage rises accordingly.

For small batch sizes the bottleneck is in high CPU overhead at the Spout. This is caused by generation of message IDs, determination of destination Bolt task. As we increase the batch size, the CPU usage gets smaller and the bottleneck starts shifting towards network.

We chose the batch size which yields a high sending event throughput. This allows CPU resources to be used for event detection. Figure 6 demonstrates that any size above 300 is good, as it maximizes the throughput.

6 Conclusions

In this paper, we study event detection problems over data streams which involve multiple sources. We put forward a novel framework based on Storm to support efficient complex event processing while remaining high scalability. The experimental results verify our framework has good performance and scalability in CEP query processing. Furthermore, we achieved high event detection throughput and high network usage by distributing event queries. We believe that this framework is usable and will become popular when dealing with continuous data streams and their computations.

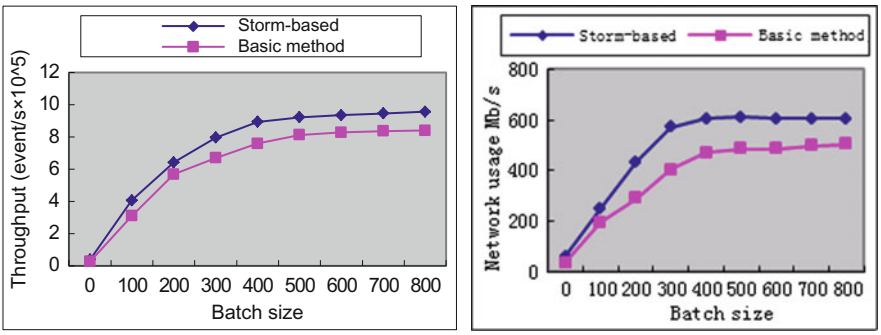

Fig. 6 Throughput and network usage experiments

Acknowledgments This project is sponsored by Hunan Provincial Natural Science Foundation of China "Context-aware and proactive complex event processing for large scale internet of things (13JJ3046)" and supported by the "complex event processing in large scale internet of things (K120326-11)" project of Changsha technological plan.

References

1. Luckham DC (2001) The power of events: an introduction to complex event processing in distributed enterprise systems. Addison-Wesley Longman Publishing Co., Inc., Boston, MA, USA
2. Zimmer D, Unland R (1999) On the semantics of complex events in active database management systems. In: ICDE, p 392–399
3. Wu E, Diao Y, Rizvi S (2006) High-performance complex event processing over streams. In: SIGMOD conference, p 407–418
4. Barga RS, Goldstein J, Ali MH, Hong M (2007) Consistent streaming through time: a vision for event stream processing. In: CIDR, p 363–374
5. Li G, Jacobsen HA (2005) Composite subscriptions in content-based publish/subscribe systems. In: Middleware'05. Springer, New York
6. Schultz-Moeller NP, Migliavacca M, Pietzuch P (2009) Distributed complex event processing with query optimization. In: DEBS'09. ACM, Nashville
7. Demers AJ, Gehrke J, Panda B, Riedewald M, Sharma V, White WM (2007) Cayuga: a general purpose event monitoring system. In: CIDR, p 412–422
8. Chen J, DeWitt DJ, Tian F, Wang Y (2000) Niagara CQ: a scalable continuous query system for internet databases. ACM SIGMOD Record 29(2):390
9. Mert Akdere, Ugur Çetintemel, Nesime Tatbul, Plan-based complex event detection across distributed sources, Proceedings of the VLDB Endowment, vol 1(1), Aug 2008
10. Arasu A, Babcock B, Babu S, Cieslewicz J, Datar M, Ito K, Motwani R, Srivastava U, Widom J (2004) STREAM: the Stanford data stream management system. In: Garofalakis, Gehrke, and Rastogi (eds) A book on data stream management
11. Arasu A, Babu S, Widom J. The CQL continuous query language: semantic foundations and query execution. Technical report, Stanford University
12. Marz N. Storm wiki. URL https://github.com/nathanmarz/storm/wiki

The Design of Traffic Monitoring Module of COFN Management

Jianli Liu, Jinying Chen, Wei Tang, and Zhan Li

Abstract By using the computer hardware platform to analog communication network data collection node, the Visual C++ 6.0 development platform, and the software of server-side and agent-side in MFC WIN API technology development traffic monitoring module, to design a custom network management protocol. With an Access database platform and DAO technology to complete the operations of read and write. Based on the future communication network architecture, to design a set of data flow management system, to provide an efficient and low cost management solutions for the network administrator.

1 Introduction

With the development of network information technology, especially the rapid development of the Internet terminal, the IPv4 address resource depletion speed greatly accelerated. And the existing network in the channel allocation and data store and forward mechanism and the routing and allocation to the bottleneck of the development, related technical bottleneck seriously affected the network transmission rate and efficiency [6]. So people need to solve the existing problems of the network in the future networks are becoming more and more intense, to establish a fully functional and reliable management system has become the inevitable trend of future communication, the significance of the design is that it can provide the corresponding fault detection and handling mechanisms of future traffic data communication network for the acquisition and analysis of real-time, and provide a set of reliable equipment operation maintenance solutions, help to improve the efficiency of IT jobs, to provide support for the network planning and traffic distribution, COFN (Connecting oriented future network) [4, 5].

J. Liu (✉) • J. Chen • W. Tang • Z. Li
College of Information Science and Technology, Chengdu University of Technology, Chengdu, China
e-mail: 2437306780@qq.com

B. Zhang et al. (eds.), *The Proceedings of the Second International Conference on Communications, Signal Processing, and Systems*, Lecture Notes in Electrical Engineering 246, DOI 10.1007/978-3-319-00536-2_78,

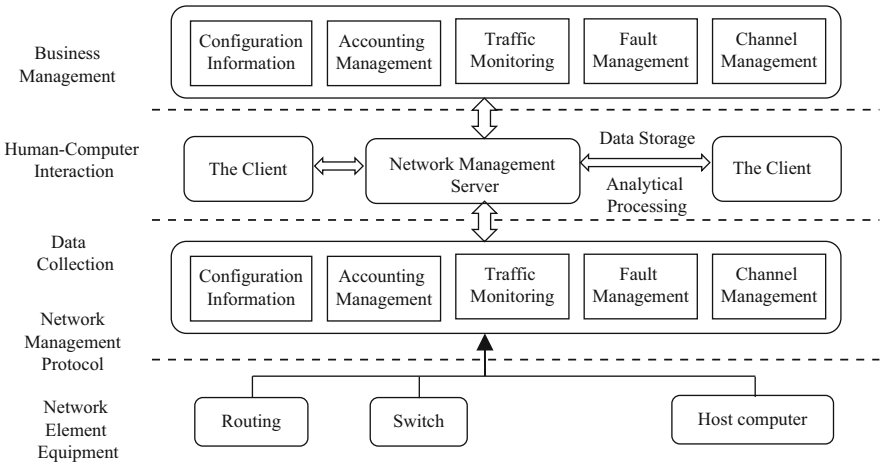

Fig. 1 The architecture of future network management

2 The Architecture of Future Network Management

The main purpose of network management is to establish a good communication link between the user requirements and the network environment. From the perspective of the demand of users, the network management system should have, such as network monitoring and configuration, business services billing methods, management of a network failure monitoring and ruled out, network flow calculation and control, and other functions. The architecture of future network management is shown in Fig. 1, the whole system architecture is divided into five parts: the service management layer, human-computer interaction layer, data acquisition layer, network management protocol layer and network elements equipment layer [2].

3 The Design of COFN Management Traffic Monitoring Module

Network traffic monitoring is an important content in network management system, is the basic work of accounting function, fault location and fault early warning function, completes the flow monitoring work could pave the way for the subsequent development. Through the extraction and analysis of network flow data, can understand the relevant segment of the use of cyber source, characteristic analysis of the corresponding data in order to find network fault occurrence and location network accident, can also according the flow size to distribution network hardware and software resources reasonable, extract the flow data information and save to the database, monitoring of these data by the network management software and display the real-time data by graphic data table. According to the actual needs of

the monitoring environment, the whole monitoring module is divided into the server, client and database storage of three modules in the function. The design of each module will be introduced in detail.

3.1 The Design of Memory Data List Structure

Flow monitoring module server as the core module of traffic monitoring, used for storage, network node data processing and information transmission. Through the network communication custom protocol to obtain real-time acquisition to realize the function, then the collected data is divided into three layers structure of city level, district level, local level, finally, the storage after processing data in real-time, this requires database technology, by using DAO technology to store the collected date into table format for later query in the processing operation of the server [1]. The server needs to implement the function in detail as follows:

(1) When the software is up and running, shows the main interface. (2) Create Access database when the program is run in the first time by DAO technology. (3) Establish a connection with the agent, and then obtain the information about the structure and the value of network data and display on the main interface. (4) According to the network data storage structure in the Network Manager. MDB database, create the tables dynamically. (5) To Monitor and judge the changes of network data, and change the value which has been written to the historical database. The server systems module can be designed into three aspects, namely the design of memory data list structure, the server side of human-computer interaction interface design and the agent communication protocol design.

3.1.1 The Design of Memory Data List Structure

When designing flow monitoring module, in order to correspond the assigned prefix address of future network transmission protocol, memory data list structure is simple to set for the municipal, district level and network level. This design is developed by using object-oriented design methods, so each level corresponds to a class, in the memory data list structure that includes four types: CCtrlModule, CCtrlCity, CCtrlCounty, CCtrlLAN. Memory data list management structure is shown in Fig. 2.

3.1.2 The Design of Human–Computer Interaction Interface in Server-Side

The design concept of server is to make the network management more simple and convenient to understand the real-time network traffic information intuitively, to add and delete data quickly. The human-machine interface is developed with Visual

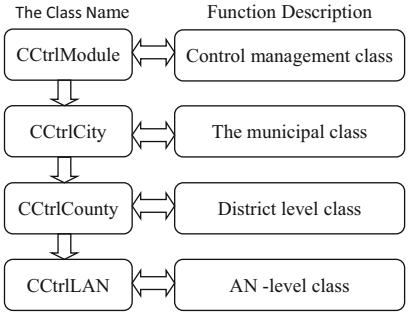

Fig. 2 The design of memory data list structure

C++6.0, by selecting the MFC AppWizard (exe) to establish engineering, d choose to set up single document interface and Windows Explorer engineering style. When the Project Wizard completed, the system will generate CCOFNManager-ServerApp, CCOFNManagerServerView, CCOFN-ManagerServerDoc, CLeftView, CAboutDlg and CMainFrame automatically. The CCOFN ManagerServerView class and the CLeftView window class is the right windows and left window class to control the man–machine interface respectively [7].

3.1.3 Design of Agent Communication Protocol

The communication connection of the server side and the agent is based on the socket in the design, but for the transmission of management information data is adopted the custom communication protocol. The communication protocol of COFN management, adopts the frame structure of data transmission mode, frame structure is unit to send data package, the management information is sent and received in a frame unit, frame format is defined by a specific structure, the variable is set into a frame format structure types can transmit instruction and data access, frame format structure code is as follows:

```
Typedef struct ModFrameTag
{
    DWORD nOrder;
    Cstrings Content;
} ModFrame;
```

Because memory data chain table adopts three layers data structures, so the content of each frame is based on three layers data hierarchy to design, different instructions, the attached data is also not the same, by judging the received instructions, can some data in the corresponding processing. In transmitting data content using different punctuation to differentiate between the "city", "county", "LAN" three layers structure, at the end of each frame data content use a semicolon ";" As a terminator (Fig. 3).

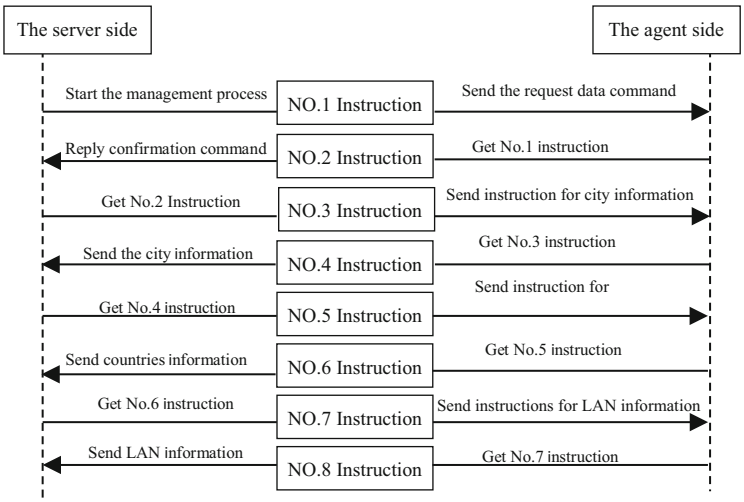

Fig. 3 The process of COFN management protocol

3.2 The Agent Design of Traffic Monitoring Module

The main function of agent is to obtain the information which is from network equipment information storehouse, use the server interface and network management server for data transmission and exchange, and then transmit the information of equipment information repository to server network management for further analysis and storage, through the special operation instruction and configuration instruction to configure the server and the corresponding network management operations. The agent is composed of equipment information database module, operation module, configuration module and server module. The agent architecture is shown in Fig. 4.

The main functions of software include the following points:

(1) Establish storage data structure to store the data extracted from the configuration file. (2) Deliver real-time traffic data to the server side, and display the contrast information at the same time. (3) Put the server-side operating instructions into the data structure which stored into the equipment database.

3.3 The Design of Database Storage Module

3.3.1 The Relevant Technology of Database Design

OLE DB (Object Link and Embedding Database) technology is a new technology provided by Visual C++ development database application, based on the COM interface, and provides a unified interface for all the file systems including

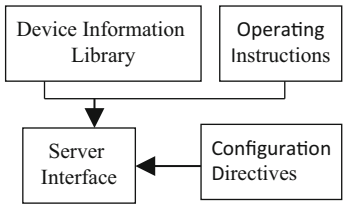

Fig. 4 The structure of agent side

relational and non-relational database. These features make OLE DB technology has more advantages than the traditional database to access technique.

DAO (Database Access Object) is an application programming interface (API), which allows programmers can use DAO technology to request Microsoft to visit Access database. Record set object is the main object to query and modify the database. Field is used to represent the column information record, including column values and other information. Access 2000 is a component of Microsoft Office suite, is a desktop type and small database management system [3].

3.3.2 Realization of Database Storage Module

Because Visual C++ 6.0 provides the MFC classes and templates class, such as AppWizard, Wizard Class and a series of Wizard to produce applications, these features greatly simplifies the design of the application. The system needs to create an Access database at run time, uses the DAO technology to create Access database, and calls the database directly by DAO technology.

All the tables in the database are generated automatically by codes, using the Create, Select, Where, Drop and the SQL statement to create, select, query, reduce and delete the specified database in the table, during the execution of the program will be generated Citys, Cityn_HisData (n city index ID), Cityn_CountyData (n city index ID), Cityn_Countym_LANData (m Cityn_NameIDData table and index).

4 Summary

In background of connection oriented network, this paper designs the architecture of future network management system. According to the characteristics of address word division crown of the future network, traffic monitoring module will be divided into three layers mode by management data, through such division mechanism to strengthen the flexibility and accuracy of data management, the three major modules respectively is the server design, the agent side storage module design and database design. The design of traffic monitoring module has the advantage that it is the basis of billing module; fault management module, channel management module, configuration management module, and the development mechanism can be applied to the development of other modules.

References

1. Xin S (2007) Further steps VC++. Electronic Industry Press, Beijing
2. Jinying Chen, Min Lin, Zhongming Zhu (2011) Five network amalgamation. The international conference on consumer electronics, communications and networks
3. Xiaoling Z (2010) Practical access database tutorial. Electronic Industry Press, Beijing
4. Hongke Zhang (2012) Key techniques of future network [EB/OL]
5. Guojie Li (2012) Some innovation about future network [EB/OL]
6. Binxing Fang (2012) The security issues in future network [EB/OL]
7. Junjie H (2001) Dissecting MFC. Huazhong University of Science and Technology Press, Wuhan

Part VII
Wireless Communication and Networks

New Blind Recognition Method of SCLD and OFDM Based on Cyclostationarity

Yilong Chen, Changzhong Zhang, and Zhuo Sun

Abstract Previous studies on blind recognition of the modulation format of a received signal is generally performed in single domain, e.g. frequency or time domain. This paper presents a new approach by defining a dual domain decision function, which makes use of signals features that the magnitude of second-order cyclic cumulants of orthogonal frequency division multiplexing (OFDM) signals and single carrier linear digitally modulated (SCLD) signals has an obvious difference in both time and frequency domain. The proposed algorithm enlarges the distinguish gap between OFDM and SCLD. The results of simulation experiments confirm the theoretical analysis.

Keywords Blind recognition • OFDM • Second order cyclostationarity

1 Introduction

Blind recognition of the modulation format of a received signal is important in a variety of military and commercial applications, such as military surveillance, information safety and wireless spectrum resource management. The evolution of communication systems continues to pose new challenges for signal recognition. One example is the recognition of multicarrier signals, such as orthogonal frequency division multiplexing (OFDM), against single carrier (SC) signals [1, 2]. A lot of research has been done in this respect, which can be generally classified into two kinds of algorithms: likelihood-based and feature-based methods [1].As one of the feature-based methods, the cyclostationarity of linear modulation signal was widely applied for signal detection and modulation recognition [3].

Y. Chen (✉) • C. Zhang • Z. Sun
Wireless Signal Processing and Network Lab, Key Laboratory of Universal Wireless Communications, Ministry of Education, Beijing University of Posts and Telecommunications, Beijing, China
e-mail: aa19880820@126.com

B. Zhang et al. (eds.), *The Proceedings of the Second International Conference on Communications, Signal Processing, and Systems*, Lecture Notes in Electrical Engineering 246, DOI 10.1007/978-3-319-00536-2_79,

However, most cyclostationary-based methods recognize signals only in time domain. The method in [4] utilized the cyclostationarity properties of orthogonal frequency division multiplexing (OFDM) in time domain, but the difference of the second-order cyclic cumulants (CCs) magnitude of OFDM and single carrier linear digitally modulated (SCLD) is not obvious in low SNR, the probability of correctly recognizing the signal is not optimal in low SNR. To achieve the high probability of correctly recognizing the signal in low SNR condition, the proposed algorithm in this paper jointly makes use of the feature of signal in time and frequency domain. The dual domain decision function enlarges the distinguish gap between OFDM and SCLD.

This paper is organized as follows: The SCLD and OFDM signal models and the analytical expressions for the second-order CCs and cycle frequencies (CFs) are presented in Sect. 2. The proposed dual domain-based algorithm is presented in Sect. 3. Simulation results are given and discussed in Sect. 4. Finally, conclusions are drawn in Sect. 5.

2 Signal Model and Second-Order Cyclostationary of SCLD and OFDM

In [5], it proved that the addition of cyclic prefix (CP) to an OFDM symbol provides a useful cyclostationary feature. Meanwhile, for SCLD signals, cyclostationarity is induced by the pulse shape. The continuous-time baseband equivalent of received SCLD signals in AWGN is given by [6]

$$r_{SCLD}(t) = ae^{j\theta}e^{j2\pi\Delta f_c t}\sum_{l=-\infty}^{\infty} s_l g(t - lT - \varepsilon T) + \omega(t) \tag{1}$$

where a is the amplitude factor, θ is the carrier phase, Δf_c is the frequency offset, T is the symbol period, $\varepsilon(0 \le \varepsilon \le 1)$ is the timing offset, g(t) is the overall impulse response of the transmit and receive filters, s_l is the symbol transmitted in the lth symbol period, ω(t) is complex Gaussian noise with zero mean.

The received baseband OFDM signals is given by [7]

$$r_{OFDM}(t) = ae^{j\theta}e^{j2\pi\Delta f_c t}\sum_{k=0}^{K-1}\sum_{l=-\infty}^{\infty} s_{k,l}e^{j2\pi k\Delta f_K(t-lT-\varepsilon T)}g(t - lT - \varepsilon T) + \omega(t) \tag{2}$$

where K is the number of subcarriers of the OFDM signal, $S_{k,l}$ is the symbol transmitted on the kth subcarrier over the lth symbol period, Δf_K is the frequency separation between two adjacent subcarriers, T is the OFDM symbol period. And $T = T_{CP} + T_u$.

The analytical closed-form expressions for the second-order (one-conjugate) CCs and the set of CFs for SCLD signals are given respectively by [8]

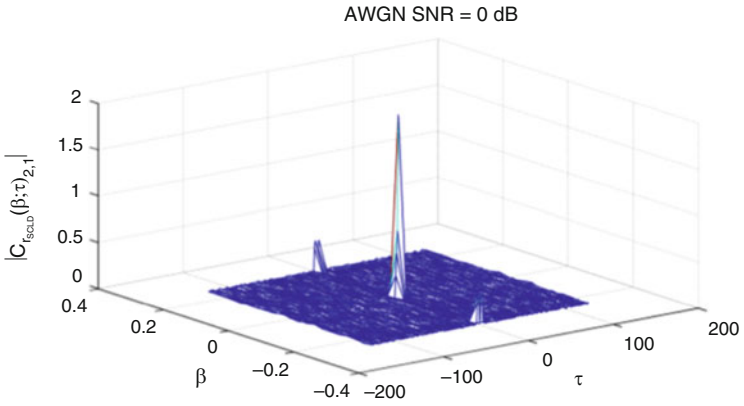

Fig. 1 CCs magnitude value of SCLD in AWGN

$$c_{r_{SCLD}}(\beta;\tau)_{2,1} = \vartheta(\tau)\rho^{-1}e^{-j2\pi\beta\varepsilon\rho}\Lambda(\tau) + c_{\omega}(\beta;\tau)_{2,1} \tag{3}$$

$$\kappa_{2,1}^{SCLD} = \left\{\beta \in \left[-1/2, 1/2\right) \middle| \beta = l\rho^{-1}, l \text{ integer}\right\} \tag{4}$$

Where $\vartheta(\tau) = a^2 e^{-j\frac{2\pi}{\rho}\Delta f_c T\tau} C_{s,2,1}$ and $\Lambda(\tau) = \sum_{u=-\infty}^{\infty} g(u)g^*(u+\tau)e^{-j2\pi\beta u}$, ρ is the oversampling factor. Similarly to SCLD signals, the second-order (one-conjugate) CCs and the set of CFs for OFDM signals are given by [9]

$$c_{r_{OFDM}}(\beta;\tau)_{2,1} = a^2 C_{s,2,1} D^{-1} e^{-j2\pi\beta\varepsilon\rho} e^{-j\frac{2\pi}{\rho K}\Delta f_c T_u \tau} \Gamma_K(\tau)\Lambda(\tau) + c_{\omega}(\beta;\tau)_{2,1} \tag{5}$$

$$\kappa_{2,1}^{OFMD} = \left\{\beta \in \left[-1/2, 1/2\right) \middle| \beta = l\rho^{-1}, l \text{ integer}\right\} \tag{6}$$

Where $\Gamma_K(\tau) = e^{j\frac{\pi}{\rho K}(K-1)\tau} \sin\left(\frac{\pi\tau}{\rho}\right) / \sin\left(\frac{\pi\tau}{\rho K}\right)$ and $\Lambda(\tau) = \sum_{u=-\infty}^{\infty} g(u)g^*(u+\tau)e^{-j2\pi\beta u}$, $D = \rho K\left(1 + \frac{T_{CP}}{T_u}\right)$

The magnitude of the second-order (one-conjugate) CC of SCLD, and OFDM signal is depicted versus CF and delay in Figs. 1 and 2 respectively.

3 Proposed Dual Domain-Based Algorithm

At the receive-side, the bandwidth of the signal is roughly estimated, and a low-pass filter is used to remove the out-of-band noise. The signal is down-converted and (over)sampled at a rate equal to ρ times.

From Sect. 2, it shows two significant differences between SCLD and OFDM. First, in the time domain (CF = 0), CCs magnitude value of OFDM signals is non-zero values with delays around ±ρK, whereas CCs magnitude value of SCLD signals is zero. Second, in the frequency domain (delay = 0), CCs magnitude value

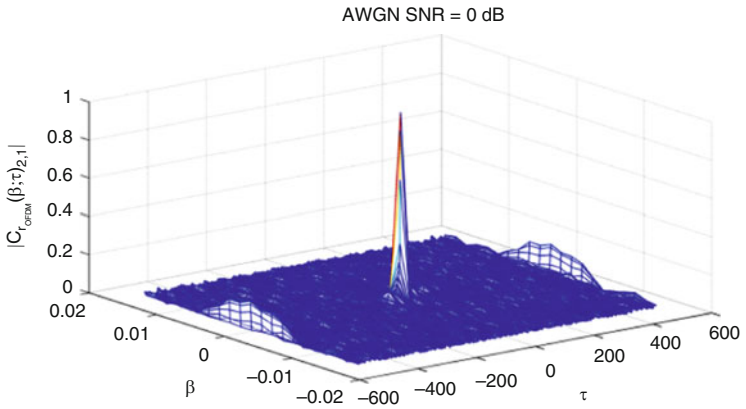

Fig. 2 CCs magnitude value of OFDM in AWGN

of SCLD signals appears peaks with CFs equaling to integer multiples of 1/ρ, whereas the CCs magnitude of OFDM is zero.

Combining the features of OFDM and SCLD in two domains, we define a dual domain joint decision function

$$z_1 = \frac{c_r(0;\rho K)_{2,1}}{c_r(\rho^{-1};0)_{2,1}} \tag{7}$$

From [10], an estimate of the second-order cyclic cumulants is given as

$$\begin{aligned}\hat{C}_{2r}(\alpha,\tau_n) &\triangleq \frac{1}{T} r(i) r^*(t+\tau_n) e^{-j2\pi\alpha i} \\ &= C_{2r}(\alpha,\tau_n) + \varepsilon_{2r}^{(T)}(\alpha,\tau_n)\end{aligned} \tag{8}$$

Where $\varepsilon_{2r}^{(T)}(\alpha, \tau_n)$ represents the estimation error which vanishes asymptotically as $T \to \infty$. Due to the existence of error $\varepsilon_{2r}^{(T)}(\alpha, \tau_n)$, the estimator $\hat{C}_{2r}(\alpha,\tau_n)$ is seldom exactly zero in practice, even if α is not a cycle frequency.

By substituting the (8) into the (7), we have:

$$z_1 = \frac{c_r(0;\rho K)_{2,1} + \varepsilon_r^{(T)}(0;\rho K)_{2,1}}{c_r(\rho^{-1};0)_{2,1} + \varepsilon_r^{(T)}(\rho^{-1};0)_{2,1}} \tag{9}$$

For OFDM signal, we can find that based on (5)

$$c_r(0;\rho K)_{2,1} \gg \varepsilon_r^{(T)}(0;\rho K)_{2,1}, c_r\left(\rho^{-1};0\right)_{2,1} = 0 \tag{10}$$

Therefore, the decision function for OFDM signal can be expressed as:

Fig. 3 z_1 of OFDM

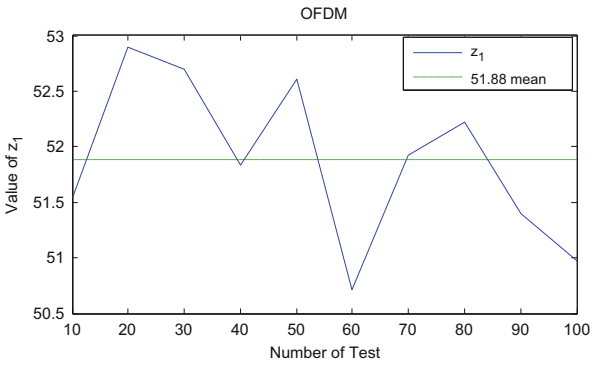

$$z_1\big|_{\text{OFDM}} \approx \frac{c_r(0;\rho K)_{2,1}}{\varepsilon_r^{(T)}(\rho^{-1};0)_{2,1}} \tag{11}$$

For SCLD, we have the similar conclusions based on (3)

$$c_r\left(\rho^{-1};0\right)_{2,1} \gg \varepsilon_r^{(T)}\left(\rho^{-1};0\right)_{2,1}, c_r(0;\rho K)_{2,1} = 0 \tag{12}$$

Therefore, the decision function for SCLD signal can be expressed as:

$$z_1\big|_{\text{SCLD}} \approx \frac{\varepsilon_r^{(T)}(0;\rho K)_{2,1}}{c_r(\rho^{-1};0)_{2,1}} \tag{13}$$

In Figs. 3 and 4, we can see that function z_1 exhibits the obvious difference between OFDM signals and SCLD signals to about 50 times.

4 Simulation Results and Analysis

4.1 Simulation Setup

In simulation, we adopt QPSK modulations for SCLD signal. The transmit filter is a root raised cosine with 0.5 roll-off factor, and the signal bandwidth is 40 kHz. For the OFDM signals, QPSK modulation is used on each subcarrier. The signal bandwidth is set to 800 kHz, and the number of subcarriers is set to 128. The useful time period of the OFDM symbol is set to 160 us and the cyclic prefix period is set to 40 us. At the transmit-side, a raised cosine window with 0.025 roll-off factor is used for OFDM signals. In addition, we set amplitude factor to 1, timing offset to 0.75, the carrier phase as a random variable uniformly distributed over $[-\pi, \pi)$, and frequency offset is set to 16 kHz and 320 kHz for SCLD and OFDM signals.

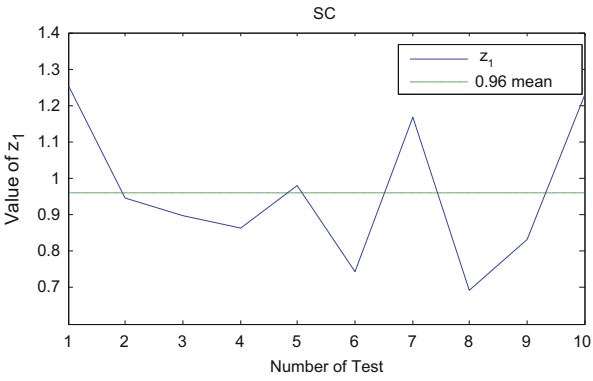

Fig. 4 z_1 of OFDM

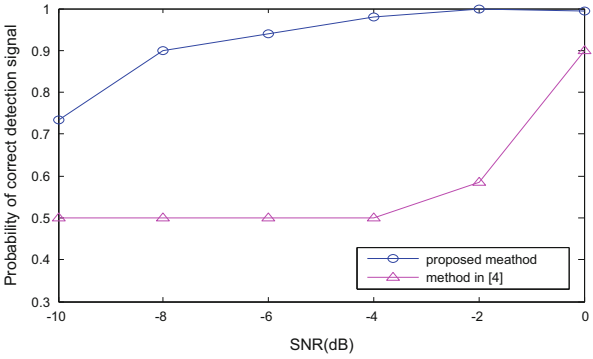

Fig. 5 Comparison between the proposed and the method in [4] in AWGN

The received signal is low-pass filtered and (over) sampled with the factor ρ set to 4. The probability of signal detection equates the probability of correctly recognizing the OFDM adding the probability of correctly recognizing the SCLD. The probability of signal detection is obtained from 100 trials for each signal type.

4.2 Simulation Results

Figure 5 shows that the proposed method performs better than the method in [4]. The probability of correct detection signal of the method in [4] is just 0.5 when SNR varies from −10 to −4 dB, which is on the reason that the threshold is too irrational high that SCLD signals cannot be detected correctly, whereas the probability of correct detection signal of the proposed method is almost 0.9 at −8 dB because the proposed method enlarge the distinguish gap between OFDM and SCLD.

5 Conclusions

The proposed algorithm exploits the non-zero CCs magnitude values in time and frequency domains for solve the OFDM and SCLD recognition problem. Considering the different features of OFDM and SCLD in two domains, we define a dual domain joint decision function to widen the distinguish gap. Compared with the traditional methods in [4], the proposed method in this paper improves the probability of signal detection in low SNR.

Acknowledgments This work was supported by the National Natural Science Foundation of China under grant 61271181, and the Fundamental Research Funds for the Central Universities under grant 2013RC0104.

References

1. Dobre OA, Abdi A, Bar-Ness Y, Su W (2007) A survey of automatic modulation classification techniques: classical approaches and new trends. IET Proc Commun 1(2):137–156
2. Cabric D, Mishra SM, Brodersen RW (2004) Implementation issues in spectrum sensing for cognitive radios. In: Proc Asilomar Conference on Signals, Systems, and Computers (ASILOMAR), Pacific, Grove, Nov 2004, pp 772–776
3. Gardner WA (1988) Signal interception: a unifying theoretical framework for feature detection. IEEE Trans Commun 36:896–906
4. Punchihewa A, Dobre OA, Rajan S, Inkol R (2007) Cyclostationarity-based algorithm for blind recognition of OFDM and single carrier linear digital modulations. In: Proc IEEE PIMRC, 2007, Athens, Greece, pp 1–5
5. Oner M, Jondral F (2004) Cyclostationarity based air interface recognition for software radio systems. In: Proc IEEE Radio and Wireless Conference, Sept 2004, pp 263–266
6. Proakis JG (2000) Digital communications, 4th edn. McGraw Hill, New York, NY
7. Nee RV, Prasad R (2000) OFDM for wireless multimedia communications. Artech House, Norwood, MA, USA
8. Zhang Q, Dobre OA, Rajan S, Inkol R (2009) On the second-order cyclostationarity for joint signal detection and classification in cognitive radio systems. In: Proc IEEE CCECE, Newfoundland, Canada, 2009, pp 204–208
9. Dobre OA, Bar-Nees Y, Su W (2003) Higher-order cyclic cumulants for high order modulation classification. In: Proc. IEEE MILCOM, Boston, MA, 2003, pp 112–117
10. Dandawate AV, Giannakis GB (1994) Statistical tests for presence of cyclostationarity. IEEE Trans Signal Proces 42(9):2355–2369

A Novel ICI-SC Scheme in MIMO-OFDM System

Zhenchao Wang, Jianping Zhang, Yanqin Wang, Zhenpeng Liu, and Zhenyang Guan

Abstract MIMO-OFDM system suffers from ICI caused by frequency offset, and the ICI-SC method is a very simple way of suppressing ICI, but the existing ICI-SC method may reduce the anti-noise performance when we improve the CIR performance. This paper proposes a novel ICI-SC scheme that subcarrier signals are remapped in complex weighted data-conjugate method to solve the problem. The proposed method with the minimum phase rotation can effectively reduce the phase error caused by phase rotation of received signal; thereby it improves the system anti-noise performance. According to the simulation, the proposed method has not only a similar CIR performance with the existing method, but also a significantly better BER performance. Another problem is the bandwidth efficiency of ICI self-cancellation method is 1/2, so this paper proposes a novel remapped method of 2/3 rate data to improve the bandwidth efficiency of MIMO-OFDM system.

Keywords MIMO-OFDM • Carrier frequency offset • ICI-SC • Bandwidth efficiency

Z. Wang (✉) • J. Zhang • Z. Guan
College of Electronic and Information Engineering, Hebei University, BaoDing, China
e-mail: 463308886@qq.com

Y. Wang
Hebei University, BaoDing, China

Z. Liu
College of Electronic and Information Engineering, Hebei University, BaoDing, China

Network Centre, HeBei University, BaoDing, China

B. Zhang et al. (eds.), *The Proceedings of the Second International Conference on Communications, Signal Processing, and Systems*, Lecture Notes in Electrical Engineering 246, DOI 10.1007/978-3-319-00536-2_80,

1 Introduction

With the rapid development of wireless network and wireless multimedia services, MIMO-OFDM (Multiple-Input Multiple-Output and Orthogonal Frequency Division Multiplexing) is a promising technique for fourth-generation (4G) broadband wireless communication system [1]. It can provide high data rate and high spectral efficiency, overcome channel frequency selective fading and improve system capacity etc, however, OFDM system suffers from ICI (Inter-carrier Interference) caused by phase noise or frequency offset, which degrades system performance.

Among the suppressing ICI schemes, the ICI self-cancellation (ICI-SC) scheme is widely used because it is a very simple way for suppressing ICI. The ICI-SC scheme and the STFBC strategy for two transmit antennas are first proposed by Y. Zhao and S. Haggman [2], the further developed in STFBC strategy for multiple transmit antennas is proposed by Y. Gong and K. B. Letaief [3], and then M. Uysal and N. Al-Dhahir introduce the ICI-SC technique employed in adjacent and symmetric subcarrier mapping scheme [3]. In recent years, researchers have proposed various improvements, adjacent data-conversion method, symmetric data-conversion method, adjacent real constant weighted data-conversion method, symmetric real constant weighted data-conversion method, adjacent data-conjugate method, and symmetric data-conjugate method etc [3–5]. The research of ICI-SC scheme is mainly for SISO-OFDM system, but for MIMO-OFDM system it's still in infancy.

In this paper, we investigate the SC techniques to mitigate ICI for MIMO-OFDM systems and a novel ICI-SC scheme that subcarrier signals are remapped in complex weighted data-conjugate method is proposed to solve the problem that the real constant weighted data-conversion method may reduce the anti-noise performance when improving the CIR. On the other hand, a remapped method of 2/3 rate data is proposed to improve a problem that the bandwidth efficiency of ICI self-cancellation method in MIMO-OFDM system is 1/2.

2 ICI Analysis in MIMO-OFDM

We consider an MIMO-OFDM system with M transmit antennas, N receive antennas, and K sub-carriers, as shown in Fig. 1.

The received kth subcarrier is expressed as follows:

$$y_n(k) = \sum_{m=1}^{M} C_m(k) H_{m,n}(k) S_{m,n}(0) + I_n(k) + z_n(k), \quad k = 0, 1, \cdots, K-1 \qquad (1)$$

Where, $z_n(k)$ is the noise, $C_m(k)$ is the STFB codewords that can be expressed as [6],

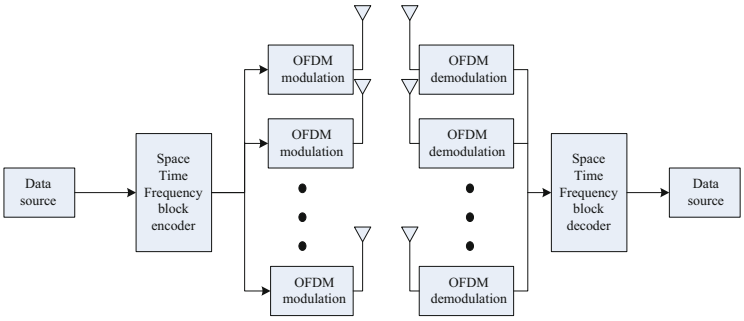

Fig. 1 Block diagram of MIMO-OFDM system with ICI

$$C_m = \begin{bmatrix} c_1(0) & c_2(0) & \cdots & c_M(0) \\ c_1(1) & c_2(1) & \cdots & c_M(1) \\ \vdots & \vdots & \ddots & \vdots \\ c_1(k-1) & c_2(k-1) & \cdots & c_M(k-1) \end{bmatrix} \tag{2}$$

$H_{m,n}(k)$ is the equivalent form of channel state information from transmitting antenna m and receiving antenna n,

$$H_{m,n}(k) = \sum_{l=0}^{L-1} \alpha_{m,n}(l) e^{-j2\pi k \Delta f \tau_l} \tag{3}$$

Suppose that frequency selective fading channels between each pair of transmitting and receiving antennas have L independent delay paths and the same power delay profile. The MIMO channel is assumed to be constant over each OFDM block period, but it may vary from one OFDM block to another [7]. The coefficients $\alpha_{m,n}(t,l)$ are complex channel gains of the lth path between transmitting antenna m and receiving antenna n. They are modeled as zero-mean complex Gaussian random variables with variance $\mathrm{E}[|\alpha_{m,n}(l)|^2] = \delta_l^2$, and $\sum_{l=0}^{L-1} \delta_l^2 = 1$. $\Delta f = 1/T_s$ is the subcarrier spacing and T_s is the OFDM symbol duration. τ_l is the delay of the lth path. The ICI term $I_n(k)$ at subcarrier k of each receiving antenna n is the superposition of M ICI terms $I_{m,n}(k)$ that can be expressed as,

$$I_n(k) = \sum_{m=1}^{M} I_{m,n}(k) = \sum_{m=1}^{M} \sum_{p=0, p\neq k}^{K-1} C_m(p) H_{m,n}(p) S_{m,n}(p-k) \tag{4}$$

The coefficient $S_{m,n}(k)$ is

$$S_{m,n}(k) = \frac{\sin\left(\pi(k+\varepsilon_{m,n})\right)}{K\sin\left(\frac{\pi}{K}(k+\varepsilon_{m,n})\right)}\exp\left(j\pi\left(1-\frac{1}{K}\right)(k+\varepsilon_{m,n})\right) \tag{5}$$

Note that coefficients $S_{m,n}(0)$ is a constant with respect to subcarrier index k = 0,

$$S_{m,n}(0) = \frac{\sin\left(\pi\varepsilon_{m,n}\right)}{K\sin\left(\frac{\pi}{K}\varepsilon_{m,n}\right)}\exp\left(j\pi\left(1-\frac{1}{K}\right)\varepsilon_{m,n}\right) \tag{6}$$

Where $\varepsilon_{m,n}$ is the normalized frequency offset of the transmission link from transmitting antenna m and receiving antenna n. From the (11) and (12), we can know that if the value of $\varepsilon_{m,n}$ becomes larger. The desired part $|S_{m,n}(0)|$ will decrease and the undesired part $|S_{m,n}(k)|$ will increase.

The received signal in (1) can be simplified as,

$$y(k) = \underbrace{X(k)Q(0)}_{\text{desired part}} + \underbrace{\sum_{p=0,p\neq k}^{K-1} X(p)Q(p-k)}_{\text{undesired part}} \tag{7}$$

Similar to the ICI-SC of the SISO-OFDM system, during ICI cancellation coding in MIMO-OFDM system, one data symbol is mapped onto two sub-carriers with predefined weighting coefficients. The weighting coefficients are calculated carefully such that the ICI signals within the two sub-carriers are cancelled by each other at the receiver end.

The received signal on the $(2k)$th and $(2k+1)$th sub-carriers can be expressed as:

$$y(2k) = X(k)[Q(0) - Q(1)] + \sum_{p=0,p\neq k}^{K/2-1} X(p)[Q(2p-2k) - Q(2p+1-2k)] \tag{8}$$

$$\begin{aligned} y(2k+1) &= X(k)[Q(-1) - Q(0)] \\ &\quad + \sum_{p=2,p\neq k}^{K/2-1} X(p)[Q(2p-2k-1) - Q(2p-2k)] \end{aligned} \tag{9}$$

The desired signal is recovered as follows:

$$\begin{aligned} y'(k) &= X(k)[2Q(0) - Q(1) - Q(-1)] \\ &\quad + \sum_{p=0,p\neq k}^{K/2-1} X(p)[2Q(2p-2k) - Q(2p+1-2k) - Q(2p-2k-1)] \end{aligned} \tag{10}$$

The coefficient of the ICI cancellation modulation (ICM) is $Q'_{p-k} = Q_{2p-2k} - Q_{2p+1-2k}$, the coefficient of the ICI cancellation demodulation (ICD) is

$Q''_{p-k} = 2Q_{2p-2k} - Q_{2p+1-2k} - Q_{2p-1-2k}$, the combination of ICM and ICD called ICI-SC method can be "self cancelled" each other.

Definite the ratio of the signal power to the power in the interference components (Carrier to Interference Ratio, CIR) as an indication of signal quality in the absence of noise. Assume that the desired signal is transmitted on subcarrier "0", and then, the CIR of normal OFDM systems is simplified as [8]:

$$\mathrm{CIR} = \frac{|S(0)|^2}{\sum_{l=1}^{N-1} |S(l)|^2} \tag{11}$$

And the CIR of the ICI-SC method can be represented as:

$$CIR = \frac{|2Q_0 - Q_1 - Q_{-1}|^2}{\sum_{p=0}^{K/2-1} |2Q_{2p} - Q_{2p+1} - Q_{2p-1}|^2} \tag{12}$$

3 Novel ICI-SC Scheme

Among the lots of ICI-SC schemes, the real constant weighted data-conversion method is the best way of suppressing ICI, and its CIR will increase with the weighting factor decreasing [9], but it will reduce the anti-noise performance when the weighting factor is too small. This problem can be solved by transmitting complex weighted data, because the method with the minimum phase rotation can effectively reduce the phase error caused by phase rotation, thereby improve the anti-noise performance.

The coefficient gradually changes with respect to the position of the sub-carriers. The closer and further the sub-carriers with respect to the desired subcarrier, the more interference will be occurred especially at the adjacent and symmetric positions [5], so the adjacent and symmetric sub-carriers mapping scheme is used in this paper to reduce the ICI.

The ICI-SC scheme of data-conjugate method is proposed in [5], from the simulation, it can be seen that the scheme can improve the CIR and reduce the BER performance. So a novel ICI-SC scheme is proposed in this paper.

3.1 Adjacent Complex Weighted Data-Conjugate Method

Subcarrier signals are remapped as the form of $X'(2k) = X(k)$, $X'(2k+1) = e^{j\pi/2}X^*(k)$ in adjacent complex weighed data-conjugate method.

The received signal on the $(2k)$ th and $(2k+1)$th sub-carriers can be expressed as:

$$y(2k) = X(k)Q(0) + e^{j\pi/2}X^*(k)Q(1) + \sum_{p=0,p\neq k}^{K/2-1} X(p)Q(2p-2k) + e^{j\pi/2}X^*(p)Q(2p+1-2k) \quad (13)$$

$$y(2k+1) = X(k)Q(-1) + e^{j\pi/2}X^*(k)Q(0) + \sum_{p=0,p\neq k}^{K/2-1} X(p)Q(2p-2k-1) + e^{j\pi/2}X^*(p)Q(2p-2k) \quad (14)$$

The desired signal is recovered as follows:

$$\begin{aligned} y'(k) &= y(2k) - e^{j\pi/2}y^*(2k+1) \\ &= X(k)(Q(0)+Q^*(0)) + e^{j\pi/2}X^*(k)(Q(1)-Q^*(-1)) \\ &+ \sum_{p=0,p\neq k}^{K/2-1} X(p)[Q(2p-2k)+Q^*(2p-2k)] + e^{j\pi/2}X^*(p)[Q(2p+1-2k)-Q^*(2p-2k-1)] \end{aligned} \quad (15)$$

The CIR can be represented as:

$$CIR = \frac{\left|Q_0 - Q_0^*\right|^2 + \left|e^{j\pi/2}(Q_1 - Q_{-1})\right|^2}{\sum_{p=0}^{K/2-1}\left(\left|Q_{2p} - Q_{2p}^*\right|^2 + \left|e^{j\pi/2}\left(Q_{2p+1} - Q_{2p-1}^*\right)\right|^2\right)} \quad (16)$$

3.2 Symmetric Complex Weighted Data-Conjugate Method

The main idea of the symmetric complex weighted data-conjugate method is mapping the sub-carriers signals as the form of $X'(k) = X(k)$, $X'(K-k-1) = e^{j\pi/2}X^*(k)$, the data is mapped onto two symmetrically allocated sub-carriers.

The received signal on the kth and (K-k-1)th sub-carriers can be expressed as:

$$y(k) = X(k)Q(0) + e^{j\pi/2}X^*(k)Q(K-1) + \sum_{p=0,p\neq k}^{K/2-1} X(p)Q(p-k) + e^{j\pi/2}X^*(p)Q(K-p-1-k) \quad (17)$$

$$y(K-k-1) = X(k)Q(1-K) + e^{j\pi/2}X^*(k)Q(0) + \sum_{p=0,p\neq k}^{K/2-2} X(p)Q(p-K+k+1) + e^{j\pi/2}X^*(p)Q(k-p) \quad (18)$$

The desired signal is recovered as follows:

$$\begin{aligned} y^{'}(k) &= y(k) - e^{j\pi/2}y^{*}(K-k-1) \\ &= X(k)(Q(0)+Q^{*}(0)) + e^{j\pi/2}X^{*}(p)(Q(K-1)-Q^{*}(K-1)) \\ &+ \sum_{p=0}^{K/2-1} X(p)[Q(p-k)+Q^{*}(k-p)] + e^{j\pi/2}X^{*}(p)[Q(K-p-1-k)-Q^{*}(p-K+k+1)] \end{aligned} \tag{19}$$

The CIR can be represented as:

$$CIR = \frac{\left|Q_0 + Q_0^{*}\right|^2 + \left|e^{j\pi/2}\left(Q_{K-1} - Q_{1-K}^{*}\right)\right|^2}{\left|Q_p + Q_{-p}^{*}\right|^2 + \sum_{p=0, p\neq k}^{K/2-1}\left|e^{j\pi/2}\left(Q_{K-p-1} - Q_{p-K+1}^{*}\right)\right|^2} \tag{20}$$

The ICI-SC scheme is a very simple way of suppressing ICI in MIMO-OFDM systems, but it's a loss of bandwidth, the system used the lower bandwidth efficiency will have the better anti-noise performance. When the channel environment is better, there is no need to waste a large of spectral resources on suppressing ICI, so we can appropriately reduce the system's ability to suppress ICI in exchange for better bandwidth efficiency.

3.3 2/3 Rate Complex Weighted Data-Conjugate Method

The problem of bandwidth efficiency in fact is a question of coding efficiency, so we propose a 2/3 rate complex weighted data-conjugate method in this paper, and this method can achieve the bandwidth efficiency of 2/3, which improves the bandwidth efficiency.

Subcarrier signals are remapped as the form of $X'_{3k} = X_{2k}$, $X'_{3k+1} = X_{2k+1}$, $X'_{3k+2} = e^{j\pi/2}X^{*}_{2k+1}$ in 2/3 rate complex weighted data-conjugate method. X_{2k} is information data in $2k$th carrier before complex weighted data-conjugate method mapping and X'_{3k} is information data in $3k$th carrier after the complex weighted data-conjugate mapping.

The received signal on the $3k$th, $(3k+1)$ th and $(3k+2)$th sub-carriers can be expressed as:

$$Y(3k) = X(2k)Q(0) + X(2k+1)Q(1) + e^{j\pi/2}X^{*}(2k+1)Q(2)$$

$$+\sum_{l=0,l\neq k}^{2/3N}\left[X(2l)Q(3l-3k)+X(2l+1)Q(3l+1-3k)+e^{j\pi/2}X(2k+1)^{*}Q(3l+2-3k)\right] \tag{21}$$

$$Y(3k+1)=X(2k)Q(-1)+X(2k+1)Q(0)+e^{j\pi/2}X^{*}(2k+1)Q(1)$$
$$+\sum_{l=0,l\neq k}^{2/3N}\left[X(2l)Q(3l-1-3k)+X(2l+1)Q(3l-3k)+e^{j\pi/2}X^{*}(2k+1)Q(3l+1-3k)\right] \tag{22}$$

$$Y(3k+2)=X(2k)Q(-2)+X(2k+1)Q(-1)+e^{j\pi/2}X(2k+1)^{*}Q(0)$$
$$+\sum_{l=0,l\neq k}^{2/3N}\left[X(2l)Q(3l-2-3k)+X(2l+1)Q(3l-1-3k)+e^{j\pi/2}X^{*}(2k+1)Q(3l-3k)\right] \tag{23}$$

The desired signals Z_{2k} and Z_{2k+1} can be recovered as follows:

$$\begin{aligned}\mathrm{Z}_{2k}&=Y_{3k}-Y_{3k+1}\\&=X_{2k}(Q_0-Q_{-1})+X_{2k+1}(Q_1-Q_0)+e^{j\pi/2}X^{*}_{2k+1}(Q_2-Q_1)\end{aligned} \tag{24}$$

$$\begin{aligned}\mathrm{Z}_{2k+1}&=Y_{3k+1}-e^{j\pi/2}Y^{*}_{3k+2}\\&=\mathrm{X}_{2k+1}\left(Q_0+Q_0^{*}\right)+e^{j\pi/2}\mathrm{X}^{*}_{2k+1}\left(Q_1-Q^{*}_{-1}\right)+\mathrm{X}_{2k}Q_{-1}-e^{j\pi/2}\mathrm{X}^{*}_{2k}Q^{*}_{-2}\\&+\sum_{l=0,l\neq k}^{2/3N}X_{2l}Q_{3l-1-3k}-e^{j\pi/2}X^{*}_{2l}Q^{*}_{3l-2-3k}+X_{2l+1}\left(Q_{3l-3k}+Q^{*}_{3l-3k}\right)+e^{j\pi/2}X^{*}_{2k+1}\left(Q_{3l+1-3k}\right.\\&\left.-Q^{*}_{3l-1-3k}\right)\end{aligned} \tag{25}$$

In the receiver, the signal of K sub-carriers is converted back into the signal with (2/3) K sub-carriers by de-mapping, and the signals Z_{2k} and Z_{2k+1}can be recovered.

The normal OFDM bandwidth efficiency is 1, but it can't suppress ICI; the ICI-SC can suppress ICI well, but bandwidth efficiency is only 1/2; the proposed method can achieve the bandwidth efficiency of 2/3, meanwhile, it also can suppress ICI, and it provides a satisfactory tradeoff between the bandwidth efficiency and ICI reduction.

4 Simulation Results

A simulation comparison is conducted to evaluate the performance.

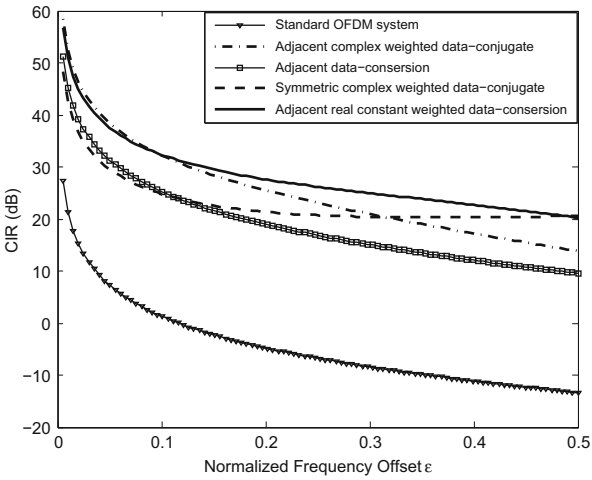

Fig. 2 A CIR comparison of different methods

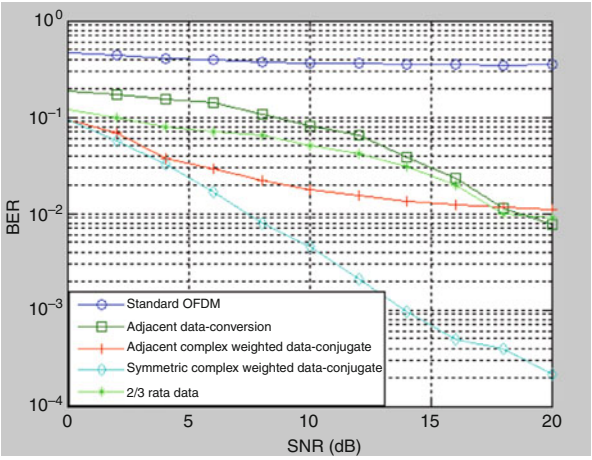

Fig. 3 A BER comparison of different methods

Figure 2 shows a CIR comparison of the standard OFDM system, adjacent data-conversion method, adjacent real constant weighted data-conversion method, adjacent complex weighted data-conjugate method and symmetric complex weighted data-conjugate method. From the Fig. 2, it is found that all the ICI-SC method can improve the system CIR, and adjacent complex weighted data-conjugate method has the larger CIR when frequency offset is small, with the frequency offset increasing, adjacent real constant weighted data-conversion method has the excellent CIR performance and it's better than the proposed method.

CIR is a performance criterion without considering the noise, so a BER comparison of different methods is showed in Fig. 3 to analyze the improvement on system performance of the different ICI-SC methods. From the simulation, all the

ICI-SC methods' BER curves can decrease with the increasing signal-to-noise ratio, it proves all the methods can improve the system anti-noise performance; it is also found that the symmetric complex weighted data-conjugate method has significantly better BER performance, which certifies the proposed method can better improve the system performance.

5 Conclusion

In this paper, a MIMO-OFDM model with frequency offset has been analyzed and researched for ICI reduction, the novel methods are proposed based on the existing ICI-SC method. From the simulation, the complex weighted data-conjugate method can suppress the ICI effectively and greatly improve the performance of BER than other schemes; the 2/3 rate data method can achieve the bandwidth efficiency of 2/3, reduce a waste of spectral resources on suppressing ICI, and provide a satisfactory tradeoff between the bandwidth efficiency and ICI reduction.

Reference

1. Stamoulis A, Diggavi SN, Al-Dhahir N (2002) Intercarrier interference in MIMO-OFDM. IEEE T Signal Proces 50(10):2451–2464
2. Zhao Y, Haggman S (2001) Intercarrier interference self-cancellation scheme for OFDM mobile communication systems. IEEE Trans Commun 49:1185–1191
3. Idris A (2011) CIR and BER performance of STFBC in MIMO OFDM system. Aust J Basic Appl Sci 5(12):3179–3187
4. Yiwleak A, Pirak C (2010) Zero-padded complex conjugate technique for intercarrier interference cancellation in MIMO-OFDM systems. ISCIT 26–29:901–906
5. Idris A, Alam S (2010) A new data-conjugate intercarrier (ICI) self-cancellation for ICI reduction in space time frequency block codes MIMO-OFDM system. IEEE Trans Computer and Network Technology 23–25:43–47
6. Jie K (2008) The research of interference cancellation technology in MIMO-OFDM system. Xi'An University of Science and Technology, Xi'An
7. Molisch AF, Win MZ, Winters JH (2002) Space-time-frequency (STF) coding for MIMO-OFDM systems. IEEE Commun, 6(9)
8. Azlina Idris, Kaharudin Dimyati (2008) Interference self-cancellation schemes for spacetime frequency block codes MIMO-OFDM system. IJCSNS, (8)9
9. Hua Y (2010) Inter-carrier interference suppression technology under high mobility environment in OFDM system. Southwest Jiaotong University, Chengdu

An Improved Blind Detection Method for PDCCH in TD-LTE System

Zengshan Tian, Li Zhang, Mu Zhou, and Qiping Zhou

Abstract As a crucial role in scheduling for the TD-LTE system, the Physical downlink control channel (PDCCH) assigns variable resources to the uplink and downlink transmission. Based on the consideration of the structure of PDCCH multiplexing data, this paper proposes an improved blind detection algorithm for the PDCCH in the TD-LTE system. The most remarkable difference from the conventional blind detection algorithms is that our proposed algorithm requires the preprocessing on the PDCCH multiplexing data in a determined search space. The simulation results demonstrate that our proposed algorithm can effectively reduce the average number of PDCCH blind detections.

Keywords TD-LTE • PDCCH • Blind detection • Search space • DCI format

1 Introduction

As a quasi-4G system, TD-LTE is based on the orthogonal frequency division multiplexing (OFDM) and multiple-input multiple-output (MIMO) technologies. The TD-LTE system supports six different transmission bandwidths including the 1.4, 3, 5, 10, 15 and 20 MHz. The peak data rate by the first release is desired to achieve the transmission rate100 and 50 Mbps in the downlink and uplink respectively within the 20 MHz frequency band. In TD-LTE system, both the transmission bandwidth and delay are significantly constrained [1].

Because the user equipment (UE) is always notified by the PDCCH about the uplink and downlink resource scheduling, the PDCCH will play a significant role in scheduling the uplink and downlink resource in the TD-LTE system [2]. Under

Z. Tian (✉) • L. Zhang • M. Zhou • Q. Zhou
Chongqing Key Lab of Mobile Communications Technology, School of Communication & Information Engineering, Chongqing University of Posts and Telecommunications, Chongqing 400065, China
e-mail: tianzs@cqupt.edu.cn; zhanglilv0830@126.com

B. Zhang et al. (eds.), *The Proceedings of the Second International Conference on Communications, Signal Processing, and Systems*, Lecture Notes in Electrical Engineering 246, DOI 10.1007/978-3-319-00536-2_81,

normal circumstances, when the UE receives the PDCCH signaling, the UE will not be informed about the location of actual physical resources which have been assigned to PDCCH and the PDCCH formats in a sub-frame. However, the information content of the current needs can be provided to the UE. For instance, in the idle state, the UE is waiting for the page and system message, and the uplink authorization message is desired by the UE when the uplink data is waiting to be sent out. Then, the UE should conduct the blind detection on each sub-frame for the PDCCH decoding to effectively schedule the uplink and downlink resource.

As the bearer of the downlink control information (DCI) format, the PDCCH can be suggested as the core element for the system resource allocation and control information scheduling. In this case, the PDCCH blind detection has significant influence on the system response speed and data processing capacity. For the UE, if the efficiency of blind detection cannot be guaranteed, a certain delay to the system and the corresponding time will be resulted. In response to this problem, this paper proposes a new blind detection method for PDCCH to not only improve the detection performance but also reduce the number of blind detections.

The remainder of this paper is organized as follows. Section 2 gives an overview of the control channels in TD-LTE downlink system. Section 3 addresses the features of the PDCCH channel multiplexing. Section 4 discusses the characteristics of the specific PDCCH multiplexing. Section 5 compares the blind detection process by the conventional and our proposed methods. Then, Sect. 6 provides some experimental results in the additive white Gaussian noise (AWGN) channel to verify the efficiency of our proposed method. Finally, we conclude this paper and give some future directions in Sect. 7.

2 PDCCH

The message carried by the PDCCH is known as the DCI which contains the resource assignment and some other control information for a UE or a group of UEs. For instance, the downlink scheduling and assignment information are used for the physical downlink shared channel (PDSCH) demodulation and decoding. The scheduling grant information is used to inform the UE about the used resource and transmission format on the physical uplink shared channel (PUSCH) transmission. The transmission power control command is used for the uplink physical channel power control. At this point, the DCI can be divided into a variety of formats: 1) format 0: scheduling information of PUSCH; 2) formats 1, 1A, 1B, 1C and 1D: scheduling information of PDSCH; 3) formats 2 and 2A: configuration information of antenna cases; and 4) formats 3 and 3A: configuration information of uplink power control [3].

In the physical layer of TD-LTE system, the processing flow of PDCCH at the receiver can be recognized as an inverse process of the transmission processing flow [4], as depicted in Fig. 1.

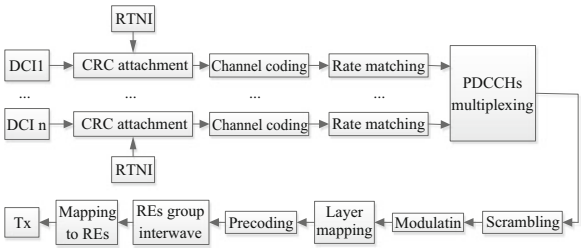

Fig. 1 PDCCH transmission flow

3 PDCCH Channel Multiplexing

In order to reduce the number of blind detection, the TD-LTE system supports four types of PDCCH formats which are named as the formats 0, 1, 2 and 3 respectively. Each format is associated with a special number of CCEs, as illustrated in Table 2. Each CCE consists of nine REGs, and thereby it will contain 72 bits of continuous resources block [4]. The multiple formats supported by the PDCCH are also presented in Table 1.

From Table 1, we can find the maximum number of OFDM symbols which are assigned to PDCCH transmission in a sub-frame. To improve the efficiency of the transmission bandwidth, we should decrease the number of OFDM symbols assigned to each PDCCH.

By using the multiplexed PDCCH to calculate the number of available CCEs, the number of available CCEs can be calculated by (1).

$$N_{\mathrm{CCE}} = \left\lfloor \left(N_{\mathrm{REG}}^{\mathrm{TOTAL}} - N_{\mathrm{REG}}^{\mathrm{PCFICH}} - N_{\mathrm{REG}}^{\mathrm{PHICH}}\right)/9 \right\rfloor \tag{1}$$

Where $N_{\mathrm{REG}}^{\mathrm{TOTAL}}$ is the total number of the REGs in the OFDM symbols of control domain; $N_{\mathrm{REG}}^{\mathrm{PCFICH}}$ is the number of the PCFICH REGs; $N_{\mathrm{REG}}^{\mathrm{PHICH}}$is the number of the PHICH REGs.

After the PDCCH is multiplexed, we can define the monitoring candidate PDCCH series in a search space $S_k^{(L)}$. $S_k^{(L)}$ are defined as continuous CCE set in (2).

$$\begin{cases} S_k^{(L)} = L \cdot \{(Y_k + m) \bmod \lfloor N_{\mathrm{CCE},k}/L \rfloor\} + i \\ i = 0, \cdots, L-1; m = 0, \cdots, M^{(L)} - 1 \end{cases} \tag{2}$$

Where $L \in \{1,2,4,8\}$; $M^{(L)}$ is the number of decoding PDCCHs in the specified search space. Y_k is calculated by (3).

$$\begin{cases} Y_k = (A \cdot Y_{k-1}) \bmod D \\ Y_{-1} = n_{RNTI} \neq 0, \quad A = 39827, D = 65537 \end{cases} \tag{3}$$

By setting the levels $L = 1, 2, 4, 8$, the multiplexed PDCCH will be mapped into ten consecutive CCEs, as shown in Fig. 2. At this point, the length of DCI will

Table 1 PDCCH formats

PDCCH format	Number of CCEs	Number of REGs	Number of PDCCH bits
0	1	9	72
1	2	18	144
2	4	36	288
3	8	72	576

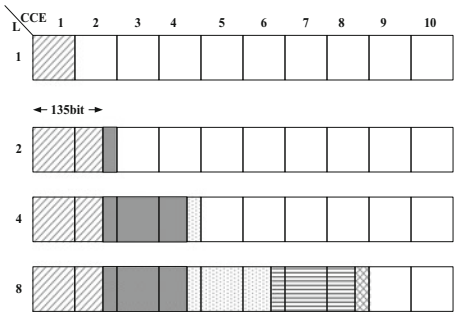

Fig. 2 CCE data structure after multiplexing

be determined by the size of bandwidth. We take the DCI with the length of 29 bits and the common search space for instance. The final length of DCI will equal to 135 bits after the cyclic redundancy check (CRC) and tail biting convolutional coding. In Fig. 2, the shaded blocks represent the different duplicate information after the rate matching. In other words, the shaded blocks with the same shape size should contain the same CCE information.

4 Characteristics of the Specific PDCCH Multiplexing

As depicted in Fig. 2, when the set level equals to 1, the interleaved concatenated information will be punched, but for the set level 2, there will be a few duplicate information with nine repeating bits. As the set level increases to 4 and 8, there a large number of complete repeating segments could be resulted.

Because of the existence of the complete repeating segments in set levels 4 and 8, we can use the slide correlation to conduct the PDCCH multiplexing segmentation. In our experiments, we select the correlation window with the length of 270 bits and divide this window into two segments with the length 135 bits each (i.e., the two repeating segments). Then, we can obtain the slide correlation value of each segment with the sliding step 1 CCE in Fig. 3. We observe that in the ideal situation, the well peak performance can be obtained by dividing the correlation window into two repeating segments.

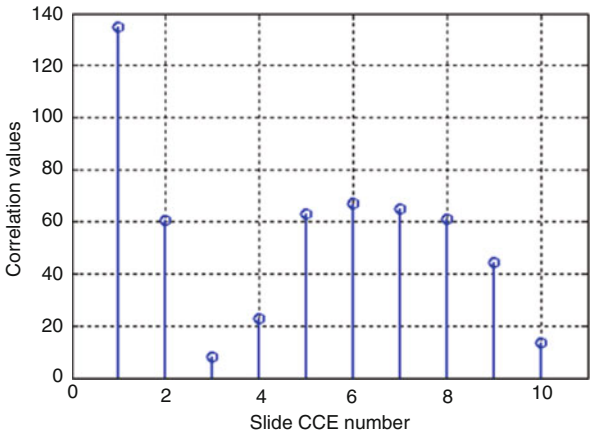

Fig. 3 Slide correlation values

After the demodulation and descrambling at the receiver, we can obtain the similar multiplexing segment in Fig. 2. At this point, for both the hard and soft demodulation [5], the PDCCH multiplexing information should always achieve the well correlation peak performance after the descrambling. Therefore, with the help of the correlation peak, we can effectively improve the detection performance and also reduce the number of blind detection by preprocessing the information in the specific search space.

5 Blind Detection

A string of data in different PDCCH channels will be obtained after the descrambling at the receiver. Because the UE cannot determine the exact multiplexing method, the blind detection process should be required.

5.1 Conventional Blind Detection Method

The steps of the conventional blind detection method are described below.

1. Calculation of the number of CCEs: Dividing the length of string data by 72, we can obtain the number of CCEs (i.e. $N_{\mathrm{CCE},k}$). The CCEs are labeled from the IDs 0 to $N_{\mathrm{CCE},k} - 1$ where k is the number of sub-frames. Moreover, the lengths of string data on both the transmission and receiver sides should be the integral multiples of the number of CCEs.
2. Determination of the radio network temporary indication (RNTI) and DCI format: Based on the expected DCI information for the UE, we can easily

determine the RNTI for CRC descrambling and the DCI format for blind detection.

3. Calculation of the starting position and the largest search space: The starting position in search space and the largest CCE search space can be calculated by (2).
4. Processing on the read-out CCEs information: Because there is no prior information about the search level, the UE should try all the set levels in search space to read the CCEs. Then, after the de-rate matching and Viterbi decoding on the CCEs, we will conduct the RNTI descrambling and CRC checksum on the obtained data.
5. Blind Detection: If the CRC checksum is correct, the data can be accepted however, if the wrong checksum occurs, the starting position will be added by L. This iterative process continues until the entire candidate PDCCHs have been searched. We take the iterations with $L = 1$ for instance. If the desired DCI information cannot be obtained after all the CCEs have been searched in the condition of level $L = 1$, we will go back to step 4 to re-calculate the starting position of the search space. Then, we continue for the next iteration with the level $L = 2$. The blind detection ends when the UE obtains the desired DCI information or all the set levels have been searched [6].

Based on the previous steps, the significant drawbacks of the conventional blind detection method are about the large amount of calculation cost and low detection accuracy because all the CCE levels and PDCCH candidates should be traveled during the iterative search process.

5.2 Improved Blind Detection Method

The steps of our improved method are described below.

Steps 1, 2 and 3 are the same steps with the conventional blind detection method.

4. Preprocessing PDCCH multiplexing data in search space: The length of calculated data in the specified search space equals to the length of sliding correlation window $L_{corr} = 3 * (L_{dci} + 16)$ where L_{dci} the calculated length of DCI information is. Because the PDCCH will be mapped by using the CCE as the minimum unit, the step size of the related offset should equal to 1 CCE. Then, each correlation value will be recorded as a starting point for the CCE. If the DCI is only associated with the public search space (e.g. $L = 4, 8$), we will order the correlation values in the descending order and then go to step 5. If the DCI is associated with the dedicated search space or both the dedicated search space and the public search space, we will first judge the correlation peak, and then select the top five staring position with the largest priority to process the step 5.
5. Blind Detection: The data obtained from each given starting position is with it's the length L_{corr}. Because the data has been de-repeated, it can be de-interleaved directly for the de-rate matching and Viterbi decoding. After that, the obtained data will be descrambled by the RNTI and CRC checksum. If the CRC

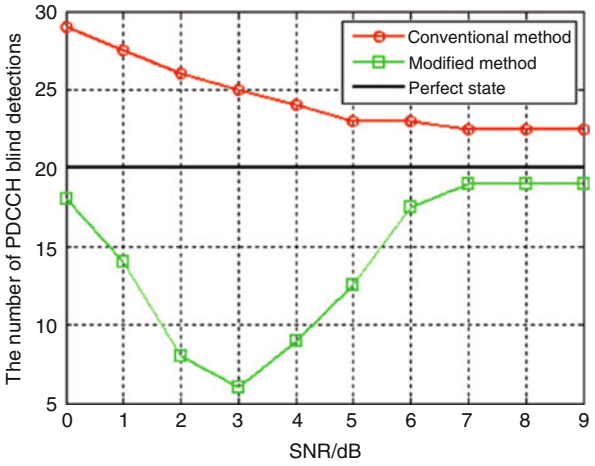

Fig. 4 Number of PDCCH blind detection

Table 2 Simulation parameters

Parameters	Simulation values
Downlink bandwidth	10 MHz
Number of transmit antennas	2
Number of PDCCH	1
RNTI type	C-RNTI
Noise type	AWGN
Transmission mode	1

checksum is correct, the blind detection is done. However, in the wrong CRC checksum condition, we will judge whether the data is associated with the specific search space or both the public search space and specific search space. If the data is not associated with the previous search spaces, we will not consider the two set levels $L = 4$ and $L = 8$, but conduct the conventional blind detection process with $L = 1$ and $L = 2$. This blind detection process ends when the UE obtains the desired DCI information or all the set levels have been blindly detected.

6 Simulation Results

The simulation environments are described as follows: (1) three DCI formats (i.e. 0, 1 and 1A) sent out from the sender; (2) AWGN channel; and (3) C-RNTI as the RNTI type. In different conditions of signal to noise ratio (SNR), we compare the average number of PDCCH blind detection by the conventional and our proposed methods in Fig. 4. There are 1,000 data blocks used for the simulation on the MAT LAB platform. The simulation parameters are listed in Table 2.

As shown in Fig. 4, it is observed that the number of blind detection will be significantly increased in the low SNR condition. For instance, in the condition of 3 dB SNR, the number of blind detection by our proposed method decreases by 70 and 76 % compared to the perfect state and the conventional method. This result is mainly cause by the significant increase of the PDCCH formats 2 (4 CCE) and 3 (8 CCE) in the bad channel condition.

Compared to the conventional blind detection method, the remarkable difference of our proposed method is that by the characteristics of the large set levels of string data. In the condition of low SNR, most of the set levels will be selected as format 3 (8 CCE). In this case, although the required conditions for the preprocessing can be satisfied, the precision for the possibility ordering by the correlation peak cannot be guaranteed. In the contrary, both the required conditions for the preprocessing and precision for the possibility ordering can be satisfied. Therefore, the number of blind detection will be substantially decreased. However, in the high SNR condition, because lower set levels are allocated to the UE, the preprocessing can only optimize the blind detection process in public search space, and thereby the decrease of the number of blind detection cannot be significant.

7 Conclusion

This paper proposes a new blind detection method for the PDCCH in TD-LTE system. Without the consideration of the impossible situations after the pretreatment on the detection information, our improved method outperforms the conventional blind detection method in the aspects of the required number of blind detection, computation cost for the reaction of UE and system delay in variable conditions of SNR.

References

1. Wang Y, Sun S (2010) The principle of TD-LTE technology and system design. People's Posts and Telecommunications Publishing House, Beijing
2. Sesia S, Toufik I, Baker M (2009) LTE-the UMTS long term evolution from theory to practice. Wiley, Hoboken NJ
3. Li X, Jia H (2011) A method to reduce PDCCH blind detection number in LTE system. Application of Electronic Technique 38(4):87–89
4. 3GPP TS 36.211 v9.1.0, 3rd generation partnership project; technical specification group radio access network; evolved universal terrestrial radio access (E-UTRA); physical channels and modulation (release 9). Accessed Mar 2010
5. Wang D, Jia H (2012) Research of calculating CFI value used in LTE system. In: Proc. 9th international conference on fuzzy systems and knowledge discovery (FSKD 2012), pp 2220–2223. doi:10.1109/FSKD.2012.6233744
6. Lang T, Jia Y (2011) Application of soft demodulation in LTE physical layer downlink. International conference on control, automation and systems engineering (CASE 2011), pp 1–5. doi:10.1109/ICCASE.2011.5997875

Simple and Efficient Algorithm for Automatic Digital Modulation Recognition

Badreldeen Ismail Dahap and Liao HongShu

Abstract In this paper we propose new features extracted from the instantaneous information (amplitude, frequency and phase) to discriminate between digital modulated signals MASK (2, 4 and 8), MFSK (2, 4 and 8) and MPSK (2, 4 and 8). By setting the appropriate threshold, the average recognition rate can reach 99.5 % when SNR = 8 dB. This algorithm is easy to implement and has small computation loads due to the use of less number of features comparing with most of the existing algorithms of automatic digital modulation recognition.

Keywords Instantaneous information • Modulation recognition and features

1 Introduction

Automatic modulation recognition has been an important theme with the development of wireless communications. It is widely applied to the non-cooperative communication field for military or civilian purposes. It is used in military applications such as surveillance, electronic warfare and threat analysis. In civilian field, it is used for the purposes such as signal confirmation, interference identification and spectrum management [1].

There are two main types of modulation recognition approaches: the statistical pattern recognition approach and the decision-theoretic approach.

Several modulation classification approaches have been established in the last few years to discriminate among MPSK, MFSK based on Cumulant [2–8], Wavelet analysis [9–12], both Wavelet and Cumulant [13], Spectrum Line Feature [14, 15], Cyclic Spectral Density [16] and Cyclic Spectral Correlation Function [17]. However, most of these approaches have some shortcomings in practical

B.I. Dahap (✉) • L. HongShu
School of Electronic Engineering, University of Electronic Science and Technology of China, Chengdu, Sichuan 610054, P. R China
e-mail: bader_6dahap@hotmail.com; hsliao@uestc.edu.cn

B. Zhang et al. (eds.), *The Proceedings of the Second International Conference on Communications, Signal Processing, and Systems*, Lecture Notes in Electrical Engineering 246, DOI 10.1007/978-3-319-00536-2_82,

implementation due to the complexity of their calculations and recognition rate at lower SNR, for the decision-theoretic approaches and statistical pattern recognition respectively. To solve the problems of lower recognition rate at lower SNR, most researchers focus on the improvement of statistical pattern recognition by choosing features that enable us to get a higher recognition rate at lower SNR using the decision tree classifier or machine learning classifier with the help of neural network.

In [18], the proposed seven features extracted from instantaneous information to discriminate between digital modulated signals {(MASK (2, 4 and 8), MPSK (2, 4 and 8) and MFSK (2, 4 and 8)} have an overall success rate of over 96 % at the SNR = 10 dB.

Our research aims at the development of a new approach for the modulation recognition of digital signals, using four features extracted from instantaneous information (amplitude, frequency and phase) to discriminate between nine signals as in [18] at low SNR. Our approach not only achieves a better recognition rate but also overcomes the weakness of traditional approaches to some extent.

This paper is organized as follows: The features extracted from instantaneous information are introduced in section two. Computer simulations including the determination of thresholds, the flowchart and the simulation results are explained in section three, while the conclusion is given in section four.

2 Feature Extraction

To discriminate the digitally modulated signals, four features extracted from instantaneous information (amplitude, phase and frequency) are used.

The first feature $\mathbf{V_{aa}}$ is defined by

$$\mathbf{V_{aa}} = \frac{1}{\mathbf{N_s}} \sum_{\mathbf{i}=1}^{\mathbf{N_s}} \mathbf{a_{cn}^2(i)} - \left(\frac{1}{\mathbf{N_s}} \sum_{\mathbf{i}=1}^{\mathbf{N_s}} \mathbf{a_{cn}(i)} \right)^2 \tag{1}$$

where N_s is the number of samples, $a_{cn}(i) = a_n(i) - 1$, and $a_n(i) = a(i)/m_a$, a (i) is the instantaneous amplitude, m_a is the sample mean value. Since the variance of the normalized-centered instantaneous amplitude of MASK satisfies $\mathbf{V_{aa(ASK2)} > V_{aa(ASK8)} > V_{aa(ASK4)}}$, only V_{aa} can be used to discriminate between ASK2, ASK4 and ASK8.

The second feature $\mathbf{V_{ph}}$ is defined by

$$\mathbf{V_{ph}} = \frac{1}{\mathbf{N_s}} \sum_{\mathbf{i}=1}^{\mathbf{N_s}} \varnothing^4(\mathbf{i}) - \left(\frac{1}{\mathbf{N_s}} \sum_{\mathbf{i}=1}^{\mathbf{N_s}} \varnothing^2(\mathbf{i}) \right)^2 \tag{2}$$

where Ns is the number of samples and ∅ is the instantaneous phase without normalization. Since the variance of the square of the instantaneous phase of MPSK satisfies $\mathbf{V_{ph(PASK4)}}>\mathbf{V_{ph\ (PASK8)}}>\mathbf{V_{ph\ (PASK2)}}$, only $\mathbf{V_{ph}}$ can be used to discriminate between (MASK) and (MPSK), and also discriminate PSK2, PSK4 and PSK8.

The third feature $\mathbf{V_{if}}$ is defined by

$$V_{if} = \frac{1}{N_s}\sum_{i=1}^{N_s} f^2(i) - \left(\frac{1}{N_s}\sum_{i=1}^{N_s} f(i)\right)^2 \tag{3}$$

where Ns is the number of samples, while f is the instantaneous frequency. $\mathbf{V_{if}}$ is used to discriminate between MPSK and MFSK.

The fourth feature **PP** is defined by

$$\mathbf{PP} = \sqrt{\frac{1}{\mathbf{c}}\left(\sum_{\mathbf{a_n(i)}>\mathbf{a_t}} \varnothing^2_{\mathbf{NL}}(\mathbf{i})\right) \Big/ \left(\frac{1}{\mathbf{c}}\sum_{\mathbf{a_n(i)}>\mathbf{a_t}} \left|\varnothing_{\mathbf{NL}}(\mathbf{i})\right|\right)^2} \tag{4}$$

where PP is the improvement of the P proposed by [18] and c is the number of non-weak samples. $a_n(i) = a(i)/m_a$, where a(i) is the instantaneous amplitude, m_a is the sample mean value, a_t is the value of threshold to get non-weak sample signals and $\varnothing_{NL}$ is normalized instantaneous phase. **PP** is used to discriminate between FSK2, FSK4 and FSK8.

3 Computer Simulations

In this section, the computer simulation results are introduced, the software used is Matlab R2011b and the simulation parameters are set as follows: carrier frequency (fc) = 150 KHz, sampling frequency (fs) = 1.2 MHz, symbol rate (fb) = 12.5 Kbps, symbol number 1000, the carrier amplitude(ac) = 1 and the noise is assumed to be additive white Gaussian noise.

3.1 Thresholds Determination

The thresholds for all features are shown in the Fig. 1, Fig. 2, Fig. 3, Fig. 4, Fig. 5, and the specific values are shown in Table 1.

From Fig. 1 we see that ASK2 can be discriminated from (ASK4, ASK8) at SNR $\geq$ 2 dB by the threshold 1 (t2), similarly (ASK4) can be discriminated from ASK8 at SNR $\geq$ 7 dB by the threshold 2 (t3).

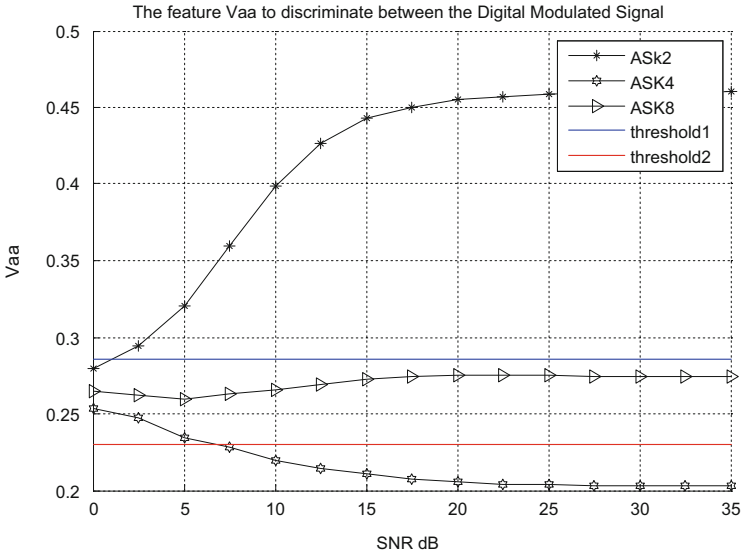

Fig. 1 Feature V_{aa}

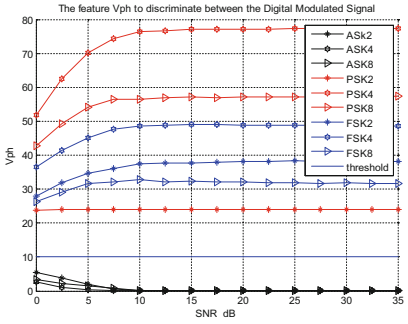

Fig. 2 Feature V_{ph}

Figure 2 shows that, the first threshold (t1) of the feature V_{ph} enables the discrimination of MASK from MPSK and MFSK at SNR $\geq$ 0 dB.

From Fig. 3 we see that (PSK2) can be discriminated from (PSK4, PSK8) at SNR $\geq$ 0 dB by the threshold 1 (t5), similarly (PSK4) can be discriminated from (PSK8) at SNR $\geq$ 3 dB by the threshold 2 (t6).

Figure 4 shows that (MFSK) can be discriminated from (MPSK) at SNR $\geq$ 0 dB by the threshold (t4).

Figure 5 shows that (FSK2) can be discriminated from (FSK4, FSK8) at SNR $\geq$ 0 dB by the threshold 1 (t7), also (FSK4) can be discriminated from (FSK8) at SNR $\geq$ 0 dB by the threshold 2 (t8).

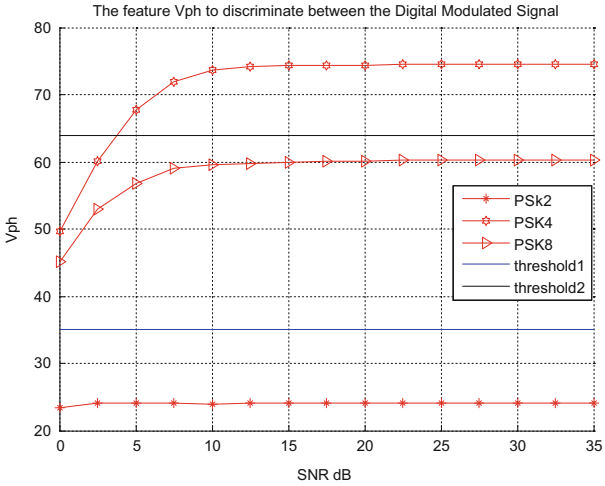

Fig. 3 Feature V_{ph}

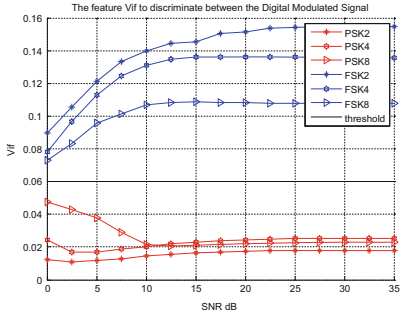

Fig. 4 Feature V_{if}

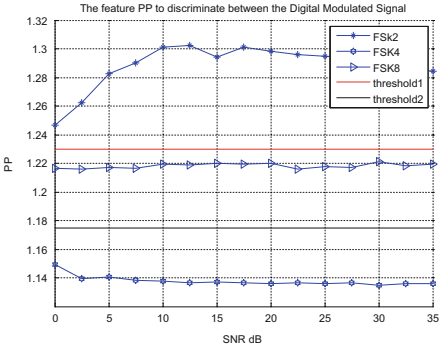

Fig. 5 Feature PP

Table 1 The values of all thresholds

Feature	Threshold	Function
Vph	t1 = 10	Discriminate (MASK) from (MPSK, MFSK)
	t5 = 35	Discriminate (PSK2) from (PSK4, PSK8)
	t6 = 64	Discriminate (PSK4) from (PSK8)
V_{if}	t4 = 0.06	Discriminate (MPSK) from (MFSK)
V_{aa}	t2 = 0.286	Discriminate (ASK2) from (ASK4, ASK8)
	t3 = 0.23	Discriminate (ASK4) from (ASK8)
PP	t7 = 1.23	Discriminate (FSK2) from (FSK4, FSK8)
	t8 = 1.18	Discriminate (FSK4) from (FSK8)

3.2 Flowchart of Automatic Recognition of Digital Modulation

As shown in the Fig. 6 below, first, we separate (MASK) from (MPSK, MFSK) using V_{ph}. Secondly, we separate (MPSK) from (MFSK) using V_{if}. Thirdly, we separate ASK2, ASK4, and ASK8 from one another using Vaa. Fourthly, V_{ph} is used to separate PSK2, PSK4, and PSK8 from one another. Finally, we separate FSK2, FSK4, and FSK8 from one another using PP.

3.3 Simulation Results and Analysis

500 iterations are used to get the recognition rates in Table 2, Table 3, Table 4.

Table 2 shows that, by using V_{aa} to discriminate among MASK (ASK2, ASK4, ASK8), the average recognition rate can reach 92.13 % when SNR =6 dB.

Table 3 shows that when V_{ph} is used to discriminate among MPSK (PSK2, PSK4 and PSK8) the average recognition rate can reach 99.6 % when SNR = 6 dB, which has a better recognition rate than [11] and is easier to compute than most existing MPSK automatic modulation recognition techniques such as [4, 19]. In addition this feature is able to discriminate (MASK) from (MPSK and MFSK) and the recognition rate reaches 100 % when SNR ≥ -2dB.

Table 4 shows that when PP is used to discriminate between MFSK (FSK2, FSK4 and FSK8). The average recognition rate reaches 96.4 % when SNR = -2 dB. This shows that the modified feature has a better recognition rate than most existing MFSK automatic modulation recognition technique such as [12, 17] and is easier to compute.

By using these four new features, an average recognition rate not less than 99.5 % can be achieved when SNR = 8dB, as shown in Fig. 7 and Table 5, which is much better than those in [18, 20] and [21].

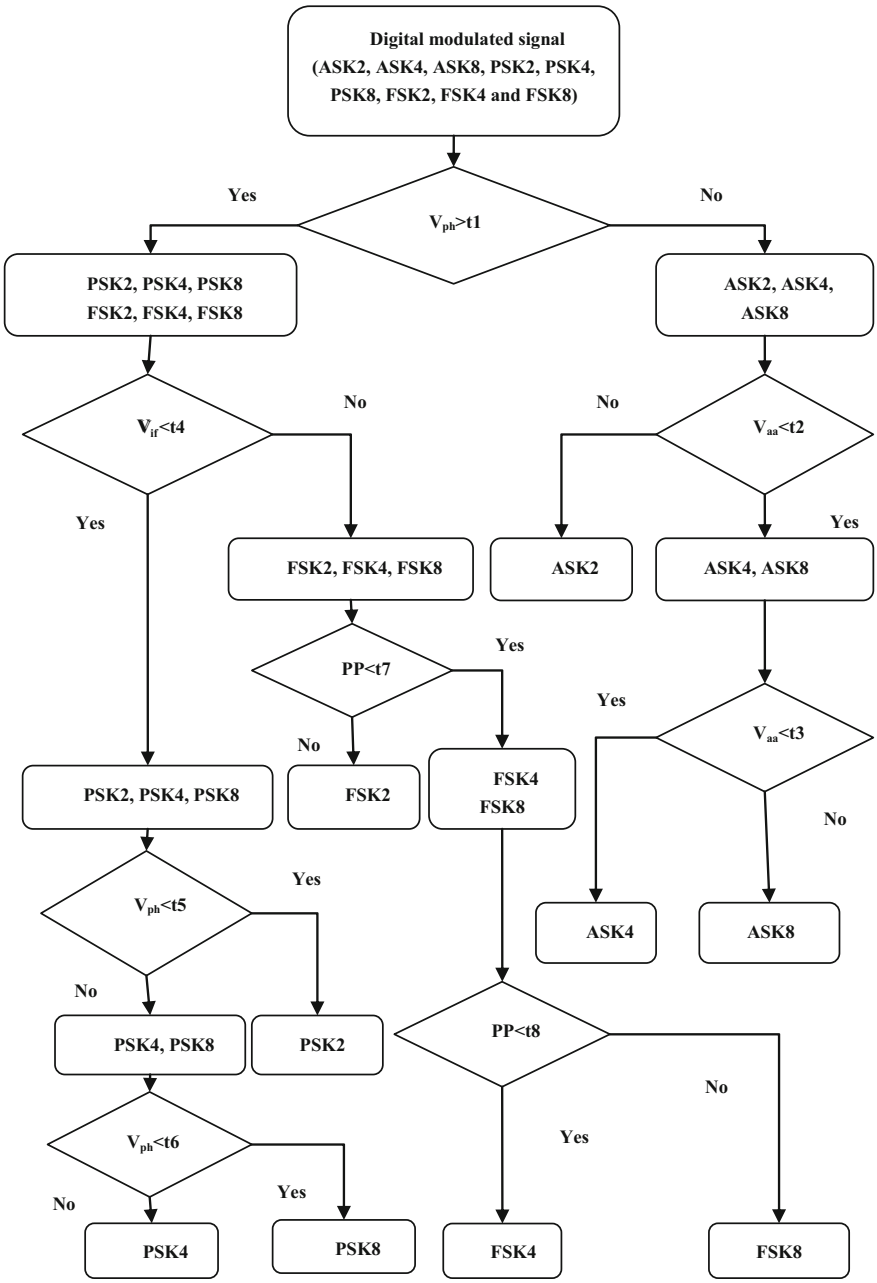

Fig. 6 Flowchart of automatic modulation recognition

Table 2 The results of feature V_{aa}

SNR (dB)	4	6	8	>10
ASK2	96.4 %	100 %	100 %	100 %
ASK4	6.6 %	76.4 %	95 %	100 %
ASK8	100 %	100 %	100 %	100 %
Average recognition rate	67.67 %	92.13 %	98.33 %	100 %

Table 3 The results of feature V_{ph}

SNR (dB)	4	6	8	>10
PSK2	100 %	100 %	100 %	100 %
PSK4	57.4 %	98.8 %	100 %	100 %
PSK8	100 %	100 %	100 %	100 %
Average recognition rate	85.8 %	99.6 %	100 %	100 %

Table 4 The results of feature PP

SNR (dB)	−4	−2	0	>2
FSK2	51.60 %	89.4 %	100 %	100 %
FSK4	100 %	100 %	100 %	100 %
FSK8	77.8 %	100 %	100 %	100 %
Average recognition rate	76.47 %	96.47 %	100 %	100 %

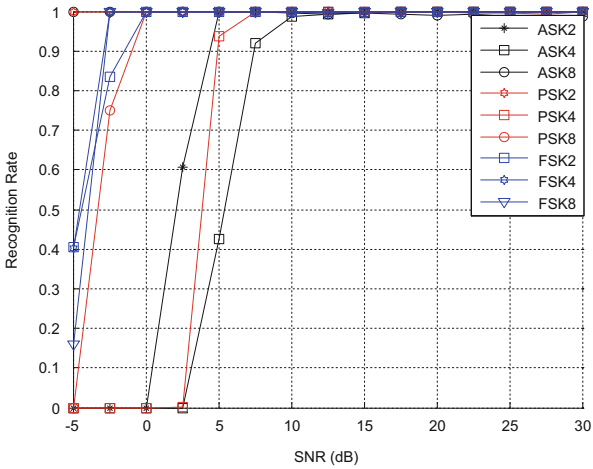

Fig. 7 The right recognition of the digital modulated signals

Table 5 The correct classification at SNR = 8 dB

ASK2	100 %	PSK8	99.8 %
ASK4	96 %	FSK2	100 %
ASK8	100 %	FSK4	100 %
PSK2	100 %	FSK8	100 %
PSK4	100 %	Average recognition rate	99.53 %

4 Conclusion

In this paper we propose four new features based on the variance of instantaneous amplitude, phase and frequency. By using these features, an average recognition rate not less than 99.5 % can be achieved when SNR = 8 dB. This technique not only gives a better recognition rate, compared to existing methods, but it is also easier to compute. The simulation results also show that only one feature can be used to discriminate the MASK, MPSK and MFSK signals subtype. It is more feasible in practical scenarios.

References

1. Yang Jie, Wang Xumeng, Wu, Hongli (2009) Modified automatic modulation recognition algorithm. In: IEEE WCNM, Beijing, 2009, pp 1–4
2. Xin Zhou, Ying Wu, Bin Wang (2008) The MPSK signals modulation classification based on kernel methods. In: IEEE Antennas, Propagation and EM Theory, Kunming, 2008, pp 1419–1422
3. Zhang S, Zhou X, Wu Y (2010) Improved modulation classification of MPSK signals based on high order cumulants. IEEE Future Computer and Communication (ICFCC) 2:V2-444–V2-448
4. Xin Zhou, Ying Wu, Guopeng Yang (2009) Modulation classification of MPSK signals based on relevance vector machines. In: IEEE Information Engineering and Computer Science, pp 1–5
5. Li Chi sheng, Xiao Jing, Xu Qingyi (2011) A novel modulation classification for PSK and QAM signals in wireless communication. In: IEEE Communication Technology and Application (ICCTA 2011), Beijing, 2011, pp 89–92
6. Sun G (2010) MPSK signals modulation classification using sixth-order cumulants. IEEE Image and Signal Processing (CISP) 9:4404–4407
7. Yu Han, Guohua Wei, Chunyun Song et al (2012) Hierarchical digital modulation recognition based on higher-order cumulants. In: IEEE Instrumentation, Measurement, Computer, Communication and Control (IMCCC), Harbin, 2012, pp 1645–1648
8. Li Shi-ping, Chen Fang-chao, Wang Long (2012) Modulation recognition algorithm of digital signal based on support vector machine. In: IEEE Control and Decision Conference (CCDC), Taiyuan, 2012, pp 3326–3330
9. Ho KC, Prokopiw W, Chan YT (2000) Modulation identification of digital signals by the wavelet transform. IEEE Proc Radar Sonar Naving 147(4):169–176
10. Cui C, Li H, Yu J (2010) MPSK modulation classification based on Morlet transform. Commun Technol 43(3):10–12
11. Ka mun Ho, Vaz C, Daut DG (2010) Automatic classification of amplitude, frequency, ad phase shift keyed signals in the Wavelet domain. In: IEEE Sarnoff symposium, Princeton, NJ 2010, pp 1–6
12. Xin Zhou, Ying Wu (2006) Automatic classification of MFSK signals by T (E Wavelet Transforms). In: IEEE Communications and Networking in China, 2006, ChinaCom' 06, 2006, pp 1–5
13. Yuan Hong (2010) Classification of MPSK signals using M-bands wavelet and high-order cumulants. In: IEEE Signal Processing Systems (ICSPS), Dalian, 2010, pp V1-66–V1-69
14. Li SK, Dong B, Liu N (2010) Modulation recognition of MPSK signals based on spectrum line feature. Commun Technol 43(8):127–128

15. Yang L, Xu XD, Lu YR et al (2009) Spectrum line based modulation classification for constant modulus digital modulation signals. Journal of University of Science and Technology of China 39(9):936–943
16. Zhu L, Cheng HW, Wu LN (2009) Identification of digital modulation signals based on cyclic spectral density and statistical parameters. Journal of Applied Sciences-Electronics and Information Engineering 27(2):137–143
17. Meng LL, Li J (2010) Research on an identification of MFSK signals based on cyclic spectral correlation function. Radio Communications Technology 36(1):22–25
18. Pan-Feng Sun, Zi-Wei Zheng, Man Li (2011) Recognition of digital modulation signals based on statistical parameters. In: IEEE Transportation Mechanical, and Electrical Engineering (TMEE), Changchun, 2011, pp 2467–2470
19. Chen Kai-Zhi, Hu Ai-Qun (2008) MPSK demodulation algorithm based on pattern recognition. In: IEEE Neural Networks and Signal Processing, Nanjing, 2008, pp 182–186
20. Chunyun Song, Yi Zhan, Lin Guo (2011) A new feature parameter for MFSK/MPSK recognition. In: IEEE Intelligence Science and Information Engineering (ISIE), Wuhan, 2011, pp 21–23
21. Wang L, Wu H (2010) Digital modulation identification by distance and fuzzy evaluation. IEEE Advanced Computer Control (ICACC) 5:70–73

The Analysis of Effect of Nonlinear Power Amplifier on Beamforming

Chen Wei, Huiyong Li, and Julan Xie

Abstract In a transmit beamforming system, the power amplifier (PA) plays an important role of affecting performance and stability of this system, because most of systems' nonlinearities are derived from the PA's nonlinearities. Generally speaking, only the lower amplitude input can gain the better linearity of PA but poor efficiency; on the contrary, the higher efficiency always means the more deteriorated linearity of PA. It's a dilemma to maintain both the efficiency and the nonlinearities of PA. Aiming to obtain a deeper understanding on this problem, this paper analyses the effect of nonlinear power amplifier on beam patterns of transmission arrays. Simulation results are also given for confirming the validity of the theoretical results.

Keywords The nonlinearities of PA • The model of PA • Transmit beamforming • Beam pattern

1 Introduction

In the past few years, boosted by the development of the receiving digital beamforming and the solid-state power amplifier (SSPA), the transmit digital beamforming has got a significant improvement. What's more, it is the digital technique that makes the system more reliable and more stable. Therefore this technique is widely used in radar, the military anti-jam communication and the civil mobile communication.

In fact, the power amplifier has an eternal contradiction in the efficiency and linearity of PA, that the lower amplitude input can gain the better linearity of PA but poor efficiency; on the contrary the higher efficiency always means the more

C. Wei (✉) • H. Li • J. Xie
School of Electronic Engineering, University of Electronic Science and Technology of China, Chengdu, Sichuan 611731, People's Republic of China
e-mail: 403773615@qq.com

B. Zhang et al. (eds.), *The Proceedings of the Second International Conference on Communications, Signal Processing, and Systems*, Lecture Notes in Electrical Engineering 246, DOI 10.1007/978-3-319-00536-2_83,

deteriorated linearity of PA. As we all know, the nonlinearity of PA will break the information of the input signal, which can make influence on the transmitting beamforming. Therefore, it is important for solve this contradiction to analyze the effect of nonlinear PA on beamforming. In [1], it only considered the AM–AM varieties, regardless of the AM–PM varieties and so on. This paper demonstrates the effect of nonlinear power amplifier on beam patterns. In particular, we concentrate on the effects that amplitude nonlinearities and phase nonlinearities have on these patterns.

Although some nonlinear amplifier models, such as the model of Taylor series of finite order, have a simple form, they only show AM–AM conversion. Meanwhile, some nonlinear amplifier models, such as the model of Volterra in [2], can show AM–AM conversion and AM–PM conversion, but they have a complex form which is inconvenient to study.

In this study, each channel and array elements are assumed ideal. We will limit ourselves to a narrow band signal. As assumed, the model of PA is quasimemoryless [3]. This is done in order to focus attention on the effects of the amplitude and phase nonlinearities. Starting from these assumptions, we develop an amplifier model from [4, 5] that is based on a band-pass orthogonal model, which can simply show nonlinear distortions in both AM–AM conversion and AM–PM conversion.

2 The Analysis of Nonlinear Power Amplifier Based on a Band-Pass Orthogonal Model

We will limit our study on the "a narrow band signal" case and focus attention on foundational frequency. The model of nonlinear PA is shown in Fig. 1.where $f(A_w A(t))$ is an odd function, representing AM–AM conversion, and $g(A_w A(t))$ is an even function, representing AM–PM conversion. There will be a separate set of function for each model.

The input signal in Fig. 1 is given by:

$$v_{in} = A_w A(t) \cos(\omega t + \theta(t) - \phi_w) \tag{1}$$

where A_w is the amplitude of each channel's weight and ϕ_w is the phase of weight. ω is the carrier frequency. $\theta(t)$ is the phase of the input signal and $A(t)$ is the amplitude of the input signal. So this output signal of a nonlinear amplifier is given by

$$v_{out} = f(A_w A(t)) \cos(\omega t + \theta(t) - \phi_w + g(A_w A(t))) \tag{2}$$

Expanding (2) results in (3).

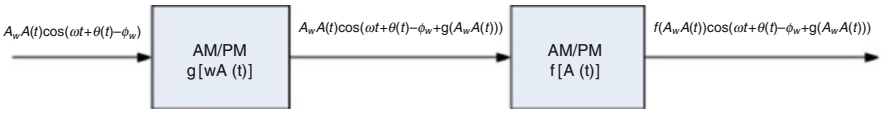

Fig. 1 The model of nonlinear PA

$$\begin{aligned} v_{out} &= f\left(A_w A(t)\right)\cos g\left(A_w A(t)\right)\cos\left(\omega t+\theta(t)-\phi_w\right) \\ &\quad -f\left(A_w A(t)\right)\sin g\left(A_w A(t)\right)\sin\left(\omega t+\theta(t)-\phi_w\right) \\ &= I[A_w A(t)]\cos\left(\omega t+\theta(t)-\phi_w\right) \\ &\quad -Q[A_w A(t)]\sin\left(\omega t+\theta(t)-\phi_w\right) \end{aligned} \tag{3}$$

where

$$\begin{aligned} I[A_w A(t)] &= f\left(A_w A(t)\right)\cos g\left(A_w A(t)\right) \\ Q[A_w A(t)] &= f\left(A_w A(t)\right)\sin g\left(A_w A(t)\right) \end{aligned} \tag{4}$$

Finally, $f(A_w A(t))$ and $g(A_w A(t))$ are given by:

$$\begin{aligned} f\left(A_w A(t)\right) &= \sqrt{I[A_w A(t)]^2+Q[A_w A(t)]^2} \\ g\left(A_w A(t)\right) &= \arctan^{-1}\frac{Q[A_w A(t)]}{I[A_w A(t)]} \end{aligned} \tag{5}$$

According to the instruction of PA, we can get the solid lines of $f(A_w A(t))$ and $g(A_w A(t))$ by which the lines of $I(A_w A(t))$ and $Q(A_w A(t))$ are finally given.

As (4) stated, both $I(A_w A(t))$ and $Q(A_w A(t))$ are odd functions. So, the two lines can be simulated by an odd number-order power series.

$$\begin{cases} I[A_w A(t)] = a_{I1}\left(A_w A(t)\right)+a_{I3}(A_w A(t))^3+\ldots\ldots \\ Q[A_w A(t)] = a_{Q1}\left(A_w A(t)\right)+a_{Q3}(A_w A(t))^3+\ldots\ldots \end{cases} \tag{6}$$

Let (6) be merged into a complex expression.

$$\begin{aligned} f\left(A_w A(t)\right)e^{jg(A_w A(t))} &= \left(a_{I1}+j*a_{Q1}\right)\left(A_w A(t)\right) \\ &\quad +\left(a_{I3}+j*a_{Q3}\right)(A_w A(t))^3+\ldots\ldots \end{aligned} \tag{7}$$

where a_{I1} and a_{Q1} decide the amplification of PA. When a_{I3} and a_{Q3} are negative, the output signal is undergoing compression by the amplifier. However, when a_{I3} and a_{Q3} are positive, the output signal is undergoing expansion. In general, because the voltages of most nonlinear devices are limited by quiescent point, the output signal is always compressed.

High order power series will get an accurate fitted result. Generally, third-order is enough to reflect the nonlinearity.

The accuracy of this model will be fallen, when PA's nonlinearities are raised. So, the model proposed is adapted not to the rich nonlinear PA, but to the poor nonlinear PA.

Besides (2), the output signal is also shown by:

$$v_{out} = \mathrm{Re}\left[f(A_w A(t))e^{jg(A_w A(t))}e^{j(\omega t+\theta(t)-\phi_w)}\right] \tag{8}$$

Because we always substitute a real signal with a complex signal for researching conveniently, we have:

$$\begin{aligned} v'_{out} &= f\left(A_w A(t)\right)e^{jg(A_w A(t))}e^{j(\omega t+\theta(t)-\phi_w)} \\ &= \left(a_{I1}+j*a_{Q1}\right)A_w A(t)e^{j(\omega t+\theta(t)-\phi_w)} \\ &+ \left(a_{I3}+j*a_{Q3}\right){A_w}^3 A(t)^3 e^{j(\omega t+\theta(t)-\phi_w)} \\ &= \left(a_{I1}+j*a_{Q1}\right)w^H A(t)e^{j(\omega t+\theta(t))} \\ &+ \left(a_{I3}+j*a_{Q3}\right)w^H {A_w}^2 A(t)^3 e^{j(\omega t+\theta(t))} \\ &= A_1 e^{j\varphi_1} w^H A(t)e^{j(\omega t+\theta(t))} \\ &+ A_3 e^{j\varphi_3} w^H {A_w}^2 A(t)^3 e^{j(\omega t+\theta(t))} \end{aligned} \tag{9}$$

where

$$\begin{aligned} A_1 &= \sqrt{{a_{I1}}^2+{a_{Q1}}^2}, \varphi_1 = \arctan^{-1}\frac{a_{Q1}}{a_{I1}} \\ A_3 &= \sqrt{{a_{I3}}^2+{a_{Q3}}^2}, \varphi_3 = \arctan^{-1}\frac{a_{Q3}}{a_{I3}} \end{aligned} \tag{10}$$

$e^{-j\phi_w}$ is the phase of weight in (9). As (9) and (10) stated, after the nonlinear PA, the output signals become $A(t)e^{j(\omega t+\theta(t)+\varphi_1)}$ and $A(t)^3 e^{j(\omega t+\theta(t)+\varphi_3)}$. When the input signal is a Linear Frequency Modulation (LFM) signal, the output signal is given by

$$\begin{aligned} v_{lfs-out} &= \left[A_1 e^{j\varphi_1} w^H A + A_3 e^{j\varphi_3} w^H {A_w}^2 A^3\right]e^{j(\omega t+\theta(t))} \\ &= A' e^{j(\omega t+\theta(t))} = \left|A'\right|e^{j\varphi_{A'}}e^{j(\omega t+\theta(t))} \end{aligned} \tag{11}$$

where

$$A' = A_1 e^{j\varphi_1} w^H A + A_3 e^{j\varphi_3} w^H {A_w}^2 A^3. \tag{12}$$

The coefficient of output signal is a constant complex in (12), which the norm of is the power of output signal, and which the phase of is the delay of transmitting signal. These factors don't affect the information of input signal.

Besides, when the input signal is a narrow band signal which the amplitude varies along the time, the output signal consists of original signal and nonlinear products which are interference signals for the input signal.

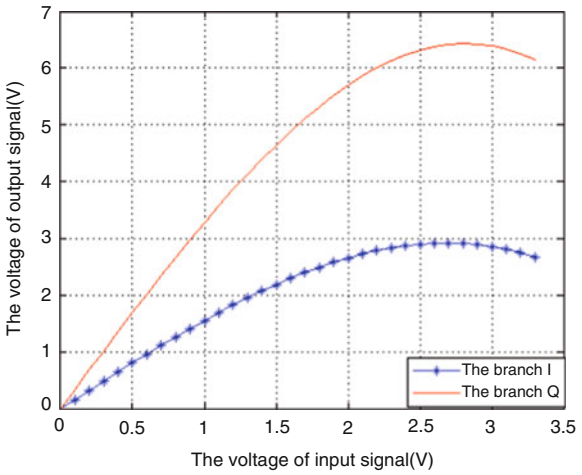

Fig. 2 The branch I and Q of AM–AM conversion

3 Simulation

We consider a 16-element array with elements uniformly spaced on the line of distance equal to half wavelength. We design a transmit beam at angle 30° and a null point at angle − 20°. We calculate the effects the nonlinear PA has on the beam patterns produced by a beamforming technique based on orthogonal projection algorithm. According to the paper [6], we let the coefficients of this PA model be $a_{I1} = 1.6285$; $a_{I3} = -0.0750$; $a_{Q1} = 3.4184$; $a_{Q3} = -0.1430$. Following the coefficients, the lines of $I(A_w A(t))$ and $Q(A_w A(t))$ are shown by Fig. 2.

As (11) showed, when the input signal is a LFM signal, the information of the output signal across nonlinear PA will be the same as the input signal, while the power of the output signal will change with the nonlinearity of PA.

Figure 3 shows a composite plot of linear PA and nonlinear PA in the signal of different amplitudes. According to this figure, we can find that a large amplitude of input signal will lead to compression of output signal, and a high voltage increased at null point.

As (9) stated, when the input signal is a narrow signal which the amplitude of is a time function, such as a DSB signal, $A(t)e^{j(\omega t + \theta(t))}$ is the input signal and $A(t)^3 e^{j(\omega t + \theta(t))}$ is the nonlinear product. In this simulation, we assumed $A(t) = As * \cos \omega t$.

Figure 4 shows a composite plot of foundational signal and a third-order harmonic product. According to this figure, we can find that large amplitude of an input signal will get a strong power of the nonlinear product, which lead to a clear nonlinearity of PA. This will make an influence on the result of transmission. Figure 5 shows the power radio of the original signal versus the nonlinear product in the different amplitudes of the input signal, when the amplitude of the input signal is $As \cos \omega t$.

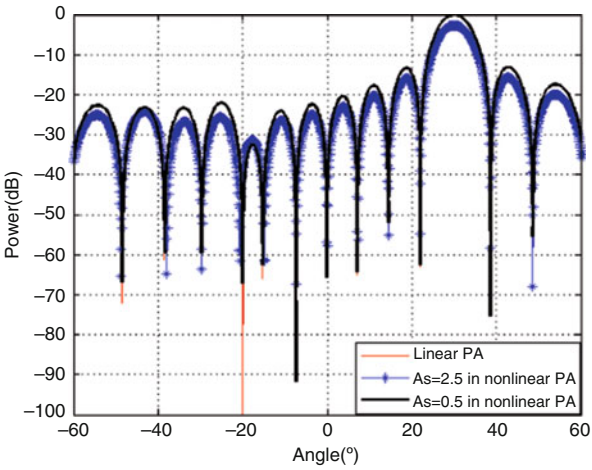

Fig. 3 Power array pattern. The input signal is a LFM signal

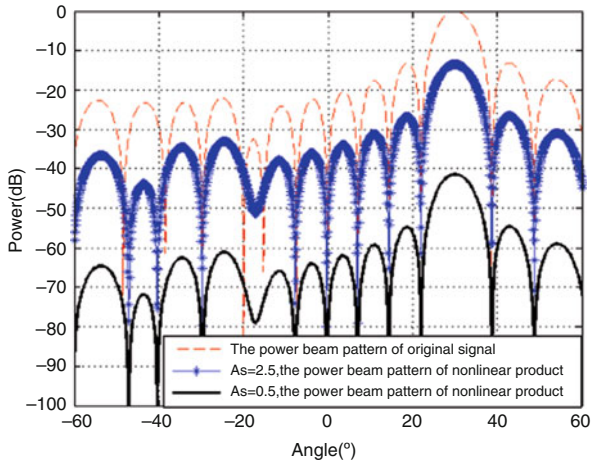

Fig. 4 Power array pattern. The input signal is a DSB signal

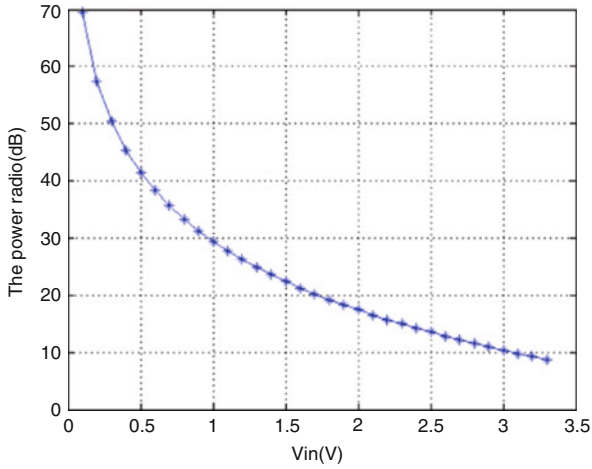

Fig. 5 The radio power of original signal versus nonlinear products, when the amplitude of the input signal is $As\cos\omega t$

4 Summary

In this paper, all array elements are thought to have the same characteristics. According to AM–AM conversion and AM–PM conversion, when the input signal is a constant envelope signal (such as a LFM signal), that is to say, the amplitude of the input signal that is constant, the nonlinear product is also a constant complex. So, it does not affect the information of signal. In general, we can transmit LFM signal by a high efficiency and rich nonlinearity of PA. However, when the input signal is an in-constant envelope signal (such as a DSB signal), that is to say, the amplitude of the input signal that is a time function, both AM–AM conversion and AM–PM conversion will affect the information of amplitude and phase of the input signal. The nonlinear product is an interference signal, which is decided by the value of a_1/a_3. At the worst case, the power of nonlinear products which are made by AM–AM varieties or AM–PM varieties will be strong and the nonlinear PA badly undermines the output signal. Thus, as expected, we can make a choice between the efficiency and the linearity of PA properly, with the radio power of original signal and nonlinear products.

Acknowledgments This work is supported partly by the China Postdoctoral Science Foundation (No.2012M520077), by Science and Technology Foundation of Sichuan Province (No. 2013JY0004) and by the Fundamental Research Funds for the Central Universities of China (ZYGX2012J018).

References

1. Real EC, Charette DP (1995) Non-linear amplifier effects in transmit beamforming arrays. IEEE Trans Acoust Speech Signal Process 5:3635–3638
2. Takeichi K, Furukawa T (2002) A Parallel fast algorithms of Volterra adaptive filters. IEEE Trans Circuit Syst l:26–29
3. Raich R, Zhou GT (2002) On the modeling of memory nonlinear effects of power amplifiers for communication applications. In: Proc.10th IEEE digital signal processing workshop, 1–6 Oct
4. Zeng Xingbin, Hu Qianmiao (2005) A nonlinear model of Radiofrequency power amplifier. Microwave and millimetre-wave symposium of China, pp 1205–1208
5. Saleh AAM (1981) Frequency-independent and frequency-dependent nonlinear models of TWT amplifiers. IEEE Trans Commun 11(11):1715–1720
6. Liu hui, Guan boran (2003) A nonlinear power amplifier based on band-pass orthogonal model. Microwave and millimetre-wave symposium of China, pp 265–268

A New Secure Transmission for Big Data Based on Nested Sampling and Coprime Sampling

Junjie Chen, Qilian Liang, Baoju Zhang, and Xiaorong Wu

Abstract There are critical requirements for security in Big Data collection and transmission of Big Data through a communication network. A new secure transmission for Big Data based on nested sampling and co-prime sampling is proposed in this paper. With nested sampling and coprime sampling, Big Data could also achieve higher PSD for BFSK signal. When the sampling spacing pairs bigger enough, the spectrum of BFSK signal performs like frequency hopping. With the same independent multitone interfering signal added to FH/BFSK system, the error probability becomes much lower using nested sampling and coprime sampling compared with the original FH/BFSK signal. This property has great advantage in the security of Big Data collection and transmission using FH/BFSK based on nested sampling and coprime sampling.

1 Introduction

The phrase "Big Data" refers to large, diverse, complex, distributed data sets generated from instruments, sensors, Internet transactions, email, video, click streams, and all other digital sources available today and in the future, as defined by U.S. National Science Foundation in its recent solicitation.

In modern data processing, the security is an important issue. Data experts and critics worry that potential abuses of Big Data may imperil personal privacy, and consumer freedoms[1, 2]. Critical requirements for security in Big Data collection

J. Chen (✉) • Q. Liang
Electrical Engineering, University of Texas at Arlington, 416 Yates St, Arlington, TX 76019, USA
e-mail: junjie.chen@mavs.uta.edu; liang@uta.edu

B. Zhang • X. Wu
College of Physics and Electronic Information, Tianjin Normal University, Tianjin 300387, China
e-mail: wdxyzbj@mail.tjnu.edu.cn; wu.xiaorong@sohu.com

B. Zhang et al. (eds.), *The Proceedings of the Second International Conference on Communications, Signal Processing, and Systems*, Lecture Notes in Electrical Engineering 246, DOI 10.1007/978-3-319-00536-2_84,

and transmission through a communication network is presented. A new secure transmission for Big Data based on nested sampling and coprime sampling is proposed in this paper.

In this paper, a brief introduction of nested sampling [3–5] and coprime sampling is given. As we will show, with the sampling spacings increasing, the mainlobe of PSD (Power Spectral Density) estimated from these two sampling methods will be much narrower, that is, the occupied bandwidth becomes smaller [6, 7]. With the sampling intervals large enough, the PSD will be as narrow as possible, which performs like frequency hopping (FH). What's more, it will be proved that for such kind of FH/BFSK signal sampled by these two sampling methods, the probability of error will becomes lower with independent multitone interference added. This property has great advantage in the security of Big Data collection and transmission when the communication system is attacked by jamming. This offers a new secure transmission method for Big Data.

The rest of this paper is organized as follows. A brief overview of nested sparse sampling and co-prime sampling is given in Sects. 2 and 3 separately. In Sect. 4, the FH/BFSK communication system with independent multitone interference is introduced. Numerical results for the PSD of nested sampling and coprime sampling are detailed in Sect. 5. The error probability performance of FH/BFSK in Rician fading channel with independent multitone interference is shown in Sect. 6. Conclusions are presented in Sect. 7.

2 Nested Sampling

The nested array was first introduced as an effective approach of array processing with enhanced degrees of freedom in [5, 8]. The nested array [4] has two uniform levels of sampling density, with the level 1 samples at the N_1 locations and the level 2 samples at the N_2 locations.

$$1 \le l \le N_1, \text{ for level 1}$$
$$(N_1 + 1)m, 1 \le m \le N_2, \text{ for level 2}$$

Using nested array structure, with sparse samples, the difference-co-array $k = (N_1 + 1)m - l$ could obtain the degrees of freedom as

$$2[(N_1 + 1)N_2 - 1] + 1 = 2(N_1 + 1)N_2 - 1 \tag{1}$$

Based on the principle above, nested sampling could be achieved as shown in Fig. 1. Two levels of sampler are involved, with N_1 level-1 samples and N_2 level-2 samples in each period, with a period of $(N_1 + 1)N_2$. It is obvious that the samples obtained from nested sampling are very sparse compared with Nyquist sampling.

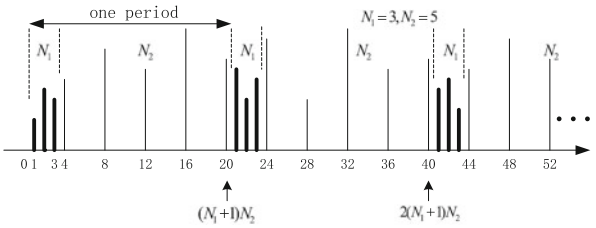

Fig. 1 Nested sampling with $N_1 = 3, N_2 = 5$

Consider the product $x(n_1)x^*(n_2)$ for the samples obtained from nested sampler, with n_1 and n_2 belong to the first period in Fig. 1, the difference-co-array $k = (N_1 + 1)m - l$ at the following locations could be obtained,

$$1, 2, \ldots, N_1, (N_1 + 1), 2(N_1 + 1), \cdots, N_2(N_1 + 1) \tag{2}$$

Although the signal is sampled sparsely and non-uniformly at $1 \leq l \leq N_1$ and $(N_1 + 1)m$,$1 \leq m \leq N_2$ for each period, the signal's autocorrelation $R_c(\tau)$ could be estimated at all lags $\tau = k$, which means that the original signal's second-order statistical property is kept using nested sampling.

The autocorrelation samples for all k could be calculated [4] by averaging the products $x(n_1)x^*(n_2)$ over L periods,

$$\hat{R}(k) = \frac{1}{L}\sum_{l=0}^{L-1} x(n)x^*(n-k) \tag{3}$$

3 Coprime Sampling

Different from nested sampling, coprime sampling has two sets of uniformly samplers as shown in Fig. 2.

Coprime sampler uniformly samples $x_c(t)$ using two sparse samplers, with sample spacing PT and QT respectively, where P and Q are coprime integers.

$$x(n) = x_c(nT) \tag{4}$$

Consider the product

$$x(Pn_1)x^*(Qn_2) \tag{5}$$

where $x(Pn_1)$ and $x(Qn_2)$ comes from the first and the second sampler. Set the difference as

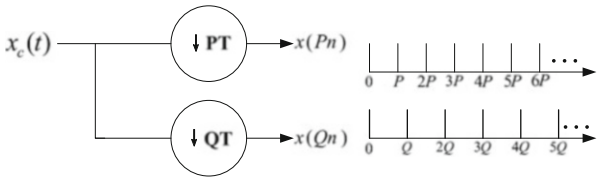

Fig. 2 Co-Prime sampling in the time domain

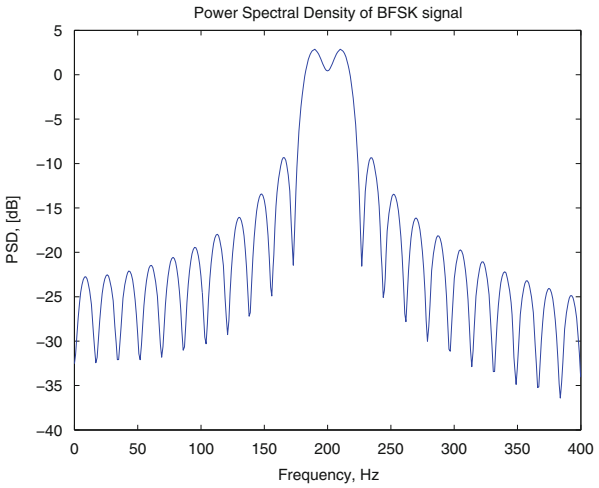

Fig. 3 original PSD calculated for BFSK signal

$$k = Pn_1 - Qn_2 \tag{6}$$

The authors in [4] have proved that the difference k can achieve any integer value in the range $0 \le k \le PQ - 1$, if n_1 and n_2 satisfy $0 \le n_1 \le 2Q - 1$ and $0 \le n_2 \le P - 1$.

Since $k = P(n_1 + Ql) - Q(n_2 + Pl)$ for any l, the estimate of autocorrelation $R(k)$ could also be obtained by averaging l,

$$\hat{R}(k) = \frac{1}{L} \sum_{l=0}^{L-1} x(P(n_1 + Ql))x^*(Q(n_2 + Pl)) \tag{7}$$

4 FH/BFSK with Independent Multitone Interference

The signal is BFSK signal with central frequency $\omega_o = 200$ Hz, and frequency offset $\Omega = 10$ Hz. $\sqrt{2P} = 1$, so that $P = 1/2$. The PSD of this BFSK signal is as shown in Fig. 3.

It is assumed that there are totally N_S nonoverlapping FH bands in the FH/BFSK communication system [9, 10]. Each FH band occupies B_h bandwidth. There are two orthogonal signaling tones in each FH band. Each two signal tones in each FH band are orthogonal to the signaling tones in all other FH bands. There are totally $2 \times N_S$ possible transmitted signaling tones.

The PSD of Additive White Gaussian Noise (AWGN) that corrupt the channel is defined as $N_0/2$. The independent multitione interference tones have a total power of P_{JT}, which is transmitted in the total of q equal power independent interfering tones and is spread uniformly over the spread spectrum bandwidth of the FH/BFSK communication system. The power for each interfering tone is $P_J = P_{JT}/q$. The independent multiple interfering tones are transmitted at the frequencies exactly corresponding to the possible $2 \times N$ signaling tones, and none of them are transmitted at the same frequency.

5 Numerical Results

As proved in [7], with the increase of sampling spacing pairs, besides the mainlobe of the PSD becomes narrower, the central of the PSD gets higher for both nested sampling and coprime sampling, which results in an efficient spectrum usage. It is also observed that with the same sampling spacings chosen for both nested sampling and coprime sampling, i.e., $N_1 = P$, $N_2 = Q$, $N = (N_1 + 1)N_2$ for nested sampling will be greater than $N = PQ$ for coprime sampling. If the sampling spacing pairs become higher, the mainlobe of PSD will becomes much narrower, and the bandwidth will be much smaller. When the sampling spacings pairs are great enough, the bandwidth occupied will become as narrow as possible, which performs like frequency hopping. The following BFSK results will show this performance for nested sampling as shown in Fig. 4 and coprime sampling as shown in Fig. 5. Besides the narrower bandwidth, as analyzed, the PSD is higher with the increase of the sampling spacing pairs.

6 Error Probability Analysis

The probability of error performance for FH/BFSK with independent multitone interference was discussed in [9]. From formula (34) in [9], the probability of error for FH/BFSK system with independent multitone interference could be calculated,

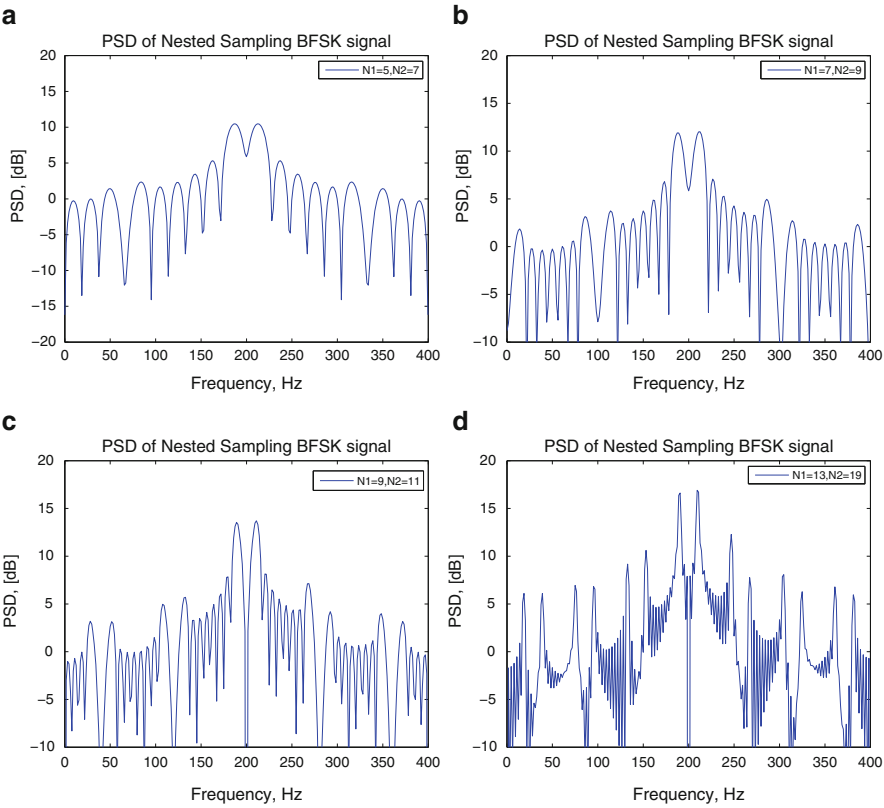

Fig. 4 Nested sampling BFSK with different N1 & N2 pairs. (**a**) Nested sampling (N1 = 5, N2 = 7), (**b**) Nested sampling (N1 = 7, N2 = 9), (**c**) Nested sampling (N1 = 9, N2 = 11), (**d**) Nested sampling (N1 = 13, N2 = 19)

$$
\begin{aligned}
P_b = {} & \frac{q}{2N_S}\left(1-\frac{q-1}{2N_S-1}\right)P_b(\textit{hop jammed} \mid 1\ \textit{jamming tone}) \\
& + \frac{q}{2N_S}\left(\frac{q-1}{2N_S-1}\right)P_b(\textit{hop jammed} \mid 2\ \textit{jamming tones}) \\
& + \left(1-\frac{q}{2N_S}\right)\left(1-\frac{q}{2N_S-1}\right)P_b(\textit{hop not jammed})
\end{aligned} \tag{8}
$$

where q is the total number of independent interference tones, and N_S is the total number of nonoverlapping FH bands [12, 13].

The Rician Fading Factor K is set to 10 dB, i.e., $K = 10$ dB. The error probability vs. SJR (Signal-to-Jamming-Ratio), $SJR = P_S/P_{JT}$ could be calculated following the procedure described in [10] and [11], where P_S is the average information signal power, and P_{JT} is the total average power of interference.

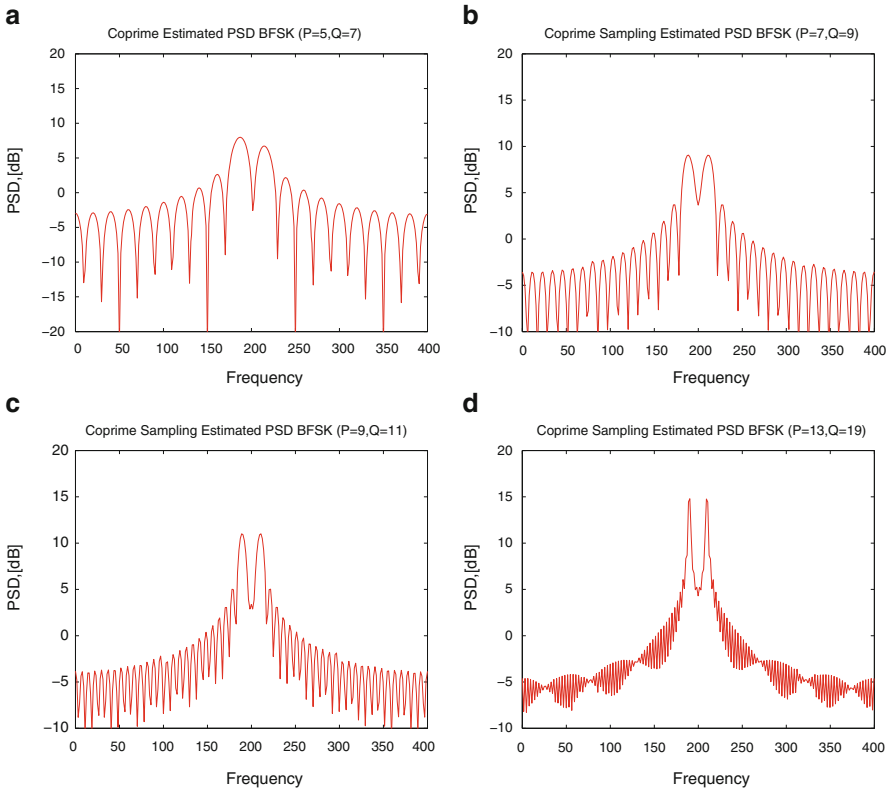

Fig. 5 Co-prime sampling BFSK with different P & Q pairs. (**a**) Coprime sampling (P = 5, Q = 7), (**b**) Coprime sampling (P = 7, Q = 9), (**c**) Coprime sampling (P = 9, Q = 11), (**d**) Coprime sampling (P = 13, Q = 19)

As discussed above, both nested sampling and coprime sampling could enhance the PSD of the signal, which means that they could increase Signal to Noise Ratio (SNR) for the same signal bandwidth and noise power. From the results in Sect. 5, the corresponding probability of error for FH/BFSK signal with nocoherent detection in Rician fading channel $K = 10$ dB with $q = 100$ independent multitone jamming in $N_S = 1{,}000$ frequency hops could be achieved.

Figure 6a,b show the results for nested sampling and coprime sampling separately. With the sampling spacing pairs increasing, i.e., N_1 and N_2 for nested sampling, and P and Q for coprime sampling, it can observed that the probability of error gets lower. It is also obvious that nested sampling could get lower probability of error compared with coprime sampling for the same sampling spacing pairs.

In Fig. 6a, with the same probability of error, for example, $P_b = 4 \times 10^{-3}$, for nested sampling case, when $N_1 = 5, N_2 = 7$, it has about 7 dB gain compared with the original FH/BFSK signal. When $N_1 = 7, N_2 = 9$, it has about 2.5 dB gain

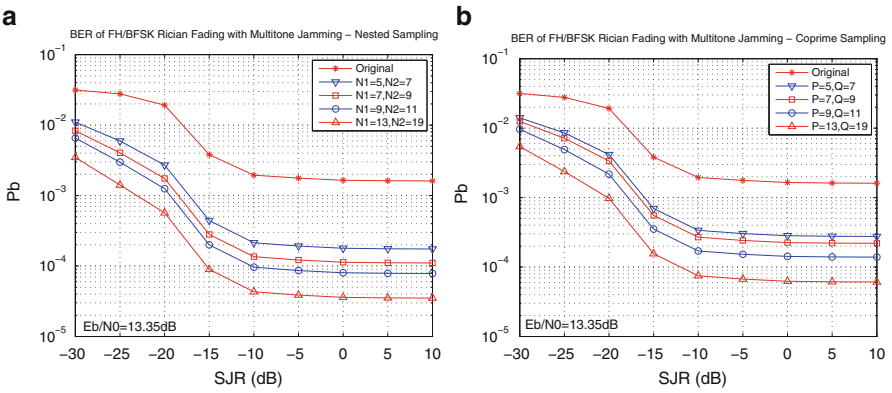

Fig. 6 BER of FH/BFSK Rician fading with multitone jamming, with Rician fading factor $K =$ 10 dB, total number of jammings q = 100, frequency hops $N_S = 1{,}000$, and $E_b/N_0 = 13.35$ dB. (**a**) Nested sampling, (**b**) Coprime sampling

compared with the case when $N_1 = 5, N_2 = 7$. Similarly, when $N_1 = 9, N_2 = 11$ has almost 2 dB gain compared with the case when $N_1 = 7, N_2 = 9$, and when $N_1 = 13, N_2 = 19$, it has about 3 dB gain compared with $N_1 = 9, N_2 = 11$. Similarly, the advantage of coprime sampling with independent multitone interference is shown in Fig. 6.

7 Conclusions

There are critical requirements for security in Big Data collection and transmission of Big Data through a communication network. A new secure transmission for Big Data based on nested sampling and co-prime sampling is proposed in this paper. With nested sampling and coprime sampling, Big Data could also achieve higher PSD for BFSK signal. When the sampling spacing pairs bigger enough, the spectrum of BFSK signal performs like frequency hopping. With the same independent multitone interfering signal added to FH/BFSK system, the error probability becomes much lower using nested sampling and coprime sampling compared with the original FH/BFSK signal. This property has great advantage in the security of Big Data collection and transmission using FH/BFSK based on nested sampling and coprime sampling.

Acknowledgements This work was supported in part by U.S. Office of Naval Research under Grants N00014-13-1-0043, N00014-11-1-0071, N00014-11-1-0865, and U.S. National Science Foundation under Grants CNS-1247848, CNS-1116749, CNS-0964713.

References

1. David Bollier, Firestone CM (2010) The promise and peril of big data. The Aspen Institute, Washington, DC, USA
2. Labrinidis A, Jagadish HV (2012) Challenges and opportunities with big data. Proceedings of the VLDB Endowment 5(12), 2032–2033
3. Pal P, Vaidyanathan PP (2011) Coprime sampling and the MUSIC algorithm. In: IEEE Digital signal processing workshop and IEEE signal processing education workshop (DSP/SPE), pp 289–294, Jan 2011
4. Vaidyanathan PP, Pal P (2011) Sparse sensing with co-prime samplers and arrays. IEEE T Signal Process 59(2):573–586
5. Pal P, Vaidyanathan PP (2010) A novel array structure for directions-of-arrival estimation with increased degrees of freedom. In: IEEE International Conference on Acoustics Speech and Signal Processing (ICASSP), pp 2606–2609
6. Chen J, Liang Q, Wang J, and Choi H.-A (2012) Spectrum efficiency of nested sparse sampling. In: Wireless algorithms, systems, and applications. Springer, Berlin, pp 574–583
7. Chen J, Liang Q, Zhang B, Wu X (2013) Spectrum efficiency of nested sparse sampling and coprime sampling. EURASIP J Wireless Comm Netw 2013(1):47
8. Pal P, Vaidyanathan PP (2010) Nested arrays: a novel approach to array processing with enhanced degrees of freedom. IEEE T Signal Process 58(8):4167–4181
9. Robertson RC, Sheltry JF (1996) Multiple tone interference of frequency-hopped noncoherent MFSK signals transmitted over Ricean fading channels. IEEE T Comm 44(7):867–875
10. Tjhung TT, Chai CC (1999) Multitone jamming of FH/BFSK in Rician channels. IEEE T Comm 47(7):974–978
11. Yu Z, Tjhung TT, Chai CC (2001) Independent multitone jamming of FH/MFSK in Rician channels. IEEE T Comm 49(11):2006–2015
12. Lindsey WC (1964) Error probabilities for Rician fading multichannel reception of binary and n-ary signals. IEEE T Inform Theory 10(4):339–350
13. Kirachaiwanich D, Liang Q (2011) The combined-jamming model for IEEE 802.11 FH/MFSK networks. Eur T Telecomm 22(1):14–24

Sparse Channel Estimation Using Overcomplete Dictionaries in OFDM Systems

Fei Zhou and Jing Tan

Abstract With the in-depth study of the wireless channel, more and more experimental evidence show that many wireless channels are sparse in the conditions of large bandwidth and long signaling durations. Thus, Compressed Sensing theory applied for sparse channel estimation can reduce the number of pilots, so as to increase spectral efficiency. However, the non-integer times of sampling period about the time-delay or Doppler frequency shift will lead to the energy leakage, and reduce the time delay-Doppler sparsity of the equivalent channel, thus affect the accuracy of channel estimation. In this paper, we utilize over-complete dictionaries based on super resolution to enhance the sparsity of the equivalent channel. Simulation results demonstrate that the overcomplete dictionary representation of the double-selective channel is much sparser than the classical delay-Doppler representation. The method proposed in this paper can effectively improve the performance of sparse reconstruction algorithms, and then obtain the better precision of channel estimation.

Keywords Channel estimation • Compressed sensing • OFDM • Over-complete dictionaries

1 Introduction

The multipath-effect and Doppler-effect in the wireless channel cause the signal time and frequency selective fading, which are the main factors to signal distortion. In Orthogonal Frequency Division Multiplexing (OFDM) Systems, the conventional training-based estimation methods of double-selection channels are assumed that channel has rich multipath, so a lot of pilot signal are utilized to obtain the

F. Zhou (✉) • J. Tan
Chongqing Key Lab of Mobile Communications Technology, Chongqing University of Posts and Telecommunications, Chongqing 400065, P R China
e-mail: zhoufei@cqupt.edu.cn

B. Zhang et al. (eds.), *The Proceedings of the Second International Conference on Communications, Signal Processing, and Systems*, Lecture Notes in Electrical Engineering 246, DOI 10.1007/978-3-319-00536-2_85,

accurate channel state information. However, it greatly reduces the utilization of spectrum resources. In fact, in wideband mobile communication, the physical multipath channel usually has a small amount significantly path. Especially, under the condition of wide bandwidth or long signal duration, most channel energy is only concentrated in a small area in time-delay and Doppler domain, so the channel can be characterized as sparse.

Taking advantage of inherent sparsity of the wireless channel, Compressed Sensing (CS) [1, 2] theory is first applied for channel estimation by Bajwa [3] and Taubock [4] et al. CS theory suggests that if the signal is sparse in certain domain, it can be accurately reconstructed by a small amount of sampling signal with a high probability [2]. Therefore, due to the inherent channel sparsity, CS-based channel estimation can greatly reduce the number of pilots, and improve the utilization rate of spectrum resource. However, the cannel estimation techniques presented in [3, 5] limits themselves to the sparsity in the delay domain only and fails to take into account the Doppler sparsity. Then, a number of authors have addressed the problem in doubly-selective channels. They focused on channels which are sparse in delay-Doppler domain [4, 6–8]. In [7], it is shown experimentally for underwater acoustic channels that CS-based channel estimation outperforms traditional algorithms (ESPRIT and root-MUSIC). Taubock found that the energy leakage caused by the non-integer times of sampling period of time-delay or Doppler obviously deteriorates channel's sparsity that limits the performance of CS-based channel estimation method of [4]. Later, he proposed an iterative basis optimization procedure that aims to maximize sparsity [8]. Though the method in [8] achieves a significant performance gains, its basis optimization has to be performed before the start of data transmission which adds additional complexity. Aimed at the decrease sparsity of the channel, we use a high resolution over-complete dictionary to improve the performance of channel estimation, and the dictionary just adds the operation time of sparse reconstruction algorithms since to the increase of basis. We find that the over-complete dictionary representation of channel is much sparser than the classical delay-Doppler representation used in other works.

The rest of this paper is organized as follows. Section 2 introduces the OFDM system model. Section 3 analyzes the sparsity of the channel's delay-Doppler representation and dictionary representation, and presents the CS-based channel estimation method. In Sect. 4 we present numerical results. Finally, Sect. 5 concludes the paper.

2 OFDM System Model

A generalized cyclic prefix (CP) OFDM transmission signal is given by

$$x(t) = \frac{1}{\sqrt{K}} \sum_{l=0}^{L-1} \sum_{k=0}^{K-1} x_{l,k} e^{j2\pi k(t-lT)/T_0} g(t - lT) \tag{1}$$

where T_0 and T denote the OFDM symbol duration and the CP-OFDM block duration, respectively. $T_{CP} = T - T_0$ is the guard interval for the CP which is used to avoid the inter symbol interference (ISI). K is the total number of subcarriers and L is the number of transmitted symbol periods, and $B = K/T_0$ is the bandwidth. $x_{l,k}$ denotes the l - th symbol transmitted at subcarrier k. $g(t)$ is 1 on [0,T] and 0 otherwise.

According to the WSSUS model, the time-varying multipath channel is expressed as [9]

$$h(t, \tau) = \sum_{q=1}^{N_q} \eta_q \delta\big(\tau - \tau_q\big) e^{j2\pi v_q t} \tag{2}$$

where N_q is the number of multipath components, η_q, τ_q, v_q are the attenuation coefficient, the delay and the Doppler shift of path q - th, respectively. δ denotes the Dirac-delta function.

Then the received signal is

$$r(t) = \sum_{q=1}^{P} \eta_q x\big(t - \tau_q\big) e^{j2\pi v_q t} + z(t) \tag{3}$$

where $z(t)$ is the zero-mean, white Gaussians noise with power σ_z^2. Assuming that the receiver has been synchronization, then the demodulated symbols can be written as

$$\begin{aligned} r_{l,k} &= \int r(t)\gamma(t - lT) e^{j2\pi k(t-lT)/T_0} dt \\ &= H_{l,k} x_{l,k} + z_{l,k} \end{aligned} \tag{4}$$

for $l = 0, \cdots, L - 1$ and $k = 0, \cdots, K - 1$, $z_{l,k}$ is equivalent noise term, and $\gamma(t)$ is 1 on [T_{CP},T] and 0 otherwise. And the equivalent baseband channel frequency response $H_{l,k}$ is

$$H_{l,k} = \sum_{q=1}^{P} A_q e^{-j2\pi k\tau_q/T_0} e^{j2\pi v_q lT} \tag{5}$$

where $A_q = \big(\eta_q e^{j2\pi v_q(2T_{CP}+T_0)} \sin c\big(v_q T_0\big)\big)$.

Let $p_{l,k}$ denotes the pilot symbols, $\mathcal{P}$ is the pilot set, $(l,k) \in \mathcal{P}$. According to (4), estimation of the channel frequency response $H_{l,k}$ can be calculated by

$$\hat{H}_{l,k} = \frac{r_{l,k}}{p_{l,k}} = H_{l,k} + \tilde{z}_{l,k} \tag{6}$$

with $\tilde{z}_{l,k} = z_{l,k}/p_{l,k}$.

3 Sparse Channel Estimation Using a Dictionary

3.1 Delay-Doppler Sparsity

The equivalent channel model (5) is difficult to analyze due to a potentially large number of physical parameters $\{(\eta_q,\tau_q,v_q)\}$. Usually, we approximate it by the basis expansion model (BEM) [9]. In this BEM, delay and Doppler are uniformly sampled at a resolution commensurate with $\Delta\tau = T_s$ and $\Delta v = 1/NLT_s$ respectively, where $T_s = T_0/K$ is the baseband sampling. Taking the discrete Fourier transform (DFT) of $H_{l,k}$, we obtain the discrete-delay-Doppler spreading function

$$\begin{aligned} S[m,i] &= \sum_{l=0}^{L-1}\sum_{k=0}^{K-1} H_{l,k} e^{-j2\pi ki/L} e^{j2\pi km/K} \\ &= \sum_{q=1}^{P} A_q \times K \times e^{j2\left(m-K\tau_q/T_0\right)\frac{K-1}{K}} dir_K\left(m-\frac{K\tau_q}{T_0}\right) \times L \times e^{-j2\pi\left(i-v_qLT\right)\frac{L-1}{L}} dir_L\left(i-v_qLT\right) \end{aligned} \tag{7}$$

where $dir_N(x) = \sin(x)/(N\sin(x/N))$.

In view of (7), $S[m,i]$ would reduce to simple Dirac-deltas if τ_q/T_s and v_qLT are integers, since both $dir_L(\pi(i - v_qT))$ and $dir_K(\pi(m - \tau_q/T_s))$ vanish at all integers except zero, where they are one. In other cases, $S[m,i]$ will have non-zero entries for all m and i with decreasing intensity due to the decay of $dir_N(x)$. Since the tail decays slowly, there still have a lot of coefficients should not be neglected, which seriously reduce the delay-Doppler sparsity.

3.2 Dictionary Sparsity

From the analysis in above section, we find that although the delay-Doppler representation can capture the full channel effect, it has a weak sparseness that limits the performance of CS-based channel estimation. In order to achieve a more sparse channel representation, we use an overcomplete basis which we often refer to as dictionary.

Writing (5) in vector form, we have

$$\mathbf{h}_{\Delta} = \sum_{q=1}^{N_q} A_q w(\tau_q, v_q) \tag{8}$$

where $[\mathbf{h}_{\Delta}]_{kL+l} = H_{l,k}$ and $w(\tau_q, v_q)_{kL+l} = e^{-j2\pi\left(k\tau_q/T_0 - v_q lT\right)}$.

Due to the random values of delay and Doppler shift in $[0,\tau_{\max}]$ and $[-v_{\max}/2, v_{\max}/2]$, respectively, a finite basis cannot contain all possible values of τ_q or v_q. So as to approximate the equivalent channel frequency response, we choose a redundant basis generated by delay and Doppler shift at a finer grained resolution of T_s/λ and $1/\lambda NLT_s$, respectively. Here, λ is the multiple of the baseband sampling time. So we choose representative sets of (τ,v) as

$$\begin{aligned} \tau_p &\in \{0, T_s/\lambda, 2T_s/\lambda, \cdots, DT_s/\lambda\} \\ v_p &\in \{-F/\lambda NLT_s, \cdots, (F-1)/\lambda NLT_s\} \end{aligned} \tag{9}$$

leading to $D = \lceil \lambda\tau_{\max}/T_s \rceil + 1$ delays and $F = \lceil \lambda v_{\max} T/2 \rceil$ Doppler shifts. Hence, the dictionary can be designed as

$$[\mathbf{U}]_{kL+l,(i+F)D+m} = w[m,i]_{l,k} = e^{-j2\pi(km/\lambda K - li/\lambda L)} \tag{10}$$

for $i \in \{-F, \cdots, F-1\}$ and $m \in \{0, \cdots, D-1\}$. Especially, if $\lambda = 1$, the dictionary is equivalent to the 2D-Fourier transform basis used in the previous section. So $\mathbf{h}_{\Delta}$ is approximate by

$$\mathbf{h}_{\Delta} = \mathbf{U}\mathsf{g} \tag{11}$$

where $[\mathsf{g}]_{(i+F)D+m} = A_{m,i}, A_{m,i}$ corresponding to the dictionary columns. But most of entries of g are zeros since the channel is sparse.

We use sparse reconstruction algorithm to find S -approximation of the channel frequency response. In Fig. 1, we notice that with the increase of S, the Mean Square Error (MSE) $E\left[\left|\mathbf{h}_{\Delta} - \hat{\mathbf{h}}_S\right|^2\right]$ can reduce to 10^{-1}. This means that the S strongest channel taps concentrate about 90 % of the channel energy. Moreover, as the increase of λ, we need less channel taps to approximate the channel frequency response. For example, the number of channel taps needed by a overcomplete basis with $\lambda = 2$ is about half of that by baseband mode ($\lambda = 1$) to achieve a MSE of 0.5×10^{-1}, while it is much less by a overcomplete basis with $\lambda = 4$. In general, channel's dictionary representation is much sparse than delay-Doppler representation.

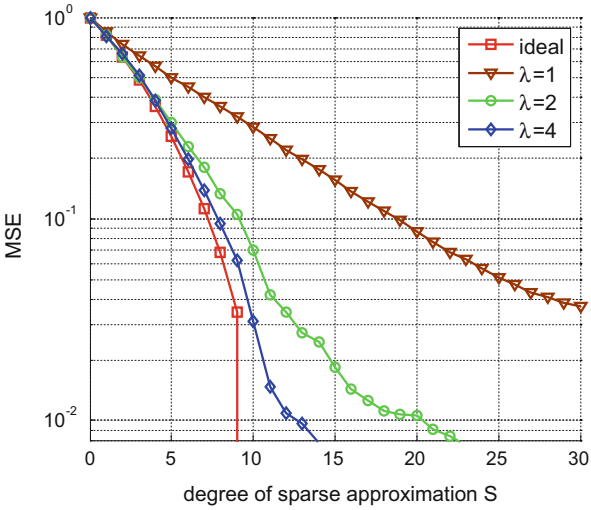

Fig. 1 Sparse approximation of frequency response

3.3 CS-Based Channel Estimation Based on an Overcomplete Dictionary

According to (6) and (11), the frequency response at pilots have arrived at the standard compressed sensing problem formulation,

$$\widetilde{\mathbf{h}}_{(p)} = \mathbf{h}_{\Delta}\big|_{(l,k)\in p} + \mathbf{z}_{(p)} = \mathbf{U}_{(p)}\mathsf{g} + \mathbf{z}_{(p)} \tag{12}$$

which is linear in the set of unknowns $\mathsf{g}\in\mathbb{C}^N$ and uses a measurement matrix $\mathbf{U}_{(p)} \in\mathbb{C}^{\mathcal{P}\times N}$ to explain the observations $\widetilde{\mathbf{h}}_{(p)}$.

So the CS-based channel estimation algorithm steps are as follows:

1. Calculate the channel estimations at pilot positions to obtain $\widetilde{\mathbf{h}}_{(p)}$ according to (6).
2. Run Orthogonal Matching Pursuit (OMP) [10] and/or Compressive Sampling Matching Pursuit (CoSaMP) [11] to obtain an estimation $\hat{\mathsf{g}}$ of g in (12), i.e., the estimation of $A_{m,i}$.
3. Calculate estimations of all the channel coefficients $H_{l,k}$ by equation (11).

4 Simulation Results

In this section we present numerical results to compare sparse channel estimation algorithms for OFDM. The CP-OFDM parameters are: $K = 256$, $T_0 = 51.2$ us, $T_{CP} = 12.8$ us, and $B = 5$MHz. The system employed a QPSK symbol alphabet.

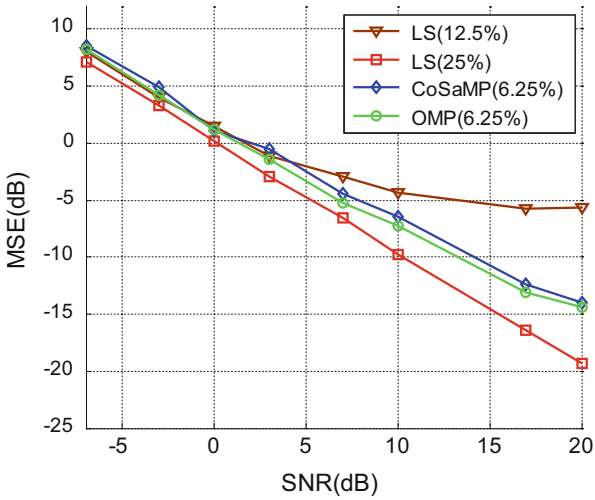

Fig. 2 Performance of CS-based and LS

During blocks of $L = 32$ transmitted OFDM symbols, we used the channel simulation tool IlmProp [12] based on geometrical structure of space to simulate doubly-selective fading channel. The noise $z_{l,k}$ was zero-mean complex white Gaussian with variance σ_z^2.

Simulation 1: this experiment mainly compared the CS-based channel estimation method with the least-squares (LS) channel estimation. Here, we measured the performance by the mean square error normalized by mean energy of the channel coefficients. For LS channel estimation, we used two different rectangular pilot constellations, i.e., selected uniformly 12.5 and 25 % of all symbols for pilots, respectively. For CS-based estimation, we selected randomly 6.25 % of all symbols for pilots. Figure 2 shows that OMP and CoSaMP algorithms with 6.25 % of resource outperform the LS algorithm with 12.5 % resources. In conclusion, the CS-based method effectively improves the resource utilization rate.

Simulation 2: this experiment mainly compared CS-based channel estimation methods based on different resolution dictionary. Figure 3 shows that by using the same pilots as simulation 1, CS-based channel estimation algorithms based on a dictionary with resolution $\lambda = 2$ outperform that with $\lambda = 1$. Especially in the low SNR range, the estimation performance yields an additional about 3 dB. This performance gain result from the sparsity improvement of channel.

Simulation 3: this experiment mainly analysis how the number of pilots effects the performance of CS-based channel estimation methods ($SNR = 10$dB). Figure 4 shows that with the increasing of the number of pilots, the performance is also increasing. On the other hand, to achieve the same performance, the higher the resolution is, the less resource the OMP and CoSaMP algorithm are required. For example, to insure the MSE under -8 dB, OMP ($\lambda = 2$) only needed about 5 % of resources, while OMP ($\lambda = 1$) required about 6.5% of resources.

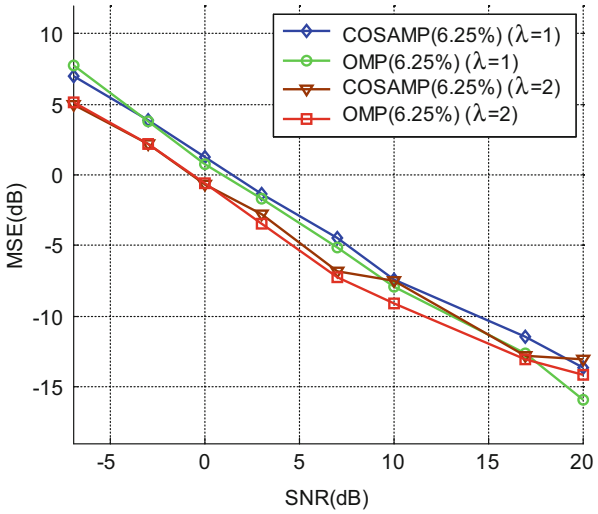

Fig. 3 Performance of CS-based channel estimation based on different resolution dictionary

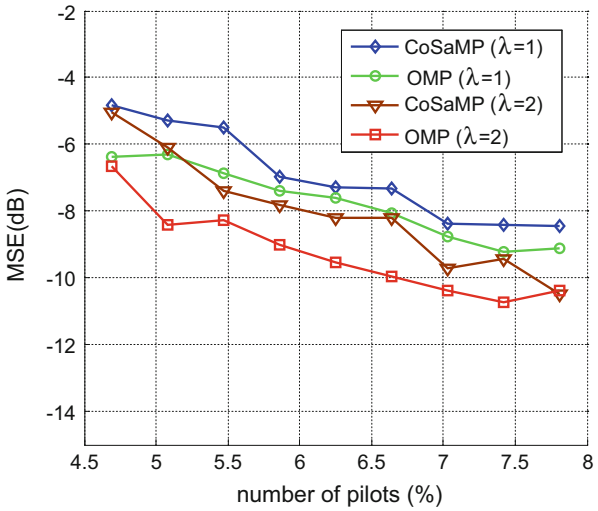

Fig. 4 Comparisons of OMP and CoSaMP under different resolution dictionary

5 Conclusion

In this paper, we considered sparse channel estimation algorithms for OFDM system. Simulations using a geometry-based channel simulator demonstrated that all sparse channel estimation algorithms significantly outperform the simple LS

estimator. Moreover, we showed that the overcomplete dictionary representation was much sparser than classical delay-Doppler representation, and then obtained the better precision of channel estimation.

Acknowledgments This work was supported by the special fund of Chongqing key laboratory (CSTC) and by the project of Chongqing Municipal Education Commission (Kjzh11206) and National Science and Technology Major Program (2011ZX03006-003 (7)) and by Fundamental and Frontier Research Project of Chongqing (cstc2013jcyjA40034).

Reference

1. Donoho DL (2006) Compressed sensing. IEEE Trans Inf Theory 52(4):1289–1306. doi:10.1109/TIT.2006.871582
2. Candes EJ et al (2006) Robust uncertainty principles: exact signal reconstruction from highly incomplete frequency information. IEEE Trans Inf Theory 52(2):489–509. doi:10.1109/TIT.2005.862083
3. Bajwa WU et al (2008) Compressed channel sensing. Information Sciences and Systems, 2008. CISS 2008. 42nd Annual Conference 42:5–10. doi:10.1109/CISS.2008.4558485. http://ieeexplore.ieee.org/xpls/abs_all.jsp?arnumber=4558485&tag=1
4. Taubŏck G, Hlawatsch F (2008) A compressed sensing technique for OFDM channel estimation in mobile environments: exploiting channel sparsity for reducing pilots. Acoustics, Speech and Signal Processing (ICASSP-08) 1:2885–2888. doi:10.1109/ICASSP.2008.4518252
5. Kang T, Iltis RA (2008) Iterative carrier frequency offset and channel estimation for underwater acoustic OFDM systems. IEEE J Select Areas Commun 26(9):1650–1661. doi:10.1109/JSAC.2008.081205
6. Bajwa WU et al (2010) Compressed channel sensing: a new approach to estimating sparse multipath channels. IEEE Proc 98(6):1058–1076. doi:10.1109/JPROC.2010.2042415
7. Berger CR (2010) Application of compressive sensing to sparse channel estimation. IEEE Commun Mag 48(11):164–174. doi:10.1109/MCOM.2010.5621984
8. Taubŏck G et al (2010) Compressive estimation of doubly selective channels in multicarrier systems: leakage effects and sparsity-enhancing processing. IEEE J Sel Top Sign Proces 4 (5):255–271. doi:10.1109/JSTSP.2010.2042410
9. Sayeed AM, Aazhang B (1999) Joint multipath-Doppler diversity in mobile wireless communications. IEEE Trans Commun 47:123–132. doi:10.1109/26.747819
10. Tropp JA, Gilbert AC (2007) Signal recovery from random measurements via orthogonal matching pursuit. IEEE Trans Inf Theory 53(12):267–288. doi:10.1109/TIT.2007.909108
11. Needell D, Tropp JA (2008) CoSaMP: iterative signal recovery from incomplete and inaccurate samples. App Comput Harmon An 26(3):301–321. doi:10.1016/j.acha.2008.07.002
12. Galdo GD; Haardt M (2003) IlmProp: a flexible geometry-based simulation environment for multiuser MIMO communications. COST 273 Temporary Documents, No. TD (03) 188. http://www.delgaldo.com/papers/delgaldo_COSTPrague.pdf. Accessed 14 Jun 2013

Amplify-and-Forward Relay Networks for Bit-Interleaved Space-Time Codes

Tao He and Susheel Kumar Chanda

Abstract This paper proposes a novel Amplify-and-Forward (AF) cooperative diversity scheme by employing the combination of bit-interleave coded modulation (BICM) and orthogonal space-time block coding (STC). The frame of the wireless network is described and the pairwise error probability (PEP) of AF protocol is derived. Based on the PEP, exact expressions of bit-error-rate (BER) are investigated over dissimilar Rayleigh fading channels. Numerical results corroborate the analysis and confirm the effectiveness of the proposed scheme.

Keywords Bit-interleave • Space-time coding • Amplify-and-forward • Bit-error-rate

1 Introduction

Cooperative communication is a new paradigm that draws from the ideas of using the broadcast nature of the wireless channels to make communicating nodes help each other. In [1], two cooperative protocols were proposed: amplify-and-forward and decode-and-forward (DF). In this paper, we consider the AF strategy, where the relays only need to transmit a scaled version of the signal received from the source, which significantly simplifies the implementation. The performance of cooperative AF relay networks has been widely studied in the literature, e.g. [2, 3].

Very recently, Bit-interleaved coded modulation [4], which is a bandwidth-efficient technique for fading channels, have been begun to be studied with

T. He (✉)
School of Aeronautics and Astronautics, The University of Electronic and Science Technology of China, Chengdu, Sichuan, China
e-mail: hetao@uestc.edu.cn

S.K. Chanda
School of ECE, Utah State University, Logan, UT, USA
e-mail: Susheel.2k7@gmail.com

B. Zhang et al. (eds.), *The Proceedings of the Second International Conference on Communications, Signal Processing, and Systems*, Lecture Notes in Electrical Engineering 246, DOI 10.1007/978-3-319-00536-2_86,

cooperative techniques. The ref. [5] derived the asymptotic bit error rate (BER) bounds of the cooperative system with the serial concatenated BICM over Additive White Gaussian Noise (AWGN) channels and Rayleigh fading channels. Meanwhile, Babarossa [6] explored the application of space-time code [7] to cooperative diversity. In [8], the GABBA codes were employed to design a practical distributed space-time codes for wireless relay networks using the amplify-and-forward scheme. To obtain both space and time diversity, concatenated BICM and ST codes (BI-STC) is extensively used for the point to point transmission [9]. BI-STC can provide robust performance under wide variety of fading conditions [10]. However, the using of BI-STC in relay networks has not been investigated thoroughly in existing literatures.

In this paper, we consider the analysis and design of AF cooperative relaying BI-STC scheme (BI-STC-AF). Our main contribution can be described as follows. Firstly, we design the AF relay networks based on the BI-STC technique. Secondly, we derive a closed-form expression for of the bit error rate (BER) of the proposed cooperative diversity scheme, which is important to evaluate the system performance and can be used to develop guidelines for modulation constellation selection, space-time code design and relay selection, etc. Simulation results confirm the validity of the derived analytical results and show the effectiveness of the proposed scheme.

2 System Models

As is shown in Fig. 1, we consider a cooperative relaying scheme with one source, n relays and one destination. The channels between the source and the relay nodes, between the relays nodes and the destination, and the direct path are assumed to be Rayleigh flat fading and independent from each other. The channel coefficients are modeled as independent complex Gaussian random variables with zero mean and variances $\rho_{i,j}^2$ ($i \in \{S,R\}$, $j \in \{R,D\}$). The additive noises are zero mean and have variance N_0.

The information bit s is first encoded by a convolutional code of rate $R_c = k_c/n_c$. Then, the encoder output is bit-interleaved and each $K = mq$ bits of the interleaved sequence are grouped as a channel symbol. The modulator maps each symbol to a complex-valued signal chosen from a 2^m -ary constellation χ according to the labeling map μ with average symbol energy equal to E_s. The space-time block encoder take the constellation signals to form an $L \times n$ ST codeword matrix $\mathbf{X}_t = [x_l^i]$, where L is the number of the time slots for transmitting one ST codeword. x_l^i, $1 \leq i \leq n$, $1 \leq l \leq L$ is the transmitted signal from the i^{th} antenna at time l.

The source broadcasts the packet to all relays. The received signal at relays are given by

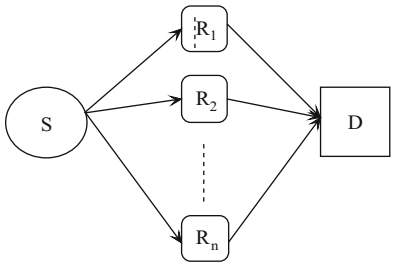

Fig. 1 A cooperative relaying network

$$y_{s,r_j} = \sqrt{P_1} h_{s,r_j} v^p + n_{s,r_j}, \tag{1}$$

where $j = 1, 2, \cdots, n$, P_1 is the source transmit power and n_{s,r_j} is noise at the j^{th} relay.

Upon receiving y_{s,r_j}, each relay will normalize the received signal by the factor $\beta \triangleq \sqrt{(P_2/n)/\left(P_1 \rho_{s,r}^2 + N_0\right)}$ to satisfy a long-term power constraint before forwarding it to the destination in phase 2 P_2 is the power of relays. The $n \times 1$ received vector data vector from the relay nodes at the destination node can be modeled as

$$\mathbf{y}_d = \beta \mathbf{X}_r \mathbf{H} + \mathbf{n}_d, \tag{2}$$

where $\mathbf{H} = [h_{s,r_1} h_{r_1,d}, \cdots, h_{s,r_n} h_{r_n,d}]^T$ and $\mathbf{X}_r = [\mathbf{A_1 s}, \cdots, \mathbf{A_n s}]$ plays the role of the Space-Time codeword. $\mathbf{n}_d$ is the noise vector.

At the receiver of the destination, the STB decoders first apply the MAP decoding algorithm to decode the signals received from the different relays. After that, the LLR for the i^{th} bit of the considered label is evaluated and are de-interleaved before being passed to the decoder.

3 BER Performance Analysis

Assuming ideal interleaving, the BICM union bound of the probability of bit error is given by [4]

$$p_b \leq \frac{1}{k_c} \sum_{d=d_f}^{\infty} W_I(d) f\left(d, \mu, \chi\right), \tag{3}$$

where d_f is the minimum Hamming distance of the convolution code and $W_I(d)$ is the total input weight of error events at Hamming distance d. $f(d,\mu,\chi)$ depends only

on the Hamming distance d, the mapping rule μ, and the signal constellation χ.For BI-STC, the union bound of the $f(d,\mu,\chi)$ can be upper-bounded using the Cherbnoff technique

$$f_{ub}(d,\mu,\chi) \le \left[\frac{1}{K2^K}\sum_{k=1}^{K}\sum_{b=0}^{1}\sum_{X\in\chi_b^k}\sum_{Z\in\chi\overline{b}^k}\min_s \Phi_{\Delta(\mathbf{X},\mathbf{Z})}(s)\right]^d, \tag{4}$$

where $\mathbf{X}$ and $\mathbf{Z}$ are the transmitted and erroneously decoded signals, respectively. $\Phi_{\Delta(\mathbf{X},\mathbf{Z})}(s)$ is the Laplace transform of the pdf of the metric difference $\Delta(\mathbf{X},\mathbf{Z})$. To evaluate (4), the key is to evaluate $\min_s \Phi_{\Delta(\mathbf{X},\mathbf{Z})}(s)$, which can be replaced by the PEP of space coding in a BI-STC system [11].

For simplicity, symmetry is assumed between all relays, i.e., $\rho_{s,r_m}^2 = \rho_{s,r}^2$, $\rho_{r_m,d}^2 = \rho_{r,d}^2$ for all $m \in \{1, \cdots, n\}$.

The conditional PEP for a certain channel realization can be given by

$$P\left(\mathbf{X}\to\mathbf{Z}\middle|\mathbf{H}\right) = Q\left(\frac{\beta}{\sqrt{2}}\|(\mathbf{X}-\mathbf{Z})\mathbf{H}\|\right). \tag{5}$$

Using the Craig expression, (5) can be written as

$$P\left(\mathbf{X}\to\mathbf{Z}\middle|\mathbf{H}\right) = \frac{1}{\pi}\int_0^{\pi/2}\exp\left(-\frac{\beta^2\|(\mathbf{X}-\mathbf{Z})\mathbf{H}\|^2}{4\sin^2\theta}\right)d\theta. \tag{6}$$

Defining a matrix Γ as $\Gamma \triangleq (\mathbf{X}-\mathbf{Z})^{\mathrm{H}}(\mathbf{X}-\mathbf{Z})$, a constant C as $C \triangleq \frac{P_1P_2\rho_{s,r}^2}{4nN_0\left(P_1\rho_{s,r}^2+P_2\rho_{r,d}^2+N_0\right)}$, where P_1 and P_2 are the power at source and relays, respectively. Defining another matrix Ω as $\Omega \triangleq C\Gamma\mathrm{diag}\left(|h_{r_1,d}|^2, \mathrm{L}, |h_{r_n,d}|^2\right)$, by taking the expectation in (6) over the source-to-relay channel coefficients, we get

$$\begin{aligned} P(\mathbf{X}\to\mathbf{Z}) &= \frac{1}{\pi}\int_0^{\pi/2} E_{\left[h_{r_1,d},\mathrm{L},h_{r_n,d}\right]}\left[1/\prod_{i=1}^{n}\left(1+\frac{\beta^2}{4\sin^2\theta}\lambda_{\Omega_i}\right)\right]d\theta \\ &\le \frac{1}{2}E_{\left[h_{r_1,d},\mathrm{L},h_{r_n,d}\right]}\left[1/\prod_{i=1}^{n}\left(1+\frac{\beta^2}{4}\lambda_{\Omega_i}\right)\right] \simeq \frac{1}{2}E_{\left[h_{r_1,d},\mathrm{L},h_{r_n,d}\right]}\left[1/\prod_{i=1}^{n}\frac{\beta^2}{4}\lambda_{\Omega_i}\right] \\ &= \frac{\beta^{2n}}{4^{n+\frac{1}{2}}}E_{\left[h_{r_1,d},\mathrm{L},h_{r_n,d}\right]}\left[1/\prod_{i=1}^{n}\lambda_{\Omega_i}\right], \end{aligned} \tag{7}$$

where λ_{Ω_i} is the i^{th} eigenvalue of matrix Ω. Since the determinant of a matrix is equal to the product of the matrix eigenvalues, and the determinant of the product of

the multiplication of two matrices is equal to the product of the individual matrices' determinants, we can write

$$\prod_{i=1}^{n}\lambda_{\Omega_i}=\prod_{i=1}^{n}C\lambda_i\prod_{i=1}^{n}|h_{r_i,d}|^2, \tag{8}$$

where λ_i is the i^{th} eigenvalue of Γ. Averaging the expression in (8) over the exponential distribution of $|h_{r_i,d}|^2$ gives

$$P(\mathbf{X}\to\mathbf{Z})=\frac{\beta^{2n}C^{-n}}{4^{n+\frac{1}{2}}}\left(1/\prod_{i=1}^{n}\lambda_i\right)\sum_{i=0}^{n}\binom{n}{i}2^i{}_2F_1\left(2n,2n+2+i;4n-1;\frac{1}{2}\right)\lambda_i, \tag{9}$$

where ${}_2F_1(x)$ is the hyper geometric function. At high SNR, (9) can be written as

$$\begin{aligned}P(\mathbf{X}\to\mathbf{Z})&\simeq\frac{1}{2}\left(\frac{\alpha^2\rho_{s,r}^3}{\alpha\rho_{s,r}^2+(1-\alpha)\rho_{r,d}^2}\right)^{-n}SNR^{-n}\\&\times\left(1/\prod_{i=1}^{n}\lambda_i\right)\sum_{i=0}^{n}(n,i)2^i{}_2F_1\left(2n,2n+2+i;4n-1;\frac{1}{2}\right)\lambda_i\triangleq\frac{1}{2}(\alpha_{AF})^{-n}g(\lambda_i)SNR^{-n}\end{aligned} \tag{10}$$

where we define the following expressions:

$SNR \triangleq P/N_0$, and $P \triangleq P_1 + P_2$ is the transmitted power per source symbol, $P_1 \triangleq \alpha P$, $\alpha \in (0,1)$, $\alpha_{AF}\triangleq\frac{\alpha^2\rho_{s,r}^3}{\alpha\rho_{s,r}^2+(1-\alpha)\rho_{r,d}^2}$ and

$$g(\lambda_i)\triangleq\left(1/\prod_{i=1}^{n}\lambda_i\right)\sum_{i=0}^{n}\binom{n}{i}2^i{}_2F_1\left(2n,2n+2+i;4n-1;\frac{1}{2}\right)\lambda_i$$

For computing briefness, (4) can be effectively expurgated to approach the "error-free feedback" performance as [12]

$$f_{ef}(d,\mu,\chi)\le\left[\frac{1}{K2^K}\sum_{k=1}^{K}\sum_{b=0}^{1}\sum_{X\in\chi_b^k}\min_s\Phi_{\Delta(X,Z)}(s)\right]^d. \tag{11}$$

Placing (10) into (11) provides

$$f_{ef}(d,\mu,\chi) \le \left[\frac{1}{K2^K}\sum_{k=1}^{K}\sum_{b=0}^{1}\sum_{X\in\chi_b^k}\tfrac{1}{2}(\alpha_{AF})^{-n}g(\lambda_i)SNR^{-n}\right]^d = (\alpha_{AF}SNR)^{-nd}\left[\frac{1}{K2^{K+1}}\sum_{k=1}^{K}\sum_{b=0}^{1}\sum_{X\in\chi_b^k}g(\lambda_i)\right]^d. \tag{12}$$

By defining $d_b^2(\chi,\mu,n) \triangleq \left[\frac{1}{K2^{K+1}}\sum_{k=1}^{K}\sum_{b=0}^{1}\sum_{X\in\chi_b^k}g(\lambda_i)\right]^{-1/n}$, (12) can be rewritten as

$$f_{ef}(d,\mu,\chi) \le \left(\alpha_{AF}d_b^2(\chi,\mu,n)SNR\right)^{-nd}. \tag{13}$$

When only including the dominant error event associated with d_f in (3), we get

$$p_b \simeq \frac{1}{k_c}W_I(d_f)f_{ef}(d,\mu,\chi) = \frac{W_I(d_f)}{k_c}SNR^{-nd}\left[\alpha_{AF}d_b^2(\chi,\mu,n)\right]^{-nd}. \tag{14}$$

From (10) (12) and (14), the BEP of AF cooperative relaying based on BI-STC systems can be calculated.

4 Simulation Results

In this section, we present simulation results to illustrate the performance of the proposed BI-ST-AF scheme and to support the analytical results in Sect. 3. In our numerical experimentations, we adopt the convolutional codes that are the best known rate 2/3 codes [13], the worst-case error event length is $d = 6$ and free distance $d_f = 5$. The bit interleaver is S-random with length of 6,144 and depth of 20. The modulation constellation is 16PSK with Gray labeling. Equation (3) are used to evaluate the LLRs at destinations. The space-time code is proposed by Alamouti [14]. All links are supposed to be independent, identically distributed Ryleigh fading with $\rho_{i,j}^2 = 1$.

Figure 2 depicts the BER against SNR with different number of relay nodes in the BI-STC-AF relay networks. The total power is equally allocated between the source and the relays, that is, $\alpha = 0.5$. From the figure, one can see that the BER performances of BI-STC-AF scheme upgrades in terms of the number of relay nodes. It can also be seen that the improvement speed of BER performance comes down with the increasing number of relays nodes.

The comparative curves of the BER performance versus mean SNR for BICM, BI-STC and BI-ST-AF are drawn in Fig. 3. As shown in this figure, the proposed BI-ST-AF scheme has better performance than the BICM and the BI-STC schemes

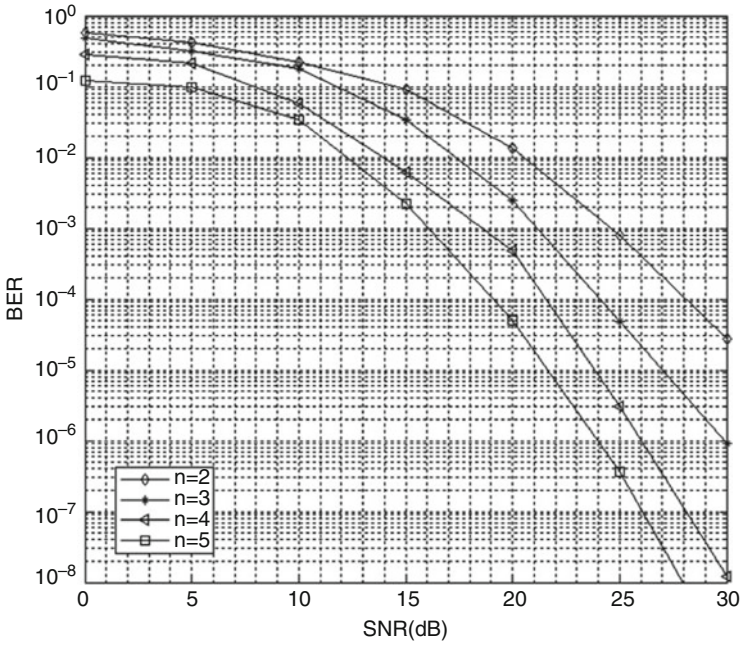

Fig. 2 BER versus SNR of the proposed cooperative diversity scheme with different number of relay nodes

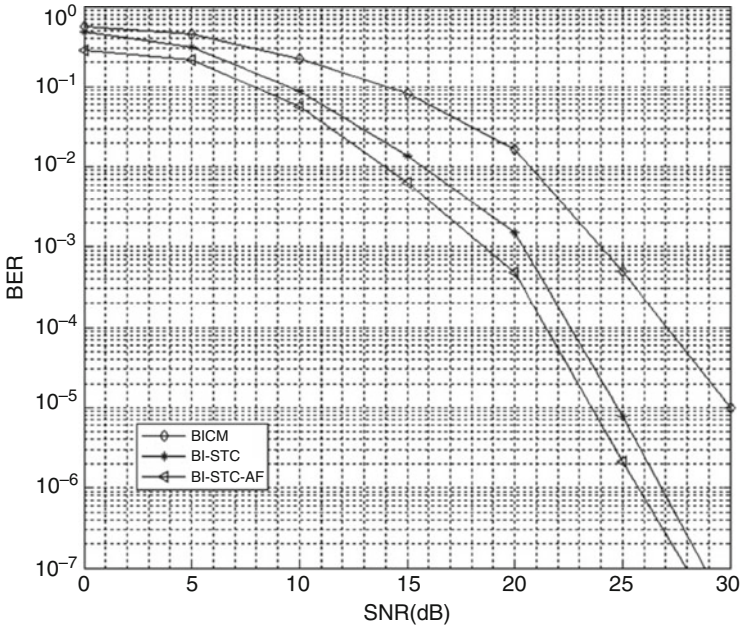

Fig. 3 BER versus SNR of various schemes

in terms of BER. The reason that the proposed scheme outperforms BICM lies in that the concatenated BICM and STC is more robust in fading channel. When compared with BI-STC scheme, the cooperative relying system performs better due to the distributed relays mitigate interference among antennas in multiple-input-multiple-output schemes. It can be also seen from the figure that these two schemes have about the similar performance when SNR is high enough.

5 Conclusion

We have proposed an Amplify-and-Forward cooperative diversity scheme based on the concatenation of bit-interleaved coded modulation and space-time block codes technique. The bit error probability of the scheme depends on the SNR, the channel conditions and the modulation and codes parameters of the BICM system. Simulation results show that the proposed scheme outperforms BICM and BI-ST schemes in terms of BER. Optimal power allocation between the source and the relays remains a future problem.

Acknowledgments This work was supported by the Applied Foundation Research Projects for Department of Science and Technology of Sichuan Province (No. 2012JY0072) and the Fundamental Research Funds for the Central University (No. ZYGX2011J125).

References

1. Laneman JN, Tse DNC, Wornell GW (2004) Cooperative diversity in wireless networks: efficient protocols and outage behavior. IEEE T Inform Theory 50:3062–3080
2. Beaulieu NC, Hu J (2006) A closed-form expression for the outage probability of decode-and-forward relaying in dissimilar Rayleigh fading channels. IEEE Commun Lett 10:813–815
3. Rodríguez LJ, Tran NH, Le-Ngoc T (2011) Bandwidth-efficient bit-interleaved coded modulation over NAF relay channels: error performance and precoder design. IEEE T Veh Technol 60:2086–2101
4. Caire G, Taricco G, Biglieri E (1998) Bit-interleaved coded modulation. IEEE Trans Inform Theory 44:927–946
5. Hoshyar R, Tafazolli R (2008) BER performance analysis of a cooperative BICM system based on post-BSC model. Proc. IEEE 19th International Symposium PIMRC. 2008, pp 1–5
6. Barbarossa S, Pescosolido L, Ludovici D, Barbetta L, Scutari G (2004) Cooperative wireless networks based on distributed space time coding. Proc. International workshop wireless Ad-hoc networks, 2004, pp 1–5
7. Tarokh V, Seshadri N, Calderbank AR (1998) Space-time codes for high data rate wireless communication: Performance criterion and code construction. IEEE T Inform Theory 44:744–765
8. Behrouz M, Are H, Giuseppe A (2009) Distributed GABBA space-time codes in amplify-and-forward relay networks. IEEE T Wirel commun 8:2036–2045
9. Tonello A (2001) Performance of space-time bit-interleaved codes in fading channels with simplified iterative decoding. IEEE international conference on communication, ICC, Rhodes, 2001, pp 1357–1361

10. Hong Z, Hughes BL (2001) Robust space-time trellis codes based on bit-interleaved coded modulation. Proc CISS'01 2:665–670
11. Huang Y, Ritcey JA (2005) Optimal constellation labeling for iteratively decode bit-interleaved space-tome code modulation. IEEE T Inform Theory 51:1865–1871
12. Huang Y, Ritcey JA (2004) Tight BER bounds for iteratively decoded bit-interleaved space-time coded modulation. IEEE Commun Lett 8:153–155
13. Moon TK (2005) Error correction coding. Wiley, Hoboken, NJ
14. Alamouti SM (1998) A simple transmit diversity technique for wireless communications. IEEE J Sel Area Comm 16:1451–1458

Adaptive Modulation Based Relay Selection and Power Allocation in Cooperative OFDM Wireless Networks

Nianlong Jia, Wenjiang Feng, Najashi Bara'u Gafai, and Weiheng Jiang

Abstract Several problems that hinder the optimal performance of multiple relays cooperative OFDM wireless networks have been identified recently. Power allocation and relay selection are some of the problems encountered in these systems. In this paper, a bit reloading (BR) OFDM relaying scheme which solves the problem of both power allocation and relay selection in multiple relays cooperative OFDM wireless networks by selecting the best relay to retransmit the OFDM signal is presented. This method varies from other methods in open literature because bit loading is executed at each hop i.e. from source to relay, and from relay to the destination. Because the bottleneck of bit loading with regard to source-to-relay-to-destination subchannel is eliminated, our proposed scheme achieves more power gain and end-to-end data rate. The theoretic analysis and simulation result also demonstrates our scheme has a better performance.

Keywords Cooperative communications • OFDM • Relay selection • Bit loading

1 Introduction

Cooperative relaying has been known as a key technique for next generation wireless communication systems. It offers wide coverage range, diversity gain and network throughput improvement. Meanwhile, OFDM is widely applied in broadband wireless networks due to its capability of eliminating inter symbol

Project supported by the Chongqing Nature Science Foundation of China (No. CSTC2009BA2064), and the Special Fund for Basic Scientific Research of Central Colleges, Chong'qing University (CDJXS11160003)

N. Jia (✉) • W. Feng • N.B. Gafai • W. Jiang
College of Communication Engineering, Chongqing University, Chongqing 400030, China
e-mail: jnl@cqu.edu.cn; fengwj@cqu.edu.cn

B. Zhang et al. (eds.), *The Proceedings of the Second International Conference on Communications, Signal Processing, and Systems*, Lecture Notes in Electrical Engineering 246, DOI 10.1007/978-3-319-00536-2_87,

interference (ISI) resulting in high data rates over frequency-selective fading channels. Incorporating these two techniques has been investigated recently [1].

In general, relays are classified into two main categories, decode-and-forward (DF) and amplify-and-forward (AF) relays. AF-OFDM relaying has been earlier investigated in [2, 3]. Pairwise error probability (PEP) is studied over frequency-selective channels, the diversity order is thus given and relay selection is performed [2]. Relay selection and sub-channel pairing are also considered in [3], the limited subchannel feedback from each node largely decrease computational complexity. However, DF-OFDM relaying has been preferred over AF-OFDM relaying due to higher SNR gain [4]. Research on DF-OFDM relaying has attracted extensive attention recently [5–9]. Two selective relaying schemes in cooperative OFDM system: selective OFDMA relaying (relay selection is performed in per-subcarrier manner) and selective OFDM relaying (relay selection based on entire OFDM block) were proposed in [5], the performance of the two schemes were analyzed with equal bit allocation (EBA) and bit loading (BL). The outage probability of selective OFDM relaying was presented for EBA, and minimal-based relay selection was shown as the only way to ensure full system diversity [6]. Moreover, SER performance of adaptive power loading was investigated in [7]. Two power allocation schemes which are based on statistical channel status information and instantaneous channel status information to minimize system outage probability were investigated in [8, 9]. In [10, 11], MIMO with space-frequency block coding was incorporated into a relay system to improve system performance.

In this paper, we propose a bit reloading (BR) selective OFDM relaying protocol. Unlike the traditional way of relay selection and power allocation based on each end-to-end subchannel e.g. $S(n)$-$R_i(n')$-D (end-to-end chain form source at n-th subcarrier to relay R_i and form relay R_i to the destination at n'-th subcarrier), the proposed scheme executes the bit loading algorithm at both the source and relay nodes separately unlike in other schemes, the best relay is selected to provide the highest end-to-end data rate. By means of bit loading at source node and relay node the cutoff bound is attained. The theoretical outage performance is evaluated and analyzed first. Then the optimal relay selection and power allocation are given. After that, simulation is carried out to validate our analysis.

2 System Model

We consider a single source-destination (S-D) cooperative OFDM system with M relays. The relays are randomly located between the source node and the destination. N subcarriers are available at each node. Decode-and-forward (DF) relaying strategy is assumed in our work and perfect time and frequency synchronization are also assumed.

A two-stage transmission is adopted. In the first stage, source node transmits to potential relay nodes. Then the relay selected retransmits the message to the destination. In particular, only the best relay is selected to retransmit the entire

OFDM symbol. The channel coefficients of subcarrier n in the first hop and subcarrier n' in the second hop are denoted by $Hsr_i(n)$ and $Hr_id(n')$ respectively. we use $Gsr_i(n)$ and $Gr_id(n')$ to denote the channel power gains of $|Hsr_i(n)|^2$ and $|Hr_id(n')|^2$, respectively, also, let $Gsr_id(n)$ refer to minimal$\{Gsr_i(n), Gr_id(n')\}$.

In previous works, selective OFDM relaying was investigated for EBA and BL. As a result of end-to-end subchannel $Gsr_id(n)$, the highest data rate at each sub-carrier is limited by the worst subchannel between the first hop and the second hop. Although subcarrier pairing helps in improving system performance, the worst hop is still a bottleneck. So we proposed a new relaying scheme, which is called bit reloading (BR) selective OFDM relaying. In this case, Gsr_i and Gr_id are considered individually instead of $Gsr_id(n)$ for bit loading at source node and relay node. In this paper, we compare the performance of BR selective OFDM relaying with classical selective OFDM relaying with BL.

The following assumptions are made:

A1) no direct transmit link is assumed, the destination node only use the signal transmitted in the second stage;

A2) Gsr_i and Gr_id are independent exponential random variables with mean $1/\lambda_{sri}$ and $1/\lambda_{rid}$, respectively. Also, $Gsr_id(n)$ are independent exponential random variables with mean $1/(\lambda_{sri}+\lambda_{rid})$.

3 Outage Analysis for BR Selective OFDM Relaying

In this section, we will evaluate the end-to-end outage performance of selective OFDM relaying and BR selective OFDM relaying. We first consider selective OFDM relaying with BL, the end-to-end outage of selective OFDM relaying scheme with BL transmission is given by [5].

$$\begin{aligned} P_{out,BL}^{OFDM} &= \prod_{i=1}^{M} \Pr\left[\sum_{n=1}^{N} \frac{1}{2}\log\left(1 + G_{sr_id}(n)\frac{\gamma}{\Gamma}\right) < NR\right] \\ &\approx \prod_{i=1}^{M} \left(\lambda_i^N 2^{2NR} (\ln 2)^{N-1} \left(\prod_{j=1}^{N-1} \frac{1}{j}\right) (2NR)^{N-1} \left(\frac{\Gamma}{\gamma}\right)^N\right) \end{aligned} \tag{1}$$

The last step is a high-SNR approximation. Where the logarithms are base-2 unless otherwise noted, R is the average number of bits at each subchannel, and where Γ is the SNR gap.

Theorem 1. The end-to-end outage of BR selective OFDM relaying scheme is given by

$$P_{out,BR}^{OFDM} \approx \prod_{i=1}^{M} \left(\lambda_{sr_i}^{N} + \lambda_{r_i d}^{N} - \lambda_{sr_i}^{N}\lambda_{r_i d}^{N} Q\right) Q \tag{2}$$

This is a high-SNR approximation, where

$$Q = 2^{NR}(\ln 2)^{N-1}\left(\prod_{j=1}^{N-1}\frac{1}{j}(2NR)^{N-1}\right)\left(\frac{\Gamma}{\gamma}\right)^{N}$$

Proof.

$$P_{out,BR}^{OFDM} = \prod_{i=1}^{M} 1 - \left(1 - P_r\left(\sum_{n=1}^{N}\frac{1}{2}\log\left(1 + G_{sr_i}(n)\frac{\gamma}{\Gamma} < NR\right)\right)\right.$$

$$\left(1 - P_r\left(\sum_{n=1}^{N}\frac{1}{2}\log\left(1 + G_{r_i d}(n)\frac{\gamma}{\Gamma} < NR\right)\right)\right)$$

$$= \prod_{i=1}^{M} P_r\left(\sum_{n=1}^{N}\frac{1}{2}\log\left(1 + G_{sr_i}(n)\frac{\gamma}{\Gamma} < NR\right) + P_r\left(\sum_{n=1}^{N}\frac{1}{2}\log\left(1 + G_{r_i d}(n)\frac{\gamma}{\Gamma} < NR\right)\right.\right.$$

$$\left. - P_r\left(\sum_{n=1}^{N}\frac{1}{2}\log\left(1 + G_{sr_i}(n)\frac{\gamma}{\Gamma} < NR\right)\right) P_r\left(\sum_{n=1}^{N}\frac{1}{2}\log\left(1 + G_{r_i d}(n)\frac{\gamma}{\Gamma} < NR\right)\right.\right. \tag{3}$$

Incorporating (1) and (3), we obtain (2). Form formula (2), we can see that BR selective OFDM relaying and selective OFDM relaying with BL achieve the same diversity gain.

Corollary 1. BR selective OFDM relaying has smaller outage probability than selective OFDM relaying with BL.

Proof.

$$\begin{aligned} P_{out,BL}^{OFDM} - P_{out,BR}^{OFDM} &= \prod_{i=1}^{M}\left(\lambda_{sr_i} + \lambda_{sr_i}\right)^{N} Q - \prod_{i=1}^{M}\left(\lambda_{sr_i}^{N} + \lambda_{r_i d}^{N} - \lambda_{sr_i}^{N}\lambda_{r_i d}^{N} Q\right) Q \\ &= \prod_{i=1}^{M}\left(\sum_{k=1}^{N-1}\binom{N}{k}\lambda_{sr_i}^{N-k}\lambda_{r_i d}^{k} + \lambda_{sr_i}^{N}\lambda_{r_i d}^{N} Q\right) Q \succ 0 \end{aligned} \tag{4}$$

4 Adaptive Bit Reloading Selective OFDM Relaying Scheme

In the previous section, we showed that BR selective OFDM relaying outperforms selective OFDM relaying with BL. In this section, we will address the issues relevant to adaptive relay selection and power allocation in our proposed protocol.

We assume a central controller is available; it is able to collect all the channel information and then make a decision on relay selection and power allocation. We focus on fixed data rate relay selection and power allocation.

We fix transmit power and bit error probability (BEP), the minimum power can be formulated as:

$$\mathbf{P1}: \min_{i=1,2,\ldots M} \sum_{n=1}^{N}\sum_{n'=1}^{N}\left(P_{sr_i}(n)+P_{r_id}(n')\right) \tag{5}$$

$$\text{C1}: \sum_{n=1}^{N} b_n = R_b, b_n \geq 0.$$

$$\text{C2}: \sum_{n'=1}^{N} b_{n'} = R_b, b_{n'} \geq 0.$$

$$\text{C3}: \begin{matrix} BER_n \leq BER_{\text{target}}, (n=1,2,\ldots N) \\ BER_{n'} \leq BER_{\text{target}}, (n'=1,2,\ldots N) \end{matrix}.$$

$$\text{C4}: P_{sr_i}(n) \geq 0, P_{r_id}(n') \geq 0.$$

where $P_{sr_i}(n)$ and $P_{r_id}(n')$ are allocated power for source node at *n-th* subcarrier and relay node at *n'-th* subcarrier, respectively. b_n is the bit number at subcarrier n and $b_{n'}$ is the bit number at subcarrier n', likewise. R_b denotes the fixed transmit rate, BER_{target} is the threshold of target SNR.

In an OFDM system, the relationship between received SNR and b_n is denoted as $b_n = \frac{1}{2}\log_2\left(1+\frac{SNR_n}{\Gamma}\right)$ and $b_{n'} = \frac{1}{2}\log_2\left(1+\frac{SNR_{n'}}{\Gamma}\right)$

Here, Γ = -ln(5**SERtarget*)/1.5 denotes SNR gap, which is related to modulation type, BEP and channel coding. If we assume the same modulation type and target SNR at each subchannel, Γ is recognized as a constant., with perfect coding $\Gamma = 1$.

For simplification, noise power σ^2 (Gauss white noise variance) at each subchannel is assumed the same.

By using Lagrange multiplier method, the optimal power allocated is obtained as:

$$P_{sr_i}(n) = X(n,G)\Gamma\sigma^2\left(\frac{2^{\frac{2R_b}{N}}}{\prod_{n=1}^{N} G_{sr_i}(n)^{\frac{1}{N}}} - \frac{1}{G_{sr_i}(n)}\right) \tag{6}$$

$$P_{r_id}(n) = X(n,G)\Gamma\sigma^2\left(\frac{2^{\frac{2R_b}{N}}}{\prod_{n=1}^{N} G_{r_id}(n)^{\frac{1}{N}}} - \frac{1}{G_{r_id}(n)}\right) \tag{7}$$

where

$$X(n,G) = \begin{cases} 1 & \text{if } \dfrac{2^{\frac{2R_b}{N}}}{\prod_{n=1}^{N} G_{\mathrm{ab}}(n)^{\frac{1}{N}}} - \dfrac{1}{G_{ab}(n)} \geq 0 \\ 0 & \text{else} \end{cases}, \quad a \in \{s, r_i\},\ b \in \{r_i, d\}$$

The optimal problem (5) is to select the relay node which resulting to minimum power requirement.

5 Numerical Results

5.1 Diversity Gain

During simulation, we consider multiple relay nodes, each of them are located at an equal distance to the source and to the destination, i.e., $G_{sri}/G_{rid} = 0$ dB, and assume QPSK modulation. The number of subcarriers is fixed at $N = 16$. For the convenience of comparison, we set $\lambda_{sri}(n) = \lambda_{rid}(n) = 1$. We assume perfect coding in our simulation with SNR gap equal to 1.

We first simulate the outage of BR selective OFDM relaying scheme, selective OFDM relaying with BL and EBA, the simulation effectively compute the outage probability for a given network realization. In order to be fair in comparisons, transmit power and receive noise is the same for all nodes and all transmissions.

Figure 1 is the simulation output with five relay nodes at the condition of R = 2 bit/s/HZ, the curve shows that BR selective OFDM relaying scheme can achieve the same diversity order as selective OFDM relaying with BL, but more power gain can be obtained. As a result of bit loading, both of them outperforms EBA scheme.

Figure 2 provides results on the comparison of different number of relay nodes in a network for BR selective OFDM relaying scheme. The results indicate the greater the number of relays, the higher the diversity order that can be achieved. This is in accordance with our theoretic analysis.

5.2 Data Rate

In this section, we simulate the end-to-end data rate performance of the proposed scheme in a coded cooperative OFDM system. We again assume QPSK modulation. Relay nodes are located at an equal distance to the source and to the destination, which is the same as in Sect. 5.1. Firstly, we fix the number of relay in a system, and we investigate the achievable data rate at different power constraints. It is depicted as in Fig. 3. The simulation result shows that more data rate can be achieved with BR selective OFDM relaying scheme compared with classical selective OFDM relaying with BL.

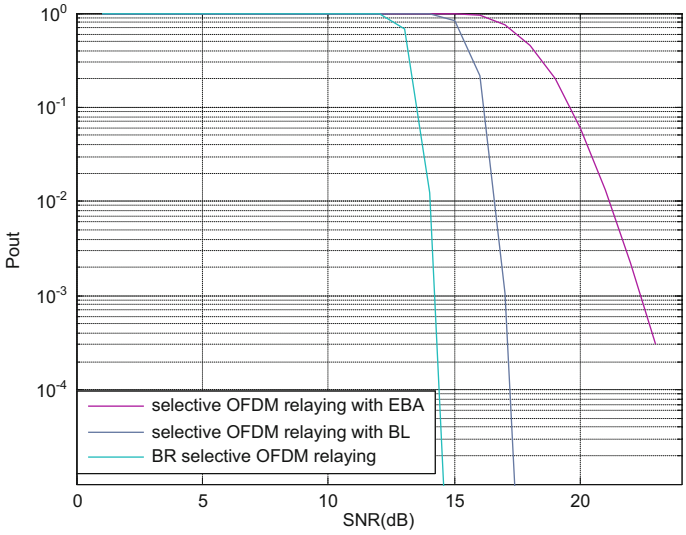

Fig. 1 Outage probability with 5 relay nodes, 16 subcarriers when R = 2 bit/s/HZ

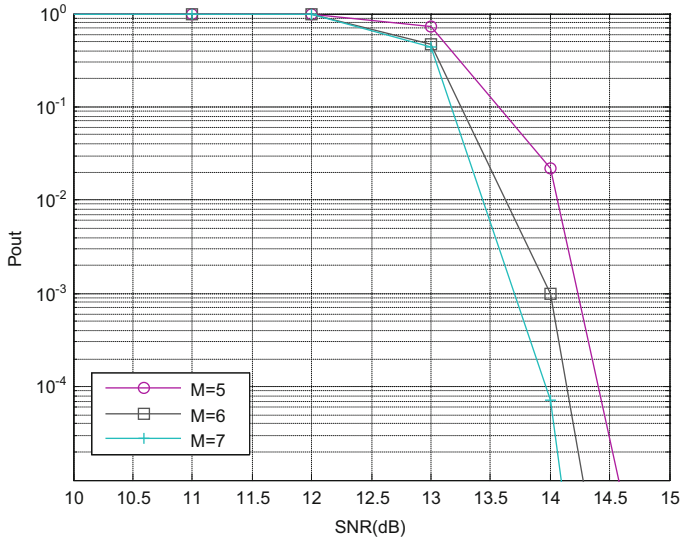

Fig. 2 Outage performance of BR selective OFDM relaying with different relay number

Figure 4 is the comparison of end-to-end transmission rate achieved by the two schemes, which is in accordance with our theoretical analysis. As the number of relays increase, more diversity gain and end-to-end data rate is achieved.

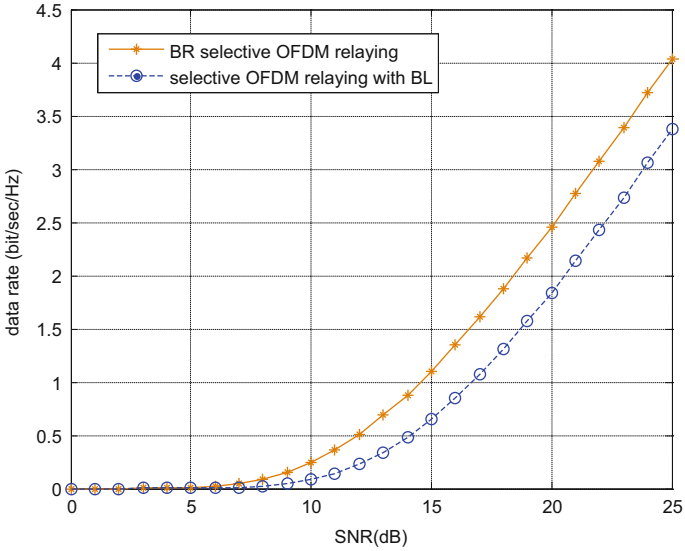

Fig. 3 Spectrum effectiveness comparison with $M = 5, N = 16$

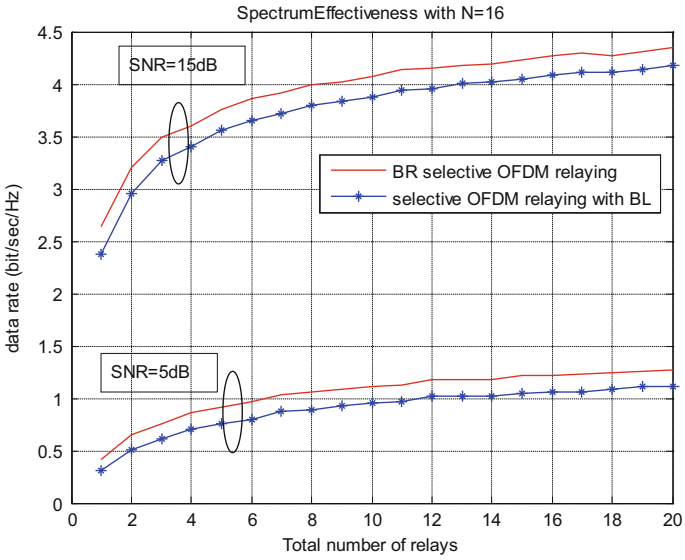

Fig. 4 Average end-to-end transmission rate achieved by different algorithm

6 Conclusions

We studied the optimal bit loading problem in a relay based OFDM system. The source transmits the data over orthogonal subcarriers to multiple relays. The information is decoded by the relays, where the best one is selected and it retransmits the information to the destination. The proposed scheme adopts bit reloading at user node and relay node which is different from the classical selective OFDM relaying with bit loading. The outage analysis demonstrates that with the same diversity order as the classical methods, more power gain is possible in the proposed scheme. We also investigated the power allocation and relay selection in two scenarios, the simulation demonstrated a good end-to-end data rate. Although it is a centralized algorithm, the optimal resource allocation algorithm presented in this paper defines the performance bounds of block based OFDM relaying.

References

1. Wanlu Sun, Lihua Li, Wei Yang (2011) Joint subcarrier pairing, relay selection and power allocation in OFDM relay systems. In: IEEE ICC, Kyoto, 2011, pp 1–5
2. Ding Y, Uysal M (2009) Amplify-and-forward cooperative OFDM with multiple-relays: performance analysis and relay selection methods. IEEE T Wireles Commun 8(10):4693–4698
3. Rui Yin, Yu Zhang, Jietao Zhang (2009) Distributed joint optimization of relay selection and subchannel pairing in OFDM based relay networks. In: IEEE PIMRC, Tokyo, 2009, pp 722–726
4. Jae Cheol Park, TanTaiDo, YunHeeKim (2010) Outage probability of OFDM-based relay networks with relay selection. In: IEEE 71st VTC conference, Taibei, 2010, pp 1–5
5. Bo Gui, LinDai, Leonard J (2008) Selective relaying in cooperative OFDM systems: two-hop random network. In: Proceeding of IEEE WCNC, Las Vegas, NV, 2008, pp 996–1001
6. Wendong Yang, Yueming Cai (2010) Distributed relay selection in OFDM-based cooperative wireless networks. In: 6th international conference on WiCOM, Chengdu, 2010, pp 1–4
7. Amin O, Uysal M (2012) Adaptive power loading for multi-relay OFDM regenerative networks with relay selection. IEEE T Commun 60(3):614–6199
8. Lijie Wang, Haitao Zhao, Yong Xi (2010) Optimal power allocation and relay selection in OFDM-based cooperative systems. In: 6th international conference on WiCOM, Chengdu, 2010, pp 1–5
9. Lijie Wang, Haitao Zhao, Yong Xi (2010) Optimizing the performance of OFDM-based cooperative networks by relay selection, power allocation and relay localization. In: IEEE international conference on ultra-wideband, Nanjing, 2010, pp 1–4
10. Munoz D, Xie B (2012) An adaptive MIMO-OFDMA relay system. IEEE Commun Lett 1 (5):496–499
11. Ibrahim Khalil Sileh, Wei Xiang (2012) Distributed space-frequency coding for OFDM-based hybrid relay selection. In: ISCIT, international symposium, Gold coast, 2012, pp 594–598

Concatenated-Code Belief Propagation Decoding for High-Order LDPC Coded Modulations

Haicheng Zhang, Guibin Zhu, and Huiyun Jiang

Abstract This paper presents and demonstrates a concatenated code model (CCM) for high order, low-density parity-check (LDPC) coded modulation, which consists of a serial concatenation of an outer LDPC encoder, an inner binary-decimal conversion (BDC) encoder and a puncture. A corresponding concatenated-code belief propagation (CCBP) decoding algorithm is derived for the proposed concatenated code. Compared to other algorithms, CCBP method provides a much more excellent parallel decoding process for high order modulations. Simulation results show that the proposed CCBP algorithm performs superior to conventional belief propagation (BP) decoding within a wide range of modulation orders.

1 Introduction

Low-density parity-check (LDPC) codes can approach the capacity on various channels at relatively low complexity using iterative decoding. Since their rediscovery in the 1990s [1], there have been various coding schemes and decoding strategies proposed for LDPC coded modulations to achieve both power and bandwidth efficiency, such as Non-binary LDPC coded modulation scheme [2], Multi-Level Coding/Multi-Stage Decoding (MLC/MSD) [3], Bit Interleaved Coded Modulation (BICM) [4], etc.. In these strategies, BICM is the most popular coded modulation (CM) scheme since it exhibits the lowest complexity. However, there still remains a gap between the BICM capacity and the modulation constrained capacity (CM capacity) since the BP decoding is used [4]. Actually, due to high sensitivity of BP decoding to the mapping, it will not work well in scenarios where

H. Zhang (✉) • G. Zhu
Department of Power Engineering, Chongqing Communication College, Chongqing, China

H. Jiang
ChongQing Municipal Infrastructure Administration Bureau, Chongqing, China

B. Zhang et al. (eds.), *The Proceedings of the Second International Conference on Communications, Signal Processing, and Systems*, Lecture Notes in Electrical Engineering 246, DOI 10.1007/978-3-319-00536-2_88,

Gray mapping is not possible, such as 32-QAM and 128QAM modulations. For example, for a 32-QAM modulation with a quasi-Gray labeling, the BICM capacity gap is 2.6 dB, and 3.5 dB for a 128-QAM modulation. Thus, a joint decoding algorithm for LDPC coded modulations should be developed to approach the CM capacity.

To approach the modulation constrained capacity, a concatenated code model (CCM) is demonstrated for high order LDPC coded modulations and a joint decoding algorithm named CCBP is derived in this paper. Related to this, Sect. 2 provides the concatenated code model. Section 3 describes the CCBP decoding algorithm. Sections 4 and 5 show some simulation results and present a conclusion, respectively.

2 CCM for High-Order LDPC Coded Modulations

The basic diagram of the proposed system is as shown in Fig. 1. At the transmitter, k information bits $\mathbf{S} = [s_0, s_1, \ldots, s_{k-1}]$ are encoded into n bits codeword $\mathbf{C} = [c_0, c_1, \ldots, c_{k-1}, c_k, c_{k+1}, \ldots, c_{n-1}]$ by an LDPC encoder [1]. And then, a systematic binary-decimal conversion (BDC) encoder concatenates subsequently, which converts each n bits string $\mathbf{C}$ to a new code $\overline{\mathbf{C}} = \left[c_0, c_1, \ldots, c_{n-1}, \widetilde{c}_0, \widetilde{c}_1, \ldots, \widetilde{c}_{p-1}\right]$. The parity symbols $\widetilde{c}_0, \widetilde{c}_1, \ldots, \widetilde{c}_{p-1}$ are non-negative integers over the field of $[0, 2^B\text{-}1]$. The BDC rule is

$$\widetilde{c}_i = \sum\nolimits_{j=0}^{B-1} 2^{B-1-j} c_{i\times B+j}, \quad 0 \le i < p, \quad p = n/B. \tag{1}$$

Next, a puncture device is used to puncture the word $\overline{\mathbf{C}}$ to obtain the parities of the BDC codes $\widetilde{\mathbf{C}} = \left[\widetilde{c}_0, \widetilde{c}_1, \ldots, \widetilde{c}_{p-1}\right]$. Then the integers of $\widetilde{\mathbf{C}}$ are mapped to symmetry symbols $\widetilde{\mathbf{X}} = \left[\widetilde{x}_0, \widetilde{x}_1, \ldots, \widetilde{x}_{p-1}\right]$, where

$$\widetilde{x}_i = \widetilde{x}_i^R + j\widetilde{x}_i^C = f_R(\widetilde{c}_i) + jf_C(\widetilde{c}_i) = f(\widetilde{c}_i), \quad 0 \le i < p \tag{2}$$

Here, $f_R(\widetilde{c})$ and $f_C(\widetilde{c})$ map the integer $\widetilde{c}$ as the real and imaginary parts of the 2^B-QAM (quadrature amplitude modulation) constellation in a gray or quasi-gray manner, respectively [5].

The symbols in $\widetilde{\mathbf{X}}$ then pass through the complex additive white Gaussian noise (AWGN) channel, and the outputs are $\widetilde{\mathbf{Y}} = \left[\widetilde{y}_0, \widetilde{y}_1, \ldots, \widetilde{y}_{p-1}\right]$, where

$$\widetilde{y}_i = \widetilde{y}_i^R + j\widetilde{y}_i^C = \widetilde{x}_i + \omega_i, \quad 0 \le i < p. \tag{3}$$

Here ω_i is the AWGN noise of variance $\sigma^2 = N_0/2$.

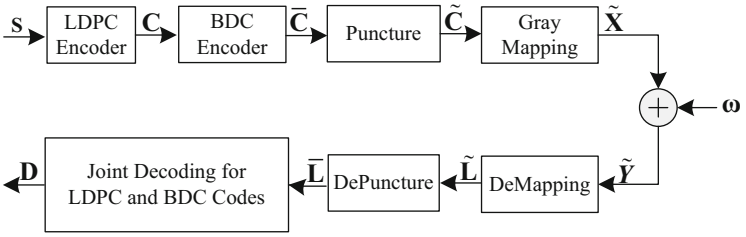

Fig. 1 System model

At the receiver, a de-mapping device is used to process the received signals $\widetilde{\mathbf{Y}}$. It computes the channel log-likelihood ratio (LLR) of the QAM symbols, and maps them as the LLR of the common integers in $\widetilde{\mathbf{C}}$: $\widetilde{\mathbf{L}} = \left[\widetilde{\mathbf{L}}_0, \widetilde{\mathbf{L}}_1, \cdots, \widetilde{\mathbf{L}}_{p-1}\right]$, where $\widetilde{\mathbf{L}}_i = \left[\widetilde{\mathbf{L}}_i(0), \widetilde{\mathbf{L}}_i(1), \cdots, \widetilde{\mathbf{L}}_i\left(2^B - 1\right)\right]$, and

$$\begin{aligned}\widetilde{\mathbf{L}}_i(v) &= \log\frac{P\left(\widetilde{y}_i|\widetilde{c}_i = v\right)}{P\left(\widetilde{y}_i|\widetilde{c}_i = 0\right)} = \log\frac{P\left(\widetilde{y}_i|\widetilde{x}_i = f(v)\right)}{P\left(\widetilde{y}_i|\widetilde{x}_i = f(0)\right)} \\ &= \frac{\widetilde{y}_i^R\left(f_R(v) - f_R(0)\right) + \widetilde{y}_i^C\left(f_C(v) - f_C(0)\right)}{\sigma^2} \\ &\quad - \frac{\left(f_R^2(v) - f_R^2(0)\right) + \left(f_C^2(v) - f_C^2(0)\right)}{2\sigma^2},\ 0 \le i < p, 0 \le v < 2^B. \end{aligned} \tag{4}$$

Subsequently, the de-puncture device retrieves the full LLR of the BDC codeword $\overline{\mathbf{C}}$:$\overline{\mathbf{L}} = \left[\overline{L}_0, \overline{L}_1, \ldots, \overline{L}_{n-1}, \widetilde{\mathbf{L}}_0, \widetilde{\mathbf{L}}_1, \ldots, \widetilde{\mathbf{L}}_{p-1}\right]$, where c_0, c_1, …, c_{n-1} of codeword $\overline{\mathbf{C}}$ are punctures in the transmitter, thus their LLR are

$$\overline{L}_i = \log\frac{P(\overline{c}_i = 0)}{P(\overline{c}_i = 1)} = 0,\ \ 0 \le i < n. \tag{5}$$

Finally, the full channel LLR $\overline{\mathbf{L}}$ of codeword $\overline{\mathbf{C}}$ are feed into the decoder to finish the decoding.

In this system, the high-order modulation is modeled by a BDC encoder concatenated after a LDPC encoder. Correspondingly, the demodulation and decoding is performed by a joint decoding algorithm for the concatenated code. With this joint decoding algorithm, CM capacity can be approached.

3 Concatenated-Code Belief-Propagation Decoding

BICM is suboptimal since BP decoding ignores statistical dependencies between the bits originating from the modulation symbol (the parity symbol of BDC code in this paper). Hence, it does not perform MAP decoding even when the code underlying tanner graph is cycle-free. Motivated by this observation, an improved CCBP decoding is derived based on a united tanner graph of the LDPC code and BDC code.

In the system, there are two encoders, the LDPC encoder and the BDC encoder, concatenated serially. Thus, the code sequence $\overline{\mathbf{C}} = [c_0, c_1, \ldots, c_{n-1}, \widetilde{c}_0, \widetilde{c}_1, \ldots, \widetilde{c}_{p-1}]$ satisfies the following equation:

$$\overline{\mathbf{HC}}^T \triangleq \begin{bmatrix} \mathbf{H} & \mathbf{0}_{m\times p} \\ \widetilde{\mathbf{H}} & -\mathbf{I}_{p\times p} \end{bmatrix} \overline{\mathbf{C}}^T = 0, \tag{6}$$

where $\mathbf{H} = [h_{ij}]_{m\times n}$ is the binary parity-check matrix of the LDPC code and $\widetilde{\mathbf{H}} = [\widetilde{h}_{ij}]_{p\times n}$ is part of the parity-check matrix of the BDC code over the integer field of [0, 2^B-1]:

$$\widetilde{\mathbf{H}} = \begin{bmatrix} 2^{B-1}, 2^{B-2}, \cdots, 2^0 & & & 0 \\ & 2^{B-1}, 2^{B-2}, \cdots, 2^0 & \ddots & \\ 0 & & & 2^{B-1}, 2^{B-2}, \cdots, 2^0 \end{bmatrix}. \tag{7}$$

Thus $\overline{\mathbf{H}}$ is the united parity-check matrix of the concatenated code. According to $\overline{\mathbf{H}}$, the united tanner graph of the concatenated code can be drawn as in Fig. 2 [6]. In the graph, there are n variable nodes and m check nodes of the LDPC code, and p variable nodes and p check nodes of the BDC code (In fact, the n variable nodes of the LDPC code are also the variable nodes of the BDC code). The variable nodes and check nodes connect by edges. Each LDPC variable node emits *several* edges to the LDPC check nodes randomly, while *one* edge to the BDC check node. Each LDPC check node just emits edges to the LDPC variable nodes. Correspondingly, each BDC variable node emits *one* edge to the BDC check node, and *none* to the LDPC check nodes. Each BDC check node emits B edges to the LDPC variable nodes. Joint decoding is performed by exchanging messages between variable nodes and check nodes through the edges of the graph, in both directions and iteratively [7, 8].

Next, we describe the joint decoding algorithm with LLR messages. For convenience, some common notations $Ri)=\{k|h_{ik}=1, h_{ik}\in\mathbf{H}\}$, $Ri)\backslash j=\{k \mid h_{ik}=1, h_{ik}\in\mathbf{H}$,

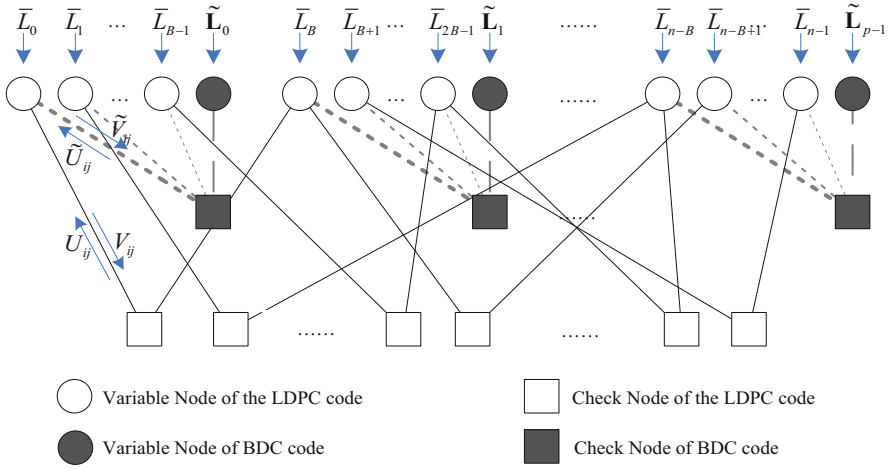

Fig. 2 Tanner graph of the concatenated code

$k \neq j\}$, $C(j)=\{k \mid h_{kj}=1, h_{kj} \in \mathbf{H}\}$ and $C(j) \backslash i=\{k \mid h_{kj}=1, h_{kj} \in \mathbf{H}, k \neq i\}$ are defined here [6]. The joint decoding algorithm is as follows:

1. *Initialization*. Initialize the channel messages $\overline{L}_i(0 \leq i < n)$ and $\widetilde{\mathbf{L}}_i(v)$ $(0 \leq i < p$, $0 \leq v < 2^B)$, and set V_{ij} $(0 \leq i < m, 0 \leq j < n)$ and $\widetilde{V}_{ij}$ $(0 \leq i < p, 0 \leq j < n)$ to 0.
2. *Check node decoding* (*CND*). There are two classes of checks: the LDPC checks by $\mathbf{H}$ and the BDC checks by $\widetilde{\mathbf{H}}$. As shown in Fig. 2, we note U_{ij} and $\widetilde{U}_{ij}$ as the check message from the ith LDPC check node to the jth LDPC variable node and the check message from the ith BDC check node to the jth LDPC variable node, respectively. According to the edges connecting with the LDPC check nodes and the BDC check nodes, messages for the two checks are propagated as follows respectively:

$$U_{ij} = 2 \cdot \tanh^{-1}\left\{\prod\nolimits_{k \in R(i) \backslash j} \tanh\{V_{ik}/2\}\right\}, \quad 0 \leq i < m, \quad 0 \leq j < n \tag{8}$$

$$
\begin{aligned}
\widetilde{U}_{ij} &= \log\frac{P\left(\sum_{k=0}^{n-1}\widetilde{h}_{ik}c_k-\widetilde{c}_i=0\middle|c_j=0,\{\widetilde{y}\}\right)}{P\left(\sum_{k=0}^{n-1}\widetilde{h}_{ik}c_k-\widetilde{c}_i=0\middle|c_j=1,\{\widetilde{y}\}\right)}\\
&= \log\frac{P\left(\sum_{k=0}^{B-1}2^{B-1-k}c_{i\times B+k}-\widetilde{c}_i=0\middle|c_j=0,\{y\}\right)}{P\left(\sum_{k=0}^{B-1}2^{B-1-k}c_{i\times B+k}-\widetilde{c}_i=0\middle|c_j=1,\{y\}\right)}\\
&= \log\frac{\sum_{a_0a_1\cdots a_{B-1}:a_{j-i\times B}=0}\left[\prod_{k=0,k\neq j-i\times B}^{B-1}P(c_{i\times B+k}=a_k)\right]\cdot P\left(\widetilde{y}_i\middle|\widetilde{c}_i=\sum_{k=0}^{B-1}2^{B-1-k}a_k\right)}{\sum_{a_0a_1\cdots a_{B-1}:a_{j-i\times B}=1}\left[\prod_{k=0,k\neq j-i\times B}^{B-1}P(c_{i\times B+k}=a_k)\right]\cdot P\left(\widetilde{y}_i\middle|\widetilde{c}_i=\sum_{k=0}^{B-1}2^{B-1-k}a_k\right)}\\
&= \log\frac{\sum_{a_0a_1\cdots a_{B-1}:a_{j-i\times B}=0}\exp\left[\prod_{k=0,k\neq j-i\times B}^{B-1}\log\frac{P(c_{i\times B+k}=a_k)}{P(c_{i\times B+k}=1)}\right]\cdot\exp\left[\log\frac{P\left(\widetilde{y}_i\middle|\widetilde{c}_i=\sum_{k=0}^{B-1}2^{B-1-k}a_k\right)}{P(\widetilde{y}_i|\widetilde{c}_i=0)}\right]}{\sum_{a_0a_1\cdots a_{B-1}:a_{j-i\times B}=1}\exp\left[\prod_{k=0,k\neq j-i\times B}^{B-1}\log\frac{P(c_{i\times B+k}=a_k)}{P(c_{i\times B+k}=1)}\right]\cdot\exp\left[\log\frac{P\left(\widetilde{y}_i\middle|\widetilde{c}_i=\sum_{k=0}^{B-1}2^{B-1-k}a_k\right)}{P(\widetilde{y}_i|\widetilde{c}_i=0)}\right]}\\
&= \log\frac{\sum_{a_0a_1\cdots a_{B-1}:a_{j-i\times B}=0}\exp\left\{\sum_{k=i\times B,k\neq j}^{i\times B+B-1}(1-a_{k-i\times B})\widetilde{V}_{ik}+\widetilde{\mathbf{L}}_i\left(\sum_{k=0}^{B-1}2^{B-1-k}a_k\right)\right\}}{\sum_{a_0a_1\cdots a_{B-1}:a_{j-i\times B}=1}\exp\left\{\sum_{k=i\times B,k\neq j}^{i\times B+B-1}(1-a_{k-i\times B})\widetilde{V}_{ik}+\widetilde{\mathbf{L}}_i\left(\sum_{k=0}^{B-1}2^{B-1-k}a_k\right)\right\}} \quad 0\le i<p,\ 0\le j<n
\end{aligned}
\tag{9}
$$

where a_i $(0 \le i < B)$ is a binary bit.

3. *Variable node decoding* (*VND*). There are two classes of sum operations: sums from the LDPC variable nodes to the LDPC check nodes, and sums to the BDC check nodes (Actually, there are three sums, and the third one is that sums from the BDC variable nodes to the BDC check nodes. However each BDC variable node just indicates one edge, thus it doesn't update messages). Two terms V_{ij} and $\widetilde{V}_{ij}$ are defined to denote the summing message from the jth LDPC variable node to the ith LDPC check node, and the summing message from the jth LDPC variable node to the ith BDC check node, respectively. These two terms are offered through the edges as follows:

$$V_{ij} = \sum\nolimits_{k\in C(j)\backslash i} U_{kj} + \widetilde{U}_{i'j}\big|_{i'=\lfloor j/B\rfloor},\ \ 0 \le i < m,\ \ 0 \le j < n. \tag{10}$$

$$\widetilde{V}_{ij} = \sum\nolimits_{k\in C(j)} U_{kj},\ \ 0 \le i < p,\ \ 0 \le j < n. \tag{11}$$

4. *Decision*. Denote Z_i $(0 \le j < n)$ as the decision message of the variable node. This message includes all the information from the LDPC check nodes and from the BDC check nodes.

$$Z_j = \sum\nolimits_{k\in C(j)} U_{kj} + \widetilde{U}_{i'j}\big|_{i'=\lfloor j/B\rfloor},\ \ 0 \le j < n. \tag{12}$$

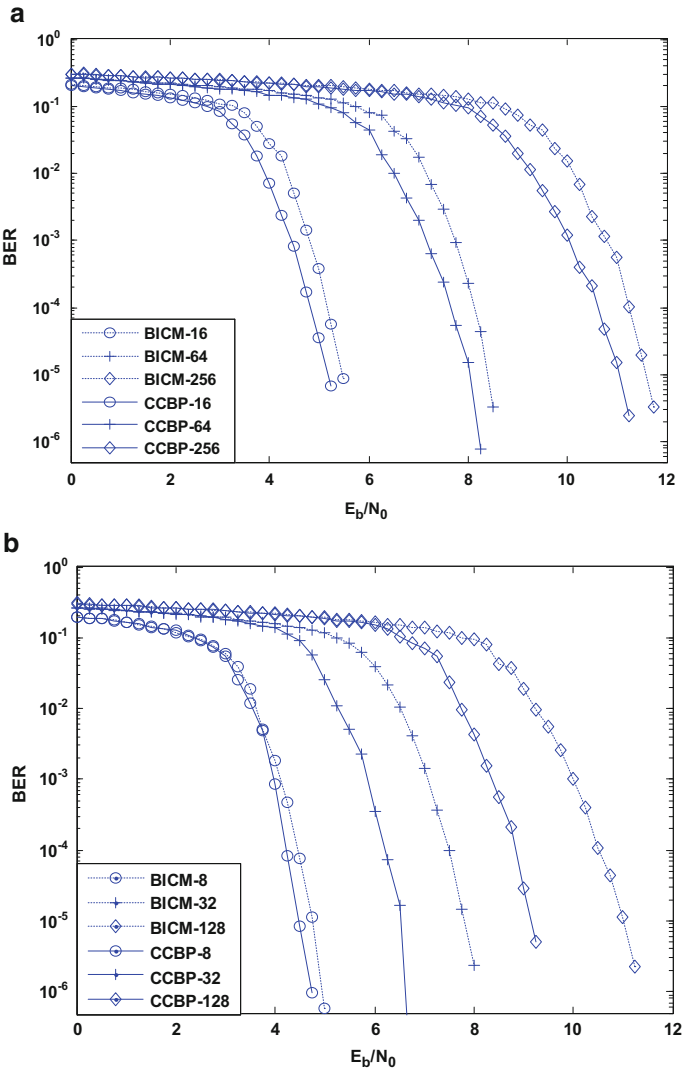

Fig. 3 Performances comparison of CCBP and BICM algorithm. (**a**) performances when 16-QAM, 64-QAM or 256-QAM are adopted; (**b**) performances when 8-QAM, 32-QAM or 128-QAM are adopted

$$d_j = \begin{cases} 0, & Z_j \geq 0 \\ 1, & Z_j < 0 \end{cases}, \quad 0 \leq j < n. \tag{13}$$

Let $\mathbf{D} = [d_0, d_1, \ldots, d_{n\text{-}1}]$, if $\mathbf{HD}^T$=0, the decoding succeeds, otherwise, the decoding fails, then repeat steps 2–4 until $\mathbf{HD}^T$=0 or a present maximum number of iterations is reached.

Compared to the conventional coding schemes and decoding strategies, this paper presents a concatenated coded modulation model and a CCBP decoding algorithm. In the concatenated coded modulation model, the BDC encoder finishes the modulation in a coding way. In the decoding, the proposed method offers a joint message processing for high order modulations. Contrast to conventional BP decoding scheme, the proposed CCBP method offers a joint message processing for high-order modulations in a concatenated code way. This brings to a more accurate decoding process, which will be verified by simulation results in Sect. 4.

4 Simulation Results

The bit error rate (BER) performances of the proposed CCBP algorithm with respect to conventional BP decoding are compared in Fig. 3. All the performances were evaluated over a QAM modulated AWGN channel and a maximum number of 50 iterations were allowed in the decoding. The code in the simulation is adopted from Mackay (3, 6) code sets of length 1008 [8], and the integer in the legend of the figure represents the order of the QAM modulations. It is observed that the proposed algorithm outperforms the BP decoding a little at a 10^{-6} BER when 16-QAM, 64-QAM or 256-QAM are adopted, while by about 0.1, 1.1, and 2.1 dB at a 10^{-6} BER when 8-QAM, 32-QAM or 128-QAM are adopted, respectively. This confirms that the CCBP algorithm performs better than the BP decoding, especially for 2^B-QAM ($B = 3, 5, 7$) modulations.

5 Conclusion

In this work, we present a concatenated code model for high-order LDPC coded modulations. A CCBP decoding algorithm is derived for the concatenated code. Good performance has been obtained with CCBP decoding algorithm for high-order modulations. As advantages with respect to this scheme, the proposed CCBP approach performs superior to the BP algorithm within a wide range of modulation orders.

References

1. MacKay DJC, Neal RM (1996) Near Shannon limit performance of low-density parity-check codes. Electron Lett 32:1645. doi:10.1049/el:19961141
2. Bennatan A, Burshtein D (2006) Design and analysis of nonbinary LDPC codes for arbitrary discrete-memoryless channels. IEEE T Inform Theory 52:549–583. doi:10.1109/TIT.2005.862080

3. Wachsmann U, Fischer RFH, Huber JB (1999) Multilevel codes: theoretical concepts and practical design rules. IEEE T Inform Theory 45:1361–1391. doi:10.1109/18.771140
4. Caire G, Taricco G, Biglieri E (1998) Bit interleaved coded modulation. IEEE T Inform Theory 44:927–946. doi:10.1109/18.669123
5. Proakis JG (2001) Digital communications, 4th edn. McGraw-Hill, Boston, MA
6. Tanner RM (1981) A recursive approach to low complexity codes. IEEE T Inform Theory IT-27:533–547. doi:10.1109/TIT.1981.1056404
7. Wiberg N (1996) Codes and decoding on general graphs. Dissertation, Linköping University
8. MacKay DJC (1999) Good error-correcting codes based on very sparse matrices. IEEE T Inform Theory 45:399–431. doi:10.1109/18.748992

Joint Detection Algorithm for Spectrum Sensing Over Multipath Time-Variant Flat Fading Channels

Mengwei Sun, Yan Zhang, Long Zhao, Bin Li, and Chenglin Zhao

Abstract A popular approach to spectrum sensing is matched filter which could achieve the optimum performance in short sensing time. Under multipath time-variant flat fading channel, this conventional spectrum sensing method could be cumbersome to implement due to channel variation. This paper puts forward a new spectrum sensing algorithm in allusion to this defect. We firstly propose a dynamic state-space model which could thoroughly characterize the evolution of two hidden states: primary user state and the multipath fading channel. Then a promising joint estimation algorithm of these two states based on maximum a posteriori probability criteria and particle filtering technology is presented. Experimental simulations are provided to demonstrate the superior performance of our presented joint detection scheme.

Keywords Spectrum sensing • Multipath time-variant flat fading channel • Dynamic state-space model • Joint estimation • Particle filtering

1 Introduction

In traditional static frequency allocation schemes, only the licensed users (primary users, PUs) have the right to use the allocated spectrum. The mismatch of this static management and the dynamic way the radio resource is used has caused the problem that the contradiction between scarce spectrum resources and under-utilization of the frequency spectrum becomes increasingly serious. Cognitive radio (CR) technique has caused wide attention over the past few years as a promising method to alleviate the scarcity of spectrum resources [1]. As one of the most important elements in CR technology, the spectrum sensing could make

M. Sun (✉) • Y. Zhang • L. Zhao • B. Li • C. Zhao
Key Lab of Universal Wireless Communications, Beijing University of Posts and Telecommunications, Beijing, China
e-mail: 18810536430@163.com

B. Zhang et al. (eds.), *The Proceedings of the Second International Conference on Communications, Signal Processing, and Systems*, Lecture Notes in Electrical Engineering 246, DOI 10.1007/978-3-319-00536-2_89,

unlicensed users (second users, SUs) to detect frequency spectrum accurately and determine whether it is available at a particular place and time.

There are three classical methods of spectrum sensing: energy detection (ED) [2], matched filter detection (MFD) [3], and cyclostationary feature detection [4]. MFD could achieve the optimum performance in short sensing time. Given that pilot, synchronization code and spread spectrum code are utilized in quantities of wireless communication systems, MFD has a wide range of application. However, MFD is a parametric hypothesis method from the statistic view, so the performance is susceptible to the parameter value set up. In the communication system with multipath time-variant flat fading (MTVFF) channel, the determination of parameters is a much more formidable undertaking. In this paper, we design a novel dynamic state-space model (DSM) to describe the model of spectrum sensing over MTVFF channel based on matched filter. And then we propose a promising algorithm which could estimate the multipath time-variant flat fading channel gain and the PU state jointly.

The rest of this paper is organized as follows. Section 2 provides a new DSM for spectrum sensing over MTVFF channel. In Sect. 3, we present the joint blind estimation algorithm based on maximum a posteriori probability (MAP) criteria and particle filtering (PF) technology [5]. Numerical simulations and performance analysis are provided in Sect. 4. Finally, conclusion is presented in Sect. 5.

2 DSM for Spectrum Sensing

The dynamic state-space model designed in this paper takes full consideration of the evolution of primary user state and the multipath fading channel gain, and it could be represented as follow:

$$\begin{cases} \mathbf{x}_n = f(\mathbf{x}_{n-1}) \\ \mathbf{h}_n = \varphi(\mathbf{h}_{n-1}) \\ y_n = g(\mathbf{h}_n, \mathbf{x}_n, \mathbf{w}_n) \end{cases} \qquad n = 0, ..., N-1 \tag{1}$$

Firstly, we employ a first-order Markov chain to abstract the PU states. Secondly, the finite-state Markov channel (FSMC) is utilized to characterize the MTVFF channel [6]. Lastly, the signal processed by matched filter is viewed as the observation. The flowchart of this model is shown in Fig. 1, and we will describe these three parts in follows.

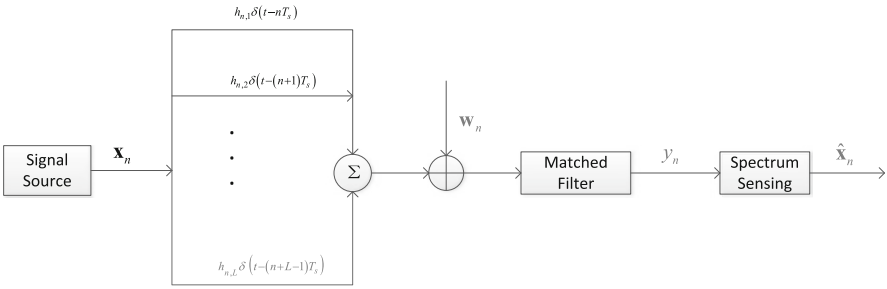

Fig. 1 The flowchart of DSM

2.1 PU States

The working state of PU comes in two forms: active and idle, and we utilize S_0 and S_1 represent them respectively. They transfer to each other with specified probability. Furthermore, we employ a transition probability matrix (TPM) to represent the transition probability, and it could be expressed as:

$$\mathbf{\Pi} = \begin{bmatrix} p_{S_0 \to S_0} & p_{S_0 \to S_1} \\ p_{S_1 \to S_0} & p_{S_1 \to S_1} \end{bmatrix} = \begin{bmatrix} p_{00} & p_{01} \\ p_{10} & p_{11} \end{bmatrix} \tag{2}$$

Here, $p_{01} = 1\text{-}p_{00}$ and $p_{10} = 1\text{-}p_{11}$. The configurations of the transition probability depend on the practical application.

2.2 MTVFF Channel Model

As the other hidden state, the multipath time-variant flat fading channel in n-th sensing slot could be written as [7]:

$$h_n = \sum_{l=0}^{L-1} h_{n,l}\delta(t - l\tau), \qquad n = 0, 1, \ldots, N-1 \tag{3}$$

Here, L is the multipath number, τ represents the sampling period. For the convenience of analysis, we assume that any channel is independent of each other. The main idea data-independent FSMC model is partitioning each channel gain into K different discrete states, and each discrete state transfer to others with specified probability [6]. The transition probability between channel states is defined as:

$$\begin{aligned}\mathbf{h}_n : p(\mathbf{h}_n|\mathbf{h}_{n-1}) &= \prod_{l=0}^{L-1} p(h_{n,l}|h_{n-1,l}) \\ &= \prod_{l=0}^{L-1} p\left(S_{h_{n,l}} = k \middle| S_{h_{n-1,l}} = k'\right) = \prod_{l=0}^{L-1} P_l(k|k')\end{aligned} \tag{4}$$

2.3 Observation

The sampled sequence of transmit signals $\mathbf{X}_{0:N\times M\text{-}1} = [\mathbf{x}_0,\mathbf{x}_1,\ldots,\mathbf{x}_{N\text{-}1}]$, and the corresponding channel gain sequence is represented by $\mathbf{H}$, and the received signal sequence could be written as:

$$\mathbf{Y} = \mathbf{H} \times \mathbf{X} + \mathbf{v} \tag{5}$$

Here, $\mathbf{v}$ represents the vector of noise value which is an additive white Gaussian noise (AWGN) process with zero mean and variance σ^2. At the receiving end, the received signals will be processed by the matched filter firstly, and the observation varies in accordance to the different hypothesis test, i.e.:

$$y_n = \begin{cases} \mathbf{s}_c \bigotimes \mathbf{w}_n & S_{\mathbf{x}_n} = H_0 \\ \mathbf{s}_c \bigotimes (\mathbf{H}_n \times \mathbf{s}_c + \mathbf{v}_n) & S_{\mathbf{x}_n} = H_1 \end{cases} \tag{6}$$

3 Joint Estimation

In this section, detailed spectrum sensing algorithm applied for MTVFF channel will be presented. It is apparent from (6) that the channel gain $\mathbf{h}_n$ will disappear thoroughly when the PU is idle, so the estimation of the channel gain becomes insurmountable in this situation. In order to solve this problem, we adopt different mechanisms to estimate the channel gain according the result of coarse detection about PU state. More specifically, the estimation algorithm consists of three steps, i.e., (1) the coarse detection about the PU state, (2) the estimation of fading channel gain based on MAP and (3) PF-based PU state detection. These steps will be described in detail in follows.

3.1 Coarse Detection

The purpose of this step is to detect the PU state roughly in order to determine the estimation mechanism for channel gain, and we could get an initial result by specify a threshold:

$$\tau_{CD} = \frac{\mathbf{s}_c}{2} \otimes [\min(\mathbf{h}_k) * \mathbf{s}_c], \qquad k = 0, \ldots, K-1 \tag{7}$$

Here, $\min(\mathbf{h}_k)$ represents the minimum fading channel gain. Based on the decision criterion above, we could get the coarse detection as:

$$\mathbf{x}_n^{\dagger} = \begin{cases} \mathbf{0} & y_n < \tau_{CD} \\ \mathbf{s}_c & y_n \geq \tau_{CD} \end{cases} \tag{8}$$

It is worthy to note that the purpose of coarse detection in this paper is to provide the basis for the choice of mechanism which could be applied to estimate the channel gain in real-time. Even though the accuracy of coarse detection is relatively low, the subsequent algorithm will modify the result for the purpose of accurate estimation.

3.2 Estimation of Multipath Fading Channel Gain

The reasons why different mechanisms are utilized for channel gain estimation include the following:

Firstly, because the channel has the character of flat fading, the channel coherence time T_c is longer than the period of sensing slot T_s. For simplicity, T_c is supposed to be multiples of T_s [6]. Therefore, due to the different location in a channel gain period, the sensing slots could be classified into two categories: first slot and non-first slot, and they are defined as (9). And the channel gain is possible to transfer into other state only in the first slot.

$$\mathrm{mod}(nT_s, T_c) \begin{cases} = 0, & first\ \ slot \\ \neq 0, & non-first\ \ slot \end{cases} \qquad n = 0, \ldots, N-1 \tag{9}$$

Secondly, the MAP criteria for channel gain becomes useless when the PU state is absent, i.e. $\mathbf{x}_n = 0$, in order to combat this problem, we should find some other effective ways to estimate the state of fading channel gain.

Based on the aforementioned reasons, this paper presents the overall design diagram for multipath time-variant flat fading channel:

If $\mathbf{x}_n^{\dagger} = 0$, and the sensing slot is the first in a channel state period, we could obtain the estimation of $\mathbf{h}_n$ based on the prior transition probability, as shown in (10a), and the $\hat{\mathbf{h}}_{pre}$ represents the final estimation of channel gain in the previous channel state period;

If $\mathbf{x}_n^{\dagger} = 0$, and the sensing slot is the non-first, the estimation of fading channel gain is assumed unchanged, like (10b);

If $\mathbf{x}_n^{\dagger} = \mathbf{s}_c$, we could obtain the MAP estimation of fading gain by (10c).

$$\hat{\mathbf{h}}_n = \arg\max_{\hat{\mathbf{h}}_n \in A} p\left(\mathbf{h}_n \middle| \hat{\mathbf{h}}_{pre}\right) \qquad \mathbf{x}_n^{\dagger} = 0 \ \& \ first \ \ slot \tag{10a}$$

$$\hat{\mathbf{h}}_n = \hat{\mathbf{h}}_{n-1}, \qquad \mathbf{x}_n^{\dagger} = 0 \ \& \ non-first \ \ slot \tag{10b}$$

$$\hat{\mathbf{h}}_n = \arg\max_{\hat{\mathbf{h}}_n \in A} p\left(y_n \middle| \mathbf{h}_n, \mathbf{x}_n^{\dagger}\right) p\left(\mathbf{h}_n \middle| \hat{\mathbf{h}}_{pre}\right), \qquad \mathbf{x}_n^{\dagger} = \mathbf{s}_c \tag{10c}$$

The likelihood function $p(y_n|\mathbf{h}_n, \mathbf{x}\dagger\ \mathbf{n})$ in (10c) follows the Gaussian distribution and the configuration is:

$$p\left(y_n \middle| \mathbf{h}_n, \mathbf{x}_n^{\dagger} = \mathbf{s}_c\right) = \frac{1}{\sqrt{2\pi\left(\mathbf{s}_c^T \times \mathbf{s}_c\right)\sigma^2}} \exp\left\{\frac{-\left[y_n - \mathbf{s}_c \bigotimes (\mathbf{h}_n * \mathbf{s}_c)\right]^2}{2\left(\mathbf{s}_c^T \times \mathbf{s}_c\right)\sigma^2}\right\} \tag{11}$$

3.3 PF-Based PU State Detection

Based on the Bayesian theory, particle filtering technology shows huge superiority when handing with blind estimation problem. The key of particle filtering is approximating a complex distribution by a series of particles with associated weights, and then, the MAP estimation could be drawn and the marginal data detection at time n is given by [8]:

$$\hat{\mathbf{x}}_n^{(MAP)} = \arg\max_{\mathbf{x}_n \in X} \left\{ \sum_{i=1}^{P} \delta\left(\mathbf{x}_n - \mathbf{x}_n^{(i)}\right) w_n^{(i)} \right\} \tag{12}$$

The process of PF technology applying for signal detection covers four basic steps as follows: (1) generate particles based on sequential importance sampling (SIS); (2) compute the associated weight; (3) re-sampling; (4) MAP estimation. We will give a detailed account of these steps [9,10].

Firstly, we begin SIS algorithm by drawing particles from important distribution. The form of the important distribution varies according to the actual situation. In this paper, we adopt the optimal importance distribution:

$$\pi(\mathbf{x}_n|\mathbf{x}_{0:n-1}, y_{0:n}, \mathbf{h}_{0:n}) \propto p\left(y_n \middle| \mathbf{x}_n, \mathbf{x}_{0:n-1}^{(i)}, y_{0:n-1}, \hat{\mathbf{h}}_n\right) p\left(\mathbf{x}_n \middle| \mathbf{x}_{0:n-1}^{(i)}\right) \tag{13}$$

Secondly, the associated importance weights could be computed recursively by [9]:

$$\widetilde{w}_n^{(i)} = w_{n-1}^{(i)} \times \frac{p\left(y_n \middle| \mathbf{x}_{0:n}^{(i)}, \hat{\mathbf{h}}_n, y_{0:n-1}\right)}{\pi\left(\mathbf{x}_n^{(i)} \middle| \mathbf{x}_{0:n-1}^{(i)}, y_{0:n}\right)} = w_{n-1}^{(i)} \times p\left(y_n \middle| \mathbf{x}_{n-1}^{(i)}, \hat{\mathbf{h}}_n\right) \tag{14}$$

Unfortunately, the degeneracy of SIS algorithm is usually inevitable after several times of iteration, as an efficient approach to alleviate this difficulty, the

re-sampling procedure is processed to eliminate particle trajectories with small normalized importance weight while concentrate upon those trajectories having larger normalized importance weight [10].

Lastly, the MAP estimation could be achieved by (12) based on the particles and associated weights computed above.

4 Computer Simulation

In this paper, we focus on a scenario of a multipath time-variant Weibull fading channel with parameters $\lambda = 1, \beta = 1.4$ and we assume the TPM of PU state is:

$$\mathbf{\Pi} = \begin{bmatrix} p_{00} & p_{01} \\ p_{10} & p_{11} \end{bmatrix} = \begin{bmatrix} 0.8 & 0.2 \\ 0.2 & 0.8 \end{bmatrix}$$

We will compare the performance of proposed algorithm with the traditional MFD method. And this investigation mainly studies the effects that the parameters of multipath channel have on the sensing performance, i.e. Doppler frequency shift fd and number of multipath channel L.

4.1 PF-Based PU State Detection

In this simulation, the number of multipath is set to be 4, the size of partitioned states number for the MTVFF channel is $K = 5$. Three configurations of maximum Doppler frequency shift f_d are adopted in this experiment, i.e., $f_d = 0.2, 0.1, 0.05$. The simulation results are shown in Fig. 2.

It is obvious from Fig. 2 that compared with traditional MFD method the sensing performance achieved by proposed algorithm could be improved significantly when operating the MTVFF channel. For example, when the detection probability surpass 0.95 and the $f_d = 0.1$, the desired SNR of new algorithm and traditional MFD method is 4.5 dB and 12 dB respectively.

4.2 Number of Multipath Channel

In this simulation, the maximum Doppler frequency shift $f_d = 0.1$, and the partitioned states size of MTVFF channel K is assumed to be 5. The number of multipath channel L is 3, 4and 5 respectively. From the numerical experiment results shown in Fig. 3, it should be noted that with the advance of L, the performance of proposed algorithm will decrease.

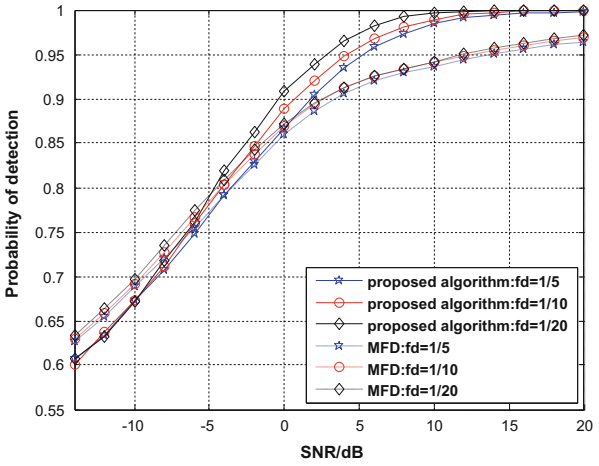

Fig. 2 Sensing performance of the proposed joint estimation algorithm and traditional MFD method under different maximum Doppler frequency shift fd

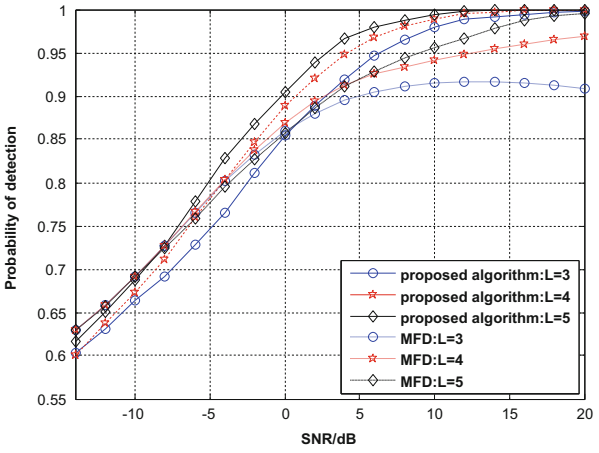

Fig. 3 Sensing performance of the proposed joint estimation algorithm and traditional MFD method under different number of multipath

5 Conclusion

In this article, we have designed a promising spectrum sensing algorithm which could find wide use in CR systems. The advantages of this algorithm could be summarized into three-fold. First of all, the sensing of allocated spectrum is accessible by detecting the pilot or synchronization code, this feature ensures that the algorithm proposed could be applied for most CR systems. Secondly, a novel DSM is developed from the Bayesian point of view which takes full consideration of the multipath time-variant fading channel. This DSM could be applied for signal estimation in other communication systems. Lastly, we propose a joint estimation algorithm which could estimate the channel gain and PU state sequentially and timely without a training sequence. And simulation verifying tests indicate that this

method could achieve better performance than traditional MFD method over multipath time-variant flat fading channel. Because of the advantages aforementioned, this proposed method could provide a referential solution to the practical design of spectrum sensing algorithms.

Acknowledgement This work was supported by the National Natural Science Foundation of China (61271180), Major National Science and Technology Projects (2012zx03001022) and Special Foundation for State Internet of Things Program (Radio frequency and communication security testing service platform of Internet of things).

References

1. Mitola J, Maguire GQ (1999) Cognitive radio: making software radios more personal. Personal Communications. IEEE 6(4):13–18
2. Digham FF, Alouini MS, Simon MK (2003) On the energy detection of unknown signals over fading channels. Proc. of IEEE international conference on communications, vol 5, Anchorage, AK, May 2003, pp 3575–3579
3. Zhang Z, Yang Q, Wang L, Zhou X (2010) A novel hybrid matched filter structure for IEEE 802.22 standard. Circuit Syst (APCCAS), IEEE Asia Pacific conference, 2010, pp 652–655
4. Cabric D, Mishra SM, Brodersen RW (2004) Implementation issues in spectrum sensing for cognitive radio. Proc. Asilomar Conf. Signals, Syst., Comput., vol 1, Nov 2004, pp 772–776
5. Djuric PM, Kotecha JH, Zhang JQ, Huang YF, Chirmai T, Bugallo MF, Miguez J (2003) Particle filtering. IEEE Signal Process Magazine 20(5):19–38
6. Sadeghi P, Kennedy R, Rapajic P, Shams R (2008) Finite-state Markov modeling of fading channels: a survey of principles and applications. IEEE Signal Process Magazine 25(5):57–80
7. Zhang D, Tian Z (2007) Adaptive game-based radio spectrum allocation in doubly selective fading channels. IEEE international conference on digital object identifier, 2007, pp 5172–5176
8. Miguez J, Djuric PM (2004) Blind equalization of frequency-selective channels by sequential importance sampling. IEEE Trans Signal Process 52(10):2738–2748
9. Liu JS, Chen R (1995) Blind deconvolution via sequential imputations. J Am Stat Assoc 90 (430):567–576
10. Doucet A (2000) On sequential Monte Carlo sampling methods for Bayesian filtering. Stat Comput 10:197–208

Empirical Likelihood-Based Channel Estimation with Laplacian Noise

Long Zhao, Qiang Ma, Bin Li, and Chenglin Zhao

Abstract This paper introduces a new method to estimate channel with Laplacian noise based on empirical likelihood algorithm. The received signal is assumed to be a transmitted signal which has been corrupted by a multipath channel, modeled as a FIR filter, the output being further disturbed by additive independent Laplacian noise. Then the channel estimation is treated as a nonparametric estimation issue in the model and the channel parameter is estimated by Empirical Likelihood approach. Furthermore, the MSE and BER performance of channel estimation are explored via numerical simulations.

Keywords Laplacian noise • Empirical likelihood • Channel estimation

1 Introduction

A number of situations exist where the problem is to estimate channel parameter in an observed signal. Examples of such problems would be channel coefficients, channel phase, time delay, etc. It is normally assumed in these cases that the noise is Gaussian [1,2]. Two common motives for this assumption are that the noise in many applications is approximately Gaussian according to the central limit theorem, and the Gaussian assumption is analytically tractable.

However, in practice, certain noises cannot be reasonably characterized as Gaussian due to their impulsive nature [3]. One form of frequently encountered non-Gaussian noise is referred to as impulsive noise [4]. Such noise can be modeled by a random variable whose distribution has an associated "heavy tail" behavior. The Laplace distribution is popular for modeling non-Gaussian, impulsive noises in engineering studies owing to its capability of characterizing the heavy tail behavior

L. Zhao • Q. Ma (✉) • B. Li • C. Zhao
Key Lab of Universal Wireless Communications, Beijing University of Posts and Telecommunications, Beijing, China
e-mail: 516139197@qq.com

B. Zhang et al. (eds.), *The Proceedings of the Second International Conference on Communications, Signal Processing, and Systems*, Lecture Notes in Electrical Engineering 246, DOI 10.1007/978-3-319-00536-2_90,

exhibited by these noise. For example, as demonstrated in [5], Laplacian approximation is more accurate than a Gaussian approximation for the distribution of the multiple access interference in time-hopping ultra-wide bandwidth communication. It also has been used in image processing [6] and in modeling noise encountered in communications at low frequencies [7]. Although estimation in non-Gaussian environments is a more complex issue, empirical likelihood, which is endowed with the advantageous character that it works when the mean of noise is zero, is effective for these problems.

The rest of the article is organized as follows. Section 2 describes the signal model for the channel estimation. The empirical likelihood algorithm for channel estimation is developed in Sect. 3. Illustrative computer simulations are presented in Sect. 4 and some concluding remarks are made in Sect. 5.

2 Signal Model

Consider a digital communication system where BPSK symbols $s_t \in \{\pm 1\}$, $t = 0,1,2,\ldots$ are transmitted in frames through a frequency-selective multipath fading channel. When the coherent time of the fading process is long enough compared with the frame size, it is commonly assumed that the channel impulse response (CIR) is constant for the duration of the frame. In such cases, the receiver signal is fed into a matched filter and then sampled with a symbol rate. The resulting sampled sequence can be expressed as (1)

$$y_i = \sum_{l=0}^{m-1} s_l h_{t-l} + v_i, \quad i = 1, 2, \ldots \tag{1}$$

where v_i is an additive white Laplacian noise process with zero mean, whereas h_i, $i \in Z$, is the discrete-time equivalent CIR. In the practical case that the transmitted pulse waveforms are causal signals with limited duration, the discrete-time equivalent CIR becomes a causal finite-length sequence that can be conveniently represented by $m \times 1$ vector

$$\mathbf{h} = [h_{m-1}, h_{m-2}, \ldots, h_0]^{\mathrm{T}} \tag{2}$$

where m is the channel order (it physically represents the number of resolvable propagation paths), and the superindex T denotes transposition. We usually assume that the channel vector complies with Gaussian distribution. Then let us reformulate model (1) with (3) to gain an easier expression for signal model (4).

$$\mathbf{S}_i = \left(s_{i0},\ s_{i1}, \ldots, s_{i(m-1)}\right)^{\mathrm{T}} \tag{3}$$

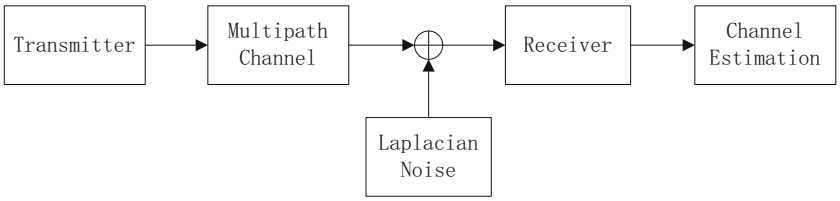

Fig. 1 Signal model

$$Y_i = \mathbf{S}_i^{\mathrm{T}}\mathbf{h} + v_i \quad i = 1, 2, \ldots \tag{4}$$

Figure 1 vividly illustrates the signal model (4).In the model the multipath channel coefficients, h_i, $i = 0,1,\ldots,m\text{-}1$, are assumed unknown. The main objective is to recover the coefficients with the help of observations Y_i and aided-data S_i.

3 Channel Estimation with Laplacian Noise

The probability density function of zero-mean Laplacian noise v is

$$f_v(x) = \frac{1}{\sqrt{2}\sigma} e^{-\frac{\sqrt{2}|x|}{\sigma}} \quad x \in \mathbf{R} \tag{5}$$

where σ^2 is the variance of the noise.

The basic idea of the algorithm is to make mean square deviation smallest, that is, to compute the best $\mathbf{h}$ minimizing the function $\mathrm{E}[(Y\text{-}\mathbf{S}^{\mathrm{T}}\mathbf{h})^2]$. Then the best vector $\mathbf{h}$ is

$$\mathbf{h} = \left(E\mathbf{S}_i\mathbf{S}_i^{\mathrm{T}}\right)^{-1} E(\mathbf{S}_i Y) \tag{6}$$

Using above relationships, the (6) can be written as (7) and we define a new variable $W(\mathbf{h})$ in (8).

$$E\ \mathbf{S}_i\left(Y - \mathbf{S}_i^{\mathrm{T}}\mathbf{h}\right) = 0 \tag{7}$$

$$W_i(\mathbf{h}) = \mathbf{S}_i\left(Y - \mathbf{S}_i^{\mathrm{T}}\mathbf{h}\right) \tag{8}$$

To gain the $\mathbf{h}$, we introduce an empirical likelihood $R(\mathbf{h})$ according to Owen's theory [8–10]. Thus the estimation becomes a nonparametric issue explicitly illustrated as follows:

$$R(\mathbf{h}) = \sup_{p_1,\cdots,p_n} \sum_{i=1}^{n} \log(np_i) \tag{9}$$

where $p_1,\ldots,p_n$ are subject to the following restrictions [11–14]

$$\sum_{i=1}^{n} p_i W_i(\mathbf{h}) = 0, \quad \sum_{i=1}^{n} p_i = 1, \quad p_i \geq 0, \quad i = 1, \ldots, n \tag{10}$$

where n is the length of observation Y and $\{p_i\}$ can be computed via Lagrange scheme [9]

$$p_i(\mathbf{h}) = \frac{1}{n\left(1 + \lambda^{\mathrm{T}} W_i(\mathbf{h})\right)} \tag{11}$$

where λ is uniquely determined by

$$\frac{1}{n} \sum_{i=1}^{n} \frac{W_i(\mathbf{h})}{1 + \lambda^{\mathrm{T}} W_i(\mathbf{h})} = 0 \tag{12}$$

The suitable solution λ of (12) can be gained by Newton algorithm. Consequently the empirical likelihood $R(\mathbf{h})$ can be obtained. Then the estimation of channel should be given by

$$\mathbf{h} = \underset{\mathbf{h}}{\operatorname{argmax}} \quad R(\mathbf{h}) \tag{13}$$

4 Simulation

In this section, we will study the performance of the estimation method for system with Laplacian noise. As illustrated in Fig. 2, we demonstrate the MSE performance of the proposed scheme in different aided-data length as the channel order m is 3. It is apparent that the estimation performance will be better as the aided-date length grows.

Then, we can detect the transmitted signal S_i using the acquired channel coefficients $\mathbf{h}$. Figure 3 depicts the detection result by obtained $\mathbf{h}$ when aided-data length is 50 and clearly shows that the detections have a relatively good BER performance.

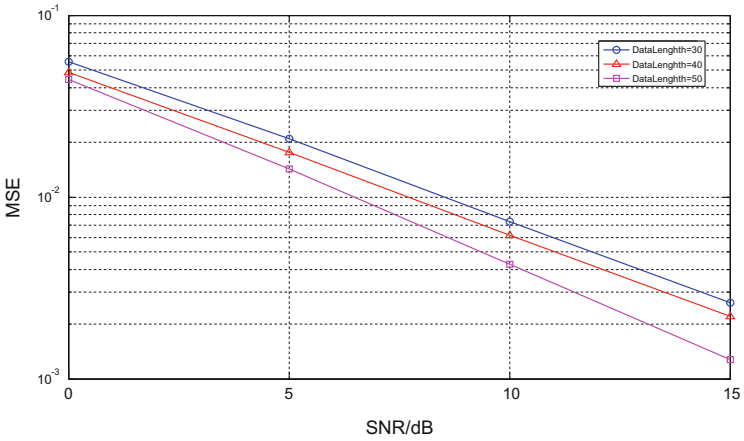

Fig. 2 MSE performance with different aided-data length

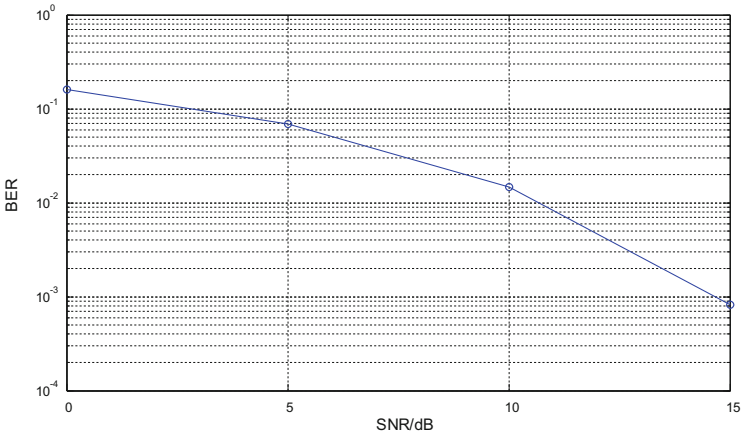

Fig. 3 BER performance when aided-data length is 50

5 Conclusion

In this paper, we provide an Empirical Likelihood scheme for channel estimation in digital communication system with Laplacian noise. Firstly, modeling for these systems is introduced. Then, we present an Empirical Likelihood for channel estimation. Simulation results show that the estimation proposed in this paper has good MSE and BER performance.

Acknowledgement This work was supported by the National Natural Science Foundation of China (61271180), Major National Science and Technology Projects (2012zx03001022) and Special Foundation for State Internet of Things Program (Radio frequency and communication security testing service platform of Internet of things).

References

1. Proakis JG, Dimitris GM (1995) Digital communications, vol 3. McGraw-Hill, New York
2. Van Trees HL (2004) Detection, estimation, and modulation theory. Wiley, New York
3. Kassam SA (1989) Signal detection in non-Gaussian noise. Sringer, Berlin
4. Marks RJ et al (1978) Detection in Laplace noise. Aerospace Electron Syst IEEE Trans 6:866–872
5. Beaulieu NC, Niranjayan S (2010) UWB receiver designs based on a Gaussian-Laplacian noise-plus-MAI model. Commun IEEE Trans 58(3):997–1006
6. Woods JW, O'Neil S (1986) Subband coding of images. Acoust Speech Signal Process IEEE Trans 34(5):1278–1288
7. Bernstein SL et al (1974) Long-range communications at extremely low frequencies. Proc IEEE 62(3):292–312
8. Owen AB (1988) Empirical likelihood ratio confidence intervals for a single functional. Biometrika 75(2):237–249
9. Owen A (1990) Empirical likelihood ratio confidence regions. Ann Stat 18(1):90–120
10. Owen A (1991) Empirical likelihood for linear models. Ann Stat 19(4):1725–1747
11. Xu F (2009) An empirical likelihood scheme for signal detection in MIMO systems with nonlinear interference. Circuit Commun Syst. PACCS'09. Pacific-Asia conference on IEEE, 2009, pp 540–543
12. Xu F, Xu X, Zhang P (2007) Semiparametric theory based MIMO model and performance analysis. J China Univ Posts Telecomm 14(4):36–40
13. Li G, Qi-Hua W (2003) Empirical likelihood regression analysis for right censored data. Stat Sinica 13(1):51–68
14. Wang Q, Jonnagadda NKR (2002) Empirical likelihood-based inference in linear errors-in-covariables models with validation data. Biometrika 89(2):345–358

Multi-path Channel Estimation Using Empirical Likelihood Algorithm with Non-Gaussian Noise

Pengbiao Wang, Yan Zhang, Long Zhao, Bin Li, and Chenglin Zhao

Abstract In this paper a novel algorithm, empirical likelihood, is employed to estimate the channel taps of multi-path channel under Non-Gaussian noise. To illustrate, multi-path channel is modeled as a FIR filter and non-Gaussian noise is taken as mixed Additive White Gaussian and impulse noise for simplicity. Thus the transmitted signal, being impacted by the multi-path fading effect and being disturbed by the non-Gaussian noise, would be sampled to form the received signal. And simulations show that the proposed algorithm is capable of obtaining good MSE and bit error rate BER performances.

Keywords Multi-path channel estimation • Non-Gaussian noise • Empirical likelihood

1 Introduction

Multi-path frequency selective fading channel is frequently encountered in wireless communications, causing considerable performance degradation. The impulse response of multi-path fading channel can be modeled as an autoregressive (AR) process. In [1], a lease-square (LS) method was proposed for the AR parameters estimation of the fading channel model. The LS criterion is considered optimal and equivalent to maximum-likelihood (ML) for channel estimation when the transmitted symbols are equi-probable and noise being additive Gaussian [2, 3]. And in [4], a coupled estimator consisting of a Kalman filter in parallel with a LS-based AR parameters estimator was introduced. Although these algorithms perform well in additive white Gaussian noise channel, their performances will significantly deteriorate in non-Gaussian noise environment, which appears often in

P. Wang (✉) • Y. Zhang • L. Zhao • B. Li • C. Zhao
Key Lab of Universal Wireless Communications, MOE Wireless Network Lab, Beijing University of Posts and Telecommunications, Beijing, China
e-mail: wangpengbiao999@126.com

B. Zhang et al. (eds.), *The Proceedings of the Second International Conference on Communications, Signal Processing, and Systems*, Lecture Notes in Electrical Engineering 246, DOI 10.1007/978-3-319-00536-2_91,

communications channel. Consequently, the received signal cannot be equalized appropriately and system performance will be degraded.

Empirical likelihood [5–7], which has a highlighted advantage that it works as long as the mean of the noise system suffers equals zero no matter what kinds of noise it is, is proposed in this paper for estimating the channel over the mixed Gaussian and impulse noise channel. That quality endows it with the ability to solve the degradation originated from the sensitivity of the traditional methods. Simulations showed good performance in estimation of fading channel in hybrid noise environment.

This work is organized as follows: Section 2 introduces the fading channel model with non-Gaussian noise. Section 3 illustrates the estimation using empirical likelihood method. Section 4 discusses the environment used for simulation and shows the results of this work. Finally, Sect. 5 exposes conclusions.

2 Problem Formulation

For simplicity, we consider the real domain model and assume that the base band received signal $y(t)$ after appropriate filtering and sampling can be modeled as:

$$y(t) = \sum_{l=0}^{L-1} s(t-l)h(t,l) + n(t) + e(t) \tag{1}$$

where $s(t)$ is the transmitted training signal at time t and $h(t,l)$ is the lth tap of the impulse response of the multi-path channel, L is the length of multi-path. Then we take mixed Additive White Gaussian Noise and impulse noise as the non-Gaussian noise. In (1), $n(t)$ and $e(t)$ indicate Additive White Gaussian Noise and impulsive noise respectively, which are mutually independent variables with zero-mean. In the vector form, we have

$$\mathbf{y} = \mathbf{Sh} + \mathbf{n} + \mathbf{e} \tag{2}$$

where $\mathbf{h} = [h_0\, h_1\ \cdots\ h_{L-1}]^T$, $\mathbf{y} = [y_0\, y_1\ \cdots\ y_{N-1}]^T$, $\mathbf{n} = [n_0\, n_1\ \cdots\ n_{N-1}]^T$, $\mathbf{e} = [e_0\, e_1\ \cdots\ e_{N-1}]^T$ and $\mathbf{S}$ is the known training matrix given by

$$\begin{aligned}\mathbf{S} &= \begin{bmatrix} s(0) & s(-1) & \cdots & s(-L+1) \\ s(1) & s(0) & \cdots & s(-L+2) \\ \vdots & \vdots & \ddots & \vdots \\ s(N-1) & s(N-2) & \cdots & s(N-L) \end{bmatrix} \\ &= [\mathbf{s}_0 \quad \mathbf{s}_1 \quad \cdots \quad \mathbf{s}_{N-1}]^T \end{aligned} \tag{3}$$

In practice, the channel taps are unknown or time-varying and thus real-time estimation is required. Commonly, periodic training sequence is transmitted to the

receiver to estimate the channel parameters. Efficient algorithms have been proposed to estimate the AR parameters using LS algorithm [1, 4]. Data symbols are then transmitted after the training period. At the receiver, each data symbol is detected using the current estimate of the channel.

Unfortunately, the algorithms above are known to be sensitive to non-Gaussian noise, such as impulse noise coming from the communications channel. The accuracy of the channel estimation would deteriorate, which will lead to significant degradation of system performance. So, we adopt the empirical likelihood method to get robust estimation of the channel taps.

3 Empirical Likelihood Estimation

Notion of Empirical Likelihood has been explicitly illustrated in [5–7] by Owen. Meanwhile, Owen developed it and utilized it in nonparametric regression problem [8–10]. According to his theory, as long as the mean of both $\boldsymbol{n}$ and $\boldsymbol{e}$ equal zero, which means true value of $\boldsymbol{h}$ satisfies the following formula:

$$E\left(\mathbf{s}^T(\mathbf{y}-\mathbf{sh})\right)=0 \tag{4}$$

thus we can define an auxiliary variable

$$Z_i = Z_i\left(\hat{\mathbf{h}}\right) = \mathbf{s}_i{}^T\left(\mathbf{y}_i - \mathbf{s}_i\hat{\mathbf{h}}\right) \tag{5}$$

where $\hat{\mathbf{h}}$ is the channel taps estimated. Then the empirical likelihood ratio function of $\hat{\mathbf{h}}$ can be computed as:

$$R\left(\hat{\mathbf{h}}\right) = \max\left\{\prod_{i=1}^{N}(Np_i)\Big|\sum_{i=1}^{N}p_iZ_i\left(\hat{\mathbf{h}}\right) = \begin{bmatrix}0\\ \vdots\\ 0\end{bmatrix}_{L\times 1}, p_i \geq 0, \sum_{i=1}^{N}p_i = 1\right\} \tag{6}$$

where $\{p_{\mathrm{i}},\ \mathrm{i} = 1\ldots\mathrm{N}\}$ is a set of probability weights allocated to the auxiliary variable Z_{i} .To figure out $p_{,}$ we adopt Lagrange method and attain the equation bellow:

$$p_i\left(\hat{\mathbf{h}}\right) = \frac{1}{N[1+\lambda(Z_i{}^T-\mu)]},\quad i=1,2,\cdots,N \tag{7}$$

where μ indicates mean of auxiliary variable Z, λ signifies the solution of the following function:

$$\sum_{i=1}^{N} \frac{Z_i{}^T - \mu}{1 + \lambda(Z_i{}^T - \mu)} = 0 \tag{8}$$

Based on the discussions above, the logarithmic empirical likelihood of $\hat{\mathbf{h}}$ can be worked out by

$$l(\hat{\mathbf{h}}) = -2\log R(\hat{\mathbf{h}}) = -2\log\left\{\prod_{i=1}^{N} N p_i(\hat{\mathbf{h}})\right\} \tag{9}$$

It has been proved in [6] that the problem becomes the process of minimizing $l(\hat{\mathbf{h}})$. It has also been verified that the problem is convex, closed and compact, thus there has a unique $\hat{\mathbf{h}}$ minimizing $l(\hat{\mathbf{h}})$.

4 Simulation Results

Simulations under mixed Gaussian and impulse noise environment are performed to evaluate the performance of the proposed channel estimation algorithm. In our experiment, the results are obtained by averaging over 100 independent runs. A multi-path channel with length L = 3 is considered. The training symbols s(t) are drawn from BPSK. Initial training period of 20, 40 and 60 samples under a series of SNR including 0, 5, 10, 15 dB are used respectively. The receiver starts to decode the data after the training period and the BER performance could be gained under the conditions proposed above.

Figure 1 shows the MSE of the channel estimation at different SNR. It is clear that higher estimation accuracy will be achieved with the SNR improved. Meanwhile, longer training sequence will assure more accurate estimation.

Figure 2 demonstrates the BER based on the channel estimators above. It illustrates that our algorithm can get relatively good BER performances when SNR is bigger than 10 dB.And it's clear the length of training sequence has a minor influence on BER.

5 Conclusion

Modern communication systems are affected by varying kinds of non-Gaussian noise, such as impulse noise originating from man-made electromagnetic interference, atmospheric noise and ignition noise, etc. In general, the non-Gaussian noise will terribly degrade the performance of the wireless system. That problem can be improved by empirical likelihood method introduced in this paper. Simulations show that the proposed algorithm performs well under the non-Gaussian noise.

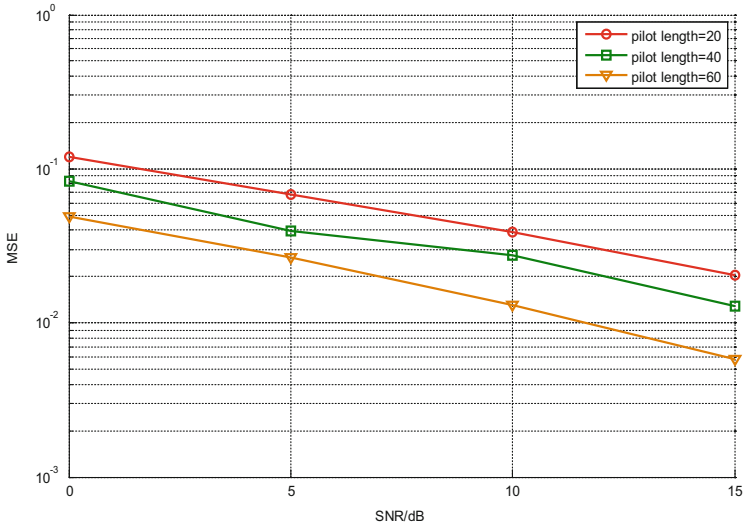

Fig. 1 Mean-square error of channel estimation

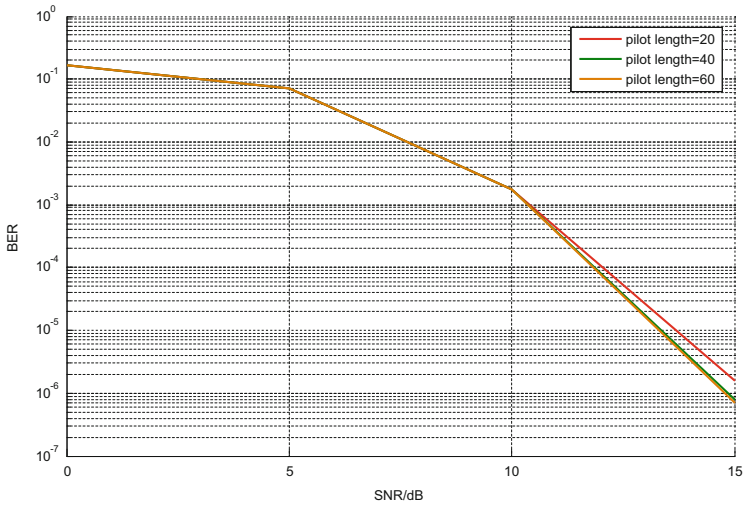

Fig. 2 Bit error rate based on the channel estimated above

Acknowledgement This work was supported by the National Natural Science Foundation of China (61271180), Major National Science and Technology Projects (2012zx03001022) and Special Foundation for State Internet of Things Program (Radio frequency and communication security testing service platform of Internet of things).

References

1. Tsatsanis MK, Giannakis GB, Zhou G (1996) Estimation and equalization of fading channels with random coefficients. Signal Process 53:211–229
2. Crozier SN, Falconer DD, Mahmoud SA (1991) Least sum of squared errors (LSSE) channel estimation. IEE Proc F 138(4):371–378
3. Van Trees HL (1968) Detection, estimation, and modulation theory, Part I. Wiley, London
4. Davis LM, Collings IB, Evans RL (1997) Identification of time-varying linear channels. Proc. ICASSP'97, Apr 1997, Munich, Germany
5. Owen AB (1988) Empirical likelihood ratio confidence intervals for a single functional. Biometrika 75:237–249
6. Owen AB (1988) Small sample central confidence intervals for the mean. Technical report 302, Dept. Statistics, Stanford Univ
7. Owen AB (1988) Computing empirical likelihoods. In: Wegman EJ, Gantz PT, Miller JJ (eds) Computing science and statistics. Proceedings of the 20th symposium on the interface. American Statistics Association, Alexandria, VA, pp 442–447
8. Owen AB (1990) Empirical likelihood confidence regions. Ann Stat 18:90–120
9. Owen AB (1991) Empirical likelihood for linear models. Ann Stat 19:1725–1747
10. Owen AB (2001) Empirical likelihood. Chapman and Hall, New York

A Training Sequence Parallel Detection Technology Based on Timeslot Sliding Window

Jian Shi, Jianfeng Huang, and Kaihua Liu

Abstract The GSM radio network's latest development status and its prominent problems were discussed with the limitations of the radio network analysis using the traditional drive test and frequency sweeping. A new training sequence parallel detection technology base on timeslot sliding window were proposed, the timeslot sliding window technology and the algorithms of the parallel correlative detection were discussed in detail. With the successful application cases of the engineering practice in Zhejiang Province, the important application valuation of the new technology proposed in this paper in the radio network planning and optimization engineering was proved.

Keywords Timeslot sliding window • Training sequence • Parallel detection • Cellular radio network

1 Introduction

With high-speed growth of mobile service, the load of radio network increases daily. The frequency bands of GSM900, DCS1800 and EGSM have been massively implemented. The number of sites with high carrier configuration and density of frequency reuse increase constantly while the distance between base stations of cellular networks is decreasing. At present the GSM radio network of China Mobile Communications Corporation has widespread problems of excessive overlapping

J. Shi (✉) • K. Liu
Tianjin University, Tianjin, China
e-mail: shijian@139.com

J. Huang
Beijing University of Posts and Telecommunications, Beijing, China

B. Zhang et al. (eds.), *The Proceedings of the Second International Conference on Communications, Signal Processing, and Systems*, Lecture Notes in Electrical Engineering 246, DOI 10.1007/978-3-319-00536-2_92,

coverage, severe cross-boundary overage and rapidly increasing probability of CCI (Co-Channel Interference) and ACI (Adjacent Channel interference), which lead to radio signal quality's degrading, 5–7 level severe interference and user perception's obviously declining [1].

Analytical methods [2–4] of traditional regular hexagon cell clusters for interference and coverage cannot meet the requirement of increasing complexity of radio network analysis. Moreover, recent regular testing methods including drive test and sweep frequency test cannot locate specific interfered frequency, interference levels of serving cell and the location of interference source cell, which becomes a technical bottleneck for further detailed optimization of current radio network. Exploring new measuring techniques and analysis methods, further scientific defining and accurate quantitative analyzing for radio network problems, and obtaining more precise optimization solution are significant for radically improving overall performance of cellular networks. Therefore, this paper proposes a kind of new full-band and high-accuracy timeslot sweeping technology—a training sequence parallel detection technology base on timeslot sliding window. According to the distribution of different training sequence code that is from each cell of radio network, it can locate and measure received power, C/I and noise floor of same carrier frequency coming from different cells of radio networks. It supplies new frequency sweeping measurement and scientific analysis methods for accurate positioning and final solution of radio networks interference and coverage problems.

2 Timeslot Measuring Frequency Sweeping Technology

2.1 The Limit of Traditional Frequency Sweeping

Traditional BCCH frequency sweeping data that is common measuring data source of present integral network structure assessment can accurately reflect the radio signal coverage status of BCCH frequency. However, traditional frequency sweeping devices can only measure and decode BCCH channel without effectively distinguishing and measuring received power of same TCH frequency coming from different cells.

Under normal circumstances, BCCH carrier frequency is full-power transmitted in normal working condition of each cell while the transmitting power of TCH frequency is influenced by factors of frequency hopping, DTX (Discontinuous Transmission) and power control etc.; in addition, BCCH frequency and TCH frequency have different reuse density, so there is a large difference between the system noise floor levels of two types of carrier frequency. In different regions (grids) of cells, the received power, C/I and noise floor level of BCCH and TCH carrier frequency certainly exist differences. Hence, improving accurate measurement for TCH frequency based on BCCH frequency sweeping measurement no

doubt has significant engineering application value for radio networks problems' analysis and optimization.

2.2 Necessity of Timeslot Measurement

The high-precision timeslot measuring frequency sweeping proposed in this paper can perform accurate measurement of each timeslot signal power for each frequency in full-band in period of full-frame for both BCCH and TCH carrier frequency, which is an innovative radio networks measuring technique method in the present industry. In different test area, it can accurately measure the received power and C/I in different timeslot from all frequency including BCCH and TCH. Moreover, it can precisely locate the value and C/I of signal power of CCI coming from different interference cells associated with the TSC allocation for each cell in the radio network, so that this new measuring technique methods can be supplied for the depth profiling of cellular radio networks coverage and interference.

Scanning per timeslot for each carrier frequency can effectively distinguish each timeslot's idle state and traffic state: in the idle state of timeslot, the corresponding correlative power of all training sequence code C/I is less than 0 ($C/I < 0$) where the timeslot power reflects the noise floor of radio networks, so the measuring in the idle state of timeslot supplies more fine grid's accurate measuring data source and new analysis methods for more precise estimation of noise floor; in the traffic state of timeslot, the correspond correlative power of all training sequence code C/I is larger than 0 ($C/I > 0$) under normal conditions, so whether the carrier power comes from serving cells or interference cells can be decided according to training sequence allocation. It offers the most scientifically objective accurate measuring data for carrier coverage and interference problems analysis.

2.3 Principle of Timeslot Measuring Technique

GSM mobile communication system defines nine groups of training sequence code (TSC) [5], eight groups of which are used for the cell traffic channel. The rest group is used for transmitting signal power filling of BCCH carrier frequency dummy burst, which is shown in expression (1).

$$
\begin{aligned}
\text{Training Bits} = [&0,0,1,0,0,1,0,1,1,1,0,0,0,0,1,0,0,0,1,0,0,1,0,1,1,1;\\
&0,0,1,0,1,1,0,1,1,1,0,1,1,1,1,0,0,0,1,0,1,1,0,1,1,1;\\
&0,1,0,0,0,0,1,1,1,0,1,1,1,0,1,0,0,1,0,0,0,0,1,1,1,0;\\
&0,1,0,0,0,1,1,1,1,0,1,1,0,1,0,0,0,1,0,0,0,1,1,1,1,0;\\
&0,0,0,1,1,0,1,0,1,1,1,0,0,1,0,0,0,0,0,1,1,0,1,0,1,1;\\
&0,1,0,0,1,1,1,0,1,0,1,1,0,0,0,0,0,1,0,0,1,1,1,0,1,0;\\
&1,0,1,0,0,1,1,1,1,1,0,1,1,0,0,0,1,0,1,0,0,1,1,1,1,1;\\
&1,1,1,0,1,1,1,1,0,0,0,1,0,0,1,0,1,1,1,0,1,1,1,1,0,0;\\
&\%\ \text{above 8 is for the TCH}\\
&0,1,1,1,0,0,0,1,0,1,1,1,0,0,0,1,0,1,1,1,0,0,0,1,0,1\\
&\%\ \text{dummy burst}\ ];
\end{aligned}
\tag{1}
$$

The three least significant bits of the BSIC (Base Station Identification Code) indicate which of the eight training sequences is used in the bursts sent on the downlink common channels of the cell [6]. The training sequence known as reference signal is used for the channel equalization in time domain when receiving signals for each cell, so that it can improve the anti-interference ability of GSM mobile communication system.

The downlink timeslot signal of different cells using same carrier frequency can use different training sequences to make the distinction. This supplies an effective technical method for the distinguishing of interference signal power between different cells.

High-accuracy timeslot sweeping measurement provides accurate measurement for carrier timeslot's power and C/I in the time dimension besides measures all carriers in frequency dimension.

The core of high-accuracy timeslot measuring technique is to perform signal sampling over one frame period (eight timeslot) for every carrier frequency. Target at the lacking problem of orthogonal property between nine groups of training sequence codes, by adopting training sequence parallel detection technology base on timeslot sliding window that this paper proposed for every timeslot of sampled signal, performing the correlative power detection of nine training sequence code can accurately measure the maximum correlative power, C/I and detecting corresponding TSC of training sequence code block for each timeslot.

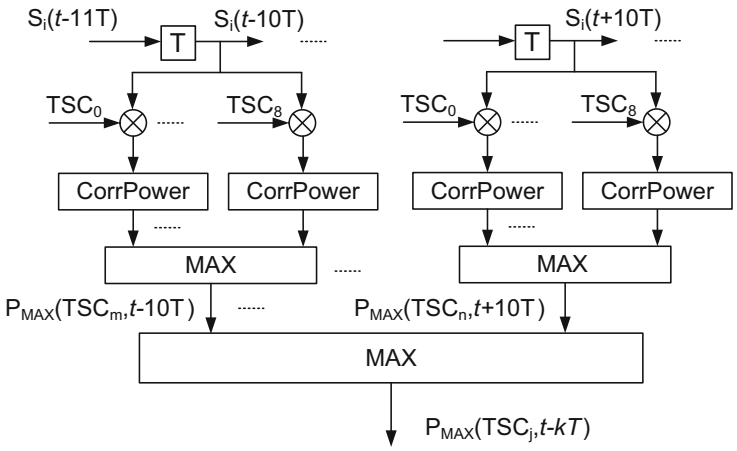

Fig. 1 Training sequence code parallel detection timeslot sliding window

3 Parallel Sliding Window Timeslot Measurement

3.1 Timeslot Sliding Window Parallel Detection Technology

In consideration of GSM as asynchronous system, down link signals between each base station don't perform timeslot synchronization. The boundary of each timeslot won't coincide in one physical frame period in the received sampled signal of same carrier coming from different cells. Hence, the detection for every timeslot power must perform sliding widow detection in a time bucket that is over one timeslot period. Moreover, parallel detecting using nine group of training sequence code for every time-delay signal is to detect that whether this timeslot exist traffic occupancy; in addition, detect the corresponding training sequence code of maximum correlative power signal when timeslot is existing traffic occupancy. Figure 2 shows the parallel sliding window time slot detection technology method.

The parallel sliding window that Fig. 1 shows consists of 21 delayers. Time delay period of every delayer T is 1 μs (T = 1 μs). The whole length of sliding window that is extended for 10 μs to both sides from central point is totally 21 μs. The sampled signal delayed every time is performed parallel correlative detection with nine groups of training sequence code.

5 bit at the beginning and 5 bit at the end that are from training sequence of 26 bit for each group are obtained by 16 bit (located in the center point) original sequence's performing period expanding, so there will be both 5 zero points on both sides of correlative peak value when using 16 original bit to perform correlative detecting for transmitted timeslot signal of the cell.

It totally needs 21 parallel strongest training sequence code correlative power detections in all for the measuring of a timeslot.

3.2 Timeslot Power Detection

Timeslot power detection mainly contains timeslot training sequence maximum correlative power detection, timeslot mean power detection and timeslot noise floor power detection.

Timeslot training sequence code maximum correlative power detection is to detect the maximum training sequence code correlative power and C/I in one timeslot period. If one timeslot SLOT_u of carrier frequency f_p is occupied by the traffic of serving cell CELL_h (means the hth cell in the radio network, which is allocated with lth training sequence code TSC_l) in the specified test zone (grid) g_q (means the qth grid in the radio network) and in the test time t, TSC_l's maximum correlative power $P_{corr\mathrm{MAX}}(\mathrm{SLOT}_u, \mathrm{TSC}_l, t\text{ - }k\mathrm{T})$ and C/I from cell CELL_h can be detected. The algorithm of $P_{\mathrm{MAX}}(\mathrm{SLOT}_v, \mathrm{TSC}_l, t\text{ - }k\mathrm{T})$ is expressed as (2).

$$P_{corr\mathrm{MAX}}(\mathrm{SLOT}_u, \mathrm{TSC}_l, t\text{-}k\mathrm{T}) = \underset{k=-10}{\overset{10}{\mathrm{MAX}}} \quad \underset{\mathrm{TSC}_i, i=0}{\overset{8}{\mathrm{MAX}}} \quad \left[P_{corr}\left(\mathrm{SLOT}_u, \mathrm{TSC}_m, S_i(t\text{-}k\mathrm{T})\right)\right] \tag{2}$$

where the symbol MAX(·) means the max value of array element within parentheses is obtained. The algorithm of training sequence code maximum correlative power in one frame (FRAME_w, the wth frame), $P^F_{corrMAX} = P_{corr\mathrm{MAX}}(\mathrm{FRAME}_w, \mathrm{SLOT}_v, \mathrm{TSC}_l, t\text{ - }k\mathrm{T})$ is expressed as (3).

$$P^F_{corr\mathrm{MAX}} = \underset{\mathrm{SLOT}_u, u=0}{\overset{7}{\mathrm{MAX}}} \quad \underset{k=-10}{\overset{10}{\mathrm{MAX}}} \quad \underset{\mathrm{TSC}_i, i=0}{\overset{8}{\mathrm{MAX}}} \quad \left[P_{corr}\left(\mathrm{SLOT}_u, \mathrm{TSC}_m, S_i(t\text{-}k\mathrm{T})\right)\right] \tag{3}$$

The maximum training sequence code correlative power and the corresponding timeslot central point in one frame, eight timeslot, period is chose as the detecting time reference of timeslot analytical timeslot central point in one frame period at this time. Moreover, each timeslot central point and timeslot boundaries' dividing in one frame period is performed based on this time reference. Figure 2 shows that the training sequence code correlative power received by SLOT_3 is strongest within one frame period. The rest of timeslot central points and timeslot boundaries' positioning extension in the whole frame period is implemented based on the corresponding of peak time of training sequence code correlative power received by SLOT_3 which is chose as SLOT_3 timeslot central point reference. In addition, each other timeslot's central and boundaries division and the maximum training sequence code correlative peak power detection in one whole frame period are performed on this basis.

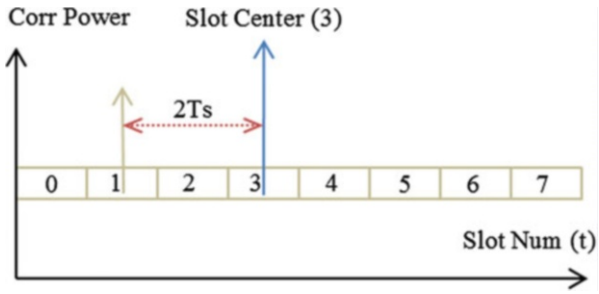

Fig. 2 Positioning of timeslot central point

The algorithm of traffic occupancy timeslot SLOT_v's timeslot mean received power $\overline{P}(\mathrm{SLOT}_v, t\text{-}k\mathrm{T})$ is expressed as (4).

$$\overline{P}(\mathrm{SLOT}_v, t\text{-}k\mathrm{T}) = \frac{1}{N}\sum_{n=0}^{N-1}\left(|\mathrm{I}_S(\mathrm{SLOT}_v, n, t-k\mathrm{T})|^2 + |\mathrm{Q}_S(\mathrm{SLOT}_v, n, t-k\mathrm{T})|^2\right) \tag{4}$$

where $\mathrm{I}_S(\mathrm{SLOT}_v, t - k\mathrm{T})$ and $\mathrm{Q}_S(\mathrm{SLOT}_v, t - k\mathrm{T})$ respectively are timeslot SLOT_v time periods' I and Q two way base band complex signal of received sampled signal—GSM modulating signal symbol series. N is a GMSK modulating symbolic number in a timeslot period. And also

$$\mathrm{I}_S(\mathrm{SLOT}_v, t\text{-}k\mathrm{T}) = \{\mathrm{I}_S(\mathrm{SLOT}_v, n, t-k\mathrm{T}), n = 0, 1, 2, \ldots, N-1\} \tag{5}$$

$$\mathrm{Q}_S(\mathrm{SLOT}_v, t\text{-}k\mathrm{T}) = \{\mathrm{Q}_S(\mathrm{SLOT}_v, n, t-k\mathrm{T}), n = 0, 1, 2, \ldots, N-1\} \tag{6}$$

The SNR $\mathrm{CtoI}(\mathrm{SLOT}_v, t - k\mathrm{T})$ of timeslot occupied by traffic can be calculated based on $P_{\mathrm{MAX}}(\mathrm{SLOT}_v, \mathrm{TSC}_l, t - k\mathrm{T})$ and $\overline{P}(\mathrm{SLOT}_v, t\text{-}k\mathrm{T})$, the algorithm of which is expressed as (7).

$$\mathrm{CtoI}(\mathrm{SLOT}_v, t\text{-}k\mathrm{T}) = 10\lg\frac{P_{corr\mathrm{MAX}}(\mathrm{SLOT}_v, \mathrm{TSC}_l, t\text{-}k\mathrm{T})}{\overline{P}(\mathrm{SLOT}_v, t\text{-}k\mathrm{T}) - P_{corr\mathrm{MAX}}(\mathrm{SLOT}_v, \mathrm{TSC}_l, t\text{-}k\mathrm{T})} \tag{7}$$

For the vacant timeslot SLOT_v not occupied by traffic, the corresponding C/I of detected training sequence code maximum correlative power is less than 0 (C/I < 0), where the timeslot detecting power is the noise floor of f_p frequency's radio network. All the noise floor statistic of vacant timeslot in the specified test grid is mean noise floor of this carrier frequency $\overline{N}_{floor}(f_p, t - k\mathrm{T})$, the algorithm of which is expressed as (8).

$$\overline{N}_{floor}\left(f_p, t-k\mathrm{T}\right) = \frac{1}{\mathrm{count}\left[v, \mathrm{CtoI}\left(\mathrm{SLOT}_v, t\text{-}k\mathrm{T}\right) < 0\right]} \times \sum_{v=0,\, \mathrm{CtoI}\left(\mathrm{SLOT}_v, t\text{-}k\mathrm{T}\right)<0}^{7} \overline{P}\left(\mathrm{SLOT}_v, t\text{-}k\mathrm{T}\right) \tag{8}$$

where count[v, CtoI(SLOT$_v$, t - kT) < 0] is the timeslot number of CtoI < 0 in (8). $\overline{N}_{floor}\left(f_p, t-k\mathrm{T}\right)$ is mean noise floor in one frame period. In the practical application, the statistical averaging of noise floor for several frame periods of several test loop from the same carrier frequency in specified test grid can be performed. It can increase effective signal's sampling quantity of the vacant timeslot to eliminate the effect brought by signal rapid fading, so that the mean value of noise floor can reflect the real situation of radio networks more accurately.

3.3 Application of Timeslot measurement

The training sequence parallel detection technology base on timeslot sliding window proposed in this paper have already been developed and realized in the frequency scanner.

In addition, the timeslot measuring frequency sweeping data have been used for Zhejiang mobile communication system daily optimization engineering of positioning problems of interference and coverage, evaluating networks noise floor and evaluating rationality of carrier frequency coverage, which has attained the results expected. Figure 3(a) shows the training sequence code's C/I measuring of each timeslot for different frequency. Figure 3(b) presents the power measuring of each timeslot for different frequency. For each BCCH frequency, both measurement results from training sequence detection match very well with the FCCH measurement with a traditional BCCH frequency scanner. These means he training sequence parallel detection technology base on timeslot sliding window proposed in this paper is a perfect way to measure both BCCH and TCH timeslots.

By two kinds of timeslot measurement with difference training sequence code allocation by each cell, combined with layer 3 LAC (Location Area Code) and CI (Cell Identification) decoding of all BCCH channels sweeping from the same measuring point, the same carrier frequency transmitted power and C/I condition coming from different cells can be positioned.

As shown Fig. 4, the NO.54 frequency of NO.30984 cell located by timeslot sweeping data analysis in the bad quality section of Beishan road in Hangzhou is severely interfered by several same frequency cells with NO.54 frequency around it, so the statistic C/I of NO.54 frequency in NO.30984 cell is only 5.47. In addition, according to the analysis of timeslot sweeping data for this section, the received power of NO.68 frequency is relatively small. It means its multiplexing density in

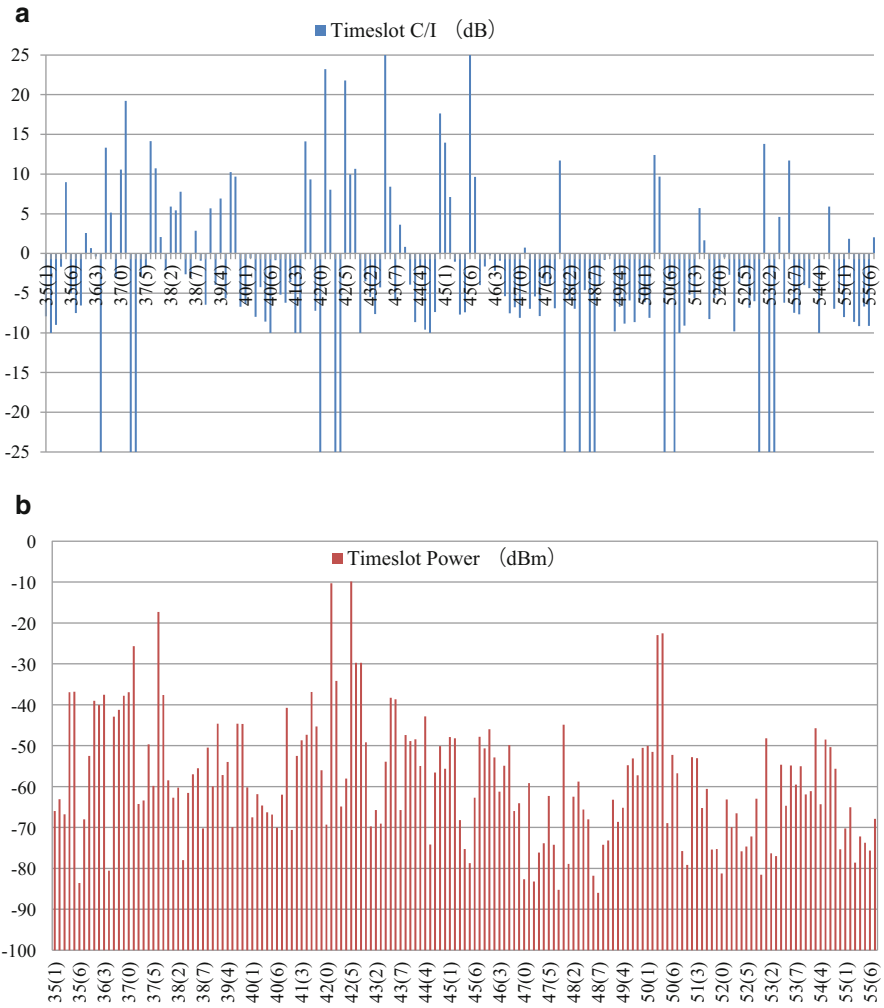

Fig. 3 (**a**) Timeslot C/I measurement. (**b**) Timeslot power measurement

this section is relatively low, so it is suited to replace the NO.54 frequency of NO.30984 cell, to improve the signal quality for this measurement point.

Timeslot measurement that supplies direct measuring technological means for frequency coverage condition analysis, noise floor analysis, interference condition and positioning of interference source analysis, etc. Timeslot measurement offers the most important radio measuring technological means for precise optimization and the improvement of radio networks' performance.

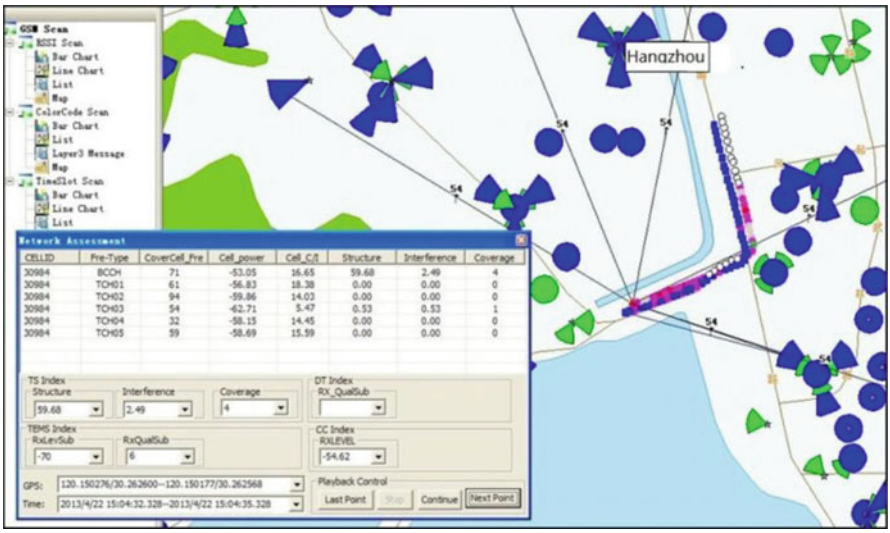

Fig. 4 Traffic timeslot measuring locating interference cell

4 Conclusions

The training sequence parallel detection technology base on timeslot sliding window proposed in this paper is a significant innovation of frequency sweeping technology. Moreover, its idea could also be applied to the radio networks measurement of 3G and 4G cellular mobile communication systems, which has indispensable core value of application for planning and optimizing engineering's accurate analysis of radio network problems and provision of high efficient solution.

Acknowledgments The research project base on network structure evaluating technology of frequency sweeping from this paper was highly valued and strongly supported by leaders and staff of China Mobile Communications Corporation and China mobile Zhejiang branch. Thanks them for the smooth establishment and good results obtained of this research project!

References

1. Zheng H, Chen F (2013) A radio network structure evaluating technology base on sweeping. Telecom Technol J 8:74–79
2. William KH (1980) Frequency assignment: theory and applications. Proc IEEE 68:1497–1514
3. Sivarajan KN, M cEliece RJ, Ketchun JW (1989) Channel assignment in cellular radio. Proc IEEE 39th VTC, pp 846–850
4. Mathar R, Mattfeldt J (1993) Channel assignment in cellular radio networks. IEEE Trans Vehicular Technol 42(4):647–656

5. GSM Technical specifications 03.03 (1998) Numbering, addressing and identification. version 7.1.0 Release, ETSI, phase 2
6. GSM Technical specifications 05.02 (1998) Multiplexing and multiple access on the radio path. version 7.1.0 Release, ETSI, phase 2

A Method to Evaluate MANET Connectivity Based on Communication Demand and Probability

Xiang Zhang, Qiang Liu, and Zhendian Li

Abstract Connectivity of MANET (Mobile Ad hoc Network) physically depends on the radio radius, node density and variability of topology changing. But when evaluate connectivity influence on MANET communication, the physical factors above and other factors like link or path status are not quite enough. This paper proposes a method to evaluate the MANET connectivity by taking node communication probability and status into consideration as well. Connectivity here stands for the communication availability of the whole MANET, and can also be used to check whether a mobility model is suitable to MANET communication. Simulation results present the connectivity of scenarios with simple uniform node communication probability. Typical mobility models are implemented and related evaluation results are compared.

Keywords MANET • Network connectivity • Communication probability

1 Introduction

A multi-hop ad hoc network [1] is an autonomous system composed of series of wireless nodes which can communicate with each other through multiple hops, even if the source node's wireless signal cannot reach the target one. Nodes in such a network are working both as terminal and wireless router. And specially, if to emphasize node mobility, we get the mobile ad hoc networks (MANETs), which have special advantages in applications of emergency communication, battlefield communication and vehicular communication.

Connectivity [2–5] is one of the most important attribute of MANET, since it represents the available paths for communication. Researches on connectivity of

X. Zhang • Q. Liu (✉) • Z. Li
School of Computer Science and Engineering, University of Electronic Science and Technology of China, Chengdu, China
e-mail: zhangx@uestc.edu.cn; 191044287@qq.com; lizhendian@126.com

B. Zhang et al. (eds.), *The Proceedings of the Second International Conference on Communications, Signal Processing, and Systems*, Lecture Notes in Electrical Engineering 246, DOI 10.1007/978-3-319-00536-2_93,

MANET usually adopt theories like six degrees of separation [6], graph theory [7] or percolation theory [8] to find conditions under which the topology of network is k-connected, such as radio radius, node density, and mobility and so on. These traditional connectivity evaluation methods usually emphasize the MANET is a connected network. But in fact, the MANET in real world is usually divided into different separate blocks. How to evaluate the connectivity of such a split MANET is a problem. ZHAO proposed a solution in [9]. His method is to take snapshot of topology in MANET of n nodes, and calculate the number of neighbors of node i, recording as N_i. Then the number of edges of this snapshot can be calculated as $\Sigma_i^n N_i/2$, and the MANET connectivity can thereafter be defined as follow:

$$\rho = \Sigma_{i=1}^{n} N_i / n(n-1) \tag{1}$$

Formula (1) gives a way to evaluate the MANET connectivity even if the MANET was divided into separate blocks. Its evaluation result will be bad if the separate blocks really exist. But in such a scenario, we cannot just simply say the connectivity of the whole MANET is bad, if there is no communication demand during these blocks at all. Therefore, evaluate the MANET connectivity based on probability of node communication is another way to understand the communication availability of the whole networks, and can also help to evaluate how a mobility model is suitable to MANET.

2 Connectivity Evaluation Method

2.1 Network Scenario Assumption

The one-dimensional MANET is what we focus on, where n represents isomorphic-nodes randomly distributed in one-dimensional region [0, L]. The initial positions of the nodes obey uniform distribution and are independent of each other. In this network, all nodes have the same transmission power so that the corresponding wireless communication radius is determined as R.

If the Euclidean distance between node u and node v is smaller than or equal the communication radius R, u and v can communicate directly with each other. But if the distance is greater than R, u and v can just communicate through other reachable intermediate nodes within the limits of the hops and QoS, only if there are reachable intermediate nodes. Then we define that u and v can indirect communicate with each other. In both cases, we say there is a reachable path between node u and v. At a special moment, a snapshot of the dynamic one-dimensional MANET can be achieved, which can be described as a geometric random graph G (V, R) that each node is located in the area of [0, L]. And the network distribution area barrier and the transceiver radio channel between nodes are assumed as symmetrical.

2.2 Algorithm of Connectivity Evaluation

MANET topology and communication status are dynamic. In case of physical connectivity status is known, if the overall demand of the whole MANET is determined, how demands of communication is satisfied is an important factors to evaluate the actual network connectivity, which represents the communication availability of the whole MANET in an actual communication process.

Thus, we set ρ as the instantaneous connectivity of MANET at some specified moment:

$$\rho = \text{communicaiton}_{\text{current\_can\_be\_satisfied}} / \text{communicaiton}_{\text{current\_whole\_demand}} \quad (2)$$

If a MANET node v_i demands to communicate at some moment, it will generate traffic flows. We abstract a flow factor function $G_i(m)$ to represent the communication demand of node v_i at moment m. If v_i want or is in process of communicating with some target, $G_i(m) = 1$, otherwise $G_i(m) = 0$. Obviously, the whole MANET communication demands is sum of demands of all the active nodes, which can be recorded as $\Sigma_i^n G_i(m)$.

As to how the current communication can be satisfied, various factors need to be considered, such as availability of physical path to the target, status of links on available paths, and what is more important, how probable the MANET nodes want to communicate with each other. Thus, we set $P_{i,j}(m)$ to represent the communication probability from node v_i to node v_j at specified moment m. And we also set a function $L_{i.\ j}(m)$ to represent the target reachability of node v_j from the source node v_i. When computing $L_{i.\ j}(m)$ various factors must be taken into consideration, such as hop limit, link failure rate, remaining capacity of each node and each link on the path and so on. Then, when applying probability analysis, if there is not any path existing between v_i and v_j, then $L_{i,j}(m) = 0$, otherwise we set $0 \leq L_{i,j}(m) \leq 1$.

Therefore, we get the formula (3) to present how the current scenario satisfied the current communication demands.

$$\sum\nolimits_{j=1j\neq i}^{n} G_i(m)P_{i,j}(m)L_{i,j}(m) \quad (3)$$

And now we can calculate the connectivity of MANET by formula (4)

$$\rho(\mathrm{m}) = \sum\nolimits_{j=1j\neq i}^{n} G_i(m)P_{i,j}(m)L_{i,j}(m) / \sum\nolimits_{i}^{n} G_i(m) \quad (4)$$

3 Simulation and Results

The MANET simulation scenario consists of 40 nodes adopting several mobility models like Random Way Point (RWP) and Random Direction (RD). Scenario area is set to 1,000 × 1,000 m^2, and the node communication radius is set to 150 m.

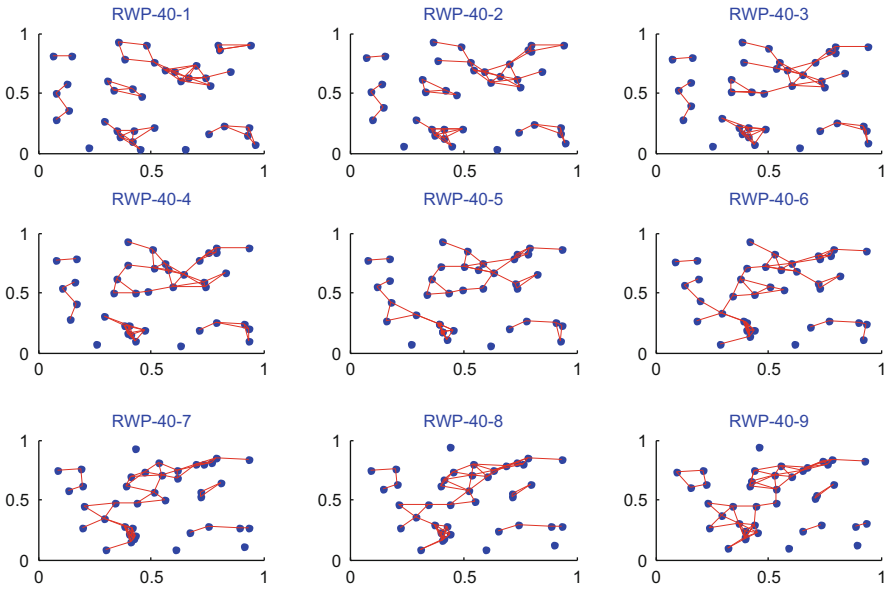

Fig. 1 Consecutive MANET topology changing

Nine consecutive network topology graphs captured in simulation is shown in Fig. 1, which depicts that MANET topology changing affects the physical network connectivity and may cut the whole network apart. But it doesn't mean the communication availability of the whole MANET is bad. Node communication demands should be taken into consideration.

In this paper, result of the simplest scenario simulation is presented. The communication demand of each MANET node assumes to obey uniform distribution, and each node has the same probability to communicate with each other. We also assume that the available capacities of each link and node are infinite. Then we get $G_i(m) \sim B(1,p)$, assuming $P_{i,j}(m) = 1/n$ (n is the total number of MANET nodes) and $L_{i,\ j}(m) = 1$. Figure 2 depicts the comparison of connectivity with consideration of communication probability calculated by formula (4), and the one without consideration of communication probability calculated by formula (1). The results are similar but obviously different. And we can imaging there will be more difference if we set $G_i(m)$ and $P_{i,j}(m)$ obey some complicated distributions.

When implementing this evaluation method with four mobility models, including RWP, RW-D, RW-T and RD, we set the number of nodes varying from 10 to 250 by increasing the step length of 10, and set the simulation time to 10,000 s. After 500 times simulation, mean results of connectivity evaluated by formula (4) are shown in Fig. 3.

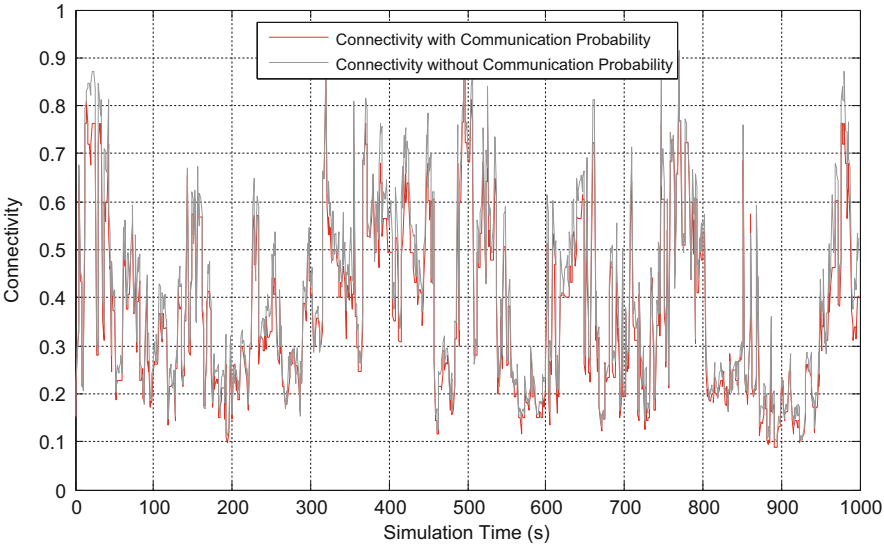

Fig. 2 Comparison of connectivity evaluation with and without consideration of communication probability in the simplest scenario

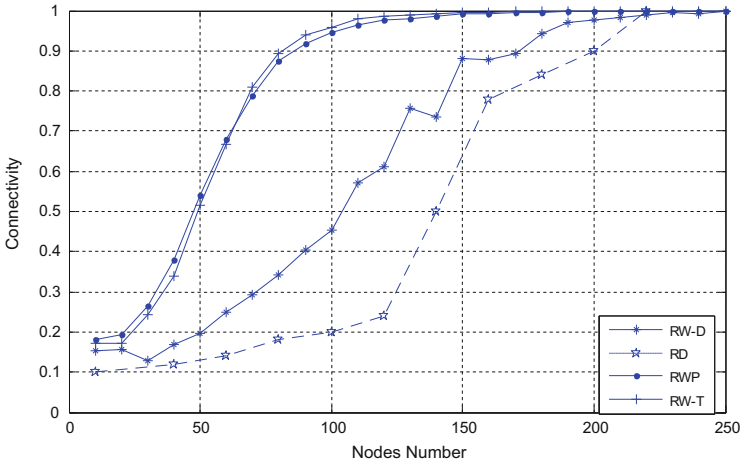

Fig. 3 Comparison of connectivity evaluation with different mobility model

4 Conclusion

Network physical connection can't completely represent the connectivity of the whole MANET, especially when MANET is divided into separate blocks. We propose a novel network connectivity evaluation method based on inter-node communication probability. Compared with other traditional methods, method in

this paper emphasizes the consideration of communication demands of MANET nodes, as well as their communication probability with other ones. Simulation demonstrate that even the simplest setup of $G_i(m)$, $P_{i,j}(m)$ and $L_{i,j}(m)$ can get different results from the traditional methods.

In the future work, we are going to create more scenarios to evaluate how precisely the communication demand and probability, as well as other factors like link reachability, will affect the evaluation of the MANET connectivity, which represent the total communication availability.

References

1. Ramanathan R, Redi J (2002) A brief overview of ad hoc network: challenges and directions [J]. IEEE Commun Magazine 40(5):20–22
2. Gupta P, Kumar PR (1998) Critical power for asymptotic connectivity in wireless networks [M]. Birkhauser, Boston, MA, pp 547–566
3. Bettstetter C (2002) On the minimum node degree and connectivity of a wireless multihop network [C]. Proc. of ACM MobiHoc'02. Lausanne, Switzerland, [s. n.]
4. Xiang H-H, Liu J-K, Kuang J-M et al (2009) Analysis of MANET connectivity based on Markov Chain Model [J]. Comput Eng 35(24):13–16
5. Xing F, Wang W (2006) Modeling and analysis of connectivity in mobile ad hoc networks with misbehaving nodes [A]. In: Proceedings of IEEE ICC 2006. New York, IEEE Press, pp 1879–1884
6. Sharma G, Mazumdar R (2005) Hybrid sensor networks: a small world [C]//MobiHoc 05. ACM, New York, pp 366–377
7. Bai X, Xuan D, Yun Z-Q et al (2008) Complete optimal deployment patterns for full-coverage and k-connectivity ($k \leq 6$) wireless sensor networks [C]. MobilHoc '08 Proceedings of the 9th ACM international symposium on Mobile ad hoc networking and computing table of contents. New York, NY, ACM, pp 401–410
8. Broadbent SR, Hammersiey JM (1957) Percolation processes. I. Crystals and mazes. Proc Cambridge Philos Soc 53:629–641
9. Zhao J-L, Shang R-Q, Sun Q-X (2006) Study of the relationship between mobility model of ad hoc network and its connectivity [J]. J Commun 27(1):119–123

Coexistence Study Based on TD-SCDMA and WCDMA System

Li Li and He Hong

Abstract Interference is one of key issues for wireless network optimization. How to work with other communication systems is a crucial issue to ensure system performance in 3G networks. This article focuses on the analysis of adjacent channel interference between TD-SCDMA and WCDMA system. The interference mathematical model was discussed, including spurious interference, intermodulation and blocking interference. The minimum coupling loss was obtained by using deterministic algorithm in order to two system coexistence and co-station., the conclusion indicated that the necessary isolation require at least 33.87 and 69 dB, which have certain significance for engineering practice.

Keywords TD-SCDMA • WCDMA • Coexistence interference • Isolation loss

1 Introduction

How to work with other communication system to maintain good isolation is a crucial issue to ensure system performance in 3G networks. As the third generation mobile communication business, interference is one of the key issues for wireless network optimization. Since different operators in different network configuration and network coverage are used more and more widely, there are interferences between different systems. There are a total of base stations in geographical location coexistence in the actual TD-SCDMA and WCDMA network construction, which will bring interference problems resulting in decreased communication quality, coverage and system capacity loss.

The Tianjin science and technology innovation special fund (No. 10FDZDGX00400).

L. Li (✉) • H. Hong
Tianjin Key Laboratory for Control Theory & Applications in Complicated Systems, Tianjin University of Technology, Tianjin, China
e-mail: green_linda@163.com

B. Zhang et al. (eds.), *The Proceedings of the Second International Conference on Communications, Signal Processing, and Systems*, Lecture Notes in Electrical Engineering 246, DOI 10.1007/978-3-319-00536-2_94,

This article is mainly based on Tianjin science and technology innovation special funds project which is cooperation with China Mobile Communications Corporation Tianjin Ltd. That is the project is key technology research demonstration and application of next-generation mobile communication network coverage. The theoretical analysis of coexistence interference was carried out from mathematical model of the main interference in TD-SCDMA and WCDMA system. Given an effective solution to reduce interference and specific indicators of spatial segregation, which not only guides engineering suppression between two systems interfere with the implementation of isolation, but also provides a certain reference value for different systems of network optimization [1].

This paper analyzed the causes of interference of coexistence systems, studied the interference between the TD-SCDMA and WCDMA systems. In order to ensure the systems can run in high performance, it got the additional isolation loss requirements for the two coexistence systems.

2 Interference Analysis

According to frequency spectrum, TD-SCDMA consists of two parts, namely, 1,880–1,920 MHz and 2,010–2,025 MHz, additional bands of 2,300–2,400 MHz. WCDMA uplink frequency band is 1,920–1,980 MHz and Downlink is 2,110–2,170 MHz. In addition, additional spectrum of the WCDMA is: 1,755–1,785 MHz and 1,850–1,880 MHz. Because sandwiched between 1,880 and 1,920 MHz is TDD frequency band, WCDMA uplink will cause interference on TD-SCDMA in the 1,920 MHz. As TD-SCDMA system applies TDD mode, using the same frequency for sending and receiving, while WCDMA system adopts FDD mode, transceiver is a different frequency, there are four interference types should be considered [2].

TD-SCDMA Uplink disturbs WCDMA Uplink, namely, TD-SCDMA mobile station for WCDMA base station, WCDMA Uplink disturbs TD-SCDMA Uplink, namely: WCDMA mobile station for TD-SCDMA base station, WCDMA Uplink disturbs TD-SCDMA downlink, namely WCDMA mobile station for the TD-SCDMA base station, TD-SCDMA downlink disturbs WCDMA Uplink namely: TD-SCDMA base stations for WCDMA base station.

Uplink and downlink frequency bands composed of a pair of frequency bands among them. Uplink is mobile phone transmit and base station receiver, downlink is the base station signal to the phone channel frequency bands. The first three kinds of interference are related to the terminal interference, which lead to loss less than 3 % in acceptable practical applications. Therefore, base stations and base stations interference is the main factors affecting adjacent channels coexistence of two systems which need to focus on.

Working in different frequencies, coexistence interference of two systems is caused by imperfect characteristics of transmitter and receiver, transmitter launches useful signal and produces band radiation in the specified working channel,

including in adjacent channel leakage and spurious radiation. The receiver receives its useful signal in the corresponding channel at the same time, interference signal falling into the channel signals may causes receiver sensitivity loss and obstruction which leaded to receiver reduced demodulation capacity. Therefore, the interference between two systems depends on the working band interval and transceiver spatial segregation and other factors [3].

Interference analysis method was used to quantitative analysis of the interference of TD-SCDMA and WCDMA system in order to obtain isolation index from spurious and intermodulation and blocking interfere in this paper, through spatial segregation to achieve coexistence and co-station.

3 Interference Model

From interfering formation to view, system interference includes spurious interference, intermodulation interference and blocking interference, in which spurious interference is an important indicator. As long as spurious interference can be avoided, blocking and intermodulation interference can be avoided in general [4, 5].

Spurious interference is that launching band noise from interfering device drop into received band of receiver, which caused interference for useful signal channel. Spurious radiation signal received from base station directly result in receiver sensitivity reduced. Sensitivity deteriorated ΔS as follow

$$\Delta S = 10\log\left(1 + 10^{\frac{Interference(BW_r) - NoiseFloor}{10}}\right) \tag{1}$$

Where $Interference(BW_r)$ is spurious interfering signal strength allowing to WCDMA receiver, $NoiseFloor$ is thermal noise level of the receiver. After equation conversion, that is:

$$Interference(BW_r) = NoiseFloor + 10\log\left(10^{\frac{\Delta S}{10}} - 1\right) \tag{2}$$

According to 3GPP TS 25.942 V8.0.0, thermal noise power level of WCDMA base station receiver is -103.16 dBm at 3.84 MHz, and then (2) can be expressed as:

$$Interfernece(BW_r) = -103 - 6 = -109 \text{ dB} \tag{3}$$

Spurious radiation from interfering base station antenna is obtained attenuation by a certain separation between two base stations, spurious interference isolation formula as follows:

$$L = S_t(\mathrm{f}, BW_t) - Interference(BW_r) - 10\log\left(\frac{BW_r}{BW_t}\right) \quad (4)$$

Where $S_t(f, BW_t)$ is spurious radiation, $10\log\left(\frac{BW_r}{BW_t}\right)$ is bandwidth conversion factor, BW_r is measured bandwidth of interfering power levels, BW_t is channel bandwidth of disturbed system.

Spurious emission power index of TD-SCDMA and WCDMA base stations in co-station or coexistence are −80 dBm at 3.84 MHz and −43 dBm at 3.84 MHz respectively [6]. That data is substituted into (4) and derived minimum spurious isolation of 23 and 60 dB.

Blocking interference means that disturbed receiver received a strong signal interference which made receiver overload and its sensitivity degradation. Blocking isolation L is equal to interfering system transmission power minus blocking index of disturbed system receiver. According to 3GPP TS25.105V8.3.1, when WCDMA and TD-SCDMA system co-site, blocking interference of −40 dBm in the 1,920–1,980 MHz frequency is allowed, and useful signal power is −115 dBm above at the moment [7]. As maximum transmit power of TD-SCDMA base station is 34 dBm, the antenna separation between TD-SCDMA and WCDMA is at least 74 dB.

Intermodulation isolation is shown in the following equation:

$$L = P_t - P_n - L_{RX\_Filter} \quad (5)$$

The third-order intermodulation is the main component of intermodulation interference, P_t is the biggest carrier transmits power of interfering base station, P_n is interfering carrier level of disturbed base station receiver input, $L_{RX\ -\ Filter}$ is receiver filter attenuation of disturbed base station in bandwidth of interfering base station transmitters.

4 Deterministic Approach

Based on deterministic analysis method, the worst interference of adjacent channel coexistence between base stations of TD-SCDMA system and WCDMA system was studied in this paper. The deterministic algorithm is to use the minimum coupling loss MCL. It is the study on the size of adjacent channel interference in the worst case which can be estimated theoretically, when interfering with the greatest power to launch. The method can be used to calculate the interference of base stations and solve coexistence interference. As shown in (6).

$$MCL = P_{TX} - ACIR - ACL_{MAX} \quad (6)$$

Where P_{TX} is maximum transmit power of interfering sources, $ACIR$ is adjacent-channel interference power ratio, ACL_{MAX} is interference level of adjacent channel.

The size of interfere is subject to two factors, that is *ACS* of disturbed system receiver and *ACLR* of interfering system transmitters. Adjacent-channel interference power ratio *ACIR* was used to measure coexistence interference between systems of different frequencies in engineering. Parallel relationship between them as shown in the following equation:

$$\frac{1}{ACIR} = \frac{1}{ACLR} + \frac{1}{ACS} \tag{7}$$

The interference of WCDMA base stations and TD-SCDMA base stations is usually more serious, which focus on their adjacent channel and coexistence.

ACIR requires three steps: (1) ACLR of WCDMA base station. According to 3GPP25.104 protocol, base band emission power limits and the maximum transmit power is 43 dBm, then WCDMA base station ACLR could be expressed as: 43 dBm − (−52 dBm/1 MHz + 10lg(1.28 MHz/1 MHz)) = 93.9 dB. (2) ACS of TD-SCDMA base station is 93 dB when systems coexistence. (3) Then using (7), ACIR values is 90.42 dB.

The maximum allowed external interference of WCDMA base station receiver is −113.87 dBm. Substituted into the (6) and obtained MCL, that is: MCL = 43 − 90.42 − (−113.87) = 66.45 dB.

According to 3GPPTS25.105 protocol, system co-station coupling requirements 30 dB. Additional isolation loss of two systems can be obtained as:

$$A = MCL - 30 \tag{8}$$

Two systems coexistence is discussed as follows:

$$A = MCL - (L - G_t\text{-}G_r) \tag{9}$$

Where G_t is the antenna gain of interference system, G_r is the antenna gain of the interfered base station, $\boldsymbol{L}$ is path loss of the interfering transmitter and the receiver system, $\boldsymbol{A}$ is additional isolation loss requirements for two systems coexistence.

Assuming the distance between base stations is 100, 200, 300 m respectively, the antenna height is 30 m. Using bilinear sight propagation mode [8], signal propagation model could be expressed as:

$$L(d) = \begin{cases} -27.56 + 20\lg(f) + 20\lg(d) & 1 < d < d_r \\ -27.56 + 30\lg(f) - 10\lg(d_r) + 30\lg(d) & d > d_r \end{cases} \tag{10}$$

Where $\boldsymbol{L}(d)$ is the path loss, f is the carrier frequency, d is the antennas distance, d_r is the first Fresnel radius, d_1, d_2 is two base station antenna height respectively.

Table 1 Additional isolation requirements (WCDMA interfering TD-SCDMA)

	WCDMA band emission requirements	WCDMA ACLR/dBc	TD-SCDMA ACS/dB	ACIR/dBm	ACL/dBm	MCL/dB	Additional isolation loss/dB		
							100/m	200/m	300/m
Coexistence	−52 dBm/3.84 MHz	93.9	93	90.42		66.45	10.53	4.51	0.99
Co-station	−86 dBm/3.84 MHz	127.9	93	93	−113.87	63.87	33.87		

Table 2 Additional isolation requirements (TD-SCDMA interfering WCDMA)

	TD-SCDMA band emission requirements	TD-SCDMA ACLR/dBc	WCDMA ACS/dB	ACIR/dBm	ACL/dBm	MCL/dB	Additional isolation loss/dB		
							100/m	200/m	300/m
Coexistence	−36 dBm/3.84 MHz	70	−52	45		99	33.7	27.7	24.2
Co-station	−80 dBm/3.84 MHz	114	−52	45	−110	99	69		

5 Conclusion

According to above analysis, the two systems can be achieved coexistence and co-station, additional isolation requirements of TD-SCDMA and WCDMA can be obtained as shown in Table 1 and Table 2. Thus, spatial segregation is useful for resolving additive noise interference, receiver blocking and intermodulation interference.

In order to reduce interference, the most practical way is to increase isolation and shielding. It is good method by designing a digital band-pass filter to effectively suppress interference coexistence [9]. Therefore, spatial isolation and shielding implementation can effectively improve the interference of TD-SCDMA and WCDMA, resolving the issue of high-end users covered by dense urban areas and improving the capacity of entire system to better meet user demands for quality.

Acknowledgments This work was partially supported by Tianjin science and technology innovation special fund project: "Research on the key technology of next-generation mobile communication network coverage and demonstration application" (10FDZDGX00400). And thanks China Mobile Communications Corporation Tianjin Ltd Tianjin Key Laboratory for Control Theory and Application in Complicated Systems, Tianjin University of Technology, Tianjin 300191, and China.

References

1. Ni S, Blogh JS, Hanzo L (2003) On the network performance of UTRA-like TDD and FDD CDMA systems using adaptive modulation and adaptive beam forming. Vehicular technology conference, VTC 2003 spring. The 57th IEEE semiannual vol 1, 22–25 Apr 2003, pp 606–610
2. 3GPP TS 25.942 V8.0.0 (2008-12) Radio frequency (RF) system scenarios (Release 8)
3. Hsueh-Jyh L, TaYung L (2003) Comparison of beamforming techniques for WCDMA communication systems. Vehicular Technol IEEE Trans 52(4):752–760
4. Yang L, Fang W, Yongyu C, Dacheng Y (2007) Theoretical and simulation investigation on coexistence between TD-SCDMA and WCDMA system. Vehicular technology conference, VTC2007-Spring, IEEE 65th 22–25 Apr 2007, pp 1198–1203
5. Suryanegara M, Hutabarat ER, Gunawan D (2006) The interference on WCDMA system in 3G coexistence network. Personal, indoor and mobile radio communications, 2006 I.E. 17th international symposium, 11–14 Sept 2006, pp 1–5

6. 3GPP TS 25.105 V8.3.1 (2009-04) Base station (BS) radio transmission and reception (TDD) (Release 8)
7. 3GPP TS 25.104 V8.6.0 (2009-03) Base station (BS) radio transmission and reception (FDD) (Release 8)
8. Chen Z, Chongxiu Y, Anjian L, Daxiong X (2006) TD-SCDMA wireless mobile communication system interference analysis. Modern Sci Technol Telecom 4(4):35–38
9. Liao H, Dongfeng Z, Liying H (2007) Analysis of TD-SCDA and WCDMA systems coexistence interference and design of filter circuit. J Yunnan Univ 29(S2):190–195

Joint Power and Spectrum Allocation for Relay Stations in Mobile Relay Networks

Xin Wang, Qilian Liang, Baoju Zhang, and Xiaorong Wu

Abstract Mobile phones are among the most popular consumer devices with the recent development of 4G networks. The ubiquity of mobile phones have resulted in increasing capacity demands and extended more and more pressures on the limited spectrum resources (Lin and Liu, IEEE T Image Process 21(5):2667–2680, 2012). Recently, relay communications with the aid of Relay Stations (RSs) have emerged as a solution to improve transmission rate between the Base Station (BS) and Mobile Station (MS). In this paper, we investigate the joint power and spectrum allocation for RSs in mobile relay networks. We first study the joint power and spectrum allocation for RSs without individual power constraint and propose an optimal power and spectrum allocation strategy. The scenario with individual power constraint is further explored. We prove that all selected RSs should adjust the transmission power in a descending order according to the channel gain, and for the selected RSs with full power allocation, the optimal spectrum allocation is proportional to the channel gain. The theoretical results obtained are instrumental to the future mobile relay network modeling and design.

1 Introduction and Motivation

As part of the National Broadband plan, the data collected by FCC shows that the North American mobile data traffic will increase roughly 20–45 times from 2009 to 2014 [1]. Recently, Cisco observes that the mobile traffic grows much faster than expectation in 2010 and predicts that by 2015 two-thirds of the mobile data will be

X. Wang (✉) • Q. Liang
Department of Electrical Engineering, University of Texas at Arlington, 416 Yates Street, Arlington, Texas 76019, USA
e-mail: xin.wang51@mavs.uta.edu; liang@uta.edu

B. Zhang • X. Wu
Department of Physics and Electronic Information, Tianjin Normal University, Tianjin, China
e-mail: wdxyzbj@mail.tjnu.edu.cn; wu.xiaorong@sohu.com

B. Zhang et al. (eds.), *The Proceedings of the Second International Conference on Communications, Signal Processing, and Systems*, Lecture Notes in Electrical Engineering 246, DOI 10.1007/978-3-319-00536-2_95,

video data [2]. To serve the increasing capacity demands in mobile cellular networks, new technologies have been introduced to Long Term Evolution (LTE) and LTE-Advanced systems, such as Multiple Input Multiple Output (MIMO), Cooperative Multiple-Point (CoMP) transmission and Relay Stations (RSs). In particular, there have been numerous researches integrating RSs into the mobile network, which results in the *mobile relay network*. With the assistance of RSs, in the downlink, the Base Station (BS) first transmits the data on the backhaul link to the RS within its cell. In the second phase, the RS forwards the data on the access link to the Mobile Station (MS).

The application of RS has already been widely studied in the literature, for example [3–20]. The seminal work by [3] initiated the study of applying RSs into the mobile networks. In [6], a comprehensive overview of about the application of RS in mobile networks is provided. Meanwhile, numerous studies have investigated the co-existence of different types of stations in cellular networks including BSs, pico BSs, femto BSs and RSs. Damnjanovic et al. [9] investigate the cell spectral efficiency optimization in relay enhanced cells. A comprehensive overview on the so-called heterogeneous networks is given in [12]. However, to the best of the authors' knowledge, it is still a significant open question on the RS selection in mobile rely networks.

In this paper, we aim to select the optimal[1] RSs to maximize the transmission rate of the mobile relay networks. The remainder of this paper is organized as follows. In Sect. 2, we formulate the relay mobile network model. The joint power and spectrum allocation for RSs without and with individual power constraint are investigated in Sects. 3 and 4, respectively. In Sect. 5, we present some concluding remarks.

2 System Model

In this section, we introduce the channel and transmission models for the mobile relay network. The system diagram is shown in Fig. 1. We assume that, for MS (user) j, there exist L Relay Stations (RSs) around that can serve as the relays from the BS to MS. In some scenarios, the mobile phones can also serve as the RSs.

The baseband model for the communications between RS i and MS j at time slot t is described as:

$$Y_t^j = h_{ij} X_t^i + Z_t^j. \tag{1}$$

[1] The "optimality" is mainly defined from the sum-rate perspective. The fairness and efficiency of such strategy go beyond the scope of this paper.

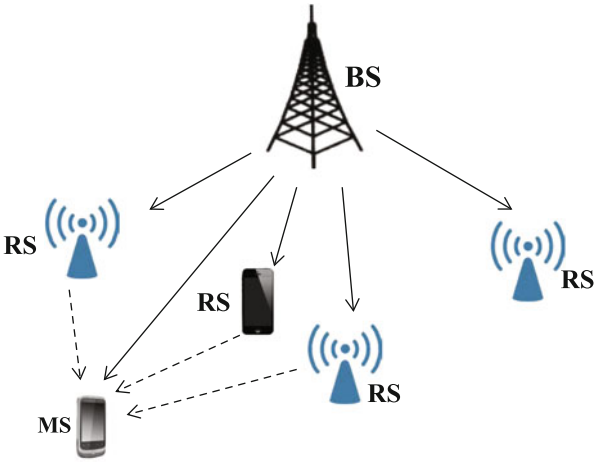

Fig. 1 Mobile relay system model

- X_t^i is the complex baseband signal RS i transmits, Y_t^j is the complex baseband MS j receives, and Z_t^j is a Gaussian independent and identically distributed (*i.i.d.*) random variable with zero mean and noise spectral density N_0.
- h_{ij} characterizes both small-scale fading of the channel.
- RS i transmits with power P_i and the signal is received at node j with power $P_i \cdot |h_{ij}|^2 = P_i \cdot g_i$, where g_i denotes the fading channel gain.

3 Joint Power and Spectrum Allocation Without Individual Power Constraint

Our goal is to maximize the transmission rate for the MS (end user). From the information theory point of view, the maximum achievable rate of reliable communication is [13]

$$x_i \cdot \log\left(1 + \frac{p_i \cdot g_i}{x_i \cdot N_0}\right) \quad bit/s \tag{2}$$

where p_i is the power allocation variable and x_i is the spectrum occupation variable.

We assume that there are L RSs that can serve as the relays from the BS to MS. Therefore, with the spectrum constraint $\sum_{i=1}^{L} x_i \leq 1$ and the total power constraint $\sum_{i=1}^{L} p_i \leq P_{tot}$, the optimization problem can be formulated as follows.[2]

[2] In the sequel, we replace log with ln for simplicity.

$$\begin{aligned} \max & \sum_{i=1}^{L} x_i \cdot \ln\left(1+\frac{p_i \cdot g_i}{x_i \cdot N_0}\right) \\ s.t. \quad & x_i \geq 0 \\ & p_i \geq 0 \\ & \sum_{i=1}^{L} x_i - 1 = 0 \\ & \sum_{i=1}^{L} p_i - P_{tot} = 0 \end{aligned} \tag{3}$$

The Lagrangian function G is given as

$$\begin{aligned} G = & -\sum_{i=1}^{L} x_i \ln\left(1+\frac{p_i \cdot g_i}{x_i \cdot N_0}\right) - \sum_{i=1}^{L} \beta_i x_i - \sum_{i=1}^{L} \lambda_i p_i \\ & + \mu\left(\sum_{i=1}^{L} x_i - 1\right) + \upsilon\left(\sum_{i=1}^{L} p_i - P_{tot}\right). \end{aligned} \tag{4}$$

From the Lagrangian function G, we can derive the following Karush–Kuhn–Tucker (KKT) conditions [14]:

$$-\ln\left(1+\frac{p_i \cdot g_i}{x_i \cdot N_0}\right) - x_i \cdot \frac{-\frac{p_i \cdot g_i}{x_i^2 \cdot N_0}}{1+\frac{p_i \cdot g_i}{x_i \cdot N_0}} - \beta_i^* + \mu^* = 0 \tag{5}$$

$$-x_i \cdot \frac{-\frac{g_i}{x_i \cdot N_0}}{1+\frac{p_i \cdot g_i}{x_i \cdot N_0}} - \lambda_i^* + \upsilon^* = 0 \tag{6}$$

$$\beta_i^* \cdot x_i = 0 \tag{7}$$

$$\lambda_i^* \cdot p_i = 0 \tag{8}$$

Lemma 1. *If A is the selected RS set, then $|A| = 1$.*

Proof. We first simplify the KKT conditions with introducing $SNR_i = \frac{p_i \cdot g_i}{x_i \cdot N_0}$, and obtain

$$\ln(1+SNR_i) - \frac{SNR_i}{1+SNR_i} = \mu^*. \tag{9}$$

$$1+SNR_i = \frac{g_i}{N_0 \cdot \upsilon^*}. \tag{10}$$

From (9), it is straightforward to prove $f(x) = \ln(1+x) + \frac{x}{1+x}$ is a monotonously increasing function. Therefore, we know that the *SNR* of the signal received from all the RSs should keep constant, since μ^* is a constant. Together with (10), we

conclude that SNR_i is unique, which means that only one RS should be selected to maximize the transmission rate. Therefore, $|A| = 1$ and we complete the proof.

With $SNR_i = \frac{p_i \cdot g_i}{x_i \cdot N_0}$, it is obvious that large p_i yields large SNR_i. Therefore, in terms of the *power allocation strategy*, the selected RS should consume the whole power constraint P_{tot} to maximize the transmission rate.

Further, we investigate the *spectrum allocation strategy*. With the introduction of $\Gamma = \frac{P_{tot} \cdot g_i}{N_0}$, the transmission rate to maximize is thus

$$f(x) = x \cdot \ln\left(1 + \frac{\Gamma}{x}\right), \tag{11}$$

where x is the spectrum allocation variable. Obviously, we obtain

$$f'(x) = \ln(1 + SNR) - \frac{SNR}{1 + SNR} \tag{12}$$

with $SNR = \frac{\Gamma}{x}$. From $f'(x) > 0$ with regard to $SNR > 0$, f(x) is also an increasing function. Therefore, the selected RS should occupy the whole spectrum.

4 Joint Power and Spectrum Allocation with Individual Power Constraint

In this section, we turn our attention to the joint power and spectrum allocation with individual power constraint. The formulated problem is similar to (3), only with the introduction of individual power constraint $p_i \leq P_0$.

$$\begin{aligned} \max \quad & \sum_{i=1}^{L} x_i \cdot \ln\left(1 + \frac{p_i \cdot g_i}{x_i \cdot N_0}\right) \\ s.t. \quad & x_i \geq 0 \\ & p_i \leq P_0 \\ & \sum_{i=1}^{L} x_i - 1 = 0 \\ & \sum_{i=1}^{L} p_i - P_{tot} = 0 \end{aligned} \tag{13}$$

From the Karush–Kuhn–Tucker (KKT) conditions, we have

$$\ln(1 + SNR_i) - \frac{SNR_i}{1 + SNR_i} = \mu^* \tag{14}$$

$$1 + SNR_i = \frac{g_i}{N_0 \cdot (\alpha_i + v^*)} \tag{15}$$

$$\alpha_i \cdot (p_i - P_0) = 0 \tag{16}$$

Lemma 2. *With the individual and total power constraint, less than one RS is not assigned with full power.*

Proof. First, from (14), we conclude the signal received from all the selected RSs should keep constant SNR.

If the selected RS is not assigned with full power, $p_i < P_0$, we obtain $\alpha_i = 0$ from the KKT condition (16). Further, from (15), we can easily prove that SNR_i is unique, which means at most one RS is not assigned with full power. The proof is complete.

In the following, Lemma 3 provides the *joint power and spectrum allocation strategy* with individual power constraint.

Lemma 3. *The power allocation for the selected RSs follow a descending order according to the channel gain* g_i*; while for the selected RSs with full power allocation, the spectrum allocation is proportional to the channel gain* g_i*.*

Proof. As is known, the signal received from all the selected RSs should keep constant SNR, i.e.,

$$\frac{g_i}{N_0(\alpha_i + v^*)} = \frac{g_j}{N_0(\alpha_j + v^*)}. \tag{17}$$

Clearly, if $g_i > g_j$, we have $\alpha_i > \alpha_j$. Meanwhile, from Lemma 2, we have proved that at most one RS is not assigned with full power ($\alpha = 0$). Therefore, RS with better channel condition (large g_i) should be assigned with full power.

In terms of the spectrum allocation strategy, we know that $SNR_i = \frac{P_0 \cdot g_i}{N_0 \cdot x_i}$ for the RS with full power allocation. With the fact that all selected RSs keep constant SNR and $\sum_{i=1}^{L} x_i = 1$, we thus obtain

$$x_i = \frac{g_i}{\sum_{i=1}^{L} g_i}. \tag{18}$$

Therefore, the spectrum allocation is proportional to the channel gain g_i and we complete the proof.

Next, we aim to evaluate the performance of our proposed joint power and spectrum allocation strategy for RSs. In the simulation, we assume that there are ten relay stations available and the total power constraint P_{tot} is 50 mW. To simulate the practical communication environment, we assume that the wireless channel h_{ij} follows Rayleigh fading. Clearly from Fig. 2, the joint power and spectrum

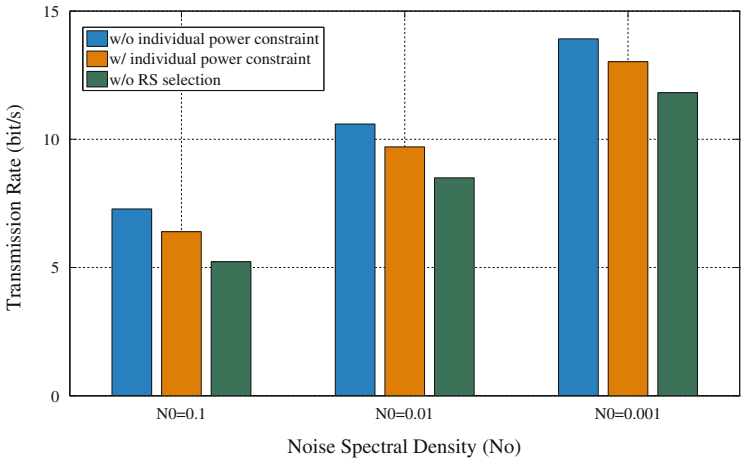

Fig. 2 Transmission rate (bit/s) with different power and spectrum allocation strategy

allocation strategy always provides the best transmission rate performance, since the individual power constraint (10 mW in this case) add one more constraint to the formulated optimization problem. To sum up, our proposed joint power and spectrum allocation strategy outperforms the scenario without RS selection, which further verifies the validity of the joint power and spectrum allocation algorithm.

5 Conclusions

In this work, we study the joint power and spectrum allocation for Relay Stations (RSs) in mobile relay networks. We first investigate the joint power and spectrum allocation without individual power constraint, and prove that only one RS should be selected per time to maximize the transmission rate. Further, in the scenario with individual power constraint, we conclude that all selected RSs should adjust the transmission power in a descending order according to the channel gain. Meanwhile, for the selected RSs with full power allocation, the optimal spectrum allocation is proportional to the channel gain. The effectiveness of our proposed joint power and spectrum allocation is demonstrated by the illustrative simulation.

Acknowledgements This work was supported in part by U.S. Office of Naval Research under Grants N00014-13-1-0043, N00014-11-1-0071, N00014-11-1-0865, and U.S. National Science Foundation under Grants CNS-1247848, CNS-1116749, CNS-0964713.

References

1. Federal Communications Commission (2010) Mobile broadband: the benefits of additional spectrum. www.fcc.gov. October 2010
2. Cisco visual networking index: global mobile data traffic forecast update, 2010–2015, Cisco white paper, www.cisco.com, February 2011
3. Walke B, Briechle R (1985) A local cellular radio network for digital voice and data transmission at 60GHz. Online Publishing, London, pp 215–225
4. Wang X, Liang Q (2013) On the throughput capacity and performance analysis of hybrid wireless network over fading channels. IEEE T Wirel Comm 12(6):2930–2940
5. Wang X, Liang Q (2012) Enhanced security and reliability with MIMO communications for smart grid. Secur Comm Networks
6. Pabst R, Walke B, Schultz D, Herhold P, Yanikomeroglu H, Mukherjee S, Viswanathan H, Lott M, Zirwas W, Dohler M, Aghvami H, Falconer D, Fettweis G (2004) A network information theory for wireless communication: scaling laws and optimal operation. IEEE Comm Mag 42(9):80–89
7. Wang X, Liang Q (2012) On the outage throughput capacity of hybrid wireless networks over fading channels. IEEE Globecom 2173–2178
8. Wang X, Liang Q (2013) Physical layer security in wireless smart grid. Secur Comm Networks
9. Damnjanovic A, Montojo J, Wei Y, Ji T, Luo T, Vajapeyam M, Yoo T, Song O, Malladi D (2011) A survey on 3GPP heterogeneous networks. IEEE Wireless Comm 18(3):10–21
10. Wang X, Liang Q (2013) Scaling laws for hybrid wireless networks over fading channels: outage throughput capacity and performance analysis. IEEE international conference on communications (ICC) 2013, Budapest, Hungary
11. Wang X, Liang Q (2013) Energy management for plug-in hybrid electric vehicles via vehicle-to-grid. IEEE international conference on communications (ICC) 2013, Budapest, Hungary
12. Lin YD, Hsu YC (2000) Multihop cellular: a new architecture for wireless communications. IEEE Infocom 3:1273–1282
13. Cover T, Thomas J (2006) Elements of information theory, 2nd edn. Wiley, New York
14. Boyd S, Vandenberghe L (2003) Convex optimization. Cambridge University Press, New York
15. Lin WS, Liu KJR (2012) Game-theoretic pricing for video streaming in mobile networks. IEEE T Image Process 21(5):2667–2680
16. Wang X, Liang Q (2012) Sensor selection schemes in smart grid. IEEE PES Innovative Smart Grid Technologies Asia 2012, May, 1–5
17. Wang X, Liang Q (2012) Stabilizing the power supply in microgrid using sensor selection. IEEE Globecom 3513–3518
18. Wang X, Liang Q (2012) Bidirectional energy management for plug-in hybrid electric vehicles via vehicle-to-grid. International conference on communications signal processing and systems 2012, Beijing, China
19. Wang X, Liang Q (2013) On the ergodic throughput capacity of hybrid wireless networks over fast fading channels. IEEE international conference on communications (ICC) 2013, Budapest, Hungary
20. Wang X, Liang Q (2013) Throughput performance analysis for hybrid wireless networks over fading channels. International conference on computer communications and networks (ICCCN) 2013, Nassau, Bahamas

Research on the Channel Estimation Algorithms in MIMO-Channel

Junsheng Zhang, Ruian Liu, and Daxi Liu

Abstract Randomness of wireless channel, in order to accurately recover the transmitter signal, requires to estimate the channel. This paper has been introduced some channel estimation algorithms which are based on the pilot frequency. It respectively analyzes and compares performances of the Least Square error (LS) and Minimum Mean Square Error (MMSE) and Linear Minimum Mean Square Error (LMMSE) algorithm in MIMO-OFDM wireless communication system. At the same time, it analyzes the performance of the three algorithms by increasing the multipath path. Experimental results show that, when the receiving signal under the condition of high SNR, considering the performance and computational complexity comprehensively in the channel estimation algorithm, the LS algorithm still has a very good application prospect.

Keywords LS • MMSE • LMMSE • MIMO-OFDM • Channel

1 Introduction

Orthogonal Frequency Division Multiplexing (OFDM) is a multi-carrier modulation technique, it can reduce the Inter-Symbol Interference (ISI) and Inter-Carrier Interference (ICI) effect on the signal. It has a high spectrum utilization rate, and can effectively resist the multipath delay spread [1]. Multiple Input Multiple Output (MIMO) technology can realize the high quality and high capacity wireless signal transmission, thus it has aroused people's wide attention in recent years. MIMO technology can exponentially improve spectrum utilization and power consumption on the basis of the original transmission bandwidth. The combined technology has

J. Zhang • R. Liu (✉) • D. Liu
College of Electronic and Communication Engineering, Tianjin Normal University, Tianjin, China
e-mail: ruianliu@sina.com

B. Zhang et al. (eds.), *The Proceedings of the Second International Conference on Communications, Signal Processing, and Systems*, Lecture Notes in Electrical Engineering 246, DOI 10.1007/978-3-319-00536-2_96,

already been one of the key technologies in the fourth generation mobile communication system [2–4].

Due to the frequency offset in OFDM system is very sensitive, it generally uses the coherent detection, there will be to use the channel estimation techniques to estimate the channel frequency response between the sender and the receiver. At the receiving terminal, according to the estimated response function can judge the distortion of the signal amplitude and phase, the channel are recognized by identifying the transfer characteristic of time domain or frequency domain. At the receiving terminal, it can use the channel equilibrium techniques to get the maximum reduction transmission signal [5].

In order to achieve an excellent transmission performance in MIMO-OFDM system, it is very necessary to carry on the accurate channel estimation. This article discusses the LS, MMSE and LMMSE channel estimation algorithm. It applies these algorithms to the MIMO-OFDM quasi static channel. Through comparing MSE or MMSE of these algorithms, the simulation results show that, considering the performance and computational complexity comprehensively in the channel estimation algorithm, the LS algorithm still has a very good application prospect.

2 Channel Estimation Algorithm

2.1 LS Algorithm

The LS algorithm is the most basic and simplest algorithm of channel estimation in MIMO-OFDM system. Suppose the pilot location sent the sub-carrier information is X_P, received information is Y_P, and the corresponding channel fading coefficient of frequency domain is H_P. So the relationship among the three is as follow:

$$Y_P = X_P H_P + N \tag{1}$$

The expression of channel estimation based on the LS algorithm can be written as follow [6]:

$$\begin{aligned} \hat{H}_{P,LS} &= [H_{P,LS}(0) \quad H_{P,LS}(1) \cdots \quad H_{P,LS}(N_P - 1)\ ]^{\mathrm{T}} \\ &= \left[\frac{Y_P(0)}{X_P(0)} \quad \frac{Y_P(1)}{X_P(1)} \cdots \quad \frac{Y_P(N_P - 1)}{X_P(N_P - 1)} \right]^{\mathrm{T}} \end{aligned} \tag{2}$$

By formula (2), the channel estimation method has a simple structure and small amounts of calculation which is based on the LS algorithm. It is very suitable for the actual system.

But the LS algorithm does not take use of the channel relevance characteristics of frequency and time domain. It also ignores the influence of noise during the

channel estimation. Therefore it is more sensitive to the noise. When the noise is bigger, the estimated accuracy has greatly reduced. According to the formula (2), the Mean Square Error (MSE) of LS estimation can be written as:

$$\begin{aligned} \mathrm{MSE}_{LS} &= \mathrm{trace}\left(E\left[\left(\hat{H}_{P,LS} - H_P\right)^{\mathrm{T}}\left(\hat{H}_{P,LS} - H_P\right)\right]\right) \\ &= \mathrm{trace}\left(\sigma_n^2\left(X_P^{\mathrm{T}}X_P\right)^{-1}\right) \end{aligned} \tag{3}$$

The MSE of LS algorithm can also be written as the following form:

$$\mathrm{MSE}_{LS} = \beta/\mathrm{SNR} \tag{4}$$

Among these, $\beta = E[|x_P|^2]E[|1/x_P|^2]$ is associated with the constellation size. σ^2 is a noise variance.

2.2 MMSE Algorithm

In order to reduce the effects of noise on the channel estimation and improve the estimation precision. MMSE algorithm can be used to design the channel estimation algorithm. It has comprehensively considered the characteristics of the channel and noise variance. As follow:

$$\mathrm{MSE}_{MMSE} = E\left[\left(H - \hat{H}\right)^{\mathrm{H}}\left(H - \hat{H}\right)\right] \tag{5}$$

MMSE algorithm is the minimize of MSE [7], the corresponding frequency domain channel fading coefficient is as follow:

$$\begin{aligned} \hat{H}_{P,MMSE} &= R_{H_PH_P}X_P^{\mathrm{T}}\left(X_PR_{H_PH_P}X_P^{\mathrm{T}} + \sigma_{N_P}^2\left(X_PX_P^{\mathrm{T}}\right)^{-1}\right)^{-1}Y_P \\ &= R_{H_PH_P}\left(R_{H_PH_P} + \sigma_{N_P}^2\left(X_PX_P^{\mathrm{T}}\right)^{-1}\right)^{-1}\hat{H}_{P,LS} \end{aligned} \tag{6}$$

$R_{H_PH_P}$ is the autocorrelation matrix of the pilot sub-channels. X_P is the pilot signal. MMSE algorithm needs to get the matrix inversion. Therefore, the biggest drawback of MMSE algorithm is the large amount of calculation.

2.3 LMMSE Algorithm

By formula (6), it can be seen that MMSE channel estimation algorithm is to transform the response of LS channel estimation algorithm. In this transform process, if the

matrix inversion calculation is taken to the shock response of each OFDM symbol, it will make the final computation is large. But if it uses a fixed and same pilot symbol or an average signal-to-noise ratio (SNR) instead of the inverse operation, this will greatly reduce the amount of calculation. In the practical application, it makes use of the average SNR instead of the pilot signal inversion. That is to say, $E[(X_P X_P^{\mathrm{T}})^{-1}]$ will be instead of $(X_P X_P^{\mathrm{T}})^{-1}$. It is also mean that, it will use the average power of sub-channels instead of the instantaneous power of symbols. This can greatly reduce the amount of calculation of MMSE algorithm. So, the formula (6) is simplified to obtain the Linear Minimum Mean Square Error (LMMSE) estimator [8]:

$$\hat{H}_{P,LMMSE} = R_{H_P H_P}\left(R_{H_P H_P} + \frac{\beta}{\mathrm{SNR}} I\right)^{-1} \hat{H}_{P,LS} \tag{7}$$

The MSE of LMMSE algorithm is:

$$\mathrm{MSE}_{LMMSE} = \frac{1}{N}\frac{\beta}{\mathrm{SNR}}\sum_{k=0}^{N-1}\frac{\lambda_k}{\lambda_k + \frac{\beta}{\mathrm{SNR}}} \tag{8}$$

The MMSE algorithm is too complex, so nowadays it commonly uses the LMMSE algorithm instead of MMSE algorithm.

3 System Model and the Channel

The MIMO-OFDM system has N_t transmitting antennas and N_r receiving antennas [9]. It is as shown in Fig. 1.

In the frequency selective fading channel, the transmitting terminal uses the STBC coding method and combines with OFDM technology. Then the frequency selective fading channel is divided into N (N points FFT) flat fading sub-channels. Suppose the time domain impulse response between the ith transmitting antenna and the jth channel receiving antenna is as:

$$h_{j,i}(t,\tau) = \sum_{p=1}^{L} a_p \delta(\tau - \tau_p) \tag{9}$$

L is the corresponding the most number of path delay. Channel has been discretization, can get $h_{j,i}(n,l)$,and its corresponding frequency domain shock response is as:

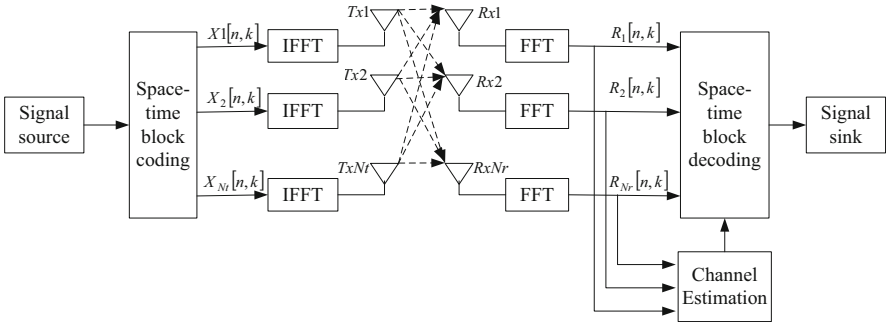

Fig. 1 MIMO-OFDM system block diagram

$$H_{j,i}(n,k) = \sum_{l=1}^{L} h_{j,i}(n,l)\exp\left(-j2\pi\frac{kl}{N}\right) \tag{10}$$

$H_{j,i}(n,k)$ is the frequency attenuation coefficient between the transmitting antenna i and receiving antenna j. At the time n of the transmission of OFDM symbol, the data source is separated into N_t groups frequency domain subcarrier symbols, corresponded the transmitting antennas, by space-time coding. For example, the $X_i(n,k)$ is the k sub-carrier symbol of the ith transmitting antenna, treated with inserted pilot frequency and zero sideband. Through the IFFT transformation, it coupled with Cyclic Prefix (CP). At the same time the antenna ($i = 1, 2, \ldots, N$) transfer out the data. At the jth antennas of the receiving terminal, it eliminates the CP. The signal of frequency domain after the FFT transformation is represented as:

$$R_j(n,k) = \sum_{i=1}^{N_t} H_{j,i}(n,k)X_i(n,k) + W_j(n,k) \tag{11}$$

$W_j(n,k)$ is the Additive White Gaussian Noise (AWGN). The variance of W_j is σ^2. The mean of W_j is zero on the k sub-carrier symbol of the jth receiving antenna at time n.

4 Simulation and Result Analysis

4.1 Experiment on Quasi-Static Multipath Fading Channel

The parameter settings of MIMO-OFDM communication system experiment are as follows: it has 64 carriers; the sub-carrier gap is 1.25 MHz; the bandwidth is 80 MHz; the integral cycle is 0.8 μs; the sampling time interval is 0.0125 μs; the cyclic prefixes are a total of 16; the modulation of the data is Quadrature Phase Shift Keying (QPSK); the simulation environment is the Quasi-static Multipath Fading Channel.

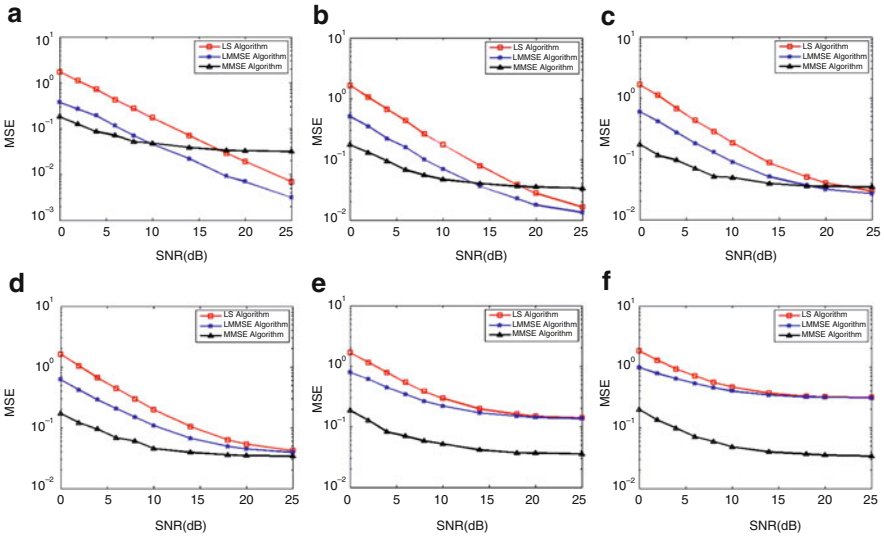

Fig. 2 Comparison of the channel estimation performance of LS, LMMSE and MMSE algorithm. (**a**) 4 paths. (**b**) 7 paths. (**c**) 9 paths. (**d**) 10 paths. (**e**) 15 paths. (**f**) 20 paths

In this part, by changing the number of multipath, we respectively make the curves as shown in Fig. 2a–f. The number of paths is: 4 paths, 7 paths, 9 paths, 10 paths, 15 paths, 20 paths. Under the condition of Quasi-static, the number of paths is increased based on the LS and MMSE and LMMSE algorithm. The LS and LMMSE algorithm are more superior than MMSE algorithm, but all the three algorithms have the floor effect. When the receiving signal SNR is less than 10 dB, the estimation performance based on MMSE algorithm is the best, followed by LMMSE. But along with the increase of SNR, the estimation performance based on MMSE algorithm appears obvious floor effect. When the SNR is more than 10 dB, the MMSE algorithm estimation performance is worse than LMMSE algorithm. Nevertheless, the use of LMMSE algorithm has some limitations, it demands to know the statistical features of channel and receiving signal SNR. The computational complexity of the MMSE algorithm is higher than the LS algorithm. Though it can design some special pilot frequency to appropriately reduce the complexity, it is only used in the low SNR environment.

4.2 Experiment on Quasi-Static Rayleigh Fading Channel

The parameter settings of MIMO-OFDM communication system experiment are as follows: it has 64 carriers; the sub-carrier gap is 1.25 MHz; the bandwidth is 80 MHz; the integral cycle is 0.8 μs; the sampling time interval is 0.0125 μs; the

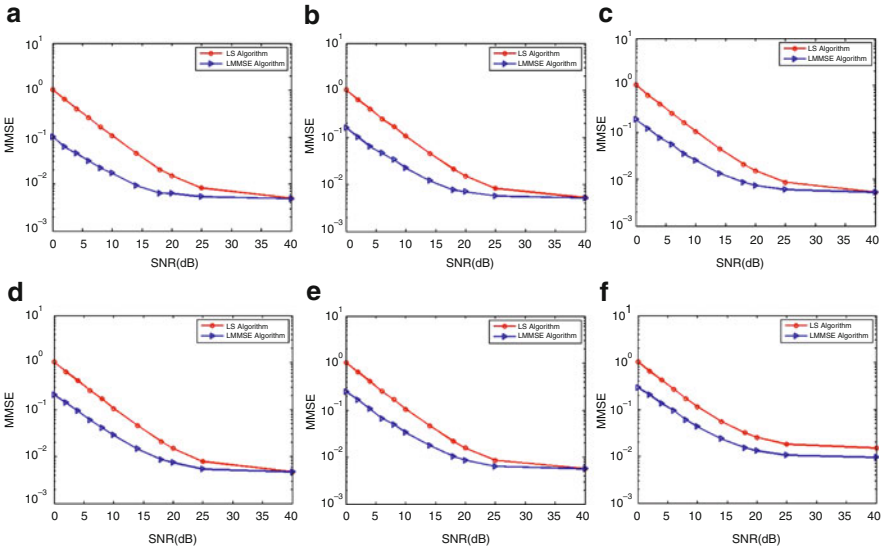

Fig. 3 Comparison of the LMMSE and LS channel estimation algorithm. (**a**) 4 paths. (**b**) 8 paths. (**c**) 10 paths. (**d**) 12 paths. (**e**) 15 paths. (**f**) 20 paths

cyclic prefixes are a total of 16; the modulation of the data is Quadrature Phase Shift Keying (QPSK); the movement speed of wireless communication equipment is 3 km/h; the simulation environment is the Rayleigh fading channel, which contains the multipath fading and Doppler frequency shift.

In this part, by changing the number of paths, we respectively make the curves as shown in Fig. 3a–f. The number of paths is: 4 paths, 8 paths, 10 paths, 12 paths, 15 paths, 20 paths. In the communication system of the combined action of the certain Doppler frequency shift and multipath effect, as shown in Fig. 3, when the SNR reaches 20 dB, the MMSE values of LS and LMMSE algorithm all appear the floor effect. With the gradual increasing of the number of paths, the MMSE values of the two algorithms, are not like before, has been separated. The superiority performance of the LS algorithm is reflected. When the receiving signal under the condition of high SNR, considering the performance and computational complexity comprehensively in the channel estimation algorithm, the LS algorithm still has a very good application prospect.

5 Conclusion

This paper researches and compares the channel estimation performance of the MIMO-OFDM system based on the LS and MMSE and LMMSE algorithm. It respectively studies on the condition of different multipath time delay of MSE and MMSE and analyzes the algorithm performance under this situation. Through the

experiments, it comprehensively considers the estimation performance and computational complexity, the performance of LS algorithm in the MIMO-OFDM system is most superior, and the LS algorithm has a good application prospect.

Acknowledgment This research was supported by the Tianjin natural science fund (13JCYBJC15800)

References

1. Zhang J, Zheng B (2003) Overview of pilot-aided channel estimation in OFDM. J Chin Inst Commun 24(11):116–124
2. Shi X, Li H (2010) Principle and key techniques of MIMO-OFDM system for wireless communication. Foreign Electron Meas Technol 29(2):1–2
3. Katariya A, Yadav A, Jain N et al (2011) BER performance criteria based on standard IEEE 802.11a for OFDM in multipath fading environments. 2011 international conference on computational intelligence and communication networks, pp 238–241
4. Yang W (2005) A road to future broadband wireless access: MIMO-OFDM based air-interface. IEEE Commun Mag 43(1):53–60
5. Coleri S, Ergen M, Puri A, Bahai A (2002) A study of channel estimation in OFDM systems. In: IEEE 56th Proceedings of Vehicular Technology Conference, VTC 2002-Fall vol. 2, pp 894–898 doi:10.1109/VETECF.2002.1040729
6. Edfors O, Sandell M, Vandebeek J et al (1998) OFDM channel estimation by singular value decomposition. IEEE Trans Commun 46(7):931–939
7. Morelli M, Mengali U (2001) A comparison of pilot-aided channel estimation methods for OFDM systems. IEEE Trans Signal Process 49(12):3065–3073
8. Minn H (2000) An investigation into time-domain approach for OFDM channel estimation. IEEE Trans Broadcast 46(4):240–247
9. Deng P, Yan Z (2011) Research on a method of the quasi-static channel estimation for MIMO-OFDM system. National conference of China institute of communications (NCCIC), pp 24–28

A Novel Wideband Dual-Polarized Dipole Antenna

Feiyun Guan, Xianhu Luo, and Xianqi Lin

Abstract In this paper, a novel dual-polarized antenna is proposed, which can be easily processed for mobile wireless communication systems. The proposed antenna has a common impedance bandwidth at both input ports from 1.61 to 2.52 GHz (44.1 %) with SWR $\leq$2. The isolation between the two ports is larger than 20 dB, at the same time, the gain of the antenna is about 7 dBi. The radiation pattern of the antenna in the corresponding frequency band has a stable performance. Moreover, the antenna can be processed in a metal plate into a flat shape then bent into the desired antenna model, so it's convenient for industrial processing.

Keywords Dipole antenna • Dual-polarization • Wideband

1 Introduction

With the rapid development of modern wireless communications, such as 3G technology, LTE, WiFi, and WiMAX, there has been increased demand for wideband and low profile antennas. Many different methods have been proposed to investigate wideband unidirectional patch antennas [1, 2]. And most of the antennas for modern wireless communications are required to be embedded easily or maintaining aerodynamic performance [3]. Meanwhile, due to this increasing mobile user and the expansion of mobile services, the system becoming increasingly crowded. During the past few years, the $\pm 45^{\circ}$ dual-polarized antennas are used widely in mobile communications to increase the capacity of mobile communications and reduce the installation cost [4]. Therefore, there are a variety of wideband dual polarization dipole antenna is designed for mobile communication.

F. Guan (✉) • X. Luo • X. Lin
School of Electronic Engineering, University of Electronic Science and Technology of China, Chengdu 610054, P.R. China
e-mail: xianhuluo@gmail.com; xianqilin@gmail.com

B. Zhang et al. (eds.), *The Proceedings of the Second International Conference on Communications, Signal Processing, and Systems*, Lecture Notes in Electrical Engineering 246, DOI 10.1007/978-3-319-00536-2_97,

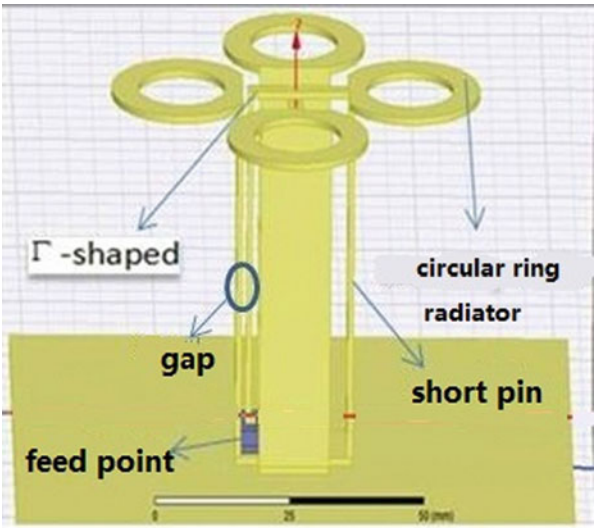

Fig. 1 Perspective view of the proposed antenna

In this paper, we will discuss the model of the novel dual-polarized broadband antenna for the third generation mobile communication system. Then, we use HFSS (3-dimensional full-wave electromagnetic simulation software) to analyze the electromagnetic parameters of the novel antenna.

2 Antenna Design and Analysis

As show in Figs. 1 and 2 (Fig. 2 is the ultimate optimized schematic), the planar structure of the mentioned antenna consists of 6 parts: Radiating elements, the coaxial feeder, nylon cushion, Γ-shaped strip feed, short pin, metal ground. In the Fig. 2, we can see the detailed dimensions for operation at about 2 GHz. The radiation of the antenna and the Γ-shaped feed strip are made of cooper for its superiority of being easy to be processed, corrosion prevention and low-cost. A schematic plan view of shaded part represents a 1 mm metal sheet, and the 2.8 mm thick metal strips as shown in the upper right corner of the Fig. 2 stands in the nylon base, which act as feed strips. The effective circumference of the circular ring radiator can be empirically approximated by

$$le = (2 * \text{pi} * \text{N} * \text{S})/\lambda \tag{1}$$

*l*e is the effective length of the antenna, λ is about $\lambda_0/\sqrt{\varepsilon_r}$, S is on behalf of the effective area of the antenna. Thus, the resonant frequency will be changed when we fine-tune the size of the radiating patch, and the height above ground of the

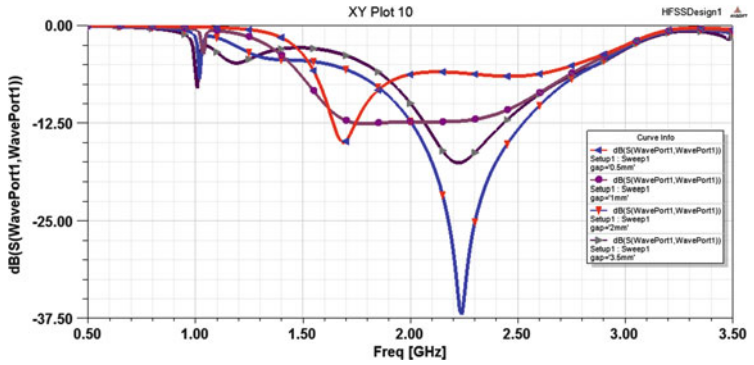

Fig. 2 Schematic diagram of dual-polarized dipole antenna

radiating element is about 1/4 wavelength, which can achieves a good performance of the mirror.

3 Results and Analysis

The width of the gap between the Rectangular columns feed strip and Γ-shaped feed strip is an important parameter for impedance matching [5]. Figure 3 shows the simulation results for return loss of the proposed antenna as an outcome of gap. An optimal value for gap is found to be 1 mm for the best impedance matching at operation frequency. The distance (H) of antenna radiating elements to ground has a conspicuous influence on the bandwidth of the proposed antenna. Figure 4 shows the simulation results for return loss of the proposed antenna as an outcome of H. An optimal value for H is found to be 51 mm for the best performance at operation frequency. Meanwhile, we can see that the d_out of the antenna outer ring size has a certain impact for impedance matching from the Fig. 5.

The simulation results of the dual-polarized dipole antenna show in Fig. 6, and the dual polarized antenna has a common impedance bandwidth at both input ports from 1.61 to 2.52 GHZ (44.1 %) with SWR ≤ 2 (S11 ≤ -10 dB). The isolation between the two ports is larger than 20 dB, at the same time, the gain of the antenna is about 7 dBi.

4 Conclusion

In this research, a wideband dual-polarized dipole antenna is presented and investigated. By optimizing the design, we finally got the wideband dual-polarized dipole antenna. Meanwhile, the radiation pattern of the antenna in the

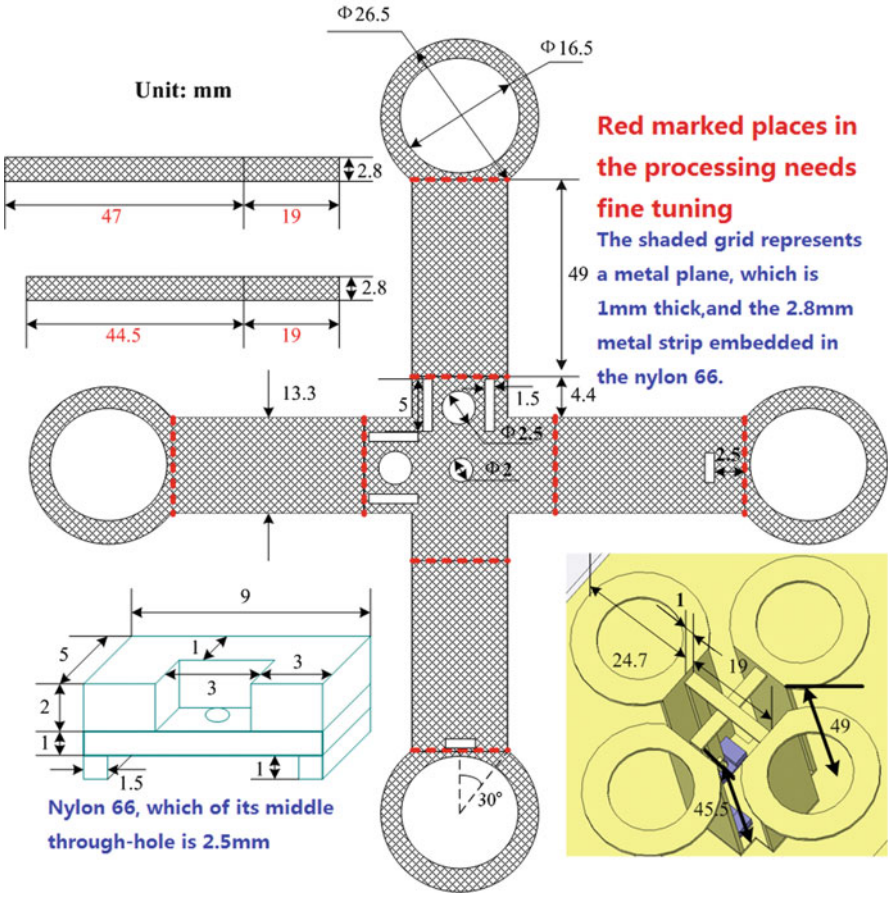

Fig. 3 Effect of the gap on the return loss of the antenna

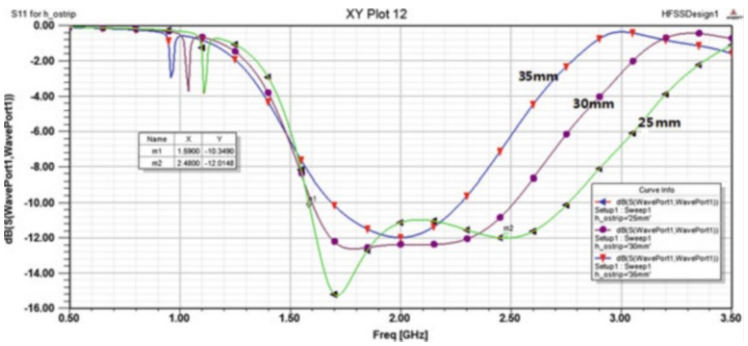

Fig. 4 Effect of the height (h_ostrip) on the performance of the antenna

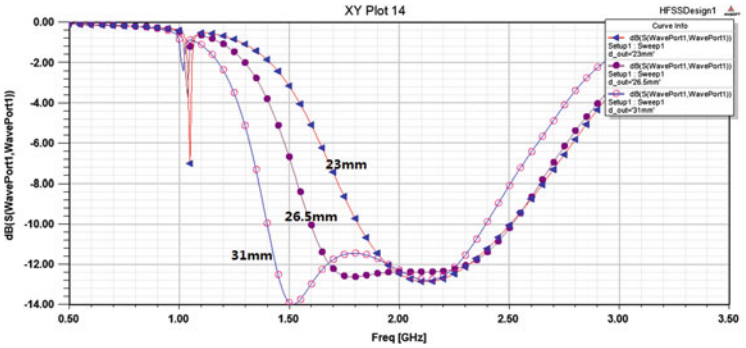

Fig. 5 Effect of d_out on the performance of the antenna

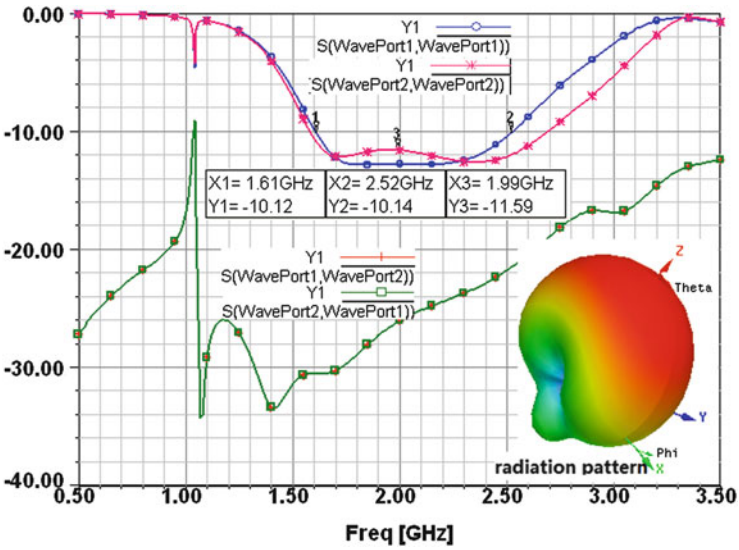

Fig. 6 Part of the simulation results for the double-dipole

corresponding frequency band has a stable performance. And duo to molding plane structure, this antenna is convenient for industrial processing.

Acknowledgement This work was supported in part by NSFC (Nos. 60901022), in part by RFDP (No. 20090185120005), in part by the Fundamental Research Funds for the Central Universities (Nos. ZYGX2010J021).

References

1. Mak CL, Luk KM, Lee KF, Chow YL (2000) Experimental study of a microstrip patch antenna with an L-shaped probe. IEEE Trans Antennas Propag 48(5):777–783
2. Lee KF, Luk KM, Tong KF, Shum S-M, Huynh T, Lee RQ (1997) Experimental and simulation studies of the coaxially fed U-slot rectangular patch antenna. Inst Elect Eng Proc Microw Antennas Propag 144(5):354–358
3. KWAI-M AN LUK (2011) The importance of the new developments in antennas for wireless communications. Proceedings of the IEEE, December 2011, vol 99, No. 12
4. Guo Y-X, Luk K-M, Lee K-F (2002) Broadband dual polarization patch element for cellular-phone base stations. IEEE Trans Antennas Propag 50:251–253
5. Mingjian LI, Kwai-Man LUKA (2012) Wideband dual-polarized antenna with very low back radiation. Proceedings of APMC 2012, Kaohsiung, Taiwan, 4–7 Dec 2012

Direct P-Code Acquisition Based on Wavelet Filtering

Qing Xu, YuXiang Gao, and HaiJiang Wang

Abstract Compared with the C/A-Code, GPS P-Code offers much higher accuracy but also the higher tolerance to jamming and spoofing. It has large Doppler frequency shift, long code period and high code rate. According to these characters, a new scheme for direct P-Code acquisition using auxiliary acquisition is proposed in the paper, which estimates the phase and Doppler of received P-Code signal in the two dimensional search. In order to finish the auxiliary acquisition rapidly, the wavelet is used to decrease the quantity of data. True phase alignment is detected using a conventional parallel search scheme, where the initial phase and Doppler are set to the values obtained by the auxiliary acquisition and whose amount of parallel channels is required less. The result of computation shows the proposed scheme achieve the priori information of phase and Doppler faster and correctly.

Keywords GPS • DSP • Direct P-code acquisition • Wavelet • Auxiliary acquisition

1 Introduction

The Global Position System (GPS) provides an all-weather, 24 h navigation capability to suit equipped users. It is a direct-sequence spread spectrum (DS/SS) system, which is first required for reception of DS/SS signals to synchronize the phase of the local PN sequence with that of the transmitter [1]. It broadcasts both a short repeating code called C/A code and a longer code called P-Code. Because of the large Doppler frequency shift, a two dimensional search must be performed: code phase and carrier frequency. Traditionally, in order to acquire the P-code, the GPS receiver locks onto the C/A code to extract the Hand-over-word (HOW),

Q. Xu (✉) • Y.X. Gao • H.J. Wang
College of Electronic Engineering, Chengdu University of Information Technology, Chengdu, Sichuan 610054, China
e-mail: xuqing68@cuit.edu.cn

B. Zhang et al. (eds.), *The Proceedings of the Second International Conference on Communications, Signal Processing, and Systems*, Lecture Notes in Electrical Engineering 246, DOI 10.1007/978-3-319-00536-2_98,

which provides the necessary timing information to tell where the P-code pattern is in its whole sequence. Compare with the P-Code, the C/A code is jammed easily intended or involuntary. During certain military operations, the C/A-code signal could be degraded so that the use of the open Standard Positioning Service to adversaries is denied and the use of the encrypted P (Y)-code is still sustained [5]. So the direct P-Code acquisition potential is a more robust functionality for GPS receivers to provide the ability to acquire the P-Code without the aid of the C/A code.

The difficulty of direct GPS P-Code acquisition is the extremely long period of the P-code, which makes the search for the correct carrier frequency and code phase very slow. In order to reduce the acquisition time, must combine with multi-technology, such as, Enhance the precision of time and frequency resource to decrease the cells of carrier frequency and code phase, which must be searched for; Increase the amounts of parallel processing channel and the processing velocity of hardware; Improve the acquisition algorithmic and the signal processing technologies to boost efficiency of researching for the carrier frequency and code phase; Enhance the Signal-to-Noise Rate of the receiver front ends.

Although the general parallel code-phase search is used due to its efficient searching speed [6], the implementation complexity becomes prohibitive especially for the long PN sequences in FPGA design because of large hardware resource requirement and design complexity.

The efficiency of a searching algorithm greatly affects the P-Code acquisition time. Under the precondition of not to increase the complexity of design fast, it is a desired method to reduce the acquisition time that boosting the efficiency of researching for the carrier frequency and code phase through improving the acquisition algorithmic and the signal processing technologies.

The promising methods to improve acquisition speed proposed by other researchers focus more on software simulation performance, such as, Circular correlation by partition and zero padding; Non-coherent circular correlation by partition; Delay and multiplication, They require large Fast Fourier Transform size [5]. So, for the direct P-code acquisition, the challenges are how to reduce the code phase search time for the extremely long period and how to avoid large size Fast Fourier Transform (FFT).

2 The Proposed Method Based on Auxiliary Acquisition

If a priori information on the phase and the Doppler frequency of the incoming PN signal is available by some means [2], direct P-Code acquisition is faster than handover from the C/A code search by starting the search from the most probable region. The promising design attempts to achieve acquisition without first acquiring the C/A code and use the P-Code directly.

The proposed method achieves direct P-Code acquisition in two approaches. First, the phase and Doppler frequency of incoming P-Code signal are estimated

utilizing DSP using FFT, called auxiliary acquisition; True phase alignment is detected using a conventional parallel search scheme, where the initial phase of local P generators and the initial value of NCO are set to a values obtained by the DSP and whose amount of parallel channels is required less. This paper describes the auxiliary acquisition mostly.

3 The Priori Information Obtaining Using Wavelet Transformation

Even just searching a segment of the P-code for several ms, the searching task is still huge. In order to limit the searching segment, a good acquisition algorithm is absolutely necessary. The direct average and overlap average method, which can speed up the correlation procedure, are proposed to decrease the quantity of data [5]. It supposes the Doppler frequency is compensated primely. But in application, Because of not any priori information of Doppler other than the changing range, a two dimensional search must be performed.

In order to decrease the quantity of data, the wavelet analysis is a desired method, which is performed using a single prototype function called a wavelet. From a signal processing point of view, a wavelet is an octave band filter. Therefore the wavelet transform can be interpreted as a constant-Q filtering with a set of octave-band filter, followed by sampling at the respective Nyquist frequencies (corresponding to the bandwidth of the particular octave band) [3, 4]. The signal processes with three steps wavelet decomposition and obtaining the approximation signal $x_0[n]$ shows in Fig. 1.

Where, $2\downarrow$ means down-sampling by 2 and $h_0[n]$ can be considered as the response of a low-pass filter, respectively. Followed the wavelet theory, the L must be even. After 3 steps decomposition, the quantity of $x_0[n]$, is only one eighth of $x_I[n]$.

Not considering the noise, the received signal can be expressed:

$$R = AP(t - \tau_1)D(t)\cos[2\pi(f + f_d)t] \tag{1}$$

where, A is the amplitude of received signal, $P(t)$ is the P code sequence, τ_1 is the unknown code phase to be estimated, $D(t)$ is the navigation data, f and f_d are the carrier and Doppler frequency. After the down-converted and wavelets processing, considering the velocity of information and Doppler are less than sampling frequency, the processed signal can be express:

$$R^{'} = AP^{'}(t - \tau_1)D(t)\cos[2\pi f_d t] \tag{2}$$

Where, $P'(t)$ is the approximation signal whose amount of data is only 2^{-j} than the original data and j is the amount of filters.

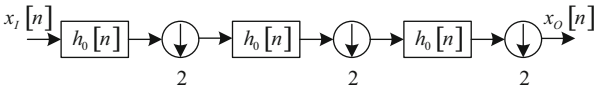

Fig. 1 Three steps wavelet decomposition

Similarly, the local generational P Code processed with Wavelets filter can be express as $G' = P'_L(t - \tau_2)$. De-spread spectrum procession with G', it can be express:

$$S = A < P^{'}(t - \tau_1)P^{'}{}_L(t - \tau_2) > D(t)\cos[2\pi f_d t] \tag{3}$$

If coarse alignment within some fraction of one code chip interval between the two PN-code sequences is achieved, that is $\tau_1 \approx \tau_2$ then

$$< P^{'}(t - \tau_1)P^{'}{}_L(t - \tau_2) >= 1 \qquad \text{(normalization)}$$

The signal can be express as:

$$S = AD(t)\cos[2\pi f_d t] \tag{4}$$

After the procession of de-spread spectrum, the signal includes Doppler frequency only, which can be estimated using FFT.

The whole processing block diagram showed in Fig. 2.

In Fig. 2, the incoming signal in-phase and quadrature components, which are processed with Wavelets filters to decrease the amount of data, are used as the real and imaginary inputs when calculating the FFT, which generates one dimension data with 32 × 1,024 points. The result is multiplied by the complex conjugate of the FFT of the local generated P code processed with Wavelets filters alike. It generates the two dimensional data of 1,024 × 32. Implement an FFT that extends the parallel testing to a maximum of 32 resolution cells in frequency for 1,024 times. Extract the Maximum of magnitude to compare with the threshold.

If the threshold is exceeded, then PN tracking is initiated; otherwise, the next code phase estimate is tested.

4 Performance of Auxiliary Acquisition

After wavelets filtering for three times, the data for FFT calculation are as many as one eighth of primal data collected by AD. If the sampling rate is 65.536 MHz and the length of FFT is 1,024, we can process the data of 125 μs for each FFT calculation.

(a) Precision of Doppler estimation

According to the length of 32 calculations for FFT, the precision of Doppler estimation can be express as:

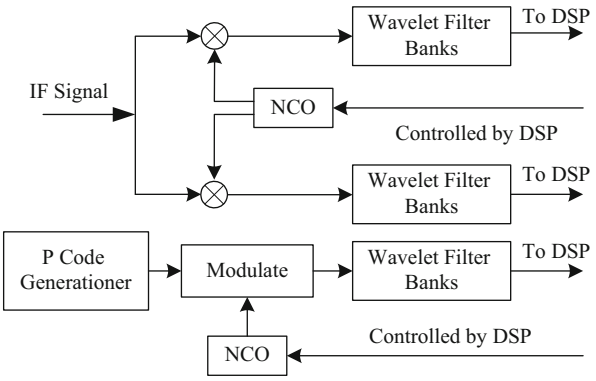

Fig. 2 The block diagram of auxiliary acquisition for direction P-code acquisition based on wavelet

$(1/T)/32 = (1/125\ \mu s)/32 = 250$ Hz

Where, T is the length of data for each FFT calculation.

(b) Max acquisition time for auxiliary acquisition

If the uncertain time is ± 1 s, we can estimate the maximal acquisition time in several parts below.

First, storage and processing for receive signal. If the receive unite saves the data of 4 ms, the time domain data are as many as 32,768 after the wavelets processing. So we must finish the FFT calculation for 32 times if the length of FFT is 1,024.

Second, storage and processing for P code signal generated by local receiver. If the uncertain time is ± 1 s, we can load the data for several times for such huge data. Like the method processing for receive signal, if we load the data of 4 ms, we must finish the FFT calculation for 32 times whose length is 1,024.

Lastly, correlation and Doppler estimation. If we use FFT to finish the correlation and estimate the Doppler range, the operation times of two dimensional search is listed below:

1,024 points complex multiplication: 32
1,024 points IFFT: 32
32 points FFT: 1,024

(c) The total acquisition time

If we finish the auxiliary acquisition by using DSP, such as TMS320C64x with the capacity of processing information at a rate of 8,800+ MIPS or nearly nine billion instructions per second at clock rates of 1.1 GHz and greater, the cycles for FFT calculation is

$$10 \times (N/8 + 19) \times \mathrm{ceil}\,(\log 4(N) - 1) + (N/8 + 2) \times 7 + 28 + N/8$$

Where, N is the scalar for FFT. The cycles for complex Multiplication is

$$9 \times nx/8 + 18$$

Table 1 The processing time for C64x DSP

Calculation	1,024 Points FFT (IFFT)	32 Points FFT	1,024 Points complex multiplication
Processing time (circle and time)	6,262 10.44 μs	192 0.35 μs	1,170 1.95 μs

Where, nx is the length of vector. If the clock rate is 600 MHz, the processing rate of C64x is listed in Table 1.

If we only consider the time consumption of FFT, we need finish 96 times 1,024 points FFT(IFFT), 1,024 times 32 points FFT and 32 times 1,024 points complex multiplication that total consume 1.5 ms.

If the uncertain time is ± 1 s, the repetitive search for all code phase is

2 s/125 μs = 16,000(times)

So the maximal time for auxiliary acquisition is 24 s.

5 Conclusion

Compared with the C/A-Code, GPS P-Code has large Doppler frequency shift, long code period and high code rate. According to these characters, it is difficult for direct P-code acquisition. This paper propose a new scheme for direct P-Code acquisition using auxiliary acquisition, which estimates the phase and Doppler of received P-Code signal in the two dimensional search cursorily. In order to finish the auxiliary acquisition rapidly, the wavelet is used to decrease the quantity of data. It cannot only save hardware resource, but also increase the flexibility by using DSP.

References

1. Pickholtz R, Schilling D, Milstein L (1982) Theory of spread-spectrum communications—a tutorial. IEEE Trans Commun COM-30:855–884
2. Kang S, Lee Y-H (2001) Rapid acquisition of PN signals for DS/SS systems using a phase estimator. IEEE J Sel Area Comm 19(6):1128–1137
3. Vetterli M, Herley C (1992) Wavelets and filter banks: theory and design. IEEE Trans Signal Process 40(9):2207–2232
4. Mallat G (1989) A theory for multiresolution signal decomposition: the wavelet representation. IEEE Trans Pattern Anal Mach Intell 11(7):674–693
5. Pang J. Global positioning system P-code direct acquisition field programmable gate array prototyping. Dissertation for the Degree Doctor of Philosophy, College of Engineering and Technology Ohio University
6. Wolfert R, Chen S, Kohli S, Leimer D, Lascody J (1998) Direct P(Y)-code acquisition under a jamming environment. Position Location and Navigation Symposium, pp 228–235, IEEE 1998 10.1109/PLANS.1998.670047

The Design of RFID Middleware Data Filtering Based on Coal Mine Safety

Jianglong Zhu, Jun Huang, Dawen He, Yujun Leng, and Shilin Xiao

Abstract This paper introduces the application of radio frequency identification (RFID) technology in coal mine safety. As one of the most important part of the radio frequency identification (RFID) system, RFID middleware is introduced. To resolve the problem of processing great number of RFID datum, the data filter method becomes a very hot filed for researching. Several filter methods are researched and analysed in the paper. The readers collect the data from the tags. The algorithm is to filter the data which is within the scope of setting. The algorithm achieves the effect of filter redundant data.

Keywords RFID • Middleware • Data filter • Redundant data • Algorithm

1 Introduction

Coal mine production is under the ground. Bad environment is the cause of coal mine accidents, in addition to the coal mine complex operation condition, severe natural hazards such as water, fire, gas, coal dust, and coal mine equipment condition, the management level and mine workers' own quality problems. Safety in production is always the first priority to coal enterprise [1]. RFID technology can identify multiple tags at the same time, the persons, equipment and supplies under the ground can be located and tracked record [2]. At the time of the accident rescue,

J. Zhu (✉) • J. Huang • Y. Leng
Chongqing Key Laboratory of Signal and Information Processing, Chongqing University of Posts and Telecommunications, Chongqing 400065, P.R.China
e-mail: zhujl24@163.com; 270021129@qq.com

D. He
Chongqing MAS Science & Technology Co., Ltd, Chongqing 400065, P.R.China

S. Xiao
State Key Laboratory of Advanced Optical Communication Systems and Networks, Shanghai Jiao Tong University, Shanghai 200240, China

B. Zhang et al. (eds.), *The Proceedings of the Second International Conference on Communications, Signal Processing, and Systems*, Lecture Notes in Electrical Engineering 246, DOI 10.1007/978-3-319-00536-2_99,

understanding the underground persons' position timely and accurate, it makes the rescue work much more easier.

RFID middleware plays an intermediary role between RFID tags and applications. RFID middleware interface defines a relatively stable high-level application environment, no matter how the underlying computer hardware and system software upgrade, as long as the middleware updates and application software is almost without any modification, thus protecting the enterprise application software development in the major investment [3]. At the same time, the use of RFID middleware helps to reduce the burden of enterprises when the second development, which makes them to upgrade existing software systems with ease, extends the function of the software system and simplifies the complexity of the development.

The coal mine monitoring system produces great amount of data. In a medium-sized coal mine as an example. The entire RFID system may generate thousands of tag data at the same time, tens of thousands of the amount of monitoring data every day. The data rarely contains really useful information, which requires the RFID system to have a strong processing capacity to filter redundant data.

2 The RFID Middleware Architecture

According to the definition of the EPC Internet of things Savant middleware [4] defined by Auto-ID Laboratory which is the RFID authoritative research institutions, EPC application layer event specification, and the bottom layer read and write device interface protocols proposed by EPC global, as shown in Fig. 1 is the RFID middleware architecture. It contains the following functional modules: read-write device interface module, read-write device driver manager module, logic read-write device mapping module, RFID data filter module, business rules filter module, read-write device configuration, management and monitoring module, the upper application program interface module.

Read-write device interface is mainly used for data communication between middleware and RFID read-write device. Its function is to send the RFID tags data received from RFID read-write device to the middleware and to accomplish the instructions received from the read-write device configuration, management and monitoring module.

Read-write device driver manager module is mainly used to connect and drive various types of read-write devices, to establish connection to read-write device with different parameters, and to complete data communication.

Logic reader and writer mapping module maps the multiple reader and writers or their multiple antenna to be a logic reader and writer, a logical reader and writer represents a data collection point with specific meaning, regardless of the number of reader and writer, antenna per collection point, which reduces the software data acquisition coupling of the upper module and the lower part.

RFID data filtering module mainly filters the collected RFID data, meanwhile, redundancy filtering the huge amount of data hardware uploaded. Since this article

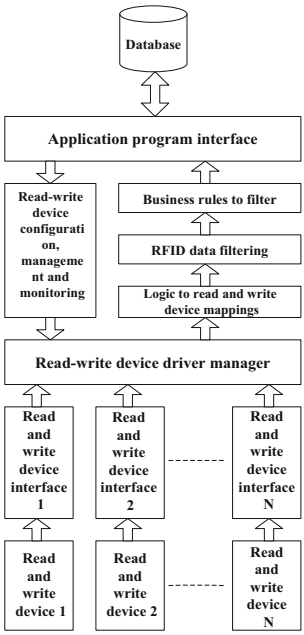

Fig. 1 The RFID architecture

focuses on RFID middleware data filtering, therefore the part will focus on introduce. RFID data filtering is unanimously recognized as one of the core functions of RFID middleware. Collected original label data from the reader and writer's is huge, while the tag is read several times per second, changes in environmental parameters is relatively small in the mining environment, that is said, really meaningful data to the user is very little, if we do not filter the redundant data, it will burden network bandwidth, processor and data storage. Therefore, filtering the redundant data collected of RFID is the primary task of RFID middleware.

Business rules filter module is mainly used to package further on RFID data after filtering by the upper application in the specific business requirements of the rules, to make it to be event data with specific meaning for the upper applications.

Reader and writer configuration, management and monitoring module is mainly used for selecting data transmission mode (serial port communications and network communications), the configuration parameters, to establish a connection with the reader and writer, and give instructions for the reader and writer.

Application program interface module is to provide data middleware processed to the upper.

3 Design of RFID Middleware Data Filtering Methods

3.1 Current Methods of Processing RFID Tag Redundancy Data and Problems Analysis

The RFID tags' original data collected from the read-write device is a huge amount. Such as that a medium-sized mining area can meet 64 substations, each of which can connect eight read-write devices, and each device reads tags with six kinds of parameters. Supposing that the time to communicating between read-write device and tag is 50 ms, and each data includes: Tag ID, read data, read time, etc. Its size is about 20 bytes. Then, according to the calculation, the amount of data is about 16G for one day. Tag is read for several times per second, but in the coal mine environment, the environment parameters within 1 s basically won't change, so that only a small part of the collected data are meaningful to the user. If we do not process these redundant data and directly transmit them to the upper application, we will bring great storage burden for the RFID system, and this is also a great challenge to the speed of the processor.

Current methods of processing redundant data are as the follows:

- Create a table to store RFID data in the database, and filter data through adding, deleting, searching, updating data. This method is easy to realize. But when dealing with large-scale RFID data, it will involve a large number of disks' I/O, which is inefficient and with no using value.
- We can open a large memory buffer from the middleware system, storing temporary RFID data to be redundant filtering; This memory operations compared to the disk I/O on the processing efficiency is greatly improved, but middleware requires real-time to process a large number of RFID data, and so it has a lower filtering lookup time and resource consumption of the memory to be low.
- The filter algorithm based on the linear form [5], put all label data read some time into linear form, when reading to the new label, it will traverse the entire linear form by the label keyword, and then comparing the new label with the linear form tags in each, if it finds the corresponding linear form tag, descripted that data of tag is repeat,, the new label information replaces the linear table tag information; otherwise, then there is a new label data, the label insert linear table; implementation of linear table lookup method is very simple, but the performance is very bad, average time complexity in linear table to find a keyword's is O (n), the total average complexity to solve the problem of internal filtering conducted search, insert, and delete is O (n^2).
- Filtering algorithm based on a hash table [6], the algorithm transforms the label redundant data filtering problem into searching tab first appear and leave events. Although the time complexity of the hash table lookup algorithm in the ideal state is O (1), its tag information is only tag ID collected, rather than to contain tag ID, read data, the reading time information of complex data structures, the

algorithms greatly reduce the efficiency of memory use. But also for the data read continuously within the reader and writer (non-label first appeared, and leave the event), the filter effect is not obvious.

The methods processed the redundant data that existed insurmountable defects to some extent, so it is needed to seek a more rapid, convenient, less memory processing method.

3.2 Hash Table and Linked List with the Combination of RFID Data Filtering Methods

The design of this part mainly improves a method that can realize filter redundant data, which combines a hash table and the linked list, and this method creates the hash table in memory, and do hash computing by using a hash function for RFID tag ID, and finds the corresponding address information of the list quickly, to compare the data stored determine whether it is redundant data, if it is, handles it. This method can overcome the defects of the previous processing of the data, the fast speed of data processing, high real-time data, small memory, and so on. It is a more reliable and practical method of redundant data processing.

As shown in Fig. 2 is a hash table and linked list with the combination of RFID data filtering flow chart.

The original RFID tag data which is collected from the reader containing tag ID, read data, the read time and other information, the received data is transferred to the filtering algorithm through the queue, the queue is a FIFO data transmission which can be guaranteed its' real-time.

The original RFID tag data which is read from the queue, then do hash calculations according to the key words of tag ID, and deal with conflicts by using Chain address method, calculate the address corresponding to the ID tag, and look up hash table address to see if there is tag information, if there is no tag information, then stored this address in the hash table and the tag data and time information which are corresponding to the address in the list.

If there is tag information, then find out the existing information, and be compared to see if the set range (such as temperature difference range of 0.5 °C, in this range is considered to be redundant data), if in this range, replace the stored data, and updated. Otherwise it is not redundant data, save this data and time in the list; such an event in a period T, the read data is processed, after the time period T the stored data in the list is transported to the background, and empty free memory list for the next event period T to prepare redundant processing the data in order to achieve the filter effect.

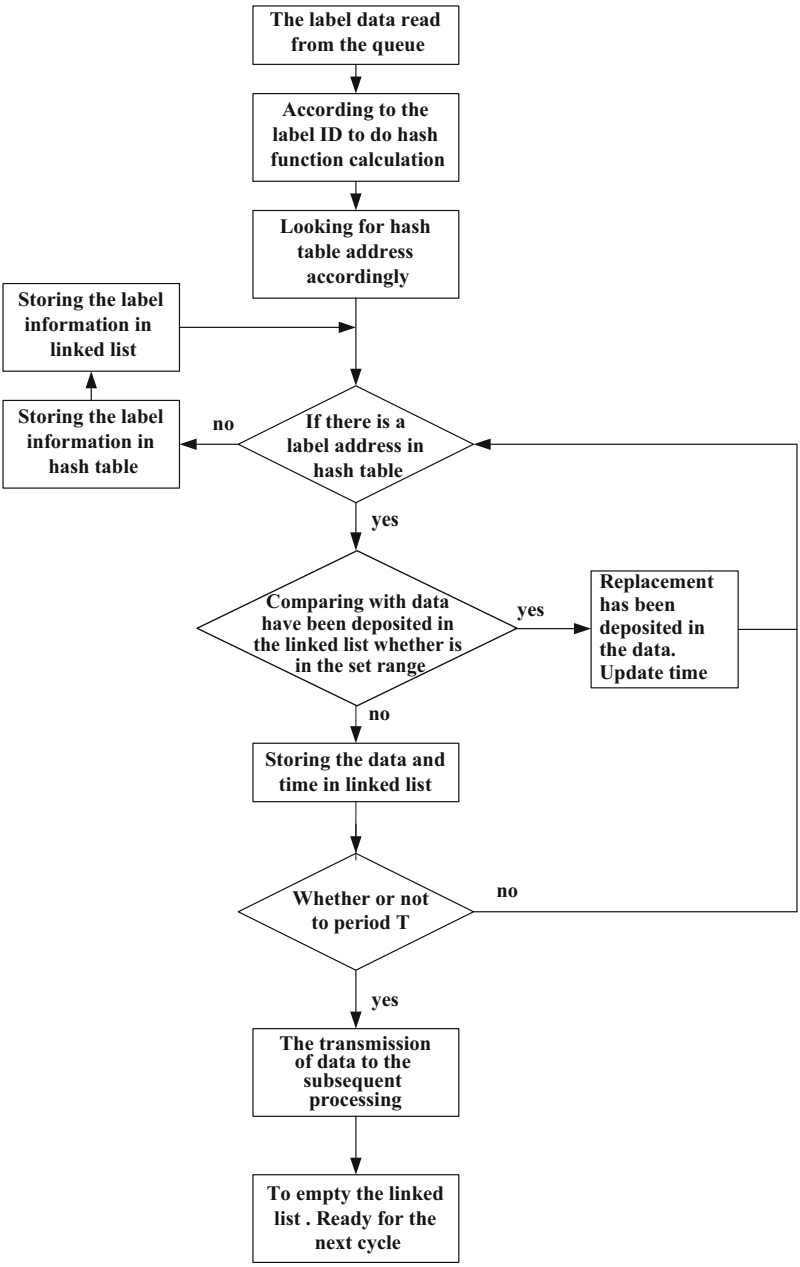

Fig. 2 Hash table and linked list with the combination of RFID data filtering flow chart

Table 1 Hash table information

Content of hash table	The meaning of each element
Elem	Data storage base element
Count	The current number of data elements
Sizeindex	Hashsize[sizeindex] current capacity

4 Algorithm Implementation and Verification

4.1 Algorithm Implementation

According to the algorithm design ideas, this article is to verify its validity. Rs485 is used in the experiments, the temperature label is collected. The period is 5 s. C++ language is used in algorithm. It receives data via serial communication.

First, creating a hash table, it contains the information as follow table 1.

Second, creating a linked list, it contains the information as follow table 2.

The data filtering processing function as follow:

```
void dataFilter()
{
  HashTable h;
  InitHashTable(h);
  if(Receive the hardware data transmission to the
middleware)
    if(Find(h,k,p)==1)
    {
      if(Label data within the set range)
        updata data and ReadTime
      else
        InsertHash(h,e);
    }
    else
    {
      InsertHash(h,e);
    }
}
```

4.2 Experimental Verification

As shown in Fig. 3 is the interface display.

Diagram on the left is the raw data which is introduced from the hardware to the middleware; the right is the data which is filtered by the RFID middleware.

By contrast can see that achieves the effect of filter redundant data.

Table 2 Linked list information

Content of linked list	The meaning of each element
Key	Key-value
Data	Data from the tag
ReadTime	Read time
pNext	Next element
Deviceid	Device identification number

Fig. 3 The received warning message

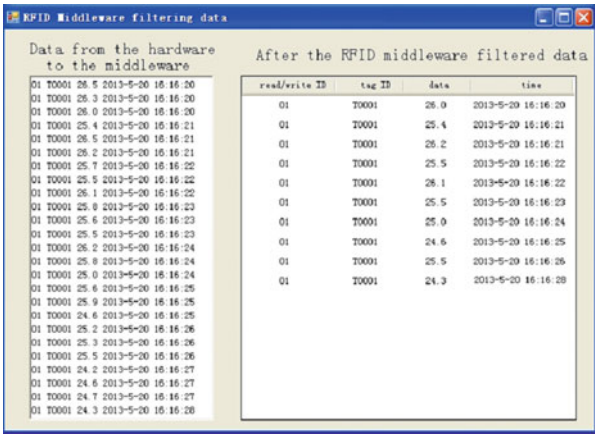

5 Conclusion

This paper analyses the RFID middleware application in coal mine safety and research the existed filtering algorithm. It improves the design of a method combining the hash table and linked list which implements the redundant data filtering. Then it uses C++ language to implement and the experiment to test and verify. The results show that the algorithm has the effect of the removal of redundant data. It has a certain practical value for RFID middleware design and development.

Acknowledgments This work was supported by the Chongqing Municipal science and technology key research projects, China (No. cstc2012gg-yyjsB40003); Also was supported by the Project of State Key Laboratory of Advanced Optical Communication Systems and Networks, Shanghai Jiao Tong University (2011GZKF031114); Also was Supported by Natural Science Foundation Project of CQ (cstc2011jjA40043).

References

1. Zhongjing Xu (2011) Coal mine safety management problems and counter measures research. The union expo: Theoretical research 10:308
2. Li Zhang (2009) Study on RFID-based tracking and locating system underground mine. Dalian university of technology, pp 1–2

3. Sharyn Leaver (2004) Evaluting RFID Middleware. Forrester Research 13:1–2
4. Auto-ID Center. Auto-ID savant specification, p 4
5. Xiaokai X (2001) Data structure and practical tutorial. Tsinghua university press, Beijing
6. Yang D (2006) Design and implementation of RFID reader based filter technology. Shanghai jiao tong university, Shanghai

The Design of the RF Front-End of Reader Based on SAW RFID

Fuhai Wu, Jun Huang, Cheng Ma, Yujun Leng, Jing Yang, and Shilin Xiao

Abstract This paper first describes the system architecture and operating principle of SAW Radio Frequency Identification Devices (RFID). Then it provides the designing scheme to the radio frequency front end of 915 MHz ultra high frequency (UHF) reader. At last, it lists the test method to the RF front end system, and system-level verification of RFID reader. The results show that, this design meets the performance index of 915 MHz reader, and has properties of reliability, efficiency and flexibility in configuration and maintenance.

Keywords SAW • RFID • System-level • Ultra high Frequency • Reader • Test

1 Introduction

Radio Frequency Identification Devices (RFID) [1] was used from the 1980s, and its theory has been enriched constantly. Technologies as well as products applying single chip electronic tag identification, multi-chips electronic tag identification, passive electronic tag identification, radio frequency identification adapting to the high speed moving and remote objects have become reality and been widely used in logistics, transportation, finance, medical treatment, power system, military, etc. In the beginning, this paper gives out the designing scheme of the entire RFID system.

F. Wu (✉) • J. Huang • Y. Leng • J. Yang
Chongqing Key Laboratory of Signal and Information Processing, Chongqing University of Posts and Telecommunications, Chongqing 400065, People's Republic of China
e-mail: fuhai_1314@163.com

C. Ma
Chongqing MAS Science & Technology Co., LTD, Chongqing 400065, People's Republic of China

S. Xiao
State Key Laboratory of Advanced Optical Communication Systems and Networks, Shanghai Jiao Tong University, Shanghai 200240, China

B. Zhang et al. (eds.), *The Proceedings of the Second International Conference on Communications, Signal Processing, and Systems*, Lecture Notes in Electrical Engineering 246, DOI 10.1007/978-3-319-00536-2_100,

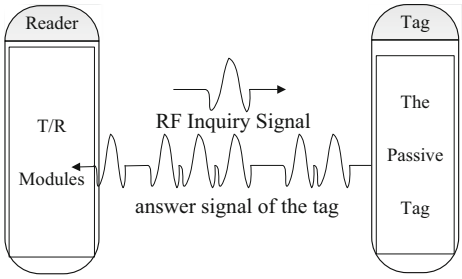

Fig. 1 The structure of RFID

And then, it accomplishes the performance test of this system, combining with the test scheme.

2 RFID Architecture and Operating Principle

Radio Frequency Identification Devices (RFID) system is composed of three parts: card reader, RF antenna and electronic tag, as shown in Fig. 1.

Electronic tag is also called radio frequency card or non-contact IC card. It consists of a small label chip (control circuit and memory) and antenna, and is inserted in the identified object when using in order to store data information of the tested object. According to the different ways of power supply, it is divided into two kinds: passive and active. In order to reduce the cost of the electronic tag and use easily, this paper use passive electronic tag (also called passive tag). Operating principle of RFID system: Card reader sends radio frequency request signal through the antenna. After receiving the signal, tag antenna absorbs part of the energy of the electromagnetic wave to active the tag. Then the tag modulates the information such as its own serial number to the RF signal using the backscattering modulation mode, and sends it out through the tag antenna. The reader receives the RF signal sent from the tag, and sends it to the background main system after demodulating and decoding for relevant processing.

3 Design Scheme of RFID Reader

The hardware design [2] of the reader is a key part of RFID system design, because the signal received is weak, which need to take more sensitive receiver technology and high speed A/D data acquisition, and it should be processed and recognized by digital signal processing (DSP). This article constructs a data acquisition system with TMS320VC5509A of TI company as the core, and designs passive RFID reader which operates in 915 MHz frequency channel and its working distance can extend up to 10 m.

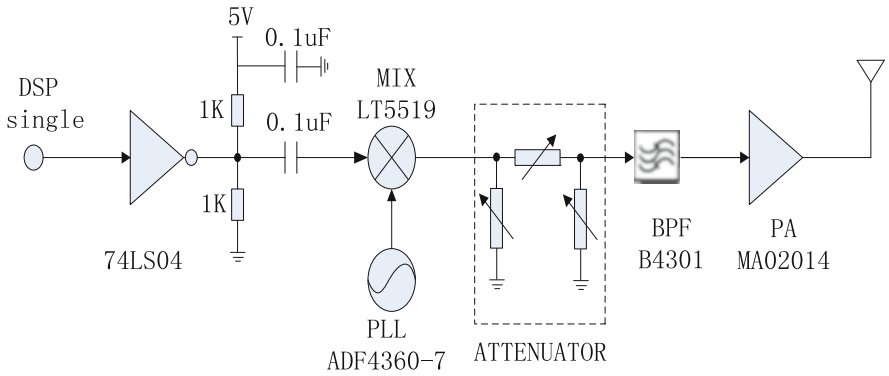

Fig. 2 The structure of transmitter

3.1 Design of the Transmitting Circuit

The transmitting circuit designed [3] is shown in Fig. 2. The mixer adopts up-conversion mixer LT5519, and the bandwidth of the RF output frequency is 0.7–1.4 GHz and the bandwidth of the IF input frequency is 1–400 MHz. The vibration uses ADF4360-7 frequency synthesizer, and its output frequency is 350–1,800 MHz. The attenuator is composed of three sliding rheostat, R1 = 17.6 Ω, R2 = R3 = 292.4 Ω, and its attenuation is 3 dB. The bandpass filter adopts surface acoustic wave filter B4301, and its center frequency is 915 MHz, bandwidth 26 MHz, insertion loss 2.9 dB. The power amplifier adopts MA02014, its output power is 30.8 dBm, and power gain is 30.8 dB.

3.2 Select Fitting Function

The receiver of the system [4] is designed by zero intermediate frequency structure. The zero intermediate frequency receiver is more flexible than super heterodyne transceiver in application, because there is no impact by intermediate frequency bandpass filter. The front end of the design structure figure consists of bandpass filter and low noise amplifier, and the radio frequency output power of the bandpass filter at room temperature can reach 12.6 W. The insertion loss is low as 1.2 dB, and the loss range is ±0.25 dB, so the performance is very good. The low noise amplifier has the advantages of low noise, high gain, wide dynamic range and so on, and the gain of the 900 MHz band can reach 17 dB, what's more the low noise is no more than 1.0 dB. The design is shown in Fig. 3.

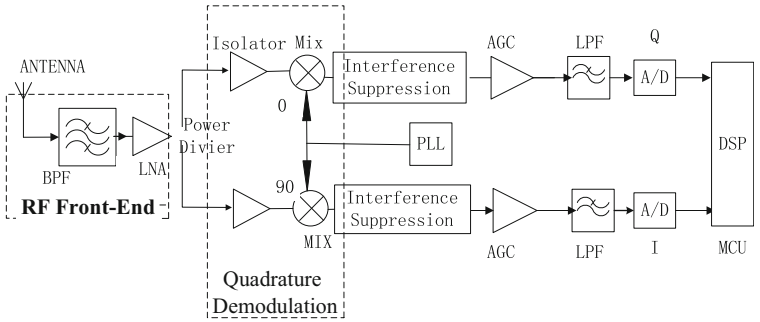

Fig. 3 The structure of receiver

3.3 The Design of Phase Locked Loop (PLL)

The PLL chip is ADF4360-7 [5] of ADI company, the design of phase-locked loop take use of the ADIsimPLL simulation software, in the software set the reference input frequency, the phase frequency, output frequency, VCO control sensitivity, the loop bandwidth, phase margin, lock indicator way and the type of loop filter. Figure 4 shows the design schematics of PLL.

4 RF Front-End Test of RFID

4.1 System Testing Platform of RFID

RFID system test platform mainly complete the detection of 915 MHz RF signal, including the carrier frequency tolerance, the transmit power, the channel bandwidth [6].

Indicators are specifically defined as follows:

1. The carrier frequency tolerance: The difference value of measuring carrier frequency and the corresponding nominal frequency, and then compared with the nominal frequency value, the formula is: |F-Fc|/Fc;
2. The transmit power: The average power of the transmitter;
3. The channel bandwidth and the channel bandwidth: Set the center frequency of the specified channel as the test center, record the corresponding bandwidth of up to 99 % of the energy in the transmission power.

In the article, in order to test above indicators, firstly build the system platform, a PC is equipped with read and write control program, connected with Agilent E4407B via GPIB, the interface of PC-side is USB and the interface of spectrum analyzer is GPIB interface. As Fig. 5 shows:

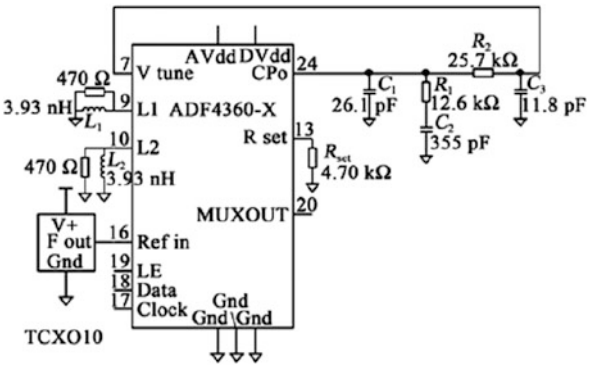

Fig. 4 The design schematic of PLL

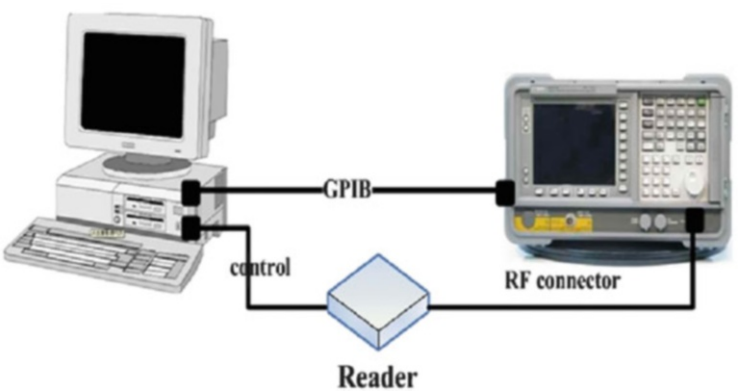

Fig. 5 System test platform

4.2 Test and Verify

4.2.1 Carrier Frequency Capacity

Carrier frequency capacity test preparation, test process and test results are as follows:

Test equipment: Spectrum analyzer, Radio frequency (RF) cable and the launch module.

Test indicators: $\leq 20 \times 10^{-6}$.

Test process: Refer to the left of Fig. 6.

Test result: Refer to the right of Fig. 6. The result is 914.987 MHz, using the carrier frequency capacity calculation formula |F-Fc|/Fc, the test result is |914.987-915|/915 = 14.2×10^{-6}, it's less than the performance indicators so it can meet the requirements.

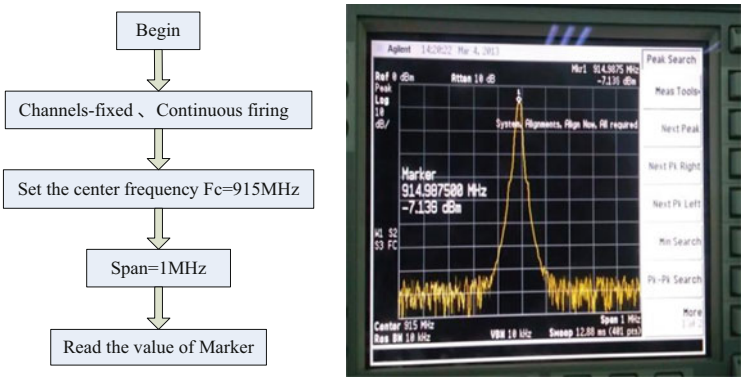

Fig. 6 Carrier frequency capacity test

4.2.2 Transmission Power Test (E.R.P)

Transmission power [7] test preparation, test process and test results are as follows:

Test equipment: Spectrum analyzer, Radio frequency (RF) cable and the launch module.
Test indicators: 2 W/33dBm.
Test process: Refer to the left of Fig. 7.

After open the spectrum analyzer, the order of the buttons is Measure——Channel Power——Mea Setup——INTEG BW.

Test result: Refer to the right of Fig. 7. The launch power is 11.46 dBm, it's less than the given index.

4.2.3 Channel Bandwidth and Channel Occupied Bandwidth

Test preparation, test process and test results of channel bandwidth and the channel bandwidth are as follows:

Test Equipment: Spectrum analyzer, RF cables, Launch module.
Measurements for testing: $\leq$250 KHZ.
Testing process: With reference to the left of Fig. 8.

After opening the Spectrum analyzer, the order of pressing the buttons is: Span——Measure——OBW——Mea Setup——Power Ratio.

Test result: With reference to the right of Fig. 8, the test result is 83.6341 KHz, it is less than the given indicator.

Fig. 7 Transmission power test

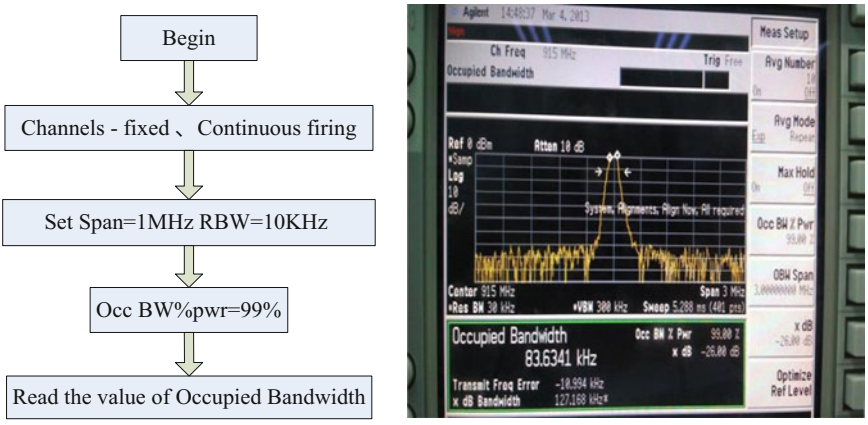

Fig. 8 Channel occupied bandwidth test

5 Conclusion

This paper describes the working principle of the RFID from the RFID architecture and gives a brief description of the design of the RF front-end of the RFID reader. Especially the paper gives the performance test of RF front-end include: the tolerance of carrier frequency, transmission power, channel bandwidth and channel occupied bandwidth. Papers proved that the reliable performance of each circuit module and the ideas feasibility of hardware designed through the analysis of experimental data and test results.

Acknowledgments This work was supported by the Chongqing Municipal science and technology key research projects, China (No. cstc2012gg-yyjsB40003); Also was supported by the Project of State Key Laboratory of Advanced Optical Communication Systems and Networks, Shanghai

Jiao Tong University (2011GZKF031114); Also was supported by Natural Science Foundation Project of CQ (cstc2011jjA40043).

References

1. Nath B, Reynolds F, Want R (2006) RFID technology and applications. IEEE Trans 5(1):22–24
2. Byeong-Seob You, Sook-Kyung Cho, Hae-Young Bae (2007). A novel architecture for cargos location and safety in networked RFID. Journal of Chongqing University of Post and Telecommunications (Natural Science Editing) 19(3):386–391.
3. Curty JP, Declercq M, Dehollain C et al (2007) Design and optimization of passive UHF RFID systems. Springer, New York, USA, pp 37–39
4. Philip Karantzalis (2005) Baseband Circuits for an RFID Receiver-Design Note 381. http://www.linear.com, pp 1–2
5. Analog Devices (2009) ADF4360-7 datesheet. http://www.analog.com, pp 2–24
6. Zheng Zhu (2004) RFID analog front end design tutorial. Auto-ID lab at University of Adelaide, pp 3–34
7. Floerkemeier C, Roduner C, Lampe M (2007) RFID application development with the Accada middleware platform. IEEE Syst J 1(2):82–94

Part VIII
Localization and Target Detection

A Scattering Model Based on GTD in Terahertz Band

Yang Yu, Jin Li, and Rui Min

Abstract Scattering center is the basic electromagnetic scattering characteristic of targets in optical region. In this paper, the parametric scattering center model is analyzed for application to THz band. Then a reduced scattering center model is derived. This model is simpler than parametric scattering model and suitable to the scattering mechanisms in THz band. On this basis, experimental results are analyzed and the validity of the scattering center model in THz band is verified.

Keywords Synthetic aperture radar (SAR) • Terahertz • Scattering center model

1 Introduction

At sufficiently high frequencies, the scattering response of an object can be well approximated as a sum of responses from individual scatters, or scattering centers [1]. These scatters provide a physically relevant, yet concise description of the object and are thus good candidates for use in both automatic target recognition and high resolution analysis of scattering data. In this paper, we consider the analysis of response from the target in THz band. We use a scattering model based on the geometrical theory of diffraction (GTD) to estimate not only the range to radar and amplitude of each scattering centers, but also the shape characteristic of scattering centers [2, 3].

There are three main scattering models to describe the return signal of the target: undamped exponential model [4], prony model [5] and the parametric scattering center model [6–8]. The undamped exponential model considers the amplitude of scattering center is independent of the frequency and of the aspect angle. The undamped exponential model is the simplest model, but if the relative bandwidth

Y. Yu (✉) • J. Li • R. Min
School of Electronic Engineering, University of Electronic Science and Technology of China, Chengdu, China
e-mail: carlyy.yuyang@gmail.com

B. Zhang et al. (eds.), *The Proceedings of the Second International Conference on Communications, Signal Processing, and Systems*, Lecture Notes in Electrical Engineering 246, DOI 10.1007/978-3-319-00536-2_101,

and accumulated angle is large, some scatterers amplitude dependence on frequency and aspect cannot be neglected. Then the model cannot predict the scattering response of complex target. Compared with the undamped exponential model, the prony model can describe not only the scattering response by simple point, but also the scattering amplitude dependence on frequency and aspect angle. However, this model cannot describe the diffraction of some non-point scattering centers such as edge diffraction, corner diffraction and singly curved surface reflection et al. The parametric scattering model is a model based on GTD and physical optics (PO). This model is the most complex and perfect model. It reveals the high frequency scattering mechanism by describe the amplitude dependence on frequency and aspect angle.

This paper analyzes the parametric scattering model in THz regime. The remainder of the paper is organized as follows. In Section II we introduce the parametric scattering model of far-field scattering as a function frequency and aspect angle. In Section III we analyze the parametric scattering model in THz band and verify the model with experimental results.

2 Parametric Scattering Center Model

From the geometrical theory of diffraction, when the wavelength of the incident excitation is small relative to the object extent, the backscattered field appears to originate from a set of discrete scattering centers and can be approximated by

$$\vec{E}^{s}(f,\theta,t) \approx \frac{\vec{E}_0 e^{j2\pi ft}}{ct} \sum_{m=1}^{M} A_m(f,\theta)\exp\{-j2\pi f t_m\} \tag{1}$$

where f is frequency, c is the propagation velocity, θ is the target aspect angle, and $t_m = \frac{2}{c}\vec{r}_m\hat{z} = \frac{2}{c}(x_m\cos\theta + y_m\sin\theta)$ is the round-trip propagation delay of the mth scattering center, $\vec{r}_m = (x_m, y_m)$ is the vector from the target center to the scattering center, $\hat{z} = (\cos\theta, \sin\theta)$ is the unit vector along the propagation.

The amplitude $A_m(f,\theta)$ is a frequency and angle dependent coefficient determined by geometry, composition, and orientation of the scattering mechanism. The corresponding normalized field for a given polarization (suppressing the $e^{j2\pi ft}$ time convention)

$$E(f,\theta) = \sum_{m=1}^{M} A_m(f,\theta)\exp\left\{\frac{-j4\pi f}{c}(x_m\cos\theta + y_m\sin\theta)\right\} \tag{2}$$

The GTD predicts that scattering amplitude follows a $(jf/f_c)^{\alpha}$ dependence, where α is an integer multiple of 0.5, f is the carrier frequency. Table 1 summarizes the α parameters.

Table 1 Type parameters for canonical scattering mechanisms

Value of α	Example scattering geometries
1	Flat plate at broadside; dihedral
0.5	Singly curved surface reflection
0	Point scattering center; doubly curved surface reflection; straight edge specular
−0.5	Curved edge diffraction
−1	Corner diffraction

Then the amplitude $A_m(f,\theta)$ in (2) can be presented as

$$A_m(f,\theta) = A'_m(f,\theta)\left(j\frac{f}{f_c}\right)^{\alpha} \tag{3}$$

Then we consider the amplitude dependence on aspect angle. As aspect angle is varied, the parametric model assumes that a scattering center behaves in one of two ways: either a scattering center is localized and appears to exist at a single point in space, or it is distributed in the imaging plane and appears as a finite, nonzeros-length current distribution. The amplitude dependence on aspect angle is different for each of these scenarios.

Examples of localized scattering mechanisms are trihedral reflection, corner diffraction, and edge diffraction. All of these mechanisms have slowly varying amplitude as a function of aspect angle. Then the $A'_m(f,\theta)$ can be presented as a slowly varying function with a damped exponential

$$A'_m(f,\theta) = A''_m \exp(-2\pi f \gamma_m \sin\theta) \tag{4}$$

The exponential function provides a mathematically convenient approximation containing only a single parameter. Although physical insight is used to arrive at the exponential model, the parameter γ_m has no direct physical interpretation.

On the other hand, examples of distributed scattering mechanisms are flat-plate reflection, dihedral reflection and cylinder reflection. Each of these scattering mechanisms has an amplitude dependence on aspect angle that contains a sinc $(x) = \sin(x)/x$ function. In all cases, this sinc(x) function is the dominant term in the physical optics far-zone scattering solution and the parametric model adopt the sinc (x) function to characterize angle dependence in the scattering model for scattering centers that are distributed

$$A'_m(f,\theta) = A''_m \mathrm{sinc}\left(\frac{2\pi f}{c} L_m \sin\left(\theta - \overline{\theta}_m\right)\right) \tag{5}$$

Where L_m is the length and $\overline{\theta}_m$ is the orientation angle of the distributed scatter.

Then the parametric scattering center model can be presented by combining (2)–(5)

$$E_m(f,\theta) = A_m\left(j\frac{f}{f_c}\right)^{\alpha_m} \operatorname{sinc}\left(\frac{2\pi f}{c}L_m \sin\left(\theta - \overline{\theta}_m\right)\right)\exp\left(-2\pi f\gamma_m \sin\theta\right) \times\exp\left(j\frac{4\pi f}{c}\left(x_m\cos\theta + y_m\sin\theta\right)\right) \tag{6}$$

where $L_m = 0$ if the scattering center is localized, and $\gamma_m = 0$ if the scattering center is distributed. The parameter A_m is a relative amplitude for each scattering center. The total scattered field is a sum of M individual scattering terms

$$E(f,\theta) = \sum_{m=1}^{M} E_m(f,\theta) \tag{7}$$

3 Scattering Model in THz Band

3.1 The Scattering Model

In this section, we analyze the parametric scattering model in THz band. First, we consider the exponential part $\exp(-2\pi f\gamma_m \sin\theta)$. When $L_m = 0$ and $\gamma_m \neq 0$, this function denotes the amplitude dependence on aspect angle and frequency of localized scattering centers. In the THz band, the frequency f range from 0.1 to 10 THz, then we can assume that the exponential part $\exp(-2\pi f\gamma_m \sin\theta) \approx 0$. This means that in THz band, the localized scattering mechanisms can be neglected.

On the other hand, in the sufficiently high frequency, the scattering mechanism of localized scattering centers is determined by its finite neighborhood. Then the localized scattering centers, which are electrically large in THz band, can be replaced by a set of distributed scattering centers.

Second, we consider the sinc function part. We assume that L_m, θ and $\overline{\theta}_m$ is fixed, then the relationship between frequency and sinc function is shown in Fig. 1.

From Fig. 1 we could see that the sinc function varies violently in the low frequency and approximate to 0 when the frequency is larger than 5 THz. This is also consistent with the electromagnetic theory. In the high frequency, the scattering amplitude is independence with aspect angle, scattering model becomes Geometrical Optics (GO) model. In the low THz band, the aspect angle dependence cannot be neglected.

Third, we consider the $(jf/f_c)^{\alpha}$, this part of parametric model denotes the amplitude dependence on fractional bandwidth. For the ultra-wideband systems, fractional bandwidth is $B/f_c \geq 0.25$. For $B/f_c = 0.25$, the ratio of frequency f and center frequency f_c is $0.875 \leq f/f_c \leq 1.125$. For different α value, the amplitude dependence is shown in Fig. 2.

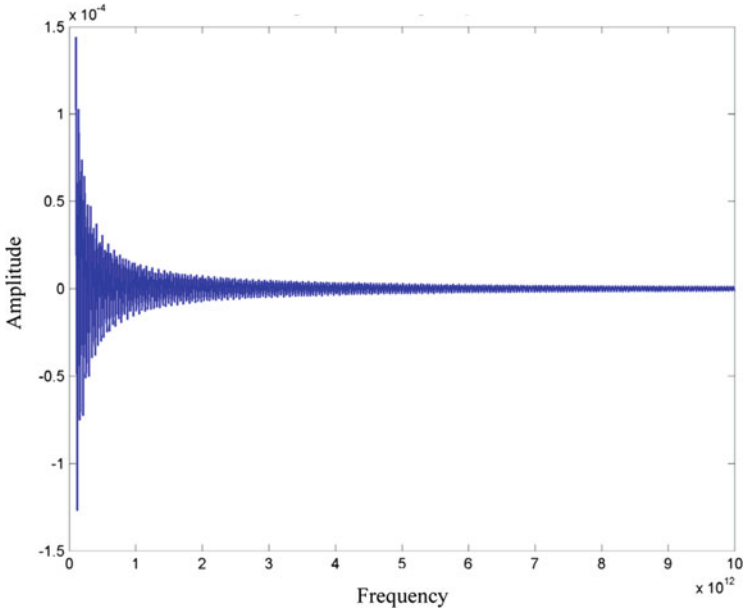

Fig. 1 The relationship between frequency and sinc function part

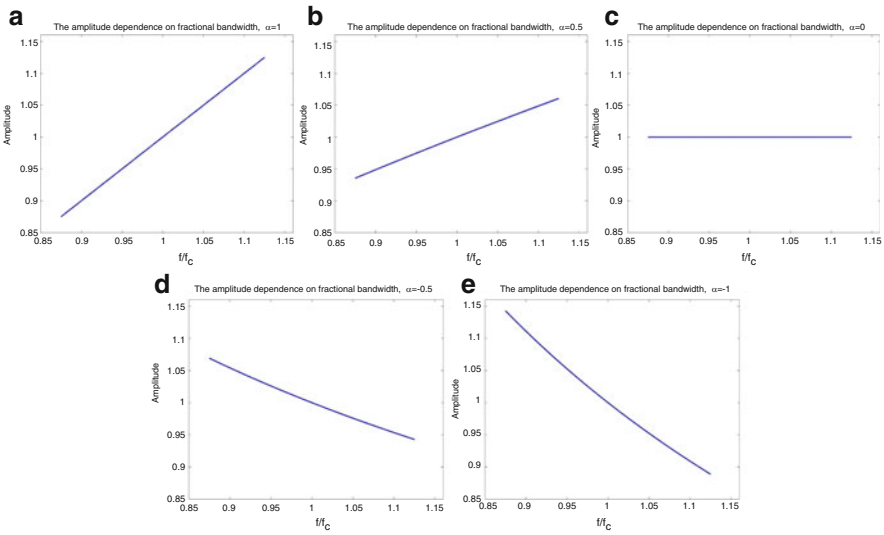

Fig. 2 The amplitude dependence on $(jf/f_c)^{\alpha}$ when $B/f_c = 0.25$. (**a**) $\alpha = 1$; (**b**) $\alpha = 0.5$; (**c**) $\alpha = 0$; (**d**) $\alpha = -0.5$; (**e**) $\alpha = -1$

When $\alpha \neq 0$, for the ultra-wideband systems, the amplitude dependence on fractional bandwidth cannot be neglected; when $\alpha = 0$, we have $(jf/f_c)^{\alpha} = 1$, then the amplitude only related to the aspect angle dependence function.

If the fractional bandwidth is less than 0.25, the amplitude change induced by fractional bandwidth is even small. For example: if $f_c = 0.2$ THz, $B = 5$ GHz, the downrange resolution is $c/2B = 3cm$, the fractional bandwidth is only 0.025. The amplitude dependence on function $(jf/f_c)^{\alpha}$ is so little that can be neglected.

Then we can get the scattering model in THz band as below

$$E_m(f,\theta) = A_m\left(j\frac{f}{f_c}\right)^{\alpha_m}\operatorname{sinc}\left(\frac{2\pi f}{c}L_m\sin\left(\theta-\overline{\theta}_m\right)\right)\exp\left(j\frac{4\pi f}{c}\left(x_m\cos\theta+y_m\sin\theta\right)\right) \tag{8}$$

Especially, in high frequency part of THz band, it becomes

$$E_m(f,\theta) = A_m\left(j\frac{f}{f_c}\right)^{\alpha_m}\exp\left(j\frac{4\pi f}{c}\left(x_m\cos\theta+y_m\sin\theta\right)\right) \tag{9}$$

3.2 Image Domain Model

The model in (14) describes scattering in frequency aspect domain. For most SAR data, imaging is approximately a unitary operator. The image domain segmentation provides several practical advantages for computing estimates of the unknown model parameters. We transform the scattering model from frequency-aspect domain into the image domain.

We use the same processing in reference [8], a single scattering center of parametric scattering model in image-domain $F_m(t_x,t_y)$ is written as (10).

$$\begin{aligned} F_m\left(t_x,t_y\right) = \int_{f_{y1}}^{f_{y2}}\int_{f_{x1}}^{f_{x2}}\Bigg\{ & \sum_{p=1}^{P}\sum_{q=1}^{Q}A_nB_p^xB_q^y\operatorname{sinc}\left[\frac{2\pi L\cos\overline{\theta}_m}{c}\left(f_y-f_x\tan\overline{\theta}_m\right)\right] \\ & \cdot\exp\left[2\pi f_y\left(-\gamma_m+j\left(\frac{2y_m}{c}+\beta_q^y+t_y\right)\right)\right] \\ & \cdot\exp\left[2\pi f_x\left(-r_m+j\left(\frac{2x_m}{c}+\beta_p^x+t_x\right)\right)\right]df_xdf_y\Bigg\} \end{aligned} \tag{10}$$

Compare (8) with (6), the scattering model in THz band is the distributed scattering center model of parametric scattering model. Then the image-domain model remains only the distributed scattering center part of model (10). For the distributed scattering center, the sinc function shows as a line with finite length in the range dimension.

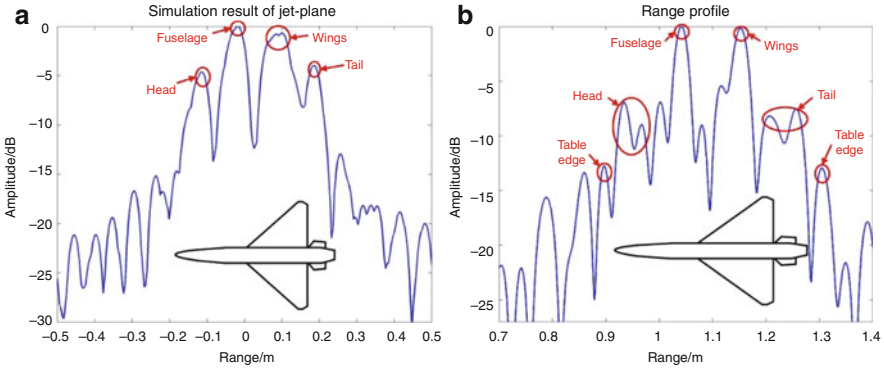

Fig. 3 Range profile of jet-plane. (**a**) simulation result; (**b**) measured data

4 Results

In this section we use the experimental results to verify the validity of scattering model in THz band. First we simulate the backscatter of a jet-plane by model (8). According to the model, the plane could be decomposed to four parts on radar line of sight: the cone shaped head, the cylinder shaped fuselage, the flat-plate shaped wings and the short-cylinder shaped tail. Then the backscatter simulation result is shown in Fig. 3a.

To verify the validity of the model, we consider the measured data of the jet-plane model on metal table. The center frequency is 220 GHz, bandwidth is 4.9 GHz. Figure 3b shows the range profile of the measured data.

From Fig. 3a, b we can see that the model predicts the scattering data perfectly. The strongest echo power comes from the fuselage and wings, head and tail take the second place, the power from table edge is the weakest. In THz scattering center model, the backscatter from plane fuselage is considered as cylinder reflection, and the backscatter from wings is considered as flat-plate reflection. They both are modeled as the longest length distributed scattering centers of plane. The length of head and tail is shorter, so that the amplitude is lower than the fuselage and wings. In range profile, the head and tail show two peaks. This is caused by the side lobe of fuselage and wings. The table edge is replaced by plenty of short length distributed scattering centers, so that its echo power becomes the weakest in the range profile.

5 Conclusion

We analyzed the scattering mechanisms and parametric scattering model in THz band. Then we presented its reduced form. This reduced model suppressed the backscattering power from the localized scattering center, describes the scattering mechanisms in THz band as distributed scattering centers. It is simpler than the

parametric scattering model and describes the scattering mechanisms perfectly. At last, model was validated using measured scattering data in THz band, which establishes the foundation for the next research of feature extracting and high resolution SAR imagery interpretation methods in THz band.

Acknowledgements This work is supported by the National Natural Science Foundation of China (Grant No. 61271287).

References

1. Borden B (2002) Mathematical problems in radar inverse scattering. Inverse Problems 18: R1–R28
2. Keller JB (1962) Geometrical theory of diffraction. J Opt Soc Am 52:116–130
3. Kouyoumjian RG, Pathak PH (1974) A uniform geometrical theory of diffraction for an edge in a perfectly conducting surface. Proc IEEE 62:1448–1461
4. Wehne DR (1995) High resolution radar, 2nd edn. Artech House, Boston, MA
5. Hurst M, Mittra R (1987) Scattering center analysis via Prony's method. Antenn Propag IEEE Trans 35:986–988
6. Potter LC, Da-Ming C, Carriere R, Gerry MJ (1995) A GTD-based parametric model for radar scattering. Antenn Propag IEEE Trans 43:1058–1067
7. Akyildiz Y, Moses RL (1999) Scattering center model for SAR imagery. In: Proceedings of the 1999 SAR image analysis, modelling, and techniques II, 22 Sept 1999, Florence, Italy, pp 76–85
8. Gerry MJ, Potter LC, Gupta IJ, Van Der Merwe A (1999) A parametric model for synthetic aperture radar measurements. Antenn Propag IEEE Trans 47:1179–1188

Through Wall Human Detection Using Compressed UWB Radar Data

Wei Wang, Baoju Zhang, and Jiasong Mu

Abstract The technology for through wall human detection with UWB radar was discussed. Due to the large amount of UWB radar data, compressive sensing theory was introduced and compressed UWB radar data can be collected. The singular value decomposition algorithm was used to acquire the singular values of compressed radar data. The compressed UWB radar data were collected at still status of human being for Gypsum wall. The experimental results showed that the singular values with human target were increased relative to the status without target.

Keywords Through wall human detection • UWB radar • Compressive sensing • Singular value decomposition

1 Introduction

Through wall human detection is a new developing technology in recent years. It can penetrate non-metallic media (such as brick wall, ruins) to detect life signal in far-off areas but not require any contacting with the living body through electrode or sensors. Through wall human detection is of great interest for many applications, such as: military reconnaissance, anti-terrorism, medical and natural disasters ambulance. And it has a positive significance in economic construction and social stability. Body electrostatic field, ultra-low frequency electromagnetic energy and Ultra-wideband (UWB) radar technologies have been used for through wall human detection currently.

The Ultra-wideband (UWB) radar can launch very short duration pulses to penetrate non-metallic wall and obstacles. Due to its strong anti-interference ability, high resolution performance and good target recognition capabilities, the

W. Wang (✉) • B. Zhang • J. Mu
College of Electronic and Communication Engineering, Tianjin Normal University, Tianjin, China
e-mail: wangweivip@tju.edu.cn

B. Zhang et al. (eds.), *The Proceedings of the Second International Conference on Communications, Signal Processing, and Systems*, Lecture Notes in Electrical Engineering 246, DOI 10.1007/978-3-319-00536-2_102,

UWB radar has emerged as one of the most optimal choices for through all human detection. In [1], the detection of trapped human beings below rubble by means of M-sequence UWB radar was demonstrated and a detection of buried people in wet rubble became possible by enhancing specific signal features by filtering algorithm. The further study of the above method has been proposed in [2–4]. The process of UWB radar signal has been presented which consisting of the solution of the signal processing tasks such as raw radar data pre-processing, background subtraction, target detection, target trace estimation, target localization and tracking, and the multiple target detection also were investigated. And for through wall moving target tracking by M-sequence UWB radar also was described in [4] as a complex procedure consisted of such phases as raw radar data pre-processing, background subtraction, detection, time of arrival estimation, wall effect compensation, localization and tracking itself. In [5], Ultra-wideband pseudo noise radar was used for detection of moving people and trapped people. The experimental results showed that the performance of antennas and of the radar electronics connected with powerful and clever algorithms were important for successful application of human detection with UWB radar. In [6] and [7], some algorithms for through wall human detection for three types of walls, that is Gypsum wall, Wooden door and Brick wall were discussed.

Although UWB radar technology can obtain good achievement in through wall human detection, UWB radar generate large amounts of data and bring great pressure to data acquisition hardware. On the other hand, the data needed by the human being detection is far less than the actual sampling amount of data that is a lot of collected data is useless. In 2006, Donoho and Candès proposed a new theory called compressive sensing (or compressed sampling, CS) based on signal decomposition and approximation theory [8, 9]. The theory suggested that a high-dimensional signal can be projected into a low-dimensional space with a random measurement matrix when the signal was sparse or compressible. Then the original signal can be reconstructed from the low-dimensional information with solving an optimization problem. That is the low-dimensional signal contained the main features of the original signal.

In this paper we would propose an algorithm for through wall human detection based on the random collected UWB radar data with compressive sensing theory. The remainder of the paper is organized as follows. In the Sect. 2 the compressive sensing theory will be introduced. Then the collecting procedure of UWB radar with compressive sensing will be described and the singular value decomposition (SVD) of compressed UWB radar data will be presented for through wall human detection in Sect. 3. Experimental results for human being detection under Gypsum wall will be showed in Sect. 4. Conclusion and discussion is in Sect. 5.

2 Compressive Sensing Theory

Assuming signal $x \in R^N$, it can be expressed as:

$$x = \sum_{i=1}^{N} \phi_i \theta_i \quad \text{or} \quad x = \Phi\theta \tag{1}$$

Where Φ is $N \times N$ orthonormal transform basis, θ is the expansion coefficients vector in the orthonormal basis. If K elements in vector θ are not zero and K is far less than N, signal x can be called K sparse signal.

Compressive sensing showed that the signal may be acquired with a small set of nonadaptive, linear measurements as long as the signal is sparse in some basis. So, we can capture the signal x via linear measurements:

$$y = \Psi x = \Psi\Phi\theta \tag{2}$$

Where Ψ is a $M \times N$ random measurement matrix and $M < N$. Here, (Φ,Ψ) is a pair of orthobases which followed the incoherence restriction. The coherence between the measurement basis Ψ and the orthonormal transform basis Φ is [10]

$$\mu(\Psi, \Phi) = \sqrt{N} \cdot \max_{1 \le k, j \le N} \left| \langle \psi_k, \phi_j \rangle \right| \tag{3}$$

The coherence measures the largest correlation between any two elements of Ψ and Φ.As for how large and how small, it follows from linear algebra that $\mu(\Psi, \Phi) \in \left[1, \sqrt{N}\right]$. And compressive sensing is mainly concerned with low coherence pairs.

If x is termed as K sparse in the orthonormal basis, we only need to collect $M = O(K \log(N/K))$ random measurements to recover the signal by searching for the l_0-sparsest that agrees with the measurements [11]:

$$\hat{\theta} = \text{argmin} \|\theta\|_0$$

Subject to

$$y = \Psi x = \Psi\Phi\theta \tag{4}$$

where the l_0 pseudo-norm $\| \cdot \|_0$ corresponds to the number of non zero elements. As we know, Equ.4 is a daunting NP-complete combinatorial optimization problem which is hardly solved directly in practice. Compressive sensing theory seeks to solve the "closest possible" tractable minimization problem with solving the l_1-minimization and it leads to a much simpler convex problem.

Compressive sensing theory showed that the signal can be sampled and compressed simultaneously. And the acquired low dimensional signal contained the main features of the signal under the premise of appropriate measurement matrix. Therefore, the CS theory provided an effectively way to overcome the complexity of through wall human detection in large amount of UWB radar data.

3 UWB Radar Data Collected and SVD Processing

The through wall detection of human being is based on the fact that the human body is always in a state of motion even if it sleeps or is trapped because of breathing. These tiny human motions would cause periodic changes of electromagnetic wave which is emitted by UWB radar and return through walls from human body target [6]. Multiple echo signals of UWB radar can reflect this periodic change. Thus, a $P \times N$ matrix E can be constructed using P echoes with length N of each echo.

$$E = \begin{bmatrix} s11 & s21 & \cdots & sP1 \\ s12 & s22 & \cdots & sP2 \\ \vdots & \vdots & \cdots & sP3 \\ s1N & s2N & \cdots & sPN \end{bmatrix} \tag{5}$$

With the random measurement matrix $\Psi \in Z^{N \times M}$, the compressed echo signals can be collected based on compressive sensing theory. Thus, a $P \times M$ matrix D can be obtained.

SVD is an effective signal processing algorithm for extraction of signal characteristics. The SVD of D can be denoted as:

$$D = USV^T \tag{6}$$

Where the columns of U are the eigenvectors of the DD^T matrix and the columns of V are the eigenvectors of the D^TD matrix. S is a diagonal matrix with the definition of the no diagonal elements of diagonal matrices being zero. The diagonal elements of S are a special kind of values of the original matrix. They are termed the singular values of D.

Combined the reconstruction theory of CS and SVD theory, the singular values can not only indicate the signal characteristics of compressed matrix D, but also original matrix E. Therefore, through wall human detection could be achieved by comparing the changes of singular values.

4 Results and Analysis

In this paper, we used the P220 UWB radar as the measurement tool which worked in monostatic mode that waveform pulses were transmitted from a single Omni-directional antenna and the scattered waveforms were received by a collocated Omni-directional antenna. In the experiments, P220 UWB radar was worked in the center frequency of 4.3 GHz with 10-dB bandwidth at 2.3 GHz and a resolution of 6.5 cm.

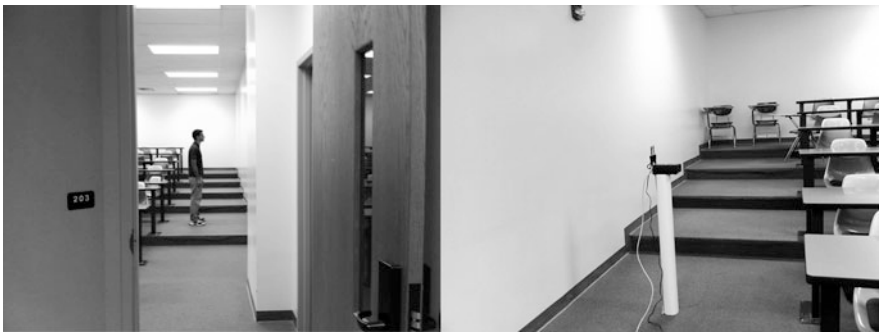

Fig. 1 Location of human target (*left*) and P220 UWB radar (*right*) at Gypsum wall

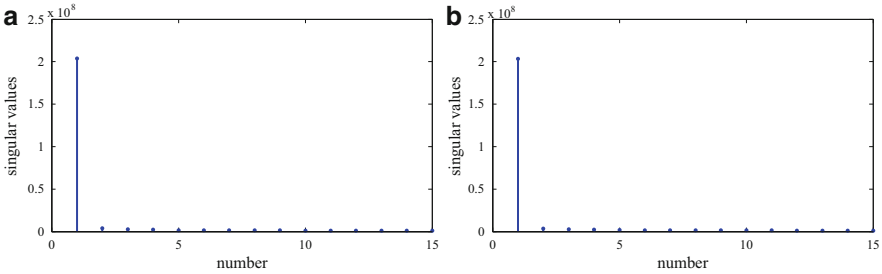

Fig. 2 The singular values of compressed UWB radar data without target

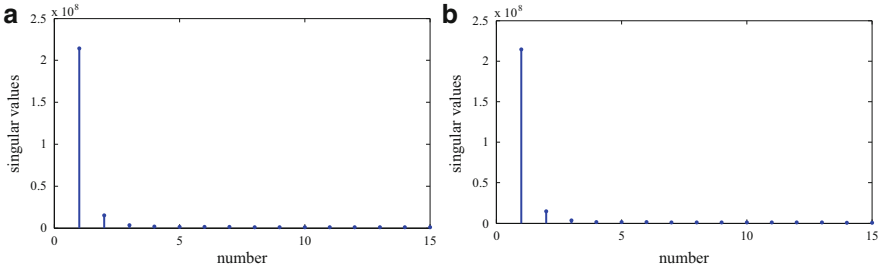

Fig. 3 The singular values of compressed UWB radar data with target

In the project, we have taken measurements of through wall detection for still human being with P220 UWB radar at Gypsum wall. Person was at a distance of 6.5 ft from the radar on the other side of the wall (Fig. 1).

Each 30 measurements were taken with people and without target. Random Gaussian matrix was used as the measurement matrix for compressed UWB radar data acquired. Then SVD of the compressed data was implemented. The results were showed in Figs. 2 and 3.

Figures 2a, b and 3a, b showed the singular values of 15 compressed measurements with human target and without human being where the compressive ratio is

0.5, respectively. From the results, it can be seen that there were minor changes in singular values at the same status of with target or without target. But the singular value was increased at the status of with target especially the second singular value. In other word, the singular values of compressed UWB radar data can be used for through wall human detection in Gypsum wall.

5 Conclusions

UWB radar is one of the most favorable methods for through wall human detection due to its strong penetration ability. Because of the large amount of UWB radar data, the paper proposed the SVD algorithm for compressed UWB radar data to detect through wall human being with compressive sensing theory. The experiments for human detection under the status for Gypsum wall were tested. And the results demonstrated that the singular values could effectively reflect the presence of the human target.

Acknowledgements The authors would love to thank Professor Qilian Liang in University of Texas at Arlington for providing the UWB radar data. This research was supported by the Tianjin Younger Natural Science Foundation (12JCQNJC00400) and National Natural Science Foundation of China(61271411).

References

1. Zaikov E, Sachs J, Aftanas M, Rovnakova J (2008) Detection of trapped people by UWB radar. Micorwave Conf (GeMIC) German 3:1–4
2. Rovnakova J, Svecova M, Kocur D et al (2008) Signal processing for through wall moving target tracking by M-sequence UWB radar. 2008 18th international conference on Radioelektronika 4:1–4
3. Kocur D, Gamec J, Svecova M, Gamcova M, Rovnakova J (2010) Imaging mehtod: an efficient algorithm for moving target tracking by UWB radar. Acta Polytechnica Hungarica 7(3):5–24
4. Kocur D, Rovnakova J, Svecova M (2009) Through wall tracking of moving targets by M-sequence UWB radar. Studies Comput Intell 243:349–364
5. Sachs J, Aftanas M, Crabbe S et al (2008) Detection and tracking of moving or trapped people hidden by obstacles using ultra-wideband pseudo-noise radar. Eur Radar Conf 10:408–411
6. Singh S, Liang Q, Chen D, Sheng L (2011) Sense through wall human detection using UWB radar. EURASIP J Wireless Comm Networking 20
7. Wei Wang, Xin Zhou, Baoju Zhang, Jiasong Mu. Anomaly detection in big data from UWB radars. Security and Comm Networks Accepted. doi:10.1002/sec.745
8. Donoho DL (2006) Compressed sensing. IEEE Trans Inform Theor 52(4):1289–1306
9. Candès E (2006) Compressive sampling. In: Proceedings of international congress of mathematicians, European Mathematical Society Publishing House, Madrid, Spain, pp 1433–1452
10. Candès E, Wakin M (2008) An introduction to compressive sampling. IEEE Signal Process Mag 25:21–30
11. Averbuch A, Shai D, Shay D (2012) Adaptive compressed image sensing using dictionaries. SIAM J Imag Sci 5(1):57–89

Scattering Model Based Hybrid TOA/AOA/AOD Localization in NLOS Environment

Zengshan Tian, Ling Yao, Mu Zhou, Fei Zhou, and Li Zhang

Abstract This paper proposes a new localization algorithm to locate the targets in non-line-of-sight (NLOS) environment by maneuverable single station. The algorithm first estimates scatters' positions in the second layer and the distances from the second-layer scatters to the mobile station (MS) based on the circular motion characteristics. Second, by selecting the second-layer scatters as the virtual base station (BS), we can convert the problem of single station localization into the one with multiple stations. Third, the time difference of arrival (TDOA) algorithm is used to estimate the positions of the first-layer scatters. Finally, we will use the positions of the first-layer scatters and the angle of departure (AOD) to estimate the real positions of MS. The efficiency of our proposed algorithm is verified based on the simulation in a simple two-layer scattering model.

Keywords Wireless localization • NLOS • Single station • Two-layer scattering model • Virtual base station

1 Introduction

The wireless localization for the special targets has caught significant attention in recent decade ranging from the public emergency rescue to the individual intelligent transportation. The practical applications always require high positioning accuracy, but there always exist many disturbing factors which deteriorate the accuracy performance of the cellular network. Among them, the non-line-of-sight (NLOS) and measurement error can be suggested as the significant ones causing serious positioning errors [1].

Z. Tian (✉) • L. Yao • M. Zhou • F. Zhou • L. Zhang
Chongqing Key Lab of Mobile Communications Technology, School of Communication & Information Engineering, Chongqing University of Posts and Telecommunications, Chongqing 400065, China
e-mail: tianzs@cqupt.edu.cn; gigi_101@163.com

B. Zhang et al. (eds.), *The Proceedings of the Second International Conference on Communications, Signal Processing, and Systems*, Lecture Notes in Electrical Engineering 246, DOI 10.1007/978-3-319-00536-2_103,

Based on the number of observation stations, the wireless localization systems can be classified into two categories: single station location (SSL) and multi-station location (MSL) [2] proposes a hybrid time of arrival (TOA) and angle of arrival (AOA) localization algorithm by considering both the Doppler frequency shift and scattering information [3] studies the positioning and tracking method for the mobile target [4] introduces the idea of using the scatter reflective characteristics to realize SSL, but the detailed steps for the scatter positioning is not given [5] applies the map matching methods to estimate the scatters' positions, while the performance of this method significantly depends on the precision of the map construction.

This paper presents a new location algorithm for the MS by using the scattering information in NLOS environment. Section 2 gives the topological structure of the two-time reflection model. In Sect. 3, we use the single station model to measure the positions of the second-layer scatters. Based on the positioning parameters of the multipath signals, the positions of the first-layer scatters and MS can be located. The experimental results are provided in Sect. 4 to verify the feasibility and efficiency of our algorithm.

2 System Model

As depicted in [6], the authors selects the scatters as the virtual BS to locate the target MS. From this idea, this paper will introduce an enhanced model to solve the two-time reflection problem. The topological structure is shown in Fig. 1.

The starting position of single station is located at the coordinate origin (0,0). The angle coordinate of the MS is denoted by (X_{ms},Y_{ms}). The waves from the MS first reflect on the first-layer scatter $M = (M_x,M_y)$, and then arrive at the single station through the second-layer scatters $B = (B_{xi},B_{yi})$. Then, the corresponding TOA model is described in (1).

$$L_i(n) = c \cdot \tau_i(n) = L_i^o(n) + n_{Li}(n) = p_i(n) + r_i + h \tag{1}$$

Where i (i = 1, 2 and 3) represents the i-th scatter, n is the movement time of single station, c is the light speed. $L_i^o(n)$ is the propagation distance of the signal. $n_{Li}(n)$ is the measurement error which obeys the normal distribution $N(0,\delta_L^2)$. $p_i(n)$ is the distance from (B_{xi},B_{yi}) to the signal observer. r_i is the distance from (M_x,M_y) to (B_{xi},B_{yi}). h is the distance from the MS to (M_x,M_y). r_i and h are constant in the conditions of the fixed positions of the MS and (M_x,M_y). At this point, The AOA model of the signals is also defined in (2).

$$\alpha_i(n) = \alpha_i^o(n) + n_{\alpha i}(n) \tag{2}$$

Where $\alpha_i^o(n)$ is the value of AOA, $n_{\alpha i}(n)$ is the measurement error obeying the normal distribution $N(0,\delta_a^2)$. From Fig. 1, both the scatter positions and $p_i(n)$ can be

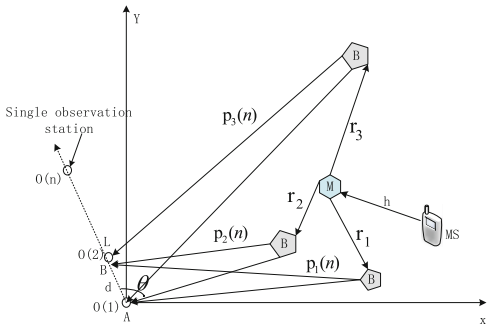

Fig. 1 Two-time reflection signal propagation model for the SSL

effectively estimated. Based on (1), the distance between the MS and (B_{xi},B_{yi}) is calculated below.

$$r_i + h = L_i(n) - p_i(n) \tag{3}$$

Finally, by selecting (B_{xi},B_{yi}) as the virtual BSs to locate (M_x,M_y) with the help of the TDOA and AOD models, the MS can be effectively located. The detailed steps of this localization process will be provided in the following section.

3 Hybrid TOA-AOA-AOD Localization

3.1 Matching Conditions of Doppler Frequency Shift

Because the separation distance by the movement of the single station is small, the frequency of signals can be assumed to be constant. Therefore, if the Doppler frequency shift [7] of two receiving signals is the same, these two signals will be recognized as the ones coming from the reflection of the same second-layer scatter.

As shown in Fig. 1, we assume that the single station moves from positions A to B with the speed v. Because the separation distance of the movement of single station is significantly smaller than the distance between the single station and (B_{xi}, B_{yi}), θ will approximately equal to the angle between the direction of single station and arrival radio wave. Obviously, the angle of the two receiving signals coming from the reflection of the same second layer scatter (θ) is approximately constant. At this point, the path difference of the radio waves coming from A and B can be calculated by $L = d\ \sin(\theta - \pi/2) = -\ v\Delta t\ \sin(\theta)$, where Δt is the movement time. Therefore, the variation of phase of the arrival radio wave is presented in (4). Where λ is the wavelength of the arrival radio wave; f_d is the Doppler frequency shift which can be calculated by

$$\Delta\varphi = \frac{2\pi L}{\lambda} = \frac{-2\pi v \Delta t \sin(\theta)}{\lambda} \tag{4}$$

$$f_d = \frac{1}{2\pi}\frac{\Delta\varphi}{\Delta t} = \frac{-v}{\lambda}\sin(\theta) \tag{5}$$

In (5), v, λ and θ of the radio waves from the same MS are constant because of the reflection from the same second-layer scatter. Therefore, the (5) illustrates that the Doppler frequency shift of two signals from the same MS is a constant. Moreover, the use of AOD model can guarantee that the two receiving signals will come from the same first-layer scatter.

3.2 Circle Fitting Method

This subsection mainly focuses on the localization of the second-layer scatter based on the track information from the single station, AOA and TOA in the condition of the movement of single station. We assume the scatters will be stable when the single station moves in short time duration.

Because the single station moves along one random path, the parameters in TOA and AOA models can be easily obtained from different observation points. After the parameters are obtained, we can use (6) to calculate the position coordinates of the pseudo-target, $V_i(n) = (x_i^f(n), y_i^f(n))$.

$$\begin{cases} x_i^f(n) = x_o(n) + L_i(n)\cos\left(a_i(n)\right) \\ y_i^f(n) = y_o(n) + L_i(n)\sin\left(a_i(n)\right) \\ n = 1, \cdots, N, i = 1, \cdots, K \end{cases} \tag{6}$$

Where n is the number of measurement points. K is the number of positioning parameters of the second layer scatter. $V_i(n)$ is the position coordinates of the pseudo-target. The pseudo-target is defined as the location target in the line of sight (LOS) condition.

In Fig. 2, $V_i(n)$ is the pseudo-target of B_i from the observation point n . If the position of scatter is not variable and there is no measurement error, $o(n)$, B_i and $V_i(n)$ will be linearly located for each given n. With the movement of single station, the locations of pseudo-targets with respect to each measurement point will be changing. Therefore, $V_i(n)$ can effectively infer the related motion trail. In this case, the locations of (B_{xi},B_{yi}), (M_x,M_y) and MS remain stable.

The motion trail of pseudo-targets is with the centre B_i and radius $(r_i + h)$. The motion equation can be calculated by (7).

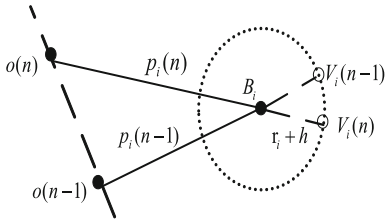

Fig. 2 Pseudo-target circular track plot

$$\left(x_i^f(n) - B_{xi}\right)^2 + \left(y_i^f(n) - B_{yi}\right)^2 = (r_i + h)^2 \tag{7}$$

We set $c_i = (r_i + h)$ and $n \geq 3$, (7) can be solved by the least square (LS) method. Letting

$$\Theta_i = \begin{bmatrix} -2B_{xi} \\ -2B_{yi} \\ {B_{xi}}^2 + {B_{yi}}^2 - {c_i}^2 \end{bmatrix}, \quad A_i = \begin{bmatrix} x_i^f(1) & y_i^f(1) & 1 \\ x_i^f(2) & y_i^f(2) & 1 \\ \cdots & \cdots & \cdots \\ x_i^f(N) & y_i^f(N) & 1 \end{bmatrix},$$

$$b_i = -\begin{bmatrix} \left(x_i^f(1)\right)^2 + \left(y_i^f(1)\right)^2 \\ \left(x_i^f(2)\right)^2 + \left(y_i^f(2)\right)^2 \\ \cdots \\ \left(x_i^f(N)\right)^2 + \left(y_i^f(N)\right)^2 \end{bmatrix} \tag{8}$$

Equation (7) is represented as $A_i \cdot \Theta_i = b_i$. The LS solution should be $\Theta_i = ({A_i}^T A_i)^{-1} {A_i}^T b_i$. The distance between (B_{xi},B_{yi}) and $o(n) = (o_x(n), o_y(n))$ is given by (10).

$$\begin{cases} B_{xi} = -1/2\Theta_i(1), \ \ B_{yi} = -1/2\Theta_i(2) \\ c_i = 1/2\sqrt{{\Theta_i}^2(1) + {\Theta_i}^2(2) - 4\Theta_i(3)} \end{cases} \tag{9}$$

$$p_i(n) = \sqrt{\left(B_{xi} - O_x(n)\right)^2 + \left(B_{yi} - O_y(n)\right)^2} \tag{10}$$

3.3 Localization of the First Layer Scatters and MS

As shown in Fig. 1, (B_{xi},B_{yi}) is selected as the virtual BS. (M_x,M_y) can be obtained based on at least three virtual BSs. From Fig. 2, $c_i = r_i + h$. $\Delta c_{1i} = c_i - c_1 = (r_i + h) - (r_1 + h)$ $(i = 2, 3)$. Then we using Chan algorithm [8] to locate (M_x,M_y). Where $x_{i1} = B_{xi} - B_{x1}$; $y_{i1} = B_{yi} - B_{y1}$ $(i = 2, 3)$.

$$\begin{bmatrix} M_x \\ M_y \end{bmatrix} = -\begin{bmatrix} x_{21} & y_{21} \\ x_{31} & y_{31} \end{bmatrix}^{-1} \times \left\{ \begin{bmatrix} \Delta c_{12} \\ \Delta c_{13} \end{bmatrix} R_1 + \frac{1}{2} \begin{bmatrix} \Delta c_{12}{}^2 - k_2 + k_1 \\ \Delta c_{13}{}^2 - k_3 + k_1 \end{bmatrix} \right\} \tag{11}$$

$$\begin{aligned} R_1{}^2 &= (B_{x1} - M_x)^2 + \left(B_{y1} - M_y\right)^2 \\ &= k_1 - 2M_x B_{x1} - 2M_y B_{y1} + M_x{}^2 + M_y{}^2, \end{aligned} \quad \begin{cases} k_1 = B_{x1}{}^2 + B_{y1}{}^2 \\ k_2 = B_{x2}{}^2 + B_{y2}{}^2 \\ k_3 = B_{x3}{}^2 + B_{y3}{}^2 \end{cases} \tag{12}$$

$$A = -\begin{bmatrix} x_{21} & y_{21} \\ x_{31} & y_{31} \end{bmatrix}^{-1} \begin{bmatrix} \Delta c_{12} \\ \Delta c_{13} \end{bmatrix}, \quad B = -\begin{bmatrix} x_{21} & y_{21} \\ x_{31} & y_{31} \end{bmatrix}^{-1} \frac{1}{2} \begin{bmatrix} \Delta c_{12}{}^2 - k_2 + k_1 \\ \Delta c_{13}{}^2 - k_3 + k_1 \end{bmatrix} \tag{13}$$

$$\begin{cases} M_x = A(1,1) \cdot R_1 + B\left(1,1\right) \\ M_y = A(2,1) \cdot R_1 + B\left(2,1\right) \end{cases}, \quad \left[M_x, M_y\right] = A \cdot R_1 + B \tag{14}$$

By Substituting (14) into (12), R_1 can be easily obtained. Then, r_i can be obtained in (15).

$$r_i(n) = \sqrt{(B_{xi} - M_x)^2 + \left(B_{yi} - M_y\right)^2} \tag{15}$$

Finally, based on the location of (M_x,M_y) and AOD model, the location of MS will be reliably estimated.

4 Simulation Results

We assume the initial position of the single station is located at the origin of coordinates. The MS is at the position (x_t,y_t) = (800m, 800m), observation period is set to be one second. The speed of the single station in the x and y directions equal to $V_{ox} = 8m/s$ and $V_{oy} = 15m/s$. The root mean-square error (RMSE) is used to evaluate the positioning performance.

$$RMSE = \frac{1}{N} \sum_{n=1}^{N} \sqrt{(\hat{x}_t(n) - x_t)^2 + (\hat{y}_t(n) - y_t)^2} \tag{16}$$

Where $(\hat{x}_t(n), \hat{y}_t(n))$ is the estimated position. N is the number of total observation points.

4.1 Simulation One

In this simulation, the variations of position accuracy with respect to the number of scatters on the second layer and the radius of scatters. The standard deviations in AOA and TOA models are $\delta_\alpha = 0.04$rad and $\delta_\gamma = 2$m.

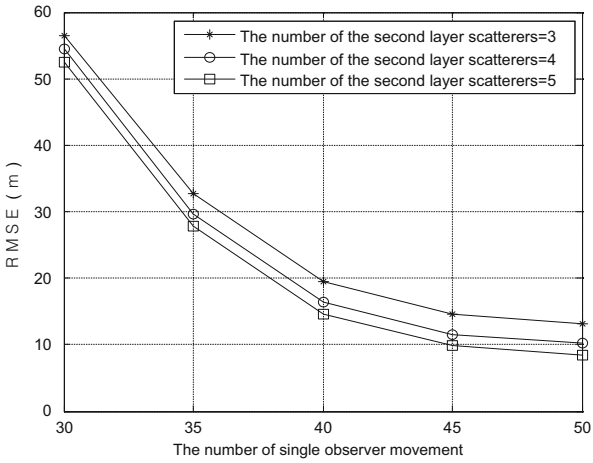

Fig. 3 RMSE with respect to the number of scatters on the second layer

In Fig. 3, the scatters on the first and second layers are distributed in a circle with the centre MS and the radius $R_1 = 200$m and $R_2 = 400$m. Obviously, as the number of single observer movement increases, the RMSE will decrease. For a given number of single observer movement, RMSE will decrease with the increase of the number of scatters on the second layer.

In Fig. 4, the number of scatters on the second layer is set to be five. With the increase of the number of single observer movement, the RMSE will decrease. Therefore, based on the collection of more useful observation information, the position accuracy can be improved. Moreover, with the increase of scatter radius, the position error will increase slightly, especially in the large number of single observer movement conditions.

4.2 Simulation Two

We continue to examine the influence on position accuracy with respect to the standard deviations of AOA and TOA. In Figs. 5 and 6, there are 5 scatters on the second layer, $R_1 = 200$m, $R_2 = 400$m.

From Fig. 5, $\delta_\gamma = [2\text{m}, 4\text{m}, 6\text{m}, 8\text{m}, 10\text{m}]$. It can be obtained that the position error will decrease as the number of single observer movement increases. In the large number of single observer movement condition, the decrease of the standard deviation of AOA can remarkably decrease the RMSE. In Fig. 6, and $\delta_\alpha = [5$ mrad, 4mrad, 6mrad, 8mrad, 10mrad]. Similarly, as the number of single observer movement increases, the RMSE will decrease. In the conditions of the largest number of single observer movement and smallest standard deviation of TOA, the smallest RMSE will be achieved as expected.

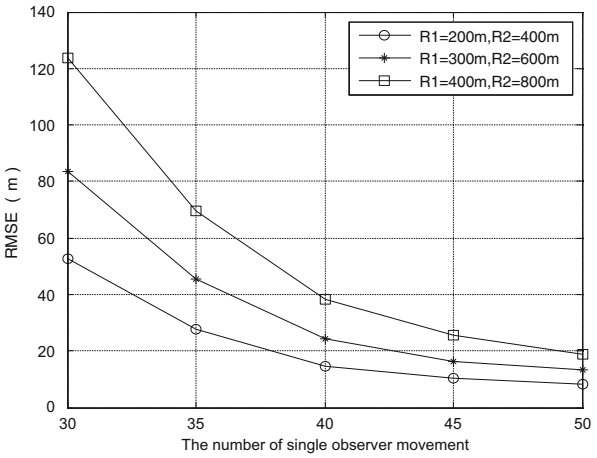

Fig. 4 RMSE in different scatter radius conditions

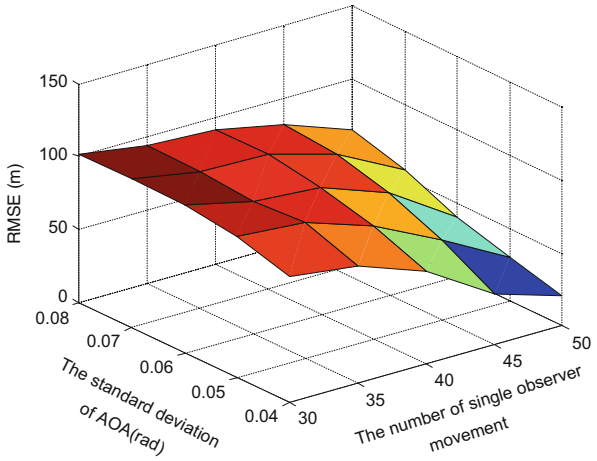

Fig. 5 Variations of RMSE with respect to the standard deviation of AOA

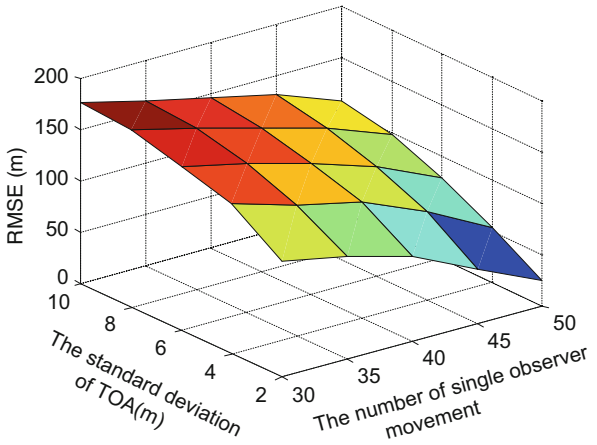

Fig. 6 Variations of RMSE with respect to the standard deviation of TOA

5 Conclusion

This paper proposes a new hybrid TOA-AOA-AOD localization algorithm based on a two-layer scattering model. An effective circle fitting method is used to realize the joint estimation of the virtual BS and the related distance to the MS. Then it uses Chan algorithm to locate (M_x,M_y). Finally, the real location of the MS can be reliably estimated based on (M_x,M_y) and AOD model. Furthermore, our proposed algorithm can be widely used for the practical use in future by the reason of the slight calculation cost.

References

1. Wang W, Xiong J, Zhu Z (2005) A new NLOS error mitigation algorithm in location estimation. IEEE Trans Vehicular Technol 54(6):2048–2053
2. Yu K, Guo Y (2009) Statistical NLOS identification based on AOA, TOA and signal strength. IEEE Trans Vehicular Technol 58(1):274–286
3. Xu T, Liu S (2009) Single observer passive location using phase rate of change with the extended Kalman particle filter. Comput Commun Control Manag 3:65–68
4. Wang Z, Zekavat SA (2012) Omni directional mobile NLOS identification and localization via multiple cooperative nodes. IEEE Trans Mobile Comput 11(12):2047–2059
5. Ji T, Wu Q, Jiang L, Tang W (2011) Disturbance detection, location and classification in phase space. Gen Transmission Distribution IET 5(2):257–265
6. Yang T, Jin L (2011) Single station location method in NLOS environment: the circle fitting algorithm. Sci China Inform Sci 54(2):381–385
7. Shames I, Bishop A, Smith M, Anderson B (2013) Doppler shift target localization. IEEE Trans Aerospace Electron Syst 49(1):266–276

The Research of Dynamic Tracking Algorithm Based on Hybrid Positioning System

Chengbiao Fu

Abstract In signal-degraded environments such as dense urban area and indoor environment, GPS (Global Positioning System) signals are either blocked or strongly degraded by natural and artificial obstacles, which cannot meet the surging demands for position information, the combination of different GNSS (Global Navigation Satellite System) could be a suitable approach to fill this gap. This paper presents a hybrid positioning method combining GPS and GLONASS, simulation results show that Extended Kalman Filter Algorithm is an effective method to deal with data fusion in hybrid positioning system, so this system can improve the positioning accuracy in the environment without enough GPS satellites.

Keywords GPS • GLONASS • Integrated navigation • Extended Kalman filter

1 Introduction

GPS is used for wide variety of scientific applications, but it cannot locate successfully in dense urban areas and mountainous areas [1], therefore, the standalone GPS isn't able to provide an accurate and continuous absolute positioning , a possible approach to solving this problem is to consider the combining positioning system.

GNSS are worldwide, all-weather navigation systems, which are able to provide three-dimensional positioning [2], velocity and time synchronization. Currently, with the development of GNSS, the number of global navigation satellites in view can be greatly increased in the same epoch moment, multi-constellation navigation system will improve navigation accuracy, integrity and reliability. The present GNSS are GPS, GLONASS, Galileo and Compass [3], but the latter two are still

C. Fu (✉)
Department of Computer Science and Engineering, Qujing Normal College, Qujing, China
e-mail: fucb305@gmail.com

B. Zhang et al. (eds.), *The Proceedings of the Second International Conference on Communications, Signal Processing, and Systems*, Lecture Notes in Electrical Engineering 246, DOI 10.1007/978-3-319-00536-2_104,

in the development phase. As of 24 January 2012, a total of 31 GLONASS satellites [4] are in orbit.

Now that GLONASS has reached its full constellation [5], and it's the positioning standard of Russian. This paper presents hybrid location method combining GLONASS and GPS to achieve accurate positioning, making up for the defects of GPS signals substantially lose accuracy and availability in dense urban areas and indoors. This method improves positioning precision and availability.

2 Hybrid Positioning System Model

An integrated GNSS system based on GPS and GLONASS, provides a significantly increased satellite availability [5], the model of GPS/ GLONASS hybrid positioning system can be expressed in Fig. 1.

The GNSS are considered quite similar to each other, but they also present several significant differences [6], the main difference is time scale adopted by system, therefore, when GPS and GLONASS are used together, an additional unknown must be estimated, there will be 5 unknown parameters at each epoch, then by analyzing the pseudo-range observation equations, the true distances between a receiver and a satellite can be expressed as:

$$\begin{cases} \rho_{GPS1} = \sqrt{(x_1 - x_u)^2 + (y_1 - y_u)^2 + (z_1 - z_u)^2} + c \cdot t_{GPS} \\ \rho_{GPS2} = \sqrt{(x_2 - x_u)^2 + (y_2 - y_u)^2 + (z_2 - z_u)^2} + c \cdot t_{GPS} \\ \rho_{GPS3} = \sqrt{(x_3 - x_u)^2 + (y_3 - y_u)^2 + (z_3 - z_u)^2} + c \cdot t_{GPS} \\ \rho_{GLOASS1} = \sqrt{(x_{a1} - x_u)^2 + (y_{a1} - y_u)^2 + (z_{a1} - z_u)^2} + c \cdot (t_{GLONASS} - t_{GPS}) \\ \rho_{GLONASS1} = \sqrt{(x_{a2} - x_u)^2 + (y_{a2} - y_u)^2 + (z_{a2} - z_u)^2} + c \cdot (t_{GLONASS} - t_{GPS}) \end{cases} \tag{1}$$

Where ρ_{GPSi} is the pseudo-range of GPS satellite, $\rho_{GLONASSi}$ is the pseudo-range of GLONASS satellite, (x_i,y_i,z_i) is the coordinate parameters of GPS satellite, (x_{ai}, y_{ai},z_{ai}) is the coordinate parameters of GLONASS satellite, $t_{GLONASS}$ is the GLONASS time, (x_u,y_u,z_u) is the position of object, t_{GPS} is the GPS time, C is the speed of light.

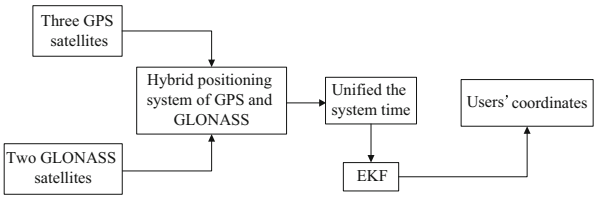

Fig. 1 The location schematic of double constellation

3 Integration Positioning Algorithm

Because of the nonlinear equation with GPS and GLONASS pseudo-orange observation model, we need to use Extended Kalman Filter (EKF) algorithm to estimate location information.

3.1 Establishment State Equation

This paper considers two dimensional case, uses Uniform motion model in the x direction, and Singer model in the y direction, the process of discretization of the state vector [7] can be described as the following:

$$X_k = [x(k), x_\circ(k), y(k), y_\circ(k), y_{\circ\circ}(k)]^T \tag{2}$$

Where $x(k)$, $x_\circ(k)$ denotes the position and the speed of the goal in x direction separately, $y(k)$, $y_\circ(k)$, $y_{\circ\circ}(k)$ denotes the position, the speed and the acceleration of the goal in y direction separately.

The process of target state equation can be defined as:

$$\boldsymbol{X}_k = \boldsymbol{A}\boldsymbol{X}_{k-1} + \boldsymbol{W}_{k-1} \tag{3}$$

The transition matrix is given as:

$$\boldsymbol{A} = \begin{bmatrix} 1 & T & 0 & 0 & 0 \\ 0 & 1 & 0 & 0 & 0 \\ 0 & 0 & 1 & T & (\alpha T - 1 + e^{-\alpha T})/\alpha^2 \\ 0 & 0 & 0 & 1 & (1 - e^{-\alpha T})/\alpha \\ 0 & 0 & 0 & 0 & e^{-\alpha T} \end{bmatrix} \tag{4}$$

The covariance matrix of the state noise is represented as:

$$\boldsymbol{Q} = E\left[W_k W_k^T\right] = 2\alpha\sigma_m^2 \begin{bmatrix} T^3/3 & T^2/2 & 0 & 0 & 0 \\ T^2/2 & T & 0 & 0 & 0 \\ 0 & 0 & q_{11} & q_{12} & q_{13} \\ 0 & 0 & q_{21} & q_{22} & q_{23} \\ 0 & 0 & q_{31} & q_{32} & q_{33} \end{bmatrix} \tag{5}$$

Where

$$q_{11} = \frac{1}{2\alpha^5}\left(1 - e^{-2\alpha T} + 2\alpha T + \frac{2\alpha^3 T^3}{3} - 2\alpha^2 T^2 - 4\alpha T e^{-\alpha T}\right)$$

$$q_{12} = q_{21} = \frac{1}{2\alpha^4}\left(e^{-2\alpha T} + 1 - 2e^{-\alpha T} + 2\alpha T e^{-\alpha T} - 2\alpha T + \alpha^2 T^2\right)$$

$$q_{13} = q_{31} = \frac{1}{2\alpha^3}\left(1 - e^{-2\alpha T} - 2\alpha T e^{-\alpha T}\right)$$

$$q_{22} = \frac{1}{2\alpha^3}\left(4e^{-\alpha T} - 3 - e^{-2\alpha T} + 2\alpha T\right)$$

$$q_{23} = q_{32} = \frac{1}{2\alpha^2}\left(e^{-2\alpha T} + 1 - 2e^{-\alpha T}\right)$$

$$q_{33} = \frac{1}{2\alpha}\left(1 - e^{-2\alpha T}\right)$$

Where α denotes motor frequency, T denotes Sampling time interval, σ_m^2 denotes acceleration variance of the goal.

3.2 Establishment Observation Equation

The observation equation with GPS and GLONASS can be defined [8] as:

$$\boldsymbol{Y}_k = h(\boldsymbol{X}_k, k) + \boldsymbol{V}_k \tag{6}$$

Where Y_k denotes the pseudo-orange measurements value of satellites, V_k denotes the observation noise, $h(X_k,k)$ denotes the observation matrix.

$h(X_k,k)$ is nonlinear function, the EKF algorithm is represented as follows:

$$\hat{\boldsymbol{X}}_{k/k-1} = \boldsymbol{A}\hat{\boldsymbol{X}}_{k-1} \tag{7}$$

$$\boldsymbol{P}_{k/k-1} = \boldsymbol{A}\boldsymbol{P}_{k-1}\boldsymbol{A}^T + \boldsymbol{Q} \tag{8}$$

$$\boldsymbol{K}_k = \boldsymbol{P}_{k/k-1}\boldsymbol{H}_k^T\left(\boldsymbol{H}_k\boldsymbol{P}_{k/k-1}\boldsymbol{H}_k^T + \boldsymbol{R}_k\right)^{-1} \tag{9}$$

$$\hat{\boldsymbol{X}}_k = \hat{\boldsymbol{X}}_{k/k-1} + \boldsymbol{K}_k\left[\boldsymbol{Y}_k - h\left(\hat{\boldsymbol{X}}_{k/k-1}, k\right)\right] \tag{10}$$

$$\boldsymbol{P}_k = (\boldsymbol{I} - \boldsymbol{K}_k\boldsymbol{H}_k)\boldsymbol{P}_{k/k-1} \tag{11}$$

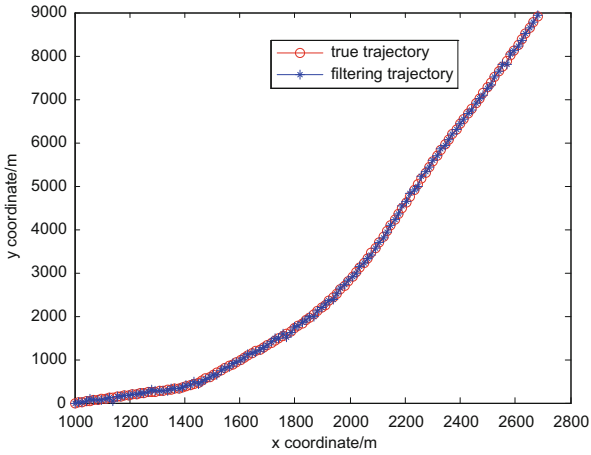

Fig. 2 Tracking trajectory

4 Simulation

In order to compare the precision of combined GPS/GLONASS positioning system, the estimator is implemented by Extended Kalman Filter, which is extensively used to integrated system. We choose a test area covered by 3 GPS satellites and 2 GLONASS satellites.

In the test process, assuming the initial clock deviation of GPS and GLONASS is known, the initial position is (1,000, 0), the initial velocity of x direction is 13 m/s, the initial velocity of y direction is 12 m/s, the initial acceleration velocity of y direction is 0, the acceleration variance in movement is 3.8, the motor frequency is 0.1, observations time interval is 1 s, a total of 120 s.

We adopt EKF algorithm to track the target trajectory, assuming the observation error of GPS obey Gaussican distribution by mean to 0, standard deviation to 5 m. Also, assuming the observation error of GLONASS obey Gaussican distribution by mean to 0, standard deviation to 25 m. Simulation results are shown in Figs. 2, 3, 4, 5, and 6.

Figure 3 shows the positioning tracking trajectory result in x direction. Figure 4 shows the positioning tracking trajectory result in y direction. We can found that simulation trajectory is consistent with true trajectory.

Figures 5 and 6 shows that the pseudo-range measurement error result. We can found that pseudo-range positioning has the precision of 20 m, which can meet the demands for position information.

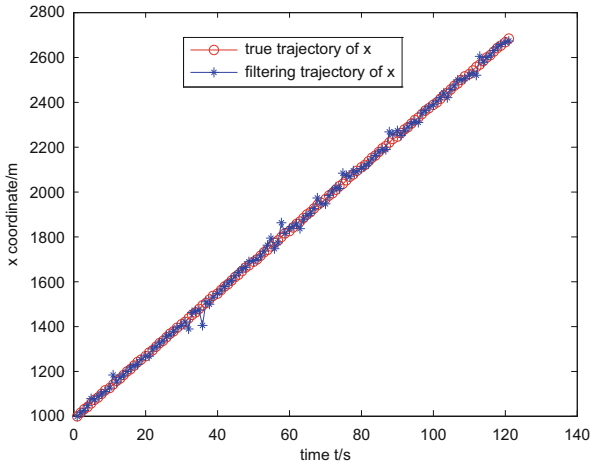

Fig. 3 Tracking trajectory of x direction

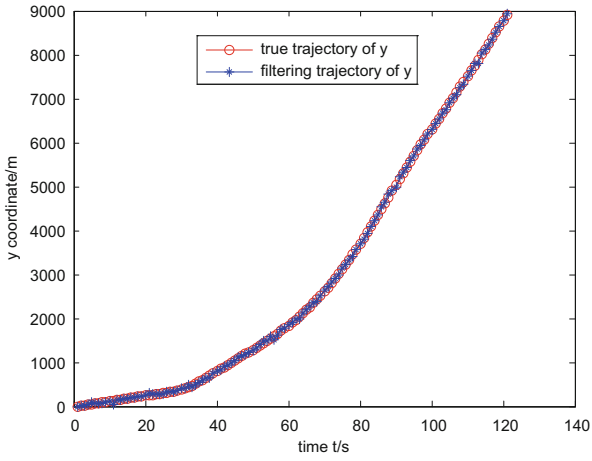

Fig. 4 Tracking trajectory of y direction

5 Conclusion

Based on the research results presented in this paper, the hybrid positioning technology based on GPS/GLONASS is effective, the integrated system not only to improve accuracy of positioning, but also to make up for the defects when the number of GPS satellites are not enough in dense urban areas and indoors. A data fusion algorithm based on EKF is designed for GPS/GLONASS hybrid positioning. Through our theoretical analysis and simulation verification, this EKF algorithm can improve the performance of hybrid navigation system, simulation filtering trajectory is consistent with true trajectory basically. The experimental results verify that the combined GPS/GLONASS navigation positioning have great applications for navigation users, especially in limited satellite conditions.

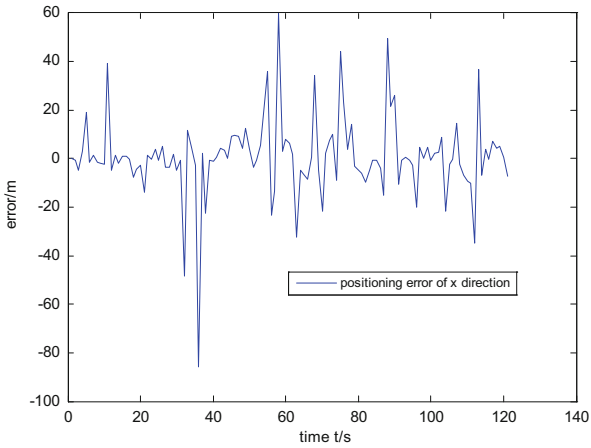

Fig. 5 Positioning error in x direction

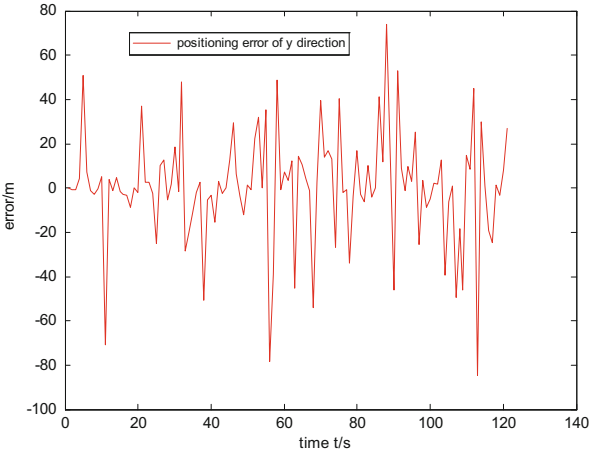

Fig. 6 Positioning error in y direction

References

1. Hideki Y, Tomoji T, Nobuaki K, Akio Y (2008) Evaluation of positioning accuracy with differential GPS/GLONASS. 21st international technical meeting of the Satellite Division of the Institute of Navigation, ION GNSS, vol 2. pp 669–674
2. Juju D, Yunzhong S (2012) An algorithm of combined GPS/GLONASS static relative positioning. Cehui Xuebao/Acta Geodaetica et Cartographica Sinica 41(6):825–830, 917
3. Xiangguang M, Jiming G (2010) GPS-GLONASS and their combined precise point positioning. Wuhan Daxue Xuebao (Xinxi Kexue Ban)/Geomatics Inform Sci Wuhan Univ 35 (12):1409–1413
4. Changsheng C, Yang G (2013) Modeling and assessment of combined GPS/GLONASS precise point positioning. GPS Solutions 17(2):223–236, doi: 10.1007/s10291-012-0273-9
5. Xiaohong Z, Fei G, Xingxing L, Xiaojing L (2010) Study on precise point positioning based on combined GPS and GLONASS. Wuhan Daxue Xuebao (Xinxi Kexue Ban)/Geomatics Inform Sci Wuhan Univ 35(1):9–12

6. Changsheng C, Yang G (2013) GLONASS-based precise point positioning and performance analysis. Adv Space Res 51(3):514–524. doi:doi: 10.1016/j.asr.2012.08.004
7. Yang Xu, Xu Qing, Wang Haijiang (2012) An Kalman filter-based method for BeiDou/GPS integrated navigation system. The 2012 Proceedings of the international conference on communications, signal processing, and systems, lecture notes in electrical engineering, vol 202. pp 485–492 doi: 10.1007/978-1-4614-5803-6_49
8. Tian Zengshan, Lei Luo (2008) Particle filter positioning and tracking based on dynamic model. 4th IEEE conference on automation science and engineering, CASE, pp 756–759. doi: 10.1109/COASE.2008.4626430

Probability Distribution-Aided Indoor Positioning Algorithm Based on Affinity Propagation Clustering

Zengshan Tian, Xiaomou Tang, Mu Zhou, and Zuohong Tan

Abstract With the rapid development of indoor positioning technology, the fingerprint-based Wireless Local Area Network (WLAN) positioning becomes a new and widely recognized research concern. This paper proposes a probability distribution-aided indoor positioning algorithm based on the affinity propagation clustering. Different from the conventional fingerprint-based positioning algorithms, our algorithm first uses the affinity propagation clustering to minimize the searching space of reference points (RPs). Then, the probability distribution-aided positioning algorithm is utilized to estimate the target's accurate position. Furthermore, because the affinity propagation clustering can effectively reduce the computation cost for the RP searching which is involved in the probability distribution-aided positioning algorithm, the positioning efficiency of our proposed algorithm can be effectively guaranteed. Experimental results demonstrate that our proposed affinity propagation clustering will significantly improve the performance of the probability distribution-aided positioning algorithm in both the positioning accuracy and real-time ability.

Keywords WLAN indoor positioning • Fingerprinting • Affinity propagation clustering • RSS • Probability distribution

1 Introduction

In recent decade, the indoor WLAN positioning technology has caught significant attention by a variety of universities and research institutes [1]. Among them, the time of arrival (ToA), angle of arrival (AoA) and received signal strength (RSS) are

Z. Tian (✉) • X. Tang • M. Zhou • Z. Tan
Chongqing Key Lab of Mobile Communications Technology, School of Communication & Information Engineering, Chongqing University of Posts and Telecommunications, Chongqing 400065, China
e-mail: tianzs@cqupt.edu.cn; tangxiaomou@foxmail.com

B. Zhang et al. (eds.), *The Proceedings of the Second International Conference on Communications, Signal Processing, and Systems*, Lecture Notes in Electrical Engineering 246, DOI 10.1007/978-3-319-00536-2_105,

the three most representative measurements for the position estimation. Compared to the ToA and AoA measurements, the RSS can be more easily measured without any additional special hardware devices in current open public WLAN networks. However, the most significant challenge of the RSS readings is about the irregular variations of RSS due to the variable radio channel attenuation, signal shadowing, multi-path interference and even the variations of indoor temperature [2].

One effective solution is the k-nearest neighbor (kNN) algorithm to estimate the mobile user's position at the centroid of the K closest neighbors. The closest neighbors are defined as the RPs which have the smallest RSS distance to the on-line new collected RSS readings [3]. The kNN algorithm can be easily implemented by the current widely-existing WLAN infrastructures, while the accuracy is limited. Another alternative approach is based on the statistical analysis on the probabilities of each candidate RP to calculate the confidence probability of each RP to be selected as the mobile user's estimated position [4].

In this paper, we present a new accurate and scalable positioning algorithm to estimate the user's position with low computation cost in a public WLAN environment. Our algorithm consists of two steps: (1) the coarse positioning step is used to obtain the cluster which the user belongs to; and (2) the fine positioning step is utilized to calculate the accurate coordinates of the user.

The paper is organized as follows. Section 2 discusses the overall structure of our algorithm. Sections 3 addresses the detailed steps of the off-line affinity propagation, on-line cluster matching-based coarse positioning and probability distribution-aided fine positioning respectively. The performance of our proposed algorithm is verified in Sect. 4. Finally, Sect. 5 concludes this paper.

2 Overall Structure of Proposed Positioning Algorithm

The block diagram of our proposed indoor positioning algorithm is shown in Fig. 1. Obviously, this algorithm contains two phases: (1) in the off-line phase, we construct the radio map and conduct the affinity propagation clustering; and (2) in the on-line phase, the cluster matching-based coarse and probability distribution-aided fine positioning will be performed respectively. The detailed steps about the block diagram in Fig. 1 will be analyzed in Sect. 3.

In the off-line phase, we first carry the WLAN mobile device to collect the RSS readings from the hearable APs to construct the radio map in the area of interest. During the construction of the radio map ψ (see details below), the corresponding physical coordinates of RPs should also be stored. Then, the affinity propagation clustering is conducted in the radio map to cluster the raw RPs.

In the on-line phase, the first step is to use the mobile device to collect the on-line new RSS readings. Then, the coarse positioning will be used before the fine positioning for the reasons of reducing the on-line computation cost and improving the accuracy performance of the probability distribution-aided positioning algorithm.

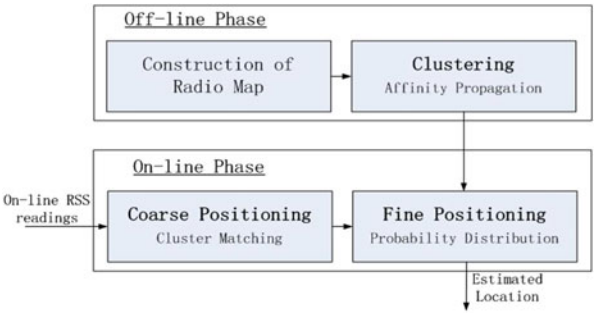

Fig. 1 Block diagram of proposed positioning algorithm

Due to the time-variation property of radio propagation in indoor WLAN environment (e.g. multi-path effect, RSS shadowing and adjacent channel interference), the fingerprint-based positioning has been more preferred in practical use [5]. During the off-line phase, the RSS readings are collected at pre-calibrated positions which are also named as the RPs. We denote the τ − th RSS readings from AP_i at RP_j as $\{\psi_{i,j}(\tau), \tau = 1, \ldots, q, q > 1\}$ where q is the number of RSS readings. Normally, the average of RSS readings will be computed and stored into a database which is known as the widely recognized radio map ψ. The radio map can effectively describe the spatial distribution property of the RSS in target area.

$$\psi = \begin{pmatrix} \psi_{1,1} & \psi_{1,2} & \cdots & \psi_{1,N} \\ \psi_{2,1} & \psi_{2,2} & \cdots & \psi_{2,N} \\ \vdots & \vdots & \ddots & \vdots \\ \psi_{L,1} & \psi_{L,2} & \cdots & \psi_{L,N} \end{pmatrix} \tag{1}$$

where $\psi_{i,j} = \frac{1}{q}\sum_{\tau=1}^{q} \psi_{i,j}(\tau)(i = 1, 2, \ldots, L; j = 1, 2, \ldots, N)$ is the average of RSS readings from AP_i at RP_j over the time domain. L and N are the number of access points (APs) and RPs respectively. Each column of the radio map ψ (i.e. $\psi_j = [\psi_{1,j}, \psi_{2,j}, \ldots, \psi_{L,j}]^T, j = 1, 2, \ldots, N$) represents a sequence of RSS readings at a RP_j. The superscript "T" denotes the transposition operation.

3 Detailed Steps of Proposed Positioning Algorithm

In response to the variation of indoor WLAN propagation channel, the affinity propagation clustering is used to mitigate the effects of RSS deviations and potential outliers on the positioning process. Different from the conventional K-means clustering [6], the basic idea of our proposed affinity propagation clustering algorithm is to use the *preference* (p) to label the RPs and the RPs with larger preference are more likely to be selected as the cluster centers. Our proposed algorithm outperforms the K-means clustering because of the initialization-independent property and better selection of cluster centers [7].

For the affinity propagation clustering, we first use the pairwise similarity $s(i,j)$ to describe the fitness of the RP_j to be selected as the cluster center with respect to the RP_i. Based on (1), we can denote the RSS vector for each RP_j as $\psi_j + \delta_j$ where δ_j is the measurement noise which obeys the Gaussian distribution. Therefore, the pairwise similarity $s(i,j)$ can be defined as the squared Euclidean distance in (2).

$$s(i,j) = -\left\|\psi_i - \psi_j\right\|^2, \quad \forall i, \quad j \in \{1,2,\ldots,N\} \tag{2}$$

Furthermore, there are two types of messages transmitted among the RPs for the affinity propagation clustering: (1) responsible message $r(i,j)$ which transmits the information about the clustering center; and (2) availability message $a(i,j)$ which informs the attachment relations between the RPs and clusters.

The RP_i will send the responsible message to each candidate cluster center RP_j to transmit the accumulated fitness for the RP_j to be selected as the cluster center for RP_i. By taking all the other potential cluster centers j ' for RP_i into account, we can obtain

$$r(i,j) = s(i,j) - \max_{j' \neq j} \{a(i,j') + s(i,j')\} \tag{3}$$

where $a(i,j)$ is the availability message, as defined in (5). Meanwhile, we define the self-responsibility $r(i,i)$, which is known as *preference (p)* as the median of input similarities, resulting in the average number of clusters.

$$p = \text{median}\{s(i,j), \forall i,j \in \{1,2,\ldots,N\}\} \tag{4}$$

The availability message $a(i,j)$ is sent from each candidate cluster center RP_j to RP_i. $a(i,j)$ describes the accumulated fitness for RP_i to select RP_j as its center, such as

$$a(i,j) = \min\left\{0, r(j,j) + \sum_{i' \neq i,j} \max\{0, r(i',j)\}\right\} \tag{5}$$

Similarly, the self-availability $a(j,j)$ will reflect the accumulated fitness for RP_j to be selected as the center. Because of the requirement of positive responsibilities, we have

$$a(j,j) = \sum_{i' \neq j} \max\{0, r(i',j)\} \tag{6}$$

The previously mentioned messages are transmitted among the neighboring RPs until the optimal cluster centers are searched out. When updating the messages, it is important that they be damped to avoid numerical oscillations that arise in some circumstances. Each message is set to λ times its value from the previous iteration

plus 1 - λ times its prescribed updated value, where the damping factor λ is between 0 and 1.

In the on-line phase, we will collect the new RSS readings at unknown positions $\vec{\psi}_r = \left[\psi_{1,r}, \ldots, \psi_{L,r}\right]^T$ where $\{\psi_{k,r}, k = 1, \ldots, L\}$ is the average of new RSS readings from AP_k. We define H and C_j as the set of cluster centers and the set of RPs with the center $RP_j \in H$. After the coarse positioning, the candidate cluster selected for the fine positioning can be obtained by (7).

$$j' = \text{argmin}_{j \in H} \left|\left|\vec{\psi}_r - \vec{\psi}_j\right|\right|^2, \vec{\psi}_r = \left[\psi_{1,r}, \ldots, \psi_{L,r}\right]^T \tag{7}$$

For the fine positioning, we will calculate the matching probability between the on-line new collected RSS readings and the pre-stored fingerprints in radio map. By assuming the Gaussian probability distribution of RSS readings at each RP, the RSS values should obey the normal distribution $N(\mu,\sigma^2)$.

First, the likelihood function is calculated by

$$L(\mu, \sigma^2) = \prod_{i=1}^{n} \frac{1}{\sqrt{2\pi}\sigma} e^{-\frac{(x_i-\mu)^2}{2\sigma^2}} \tag{8}$$

Second, we can obtain the logarithmic equation in (9).

$$\lg L(\mu, \sigma^2) = -\frac{n}{2}\lg(2n) - \frac{n}{2}\lg(\sigma^2) - \frac{n}{2\sigma^2}\sum_{i=1}^{n}(x_i - \mu)^2 \tag{9}$$

Third, likelihood equations should be

$$\begin{cases} \dfrac{\partial \lg L(\mu, \sigma^2)}{\partial \mu} = \dfrac{1}{\sigma^2}\displaystyle\sum_{i=1}^{n}(x_i - \mu)^2 = 0 \\ \dfrac{\partial \lg L(\mu, \sigma^2)}{\partial \sigma^2} = -\dfrac{n}{2\sigma^2} + \dfrac{1}{2\sigma^4}\displaystyle\sum_{i=1}^{n}(x_i - \mu)^2 = 0 \end{cases} \tag{10}$$

Last, by calculating the (10), one has

$$\mu^* = \overline{x} = \frac{1}{n}\sum_{i=1}^{n} x_i \tag{11}$$

$$\sigma^{*2} = \frac{1}{n}\sum_{i=1}^{n}(x_i - \overline{x})^2 \tag{12}$$

The likelihood equations have a unique solution (μ^*,σ^{*2}) which should also be a local maximum point. This result can be interpreted that when $|\mu| \to \infty$ or $\sigma^2 \to 0$

or $\sigma^2 \to \infty$, the non-negative function $L(\mu,\sigma^2) \to 0$. Therefore, the maximum likelihood estimation of μ and σ^2 will be

$$\mu^* = \overline{X} \tag{13}$$

$$\sigma^{*2} = \frac{1}{n}\sum_{i=1}^{n}\left(X_i - \overline{X}\right)^2 \tag{14}$$

where X is defined as the set of RSS readings. Based on the statistical property of the maximum likelihood estimation μ^* and σ^{*2}, we can approximately recognize μ^* as the RSS fingerprint at each RP. With this idea, the mean of RSS reading e_i and the corresponding variance d_i from each hearable AP AP_i should be calculated for the construction of radio map in the off-line phase.

In the on-line phase, after collecting the new RSS readings $\{rss_i,\ i = 1, 2, \ldots, L\}$, according to (15), we can calculate the probability of the RP (x,y) with respect to the i − th AP $P_i(x,y)$. In (15), we have $\mu = e_i$ and $\sigma = d_i$.

$$P_i(x,y) = \frac{1}{\sqrt{2\pi}\sigma} e^{-\frac{(rss_i-\mu)^2}{2\sigma^2}} (\sigma > 0) \tag{15}$$

Then, the probability of each RP $P(x,y)$ can be calculated. Finally, we will locate the user's position at the RP which has the maximum probability.

$$P(x,y) = \prod_{i=1}^{L} P_i(x,y) = \prod_{i=1}^{L}\left(\frac{1}{\sqrt{2\pi}d_i} e^{-\frac{(rss_i-e_i)^2}{2d_i^2}}\right) \tag{16}$$

4 Experimental Results and Analysis

Figure 2 shows the target indoor WLAN positioning environment for our testing. By using RSS readings collected from 9 public APs (Cisco WRT54G), we will compare the performance of our proposed algorithm with other three typical positioning algorithm; (1) kNN positioning algorithm with K-means clustering (K-means + Knn); (2) probability distribution-aided positioning algorithm with K-means clustering (K-means + Probability Distribution); and (3) kNN positioning algorithm with affinity propagation clustering (Affinity Propagation + Knn). The dimensions of our testing area are 66 × 22 m^2.

4.1 Positioning Results

Figure 3 gives the results of the affinity propagation clustering on the RPs. The solid circles represent the calibrated RPs and the RPs belonging to different clusters are

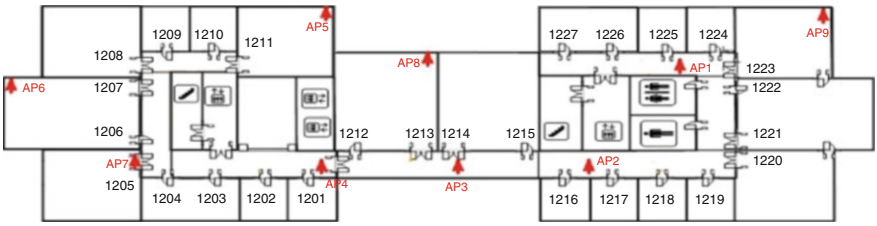

Fig. 2 Indoor WLAN positioning environment

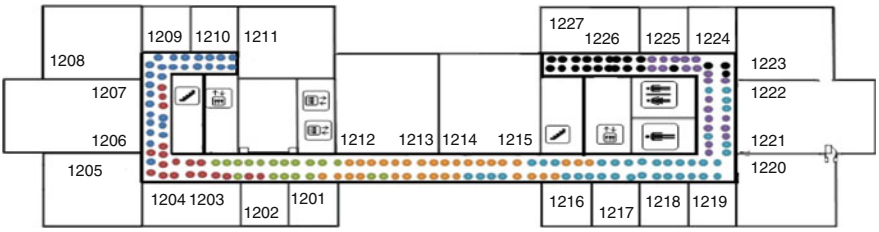

Fig. 3 Results of affinity propagation clustering on RPs

labeled by different color. The 182 RPs have been clustered into 7 clusters and the RPs in the same cluster are physically adjacent.

By randomly selecting 81 test positions in target area (see Fig. 4), we can compare the error performance of the K-means + Knn, K-means + Probability Distribution, Affinity Propagation + Knn and our proposed algorithm in Table 1 Furthermore, the comparisons of the cumulative density functions (CDFs) of positioning errors are also illustrated in Fig. 5.

4.2 Error Analysis

Based on the previous experimental results which are conducted in a public indoor WLAN environment, we can observe that: (1) our proposed probability distribution-aided positioning algorithm has reduced the mean of errors by 34.02 %, 28.3 % and 16.17 %, respectively compared to the K-means + Knn, K-means + Probability Distribution and Affinity Propagation + Knn positioning algorithms; and (2) our proposed algorithm has also increased the confidence probability of errors within 3 m to 80.49 % which is significantly larger than the probabilities 43.9 %, 62.2 %, and 65.85 % achieved by the K-means + Knn, K-means + Probability Distribution and Affinity Propagation + Knn positioning algorithms.

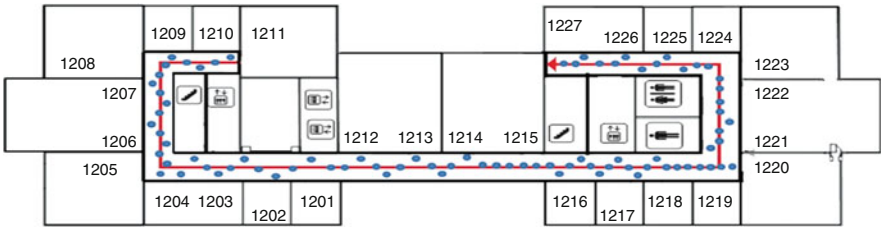

Fig. 4 The experimental curve selected randomly

Table 1 Results of statistical positioning errors

Algorithm	Mean (m)	Max (m)	Variance (m^2)
K-means + Knn	3.38	6.72	2.82
K-means + probability distribution	3.11	6.70	3.24
Affinity propagation + Knn	2.66	6.67	3.02
Proposed algorithm	2.23	6.52	2.52

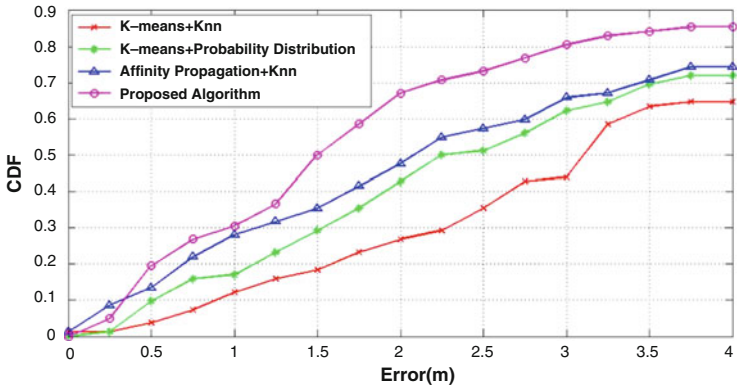

Fig. 5 CDFs of positioning errors

5 Conclusion

This paper proposes a new probability distribution-aided indoor positioning algorithm to not only improve the accuracy performance, but also decrease computation cost for the fingerprint searching and matching. Because the affinity propagation clustering can be recognized as a preprocessing of the conventional kNN and probability distribution-aided positioning algorithms, our method can also be easily applied to the other fingerprint-based wireless positioning systems, like the RFID and mobile cellular network. However, due to the significant dependence on the RSS distributions and deployment of RPs, the optimization of the layout of APs and fingerprint modification will form our interesting work in future.

References

1. Zhou M, Wong AKS, Tian ZS, Zhang VY, Yu X, Luo X (2013) Adaptive mobility mapping for people tracking using unlabelled Wi-Fi shotgun reads. IEEE Comm Lett 17(1):87–90
2. Zhou M, Tian Z, Xu K, Yu X, Wu H (2013) Theoretical entropy assessment of fingerprint-based Wi-Fi localization accuracy. Expert Syst Appl 40(15):6136–6149
3. Khodayari S, Maleki M, Hamedi E (2010) A RSS-based fingerprinting method for positioning based on historical data. Proc IEEE SPECTS 306–310
4. Kushki A, Plataniotis KN, Venetsanopoulos AN (2007) Kernel-based positioning in wireless local area networks. IEEE Trans Mobile Comput 6(6):689–705
5. Jain VK, Tapaswi S, Shukla A (2012) Distributed location estimation system using WLAN received signal strength fingerprints. Proc IEEE WCNC 3102–3106
6. Gokcay E, Principe J (2002) Information theoretic clustering. IEEE Trans Pattern Anal Machine Intell 24(2):158–172
7. Wang Y, Li WY, Sun Y (2011) Wireless sensor network cluster locations: a probabilistic inference approach. Proc IEEE ICAL 76–80

Detecting and Separating Different Moving Styles Targets of the Over-the-Horizon Radar

Cheng Luo, Dingwen Xu, and Zishu He

Abstract The problem of detecting and separating different moving styles targets of the over-the-horizon radar (OTHR) is studied. The echo of the moving target is educed, and a scheme for detecting and separating targets is proposed. The scheme, without any prior information of the targets, combines the Radon-Fourier transform (RFT) with the high-order ambiguity function (HAF), compensates the range-cell crossing and Doppler-cell crossing. Simulation results proved that the scheme is a valid approach to detect and separate different moving styles targets.

1 Introduction

The OTHR [1, 2] submits a high frequency (HF) skywave, makes use of the reflection of the ionosphere, which could largely prolong the early warning time. For some native advantages, the OTHR has been set great store by more and more scholars and study organizations [3–6]. However, the OTHR works in a complex environment, because of the heavy clutter and noise, the OTHR needs to accumulate in a longer time to gain enough SNR. For a high-speed moving target, longer accumulation time means it may cross the range-cell, the Doppler-cell and the radar beam, so compensations must be done before accumulation in this scenario [7].

Fortunately, because of the hyper-far range between the target and the radar, crossing-beam would hardly happen in the accumulation period, so only range-cell crossing and Doppler-cell crossing are needed to be compensated. Considering the lack of prior information of the targets in practice, four different scenarios will be discussed in this paper: no target, or only constant velocity target, or only constant acceleration target, or constant velocity target and constant acceleration target.

C. Luo (✉) • D. Xu • Z. He
School of Electronic Engineering, University of Electronic Science and Technology of China, Chengdu, China
e-mail: genielc@yahoo.cn

B. Zhang et al. (eds.), *The Proceedings of the Second International Conference on Communications, Signal Processing, and Systems*, Lecture Notes in Electrical Engineering 246, DOI 10.1007/978-3-319-00536-2_106,

In order to improve the applicability, in this paper, without any prior information of the targets, the echo model with range-cell crossing and Doppler-cell crossing will be educed, then the RFT [8, 9] and HAF [10, 11] will be employed to compensate the effort caused by the velocities and the accelerations of the targets, and the accumulation will be done at last.

2 Echo Model

The HF OTHR submits LFMCW signal, which could be written as

$$s_t = e^{j\pi\mu\hat{t}^2} \tag{1}$$

where μ is the FM slope, $\hat{t}$ is the fast time. The echo after pulse compression is

$$s_{rm}(t,\hat{t}) = A\text{sinc}\{\pi B_s[\hat{t} - 2R(t)/c]\}\exp[-j4\pi R(t)/\lambda] \tag{2}$$

where A is the complex amplitude, B_s is the bandwidth, the range between the target and the radar is $R(t) = R_0 + vt$, R_0 is the original range, v is the radial velocity. By simplifying equation (2)

$$s_{rm}(t,R) = A_T\text{sinc}\{\pi[R - R(t)]/\rho_r\}\exp(-j2\pi f_d t) \tag{3}$$

where $R = c\hat{t}/2$, and the complex amplitude $A_T = A\ \exp(-j2\pi R_0)$, $\rho_r = c/2B_s$ is range resolution, f_d is Doppler frequency.

It is easy to see from (3), because the time delay is changing, the range-cell crossing and the Doppler-cell crossing would happen, which should be compensated before coherent accumulation.

3 Solve Scheme

The whole processing scheme is shown in Fig. 1. No matter what the echo contains, the RFT is used to compensate the range-cell crossing firstly, and then matched filtering. Select the highest peak of the matched filtering output and let the corresponding velocity as the real velocity of the target. Secondly, the HAF is used to estimate the acceleration and compensate the effect. Lastly, judge a target is presented or not by coherent accumulation.

If there is a constant acceleration target in the detection area, the range-cell crossing and the Doppler-cell crossing can be compensated by Fig. 1. If there is a constant velocity target or no target, a fake acceleration would be estimated, but after compensation and accumulation, not enough gain can be gained, and whether

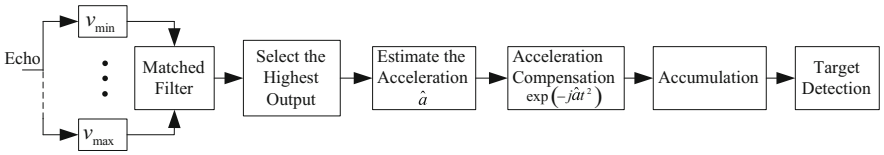

Fig. 1 The flow chart of long time accumulation and detection of OTHR targets

there is a constant velocity target or not can be made by matched filtering. If there are more than one targets, accumulation output of these targets can be get, and then cancel the biggest one, repeat the steps until every target been detected and separated, the detail will be explained in the simulations.

4 Ways of Compensation

Coherent accumulation needs strict precondition. In this section, the RFT is employed to compensate the range-cell crossing while the HAF is employed to estimate the acceleration and compensate the Doppler-cell crossing.

Assume that (ρ_T,θ_T) is the target location in the system of the polar coordinates. Considering the lack of the prior information in practice, the velocities and ranges of the targets must be searched, so the definition of the RFT should be

$$G_{\rho\theta}(\rho,\theta)=\int_{-T/2}^{T/2} s_{rm}\left(t,\frac{\rho}{\sin\theta}-t\cot\theta\right)H_\theta(t)dt,\rho\in(-\infty,\infty),\theta\in[0,\pi] \tag{4}$$

where (ρ,θ) is the searching polar coordinates. At the very location where the target lies, the RFT of the pulse compression signal is

$$\begin{aligned}G_{\rho\theta}(\rho_T,\theta_T)&=\int_{-\infty}^{\infty}\int_{-T/2}^{T/2} s_{rm}(t,R)\delta(\rho_T-t\cos\theta_T-R\sin\theta_T)H_\theta(t)dtdR\\&=A_TT.\end{aligned} \tag{5}$$

From (5), it is clearly to see that when the searching location (ρ,θ) is near the real one (ρ_T,θ_T), RFT can compensate the range-cell crossing validly.

The echo of a moving target can be approximated by a polynomial phase signal (PPS), and the HAF is often used to estimate parameters of a PPS, so the HAF can be used here for the compensation. An Mth order PPS could be written as

$$s(n) = \exp\left(j\sum_{m=0}^{M} a_m n^m\right), 0 \le n \le N-1 \tag{6}$$

where a_0, a_1, $\cdots$ a_M are coefficients for each order, N is the number of samples. The echo after matched filtering can be modeled as a PPS

$$y^{'}(n) = \exp\left\{j2\pi\left(\frac{2f_0}{c}\right)\left[\sum_{k=0}^{M}\frac{v_k}{k!}\left(nT_p\right)^k\right]\right\} \tag{7}$$

where v_i are radial moving parameters of each order of the target, as v_1 is the original radial velocity, v_2 is the original radial acceleration. Compare (6) with (7), one can get

$$a_i = 2\pi\left(\frac{2f_0}{c}\right)\left(\frac{v_i}{i!}\right)(T_{sw})^i, i = 0, 1, \cdots M. \tag{8}$$

So the moving parameters can be get from (8) by HAF.

In order to estimate the highest-order coefficient a_M, the high-order instantaneous moment (HIM) can be calculated as a 1-order monochromatic signal

$$\begin{aligned} &HIM_M[s(n);\tau] = \exp[j(w_0 n + \phi_0)], 0 \le n \le N-(M-1)\tau-1 \\ &\omega_0 = M!\tau^{M-1}a_M, \phi_0 = (M-1)!\tau^{M-1}a_{M-1} - (M-1)M!\tau^M a_M/2. \end{aligned} \tag{9}$$

In (9), the frequency ω_0 has a linearity relationship with a_M, then the Mth order HAF can be expressed as

$$HAF_M[s(n);\omega,\tau] = \sum_{n=0}^{N-(M-1)\tau-1} HIM_M[s(n);\tau]e^{-j\omega n}. \tag{10}$$

By calculating the maximum of $|HAF_M[s(n);\ \omega,\ \tau]|$, $\hat{a}_M$ can be estimated as

$$\hat{a}_M = \frac{\arg\max_\omega |HAF_M[s(n);\omega,\tau]|}{M!(\tau)^{M-1}}. \tag{11}$$

Combine (10) and (11), the corresponding radial moving parameter can be get, and then put $\hat{a}_M$ into $s(n)$ to cancel the phase with a_M, a 1-order lower signal can be get after the compensation. Repeat the steps above, all of the phase parameters can be estimated and canceled.

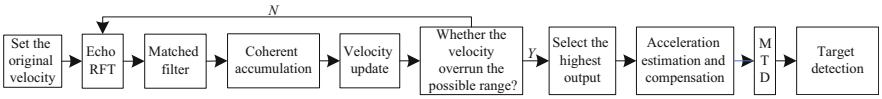

Fig. 2 The flow chart of simulations

5 Simulations

Main parameters are set as: the pulse repeat interval is $10ms$, the bandwidth is $40kHz$, the carrier frequency is $10MHz$, the period of the coherent time is $5s$, the SNR is $-25dB$, repeat every simulations 200 times to calculate the average. In order to prove the generality of the scheme above, four different simulation backgrounds are selected: (1) no target, (2) only constant velocity target, (3) only constant acceleration target, (4) constant velocity target and constant acceleration target. The flow chart of simulations is shown in Fig. 2.

If no target exists, the echo only contains noise. The MTD result without any compensation is shown in Fig. 3 left, and nothing but noise can be seen.

As is shown in Fig. 3 right, after the compensation by RFT and HAF, there is also only noise. In this scenario, acceleration can be estimated, but after the compensation, not enough gain can be get. The conclusion of this scenario is: no target exists, which is coincide to the simulation conditions.

If there is a constant velocity target, and the target original states are: the level range is $850km$, the altitude is $10km$, the level velocity is $300m/s$.

The MTD result without any compensation is shown in Fig. 4 left. Because the velocity is low and the acceleration is 0, the range movement is lightly, and the range-cell crossing and the Doppler-cell crossing are not happen, an obvious peak is showing in the MTD result. For a constant velocity target, the acceleration estimated by HAF is 0, the MTD result after the compensation is nearly the same with that before compensating, as is shown in Fig. 4 right.

If there is a constant acceleration target, and the target original states are: the level range is $850km$, the altitude is $10km$, the rise velocity is $3000m/s$, the rise acceleration is $30m/s^2$, the level velocity is $1000m/s$, the level acceleration is $50m/s^2$.

The MTD result without any compensation is shown in Fig. 5 left, the high velocity caused range-cell crossing and the high acceleration caused Doppler-cell crossing, the target cannot be detected before compensating. The MTD result after the compensation is shown in Fig. 5 right, it is easy to see the target in that Figure.

If a constant velocity target and a constant acceleration target are exist, the multi-target detecting steps are shown in the flow chart

The targets original states are: the constant acceleration target: the level range is $850km$, the altitude is $10km$, the rise velocity is $1000m/s$, the rise acceleration is $30m/s^2$, the level velocity is $100m/s$, the level acceleration is $10m/s^2$. The constant velocity target: the level range is $850km$, the altitude is $5km$, the level velocity is $300m/s$.

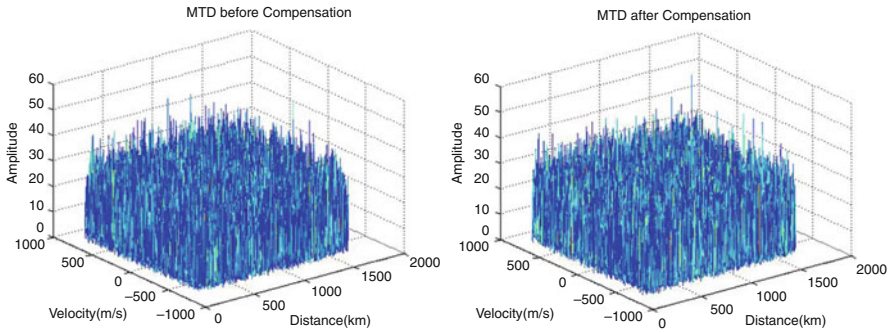

Fig. 3 MTD results before (*left*)/after (*right*) compensation without target

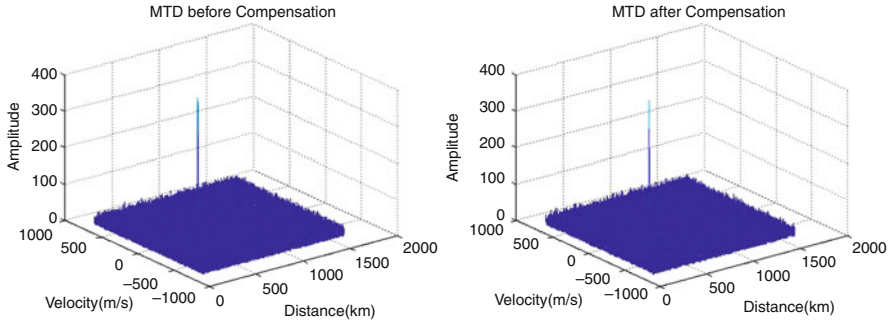

Fig. 4 MTD results before (*left*)/after (*right*) compensation with a constant velocity target

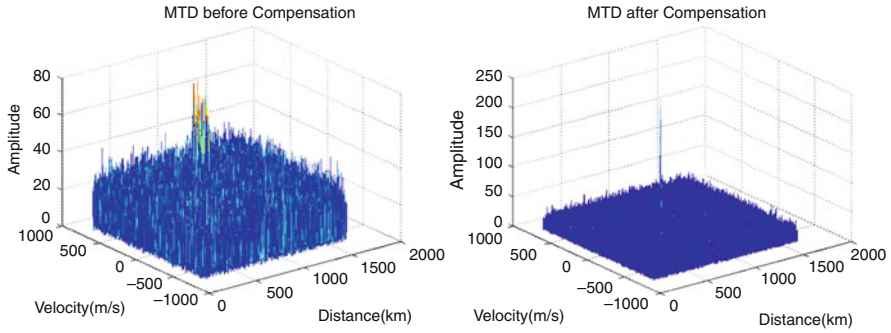

Fig. 5 MTD results before (*left*)/after (*right*) compensation with a constant acceleration target

The MTD results without any compensation are shown in Fig. 7 left. It is obviously to see, because of the high velocity and the large acceleration, the constant acceleration target echo cannot get enough gain by MTD and it is hardly seen in the Figure, while the low velocity and zero acceleration for the constant

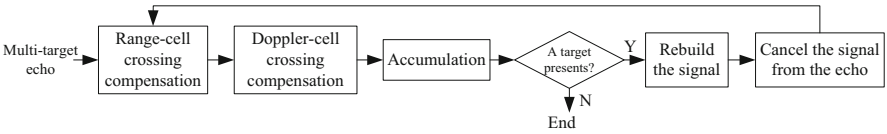

Fig. 6 The flow chart for multi-target detection

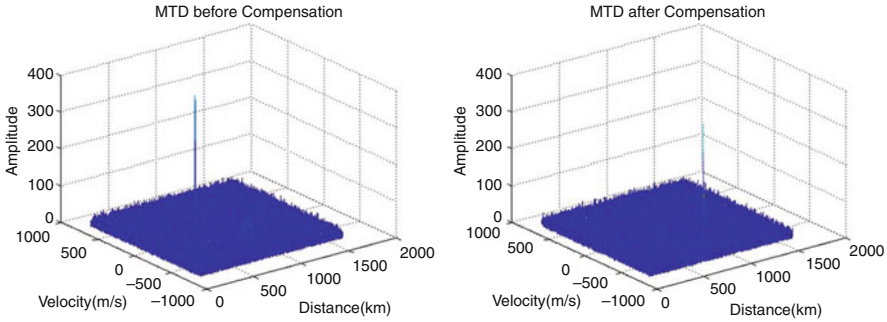

Fig. 7 MTD results before (*left*)/after (*right*) compensation with two targets

velocity target, its echo gains an obvious peak by MTD. From this, the constant velocity target can be detected, but the constant acceleration one cannot.

According to Fig. 6, cancel the constant velocity target from the echo, and repeat the compensation and accumulation. The MTD result is shown in Fig. 7 right, and the constant acceleration target can be detected now.

6 Conclusions

Detecting and separating different moving styles targets of OTHR is studied. The echo with range-cell crossing and Doppler-cell crossing is educed firstly, and then a scheme for coherent accumulation of multi-target is proposed. This scheme combines RFT with HAF, compensates the range-cell crossing and Doppler-cell crossing very well, and actualizes the coherent accumulation of the echo, on condition that there's no prior information of the targets. Lastly, four possible target detection backgrounds are based to carry out the simulations, and the simulations results show that the scheme proposed can detect different moving styles targets validly.

Acknowledgements This work is supported by the National Natural Science Associated Foundation (no. 11076006) and National Natural Science Foundation of China (no. 61032010 and no. 61201280).

References

1. Headrick JM, Skolnik MI (1974) Over-the-horizon radar in the HF band. J Proc IEEE 62:644–673
2. Barnum JR (1986) Ship detection with high resolution HF skywave radar. J IEEE J Ocean Eng OE-11:196–210
3. Headrick JM, Thomason JF (1998) Application of high-frequency radar. J Radio Sci 33:1045–1054
4. Harmanci K, Krolik J (2000) Adaptive temporal processing for equatorial spread Doppler clutter suppression. C In Proceedings of ICASSP'00, p 3041–3044
5. Kun Lu, Xingzhao Liu (2004) Enhanced maneuvering targets detection via po1ynomia1 phase modeling in over-the-horizon radars. C Proceedings of 2004 I.E. radar conference, pp 444–449
6. Turley MDE (1997) Hybrid CFAR techniques for HF Radar. C IEE Radar 97:36–40
7. Kun L, Liu X (2005) Enhanced visibility of maneuvering targets for high-frequency over-the-horizon radar. J IEEE Trans Antennas Propag 53:404–411
8. Jia X, Ji Y, Peng Y, Xia X (2011) Radon-Fourier transform for radar target detection, 1: generalized Doppler filter bank. J IEEE Trans Aerosp Electron Syst 47:1186–1202
9. Jia X, Xia X, Peng S, Ji Y, Peng Y, Qian L (2012) Radar maneuvering target motion estimation based on generalized Radon-Fourier Transform. J IEEE Trans Signal Process 60:6190–6201
10. Fraser GJ, Boashash B (1992) High-order ambiguity functions and time-varying higher-order spectra. C In Proc ISSPA 92:242–245
11. Peleg S, Friedlander B (1995) The discrete polynomial-phase transform. J IEEE Trans Signal Process 43:1901–1914

The Performance Study of Positioning and Tracking in Dynamic Model

Anhong Tian, Mu Zhou, and Chengbiao Fu

Abstract In the process of maneuvering target tracking, there has the phenomenon of non-linear and linear model estimation. In order to deal with this problem, this paper studies the dynamic positioning and tracking algorithm based on EKF (Extended Kalman Filter), which adopts Singer model in y direction and Uniform motion model in x direction . The simulation results show that positioning result has a precision of 15 m, the EKF method can be used effectively to restrain errors and get high precision.

Keywords Global positioning system • Positioning tracking error • Kinematic model • Extended kalman filter

1 Introduction

GPS (Global Positioning System) are worldwide, all-weather navigation system, which can provide three-dimensional positioning, velocity and time synchronization. So, localization or position estimation is one of the most important capabilities of GPS navigation system.

Design of state space model and estimation filter is the key technology [1] in the field of maneuvering target tracking. The estimation theoretic algorithm based on Kalman filter (KF) is the optimal approaches to positioning, but KF is only applied to the situation that filter error and the forecast error is small, otherwise the initial covariance estimate would fall too fast, which leads to instability and even divergent.

A. Tian (✉) • C. Fu
Department of Computer Science and Engineering, Qujing Normal College, Qujing, China
e-mail: tianfucb@gmail.com; tianah841023@gmail.com

M. Zhou
Department of Communication and Information Engineering, Chongqing University of Posts and Telecommunications, Chongqing, China

B. Zhang et al. (eds.), *The Proceedings of the Second International Conference on Communications, Signal Processing, and Systems*, Lecture Notes in Electrical Engineering 246, DOI 10.1007/978-3-319-00536-2_107,

In order to solve the problem of non-Gaussian and non-linear filtering, we can adopt EKF algorithm, which is based on the principle of linearizing the state and measurement models by using Taylor series expansions [2]. This paper presents EKF to track positioning trajectory, theoretical analysis and simulation results demonstrate that EKF algorithm is an effective method to track the target in GPS positioning system.

2 Extended Kalman Filter Basic Principle

The filtering model [3] used in the EKF is defined as follows:

$$X_k = F(X_{k-1}, k-1) + Q_{k-1} \tag{1}$$

$$Z_k = H(X_k, k) + R_k \tag{2}$$

Where X_k is the state, Z_k is the measurement, Q_{k-1} is the process noise, R_k is the measurement noise, F is the dynamic model function and H is the measurement model function.

The EKF algorithm is represented [4] as follows:

$$\hat{\boldsymbol{X}}_{k/k-1} = \boldsymbol{A}\hat{\boldsymbol{X}}_{k-1} \tag{3}$$

$$\boldsymbol{P}_{k/k-1} = \boldsymbol{A}\boldsymbol{P}_{k-1}\boldsymbol{A}^T + \boldsymbol{Q} \tag{4}$$

$$\boldsymbol{K}_k = \boldsymbol{P}_{k/k-1}\boldsymbol{H}_k^T\left(\boldsymbol{H}_k\boldsymbol{P}_{k/k-1}\boldsymbol{H}_k^T + \boldsymbol{R}_k\right)^{-1} \tag{5}$$

$$\hat{\boldsymbol{X}}_k = \hat{\boldsymbol{X}}_{k/k-1} + \boldsymbol{K}_k\left[\boldsymbol{Y}_k - h\left(\hat{\boldsymbol{X}}_{k/k-1}, k\right)\right] \tag{6}$$

$$\boldsymbol{P}_k = (\boldsymbol{I} - \boldsymbol{K}_k\boldsymbol{H}_k)\boldsymbol{P}_{k/k-1} \tag{7}$$

3 GPS State Equations

Singer model and Uniform motion model are typical maneuvering model, which are flexible to describe the movement of targets [5], the maneuvering target dynamics can be described to a standard form as follows:

$$\boldsymbol{X}_k = \boldsymbol{A}\boldsymbol{X}_{k-1} + \boldsymbol{W}_{k-1} \tag{8}$$

Where $X_k = [x(k), x_\circ(k), y(k), y_\circ(k), y_{\circ\circ}(k)]^T$, $x(k)$, $x_\circ(k)$ are the position and the speed in x direction respectively, $y(k)$, $y_\circ(k)$, $y_{\circ\circ}(k)$ are the position, the velocity and the acceleration in y direction respectively.

The transition matrix A is given by:

$$\boldsymbol{A} = \begin{bmatrix} 1 & T & 0 & 0 & 0 \\ 0 & 1 & 0 & 0 & 0 \\ 0 & 0 & 1 & T & (\alpha T - 1 + e^{-\alpha T})/\alpha^2 \\ 0 & 0 & 0 & 1 & (1 - e^{-\alpha T})/\alpha \\ 0 & 0 & 0 & 0 & e^{-\alpha T} \end{bmatrix}$$

Where α is the reciprocal of maneuver time constant, T is the sampling time. The covariance matrix $\boldsymbol{W}_k$ is represented by:

$$\boldsymbol{Q} = E\left[W_k W_k^T\right] = 2\alpha\sigma_m^2 \begin{bmatrix} T^3/3 & T^2/2 & 0 & 0 & 0 \\ T^2/2 & T & 0 & 0 & 0 \\ 0 & 0 & q_{11} & q_{12} & q_{13} \\ 0 & 0 & q_{21} & q_{22} & q_{23} \\ 0 & 0 & q_{31} & q_{32} & q_{33} \end{bmatrix}$$

Where

$$q_{11} = \frac{1}{2\alpha^5}\left(1 - e^{-2\alpha T} + 2\alpha T + \frac{2\alpha^3 T^3}{3} - 2\alpha^2 T^2 - 4\alpha T e^{-\alpha T}\right)$$

$$q_{12} = q_{21} = \frac{1}{2\alpha^4}\left(e^{-2\alpha T} + 1 - 2e^{-\alpha T} + 2\alpha T e^{-\alpha T} - 2\alpha T + \alpha^2 T^2\right)$$

$q_{13} = q_{31} = \frac{1}{2\alpha^3}(1 - e^{-2\alpha T} - 2\alpha T e^{-\alpha T})$, $q_{22} = \frac{1}{2\alpha^3}(4e^{-\alpha T} - 3 - e^{-2\alpha T} + 2\alpha T)$
$q_{23} = q_{32} = \frac{1}{2\alpha^2}(e^{-2\alpha T} + 1 - 2e^{-\alpha T})$, $q_{33} = \frac{1}{2\alpha}(1 - e^{-2\alpha T})$

4 GPS Measurement Equation

As everyone knows, it needs at least four satellites to calculate the receiver's dimensional coordinate and clock offset, the true distances between a receiver and a satellite can be expressed as follows:

$$\begin{cases} r_1 = \sqrt{(x_1 - x_u)^2 + (y_1 - y_u)^2 + (z_1 - z_u)^2} + ct_u \\ r_2 = \sqrt{(x_2 - x_u)^2 + (y_2 - y_u)^2 + (z_2 - z_u)^2} + ct_u \\ r_3 = \sqrt{(x_3 - x_u)^2 + (y_3 - y_u)^2 + (z_3 - z_u)^2} + ct_u \\ r_4 = \sqrt{(x_4 - x_u)^2 + (y_4 - y_u)^2 + (z_4 - z_u)^2} + ct_u \end{cases} \tag{9}$$

Where (x_i,y_i,z_i) denotes the coordinate of the GPS satellite, (x_u,y_u,z_u) denotes the receiver position, r_i denotes pseudo-range observation, t_u denotes receiver clock offset, c is the speed of light, (x_u,y_u,z_u,t_u) are four unknowns parameters.

Then, the nonlinear measurement model can be presented [6] as follows:

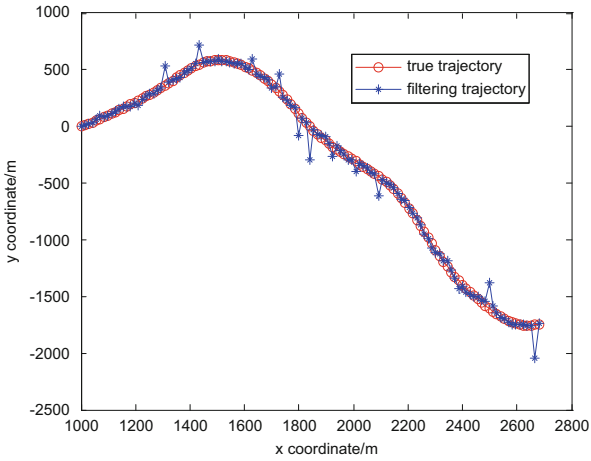

Fig. 1 The trace of target tracking

$$\boldsymbol{Y}_k = h(\boldsymbol{X}_k, k) + \boldsymbol{V}_k \tag{10}$$

Where $\boldsymbol{V}_k$ is the measurement noise vector, $h(X_k,k)$ denotes the observation matrix.

5 Simulation Results and Analysis

In order to test the performance of algorithm, this paper adopts 4 GPS satellites to simulate. The experiments are developed under the MATLAB 7.1 simulation environment. In x direction, the target model is Uniform motion model, and the target model is Singer model in y direction.

Supposing initial state vector is $X(0) = [1000,12,0,10,0]^T$, the total simulation time is 200 s, the sample interval is 1 s, the acceleration variance is 3.6, the motor frequency is 0.1.

The simulation results are shown in Figs. 1 and 2.

Figure 1 compares their motion trace between true trajectory and filtering trajectory. Figure 2 compares their positioning tracking error. According to these simulation results, we know that Fig. 1 shows the motion trace obtained by EKF algorithm, filtering trajectory can make the good match with the true trajectory, filtering trajectory is consistent with the true trajectory basically. Figure 2 shows their tracking error in x direction and y direction, the average position estimation error obtained by EKF algorithm in x direction is 15 m, the average position estimation error obtained by EKF algorithm in y direction is 16 m. The simulation results have demonstrated that EKF can still be relatively satisfied with the positioning and tracking performance

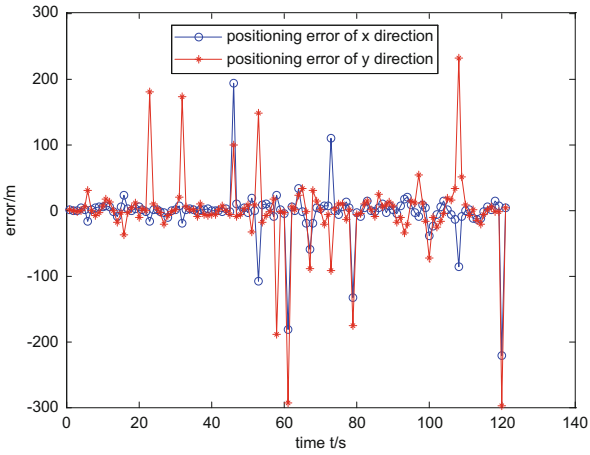

Fig. 2 The positioning tracking error

6 Conclusion

In this paper, the Extended Kalman Filter algorithm is introduced to be applied in the state estimation of GPS navigation system, and the simulation results show the superior performance of the EKF, filtering trajectory is consistent with true trajectory basically, the positioning error is small, which can meet the demands of positioning accuracy and real-time.

Acknowledgments This work was supported by Science and Technology Project of Chongqing Municipal Education Commission under Grant KJ130528, and Nature Science Foundation of Yunnan Province Education Department under Grant 2013Y017 about "the research of optimized satellite selection algorithm based on maximum determinant in positioning system", and Nature Science Foundation of Qujing Normal College under Grant 2012QN022 & 2012QN023 about "the research of satellite selection algorithm in global positioning system".

References

1. Ma Di, Er Meng Joo, Lim Hock Beng (2008) A Comprehensive study of Kalman Filter and Extended Kalman Filter for target tracking in Wireless Sensor Networks. IEEE International conference on systems, man and cybernetics, pp 2792–2797. doi:10.1109/ICSMC.2008.4811719
2. Ping Y, Xingqun Z, Yanhua Z (2011) Mended EKF-based GPS/INS tight coupling simulator. Adv Mat Res 271–273:609–615. doi:10.4028/www.scientific.net/AMR.271-273.609
3. Zhang Haitao, Rong Jianet et al (2008) The application and design of EKF smoother based on GPS/DR integration for land vehicle navigation. In: Proceedings of 2008 Pacific-Asia workshop on computational intelligence and industrial application, PACIIA 2008, vol 1, pp 704–707. doi:10.1109/PACIIA.2008.131

4. Haitao Z, Yujiao Z (2011) The performance comparison and analysis of extended Kalman filters for GPS/DR navigation. Optik 122(9):777–781. doi:10.1016/j.ijleo.2010.05.023
5. Kang Hangoo, Yun Jaeoh, Kim Seokyoung, Lee Jihong (2010) Mobile robot localization by EKF and indoor GPS based on eliminated maximum error anchor. Proceedings of the IASTED International conference on robotics, Robo, p 84–88. doi:10.2316/P.2010.703-054
6. Tian Zengshan, Lei Luo (2008) Particle filter positioning and tracking based on dynamic model. 4th IEEE conference on automation science and engineering, CASE, p 756–759. doi:10.1109/COASE.2008.4626430

Adapting Traceability System to Origin Positioning System for Agricultural Product from an Electronic Scale Using GPS

Jing Xie and Chuanheng Sun

Abstract To overcome the limitations of current agricultural products traceability information obtaining methodology, we developed the OPSAP (origin positioning system of agricultural product) with electronic scales. The positioning system is a software model working with the electronic scale and providing objective location information for the whole traceability system. The electronic scale not only has the weighting function, but also provides a method for determining location where the scale positioned. This article establishes the OPSAP and changes traceability system made to support the TSAP (traceability system of agricultural product). Together, the two modules provide customers the unique ability to obtain the agricultural products' origin information through the traceability system. The application experiments showed that this was an effective way to complete agricultural products traceability chain.

Keywords Origin positioning • IOT • QuickHull algorithm • Point in polygon • Traceability system

1 Introduction

Nowadays consumers are informed and aware and they demand much more information about agricultural products and food, not only its prices, but also the safety information [1, 2]. Meanwhile, demand from consumers for organically produced agricultural products and foodstuffs, which contribute to the health and well-being of people, is increasing. In China, farmers have been developing organic farming systems for decades. In response to the rising demand, agricultural products and foodstuffs are being placed on the market with indications stating or implying to

J. Xie • C. Sun (✉)
National Engineering Research Center for Information Technology in Agriculture, Beijing 100097, China
e-mail: xiej@nercita.org.cn; sunchh@nercita.org.cn

B. Zhang et al. (eds.), *The Proceedings of the Second International Conference on Communications, Signal Processing, and Systems*, Lecture Notes in Electrical Engineering 246, DOI 10.1007/978-3-319-00536-2_108,

purchasers that they have been produced organically or without using synthetic chemicals. Measures for protecting organic farming have been taken.

Traceability is considered as one of the most effective ways to provide assurance with regard the source and production systems. It can provide consumers with accurate information, ensure conditions of fair competition for the producers of organic products and improve the credibility of such products in the eyes of consumers [3]. The present study of determining agricultural product origin, which is the starting point of the traceability system, was encoding for each product origin. It was simple, but lack of security and objective [3, 4].

Global Positioning System (GPS) receivers provide a method for determining location anywhere on the earth. Accurate, automated position tracking with GPS receivers allows farmers and agricultural service providers to automatically record data. In this article, an origin positioning system of agricultural product based on GPS is developed and intended to record the location information of origin. This is applied in the traceability chain to meet the growing requirements of food security [5, 6].

2 System Description

2.1 Equipment

Whereas the traceability system of agricultural product runs on a web service to provide customers traceability information, the origin positioning system runs on an electronic scale (connected with computer) in the field. Agricultural products' information is generated through a connection to the traceability system database that stores the products' basic descriptions, origin informational, circulation process information and so on. Products' basic information and origin information are acquired by the electronic scale with GPS module, after that the whole information is uploaded to the server (Fig. 1).

Each acquisition system of agricultural product information consists of the following:

1. Electronic scale with GPS module and Ethernet interface;
2. Local storage unit;
3. Computer.

The electronic scale is commonly used in the field. Therefore, it registers products' information by communicating with a local database. When work ended, the records in the local database would be transferred to a work computer, and uploaded to the remote server after data processing.

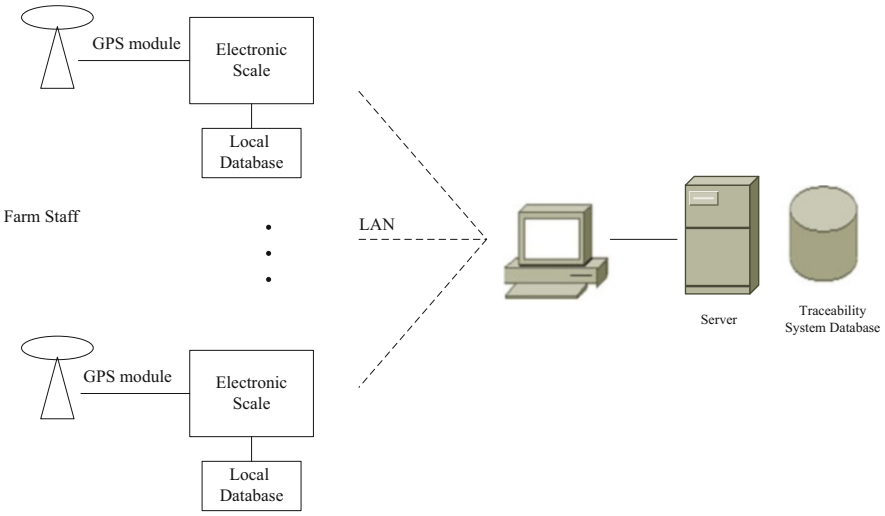

Fig. 1 Origin positioning system of agricultural product

2.1.1 Electronic Scale with GPS

Electronic scale is widely used in agricultural occasions, which usually measures weight of an item and calculates a price of the item by multiplying the weight of the item by a unit price of the item. It has printing device for printing out item data on a label paper. In this paper, we developed an electronic scale consisting of a GPS device for positioning current location in agricultural product origin. The whole system consists of CPU, load cell, operating panel, display module, storage unit and GPS module (Fig. 2):

Basic information of agricultural products, such as names, prices, are entered through load cell, and saved to flash-memory ROM. The information can be displayed, encrypted, transferred and printed in labels. RFID model records responsibility subject information. Data, include the basic information, weights, GPS information, can be saved in the local storage unit.

Global Positioning System (GPS) receivers provide a method for determining location anywhere on the earth [7–11]. Accurate, automated position tracking with GPS receivers allows farmers and agricultural service providers to automatically record data. The project adopts GS-216 to obtain location information. GS-216 is an outstanding high sensitivity personal GPS receiver which position accuracy is 10 meters CEP. While GS-216 is connected with the electronic scale with RS-232. Material object image such as the one is shown in Fig. 3.

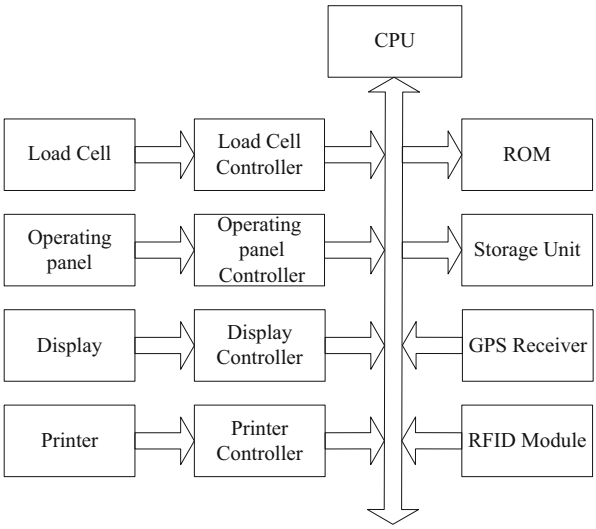

Fig. 2 Composition of traceable electronic scales

Fig. 3 Electronic scale with GS-216

2.1.2 Data Receiving Software

The data which electronic scale upload includes date, products' name, price, trace code, latitude and longitude. A data receiving software was designed to store the data transformed by the electronic scale (Fig. 4).

2.2 Traceability System: Adaptations to Support OPSAP

The customers use traceability system to obtain safety information of agricultural product. Now with OPSAP, traceability system supports the customers the capability to know exactly where the agricultural products come from. In order to realize this function, we added an algorithm to the traceability system (Fig. 5).

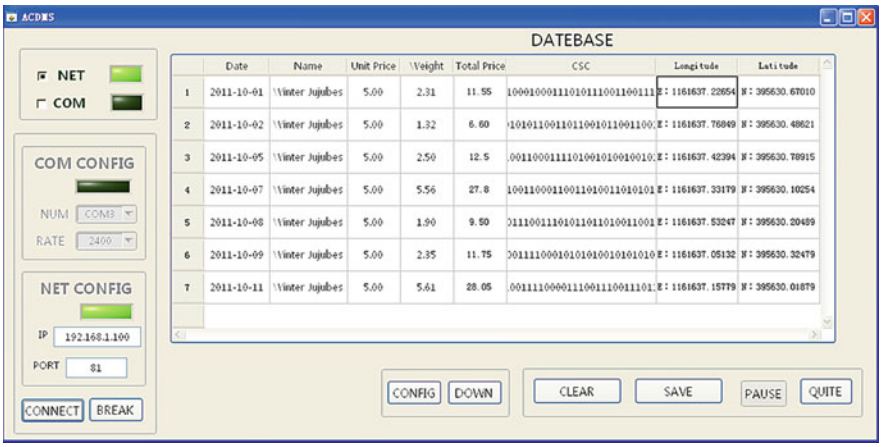

Fig. 4 Receive data from an electronic scale

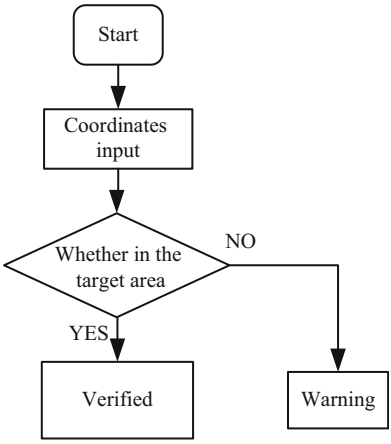

Fig. 5 Origin judgment flow chart

2.2.1 Bounding Areas Determination

When received these information, data processing system in the computer of the farm area needs an algorithm to establish the correspondence between coordinates and the origin. In the August of 2012, we did positioning experiments in the experimental plot of Beijing Academy of Agriculture and Forestry Sciences to see the real coordinates distribution. The experiments were designed to record the coordinate when the scale was printing the label. In a month later, the general data obtained by scales was shown in Fig. 6.

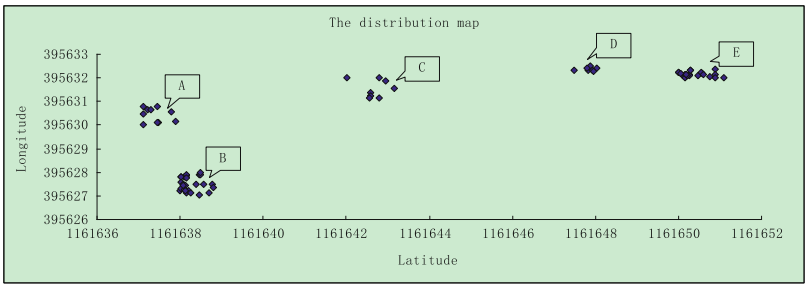

Fig. 6 The distribution map of coordinates

We can find that these points are mainly concentrated in five locations. Now what we need to do is to calculate boundary of each region, which is the proper convex set that contains the whole points. Due to the number of the coordinates is not too big, we use the QuickHull algorithm to find the minimum convex hulls of polygons [12]. The algorithm uses a divide approach, and it is quite fast in most average cases, as well as its recursive nature allows a fast and yet clean implementation (Fig. 7).

Using C language to realize QuickHull algorithm, we got the convex hull of the five sets of points. The convex hull of Part A is shown in Fig. 8

2.2.2 Point in Polygon

According to the analyses above, we can get the boundary points of the positioning area of electronic scales. Then when customers using traceability system to find out whether the coordinates printed on the product's label are belonging the target origin, the problem becomes into testing whether a point is inside a polygon.

Testing whether a point is inside a polygon is a basic operation in computer graphics. Essentially, it says that a point is inside a polygon if, for any ray from this point, there is an odd number of crossings of the ray with the polygon's edges. In this paper, we use the ray casting algorithm which is to test how many times a ray, starting from the point and going any fixed direction, intersects the edges of the polygon. If the point in question is not on the boundary of the polygon, the number of intersections is an even number if the point is outside, and it is odd if inside. The schematic of ray casting algorithm is shown in Fig. 9.

Writing this algorithm into the origin positioning software, we can realize the function that trace the origin of agricultural products through the coordinates. However, we have to verify the accuracy of the positioning software. So this software has not been applied to the traceability website (Fig. 10).

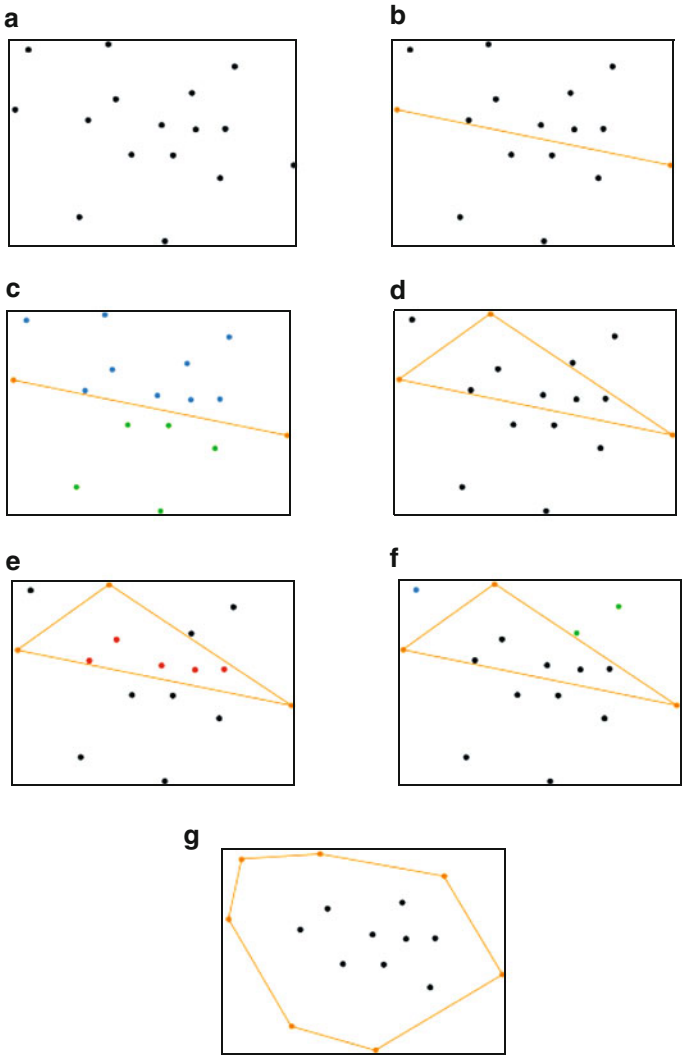

Fig. 7 Schematics of QuickHull algorithm. (**a**) Initial set of points. (**b**) Min/Max horizontal points. (**c**) Divide the point set into left and right. (**d**) Point with maximal distance to the line. (**e**) Points inside the triangle are ignored. (**f**) Divide the point set into left and right again. (**g**) the convex hull polygon

3 Conclusions and Future Outlook

Traceability is ultimately about trust. Consumers trust for the products and brands that they purchase, and suppliers trust within a complete food security chain. Especially nowadays, traceability has been driven by issues of food safety, product

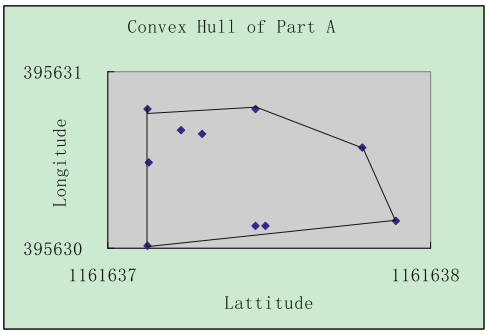

Fig. 8 The Convex Hull of Part A

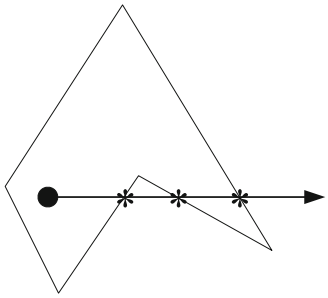

Fig. 9 Schematic of ray casting algorithm

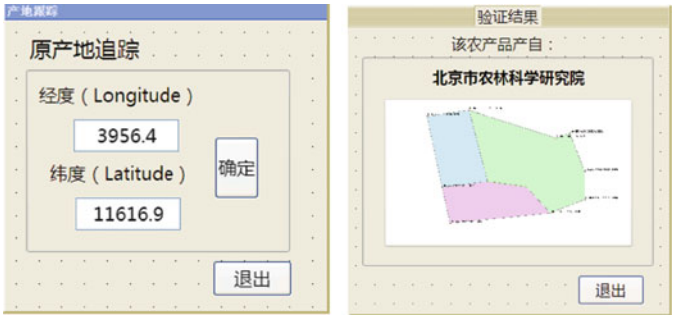

Fig. 10 OPSAP verify a coordinate

recalls and fraudulent claims for higher value food products such as organic. To achieve requirements of the organic agricultural products traceability, more and more information technologies have been employed.

It is necessary to manage a system to enhance the objectivity and credibility of the retroactive chain. This article presented a system for organic agricultural products origin anti-counterfeiting, through an electronic scale equipped with

GPS model, by recording the current location while weighting the agricultural products. To achieve the anti-counterfeiting target, default coordinates which were achieved by doing prepare experiments were presented in the electronic scale, and compared with the current coordinate. The comparison result is encrypted and printed to labels.

So far, we have focused on perfecting the electronic scale with GPS model and doing experiments to determine the range where the device usually be used. The results have not been verified in practical. So we plan to test our approach on additional agricultural products origins in the near future.

Acknowledgments This research was supported by the High-Tech Research and Development Program of China (No: 2012AA101905-02). The team included Yang Xinting, Sun Chuanheng, Li Wenyong, Zhou Chao, Wu Xiaoming, Du Xiaowei. All of the mentioned support and assistance are gratefully acknowledged.

References

1. Xi Wang, Xinzhong Wang, Weidong Zhuang (2011) Study for organic soybean production information traceability system based on web. Computer and Computing Technologies in Agriculture IV-IFIP Advances in Information and Communication Technology 345:567–572
2. Xue Dong (2010) A review of studies on controlling of quality of organic vegetable and traceable system. J Jilin Agric Sci 35(3):51–56
3. Guangwei Tan, Xi Wang, Weidong Zhuang (2010) Research on management of traceability of organic agricultural products quality based on ASP. J Agric Mechanization Res 1:24–29
4. Wenjun Zhang (2005) Development of interface and program of navigation information retrieval between embedded system and GPS. Comput Eng 31(18):210–212
5. Bernhard Buchli, Felix Sutton, Jan Beutel (2012). GPS-equipped wireless sensor network node for high-accuracy positioning applications. 9th European conference on wireless sensor networks (EWSN2012). Lecture notes on computer science, pp 179–195
6. Yuqi Wang, Hui Qi (2012) Research of intelligent transportation system based on the internet of things frame. Wirel Eng Technol 3:160–166
7. Atanas Atanasov, Plamen Kangalov, Kaloyan Stoianov et al (2010) Some aspects in preparation of transport and field operations on large Bulgarian farms by using GPS and Google earth engineering for rural development 5: 27–28
8. Hnin Si, Zaw Min Aung (2011) Position data acquisition from NMEA protocol of global positioning system. Int J Comput Electr Eng 3(3):353–357
9. Jianhua Tang (2009) Design and implementation of anti-fake original label management system. Agr Netw Inf 6:13–16
10. NMEA-0183: the National Marine Electronics Association
11. Dejun Qian, Zhe Zhang, Chen Hu (2007) On parsing of NMEA0183 protocol. Chin J Electron Devic 30(2):698–701
12. C. Bradford Barber, David P. Dobkin, Hannu Huhdanpaa (1996) The Quickhull algorithm for convex hulls. ACM Trans Math Softw 22(4):469–483

Improved Positioning Algorithm Using the Linear Constraints of Scatterer in Two Base Stations

Zhou Fei and Fan Xin-Yue

Abstract How to restraint non-line-of-sight (NLOS) error is an interesting field. Traditional way to restraint NLOS mainly includes: NLOS identify and NLOS reconstruction. In high multipath environment, these ways can not get good performance. The way proposed by this paper mainly utilizes the linear constraints of scatterer in two base stations to improve traditional way. Simulation results shows improved positioning algorithm can suit for complicate multipath environment and get good positioning precision.

Keywords NLOS • Multipath • Reconstruction • Scatterer

1 Introduction

Positioning Algorithm Using scatterer information is a developing idea to restraint NLOS error in recent years. These are mainly divided into two kinds, one way is utilizing different scatterer model to get some statistic information, e.g. Probability density function (pdf) of time-of-arrival (TOA) or angel-of-arrival (AOA). Then some algorithms was used to reconstruct parameters that relate to positioning [1, 2]. Another way does not need scatterers model and statistic information. It mainly utilizes geometry layout relation among base station, scatterer and mobile station (MS) to design positioning model. And uncertain NLOS is transformed to fixed factor. Influence of NLOS error would be weakened. So positioning error mainly influenced by measurement parameters. It can improve positioning precision very much without doubt [3–5].

Z. Fei (✉) • F. Xin-Yue
School of Communication and Information Engineering, Chongqing University Posts and Telecommunication, 400065 ChongQing, China
e-mail: zhoufei@cqupt.edu.cn

B. Zhang et al. (eds.), *The Proceedings of the Second International Conference on Communications, Signal Processing, and Systems*, Lecture Notes in Electrical Engineering 246, DOI 10.1007/978-3-319-00536-2_109,

In this paper, we mainly consider the kind of algorithm, If MS and several scatterer are in the same line, their Doppler frequency shift of signal is the same. So three cases are exits: (1) One scatterer and MS are in the same line; (2) Two scatterers and MS are in the same line; (3) Three or more scatterers and MS are in the same line.

The third case is studied in literature [6]. However, the second case is more generally than the first case. So how to implement positioning in second cases is more valuable. Aimed to high performance of line constraint positioning and inappeasable precondition, this paper proposed an improved positioning algorithm using the linear constraint in two base stations.

This paper is organized as follows, in Sect. 2, multipath signal match is presented and analyzed. In Sect. 3, based on signal match results, TOA reconstruction is implemented to positioning estimation. In Sect. 4, a common positioning algorithm is introduced. Lastly, the conclusion and simulation are drawn in Sect. 5

2 Pairing of Multi-Path Signal About Different Base Station

Figure 1 gives brief frame of the improved algorithm, the whole algorithm includes three steps.

(1) Multipath Signal Match: Base station receives multipath signal and measures its Doppler frequency shift. Signal that reflected from scatterers to base station are matched and selected to acquire two scatterers that in the same line with MS.
(2) TOA Reconstruction: After multipath signal match and scatterer selection, scatterer can be positioned based on its AOA that measured by two base stations. Base on serious research proposed by this paper, distances between MS and two scatterers can be computed. Lastly, combined to linear constraint of two scatterers, TOA reconstruction can be implemented.
(3) Positioning estimation using TOA: Two scatterers are regard as virtual base station. Added that two real base stations, four TOA can be gotten. So some mature algorithms can be used to compute positioning of mobile station.

Mentioned previously, multipath components that reflected from the same scatterer to different base stations and from different scatterer that the same line with MS to the same base station is all equivalent. So the key of multipath signal match is how to distinguish the same Doppler frequency multipath signals that received from the same base station and how to pair multipath signal that reflected from the same scatterers to different base station correctly. In Fig. 2, positioning parameter (xsi,ysi) of ith scatterer is derived by (1)

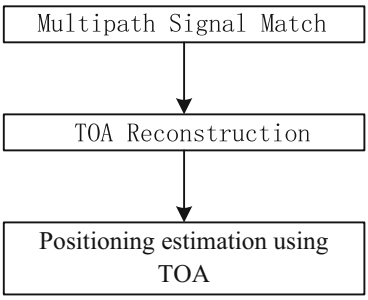

Fig. 1 Positioning Algorithm Frame

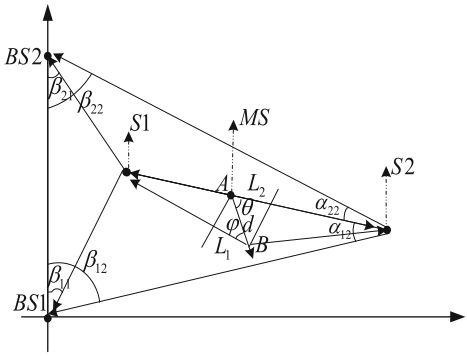

Fig. 2 Layout of Mobile Terminal

$$x_{Si} = \frac{x_2 - x_1 \tan\beta_{2i} \tan\beta_{1i} + (y_1 - y_2)\tan\beta_{2i}}{1 - \tan\beta_{1i}}$$
$$y_{Si} = (x_{Si} - x_1)\tan\beta_{1i} + y_1 \tag{1}$$

Where, (x_1,y_1) and (x_2,y_2) are positioning parameter of two base stations. β_{ji} is DOA of ith Scatterer that measured by jth base station. And the linear distance between ith base station and jth base station is derived by (2)

$$L_{ji} = \sqrt{\left(x_{Si} - x_j\right)^2 + \left(y_{Si} - y_j\right)^2} \tag{2}$$

If measurement error is zero, (3) is logical.

$$L_i = l_{1i} - L_{1i} = l_{2i} - L_{2i} \tag{3}$$

Where, (4) is the measurement error.

$$EN = [(l_{2i} - L_{2i}) - (l_{1i} - L_{1i})]^2 \tag{4}$$

When EN is close to minimum, two sets of data is matching. So four sets of data from two base stations, (l_{11},β_{11}) and (l_{21},β_{21}), (l_{11},β_{11}) and (l_{22},β_{22}), (l_{12},β_{12}) and

(l_{21},β_{21}), (l_{12},β_{12}) and (l_{22},β_{22}), are grouped four pair. Their EN can be computed by (4). The set of data that its EN is minimum must be reflected by the same scatterer and measured by two base stations separately, in others word, the set is correct pair. So the others set of data measured by the same two base stations is the others correct pair.

3 TOA Reconstruction

If multipath signal that different base stations is success to pair, their positioning parameter of Scatterers S_i and S_j, (x_{Si},y_{Si}) and (x_{Sj},y_{Sj}), can by computed by (1). And distance between two Scatterers can by derived by (5)

$$L_S = \sqrt{\left(x_{Si} - x_{Sj}\right)^2 + \left(y_{Si} - y_{Sj}\right)^2} \tag{5}$$

So their line relation among S_i, S_j and MS can be determined by L_i, L_j and L_S.
if $L_j > L_S$ and $L_j > L_i$, S_i is located between S_j and MS.
if $L_i > L_S$ and $L_i > L_j$, S_j is located between S_i and MS
if $L_S > L_i$ and $L_S > L_j$, MS is located between S_j and S_i.
In case (1), S_i, S_j and $BS1$ can form a triangle, So (6) can be derived.

$$\cos\alpha_{1j} = \frac{L_S^2 + L_{1j}^2 - L_{1i}^2}{2L_S L_{1j}} \tag{6}$$

And In another triangle formed by S_j, MS and $BS1$, the line distance L_{line1} between MS and $BS1$, can be derived by (7), So TOA of $BS1$ is success to reconstruct.

$$L_{line1} = \sqrt{r_j^2 + L_{1j}^2 - 2r_j L_{1j}\cos\alpha_{1j}} \tag{7}$$

Similarly, the distance, L_{line2}, between MS and $BS2$,also can be derived by (8)

$$L_{line2} = \sqrt{r_j^2 + L_{2j}^2 - \frac{\left(L_S^2 + L_{2j}^2 - L_{2i}^2\right)r_j}{L_S}} \tag{8}$$

In case (2), according to triangle relations among S_j, S_i and $BSi(i = 1,2)$, L_{line1} and L_{line2} also can be acquired by (9). In others word, TOA reconstruction also can implemented.

$$L_{line1} = \sqrt{r_i^2 + L_{1i}^2 - \frac{\left(L_S^2 + L_{1i}^2 - L_{1j}^2\right) r_i}{L_S}}$$
$$L_{line2} = \sqrt{r_i^2 + L_{2i}^2 - \frac{\left(L_S^2 + L_{2i}^2 - L_{2j}^2\right) r_i}{L_S}} \quad (9)$$

Similarly, in case 3, The resolution of case (1) and (2) is still in effect.

4 Positioning Parameter of Mobile Computation

In Fig. 2, S_i,S_j can be consider as virtual base station. r_i and r_j are TOA about Line-of-Sight(LOS) from MS to two scatterers (Si,Sj). And TOA about LOS of $BS1$ and $BS2$ can be reconstruct effectively. So four TOA from different BS to MS can be used to compute positioning parameter about MS. Here, Least-Square algorithm is preferred and useful algorithm.

$$\left(x_j - x_1\right)x + \left(y_j - y_1\right)y = \frac{1}{2}\left[x_j^2 + y_j^2 - \left(x_1^2 + y_1^2\right) + r_1^2 - r_j^2\right] \quad (10)$$

Where, $r_j^2 = (x_j - x)^2 + (y_j - y)^2$; So (10) can be derived and represented by vector matrix form, (11):

$$AX = B \quad (11)$$

Where, $X = \begin{bmatrix} x \\ y \end{bmatrix}$ $A = \begin{bmatrix} x_2 - x_1 & y_2 - y_1 \\ x_{Si} - x_2 & y_{Si} - y_2 \\ x_{Sj} - x_{Si} & y_{Sj} - y_{Si} \end{bmatrix}$

$$B = \begin{bmatrix} \frac{1}{2}\left[x_2^2 + y_2^2 - \left(x_1^2 + y_1^2\right) + L_{line1}^2 - L_{line2}^2\right] \\ \frac{1}{2}\left[x_{Si}^2 + y_{Si}^2 - \left(x_2^2 + y_2^2\right) + L_{line2}^2 - r_i^2\right] \\ \frac{1}{2}\left[x_{Sj}^2 + y_{Sj}^2 - \left(x_{Si}^2 + y_{Si}^2\right) + r_i^2 - r_j^2\right] \end{bmatrix}$$

Lastly, positioning of MS can be computed by (12)

$$X = \left(A^T A\right)^{-1} A^T B \quad (12)$$

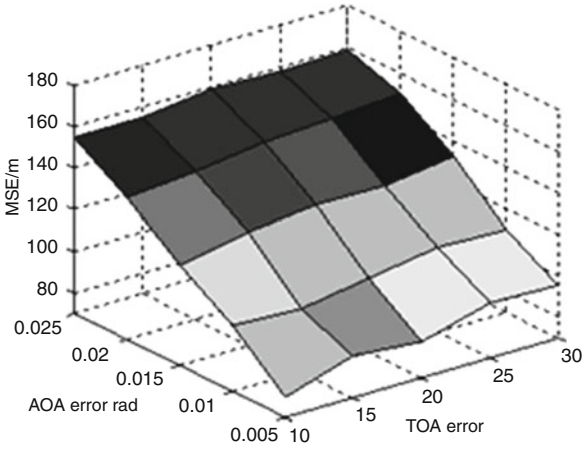

Fig. 3 MSE of different error about AOA and TOA

5 Simulation and Analysis

A macrocellular district is assumed, *BS*1 is located in the original point of Cartesian coordinate system, *BS*2 is located in (0,2000)m, and Base Station is stationary. Other parameters of simulation refer to the following table.

Figure 3 shows MSE of different TOA and AOA measurement errors in Disk of scatterers (DOS) model that its radius is 500 m. It concludes that AOA error influences positioning precision greater than the TOA error. So when AOA error is enough small, the influence of TOA error is a littler obvious. But if AOA error is enough large, positioning error mainly is influenced by AOA error.

Figure 4 shows RMSE comparison of different radius of model. Its model is DOS, its standard error of TOA measurement error is 1.5 m, and its standard error of AOA measurement error is 0.005rad. It concluded that performance of improved algorithm that proposed by this paper is better than traditional algorithm. The performance of traditional algorithm degrades obviously when radius of model turn large. But improved positioning algorithm using the linear constraints of scatterers in two base stations has better performance. Its positioning error is briefly stable.

Figure 5 gives comparison of positioning error of different multipath number in DOS model. It concluded that when multipath number is more, RMSE of positioning is smaller.

Lastly, from the above comparisons, improved algorithms have the better performance than traditional algorithm. So it is necessary to continue research further.

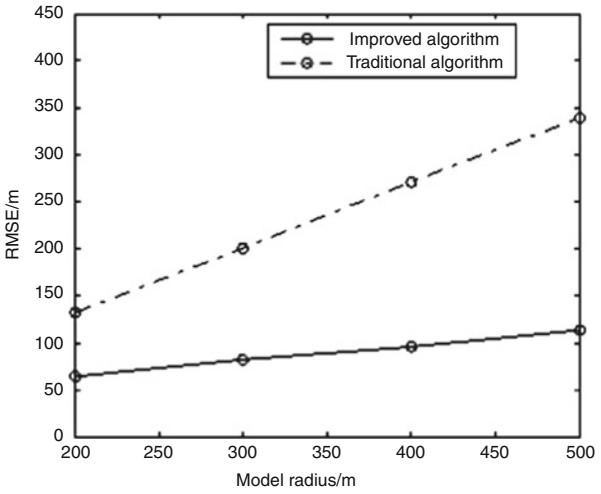

Fig. 4 RMSE of different radius of model

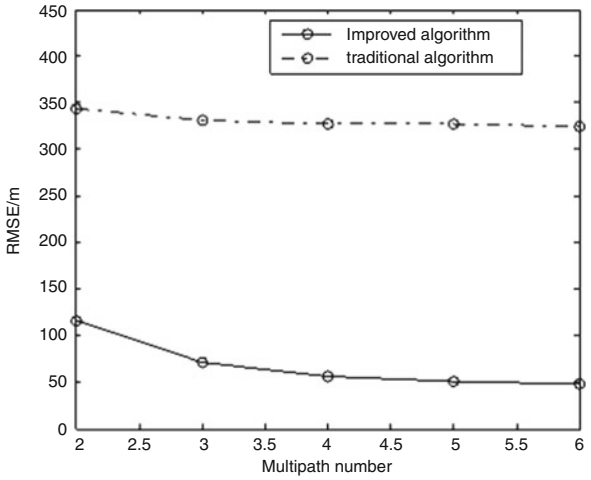

Fig. 5 Positioning Error of Different Multipath Number in DOS Model

References

1. Thomas NJ, Cruickshark DGM, Laurenson DI (2001) Calculation of mobile location using scatter information. Electronic Lett 37(19):1193–1194
2. Wan Q, Yang WL, Peng YN (2004) Closed-form solution to mobile location using linear constraint on scatterer. Electron Lett 40:883–884
3. TianChi YANG, Liang JIN (2011) Single station location method in NLOS environment: the circle fitting algorithm. SCIENCE CHINA Inf Sci 54(2):381–385
4. TianChi YANG, ChaoQun YU, TianPeng WANG, Liang JIN (2011) A single observer location method under the scatter signals position disturbance situation: the constraint total least square method. SCIENCE CHINA Inf Sci 54(1):146–152

5. Miao H, Yu K, Juntti M (2007) Positioning for NLOS propagation: algorithm derivation and Cramer-rao bounds. IEEE Trans Veh Technol 56(5):2568–2580
6. Venkatraman S, James Caffery JR. (2002) A statistical approach to non-line-of-sight BS identification. IEEE Wireless Personal Multimedia Communications(WPMC) Conference, 296–300

An Effective Phase-Based Localization Approach Under Multipath Environments

Yang Zhao, Kaihua Liu, Yongtao Ma, Liuji Zhou, and Jinlong Wang

Abstract Multipath channel has always been a big challenge in accurate indoor localization based on Radio Frequency Identification (RFID) technique. To mitigate this problem, we present a simple but effective localization approach which utilizes Phase of Arrival (POA) as the measurement information and linear least squares as geometrical localization estimation algorithm. In this approach, we make an accurate phase extracting criterion and also propose a reasonable line of sight (LOS) computation method which depends on the addition of the reference tags. Experimental results show that the proposed approach can achieve a position error of about 1 m under multipath environments and is robust to the environmental dynamics.

Keywords Phase of arrival (POA) • Linear least squares • Reference tags • Multipath environments

1 Introduction

With the popular of wireless localization services, high accuracy localization method under multipath environments is urgently needed for both commercial and governmental interests. Generally location estimation schemes can be classified as ranging approach (geometrical approach) and non-ranging approach (statistical approach). As for the ranging approach, the target location can be estimated by the geometrical relationship with the Euclidean distance between the reader and the tag. While in the non-ranging approach, the objective is to statistically minimize

Y. Zhao (✉) • K. Liu • Y. Ma • L. Zhou
School of Electronic Information Engineering, Tianjin University, Tianjin, China
e-mail: zyangtj@gmail.com

J. Wang
ZTE Corporation, Tianjin, China

B. Zhang et al. (eds.), *The Proceedings of the Second International Conference on Communications, Signal Processing, and Systems*, Lecture Notes in Electrical Engineering 246, DOI 10.1007/978-3-319-00536-2_110,

the estimation error of the channel parameters or the controlling parameters of the objective function [1], thus getting the minimized location error for the target localization. There are several kinds of signal measurement information used in the location estimation, such as Time of Arrival (TOA) [2, 3], Time Difference of Arrival (TDOA) [4], Direction of Arrival (DOA, angle of arrival (AOA)) [5], phase of arrival (POA) [6–8],and Received Signal Strength (RSS) [9]. And of course, these kinds of measurement information can also be combined to get a hybrid localization scheme, such as a fusion of TDOA and AOA [10].

Many researches have been devoted to the study of ranging approach by the above information. An important premise in TOA-based or TDOA-based ranging approach is that the multipath signals should be separable in time space, so most approaches are based on ultra wideband. As for DOA-based ranging approach, antenna arrays are widely used and many papers have demonstrated their effectiveness. Considering that the ambiguity of whole cycles is the main problem in POA-based ranging approach, dual frequency subcarriers and single frequency subcarrier were proposed [7], both of which could solve this problem effectively. Through previous study, we know there is a non-linear relationship between RSS and the distance, so RSS is rarely used in ranging approach and always mentioned in non-ranging approach where the reference tags contribute a lot.

The main work of this paper is that a POA-based localization approach under multipath environments is proposed, which is simple but very effective. The rest of the paper is organized as follows. In Sect. 2, a new phase extracting criterion after All-phase-FFT conversion are explained in detail and the line of sight (LOS) distance estimation method based on the addition of the reference tags is also proposed. In Sect. 3, experimental results are illustrated and show the improvement in location accuracy which can prove the effectiveness of this proposed method. In the end, the conclusion is presented in Sect. 4.

2 A POA-Based Localization Approach with Reference Tags

The most challengeable problem in POA-based localization approach is about the ambiguity of whole cycles. Subcarriers [7] can solve this problem successfully under line of sight (LOS), but still exist some problems unsolved in phase extracting. Here considering the multipath environments, we make a new phase extracting criterion and propose a more accurate LOS computation method with the addition of reference tags based on a single frequency subcarrier.

2.1 Phase Extracting Scheme

Here the location estimation depends on the phase difference $\Delta\Phi$ of the single subcarrier f_0. For the purpose of eliminating the ambiguity of whole cycles, the frequency of the subcarrier should be not too high, and guarantee that the round trip distance is shorter than the wavelength of the signal. Thus the duration of the subcarrier wave is among one period and the ambiguity problem is eliminated. The detailed procedure is expressed in [7], here we just propose a new and accurate phase extracting scheme. The propagation length L can be written as (1), the location estimation can be got by linear least squares (LLS).

$$L = \frac{c\Delta\phi}{4\pi f_0} \tag{1}$$

Among them, All-phase FFT can be used to get the accurate phase estimation, and the detailed algorithm process can be found in [11]. But some problems exist in phase extracting after All-phase FFT conversion, the corresponding criterion is proposed as follows.

Step1: All though the Sub-Nyquist Sampling can reduce the sampling requirement of the analog-to-digital converter, it will bring the cyclic extension in the frequency domain after All-phase FFT, as the frequency of the carrier (or - sub-carrier) is integer multiples of Sub-Nyquist Sampling frequency f_s. So we use (2) to limit the spectrum lines K of the carrier f to the sampling number N. As for the sum frequency and the difference frequency, the same processing is implemented. Where [•] means the integer conversion, it helps make the content integer. Then we can extract the phase value in the phase spectrum according to the spectrum line.

$$k = [(f - [f/f_s] \times f_s) \times N/f_s] \tag{2}$$

Step2: if the phase of the sum frequency is smaller than that of the difference frequency, we just add an extra 2π in the phase computation of the sum frequency.

Step3: Theoretically, the sum of the sum frequency phase φ_3 and the difference frequency phase φ_1 is as much as the twice of the carrier phase φ_2. Considering the addition of the noise, we set a new judging principle in (3).

$$\begin{cases} \varphi_2 + 360; & \varphi_1 + \varphi_3 > \alpha\varphi_2 \\ \varphi_3 + 360; & \varphi_1 + \varphi_3 > \beta\varphi_2 \end{cases} \quad \alpha \in (2,3) \quad \beta \in (1,2) \tag{3}$$

Through many experiments, the above principles are proved effective in phase extraction. Then we test the phase estimation accuracy under one path situation, i.e. line of sight (LOS), the results show that the phase extraction accuracy is

perfect, but under multipath environments, the results are becoming worse, which will be discussed in Sect. 3.

2.2 Refer-All-Phase-FFT

Considering that the single frequency subcarrier cannot provide preferable LOS estimation under multipath environments, we consider the addition of reference tags and name this approach Refer-All-phase-FFT. The key reason for the addition of reference tags is that the reference tags and the targets are subject to the same effect in the environment, so it can help increase location accuracy to some extent.

The simple propagation model in indoor condition can be shown in Fig. 1. Here we take three paths as an example, including the direct path (LOS), the wall reflection path (NLOS1) and the ground reflection path (NLOS2).

In this model, the wall reflection path (NLOS1) is supposed to be emanated from the V-reader1 which is symmetric with the reader by the wall, the ground reflection path (NLOS2) is supposed to be emanated from the V-reader2 which is symmetric with the reader by the ground. The three mixed paths can make the received phase complex, and the reflective coefficient will also add extra phase deviation. So the mixed receiving phase cannot extract the accurate phase difference under LOS, then the distance calculated from the (1) will bring huge error in location estimation.

Here we introduce the reference tags to increase the location accuracy, for the extraction of LOS phase from the mixed receiving phase is so difficult. In LANDMARC [9], the reference tags are chosen by the adjacent RSSI value between the target tag and the reference tag, and the K Nearest Neighbor (KNN) is used to estimate the location of the target.

From the (1), we can find that the phase has a linear relationship with the distance, so our principle of choosing the reference tags is the nearest neighbor in the mixed receiving phase value between the reference tag and target tag under one reader. Then we don't utilize the coordinate location of the reference tag for the location estimation like LANDMARC, we calculate the direct distance between the selected reference tag and the reader, and mark it as the direct distance between the target tag and the reader. After getting the corresponding direct distance between the target tag and all the readers, LLS can be utilized to get the final location estimation.

The reason that we prefer the direct distance of the reference using the LLS to the coordinate location of the reference using KNN can be discussed in Fig. 2. The four red boxes stand for the four readers (*R_1*, *R_2*, *R_3*, and *R_4*) in the four corners. The red circle stands for the target tag *T*, and the green circles (*VT_1* and *VT_2*) stand for the virtual tag symmetric with a certain reader. The virtual tag has the same mixed phase deviation as the target tag under one reader. In addition, the blue triangles (*RT_1*, *RT_2* and *RT_3*) stand for the reference tags.

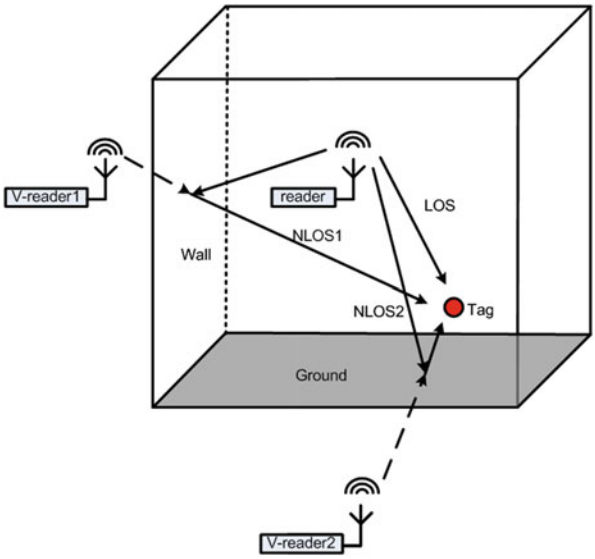

Fig. 1 Simple propagation model in indoor condition

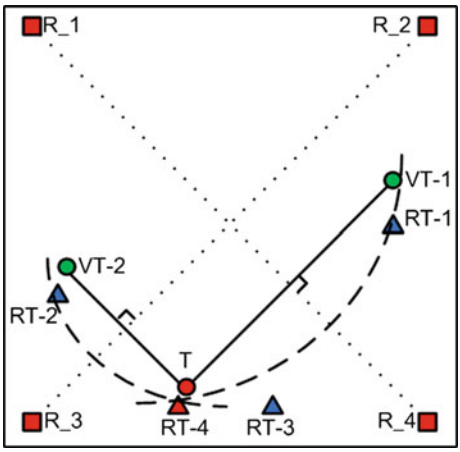

Fig. 2 The choosing principle of the reference tags

The choosing of the reference depends on the similarity between the reference and the target. Under multipath environments, there is always a virtual tag which is symmetric with the target under one reader, like the virtual tag *VT_1* under the reader *R_1*. The symmetric virtual tag experiences the same propagation distance under each path, so the receiving mixed phase deviation of the virtual tag is equal to the target theoretically. While in practice the reference tags cannot be exactly the virtual tag, but sometimes there are reference tags which are close to the virtual tags. Of course, there are also some reference tags adjacent with the target itself. As shown in Fig. 1, the reference *RT_1* is close to the virtual tag *VT_1*, while the reference *RT_3* is the nearest one for the target. In our principle, we will choose the *RT_1* as the reference tag under the reader *R_1*, and similarly, choose the *RT_2* as

the reference tag under the reader *R_2*. Then we can draw two circles, one is about the reader *R_1* with a radius of the distance between the *R_1* and *RT_1*, the other is about the reader *R_2* with a radius of the distance between the *R_2* and *RT_2*. Then final location can be set as the intersection *RT_4* (marked as red triangle) of the two circles which is marked as two dotted lines in Fig. 2.

3 Experimental Results

For testing the location performance of our approach, we conduct a series of simulation experiences. Here we use four readers placed in the ceiling and around the four corners of an indoor scene which is modeled in a space of $10 \times 10 \times 5$ m. And 200 tags are randomly distributed in the horizontal space with a same height of 1 m. As for the reference tags, we choose 9 tags which are evenly arranged on the horizon and the height of the reference tags are also 1 m. For simplicity, we just consider the case that the signal propagates back just in the way it sends. After 2,000 times experiments with Monte Carlo method, the final results are shown in the following.

After executing the three steps in Sect. 2.1, we can get more accurate phase estimation for the further location estimation. Through experiments we can find that the worse phase estimation error in LOS under signal to noise rate (SNR) of 10 dB is about 1.2°, and when the SNR is 40 dB, the phase error can reach 0.03°. While under multipath environments, the worse deviation reaches about 11°, and even though the SNR can improve the estimation performance, the best error result still stands above 4°. So the direct using of the phase estimation result in LOS distance computation can bring huge mistakes in location estimation under multipath case.

In Fig. 3, we make a performance comparison between four different approaches under multipath environments, and the four approaches include Refer-All-phase-FFT which is proposed in this paper, All-phase-FFT which directly uses the phase results extracted from the All-phase-FFT for LOS estimation, LANDMARC which follows the same location procedures in [9] and uses the Received Signal Strength Indicator (RSSI) of the channel model under multipath environments in [8], and LANDMARC-ranging which takes use of the geometrical approach (LLS) with the selected nearest reference tag's direct distance instead of the K nearest neighbor (KNN) location scheme.

Form the simulation performances shown in Fig. 3, the worse performance is All-phase-FFT whose location error is between 4.8 m and 2.7 m under diverse SNR values, which can be explained from the bad phase estimations. The LANDMARC and LANDMARC-ranging performed approximate results, and via comparison, the result of LANDMARC is better. The most understandable reason can be explained that there is non-linear relationship with RSS and the distance, so the geometrical approach using the direct distance information selected from the RSS is not completely correct. In the end, we can prove that our proposed scheme Refer-All-phase-FFT can reduce the location error below 1 m, and the value of SNR has small influence on the location estimation error, which provides the effectiveness of this approach utilized in practice.

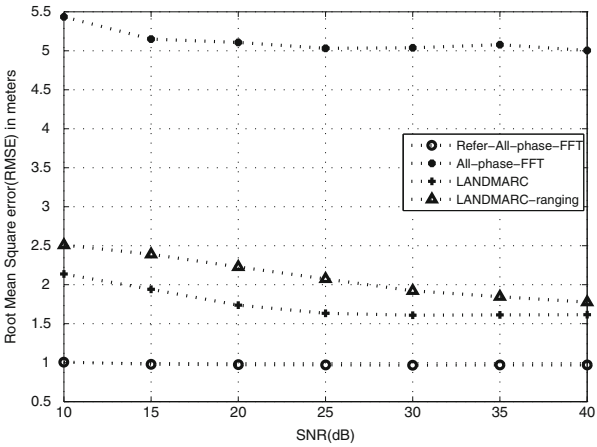

Fig. 3 Performance comparison between four different approaches

4 Conclusions

This paper proposes a simple but effective localization approach under multipath environments with the RFID technique. In this approach, we choose the POA based on a single frequency subcarrier as the signal measurement information to capture the LOS distance estimation for the final localization estimation by the geometrical approach LLS. And we also improve the phase accuracy by a new phase extracting criterion after the All-phase-FFT conversion. Though the performances of the phase estimation are perfect in LOS, the results fall severely under multipath environments and will introduce more localization estimation error. Considering this, we consult the idea of the addition of the reference tags, and still follow the ranging approach for localization based on LLS. The experiments compare our approach with other three approaches under multipath environments and the results prove that our approach has a good localization performance and is robust to the environmental dynamics.

Acknowledgments This research is supported by research forums cooperation project of ZTE Corporation.

References

1. Seow CK, Tan SY (2008) Non-line-of-sight localization in multipath environments. IEEE Trans Mob Comput 7(5):647–660. doi:10.1109/TMC.2007.70780
2. Setlur P, Smith GE, Ahmad F, Amin MG (2012) Target localization with a single sensor via multipath exploitation. IEEE Trans Aerosp and Electron Syst 48(3):1996–2014. doi:10.1109/TAES.2012.6237575
3. Alsindi NA, Alavi B, Pahlavan K (2009) Measurement and modeling of ultrawideband TOA-based ranging in indoor multipath environments. IEEE Trans Veh Technol 58 (3):1046–1058. doi:10.1109/TVT.2008.926071

4. Steffes C, Rau S (2012) Multipath detection in TDOA localization scenarios. SDF 88–92. doi: 10.1109/-SDF.2012.6327914
5. Azzouzi S, Cremer M, Dettmar U, Kronberger R, Knie T (2011) New measurement results for the localization of UHF RFID transponders using an Angle of Arrival (AoA) approach. RFID 91–97. doi: 10.1109/RFID.2011.5764607
6. Steiner C, Wittneben A (2011) Efficient training phase for ultrawideband-based location fingerprinting systems. IEEE Trans Signal Process 59(12):6021–6032. doi:10.1109/TSP.2011.2166390
7. Weiguang Shi (2011) Research of Indoor localization Algorithm based on Radio Frequency Identification Technology. Dissertation, Tianjin University
8. Nikitin PV, Martinez R, Ramamurthy S, et al. (2010) Phase based spatial identification of UHF RFID tags. RFID 102 -109. doi: 10.1109/RFID.2010.5467253
9. Ni LM, Liu Y, Lau YC, Patil AP (2004) LANDMARC: indoor location sensing using active RFID. Wirel Netw 10(6):701–710. doi:10.1023/B:WINE.0000044029.063-44.dd
10. Cong L, Zhuang W (2002) Hybrid TDOA/AOA mobile user location for wideband CDMA cellular systems. IEEE Trans Wirel Commun 1(3):439–447. doi:10.1109/TWC.2002.800542
11. Wang Z, Huang X, Yang W (2007) The measuring phase method of all-phase FFT. World Sci-Tech R & D 29(4):28–32. doi:10.3969/j.issn.1006-6055.2007.04.006

Human Action Recognition Using Maximum Temporal Inter-Class Dissimilarity

Haijun Liu and Lan Li

Abstract Human action sequences can be considered as nonlinear dynamic manifolds in image frames space. In this paper, a novel manifold embedding method, Maximum Temporal Inter-class Dissimilarity (MTID), is proposed for human action recognition, which is based on the framework of Locality Preserving Projections (LPP). Being different from LPP whose goal is to minimize the intra-class distance in local neighborhood, MTID can make best of both the class label information and the temporal information to maximize the inter-class distance in local neighborhood, Namely, focusing on maximizing the dissimilarity between frames that are similar in appearance but are from different classes. At last the Nearest Neighbors classifier based on Hausdorff distance is introduced for recognition. The experimental results demonstrate the effectiveness of the proposed method for human action recognition.

Keywords Human action recognition • Manifold learning • Maximum temporal inter-class dissimilarity

1 Introduction

Human action recognition is an important research topic in computer vision. It aims to recognize or understand human actions based on features extracted from human posture sequences. This interest is driven by a wide spectrum of promising application areas such as human-machine interaction, intelligent video surveillance and sports event analysis etc.

In recent years, some researchers proposed to preprocess human action sequences and use the obtained human silhouettes as features [1, 2]. Compared

H. Liu (✉) • L. Li
School of Electronic Engineering, University of Electronic Science and Technology of China, 2006 Xiyuan Ave., Chengdu 611731, China
e-mail: haijunliu518128@gmail.com

B. Zhang et al. (eds.), *The Proceedings of the Second International Conference on Communications, Signal Processing, and Systems*, Lecture Notes in Electrical Engineering 246, DOI 10.1007/978-3-319-00536-2_111,

with other features, silhouettes can offer detailed body shape information. Assuming an underlying lower-dimensional representation for frames of human action sequences, manifold learning approaches have been introduced to recover such a lower-dimensional representation that best describes frames' relationships. Wang and Suter [2] proposed to use the Locality Preserving Projections (LPP) [3] to obtain dynamic shape manifolds for human action recognition. Blackburn and Ribeiro [4] employed the ISOMAP to embed frames of human action sequences into sub-manifolds.

Some researchers extended existing manifold learning methods with additional temporal information to recover spatio-temporal relationships between frames. Lewandowski et al. [5] presented a temporal extension for the Laplacian Eigenmap (LE) by constructing two graphs that encode temporal neighbor relations and the temporal repetition relations, respectively. Fang and Chen [6] calculated pairwise affinities between frames based on several temporal relationships and learned the manifold following the Locality Preserving Projections (LPP) framework. In [1], each frame is associated with a short video segment as its feature. Those frames are embedded via Local Spatio-Temporal Discriminant Embedding (LSTDE) [1] into a subspace such that frames from the same action class are close to each other after the embedding.

Motivated by Locality Preserving Projections (LPP) [3] and its variants, such as the Supervised LPP [7] and the Orthogonal LPP [8], we propose a novel manifold learning based method, Maximum Temporal Inter-class Dissimilarity (MTID), to recover the underlying relationships between frames from all training sequences. It combines both temporal and class label information from all frames in the embedding process. However, unlike the LSTDE [1], which utilizes all class label information, our method only focuses on the frames that are most difficult to distinguish, i.e., frames that are highly similar in terms of appearance but are from different classes. We argue that by focusing on those frames, the embedded samples (frames) can be classified more easily. After all training samples are embedded into a lower dimensional space, frame classification and sequence classifications are performed using a Nearest Neighbors classifier based on Hausdorff distance [2].

2 Maximum Temporal Inter-Class Dissimilarity (MTID)

Human action sequences can be preprocessed to obtain the silhouette of human in every frame. By concatenating all pixels' labels in a silhouette frame, we obtain a vector $\mathbf{x} \in \mathbf{R}^m$ for the frame, where m is the number of pixels in a frame. Let $\mathbf{X} = [\mathbf{x}_1, \mathbf{x}_2, \cdots, \mathbf{x}_n] \in \mathbf{R}^{m \times n}$ represent all n training silhouette frames, where $\mathbf{x}_i \in \mathbf{R}^m$ for all $\mathbf{x}_i \in \mathbf{X}$.

In manifold learning based recognition methods [1, 2, 5, 6, 9], every frame in action sequences is treated as a training sample. And each frame $\mathbf{x}_i$ in a time

sequence is associated with a frame number, $t(\mathbf{x}_i)$, specifying its position in a sequence, and a class label, $c(\mathbf{x}_i)$, specifying its class.

The goal of our method is to recover a lower-dimensional representation $\mathbf{Y} = [\mathbf{y}_1, \cdots, \mathbf{y}_n] \in \mathbf{R}^{d \times n}$ for the training samples $\mathbf{X}$, where $\mathbf{y}_i \in \mathbf{R}^d$ $(d < m)$ is the representation for $\mathbf{x}_i$. In this method, we focus on distinguishing frames that are of similar appearance but from different classes. We argue that by maximizing the distances between those frames during the embedding process.

To robustly determine samples of similar appearance, we first calculate the $L2$ distances between all training samples and obtain each sample $\mathbf{x}_i$'s k nearest neighbors $\mathcal{N}_k(\mathbf{x}_i)$. If two samples $\mathbf{x}_i$ and $\mathbf{x}_j$ are within each other's k nearest neighbors, i.e., $\mathbf{x}_i \in \mathcal{N}_k(\mathbf{x}_j)$ and $\mathbf{x}_j \in \mathcal{N}_k(\mathbf{x}_i)$, we judge that $\mathbf{x}_i$ and $\mathbf{x}_j$ are of similar appearance.

We define an appearance dissimilarity weight w_{ij}^a between samples $\mathbf{x}_i$ and $\mathbf{x}_j$ as follows:

$$w_{ij}^a = \{\cos(\mathbf{x}_i, \mathbf{x}_j) \mathbf{x}_i \in \mathcal{N}_k(\mathbf{x}_j), \mathbf{x}_j \in \mathcal{N}_k(\mathbf{x}_i), c(\mathbf{x}_i) \neq c(\mathbf{x}_j)\, 0 \,\text{otherwise}, \quad (1)$$

where

$$\cos(\mathbf{x}_i, \mathbf{x}_j) = \frac{\mathbf{x}_i \cdot \mathbf{x}_j}{\|\mathbf{x}_i\| \|\mathbf{x}_j\|} \quad (2)$$

is the cosine similarity function [2] measuring the dissimilarity weight between two similar samples $\mathbf{x}_i$ and $\mathbf{x}_j$, and $\cdot$ represents the dot product of two vectors. $\cos(\mathbf{x}_i, \mathbf{x}_j)$ equals 1 when $\mathbf{x}_i = \mathbf{x}_j$ and decreases as the appearance dissimilarity between $\mathbf{x}_i$ and $\mathbf{x}_j$ increases. Equation (1) denotes that we focus on samples that are of similar appearance, $\mathbf{x}_i \in \mathcal{N}_k(\mathbf{x}_j)$, $\mathbf{x}_j \in \mathcal{N}_k(\mathbf{x}_i)$, but are from different classes, $c(\mathbf{x}_i) \neq c(\mathbf{x}_j)$.

To take account of temporal information, we define a temporal dissimilarity weight between samples $\mathbf{x}_i$ and $\mathbf{x}_j$ as

$$w_{ij}^t = \exp\big(-\big|t(\mathbf{x}_i) - t(\mathbf{x}_j)\big|\big). \quad (3)$$

The overall dissimilarity weight between $\mathbf{x}_i$ and $\mathbf{x}_j$ is then defined as the product of w_{ij}^a and w_{ij}^t,

$$w_{ij} = w_{ij}^a w_{ij}^t. \quad (4)$$

Most importantly, w_{ij}^a and w_{ij}^t are both normalized before the product in Eq. (4).

Our proposed method looks for a lower-dimensional representation $\mathbf{Y}$ that maximizes squared distances between samples $\mathbf{X}$ according to the dissimilarity weights w_{ij}:

$$\underset{y_1,\cdots,y_n}{\text{maximize}} \quad \frac{1}{2}\sum_{i}^{n}\sum_{j}^{n}\|\mathbf{y}_i-\mathbf{y}_j\|_2^2 w_{ij}. \tag{5}$$

The above objective function is optimized following the Orthogonal Neighborhood Preserving Projection (ONPP) [8] framework, where every sample $\mathbf{x}_i$ is embedded to a position $\mathbf{y}_i$ in the lower dimensional space via a linear projection $\mathbf{V} \in \mathbf{R}^{m\times d}$ as $\mathbf{y}_i = \mathbf{V}^T\mathbf{x}_i$. Equation (5) can then be reformulated to

$$\underset{\mathbf{V}}{\text{maximize}}\ \frac{1}{2}\sum_{i}^{n}\sum_{j}^{n}\|\mathbf{V}^T\mathbf{x}_i-\mathbf{V}^T\mathbf{x}_j\|_2^2 w_{ij}, \text{subject to } \mathbf{V}^T\mathbf{V}=\mathbf{I}, \tag{6}$$

where $\mathbf{V}^T\mathbf{V} = \mathbf{I}$ denotes that columns of $\mathbf{V}$ must be orthogonal to better preserve the metric structure of the frame space [8].

Further reformulating the objective function using matrix notation leads to the following concise form:

$$\begin{aligned}&\underset{\mathbf{V}}{\text{maximize}}\ tr\left(\mathbf{V}^T XLX^T\mathbf{V}\right),\\ &\text{subject to } \mathbf{V}^T\mathbf{V}=\mathbf{I},\end{aligned} \tag{7}$$

where $\mathbf{L} = \mathbf{D} - \mathbf{W}$, $\mathbf{W} \in \mathbf{R}^{n\times n}$ is a symmetric affinity matrix created by setting w_{ij} as $\mathbf{W}$'s entry at the ith row and jth column, and $\mathbf{D} \in \mathbf{R}^{n\times n}$ is a diagonal matrix with its ith entry as $\mathbf{D}_{ii} = \sum_{j=1}^{n} w_{ij}$. Let $v_1, v_2, \cdots, v_d$ be XLX^T's eigenvectors corresponding to its d largest eigenvalues. The optimum of Eq. (7) can then be obtained as $\mathbf{V} = [v_1, v_2, \cdots, v_d]$.

3 Experiments

To evaluate our proposed method, we performed two experiments on the human action recognition dataset [10]. Both experiments are performed using a Nearest Neighbors (NN) classifier based on the Hausdorff distance [2].

We slightly revise the dissimilarity weight (4) by removing the temporal term w_{ij}^t to create a baseline algorithm for comparison, i.e.,

$$w_{ij} = w_{ij}^a. \tag{8}$$

We call the baseline algorithm Maximum Inter-class Dissimilarity (MID) in contrast to Maximum Temporal Inter-class Dissimilarity (MTID).

3.1 Dataset and Pre-Processing

The human action dataset from [10] is chosen to evaluate our proposed method for the task of human action recognition. In this dataset, there are 9 human subjects, and each of which performs 10 different actions (90 sequences in total). The human silhouette masks are provided with original frame images.

In this dataset, every time sequence might record a human subject performing a same action for several times. We create a DatasetA by cropping every time sequence to let it include only a single and complete action. The beginning frames of all time sequences in DatasetA within the same class record a same beginning posture. The original and more challenging time sequences with repetitive actions are denoted as DatasetB. All frames are centered at silhouettes' positions and cropped to the size of 80×40, which are then concatenated to create 3200-dimensional column vectors. To avoid the singular matrix problem and improve the computational efficiency, Principal Component Analysis with 99% of variance retained is adopted to reduce the dimension of training samples.

3.2 Recognition Results on DatasetA

For each test sequence, we recognize its action class using a Nearest Neighbors (NN) method based on the Hausdorff distance. A nine-fold cross validation was adopted to evaluate the proposed method and the compared ones using DatasetA. At each time, 8 out of 9 subjects' actions from DatasetA are used as training sequences. The remaining subject's 10 sequences are used for testing. The average sequence recognition rates for all cases of the cross validation settings are recorded as the final results.

Following the experimental setup in [2, 9], we first conduct experiments on DatasetA where each sequence only includes a single and complete action. The performance of the proposed method MTID and the baseline method MID are compared. In Fig. 1a, we show the recognition rates of the two methods with d and a fixed number of neighbors $k = 20$. It shows that if the dimension number is no less than 14, the recognition rate of the proposed MTID is always greater than 95%. In Fig. 1b, we show the recognition rates of the two methods with varying k and a fixed dimension number $d = 20$. The recognition rate of the MTID is always 100% if $k \geq 55$. In both cases, our proposed MTID outperforms the baseline method MID, which demonstrates the necessity of incorporating temporal information in action recognition. These results by MTID and MID are also comparable with those by [2, 9].

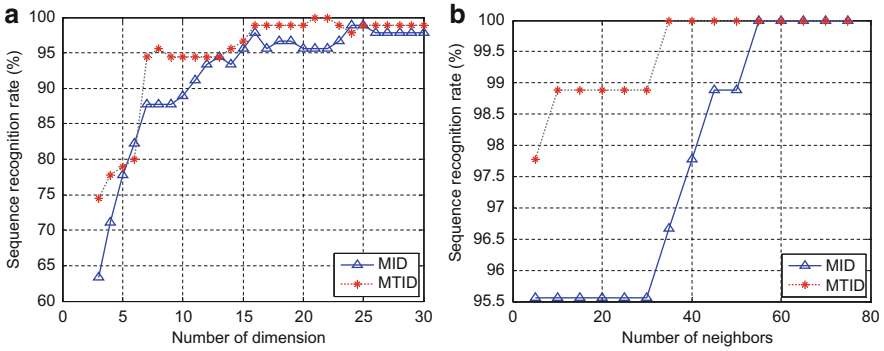

Fig. 1 Sequence recognition rates for DatasetA by our proposed MTID and the baseline method, MID. (**a**) Recognition rates with increasing dimension numbers while fixing $k = 20$. (**b**) Recognition rates with increasing number of neighbors while fixing $d = 20$

3.3 Recognition Results on DatasetB

We then compare our methods with some state-of-the-art manifold embedding methods, which include Locality Preserving Projections (LPP) [3], Temporal-Vector Trajectory Learning (TVTL) [6], Locality Sensitive Discriminant Analysis (LSDA) [11] and Local Spatio-Temporal Discriminant Embedding (LSTDE) [1], using the more challenging DatasetB.

We utilized the cropped sequences in DatasetA for training and the original sequences in DatasetB for testing. Similarly to the previous experiment, a nine-fold cross validation is used where 8 out of 9 subjects' actions from the same datasets are used for training. The remaining subject's 10 actions were used for testing. Since each test sequence might record a same action for several times, each frame is classified using a Nearest Neighbors (NN) classifier based on the Hausdorff distance. We empirically set $k = 28$, $d = 10$, and $t = 13$.[1] The average frame recognition rates for our proposed MTID and compared methods are shown in Table 1. The experimental results show that our method outperforms all compared methods with a much smaller dimension number (showing in bold).

To analyze which actions are misclassified, confusion matrices of our proposed MTID, LPP [3], and LSTDE [1], are shown in Fig. 2, where the entry at row A and column B denotes the percentage of classifying a frame in action A as action B. Those matrices show that most actions can be recognized correctly, except for *jump*, *run* and *wave1*, which are more likely to be misclassified. This is because silhouettes of those actions have high inter-class similarities. For those actions, LPP misclassify them more frequently than MTID does. By focusing on maximizing the spatio-temporal dissimilarities between those actions, MTID could embed frames from different classes far away from each other.

[1] t is a temporal segmentation parameter like in LSTDE [1].

Table 1 Average frame recognition rates on DatasetB by proposed MTID and compared methods

Methods	MTID (ours)	MID (baseline)	LPP [3]	LSDA [11]	TVTL [6]	LSTDE [1]
Recognition rates (%)	**93.18**	92.61	90.51	90.81	90.21	90.91
dimension	**10**	31	23	41	n/a	28

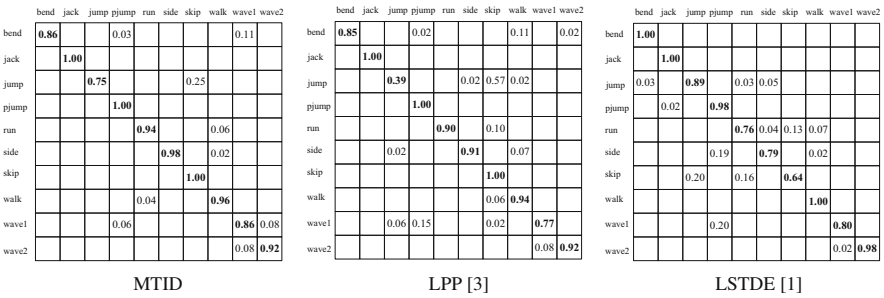

Fig. 2 Confusion matrixes by our proposed MTID, LPP [3] and LSTDE [1] on DatasetB. For each matrix, the entry at row *A* and column *B* denotes the percentage of classifying action *A* as action *B*

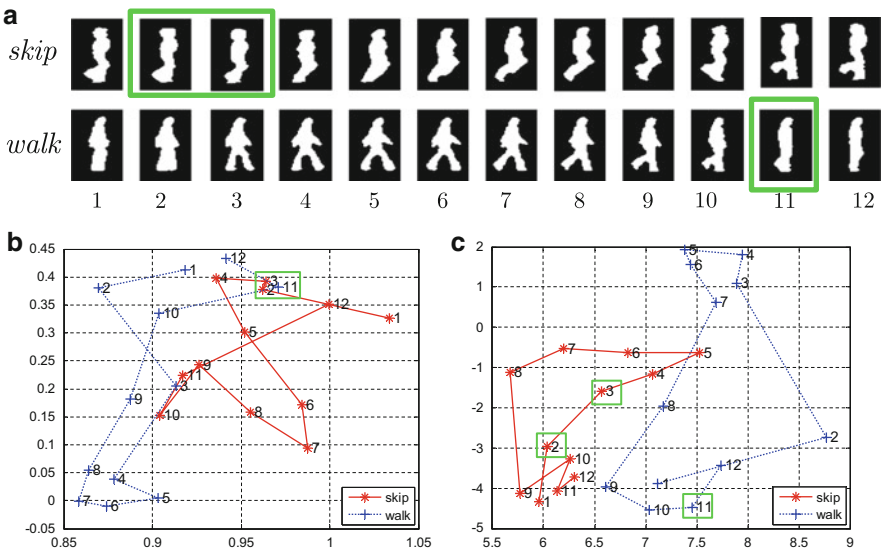

Fig. 3 Illustration of the differences between LPP and MTID. (**a**) The silhouette frames of a sequence in *skip* and a sequence in *walk*. Some frames with similar appearance are labeled by green rectangles. (**b**) Embedding result by LPP with $d = 2$. The frames in green rectangles are embedded close to each other. (**c**) Embedding result by MTID with $d = 2$. The frames in green rectangles are embedded far away from each other

In Fig. 3, we illustrate the differences between the LPP [3] and our MTID using two time sequences from *skip* and *walk*. The 2nd, 3rd frames of the *skip* sequence and the 11th frame of the *walk* sequence have similar appearances. After embedding the two sequences using both methods with $d = 2$, we plot the embedding results by LPP and MTID in Fig. 3b,c. Obviously, our method embeds the similar frames (in green rectangles), especially those from different actions, further away than the LPP does, which makes the classification step easier to perform.

4 Conclusions

We presented a novel dimension reduction method, Maximum Temporal Inter-class Dissimilarity (MTID), for human action recognition. Posture silhouettes are used as features for the action frames. By focusing on maximizing the distances between the frames with high appearance similarities but from different action classes, our proposed MTID is able to recover an optimal embedding for the frames that best preserves the appearance, temporal, and discriminant relationships between them. Extensive experimental and comparison results show that our method outperforms state-of-the-art manifold embedding based methods.

Acknowledgements This research is supported by National Natural Science Foundation of China (61201271), Specialized Research Fund for the Doctoral Program of Higher Education (20100185120021), and Sichuan science and technology support program (cooperated with Chinese Academy of Sciences) (2012JZ0001).

References

1. Jia K, Yeung D (2008) Human action recognition using local spatio-temporal discriminant embedding. IEEE Conf Comput Vis Pattern Recogn 1–8
2. Wang L, Suter D (2007) Learning and matching of dynamic shape manifolds for human action recognition. IEEE Trans Image Process 16(6):1646–1661
3. He X, Niyogi P (2004) Locality preserving projections. Neural Inform Process Syst 16:153–160
4. Blackburn J, Ribeiro E (2007) Human motion recognition using isomap and dynamic time warping. In: International conference on computer vision workshop on human motion, pp 285–298
5. Lewandowski M, Martinez-del-Rincon J, Makris D, Nebe J (2010) Temporal extension of laplacian eigenmaps for unsupervised dimensionality reduction of time series. Int Conf Pattern Recogn 161–164
6. Fang C, Chen J, Tseng C, Lien J (2009) Human action recognition using spatio-temporal classification. Asian Conf Comput Vis 98–109
7. Zheng Z, Yanga F, Tana W, Jiaa J, Yangb J (2007) Gabor feature-based face recognition using supervised locality preserving projection. Signal Process 87(10):2473–2483

8. Kokiopoulou E, Saad Y (2007) Orthogonal neighborhood preserving projections: A projection-based dimensionality reduction technique. IEEE Trans Pattern Anal Mach Intell 29(12):2143–2156
9. Wang L, Suter D (2008) Visual learning and recognition of sequential data manifolds with applications to human movement analysis. Comput Vis Image Understand 110(2):153–172
10. Gorelick L, Blank M, Shechtman E, Irani M, Basri R (2007) Action as space-time shapes. IEEE Trans Pattern Anal Mach Intell 29(12):2247–2253
11. Cai D, He X, Zhou K (2007) Locality sensitive discriminant analysis. Int Joint Conf Artif Intell 708–713

Single Point Positioning Algorithm of Integrated System Based on Improve Least Squares Algorithm

Anhong Tian, Chengbiao Fu, and Jian Xu

Abstract In order to obtain position and clock bias, at least four GPS (Global Positioning System) pseudo-range measurements are needed, which are based on least squares iteration algorithm, the accuracy is dependent on the number of iterations and the deviation between initial value and true value, and GPS satellite is partly blocked indoors and dense urban areas. Therefore, a simple novel method is developed to solve the navigation equations directly without linearization and iteration, which is combining GPS and GLONASS. The results show that novel method is effective for navigation precision, the method reduces the computational complexity significantly and is highly suitable for single point positioning.

Keywords Navigation equations • Single point positioning • Least squares • Hybrid positioning

1 Introduction

GPS (Global Positioning System) are worldwide, all-weather navigation systems, which are able to provide three-dimensional positioning [1], velocity and time synchronization, but it cannot locate successfully indoors and dense urban areas [2], therefore, the single GPS system can't completely meet the demands of single point positioning.

Currently, with the development of Global Navigation Satellite System (GNSS), the number of global navigation satellites in view can be greatly increased in the same epoch moment [3]. The present GNSS are GPS, GLONASS, Galileo and Compass, but the latter two are still in the development phase. This paper presents

A. Tian (✉) • C. Fu • J. Xu
Department of Computer Science and Engineering, Qujing Normal College, Qujing, China
e-mail: tianfucb@gmail.com

B. Zhang et al. (eds.), *The Proceedings of the Second International Conference on Communications, Signal Processing, and Systems*, Lecture Notes in Electrical Engineering 246, DOI 10.1007/978-3-319-00536-2_112,

integrated positioning system combining GPS and GLONASS to settle single point positioning.

The most mentioned positioning method should be pseudo-range measurement based on least-squares iteration algorithm, but its accuracy depends on the number of iterations and the deviation between initial value and true value. So this paper gives a novel model to realize the precise positioning, the performance of this algorithm is analyzed theoretically and evaluated by computer simulation.

2 Least Squares Iteration Algorithm

GPS satellite is partly blocked in indoor environment and dense urban area, there are less than four satellites, it is difficult to get the precise location information, in this situation, auxiliary positioning technology will be adopted, in order to make up for the defects of GPS signals performs badly or even fails to work. The GLONASS satellites are similar to GPS satellites, we can adopt the integrated system combing GPS and GLONASS, the hybrid positioning system model can be expressed in Fig. 1.

According to the principle of GPS and GLONASS positioning, they has the same pseudo-range equation. Assuming we can ignore the pseudo-ranges error of ionospheric delay and tropospheric delay [4], then the GPS or GLONASS pseudo-range mathematical model can be expressed as follows:

$$r = \sqrt{(x_i - x_u)^2 + (y_i - y_u)^2 + (z_i - z_u)^2} + c \times t_u \tag{1}$$

Where r is the geometrical range between satellite and receiver, (x_i,y_i,z_i) denotes the coordinate of satellite, (x_u,y_u,z_u) denotes the receiver position, c is the speed of light, $c \times t_u$ is the unknown distance caused by the clock offset, (x_u,y_u,z_u,t_u) is unknown parameters.

Obviously (1) is non-linear, the pseudo-range equation can be linearized with Taylor's series expansion at the approximate point, assuming (X_0,Y_0,Z_0,B_0) is initially estimated position of unknown parameters, $(\Delta x, \Delta y, \Delta z, \Delta t_u)$ is the increment, which can update the receiver coordinates [5], this is shown as follows:

$$X_u = X_0 + \Delta x, \quad Y_u = Y_0 + \Delta y, \quad Z_u = Z_0 + \Delta z, \quad B_u = B_0 + c \times \Delta t_u \tag{2}$$

Let $R_{i0} = \sqrt{(X_i - X_0)^2 + (Y_i - Y_0)^2 + (Z_i - Z_0)^2}$, Taylor's series expansion is adopted to linearize the pseudo-range equation, observation equation is becomes:

$$r_i = R_{i0} + m_i \times \Delta x + n_i \times \Delta y + k_i \times \Delta z + c \times \Delta t_u \tag{3}$$

Where $m_i = \frac{X_i - X_0}{R_{i0}}, n_i = \frac{Y_i - Y_0}{R_{i0}}, k_i = \frac{Z_i - Z_0}{R_{i0}}$

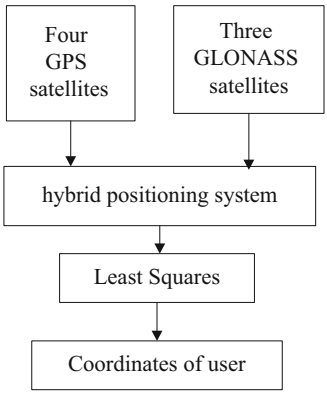

Fig. 1 The hybrid positioning system

The four unknown parameters can be solved according to the rules of Least Squares. The observation equation [1] can be expressed as follows:

$$\begin{cases} r_1 - R_{10} = m_1\Delta x_u + n_1\Delta y_u + k_1\Delta z_u + c\Delta t_u \\ r_2 - R_{20} = m_2\Delta x_u + n_2\Delta y_u + k_2\Delta z_u + c\Delta t_u \\ r_3 - R_{30} = m_3\Delta x_u + n_3\Delta y_u + k_3\Delta z_u + c\Delta t_u \\ \cdots \\ r_n - R_{40} = m_n\Delta x_u + n_n\Delta y_u + k_n\Delta z_u + c\Delta t_u \end{cases} \tag{4}$$

The equation can be expressed as

$$V - L = H \cdot X \tag{5}$$

Where

$$H = \begin{bmatrix} a_{x1} & a_{y1} & a_{z1} & 1 \\ a_{x2} & a_{y2} & a_{z2} & 1 \\ a_{x3} & a_{y3} & a_{z3} & 1 \\ a_{x4} & a_{y4} & a_{z4} & 1 \end{bmatrix}, \quad X = \begin{bmatrix} \Delta x_u \\ \Delta y_u \\ \Delta z_u \\ c\Delta t_u \end{bmatrix}, \quad V - L = \begin{bmatrix} r_1 - R_{10} \\ r_2 - R_{20} \\ r_3 - R_{30} \\ \cdots \\ r_n - R_{n0} \end{bmatrix}$$

According to Least Square theorem, the normal equations become:

$$\left(H^T \cdot H\right) \cdot X = H^T \cdot L \tag{6}$$

Hence,

$$X = \left(H^T H\right)^{-1} H^T Y \tag{7}$$

(Δx, Δy, Δz, Δt_u) is used to recalculate estimated position of (x_u,y_u,z_u,t_u) in accordance with (2), as the initial value may involve large errors, therefore, in

order to get close to the true value, (4) need to be repeated with initial value, until error components (Δx, Δy, Δz, Δt_u) are smaller than the desired error (e.g.0.01 m) [6], the desired error is defined as δ, this is shown as follows:

$$|\Delta x| + |\Delta y| + |\Delta z| + |c \times \Delta t_u| < \delta \tag{8}$$

3 A New Model for Solving the Navigation Equations

As mentioned in above, positioning accuracy of iterative Least Squares method depends on the number of iterations [7] and the deviation between initial value and true value. When the deviation is big, there are a lot of iterations [8]. Then, we give a novel model to solve positioning accuracy.

$$\begin{cases} (r_i - b)^2 = (x_i - x_u)^2 + (y_i - y_u)^2 + (z_i - z_u)^2 \\ (r_{i+1} - b)^2 = (x_{i+1} - x_u)^2 + \left(y_{i+1} - y_u\right)^2 + (z_{i+1} - z_u)^2 \end{cases} \tag{9}$$

Where $b = c \cdot t_u$, r_i is pseudo-range.
The (9) is subtracting:

$$d_i x_u + m_i y_u + n_i z_u + k_i b = l_i \tag{10}$$

Where

$$\begin{aligned} d_i &= 2(x_{i+1} - x_i), \\ m_i &= 2\left(y_{i+1} - y_i\right), \\ n_i &= 2(z_{i+1} - z_i), \\ k_i &= 2(r_i - r_{i+1}), \\ l_i &= x_{i+1}^2 - x_i^2 + y_{i+1}^2 - y_i^2 + z_{i+1}^2 - z_i^2 + r_i^2 - r_{i+1}^2 \end{aligned}$$

Equation (10) is transformed into matrix form:

$$\mathbf{A} \cdot W \cdot \boldsymbol{\sigma}_x = \mathbf{L} \cdot W \tag{11}$$

Where

$$\mathbf{A} = \begin{bmatrix} d_1 & m_1 & n_1 & k_1 \\ d_2 & m_2 & n_2 & k_2 \\ \cdots & \cdots & \cdots & \cdots \\ d_{n-1} & m_{n-1} & n_{n-1} & k_{n-1} \end{bmatrix}, \quad \boldsymbol{\sigma}_x = \begin{bmatrix} x_u \\ y_u \\ z_u \\ b \end{bmatrix}, \quad \mathbf{L} = \begin{bmatrix} l_1 \\ l_2 \\ \cdots \\ l_{n-1} \end{bmatrix},$$

$$W = \frac{x_{i+1}x_i + y_{i+1}y_i + z_{i+1}z_i}{\sqrt{(x_{i+1} - x_i)^2 + \left(y_{i+1} - y_i\right)^2 + (z_{i+1} - z_i)^2}},$$

According to Least Square theorem, the normal equations become:

$$\boldsymbol{\sigma}_x = \left[\mathbf{A}^{\mathrm{T}} \cdot W \cdot \mathbf{A}\right]^{-1}\left[\mathbf{A}^{\mathrm{T}} \cdot W \cdot \mathbf{L}\right] \tag{12}$$

We adopt weighted least squares to get positioning results.

4 Simulation Results and Analysis

In signal-degraded environments such as dense urban area and indoor environment, we can use hybrid positioning system to obtain accurate location information, in order to test the performance of algorithm, we choose a test area covered by 4 GPS satellites and 3 GLONASS satellites. Simulation results are shown in Tables 1 and 2.

Table 1 indicates the comparison of positioning error for least squares iteration algorithm, in the certain initial value of (0,0,0,0), when there is one iteration, the deviation between calculated position and true position is very large, where there is six iteration, average localization error is below 5 m, and when the number of iteration achieves eight, the localization error is smaller than δ,which can meet the demands of positioning precision.

Table 2 indicates that there is less iterations number in the initial value of (−1,332,600, 5,329,400, 3,237,000), it reduces the computation time greatly, and has lower computational burden than that of Table 2. But the improve algorithm has higher positioning accuracy without initial value in one iteration, and shortens computational complexity.

5 Conclusion

This paper studies the single point pseudo-range positioning algorithm of GPS and GLONASS hybrid positioning system, which is based on least-squares iterative algorithm and improved algorithm, and analysis the performance of algorithm by obtaining true satellite date. Simulation results show that the superior performance of the improved algorithm, which has higher positioning accuracy and lower iterations number.

Table 1 Comparison of the positioning error for least squares iteration algorithm

Algorithm	Initial value	Iteration	Δx	Δy	Δz	Δt_u
LS	(0,0,0,0)	1	−1.8463e + 006	4.0929e + 006	6.7231e + 006	1.1363e + 006
LS	(0,0,0,0)	2	2.6640e + 005	−5.7947e + 005	−9.5927e + 005	−1.8204e + 005
LS	(0,0,0,0)	3	−1.8288e + 003	−2.8355e + 003	5.9504e + 003	−2.0494e + 005
LS	(0,0,0,0)	4	130.9408	−306.5060	−82.0831	−2.0509e + 005
LS	(0,0,0,0)	5	−2.1594	−9.0653	6.1315	−2.0509e + 005
LS	(0,0,0,0)	6	0.2350	−0.5792	−0.0620	−2.0509e + 005
LS	(0,0,0,0)	7	−0.0035	−0.0199	0.0106	−2.0509e + 005
LS	(0,0,0,0)	8	4.5149e − 004	−0.0012	−7.7003e − 005	−2.0509e + 005
LS	(0,0,0,0)	9	−5.7719e − 006	−4.1913e − 005	2.0320e − 005	−2.0509e + 005
LS	(0,0,0,0)	10	8.7498e − 007	−2.4007e − 006	−1.0151e − 007	−2.0509e + 005

Table 2 Comparison of the positioning error for least squares iteration algorithm and improved algorithm

Algorithm	Initial value	Iteration	Δx	Δy	Δz	Δt_u
LS	(−1,332,600, 5,329,400, 3,237,000)	1	−2.6563e + 005	−1.8022e + 006	2.4598e + 006	−6.8047e + 004
LS	(−1,332,600, 5,329,400, 3,237,000)	2	1.7293e + 004	−1.4309e + 004	7.9141e + 004	−2.0438e + 005
LS	(−1,332,600, 5,329,400, 3,237,000)	3	−695.0781	−2.5140e + 003	152.4533	−2.0503e + 005
LS	(−1,332,600, 5,329,400, 3,237,000)	4	69.6997	−118.8331	−9.5169	−2.0509e + 005
LS	(−1,332,600, 5,329,400, 3,237,000)	5	−1.7689	−3.9029	2.8032	−2.0509e + 005
LS	(−1,332,600, 5,329,400, 3,237,000)	6	0.1426	−0.2641	−0.0535	−2.0509e + 005
Improved	No initial value	1	−2.1732	2.5738	8.6257	−0.0214291

Acknowledgments This work was supported by Nature Science Foundation of Yunnan Province Education Department under Grant 2013Y017, about "the research of optimized satellite selection algorithm based on maximum determinant in positioning system," and Nature Science Foundation of Qujing Normal College under Grant 2012QN022 & 2012QN023 about "the research of satellite selection algorithm in global positioning system."

References

1. Chen Wantong, Qin Honglei, Zhang Yanzhong, Jin Tian (2012) Accuracy assessment of single and double difference models for the single epoch GPS compass. Adv Space Res 49 (4):725–738. doi: 10.1016/j.asr.2011.11.022
2. Zhang Xiaohong, Guo Fei, Li Xingxing, Lin Xiaojing (2010) Study on precise point positioning based on combined GPS and GLONASS. Wuhan Daxue Xuebao (Xinxi Kexue Ban)/Geomatics Inform Sci Wuhan Univ 35(1):9–12
3. Roongpiboonsopit Duangduen, Karimi Hassan A (2009) A multi-constellations satellite selection algorithm for integrated global navigation satellite systems. J Intell Transport Syst Technol Plann Oper 13(3):127–141.doi: 10.1080/15472450903084238
4. Du Xiaojing, Liu Li, Li Huaijian (2010) Experimental study on GPS non-linear least squares positioning algorithm. Int Conf Intell Comput Technol Autom 2:262–265.doi: 10.1109/ICICTA.2010.651
5. Tong H-B, Zhang G-Z, Ou G (2012) Iterative reweighted recursive least squares for robust positioning. Electron Lett 48(13):789–791. doi:10.1049/el.2012.0546
6. Wielgosz P (2011) Quality assessment of GPS rapid static positioning with weighted ionospheric parameters in generalized least squares. GPS Solutions 15(2):89–99. doi:10.1007/s10291-010-0168-6
7. Abdel-Hafez MF (2010) The autocovariance least-squares technique for GPS measurement noise estimation. IEEE Trans Veh Technol 59(2):574–588. doi:10.1109/TVT.2009.2034969
8. Wan Xiaoguang, Zhan Xingqun, Du Gang (2011) Effects of linearization on positioning algorithm in pseudolite positioning system. J Aeronautics Astronautics Aviation Ser A 43 (3):201–208

Indoor Localization Technology Based on NLOS Identification and Offset and Improved Particle Filter

Jiaojiao Wang, Yu Zhao, Kaihua Liu, Yongtao Ma, and Xiangxi Zeng

Abstract Due to the effect of non-line-of-sight (NLOS) propagation in harsh indoor environment, the accuracy of measured distance will drop sharply, and the inaccuracy of measurement will finally reduce the localization accuracy. This paper is conducted under the condition that environment map is known. Firstly identifying the state of the mobile node (MN), then adopting certain offset to mitigate positive biases introduced by NLOS propagation, at last introducing the current observation data in the process of prediction and resample of particle filter and use this improved particle filter (IPF) to track MN. Simulation results show that by using the proposed algorithm, the localization accuracy will be improved obviously.

Keywords Indoor location • NLOS identification and offset • Particle filter • Least squares

1 Introduction

Indoor localization technology that with various application prospects makes itself widely concerned by scholars. However, the effects of non-line-of-sight (NLOS) in complicated indoor environment such as reflection, refraction, transmission seriously reduce localization accuracy. In order to reduce or imitate the influence brought by NLOS, lots of scholars have proposed different solutions [1, 2]. Markov model is used to forecast NLOS condition and estimate particles [3], utilizing the positive effect of the NLOS measurements while restraining their negative effect.

J. Wang (✉) • Y. Zhao • K. Liu • Y. Ma
School of Electronic Information Engineering, Tianjin University, Tianjin, China
e-mail: belajiao@gmail.com

X. Zeng
ZTE Corporation, Tianjin, China

B. Zhang et al. (eds.), *The Proceedings of the Second International Conference on Communications, Signal Processing, and Systems*, Lecture Notes in Electrical Engineering 246, DOI 10.1007/978-3-319-00536-2_113,

Localization methods that integrated the indoor map improve the localization accuracy in a certain degree [4–6] discussed the pulse signal propagation characteristics caused by multipath error and NLOS error modeling problems, used NLOS distance error information directly to correct TOA ranging result to improve localization accuracy. But [6] did not detect the state (NLOS or LOS) of mobile nodes.

Since Dellaert and his fellows proposed the idea that putted particle filter into use of mobile robot localization in the meeting IEEE ICRA in 1999 [7], particle filter is being popular in the area of mobile target tracking and localization. But current measured information of standard particle filter (SPF) could be missed easily and particles will be exhausted after several round of resample. In this paper, we introduce one kind of IPF that partially solves the above problems of SPF. IPF algorithm will be elaborated in Sect. 3.

2 State Detection and Distance Offset

The distance model on LOS condition can be described as $d_k^m = d_k^{real} + n_k^{los}$, d_k^m is measured distance from MN to the m-th anchor node(AN), d_k^{real} is the real distance between them, n_k^{los} is measurement noise and it follows Gaussian distribution with mean $\mu = 0$ and variance σ_m^2. The distance model on NLOS condition is $d_k^m = d_k^{real} + n_k^{los} + n_k^{nlos}$, n_k^{nlos} means the NLOS error. We suppose that n_k^{nlos} follows truncation Gaussian distribution with mean b and variance σ^2, its probability density function can be written as:

$$\begin{cases} p\left(n_k^{nlos} = x\right) = \dfrac{1}{\sqrt{2\pi}\sigma} \exp\left(-\dfrac{(x-b)^2}{2\sigma^2}\right), 0 \le x \le 2b \\ p\left(n_k^{los} = x\right) = \dfrac{2}{\sqrt{2\pi}\sigma} \exp\left(-\dfrac{(x-b)^2}{2\sigma^2}\right), x \ge 2b \end{cases} \tag{1}$$

In real measurement, we can use the following two formulas to approach b and σ^2. Here $\hat{b} = \frac{1}{N'}\sum_{i=1}^{N'} x_i$ and $\hat{\sigma}^2 = \frac{1}{N'}\sum_{i=1}^{N'} (x_i - b)^2$ are likelihood estimations of b and σ^2, respectively. x_i is the i-th measured error on NLOS condition, the experiments number is N'. Assume the actual axis of MN at time k is (x_k,y_k), i-th AN's axis is (a_i,b_i), $i = 1, 2, \ldots M$, ANs' number is M. The obstacle in indoor environment is even and location known.

Figure 1 shows the procedure of algorithm of NLOS detection and offset. We suppose $D = [d_k^1, d_k^2, \ldots d_k^M]$ represent measured distance between MN and M-th anchor, respectively. Via least square method to get MN's first estimated location

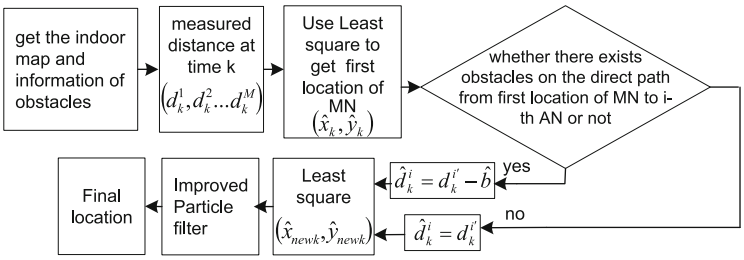

Fig. 1 Flowchart of NLOS detection and offset algorithm

axis $(\hat{x}_k, \hat{y}_k)$,then judge whether there have obstacles from $(\hat{x}_k, \hat{y}_k)$ to the i-th anchor (ANi) or not. If there exists obstacle, we mark the state between MN and ANi as NLOS, use the formula $\hat{d}_k^{\,i} = d_k^{i'} - \hat{b}$ to calculate the offset distance. If obstacle doesn't exist, then the state is marked as LOS, and the offset distance equals the measured distance, so that $\hat{d}_k^{\,i} = d_k^{i'}$. $\hat{d}_k^{\,i}$ represents the offset distance and $d_k^{i'}$ is distance between MN and ANi. Then we calculate location of MN by least square method according to the offset distances, and get the new estimated position $(\hat{x}_{newk}, \hat{y}_{newk})$.

3 Improved Particle Filter Algorithm

Particle filter [8] samples the posterior probability of the system state through Monte Carlo method and replace the integral operation of Bayesian estimation by a series of discrete particles to estimate state variables. State space model of Bayesian estimation system can be described as:

$$\begin{aligned} x_k &= f(x_{k-1}) + u_{k-1} \\ z_k &= h(x_k) + v_k \end{aligned} \tag{2}$$

$f(\cdot)$, $h(\cdot)$ represent the state equation and observation equation respectively, x_k is system state, z_k is observed value, u_k is process noise, v_k is observed noise. SPF choose the transition probability density of system state variables as the importance density function [9]. However this will lose the current measured value information in the prediction process of particles that makes the current estimated value heavily rely on model. Another problem is that though resample algorithm effectively resolves particle degradation problem, it inevitably brings particle exhausted problem. Therefore in this paper we introduce the current measured value during the prediction process of particles and the resample process. It will be coordinated by the weighted factor. We solve the problem that the prediction heavily depends on the system model, at the same time we ensure the diversity of particles. Moreover using the measured value of the start time to initialize the particles can avoid error

brought by inaccuracy initialization of particles to some degree. The following steps describe the improved particle filter:

1. Initialization: Set the start point k =1, in order to initialize particles $\{s_0^{(i)}\}_{i=1}^{N}$, we use location of MN $(\hat{x}_{new1}, \hat{y}_{new1})$ or measured distance at the start moment, $s^{(i)}$ represents the position state.
2. Prediction: By using distance prediction model and current observation information to predict particles of next moment.

$$s_k^{(i)} \sim p\left(s_k \middle| \left(s_{k-1}^{(i)} * \omega 1 + s_{ob} * \omega 2\right)\right), i = 1, 2 \ldots N \tag{3}$$

N is number of particles, $\omega 1$ and $\omega 2$ represent weighted factors and they satisfy the relationship $\omega 1 + \omega 2 = 1$, s_{ob} is current observation value.

3. Filtering

(a) Calculate importance weights:

When using the position $(\hat{x}_{newk}, \hat{y}_{newk})$ to update particles at next moment, importance weights can be calculated by the way :

$$w_k^{(i)} = p\left(z_k \middle| s_k^{(i)}\right), i = 1, 2, \ldots N \tag{4}$$

When using current observed offset distance to update weights of particles, the formula is:

$$w_k^{(i)} = \left(\prod_{j=1}^{M} p\left(z_k^j \middle| d_k^j\right)\right)^{\frac{1}{M}} \tag{5}$$

M is number of anchor nodes, $z_k^j = d_k^j + \zeta_k$, $j = 1, 2, \ldots M$. This observation model will be discussed in detail in Sect. 4.1.

(b) Weights normalization

$$\overline{w}_k^{(i)} = w_k^{(i)} / \sum_{i=1}^{N} w_k^{(i)}, i = 1, 2 \ldots N \tag{6}$$

(c) Output

$$\hat{s}_k = \sum_{i=1}^{N} \overline{w}_k^{(i)} s_k^{(i)} \tag{7}$$

(d) Resample

In this step, we introduce the current observation by multiplying a small weight, and regenerate N particles. Here we adopt the roulette wheel to

resample particles. The pseudocode of roulette resample is described as follows:

FUNCTION [pxpart] = rouletteresample(N,weights, pxpartminus, pxpart)
FOR i = 1 TO N
pu = rand;
pqtempsum = 0;
FOR j = 1 TO N
pqtempsum = pqtempsum + weights (j);
IF pqtempsum >= pu
*pxpart(i) = pxpartminus(j) *α+s_{ob}*β;%(it indicates that j-th particle is copied to the i-th particle through resample. α and β satisfy the relationship α + β=1 and α>>β, pxpart is the output of resample)*
BREAK;
END
END
END

4. Set k: $= k + 1$, go to (2) and conduct loop iteration.

4 Model Building and Simulation Analysis

In this paper we use two models to conduct experiment simulation, one is position prediction model and the other is distance prediction model. Suppose (x_k,y_k) is the estimated position of MN at time k, $\left(v_{x_k}, v_{y_k}\right)$ is MN's velocity at time k. z_k is observation variable which represents the actual position of MN at time k, d_k^i is the predicted distance from MN to the i-th AN at time k. $\zeta_k \sim N(0,\sigma_\zeta^2)$ is observation noise, $\eta_k \sim N(0,\sigma_\eta^2)$ is system noise, $i = 1, 2 \ldots M$, M is number of AN.

4.1 Position Prediction Model and Distance Prediction Model

Position prediction system model:

$$\begin{bmatrix} x_k & y_k \end{bmatrix}^T = \begin{bmatrix} x_{k-1} + v_{x_k}\Delta t & y_{k-1} + v_{y_k}\Delta t \end{bmatrix}^T + \eta_k \tag{8}$$

Position prediction observation model:

$$z_k = \begin{bmatrix} x_k & y_k \end{bmatrix}^T + \zeta_k \tag{9}$$

Distance prediction model:

$$d_k^i = \sqrt{(x_k - a_i)^2 + (y_k - b_i)^2} + \eta_k = \sqrt{(x_{k-1} + v_{x_k}\Delta t - a_i)^2 + \left(y_{k-1} + v_{y_k}\Delta t - b_i\right)^2} + \eta_k \tag{10}$$

Distance prediction observation model:

$$z_k = \left[d_k^1, d_k^2, \ldots d_k^M\right] + \zeta_k \tag{11}$$

4.2 Simulation and Analysis

The experiment is conducted at the platform MATLAB (version: 7.10.0.499) and computer processor is win32. Set the size of indoor environment to 10 m × 10 m. The ANs are on four corners of the room and obstacle is putted on the center of the room. The long of obstacle is set to 4 m and ignoring the width. MN moves along one side of obstacle in constant speed along a straight line. Its speed is $v = 0.2\ m/s$, and observation interval $\Delta t = 1s$. $\sigma_\eta^2 = 0.09$, $\sigma_\zeta^2 = 1.69$, weights are set as follows: $\alpha = 39/40$, $\beta = 1/40$; $\omega 1 = 2/3$, $\omega 2 = 1/3$, the number of particles N = 100. We compare 5 different methods in the simulation as follows:

1. Directly use the measured distance to locate the MN by the method least square (NLOS)
2. Use the SPF to track MN (NLOS + SPF)
3. Use the offset distance to locate MN by least square (NLOS offset)
4. Combine the method in (3) with SPF to track the MN (NLOS offset + SPF)
5. Combine the method in (3) with IPF to track the MN (NLOS offset + IPF)

Figure 2 depicts accumulated error curves of the above five kinds of cases. We can see that the localization error is decreased obviously by using the method which adopts NLOS detection and offset method and also we can see the performance of IPF is better than SPF. The method that combines NLOS detection and offset with improved particle filter can obtain the best performance of all. From Table 1 we can see that the localization average error of NLOS case is about 1.4 m, being reduced to about 0.3 m after using the proposed method in this paper. It confirms the effectiveness of the adopted method.

5 Conclusion

This paper discusses a new localization algorithm for indoor mobile target tracking under the condition indoor environment map is known. In the beginning, the algorithm uses least square method to locate MN and use this position to detect if there is an obstacle on the direct path from moving target to anchor. If there exists an obstacle, using the offset method to fix range value, and then through the improved particle filter to track moving target. Simulation results indicate that the

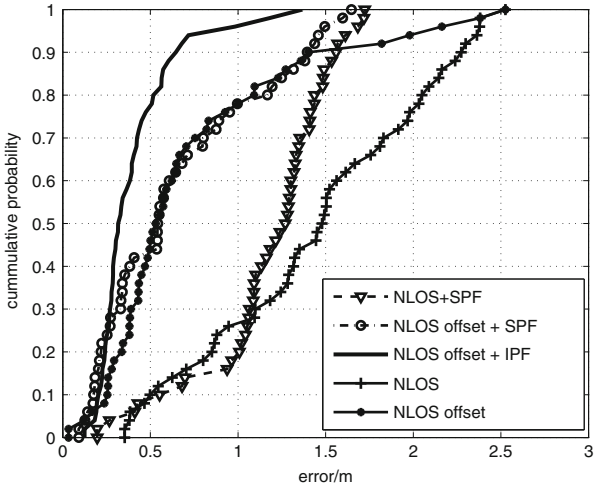

Fig. 2 CDF of five methods

Table 1 Average error of in dependent experiments (m)

Experiment times	1	2	3	4	5
NLOS	1.4419	1.4043	1.5756	1.4852	1.4680
NLOS + SPF	1.0703	1.2022	1.2403	1.2045	1.2203
NLOS offset	0.6928	0.7347	0.6598	0.6947	0.5789
NLOS offset + SPF	0.5573	0.5211	0.4170	0.5450	0.3008
NLOS offset + IPF	0.4351	0.3125	0.3366	0.4280	0.2686

NLOS detection and offset algorithm can improve the localization accuracy to a certain extent and due to the introduction of the current observation information, the performance of improved particle filter is better than standard particle filter. The method this paper proposed effectively improves the localization accuracy in complex indoor environment.

Acknowledgments This research is supported by research forums cooperation project of ZTE Corporation.

References

1. Marano S, Gifford WM, Wymeersch H et al (2010) NLOS identification and mitigation for localization based on UWB experimental data. IEEE J Sel Area Comm 28(7):1026–103. doi:510.1109/JSAC.2010.100907
2. Prieto J, Mazuelas S, Bahillo A et al (2010) NLOS mitigation prior to range estimation smoothing for wireless location systems. Proceedings of 2010 I.E. international conference on communications (ICC), pp 1–5

3. Jie Wang, Qinghua Gao, Yan Yu et al (2012) Toward robust indoor localization based on Bayesian filter using chirp-spread-spectrum ranging. IEEE Trans Ind Electr 59(3):1622–1629. doi: 10.1109/TIE.2011.2165462
4. Zhao Lijun, Sun Lining, Li Ruifeng et al (2009) On an improved SLAM algorithm in indoor environment. ROBOT 31(5):438–444
5. Evennou F, Marx F (2005) Map-aided indoor mobile localization system using particle filter. IEEE Comm Soc/WCNC 4:2490–2494
6. Meng Jing, Zhang Qinyu, Zhang Naitong et al (2011) Modeling the distance error and performance analysis in IR-UWB localization system. J Comm 32(6):10–16
7. Dellaert F, Fox D, Burgard W et al (1999) Monte Carlo localization for mobile robots. Proceedings of IEEE international conference on robotics and automation. Detroit, Michigan. pp 1322–1328
8. Sanjeev A, Maskell S, Gordon N et al (2002) A tutorial on particle filters for online nonlinear/non-Gaussian Bayesian tracking. IEEE Trans Signal Process 50(2):174–188
9. Djutić M, Kotecba H, Jianqui Zhang et al (2003) Particle filtering. IEEE Signal Process Mag 20 (5):19–38

A Kind of Localization Algorithm Based on Driver Test Data

Jian Shi, Jianfeng Huang, and Kaihua Liu

Abstract In this paper, we analyze several existing problems in the cellular radio network performance comparative analyses due to information barrier inter mobile operators. We propose an improved LEE propagation model to get more accurate prediction by collecting the massive driver test data for the correction factors' scientific computing within fine-granularity testing area. The new sliding aggregation window and the geometric Barycenter algorithms proposed in this paper are used to locate the base stations of competitor's networks more accurately.

Keywords Propagation model • Sliding aggregation window • Base station locating • Base station analysis

1 Introduction

With the rapid development of mobile communication technology, there is rapid growth in users and volume of business, which leads the competition between the various mobile network operators to become increasingly intense. For the data is not open, it is impossible to get the basic data of other operators' networks, because of the widespread information barriers between network operators. Contrast-type test indicators are generally used in horizontal contrast between operators. The away is the conventional DT/CQT (Drive Test/Call Quality Test) test, that is according to the coverage, connection rate, drop-call rate and MOS (Mean Opinion Score) test indicators. There are the following deficiencies between the different network comparative analysis technologies.

J. Shi (✉) • K. Liu
Tianjin University, Tianjin, China
e-mail: shijian@139.com

J. Huang
Beijing University of Posts and Telecommunications, Beijing, China

B. Zhang et al. (eds.), *The Proceedings of the Second International Conference on Communications, Signal Processing, and Systems*, Lecture Notes in Electrical Engineering 246, DOI 10.1007/978-3-319-00536-2_114,

1. Although it can collect a certain amount of service contrast between operators within the test area, it is unable to test and evaluate the rival networks' carrying capacity.
2. In the designated test area, the statistics cannot get the percentage traversing all the base stations of regional competitors' network.
3. It is unable to obtain current network base stations layout of other operators and to implement comparison analysis with competitors' operating network as a whole or partial performance.

In response to these problems, this paper proposes a new technical method increasing the geographical environment correction factor on the traditional LEE cellular propagation models for radio propagation model to implement fine-grained zone correction, which can effectively improve the predictive accuracy of the LEE model. On this basis, a set of algorithm to locate competitors' network sites based on driver test data is proposed, which is the application of one operator's own network test data correction factor for distance attenuation, propagation model and geographical environment in the near frequency range and the same test area. Combined with the convergence of sliding window technique and the geometric Barycenter algorithm, the method is also applied to competitors in the wireless locating of the base station to effectively improve the accuracy of sites positioning algorithm.

2 The Improved LEE Dissemination Model

2.1 The Traditional LEE Model

Equation (1) shows the traditional LEE model:

$$P_r = P_{r1} + (-\gamma) \cdot \lg \frac{d}{d_0} + \alpha_0 - n \lg \frac{f}{f_0} \tag{1}$$

In (1), P_r is the received power, d is the horizontal distance between the transmitting and receiving antennas, γ is the distance attenuation factor, P_{r1} is the received power away from 1 km in a particular city when measured using the base station antenna in the normal launch state. d_0 is taken as 1 km, f_0 is taken as 850 MHz, n is determined by f and f_0, as shown in (2).

$$n = \begin{cases} 20 & f < f_0 \\ 30 & f > f_0 \end{cases} \tag{2}$$

α_0 is the transceiver correction factor, it is used actually when the base station antenna and the standard antenna are not in the same correction, the calculation formula of α_0 is in (3) [1]

$$\alpha_0 = \left(\frac{h_t}{h_{tREF}}\right)^2 \frac{P_t}{P_{tREF}} 10^{\frac{G_t - G_{tREF}}{10}} \tag{3}$$

In (2), h_t, P_t, G_t is respectively the actual antenna height of base station, the transmitting power of base station and antenna gain of base station, h_{tREF}, P_{tREF}, G_{tREF} are respectively the antenna height of base station, transmission power of base station and the base station antenna gain, when P_{r1} and γ are measured.

2.2 The Improved LEE Propagation Model

The geographical attributes, such as geology, topography, geomorphology, vegetation, construction and environmental impact have effect on the accuracy of propagation model. And in each test region, the impacts of these different geographic attributes are different. Thus, it has important engineering significance to estimate scientifically the geographic environmental factors for different test areas. In order to have further improvement of the traditional LEE propagation model, an accurate description of the combined effects of the different geographical attributes of different test areas with different sizes, variable G_{AREA} is proposed. The improved propagation model of LEE is as follows in (4).

$$P_r = P_{r1} + (-\gamma) \cdot \lg \frac{d}{d_0} + \alpha_0 - n \lg \frac{f}{f_0} + G_{AREA} \tag{4}$$

In (4), G_{AREA} is the local correction for the dissemination of environmental correction factor, which is based on the geographical attributes within propagation loss of the test area. By analyzing mass data of DT, the differences generated by radio propagation loss can be performed more granular partial accurate correction according to different geographical and environmental properties of different areas, so that the precision forecasted by propagation model can be improved.

3 Sites Positioning of Driver Test Data

3.1 Acquisition and Processing of Driver Test Data

In order to ensure the sufficiency of the sampling data, driver test of own network and the competitors' network should be done in the same car. Both the data acquisition of the originating and terminating call test modules are implemented synchronously. All the test modules share the same GPS to receive positioning data and try to keep the constant speed at the same time. Moreover, the speed should remain moderate and be less than 20 km/h.

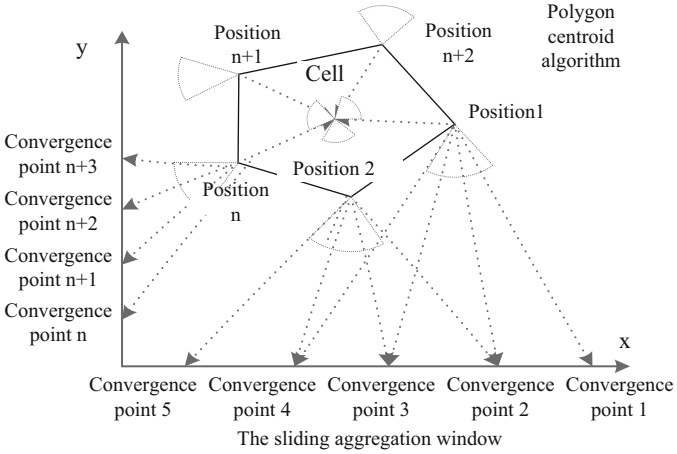

Fig. 1 Sliding aggregation geometric center location

Considering the test data is sampled in accordance with Lee's law, which needs that the difference between the test data and the local mean is less than 1 dB and wireless signal remains in slow fading and effective smooth fast fading, 36–50 sampling points are required in the range of 40 wavelengths [2]. Mean convergence window (raster) is used to converge the test sample points, the method of which is to segment the test route per 6 m, take every 6 m within the test area, and take the average of the reception level of the test samples in the same cell, thereafter, the average is taken as the signal field strength of the center in the area.

Combining the improved LEE radio propagation model that this paper proposed, the station of rival network can be effectively located base on the effective collecting and rasterize processing for mass data of DT. For further improving the accuracy of locating station, this paper proposes a new sliding aggregation geometric Barycenter algorithm which can locate the locating of station more accurately by making full use of mass data of radio signal measurement in DT.

3.2 Location Algorithm of Cell Site

The site localization algorithm of the competitor based on sliding aggregation window and geometric center positioning is shown in Fig. 1. First, this algorithm can perform multiple operations for the DT data of each aggregation window and fully exploit the useful location information by using the mechanism of sliding aggregation window. The number of operations of each aggregation window's DT data is related with parameters and factors to be determined in the improved LEE model. Second, by using the Barycenter algorithm of polygon, all the single cell's base station locating results can be performed effective error correction, so that the locating accuracy can be improved. At last, by using the cell's total base station analysis matching algorithm, the base station locating accuracy can be further improved.

The key to the sites location algorithm is the use of test data of cells and sites location of one's own network to calculate the distance attenuation factor γ_q and environmental correction factor $G_{AREA}(q)$ of the specified aggregating interval for the propagation model. The algorithm is described as follows, the four consecutive sampling convergence points q, $q + 1$, $q + 2$, $q + 3$ of CELL_i are used to create two sets of propagation (5) and (6) in convergence regions of **CON**(q), **CON**($q + 1$), **CON**($q + 2$), **CON**($q + 3$).

$$\begin{cases} P_r[\mathrm{CELL}_i(q)] = P_{r1} - \gamma_{\mathrm{CELL}_i(q)} \cdot \lg \dfrac{d_{[lon(q),lat(q)]}}{d_0} + \alpha_0 \left[\mathrm{CELL}_i(q)\right] \\ \qquad\qquad -n\lg \dfrac{f}{f_0} + G_{AREA}\left[\mathrm{CELL}_i(q)\right] \\ P_r[\mathrm{CELL}_i(q+1)] = P_{r1} - \gamma_{\mathrm{CELL}_i(q)} \cdot \lg \dfrac{d_{[lon(q+1),lat(q+1)]}}{d_0} + \alpha_0 \left[\mathrm{CELL}_i(q)\right] \\ \qquad\qquad -n\lg \dfrac{f}{f_0} + G_{AREA}\left[\mathrm{CELL}_i(q)\right] \\ P_r[\mathrm{CELL}_i(q+2)] = P_{r1} - \gamma_{\mathrm{CELL}_i(q)} \cdot \lg \dfrac{d_{[lon(q+2),lat(q+2)]}}{d_0} + \alpha_0 \left[\mathrm{CELL}_i(q)\right] \\ \qquad\qquad -n\lg \dfrac{f}{f_0} + G_{AREA}\left[\mathrm{CELL}_i(q)\right] \end{cases} \tag{5}$$

$$\begin{cases} P_r[\mathrm{CELL}_i(q+1)] = P_{r1} - \gamma_{\mathrm{CELL}_i(q)} \cdot \lg \dfrac{d_{[lon(q+1),lat(q+1)]}}{d_0} + \alpha_0 \left[\mathrm{CELL}_i(q)\right] \\ \qquad\qquad -n\lg \dfrac{f}{f_0} + G_{AREA}\left[\mathrm{CELL}_i(q)\right] \\ P_r[\mathrm{CELL}_i(q+2)] = P_{r1} - \gamma_{\mathrm{CELL}_i(q)} \cdot \lg \dfrac{d_{[lon(q+2),lat(q+2)]}}{d_0} + \alpha_0 \left[\mathrm{CELL}_i(q)\right] \\ \qquad\qquad -n\lg \dfrac{f}{f_0} + G_{AREA}\left[\mathrm{CELL}_i(q)\right] \\ P_r[\mathrm{CELL}_i(q+3)] = P_{r1} - \gamma_{\mathrm{CELL}_i(q)} \cdot \lg \dfrac{d_{[lon(q+3),lat(q+3)]}}{d_0} + \alpha_0 \left[\mathrm{CELL}_i(q)\right] \\ \qquad\qquad -n\lg \dfrac{f}{f_0} + G_{AREA}\left[\mathrm{CELL}_i(q)\right] \end{cases} \tag{6}$$

In (5) and (6), [$lon(q)$, $lat(q)$], [$lon(q + 1)$, $lat(q + 1)$], [$lon(q + 2)$, $lat(q + 2)$] and [$lon(q + 3)$, $lat(q + 3)$] are respectively the latitude and longitude of the center

point of the four consecutive convergence regions **CON**(q), **CON**(q + 1), **CON** (q + 2), **CON**(q + 3). Two propagation factors of the specified cell CELL_i in three consecutive convergence regions, $\gamma_{\mathrm{CELL}_i(q)}$ and $G_{AREA}[\mathrm{CELL}_i(q)]$, can be determined. Then take the mean of the various propagation factors derived from the two equations as the distance attenuation factor $\overline{\gamma}_{\mathrm{CELL}_i(q)}$ and environmental correction factor $\overline{G_{AREA}}[\mathrm{CELL}_i(q)]$ of the four successive convergence regions.

$$\overline{\gamma}_q = \sum_{\mathrm{CELL}_i \in \mathbf{CON}_4(q)} \overline{\gamma}_{\mathrm{CELL}_i(q)} / count_4(q) \tag{7}$$

$$\overline{G_{AREA}}(q) = \sum_{\mathrm{CELL}_i \in \mathbf{CON}_4(q)} \overline{G_{AREA}}[\mathrm{CELL}_i(q) / count_4(q) \tag{8}$$

In (7) and (8), $\mathbf{CON}_4(q) = \mathbf{CON}(q) \cup \mathbf{CON}(q+1) \cup \mathbf{CON}(q+2) \cup \mathbf{CON}(q+3)$ is the set of the measured cells in the four consecutive convergence regions within one's own wireless network. Variable $count_4(q)$ is the total number of the cells in one's own wireless network.

In order to locate the tested cell $\mathrm{CELL}_j^{'}$ of the competitors' network in the area of $\mathbf{CON}_4(q)$, positioning equations of the measured cell station is established using the measurement level of the tested cell $\mathrm{CELL}_j^{'}$ in four consecutive sliding aggregation intervals, the following (9) is shown.

$$\begin{cases} P_r\left[\mathrm{CELL}_j^{'}(q)\right] = P_{r1}^{'} - \gamma_{\mathrm{CELL}_i(q)} \cdot \lg \dfrac{d_{[lon(q),lat(q)]}}{d_0} + \alpha_0 \left[\mathrm{CELL}_j^{'}(q)\right] \\ \qquad\qquad -n \lg \dfrac{f}{f_0} + G_{AREA}\left[\mathrm{CELL}_i(q)\right] \\ P_r\left[\mathrm{CELL}_j^{'}(q+1)\right] = P_{r1}^{'} - \gamma_{\mathrm{CELL}_i(q)} \cdot \lg \dfrac{d_{[lon(q+1),lat(q+1)]}}{d_0} + \alpha_0 \left[\mathrm{CELL}_j^{'}(q)\right] \\ \qquad\qquad -n \lg \dfrac{f}{f_0} + G_{AREA}\left[\mathrm{CELL}_i(q)\right] \\ P_r\left[\mathrm{CELL}_j^{'}(q+2)\right] = P_{r1}^{'} - \gamma_{\mathrm{CELL}_i(q)} \cdot \lg \dfrac{d_{[lon(q+2),lat(q+2)]}}{d_0} + \alpha_0 \left[\mathrm{CELL}_j^{'}(q)\right] \\ \qquad\qquad -n \lg \dfrac{f}{f_0} + G_{AREA}\left[\mathrm{CELL}_i(q)\right] \\ P_r\left[\mathrm{CELL}_j^{'}(q+3)\right] = P_{r1}^{'} - \gamma_{\mathrm{CELL}_i(q)} \cdot \lg \dfrac{d_{[lon(q+3),lat(q+3)]}}{d_0} + \alpha_0 \left[\mathrm{CELL}_j^{'}(q)\right] \\ \qquad\qquad -n \lg \dfrac{f}{f_0} + G_{AREA}\left[\mathrm{CELL}_i(q)\right] \end{cases} \tag{9}$$

Through solution of (9), geographical latitude and longitude of the station of $CELL_j'$ can be obtained. The sliding window technique, as shown in Fig. 1, is reused to analyze and process the test data of the entire network. Then multiple solutions of the latitude and longitude of the stations of $CELL_j'$ are acquired to construct a geometric polygon. By calculating the gravity center of the geometric polygon, the geographical latitude and longitude with higher degree of accuracy of the transceiver antenna of base station is computed.

$$\overline{X} = \frac{X_1 + X_2 + \ldots + X_i + \ldots + X_N}{N} \tag{10}$$

$$\overline{Y} = \frac{Y_1 + Y_2 + \ldots + Y_i + \ldots + Y_N}{N} \tag{11}$$

In (10) and (11), (X_i,Y_i) is the solution of the latitude and longitude of the ith positioning point of cell station, $(\overline{X}, \overline{Y})$ is the latitude and longitude of the polygon's center of gravity.

3.3 Analysis of Cell Co-location

In the existing cellular wireless network, in order to improve the capacity of wireless network and save the cost of station arrangement, outdoor sites usually contain three cells, which means three cells with three different coverage azimuths are in the same base station. Through the analyzing signals of driver test data, the ID number of related cell in competitors' wireless network is derived and information of the cells with the same base station is calculated according to the numbers of different operators. Through a comprehensive analysis, the general naming rules of ID number of the WCDMA network [3] and CDMA network are as follows.

$$\text{WCDMA} : \text{Cell\_Identity} = \text{RNC\_ID} * 65536 + \text{Cell\_ID} \tag{12}$$

$$\text{CDMA} : \text{BASE\_ID} = \text{Site\_ID} * 16 + \text{Sector\_ID} \tag{13}$$

The cell number of the competitors should match with the number of the base station. Through analysis of driver test data signals, the ID numbers of competitors' cells are obtained and the information of the competitors' wireless base station numbers are deduced according to the principles of China Unicom and China Telecom rules. In the sites positioning process, the information is used to determine whether the cells are using the same base station. In order to improve the validity and accuracy of positioning of the sites, it is necessary consolidate the latitude and longitude of the cells with the same station according to the principles of the geometric Barycenter.

3.4 Application of the Sites Positioning

The proposed site location analysis algorithm and system has completed the research, development and on-line application in Tianjin Branch of China Mobile Group. The system makes full use automatic driver test mass data of China Mobile Group to explore competitors' sites information. Combined with Tianjin's automatic driver test system, the system supports contrast of the number of competitors' site structure, the GIS positioning of the sites and analysis of sites trends, which provides decision-making reference for planning projects and forms a set of technical support and management system for the whole life cycle of network management.

Engineering practice of Tianjin shows that the proposed sliding aggregation window of base station and the geometric Barycenter algorithm of positioning technology make a percentage of 36.74 with positioning accuracy within 50 m, a percentage of 57.37 with positioning accuracy within 50–100 m, a percentage of 5.89 with positioning accuracy above 50 m, when the driver test data adequacy is guaranteed. The positioning accuracy of the system is good enough to meet the requirements of the sites analysis system for engineering applications. Through several rounds of historical accumulated data of Tianjin, higher traversal rate of the competitors' wireless network sites is obtained. The traversal rate of base station of Tianjin Telecom CDMA network and Tianjin Unicom WCDMA network is respectively up to 94.45 and 95.23 %, which can meet the basic requirements of sites analysis in engineering applications.

After taking the proposed site location analysis technology to analyze site location of the two operators in the main city of Tianjin, China Telecom and China Unicom, as shown in Fig. 2, In Table 1 the number of sites of the three major mobile network operators in the main city of Tianjin is deduced.

4 Conclusions

Application of the paralleling test capability of multi-module driver test equipment in the present industry makes it a reasonable thought to collect massive wireless network test data of various systems and implement fine-granularity calibration of the propagation model, and then to position accurately base station sites. Practice has proved that the proposed site location analysis algorithm is of great engineering reference value to planning, optimizing and constructing decisions of wireless networks for mobile communication operators.

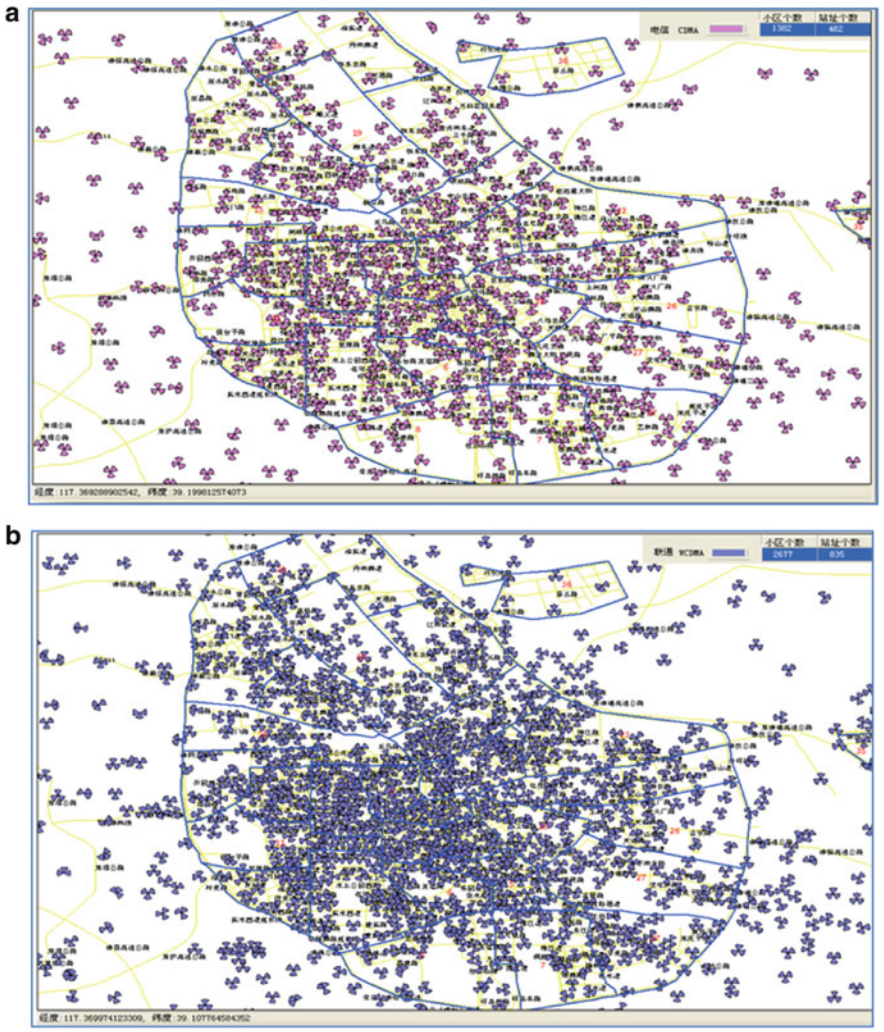

Fig. 2 (**a**) Distribution of the main city of Tianjin's CDMA network sites (**b**) Distribution of the main city of Tianjin's WCDMA network sites

Table 1 Contrast in the number of sites of the three major operators in Tianjin

Operator	Network type	Number of base stations
China mobile	GSM900	660
	GSM1800	629
	TD-SCDMA	597
China telecom	CDMA	462
China unicom	WCDMA	835

References

1. Lee DJY, Lee WCY (2000) Fine Tune Lee Model. J Personal Indoor Mobile Radio Communications
2. Lee CY (1997) Mobile communication engineering: theory and applications, 2nd edn. McGraw-Hill Professional, New York, USA
3. 3GPP Technical Specification 25.301, Radio Interface Protocol Architecture 3GPP Technical Specification

The Research of Satellite Selection Algorithm in Positioning System

Anhong Tian, Chengbiao Fu, Dechun Dong, and Siyuan Yang

Abstract In Global Navigation Satellite System (GNSS), the integrated system will provide twice and more satellites than individual system, visible satellite number can reach more than 40 in the same epoch moment, the satellite selection algorithm is very important for increasing navigation location precision, and visible satellite geometry is the most crucial factor. The classical optimal algorithm selects n satellite subsets from m visible satellites with the minimum GDOP (Geometry Dilution of Precision), its computation amount is very large especially for much many satellites. This paper presents a new satellite selection algorithm, the selection algorithm is simulated and validated by a software simulation. This algorithm can get the GDOP value close to the minimal GDOP value, and its computation amount is very small.

Keywords GDOP • Optimal satellite selection • The maximum tetrahedral volume • GNSS

1 Introduction

GNSS (Global Navigation Satellite Systems) are worldwide, all-weather navigation systems, which can provide three-dimensional positioning [1], velocity and time synchronization. Currently, with the development of GNSS, the number of global navigation satellites in view can be greatly increased to 40 in the same epoch moment, the present GNSS are GPS, GLONASS, Galileo and Compass, multi-constellation navigation system will improve navigation accuracy, integrity and reliability, however, the excessive redundancy information [2] will bring about

A. Tian • C. Fu (✉) • D. Dong • S. Yang
Department of Computer Science and Engineering, Qujing Normal College, Qujing, China
e-mail: fucb305@gmail.com

B. Zhang et al. (eds.), *The Proceedings of the Second International Conference on Communications, Signal Processing, and Systems*, Lecture Notes in Electrical Engineering 246, DOI 10.1007/978-3-319-00536-2_115,

heavy calculation load. Furthermore, how to choose a subset of satellites with good geometry distribution is significant.

As everyone knows, GDOP is the most important indicator to measure user position accuracy, and the receiver usually adopts GDOP minimum criteria as the traditional satellite selection algorithm, but the algorithm based on GDOP minimum criteria will bring enormous amount of computation, it requires a long time for computing especially for much many satellites.

In order to further reduce the calculation load and improve the effect of satellite selection, this paper studies the relationship between GDOP and tetrahedral volume value, and compare the performance about them, the performance of this algorithm is analyzed theoretically and evaluated by computer simulation.

2 The Calculation Method of GDOP

As everyone knows, it needs at least four satellites to calculate the receiver's dimensional coordinate and clock offset [3], this is shown in Fig. 1.

GPS pseudo-range observation equations are defined as follows:

$$\begin{cases} r_1 = \sqrt{(x_1 - x_u)^2 + (y_1 - y_u)^2 + (z_1 - z_u)^2} + ct_u \\ r_2 = \sqrt{(x_2 - x_u)^2 + (y_2 - y_u)^2 + (z_2 - z_u)^2} + ct_u \\ r_3 = \sqrt{(x_3 - x_u)^2 + (y_3 - y_u)^2 + (z_3 - z_u)^2} + ct_u \\ r_4 = \sqrt{(x_4 - x_u)^2 + (y_4 - y_u)^2 + (z_4 - z_u)^2} + ct_u \end{cases} \tag{1}$$

Where (x_i,y_i,z_i) denotes the coordinate of the GPS satellite, (x_u,y_u,z_u) denotes the receiver position, r_i denotes pseudo-range observation, t_u denotes receiver clock offset, c is the speed of light, (x_u,y_u,z_u,t_u) is four unknowns parameters.

Obviously (1) is non-linear, the pseudo-range equations can be linearized with Taylor's series expansion at the approximate point, then (1) can be shown as follows:

$$\begin{cases} \Delta r_1 = a_{x1}\Delta x_u + a_{y1}\Delta y_u + a_{z1}\Delta z_u - c\Delta t_u \\ \Delta r_2 = a_{x2}\Delta x_u + a_{y2}\Delta y_u + a_{z2}\Delta z_u - c\Delta t_u \\ \Delta r_3 = a_{x3}\Delta x_u + a_{y3}\Delta y_u + a_{z3}\Delta z_u - c\Delta t_u \\ \Delta r_4 = a_{x4}\Delta x_u + a_{y4}\Delta y_u + a_{z4}\Delta z_u - c\Delta t_u \end{cases} \tag{2}$$

Where Δr_i denotes the pseudo-range increment, (Δx_u, Δy_u, Δz_u, Δt_u) denotes the user's coordinate increment and clock offset increment.

And,

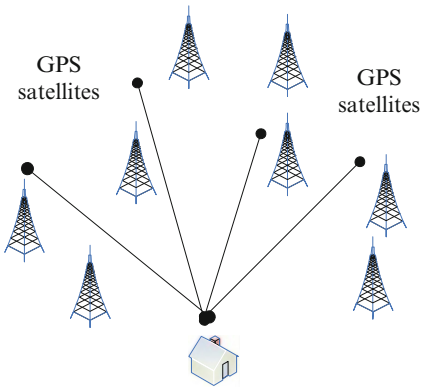

Fig. 1 GPS positioning

$$\Delta r = \begin{bmatrix} \Delta r \\ \Delta r_2 \\ \Delta r_3 \\ \Delta r_4 \end{bmatrix}, H = \begin{bmatrix} a_{x1} & a_{y1} & a_{z1} & 1 \\ a_{x2} & a_{y2} & a_{z2} & 1 \\ a_{x3} & a_{y3} & a_{z3} & 1 \\ a_{x4} & a_{y4} & a_{z4} & 1 \end{bmatrix}, \Delta x = \begin{bmatrix} \Delta x_u \\ \Delta y_u \\ \Delta z_u \\ -c\Delta t_u \end{bmatrix} \tag{3}$$

We can use least squares method to obtain an estimated value of X, this is shown as follows:

$$X_{LS} = \left(H^T H\right)^{-1} H^T Y \tag{4}$$

Then, GDOP can be shown as follows:

$$GDOP = \sqrt{trace\left(H^T H\right)^{-1}} \tag{5}$$

Hence, GDOP involves matrix inversion and matrix multiplication [3], whose computational complexity will be greatly increased with the dimensions of matrix growing.

3 Traditional Optimal Satellite Selection Algorithm

We can use GPS technology to locate object information, which is used for wide variety of scientific applications. Assuming that m visible satellites can provide measurements, satellite selection algorithm is to choose n satellite subsets from m visible satellites ($n \leq m$), then the optimal satellite selection algorithm is to choose the satellite subset with the minimal GDOP as the selection result by calculating all satellite subsets' GDOP, thus there are altogether C_m^n subsets [4]. Although it can get the best selection result, the optimal algorithm has a large

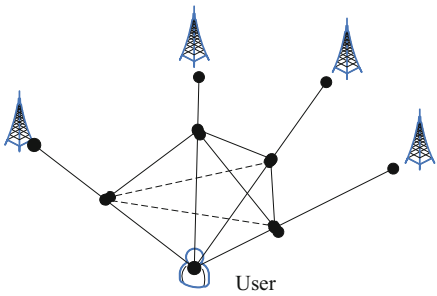

Fig. 2 The tetrahedral algorithm of 4-satellite

amount of computational burden, such as matrix and inverse matrix multiplication, so it is not appropriate for engineering application.

4 The Maximum Tetrahedral Volume Satellite Selection Algorithm

The tetrahedral volume algorithm of 4-satellite is shown in Fig. 2.

The relationship between GDOP and volume can be expressed as follows:

$$\mathrm{GDOP} = \sqrt{trace\left(H^T H\right)^{-1}} = \sqrt{trace\frac{\left(H^T H\right)^*}{|H|^2}} = \frac{\sqrt{trace\left\{\left(H^T H\right)^*\right\}}}{|H|} \tag{6}$$

Where $(H^T H)^*$ is the adjoint matrix of $(H^T H)$, trace() is the trace of a matrix.

Assume, $B = \sqrt{trace\left\{\left(H^T H\right)^*\right\}}$

Hence, $GDOP = \frac{B}{|H|}$

The relationship between tetrahedral volume and determinant can be expressed as follows [5]:

$$V = \frac{1}{6}|H| \tag{7}$$

Where V denotes tetrahedral volume.

Hence,

$$GDOP = \frac{1}{6} \cdot \frac{B}{V} \tag{8}$$

We can see that GDOP is approximately inversely proportional [6] to the volume of satellite tetrahedron.

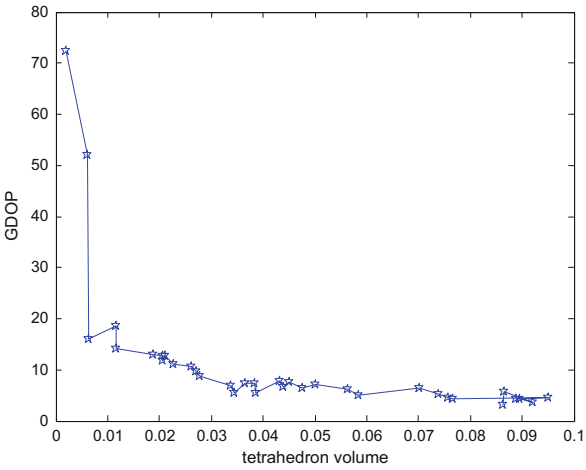

Fig. 3 The relationship between tetrahedron volume and GDOP

5 Simulation

In order to testify the relationship between tetrahedron volume and GDOP value, the simulation result is shown in Fig. 3. We select four visible satellites from seven visible satellites, there are altogether C_7^4 subsets.

The simulation result shows that as the tetrahedron volume increases, the GDOP value is becoming small basically, and this relationship can also be shown in Table 1. We select randomly five visible satellites from seven visible satellites, assumption for the satellite 1, 3, 4, 5, 7, there are altogether C_5^4 subsets.

In Table 1, according to the principle of inversely proportional relationship between tetrahedral volume and GDOP, we select the combination satellites about (1,3,5,7) as optimal constellation, but in fact, because of the GDOP minimum of combination satellites (1,3,4,5), it is the true optimal constellation. Therefore, this method is feasible in theory, and reduce the calculation load, but it is not as accurate as optimal satellite selection algorithm. However, the deviation is so little that we can ignore it.

In order to compare the computational complexity between maximum tetrahedral volume algorithm and traditional optimal satellite selection algorithm, we can get Table 2.

Table 2 indicates that the multiplication and inversion calculation times of traditional optimal algorithm is far more than that of the maximum tetrahedral volume algorithm, and with the number of visible satellites increasing, the accelerated speed of calculation times in the maximum tetrahedral volume algorithm is faster.

Table 1 Comparison the tetrahedral volume and GDOP of four satellites

Four Satellites	GDOP	Tetrahedral volume
1,3,4,5	4.9005	0.0539
1,3,4,7	5.0768	0.0680
1,3,5,7	4.9529	0.0735
1,4,5,7	5.6374	0.0507
3,4,5,7	51.8726	0.0086

Table 2 Comparison of the computational complexity for satellite selection algorithm

	Traditional optimal algorithm			Maximum tetrahedral volume algorithm		
Visible satellites	Matrix inverse times	Matrix multiplication times	Tetrahedral volume	Matrix inverse times	Matrix multiplication times	Tetrahedral volume
C_7^4	35	35	0	0	0	35
C_8^4	70	70	0	0	0	70
C_9^4	126	126	0	0	0	126
C_{10}^4	210	210	0	0	0	210

6 Conclusion

This paper studies the traditional satellite selection algorithm, which has a large amount of operation and requires a long time for computing, the computation time is still not acceptable when the number of visible satellites is very large. Then this paper studies the relation between tetrahedral volume and GDOP, and a new satellite selection algorithm is designed and the performance is validated by computer simulation. The simulation result shows that its computation is much less than optimal satellite selection algorithm. Furthermore, this algorithm can reduce the demand of capturing and tracking channels in receiver, and could reduce the designed costs of receiver to meet the needs of general market.

Acknowledgments This work was supported by Nature Science Foundation of Yunnan Province Education Department under Grant 2013Y017, about "the research of optimized satellite selection algorithm based on maximum determinant in positioning system," and Nature Science Foundation of Qujing Normal College under Grant 2012QN022 & 2012QN023 about "the research of satellite selection algorithm in global positioning system."

References

1. XuBo, BingjunShao (2009) Satellite selection algorithm for combined gpsgalileo navigation receiver. Proceedings of the 4th international conference on autonomous robots and agents, p 149–154. doi:10.1109/ICARA.2000.4803918

2. Li Guangyao, Xu Chengdong, Zhang Pengfei, Hu Chunsheng (2012) A modified satellite selection algorithm based on satellite contribution for GDOP in GNSS. Lecture Notes in Electrical Engineering 176(1):415–421. doi: 10.1007/978-3-642-31507-7_67
3. Wei Miaomiao, Wang Ju, Li Jiaqi (2012) A new satellite selection algorithm for real-time application. International conference on systems and informatics, ICSAI, p 2567–2570. doi:10.1109/ICSAI.2012.6223578
4. Zhang Miaoyan, Zhang Jun, Qin Yong (2007) A new quickly algorithm for GPS/Galileo/BD satellite selection. Second international conference on space information technology, vol 6795, p 67957I-1–67957I-6. doi: 10.1117/12.775523
5. Wan Qun, Peng Ying-Ning (2002) An improved 3-dimensional mobile location method using volume measurements of tetrahedron. In: Proceedings of the world congress on intelligent control and automation, vol 3, p 2181–2185. doi:10.1109/WCICA.2002.1021473
6. Sultana Quddusa, Hussain Md Abid, Malik MA (2013) Investigations into the relationship between GPS-DOP and unit-vector tetrahedron volume. International conference on emerging trends in VLSI, Embedded System, Nano electronics and telecommunication system, ICEVENT. doi:10.1109/ICEVENT.2013.6496546

A Fast Active Contour Tracking Method Based on Gaussian Mixture Model

Yuchen Wang, Xiaofeng Lu, and Mingyao Zhu

Abstract This paper proposed a Gaussian mixture model based gradient level set method (GMM-GLS) for moving target contour tracking in video sequences to handle automatic initialization and background variation. In contrast with conventional level set models, adaptive GMM background subtraction is applied to get the rough location of moving target as foreground in current frame. And more accurate mask image according to the rough location of foreground with dilatation operation indicates the initialization contour of level set evolution. Then, the gradient level set model can evolve the curve quickly and ensure more accurate convergence to the target contour in tracking procedure. Based on this accurate mask, the GMM-GLS method can greatly reduce the uncertain iteration time in curve convergence and optimize the initialization of GLS eliminating the interferential background. Experimental results on many real-world video sequences validate that our approach greatly improves the performance of object contour tracking.

Keywords Geometric active contours • Level set • Gaussian mixture model

Y. Wang • M. Zhu
School of Communication and Information Engineering, Shanghai University, Shanghai, China
e-mail: wangyuchen@shu.edu.cn

X. Lu (✉)
School of Communication and Information Engineering, Shanghai University, Shanghai, China

Shanghai Key Laboratory of Digital Media Processing and Transmissions, Shanghai Jiao Tong University, Shanghai, China
e-mail: luxiaofeng@shu.edu.cn

B. Zhang et al. (eds.), *The Proceedings of the Second International Conference on Communications, Signal Processing, and Systems*, Lecture Notes in Electrical Engineering 246, DOI 10.1007/978-3-319-00536-2_116,

1 Introduction

The target contour tracking in video sequences is important in computer vision. The continuous detection of accurate contours can benefit several video analysis tasks.

There are many algorithms to detect the contour of target in static images in recent years. The active contour model (ACM) [1] firstly proposed by Kass can detect object contour combining low and high level cues and it is convenient to model curve formulation. The ACM can be divided into two categories: parametric active contours (PAC) [2] and geometric active contours (GAC) [3]. Recently, researchers extend the ACM to object tracking in video. The contour detection of the target in video is difficult for object deformation, illumination, scale changes, etc. It is also easy to be confused with incorrect feature in background. The GAC can solve the topology changes to deal with complex targets. Some improvements of GAC have been proposed in these years. They improved the result of detected contour in images. GAC is based on curve evolution theory since Caselles et al. [4] introduced level set method into the GAC model in 1997. And the level set was first proposed in 1988 by Osher and Sethian [5]. AOS method of Weickert et al. [6] speed up the level set method. However, the computational load of these methods is unstable and result will be disturbed when we apply them into video. Li et al. [7] proposed the gradient level set method (GLS) to get rid of re-initialization procedure, but there is a huge computational cost in some frames if the initial curve location is far from the accurate object. In order to detect the contour in weak edge images, the Mumford-Shah (MS) model [8] was proposed to make use of global region information. One step forward, Chan and Vese [9] simplified the MS model to improve the computational efficiency. But the contour will gradually tend to worse because it use global feature to evolve the curve and it will be polluted by the complex background.

Therefore, GAC evolve object contour according to the edge or global information, the iterations are uncertain and time cost is high. The iterations can be reduced by proper initialization and accurate contour can be obtained if we can reduce the background interference when we apply the GAC model to video sequences. Rathi [10] proposed a GAC based particle filter to track object contour, but it still suffers from unstable convergence iterations because of the rectangle initialization. The work of Sun [11] introduced a supervised level set method to track contour in videos accurately, but the score map calculated in this method is complex and time cost.

In this paper, we proposed a fast and simple active contour tracking method based on Gaussian mixture model (GMM) [12]. The proposed GMM-GLS method improved the GLS algorithm in [7] on contour accuracy and convergence iterations. GMM is a fast and automatic method, and it reduced the total evolution time cost. On making use of the GMM calculated result, we can easily define the initial curve in each frame automatically and adjust the level set distance function to fit the initial curve. The GMM-GLS can ensure more efficient and reliable object contour result. At the same time, it needs less convergence iterations than conventional GAC model.

2 Active Contour Tracking Method Based on GMM

2.1 Gradient Based Level Set Method

Level Set as an implicit representation of the object contour is referenced from hydromechanics. The target contour is expressed as the zero level set of the graph of a higher dimensional curved surface function, and it minimizes an energy function based on the different constraints to the convergence result. So, the 2D curve $C(t)$ will be represented as the zero level set function $\Phi(h = 0)$ of the 3D curved surface. For this reason, the curve evolution can deal with topology changes and gives a closed expression. Equation (1) shows the level set function $\Phi(x,y,t)$.

$$\begin{cases} \dfrac{\partial \Phi}{\partial t} = g(x,y)|\nabla \Phi| \left(div\left(\dfrac{\nabla \Phi}{|\nabla \Phi|} \right) + k \right) \\ \Phi(x,y,0) = \Phi_0(x,y) \end{cases} \tag{1}$$

Where $g(x,y)$ is the evolution speed of the level set function. And Φ is altered through time t in the gradient direction. Another item is the rate of change of Φ and it is represented as the curvature multiplied by the gradient direction. When $t = 0$, $\Phi = \Phi_0$ will be formed by the initial curve. Φ_0 can also called symbol distance functions as (2). Φ_0 is calculated through the distance from each pixel to the initial curve.

$$\Phi_0(x,y) = \begin{cases} d(x,y,C_0) & (x,y) \text{ is inside } C_0 \\ 0 & (x,y) \text{ is on } C_0 \\ -d(x,y,C_0) & (x,y) \text{ is outside } C_0 \end{cases} \tag{2}$$

When the points on Φ_0 are inside C_0, the distance to curve is greater than zero. In the contrary, the Φ_0 will be negative if the pixel is outside C_0. The zero level set is the case that points are on C_0.

After initializing the distance function, the level set function will iterate as (1) shown. $g(x,y)$ can be represented as (3) since such level set method (GLS) evolves in the consideration of the gradient result. The $g(x,y)$ is monotone decreasing positive function. In (3), G_σ is the Gaussian kernel with variance σ. I is the gradient of current image. As a result, curves will slow down the evolution speed at edges of object after several iterations. The final convergent curve at last overlaps with the contour we want to detect. Figure 1 shows the evolution procedure and result of GLS. The initialization is manually represented as a red rectangle.

$$g(x,y) = \frac{1}{1 + |\nabla G_\sigma * I|} \tag{3}$$

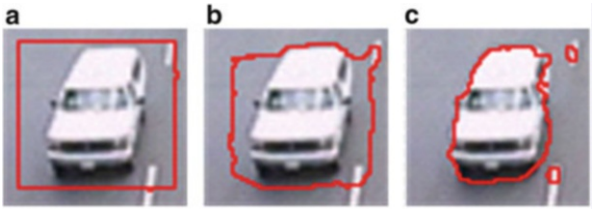

Fig. 1 GLS evolution initial contour (**a**), GLS intermediate result of 50 iterations (**b**), GLS result contour with 100 iterations (**c**)

The Fig. 1 shows that the final contour is on edge of target, and it will lead to different convergence result if the initial rectangle is different. However the convergence iterations are indeterminate because the initial position is changeful from the ideal target contour. This also makes the convergence computational time cost unstable. If the background is simple, the evolution result is very good. While in Fig. 1a–c, there is a sharp deterioration in result contour when some obstructive edges or patterns are near the object in background.

2.2 Gaussian Mixture Model for Background Subtraction

In order to reduce the convergence time cost and contour deterioration, in this paper we introduce background subtraction into GLS. Gaussian mixture model (GMM) [10] is suitable for foreground detection for speed and accuracy.

GMM build M Gaussian distributions for each pixel independently (M ranges from 3 to 7 generally). All Gaussian distributions have different weights and priorities, and they are sorted according to the priority. In video sequences, we calculate proper background weights and thresholds, then the elimination mechanism is used to judge whether the current pixel is suited to the specified distribution. Only the distributions of these pixels are larger than the threshold, they can be considered as background while the remaining ones are foreground. GMM can identify the background with small sample perturbations. Equation (4) is the N Gaussian distribution models of each pixel.

$$p(X_N) = \sum_{j=1}^{K} w_j \eta\left(X_N, \mu_j, \Sigma_j\right) \tag{4}$$

Where w is the corresponding weight. $\eta(X_N, \mu_j, \Sigma_j)$ is the *jth* Gaussian distribution. μ_j is the mean of Gaussian distribution. Σ_j is covariance matrix. According to the GMM algorithm procedure, the principle is that these pixels that their values are with low mean and high variance will be eliminated gradually for they are with high probability as new foreground pixels coming into the scene. GMM is competent to the small scale and fast moving objects detection with illumination changing not so drastic environment. The proposed GMM model in [10] can eliminate the shadow influence. When the illumination is changing, corresponding shadow region can cause the failure of foreground detection. GMM can generate mask image in each

frame where white part stand for moving foreground and black part is background. Mask images are the same in size as the video frames.

2.3 GMM Based Gradient Level Set Method

When the mask image is obtained, we can get the dilated mask image with morphology post-processing. And the biggest connected domain that can cover the whole target location and the "band of the background" in video sequence can be used to initialize our proposed GMM-GLS method as the initial contour.

In our proposed GMM-GLS method, the GMM procedure with dilated mask image is the first step, and in the second step of modified GLS with automatic location initialization instead of conventional rectangle, the final contour will be more accurate and with less iterations computational time cost.

In the background initialization, we can establish the GMM for tested video sequence. For current frame, the mask image eliminated the shadow influence will be obtained by this GMM module for foreground detection. The GMM module will update its background module, while sub-image rectangle that covers the whole the dilated mask image will be generated for curve convergence procedure. The modified GLS convergence module based on this dilated mask image can extract the accurate object contour with fewer iterations comparing with conventional GLS method. The computational time cost is reduced. And the proposed GMM-GLS algorithm procedure is shown in Table 1.

3 Experimental Results

In this section, we test the performance of the proposed GMM-GLS method on two video sequences. Video I is captured by ourselves, named "ycar." Video II, called "OneLeaveShopReenter" is from [13]. In this paper, we compare our experimental results with Li's GLS method [7], and the initialization GLS is manual rectangle.

3.1 Comparison with GLS Tracker

The GLS method is initialized manually with a rectangle encircling the target. While our proposed GMM-GLS is initialized by the dilated mask image generated by GMM.

In Video I, the luminance characteristics and texture of this yellow toy car is close to the background, and the background pixels will be included into the tracked target region frequently. As Fig. 2 shown, the whole toy car appears in 308th frame firstly. In 363rd frame, because the GLS algorithm [7] is initialized manually as a

Table 1 GMM-GLS algorithm procedure

Background initialization with m frames
  Set up and renew GMM for each pixel
For frame_num = m to the end
  Contour initialization
    1. Update GMM in current frame
    2. Calculate the mask image
    3. Eliminate the shadow and generate the dilated mask image
    4. Set the initial curve according to the dilated mask image
  Contour tracking
    For iteration_num = 0 to convergence
      Modified GLS iterates as (1)
    End
    Show the convergent evolution result in current frame
End

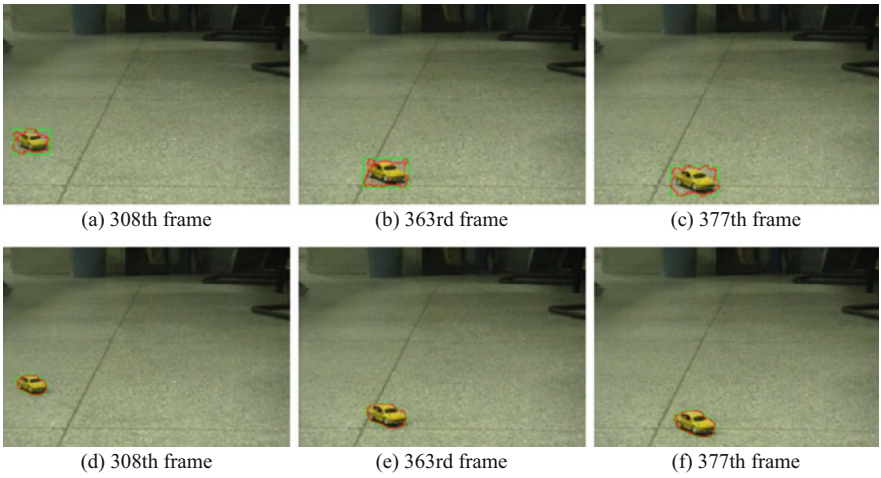

(a) 308th frame (b) 363rd frame (c) 377th frame

(d) 308th frame (e) 363rd frame (f) 377th frame

Fig. 2 Video I tracking results. (**a–c**) GLS with rectangle initialization (*green*) and its result contour (*red*). (**d–f**) GMM-GLS automatic initialization (*green*) and its result contour (*red*)

rectangle including foreground and background pixels, the dark lines in background around the car will be mistaken for the object edge as Fig. 2b, c shown. These lines and texture obstruct the evolution of GLS and increase the iterations. However, the proposed GMM-GLS can obtain good contour result as Fig. 2e, f shown. Based on the GMM module, GMM-GLS method can evolve the curve in the narrow "background band" to reduce convergence iterations computational time cost and improve the contour detection accuracy.

The second experimental results are presented in Fig. 3. The illumination changing on the non-rigid walking woman body is the most difficult for the accurate contour evolution. In GLS [7], contour evolution results are greatly hindered by

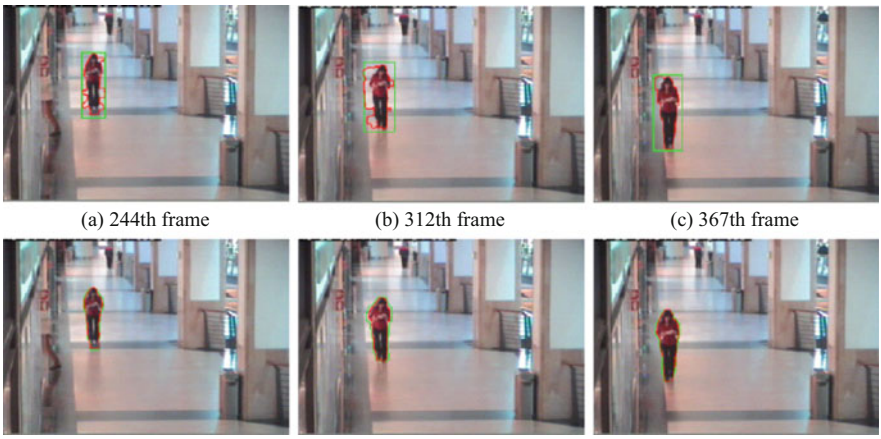

(a) 244th frame (b) 312th frame (c) 367th frame

(d) 244th frame (e) 312th frame (f) 367th frame

Fig. 3 Video II tracking results. (**a–c**) GLS with rectangle initialization (*green*) and its result contour (*red*). (**d–f**) GMM-GLS automatic initialization (*green*) and its result contour (*red*)

Table 2 Time consuming and iterations of GLS and GMM-GLS in specific frames

		GLS [7]		GMM-GLS		
Video	Frame	Time	Iterations	Time	Iterations	Decreasing (%)
I	308th	1764	202	292	24	83.4
	363rd	1859	214	309	25	83.3
	377th	1951	225	320	27	83.5
II	244th	2104	270	333	29	84.1
	312th	2296	278	343	31	85.1
	367th	2420	295	351	34	85.4

reflect light from the bright ground. As shown in Fig. 3a–c, many background edges are treated as object contour. While our proposed GMM-GLS method can solve this problem stably as shown in Fig. 3d–f.

3.2 Time Consuming Comparison with GLS Tracker

The computational time costs and iteration are measured in Table 2. The unit of time is ms/frame. The tested frames in two video sequences are 308–380th frame in Video I and 240–390th frame in Video II.

In these frames the interested targets are captured accurately. The average time decreasing is obvious and great. Additionally, Table 2 illustrates the tested results of GLS [7] and our proposed GMM-GLS in corresponding specific frames. The iterations here are ascertained when the evolution converges. The decreasing of the evolution iterations and time cost exceeding 80 % with more stable contour evolution results.

4 Conclusion

The article introduces the novel GMM-GLS method to track the object contour in video sequences. This method applies the motion information into the geometric active contour based on GMM to set better initial curve instead of rectangle initialization. Benefited from the dilated mask image based initial curve, the iteration time is stable with more accurate evolution results. And the curve evolution won't be obstructed by wrong edges near the target in the background. The experimental results show the improvement of this method in accuracy and computing speed.

References

1. Kass M, Witkin A, Terzopoulos D (1987) Snakes: active contour models. Int J Comput Vis 1:321–331. doi:10.1007/bf00133570
2. Xu C, Prince J (1998) Snakes, shapes, and gradient vector flow. IEEE Trans Image Process 7:359–369. doi:10.1109/83.661186
3. Caselles V, Catte F, Coll T, Dibos F (1993) A geometric model for active contours in image processing. Numer Math 66:1–31. doi:10.1007/BF01385685
4. Caselles V, Kimmel R, Sapiro G (1997) Geodesic active contours. Int J Comput Vis 22:61–79. doi:10.1023/A:1007979827043
5. Osher S, Sethian JA (1988) Fronts propagating with curvature dependent speed: algorithms based on Hamilton-Jacobi formulation. J Comput Phys 79:12–49. doi:10.1016/0021-9991(88)90002-2
6. Weickert J, Romeny BMH, Viergever MA (1998) Efficient and reliable schemes for nonlinear diffusion filtering. IEEE Trans Image Process 7:398–410. doi:10.1109/83.661190
7. Li C, Xu C, Gui C (2005) Level set evolution without re-initialization: a new variational formulation. Proc IEEE Conf Comput Vis Pattern Recogn 1:430–436. doi:10.1109/CVPR.2005.213
8. Mumford D, Shah J (1989) Optimal approximation by piecewise smooth functions and associated variational problems: commun. Comm Pure Appl Math 42:577–685. doi:10.1002/cpa.3160420503
9. Chan T, Vese L (2001) Active contours without edges. IEEE Trans Image Process 10:266–277. doi:10.1109/83.902291
10. Rathi Y, Vaswani N, Tannenbaum A, Yezzi A (2005) Particle filtering for geometric active contours with application to tracking moving and deforming objects. IEEE Comput Soc Conf Comput Vis Pattern Recogn 2:2–9. doi:10.1109/CVPR.2005.271
11. Sun X, Yao H, Zhang S (2011) A novel supervised level set method for non-rigid object tracking. IEEE Conf Digital Object Identifier Comput Vis Pattern Recogn 3393–3400. doi: 10.1109/CVPR.2011.5995656
12. Zivkovic Z (2004) Improved adaptive Gaussian mixture model for background subtraction. Proceedings of the 17th international conference on pattern recognition, vol 2, pp 23–26. doi: 10.1109/ICPR.2004.1333992
13. The School of Informatics of the University of Edinburgh (2004) CAVIAR Test Case Scenarios. http://groups.inf.ed.ac.uk/vision/CAVIAR/CAVIARDATA1. Accessed 31 Apr 2013

Decision Fusion in Target Detection Using UWB Radar Sensor Network

Ishrat Maherin and Qilian Liang

Abstract Ultra Wide Band (UWB), Radar Sensor Network (RSN) can be used to detect target in foliage environment. Information theoretic algorithms like entropy, relative entropy and mutual information are proven methods that can be applied to data collected by various sensors. However, the complexity of the environment posses uncertainty in fusion center and correct decision can only be made by decision fusion. In this paper we propose two methods Dempster and Shafer (D–S) theory of evidence and bayesian network for combining the decision of target detection. We resolved the conflict of decision by applying these methods. We also introduce the improved version of D–S theory for conflicting evidence and compared the performance with D–S and bayesian network. Accurate detection can be achieved by applying these methods, when echoes are in poor quality. The performance of the algorithm was evaluated, based on real world data.

1 Introduction

Time varying and rich scattering complex environment of forest makes target detection through foliage an ongoing challenge. However, forest provides safe harbor to hostile forces and their malicious activities where war fighter has poor sensing capabilities. In Radar Sensor Network (RSN), multiple distributed radar sensors survey a large area and observe targets from different angles. Radars used in our experiments were mono-static and acts independently. From the experimental data collected by Air Force, it has been found that echoes with target has more random phenomenon than the region without target, [1]. This finding leads us to use Maximum Entropy Method (MEM) and mutual information as the target detection tool [2]. In our method, radars in RSN are not collecting the information at the same

I. Maherin (✉) • Q. Liang
Electrical Engineering, University of Texas at Arlington, 416 Yates St, Arlington, TX 76019, USA
e-mail: ishrat.maherin@mavs.uta.edu; liang@uta.edu

B. Zhang et al. (eds.), *The Proceedings of the Second International Conference on Communications, Signal Processing, and Systems*, Lecture Notes in Electrical Engineering 246, DOI 10.1007/978-3-319-00536-2_117,

time and place, it is possible that decision based on entropy and mutual information can be different. Decision Fusion, achieve better decision that are not possible by individual radars operating individually [3, 4]. Bayesian inference and Dempster and Shafer's reasoning are the two popular inference algorithms for decision fusion [5–8] and [9]. Lack of a proposition's probabilistic information makes the Bayesian inference not useful. In our study, we use three different inference algorithms and compare their performance.

The rest of the paper is organized as follows. The system model is described in Sect. 2. D–S theory, PCR5 and bayesian network for high level decision fusion are described and proposed in Sect. 3. In Sect. 4, we present the simulation results. We conclude this paper and propose some future research in Sect. 5.

2 System Model

Our work is based on the sense-through-foliage data from Air Force Research Lab [10]. The target is a trihedral reflector with a slant length of 1.5. This kind of reflector is used to represent metallic military equipment under foliage cover. The target was located 300 feet away from the lift where the entire measurement equipment was located. Each sample is spaced at 50 ps interval, and 16,000 samples were collected for total time duration of 0.8 μs at a rate of approximately 20 Hz [10]. The target should then be located around sample 13,900. The block diagram of target detection is shown in Fig. 1. Radars in nine different positions collected 35 readings. Two information theoretic methods entropy and mutual information are applied in two different set of reflected echoes. Entropy is a measure of uncertainty of a random variable [11]. Let X be a discrete random variable with alphabet X and probability mass function (pmf) as p(x), then the entropy H(X) of the discrete random variable is,

$$H(X) = -\sum_{x \in X} p(x) log_2 p(x) \tag{1}$$

Maximum Entropy Method (MEM) finds the distribution which maximizes the entropy. The distribution without constraints that maximizes the entropy is uniform distribution [1]. Mutual information can be defined by the following equation

$$MI(X;Y) = H(X) - H(X|Y) \tag{2}$$

where $H(X)$ is the entropy of X and $H(X|Y)$ is the conditional entropy of X given Y. In our method, we have to find the $MI(Q_k;Q_{k-1})$, where Q_k is the quantized received echoes and k denotes the current sample index and $k-1$ denotes the previous sample index. The last stage of the decision fusion is explained in Sect. 3. The numerical values of the BBA are given in the result part of the Sect. 4 which is calculated based on the threshold values.

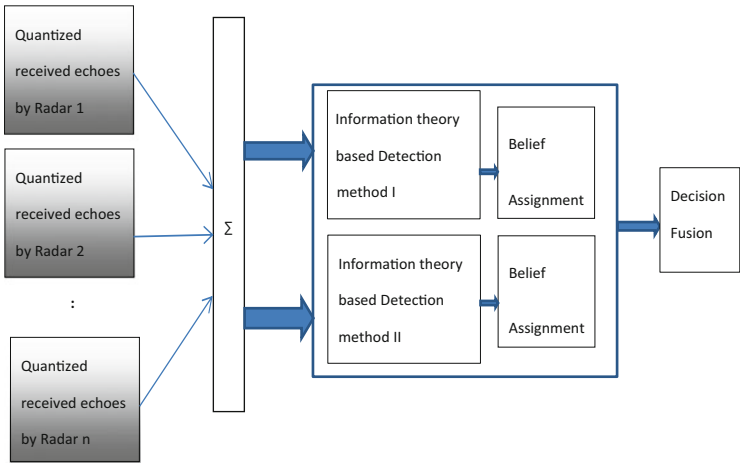

Fig. 1 Detailed block diagram for target detection through foliage

3 Decision Fusion

3.1 D–S Theory

This section provide some overview of the Dempster and Shafer's theory of evidence. This mathematical theory of evidence is commonly used in sensor fusion [9]. The biggest advantage for this theory is, it can provide an optimal result from a set of options, without prior probability.

Definition 1. Let **U** be a finite set of mutually exclusive proposition commonly known as frame of discernment. The power set of 2^U is the set of all subsets, including the null set ϕ and itself. Each subset in the power set is called the focal element. A value between [0,1] is given to each focal element, which is based on the evidence. Basic Belief Assignment (BBA) is also known as the mass function (m) of the individual proposition. It is assigned to every subset of the power set, satisfying the following:

$$m(\phi) = 0 \tag{3}$$

$$\sum_{A \subset U} m(A) = 1 \tag{4}$$

where m(A) can be considered as the accurate belief degree of proposition A.

Rule of combination: Dempster's rule of combination combines two independent sets of mass assignments by orthogonal sum. If m_1 and m_2 are two BBAs pertaining to two different evidential sources, the combined basic belief assignments is obtained via Dempster's rule of combination as follows:

$$m_1 \oplus m_2(C) = \frac{\sum_{B \cap A = C} m_1(A) \times m_2(B)}{1 - \sum_{B \cap A = \phi} m_1(A) \times m_2(B)} \tag{5}$$

where A and B are the beliefs from two different sources that indicate C is true. This rule ignores the conflict of evidence by a normalizing factor K, while K is given by the following,

$$K = \sum_{A \cap B = \phi} m_1(A) \times m_2(B) \tag{6}$$

In our study we have frame of Discernment as

$$\mathbf{U} = \{t, nt\} \tag{7}$$

where t means target present and nt means target not present. m_1 and m_2 are the two different evidential sources that are set of UWB radar sensors that calculate either entropy or mutual information as an evidence to the support of target detection. We decide the weight on the belief based on the threshold value. The combined belief of target present can be calculated as follows,

$$m_1 \oplus m_2(t) = \frac{m_1(t) \times m_2(t)}{1 - m_1(nt) \times m_2(t) - m_2(nt) \times m_1(t)} \tag{8}$$

$$m_1 \oplus m_2(t) = \frac{m_1(t_1) \times m_2(t_2)}{1 - m_1(nt_1) \times m_2(t_2) - m_2(nt_2) \times m_1(t_1)} \tag{9}$$

3.2 Proportional Conflict Redistribution Rule 5

Researchers found that normalization procedure in the D–S combination rule involves counterintuitive result when there is high conflict in evidence. One of the popular modified rule is Proportional Conflict Redistribution Rule 5 (PCR5) [12]. For our frame of discernment as given by (7) the PCR5 rule will be

$$m_1 \oplus m_2(t) = m_1(t_1) \times m_2(t_2) + \frac{m_1^2(t_1) \times m_2(nt_2)}{m_1(t_1) + m_2(nt_2)} + \frac{m_2^2(t_2) \times m_1(nt_1)}{m_2(t_2) + m_1(nt_1)} \tag{10}$$

To compare the combination of the two rules, a numerical example can be presented here. A Body of Evidence (BOE) is the set of all the focal elements, $(\mathfrak{R}, m) = ([\{A\}, m(A)] | A \subset P(U), m(A) > 0\}$; here $P(U)$ is the power set of frame of discernment, U. Three body of evidence are showed as follows:

$$(\mathfrak{R}_1, m_1) = ([\{t\}, .8], [\{nt\}, .2]); \tag{11}$$

Table 1 Combination result for D–S and PCR5

Rule	Combination	$m_1 \bigoplus m_2$	$m_1 \bigoplus m_3$
D–S rule	m(t)	0.903	0
	m(nt)	0.097	1
PCR5 rule	m(t)	0.843	0.356
	m(nt)	0.157	0.644

$$(\Re_2, m_2) = ([\{t\}, .7], [\{nt\}, .3]); \tag{12}$$
$$(\Re_3, m_3) = ([\{t\}, .0], [\{nt\}, 1]); \tag{13}$$

The comparison of the calculation for the D–S and PCR5 method is shown in Table 1. From Table 1 it is clear, when there is less conflict, D–S and PCR5 give similar results, as sown in combining m_1 and m_2. But when the conflict is high PCR5 gives better result than D–S as shown by the last column while combining m_1 and m_3.

3.3 Bayesian Network for Target Detection Using Information Theory

Bayesian Network (BN), belongs to family of probabilistic Graphical Models (GMs) known as a Directed Acyclic Graph (DAG) [13]. A BN can represent a Joint Probability Distribution (JPD) in factored form by Conditional Probability Table (CPT). Consider the case where we have n no of evidential sources $S_1, S_2, S_3, \cdots S_n$ for a particular node D. We can write Bayes theorem as,

$$P(D|S_1, S_2, S_3, \cdots S_n) = \frac{P(D) \times P(S_1, S_2, \cdots S_n|D)}{P(S_1, S_2, \cdots S_n)} \tag{14}$$

If we make assumption as sources are independent given D then we can write,

$$P(S_1, S_2, S_3, \cdots S_n|D) = P(S_1|D) \times P(S_2|D) \times \cdots P(S_n|D) \tag{15}$$

The term $P(S_1, S_2, \cdots, S_n)$ can be eliminated by normalization.

In our study we have two variables as E_h and MI_h which represent high entropy and high Mutual information respectively. These variables are two nodes of the directed graph of the target detection as shown in Fig. 2. We can use inference from bayesian network and the probability of target present can be written as,

$$P(T|E_h, MI_h) = P(T) \times P(E_h|T) \times P(MI_h|T) \tag{16}$$

Computational complexity of this algorithm is fairly low. There is no computationally exhaustive process such as FFT or JPD involved. From MATLAB profiler it was checked that the complexity was in the O(N) where N is the data size.

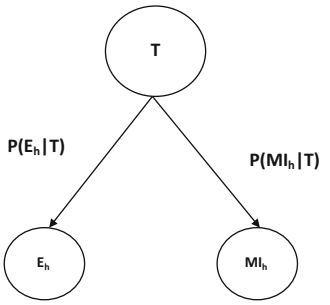

Fig. 2 Bayesian network for target detection

All other target detection algorithm where signal processing is involved is highly dependent on FFT, complex multiplication, matrix multiplication and can have very high computational load. The computational complexity for the D–S is related to the element in the frame of Discernment, which in our case is only two.

4 Simulation Results

In this section, we will discuss the simulation result we found in this paper. The belief function of entropy, $m_1(t)$ is assigned as shown by the following,

$$m_1(t) = \begin{matrix} 0.8, when H(Q) \geq 3 \\ 0.5, when, 2.5 \leq H(Q) < 3 \\ 0.0, when, H(Q) < 2.5 \end{matrix} \tag{17}$$

where H(Q) is the entropy of the quantized received echoes in the k^{th} window. The belief function of mutual information, $m_2(t)$ assigned is shown by the following,

$$m_2(t) = \begin{matrix} 0.8, when MI(Q_k) : (Q_{k-1}) \geq 2.1 \\ 0.5, when, 1.5 \leq MI(Q_k) : (Q_{k-1}) < 2.1 \\ 0.0, when, MI(Q_k) < 1.5 \end{matrix} \tag{18}$$

where $MI(Q_K;Q_{k-1})$ is the mutual information of the quantized received echoes in the subsequent radar return in the window. We select a set of data and applied D–S rule of combination. It gives several windows with higher values as shown in Fig. 3. As we have already shown in Table 1 that D–S sometimes are not so efficient for high conflict. However this were resolved better by PCR5 as shown in Fig 4a. Also with the assumption that we know the distribution of the probability of target present, bayesian network can also make inference as shown in Fig. 4b. When the entropy and mutual information both methods had less conflict then using only D–S the target is detected with certainty as shown in Fig. 5.

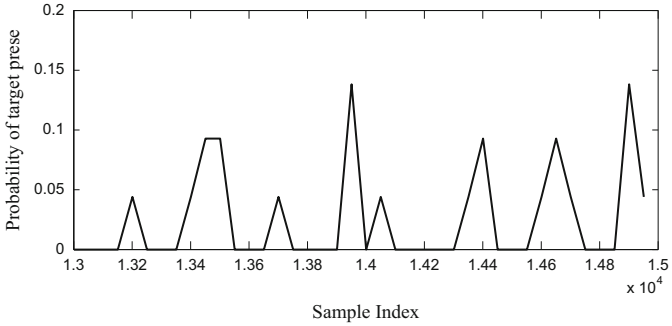

Fig. 3 Probability of target present after decision fusion by D–S with high conflict

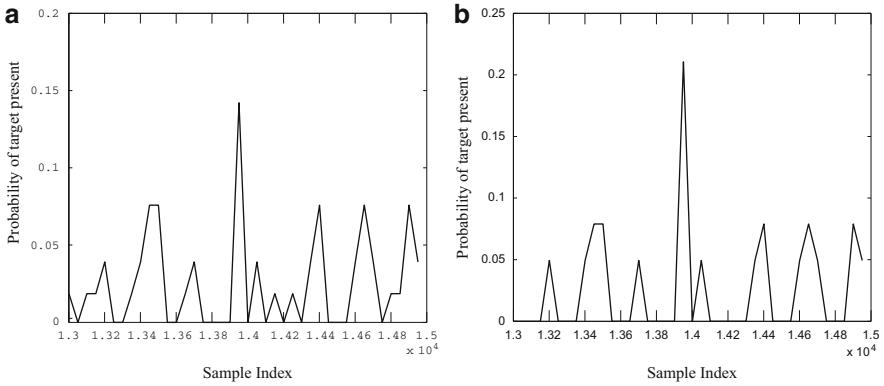

Fig. 4 Performance evaluation in terms of probability of detection for high conflict by (**a**) PCR5 and (**b**) Bayesian

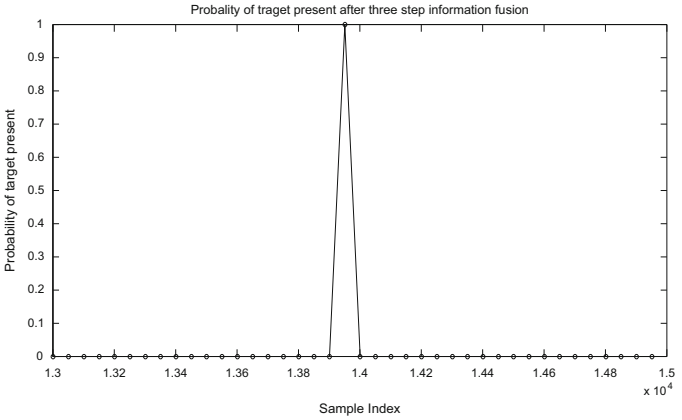

Fig. 5 Probability of target present after decision fusion by D–S with less conflict. Target is detected around sample 13,900 with certainty

5 Conclusions

Challenging environment of forest can produce uncertainty and UWB Radar Sensors can produce conflicting decision on target detection. In this paper, we propose a scheme where conflict of decision in target detection can be resolved either by Dempster and Shafer (D–S) theory of evidence or by bayesian network. We also introduce the improved version of D–S theory for conflicting evidence and compared the performance with D–S and bayesian network. Results show that when echoes are in poor quality, with this novel approach, accurate detection can be achieved. In future, this method can also be applied for multi-target detection.

Acknowledgements This work was supported in part by U.S. Office of Naval Research under Grants N00014-13-1-0043, N00014-11-1-0071, N00014-11-1-0865, and U.S. National Science Foundation under Grants CNS-1247848, CNS-1116749, CNS-0964713.

References

1. Maherin I, Liang Q (2011) An entropy based approach for sense-through foliage target detection using UWB radar. In: 6th international conference on wireless algorithms, systems and application (WASA), Chengdu, pp 180–189
2. Maherin I, Liang Q (2012) A mutual information based approach for target detection through foliage using UWB radar. In: IEEE international conference on communications (ICC), pp 6406–6410, 10–15 June, 2012
3. Luo RC, Kay MG (1990) A tutorial on multisensor integration and fusion. In: Proceedings of 16th annual conference on IEEE industrial electronics society, vol 1, pp 707–722
4. Luo RC, Chang CC, Lai CC (2011) Multisensor fusion and integration: theories, applications, and its perspectives. IEEE Sensors J 11(12):3122–3138
5. Li X, Zhu W (2010) Multi-feature fusion in weed recognition based on Dempster-Shafer's theory. In: International conference computer application and system modeling (ICCASM), vol 5, pp 127–130, 22–24 October 2010
6. Poulain V, Inglada J, Spigai M, Tourneret JY, Marthon P (2011) High-resolution optical and SAR image fusion for building database updating. IEEE Trans Geosci Remote Sens 49 (8):2900–2910
7. Nguyen-Thanh N, Koo I (2011) Evidence-theory-based cooperative spectrum sensing with efficient quantization method in cognitive radio. IEEE Trans Veh Technol 60(1):185–195
8. Cai C, Ferrari S (2007) Comparison of information-theoretic objective functions for decision support in sensor systems. In: American Control Conference, pp 3559–3564, 9–13 July 2007
9. Chen X, Yang Y, Cheng H (2010) Conflict problems of D–S evidence in multi-sensor information fusion technology. In: International conference on computer application and system modeling (ICCASM), vol 4, pp 314–318, October 2010
10. Dill C Foliage penetration(phase II) field test narrow band vesus wideband foliage penetration. Final report of contract number F41624-03-D-700/04, July 2005 to Feb 2006
11. Cover TM, Thomas JA (1991) Elements of information theory. Wiley, Newyork
12. Smarandache F, Dezert J (2005) Information fusion based on new proportional conflict redistribution rules. In: 8th international conference on information fusion, vol 2, p 8
13. Russell SJ, Norvig P (2010) Artificial intelligence: a modern approach, 3rd edn. Prentice Hall, New Jersey

A Target Tracking Algorithm Based on Optical Transfer Function and Normalized Cross Correlation

Xin Yin, Yaqiu Sun, Shidong Song, and Xueyan Ma

Abstract Cell image tracking pose many challenges to existing target tracking method due to too much noise and detail information, this paper proposed a cell image tracking method of optical transfer function and normalized cross correlation. Cell image's noise and detail information is weakened after processing by optical transfer function and cell image's frequency characteristics are acquired. Normalized cross correlation has better robustness and overcome the lack of sensitivity of light change, so cell image can be precisely matched and tracked, cell movement track is gained. The effectiveness and accuracy of this algorithm is simulated by MATLAB.

1 Introduction

Moving target tracking is a key technique in computer vision system. It was available to military areas, medical field and traffic control [1]. Moving target tracking is mean to template image is found accurately and effectively in continuous matched image. Moving target tracking is in order to draw out move curve by the data measurement and data process and provide information for object detection and background update [2]. Currently, tracking algorithm based on Kalman [3], tracking algorithm based on particle filter [4], and tracking algorithm based on character [5] are common using tracking algorithm. Tracking algorithm based on Kalman can reliably predict positions of a moving target and has less calculation, however, the track of tracking algorithm based on Kalman is not accurate. Tracking

X. Yin (✉) • Y. Sun • X. Ma
College of Electronic and Communication Engineering, Tianjin Normal University, Tianjin 300387, China
e-mail: yinxin1025@126.com

S. Song
School of Chemical and Environment Engineering, China University of Mining and Technology, Beijing 100083, China

B. Zhang et al. (eds.), *The Proceedings of the Second International Conference on Communications, Signal Processing, and Systems*, Lecture Notes in Electrical Engineering 246, DOI 10.1007/978-3-319-00536-2_118,

algorithm based on particle filter has great effect in nonlinear and non-Gaussian area, but the computation is large and real-time performance is weak. The expression of moving target and the similarity measure determine the precision and robustness of tracing algorithm, searching strategy and predictive filter determine the real-time performance.

Normalized cross-correlation algorithm is an improvement of cross correlation. This method overcomes the weakness of the sensitive for complicated illumination and has more accurate and better robustness, but at the cost of the enhancement in precision of detection has been achieved at the cost of causing algorithm complication. So it has poor efficiency and can not meet the requirement of the real-time and fast processing [6]. The noise and detail information of the image is weakened and the frequency feature is enhanced after processing by the filter based on optical transfer function of microscope. Then get frequency feature of the processed image, reduce the matched areas, improve the real-time performance is improve. Above all, in this paper, a target tracking algorithm based on optical transfer function and normalized cross correlation was proposed. The frequency feature of image is obtained by optical transfer function of microscope, then search for the position of most significant relationship between template images and matched, last the simulation experiment shows that this algorithm is accurate and effective.

2 Experimental Principles

Because the cell image features is less, the cell intensity is weaker and more sensitive to noise, extracting the feature of target in space domain is hard. Therefore, a target tracking algorithm based on optical transfer function and normalized cross correlation was proposed. The noise is weakened, the frequency features is enhanced. So the frequency features are extracted accurately.

Frequency domain of image is a way to express the extent of the image gray change. Image gradient can be expressed by frequency domain of image. The gray distribution of image is transformed to frequency distribution by Fourier. The spectrum is viewed as intensity distributions of image gradient. In spectrum, bright-dark points are mean to the different gradient between a certain point in the image and its neighborhood points. The frequency features of the image processed by this novel algorithm are enhanced, the image gradient values is increased, obvious frequency features are gained. The formulas are as followed.

$$X(u,v) = \frac{1}{M}\sum_{x=0}^{M-1}\sum_{y=0}^{M-1} f(x,y)\cdot \exp[-j2\pi(ux+vy)/M], \quad u,v = 0,1,2,\ldots,M-1 \tag{1}$$

The optical transfer function is set to $h(x,y)$, its Fourier transform is set to $H(u,v)$.

Construct filter, the function of this filter is $H_1(u,v) = 1 - H(u,v)$. Construct enhanced filter, the function is $H_{11}(u,v) = a + bH_1(u,v)$ [7].

The frequency image is processed by enhanced filter. The formulas are as followed.

$$\begin{aligned} XH(u,v) &= X(u,v) \cdot H(u,v) \\ &= \frac{1}{M} \sum_{x=0}^{M-1} \sum_{y=0}^{M-1} f(x,y) * h(x,y) \cdot \exp[-j2\pi(ux, vy)/M] \end{aligned} \tag{2}$$

In formula (2), u and v are set to 0.

$$XH(0,0) = \frac{1}{M} \sum_{x=0}^{M-1} \sum_{y=0}^{M-1} f(x,y) * h(x,y) \tag{3}$$

(2) is transformed by Fourier, as shown in (4).

$$\begin{aligned} f'(x,y) &= \frac{1}{M} \sum_{x=0}^{M-1} \sum_{y=0}^{M-1} X(u,v) \cdot H(u,v) \cdot \exp[j2\pi(ux + vy)/M], \\ x, y &= 0, 1, 2 \ldots M-1 \end{aligned} \tag{4}$$

(5) stands for mean gray values of the processed image.

$$\overline{f'}(x,y) = \frac{1}{M} \sum_{x=0}^{M-1} \sum_{y=0}^{M-1} f'(x,y) \tag{5}$$

(6) is got by (2) and (5).

$$\overline{f'}(x,y) = \frac{1}{M} X(0,0) \cdot H(0,0) \tag{6}$$

Mean gray values of the processed image is directly proportional to its zero frequency. The processed image template's energy changes the energy on all frequencies changes. The change is obvious with closing to zero frequency [7], pixel values change, in space domain, mean gray values of the image change. In frequency domain, the energy of all frequencies is changed. In frequency domain, the energy of all frequencies after processing by the filter based on optical transfer function is changed more obviously. Due to space constraints, Optional some date is selected. Table 1 is the partial data of the template image in space domain, Table 2 is the partial data of the processed template image in frequency domain, Table 3 is the partial data of the matched image in space domain, and Table 4 is the partial data of the processed matched image in frequency domain. Table 5 is the partial data of the matched image in frequency domain.

Table 1 The partial data of the template image in space domain

255	255	255	255
255	255	255	255
255	255	255	246
244	255	255	255

Table 2 The partial data of the processed template image in frequency domain

1.4e + 03	4.3e + 02	−1.2e + 03	2.5e + 02
1.3e + 03	1.1e + 03	−6.7e + 02	−9.9e + 01
−1.6e + 03	1.4e + 03	−1.2e + 03	−1.6e + 01
−5.3e + 03	−2.1e + 03	5.3e + 01	2.3e + 02

Table 3 The partial data of the matched image in space domain

255	255	255	255
255	255	255	255
255	255	254	255
255	241	255	255

Table 4 The partial data of the processed matched image in frequency domain

2.3e + 03	2.7e + 03	4.1e + 03	1.5e + 03
3.0e + 02	1.7e + 03	2.1e + 03	1.7e + 03
−1.3e + 03	−1.5e + 03	4.2e + 02	1.7e + 03
−1.1e + 02	−8.8e + 02	−1.4e + 03	2.3e + 03

Table 5 The partial data of the matched image in frequency domain

−1.8e + 05	−0.7e + 04	3.7e + 04	5.7e + 04
−1.0e + 05	−1.8e + 05	−4.3e + 04	8.4e + 04
−2.4e + 04	−1.8e + 05	−7.5 + 04	7.0e + 04
1.5e + 04	−10.0e + 04	−1.5e + 05	−3.0e + 04

The contrast among Tables 1 and 3, Tables 2 and 5 shows that in space domain, there are four different points between template image and matched image, but after template image and matched image processed by the filter based on optical transfer function, there are significant differences in frequency domain. Image characteristics in frequency domain become obvious, distinguish ability is improved. Image gradient can be expressed by Fourier transform of image. In frequency domain, after the image is processed by the filter based on optical transfer function, the horizontal and the vertical component increase. So this algorithm is more suited for micro image and small targets tracking.

Contrast the data of frequency domain between Tables 4 and 5, the data of frequency domain is increased except three values in the upper right-hand corner and one value in the lower left-hand corner. So image gradient values are increased, image characteristics in frequency domain are enhanced, the result of tracking is more accurate.

The characteristics in frequency domain are extracted from template image, calculate the similarity by normalized cross correlation algorithm. The formula of calculate the similarity is as followed.

$$C = \frac{\sum\sum[f(k,l) - f_m][g(k+m,l+n) - g_m]}{\sqrt{\sum\sum[f(k,l) - f_m]^2}\sqrt{\sum\sum[g(k+m,l+n) - g_m]^2}} \tag{7}$$

Where J and g are gray distribution function of the interrogation windows; Where J_m and g_m are mean gray values of the interrogation windows.

3 Experiments

Six continuous micro images of chicken embryonic are tracked. The sizes of micro images of chicken embryonic are 1,344 × 1,024, respectively. The size of the temple image is 30 × 30.

The step based on optical transfer function and normalized cross correlation algorithm are as followed.

Step One: Microscopic optical transfer function is set to $H_{lp}(u,v)$, construct the filter based on optical transfer function. The function of the filter is $H_{hp} = 1 - H_{lp}(u,v)$.

Step Two: Increase high-pass filter compensation. The function of the filter is $H_{hfe}(u,v) = a + bH_{hp}(u,v)$.

Step Three: Two continuous micro images of chicken embryonic are set to Ti, Ti + 1, respectively. C1 is a cell on Ti, an interrogation window, wi is selected around C1. The image of the interrogation window wi is set to $f_1(x,y)$. The characteristics in frequency domain are extracted from interrogation window wi. The function is $H_{hfe}(u,v)*G(u,v)$.

Step Four: Calculate the similarity by normalized cross correlation algorithm. Look for maximum cross correlation value.

Step Five: Record the position of C1 cell on Ti + 1. Draw out its tracking.

MATLAB software simulation result is shown in Figs. 1 and 2.

4 Conclusions

In this paper, a target tracking algorithm based on optical transfer function and normalized cross correlation was put forward. Construct enhanced filter by optical transfer function, reduce image noise by this filter, and enhance the image characteristics in frequency domain. Matching target is more accurate and more efficient. The simulation experiment shows that this algorithm can accurately and effectively track target and has better tracking performance.

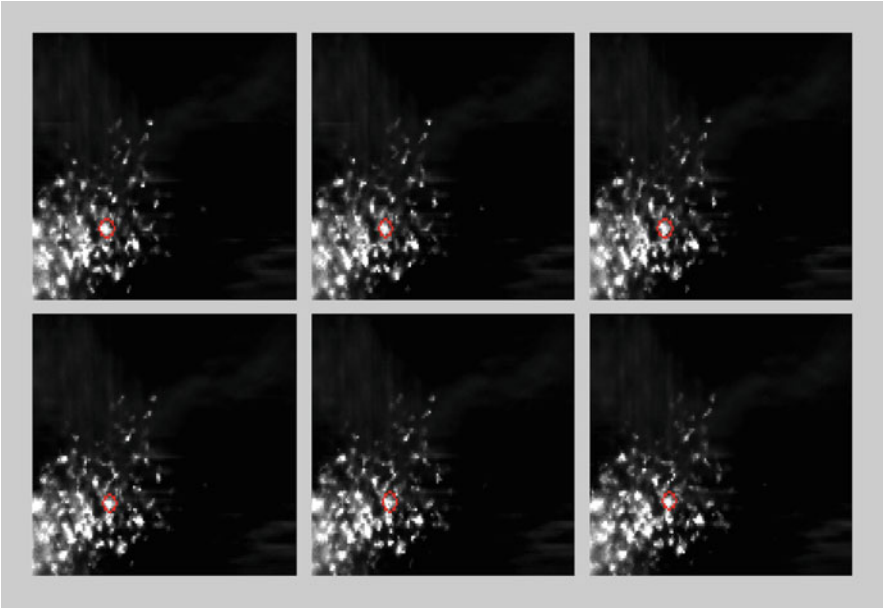

Fig. 1 Tracking process of moving target

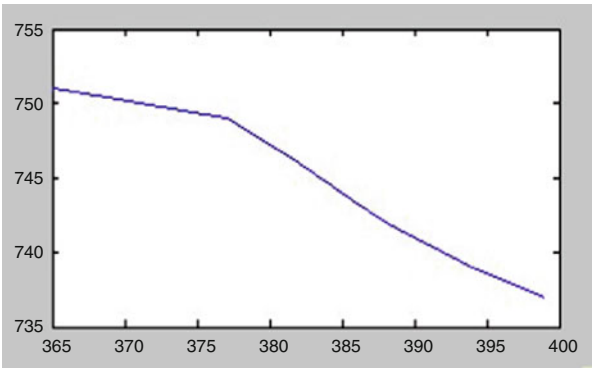

Fig. 2 The track of moving target

Acknowledgments This work was sponsored by Program for New Century for New Century Excellent Talents in University (No.80051803), Scientific Research Foundation for the Returned Overseas Chinese Scholars (No.L02003), the Doctor Scientific Research Foundation of the Tianjin Normal University (52LX14, 52X09008).

References

1. Wenting G, Nian C (2012) Object tracking based on contourlet histogram. Laser Infrared 42 (10):1177–1180. doi:10.3969/j.issn.1001-5078.2012.10.020

2. Yongmei D, Xiaoping J, Xiaoshan D (2011) Tracking algorithm of moving object based on particle swarm optimization and Kalman filter. Modern Electron Tech 34(8):133–136. doi:10.3969/j.issn.1004-373X.2011.08.042
3. Fang L (2012) The method to manage and control the software requirement in radar software system. Inform Res 38(4):45–49
4. Yuanting Y (2012) A gray object tracking algorithm based on particle filter. J Xiamen Univ (Nat Sci) 51(1):33–36
5. Huaiyang R, Yong Z (2012) Small infrared target tracking algorithm based on frequency region feature. Laser Infrared 42(8):959–964. doi:10.396/j.issn.1001-5078.2012.08.028
6. Wei G, Yigong Z, Zhenhua X (2009) An improved normalized cross-correlation for template matching of infrared image. Acta Photonica Sinica 38(1):189–193
7. Weixing Z, Huan L (2010) Fog image enhancement algorithm based on high frequency emphasize and CLAHE. Video Eng 34(7):38–40. doi:10.3969/j.issn.1002-892.2010.07.011

Analysis for Low Cost Inertial Sensors Based Pedestrian Dead Reckoning

Shaochu Wang, Kaihua Liu, Yu Liu, and Xiaokang Sun

Abstract Compared with other localization technologies, Dead Reckoning (DR) can be used for pedestrian tracking without any extra infrastructure deployed in the location areas. The chapter proposes a scheme for Pedestrian Dead Reckoning (PDR) using low cost inertial sensors, and analyses each component by technical methods. Strap-down inertial navigation based step length calculation, compensated geomagnetic field based traveling direction estimation and 3D grid models' connectivity database for map matching are applied to improve the positioning accuracy of the system. Total cost of the system merely depends on the unit price of equipment mounted on the pedestrian and the number of tracked targets. Administrators and users can track any target anywhere in real-time and remotely.

1 Introduction

GNSS can not be deployed for indoor application, as the line-of-sight transmission between receivers and satellites is not possible in an indoor environment [1]. Consequently, seeking a combination of indoor and outdoor positioning solutions becomes a hot issue. Although numerous solutions have been proposed by scholars and various kinds of indoor positioning systems (IPS) have been developed based on different techniques and technologies. Unfortunately, a standard solution for indoor localization does not exist yet [2].

Location fingerprinting technique applies signal propagation modeling which takes the reflection, refraction, diffraction, absorption and scattering of radio signal into account to build a radio map of the location environment [3]. However the accuracy depends on the density of location beacons, and the systems need a lot of preliminary work to build the fingerprint-location database.

S. Wang (✉) • K. Liu • Y. Liu • X. Sun
School of Electronic Information Engineering, Tianjin University, Tianjin, China
e-mail: wangshaochu@tju.edu.cn

B. Zhang et al. (eds.), *The Proceedings of the Second International Conference on Communications, Signal Processing, and Systems*, Lecture Notes in Electrical Engineering 246, DOI 10.1007/978-3-319-00536-2_119,

Triangulation technique uses the geometric properties of triangles to predict the target's position [3]. These techniques, from the basic principle of geometry, can achieve a high positioning accuracy. For example, Ubisense using TDOA of UWB signals provides about 20 cm at free space without obstacles [4]. But the demerit of these techniques is that the measurements are easily affected by the motion of people, multipath, reflection, alters of the objects' position and Non-Line-of-Sight (NLOS). High cost of the system is attributed to the high precision measurements and manufacturing costs.

Pedestrian Dead Reckoning systems are becoming feasible options for indoor tracking. The low deployment costs associated with dead-reckoning whilst successfully addressing many of the shortcomings [5]. Firstly, it is a complete autonomous system without interferences from the surrounding environments. Secondly, the accuracy of the PDR system only depends on sensors' accuracy and position estimating algorithms, and it has no relationship with the location areas.

Inertial Measuring Units (IMU), including accelerometers, gyroscopes and magnetometers, can be used to estimate the movement of a person by detecting steps, estimating stride lengths and the directions of motion [6]. Jimenez and Chengliang H. mount IMU onto foot by laces [6, 7], evaluate and demonstrate some position modules. Robert Harle surveys an emerging subset of tracking systems that use inertial sensors to perform dead reckoning [5], and the literatures reviewed by him only propose some improved algorithms. DARPA continuously supports the study of PRD theories, has developed a PDR system called "Personal Inertial Navigation System" (PINS) [8], but it comes with military purposes, and no additional relevant materials can be found.

This chapter presents a complete solution for PDR system by using low cost Micro-Electro-Mechanical Systems (MEMS) inertial sensors, analyses the requirements of the system and decomposes the system into a number of functional units, and presents the implementation method of each unit. Then proposes a dead-reckoning algorithm based on 3D grids connectivity database of the building. At last, the advantages and the feature works are given in the conclusion.

2 Scheme Design for PDR

Dempsey defines an IPS as a system that determines the position of something or someone continuously and in real-time in a physical space such as in a hospital, a gymnasium, a school, etc. [9]. The real-time and position performance are two important aspects of the system. Taking these factors into full account, we propose a PDR system using low cost inertial sensors. The schematic diagram of the system is shown in Fig. 1. It can be divided to two parts: the User Side and Server Side. The number of User Side can be infinite with only one Server Side.

The User Side fetches the inertial data produced by the pedestrians' movements, analyses and recognizes the motion types, calculates the step length and traveling headings, then transmits these positional parameters data frames to Server Side via

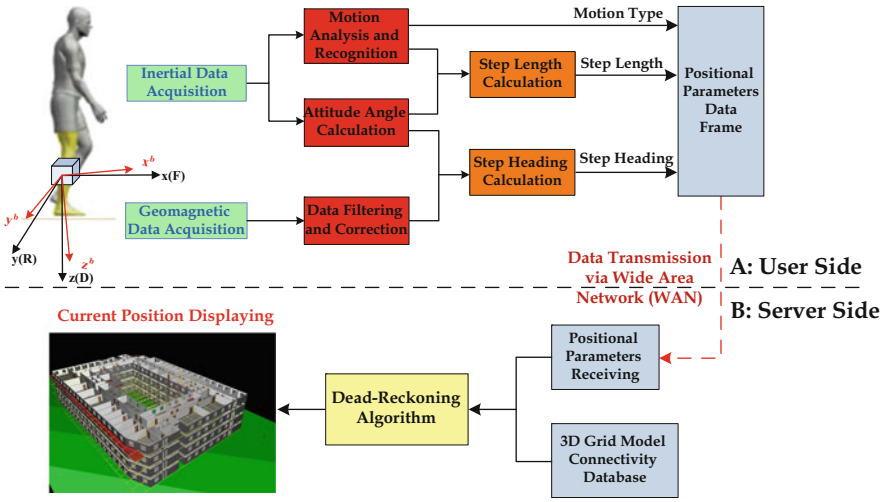

Fig. 1 The schematic diagram of the proposed PDR system

the Wide Area networks (WAN). The Server Side receives the positional parameters from each User Side, processes dead-reckoning algorithm and shows current position of the targets which the administrator and the remote users are interested in. The 3D grid model connectivity properties of the building are used to correct the position estimated by the proposed dead-reckoning algorithm.

3 Analysis for Pedestrian Dead Reckoning

3.1 Data Acquisition

Many inertial sensor manufacturers hold their high performance IMUs. The IMUs can be divided into three grades: tactical grade, industrial grade and consumer grade. In this chapter, we choose an industrial grade IMU named ADIS16405 from ADI for demonstration. It integrates with 3D accelerometers, 3D gyroscopes and 3D magnetometers. The dynamic ranges fully comply with the requirements of the system we are proposed. In order to implement the demonstration system as soon as possible, we also use the evaluation board of ADIS16405, which can be used directly to fetch inertial data via a USB cable connected to the host computer. The size of evaluation board is small enough to be installed unobtrusively on the shank, just like Fig. 1 shows.

IMU senses angular velocity, the linear acceleration produced by pedestrian's movements together with the gravitational field, and geomagnetic fields. We mark the 3 axes acceleration dataset as $\{a_{x\_i}, a_{y\_i}, a_{z\_i}\}$, 3 axes angular velocity dataset

as $\{\omega_{x\_i},\omega_{y\_i},\omega_{z\_i}\}$ and 3 axes magnetic data as $\{m_{x\_i},m_{y\_i},m_{z\_i}\}$, where $i = 1,2,\ldots,N$.

Inertial datasets are in the IMU's body axes $x^by^bz^b$ with forward-right-down configuration. When the shank stand straightly, x^b points to the waking direction, y^b points to the right and z^b points to the direction of earth's gravity. Name this position as local coordinate system (LCS) *x(F)y(R)z(D)*, LCS represents forward, right and down fixed to the surface of earth. The global coordinate system (GCS), marked as *x(N)y(E)z(D)*, represents north, east and down fixed to surface of earth.

3.2 Step Length Calculation

3.2.1 Motion Analysis and Recognition

As we all know, the accumulated error of inertial navigation increases exponentially over the time. Decomposing the continuous moving into several single steps is a common practice. Zero Velocity Update (ZUPT) technology is also used to initialize the parameters of inertial navigation.

The displacement of pedestrian is generated by the foot contact with ground periodically. Many researchers indicate that the ZUPT can be applied when the shank is perpendicular to the ground. The linear acceleration and angular velocity are close to zeros at the ZUPT points. So we decompose the continuous motions into several single steps by angular velocity of Y axis as Fig. 2 shows.

A step starts and ends with two adjacent ZUPT points. So the ZUPT points are used to segment inertial dataset of each step. It has an inherent advantage that the ZUPT initialize the parameters of step length calculation.

3.2.2 Attitude Angle Calculation

The position of IMU body axes $x^by^bz^b$ alters with the movement of shank. In order to apply inertial navigation algorithm, the inertial data in $x^by^bz^b$ coordinate must be transformed to GCS. Relative to the GCS, LCS holds the heading angle called yaw (ψ), and two zero tilt angles pitch (ρ) and roll (γ). Similarly, the relationship between the $x^by^bz^b$ and GCS also can be described by these attitude angles or azimuth angles. Mathematically the Direct Cosine Matrix (DCM) is accomplished by transformation of three sequential rotations from the axes in the GCS, the expression of the DCM based on attitude angles can be written as:

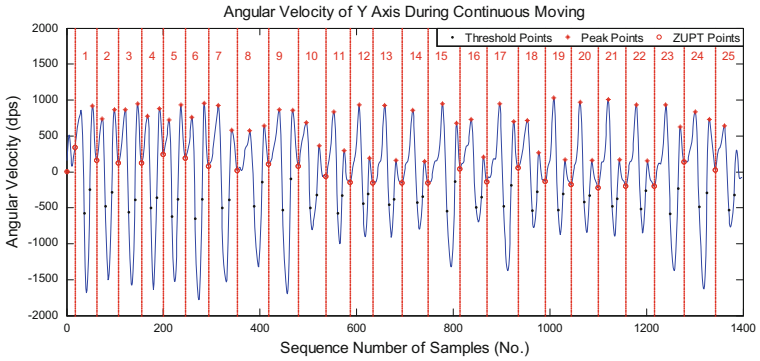

Fig. 2 Decompose the continuous process of moving into several single steps

$$R(\psi,\rho,\gamma) = \begin{bmatrix} \cos\rho\cos\psi & \cos\psi\sin\rho\sin\gamma - \cos\gamma\sin\psi & \cos\psi\sin\rho\cos\gamma + \sin\gamma\sin\psi \\ \cos\rho\sin\psi & \cos\gamma\cos\psi + \sin\rho\sin\gamma\sin\psi & -\sin\gamma\cos\psi + \sin\rho\cos\gamma\sin\psi \\ -\sin\rho & \cos\rho\sin\gamma & \cos\rho\cos\gamma \end{bmatrix} \tag{1}$$

In the period of one step, there are N samples, at sample time i, the DCM can be calculated as follows [7]:

$$R\left(\psi_{i+1},\rho_{i+1},\gamma_{i+1}\right) = R(\psi_i,\rho_i,\gamma_i)\cdot R_{i+1} \tag{2}$$

Where

$$R_{i+1} = I + \sin\left(\overline{\omega}\delta t\right)\overline{\omega}\Omega + \frac{1-\cos\left(\overline{\omega}\delta t\right)}{\overline{\omega}^2}\Omega^2, \quad \overline{\omega} = \left\|\omega_{x\_i+1},\omega_{y\_i+1},\omega_{z\_i+1}\right\|$$

So, the attitude angles at sample time i can be obtained from the DCM as:

$$\begin{aligned} \rho_i &= -\arcsin\left(R(\psi_i,\rho_i,\gamma_i)(3,1)\right) \\ \gamma_i &= \arctan\left(\frac{R(\psi_i,\rho_i,\gamma_i)(3,2)}{R(\psi_i,\rho_i,\gamma_i)(3,3)}\right) \end{aligned} \tag{3}$$

3.2.3 Strap-Down Inertial Navigation Based Step Length Calculation

The block diagram of strap-down inertial navigation system is shown in Fig. 3. Each level walking step executes the strap-down inertial navigation algorithm once.

A ZUPT point starts the step period with an initial azimuth, and the gyroscope measurements of the step fed to attitude angle calculation module to obtain instantaneous azimuth. Then project the acceleration data to GCS, subtract the

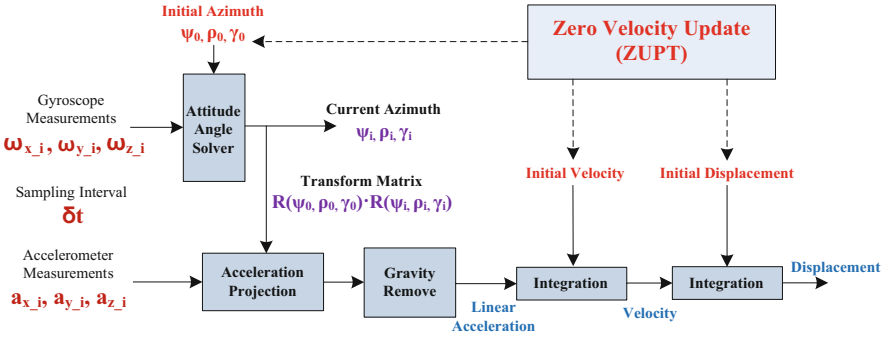

Fig. 3 Block diagram of strap-down inertial navigation system

acceleration of gravity, integrate the remaining acceleration once to obtain global velocity and twice to obtain the displacement in the GCS.

In accordance with above, the 3 axis linear acceleration in the GCS is:

$$\begin{bmatrix} a_{x(N)\_i} \\ a_{y(E)\_i} \\ a_{z(D)\_i} \end{bmatrix} = R(\psi_0, \rho_0, \gamma_0) \cdot R(\psi_i, \rho_i, \gamma_i) \cdot \begin{bmatrix} a_{x\_i} \\ a_{y\_i} \\ a_{z\_i} \end{bmatrix} - \begin{bmatrix} g_{x(N)} \\ g_{y(E)} \\ g_{z(D)} \end{bmatrix} \tag{4}$$

Where $g_{x(N)} = g_{y(E)} = 0$ and $g_{z(D)} = g \approx 9.8m/s^2$

The horizontal walking in an indoor environment is very common, whose displacement of *z(D)* axis is nearly zero. The shank is perpendicular to the ground at ZUPT point, γ_0 is also closed to zero. So there are some constraint equations:

$$\begin{aligned} s_{z(D)} &\approx 0 \\ \gamma_0 &\approx 0 \end{aligned} \tag{5}$$

Combine (2), (4) and (5), $s_{x(N)}$ and $s_{y(E)}$ can be calculated. So the step length is:

$$Step\_Length = \sqrt{s_{x(N)} + s_{y(E)}} \tag{6}$$

3.3 Step Heading Calculation

The magnetometers are easily affected by some interference: the ferrous materials nearby will cause hard iron distortion, and magnetically soft material surrounding affecting the earth's magnetic field will cause soft iron distortion. Application note [10] gives a perfect method for calibrate the geomagnetic data.

Accelerometers and magnetometers can be used to implement an electronic compass. But it is limit in stationary case as the tilt angles calculated by gravity. 3D gyroscopes can be used to track the tilt angles dynamically as the (3) shows. Project the magnetic field to a horizontal plane with tilt angles:

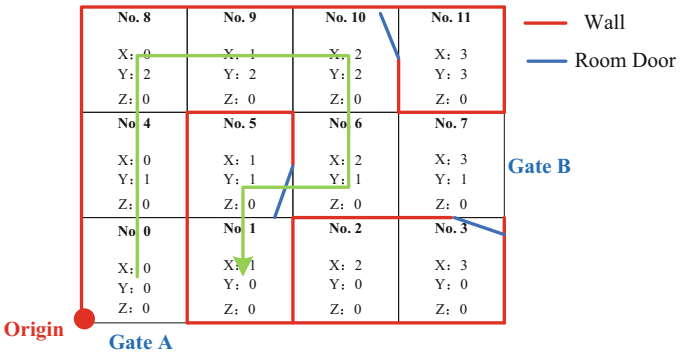

Fig. 4 An example of 3D grid model

Table 1 The properties of grid model

Grid properties	Description	Example
ID of grid model	Grid number	5
Horizontal coordinate X	X position	1
Horizontal coordinate Y	Y position	1
Vertical coordinate Z	Z position	0
Connectivity with (x + 1,y,z)	1: Yes 0: No	1
Connectivity with (x − 1,y,z)	1: Yes 0: No	0
Connectivity with (x,y + 1,z)	1: Yes 0: No	0
Connectivity with (x,y − 1,z)	1: Yes 0: No	1
Connectivity with (x + 1,y + 1,z)	1: Yes 0: No	0
Connectivity with (x + 1,y − 1,z)	1: Yes 0: No	0
Connectivity with (x − 1,y + 1,z)	1: Yes 0: No	0
Connectivity with (x − 1,y − 1,z)	1: Yes 0: No	0

$$\begin{aligned} X_h &= m_x \cos\rho + m_z \sin\rho \\ Y_h &= m_x \sin\gamma \sin\rho + m_y \cos\gamma - m_z \sin\gamma \cos\rho \end{aligned} \tag{7}$$

So the heading can be calculated as follows:

$$heading = \arctan(Y_h / X_h) \tag{8}$$

3.4 3D Grid Model Based Dead Reckoning Algorithm

The same as vehicles usually do not leave the road, pedestrians only move in the areas without obstacles like furniture, walls and doors. So the map matching is an important tool for PDR systems.

The location areas are divided into several 3D square grids. The connectivity properties with adjacent grids built a database like a 3D map. Figure 4 gives an example to describe the 3D grid model for map matching applied in the proposed

system. The red line represents walls and the blue line represents doors. The green line shows the only way from grid No. 0 to No. 1 with the shortest distance. The properties of grid model are list in the Table 1 Take grid No. 5 for an example, the 3D position can be marked as (1,1,0). With the presence of walls, the connectivity with the surrounding grids almost closed except No. 6.

Calculate the probability from current grid to any other grids with the grid distance, connectivity properties, step length and headings. For example, current grid ID is M, *p(M,N)* is the probability of arriving at grid N. If the connectivity between M and N is 0, *p(M,N)* will be zero. The grid with the maximum probability is the next position of the target.

4 Conclusion

Fully taken the requirements of stability, convenience and low cost into account, a scheme for Pedestrian Dead Reckoning system with low cost inertial sensors is proposed in this chapter. Outline the architecture of the PDR system and describe how the various components work together, then analyses each component by technical methods. Several improved algorithms are proposed to reduce the accumulated errors of inertial navigation. Map matching with 3D grid connectivity database is applied to improve the positioning accuracy of the system. The number of the targets and users can be infinite, and the administrator or users can track any target real-time and remotely. In the future, wearable devices will be independent designed. Absolute positioning technologies also can be integrated to the system for better performance.

References

1. Yanying G, Lo A et al (2009) A survey of indoor positioning systems for wireless personal networks. Comm Surv Tutorials IEEE 11(1):13–32
2. Deak G, Curran K et al (2012) A survey of active and passive indoor localization systems. Comput Comm 35(16):1939–1954
3. Abdat M, Tat-Chee W et al (2010) Survey on indoor wireless positioning techniques: towards adaptive systems. Distributed framework and applications (DFmA) international conference
4. Hui L, Darabi H et al (2007) Survey of wireless indoor positioning techniques and systems. Syst Man Cybern C: Appl Rev IEEE Trans 37(6):1067–1080
5. Harle R (2013) A survey of indoor inertial positioning systems for pedestrians. Comm Surv Tutorials IEEE 99:1–13
6. Jimenez AR, Seco F et al (2009) A comparison of pedestrian dead-reckoning algorithms using a low-cost MEMS IMU. Intell Signal Process WISP 2009. IEEE Int Symp
7. Chengliang H, Zaiyi L et al (2010) Synergism of INS and PDR in self-contained pedestrian tracking with a miniature sensor module. Sens J IEEE 10(8):1349–1359
8. Sher L. Personal inertial navigation system (PINS), DARPA

9. Dempsey M (2003) Indoor positioning systems in healthcare. Radiance Inc., White Paper, http://www.cimit.org/pubs/ips_in_healthcare.pdf
10. STMicroelectronics Inc (2010) Using LSM303DLH for a tilt compensated electronic compass. STMicroelectronics Inc., Application Note, http://www.st.com/web/en/resource/technical/document/application_note/CD00269797.pdf

A Campus Based Mobility Model for Opportunistic Network

Daru Pan, Jiajia Sun, Xiong Liu, Xuhan Feng, and Wenfeng Pang

Abstract Mobility model in Opportunistic Network is one of the important technologies. The simple mobility models, such as Random Waypoint (RWP) and Random Walk (RW) are unable to capture the normal human behavior in daily life. To capture the real movement of teachers and students in campus, we propose the mobility model based on the daily life of campus, which mainly classify the nodes into three sorts: nodes which go back to the dormitory for sleeping at night, nodes which have classes at the daytime and nodes which have night activities. We simulate and analysis the model, using the contact duration and inter-contact times of nodes as the index of its functioning evaluation, and compare with the real datasets and RWP, it shows that our model is closer to the real datasets and follows the Power-law distribution, possesses the social feature.

Keywords Opportunistic network • Mobility models • Contact duration • Inter-contact times

1 Introduction

Opportunistic networks [1] are wireless mobile networks built entirely on users' devices. With respect to traditional MANET, the network partition and disconnections are very common, and there is no guarantee that a fully connected path between source and destination exists at any time, so the routing protocol is unable to find a path to the destination. The opportunistic networks are such network which does not need the entire connected path between the source node and the destination node, while they exploit contacts of nodes to transmit messages. Opportunistic networks use the store, carry and forward principle: store data locally on a device,

D. Pan (✉) • J. Sun • X. Liu • X. Feng • W. Pang
School of Physics and Telecommunication Engineering, South China Normal University, Guangzhou 510006, China
e-mail: pandr@scnu.edu.cn

B. Zhang et al. (eds.), *The Proceedings of the Second International Conference on Communications, Signal Processing, and Systems*, Lecture Notes in Electrical Engineering 246, DOI 10.1007/978-3-319-00536-2_120,

carry it around as the user moves, and forward it to the next hop when there is an opportunity [2]. It is a specific form of network, and also a different network communication technology. Opportunistic networks have significantly meaningful to the future ubiquitous computing.

It is important for mobility model to truly reflect the real-world scenarios,which has great impact on the cache management and routing. The same routing algorithm may have distinguished different performance in different mobility models. In this paper, we propose a campus mobility model that is focus on the daily life traces of teachers and students in campus. We use simulator, the ONE, to validate the proposed model by comparing it to actual user traces and synthetic traces generated using a Random Waypoint model in terms of contact times and inter-contact times. From the analysis results, we show a good matching between the proposed model which simulates the daily movement of teachers and students in campus and the real user datasets.

The rest of the paper is organized as follows. In Sect. 2, we discuss related work and briefly describe the current classification of the mobility model. In Sect. 3, we present the details of campus based mobility model for opportunistic network. The simulation tool we use for evaluation and result analysis are introduced in Sect. 4. We conclude the paper in Sect. 5.

2 Related Work

The mobility model is referred to the node movement route rule, movement speed and pause times, etc. The mobility model plays an important role in the delivery and efficiency of data communication in the network. At present, the mobility can be classified with a different kind of mobility metrics classes thus according to the features of node mobility can be divided into two categories: the individual mobility model and the group mobility model.

The individual mobility model is dealing primarily with movement of independent nodes, which is completely independent of the other nodes. In this case, the mobility model mainly depicts the individual characteristics of the nodes. Such as, Random Walk (RW) [3], Random Waypoint (RWP) [4] and the Random Direction (RD) mobility model [5]. These models are simple, easy to build and a widely used mobility model. But, they may lead to some unrealistic movement and nodes distribution is non-uniform in the network. Besides, the RWP node is irregular and changes sharply. The node can appear urgent turning and suddenly stop. So distribution and movement of the node across the simulation area do not fit to the characteristics of realistic movements. Therefore, in recent years, some modified RWP models are proposed [6].

The group mobility model includes Reference Point Group Mobility Model (RPGM) [7] and Community Mobility model, which are proposed based on CMM [8] and HCMM [9]. The main idea is that the destination for the next

movement of a user depends on the position of people with whom the user shares social ties.

Most of the above mentioned mobility models do not capture social properties of human mobility or only model one aspect of human mobility. To the best of our knowledge, now there are few models to study the behavior of teachers and students in campus. In order to reflect the mobility traces of this special group, this paper presents a new mobility model which reproduces realistic daily mobility pattern of teachers and students in campus.

3 The Campus Mobility Model

In order to overcome the disadvantages of random mobility model and better model the daily life activities of students and teachers, in this paper, we propose a campus based mobility model for opportunistic network, according to the daily life of students and teachers in campus. The campus mobility model consists of three parts: the teachers and students stay in their apartment at night, have class in the classrooms during the day and have night activities. There are three types of node, namely the students who have more social activities (outgoing students), the students who have less social activities (Introverted students) and the teachers who have regular social activities in campus. Our definition for the movement of the mobile node is as follows:

- Student nodes are initialized at a point of the dormitory area of the map file as their own dormitory location when the simulation starts. Each node can have only one location. Once nodes arrived near this location, they go back to their dormitory by using the shortest path algorithm. And then go to sleep mode, waiting for wakeup time. During this time, the node is kept staying at a certain coordinate point until the morning.

  The shortest path algorithm used in our paper is Dijkstra algorithm [10]. In this algorithm, set D (v) is defined as a distance from the source node (denoted as node 1) to a destination node v. It is also the sum of the lengths of all links from node 1 to node v. And set l (i, j) as the distance between node i and node j. The algorithm consists of two parts:

  (a) *Initialization*. Assuming that the N represents the set of network nodes, and we set N = {1} at the beginning. All nodes that do not belong to set N, we have:

$$D(v) = \begin{cases} l(1, v) & \text{node v and node 2 are directly connected} \\ \infty & \text{node v and node 2 are not directly connected} \end{cases} \quad (1)$$

  (b) Looking for a node w that is outside of set N and it has the minimum value of D(w), then add the node w into set N, and update the original value of D(v) by using the smallest value from [D(v), D(w) + l(w, v)]:

$$D(v) \leftarrow Min[D(v), D(w) + l(w, v)] \tag{2}$$

(c) Repeat step b until all the nodes are included into set N.

- After a predetermined sleep time, students will enter the active state. Furthermore, in order to make the model closer to the real situation, the wakeup time of every node has a certain difference. The nodes will enter the teaching area after they wake up. In the area, each node is assigned a coordinate which represents their positions. After each class (40 min), the student nodes move randomly for a while (such as recess or change the classroom), and then they pause another 40 min to continue classes until the end of school. The time is following Pareto distribution, that is, if X is a random variable with a Pareto distribution, then the probability that X is greater than some number x is given by:

$$P(X > x) = \left(\frac{\mathrm{x}}{\mathrm{x_{min}}}\right)^{-\mathrm{k}} \tag{3}$$

  Where $\mathrm{x_{min}}$ is the (necessarily positive) minimum possible value of X, and k is a positive parameter.
- After school, students randomly decide whether to proceed with night activities. The nodes of outgoing student have a greater chance to have night activities. Those nodes of students who decide to have night activities meet together at a predetermined place and start group activities after the number of student members has reached a predetermined probability value. While the nodes of students who do not have night activities go back to the dormitory immediately. At the beginning of the simulation, every node is assigned a meeting spot. Once after school, the active node is arranged into a group of collective activities. The nodes may move to the meeting spot by choosing either on foot or cycling and follow the shortest path algorithm.

  Each node can randomly choose the movement way including cycling or on foot. Outgoing students have a greater chance to ride a bicycle. Teachers' nodes conduct regularly the two kinds of social activities at between giving a lesson and going back to the teacher apartment. This model is close to the daily life style of students and teachers in campus. It also has the function of modeling the basic social activities of students and teachers, and keeps the balance between the regular and random behaviors.

In wireless network design and simulation process, the mobility model design is essential, and it is also indispensable for the mobility model to choose appropriate assessment parameter. Contact duration and inter-contact times are often used to evaluate the mobility model. Therefore, we use them to evaluate the performance of the proposed model.

Definition: Complementary Cumulative Distribution Function (CCDF) of nodes' contact duration and inter-contact times is given as follow:

Supposed t represents the contact duration or inter-contact times, and N represents the number of t in the datasets, t_i (i = 1, 2, 3……N) is the ith of contact duration or inter-contact times in the datasets. Therefore, the count that t is greater than the constant T is given by

$$num = \sum_{i=1}^{N} 1, \quad \text{where } t_i > T \tag{4}$$

So, the CCDF of nodes' contact duration and inter-contact times is given by the following:

$$P(T) = P(t > T) = \frac{num}{N}, \quad \text{where } T \geq 0 \tag{5}$$

The P (T) is used to the probability that the value of time of nodes' contact times or inter-contact times is greater than a certain constant T in datasets.

4 Simulations and Performance Analysis

In this paper, the ONE (Opportunistic Network Environment) [11] is used to simulate the proposed mobility model, and, a open source GIS program, OpenJUMP [12] is used for editing and converting the maps in our experiments.

We set over 315 nodes move on a map of the campus with the size of roughly 4,500 × 3,400 m^2. The simulation time is set to 43,200 s. These nodes are divided into two kinds: students and teachers, where students consist of two groups and each group have 150 nodes, and teacher group has 15 nodes. In simulation, we set 5 meeting points as their Points of Interest. The walking speed for nodes is set to 0.5–1.5 m/s and for bicycle 3–5 m/s. The probability to do some evening activity after school is set to 0.4. The probability to go to class by bicycle is set to 0.5. The sleeping length and class length is 14,400 s, and the length of each class is 2,400 s. Pause times after each class are drawn from a Pareto distribution with coefficient 0.5 and minimum value 600 s. Figure 1 depicts that we observe the moving states of nodes at different time periods in the simulation.

For comparison, we simulated a RWP on a same sized simulation area. The moving speed is set 1–5 m/s and pause time 1–800 s, both uniformly distributed.

We use two experimental datasets gathered by the CRAWDAD Project [13] in our paper. We show that the proposed model is the approximately the same of a given real scenario. We will refer to these traces as Cambridge and Infocom 06 [13]. The characteristics of these datasets such as inter-contact times and contact duration have been explored. Here, we also use these two parameters as the proposed model evaluation metrics. In order to improve the effectiveness and correctness, we do not consider time distribution between carrying iMotes device and external devices.

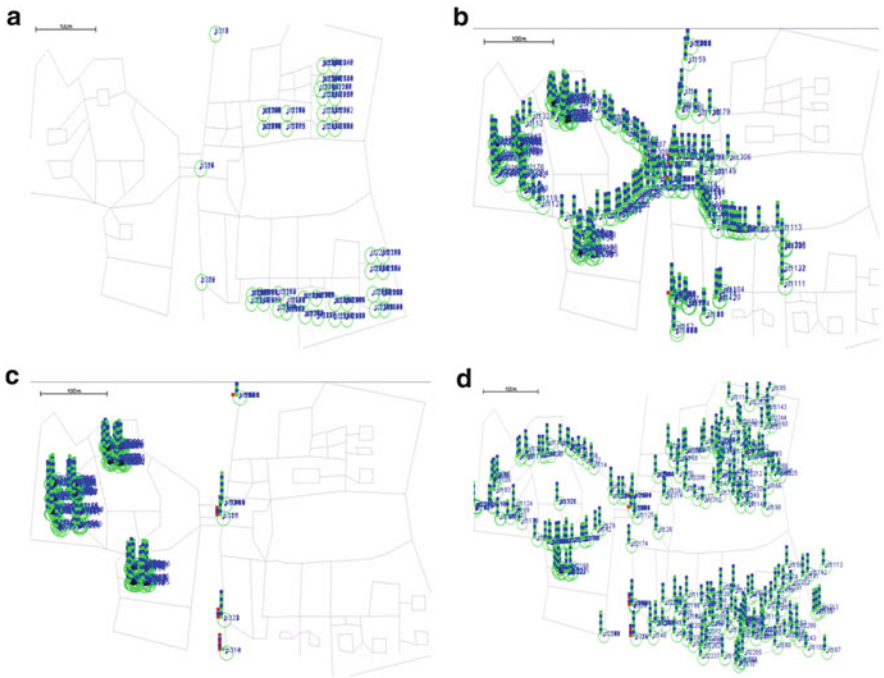

Fig. 1 The states of nodes in simulation. (**a**) initialization; (**b**) students attending class to teaching area; (**c**) students having classes in the teaching area; (**d**) student nodes' distribution after school

Figure 2a, b give the CCDF of Infocom 06, Cambridge, Random Waypoint mode (RWP), and Campus, respectively. Contact duration approximately follows the power-law distribution in Log–log coordinate in real dataset, with power-law characteristics, and the Campus model also has similar properties. While the RWP follows the exponential distribution, the distribution function is a straight line in semi-log coordinate. Because RWP model is synthesis model, node movement has a great deal of randomness. Therefore, RWP does not show good social properties in semi-log coordinate.

Figure 3a, b, respectively depict the CCDF of inter-contact times under the Log–log coordinates and semi-log coordinate in datasets. The traces of the campus model are the approximately the same as a given real traces. In the previous time, the probability is bigger than other dataset in Log–log coordinate, while the RWP is greatly different from the real traces. The reason is, in the RWP, the nodes can choose their movement patterns and states in random and individually, the probability of a node which communicates with any other nodes is the same. Finally, in the proposed model, the figure shows that the distribution curve of Campus is similar to a lean line towards down and has a better feature of the power-law distribution. Because students are the relative concentration in the living area, the density of the nodes is greater. Therefore, this situation will lead some of the nodes

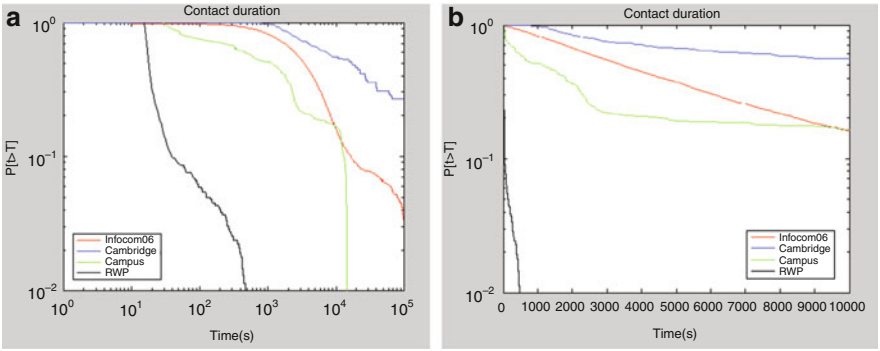

Fig. 2 Contact duration. (**a**) Log–log coordinate; (**b**) Semi-log coordinates

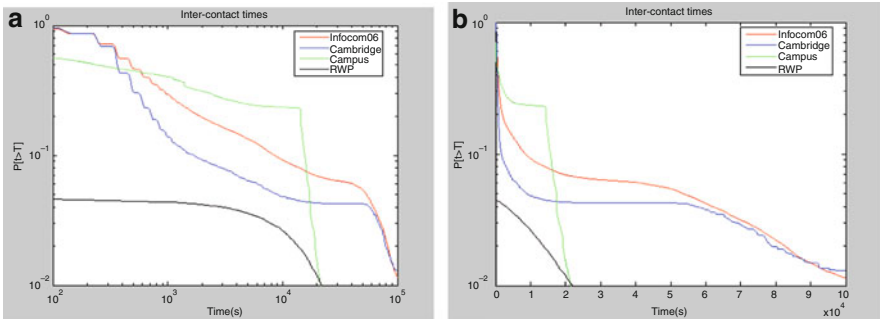

Fig. 3 Inter-contact times. (**a**) Log–log coordinate; (**b**) Semi-log coordinates

to have a very long contact time and CCDF curve has a sudden jumping down under the double logarithmic coordinates in the figure.

5 Conclusions

Mobility model is of significance for the analysis and research of all kinds of routing protocol in the opportunistic networks. In this paper, we have proposed the campus mobility model, which simulates the daily life of teachers and students in campus. By capturing several different mobility characteristics in this specific environment, i.e., sleeping, having class and having night activities of students, we have modeled the real human mobility in campus. It reflects the different aspects of campus life, while most of the other models do not capture this aspect. The proposed model is important to design more practical routing algorithms in opportunistic network. We have shown that the proposed model is more close to the real traces of gathering data from actual devices carried by people and have a better

power-law feature of contact duration and inter-contact time of the nodes. Compared with the RWP model, Campus mobility model,the proposed mobility model better reflects the sociality of node mobility under a certain social environment.

Acknowledgments This study was supported by the National Natural Science Foundation of China under Grant no. 61172087 and by Postdoctoral Science Foundation of China under Grant no. 013M530701.

References

1. Pelusi L, Passarella A, Conti M (2006) Opportunistic networking: data forwarding in disconnected mobile ad hoc networks. IEEE Comm Mag 44(11):134–141
2. Xiong YP, Sun LM, Niu JW, Liu Y (2009) Opportunistic networks. J Software 20(1):124–137
3. Camp T, Boleng J, Davies V (2002) A survey of mobility models for ad hoc network research. Wireless Comm Mobile Comput 2(5):483–502
4. Christian B, Hannes H, Hannes PC (2004) Stochastic properties of the random waypoint mobility model. Wireless Networks 10(5):555–567
5. Mohd I, Zuriati A (2009) Performance analysis of random-based mobility models in MANET routing protocol. Eur J Sci Res 32(4):444–454
6. Suvadip Batabyal, Parama Bhaumik (2012) Improving network performance with affinity based mobility model in opportunistic network. Int J Wireless Mobile Networks 4(2):189–202
7. Jian L, Pmohapatra L (2003) Location aided knowledge extraction routing for mobile ad hoc networks.Wireless communications and networking, California, USA, pp 1180–1184
8. Musolesi M, Mascolo C (2007) Designing mobility models based on social network theory. ACM SIGMOBILE Mobile Comput Comm Rev 11(3):59–70
9. Boldrini C, Passarella A (2010) HCMM: modelling spatial and temporal properties of human mobility driven by users' social relationships. Comput Commun 33(9):1056–1074
10. Xiren Xie (2011) Computer network, 5th edn. Publishing House of Electronics Industry, Beijing, China
11. Ari Keranen, Teemu Karkkainen, Jorg Ott (2010). Simulating mobility and DTNs with the ONE. J Comm 5(2):1796–2021
12. OPENJUMP-The free, java based and open source Geographic Information System for the World. http://sourceforge.net/projects/jump-pilot. Accessed 26 Feb 2013
13. CRAWDAD, A Community Resource for Archiving Wireless Data At Dartmouth. Haggle project. http://crawdad.cs.dartmouth.edu/data.php. Accessed 26 Feb 2013

GPS Multipath Mitigation Algorithm Using C/A Code Correlation Character

Jie Li, Yuliang Li, and Yingwu Zhou

Abstract The effect of signal multipath is one of the main reasons which lead to positioning error in Global Positioning System (GPS). Although the differential technology can improve the positioning accuracy of the navigation system, but the reference stations and users being in different geographical environment, the differential GPS system still can't eliminate the positioning error caused by multipath signal. In the light of the characters of GPS multipath signal model, a GPS multipath mitigation algorithm based on C/A code correlation character is proposed in this paper. Firstly, Doppler frequency is estimated when the signal delay is unknown. Then, we use the estimated Doppler frequency to get signal delay information with C/A code correlation character which is realized by correlating the reconstructed zero delay signal with the original signal. In addition, we consider the previous estimated results as the initial value and a two-dimension search method is implemented in a small range so as to further improve the estimation accuracy. It can be shown from the simulation results that the proposed method has a better time delay and Doppler frequency estimation performance compared with the conventional method and narrow correlator spacing algorithm.

Keywords Global positioning system • Multipath mitigation • C/A code correlation character • Improve the estimation accuracy

1 Introduction

Global Positioning System (GPS) has been extremely wide used in various fields and become a basic and important tool in social daily life. Most of the errors in GPS such as satellite ephemeris error, clock error, ionospheric error, tropospheric error

J. Li (✉) • Y. Li • Y. Zhou
Department of Physics and Electronics Information Engineering, Minjiang University, Fuzhou, China
e-mail: themilkyway79@126.com

B. Zhang et al. (eds.), *The Proceedings of the Second International Conference on Communications, Signal Processing, and Systems*, Lecture Notes in Electrical Engineering 246, DOI 10.1007/978-3-319-00536-2_121,

can be absolutely or mostly eliminated by the differential technique which is based on the principle that errors are related within a certain range. In reality, the antenna receives not only signals direct from the satellite but also signals reflected back from the other objects. Direct signal and multipath signal being the different path, the received mixed distortion signal would lead to measurement error [1–4]. In another word, it is called the multipath effects.

Multipath interference has become one of the main error sources of satellite navigation system [5]. Differential technique has greatly improved the positioning accuracy of the navigation system, but the differential GPS system still can not eliminate the positioning error caused by multipath because the geographical location and relative position between the reference station and user as well as the amplitude, direction and number of the multipath are quite different [6].

Lots of research organizations and universities have been seeking for the methods to mitigate the errors brought from the multipath. The main method is divided into two parts: antenna-based method and signal and data processing method. Antenna-based method is mainly composed of using a special type of antenna, drawing multipath environment map around the antenna and selecting the appropriate location to set up antenna [7, 8] etc. Multipath signals from the ground can be suppressed by the antenna design but it is hardly effective for the multipath from the top of the antenna.

Narrow correlator spacing, which decreases the early-late spacing to reduce the influence of multipath on the code tracking loop, is the most common used method to eliminate the multipath [9, 10]. The smaller of the correlator spacing, the smaller of tracking error caused by multipath. Narrow correlator spacing technology is under the hypothesis of unlimited bandwidth, but in practice, this assumption can not be satisfied. Therefore, the Delay Lock Loop (DLL) tracking error tends be to a constant when the correlator spacing is less than the reciprocal of the double-sided bandwidth [11, 12].

In this paper, a parametric model of Doppler frequency and signal time delay is proposed. Firstly, Doppler frequency is estimated when the signal time delay is unknown. Then, the estimated Doppler frequency is taken advantage of to obtain the direct and multipath time delay information with C/A code correlation character. In the satellite navigation system, the pseudorange measurement accuracy which depends on the accuracy of the signal propagation delay directly determines the positioning accuracy. What's more, in order to further improve the delay estimation accuracy, the estimation results of Doppler frequency and time delay obtained by the previous method is taken as the initial value and a two-dimension search is carried out in a small range. A more accurate time delay estimation result of direct path signal can be obtained by this kind of two-dimension optimization method.

2 Data Model and Problem Description

For the convenience of the multipath performance analysis of the satellite navigation signal and without loss of generality, the single-reflection path model is typically used. Since C/A code of different satellite is absolutely not correlated, only one satellite is taken into account in this data model. Considering one satellite with single-reflection path, the received signal model can be expressed as

$$y(t) = \sum_{p=1}^{2} \alpha_p d(t-\tau_p) c(t-\tau_p) e^{j\omega_{dp}(t-\tau_p)} + e(t) \tag{1}$$

where $d(t)$ is the navigation data, $c(t)$ is the C/A code, $e(t)$ is the thermal noise, α_1, τ_1, ω_{d1} is the amplitude, time delay and Doppler frequency of the direct signal, α_2, τ_2, ω_{d2} is the amplitude, time delay and Doppler frequency of the multipath signal respectively.

In GPS system, when the additional time delay of the multipath signal is greater than two chips, the effect on the pseudorange measurement can be neglected [13]. Because the receiver is close to reflecting surface, we can approximately consider that they have the same movement relative to the satellite. Accordingly, we can suppose that the direct signal and multipath signal have the same Doppler shift.

Thence, (1) can be rewritten as

$$y(t) = \sum_{p=1}^{2} \alpha_p d(t-\tau_p) c(t-\tau_p) e^{j\omega_{d}(t-\tau_p)} + e(t) \tag{2}$$

After A/D conversion, the transformed signal model is given as

$$y(n) = \sum_{p=1}^{2} \alpha_p d(n-\tau_p) c(n-\tau_p) e^{j\omega_{d}(n-\tau_p)} + e(n) \tag{3}$$

In the above equation, the parameters $\hat{\omega}_d$ and $\{\hat{\alpha}_p, \hat{\omega}_p\}_{p=1}^{2}$ are unknown and need to be estimated. In this paper, a new approach is presented to estimate the above parameters. The whole process can be divided into the following three steps to achieve:

1. Estimated the Doppler frequency $\hat{\omega}_d$ in the case of signal time delay is unknown.
2. According to the GPS C/A code correlation character, the time delay and amplitude $\{\hat{\alpha}_p, \hat{\omega}_p\}_{p=1}^{2}$ can be estimated respectively with obtained Doppler frequency $\hat{\omega}_d$.
3. In order to further improve the estimation accuracy, we consider the previous estimated results as the initial value and do the local two-dimension search in a

small range. The time delay of the direct signal would be estimated precisely so as to mitigate the effect of multipath.

3 Doppler Frequency Estimation

Due to the navigation data and C/A code are ± 1 in the GPS system, it can be seen from (3) that the spectrum of each satellite contains multiple frequency components. The conventional spectral analysis methods do not work here. For the sake of eliminating the influence on frequency estimation brought by the navigation data and C/A code, we square (3) as [14, 15]

$$\begin{aligned} y^2(n) = {} & \alpha_1^2 c^2(n-\tau_1)e^{2j\omega_d(n-\tau_1)} + \alpha_2^2 c^2(n-\tau_2)e^{2j\omega_d(n-\tau_2)} \\ & + 2\alpha_1\alpha_2 c(n-\tau_1)c(n-\tau_2)e^{-j\omega_d(2n-\tau_1-\tau_2)} + e_1(n) \end{aligned} \tag{4}$$

where $e_1(n) = 2\alpha_1\alpha_2 d(n-\tau_1)d(n-\tau_2)c(n-\tau_1)c(n-\tau_2)e^{-j\omega_d(2n-\tau_1-\tau_2)} + 2\alpha_1 d(n-\tau_1)c(n-\tau_1)e^{-j\omega_d(n-\tau_1)}e(n) + 2\alpha_2 d(n-\tau_2)c(n-\tau_2)e^{-j\omega_d(n-\tau_2)}e(n) + e^2(n)$.

The navigation data and C/A code being ± 1 in the GPS system, the above equation can be simplified as

$$\begin{aligned} y^2(n) = {} & \alpha_1^2 e^{2j\omega_d(n-\tau_1)} + \alpha_2^2 e^{2j\omega_d(n-\tau_2)} + 2\alpha_1\alpha_2 c(n-\tau_1)c(n-\tau_2)e^{-j\omega_d(2n-\tau_1-\tau_2)} \\ & + e_1(n) \end{aligned} \tag{5}$$

After the square processing, the spectrum of each satellite only contains a single frequency component. Fourier analysis method can be used to estimate the signal frequency.

Not only the C/A code correlation coefficient of the same satellite is very small but also the signal and noise are quite not correlated when the code delay is different. Consequently, it is obvious that Fourier analysis results of the product terms of C/A code with different time delay as well as noise and signal are close to zero. Accordingly, the frequency of satellite signal can be estimated by using Fourier analysis method. From (5), the Fourier transform spectrum can be expressed as

$$F(\omega) = \left| \sum_{n=-N/2}^{N/2-1} y^2(n)e^{-j\omega n} \right| \tag{6}$$

where $\omega = 2\omega_d$.

In (6), we have the value of $2\omega_d$ as ω which can be obtained as the location of the first p dominant peaks of the magnitude of the Fourier transform $F(\omega)$.

The implementation of improving estimation accuracy can be achieved by padding with zeros.

The estimated value of $\hat{\omega} \in [-\pi, \pi]$, thus from (5) we know the estimated value of $\hat{\omega}_d \in [-\pi/2, \pi/2]$. As the true value of $\omega_d \in [-\pi, \pi]$, the estimated frequency could be $\hat{\omega}_d$ or $\hat{\omega}_d + \pi$.

Therefore, the frequency ambiguity problem would result in miscalculation. Due to the Intermediate Frequency (IF) of the satellite signals is definitely known after down conversion and the range of Doppler shift is between $\pm$ $10kHz$ [2], frequency error between the true frequency and ambiguity frequency is generally greater than the Doppler shift. Thence, we can get rid of ambiguity frequency by distinguishing whether or not the frequency is in the range of Doppler shift.

4 Time Delay Estimation

After obtaining Doppler frequency estimates, the estimation value of time delay and amplitude $\{\hat{\alpha}_p, \hat{\omega}_p\}_{p=1}^{2}$ can be achieved with the above estimated Doppler frequency based on the C/A code correlation character.

As the Doppler frequency $\hat{\omega}_d$ has been estimated, we use $\hat{\omega}_d$ instead of ω_d to reconstruct $s(n)$ and get

$$\hat{s}(n) = d(n)c(n)e^{j\hat{\omega}_d n} \tag{7}$$

$$\hat{s}(n - \tau_p) = d(n - \tau_p)c(n - \tau_p)e^{j\hat{\omega}_d (n - \tau_p)} \tag{8}$$

Equation (3) can be further rewritten as

$$y(n) = \sum_{p=1}^{2} \alpha_p \hat{s}(n - \tau_p) + e_2(n) \tag{9}$$

where $e_2(n) = \sum_{p=1}^{2} \alpha_p s_p(n - \tau_p) - \alpha_p \hat{s}(n - \tau_p) + e(n)$.

The cycle of the navigation data is much larger than that of the C/A code and the length of the data block used for delay estimation is generally one C/A code cycle, therefore we ignore the effect of navigation data slip during the signal reconstructed process.

In order to obtain initial C/A code phase of the direct signal and the multipath signal, the following function is introduced

$$r(n) = E\left(\left|\sum_{m=0}^{M-1} s(m)y(n+m)\right|\right) = E(|R(s(n), y(n))|) \tag{10}$$

where R is the correlation operation.

Since the signal and noise are quite not correlated, (10) can be further expressed as

$$\begin{aligned} r(n) &= \alpha_1 E(|R(s(n), s(n-\tau_1))|) + \alpha_2 E(|R(s(n), s(n-\tau_2))|) \\ &= \sum_{p=1}^{2} \alpha_p q_{pn}(\tau_p) \\ &= r_1(n) + r_2(n) \end{aligned} \tag{11}$$

where $q_{pn}(\tau_p)$ is the result that the zero delay reference signal correlates with the reference signal which is delay τ_p, α_p is the corresponding amplitude.

According to the auto-correlation character of the C/A code, only two C/A code chips of the same satellite are fully aligned, can the dominant peak of the correlation results obtain its maximum value. When containing the signal multipath, there will be two correlation peaks corresponding to the initial C/A code phase of the direct signal and the multipath signal respectively.

The amplitude of the multipath signal is lower than that of the direct signal because there is certain energy loss when multipath signal reflected by the surface. The delay information of the direct signal and the multipath signal can be achieved by the location of the first two dominant peaks of the magnitude of the correlation function.

We consider below estimating the unknown parameters $\hat{\alpha}_p$ and $\hat{\tau}_p$ by minimizing the Nonlinear Least Squares (NLS) criterion [16–18]

$$Q\left(\{\hat{\alpha}_p, \hat{\tau}_p\}_{p=1}^{2}\right) = \min_{\hat{\alpha}_p, \hat{\tau}_p} \left\| \mathbf{r} - \sum_{p=1}^{2} \hat{\alpha}_p \mathbf{q}_p(\hat{\tau}_p) \right\|^2 \tag{12}$$

where $\mathbf{q}_1(\tau_1) = \left[q_{1,2}(\hat{\tau}_1), q_{1,2}(\hat{\tau}_1), \ldots, q_{1,2N-1}(\hat{\tau}_1)\right]$, $\mathbf{q}_2(\tau_2) = \left[q_{2,1}(\hat{\tau}_2), q_{2,2}(\hat{\tau}_2), \ldots, q_{2,2N-1}(\hat{\tau}_2)\right]$,

$\mathbf{r} = [r(1), r(2), \ldots, r(2N-1)]$, N is the sample points.

$\{\hat{\alpha}_k, \hat{\tau}_k\}_{k=1,k\neq p}^{2}$ is assumed to be given, then

$$\mathbf{r}_p = \mathbf{r} - \sum_{\substack{k=1 \\ k\neq p}}^{2} \hat{\alpha}_k \mathbf{p}_k(\hat{\tau}_k) \tag{13}$$

Substituting (13) into (12), we have

$$Q(\hat{\alpha}_p, \hat{\tau}_p) = \min_{\hat{\alpha}_p, \hat{\tau}_p} \left\| \mathbf{r}_p - \hat{\alpha}_p \mathbf{q}_p(\hat{\tau}_p) \right\|^2 \tag{14}$$

Solving (14), we get

$$\hat{\alpha}_p = \left(\mathbf{q}_p^T(\hat{\tau}_p) \mathbf{q}_p(\hat{\tau}_p) \right)^{-1} \mathbf{q}_p^T(\hat{\tau}_p) \mathbf{r}_p \tag{15}$$

where the parameters $\hat{\tau}_p$ can be gotten in the light of the location of p^{th} dominant peak of the magnitude of the correlation function.

The estimation of $\{\hat{\alpha}_p, \hat{\tau}_p\}_{p=1}^2$ can be realized by the following steps:

1. Assume that only direct signal is exist, that is $\mathbf{r} = \mathbf{r}_1$. Estimate $\hat{\tau}_1$ from the location of the dominant peak of the magnitude of $\mathbf{r}$. Reconstruct the reference signal $\mathbf{s}(\tau_1)$ which delay is $\hat{\tau}_1$ from (8). Correlate $\mathbf{s}(\tau_1)$ with the zero delay reference signal $\mathbf{s}$ to achieve $\mathbf{q}_1(\hat{\tau}_1)$, then get $\hat{\alpha}_1$ according to (13) ;
2. Assume that multipath signal is exist as well. Compute $\mathbf{r}_2$ with (13) by using $\{\hat{\alpha}_1, \hat{\tau}_1\}$ obtained in Step 1). Obtain $\hat{\tau}_2$ from $\mathbf{r}_2$. Then, Reconstruct the reference signal $\mathbf{s}(\tau_2)$ which delay is $\hat{\tau}_2$ and correlate $\mathbf{s}(\tau_2)$ with the zero delay reference signal $\mathbf{s}$ to achieve $\mathbf{q}_2(\hat{\tau}_2)$ and $\hat{\alpha}_2$.
3. Estimate $\mathbf{r}_1$ by using $\{\hat{\alpha}_2, \hat{\tau}_2\}$ and then redetermine $\{\hat{\alpha}_1, \hat{\tau}_1\}$ from $\mathbf{r}_1$.
4. Iterate the previous three substeps until convergence is achieved to get the final result of $\{\hat{\alpha}_p, \hat{\tau}_p\}_{p=1}^2$.

5 Precise Estimation of Parameters

So as to further improve the estimation accuracy, a fine estimation method of two-dimension search which takes the previous estimated results as the initial values is presented in this paper. Multipath delay not taken part in the positioning processing, it is unnecessary to estimate the multipath delay accurately to bring in the extra computation.

Note that $\hat{\tau}_1, \hat{\omega}_d$ represent the estimates of time delay and Doppler frequency of direct signal while τ_1, ω_d represent the true value of them. Let

$$s_1(n) = c(n - \tau_1) e^{j\omega_d (n - \tau_1)} + \widetilde{e(n)} \tag{16}$$

The fine estimates of time delay and Doppler frequency of direct signal can be expressed as

$$\begin{aligned}\left\{\hat{\tau}_{1\_p}, \hat{\omega}_{d\_p}\right\} &= \max_{\hat{\tau}_{1\_p}, \hat{\omega}_{d\_p}} \left\{R\left(S_1(n)e^{-j\omega_{d\_p}n}, c\left(n-\tau_{1\_p}\right)\right)\right\} \\ &= \max_{\hat{\tau}_{1\_p}, \hat{\omega}_{d\_p}} \left\{R\left(c(n-\tau_1)e^{j\omega_d n}e^{-j\omega_{d\_p}n}, c\left(n-\tau_{1\_p}\right)\right)\right\}\end{aligned} \tag{17}$$

where $\tau_{1\_p} \in [\hat{\tau}_1 - \delta_1, \hat{\tau}_1 + \delta_1]$, $\omega_{d\_p} \in [\hat{\omega}_d - \delta_2, \hat{\omega}_d + \delta_2]$, δ_1, δ_2 is a small offset relative to $\hat{\tau}_1, \hat{\omega}_d$, R is correlation operation. The proper δ_1, δ_2 should be selected to make sure that $\tau_1 \in [\hat{\tau}_1 - \delta_1, \hat{\tau}_1 + \delta_1]$ and $\omega_d \in [\hat{\omega}_d - \delta_2, \hat{\omega}_d + \delta_2]$.

When the estimated value $\hat{\omega}_d$ is in accord with the true value ω_d, the C/A code information can be correctly demodulated from $s_1(n)$. According to the autocorrelation character of C/A code, the correlation function can't achieve the maximum value unless C/A code is completely aligned and $\hat{\tau}_1$ is exactly consistent with τ_1. Therefore, we can precisely estimate time delay and Doppler frequency of the direct signal $\left\{\hat{\tau}_{1\_p}, \hat{\omega}_{d\_p}\right\}$ by implementing a two-dimension search within a small range. In (6) and (15), relatively accurate estimation results has been given as initial values, consequently, a small-scale two-dimension search does not bring in extravagant computation. Even so, the search step is still one of the main factors to determine the computational complexity of the algorithm. Although a comparatively coarser step can make the estimation process faster, the accuracy would have a partial loss in the meantime. A compromise between the processing speed and the accuracy should be taken into account in this method.

The basic diagram of the whole algorithm is shown below as Fig. 1.

6 Simulation Results

To test and verify the method in this paper, signals with single multipath have been simulated by the GPS simulator. On the basis of the hypothesis of (2), frequency of direct signal and multipath signal is set to the same as 1.251924 MHz. We consider the signal with the sampling rate of 7.5 MHz, integration time of 1 ms, the DLL loop noise bandwidth of 2 Hz. Although small noise bandwidth may cut down the dynamic performance of the loop, at the same time, it is facilitate reducing the noise which results in a lower tracking error and ensuring that the narrow correlator spacing achieve the best performance at the same time.

Mean square errors (MSE) of time delay and Doppler frequency change with signal to noise ratio (SNR) are shown in Figs. 2 and 3 where correlator spacing is 0.1 chips and multipath signal has an additional time delay of 700 ns relative to direct signal. It can be seen from the Fig. 2 that time delay estimation error of conventional method is too large to have a good suppression of the multipath. Narrow correlator spacing algorithm can mitigate the multipath effectively. The proposed method in this paper has a better performance compared with narrow correlator spacing before fine estimation and estimation error has been further eliminated after that. Doppler frequency error is given in Fig. 3. The results of

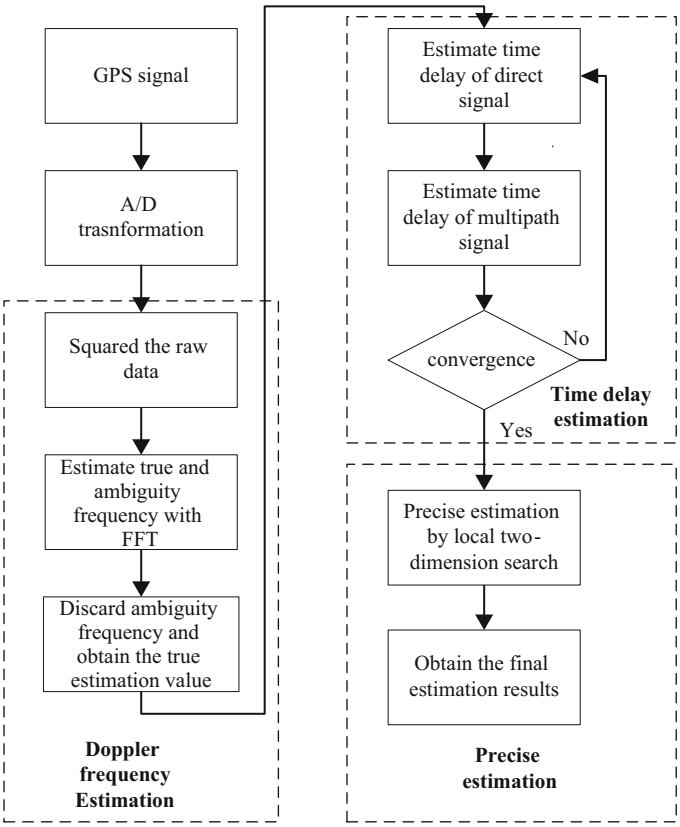

Fig. 1 Basic diagram of doppler frequency and time delay estimation

Fig. 2 Time delay error changes with SNR

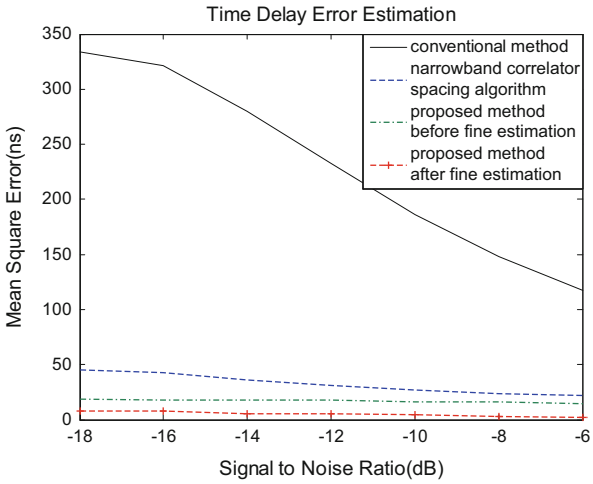

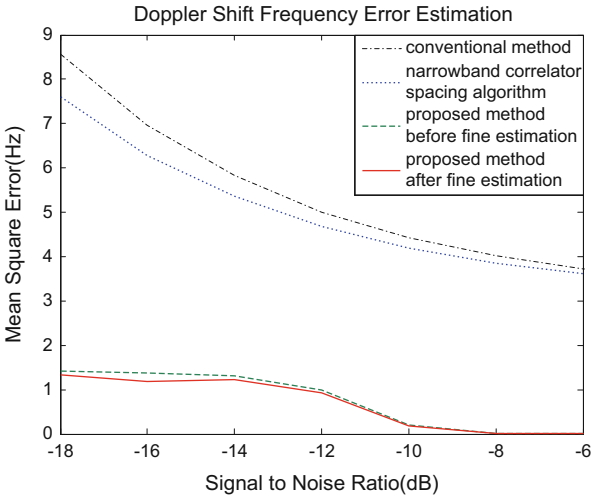

Fig. 3 Doppler frequency error changes with SNR

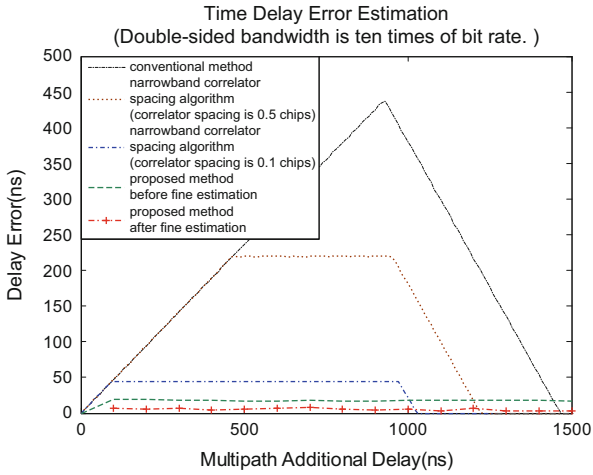

Fig. 4 Time delay error changes with additional delay

proposed method precede others as well. Doppler frequency error is rather small therefore there is no distinct improvement after fine estimation.

It is shown in Fig. 4 that time delay error of different methods changes with different multipath additional time delay when SNR is −18 dB. The conventional algorithm can not mitigate the multipath effectively. When double-sided bandwidth is ten times of bit rate, according to the conclusions given in [12], the delay error will tend to be a constant if the correlator spacing is less than 0.1 chips. It is invalid to decrease the error by means of lowering correlator spacing. In the same condition, the proposed method in this paper surpass the best performance of narrow correlator spacing algorithm when multipath additional delay has a medium length from 0.1 chips to 1 chips before fine estimation. While after fine estimation, the

performance of proposed method absolutely exceed narrow correlator spacing algorithm.

7 Conclusion

According to the characteristics of GPS multipath signal model, a new estimation algorithm of Doppler frequency and time delay, which is based on C/A code correlation character, is presented in this paper. Firstly, Doppler frequency is estimated when the signal time delay is unknown. Then, the estimated Doppler frequency is taken advantage of to obtain the direct and multipath time delay information with C/A code correlation character. In order to further improve the estimation accuracy, a two-dimension fine estimation method is proposed, which takes the previous estimated results as the initial values of search. Simulation results show that the proposed method could estimate the Doppler frequency and the time delay precisely. Narrow correlator spacing algorithm can not always reduce the estimation error by continuing decreasing the correlator spacing while the proposed method is better than its best performance in the same condition. In addition, the computation time of is lower than signal separation estimation theory method with approximately same precision.

References

1. Li CX, Liu WM (2012) Effective GPS positioning algorithm with New fast integer ambiguity resolution and kalman filter model. J Convergence InformTech 7(9):253–260
2. Liang HJ (2012) The study on the capturing technology based on the GPS signals under multiplicative noises. Int J Adv Comput Technol 4(22):771–778
3. Kong S (2011) Statistical analysis of urban GPS multipaths and pseudo-range measurement errors. IEEE Trans Aerosp Electron Syst 47(2):1101–1113. doi:10.1109/TAES.2011.5751245
4. Pinana-Diaz C, Toledo-Moreo R, Betaille D, Gomez-Skarmeta AF (2011) GPS multipath detection and exclusion with elevation-enhanced maps. 14th international IEEE conference on intelligent transportation systems, p 19–24
5. Cote FD, Psaromiligkos IN, Gross WJ (2011) GNSS modulation: a unified statistical description. IEEE Trans Aerosp Electron Syst 47(3):1814–1836. doi:10.1109/TAES.2011.5937267
6. Braasch M (1994) Optimum antenna design for DGPS ground reference stations. In: Proceedings of the 7th international technical meeting of the satellite division of the institute of navigation (ION GPS 1994), p 1291–1297
7. Scire-Scappuzzo F, Makarov SN (2009) A Low-multipath wideband GPS antenna with cutoff or non-cutoff corrugated ground plane. IEEE Trans Antennas Propag 57(1):33–46
8. Maqsood M, Gao S, Brown T and Unwin M (2010) Effects of ground plane on the performance of multipath mitigating antennas for GNSS. Antennas & propagation conference, p 241–244. doi:10.1109/LAPC.2010.5666164
9. Dierendonck AJV, Fenton P, Ford T (1992) Theory and performance of narrow correlator spacing in a GPS receiver. Navigation 39(3):265–283

10. Li L, Zhou WH, Tan SS (2006) Tracking accuracy of narrow correlator spacing gps receiver, ICSP2006 Proceedings. doi:10.1109/ICOSP.2006.346123
11. Liu HC, Xu XY, Wang FX (2005) Analysis and mitigation of the code tracking error caused by multipath in spread-spectrum ranging systems. GNSS World of China 30(6):34–38
12. Rechard DJ, Nee V (1993) Spread-spectrum code and carrier synchronization errors caused by multipath and interference. IEEE Trans Aerosp Electron Syst 29(4):1359–1365
13. Sánchez-Fernández M, Aguilera-Forero M, García-Armada A (2007) Performance analysis and parameter optimization of DLL and MEDLL in fading multipath environments for next generation navigation receivers. IEEE Trans Consum Electron 53(4):1302–1308
14. Besson O, Stoica P (1999) Nonlinear least-squares frequency estimation and detection for sinusoidal signals with arbitrary envelope. Digit Signal Process 9(1):45–56. doi:10.1006/dspr.1998.0330
15. Besson O, Stoica P (1998) Frequency estimation and detection for sinusoidal signals with arbitrary envelope: a nonlinear least-squares approach. In: Proceedings of the 1998 I.E. international conference, p 2209–2212. doi:10.1109/ICASSP.1998.681586
16. Wu RB, Naren T, Lu XG (2009) Estimation of direction of arrival for wideband coherent signals with known waveforms. Radar conference, 2009 IET international, p 827–828
17. Li J, Wu RB (1998) An efficient algorithm for time delay estimation. IEEE Trans Signal Process 46(8):2231–2235. doi:10.4028/www.scientific.net/KEM.474-476.1201
18. Li J, Zheng DM, Stoica P (1997) Angle and waveform estimation via RELAX. IEEE Trans Aerosp Electron Syst 33(3):1077–1087

On-Line Anomaly Detection in Big Data Based on Compressive Sensing

Wei Wang, Dunqiang Lu, Xin Zhou, Baoju Zhang, and Jiasong Mu

Abstract The definitions of anomaly detection and big data were presented. Due to the sampling and storage burden of anomaly detection in big data, compressive sensing theory was introduced and used in anomaly detection algorithm. The anomaly detection criterion based on wavelet packet transform and statistic process control theory was deduced. The anomaly detection method was used for through wall human detection. The experiments for detecting human behind Brick wall based on UWB radar signal was carried out. The results showed that the proposed anomaly detection algorithm could effectively detect the existence of human being through compressed signals.

Keywords Anomaly detection • Big data • Through wall human detection • Compressive sensing

1 Introduction

Anomaly detection refers to find inconsistent with the desired pattern in data, also known as novelty detection, anomaly mining, noising mining. Anomaly detection has many applications, such as credit card fraud detection, medical diagnostics information anomaly detection, industrial equipment fault detection and structural defect detection, network intrusion detection and novel theme of text mining. Currently, anomaly detection method has anomaly detection based on classification, anomaly detection based on the nearest neighbor method, anomaly detection based on clustering, statistical anomaly detection, anomaly detection based on information theory, spectral theory anomaly detection and so on [1].

W. Wang (✉) • D. Lu • X. Zhou • B. Zhang • J. Mu
College of Electronic and Communication Engineering, Tianjin Normal University, Tianjin, China
e-mail: wangweivip@tju.edu.cn

B. Zhang et al. (eds.), *The Proceedings of the Second International Conference on Communications, Signal Processing, and Systems*, Lecture Notes in Electrical Engineering 246, DOI 10.1007/978-3-319-00536-2_122,

"Big Data" refers to large, diverse, complex, longitudinal and distributed data sets generated from instruments, sensors, internet transactions, email, video, click streams, and other digital sources available today and in the future. Existing anomaly detection algorithms are mainly based on the complete data. And it greatly limits the application of anomaly detection algorithms in big data [2, 3]. The main reason is that big data acquisition and storage becomes increasingly difficult with the amount of data increasing because of the sampling bandwidth and storage space constraints.

Compressive sensing (or compressed sampling, CS) theory suggested that a high-dimensional signal can be projected into a low-dimensional space with a random measurement matrix when the signal was sparse or compressible which proposed by Donoho and Candès in 2006 [4, 5]. Then the original signal can be reconstructed from the low-dimensional information with solving an optimization problem. In other word, the low-dimensional signal contained the main features of the original signal. So CS theory can provide an effective method for anomaly detection in big data.

According to the problem in anomaly detection of big data, an anomaly detection algorithm in compressed domain is proposed which makes full use of the advantage of compressive sensing technology. The experiment for through wall human detection with the provided algorithm is carried out to test the effective of the algorithm. The remainder of the paper is organized as follows. In the Sect. 2 the compressive sensing theory will be introduced. Then the criterion and procedure of anomaly detection will be deduced base on wavelet packet transform and statistical method. Experimental results for human being detection will be showed in Sect. 3. Conclusion and discussion is in Sect. 4.

2 Background and Anomaly Detection Procedure

2.1 Anomaly Detection Procedure

The Wavelet Packet Transform (WPD) of a time-domain signal $x(t)$ can be calculated using a recursive filter-decimation operation. After the signal $x(t)$ is decomposed into j levels of decomposition and the node signals are reconstructed as $x_j^i(t)$. Then the signal $x(t)$ can be expressed as:

$$x(t) = \sum_{i=1}^{2^j} x_j^i(t) \tag{1}$$

The node signal energies E_j^i can be defined as

$$E_j^i = \int_{-\infty}^{\infty} x_j^i(t)^2 dt = \sum x_j^i(t)^2 \tag{2}$$

According to the theory of WPT, each node signal contains information of the original signal in a specific time-frequency window. Hence (2) illustrates that the node signal energy E_j^i is the energy stored in corresponding frequency band. Obviously, the frequency components will be varied when anomaly occurs in the original signal. Thus, the anomaly detection can be achieved by investigated the changing trend of E_j^i.

The wavelet packet components with small energy magnitudes are easily jammed by the measurement noise. Thus, in this paper, instead of directly observe node signal energies on an individual basis, the criterion for anomaly detection is designed as:

$$ADC = \sum_{i=1}^{m} \frac{|\Delta E_j^i - \overline{\Delta E_j^i}|}{\overline{\Delta E_j^i}} \tag{3}$$

Where ΔE_j^i is the node signal energy ratio in the total signal energy, $\overline{\Delta E_j^i}$ is the reference baseline of node signal energy ratio which is the mean value of node signal energy by measuring some subsequent signals. In order to eliminate the noise effect, the first m dominant nodes are retained. It can be deduced that anomalies in the signal would affect the wavelet node signal energies and subsequently alter the criterion "ADC". But the anomalies are not the only factor that can affect the criterion which also can be influenced by measurement noise. It is essential to establish threshold values for anomaly detection criterion so that the criterion can be use to extract anomalies from measurement noise with a large probability [6]. In this paper, the threshold values would be fixed based on statistical process control (SPC) and statistical process control charts which are used to describe the output characteristics of process in coordinate graph.

Assume that continuous measuring m sets of time-domain signals under the same status. In other words, there are no anomalies during the measurements. According to (1)–(3), a total of p ADCs can be acquired using the average node energies as the reference baseline. Furthermore, the mean values and the standard deviation of p ADCs can be obtained as μ_{ADC} and S_{ADC}. On the basis of SPC theory, an X-bar control chart is used to determine threshold values of ADC. Suppose that the p ADCs are divided into subgroups of size q. Then, the one-side $1 - \alpha$ upper confidence level for average ADCs of a subgroup can be defined as:

$$UCL_\alpha = \mu_{ADC} + Z_\alpha \left(\frac{S_{ADC}}{\sqrt{q}} \right) \tag{4}$$

Where Z_α is the value of a standard normal distribution with zero mean and unit variance such that the cumulative probability is $100(1 - \alpha)\%$. The level UCL_α can

be regarded as the threshold value of the criterion. Therefore, if no anomalies happen, the average criterion ADC of a followed subgroup would be in the range of UCL_α with a high probability $100(1 - \alpha)\%$. On the other hand, when the average criterion ADC of a consecutive subgroup is beyond the limit, it shows that there are some anomalies. However, it should indicate that the SPC is a statistical principle of hypothesis testing. So there are two types of hypothesis testing errors. Usually, the confidence limit can be improved by increasing the size p and q. From the anomaly detection procedure, it can be seen that no training data is required to construct a mathematical mode for anomaly detection. That is to say that the proposed algorithm belongs to unsupervised anomaly detection and can achieve on-line anomaly detection.

2.2 Compressive Sensing Theory

Although the proposed algorithm can overcome the noise interference and achieve anomaly detection with high probability, this algorithm is based on the complete data which greatly limits the application in the big data field. Compressive sensing theory overwhelms the limitation of Nyquist sampling theory and can acquire and compress data simultaneously. The theory provides a feasible basis for the proposed anomaly detection algorithm in big data field.

For signal $x \in R^N$,it can be expressed as:

$$x = \sum_{i=1}^{N} \phi_i \theta_i \quad , \text{or} \quad x = \Phi\theta \tag{5}$$

Where Φ is $N \times N$ orthonormal transform basis, θ is the expansion coefficients vector under the orthonormal basis. If signal x is a K sparse signal, that is K elements in vector θ are not zero and K is far less than N, the signal x can be collected with a small set of nonadaptive, linear measurements according to compressive sensing theory. Then, it can be described as follows [7–12]:

$$y = \Psi x = \Psi\Phi\theta \tag{6}$$

Where Ψ is a $M \times N$ random measurement matrix and $M < N$. Here, (Φ,Ψ) is a pair of orthobases which followed the incoherence restriction.

If x is termed as K sparse in the orthonormal basis, we only need to collect $M = O(K \log(N/K))$ random measurements to recover the signal by iterative algorithm such as Basis Pursuit (BP), matching pursuit (MP), orthogonal matching pursuit (OMP), StOMP, Subspace Pursuit (SP), and CoSaMP and so on.

According to Compressive sensing theory, the acquired low dimensional signal contained the main features of the signal under the premise of appropriate measurement matrix. So the frequency component would be included in the gathered

low dimensional signal. Therefore, the proposed anomaly detection procedure could be carried out in the compressed domain data.

3 Experiments Results

Through wall human detection is of great interest for many applications, such as: military reconnaissance, anti-terrorism, medical and natural disasters ambulance, which can penetrate non-metallic media to detect life signal in far-off areas. Due to the strong anti-interference ability, high resolution performance and good target recognition capabilities, the Ultra-Wideband (UWB) radar has emerged as one of the most optimal choices for through wall human detection. But the UWB echo signals usually are the big data which increase the burden of data sampling and storage. In this paper, we would use the proposed anomaly detection procedure in compression domain for through wall human detection to verify its feasibility.

In the experiments, we used the P220 UWB radar of Time Domain Company as the detection tool and it worked in monostatic mode that the waveform pulses were transmitted from a single Omni-directional antenna and scattered waveforms were acquired by a collocated Omni-directional antenna. In the project, the P220 UWB radar was worked in the center frequency of 4.3 GHz. The echo signals were collected at two statuses: no person behind Brick wall and still human being standing behind Brick wall which the person was at a distance of 6.5 ft from the radar on other side of the wall.

For verify the feasibility of the proposed algorithm, each 30 sets of echo signals at status of without human being and with human being were acquired. The signals were decomposed by 8-lyaer wavelet packet with db10'wavelet. And the first 20 nodes signals were used to construct the criterion ADC. The length of subgroup is $q = 5$. The upper confidence level is $1 - \alpha = 0.95$. The random Gaussian measurement matrix was chose for anomaly detection in compression domain based on compressive sensing. The experimental results of through wall human detection for original data and compressed data were shown in Fig. 1, Fig. 2 and Table 1.

According to the proposed anomaly detection procedure , from the experimental results , it can be seen that the identification method could effectively detect the existence of human being in original data and compressed data with high probability 95 %. Meanwhile, the results showed that the difference of average criterion of a subgroup between without human being and with human being became more obvious in pace with increasing compressive ratio. It is mainly because more features of original signal has eliminated with the increased compressive ratio and affected the reference baseline of node signal energy $\overline{\Delta E_j^i}$.

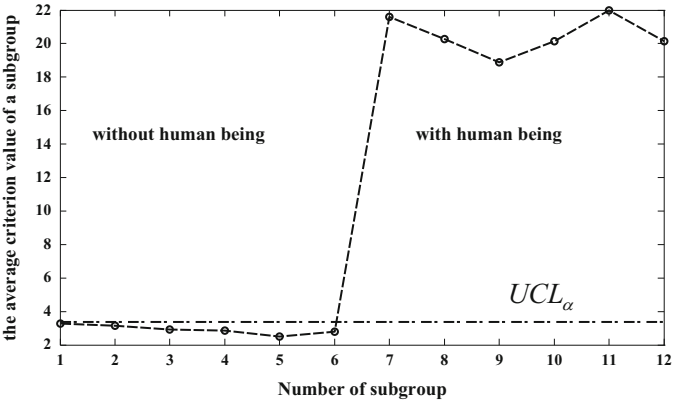

Fig. 1 Through wall human detection with original data

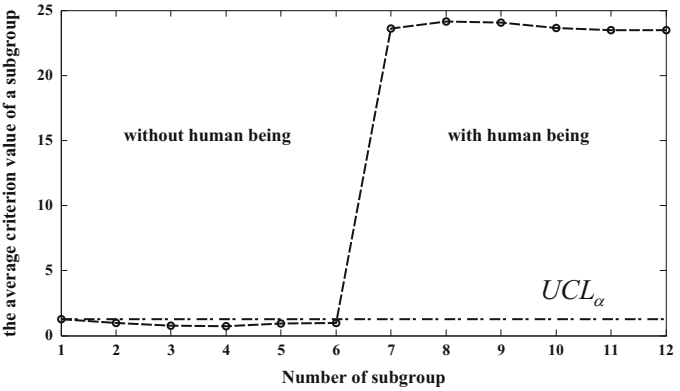

Fig. 2 Through wall human detection with compressed data at compressive ratio 1/3

Table 1 Through wall human detection with compressed data at compressive ratio 1/5 and $UCL_\alpha = 0.973$

Average criterion value of a subgroup	without human being					
	0.9231	0.7760	0.6595	0.6153	0.5798	0.6996
	with human being					
	128.205	128.433	133.584	134.44	133.735	131.339

4 Conclusions

According to the principle that the frequency components would vary because of the existence of anomaly, the paper proposed an anomaly detection algorithm based on wavelet packet transform and statistic process control theory. Due to the sampling and storage burden of anomaly detection in big data, compressive sensing

theory was used in the proposed anomaly detection method. The experiments for through wall human detection were tested. The results demonstrated that the algorithm could effectively reflect the presence of anomaly in compressed data.

Acknowledge The authors would love to thank Professor Qilian Liang in University of Texas at Arlington for providing the UWB radar data. This research was supported by the Tianjin Younger Natural Science Foundation (12JCQNJC00400) and National Natural Science Foundation of China (61271411).

References

1. Chandola V, Banerjee A, Kumar V (2009) Anomaly detection: a survey. ACM Comput Surv 41(3):1–72
2. Chun Tung Chou, Rajib Rana, Wen Hu (2009) Energy efficient information collection in wireless sensor networks using adaptive compressive sensing. 2009 I.E. 34th conference on local computer networks, vol 10, Zurich, Switzerland, p 443–450
3. Jin Wang, Shaojie Tang, Baocai Yin, et.al. (2012) Data gathering in wireless sensor networks through intelligent compressive sensing. 2012 Proceedings IEEE INFOCOM, p 603–611
4. Donoho DL (2006) Compressed sensing. IEEE Trans Inf Theory 52(4):1289–1306
5. Candès E (2006) Compressive sampling. In: Proceedings of international congress of mathematicians. European Mathematical Society Publishing House, Madrid, Spain, p 1433–1452
6. Sun Z, Chang CC (2004) Statistical wavelet-based method for structural health monitoring. J Struct Eng 130(7):1055–1062
7. Candès E, Wakin M (Mar. 2008) An introduction to compressive sampling. IEEE Signal Process Mag 25:21–30
8. Lei Xu, Qilian Liang, Xiuzhen Cheng, Dechang Chen (2013) Compressive sensing in distributed radar sensor networks using pulse compression waveforms. EURASIP J Wirel Commun and Netw. doi:10.1186/1687-1499-2013-36
9. Lei X, Liang Q (2012) Zero correlation zone sequence pair sets for MIMO radar. IEEE Trans Aerosp Electron Syst 48(3):2100–2113
10. Lei Xu, Qilian Liang (2010) Orthogonal pulse compression codes for mimo radar system. IEEE Globecom, Miami, FL
11. Lei Xu, Qilian Liang (2010) Waveform design and optimization in radar sensor network. IEEE Globecom, Miami, FL
12. Liang Q, Mendel JM (2000) Design interval type-2 fuzzy logic systems using SVD-QR method: rule reduction¿. Int J Intel Syst 15(10):939–957

Part IX
Biological Signal Processing

Using Canonical Correlation Method to Extract SSVEP at One Channel

Zhenghua Wu

Abstract Many methods have been proposed aiming at improving the transfer rate of Steady-State Visually Evoked Potential (SSVEP) based Brain–Computer Interface (BCI). In this work, we propose a method in which a filter technique is combined with the canonical correlation method, and this method called as filter and canonical correlation (FACC) is insensitive to the initial phase of SSVEP and the background noise, and only one signal channel is needed. The FACC method and the Power Spectrum (PS) method are used to extract the SSVEP within 1s length EEG segments, and the results are compared to each other. The comparison shows that FACC method is more valid than PS method when extracting SSVEP within a short span.

Keywords Steady-state visually evoked potential (SSVEP) • Brain–computer interface (BCI) • Power spectrum (PS) method • Filter and canonical correlation (FACC) method

Z. Wu (✉)
School of Computer Science and Engineering, University of Electronic Science and Technology of China, ChengDu 610054, China

Key Laboratory for NeuroInformation of Ministry of Education, School of Life Science and Technology, University of Electronic Science and Technology of China, ChengDu 610054, China

Department of Biomedical Engineering, University of Florida, Gainesville, FL 32611, USA
e-mail: wzhzxwz@sina.com

B. Zhang et al. (eds.), *The Proceedings of the Second International Conference on Communications, Signal Processing, and Systems*, Lecture Notes in Electrical Engineering 246, DOI 10.1007/978-3-319-00536-2_123,

1 Introduction

In recent years, an outstanding number of experiments have been executed by various researchers to build a SSVEP-based BCI [4–7]. In order to obtain a high transfer rate in BCI, a variety of methods of extracting SSVEP have been proposed [1–4, 9], among which a very widely used one is the PS method [1, 5–7].

The Canonical Correlation (CC) method was proposed to detect SSVEP in 2007 [2]. In this approach, a few sine signals with same frequencies as the harmonics of SSVEP are produced, and the correlation coefficient between these signals and the original EEG signals at a few channels are calculated to detect SSVEP, respectively. However, if applying this method on the signal at only one electrode, because it is very sensitive to the initial phase of SSVEP, there can not come out a good result.

In the work presented in this article, a new approach is proposed to overcome the drawback of the CC method. In this method, there is only one electrode used as the signal electrode, instead of computing the correlation coefficient between the developed sine signals with original EEG, the correlation coefficient between the original signal within a frequency band and its remained part filtered out the target frequency is computed. This new method is called as the filter and canonical coefficient (FACC) method. FACC method and PS method are used to detect SSVEP within 1s length segment, respectively. The results show the FACC method has a higher detection accuracy than the PS method for the short EEG segment.

2 Methods

2.1 Data Acquirement

Eleven healthy adults with normal or corrected normal vision served as the volunteer subjects upon giving informed consent. While seated in a comfortable chair in a shielded recording chamber, the subjects looked at the LED 60 cm in front of them. Six different stimulating frequencies, i.e. 33.33, 25, 16.67, 12.5, 8.33, and 6.25 Hz were used. Before the beginning of the repetitive stimulus, 40s spontaneous EEG signal was recorded, then 40s SSVEP under each frequency was recorded. The recording was made by using EGI system with a 129 channel electrode cap, referenced at electrode Cz. Electrode No.76 (Oz) in the occipital area was selected as the signal electrode for all the subjects under all stimulating frequencies according to the suggestion in BCI studies [8].

2.2 Methodology

First of all, the signal to noise ratio (SNR) of SSVEP under each frequency at electrode Oz is computed like this: for a certain frequency SSVEP, the original EEG signal with a length of 40s are processed by Fast-Fourier Transform (FFT) directly, and the power of SSVEP is divided by the average power of the band ± 1 Hz around stimulating frequency.

The spontaneous EEG and SSVEP are divided into segments of 1s length, and then is processed by FFT to get a spectrum. In this spectrum, the power of the frequencies lower than 5 Hz are set to zero to cancel the strong background noise, and the power from 9 to 11 Hz are set to zero to avoid the strong α signal. This new power spectrum P1 is processed by Inverse Fast-Fourier Transform (IFFT) to get a new signal S1. Then the first and/or second harmonics of a certain frequency in P1 are set to zero to get a power spectrum P2. This P2 is processed by IFFT again to get a new signal S2. After that, the correlation coefficient between S1 and S2 is calculated. The above introduced technique is called the filter and canonical correlation (FACC) method.

FACC and PS method are applied on each segment to detect SSVEP. Two types of detection accuracy are defined. The first type is that the SSVEP of a certain frequency is explicitly detected in the segment surely containing this frequency SSVEP. The second type is that the SSVEPs of other frequencies are not detected in the same segment. The two types of accuracy under different methods are evaluated by using one-way analysis of variance (ANOVA). The results by ANOVA can stand by the significance of difference between the two methods, and the significance level is set to 0.05.

3 Result

3.1 Relation Between the SNR and Detection Accuracy

In this test sample, the biggest SNR is 42 for subject S1 at stimulus 33.33 Hz and the smallest SNR is 3.7 for subject S8 at stimulus 16.67 Hz, with an average SNR of 14.9 in this sample. Some subjects have a high SNR for every stimulus, some subjects has a high SNR for some stimuli while a low SNR for other stimuli, and some subjects has a low SNR for every stimulus. Figure 1 shows the average SNR of every subject. Subject S1 has the highest average SNR of 24, while subject S11 has the lowest average SNR of 7.2. The SNR has a high positive correlation for the first-type accuracy, and the correlation coefficient is 0.9 for PS method and 0.94 for FACC method. While a low correlation coefficient 0.3 for PS and 0.7 for FACC are observed for the second-type accuracy.

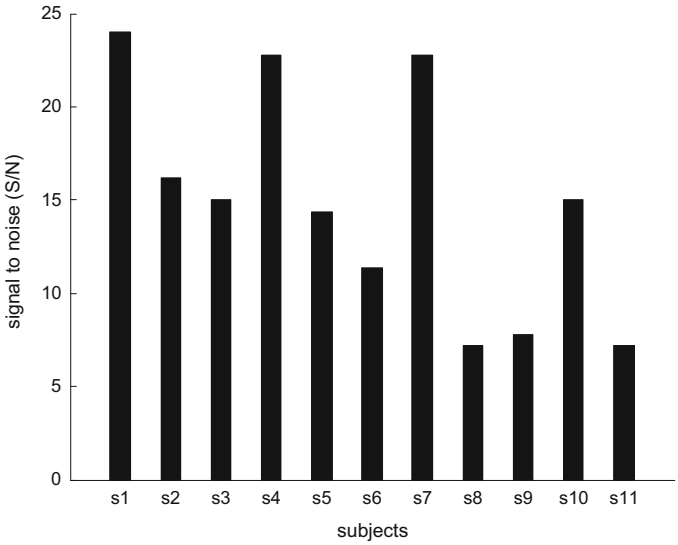

Fig. 1 The average SNR of six stimulus frequencies at electrode Oz for every subject

3.2 Comparing First-Type Accuracy

Experiment shows quite different results of SSVEP amplitude across various subjects. For some subjects, all SSVEPs under every stimulus are strong, and then can be easily extracted with a high accuracy by using both the FACC and PS methods. While for some other people, SSVEPs are strong for certain stimuli, while weak for some other stimuli. This leads to differentiated accuracy in detecting SSVEP. The overall average of first-type accuracy for PS and FACC are 60 and 68 %, respectively, and the ANOVA result is ($F(1,20) = 0.95$, $p = 0.34$). Figure 2 shows the average first-type accuracy of PS and FACC methods for every subject.

3.3 Comparing Second-Type Accuracy

Both of the second-type accuracy of PS and FACC are high for every subject under any stimulus. The average second-type accuracy for PS and FACC is 87 and 92 %, respectively. A significant difference of the average second-type accuracies between the two methods ($F(1,20) = 8.3$, $p = 0.009$) has been observed. Figure 3 illustrates the average second-type accuracy of the two methods for every subject.

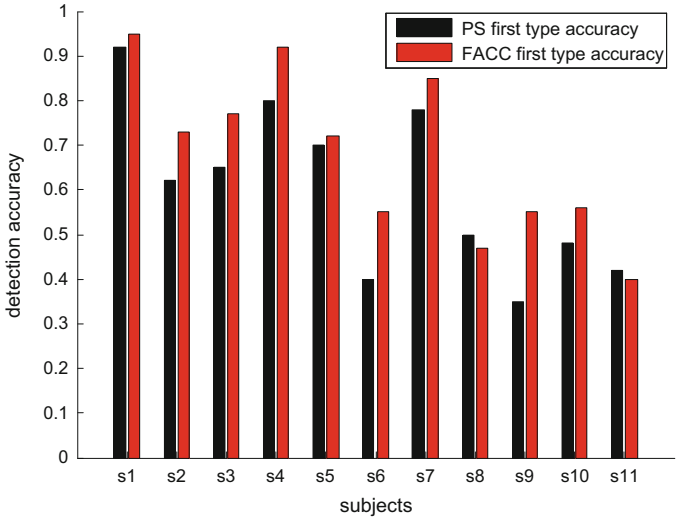

Fig. 2 The average first-type accuracy of PS and FACC method for every subject

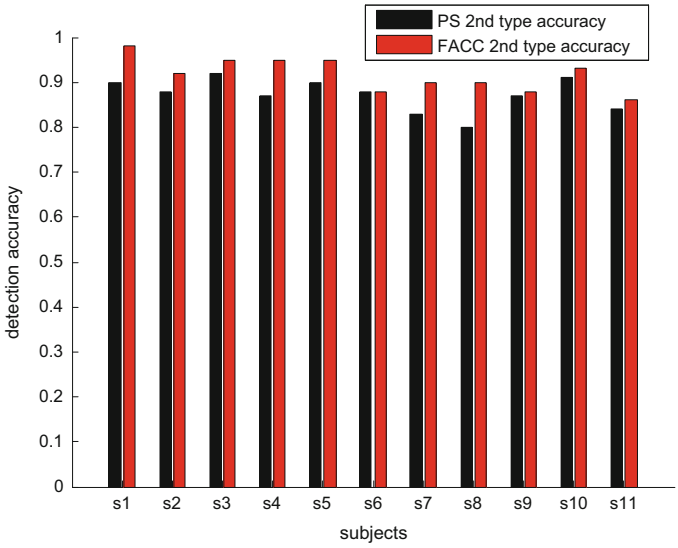

Fig. 3 The average second-type accuracy resulted by FACC and PS for every subject

4 Discussion

The detection accuracy of SSVEP can be influenced by three factors for a fixed length EEG segment: the initial phase of SSVEP, the background noise in EEG, and the power of SSVEP. The correlation coefficient between a constructed sine signal

and EEG is very sensitive to the initial phase of the sine signal. The FACC approach has overcome the drawback of the phase sensitivity of the normal CC method. Although only one signal electrode is used in this method, a high detection accuracy can be gotten.

PS method is sensitive to the background noise to some extent. While in the FACC method, the correlation coefficient is computed between the background noise and the rest part filtered out the SSVEP frequency, and this coefficient is only related to the SSVEP power. So, when applying FACC method to the SSVEP segment to detect other frequencies, the correlation coefficient holds unvaried compared to their threshold for the power of those frequencies are almost at the same level as that in spontaneous EEG, which means there are no SSVEP of these frequencies in the segment, then a high second-type accuracy is obtained. So, although the second-type accuracies of both methods are high, there is still a significant difference between them.

Of course, any method would be sensitive to the power of SSVEP itself, so it is for the PS method and FACC method. That is why a positive correlation between the SNR and the first-accuracy has been observed. In a real BCI system, there are many flickers used. When processing the EEG data, normally all the frequencies used in the system should be tested. If the second-type accuracy is low, the accuracy of the system is demonstrated low, too. So it is the same importance of the first-type and second-type accuracy.

5 Conclusion

For the insensitivity to the initial phase and the immunity of to background noise, FACC method can improve the first-type and second type accuracy in detecting SSVEP compared with the PS method, and this suggests that it can be used in a real time BCI system.

Acknowledgements The work was supported by Science and Technology Bureau of Sichuan Province (#2013GZ0017).

References

1. Friman O, Volosyak I, Graser A (2007) Multiple channel detection of steady-state visual evoked potentials for brain–computer interfaces. IEEE Trans Biomed Eng 54(4):742–750
2. Lin ZL, Zhang CS, Wu W et al (2007) Frequency recognition based on canonical correlation analysis for SSVEP-based BCIs. IEEE Trans Biomed Eng 54(6):1172–1176
3. Lopez MA, Praetor A, Playa F (2010) Use of phase in brain–computer interfaces based on steady-state visual evoked potentials. Morillas Neural Process Lett 32:1–9
4. Luo A, Sullivan TJ (2010) A user-friendly SSVEP-based brain–computer interface using a time-domain classifier. J Neural Eng 7:1–10

5. Ortner R, Allison BZ, Korisek G et al (2011) An SSVEP BCI to control a hand orthosis for persons with tetraplegia. IEEE Trans Neural Syst Rehabil Eng 19(1):1–5
6. Volosyak I (2011) BCI demographics II: how many (and what kinds of) people can use a high-frequency SSVEP BCI? IEEE Trans Neural Syst Rehabil Eng 19(3):232–239
7. Wolpaw JR, Birbaumer N, McFarland DJ et al (2002) Brain–computer interfaces for communication and control. Clin Neurophysiol 113:767–791
8. Wang YJ, Zhang ZG, Gao XR et al. (2004) Lead selection for SSVEP-based brain-computer interface. Proceeding of the 26th annual international conference of the IEEE EMBS, San Francisco, CA, USA, 1–5 Sept 2004, pp 4507–4510
9. Wu ZH, Yao DZ (2008) Frequency detection with stability coefficient for SSVEP based BCIs. J Neural Eng 5:36–43

Research on Target Identification Algorithm in Micromanipulation

Xin Yin, Cuiping Zhang, Shidong Song, Ningning Ma, and Xueyan Ma

Abstract Target identification is one of difficult problems in micromanipulation, according to this problem, this paper studies on three kinds of commonly used target identification algorithms based on the characteristics of target identification algorithm, based on the training target identification algorithm, based on the Template target identification algorithm. And the three kinds of algorithm in microscopic field were experimentally simulation comparison from the experimental results. In the end, it analyzes merit and demerit of every target identification methods and the development foreground of the identification are analyzed.

1 Introduction

One of the key issues of a micro-manipulation robot system operated in the wide scope and half structured environment is the target identification. Target identification plays an important role in economics, military affairs and science technology fields. In target identification, algorithms can be broadly divided into three categories: (a) the target identification algorithm based on the characteristics; (b) the target identification algorithm based on Neural Networks; (c) the target identification algorithm based on template [1]. Among them, the Scale-invariant feature transform (SIFT) algorithm based on feature is proposed in recent years and achieved good results in the field of target identification of an algorithm. The SIFT feature vector has a strong robustness. It is a kind of partial feature extraction algorithm; Image data has local scale-invariant features. The scaling, rotation, scale brightness

X. Yin (✉) • C. Zhang • N. Ma • X. Ma
College of Physics and Electronic Information, Tianjin Normal University, Tianjin 300387, P. R. China
e-mail: yinxin1025@126.com

S. Song
School of Chemical and Environment Engineering, China University of Mining and Technology, Beijing 100083, P. R. China

B. Zhang et al. (eds.), *The Proceedings of the Second International Conference on Communications, Signal Processing, and Systems*, Lecture Notes in Electrical Engineering 246, DOI 10.1007/978-3-319-00536-2_124,

change keeps invariance, the perspective changes, affine transform, noise also maintain stability. Target identification algorithm based on the training of BP network is the most used a form of neural network. In neural network information processing, past and present data is treated as learning sample set. By some nonlinear processing to establish model, the behavior of the system variables is got as a scientific and quantitative judgment. Target identification algorithm based on template algorithm is the most typical in template matching algorithm; Template matching is to search for target in one of the big picture. Target and template have the same size, direction and image, through a certain algorithm can find the target and determine its coordinates. The above three kinds of algorithms has made very good result in the field of target identification. With modern science and technology rapid development into tiny, ultra-precision field, people give more and more attention to micro operating system application in the biomedical field [2], cloning [3], transgenic experiment [4], etc., In micro operating system engineering, target identification under the microscopic vision become a research hotspot of machine vision. In this paper, the target identification algorithm under microscopic view is comparative analysis. This paper is divided into four parts. In Sect. 2, the typical target identification algorithm is introduced respectively; Sect. 3 is the simulation experimental study. Section 4 is the conclusion.

2 The Typical Target Identification Algorithm

In target identification, algorithms can be broadly divided into three categories.

2.1 The Target Identification Algorithm Based on Sift

SIFT is put forward by David Lowe in 1999. The algorithm is divided into five steps.

2.1.1 Generate Scale Space and Extreme Value Point

Gaussian convolution kernel is the only linear nuclear scale conversion. Gaussian scale space is defined as:

$$L(x, y, \sigma) = G(x, y, \sigma) * I(x, y) \tag{1}$$

$G(x,y,\sigma)$ is the scale variable Gaussian function.

$$G(x, y, \sigma) = \frac{1}{2\pi\sigma^2} e^{-\left(x^2+y^2\right)}/2\sigma^2 \tag{2}$$

In (2), (x, y) is the spatial coordinates, σ is a scale coordinates.

In order to effectively detect stable point in scale space, the differential Gaussian scale space is put forward.

$$D(x, y, \sigma) = (G(x, y, k\sigma) - G(x, y, \sigma)) * I(x, y) = L(x, y, k\sigma) - L(x, y, \sigma) \tag{3}$$

In search of the scale space of extreme value point, each sample point is compared to all of its adjacent points, the sample point and eight adjacent points, as well as the corresponding 18 points in the upper and lower adjacent scales were compared, in order to ensure that the extreme value point can be detected in the scale space and the two dimension image space.

2.1.2 Position the Extreme Value Point

By fitting three-dimensional quadratic function, the position and scale of the key points are accurately obtained, at the same time, the edges of the key points and unstable response of the low contrast points are removed.

2.1.3 Key Point Direction Distribution

Each key point's specified direction parameters is got using gradient direction distribution characteristics of neighborhood pixels of key points, which makes the operator possess rotation invariance.

$$m = \sqrt{\left(OL_{x+1,y} - OL_{x-1,y}\right)^2 + \left(OL_{x,y+1} - OL_{x,y-1}\right)^2} \tag{4}$$

$$\theta = \arctan x\left(\left(OL_{x,y+1} - OL_{x,y-1}\right)/\left(OL_{x+1,y} - OL_{x-1,y}\right)\right) \tag{5}$$

Formula (4) and (5) is the gradient value and direction formula of the (x, y) point.

2.1.4 Feature Point Descriptor

To enhance the robustness of matching, each key point is described using the 4 × 4, a total of 16 seeds, which eventually a key point produce a 128 dimension SIFT feature vector.

2.1.5 Key Point Feature Matching

The feature of key points is matched using Euclidean distance as similarity measure [5, 6].

2.2 *Target Identification Algorithm Based on BP Neural Network*

The BP neural network is a kind of typical forward multi-layer neural network. Three layer BP network can approximate any nonlinear function [7–9]. For example: the transfer function of network unit is Sinmoid function, which assume it includes n input layer neurons, and c hidden layer neurons and m output layer neurons. Input layer neuron is X. Neurons in hidden layer is O and output layer neurons are Y.

$$O_j = f\left(\sum_{j=1}^{n} a_{ij}x_j + \theta_i\right) \quad i = 1, 2, \ldots, c \tag{6}$$

$$y_i = {}^{i}f\left(\sum_{j=1}^{c} b_{ij}o_j + \theta_j\right) \quad i = 1, 2, \cdots m \tag{7}$$

According to the error back propagation algorithm and the theory of minimum mean square error, can adjust the formula for get connection weights.

$$b_{ij}(t+1) = b_{ij}(t) + \eta o_i(1 - o_i)(d_i - O_i)y_j \tag{8}$$

$$a_{ij}(t+1) = a_{ij}(t) + \eta y_i(1 - y_i)(d_i - o_i)x_j \sum_{k=1}^{m} o_i(1 - o_i)(d_i - o_i)b_{kj} \tag{9}$$

In (9), parameter t is learn-times. BP algorithm's specific training steps as follows [8–10]:

Firstly, neural network initialization, randomly allocate some smaller threshold values initial amount.

Secondly, the forward calculation is done to each input sample data according to formula (6) and (7). Then, the ownership value and threshold value are modified according to the formula (8) and (9).

Finally, loop iteration until network error meets the requirements or the maximum training number is reached.

Fig. 1 The original image in the macro visual field

2.3 Template Matching Algorithm [10, 11]

The similarity between the template T (m, n) and the sub graph S^{ij} is described in (10) [12–15].

$$D(i,j) = \sum_{m=1}^{M}\sum_{n=1}^{N}\left[s^{ij}(m,n) - T(m,n)\right]^2 = \sum_{m=1}^{M}\sum_{n=1}^{N}\left[S^{ij}(m,n)\right]^2 - 2\sum_{m=1}^{M}\sum_{n=1}^{N} s^{ij}(m,n) \times T(m,n) + \sum_{m=1}^{M}\sum_{n=1}^{N}\left[T(m,n)\right]^2 \tag{10}$$

$$E(i,j) = \sum_{m=1}^{M}\sum_{n=1}^{N}\left[s^{ij}(m,n) - T(m,n)\right] \tag{11}$$

In (11), the vector error is calculated.

3 Experiment Research

In Windows XP, CPU 2.93 GHz, NKTYMR601 micro-operation robot system is used in experiment [16, 17].

The system has a movement range, which is 5 cm × 5 cm and has a movement error within 5 μm.

At first, stitch microscopic images in the 4× objective microscope, Fig. 1 is the original image. Fig. 2 is stitched image. Targets are identified using the Sift in Fig. 3 and using Template matching algorithm in Fig. 4. In Fig. 5, the targets are identified using BP Neural Networks. Table 1 give the consuming time in the different algorithm, which 26 English letters is used as the training sample in the BP Neural network algorithm.

Fig. 2 Stitched microscopic images in the 4× objective microscope

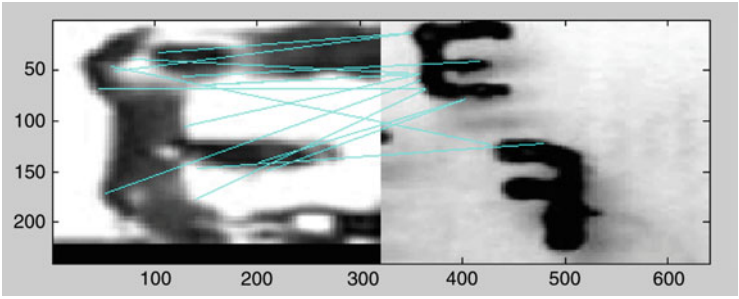

Fig. 3 Targets is identified using the sift algorithm

Fig. 4 Targets is identified using template matching algorithm

By comparing the effect of target identification and time efficiency, Sift algorithm has the highest accuracy. Template matching algorithm can accurately identify, the objects only under the condition which the object is the same as the template. When object's scale change in micro visual field, the object can not be identified. The BP neural network algorithm can accurately identify the object at the expense of the elapsed time. Therefore, the Sift algorithm if fit for the object identify in the micromanipulation.

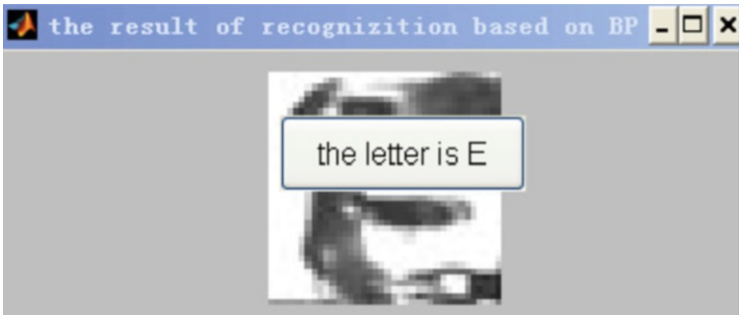

Fig. 5 The targets is identified using BP neural networks

Table 1 Comparison of the matching time in three kinds of target identify algorithm

	Sift	Template matching algorithm	Target identification algorithm based on BP neural network
Training time (S)	–	–	35.844
Preprocessing time (S)	9.771	0.265	0.094
Matching time (S)	0.140	0.219	0.015
Total time (S)	9.911	0.484	35.953

4 Conclusions

Target identification is a hot and difficulty spot in the research of machine vision field. Because the microscopic image has scale variation, much noise characteristics, the target tracking algorithm in the macro field is not entirely suitable for the object identification in the micro field. By analyzing the experimental result, the sift algorithm can meet the demand of target identification in the micro field.

Acknowledgments This work was sponsored by Program for New Century for New Century Excellent Talents in University (No. 80051803), Scientific Research Foundation for the Returned Overseas Chinese Scholars (No. L02003), the Doctor Scientific Research Foundation of the Tianjin Normal University (52LX14, 52X09008)

References

1. Lowe DG (1999) Object recognition from local scale-invariant features. IEEE Proceedings of the 7th International Conference on computer vision, Kerkyra, 1999, pp 1150–1157
2. Zhang F, Huang XF, Fang W et al (2011) Non-rigid registration of mural images and laser scanning data based on the optimization of the edges of interest. Sci Chin Inform Sci 56:1–10
3. Garcés-Chávez V, McGloin D, Melville H et al (2002) Simultaneous micromanipulation in multiple planes using a self-reconstructing light beam. Nature 419(6903):145–147

4. Arlt J, Garces-Chavez V, Sibbett W et al (2001) Optical micromanipulation using a Bessel light beam. Opt Commun 197(4):239–245
5. Cheung W, Hamarneh G (2009) n-SIFT: n-dimensional scale invariant feature transform. IEEE Trans Imag Process 18(9):2012–2021
6. Lowe DG (2004) Distinctive image features scale invariant key point. Int J Comput Vis 60 (2):91–110
7. Sadeghi BHM (2000) A BP-neural network predictor model for plastic injection molding process. J Mater Process Tech 103(3):411–416
8. Jin W, Li ZJ, Wei LS et al (2000) The improvements of BP neural network learning algorithm. Signal Processing Proceedings, WCCC-ICSP 2000. 5th International Conference on IEEE, Beijing, 2000, Vol. 3, pp 1647–1649
9. Yi J, Wang Q, Zhao D et al (2007) BP neural network prediction-based variable-period sampling approach for networked control systems. Appl Math Comput 185(2):976–988
10. Xiao Z, Ye SJ, Zhong B et al (2009) BP neural network with rough set for short term load forecasting. Expert Syst Appl 36(1):273–279
11. Lu W, Lu H, Chung FL (2006) Feature based watermarking using watermark template match. Appl Math Comput 177(1):377–386
12. Olson CF (2000) Maximum-likelihood template matching. Computer Vision and Pattern Recognition, Proceedings, IEEE Conference on IEEE, Hilton Head Island, SC, 2000, Vol. 2, pp 52–57
13. Müller C, Strube M (2006) Multi-level annotation of linguistic data with MMAX2. Corpus technology and language pedagogy: new resources, new tools, new methods. Peter Lang, Frankfurt am Main, pp 197–214
14. Sussman MS, Wright GA (2003) Factors affecting the correlation coefficient template matching algorithm with application to real-time 2-D coronary artery MR imaging. IEEE Trans Med Imag 22(2):206–216
15. Xingling W (2006) Template match algorithm of maximum variance between clusters and license plate characters' segmentation. Comput Eng 32:193–195
16. Huang HB, Sun D, Mills JK et al (2009) Robotic cell injection system with position and force control: toward automatic batch biomanipulation. IEEE Trans Robot 25(3):727–737
17. Lu Z, Chen PCY, Nam JH et al (2007) A micromanipulation system for automatic batch micro injection. Robotics and automation, IEEE International Conference on IEEE, Roma, 10–14 April, 2007, pp 3134–3135

An Information Integration Approach for Classifying Coding and Non-Coding Genomic Data

Ashis Kumer Biswas, Baoju Zhang, Xiaoyong Wu, and Jean X. Gao

Abstract Reliable methods to classify coding and non-coding transcripts from large scale genomic data will help researchers annotate novel RNA transcripts. In this manuscript we explored some of the distinguishing properties of these two classes of transcripts, such as the features of their secondary structures, differential expression scores obtained from typical RNA-seq experiments, and G+C content scores. We trained two classification methods—Conditional Random Forest (CRF) and the Support Vector Machines (SVMs) with the extracted features from the genomic data and applied the trained model to predict a test set comprised of the two classes of transcripts from three well known annotation sources and found important characteristics of the extracted features regarding the classification problem. A comparative analysis shows that our method outperforms the existing two state-of-the-art methods—the CPC (Coding Potential Calculator) and the PORTRAIT in classifying transcripts from the test dataset.

1 Introduction

The central dogma of molecular Biology was proved incomplete after the discovery of genes that are transcribed into RNAs but surprisingly stay inside the cell without being translated to any proteins. These are the non-coding RNA (ncRNA) transcripts that participate in various cellular activities including gene silencing, replication, gene expression regulation, transcription, chromosome stability, protein stability, translocation, localization and RNA modifications, processing, and their

A.K. Biswas (✉) • J.X. Gao (✉)
Department of Computer Science and Engineering, University of Texas at Arlington, Arlington, Texas 76019, USA
e-mail: ashis.biswas@mavs.uta.edu; gao@uta.edu

B. Zhang • X. Wu
School of Physics and Electronic Information, Tianjin Normal University, Tianjin, 300387, China

B. Zhang et al. (eds.), *The Proceedings of the Second International Conference on Communications, Signal Processing, and Systems*, Lecture Notes in Electrical Engineering 246, DOI 10.1007/978-3-319-00536-2_125,

stability [11]. Classifying the non-coding and coding genes that produce the RNA transcripts will help the researchers exploring the two types of genes separately as well as determining activities in which a group of ncRNAs are involved.

Due to the fact that the most of the ncRNA transcripts are engaged in one or more functions inside the cell and they require a stable structure for their respective functions [16]. Using the structural potential of RNA transcripts, coding and non-coding genes can be distinguished. However, it was later investigated that the secondary structures are not sufficiently different from the predicted stability of a random RNA sequence [14] that makes harder the classification strategies that utilize structural information only. Therefore, researchers focused on multi-domain features to distinguish a non-coding RNA from a protein coding one.

Among the several multi-domain strategies, the CPC [10] approach employed few features of the transcripts pertaining to the Open Reading Frames (ORFs) and the possible proteins for the transcript. However, it is not suitable for the reason that it is prone to be biased for classifying as non-coding those transcripts that do not have good hits on the protein databases. Again, the PORTRAIT [1] uses a software called ANGLE that translates the Expressed Sequence Tags (ESTs) from a given input sequence into possible protein. The SVM induced protein coding and non-coding transcript discriminating models were built by employing some features of these. However, the PORTRAIT classifies only the transcripts which are at least 80 nucleotides long. But there may be cases where it would be required to classify transcripts much shorter than 80 nucleotides.

With the advent of the Next Generation Sequencing platform—RNA-seq [15], transcript expressions can be quantified from the short-reads more effectively and accurately than using microarrays. Such expression scores were never employed as feature to discriminate a non-coding RNA transcript from a coding transcript. In this paper, we presented a methodology to classify the non-coding and coding transcripts from a given list of genomic coordinates by employing the expression scores as well as sequence and structure based features of the transcripts. We built discriminatory models using the Conditional Random Forest (CRF) classifier and the Support Vector Machines (SVMs). We evaluated our system in database specific and database independent manner and it showed no bias towards any specific class. We also performed a comparative analysis of our system with the CPC [10] and PORTRAIT [1] and justified our results.

2 Methods

2.1 Obtaining Dataset

We worked with the RNA-seq experiment data that was generated from the High Throughput Sequencing of RNAs from mouse cortical cultures under three different potassium stimulation conditions, which are—no stimulation condition, stimulating for 1 h and stimulating for 6 h [9]. The dataset from the experiment was

Table 1 Summary of coding and ncRNA transcript annotations used in this study

Data source	No. of coding transcripts	No. of non-coding transcripts
Ensembl [6]	6,000	5,627
RefSeq [13]	1,100	1,064
UCSC [8]	1,565	1,501

collected from NCBIs Gene Expression Omnibus [5] and are accessible through GEO series accession number GSE21161 (http://www.ncbi.nlm.nih.gov/geo/query/acc.cgi?acc=GSE21161).

The coding RNA and the ncRNA annotations of mouse (*Mus musculus* (mm9)) were retrieved from the UCSC Table Browser (knowngene track) [8]. Additionally we included Ensembl NCBIM37.67 ncRNA annotations [6], and RefSeq mRNA annotations [13]. For the three datasets, both coding and non-coding transcripts were chosen which have length less or equal to 1000nt. Table 1 summarizes the number of transcripts of each class from the three datasets.

2.2 *Feature Extraction*

We extracted three categories of features from the transcript information available in the datasets (Table 1), which are—properties of the predicted secondary structures, G+C content scores, and expression scores.

RNA transcripts are single-stranded molecules and can fold to itself by forming base pairings. These pairings often occur between the bases G and C, U and A, and sometimes G and U. The base pairings form the structural components of the RNA transcript. The components are shown in Fig. 1. We applied "RNAfold" [7] to predict the secondary structures of all the transcripts listed in Table 1. The program reported the minimum free energy (MFE) of each of the transcripts and generated a text file containing the predicted secondary structures in bracket notation. Then we extracted the following properties of the predicted structures—(1) number of paired bases, (2) number of hairpin loops of length 1, 2, 3, 4, 5, 6, 7 and greater than 7, (3) number of multi-loops of length 1, 2, 3, 4, 5, 6, 7 and greater than 7, (4) Minimum Free Energy (MFE) of the predicted structure.

The G+C content of the transcripts is the only sequence-based feature considered in our study. It is computed using Eq. (1).

$$\text{G+C Content} = \frac{n(G) + n(C)}{n(A) + n(U) + n(G) + n(C)} \tag{1}$$

Here, the function $n(x)$ is the frequency of occurrence of the base "x" in a transcript under consideration, where $x \in \{\text{A,C,G,U}\}$, the four-base alphabet required to form all RNA transcripts.

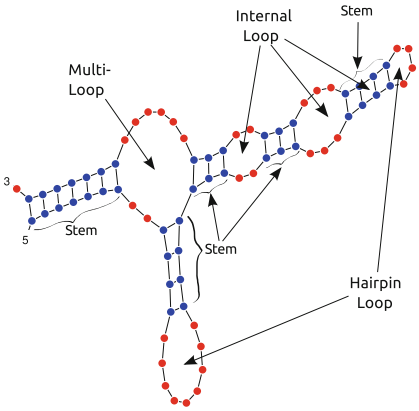

Fig. 1 Components of the secondary structure of the RNA sequence: GCGCCCGUAGCUCAAU UGGAUAGAGCGUUUGACUACGGAU CAAAAGGUUAGGGGU UCGACUCCUCUCGGGCGCG

Finally, from the RNA-seq experiment data, we analyzed the binary indexed-BigWig files for the three different conditions. Each one of the BigWig file contains coverage scores for RNA transcripts with one nucleotide span under specific condition which were used to measure expression of transcripts in the annotation sources. Expressions of RNA transcripts from an RNA-seq experiment is quantified by the "RPKM" (Reads Per Kilobase exon model per Million mapped reads) measure [12] (Eq. (2)).

$$\text{RPKM} = \frac{\text{exonReads}}{\text{totalReads(millions)} \times \text{exonLength(kB)}} \tag{2}$$

In Eq. (2), "exonReads" is the total number of short-reads mapped to a specific exon or transcript under consideration, "totalReads" is the total number of short-reads mapped in the experiment (in Million unit), and "exonLength" is the length of the exon or transcript under consideration (in kilo base unit). In order to compute RPKM score of a transcript, we added all the one-nucleotide span scores of all the coordinates that map within the start and the end coordinates of the transcript. The summation is the "exonReads" for Eq. (2). The RNA-seq experiment [9] mapped a total of 50 million short-reads, so the "totalReads" here will be 50. Finally, the absolute difference between the start and end coordinates of the transcript is the length of the transcript ("exonLength"). By plugging in the three values into the Eq. (2) we can compute RPKM expression scores of all the transcripts from the dataset (Table 1).

2.3 Measuring Influences of the Feature Combinations

In this step we tried to measure the relative importance of each of the feature combinations on the overall classification task. We extracted three types of features from the transcripts—sequence (S), secondary structure (T) and differential expression (E). Here, we built the classification models by applying all the possible combinations of the available features, which are—(1) sequence only {S}, (2) secondary structure only {T}, (3) expression only {E}, (4) sequence and structure {S,T}, (5) structure and expression {T,E}, (6) sequence and expression {S,E} and (7) all the three features {S,T,E}. Thus, to measure the influences of the features on the classification task, we split the three datasets—UCSC, RefSeq and Ensembl along with the Combined dataset (i.e., the set of all the three datasets) into training and test sets and employed the combinations of features in classifying the test sets.

2.4 Classifier Selection

We experimented with two classification algorithms—Conditional Random Forest (CRF) [2] and the Support Vector Machines (SVMs) [3]. The random forest is an ensemble classifier that consists of many decision trees and it outputs the class that is the mode of the class outputs by all the individual trees. Each tree is constructed using the following algorithm: (1) if the number of training examples is N, and the number of features of each example is M, a revised training set is prepared using any n of the N available training examples (here, $n < N$). The rest of the training examples are used to estimate the errors of the tree, (2) For each node of the tree, m out of M features are randomly chosen on which to make the decision at that node, where, $m < M$. The best split with the m features are determined by the revised training set. For prediction a new sample is pushed down the tree. It is assigned the label of the training sample in the terminal node it ends up in. This procedure is iterated over all trees in the ensemble, and the mode vote of all trees is reported as random forest prediction.

However, the Support Vector Machines [4] classifier is the most widely used supervised learning algorithm for two-class classifications. The SVMs map the feature vector into a high dimensional feature space and classify the samples by separating the hyperplane in the space. In the training phase, the SVMs perform a search for an optimal hyperplane by solving a quadratic optimization problem. This hyperplane, determined by the criterion that maximizes the distance of the nearest feature vector, has good generalization performance. We used the Radial Basis Function as the kernel of the classifier. In the training step, the *cost* and *gamma* parameters were tuned by a grid search approach in the range, $cost \in [1, 2^4]$ and $gamma \in [2^{-8}, 2]$.

2.5 Training, Testing and Evaluation

The sequence, structural and expression features were extracted in the same way for both the training and test datasets. All data values for each of the feature were normalized by standardization (i.e., $\frac{x-\mu}{\sigma}$, where x is a data value, μ is the arithmetic mean of all the data values of a certain feature, and σ is the standard deviation of all the data values of that feature). Then the two classification models were built by training the classifiers—(1) on the UCSC dataset, (2) on the RefSeq dataset, (3) on the Ensembl dataset, and (4) on the combined dataset (i.e., total set of UCSC, RefSeq and Ensembl sets). For each run, the datasets were randomly split into two partitions— 80 % were kept for training and 20 % for testing. These fractions were randomly selected during the experiments.

Based on the true class labels and the predicted class labels the confusion matrices for the classification experiments were prepared for both the classifiers. Since we built binary classifiers, non-coding RNA was treated as "positive" class and coding RNA was treated as "negative" class. Finally for all the classification runs, we computed "precision", "recall", "accuracy" and "F1-measure".

3 Results and Discussion

After testing with all the possible combinations of the classifiers trained with the three categories of features, we obtained eight bar plots as shown in Fig. 2. In the figure, the top four plots are the results of classification by the Conditional Random Forest (CRF) classifier, and the bottom four plots denote the performance of the Support Vector Machines (SVMs) classifier trained with the seven possible combinations of the three feature categories. For each of the classifier, the performance on the four test datasets (UCSC, RefSeq, Ensembl and the combined dataset) were reported separately, while in each of the plot four adjacent bars in four different grayscale shades (darkest to lightest) were drawn which represent the four performance metrices—accuracy, precision, recall and F1 measure for a classifier trained with a particular combination of features. From the figure it can be easily realized that the secondary structure properties as a feature is more influential than the other two, which can be seen by the sharp peaks at the points T, ST, TE and STE on the X-axis representing the application of secondary structure alone, sequence and structure, structure and expression and all together respectively. From the plots, it is evident that both the Conditional Random Forest (CRF) classifier and the Support Vector Machines (SVMs) are similar in terms of classification performance. But in terms of CPU time for training and prediction, the SVMs based classifier is faster than the Conditional Random Forest classifier.

Next, we compared our system (based on the application of the three features all together, {S,T,E}) with the two existing systems—CPC (Coding Potential Calculator) [10] and the PORTRAIT [1]. Both of these two systems used the SVMs in

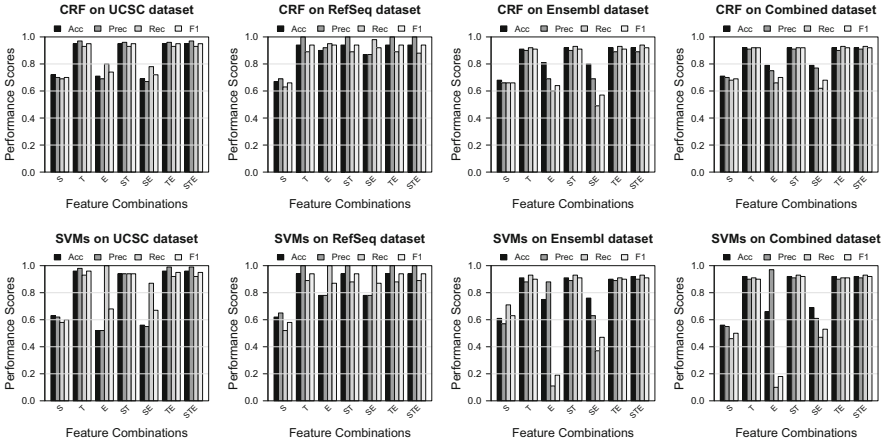

Fig. 2 Evaluating the classification performance by employing all the seven possible combinations of the three features—(i) Sequence, (ii) Secondary Structure and (iii) Differential expressions on the four datasets. The combinations are listed in X-axis as the combinations of these three letters—*S*, *T* and *E*, for the sequence, secondary structure and differential expressions respectively. Here *CRF* means our method based on the Conditional Random Forest Classifier and *SVMs* is based on the Support Vector Machines

classification and provided publicly accessible web services to perform the predictions based on the user inputs. We evaluated our system and the existing two with the same test datasets obtained from each of the three data sources and a combined dataset. However, the PORTRAIT prediction system did not report some input RNA transcripts that were less than 80 nucleotides long. Thus, in order to obtain a fair comparison we removed those transcripts from the test dataset before evaluating all the systems. Table 2 summarizes the comparison statistics of the two existing systems along with our proposed systems based on both the SVMs and the CRF based classification methods. From the results it can be noticed that the metric "recall" for each of the existing two systems is higher than that of ours. This is because of the fact that the CPC [10] and PORTRAIT [1] systems showed bias towards the prediction of "non-coding" to given transcripts. Other than this metric, our system is better than the two methods in terms of accuracy, precision and F1-measure for all the data sources. The experimental result shows that our system does not have any bias to a certain class. From this experiment, we were also able to show the significant contribution of the features we chose—sequences, structures and expressions in building a reliable non-coding and coding RNA classifier.

Table 2 Comparing classification performance of our proposed system with the CPC [10] and the PORTRAIT [1] systems, on the UCSC, RefSeq, Ensembl and combined datasets. Four performance scores are reported—accuracy (*Acc*), precision (*Prec*), recall (*Rec*) and F1-measure (*F1*)

	UCSC				RefSeq				Ensembl				Combined dataset			
Systems	Acc	Prec	Rec	F1	Acc	Prec	Rec	F1	Acc	Prec	Rec	F1	Acc	Prec	Rec	F1
CPC [10]	0.56	0.27	0.82	0.41	0.65	0.55	0.94	0.69	0.68	0.58	0.99	0.73	0.67	0.55	0.98	0.70
PORTRAIT [1]	0.72	0.39	0.86	0.53	0.80	0.71	0.91	0.80	0.73	0.62	0.98	0.76	0.74	0.61	0.97	0.75
proposed CRF	0.93	0.86	0.74	0.79	0.94	1.00	0.85	0.92	0.92	0.89	0.92	0.91	0.92	0.90	0.90	0.90
proposed SVM	0.93	0.93	0.70	0.80	0.93	1.00	0.84	0.91	0.92	0.89	0.93	0.91	0.92	0.90	0.90	0.90
	$c = 2, \gamma = 0.003906$				$c = 1, \gamma = 0.007812$				$c = 2, \gamma = 1$				$c = 2, \gamma = 0.5$			

In the last row, the c and γ represent the values of the two essential parameters of the SVMs which were obtained at the SVMs parameter tuning step

4 Conclusions

In this paper, we proposed a method to build a classifier to distinguish between a coding and a non-coding RNA transcript using a sequence based property (the G+C content), some structure based properties and three expression scores of RNA transcripts. The method can be further extended to identify random genomic sequences by employing some heuristics that will enable the discovery of novel non-coding RNA transcripts. Compared with the CPC [10] and PORTRAIT [1] methods, the method we introduced operate more accurately and reliably.

References

1. Arrial R, Togawa R, Brigido M (2009) Screening non-coding RNAs in transcriptomes from neglected species using PORTRAIT: case study of the pathogenic fungus Paracoccidioides brasiliensis. BMC Bioinformatics 10(1):239
2. Breiman L (2001) Random forests. Mach Learn 45(1):5–32
3. Chang C, Lin C (2011) LIBSVM: a library for support vector machines. ACM T Intell Syst Technol (TIST) 2(3):27
4. Cortes C, Vapnik V (1995) Support-vector networks. Mach Learn 20(3):273–297
5. Edgar R, Domrachev M, Lash A (2002) Gene expression omnibus: NCBI gene expression and hybridization array data repository. Nucleic Acids Res 30(1):207–210
6. Flicek P, Amode M, Barrell D, Beal K, Brent S, Chen Y, Clapham P, Coates G, Fairley S, Fitzgerald S et al (2011) Ensembl 2011. Nucleic Acids Res 39(suppl 1):D800–D806
7. Hofacker I, Fontana W, Stadler P, Bonhoeffer L, Tacker M, Schuster P (1994) Fast folding and comparison of RNA secondary structures. Monatshefte für Chemie (Chemical Monthly) 125 (2):167–188
8. Karolchik D, Hinrichs A, Furey T, Roskin K, Sugnet C, Haussler D, Kent W (2004) The UCSC table browser data retrieval tool. Nucleic Acids Res 32(suppl 1):D493–D496
9. Kim T, Hemberg M, Gray J, Costa A, Bear D, Wu J, Harmin D, Laptewicz M, Barbara-Haley K, Kuersten S et al (2010) Widespread transcription at neuronal activity-regulated enhancers. Nature 465(7295):182–187
10. Kong L, Zhang Y, Ye Z, Liu X, Zhao S, Wei L, Gao G (2007) CPC: assess the protein-coding potential of transcripts using sequence features and support vector machine. Nucleic Acids Res 35(suppl 2):W345–W349
11. Machado-Lima A, Del Portillo H, Durham A (2008) Computational methods in noncoding RNA research. J Math Biol 56(1):15–49
12. Mortazavi A, Williams B, McCue K, Schaeffer L, Wold B (2008) Mapping and quantifying mammalian transcriptomes by RNA-Seq. Nat Meth 5(7):621–628
13. Pruitt K, Tatusova T, Brown G, Maglott D (2012) NCBI Reference Sequences (RefSeq): current status, new features and genome annotation policy. Nucleic Acids Res 40(D1): D130–D135
14. Rivas E, Eddy S (2000) Secondary structure alone is generally not statistically significant for the detection of noncoding RNAs. Bioinformatics 16(7):583–605
15. Wang Z, Gerstein M, Snyder M (2009) RNA-Seq: a revolutionary tool for transcriptomics. Nat Rev Genet 10(1):57–63
16. Waterman M et al (1995) Introduction to computational biology: maps, sequences and genomes. Chapman & Hall, London

A Unified Probabilistic PLSR Model for Quantitative Analysis of Surface-Enhanced Raman Spectrum (SERS)

Shuo Li, Jean Gao, James O. Nyagilo, Digant P. Dave, Baoju Zhang, and XiaoYong Wu

Abstract Gold Surface-enhanced Raman Scattering (Au SERS) nano-particles in combination with Raman spectroscopy have occurred as a newly sensitive, non-invasive molecular imaging technology. The multiplexing capability enables the technology to detect and separate multiple biomarkers with picomolar sensitivity. In this study, we demonstrate the ability of Raman spectroscopy to separate different fingerprints of Au SERS nanotags. Quantitative analysis of Raman spectrum data usually faces the challenge as high dimensional variables with a low sample number. The commonly applied partial least squares (PLS) regression algorithms, including PLS2 and SIMPLS, can not avoid overfitting to small data sets. In this paper, we present a unified probabilistic PLSR model, called PPLSR, stemmed from the concepts of probabilistic principal component analysis (PPCA) and probabilistic canonical correlation analysis (PCCA) to identify the spectral fingerprints from the measured mixing Raman signals. This model partitions the observed variables into the systematic part governed by a few latent variables and the unrelated noise part controlling the uncertainty of data sets. As a general methodology, this provides a solid foundation to develop Bayesian nonparametrics models and helps to build more robust models. Experimental results of Raman spectrum data using up to five different types of Au SERS nanotags with different

S. Li (✉) • J. Gao
Department of Computer Science and Engineering, The University of Texas at Arlington, Arlington, Texas 76019, USA
e-mail: shuo.li@mavs.uta.edu; gao@mavs.uta.edu

J.O. Nyagilo • D.P. Dave
Department of Bioengineering, The University of Texas at Arlington, Arlington, Texas 76019, USA
e-mail: james.nyagilo@uta.edu; ddave@uta.edu

B. Zhang • XiaoYong Wu
College of Physics and Information Science, Tianjin Normal University, Tianjin 300387, China
e-mail: wdxyzbj@163.com

B. Zhang et al. (eds.), *The Proceedings of the Second International Conference on Communications, Signal Processing, and Systems*, Lecture Notes in Electrical Engineering 246, DOI 10.1007/978-3-319-00536-2_126,

combinations and mixing ratios are shown. Quantitative analysis using the proposed model and comparison methods are given with two cross-validation methods.

1 Introduction

The development of the gold surface-enhanced Raman scattering (SERS) nanoparticles offers an exciting opportunity to overcome the low signal-to-noise problem inherent in existing Raman spectroscopy. It is regarded as one of the most sensitive, noninvasive techniques for quantitative biomarker analysis that can provide unique spectral fingerprints from biological samples. To identify and quantify the underlying fingerprints from the multiplexing Raman signal, the basic model is usually a linear calibration model:

$$\mathbf{Y} = \mathbf{XB} + \mathbf{E}, \tag{1}$$

where $\mathbf{X} = [\mathbf{x}_1, \ldots, \mathbf{x}_N]^T \in R^{N \times d_x}$ are N zero-mean mixture Raman spectra, each with d_x wavelengths; $\mathbf{Y} = [\mathbf{y}_1, \ldots, \mathbf{y}_N]^T \in R^{N \times d_y}$ are the zero-mean ground truth concentrations of d_y components in each mixture sample; $\mathbf{B} \in R^{d_x \times d_y}$ is the matrix of regression coefficients and $\mathbf{E}$ is the residual matrix. For spectrum data, it is common that $d_x \gg N$ and variables of $\mathbf{X}$ are correlated. Latent variable regression methods, including principal component regression (PCR), canonical correlation regression (CCR) and partial least squares regression (PLSR), are usually used to solve this high dimensional, ill-conditioned, multicollinearity multivariate linear regression problem [2].

Among these methods, PLSR is commonly used because of its robust objective function [7]. It is derived from the partial least squares (PLS) technique, which represents a class of methods first used for modeling between data sets [11]. A recent overview of PLS can be found in [9]. PLSR is the variant of PLS that is especially for the prediction purpose. One PLSR algorithm, called PLS2 in [9], is based on NIPALS algorithm, which can be found in [6, 9]. An analysis of the properties of PLS2 can be found in [6]. Wold et al. [12] gives a good picture of PLS2. References [4, 5, 7] illustrate the statistic properties of the objective function and equivalent optimization process of PLS2 algorithm. Another PLSR algorithm, named SIMPLS [3], improves NIPALS algorithm based PLS2 by avoiding the deflation of original data matrixes.

Traditional PLSR algorithms are frequentist statistic methods, which suffer several inherent drawbacks, such as (1) Data inference and prediction are only based on a single model, and if the size of the training data set is small, the model would be biased; (2) It is difficult to incorporate the prior knowledge into the model and is hard to do on-line learning; (3) It needs to use the time consuming cross-validation methods to decide the model complexity, for example to find the best number of principle components. Inspired by the idea of probabilistic PCA [10] and probabilistic CCA [1], in this paper, we present a unified probabilistic model for the

traditional PLSR algorithms, named probabilistic PLSR (PPLSR), which is a solid foundation for Bayesian models that can deal with those drawbacks.

The paper is organized as follows: in Sect. 2, the differences and connections between two PLSR algorithms are analyzed; in Sect. 3, the unified probabilistic model is presented; Sect. 4 gives an EM algorithm to estimate the parameters of the model and in Sect. 5, PPLSR is evaluated on three Raman spectra data sets using three cross-validation methods.

2 PLSR Algorithms

PLSR algorithms linearly combine the explanatory variables $\mathbf{x}$ with the weights vectors as columns of matrix $\mathbf{W} = \{\mathbf{w}_i\}_{i=1}^{k} \in R^{d_x \times k}$, and get k unrelated latent variables $\mathbf{z} = \mathbf{W}^T\mathbf{x} = \{z_i\}_{i=1}^{k}$ that best represent $\mathbf{x}$ and most correlate with dependent variables $\mathbf{y}$, which can be described as obj. $\max_{\mathbf{w}_i} var(z_i)\sum_{t=1}^{d_y} corr(z_i,y_t)^2 \propto ||cov(z_i,\mathbf{y})||^2$, s.t. $||\mathbf{w}_i||^2 = 1$; $corr(z_i,z_j) = 0$, for $i = 1,\ldots,k$ and $j = 1,\ldots,(i-1)$. $var(z_i)$ and $corr(z_i,y_t)$ are variance of z_i and correlation coefficient between z_i and y_t respectively, elements of vector $cov(z_i,\mathbf{y})$ are covariance coefficients between z_i and elements of $\mathbf{y}$, $\propto$ means be proportional to, $||.||$ means Euclidean norm of vectors. Then the linear regression is done between $\mathbf{z}$ and $\mathbf{y}$. For $i = 1$, $\mathbf{w}_1$ is the first eigenvector of $\mathbf{X}^T\mathbf{Y}\mathbf{Y}^T\mathbf{X}$ corresponding to the biggest eigenvalue. For $i = 2,\ldots,K$, in order to satisfy the constraints of unrelated latent variables $corr(z_i,z_j) = 0$, $\mathbf{w}_i$ are found iteratively in both PLS2 and SIMPLS.

Algorithm 1 PLS2 Deflation process.

1: **for** $i = 1$ to k **do**
2: $\mathbf{r}_i = eig(\mathbf{X}_i^T\mathbf{Y}\mathbf{Y}^T\mathbf{X}_i)$; % Get projection directions $\mathbf{r}_i$
3: $\mathbf{z}_i = \mathbf{X}_i\mathbf{r}_i$; % Get score vectors $\mathbf{z}_i$
4: $\mathbf{p}_i = \mathbf{X}_i^T\mathbf{z}_i/(\mathbf{z}_i^T\mathbf{z}_i)$; % Get loading vectors $\mathbf{p}_i$
5: $\mathbf{X}_{i+1} = \mathbf{X}_i - \mathbf{z}_i\mathbf{p}_i^T$; % Get the residual matrices of $\mathbf{X}_i$
6: **end for**
7: Store $\mathbf{R} = [\mathbf{r}_1,\ldots,\mathbf{r}_k]$; $\mathbf{P} = [\mathbf{p}_1,\ldots,\mathbf{p}_k]$

PLS2 iteratively deflates on $\mathbf{X}$ to get residual matrix $\mathbf{X}_i$ and get the corresponding projection direction $\mathbf{r}_i$ by solving: obj. $\max_{\mathbf{r}_i} \mathbf{r}_i^T\mathbf{X}_i^T\mathbf{Y}\mathbf{Y}^T\mathbf{X}_i\mathbf{r}_i$, s.t. $\mathbf{r}_i^T\mathbf{r}_i = 1$, with $\mathbf{X}_i$ is got from a deflation process described in Algorithm 1, in which, $eig(.)$ means getting the first eigenvector of the matrix corresponding to the biggest eigenvalue, and different with the random variable z_i, $\mathbf{z}_i$ are the sample vector of the ith latent variable. The projecting direction $\mathbf{r}_i$ is to project residual matrix $\mathbf{X}_i$, and the weights vectors can be calculated as $\mathbf{W} = \mathbf{R}(\mathbf{P}^T\mathbf{R})^{-1}$ [12] or $\mathbf{W} = \mathbf{P}(\mathbf{P}^T\mathbf{P})^{-1}$ [8]. Hoskuldsson [6] proved that after the deflation, it will satisfy the unrelated constraints.

Instead of finding projection directions of residual matrixes $\mathbf{X}_i$, SIMPLS directly finds the weights vectors as the left singular vectors of a projected cross covariance matrix $\mathbf{P}_i^{\perp}\mathbf{X}^T\mathbf{Y}$ with $\mathbf{P}_i^{\perp} = \mathbf{I} - \mathbf{P}_{i-1}\mathbf{P}_{i-1}^{+}$ is the matrix of projecting directions, $\mathbf{P}_{i-1}^{+} = \left(\mathbf{P}_{i-1}^T\mathbf{P}_{i-1}\right)^{-1}\mathbf{P}_{i-1}^T$ is the Moore–Penrose inverse of $\mathbf{P}_{i-1}$ and $\mathbf{P}_{i-1} = [\mathbf{p}_1, \ldots, \mathbf{p}_{i-1}]$ is the loading matrix with the ith column calculated as $\mathbf{p}_i = \mathbf{X}^T\mathbf{z}_i/(\mathbf{z}_i^T\mathbf{z}_i)$. In each iteration the objective function of SIMPLS can be written as: obj. $\max_{\mathbf{w}_i} \mathbf{w}_i^T\mathbf{P}_i^{\perp}\mathbf{X}^T\mathbf{Y}\mathbf{Y}^T\mathbf{X}\mathbf{P}_i^{\perp}\mathbf{w}_i$, s.t. $\mathbf{w}_i^T\mathbf{w}_i = 1$. de Jong [3] proved that these $\mathbf{w}_i$ satisfy the unrelated constraints, and the detail algorithm can be found in [3].

The process of both PLS2 and SIMPLS can be summarized as: $\mathbf{X} = \sum_{i=1}^{k}\mathbf{z}_i\mathbf{p}_i^T + \mathbf{X}_{i+1} = \mathbf{Z}\mathbf{P}^T + \mathbf{X}_{i+1}$ and $\mathbf{Y} = \mathbf{Z}\mathbf{Q}^T + \mathbf{E}_y$, in which the unrelated latent variables $\{\mathbf{z}_i\}$ together with loadings $\{\mathbf{p}_i\}$ best represent the predictor matrix $\mathbf{X}$. Residual matrix $\mathbf{X}_{i+1}$ describes random noises outside the subspace spanned by the PLS principle components. Regression is done between $\mathbf{Z}$ and columns of $\mathbf{Y}$, with columns of $\mathbf{Q}$ are regression coefficients. So $\mathbf{Z}\mathbf{Q}^T$ best predicts the response matrix $\mathbf{Y}$ and $\mathbf{E}_y$ represents regression errors.

3 Unified Probabilistic PLSR Model

In this part we give the unified probabilistic PLSR that covers PLS and SIMPLS under the same model. It is reasonable to assume that any mixture Raman spectrum $\mathbf{x} \in R^{d_x}$ is composed of k principal components and random noises $\mathbf{x} = \mathbf{W}_x\mathbf{z} + \mathbf{m}_x + \mathbf{e}_x$, with columns of $\mathbf{W}_x \in R^{d_x \times k}$ and elements of $\mathbf{z} \in R^k$ being loadings and scores. $\mathbf{m}_x \in R^{d_x}$ represents the mean vector of $\mathbf{x}$, so the mean of $\mathbf{z}$ is zero. Elements of $\mathbf{e}_x$ are random noise at all Raman shifts. Also, since the principal components are unrelated, the covariance of $\mathbf{z}$ is a diagonal matrix. For easier calculation, it is reasonable to assume $\mathbf{z}$ following the unit Gaussian distribution $p(\mathbf{z}) = \mathcal{N}(\mathbf{z}|\mathbf{0}, \mathbf{I})$, here the scale on each dimension of $\mathbf{z}$ is normalized, so the lengths of loadings vectors $\{\mathbf{w}_{xi}\}_{i=1}^{k}$ are different. It is also reasonable to assume that random noise $\mathbf{e}_x$ has the same effect on each frequency of Raman spectrum and so follows an isotropy zero-mean-Gaussian distribution $p(\mathbf{e}_x) = \mathcal{N}(\mathbf{0}, \sigma_x^2\mathbf{I})$. Meanwhile the inherent linear relation between Raman spectrum $\mathbf{x}$ and mixing concentrations $\mathbf{y} \in R^{d_y}$ can be described in a multiple linear regression model $\mathbf{y} = \mathbf{W}_y\mathbf{z} + \mathbf{m}_y + \mathbf{e}_y$, with rows of $\mathbf{W}_y \in R^{d_y \times k}$ are regression coefficients between elements of $\mathbf{y}$ and $\mathbf{z}$, elements of $\mathbf{m}_y$ are the bias parameters and $\mathbf{e}_y$ are the regression errors that also follows an isotropy zero-mean-Gaussian distribution $p(\mathbf{e}_y) = \mathcal{N}(\mathbf{0}, \sigma_y^2\mathbf{I})$. Then the PPLS model can be summarized as:

$$\mathbf{x}|\mathbf{z} \sim \mathcal{N}(\mathbf{W}_x\mathbf{z} + \mu_x, \sigma_x^2\mathbf{I}) \text{ and } \mathbf{y}|\mathbf{z} \sim \mathcal{N}(\mathbf{W}_y\mathbf{z} + \mu_y, \sigma_y^2\mathbf{I}). \tag{2}$$

From (2), the joint distribution of $\mathbf{x}$ and $\mathbf{y}$ given $\mathbf{z}$ is formed as:

$$p(\mathbf{t}|\mathbf{z};\mathbf{W}_x,\mathbf{W}_y,\mathbf{m}_x,\mathbf{m}_y,\Psi)=\mathcal{N}(\mathbf{W}\mathbf{z}+\mathbf{m},\Psi), \tag{3}$$

with $\mathbf{t}=\begin{pmatrix}\mathbf{x}\\ \mathbf{y}\end{pmatrix}\in R^{d_x+d_y}, \mathbf{W}=\begin{pmatrix}\mathbf{W}_x\\ \mathbf{W}_y\end{pmatrix}, \mathbf{m}=\begin{pmatrix}\mathbf{m}_x\\ \mathbf{m}_y\end{pmatrix}, \Psi=\begin{pmatrix}\sigma_x^2\mathbf{I} & 0\\ 0 & \sigma_y^2\mathbf{I}\end{pmatrix}$. Ψ is diagonal matrix because in PPLS model, we assume all relation between $\mathbf{x}$ and $\mathbf{y}$ are expressed by $\mathbf{z}$, which means if $\mathbf{z}$ is fixed, the uncertainty of $\mathbf{x}$ and $\mathbf{y}$ are independent. Then the marginal distribution of $\mathbf{x}$ and $\mathbf{y}$ is calculated as $p(\mathbf{x},\mathbf{y})=\mathcal{N}(\mathbf{m},\Psi+\mathbf{W}\mathbf{W}^T)$, and the conditional distribution of $\mathbf{z}$ given observation $\mathbf{x}$ and $\mathbf{y}$ is calculated as $p(\mathbf{z}|\mathbf{x},\mathbf{y})=\mathcal{N}(\mathbf{m}_{z|xy},\mathbf{S}_{z|xy})$ with $\mathbf{S}_{z|xy}=(\mathbf{I}+\mathbf{W}^T\Psi^{-1}\mathbf{W})^{-1}$ and $\mathbf{m}_{z|xy}=\mathbf{S}_{z|xy}\mathbf{W}^T\Psi^{-1}(\mathbf{z}-\mathbf{m})$

The final goal of PLS regression is given a testing signal $\mathbf{x}$ to predict its response $\hat{\mathbf{y}}$. Here we give an estimation method using PPLS model. We can get $\mathbf{z}|\mathbf{x}\sim\mathcal{N}(\mathbf{m}_{z|x},\mathbf{S}_{z|x})$ with $\mathbf{S}_{z|x}=(\mathbf{I}+\sigma_x^{-2}\mathbf{W}_x^T\mathbf{W}_x)^{-1}$ and $\mathbf{m}_{z|x}=\sigma_x^{-2}\mathbf{S}_{z|x}\mathbf{W}_x^T(\mathbf{x}-\mu_x)$. Then we get $\mathbf{y}|\mathbf{x}\sim\mathcal{N}(\mathbf{m}_{y|x},\mathbf{S}_{y|x})$ with $\mathbf{m}_{y|x}=\mathbf{W}_y\mathbf{m}_{z|x}+\mu_y$ and $\mathbf{S}_{y|x}=\sigma_y^2\mathbf{I}+\mathbf{W}_y\mathbf{S}_{z|x}\mathbf{W}_y^T$. The mean value $\mathbf{m}_{y|x}$ of $\mathbf{y}$ given $\mathbf{x}$ can be used as the prediction of $\hat{\mathbf{y}}$. The regression coefficients are $\mathbf{B}=\mathbf{W}_y(\mathbf{W}_x^T\mathbf{W}_x+\sigma_x^2\mathbf{I})^{-1}\mathbf{W}_x^T$.

4 EM Algorithm for PPLSR

Having the PPLSR model, given train samples, we want to estimate the parameters of the model. It is complicated to directly estimate parameters by maximizing the log likelihood function $\sum_{n=1}^{N}\ln p(\mathbf{x}_n,\mathbf{y}_n)$. Here we give an EM algorithm for parameters estimation. In the expectation (E) step, we build the distribution of latent variables $p(\mathbf{z}_n|\mathbf{x}_n,\mathbf{y}_n;\hat{\Theta})$ with training data and previously estimated parameters, $\hat{\Theta}$ denotes all the estimated parameters. In the maximization (M) step, we estimate the parameters by maximizing the log likelihood function $\max_{\Theta}\sum_{n=1}^{N}\ln p(\mathbf{x}_n,\mathbf{y}_n|\mathbf{z}_n;\Theta)$ with the knowledge of distribution of $\mathbf{z}_n$. Θ denotes the unknown parameters. Setting derivative of the log likelihood function with respect to all parameters to zero, we get means of $\mathbf{x}$ and $\mathbf{y}$ as $\boldsymbol{\mu}_x=\frac{1}{N}\sum_{n=1}^{N}\mathbf{x}_n$ and $\boldsymbol{\mu}_y=\frac{1}{N}\sum_{n=1}^{N}\mathbf{y}_n$. These two parameters only relate to original data, so we can get them without EM algorithm. The loading matrixes are updated as: $\hat{\mathbf{W}}_x=\left[\sum_{n=1}^{N}(\mathbf{x}_n-\mathbf{m}_x)E[\mathbf{z}_n]^T\right]\left[\sum_{n=1}^{N}E[\mathbf{z}_n\mathbf{z}_n^T]\right]^{-1}$ and $\hat{\mathbf{W}}_y=\left[\sum_{n=1}^{N}(\mathbf{y}_n-\mathbf{m}_y)E[\mathbf{z}_n]^T\right]\left[\sum_{n=1}^{N}E[\mathbf{z}_n\mathbf{z}_n^T]\right]^{-1}$, with $E[\mathbf{z}_n]=\mathbf{m}_{z|xy}(\mathbf{z}_n)$ and $E[\mathbf{z}_n\mathbf{z}_n^T]=\mathbf{S}_{z|xy}+E[\mathbf{z}_n]E[\mathbf{z}_n]^T$ are calculated in the E step. Finally the noise levels are updated as $\hat{\sigma}_x^2=\frac{1}{D_xN}\sum_{n=1}^{N}\{Tr(E[\mathbf{z}_n\mathbf{z}_n^T]\hat{\mathbf{W}}_x^T\hat{\mathbf{W}}_x)-2E[\mathbf{z}_n]^T\hat{\mathbf{W}}_x^T(\mathbf{x}_n-\mu_x)+$

$\|\mathbf{x}_n-\mu_x\|^2\}$ and $\hat{\sigma}_y^2=\frac{1}{D_yN}\sum_{n=1}^{N}\{Tr(E[\mathbf{z}_n\mathbf{z}_n^T]\hat{\mathbf{W}}_y^T\hat{\mathbf{W}}_y)-2E[\mathbf{z}_n]^T\hat{\mathbf{W}}_y^T(\mathbf{y}_n-\mu_y)+\|\mathbf{y}_n-\mu_y\|^2\}$. The above estimation iterates until estimated parameters converge. The pseudo-code of the EM algorithm is summarized in Algorithm 2.

Algorithm 2 EM Algorithm for PPLSR.
Input: $\mathbf{X}$, $\mathbf{Y}$, k
Output: $\mathbf{B}$

1: $\mathbf{m}_x \leftarrow \frac{1}{N}\sum_{n=1}^{N}\mathbf{x}_n$; $\mathbf{m}_y \leftarrow \frac{1}{N}\sum_{n=1}^{N}\mathbf{y}_n$;
2: $\mathbf{X} \leftarrow \mathbf{X}-\mathbf{m}_x$; $\mathbf{Y} \leftarrow \mathbf{Y}-\mathbf{m}_y$;
3: Initialize parameters: $\hat{\Theta}=[\hat{\sigma}_x,\hat{\sigma}_y,\hat{\mathbf{W}}_x,\hat{\mathbf{W}}_y]$
4: **while** $\mathbf{m}_{z|xy}(\mathbf{Z})$ is not converge **do**
5: Calculate $\mathbf{m}_{z|xy}(\mathbf{Z}),\mathbf{S}_{z|xy}$ for N samples: $\mathbf{S}_{z|xy}=(\hat{\sigma}_x^2\hat{\mathbf{W}}_x^T\hat{\mathbf{W}}_x+\hat{\sigma}_y^2\hat{\mathbf{W}}_y^T\hat{\mathbf{W}}_y+\mathbf{I})^{-1}$ and $\mathbf{m}_{z|xy}(\mathbf{Z})=\mathbf{S}_{z|xy}(\hat{\sigma}_x^{-2}\hat{\mathbf{W}}_x^T\mathbf{X}^T+\hat{\sigma}_y^{-2}\hat{\mathbf{W}}_y^T\mathbf{Y}^T)$ with $\mathbf{Z}=[\mathbf{z}_1,\ldots,\mathbf{z}_N]$.
6: Calculate $\Sigma_{\mathbf{Z}}=\sum_{n=1}^{N}E[\mathbf{z}_n\mathbf{z}_n^T]$ as: $\Sigma_{\mathbf{Z}}=N\mathbf{S}_{z|xy}+\mathbf{m}_{z|xy}(\mathbf{Z})\mathbf{m}_{z|xy}(\mathbf{Z})^T$
7: Estimate new $\hat{\mathbf{W}}_x$ and $\hat{\mathbf{W}}_y$: $\hat{\mathbf{W}}_x=\mathbf{X}^T\mathbf{m}_{z|xy}(\mathbf{Z})^T\Sigma_{\mathbf{Z}}^{-1}$; $\hat{\mathbf{W}}_y=\mathbf{Y}^T\mathbf{m}_{z|xy}(\mathbf{Z})^T\Sigma_{\mathbf{Z}}^{-1}$
8: Estimate new parameters $\hat{\sigma}_x$ and $\hat{\sigma}_y$: $\hat{\sigma}_x^2=Tr\{\Sigma_{\mathbf{Z}}\hat{\mathbf{W}}_x^T\hat{\mathbf{W}}_x+\mathbf{X}\mathbf{X}^T-2\mathbf{X}\hat{\mathbf{W}}_x\mathbf{m}_{z|xy}(\mathbf{Z})\}/d_xN$ and $\hat{\sigma}_y^2=Tr\{\Sigma_{\mathbf{Z}}\hat{\mathbf{W}}_y^T\hat{\mathbf{W}}_y+\mathbf{Y}\mathbf{Y}^T-2\mathbf{Y}\hat{\mathbf{W}}_y\mathbf{m}_{z|xy}(\mathbf{Z})\}/d_yN$
9: **end while**
10: $\mathbf{B}=\mathbf{W}_y(\mathbf{W}_x^T\mathbf{W}_x+\sigma_x^2\mathbf{I})^{-1}\mathbf{W}_x^T$

Theoretically, the conditional log likelihood would be the criterion to control the convergence, since it is monotonically increasing and converges to a upper bound. But for high dimensional Gaussian distribution, the probability of single data point as well as the likelihood is zero. So in real case it can not be used to control the convergence. Here we use $\mathbf{m}_{z|xy}$, since it is a function of all parameters. Its convergence means the convergence of all parameters.

5 Experiments

To evaluate the effectiveness of the PPLSR model, in this section, we compare it with PLSR (PLS2 and SIMPLS) and other latent variables regression methods, on three Raman signals data sets, using two cross-validation methods. The Raman signals are collected from the Raman spectroscopy with $20\times$, 0.4_{NA} lens and 785 nm laser wavelength. Raman shifts range from $-79.65\ \text{cm}^{-1}$ to $2071.80\ \text{cm}^{-1}$ with 1,044 values. To avoid the influence of the strong intensity from Rayleigh Scattering, from 1,044 Raman shifts, we extract 896 (71th–966th). All nano-tags are made from 54.67 nm Au nano-particles, coated with dyes: DTTC and Cresyl violet (CV) (in data set one); HITC and IR140 (in data set two); DOTC, DTTC, HITC and IR140 (in data set three). All pure nano-tag solutions are made with a concentration of $1.1e^{10}$ nanotags/ml. Then with 11 mixing volume ratios (shown in Fig. 1) we mix two pure nano-tags solutions in the first two data sets,

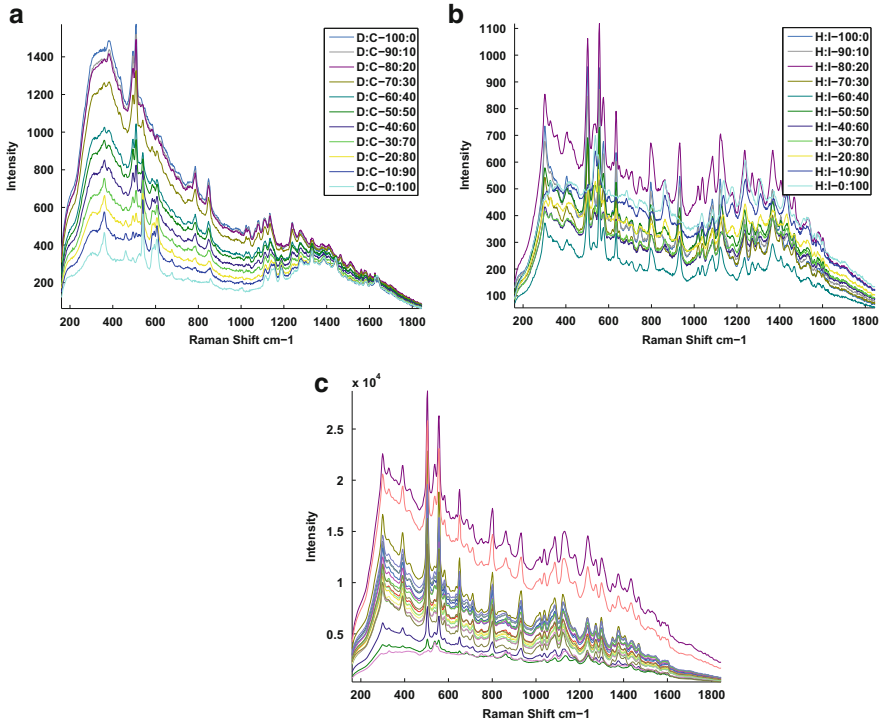

Fig. 1 Average Raman signals and mixing volume ratios. D:C-90:10, for example, means the ratio of mixing volumes of DTTC and CV is 90 %: 10 %. (**a**) DTTC-CV(D:C) (**b**) HITC-IR140(H:I) (**c**) DOTC-DTTC-HITC-IR140

with 21 mixing volume ratios $\{(25\%{:}25\%{:}25\%{:}25\%),(20\%{:}25\%{:}25\%{:}25\%),\ldots,(0{:}25\%{:}25\%{:}25\%),(25\%:20\%:25\%:25\%),\ldots,(25\%:25\%:25\%:0)\}$, we mix four pure nano-tags solutions in the third data set, and get three groups of mixture nano-tag solution samples. These mixing volume ratios can be treated as relative concentrations of each pure nano-tags. From each sample, five duplicate Raman signals are collected, with 20 s time interval. So for data set one and two, we have 55 mixture signals, and for data set three, we have 105. In order to reduce the influence of instability of Raman signals, we also get the average signals by taking average of each five duplicates. These average signals are shown in Fig. 1.

To fully use the three data sets to evaluate the predicting ability of methods, we design two cross-validation methods: Cross Validation on Duplicate testing spectra (CVD): each five duplicate spectra that from the same mixture nanotags are tested. The other duplicate mixture signals with different mixing ratios are used as training signals; Cross Validation on Average testing spectra (CVA): take the average spectra of five duplicates as testing sample to reduce the influence of instability of Raman spectra and leave other duplicate mixture signals as training data.

Table 1 RMSE and k^* of different regression methods using different cross-validation methods

	Data set one		Data set two		Data set three	
Methods	CVD	CVA	CVD	CVA	CVD	CVA
RR	2.94 (/)	1.61 (/)	4.36 (/)	4.23 (/)	4.46 (/)	4.84 (/)
PCR	2.81 (6)	1.63 (9)	4.14 (5)	4.04 (5)	4.11 (13)	4.49 (13)
OPLS	2.94 (1)	1.54 (2)	4.20 (2)	4.09 (2)	4.46 (4)	4.84 (4)
PLS2	2.93 (8)	1.59 (9)	4.22 (5)	4.11 (5)	**3.95** (10)	**4.33** (10)
SIM	**2.72** (4)	1.61 (9)	4.13 (4)	4.03 (4)	4.15 (10)	4.53 (10)
PPLSR	2.75 (8)	**1.53** (37)	**4.07** (5)	**3.97** (5)	4.11 (13)	4.45 (8)

The results are shown as: RMSE(k^*)

Square Root of Mean Squares Error (RMSE) is used to evaluate the predicting accuracy of methods, which is defined as: $RMSE=\left(\sum_{i=1}^{N}\sum_{j=1}^{d_y}(\hat{y}_{i,j}-y_{i,j})^2/Nd_y\right)^{1/2}$, with $\hat{y}_{i,j}$ and $y_{i,j}$ are the estimated ratio and ground truth ratio respectively of the ith sample and the jth dye.

To solve the ill-conditioned multiple multivariate regression problem in (1), several methods can be used: Ridge Regression (RR); Principal Component Regression (PCR); Orthonormalized PLS (OPLS) [13]; PLS2; SIMPLS.

To maximize the performance of the latent variable regression methods, we tested every possible component number to find the optimized one: for methods PCR, PLS2, SIMPLS and PPLS, $k \in [1,Rank(\mathbf{X})]$, and for OPLS, $k \in [1,Rank(\mathbf{Y})]$. The results of k^* are shown in Table 1. The EM algorithm of PPLSR converges easily, so we reasonably set the iteration time as 30. Using the three data sets and two cross-validation methods, we tested the prediction ability of different regression methods with the RMSE shown in Table 1, with bold face indicating the best result for each cross-validation measurement. RR is worse than most latent variable regression methods because of the sparsity of the high dimensional spectra data. OPLS uses a very small number of components since it is limited by $rank(\mathbf{Y})$, but the accuracy is acceptable. This efficiency is because of the normalization of the variances of predictor components of OPLS which removes the variance of $\mathbf{X}$ that is unrelated with prediction.

The results of PPLSR are not the best but similar to those of PLS2 and SIMPLS. This is because PPLSR model is a probabilistic view of PLSR method, and essentially they are the same. The merit of PPLSR over PLSR is that it models the observations as the systematic part and the unrelated noise part with parameters, which provides a foundation for future Bayesian models to avoid the over-fitting problem that PLSR can not avoid.

6 Conclusions

Based on the ideas of PPCA and PCCA and the connection between PLS2 and SIMPLS, this paper presents a unified probabilistic PLSR model, PPLSR, to illustrate the traditional PLS regression from a probabilistic point of view. It provides a solid foundation for future Bayesian nonparametric model of PLSR, which can solve the over-fitting problem by given prior distributions of parameters without the time consuming cross-validation. Right now, all parameters are assumed to follow Gaussian distributions, which is not robust to outliers. Our future work will also combine different distributions to the models to make them suitable for more sophisticated situations.

References

1. Bach FR, Jordan MI (2005) A probabilistic interpretation of canonical correlation analysis. Technical report, 688, Department of Statistics, University of California, Berkeley, 2005
2. Burnham AJ, Viveros R, MacGregor JF (1996) Frameworks for latent variable multivariate regression. J Chemometr 10:31–45
3. de Jong S (1993) SIMPLS: an alternative approach to partial least squares regression. Chemom Intell Lab Syst 18:251–263
4. Frank IE, Friedman JH (1993) A statistical view of some chemometrics regression tools. Technometrics 35:109–135
5. Gustafsson MG (2001) A probabilistic derivation of the partial least-squares algorithm. J Chem Inf Model 41:288–294
6. Hoskuldsson A (1988) PLS regression methods. J Chemometr 2:211–228
7. Li S, Gao J, Nyagilo JO, Dave DP (2010) Eigenspectra, a robust regression method for multiplexed Raman spectra analysis. In: Proceedings of IEEE BIBM, Hong Kong, China, 2010
8. Li S, Gao J, Nyagilo james O, Dave DP (2011) Probabilistic partial least square regression: a robust model for quantitative analysis of Raman spectroscopy data. In: Proceedings of IEEE BIBM, Atlanta, GA, USA, 2011
9. Rosipal R, Kramer N (2006) Overview and recent advances in partial least squares. LNCS 3940:34–51
10. Tipping ME, Bishop CM (1999) Probabilistic principal component analysis. J Roy Stat Soc Ser B (Stat Methodol) 61:611–622
11. Wold H (1975) Path models with latent variables: the NIPALS approach. Academic Press, London
12. Wold S, Sjstrma M, Eriksson L (2001) PLS-regression: a basic tool of chemometrics. Chemometr Intell Lab Syst 58:109–130
13. Worsley K, Poline JB, Friston KJ, Evans AC (1997) Characterizing the response of PET and fMRI data using multivariate linear models. Neuroimage 6:305–319

Part X
Sensor and Measuring Network

Performance Evaluation of Multiuser Selection Scheme in HANs of Smart Grid

Zhuo Li, Qilian Liang, Baoju Zhang, and Xiaorong Wu

Abstract In Home Area Networks (HANs) of Smart Grid with the promising WiFi Direct technique, multiuser selection scheme is employed to reduce the effects of fading at the receiver part of the smart meter. In this paper, the performance of multiuser selection scheme in HANs over indoor Saleh–Valenzuela (S–V) channel is evaluated from two aspects: outage probability and bit error rate (BER). The probability density function (PDF) of signal to noise ratio (SNR) of the selected user is derived from the amplitude distribution property of the indoor S–V channel. Considering the characteristic of Power Saving Mechanism in WiFi Direct networks, the closed-form outage probability are obtained. Numerical results show that the performance of multiuser selection scheme in HANs of Smart Grid is related with several factors, i.e. total number of devices in HANs, traffic intensity, and modulation scheme, etc.

1 Introduction

Smart Grid can be considered as a combination of wireless communication networks and power line communication (PLC) systems with some new characteristics, such as energy saving, self-healing, and high attack-resistance, etc. A typical smart grid communication system consists of an advanced metering infrastructure (AMI) with a multi-tier communication infrastructure that includes: home area network (HAN), which is used to gather sensor information from a variety of devices within the home, and optionally send control information to these devices to better control energy consumption, and provides access to in-home appliances;

Z. Li (✉) • Q. Liang
Department of Electrical Engineering, University of Texas of Arlington, TX, USA
e-mail: zhuo.li@mavs.uta.edu; liang@uta.edu

B. Zhang • X. Wu
College of Electronic and Communication Engineering, Tianjin Normal University, China
e-mail: wdxyzbj@mail.tjnu.edu.cn; wu.xiaorong@sohu.com

B. Zhang et al. (eds.), *The Proceedings of the Second International Conference on Communications, Signal Processing, and Systems*, Lecture Notes in Electrical Engineering 246, DOI 10.1007/978-3-319-00536-2_127,

neighborhood area network (NAN) to connect the smart meters to the local access points; and a wide area network (WAN) to connect the grid to the core utility system [2, 15].

WiFi is a mature, proven technology that implements many of the Smart Grid communication scenarios in the Home Area Network (HAN) [10]. Particularly, WiFi Direct technology is attracting attentions for Smart Grid solutions, which are driven by the desire of more efficient energy usage worldwide. Different from the conventional WiFi infrastructure, WiFi Direct is a standard that allows WiFi devices to communicate with each other without the need for wireless access point (AP). In this way, devices in the WiFi Direct network establish an ad-hoc peer-to-peer connectivity [13]. Power saving mechanism is exploited in WiFi direct technique which attempts to conserve energy on idle devices by powering off their wireless interfaces for specific period of time [4]. Consequently the WiFi Direct users could alternate between active state and doze state.

One goal of communications of the HAN in Smart Grid is to convey data from home appliances or smart sensors to the smart meter reliably and stably with as low outage probability as possible. In the existing literatures, Kim and Poor point out that one of the fundamental issues for the communication in a Smart Grid is the link capacity which should be able to convey the system state information with negligible error [5]. Liu et al [7] investigate the performance of wireless optical links including amount of fading, outage probability and BER due to weak influence. The total uplink (device to smart meter) capacity can be maximized by picking the device with the best channel to transmit [12]. This scheme is often referred to as multiuser selection diversity where the link with the largest SNR is selected among all the available links [9]. The performance of multiuser selection scheme was widely studied. The performance of multiuser selection diversity was analyzed under an absolute SNR-based scheduling scheme and a normalized SNR-based scheduling scheme in [11]. It was shown that an absolute SNR-based scheduling scheme achieves maximum capacity without fairness consideration, while a normalized SNR-based scheduling scheme guarantees fairness among all users at the expense of a certain capacity penalty.

In this paper, we evaluate the performance of multiuser selection scheme of HANs in Smart Grid communication under indoor S–V channel environment, in which the number of active users are modeled as a Markov chain[6], and the amplitude of the channel gain follows Rayleigh distribution [8]. The PDF of SNR of received signal from the selected user is derived from the amplitude distribution property of indoor S–V channel, and thus the closed-form outage probability is obtained considering the dynamic number of active users. In addition, BER of multiuser selection scheme is studied by numerical simulation.

The rest of this paper is organized as follows. Multiuser selection scheme is proposed in Sect. 2. Section 3 provides the evaluation of multiuser selection scheme in HANs of smart Grid in two categories: outage probability and BER. Simulation and results are presented in Sect. 4, followed by the discussion according to the numerical results. Finally, conclusions are drawn in Sect. 5.

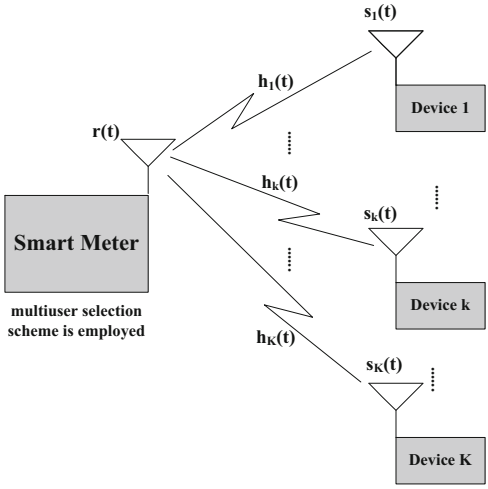

Fig. 1 Uplink multi-device communication system

2 Multiuser Diversity Selection Scheme

In a typical uplink multiuser communication scenario as shown in Fig. 1, the signal $r_k(t)$ from the k_{th} device through the channel at symbol time t can be expressed as:

$$r_k(t) = h_k(t)s_k(t) + n_k(t), \quad k = 1, 2, \ldots, K \tag{1}$$

where $s_k(t)$ is the transmitted signal at symbol time t from the k_{th} device, $h_k(t)$ is the channel gain of link k from device k to the smart meter at symbol time t, $n_k(t)$ is an independent and identically distributed (i.i.d.) sequence of zero-mean complex Gaussian noise, and K is the total number of active devices.

Thus the received SNR from the k_{th} device γ_k is:

$$\gamma_k = \frac{E_k |h_k|^2}{N_0} \tag{2}$$

where E_k is the average power of the transmitted signal from the k_{th} device, N_0 is the power of Addictive White Gaussian Noise (AWGN). Saleh–Valenzuela (S–V) channel model is often adopted for indoor communication scenarios. Since the amplitude of S–V channel gain follows Rayleigh distribution, γ_k follows exponential distribution, where E_k and N_0 are assumed to be constant. The PDF of γ_k is written as [14]:

$$f_{\gamma_k}(\gamma) = \frac{1}{\overline{\gamma}_k} \exp(-\frac{\gamma}{\overline{\gamma}_k}) \tag{3}$$

where $\overline{\gamma}_k$ is the average SNR from device k. Thus the cumulative density function (CDF) of γ_k is:

$$F_{\gamma_k}(\gamma) = 1 - \exp(-\frac{\gamma}{\overline{\gamma}_k}) \tag{4}$$

By employing multiuser selection scheme at the smart meter, the link with the maximum SNR among all the K active links is selected at each symbol time. So the received SNR at the smart meter is

$$\gamma_s = \max \gamma_k, \quad k = 1, 2, \ldots, K \tag{5}$$

For i.i.d. random variable γ_k k = 1,2,. . ., K, the CDF of γ_s with K active devices can be calculated as:

$$\begin{aligned} F^K_{\gamma_s}(\gamma) = \Pr[\gamma_s \le \gamma] &= \prod_{k=1}^{K} P_r[\gamma_k \le \gamma] \\ &= \prod_{k=1}^{K} F_{\gamma_k}(\gamma) = [F_{\gamma_k}(\gamma)]^K \\ &= [1 - \exp(-\frac{\gamma}{\overline{\gamma}})]^K \end{aligned} \tag{6}$$

where $\overline{\gamma} = \overline{\gamma}_k, k = 1, 2, \ldots, K$, which denotes that all the links have the same average received SNR. The PDF of γ_s with K active devices is obtained by taking the derivative of $F^K_{\gamma_s}(\gamma)$ as to γ:

$$\begin{aligned} f^K_{\gamma_s}(\gamma) = \frac{dF^K_{\gamma_s}(\gamma)}{d\gamma} &= K[1 - \exp(-\frac{\gamma}{\overline{\gamma}})]^{(K-1)} f_{\gamma_k}(\gamma) \\ &= \frac{K}{\overline{\gamma}}[1 - \exp(-\frac{\gamma}{\overline{\gamma}})]^{(K-1)} \exp(-\frac{\gamma}{\overline{\gamma}}) \end{aligned} \tag{7}$$

Considering that each device with WiFi Direct technique in HANs of Smart grid alternates between active state and doze state, the total number of active devices K is modeled as a Markov chain with the steady state probability P_K, K = 0,1,2,. . .,M and traffic intensity ρ, where M is the total number of devices with WiFi-Direct technique of a HAN in Smart Grid [6]. The steady state probability P_K is expressed as below:

$$P_K = \frac{\frac{1}{K!}\rho^K}{\sum_{i=0}^{M} \frac{1}{i!}\rho^i}, \quad K = 0, 1, \ldots, M \tag{8}$$

In this scenario, the average PDF of γ_s is consequently written as:

$$\begin{aligned} \overline{f}_{\gamma_s}(\gamma) &= \sum_{K=0}^{M} P_K f^K_{\gamma_s}(\gamma) \\ &= \sum_{K=0}^{M} P_K \frac{K}{\overline{\gamma}}[1 - \exp(-\frac{\gamma}{\overline{\gamma}})]^{(K-1)} \exp(-\frac{\gamma}{\overline{\gamma}}) \end{aligned} \tag{9}$$

3 Performance Analysis

3.1 Outage Probability

The HAN is said to be in *outage* when the averaged capacity is below a certain capacity threshold C_{Th}. Thus the closed-form outage probability is expressed as [1]:

$$\begin{aligned} P_{out} &= \Pr[C(\gamma_s) \le C_{Th}] \\ &= \Pr[\log_2(1+\gamma_s) \le C_{Th}] \\ &= \int_0^{(2^{C_{Th}}-1)} \overline{f}_{\gamma_s}(\gamma) d\gamma \\ &= \sum_{K=0}^{M} P_K F_{\gamma_s}^K (2^{C_{Th}} - 1) \\ &= \sum_{K=0}^{M} P_K [1 - \exp(-\frac{2^{C_{Th}} - 1}{\overline{\gamma}})]^K \end{aligned} \tag{10}$$

3.2 Bit Error Rate (BER)

For M-ary signaling, the SNR per bit γ_b could be approximately expressed as:

$$\gamma_b \approx \frac{\gamma_s}{\log_2 M} \tag{11}$$

Combining with (9), we can get the average PDF of γ_b as:

$$\overline{f}_{\gamma_b}(\gamma) = \sum_{K=0}^{M} P_K \frac{K}{\overline{\gamma_b}} [1 - \exp(-\frac{\gamma}{\overline{\gamma_b}})]^{(K-1)} \exp(-\frac{\gamma}{\overline{\gamma_b}}) \tag{12}$$

where $\overline{\gamma_b}$ is the average SNR per bit.

Assuming γ_b is roughly constant over each bit time, the average BER in the absence of interference is:

$$P_b = \int_0^{\infty} p_b(\gamma) \overline{f}_{\gamma_b}(\gamma) d\gamma \tag{13}$$

where $p_b(\gamma)$ is the BER for a certain modulation scheme under AWGN channel [3]. For WiFi technique, the High Throughput (HT) physical(PHY) data subcarriers are modulated using BPSK, QPSK, 16-QAM or 64-QAM. The BER of these four modulation schemes over AWGN channel can be found in [3].

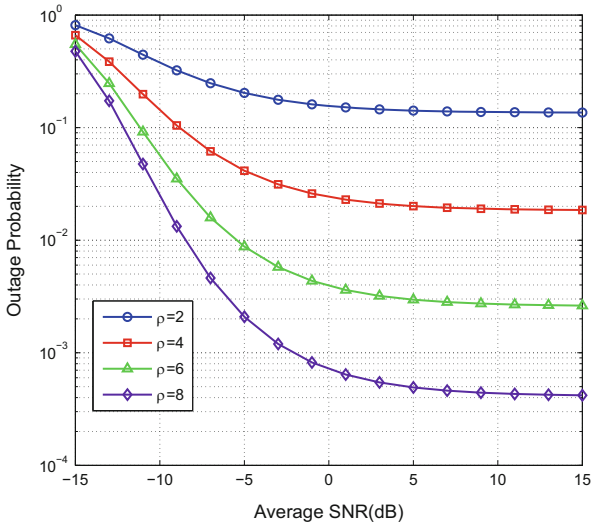

Fig. 2 Outage probability of multiuser selection scheme in a HAN, $M = 10$

4 Numerical Results and Discussion

4.1 Outage Probability

Figure 2 shows the outage probability of multiuser selection scheme of a HAN in smart grid due to different traffic intensity when the total number of WiFi Direct devices is 10. Meanwhile, for a fixed traffic intensity $\rho = 8$ but different total number of WiFi-Direct devices in a HAN, the outage probability of the multiuser selection scheme is illustrated in Fig. 3.

From Figs. 2 and 3 we can see that (1) the outage probability changes dramatically at low average SNR but has a constant tendency when the average SNR is relatively high. (2) The traffic intensity of a certain HAN in smart grid has considerate impact on the outage probability of multiuser selection scheme. Intensive traffic intensity indicates frequent switching between active state and doze state, and high probability that more devices are involved in the uplink communication with the smart meter. Consequently, a lower outage probability is achieved by selecting the link with maximum SNR among all the active links. (3) It is figured out that the values of steady state probability P_K for larger K are rather small when $M = 12$ and $M = 16$ according to (8), so that the HANs with $M = 12$ and $M = 16$ exhibit similar characteristics, which could explain the approximate overlap between the curves of outage probability with $M = 12$ and $M = 16$ in Fig. 3.

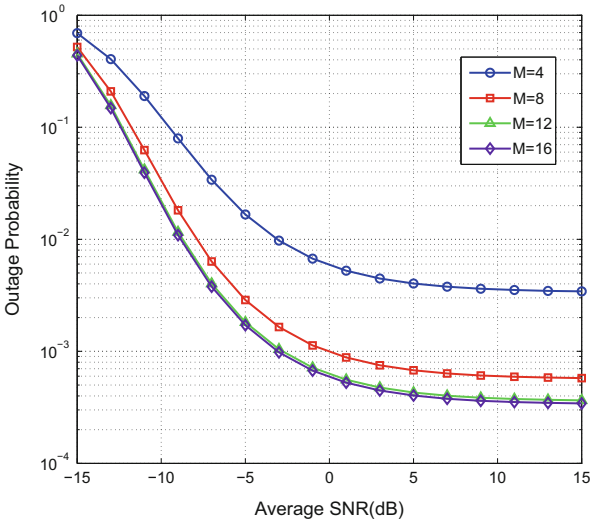

Fig. 3 Outage probability of multiuser selection scheme in a HAN, $\rho = 8$

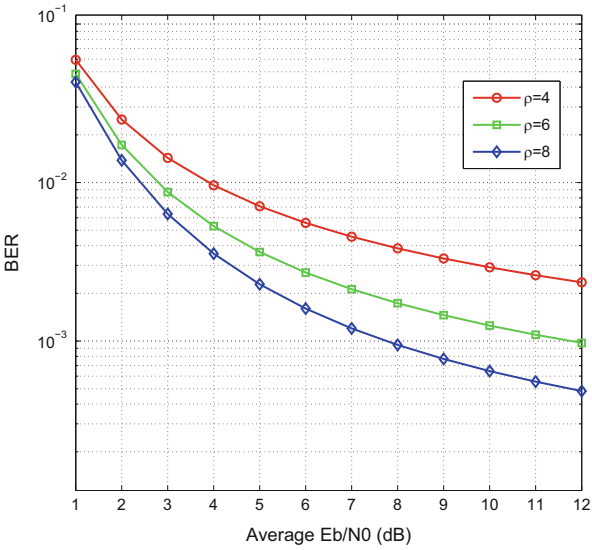

Fig. 4 BER of multiuser selection scheme in a HAN with BPSK, $M = 5$

4.2 Bit Error Rate

The numerical values of BER are determined by mainly three factors: the total number of WiFi-Direct devices in a HAN, the traffic intensity and the modulation scheme of symbols. The numerical results of BER are compared with two fixed factors and the other changing parameter. Particularly, the BER with BPSK due to different traffic intensity when $M = 5$ is shown in Fig. 4. Figure 5 illustrates the

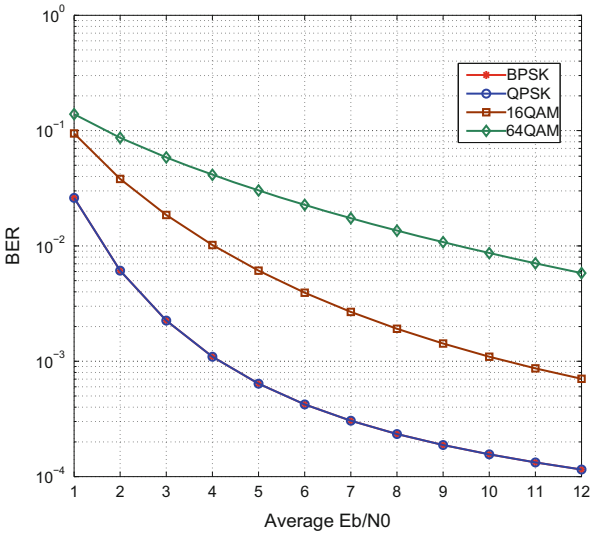

Fig. 5 BER of multiuser selection scheme in a HAN with $\rho = 8, M = 10$

BER with four kinds of modulation schemes: BPSK, QPSK, 16-QAM and 64-QAM when $\rho = 8, M = 10$. For a certain traffic intensity of $\rho = 8$ and BPSK modulation scheme,

According to Figs. 4 and 5, it is obvious to see that (1) for a certain HAN in smart grid, larger traffic intensity results in better BER performance with fixed modulation scheme and average SNR. (2) Different modulation schemes have obviously different impact on the BER performance. It is noteworthy that BPSK and QPSK exhibit the same BER performance even over the fading channel.

5 Conclusions

In this paper, the performance of multiuser selection scheme that is employed in HANs of Smart Grid with WiFi Direct technique under indoor S–V channel environment is evaluated from two aspects: outage probability and symbol error rate. The closed-form outage probability expression is derived from the amplitude distribution property of indoor S–V channel gain, combining with the characteristic that each WiFi-Direct device would alternate between active state and doze state due to power saving mechanism. In addition, the BER expressions of different modulation schemes under AWGN channel are included in the calculation of BER of the multiuser selection scheme. Numerical results show that the performance of multiuser selection scheme in HANs of Smart Grid is related with several factors, i.e. total number of devices in HANs, traffic intensity, modulation scheme, and etc.

Acknowledgements This work was supported by U.S. National Science Foundation under Grant CNS-1116749.

References

1. Cover MT, Thomas AJ (2006) Elements of information theory, 2nd edn. Wiley, Hoboken, NJ
2. Ghassemi A, Bavarian S, Lampe L (2010) Cognitive radio for smart grid communications. In: 2010 First IEEE International Conference on Smart Grid Communications, pp 297–302
3. Goldsmith A (2005) Wireless communications. Cambridge University Press, Cambridge
4. He Y, Yuan R, Ma X, et al (2008) The IEEE 802.11 power saving mechanism: An experimental study. In: IEEE Wireless Communications and Networking Conference (WCNC), pp 1362–1367
5. Kim TT, Poor HV (2011) Scheduling power consumption with price uncertainty. IEEE Trans Smart Grid 2(3):519–527
6. Li Z, Liang Q, Cheng X, et al (2012) Outage performance evaluation over rayleigh fading channels of WiFi direct networks in smart grid application. In: 2012 I.E. Innovative Smart Grid Technologies Asia (ISGT Asia), pp 1–5
7. Liu X (2012) Quality of optical channels in wireless SCADA for offshore wind farms. IEEE Trans Smart Grid 3(1):225–232
8. Saleh AAM, Valenzuela RA (1987) A statistical model for indoor multipath propagation. IEEE J Sel Area Comm SAC-5(2):128–137
9. Tan BS, Li KH, Teh KC (2010) Performance analysis of LDPC codes with selection diversity combining over identical and non-identical rayleigh fading channels. IEEE Comm Lett 14 (4):333–335
10. Wi-Fi Alliance (2010) Wi-Fi for the smart grid. http://www.wi-fi.org/knowledge_center_overview.php?docid=4686, Sep
11. Yang L, Kang M, Alouini MS (2006) Performance analysis of multiuser selection diversity. IEEE Trans Veh Tech 55(6):1848–1861
12. Yang L, Kang M, Alouini MS (2007) On the capacity-fairness tradeoff in multiuser diversity systems. IEEE Trans Veh Tech 56(4):1901–1907
13. Yoon H, Kim J (2010) Collaborative streaming-based media content sharing in WiFi-enabled home networks. IEEE Trans Consum Electron 54(4):2193–2200
14. Zhang X, Lv Z, Wang W (2008) Performance analysis of multiuser diversity in MiMO systems with antenna selection. IEEE Trans Wireless Comm 7(1):15–21
15. Zhang Y, Wang L, Sun W, et al (2011) Distributed intrusion detection system in a multi-layer network architecture of smart grids. IEEE Trans Smart Grid 2(4):796–808

Research of Coal Temperature Early Warning Method Based on Curve Fitting

Yujun Leng, Jun Huang, Qiang Wu, Jianglong Zhu, and Shilin Xiao

Abstract The main purpose of this paper is to introduce a kind of coal temperature early warning method based on Curve fitting. The method is to analysis the real-time sampled data, obtain the fitting sequence, plot the fitted curve, and Calculating time difference, then judge warning level and take appropriate measures. This early warning method can timely reaction temperature parameters in mine anomalies, and take reasonable precautions, automatically, effectively reduce the incidence of coal mine safety accidents.

Keywords Curve fitting • Coal temperature • Time difference • Early warning method

1 Introduction

Coal is the main body of China's primary energy. The coal industry carries the historic tasks of China's economic development, social progress and national revitalization [1]. With the development of the national economy, the demand for coal is also increasing year by year. However, while the coal industry makes great contributions to China's economic development, the mine accidents frequently threat to the miners seriously. Compared with developed countries, the safety of China's coal mine is not optimistic. In our country's basic industries, the coal is up

Y. Leng (✉) • J. Huang • J. Zhu
Chongqing Key Laboratory of Signal and Information Processing, Chongqing University of Posts and Telecommunications, Chongqing 400065, P. R. China
e-mail: lyj11abc@163.com

Q. Wu
Chongqing MAS Science & Technology Co., LTD, Chongqing 400065, P. R. China

S. Xiao
State Key Laboratory of Advanced Optical Communication Systems and Networks, Shanghai Jiao Tong University, Shanghai 200240, China

B. Zhang et al. (eds.), *The Proceedings of the Second International Conference on Communications, Signal Processing, and Systems*, Lecture Notes in Electrical Engineering 246, DOI 10.1007/978-3-319-00536-2_128,

to the accident and casualty largest industry, accounting for 60 % of industrial deaths over [2]. According to the statistics, in 2011 the coal mine mortality was 0.564 per one million tons, caused great economic loss and bad social influence.

In addition to the gas concentration, fire and heat damage is also an important reason of coal mine accidents. According to statistics, the 51.3 % of China's key coal mines exists the mine danger of spontaneous combustion, then, the mine temperature warning has gradually became an important topic in coal mine production safety [3].

At present, the warning of the temperature in the coal mine always use overrun warning by setting the temperature warning threshold, when the temperature reaches this threshold, the sound and light alarms. This method is the simplest and direct, but it has also some flaws. For example, the method can't determine the speed of temperature change, at the meantime, it lacks of reasonable measures taken by the different levels of warning, when the exception break out, after the alert was issued may not have enough time to take early warning measures, thus causing casualties [4, 5]. In order to solve the above problems, this paper put forward the temperature warning mechanism by curve fitting to calculate the time difference, it can effectively achieve the purpose of the security warning.

2 Overall Design

Temperature early warning method proposed in this paper are mainly collected real-time temperature as the data source, after the filtering algorithm we can obtain fitting data sequence. Draw the real-time temperature fitted curve with linear function in a certain period of time. According to the fitted curve, we can calculate the time difference and then compare with the setting warning time parameters to determine whether it is an abnormal data, if the data is abnormal, it will determine the warning level, and then to take early warning measures. The overall design process of the early warning program is shown in Fig. 1.

3 Forecast of Mine Temperature

Environment that overrun warning method widely used, the temperature monitoring system needs to mine the real-time temperature, so the mine temperature prediction has been neglected, the technology is not mature. This paper using the curve fitting method to achieve the purpose of the forecast mine temperature.

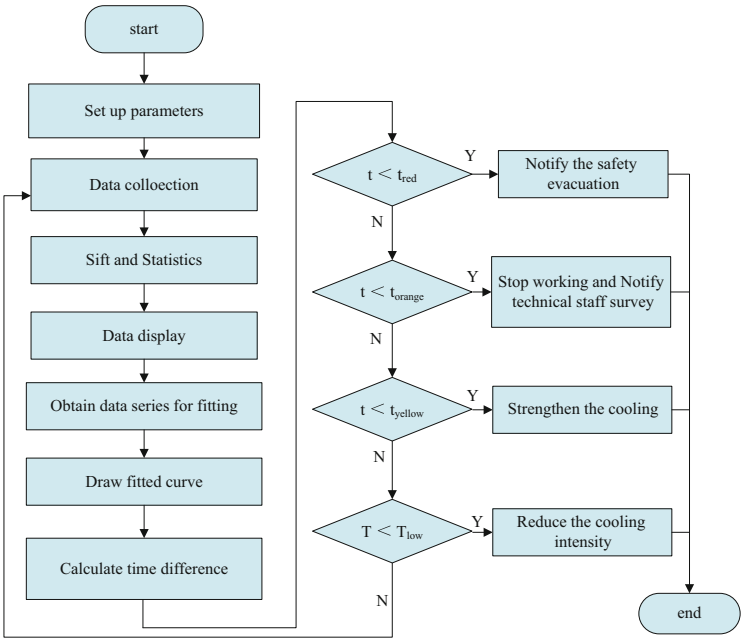

Fig. 1 The overall design

3.1 Obtain Fitting Sequence

In order to ensure the higher accuracy of fitting curve, the fitting sequence obtained can't be too short or too long. If it's too short, the data may be possess the special nature, and then leading to that reference value of the fitting curve has gone. On the contrary, too long will lead the fitting curve to be not obvious, affecting the accuracy of prediction of the temperature. Therefore, this paper get the fitting sequence using the following method: set the amplitude threshold value Tscope of the temperature variation amplitude, calculate the amplitude of the temperature change value ΔT each time, record three times consecutive ΔT, if every ΔT is smaller than Tscope, indicating that the temperature of the mine is normal or abnormal slightly. Twelve data points are used to draw the fitting curve, it is possible to response the overall variation trend of the reaction temperature. If every ΔT is greater than Tscope, indicating that the temperature is in an abnormal condition, it is gradually increased and a variation speed is relatively fast, in order to gain a clearer temperature change tendency, we get six data points to be used to draw the fitting curve.

The above temperature variation amplitude threshold needs to be set through the analysis of the actual situation of the mine.

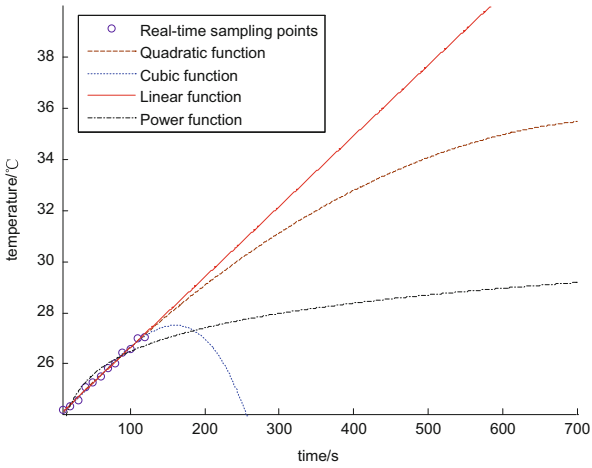

Fig. 2 Fitting curve of the usual functions

3.2 Select Fitting Function

In this paper, the temperature change in the actual inspection of a mine within a certain time, in their daily work, ventilation intensity is constant and the downhole temperature trend change very slow, only when an exception occurs, the temperature will change dramatically.

Data acquisition frequency is 10 s one time, to facilitate to explain the reason to select the fit function, the paper intercept one abnormal data and choosing its 12 data points as a fitting sequence Sn = {24.20 24.32 24.58 25.08 25.26 25.50 25.85 26.03 26.45 26.60 26.98 27.06}. Set the temperature variable is T, the time variable is t, the abscissa is time and the vertical axis is the temperature, then call Matlab, draw out several usual functions curve fitting, as shown in Fig. 2.

From Fig. 2 can be seen, quadratic function, cubic function, power function, such as non-linear function fitting curve will change very rapidly outside the scope of the data sequence. We found that the trend of the curve is influenced by the positional relationship of the last two data points larger through the observation curve, it is not suitable for the prediction of future temperature, while the linear function influence of the positional relationship of the last two data points is smaller, can be better able to describe the temperature change tendency within a certain period of time. This article uses the linear function to fit the temperature data.

3.3 Obtain Time Difference

The relevant parameters must be set before getting time difference, including the temperature upper limit T. According to the “Coal Mine Safety Regulations,” the

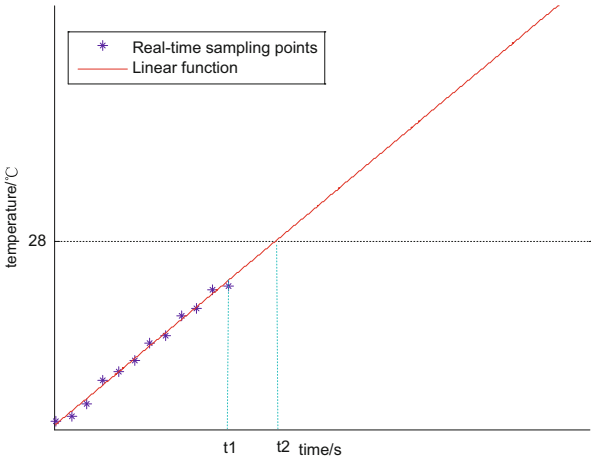

Fig. 3 Obtain time difference

underground temperature of a mine does not allow more than 28 °C (underground substation, substation chamber at 30 °C), to facilitate the interpretation of the principle of early warning method, this paper set the temperature upper limit is 28 °C, while the actual we set the upper and lower limits in conjunction with the actual situation of the mine ventilation and cooling rate in the temperature.

After fitting curve drawing, record abscissa t1 of this moment, find the fitting curve of temperature for 28 °C, record that point the abscissa of t2, as shown in Fig. 3.

According to the two abscissa the time difference can be calculated by the following Formula (1):

$$\Delta t = t2 - t1 \tag{1}$$

After getting the time difference, we can analysis the time difference to determine the current warning level, to take the appropriate measures.

4 Early Warning Processing

4.1 Early Warning Hierarchies

In this paper, the early warning method we studied adopts three-level warning method, the warning severity is divided from low to high: III level warning (yellow alert), II level warning (orange alert), I level warning (red alert). Due to the complexity of coal mine structure, there are many factors affecting the ability of the early warning measures implementation, including: roadway width, cooling speed of refrigerating equipment, staff safety evacuation speed, etc. Therefore the

mine's early warning level must be divided by the related technicists synthetically on the basis of the above-mentioned factors. It mainly sets three time difference standard to be the early warning trigger condition such as t_{red}, t_{orange}, t_{yellow}.

After the coal mine safety monitoring software calculating the time difference, it finds that the temperature is abnormal, it will start warning, according to the different warning levels for different sound and light alarm, and take corresponding early warning measures. At the same time, the software starts the GSM module to send alarm information in text form SM to the cell phone of the head in the region using the AT command [6]. The alarm information includes: abnormal temperature sensor number, installation location, temperature at the moment, time difference, warning level. This allows that the problems can be solved in time.

5 Experimental Test and Analysis of the Results

5.1 Build Test Platform

In order to verify the feasibility of the warning method described in this paper, we build test platform for testing. The data collection terminal of test platform uses three surface acoustic wave (SAW) temperature sensor tags, their ID is 01B1, 01B2, 01B3, the upper layer uses coal mine safety supervision system based on C# client software to analysis processing and display the temperature collected.

5.2 Test and Analysis

We placed 01B1 tag in the environment of normal temperature, held 01B2 tag gradually to close to the heat source which the temperature is close to 50 °C, 01B3 to 100 °C. Set the temperature upper limit is 28 °C, Standard time difference is as following: t_{yellow} is 240 s, t_{orange} is 120 s, t_{red} is 60 s, At the meantime, set the phone number when the warning is triggered to send a message to. The experimental results were shown in Figs. 4 and 5.

In Fig. 4, the monitored parameters of 01B2 tag is the real-time temperature data, the temperature begins to rise during 50 s, due to the temperature changes fast, the system selects six points as a fitting sequence. A straight line parallel to the x axis is the upper temperature limit, it can be seen from the figure, the time of the fitting curve reached the maximum temperature is 210 s, now the time is 100 s, so we can calculate time difference $\Delta t = 110$ s, at this time $\Delta t < t_{orange}$, it will trigger level II warning. As can be seen from Fig. 5, the warning information of the 01B3 tag which its temperature change fastest is also displayed, so the software system can process the data from different labels in background, if abnormal, then warning.

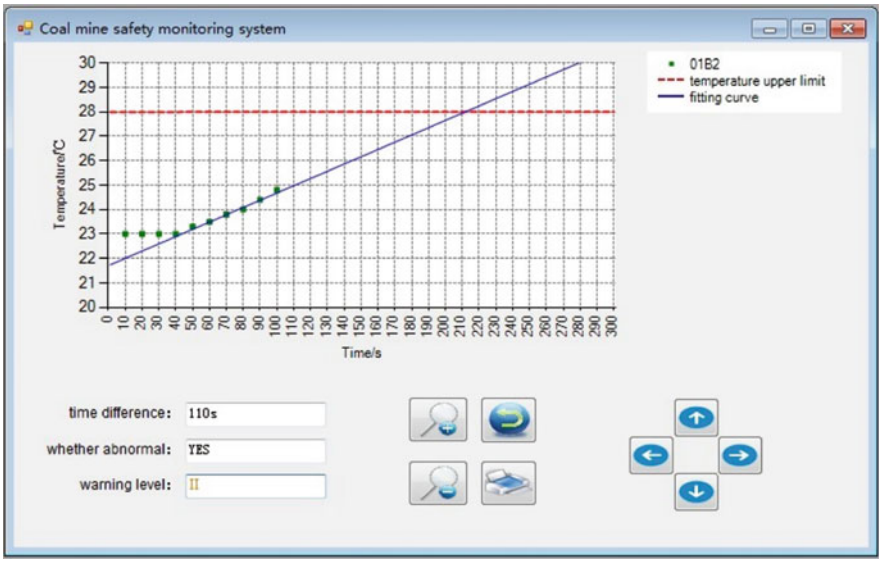

Fig. 4 Real-time temperature display

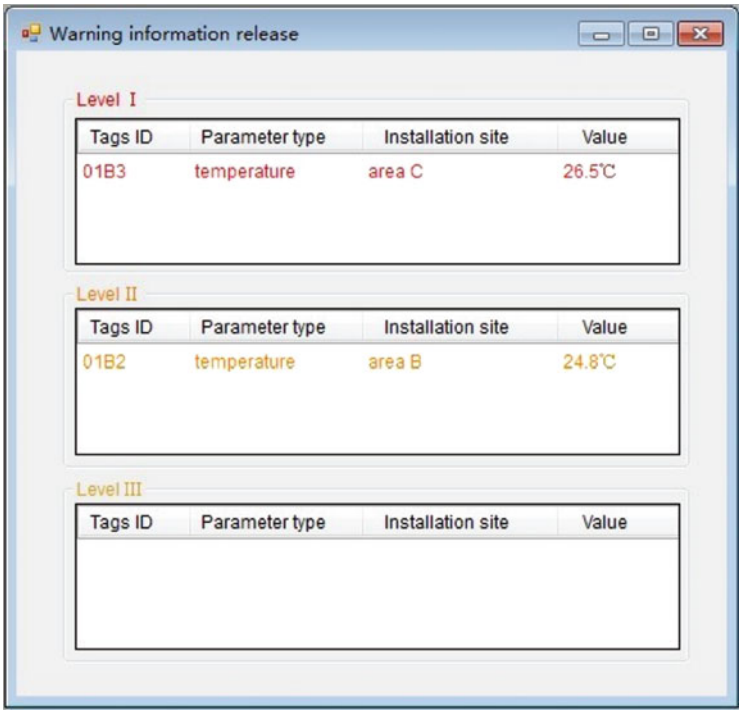

Fig. 5 Early warning information release

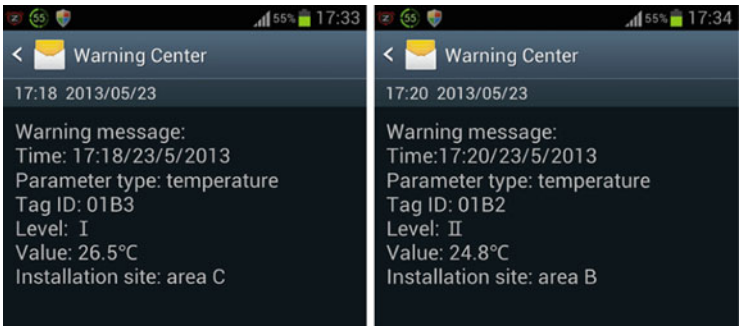

Fig. 6 The received warning message

At the same time, the software send warning information to the designated phone number. The received message is shown in Fig. 6.

6 Conclusion

In this paper, the coal temperature warning method adopt curve fitting method to predict the temperature and calculate the time difference, by comparing the time difference to the warning level, we can make warning judgment. Compared to the traditional overrun warning method, this method has the following advantages:

- It can judge the current speed of temperature changes and predict the temperature in the next period of time.
- Based on the standard of time, the warning level can be divides, and according to the actual situation of different mine, we can set a reasonable warning measures.

In summary, the method used in coal mines temperature warning will improve the safety of coal production to some extent.

Acknowledgments This work was supported by the Chongqing Municipal science and technology key research projects, China (No. cstc2012gg-yyjsB40003); Also was supported by the Project of State Key Laboratory of Advanced Optical Communication Systems and Networks, Shanghai Jiao Tong University(2011GZKF031114); Also was Supported by Natural Science Foundation Project of CQ (cstc2011jjA40043).

References

1. Notice of the State Council on Further Strengthening the safe production work [EB/OL] [2012.7.23], http://www.gov.cn/zwgk/2010-07/23/content_1662499.htm

2. Li SX, Wang WT, Xiao SY (2008) An analysis of the current situation of security production in Chinese coal enterprises and its influential factors. J Changsha Univ Sci Tech (Soc Sci) 2008:20–25
3. Peng L (2011) Fuzzy comprehensive assessment of mine natural fire risk. Xi'an, Shaanxi Coal, pp 24–25
4. Chen FK, Liu JZ, Yin H (2009) Brief probe into early warning mechanism of safety management at coal mines. Coal Mine Modernization. The American Mining Congress, Washington, DC, pp 50–51
5. Zhao Y, Yi XQ, Luo XS (2008) Formalization of task and resource for space-based early warning system. J Chongqing Univ Post Telecommun (Nat Sci Ed) 2008:500–502
6. Xie XF, Huang J, Tan CY (2013) The software analysis and design of power temperature monitoring system based on RFID, pp 23–26.

Continuous Detection Anti-collision Algorithm for EPC Gen2 RFID Systems

Zhenpeng Liu, Zhenyang Guan, Kaiyu Shang, Wenlei Chai, and Zhenchao Wang

Abstract Tag estimation can improve the throughput of the UHF passive RFID systems. It plays an important role in anti-collision algorithm. In order to reduce the complexity of the estimation algorithm and the hardware support, a new algorithm based on the continuous detection mechanism has been proposed. According to the different probability of the collision and idle, the number of the continuous detected slots must be set independently. This scheme can simplify the system and reduce the extra consumption by less detecting timeslot. Simulation results indicate the proposed scheme can improve the efficiency without complicate system.

Keywords RFID • Q-algorithm • Tag estimation • Continuous detection • Probability of collision

1 Introduction

Radio frequency identification (RFID) technology has been widely used as one of the key technology of the Internet of Things. Ultra high frequency (UHF) (860 – 960 MHz) identification with higher efficiency and further read range has been deemed to have bright future comparing with the lower one. In the RFID system, if there are multiple tags in the range of the antenna, tags will respond the reader simultaneously. Tag collision will happen inevitably. As a result, the

Z. Liu (✉)
College of Electronic and Information Engineering, HeBei University, BaoDing, China

Network Centre, HeBei University, BaoDing, China
e-mail: lzp@hbu.edu.cn

Z. Guan • Z. Wang
College of Electronic and Information Engineering, HeBei University, BaoDing, China

K. Shang • W. Chai
Network Centre, HeBei University, BaoDing, China

B. Zhang et al. (eds.), *The Proceedings of the Second International Conference on Communications, Signal Processing, and Systems*, Lecture Notes in Electrical Engineering 246, DOI 10.1007/978-3-319-00536-2_129,

collision problem has become the important factor that influences the efficiency and accuracy of RFID system.

The most popular international solution of anti-collision is the time division multiple access (TDMA) technology. Because the tag structure is simple and the TDMA scheme is convenient. In the low frequency band, mainly approaches include pure ALOHA algorithm, timeslot ALOHA algorithm, frame timeslot ALOHA algorithm, dynamic frame timeslot ALOHA algorithm, etc. In the high frequency band, the solution is the EPCglobal UHF Class1 Gen2 algorithm [1] (standard Q-algorithm) which has been promulgated by the International Organization for Standardization in 2005. Although due to the standard Q algorithm has the problem that it adapt the Q value slowly especially there are large number of tags [2], the tag estimation mechanism has been introduced into the algorithm. In other hand, these algorithms will increase the complexity of the system unexpectedly. In order to solve those problems, a new improved algorithm called an anti-collision algorithm for RFID based on continuous detection has been proposed in this paper. This approach can determine the number of continuous detection slots independently according to the difference of the idle and collision probabilities.

2 Standard Q-Algorithm

The standard Q-algorithm promulgated by the EPC Gen2 is general similar as the dynamic frame timeslot ALOHA anti-collision algorithm (DFSA) actually. Unlike the traditional DFSA, the Gen-2 algorithm allows early adjustment of frame length within each slot frame. The frame size can be decided by (1). This early adjustment can improve read performance when frame length is extremely appropriate [3].

$$Frame = 2^{Q} \tag{1}$$

During the process of identification there will be three states: Idle state (idle),no tag response; successful state (succeed),only one tag response; collision state (collision),multiple tags response.

$$Q = round(Qfp) \tag{2}$$

In order to adjust the length of identification frame, floating point number Q_{fp} and accumulating parameter c (c∈[0.1,0.5]) are used to adjust Q. Q value is calculated by round Q_{fp} (2). When the interrogator observes collision state, the Q_{fp} value increases by c. When the interrogator observes idle state, the Q_{fp} value decreases by c. When the interrogator observes succeed state, the Q_{fp} value remains unchanged. The method for choosing the slot-count parameter is shown in Fig. 1.

Main command of inventory round: Query, QueryRep, QueryAdjust [4].

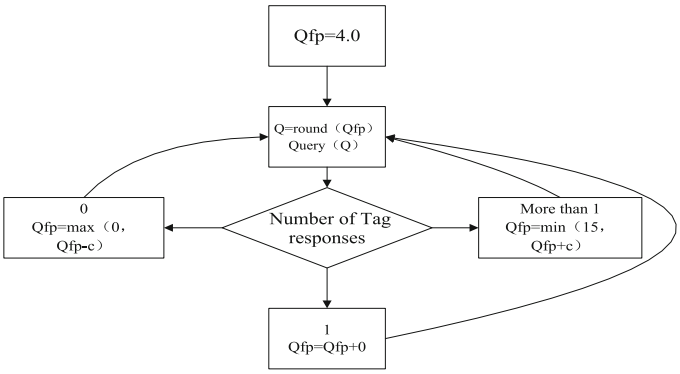

Fig. 1 Q value adjustment flow chart

Query: Initialize identification program. Set the initial Q of each tag. Each tag counter will select a number in the range $[0,2^{Q}-1]$randomly. Tags with the random number zero will reply the reader in this timeslot immediately.

QueryRep: Auto decreased command. If tags receive this command, their counters will be decreased by 1. Tags with the number zero will reply the reader.

QueryAdjust: Adjust the value of Q. When the value of Q has been changed by (2), reader will send this command. Tags choose another number between $[0,2^{Q}-1]$, then a new round of identification will start.

QueryRep command will be sent after the idle and succeed state. If the round value of Q_{fp} is different from the current Q value, the interrogator will send the QueryAdjust command to adjust the Q value for identifying unread tags. Call these commands in accordance with the provisions of the order. The reader will identify the tags constantly until all tags are identified.

3 An Anti-collision Algorithm Based on Continuous Detection

Although the EPCglobal Gen-2 provides early adjustment of frame length for anti-collision algorithm, the parameter Q can't obtains appropriate initial value quickly especially in the excessive tags situation. So estimation number of tags should be executed before the identification started. The value of Q will be selected by the estimation result. Studies have provided the relationship between timeslot number and tag number. When the timeslot number is equal to the unread tags, the system will reach the maximum efficiency [5]. These methods which provided by previous studies mainly include the lower limit value algorithm (Low Bound, LB) [6], Schoute estimation algorithm [7], chebyshev inequality estimation algorithm [8], etc. But these tag estimation algorithms need a strong hardware support and will

bring huge additional power consumption in reality. Relative to the simple structure of reader, it will bring lots of operation cost.

In order to solve this problem, a more simple tag estimation method called anti-collision algorithm based on continuous detection is proposed. Basic idea: Set the first m slots as estimating timeslots and monitor them. Get the communication state (free, success, collision) of the first m slots. If the continuous idle slots or collision slots have been detected, the value of Q will minus or plus 1 immediately. In this way, the interrogator can adjust the frame length only after three or four time slots. So identification process will be more effective. Unlike previous algorithm, this approach determine the number of continuous detection slots independently.

Next three parts, the principle of the continuous detection mechanism will be given.

3.1 Difference of the Monitoring Slots

Suppose there are n tags to be read. According to the Bernoulli experiment, if there are x tags choose a same slot, the probability will be calculated by:

$$P_e = C_n^x \left(\frac{1}{N}\right)^x \left(1 - \frac{1}{n}\right)^{n-x} \tag{3}$$

The probability of the idle slot is calculated by:

$$P_{idle} = C_n^0 \left(\frac{1}{N}\right)^0 \left(1 - \frac{1}{n}\right)^n \tag{4}$$

The probability of the success slot is calculated by:

$$P_{suc} = C_n^1 \left(\frac{1}{N}\right)^1 \left(1 - \frac{1}{n}\right)^{n-1} \tag{5}$$

The probability of the collision slot is calculated by:

$$P_{col} = 1 - P_{idle} - P_{suc} \tag{6}$$

Calculate the derivative of P_{suc} and set it equal to 0.

If P_{suc} want to approach the maximum, there must be $N = n$ and $P_{suc}(max) = 0.368$.

When $N = n$, $P_{idle} = (1\text{-}1/n)^n$ and $P_{suc} = (1\text{-}1/n)^{n\text{-}1}$.

If n is big enough, $P_{suc} \approx P_{idle}$, then:$P_{col} = 1\text{-}\ P_{idle}\ -\ P_{suc} = 1\text{-}0.368\text{-}0.368 = 0.264$.

Obviously, in the condition of high efficiency the probability of collision time slot is less than the probability of idle time slot, $P_{col} < P_{idle}$. So the detected number of continuous idle slots (m_i) should bigger than the collision ones(m_c).

$$m_i > m_c \tag{7}$$

3.2 Analysis of the Continuous Idle Slots

Suppose n' is the estimated number of tags. Then define the estimate error as: $dev(n') = \frac{|n-n'|}{n}$

dev(n') is used to measure the deviation of tag estimation.

Identifying tags is a Poisson process. Due to the concept of the timeslot, the process has been simplified. The number of the estimated value is n'. Each frame has N slots. For monitoring timeslot, the probability for first m_i continuous idle slots is:

$$P_{m_i} = \left(1 - \frac{m_i}{N}\right)^n = \left(1 - \frac{m_i}{N}\right)^{\frac{N}{m_i} * \frac{m_i n}{N}} \approx \left(\frac{1}{e}\right)^{\frac{m_i n}{N}} \tag{8}$$

Set $\lambda = n/N(\lambda > 0)$,then $P_{m_i} = (1/e)^{m_i \lambda}$ (m is positive integer). In (0,+∞) area, P_{m_i} is monotone decreasing function. Then the critical value of dev(n') will be calculated as: dev(N) = dev(2N).

Then $dev(N) = \frac{|n-N|}{n} = \frac{N-n}{n} = \frac{1}{\lambda} - 1$, $dev\left(\frac{N}{2}\right) = \frac{\left|n-\frac{N}{2}\right|}{n}$.

As $\frac{N}{2} \le n \le N$, then $dev\left(\frac{N}{2}\right) = \frac{n-\frac{N}{2}}{n} = 1 - \frac{1}{2\lambda}$.

Set dev(N) $\ge$ dev(N/2),so $\lambda = 0.75$.

As a result, when $\lambda < 0.75$,dev(N) $\ge$ dev(N/2). Set $\lambda = 0.75$, then $P_{m_i} = (1/e)^{0.75 m_i}$.

In the probability theory, if the probability is very close to zero (which means event appears with very low frequency in a large number of repeated tests), this event will be called as the small probability event. Range (0.01 – 0.05) is commonly used as the standard range.

$m_i = 3$, $P_{mi} \approx 0.1054$; $m_i = 4$, $P_{mi} \approx 0.0498$.

When $m_i = 4$, P_{m_i} achieves the requirement and choose 4 as the continuous idle slots finally. So m_i is set to 4, which means that when 4 continuous idle slots are detected $\lambda > 0.75$ would be the small probability event. Then $\lambda \le 0.75$ can be inferred. The slots number of each frame will be N/2 and that will perform better than *N*.Q will minus 1, Frame = N/2.

3.3 Analysis of the Continuous Collision Slots

When collision happen, there must be multiple tag counters value are zero. Then the system will start the collision algorithm. Processing method: Change collision tags counters value from 0 to 0 XFFFF. These collision tags will stay in epicyclic inventory and wait for the system adjusting Q and dispersing the collision tags. This process continues until the whole inventory cycle is end.

Because $m_i > m_c$, the range of m_c can be inferred. It should be {2,3}. The probability for first m_c continuous collision slots is:

$$P_{m_c} = P_c{}^{m_c} = \left[1 - \left(1 - \frac{1}{N}\right)^n - \frac{n}{N}\left(1 - \frac{1}{N}\right)^{n-1}\right]^{m_c}$$
$$= \left[1 - \left(1 - \frac{1}{N}\right)^{N*\frac{n}{N}} - \frac{n}{N}\left(1 - \frac{1}{N}\right)^{N*\frac{n-1}{N}}\right]^{m_c} \quad (9)$$
$$= \left[1 - \left(\frac{1}{e}\right)^{\frac{n}{N}} - \frac{n}{N}\left(\frac{1}{e}\right)^{\frac{n}{N}-\frac{1}{N}}\right]^{m_c}$$

As $\lambda = \frac{n}{N}(\lambda > 0)$, then $P_{m_c} = \left[1 - \left(\frac{1}{e}\right)^{\lambda} - \lambda\left(\frac{1}{e}\right)^{\lambda-\frac{1}{N}}\right]^{m_c}$

In (0,+∞)area, P_{m_c} is monotone increasing function.

As $N \leq n \leq 2N$,

$dev(2N) = \frac{2N-n}{n} = \frac{2}{\lambda} - 1$ $dev(N) = \frac{|n-N|}{n} = \frac{n-N}{n} = 1 - \frac{1}{\lambda}$

Set dev(N) = dev(2N), then $\lambda = 1.5$ When $\lambda > 1.5$, dev(N) ≥ dev(2N).

Set $\lambda = 1.5$, then P_{m_c} value can be calculate, When N is big enough, there is λ-1/N ≈ λ.

$m_c = 2$, $P_{mc} \approx 0.1958$;$m_c = 3$, $P_{mc} \approx 0.0866$.

When $m_c = 3$, P_{m_c} is very near to the range (0.01,0.05)and it has achieved the requirements of the range of m_c ({2,3}). Choose 3 as the continuous collision slots finally. So m_c is set to 3, which means that when 3 continuous collision slots are detected $\lambda < 1.5$ will be the small probability event. Then $\lambda \geq 1.5$ can be inferred. The slots number of each frame will be 2N and that will perform better than N. Q will plus 1, Frame = 2N.

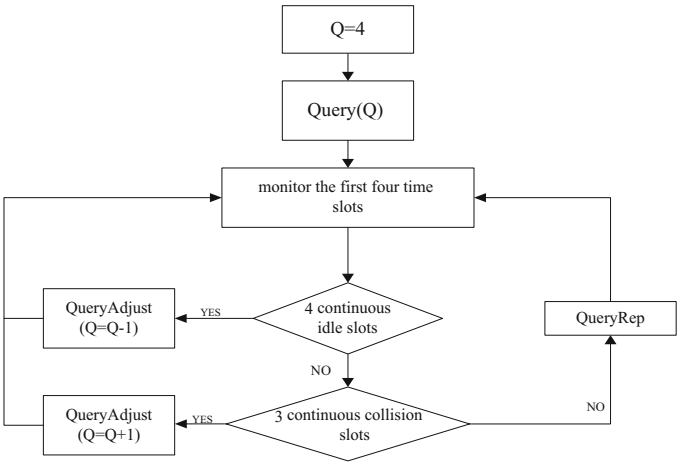

Fig. 2 The proposed continuous detection mechanism

3.4 An Anti-collision Algorithm Based on Continuous Detection

In conclusion, the process of the new algorithm can be described as follow: In the beginning of each inventory cycle, the reader will monitor the first four slots. If there are four continuous idle slots or three continuous collision slots be detected, the reader will order Q minus or plus 1. Then the reader send the Query Command again and start a new inventory round. This continuous detection mechanism is shown in Fig. 2. According to this method, the interrogator can adapt the frame length only after four slots which is more quickly than the normalized rule.

4 Simulation Result and Performance Comparison

We use MatLab to simulate the improved algorithm and compare it with the conventional Q-algorithm. G (the average packet exchange capacity) is offered traffic and it indicate the load of the interrogator. Define the system efficiency (S) as follows:

$$S = {}^{Splen}/_{Srate now\_time} \tag{10}$$

Splen is the sum of packet length. Srate is the symbol rate. now_time is the time that identify all tags. So S can also be described as:

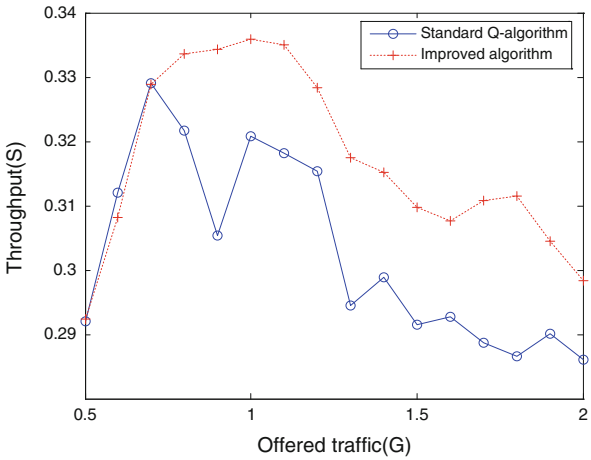

Fig. 3 Throughput of system

$$S = \frac{Packet\ transmission\ time}{Tag\ identification\ time} \tag{11}$$

When simulating this program, the scope of G is [0.5,2.0]. Hundred times tests have been done for each tag. The bit rate is 512 kpbs and the symbol rate is 256 kpbs, packet length is 128, normalized transmission delay is 0.01 s. Then simulate the standard Q-algorithm in the same experiment environment.

From Fig. 3 we can get conclusions as follows: (1) When the offered traffic G is same, the improved algorithm identification efficiency S is higher than standard Q value algorithm. It is closer to the theoretical optimum. The improved quantity is about 3%; (2) With G (number of tags) increasing, throughput will increase firstly but then decrease. The decline of the improved algorithm is less than standard Q-algorithm. The influence of increasing number of tags is smaller than the standard Q-algorithm. System has better stability comparing to the pure ALOHA, timeslot ALOHA (SA), frame timeslot ALOHA (FSA) algorithm. These algorithms will make the identification efficiency decline seriously when tags increase rapidly [9]. The improved algorithm has advantages.

Average Delay time is defined as:

$$ADT = \frac{Tplen}{Srate * spend} * \frac{Srate}{plen} \tag{12}$$

Tplen is the sum of all the identify date length, spend is the number of packet. Then ADT is normalized.

From Fig. 4 we can get conclusions as follows: (1) Continuous detection mechanism has decreased average time delay of the system significantly, which also means that it won't bring much extra consumption and the system become more efficient. (2)With G (tags number) increasing, the average delay of the system

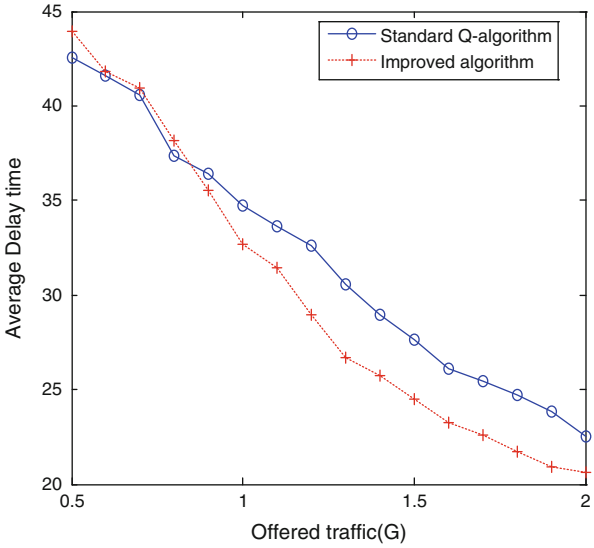

Fig. 4 Average delay time of system

would decrease gradually. So advantages of the new algorithm will become more and more obviously especially for the massive tags.

We can draw the conclusion through the experimental results: The new algorithm not only improves the system efficiency but also enhances the ability to confront the problem of tags increasing quickly.

5 Conclusion

Tag estimation algorithm plays an important role in the anti-collision algorithms of RFID UHF systems. In order to reduce the complexity of the tag estimation and the demand of high-level hardware support, the continuous detection mechanism has been introduced into the tag collision algorithm. The difference between the collision probability and idle probability has been proved by the math analysis. Then the number of the continuous frame must be considered independently (3 and 4). Simulation results prove that the new algorithm speeds up the frame length adjustment and improves the recognition efficiency without increasing any complexity of the system. It can also reduce the average delay time and enhance the ability for dealing with the surging tags.

References

1. EPC Global (2006) ISO18000-6c. EPC® radio-frequency protocols class-1 generation-2 UHF RFID protocol for communications at 860 MHz–960 MHz version. International Organization for Standardization. Singapore
2. Chen Wen-Tzu (2012) A new RFID anti-collision algorithms for the EPCglobal UHF Class-1 Generation-2 standard. Ubiquitous Intelligence & Computing and 9th International Conference on Autonomic & Trusted Computing (UIC/ATC), Fukuoka, 4–7 September, 2012, pp 811–815
3. Maguire Y, Pappu R (2009) An optimal Q-algorithm for the ISO 18000-6C RFID protocol. IEEE Trans Autom Sci Eng 6(1):19–20
4. Zhen-wei H, Ke-fei S (2011) Improved anti-collision Q-algorithm for RFID system. J Comput Eng Des 32(7):2314–2318
5. Li B, Wang J (2011) Efficient anti-collision algorithm utilizing the capture effect for ISO 18000-6C RFID Protocol. IEEE Commun Lett 15(3):352–354
6. Jae-Ryong Cha, Jae-Hyun Kim (2006) Dynamic framed slotted ALOHA algorithms using fast tag estimation method for RFID systems, Proceedings of the IEEE International Conference on Communication Technology, 8–10 January, 2006, pp 768–772
7. Inwhee Joe, Juno Lee (2007) A novel anti-collision algorithm with optimal frame size for RFID system. 5th ACIS International Conference on Software Engineering Research, Management & Applications, Busan, 20–22 August, 2007, pp 424–428
8. Qing-qing L, Hong-wu L, Xiao-lin Z (2011) An anti-collision algorithm based on unequal timeslots in radio frequency identification system. J Electron Inform Rep 31(11):2628–2633
9. Jin W, Ling-zhi Y, Gen-ping W (2011) Research on an enhanced anti-collision algorithm for RFID. J Comput Eng Sci 33(6):182–185

A Strategy of Network Coding Against Wiretapping Attack Based on Network Segmentation

Rong Du, Chenglin Zhao, Shenghong Li, and Jian Li

Abstract Compared with the traditional route-based network theory, there are lots of characteristics and advantages of network coding technology in Wireless Sensor Networks (WSN). At the same time, it is facing a variety of security threats, especially wiretapping Attack. Existing network coding security policies are mostly focused on building secure coding strategy, compared to the secure coding design strategies, security topology design strategies are much less. In this paper, we propose a weakly-secure network topology algorithm based on network segmentation. Simulations show that the proposed strategy can prevent cooperative eavesdroppers from acquiring any useful information transmitted from source node to sink node.

Keywords Network segmentation • Weakly-secure • Network coding • Wiretapping attack

1 Introduction

Different from traditional approach that a forwarder always duplicates every forwarding message, network coding [1, 2] is a new technique that allows intermediate nodes to encode multiple input messages together to form multiple output messages. Network coding can maximize the throughput of multicast networks. In 2003, Li [3] demonstrated that with a finite field size, the maximum flow from the

R. Du • S. Li (✉) • J. Li
School of Electronic Information and Electronic Engineering, Shanghai Jiao Tong University, Shanghai 200240, P.R. China
e-mail: durongorc@163.com; shli@sjtu.edu.cn

C. Zhao
School of Information and Communication Engineering, Beijing University of Posts and Telecommunications, Beijing 100876, P.R. China
e-mail: clzhao@bupt.edu.cn

B. Zhang et al. (eds.), *The Proceedings of the Second International Conference on Communications, Signal Processing, and Systems*, Lecture Notes in Electrical Engineering 246, DOI 10.1007/978-3-319-00536-2_130,

single source to sinks can be achieved by linear network coding. Because of this theory, network coding has been widely used in both wired networks and wireless networks.

Network coding systems is facing various attacks. Based on attack models, existing studies on secure network coding can be separated into two groups. Polluting attacks (active attack) [4–8] and Wiretapping attacks (passive attacks) [9–21]. The focus of this paper is the wiretapping attack, defined by Cai et al. [9]. In this attack, adversaries try to wiretap a subset of the links and acquire enough data to decode the complete packet that pass through the network. Feldman et al. [10] proposed a coding scheme in small infinite field at the expense of a small amount of bandwidth. Cai and Yeung [11, 12] proposed a multicast network coding against wiretapping attacks. Chan [13] gave the boundaries of the multicast capacity in secure network coding. Bhattad and Narayanan [14] proposed a weakly-secure network coding system. On the basis of [14], Silva [15] proposed a general weakly-secure network coding system. When the calculation ability of eavesdroppers is limited, Jain [16] designed a weakly-secure networking system by using One-way function. In [17, 18], the authors discussed the security issues in the light of the different conditions and different other safety requirements in WSN. Fancsali et al. [19–21] did the corresponding research and gave the respective security coding system.

Most existing researches are mainly concentrated on secure coding design with a given topology, but there is almost no research in secure topology design. In some small network, topology design performance more convenient than complicated coding design algorithm.

In view of the fact, the secure topology design is worthy of study. In this paper, we study security policy in a topology angle and propose a weakly-secure network topology algorithm based on network segmentation. The rest of paper is organized as follows. In Sect. 2 we discuss related work and the security goals we aim to. We discuss the problem and present an algorithm for secure network code design in Sect. 3. Performance evaluation is addressed in Sect. 4 and concluded the paper in Sect. 5.

2 Problem Statement

2.1 Network Coding

In traditional communication networks, a forwarder always duplicates every forwarding messages, network coding is a new technique that allows intermediate nodes to encode multiple input messages together to form multiple output messages. Figure 1b is a classic example of network coding, each link has unit capacity. Node W encodes the message that transmitted from W to X through linear combination $b1 \bigoplus b2$. Thus, the source S transmitted 2 bit stream b1 and b2 can

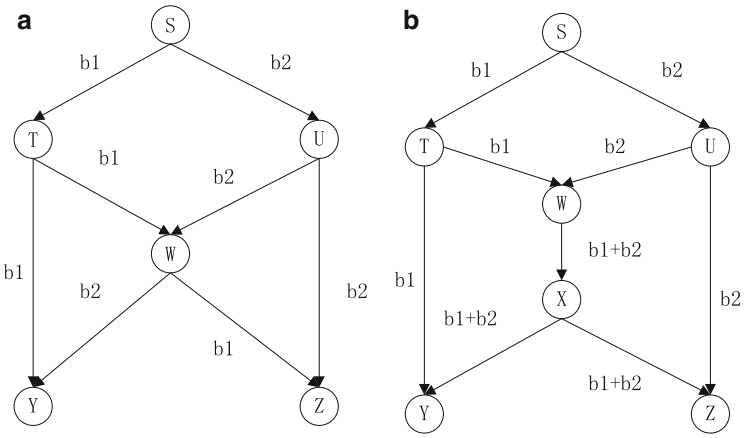

Fig. 1 Network coding

multicast to the nodes Y and Z simultaneous, the transmission rate can achieve the multicast rate of 2 bits per unit time.

2.2 System Model

In our study, a directed acyclic graph $G = \langle V,E \rangle$ is considered, where V and E are the node set and the edge set respectively. Each edge has the same unit capacity, which is 1 data stream unit per time slot. Source node S generates and sends out an n symbols message vector $X = (x_1, x_2, \cdots x_n)^T$ in a finite field F_q. $C_{\min}(G)$ is the minimum cut of G, the capacity $C_{\min}(G)$ is the maximal possible information rate of network G. In linear coding systems, the messages on outgoing edges of node v_n are linear combinations of messages on its incoming edges. We can understand each edge of the network carries an equation of source symbols.

2.3 Threat Model and Security Goals

For secure linear network coding, there are mainly two secure models in previous, Shannon-secure and weakly-secure. The difference of these two classes is that the former does not allow any information leakage and the latter disallows any meaningful information leakages. For example, given two data streams x_1 and x_2, in weakly-secure schemes, the adversaries are permit to get the combination value of $x_1 + x_2$ but not x_1 or x_2 alone; while in Shannon-secure, they cannot learn neither of them. In our paper, we focus on design weakly-secure network coding schemes.

In wiretapping attack, the malicious nodes are able to gain access to the information transmitted on these nodes. Suppose the positions of malicious nodes are known. And they can cooperate with each other to decode the packet sent from the source S. precisely, they can wiretap on a collection of $M = \langle M_1, M_2, \cdots M_K \rangle$ where M represents a set of malicious nodes. In this paper, our security goal is to prevent the source information from leaking to the adversaries.

3 Problem Analysis Proposed Scheme

3.1 Related Work

Assume $C_G(s,t) = k$, for any intermediate node v_i in G, if the In (v_i) is less than the capacity of the graph $C_G(s,d)$, then for sufficiently large size q, the generated network code is said to be secure with high probability, because the intermediate node v_i cannot recover any of the k symbols based on $k - 1$ or fewer linear equations. On the other hand, if $C_G \leq |\text{In}(v_i)|$, the security is said to be topology dependent, the network is considered secure if and only if $rank(in(v_i)) < C_G$.

In [22], the sibling work of this paper, we analyzed how the topology design influenced the security of networks, and we proposed a secure strategy against nodes conspiracy attack by topology design. This method is suitable for the small network environment, when in a large network, the wiretapping nodes becomes more, faster increase in the number of the link that needs to be removed. Therefore, we propose a strategy of network coding against wiretapping attack based on network segmentation.

3.2 Security Analysis and Discussion

Figure 2 is a directed acyclic graph and each link has a unit capacity. The source node s wants to transmit some information to the destination node t without leaking meaningful information to the wiretappers. Suppose there are m malicious nodes, each node have n incoming links $C_G(s,t) = k$. We need to remove $mn - k$ links to ensure the network security. If we divide the network into two sub-networks, assume that malicious nodes are uniformly distributed, we just need to remove approximately $^{mn-k}/_{2}$ links to the network security.

In Fig. 2, We randomly generate a 50-node network diagram, after path enforcement, we get a directed graph $G(V,E)$. The entire network is divided into two sub-networks $G_1(V_1,E_1)$ and $G_2(V_2,E_2)$ by the red line, the dashed line is the link to be removed. $C(G_1) = C(G_2) = 3$, any one of the sub-network is safe and leads the whole network security.

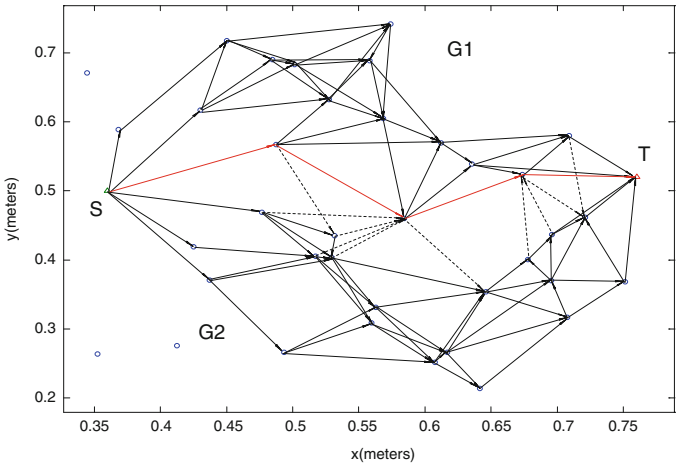

Fig. 2 Division chart of the network

How to find the best split routing is the problem that we mainly faced with, we get two objective functions.

We know that the min-cut sum of the two sub-networks is no more than the min-cut of the whole network:

$$C_{G_1} + C_{G_2} \leq C_G \tag{1}$$

To ensure the throughput of the network, the divided maximum flow as close as possible to the original maximum flow.

We find the split routing, remove the dashed links, the removed links E_{p_1}. Then we pick one sub-network, with the algorithm of [22], the removed links E_{p_2}.

$$E_p = E_{p_1} + E_{p_2} \tag{2}$$

The two objective functions are max $(C_{G_1} + C_{G_2})$ and min E_p.

4 Simulation and Discussion

4.1 Simulation

In this section, simulations are conducted based on ns-2 simulator and MATLAB to evaluate the effectiveness of proposed algorithm. The network is defined by these parameters, the number of nodes, N, (the number of edges, E_{all}), the probability of malicious nodes in intermediate nodes, p. the removed links E_p. The algorithm in

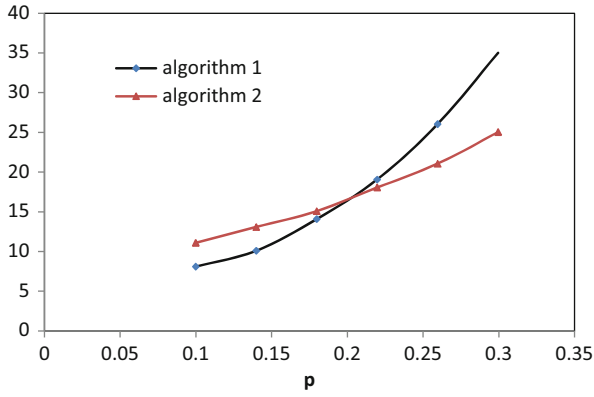

Fig. 3 Removed links E_p vs. p

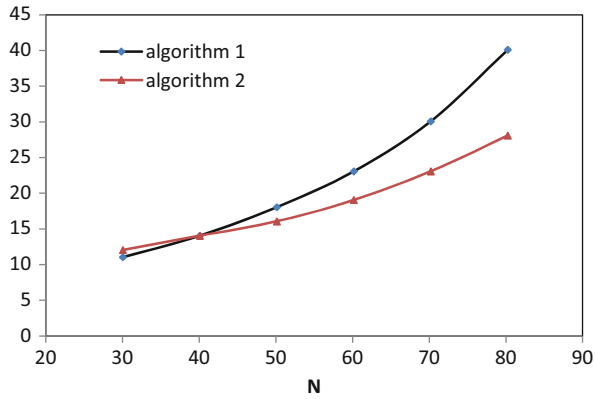

Fig. 4 Removed links E_p vs. N

[22] is algorithm 1, and the algorithm in this paper is algorithm 2. For each combination of parameters, we generate 50 instances.

In Fig. 3, we set $N = 50$, and vary p in range of $[0.1 - 0.3]$ to calculate E_p. In Fig. 4, we set $p = 0.2$, and vary N in range of $[30 - 70]$.

4.2 Performance Discussion

We can see from Figs. 3 and 4, with the increases of p and N, algorithm 2 removes few links than algorithm 1. It improves the link utilization, when faced with a large number of wiretapping nodes, algorithm 2 performances particularly well. Compared to algorithm 1, the proposed algorithm in this paper has been greatly improved, especially suitable for larger networks.

5 Conclusion

In this paper, we have investigated the problem of wiretapping Attack in network coding system. We analyzed how the network segmentation design influenced the security of networks. We proposed a secure strategy against nodes wiretapping Attack by network segmentation design. We compared the pros and cons of the proposed algorithm. Simulations showed that the proposed routing algorithm achieved good performance. As a future research, we will study the secure topology design strategy in multicast system.

Acknowledgment This work is funded by National Science Foundation of China (61271316, 61071152, 61271180), 973 Program (2010CB731403, 2010CB731406, 2013CB329605) of China, Chinese National "Twelfth Five-Year" Plan for Science & Technology Support (2012BAH38 B04), Key Laboratory for Shanghai Integrated Information Security Management Technology Research, and Chinese National Engineering Laboratory for Information Content Analysis Technology.

References

1. Ahlswede R, Cai N, Li S-YR, Yeung RW (2000) Network information flow. IEEE Trans Inf Theory 46(4):1204–1216
2. Koetter R, Medard M (2003) An algebraic approach to network coding. IEEE/ACM Trans Networking 11(5):782–795
3. Li S, Yeung R, Cai N (2003) Linear network coding. IEEE Trans Inf Theory 49(2):371–381
4. Yu Z, Wei Y, Ramkumar B, Guan Y (2008) An efficient signature-based scheme for securing network coding against pollution attacks. Proceedings of IEEE INFOCOM 2008, the 27th conference on computer communication, Phoenix, Arizona, USA, pp 1409–1417
5. Ho T, Leong B, Koetter R, Medard M, Effros M, Karger D (2004) Byzantine modification detection in multicast networks using randomized network coding. Proceedings of IEEE international symposium on information theory (ISIT), Chicago, Illinois, USA, p 144
6. Jaggi S, Langberg M, Katti S, Ho T, Katabi D, Medard M (2007) Resilient network coding in the presence of byzantine adversaries. Proceedings of IEEE INFOCOM 2007, the 26th conference on computer communications, Nice, pp 616–624
7. Krohn M, Freedman M, Mazières D (2004) On-the-fly verification of rateless erasure codes for efficient content distribution. In: IEEE Symp on Security and Privacy, Oakland, CA, pp 226–240
8. Gkantsidis C, Rodriguez PR (2006) Cooperative security for network coding file distribution. Proceedings of INFOCOM 2006, the 25th IEEE international conference on computer communications, Barcelona, Spain, pp 1–13
9. Cai N, Yeung R (2002) Secure network coding. Proceedings of IEEE international symposium on information theory (ISIT), Palais de Beaulieu, Lausanne, Switzerland, p 323
10. Feldman J, Malkin T, Stein C, Servedion RA (2004) On the capacity of secure network coding. Proceedings of the 42nd annual allerton conference on communication, control, and computing, Monticello, Illinois, USA
11. Cai N, Yeung RW (2007) A security condition for multi-source linear network coding. IEEE international symposium on information theory, Nice, France, pp 561–565
12. Zhang Z, Yeung Raymond W (2009) A general security condition for multi-source. Linear network coding.http://iest2.ie.cuhk.edu.hk/Whyeung/publications/zxzhang-security.pdf

13. CaI NT, Grant A (2008) Capacity bounds for secure network coding. IEEE communication theory workshop, St. Croix, US Virgin Islands, pp 95–100
14. Bhattad K, Narayanan KR (2005) Weakly secure network coding. First workshop on network coding, theory and applications, Riva del Garda, Italy
15. Silva D, Kschischang FR (2009) Universal weakly secure network coding. Information theory workshop on networking and information theory, Volos, Greece, pp 281–285
16. Jain K (2004) Security based on network topology against the wiretapping attack. IEEE Wirel Commun 11(1):68–71
17. Jing D, Curtmola R, Sethi R, et al (2008) Toward secure network coding in wireless networks: threats and challenges. 4th workshop on secure network protocols, Orlando, Florida, pp 33–38
18. Mills A, Smith B, Clancy TC et al (2008) On secure communication over wireless erasure networks. IEEE international symposium on information theory, Toronto, Ontario, Canada, pp 161–165
19. Fancsali SZ, Ligeti LP (2008) Some applications of finite geometry for secure network coding. J Math Cryptol 2(3):1862–2984
20. Hassanzadeh MM, Ravanbakhsh M, Ytrehu SO (2008) Two layer secure network coding-(2-LSNC). IEEE international symposium on telecommunications, Tehran, Iran, pp 7.12
21. Harada K, Yamamoto H (2008) Strongly secure linear network coding. IEICE Trans Fundam E91-A(10):2720–2728
22. Du R, Zhao C, Zhao F, Li S (2012) A strategy of network coding against nodes conspiracy attack. The international conference on communications, signal processing, and systems, Beijing, China

Research on Time Triggered Ethernet Based on Deterministic Network Calculus

Yu Xiang, Xiang Zhang, Zhenwei Li, and Wei Wang

Abstract In this paper, we present a service-performance network calculus model based on Time-Triggered Ethernet, a deterministic safety critical real-time network protocol, which is used in avionics systems. We firstly design and implement the TTE clock synchronization, redundancy fault-tolerant, multi-data communication, service-performance model, node model and network model successfully on the simulation platform. Then, we analyze the performance of TTE and compare simulation results with theoretical values from the time-triggered Ethernet network calculus. In this way, the performance and efficiency of TTE are analyzed and verified through two levels.

Keywords Time-triggered • Deterministic • Safety critical • Network calculus • Simulation

1 Introduction

In recent years, the development of real-time tasks based on the existing Ethernet has become a hot-spot issue. In this fierce competition, the time-triggered Ethernet (TTE) stands out, which combines time-triggered technology certainty, fault-tolerant mechanisms and real-time performance with the ordinary Ethernet's performances, like flexibility, dynamic, as well as "best-effort" [1, 2]. TTE provides support for synchronous, highly reliable embedded computing and networking, fault-tolerant design. Because of its characteristics, TTE is widely used in the safety-critical system, such as aviation electronic technology, transport system, industrial automation and so on.

Y. Xiang • X. Zhang • Z. Li • W. Wang (✉)
School of Computer Science and Engineering, University of Electronic Science and Technology of China, Chengdu, China
e-mail: jcxiang@uestc.edu.cn; zhangx@uestc.edu.cn; 573393612@qq.com; 874614101@qq.com

B. Zhang et al. (eds.), *The Proceedings of the Second International Conference on Communications, Signal Processing, and Systems*, Lecture Notes in Electrical Engineering 246, DOI 10.1007/978-3-319-00536-2_131,

"Time-Triggered" [3] refers to predictable and deterministic, which means all activities in the network would run in a planned way over time. The definition of the Time Triggered Ethernet is as follows [4, 5]:

TTE = Ethernet + Clock synchronization + Time-Triggered Communication + Rate-Constrained traffic + Guaranteed Transport

In this article, we firstly construct a service-performance network calculus model which is triggered by time. Based on the protocol, we realize the TTE clock synchronization algorithm, protocol and network components. We construct simulation model and then use this model to analyze the performance and parameters of the TTE. Finally, we compare simulation results with the network calculus results based on the theory and simulation results. Conclusions show that TTE can well meet the needs of safety-critical systems.

2 The Service-Performance Model of TTE Based on Network Calculus

Network Calculus is a newly-developed network QoS (Quality of Service) theory and it is based on the Idempotent Mathematics and Residuation Theory [6]. The foundation of network calculus lies in the mathematical theory of algebra, the Min-Plus algebra and the Max-Plus algebra. Network calculus can give out the network performance boundary. Deterministic network calculus makes use of arrival curve and service curve to work out the deterministic boundary of the network performance parameters [6–8], such as the maximum delay of the network data flow, the cache backlog data in the network communication nodes and backlog length, etc.

2.1 The Service-Performance Model Parameter of TTE

Based on the network calculus theory, we define that F_j is the micro-data stream as the data bit stream of the same type from transmitting node. By convention, data stream indicates the data bit stream of the same type micro-data stream through the switch. Similarly, $p(j)$ indicates the priority of the data stream and the micro-data stream. The symbol $G_j = \cup_{\{i\,:\,p(i)\,=\,p(j)\}} F_i$ indicates the aggregated flow of the micro-data stream whose priority is same with stream F_j. The symbol $G_j^H = \cup_{\{i\,:\,p(i)\,>p(j)\}} F_i$ indicates the aggregated flow of the micro-data stream whose priority is bigger than stream F_j. By convention, the symbol $PG_j = \cup_{\{i\,:\,p(i)\,>p(j)\}} F_i$ refers to the aggregated flow after the aggregation of aggregated flow G_j and the aggregated flow of the aggregated flow G_j^H. We define that $l_{\max}^j = \max\{l_i : p(i) < p(j)\}$ indicates the maximum data frame length of the stream whose priority is lower than the priority $p(j)$ of the data stream.

2.2 Network Service Curve and Service Delay

We assume that the arrival curve of the micro-data stream with the priority $p(j)$ is $\alpha_j(t) = r_j t + b_j$. The two symbols $A_j(t) = \sum_{\{i\,:\,p(i)=p(j)\}}\alpha_i(t)$ and $A_j^H = \sum_{\{i\,:\,p(i)>p(j)\}}\alpha_i(t)$ indicate the arrival curve of G_j and G_j^H respectively.

We also assume that the service capabilities of the switch are C. Namely, the total service curve of the switch providing all the data stream through this switch is $\beta_{R,T}(t) = C[t-0]^+$. Based on corollary 6.2.1 inference 1 in the reference [9], we can obtain the service curve of the aggregated flow as formula (1):

$$B\left(PG_j, t\right) = \left[\beta_{R,T}(t) - l_{\max}^j\right]^+ = C\left[t - l_{\max}^j/C\right]^+ \tag{1}$$

Based on corollary 6.2.1 inference 2 in the reference [9], we can obtain the service curve of the aggregated flow G_j as formula (2):

$$\beta\left(G_j, t\right) = \left[\beta\left(PG_j, t\right) - A_j^H(t)\right]^+ \tag{2}$$

Combining the symbol $A_j^H = \sum_{\{i\,:\,p(i)>p(j)\}}\alpha_i(t) = \sum_{\{i\,:\,p(i)>p(j)\}} r_i \times t + \sum_{\{i\,:\,p(i)>p(j)\}} b_i$, with (2), conclusion can be obtained as formula (3):

$$\begin{aligned}\beta\left(G_j, t\right) &= \left[C\left(t - l_{\max}^j/C\right) - \sum\nolimits_{\{i:p(i)>p(j)\}} r_i \times t - \sum\nolimits_{\{i:p(i)>p(j)\}} b_i\right]^+ \\ &= \left(C - \sum\nolimits_{\{i:p(i)>p(j)\}} r_i\right)\left[t - \frac{l_{\max}^j + \sum_{\{i:p(i)>p(j)\}} b_i}{C - \sum_{\{i:p(i)>p(j)\}} r_i}\right]^+\end{aligned} \tag{3}$$

Thus, the service rate and service delay parameter of the data stream G_j are respectively as formulas (4) and (5):

$$R_j^G = C - \sum\nolimits_{\{i:p(i)>p(j)\}} r_i \tag{4}$$

$$T_j^G = \left(L_{\max}^j + \sum\nolimits_{\{i:p(i)>p(j)\}} b_i\right)/R_j^G \tag{5}$$

Considering micro-data stream F_j as the investigation target again, all the micro-data in the stream G_j is serviced in the order of FIFO. In this way, we can deduce the service curve of micro-data stream F_j. Based on the assuming 6.2.1 in the reference [9], the service curve of the micro-data stream F_j is

$$\beta\left[F_j, t\right] = \left[\beta\left(G_j, t\right) - \left(A_j(t-\theta) - \alpha_j(t-\theta)\right)\right]^+ \tag{6}$$

Based on the symbol $\beta_{R_j^G, T_j^G}\left(G_j, \theta\right) = \left(\theta - T_j^G\right)R_j^G = A_j(0) - b_j$, we can obtain $\theta = T_j{}^G + (A_j(0) - b_j)/R_j^G$.

Combining the symbol $A_j(t) - \alpha_j(t) = \sum_{\{i\,:\,p(i)\,=\,p(j)\}}\alpha_i(t) - \alpha_j(t) = (\sum_{\{i\,:\,p(i)\,=\,p(j)\}}r_i - r_j) \times t + (\sum_{\{i\,:\,p(i)\,=\,p(j)\}}b_i - b_j)$ with (6), conclusions can be obtained as formula (7):

$$\begin{aligned}\beta(F_j,t) &= \left[R_j^G\left(t-T_j^G\right) - \left(\sum\nolimits_{\{i:p(i)=p(j)\}} r_i - r_j\right)\right. \\ &\left.\times\left[t-T_j^G-\frac{\sum_{\{i:p(i)=p(j)\}} b_i - b_j}{R_j^G}\right] - \left(\sum\nolimits_{\{i:p(i)=p(j)\}} b_i - b_j\right)\right]^+ \\ &= \left(R_j^G - \sum\nolimits_{\{i:p(i)=p(j)\}} r_i + r_j\right) \times \left[t - \frac{R_j^G \times T_j^G + \sum_{\{i:p(i)=p(j)\}} b_i - b_j}{R_j^G}\right]^+\end{aligned} \tag{7}$$

So, the service rate and service delay parameter of the micro-data stream F_j are respectively as formulas (8) and (9):

$$R_j = R_j^G - \sum\nolimits_{\{i:p(i)=p(j)\}} r_i + r_j \tag{8}$$

$$T_j = T_j^G + \frac{\sum_{\{i:p(i)=p(j)\}} b_i - b_j}{R_j^G} + l_j/R_j^G \tag{9}$$

If there is no cascade switch in the network, we can directly use (8) and (9) to obtain network service delay. If not, we can make use of the above reasoning process to work out the service curve of the cascade switch, and then obtain the services of the cascade system curve. The min-plus deconvolution of the two functions f and g ($f \in F$, $g \in F$) are $f \oslash g(t) = \sup_{u>=0}\{f(t+u) - g(u)\}$.

Given a server S in the network, F_j refers to the data stream through the server S. The arrival curve of F_j is α. And the service curve that the server S provides to F_j is β. Thus, the output curve of the data stream F_j through the server S is $\alpha^* = \alpha \oslash \beta$ (Proof showed in reference [9] theorem 1.4.3).

For the first level switch which is directly connected to the terminals, the arrival curve is $\alpha_{r,\,b}$ and the service curve is $\beta_{R,T}$. So, the output curve of the level switch is

$$\begin{aligned}&\alpha^* = \alpha_{r,b} \oslash \beta_{R,T}(t) = \sup_{u>=0}\{\alpha_{r,b}(t+u) - \beta_{R,T}(u-T)^+\} \\ &= \sup_{T>=u>=0}\{\alpha_{r,b}(t+u) - \beta_{R,T}(u-T)^+\} \vee \sup_{u>T}\{\alpha_{r,b}(t+u) - \beta_{R,T}(u-T)^+\} \\ &\quad = \sup_{T>=u>=0}\{\alpha_{r,b}(t+u)\} \vee \sup_{u>T}\{\alpha_{r,b}(t+u) - Ru + RT\} \\ &\quad = \alpha_{r,b}(t+u) \vee \sup_{u>T}\{\alpha_{r,b}(t+u) - Ru + RT\}\end{aligned}$$

If t > -T, we can obtain

$$\alpha^* = \alpha_{r,b} \odot \beta_{R,T}(t) = \{b + r(t+T)\} \vee \sup_{u>T}\{\alpha_{r,b}(t+u) - Ru + RT\}$$
$$= \{b + r(t+T)\} \vee \{b + r(t+T)\} = b + r(t+T) \quad (10)$$

With cascade switches in the cascade system, we can apply the min-plus convolution to obtain the service curve of double-channel scene and the service curve is as formula (11):

$$\beta_j^{\varepsilon}(F_j, t) = \beta_j^{s_1}(F_j, t) \otimes \beta_j^{s_2}(F_j, t) = \beta_j^{\varepsilon}\left(R_j^{\varepsilon} = \min(R_i, R_i^*), T_j^{\varepsilon}\right) = T_i + T_i^* \quad (11)$$

According to the above reasoning process, we can apply the theory into the TTE network scenario to respectively deduce the upper deterministic boundary of the delay in single-channel and double-channel.

3 The Design and Realization of the Simulation Model

3.1 The Design of TTE Simulation Model

TTE consists of two kinds of network devices including TTE switches and TTE terminals. With the difference of TTE network nodes' position and role in TTE clock synchronization, TTE network nodes are divided into three different roles: Synchronization Master (SM), Compression Master (CM), Synchronization Client (SC). TTE switches can be as the role of SM, CM and SC. While TTE terminals can be as the role of SM and SC.

3.1.1 TTE Switches

The main function of TTE Switch is to forward time-triggered data (TT data), traditional Ethernet "best effort" data (BE data) or rate-limited data (RC data). The workflow of TTE Switch is as shown in Fig. 1.

The most important two differences between TTE switches and traditional switches are clock synchronization module and admission control module.

3.1.2 TTE Terminals

The main function of TTE terminal is to transmit and receive data. As the same of TTE switches, TTE terminals supports time-triggered data (TT data), the traditional Ethernet's "best effort" data (the BE data) and the rate-constrained data (RC data). The workflow of TTE terminals is shown in Fig. 2.

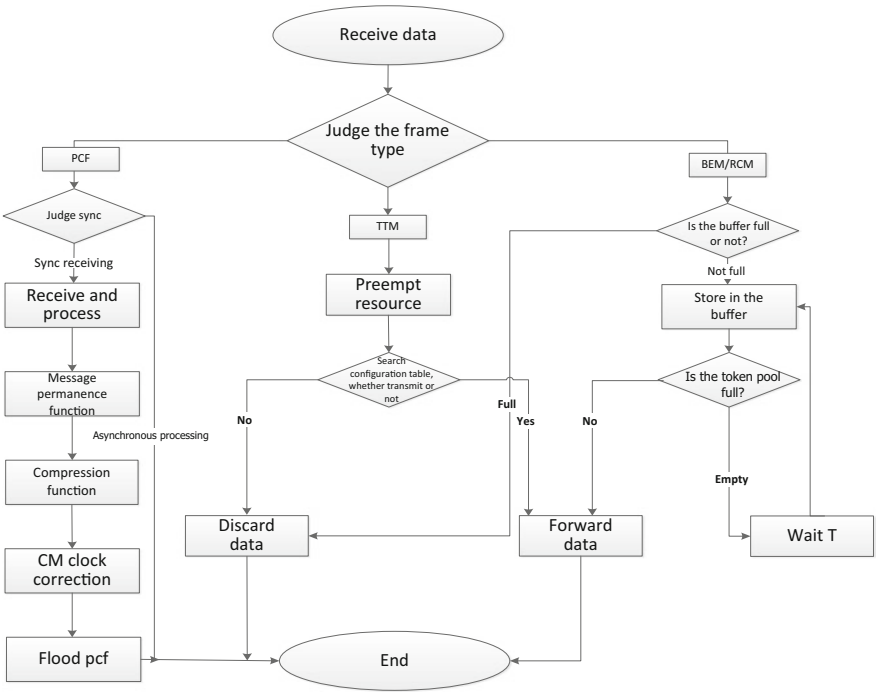

Fig. 1 The work flow of TTE switch

3.2 TTE Simulation Performance

- TTE delay
  Figure 3 describes the end-to-end delay when host A communicates with host B. Generally, the end-to-end delay divides into round-trip delay and one-way delay.

  (1) Round-Trip Delay (RTD)
  RTD of packet1: RTD1 = T6–T2
  RTD of packet2: RTD2 = T11–T7
  (2) One-Way Delay (OWD)

This test needs clock synchronization between host A and host B:
S-Source(host A) D-Destination(host B).

$$\text{Packet1 SD-Delay1} = \text{T4 - T2} \quad \text{DS-Delay1} = \text{T6 - T4} \tag{12}$$

$$\text{Packet2 SD-Delay2} = \text{T9 - T7} \quad \text{DS-Delay2} = \text{T11 - T9} \tag{13}$$

As the function op_sim_time () being able to get simulation time in simulation platform, we call the function when one nodes receives a frame. We can also get the simulation time of the frame with function op_pk_creation_time_get (pkt_ptr)

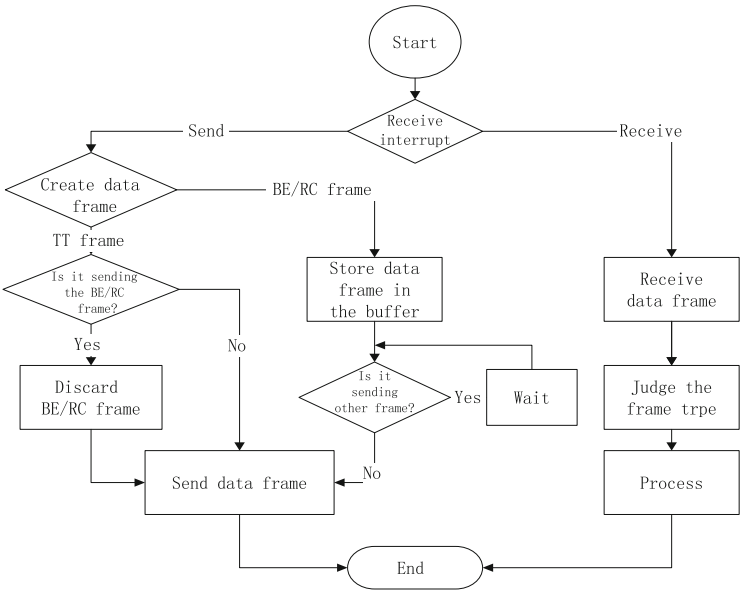

Fig. 2 The work flow of TTE terminal

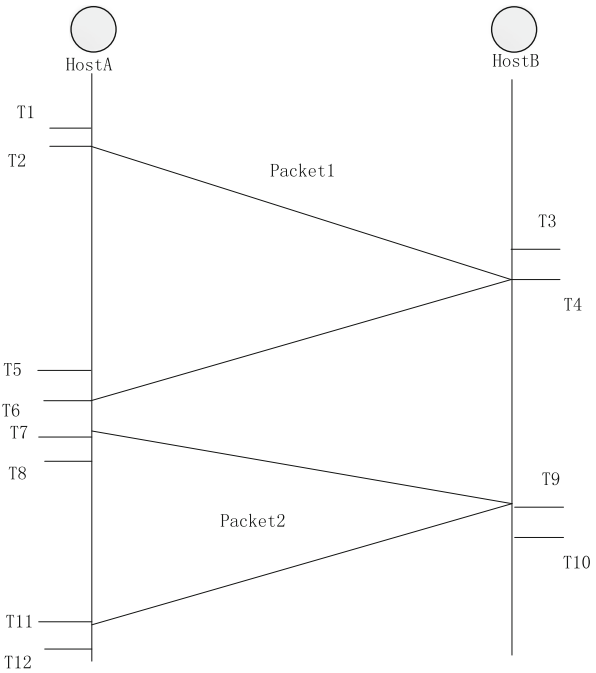

Fig. 3 Host A communicates with host B

getting the time of the creation of frames (pkt_ptr is the point which points to the frame) and tt_ete_delay means one-way delay.

$$\text{tt\_ete\_delay} = \text{op\_sim\_time}\ ()\ -\ \text{op\_pk\_creation\_time\_get}\ (\text{pkt\_ptr}) \tag{14}$$

4 Comparison Analysis of Simulation and Network Calculus

In the second section, we analyze and derivate the maximum delay of TTE data in a specified network topology with the use of the theory of network calculus. Then we conduct the statistical analysis on time-triggered Ethernet network performance parameters with simulation tools. Here we use the results of the two research tools to conduct comparative analysis, to verify whether the results of the TTE simulation can meet the delay constraints of the maximum delay derived from network calculus.

4.1 Comparison Analysis of Single Channel

In the single-channel topology network simulation model, there are three types of data traffic (time-triggered real-time data (TT), rate-constrained data (RC) and best-effort data (BE)). Figure 4 describes single-channel topology. There are seven TTE terminals and one TTE switch in the topology. Each TTE terminal communicates with other terminal through the TTE switch. TTE switch forwards three kinds of data: TT data, RC data and BE data.

Rules of Terminal nodes sending frame are as follows:

TT data stream: three nodes send two frames per 0.025 s; four nodes send one frame per 0.025 s; the TT data frame size is 1050B;

RC data stream: each node sends one frame per second; the frame size of RC data stream is 1050B;

BE data stream: each node sends 10,000 frames per second; the frame size of BE data is also 1050B.

According to the topology and rules of single-channel, the arrival curve of three kinds of data streams is:

$$\alpha_{TT} = (42000t + 1050)bytes \quad \alpha_{RC} = (1050t + 1050)bytes$$
$$\alpha_{BE} = (10500000t + 1050)bytes$$

Therefore, the separate service curve of micro-data flow F_j (TT, RC, BE) supported by switch is:

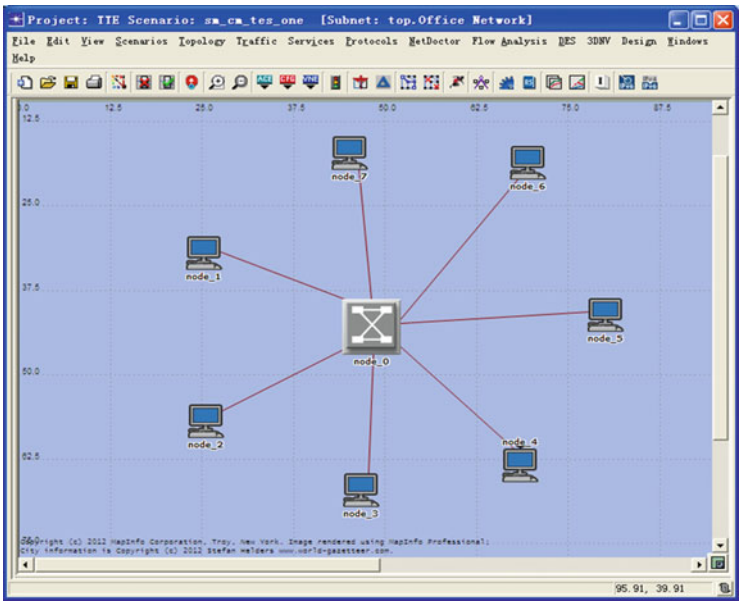

Fig. 4 Single-channel scene topology

$$\beta_{tt}^{s}\left(R^{tt} = 1.0179^{*}10^{8}bps, T_{tt} = 0.8809^{*}10^{-3}s\right)$$
$$\beta_{rc}^{s}\left(R_{rc} = 1.0139^{*}10^{8}bps, T_{rc} = 1.4908^{*}10^{-3}s\right)$$
$$\beta_{be}^{s}\left(R_{be} = 0.3839^{*}10^{8}bps, T_{be} = 2.0712^{*}10^{-3}s\right)$$

As the single-channel simulation scenario being a star-topology network, it has only one switch and has no cascading switches. So the max-delay of each type data stream is:

$$\mathrm{D}_{tt}^{\max} = 0.8809ms \quad \mathrm{D}_{rc}^{\max} = 1.4908ms \quad \mathrm{D}_{be}^{\max} = 2.0712ms$$

In the single channel simulation test, the delays of data streams are as follows:

The comparison chart between the maximum delay based on network calculus and actual delay obtained by simulation results statistics is shown as follows.

Figure 5 shows that the TT Network delay is 0.168×10^{-3} s, which proved that the determine performance of TT data traffic has been guaranteed in TTE network.

According to the single-channel results comparison chart of the three types of data, we can obtain that the simulation results well meet actual delay of the largest network delay constraint derived from network calculus.

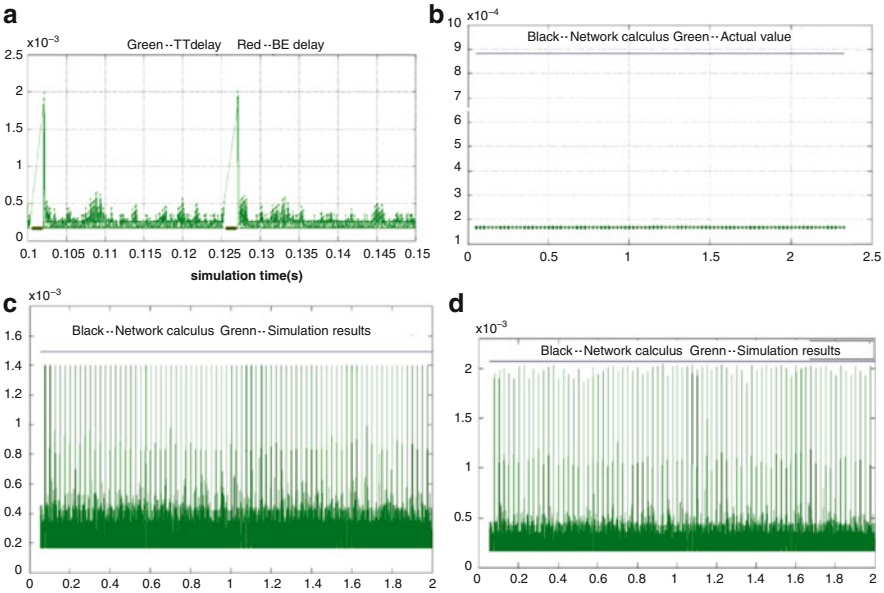

Fig. 5 Single-channel scene topology. (**a**) TT and BE data delay. (**b**) The comparison analysis of time-triggered data between simulation and network calculus results. (**c**) The comparison analysis of rate-constrained data between simulation and network calculus results. (**d**) The comparison analysis of best-effort data between simulation and network calculus results

4.2 Comparison Analysis of Double-Channel

In the double-channel topology network simulation model, there are three types of data traffic including time-triggered real-time data (TT), rate-constrained data (RC), and the best-effort (BE). Figure 6 describes double-channel topology. There are also TTE swithes and TTE terminals in the topology. TTE terninals generate data and TTE switches forward data.

Rules of Terminal nodes sending frame are as follows:

TT data stream: each node sends data frames three times per 0.25 ms; TT data frame size is 100B;

The RC data stream: each node sends data frames eight times per 0.25 ms; RC data frame size is 100B;

The BE data stream: each node sends data frames per second 10000/7; the BE frame length is 100B.

According to the rules of double-channel sending frames, the arrival curves of the level switch are:

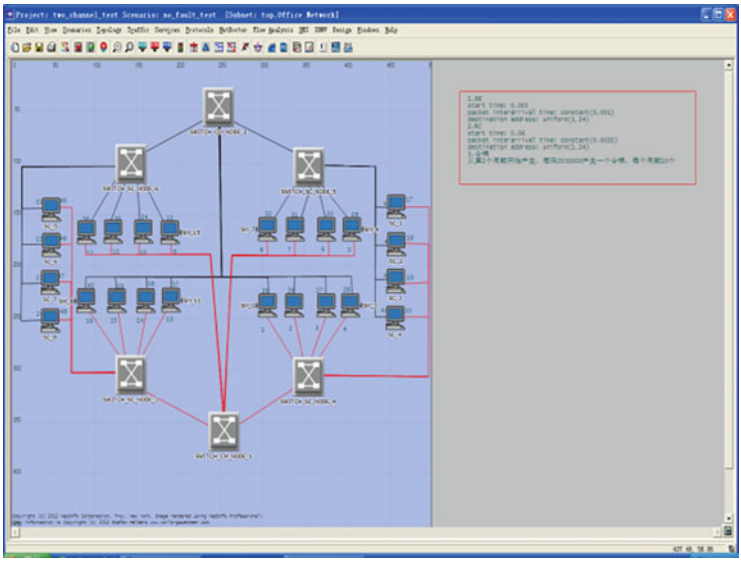

Fig. 6 Double-channel scene topology

$$\alpha_{TT} = (15120t + 378)bytes \quad \alpha_{RC} = (40320t + 1008)bytes$$
$$\alpha_{BE} = (180000t + 126)bytes$$

The service curve of micro-data flow (F_{tt}, F_{rc}, F_{be}) supported by switch is as follows:

$$\beta_{tt}^{s1}\left(R_{tt} = 1.041^{*}10^{8}bps, T_{tt} = 2.210^{*}10^{-4}s\right)$$
$$\beta_{rc}^{s1}\left(R_{rc} = 1.016^{*}10^{8}bps, T_{rc} = 0.798^{*}10^{-3}s\right)$$
$$\beta_{be}^{s1}\left(R_{be} = 0.912^{*}10^{8}bps, T_{be} = 0.965^{*}10^{-3}s\right)$$

Using the same way, we can get the arrival curves of first level switch are:

$$\beta_{tt}^{s2}\left(R_{tt} = 1.030^{*}10^{8}bps, T_{tt} = 2.237^{*}10^{-4}s\right)$$
$$\beta_{rc}^{s2}\left(R_{rc} = 1.008^{*}10^{8}bps, T_{rc} = 8.146^{*}10^{-4}s\right)$$

$$\beta_{be}^{s2}\left(R_{be} = 0.816^{*}10^{8}bps, T_{be} = 2.537^{*}10^{-3}s\right)$$

Following (11), we can obtain as

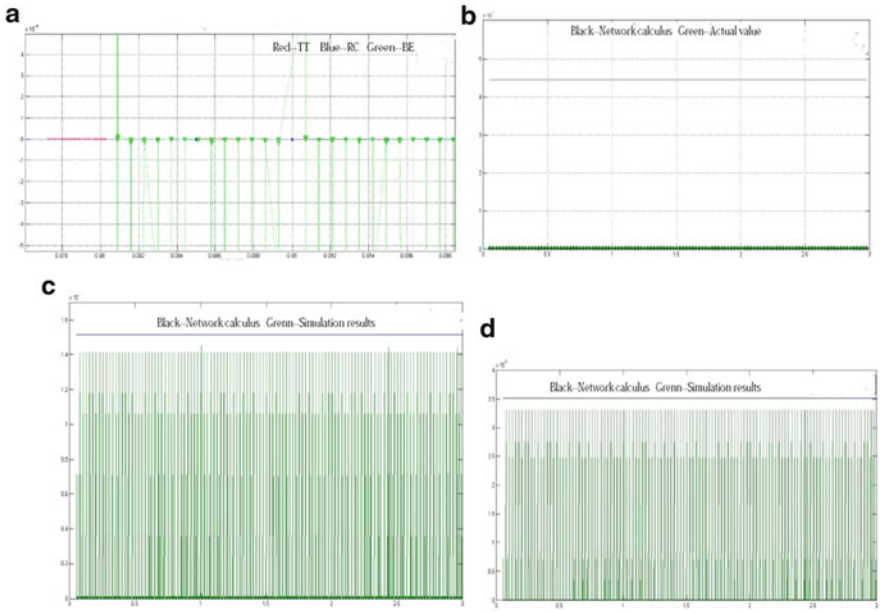

Fig. 7 Double-channel data delay. (**a**) TT and BE data delay. (**b**) The comparison analysis of time-triggered data between simulation and network calculus results. (**c**) The comparison analysis of rate-constrained data between simulation and network calculus results. (**d**) The comparison analysis of best-effort data between simulation and network calculus results

$$\beta_{tt}^{\varepsilon}\left(R_{tt} = 1.030^{*}10^{8}bps, T_{tt} = 4.447^{*}10^{-4}s\right)$$
$$\beta_{rc}^{\varepsilon}\left(R_{rc} = 1.008^{*}10^{8}bps, T_{rc} = 1.513^{*}10^{-3}s\right)$$
$$\beta_{be}^{\varepsilon}\left(R_{be} = 0.816^{*}10^{8}bps, T_{be} = 3.502^{*}10^{-3}s\right).$$

So, in the time triggered Ethernet double-channel topology, the maximum delay of time-triggered, rate constraint and best-effort respectively is:

$$\mathrm{D}_{tt}^{\max} = 0.4447ms \quad \mathrm{D}_{rc}^{\max} = 1.513ms \quad \mathrm{D}_{be}^{\max} = 3.502ms$$

In the double-channel simulation test, the delay of the network data stream is as follows:

The comparison chart between the maximum delay based on network calculus and actual delay obtained by simulation results statistics is shown as follows.

Figure 7a shows the TT Network delay is 0.2016×10^{-3} s, which proved the TT data traffic's determine performance has been guaranteed of TTE network.

According to results comparison chart of three types of data stream in double-channel, we can get that the actual delay of the simulation statistical results fully meets the maximum network delay obtained by network calculus and it also verifies

the TTE simulation results are reasonable. Then, we can verify that the TTE specification is feasible.

5 Conclusion

As a new real-time deterministic network, Time Triggered Ethernet has not yet formed a standardized protocol specification and has no mature products for the market. This paper first uses network calculus and network simulation to analyze and study the TTE. We present a service-performance network calculus model, which is triggered by time and obtain the upper deterministic boundary of the delay. With the TTE clock synchronization, redundancy fault-tolerant, multi-data communication, node model and network model designed and implemented on the simulation platform, we analyze the performance of TTE and compare simulation results with theoretical values from the time-triggered Ethernet network calculus. The final conclusion shows that TTE can be compatible with the traditional Ethernet [10] and well meet the needs of real-time and safety-critical systems in the fields of avionics and industry.

References

1. Hermann K, Gunter G (1994) TTP—a protocol for fault-tolerant real-time systems. IEEE Comput 27(1):14–23
2. TTTech. Time-triggered protocol, high level specification document. Vienna, Austria, D-032-S-10-28. Available at http://www.ttech.com
3. Time-Triggered protocol TTP/C high-level specification document. TTTech Computer Technology AG, Vienna, 2008
4. Kopetz H (2003) Fault containment and error detection in the time-triggered architecture autonomous. In: Proc. of the 6th int'l symp. on decentralized systems, IEEE Computer Society Press, Pisa, pp 139–146
5. TTTech. TTEthernet Specification v.9.1-22968[Z]. TTTech Computertechnik AG.D-INT-S-10-002, 200.11.GE
6. Firoiu V, Boudec JYL, Towsley D et al (2002) Theories and models for internet quality of service. Proc IEEE 90(9):1565–1591
7. Kopetz H, Ademaj A, Grillinger P, Steinham-mer K (2005) The time-triggered ethernet (TTE) design. In: 8th IEEE International Symposium on Object-oriented Real-time distributed Computing (ISORC), Seattle, Washington, May 2005
8. Boudec JYL, Thiran P (2004) Network calculus: a theory of deterministic queuing system for the internet. Online Version, Springer
9. Le boundec JY, Thiran P (2004) Network calculus, vol 2050, Lecture note in computer science. Springer, London
10. Hermann Kopetz, Astrit Ademaj, Petr Grillinger, Klaus Steinhammer. The time-triggered ethernet (TTE0 Design). Vienna University of Technology Real-time Systems Group. Treitlstr. 3/182-1, A-1040, Vienna, Austria, D-032-S-10-28. Available at http://www.ttech.com

Research on Distance Measurement Based on LQI

Yu Xiang, Jin Li, and Wenyong Wang

Abstract Range-based localization must measure distances between neighboring nodes. Distance measurement based on LQI, featuring low communication overhead and low complexity, is increasingly applied in the range-based localization of the Wireless Sensor Networks. We first analyze the relationship of LQI and signal transmission distance, and then we propose a kind of LQI processing method. The method includes three phases: first, LQI pre-correction before LQI converted to distance; second, the error compensation after LQI converted to distance; third, distance result correction to eliminate biggish error. After using the ZigBee-based hardware platform to test the measurement error, we draw the conclusion that this algorithm has higher accuracy and can achieve better results in distance measurements. The experiments show that measurement error is below 1 m within 10 m.

Keywords LQI • Wireless sensor network • Distance measurement

1 Introduction

In Wireless Sensor Networks, determining where an event occurs or a message be captured is one of the basic functions, and it also plays a pivotal role in indicating the effectiveness of the network. Therefore, obtaining the location of sensors is a key step in WSNs. And because of the nodes are randomly deployed and the network' data-centric characters, getting nodes' accurate location information seems more important [1].

Nodes' localizations usually realized through measuring the distances between neighboring nodes, and then applying the data to localization algorithm to estimate

Y. Xiang • J. Li (✉) • W. Wang
School of Computer Science and Engineering, University of Electronic Science and Technology of China, Chengdu, China
e-mail: jcxiang@uestc.edu.cn; 2433971887@qq.com; wangwy@uestc.edu.cn

B. Zhang et al. (eds.), *The Proceedings of the Second International Conference on Communications, Signal Processing, and Systems*, Lecture Notes in Electrical Engineering 246, DOI 10.1007/978-3-319-00536-2_132,

the location of those unknown location nodes. So, research on the distance measurement of nodes in WSNs is very necessary.

Common measuring techniques are RSSI (Received Signal Strength Indication), GPS (Global Positioning System), infrared method, ultrasonic measurement, etc. The latter three need additional hardware. And for ultrasonic measurement, in spite of its high-accuracy, it not only costs high, but also is easily affected by environment. The first method does not need any additional hardware. RSSI calculates distance between two nodes based on the signal strength, which has a relationship with the distance. As RSSI needs no additional hardware feature, the module of providing RSSI value is always embedded in the wireless transceiver chips, and RSSI-based distance measurement is often used [2].

Now, a new indicator, the Link Quality Indicator, is provided in some new wireless chips, which based on the 802.15.4 standard, to help measure distance. It shows a better performance than RSSI within a certain distance range. The LQI has a higher dynamic range and a higher resolution than RSSI [3]. When the nodes are close, the estimated distance using LQI has a smaller average deviation and standard deviation. What's more, seen from the comparison of LQI and RSSI's fading curves in reference [4], LQI has a wider linearity, a better stability and is more suitable for the localization in the condition that the distance of two nodes is less than 10 m. In this paper, we establish a distance measurement model based on the relationship between LQI and the distance of two nodes, and analyze its precision.

2 LQI-Based Experiment

2.1 Hardware Preparation

We choose our own-developed Tarax chips for sensor nodes, and Freescale MC13224v chip for master control chip to experiment. MC13224v is a ZigBee-chip solution, integrated with completed low-power 2.4 GHz radio transceiver, embedded 32-bit ARM7 processor, integrated with IEEE802.15.4, MAC, AES as well as MCU peripherals, which is also a IEEE802.15.4 integrated solution for high density and low count component [5].

2.2 Introduction to LQI

LQI is a indicator to link quality, which is used to represent the quality of link connection. It can be obtained from every data reception, and is main influenced by the receiving sensitivity and signal strength between receiver and sender [6]. LQI is from the physical layer, and then be calculated by the MAC layer. Finally, it

provides the signal strength and quality information of the received data frames, usually associated with the probability of correct receives the data frame [7], to the network layer and application layer.

More specifically, LQI is an indicator that represents the link quality and signal strength of the received packet. Its value is defined by IEEE802.15.4 standard, but its use of specific laws and characteristics do not give a clear indication. Generally, the higher the LQI value is, the better link quality is, and also the lower the link cost.

In MC13224v, the LQI value is an integer with a range of 0x00 to 0xFF (0–255), in which 0x00 corresponds to -100 dBm, and 0xFF corresponds to -15 dBm. The calculating formula shows in (1):

$$LQI(dBm) = (LQI(dec))/3 - 100 \tag{1}$$

The calling function MLMELinkQuality () returns a pointer that point to a 8-bit data, and the pointed value is LQI, which can be used after reading [8]. In order to get a stable value, it should be read after at least one reception finished, and this value will be saved to the arrival of the next data. So every time the LQI value we read has already been updated by the latest received data. In addition, LQI value is presented in the form of multiple of 3, that's the interval, is 3.

2.3 Relationship with LQI and Distance

Experiments are conducted in open outdoor. Transceiver nodes are all about 0.5 m above the ground, and the positions of receiving node is fixed. The sending node, whose transmitted power is 0 dBm, moves from 0 to 40 m with a meter for stepping. We measure 100 LQI values in every distance point, calculate their average values, and plot the LQI signal decline curve shown in Fig. 1.

From the distribution of the measured data shown in Fig. 1, we can see that the actual LQI decline curve has some irregular oscillation and decline. LQI attenuation goes sharply in a short distance, then more gentle in the middle, and in the long distance, the attenuation also exists but carries with more severe fluctuations. Near the 5-m distance, the first rise appears. After a lot of measured results in different locations, we found that the concave rise phenomenon is not accidental; it is caused by the certain deviation of node's each position. LQI value of two adjacent distance point basically differs by at least one jump interval, and the degree of differentiation is obvious.

Through analysis, although the LQI is affected by the node itself and environmental factors, the LQI does exist a certain relation with the distance of transceiver nodes. Because of certain repeatability in LQI measurement and certain regularity in LQI change, the LQI can be used for distance measurement and positioning through proper processing. In addition, although the LQI and signal transmission distance is showing an obvious attenuation trend, but it is not a smooth curve, which shows that there must be a certain degree of error, when use LQI for ranging and

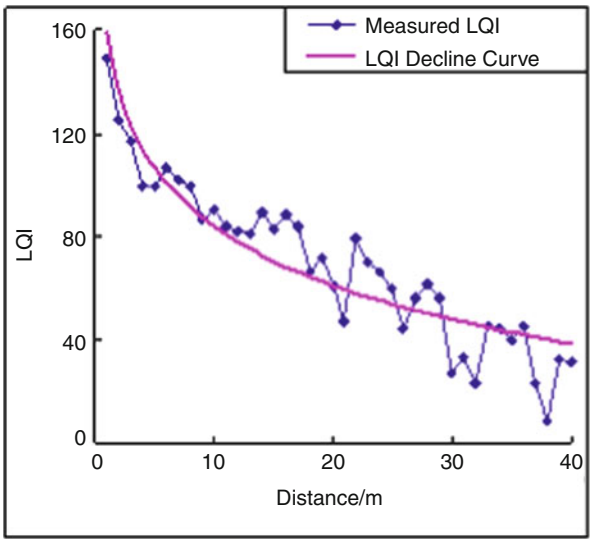

Fig. 1 LQI signal decline curve

location. LQI fluctuates gently when transmission distance is close, and when transmission distance is far, LQI fluctuates so severely that LQI variation is no longer obvious to transmission distance. Overall, ranging and location technology based on LQI shows that the closer the transmission distance is, the more accurate this technology can be, the more far transmission distance is, the greater the error this technology can generate. So, we discuss the ranging and location based on LQI value within the distance of 10 m.

3 Distance Measurement Model

Establishing distance measurement model is to find out the relationship between LQI and distance, and fit out a simple and effective curve that LQI changes over distance. This curve would be simulated by a suitable mathematical formula, as a reference to estimate the distance between unknown position sensors. LQI would be influenced by various factors, so the effective method to measure LQI in specific experimental scenario is through a number of experiments. After getting LQI values, we can proceed to next steps: figure out the relationship between LQI and distance, build the LQI-d empirical formula, and finally calculate the distance of two nodes according to their LQI value. Now, we choose two suitable fitting manners to analysis, the logarithmic function fitting and cubic polynomial function fitting, as shown in Fig. 2.

R^2 in Fig. 2 is an indicator represents fitting degree of trend line, the value can reflect the fitting degree between estimated data from trend line and its corresponding actual data. The higher the fitting degree is, the higher the correlation

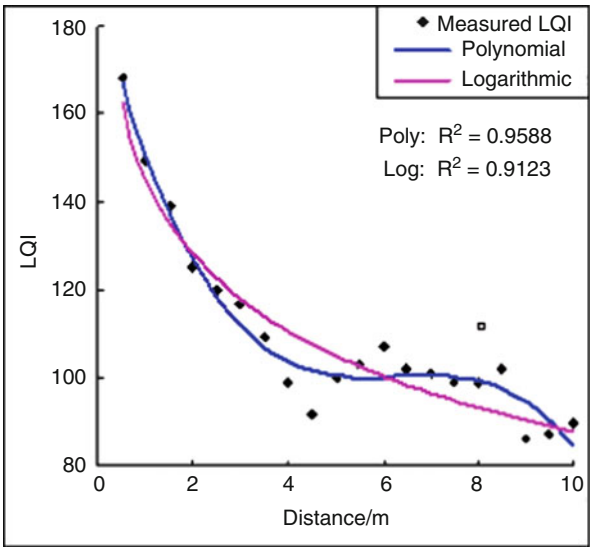

Fig. 2 LQI fitting curves

can get, and the closer the estimated value is to the actual value. Especially, when $R^2 = 1$, the estimated value and actual value are completely the same. In Fig. 2, both of the two fitting methods' $R^2 > 0.9$, which shows that both fitting degrees are good, and the LQI trends with distance are relatively consistent with the curve fitting results. Furthermore, the polynomial model has a better fitting degree with the original data; therefore, we choose the polynomial function as the empirical formula to estimate the nodes' distance.

4 QI Pre-correction Algorithm

When experimental scene stays the same, the main factors that influence the LQI is not geographical environment factors (like air pressure, humidity, etc). We need to study deviation degree between measured LQI value and model data at the same distance point in the same geographical environment, but on different days. In the same experiment scenarios, we choose two groups of experiments, respectively called Experiment 1 and Experiment 2, to discuss the data measured on two different days. Figure 3 shows the contrast figure of three attenuation curves of three experimental data.

Observed from Fig. 3, although the LQI measured in three times do exist difference in deviation at each distance, the LQI attenuation trends are the same in the overall trend. Therefore, this empirical ranging model is feasible. But due to the different experimental time, there are various influencing factors leading to huge difference in data. So if directly put the LQI into distance measurement model

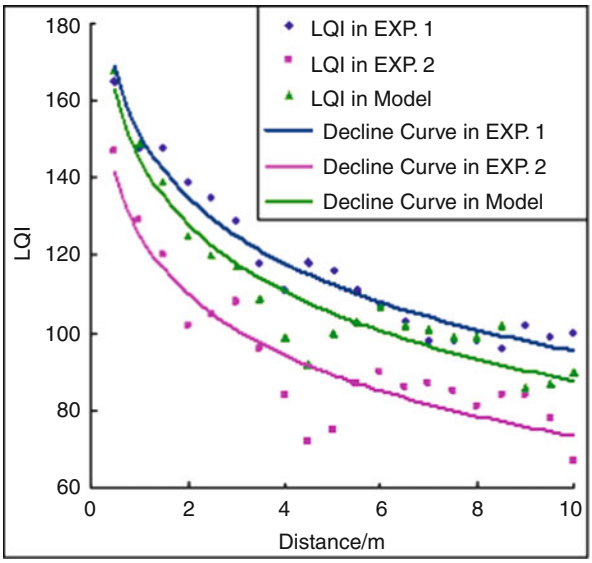

Fig. 3 Contrast fig of three experimental data

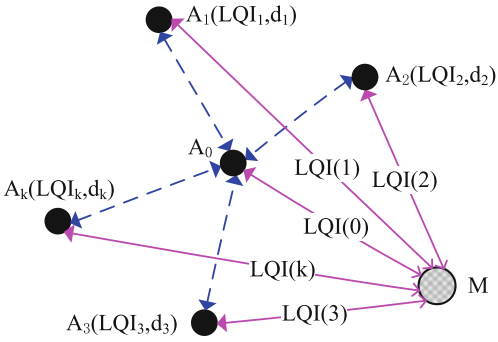

Fig. 4 Pre-correction diagram using known position nodes

instead of pre-correction, the error will be large. Therefore, we must correct the LQI according to the current environmental conditions in advance.

Within a small range, the best way to solve environmental influences is pre-correcting LQI using known position nodes. The basic idea of the algorithm is as follows. Acquire the LQI value and the actual distance between two known position nodes, and establish their corresponding relation. After compared with distance measurement model, difference of LQI value is obtained. Then use this difference to correct other LQI of those nodes' distance that would be estimated. Correction here can be divided into two ways: first, using average value of LQI differences to correct LQI uniformly; second, according to the range of LQI differences to correct LQI in groups.

As shown in Fig. 4, A_0, A_1, and A2. . . A_k are the known position nodes, and M is the unknown position node. Follow the steps mentioned above, we will acquire LQI values between A_0 and A_1, A_2,. . . , A_k at first, and secondly, set corresponding

relation groups: A_1 (LQI_1, d_1), A_2 (LQI_2, d_2),. . . , A_k (LQI_k, d_k). Thirdly, record the LQI values between M with each known position nodes, the values were LQI(1), LQI(2),. . . and LQI(k) respectively.

In relation groups A_k (LQI_k, d_k), we will calculate the differences between measured LQI and computed LQI based on the distance measurement model at each distance, the differences are expressed as d_1 <LQI>, d_2 <LQI>. . . d_k<LQI>.

1. Unified Correction

If there is little difference between d_k<LQI>, we can directly use their average value to correct the LQI(k), and the corrected LQI value can be used in the calculation of the distance. Calculation formula of corrected value $\overline{LQI}$ shows in (2):

$$\begin{aligned} &\overline{LQI} = \sum_{n=1}^{k} (d_n < LQI >)/k \\ &\left(d_i < LQI > -d_j < LQI >\right) < \varepsilon_1, (i,j) \subseteq \left(1_{\ldots}k\right) \end{aligned} \tag{2}$$

The ε_1 will be set according to the practical application.

2. Grouping Correction

If there is a big difference between d_k<LQI>, the correction effect will not be obvious if we still adopt unified correction method. Especially, when the differences have both positive and negative values, and they are far diverting from the average, there will be a large error existing in final distance result.

Grouping correction is dividing LQI values into groups according to d_k<LQI> at first, the number of groups would based on distribution of d_k<LQI>. Then the unified correction method will be used in each group. Correction formula for each group is (3).

$$\begin{aligned} &\overline{LQI} = \sum_{n \subseteq \overline{K_m}} (d_n < LQI >)/k_m \\ &\left(\mathrm{d_i} < \mathrm{LQI} > -\mathrm{d_j} < \mathrm{LQI} >\right) < \varepsilon_m, (i,j) \subseteq \overline{\overline{k_m}} \end{aligned} \tag{3}$$

m represents the mth group, $\overline{\mathrm{LQI}}_{\mathrm{m}}$ is the LQI's corrected value of mth group, $\overline{\overline{\mathrm{k_m}}}$ represents all the d_k<LQI> in mth group, k_m is the number of d_k<LQI> in mth group, and ε_m represents the difference range between d_k<LQI> in mth group. In addition, ε_m is set according to the practical application, it determines the number of groups.

Figure 5 shows the grouping situation of Experiment 2, there exists obvious gaps between each group and the respective mean values can well reflect the differences of LQI in their own groups.

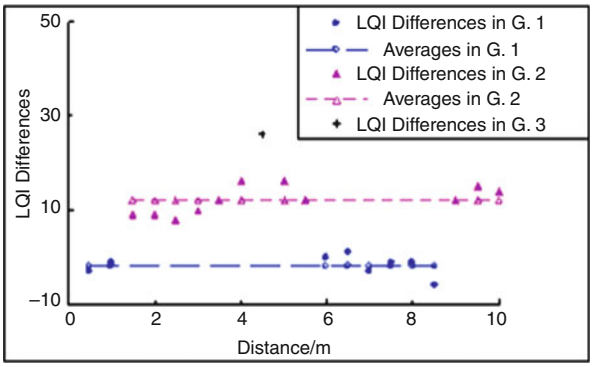

Fig. 5 Distribution of LQI differences of Exp. 2

Now, it's necessary to note two things for grouping correction. First, due to the fluctuations of LQI, two similar or same LQI values' differences may vary widely. Second, LQI(k) might not exist in Ak (LQIk, dk).

Steps of grouping correction are as follows:

Step 1: Group LQI_k in $A_k(LQI_k, d_k)$ according to intervals of LQI differences, and treat the groups as set B. Group the d_k<LQI> starting from the smallest d_k<LQI> with the interval M (M is set according to the accuracy requirement) and put its corresponding LQI values into B_1. Then same grouping way to deal with remaining LQI_k still starts from the smallest d_k<LQI> until all LQI are put into B_m. After grouping is over, calculate the average value for LQI values in each B_m. The set B can be expressed as $B(B_m, b_m)$, where B_m contains all LQI_k in mth group, and b_m is the average value of B_m.

Step 2: In the process of distance measuring, if LQI(k) appears in one of groups B_m, then go to Step 3, otherwise the Step 4.

Step 3: If LQI(k) only appears in one group B_m, then treat the b_m as corrected value. If it appears in two groups (B_m, B_n), then treat the average of b_m and b_n as corrected value, and so on.

Step 4: For the LQI(k) that does not appear in the group, we choose a nearby LQI_k, and turn to Step 3. If the intervals to two adjacent LQI_k are the same, find out their corrected values in Step 4 respectively, and calculate the average as the final correction.

Through analysis, we can find that measurement of known position nodes can help reduce the LQI fluctuation that caused by environmental factors. First, we need to calculate the difference between measured LQI and computed LQI. Then use the unified correction or grouping correction to correct the LQI in order to reduce the conversion error from LQI value to distance.

5 The Distance Processing Algorithm

5.1 Error Compensation

In the almost unchanged regional environment, LQI is still affected by the other factors, which will absolutely cause distance error. Distance measurement plays a crucial role in localization algorithm, and ranging error value will be accumulated into the localization algorithm, causing increase in position error and reducing location accuracy of the whole sensor network. So to improve the ranging precision, it is significant important to improve the positioning precision [9]. According to the preliminary analysis of the distance measuring results in sections above, we first need to examine the inherent errors of range model, and then find out its error compensation method.

Figure 6 shows the curve of distance measurement model's inherent errors, compared with LQI decline curve, we find that the error rush basically at the concave of decline curve. Therefore, we use the inherent error of range model to compensate distance results, and the compensation operation is still use the ideas of LQI value segmentation, which also used in grouping correction processing.

Because measurement model is built on a certain experiment, inevitably, there may exist some exceptions like a mutation occurs in certain distance, or abnormal values measured due to environmental impact. So we need to deal with these rare exceptions:

- Set the initial value as the ranging result, when value after compensated is obviously unreasonable.

For example, when a smaller LQI compensated value corresponding to a smaller distance value, we should examine its rationality. From Fig. 2 and experimental data statistics, LQI value is monotone decreasing within 3.5 m, which means there is no one-to-many relations between LQI and distance, and LQI values after 3.5 m are smaller than the values within 3.5 m. So we can establish a rule reference: when LQI $>$ LQI[3.5 m], the LQI can directly estimate its corresponding distance, if the LQI $<$ LQI[3.5 m], its corresponding distance should greater than 3.5 m, otherwise the result is unreasonable. By the way, the LQI[3.5 m] said average value of LQI in 3.5 m distance.

- Set the initial value as the result when value after compensated is larger than estimate maximum distance range, and also larger than a certain threshold.

5.2 Distance Result Correction

Due to the close to model strategy, idea of distance correction is: compare the distance results from four curve fitting methods of measurement model, and

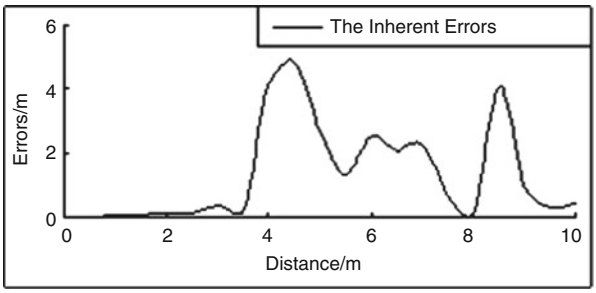

Fig. 6 Curve of model's inherent error

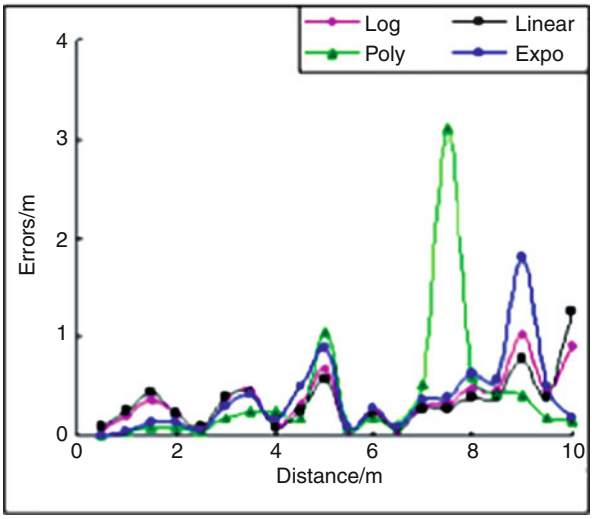

Fig. 7 Comparison fig of four fitting curves

eliminate biggish error and correct distance based on polynomial fitting, and also combined with other curve fitting.

Figure 7 shows four different fitting curves of the experiment's range error, they are exponential, linear, polynomial and logarithm curves. Seen from Fig. 7 and summarize of experiments' result, we can get:

1. The trends of these four curves are similar, but due to the fitting curve's own differences and inherent error, different kinds of curves might have differences in probability of error and amplitude at the same distance.
2. Within 5 m, polynomial fitting is the best, we will directly use it as the final result.
3. Larger than 5 m, polynomial fitting has the minimum errors in most cases, but it exists large occasional mutation errors.

Segmentation processing can be used to solve the problem above:

1. Determine the standard of segmentation. Based on the rule reference before, we set LQI[3.5 m] as boundary.

2. When LQI $\geq$ LQI[3.5 m], the distance between the sending and receiving nodes are close, so calculate result using polynomial fitting model directly. When LQI $<$ LQI[3.5 m], the distance between the sending and receiving nodes are little far, so calculate result using multiple curve fitting models. The exact way is calculating differences between the results from four kinds of fitting, grouping the distances according to the differences, and calculates the average of the distances in the biggest group. If there is more than one biggest group, we will choose the group that contain polynomial fitting. At last, the final average value is the corrected distance result.

6 Experiment Analysis

In order to verify the validity of the ranging model, we experimented under the same experimental scene, and got two groups of data: the first group is measured LQI value at ten randomly selected distance. We record relation groups between distance and LQI, as reference for LQI pre-correction. The second group of data is measured LQI value at the distance with 0.5 m stepping, which are used to estimate the distance. In order to guarantee the real-time, we only obtain LQI data for 20 times at each distance. Process is as follows:

Step 1: Calculate the averages of LQI values at each distance as the final measured results.

Step 2: Follow the steps of grouping correction, correct the LQI in second group using the LQI in the first group. The correction effect shows in Fig. 8.

Step 3: Based on the distance measurement model, use corrected LQI values to calculate distance results.

Figure 9 shows the results of four times error processing. The first curve shows error of the results that LQI directly substitute the experimental data into range model. The second curve shows the errors when substitute the corrected LQI into range model. The third curve shows the error that results has already been compensated based on the second step. And the fourth curve is plotted by the error after distance correction based on the third step.

Table 1 gives a summary of several aspects on the results of the ranging experiment.

In subsequent localization algorithm, we can add the weight design to the distance that is relatively close to the nodes (especially nodes within 3.5 m), which can help further improve the accuracy of the localization algorithm.

Table 2 compared with the results from other references upon the perspective of ranging error. We can find that the measurement based on LQI can get better effect within a close range. The distance measurement algorithm in this paper has a higher ranging precision.

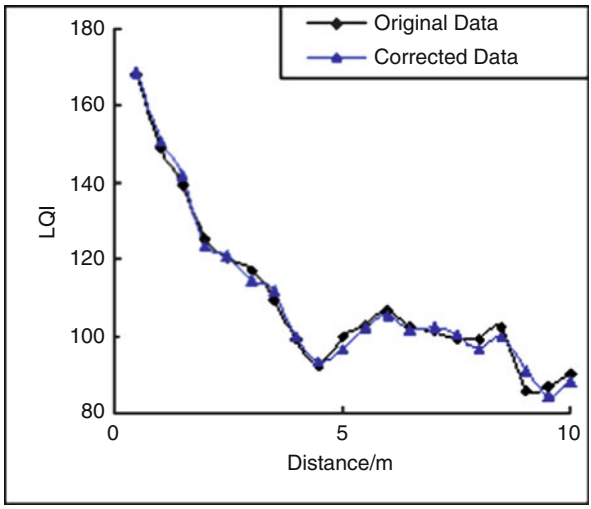

Fig. 8 Correction effect of LQI

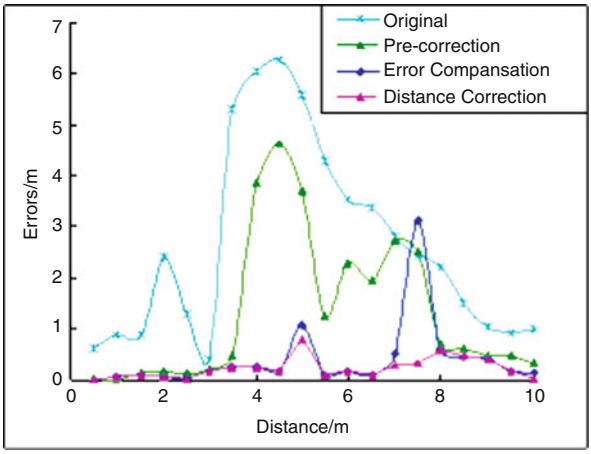

Fig. 9 Results of distance measurement

Table 1 Summary on distance measurement

Error <1 m (%)	Error <0.5 m (%)	Average error (m)	Maximum error (m)	Minimum error (m)
100	90	0.25	0.80	0.01

Table 2 Result comparison

Algorithm	Average error (m)	Method	Field/range
Algorithm in this paper	0.25	LQI	Outdoor/10 m
Algorithm in reference [4]	1.23	RSSI	Outdoor/10 m
	0.86	LQI	
	0.71	RSSI and LQI	
Algorithm in reference [10]	0.24	LQI	Indoor/8 m

7 Conclusion

In the distance measurement model, the distance results fluctuate between the true value, and the precision of results is lower at the concave of LQI signal decline curves. Observed from many times ranging experimental data, there is no obvious regularity in the range error changes, that is to say, the influences from LQI's own characteristics and the environmental factors are random.

The distance measurement algorithm based on LQI proposed in this article, including the LQI pre-correction, error compensation and distance results correction algorithm, can well reduce the differences brought from LQI fluctuations, and also reduce the errors caused by environmental factors effectively. Verified by experimental results, the LQI distance measurement algorithm improves the ranging accuracy effectively, and the final result of ranging can meet the demand of nodes localization in most wireless sensor networks when the range is in 10 m and its accuracy within 1 m.

It is a common method to measure distance using signal strength (LQI). Its requirements in node hardware, cost and energy consumption are relatively low. Although it is vulnerable to environmental conditions, constrained to the features of node itself as well as transmission power, all of which will make precision limited, this method is still popular. For most of the wireless sensor network applications, whose location requirements are not particularly accurate, this method is really a good choice.

References

1. Gao X-H, Li Y, Feng H (2009) Research on location of node for wireless sensor network. Inf Technol 7:233–235
2. Zhang J-W, Zhang L, Ying Y (2009) Research on location of RSSI based on Zigbee. Chin J Sens Actuators 22(2):285–288
3. Hu Q-Q, Zhang Q-H, Zhao F, Liang Y-Q (2011) Research on LQI location algorithm and errors for wireless sensor networks. J Chin Comput Syst 1(32):95–98
4. Zhang J-Y, Sun M-H, Wang X (2007) Dynamic distance estimation method based on RSSI and LQI. Electron Meas Technol 30(2):142–145
5. MC1322x Reference Manual (2008) Advanced ZigBee™-compliant SoC platform for the 2.4 GHz IEEE® 802.15.4 standard. Document Number: MC1322xRM Rev. 0.0, p 21–22
6. Zigbee Alliance (2004) ZigBee Document 053474r06, Version 1.0, 14 Dec 2004
7. IEEE (2003) Standard for telecommuting- cations and information exchange between system-local area medium access control (MAC) and physical layer (PHY) specifications for low rate wireless personal area networks (WPAN)
8. http://www.ieee802.org/15/pub/TG4 html
9. Simple Media Access Controller (SMAC) User's Guide. Document Number: SMACRM Rev. 1.5 03/2008
10. Qianjie Z, Hongyan C (2010) Experimental analysis of nodes distance measurement based on LQI. J Nanjing Normal University (Engineering and Technology Edition) 10(3):40–43

A 3-D Channel Model for High-Speed Railway Communications in Mountain Scenario

Jia Guiyuan, Wu Muqing, Zhao Min, and Zhao Ruojun

Abstract This paper proposes a novel three-dimensional (3-D) geometry-based stochastic channel model (GSCM) for high-speed railway (HSR) communications in mountain scenario. The proposed model not only takes the local scatterers into consideration, but also accounts for the effect of mountains on the wireless channel, which is not considered in existing models for HSR. The mathematical representation of the channel impulse response is given in this paper. Then the cumulative distribution function (CDF) of angle of departure (AoD) and space-time correlation function (STCF) are derived based on the proposed model. Finally, some numerical results and comparisons are given.

Keywords High-Speed railway • Geometry-Based stochastic channel model • Angle of departure • Space-Time correlation function

1 Introduction

The high-speed railway (HSR) has been rapidly developed recently. There is a rising demand to transmit large amount of data for the train safety and passenger service. However the Doppler effect and the unexpected environments around the train make the wireless channel more complicated, where the communication quality of the HSR is poor. To develop future HSR communication systems, an exact knowledge of the fading channel is of great importance.

Channel model is fundamental to analyze the performance of communication system. The standardized channel model WINNER II can be used in HSR environment by choosing the scenario as D2a [1]. But the special propagation scenarios

J. Guiyuan (✉) • W. Muqing • Z. Min • Z. Ruojun
Beijing University of Posts and Telecommunications, Beijing, China
e-mail: jeansyuanjgy@163.com; wumuqing@bupt.edu.cn; zhaomin@bupt.edu.cn; zhaoruojun@bupt.edu.cn

B. Zhang et al. (eds.), *The Proceedings of the Second International Conference on Communications, Signal Processing, and Systems*, Lecture Notes in Electrical Engineering 246, DOI 10.1007/978-3-319-00536-2_133,

along the railway, such as mountain and viaduct, were not taken into account in WINNER II model, which results in that the WINNER II model cannot describe the HSR wireless channel accurately. Moreover, some channel parameters in HSR were discussed in later literatures. In [2], the effects of viaduct height and base station antenna relative height on path loss were investigated. Tuned free-space path loss models in viaduct and plain scenarios were proposed in [3]. The Ricean K factors in viaduct and cutting scenarios were estimated in [4]. A novel and practical study on the position-based radio propagation was presented by performing extensive measurements at 2.35 GHz [5]. In our campaign, we performed a measurement at 2.6 GHz on Harbin–Dalian railway and obtained some channel parameters.

In this paper, we propose a 3-D geometry-based stochastic channel model (GSCM) for HSR communications in mountain scenario. Taking the scenario feature into consideration, we model the channel as having both distant and local scatterers [6]. The mountains are modeled as distant scatterers within a semi-ellipsoid, while the buildings and other scatterers around the train are modeled as local scatterers within a sphere. Hence the received signal at the train results from the distant scattering process and the local scattering process. Then the expressions for cumulative distribution function (CDF) of angle of departure (AoD) and space-time correlation function (STCF) are given based on the proposed model. Finally, numeric comparisons with WINNER II and measurements are conducted to validate the model.

The rest of the paper is organized as follows. The mountain scenario and the corresponding channel model are described in Sect. 2. The CDF of AoD and the STCF are derived in Sect. 3. The simulation results are presented in Sect. 4. Conclusions are drawn in Sect. 5.

2 The Channel Model

The mountain scenario around the railway is shown in Fig. 1. The signal emitted from the BS reaches the train in three main ways: LOS, scattered by the local scatterers and scattered by the mountains. Then a 3-D GSCM for HSR mountain scenario is proposed as shown in Fig. 2. Here we introduce the model and then give the expression of the channel impulse response.

We consider a 2*2 MIMO configuration. The BS is set at the origin of the coordinates with the relative height h denoted by O_{BS}. BS_p and BS_q are the antenna elements of BS, spaced by ξ_{pq}. The train, denoted by O_U, located at (D,0,0) with a velocity of v. U_l and U_m are the antenna elements on the train, spaced by ξ_{lm}.

The mountains are modeled as distant scatterers distributed inside a semi-ellipsoid. The semi-ellipsoid centers at $(x_d, y_d, 0)$ with three semi-principal axes as a, b and c, respectively. The k-th scatter is denoted by D_k. The blue solid lines in Fig. 2 show the link paths scattered by D_k. The buildings, trees and other scatterers

Fig. 1 The HSR mountain scenario. The train moves on the viaduct at a high speed. The BS is located about 20 m away from the track. There are mountains in the distance

around the train are modeled as local scatterers distributed inside a sphere. The sphere has a radius of R, centers at the train. The i-th scatter is represented by S_i. The red solid lines in Fig. 2 show the link paths scattered by S_i.

In this model, only single-bounce path and only plane wave in this channel is considered. It is assumed the scatterers are uniformly distributed in both the semi-ellipsoid and the sphere.

We now give the expression of the channel impulse response. The waves emitted from the BS travel over different paths with different AoDs, and after being scattered by local and distant scatterers, impinge the antenna arrays on the train. We assume the scatterers are equal. In other words, the contributions of all scatterers to path power to the channel are the same. The channel is composed of three parts: the LOS, the contribution from local scatterers and distant scatterers, indentified by the superscripts LOS, S and D, respectively. Mathematical representation of the channel impulse response between BS_p and U_l results in the following expressions.

$$h_{lp}(t) = h_{lp}^{LOS}(t) + h_{lp}^{S}(t) + h_{lp}^{D}(t) \tag{1}$$

$$h_{lp}^{LOS}(t) = \sqrt{\Omega_{lp}^{LOS}} \exp\left\{ -j\frac{2\pi}{\lambda}\xi_{lp} + j2\pi v^{LOS} t \right\} \delta(\tau - \tau^{LOS}) \tag{2}$$

$$h_{lp}^{S}(t) = \lim_{N\to\infty} \sum_{i=1}^{N} \sqrt{\frac{\Omega_{lp}^{S}}{N}} \exp\left\{ -j\frac{2\pi}{\lambda}(\xi_{ip} + \xi_{il}) + j2\pi v_i^{S} t \right\} \delta(\tau - \tau_i^{S}) \tag{3}$$

$$h_{lp}^{D}(t) = \lim_{N\to\infty} \sum_{k=1}^{N} \sqrt{\frac{\Omega_{lp}^{D}}{N}} \exp\left\{ -j\frac{2\pi}{\lambda}(\xi_{kp} + \xi_{kl}) + j2\pi v_k^{D} t \right\} \delta(\tau - \tau_k^{D}) \tag{4}$$

In particular, we define that in this paper ξ_{st}, $\overrightarrow{\xi}_{st}$ and $\overrightarrow{\Phi}_{st}(s, t = p, q, i, k, l, m, O_{BS}, O_U)$ represent the scalar distance between s and t, the vector from s to t and the unit vector from s to t, respectively. In the equations above, λ is the wavelength. $\delta(\cdot)$ is the Dirac delta function. The parameters $\Omega_{lp}^{LOS}, \Omega_{lp}^{S}$ and Ω_{lp}^{D} define the mean power of

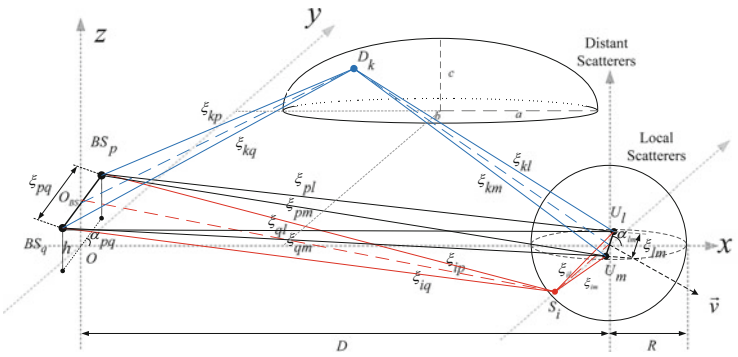

Fig. 2 The 3-D GSCM for HSR communication in mountain scenario

the LOS, local and distant scatterers parts. We impose the boundary condition $\Omega_{lp}^{LOS} + \Omega_{lp}^{S} + \Omega_{lp}^{D} = 1$ to ensure that the average power is normalized to unity [7]. τ^{LOS} is the delay of LOS path, defined as the ratio of the distance between BS_p and U_l to speed of electric wave: $\tau^{LOS} = \xi_{lp}/c$. τ_i^S and τ_k^D are defined in the same way for local and distant scatterers: $\tau_i^S = (\xi_{ip} + \xi_{il})/c$ and $\tau_k^D = (\xi_{kp} + \xi_{kl})/c$. The Doppler shift is calculated from the velocity $\overrightarrow{v}$, unit vector $\overrightarrow{\Phi}$ and wavelength λ: $\upsilon^{LOS} = \overrightarrow{v} \cdot \overrightarrow{\Phi}_{pl}/\lambda$, $\upsilon_i^S = \overrightarrow{v} \cdot \overrightarrow{\Phi}_{il}/\lambda$ and $\upsilon_k^D = \overrightarrow{v} \cdot \overrightarrow{\Phi}_{kl}/\lambda$, where $(\cdot)$ is the dot product operator of two vector.

3 The Statistical Properties of the Model

In this section, we try to analyze two aspects of HSR mountain scenario model: AoD statistics and space-time correlation property.

3.1 The CDF of AoD

Here we develop the mathematical framework for the description of the AoD statistics of the multipath at the BSs antennas.

Let us consider the local scatterers first. In our model, the scatterers are uniformed distributed in the sphere. Therefore the volume of the intersection of the sphere and the tetrahedron that has the tip at O_{BS} and sizes as the rays that emanate from O_{BS} at angle (θ,ϕ) $(\theta + \Delta\theta,\phi)$ $(\theta,\phi + \Delta\phi)$ and $(\theta + \Delta\theta, \phi + \Delta\phi)$, denoted by $O_{BS}EFGH$ in Fig. 3, is proportional to the probability of the AoD statistics of the multipath at the BSs antennas [8]. The volume of the tetrahedron

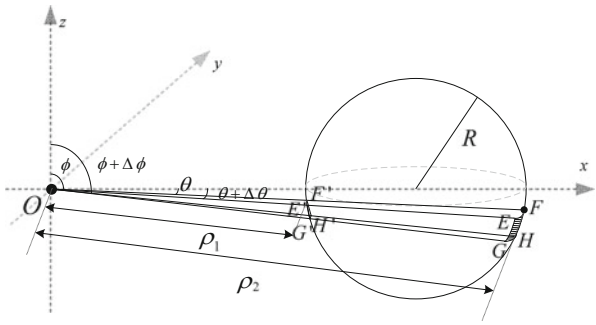

Fig. 3 The CDF of AoD for local scatterers. The volume of the intersection of the sphere and the tetrahedron is proportional to the probability of the AoD

$O_{BS}EFGH$ is $V_2(\theta,\phi)=\rho_2^3(\theta,\phi)\Delta\theta\Delta\phi/3$. The volume of intersection of the sphere and the tetrahedron is the difference between $O_{BS}EFGH$ and $O_{BS}E'F'G'H'$

$$V_i(\theta,\phi)=[\rho_2^3(\theta,\phi)-\rho_1^3(\theta,\phi)]\Delta\theta\Delta\phi/3 \tag{5}$$

Then, the CDF of the AoD at the BS side is obtained from the integral over θ and ϕ of the ratio of the intersection volume to the sphere volume.

$$F^S(\theta,\phi)=\int_{\theta^S_{\min}}^{\theta}\int_{\phi^S_{\min}}^{\phi}[\rho_2^3(\theta',\phi')-\rho_1^3(\theta',\phi')]/(4\pi R^3)d\theta' d\phi' \tag{6}$$

where

$$\begin{aligned}\rho_1&=D\sin\phi\cos\theta-\sqrt{D^2\sin^2\phi\cos^2\theta-D^2+R^2}\\ \rho_2&=D\sin\phi\cos\theta+\sqrt{D^2\sin^2\phi\cos^2\theta-D^2+R^2}\end{aligned}\quad,\sin\phi\cos\theta\geq\sqrt{1-(R/D)^2}$$

We deal with the distant scatterers in the same way, and get the CDF of the AoD caused by distant scatterers.

$$F^D(\theta,\phi)=\int_{\theta^D_{\min}}^{\theta}\int_{\phi^D_{\min}}^{\phi}(B^2-4AC)^{3/2}/(8\pi abcA^2)d\theta' d\phi' \tag{7}$$

where

$$\begin{aligned}A&=b^2c^2\sin^2\phi\cos^2\theta+a^2c^2\sin^2\phi\sin^2\theta+a^2b^2\cos^2\phi\\ B&=2b^2c^2x_d\sin\phi\cos\theta+2a^2c^2y_d\sin\phi\sin\theta\\ C&=b^2c^2x_d^2+a^2c^2y_d^2-a^2b^2c^2\end{aligned} \tag{8}$$

Finally, the CDF of AoD is the sum of CDF with respect to local and distant scatterers. The cumulative distribution function (CDF) of the AoD with respect to azimuth angle θ will be plotted in Sect. 4.

$$F(\phi,\theta) = F^S(\phi,\theta) + F^D(\phi,\theta) \tag{9}$$

3.2 The Space-Time Correlation Function

Here we derive the STCF based on the proposed channel model. The normalized space-time correlation function between any two complex fading envelopes $h_{lp}(t)$ and $h_{mq}(t)$ is defined as [9]

$$\rho_{lp,mq}(\Delta t) = \frac{\mathrm{E}[h_{lp}(t)h^*_{mq}(t+\Delta t)]}{\sqrt{\Omega_{lp}\Omega_{mq}}} = \rho^{LOS}_{lp,mq}(\Delta t) + \rho^{S}_{lp,mq}(\Delta t) + \rho^{D}_{lp,mq}(\Delta t) \tag{10}$$

where $(\cdot)^*$ denotes the complex conjugate operation, $\mathrm{E}[\cdot]$ is the statistical expectation operator.

Here we transform (10) to make it an explicit function of time and space separation. We substitute (2), (3), (4) into (10) and use the appropriate assumption of $D >> R >> \max(\xi_{lm}, \xi_{pq})$ which is often the case in HSR mountain scenario and approximate relations $\sqrt{1+t} \approx 1 + t/2$, when t is very small. For example, ξ_{il} can be written as

$$\xi_{il} = \left| \overrightarrow{\xi}_{iO_U} + \overrightarrow{\xi}_{O_U l} \right| \approx \left| \overrightarrow{\xi}_{iO_U} \right| + \overrightarrow{\Phi}_{iO_U} \cdot \overrightarrow{\xi}_{O_U l} \tag{11}$$

Similarly, we deal with ξ_{st} (s,$t = p$,q,i,k,l,m), then we get

$$\begin{aligned}
\rho^{S}_{lp,mq}(\Delta t) &= \lim_{N\to\infty} \sum_{i=1}^{N} \sqrt{\frac{\Omega^S_{lp}\Omega^S_{mq}}{\Omega_{lp}\Omega_{mq}}} \exp\left[j\frac{2\pi}{\lambda}(\Delta t \overrightarrow{v} + \overrightarrow{\xi}_{lm}) \cdot \overrightarrow{\Phi}_{iO_U} + j\frac{2\pi}{\lambda}\overrightarrow{\xi}_{pq} \cdot \overrightarrow{\Phi}_{O_{BS}i} \right] \\
\rho^{D}_{lp,mq}(\Delta t) &= \lim_{N\to\infty} \sum_{k=1}^{N} \sqrt{\frac{\Omega^D_{lp}\Omega^D_{mq}}{\Omega_{lp}\Omega_{mq}}} \exp\left[j\frac{2\pi}{\lambda}(\Delta t \overrightarrow{v} + \overrightarrow{\xi}_{lm}) \cdot \overrightarrow{\Phi}_{kO_U} + j\frac{2\pi}{\lambda}\overrightarrow{\xi}_{pq} \cdot \overrightarrow{\Phi}_{O_{BS}k} \right] \\
\rho^{LOS}_{lp,mq}(\Delta t) &= \sqrt{\frac{\Omega^{LOS}_{lp}\Omega^{LOS}_{mq}}{\Omega_{lp}\Omega_{mq}}} \exp\left[j\frac{2\pi}{\lambda}(\Delta t \overrightarrow{v} + \overrightarrow{\xi}_{lm} + \overrightarrow{\xi}_{pq}) \cdot \overrightarrow{\Phi}_{O_{BS}O_U} \right]
\end{aligned} \tag{12}$$

The STCF is a function of time separation Δt, space separation $\overrightarrow{\xi}_{pq}$ and $\overrightarrow{\xi}_{lm}$. Given specific angle distribution (like the von Mises distribution), the mathematic representation is provided in [9].

4 Numerical Result

In this section, we take some simulations for the CDF of AoD and make comparison with WINNER II and measurements to illustrate that the proposed model accounts for the effect of mountain on the wireless channel, which is not considered in existing models. Then we study the properties of the STCF.

We set the main channel parameters as follows. The carrier frequency of the signal is 2.6 GHz. So the carrier wavelength is 0.115 m. The train is moving towards the x-axis positive direction. The speed of the train is 360 km/h, i.e. 100 m/s. The relative height of BS is about 20 m. The distance between BS and the train is 1,000 m. The three principal axes of distant semi-ellipsoid a, b, and c are 1,000, 300 and 70 m, respectively. The radius of local sphere R is 30 m. Number of scatterers is limited to fit the research in [5]. The Ricean K factor follows a Gaussian distribution as K (in dB) $\sim N(6.2, 6)$ [10]. The model is generated in a deterministic approach.

Figure 4 shows the CDF of AoD with respect to azimuth angle θ. To validate our model, we compare our model with the measurement. The CDF of AoD developed in WINNER II D2a is also plotted in this figure. We can see model proposed in this paper can fit the measurement more accurately. In the HSR mountain scenario, the local scatterers play a dominant role in the CDF of AoD with small azimuth angles. But the effect of distant scatterers can't be ignored. Due to the large bulk of mountain, a wide span of azimuth angle can be seen as a result. In contrast to WINNER II D2a model which only takes the local scatterers into consideration, the model proposed in this paper accounts for the effects of distant scatterers.

In Fig. 5, we plot the absolute value of the temporal auto-correlation function versus time. A comparison to measurement and WINNER II D2a is also shown in this figure. We can see model proposed in this paper is in better agreement with the measurement result than WINNER II D2a is. The vibration degree of ACF decreases as the Δt becomes larger as a result of the effects of distant scatterers.

Figure 6 shows the effect of antenna spacing on the space correlation. The x-axis and y-axis denote the antenna spacing on the BS and train, respectively. We can find that the correlation decreases sharply when antenna spacing on the train ranges from zero to about $\lambda/2$. A reason is that the scatterers are mainly distributed around the train, thus the paths impinge on the antenna in all directions with different angles [9], while the angle span on the BS side is smaller. Therefore we see the antenna spacing on the train has a larger impact on the space correlation function than that of the BS does.

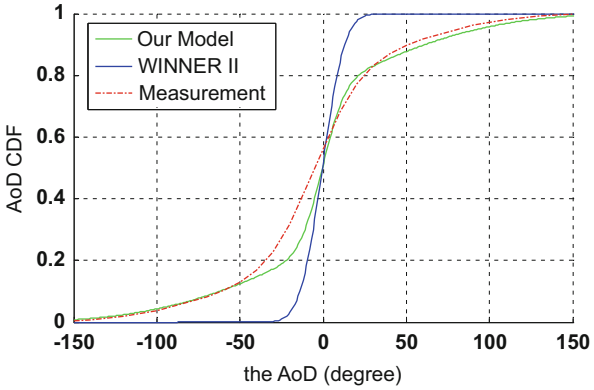

Fig. 4 The CDF of AoD in simulation. Due to the large bulk of mountain, a wide span of azimuth angle can be seen in measurement

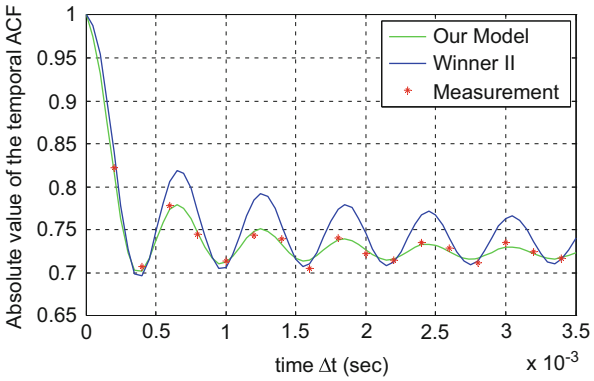

Fig. 5 The CDF of AoD in simulation. Due to the large bulk of mountain, a wide span of azimuth angle can be seen in measurement

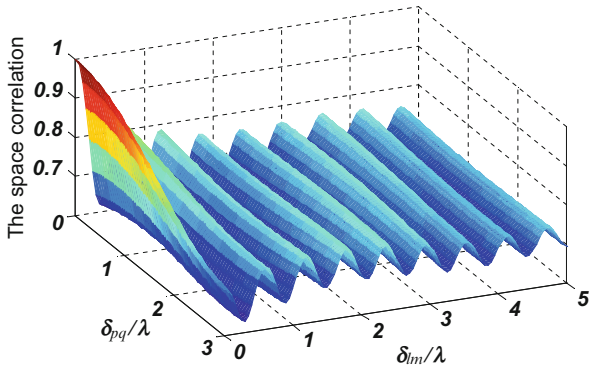

Fig. 6 The temporal auto-correlation function versus time Δt. Our model is in better agreement with the measurement result than WINNER II D2a is

5 Conclusion

This paper proposes a 3-D GSCM for HSR in mountain scenario. In our model, the mountains are modeled as distant scatterers within a semi-ellipsoid while other scatterers around the train are modeled as local scatterers within a sphere centered on the train. The channel is composed of three parts: LOS, components diffused by distant and local scatterers. The mathematical representation of the channel impulse response is given in this paper. Then we derived the CDF of AoD and STCF. By numerical simulation, we can see our model takes the effect of distant scatterers into consideration, which makes it fit the measurements more accurately.

Acknowledgements This project is supported by the National Science and Technology Major Projects of China under Grant No. 2011ZX03001-007-03.

References

1. Kyosti P, Meinila J, Hentila L et al (2007) WINNER II channel models, IST, Tech Rep IST-4-027756 WINNER II D1.1.2 v1.2
2. He R, Zhong Z, Ai B, Ding J (2011) An empirical path loss model and fading analysis for high-speed railway viaduct scenarios. IEEE Antennas Wireless Propagat Lett 10:808–812
3. Wei H, Zhong Z, Guan K, Ai B (2010) Path loss models in viaduct and plain scenarios of the high-speed railway. In: Proceedings of the 5th International ICST Conference on Communications and Networking in China (ChinaCom 2010), 1–5 August 2010
4. Lu J, Zhu G, Ai B (2010) Radio propagation measurements and modeling in railway viaduct area. In: Proceedings of the 6th International Conference on Wireless Communications, Networking and Mobile Computing (WiCOM 2010), 1–5 September 2010
5. Liu L, Tao C, Qiu J, Chen H, Yu L, Dong W, Yuan Y (2012) Position-based modeling for wireless channel on high-speed railway under a viaduct at 2.35 GHz. IEEE J Select Areas Comm 30:834–845
6. Nicolai C, Claude O (2008) The COST 273 MIMO channel model: three kinds of clusters. In: Proceedings of the 10th International Symposium on Spread Spectrum Techniques and Applications, pp 282–286
7. He Z, Chen W, Zhou W, Matthias P, Ali C (2009) Modelling of MIMO vehicle-to-vehicle fading channels in T-junction scattering environments. In: Proceedings of the 3rd European Conference on Antennas and Propagation (EuCAP 2009), pp 652–656
8. Konstantinos BB (2012) A generalized elliptical scattering model for the spatial characteristics of mobile channels. Wireless Pers Comm 67(4):971–984
9. Ali A, Mostafa K (2002) A space-time correlation model for multielement antenna systems in mobile fading channels. IEEE J Select Areas Comm 20:550–560
10. Gao L, Zhong Z, Ai B, Xiong L (2010) Estimation of the Ricean K factor in the high speed railway scenarios. In: Proceedings of the 5th International ICST Conference on Communications and Networking in China (ChinaCom 2010), pp 1–5

Adaptive Control Algorithm Improving the Stability of Micro Force Measurement System

Yelong Zheng, Xiaoli Yang, Meirong Zhao, Tao Guan, and Meihua Jiang

Abstract Based on the electrostatics principle, the measurement and realization of micro forces in the order of 10^{-6} N to 10^{-4} N (the resolution is 10^{-8} N) can be realized and it can be traced back to the SI such as length, voltage, capacitance, etc. Because the stiffness and damping ratio of the system are very small, both the external interference and the parameter variation would make the system unstable so that it is hardly to make the system get optimal by using the traditional PID control algorithm. This dissertation introduces an adaptive control algorithm based on minimum variance. Adjust the parameter values of the controller continuously to make the transient response and the output of the control object get optimal when the measurement system working. The system performance is tested by measuring standard weights of 5, 10 and 20 mg. The result shows that it can not only speed up the convergence but also reduce residual vibration, decreasing variance to 0.01 μm.

Keywords Electrostatic force • Traceability • Adaptive • Control • Measurement • Minimum variance

1 Introduction

With the development of new materials, microelectronics and biological science, the application and measurement of micro forces can play key roles. It's an urgent need to establish a measurement standard for micro forces to realize the traceability of micro forces to SI. There are a lot of cases in which micro forces need to be measured accurately such as the elastic constant calibration of the atomic force

Y. Zheng (✉) • M. Zhao • T. Guan • M. Jiang
State Key Laboratory of Precision Measuring Technology and Instruments, Tianjin University, Tianjin, China
e-mail: zhengyelong_tju@126.com

X. Yang
China Petroleum Technology & Development Corporation, Beijing, China

B. Zhang et al. (eds.), *The Proceedings of the Second International Conference on Communications, Signal Processing, and Systems*, Lecture Notes in Electrical Engineering 246, DOI 10.1007/978-3-319-00536-2_134,

microscope cantilever beam, the measurement of the micro forces in biochips and micro organism tissue, the measurement of micro-mass.

Scientific research institutes have carried out researches from country to country. Gunma University of Japan has realized the measurement of micro static forces using the downwards component of gravity. The result of the experiment shows: its minimum measured value is 1.83×10^{-4} N, the standard uncertainty is 2×10^{-6} N [1]. In order to reproduce and measure forces less than 10^{-5} N, the National Institute of Standards and Technology (NIST) in USA carried out a research of measurement technology, established corresponding measuring devices and set up the Small Force Measurement Laboratory (SFML) [2]. The Physikalisch Technische Bundesanstalt (PTB) in Germany nano-newton force metrology group came up with an aluminum plate pendulum based on the electrostatics principle which can measure forces less than 10^{-5} N, whose resolution is 10^{-12} N, when the force is 10^{-10} N, the relative uncertainty is 0.8 % [3].

The research core of this topic is a high-precision capacitive micro force sensing device based on the electrostatics principle which can tack back to SI such as voltage, displacement, etc. It uses electrostatic forces to reproduce micro forces, changing mechanical quantities into electrical quantities like capacitance and voltage, and use the balance between the gravity of weights and the electrostatic force to realize the correction of forces at μN level. Our research group has designed a rotating elastic support with stiffness at 0.8 N/m.

Because the system has a small stiffness at $k = 0.8$ N/m and a small damping ratio at $c = 0.1$, the external interference and the parameter variation both can make the system unstable and it causes sustained oscillation when there is a big external interference. In the traditional PID control algorithm, when the measurement system working in a stable state, the output of the controlled object is relatively stable as well. At this time the parameters of the PID controller once be set, they keeps almost unchanged. However, in the actual measurement process, if the input changes greatly or the operation state of the control system changes and because there are many kinds of interference like external vibration and air disturbance, the output will be changed. If we still keep the parameters of the PID controller unchanged, it is hardly to get the optimal control. Adaptive control can be adopted to ensure the output of the control system to achieve the optimal. The purpose of this design is to make the transient response and the output of the control object get optimal by adjusting continuously the parameter values of the controller. If the advanced algorithm is introduced to the controller system, the transient response and the output both can get optimal, the convergence will be speeded up and the residual vibration will be reduced so that the variance can be reduced as well.

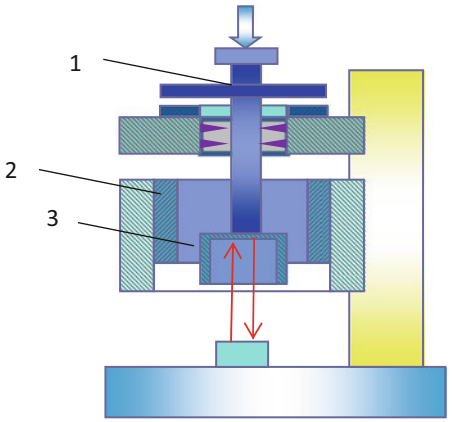

Fig. 1 System schematic diagram (1) rotating elastic support; (2) outer electrode; (3) inner electrode

2 System Structure

The system uses the electrostatics principle to reproduce the force. The system schematic diagram is shown as Fig. 1. The part for generating electrostatic forces is a variable cross-section cylindrical capacitor. The capacitor consists of a set of concentric cylindrical electrodes. The outer electrode is fixed on the combined translation platform and the inner electrode can move along the vertical direction with the motion of the lever. When there is voltage between the outer electrode and the inner electrode, there will be an electrostatic force. By controlling the voltage between the two electrodes, the micro force (standard mass) to be measured will be balanced by the electrostatic force so that the measurement and traceability of micro forces can be realized.

If the outer electrode and the inner electrode are concentric, the capacitance gradient in the plane will possess radial symmetry. The resultant force acted on the inner electrode is along the vertical direction. The relation between the electrostatic force and the applied control voltage is shown as (1) [3].

$$F = \frac{1}{2}U^2\frac{\mathrm{d}C}{\mathrm{d}Z} \tag{1}$$

In (1), F is the electrostatic force (the unit is N), U is the voltage difference between the electrodes (the unit is V). dC/dZ is the capacitance gradient (the unit is F/m), i.e. the rate of change of the capacitance along with the displacement in the vertical direction. When the parameters of the capacitor are determined, the capacitance gradient is a constant value, so the electrostatic force is determined by the voltage.

3 Adaptive Control Algorithm

In order to achieve higher resolution, the system stiffness is reduced to 0.8 N/m while the damping ratio c is only 0.1 which results the poles of the system are close to the right half plane in s domain. The external interference and the parameter variation can make the system unstable and result in oscillation. In the PID control algorithm, it causes sustained oscillation easily when there is a big external interference. This design introduces an adaptive control algorithm aiming at outputting the minimum variance. Adjust continuously the parameter values of the controller during the system working to make the transient response and the output of the control object get optimal.

3.1 Basic Idea

Design the adaptive control law with the aim of outputting the minimum variance. Use the recursive least-squares method to estimate the parameters of the controller directly. The minimum variance adaptive structure is shown as Fig. 2. y (k) is the input; u (k) is the output; d is time delay; $\xi(k)$ is the white noise sequence; B/A is the control object model; C/A is the disturbance channel model, $u(k)$ is the output of the minimum variance adaptive controller [4, 5].

Suppose the control object model can be expressed by differential equations as follows:

$$A\left(z^{-1}\right)y(k) = z^{-d}B\left(z^{-1}\right)u(k) + C\left(z^{-1}\right)\xi(k)$$

where: $A(z^{-1}) = 1 + a_1z^{-1} + a_2z^{-2} + \cdots + a_nz^{-n}$

$$B\left(z^{-1}\right) = 1 + b_1z^{-1} + b_2z^{-2} + \cdots + b_nz^{-n}$$
$$C\left(z^{-1}\right) = 1 + c_1z^{-1} + c_2z^{-2} + \cdots + c_nz^{-n}$$

So the output of the closed-loop system is [6, 7]:

$$y(k) = \frac{CBz^{-d}y_r(k+d) + CF\xi(k)}{AF + z^{-d}BG}.$$

3.2 Design of the Controller

Suppose the control objective is to make the accumulative error J [8, 9] of the actual output $y(k + d)$ and the expected output $y_r(k + d)$ to be minimum.

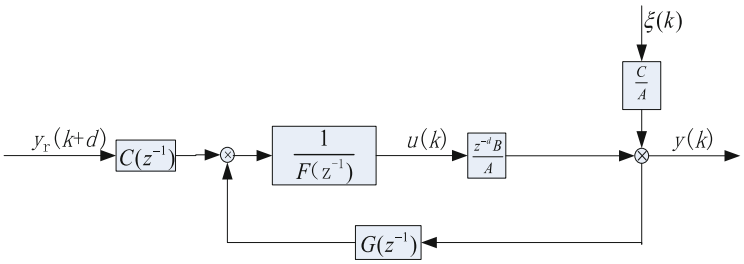

Fig. 2 The block diagram of minimum variance adaptive controller

$$J = E\left\{[y(k+d) - y_r(k+d)]^2\right\}$$

So the minimum variance control law is:

$$F\left(z^{-1}\right)u(k) = C\left(z^{-1}\right)y_r(k+d)\text{-}G\left(z^{-1}\right)y(k)$$

where: $y_r(k)$ is the expected output; $y(k + d)$ is the $(k + d)$ th output, $u(k)$ is the k th control.

$$u(k) = \frac{Ayr(k+d) - G\xi(k)}{B}$$

3.3 Simulation

The transfer function of the micro force system can be expressed as:

$$H(s) = \frac{1}{ms^2 + cs + k}$$

where m is the mass of the elastic supporting; c is the damping ratio; k is the stiffness of the elastic supporting. Sampling period is T_s. The expression in z domain is:

$$H(z) = \frac{0.09945z + 0.09765}{z^2 + 0.01979z + 0.9512}$$

From which we can calculate the poles of the system are $z_1 =$ -0.009895 + 0.975i and $z_2 =$ -0.009895-0.975i. We also can get:

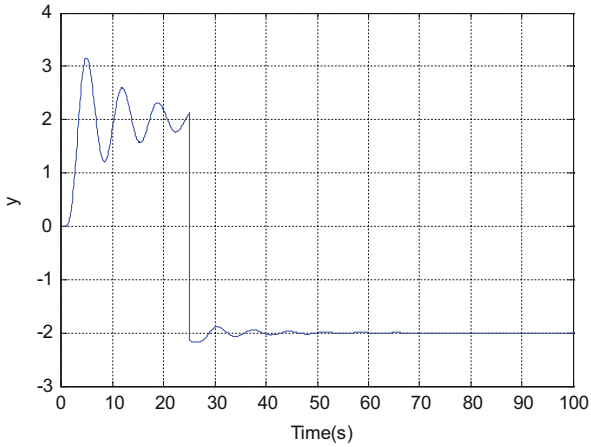

Fig. 3 The adaptive control

$$A = 1 + 0.01979z^{-1} + 0.9512z^{-2}$$
$$B = 0.09945z^{-1} + 0.09765z^{-2}$$
$$d = 1$$

Since the ground vibration variance of the laboratory is about 0.2 μm, suppose the interference signal of system $\xi(k)$ is a Gaussian white noise with variance at 0.2. When the step input is 2 at 0 s and decreases to -2 at 25 s, the output of the adaptive controller is shown as Fig. 3.

4 Experimental Comparison

Figure 4 is the photo of the electrostatic force measuring system. In order to reduce the influence of the ground vibration, the system is put on the center of the optical vibration isolation platform. The polished face of the capacitor inner electrode is used as the reflector of the laser scale RLE10 (the resolution is 10 nm) to measure the displacement caused by the micro applied force.

A group of capacitors are fixed on one end of the lever structure while the micro force to be measured is applied on the other end. The variation of the displacement of the capacitor electrode is measured by the laser scale. Then the displacement value is inputted to the PC as a feedback quantity, and the PC figures out the voltage value needed to be applied on the capacitor electrode to make it gradually restore to its original equilibrium position. Record the voltage when the laser scale restores to its original value. At this time, the electrostatic force between two electrodes generated by the voltage is equal to the micro force to be measured.

Load the standard weights of 5 mg, 10 mg and 20 mg mass respectively on the experimental device. Load the gravity of the weight on the electrostatic force system, and unload after 100 s. Figure 5 is the effect picture of traditional PID

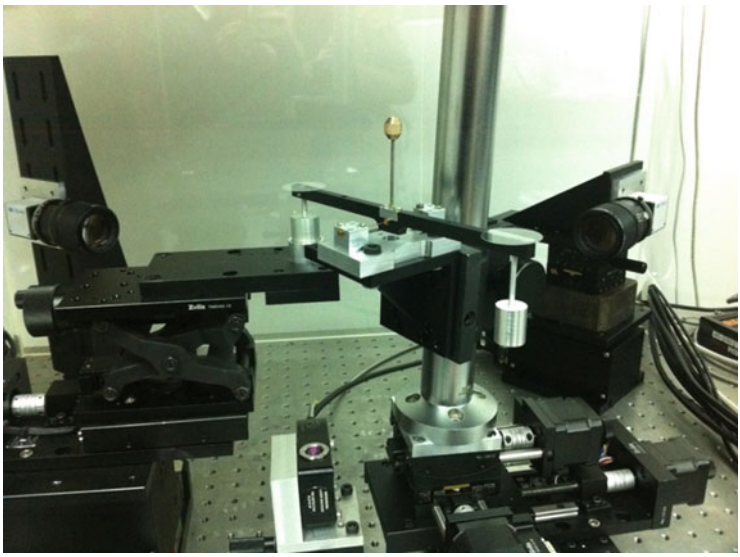

Fig. 4 The photo of the experimental device

Fig. 5 The effect picture of PID

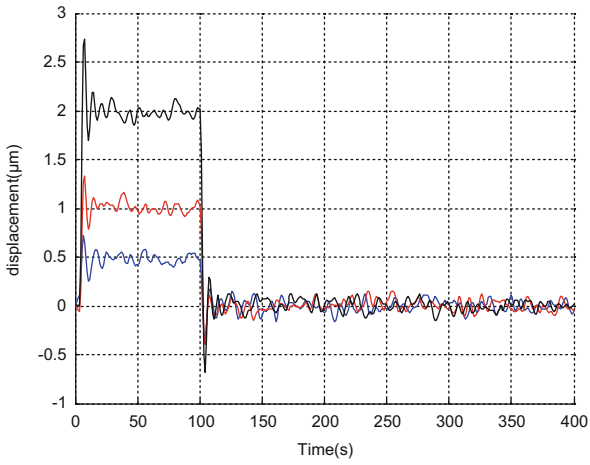

control arithmetic. Figure 6 is the effect picture of adaptive control arithmetic. In the pictures, blue lines, red lines, black lines stand for the effect pictures for 5 mg, 10 mg, 20 mg respectively.

Comparing Fig. 5 with Fig. 6, the system produces residual oscillation under the PID control, and the system can't be localized on the expected position. After the minimum variance adaptive filter is introduced, when the load is 5, 10 and 20 mg, the convergence is faster, the residual oscillation is suppressed and its variance is decreased to 0.01 μm. The result shows that this method is feasible.

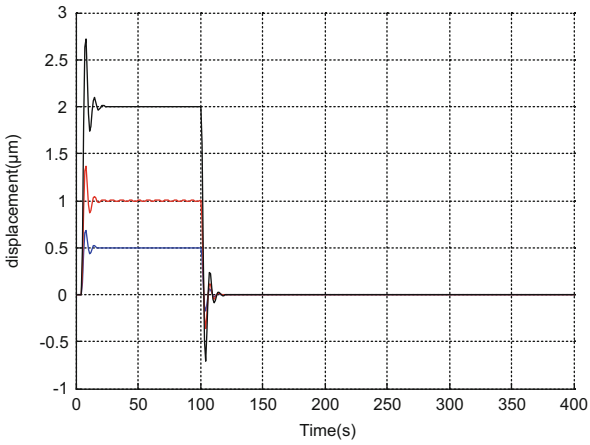

Fig. 6 The effect picture of adaptive control

5 Conclusion

This paper has introduced the micro force measuring system based on the electrostatics principle. The structure of the system makes the system sensitive to external interference. This paper adopts the adaptive control to improve the stability and the anti-interference ability of the system. Concluded from the experiment result, the adaptive control arithmetic is better than the traditional PID arithmetic.

Acknowledgements This work was supported by National Natural Science Foundation (No. 51175377) and Tianjin Natural Science Foundation (No. 12JCQNJC02700).

References

1. Newell DB, Kramar JA, Pratt JR, Smith DT, Williams ER (2003) The NIST microforce realization and measurement project. IEEE Trans Instrum Meas 52(2):508–511. doi:10.1109/tim.2003.810032
2. Fujii Y (2007) Method of generating and measuring static small force using down-slope component of gravity. Rev Sci Instrum 78(6):066104. doi:10.1063/1.2746823
3. Pratt JR, Newell DB, Kramar JA, Mulholland J, Whitenton E (2003) Probe-force calibration experiments using the NIST electrostatic force balance. Proceedings of American Society for Precision Engineering, Winter Topical Meeting, University of Florida, vol 9(61), pp 161–5
4. Sendjaja AY, Kariwala V (2009) Achievable PID performance using sums of squares programming. J Process Control 19(6):1061–1065. doi:10.1016/j.jprocont.2008.12.005
5. Harris TJ (1989) Assessment of control loop performance. Can J Chem Eng 67(5):856–861. doi:10.1002/acs.767
6. Boyd S, Barrat C (1991) Linear control design. Prentice Hall, Englewood Cliffs, NJ
7. Huang B (2003) A pragmatic approach towards assessment of control loop performance. Int J Adapt Control Signal Process 17:589–608. doi:10.1002/acs.767

8. Lofberg J (2004) YALMIP: a toolbox for modeling and optimization in MATLAB. Proceedings of IEEE international symposium on computer-aided control system design, Taipei, Taiwan, No. 04TH8770, pp 284–89
9. Kariwala V (2007) Fundamental limitation on achievable decentralized performance. Automatica 43(10):1849–1854. doi:10.1016/j.automatica.2007.03.004

QoS Performance Evaluation Methods for High-Speed Railway Mobile Communication

Dan Fei, Lei Xiong, and Jianqiang Wu

Abstract In recent years, the high-speed railway has achieved rapid development in China. To ensure the operation security of high-speed trains, providing reliable communication services is the basic requirement. Since the complex radio propagation environment, the research on the high-speed wireless communication system performance evaluation methods has caused the concern of related researchers. In this paper, we introduce a new method, hardware-in-the-loop simulation (HILS) to measure and evaluate the system QoS (Quality of Services) performance in different mobile speed. We build the simulation system with a radio channel emulator and the GSM-R (Global System for Mobile Communication for Railway) network. In addition, we accomplish an accurate emulation of the propagation environment of Beijing–Shanghai high-speed railway testing segment with actual measured data. Based on this, we finally get the conclusion that the mobile speed has little impact on CSD (Circuit Switched Data) QoS performance, while affects GPRS (General Packet Radio Service) QoS performance obviously.

1 Introduction

Compared to the public mobile communication, the propagation environment of high-speed railway communication has its particularity, such as special propagation scenes, complex large-scale fading, and of most important, severe Doppler shift caused by terminal moving in high speed and handing over frequently [1, 2]. GSM-R [3] is a new generation of railway mobile communication system which is proposed by International Union of Railway (UIC) in 1990s and has been widely used in high-speed railway lines in China.

D. Fei • L. Xiong (✉) • J. Wu
State Key Laboratory of Rail Traffic Control and Safety, Beijing Jiaotong University, Beijing 100044, P.R. China
e-mail: lxiong@bjtu.edu.cn; 12125006@bjtu.edu.cn

B. Zhang et al. (eds.), *The Proceedings of the Second International Conference on Communications, Signal Processing, and Systems*, Lecture Notes in Electrical Engineering 246, DOI 10.1007/978-3-319-00536-2_135,

To evaluate the performance of high-speed railway communication business, the corresponding concept of QoS [4, 5] is put forward. It refers to the information transmission quality between the transmitting and receiving users, as well as the users and the information transmission networks. The traditional methods for QoS performance evaluation are manly software simulation and site test, and both of them have fatal weaknesses. Software simulation is difficult to take into account many environmental factors since it has to make many assumptions, so it has poor reliability. Site test is limited by actual test conditions and consumes enormous human and financial resources, so it has poor flexibility and repeatability. HILS introduced in this paper is a new method which makes a compromise for the two traditional methods and has a good real-time property.

The remaining part of this paper is organized as follows. Section 2 describes the structure of the HILS system as well as the propagation environment emulation. Section 3 implements the analysis and evaluation for the test results on the basis of performance parameters introduction.

2 HILS Methods Description

HILS [6] is an advanced simulation method with practical equipments to replace parts of the mathematical models in the simulation system. It overcomes the weakness of bad reliability and lower efficiency in traditional pure computer simulation methods, by the combination of simulation computers and field equipments. The HILS system used in this paper is shown in Fig. 1, it mainly consists of a radio channel emulator, GSM-R network, and QoS test subsystem. The GSM-R network consists of base stations (BS), base station controller (BSC), and core network. The QoS test subsystem consists of test sever, mobile terminals, auto-test system, and Abis interface monitor. In the system, except the radio channel emulator, all the others are practical equipments, so it could accurately emulate the real-world system.

2.1 Static Propagation Environment Emulation

Taking into count the particularity of high-speed railway propagation environment, we set the co-channel interference ratio (C/I) at 18 dB and choose the COST207 [7] rural area (RA) six taps model whose parameters are listed in Table 1 as the channel model.

Standard models are widely used fading processes with certain amplitude distributions and Doppler spectrums. Classical model simulates a multipath environment where all multipath components have the same delay and equal occurrence for all incident angles and there is no line of sight (LOS) signal. So it has Rayleigh

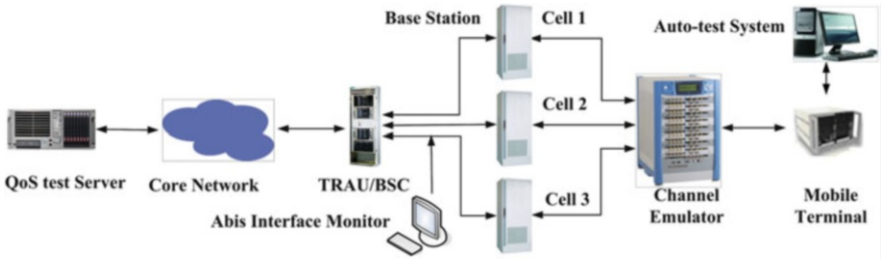

Fig. 1 HILS system block diagram

Table 1 COST207 RA six taps model parameters

Tap	Delay (ns)	Power (dB)	Doppler spectrum
1	0	0.00	Rice
2	100	−4.00	Classical
3	200	−8.00	Classical
4	300	−12.00	Classical
5	400	−16.00	Classical
6	500	−20.00	Classical

amplitude distribution whose probability density function is shown as Eq. (1) and Jakes Doppler spectrum, see Eq. (2).

$$p_{Ra}(r) = \frac{r}{\sigma^2} \exp(-\frac{r^2}{2\sigma^2}) \tag{1}$$

where r is amplitude and σ^2 is the variance of both the real and imaginary components alone.

$$S(f) = \frac{1}{\pi f_d \sqrt{1 - (\frac{f}{f_d})^2}} \tag{2}$$

where f_d is the maximum Doppler frequency shift. The Rice model is a combination of the Classical model and a LOS path with pure Doppler shift. So the Rice probability density function of amplitude is given by Eq. (3).

$$p_{Ri}(r) = \frac{2rK}{{r_s}^2} \exp(-\frac{K(r^2 + {r_s}^2)}{{r_s}^2}) I_0(\frac{2rK}{r_s}) \tag{3}$$

where r_s is the magnitude of the LOS component, $I_0(*)$ is the modified Bessel function of the first kind and zero order and K is the Rician factor which refers to the power ratio between direct wave (LOS) and scattered waves. In our simulation, K is set at 6 dB and the incident angle of LOS path is 45°.

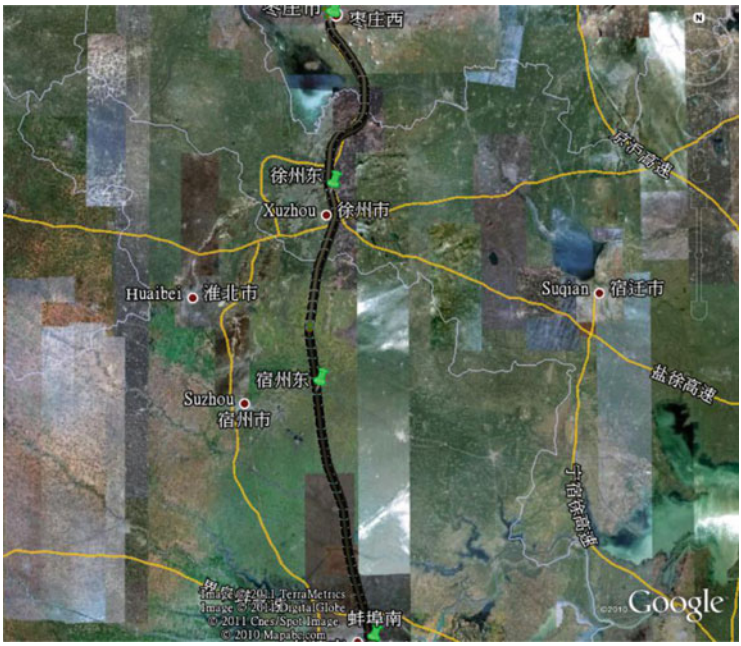

Fig. 2 Beijing–Shanghai high-speed railway testing segment map

2.2 Dynamic Propagation Environment Emulation

Here, it's necessary to emphasize the simulation of the high-speed dynamic propagation environment in which the train is running. As a representative, we choose the field strength data measured in the testing segment of Beijing–Shanghai high-speed railway to simulate the dynamic propagation environment. Beijing–Shanghai high-speed railway is one of the grand trunk railway in eastern China. It is the fastest high-speed railway in the world and has the highest technical standards. Its testing segment is from Zaozhuang West to Bengbu South with the length of 223.4 km and 68 BSs as illustrated in Fig. 2.

In the radio channel emulator, we can emulate the dynamic coverage levelby generating shadow fading script file with the measurement data asfollows:

1. calculate the loss values (including the path loss and shadow fading) according to the measured and the base station transmitting power level.
2. convert the loss value changing with the position of the base station to the one changing with time, and write it into the script file.
3. import the shadow fading script file into the corresponding channels of the channel emulator.

In our simulation, we use three testing BSs to emulate the coverage of the 68 practical BSs in a multiplexed manner. All the practical BSs are divided into

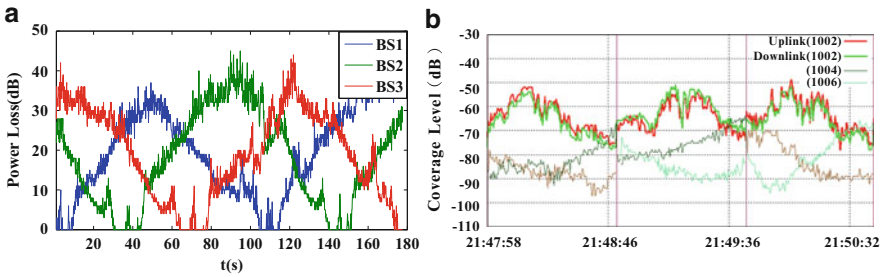

Fig. 3 Dynamic propagation environment simulation and measurement results. (**a**) Simulation power loss (**b**) RXLEVEL measured in Abis

three groups and each group is emulated by the same testing BS. Figure 3 shows the simulation power loss calculated from the measured data, which contain the path loss and shadow fading and the RXLEVEL measured in the Abis interface by the monitor.

3 Measurement Results and Performance Evaluation

GSM-R network need to meet different QoS indicators for different services types which are mainly divided into CSD and GPRS. The CSD QoS parameters mainly contain connection establishment delay, connection establishment error ratio, transfer delay, connection loss rate and transmission interference, and the GPRS QoS parameters mainly contains UDP (User Datagram Protocol) transfer delay, UDP packet loss ratio and throughput. In our simulation, we measure all the parameters to evaluate the QoS performance of this system. In addition, we measured the RXQUAL as a comparison.

3.1 CSD Performance Evaluation

In GSM-R network, the train dispatching command is transferred in CS domain, so the performance of CSD has a significant impact on the operation security of the trains. In the following, let's pay our attention to the concept and measurement results of the parameters including RXQUAL, transmission interference, and transfer delay.

RXQUAL indicates the bit error rate (BER) of the receiver, it has eight grades from 0 to 7 and each grade corresponds a certain range of BER, which is shown in Table 2. RXQUAL is a typical parameter to evaluate the physical layer performance of GSM-R system. The transmission interference refers to the number of transmission interference period in a unit time. The transmission interference

Table 2 Correspondence between BER and RXQUAL

RXQUAL	BER (%)	Average of BER (%)
0	<0.2	0.14
1	0.2 ~0.4	0.28
2	0.4 ~0.8	0.57
3	0.8 ~1.6	1.13
4	1.6 ~3.2	2.26
5	3.2 ~6.4	4.53
6	6.4 ~12.8	9.05
7	>12.8	18.10

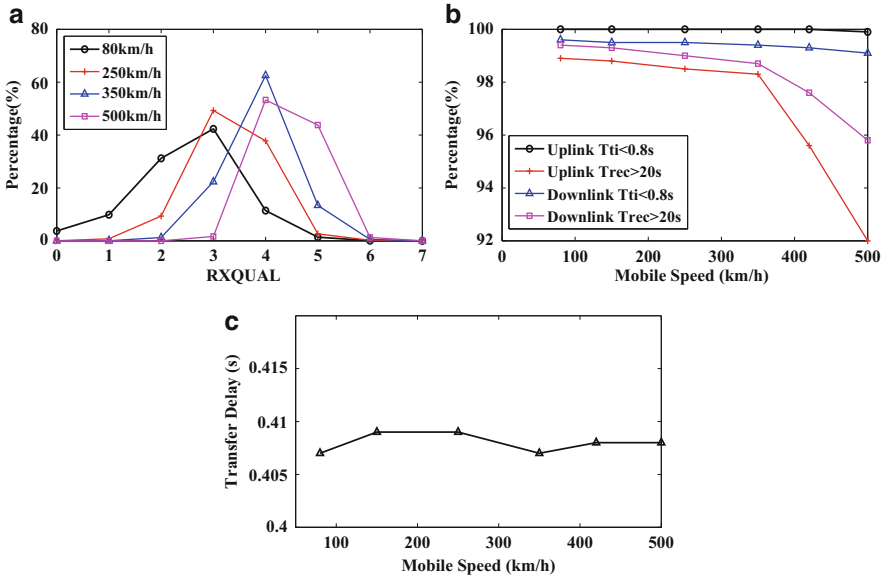

Fig. 4 CSD measurement results statistical diagram. (**a**) Downlink RXQUAL (**b**) Tansmission interferance (**c**) Transfer delay

period consists of transmission time with error (T_{TI}) and transmission time with no error (T_{REC}). T_{TI} is the time interval from the time of first error data block transferred to the time of first correct data block transferred and the T_{REC} is reverse. The transfer delay refers to the time interval from the user data blocks transfer request to the successful end-to-end transmission.

The measurement results are shown in Fig. 4. As we can see, the percentage of RXQUAL $P(RXQUAL)$ of higher grades increases obviously with the mobile speed increasing which means the RXQUAL performance becomes worse. For instance, when the speed is 80 km/h, $P(RXQUAL < 4) = 87.11$ %, and decrease to 23.59 % when the speed increases to 350 km/h, and when the speed rises as high as 500 km/h, $P(RXQUAL < 4) = 1.65$ %. For the transmission interference, both the ratio of $T_{TI} < 0.8$ s and the $T_{REC} > 20$ s are above 98 % when the speed is lower than 420 km/h. But when the speed is higher than 350 km/h, they encounter a obviously

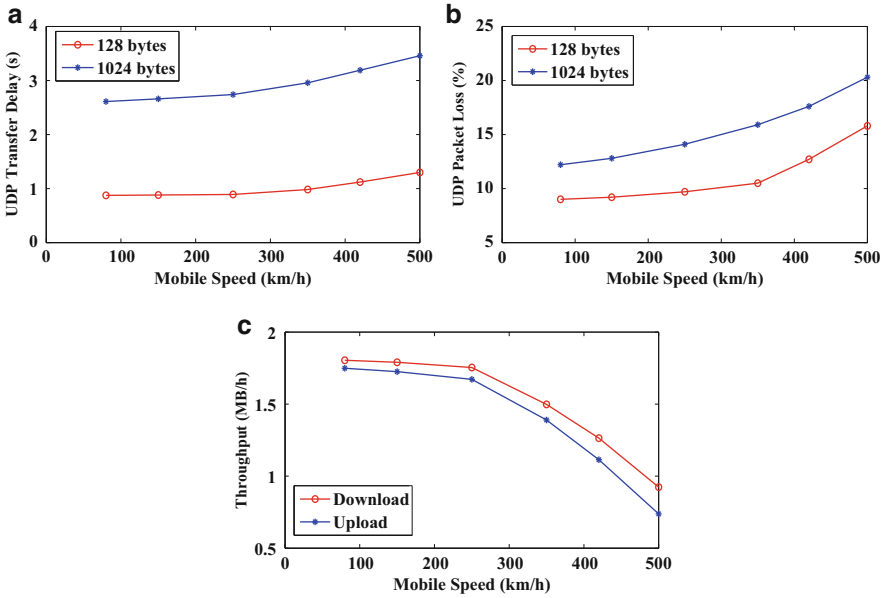

Fig. 5 GPRS test results statistical diagram. (**a**) UDP delay (**b**) Packet loss ratio (**c**) Throughput

decrease as illustrated in Fig. 4b. Especially, except the transmission interference, the impact of mobile speed on the transfer delay, as well as the other CSD QoS parameters is little from the test results. The test result of transfer delay is shown in Fig. 4c.

3.2 GPRS Performance Evaluation

In UMTS (Universal Mobile Telecommunications System), GPRS network is a best-effort network, but in railway applications, it must be reasonably configured and optimized to ensure the special services performance requirements. The measured GPRS parameters, including UDP transfer delay, UDP packet loss ratio and throughput, are briefly introduced as follows.

The UDP transfer delay refers to the time interval from the data packet transfer request to the successful end-to-end transmission to the Gi port of GGSN (gateway GPRS support node). The UDP packet loss ratio refers to the ratio of the unsuccessful transferred packets amount and the successfully transferred packets amount. The throughput refers to the amount of the data passed through the radio channel in a unit time.

The GPRS test results are shown in Fig. 5. From the figures, it is easy to distinguish the impact of mobile speed on these indicators. Both the UDP transfer

delay and the packet loss ratio are measured with two kinds of packet sizes, 128 bytes and 1024 bytes. No matter what size the packet is, the UDP transfer delay and packet loss ratio are gradually increasing with the speed increasing, and in higher speed, above 350 km/h, the growth become stronger. For the throughput as illustrated in Fig. 5c, both the upload and the download throughput are measured. As we can see, with the speed increasing, the throughput declines significantly, especially when the speed rises above 250 km/h.

4 Conclusion and Future Work

In this paper, we build the HILS system with GSM-R network and the radio channel emulator to measure the RXQUAL and the QoS for the CSD and GPRS in different mobile speed. And we get the conclusion that the mobile speed has little impact on the CSD QoS indicators except transmission interference which has a significant decline when the speed is above 350 km/h. However, the impact of mobile speed on all the GPRS QoS indicators is obviously, the higher the speed, the worse the QoS performance. It guides us that apart from the transmission speed, it's necessary to take into count the reliability of different services when we need data transmission with different security in high-speed railway environment.

In addition, there is a need to emphasize the HILS method used in this paper. GSM-R is widely used in the world and its advanced performance has been proved by many practical applications. The EB Propsim C8 has a powerful channel simulation ability with flexible functions. We combine them seamlessly to form HILS system which could meet the requirements on simulation speed and reliability. In future work, we plan to research how the mobile speed affects the communication quality or the QoS performance in high-speed railway environment. And the research work in this paper has laid a good foundation for us.

Acknowledgements This research was supported by the National Natural Science Foundation of China under Grant (No.61222105), the Key grant Project of Chinese Ministry of Education (No.313006), the Program for Changjiang Scholars and Innovative Research Team in University under Grant (IRT0949), the Beijing Jiaotong University basis research Grant (2010JBZ008), the State Key Laboratory of Rail Traffic Control and Safety (RCS2011ZZ002), Beijing Municipal Natural Science Foundation under Grant (4112048), Interdiscipline cooperation projects of the New-Star of Science and Technology supported by Beijing Metropolis, under grant no. xxhz201201.

References

1. Chang J (1987) The effects of time delay spread on portable communications channels with digital modulation. IEEE J Sel Area Comm SAC-5(5):879–889
2. Uhlirz M (1994) Concept of a GSM-based communication system for high-speed trains. In: IEEE 44th vehicular technology conference, Stockholm, Sweden, 1994

3. Zhangdui Zhong, Bo Ai, Qiuyan Liu, Siyu Lin (2009) Basis theory of railway digital mobile communication system. Tsinghua University Press and Beijing Jiaotong University Press, Beijing
4. UNISIG. ERTMS/ETCS-Class 1 GSM-R Quality of Service Class 1 Requirments SUBSET-093, 2005
5. European Econamic Interest Group European Rail Traffic Management System. ETCS/GSM-R Quality of Service Operational Analysis, Reference EEIG: 04E1171, 2005
6. Zhu M, Zhong Z, Xiong L, Ding J, Lin S (2011) Hard-in-the-loop simulation of high-speed railway mobile communication. In: CHINACOM 2011 6th international ICST conference on, 2011, pp 1206–1210
7. COST207, Digital land mobile radio communications. Office for Official Publications of the European Communities, 1989

Design of Infrared Digital Tachometer

Jingrui Sun, Mingcheng Liu, Jincheng Wu, and Li Zhou

Abstract This paper introduces the design of the non-contact method to measure the rotational speed. Compared with the traditional mechanical method and magnetic method, more convenient and efficient for future speed measurement is of great significance with measure the rotational speed of the object with a photoelectric. The design circuit includes photoelectric conversion circuit, 1 s pulse generation circuit, 60 s frequency multiplication circuit, counting latch circuit and decoding display circuit. Pulse waveforms is produced by photoelectric conversion circuit, after a Schmitt trigger wave shaping, the pulse waveform excite latch working, by the circuit latch, decoding, display, finally the mechanical speed will dynamic display on the common cathode 7-segment digital tube.

Keywords Photoelectric conversion • 1 s Pulse generating circuit • 60 s Timing and latching circuit • Decoding and displaying circuit

1 Introduction

According to the measurement mode, tachometer is divided into two categories, contact type and non-contact. According to the working principle and the way of sampling points, there are laser type, magnetoelectric type, stroboscopic type, mechanical and photoelectric type, etc. At present, measuring speed methods [1] contain mainly frequency spectrum analysis, software and hardware counting method. The hardware counting method includes the weeks method, frequency measurement method, frequency cycle method. The measuring accuracy of this method related to the received pulse number. Software counting method is converting analog signals to digital signals and then test. Through the methods of

J. Sun (✉) • M. Liu • J. Wu • L. Zhou
College of Electronic and Communication Engineering, Tianjin Normal University, Tianjin, China
e-mail: sun_jingrui@126.com

B. Zhang et al. (eds.), *The Proceedings of the Second International Conference on Communications, Signal Processing, and Systems*, Lecture Notes in Electrical Engineering 246, DOI 10.1007/978-3-319-00536-2_136,

comparative analysis, design this topic measuring method, can realize the purpose of high precision, small error, strong anti-interference ability.

2 The Basic Concept

2.1 Noun Explanation

Rotated speed refers to the number of turns that the objects of circular motion turned in unit time around the sports center of the circle. Its size and change can show machine equipment operation is normal or not. So the speed is important in the field of industrial measurement. Rotated speed and frequency with common dimensions, shall mean number of pulses in a unit time or the number of occurrences of rotational speeds, in theory, rotational speed can be directly compared with frequency values. Usually complete to each kind of tachometer test and calibration work with rotational speed standard source.

2.2 The Current Research Status of Tachometer

Current our country, rotational speed measuring instrument [1] exist flaws in measurement range, measurement accuracy, the cost performance and real-time monitoring, etc. In the non-contact measurement of tachometer, it is discussion focus problems of current speed measuring field that rotational speed standard source device can coexist with speed sensor pulse light source type. On the one hand, as a non-contact speedometer detection standard device of pulse light source detection device can improve the measurement accuracy; On the other hand, this way may cause chaos in the field of rotating speed measurement. The majority of people hold the view that using the standard source of tachometer speed for testing and calibration is more scientific rationality.

2.3 Tachometer Research Significance

Digital infrared tachometer is a speed measuring instrument with non-contact, use of photoelectric signal sensing. This system is mainly composed of photoelectric conversion circuit, seconds counting pulse generating circuit, frequency multiplication circuit, register circuit, decoding display circuit [1]. When the axis of rotation, posted on rotating objects infrared reflection paper will be received by the infrared led emit infrared reflection to photosensitive transistor's base, through the photoelectric triode conduction deadline, get really need speed pulse output

signal, then the signal into the lower count control counts, latches, decoding and ultimately displayed on the LED digital tube, so as to realize the speed of remote control.

At present, the speed control of our country compared with the developed countries, there are high accuracy measuring gap. In China, there is 90 % of the measuring instrument that accuracy can reach 0.1 %, while foreign can reach 0.05 %. Speed is very important parameter of rotating machinery in the industrial and life, Precise speed measurement of object is great significance to guarantee the normal work of the high-speed rotating machinery, Accuracy and measuring way of photoelectric speed measuring instrument is superior than mechanical tachometer of traditional way. So infrared digital tachometer will be an inevitable trend in the development of speed measuring instrument.

2.4 Tachometer Design Requirements

1. Infrared tachometer design with four digital displays, the speed range from 0000 to 9999 r/min. Realizing remote speed control;
2. Modulation infrared with a certain frequency pulse, To receive the pulse modulation, rotational speed of object is obtained by demodulation;
3. Design, material selection, commissioning the tachometer designed;
4. Draw circuit diagram;
5. Try to apply experiment to speed tests over a long distance.

3 Circuit Design and Calculation of [2]

3.1 The Total Circuit Design [3]

As shown in Fig. 1.

3.2 The Infrared Reflection Code Plate Design

Self-made infrared reflection coder plate: made a radius of about 3–4 cm round with about 2–3 mm thick paper (Coated with paint on the back or not transparent, opaque material, positive for the pure white), It is divided into 16 points on average (22.5 degrees per serving, as far as possible equal, and each interval of a sector with a sector or painted black). Try to stick on the mechanical rotation of objects, as shown in Fig. 2.

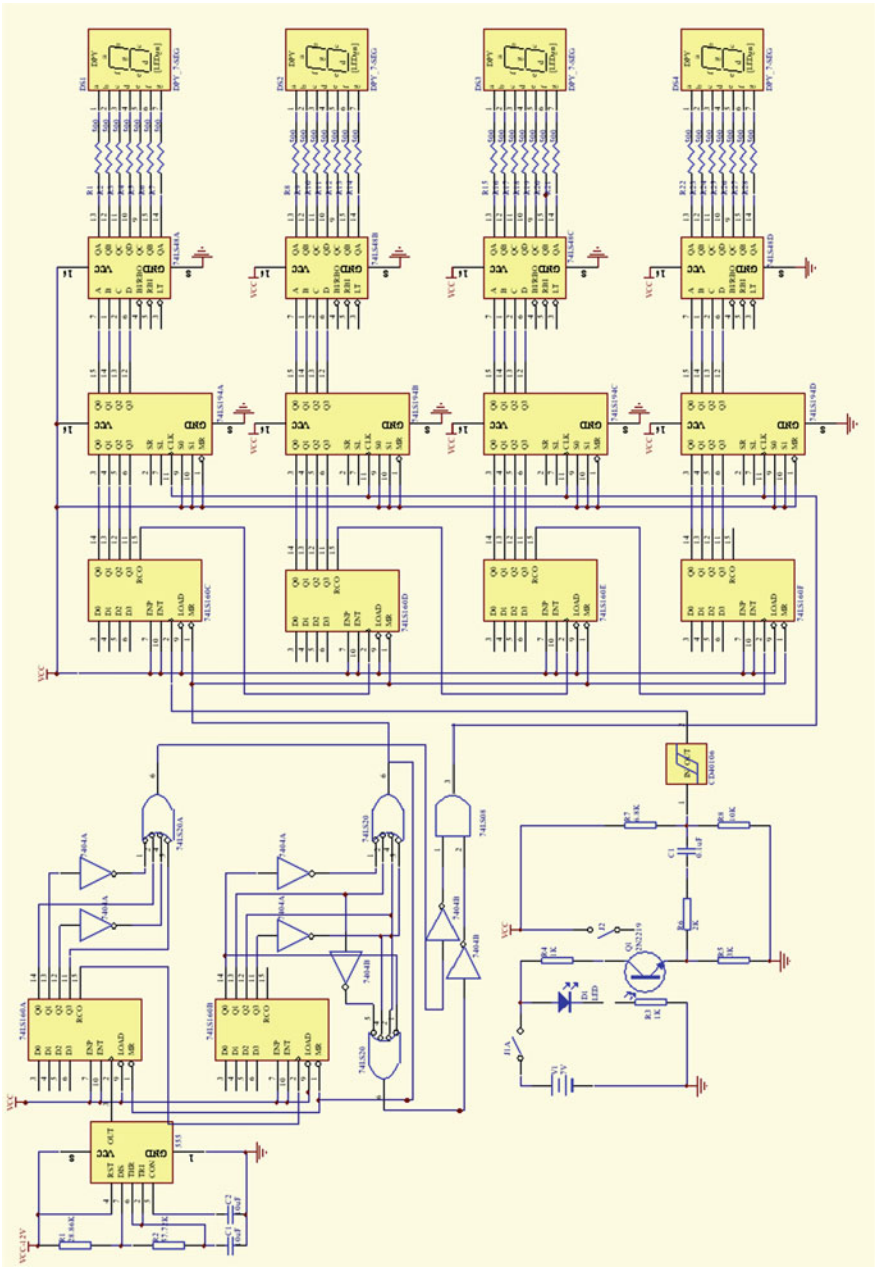

Fig. 1 The total circuit diagram

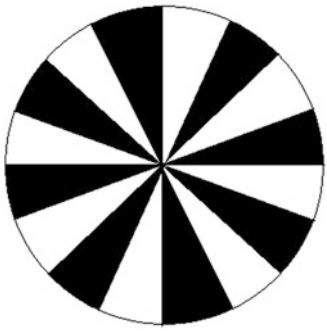

Fig. 2 Infrared reflection coder plate

3.3 Photoelectric Conversion Circuit

More convenient way is to use infrared measurement of rotational probe near objects, receive the infrared signal from the pulse. Infrared tachometer used a reflection type probe and direct type probe. In-line light-emitting tube, control head, and receiving light tube in different side of the object to be tested, Infrared led emit light to the receiving light tube, the rotating object to be tested block the light, produce the count signal. This approach is commonly used in photoelectric counting. Reflective luminous tube, control head, and receiving light tube in the same side of the object to be tested, when the probe is close to rotate the objects, receive the infrared signal, speed measurement is more convenient. This design adopts the reflex light tube.

This design adopts the infrared non-contact measuring method, tachometer use reflection type probe. When the probe is close to body or shaft rotation, the reflected infrared by reflection coder plate shines in base of the photoelectric triode, to control the triode conduction and deadline.

When the shaft turns code plate, emission of infrared radiation by the infrared diode reflect to the code plate, when infrared shine to the white area, the white areas reflect light, so the Q1 is conductive, Vb $\approx$ 0 (Low level); When the infrared radiate to the black area, black areas absorb light, so the Q1 is closing, Vb $\approx$ VCC (high level); Each exposure to one white one black area, photoelectric triode emitter would send a pulse signal. And so on, reflection code plate each roll round, will produce eight count pulses, unit time the number of received optical signal measure the rotational speed. It is important to note: doing the experiment, Because of the natural light interference and the human body infrared interference, there will be some noise superimposed on pulse wave. Experiment adopt to plus a CD40106 Schmidt waveform shaping circuit behind the count pulse, the irregular wave will be shaped for the standard rectangular wave, For following the lower circuit to count, etc. Circuit diagram is shown in Fig. 3.

Through access to information, infrared photodiode and photoelectric triode working voltage is 5 V; the maximum current value through the infrared diode does not exceed 30 mA, because of the infrared diode forward voltage from 1.3 to

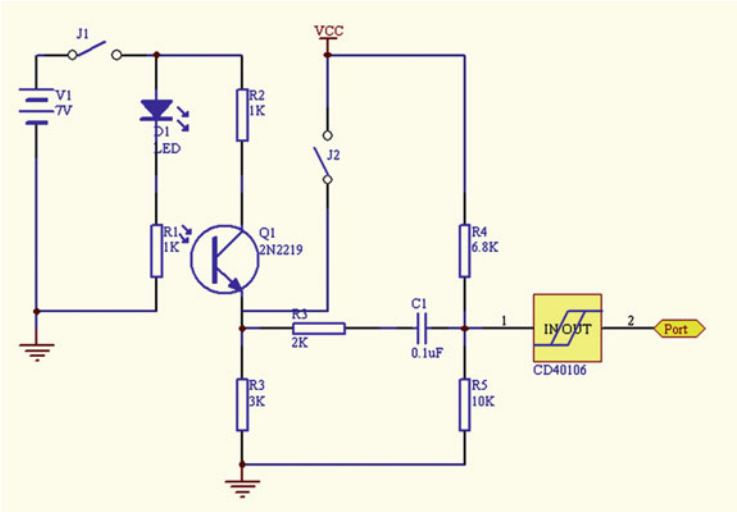

Fig. 3 Photoelectric conversion circuit

1.5 V, so the protection current limiting resistor value of diode is between 117 and 123 Ω; to control photoelectric triode conduction and deadline signal, get the required count pulse. By the Schmitt trigger CD40106 plastic, rectangular square wave is obtained.

3.4 1 s Pulse Generating Circuit [4]

The pulse signal and the timing control signal played an important role in the digital system. The pulse signal and the timing control signal can be produced by self-exciting multivibrator, Schmitt trigger and monostable trigger circuit, etc. Schmitt trigger is mainly used in waveform shaping circuit, it make the output for the rectangular wave; Monostable trigger output rectangular waves under plus pulse; Self-exciting multivibrator without plus trigger pulse. Seconds pulse circuit can produce 1 s clock pulse by using 555 and RC circuit. As shown in Fig. 4.

According to the cycle formula of multivibrator, calculate resistance and capacitance value to match the 555 timer. Because: $T = (R1 + 2 \times R2) \times C \times \ln 2$, $R1 = 28.82$ K Ω, $R2 = 57.72$K Ω, $C = 10$ μF,

So $T = (28.82 + 2 \times 57.72) \times 103 \times 10 \times 10\text{-}6 \times \ln 2 \approx 1$ s, frequency $F = 1/T = 1$ Hz. By pin3 of the 555 timer output 1 s pulse signal to the after level circuit.

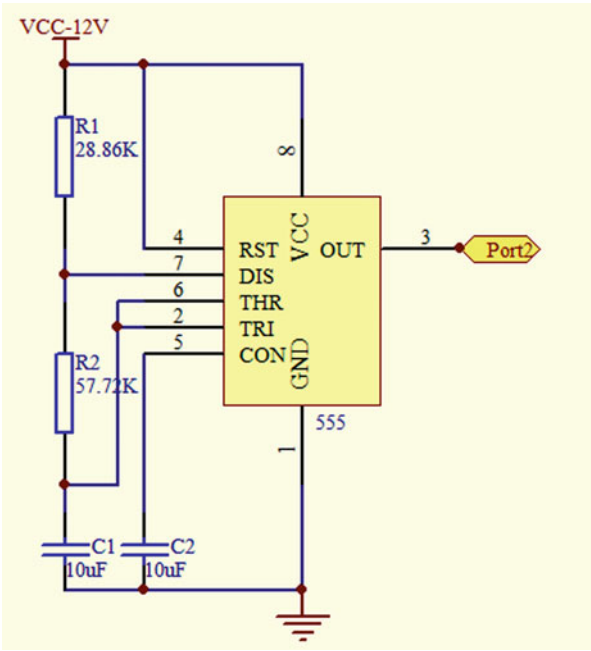

Fig. 4 1 s Pulse generating circuit

3.5 60 s Timer Latch Circuit

The circuit diagram as shown in Fig. 5, of six decimal frequency multiplier [3], will be above 555 timer 1–60 s, and output to carry pulse at a lower level circuit, trigger a lower level circuit working. When the count reaches 60 s, U2's Qa and Qb, Qc, Qd in the figure output for 0110, through the negater, pin8 in the first 74LS20 after NAND gate output is 0 (low level) that trigger addition counter 74LS160 make a reset action, at this time, output of 74LS48 pin3 is 0 (low level) that trigger data latches 74LS194 to latch.

3.6 Count Latches Decoding Display Circuit [3]

This circuit with four pieces of 74LS160 BCD synchronous addition counter will be addition 1 s pulse signal counting, when a counter count to 59, the next pulse trigger another counter to count, the original counter reset to start counting; a bidirectional shift register is composed of four pieces 74LS 194 shift register. Lock addition counter count in register, after the 74LS48 display decoder to binary Numbers to decimal decoding of the shift register, and the electrical signal to the LED display after decoding, in anode tap of the common cathode LED, high and low level is given, so that a - g of the digital tube shows or go out, to achieve the objective of the

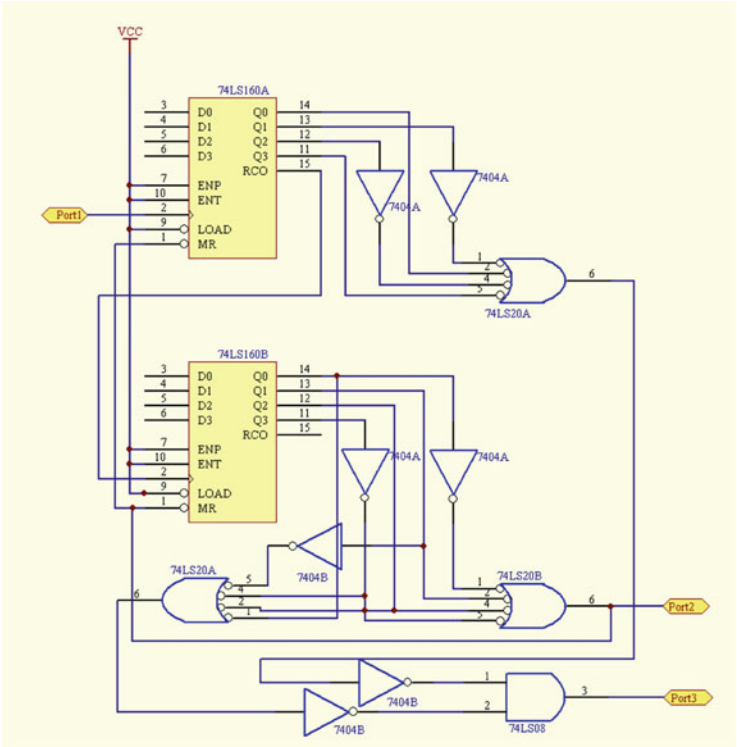

Fig. 5 60 s Timer latch circuit

digital display. In practical circuit, there are the resistance of a 500 Ω or so in the digital tube paragraphs and decoder output, in order to prevent digital tube burn out with high level. Circuit diagram is shown in Fig. 6.

By the count to 59 s as shown in Fig. 6, count pulse which the photoelectric triode emitter of photoelectric conversion circuit generate arrive, get a high level, trigger four pieces of 74LS194, frequency of 60 s on the left adding counter 74LS160 come in, reached the lower decoding circuit 74 LS48 and digital tube of display through the output port, number will be display; When the count to 60 s, 1 s clock circuit that composed of 555 timer generates a high level, Trigger the four pieces of 74LS160 reset, so that next time measurement is set to start counting.

4 The Main Problems in the Experiment and the Solution

The main problems in the debugging of hardware circuit [5]: in the process of using bread board test, circuit is complicated, chip is too much, easy to get wrong. So it need very carefully. Power supply and grounding the best distinguished by the red

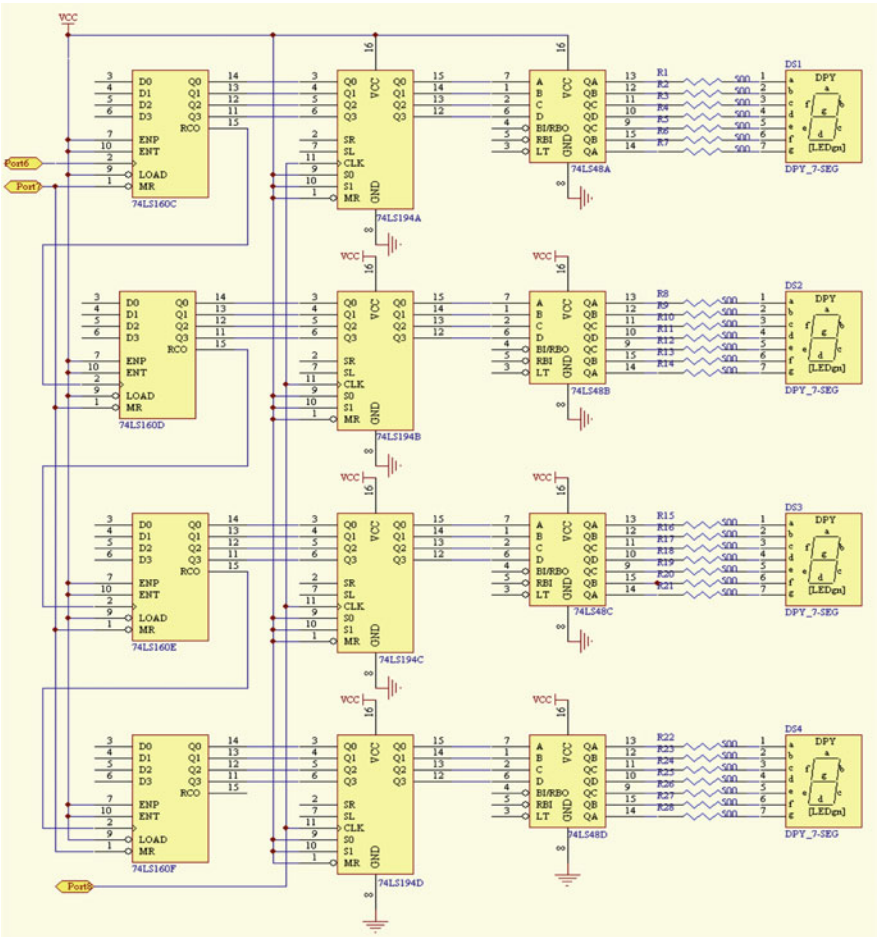

Fig. 6 Count latches decoding display circuit

line and black line, signal lines in blue or yellow. In the experiment, for example, pin9 and pin10 of 74LS1607 take power, but the pin14 still need to connect power, this is voltage to make the chips work, it would be paid attention to. At the same time, the infrared transmitting and receiving part need to use professional infrared reflective film, general reflection film is unable to complete the function. Launching tube and receiving tube would be in parallel, the light interchange is more than 15 cm.

Acknowledgment This research was supported by the Tianjin natural science fund (13JCYBJC15800).

References

1. Qiu G (2009) Permanent magnet DC motor design and application of the practical technology. Mechanical Industry Press, Beijing, pp 263–269
2. Bihu L, Jianguo S (eds) (1999) The digital logic circuits [M]. Science Press, Beijing, pp 244–249
3. Junfeng W (ed) (2005) Electronic product development and manufacture [M]. People's Posts and Telecommunications Publishing House, Beijing, pp 88–116
4. Changshu L (ed) (2002) The digital logic circuits [M]. National Defence Industry Press, Beijing, pp 145–159
5. Ziyan W (2005) Infrared technology applied in tongue inspection of traditional Chinese medicine [J]. Directory of Open Access Journals. Combine Tradition Chinese Western Med J 3(4): 326

The SVA-MUSIC Algorithm Based on a Simple Vector Array

Mingtuan Lin, Yiling Guo, Jibin Liu, and Peiguo Liu

Abstract The MUSIC algorithm based on a vector array can estimate the direction of arrivals (DOA) and polarization parameters with the impinging signals carrying the polarization information. The conventional vector unit consists of two orthogonal dipoles which are always not orthogonal since the isolation between two dipoles is not ideal. Moreover the design of the two orthogonal dipoles is always complex. In this paper, a simple vector array (SVA) is proposed to overcome the disadvantage of the conventional vector array (CVA). Instead of using two orthogonal dipoles, the vector sensor unit only includes one dipole in such a SVA with the adjacent unit orthogonal. The SVA-MUSIC algorithm based on a SVA is also proposed in the paper. The simulation results presented in the paper prove its feasibility and show that the SVA-MUSIC algorithm has a better resolution and performance than the CSA-MUSIC (Conventional Scalar Array MUSIC).

Keywords DOA • Polarization parameters • SVA • SVA-MUSIC

1 Introduction

The DOA estimation had received a significant amount of attention over the last several decades. The Conventional Beam Forming (CBF) [1] algorithm was proposed to estimate the DOA firstly. Due to the limit of the beam, its resolution was confined to the Raleigh limit. To break out the Raleigh limit, numerous of high-resolution algorithms based on the linear ARMA, AR and MA models were studied, such as the MEM [2], MVM [3] and so on. However, the algorithms were not

M. Lin (✉) • J. Liu • P. Liu
National University of Defense Technology, Changsha, China
e-mail: linmingtuan08@163.com

Y. Guo
National Huaqiao University, Quanzhou, China

B. Zhang et al. (eds.), *The Proceedings of the Second International Conference on Communications, Signal Processing, and Systems*, Lecture Notes in Electrical Engineering 246, DOI 10.1007/978-3-319-00536-2_137,

applied to the estimation since the consumptions were not accurate actually. During the 1970s, the approaches based on the subspace decomposition were introduced to the DOA estimation, among which MUSIC [4–6] and ESPRIT [7–9] were most classical techniques. The MUSIC proposed by R.O. Schmidt has well established as an effective high-resolution DOA approach and is capable of discriminating closely spaced sources. Without taking the polarized sources into consideration, the above algorithms are only confined to the DOA estimation and can not estimate the polarization parameters of the sources. As the vector sensor become more and more realizable, polarization parameters have been added to estimation process as necessary information to discriminate sources, in addition to the DOA. Compared with the conventional scalar array (CSA), CVA has many advantages, such as the good performance of anti-interference, high resolution and so on. The Vector MUSIC (V-MUSIC) was introduced in [10–12] to obtain the DOA and polarization parameters which include the polarization auxiliary angle and skewing angle. The convention vector unit consists of two orthogonal dipoles that can record two components of the signal. However the two dipoles are not always orthogonal. Moreover, the design of the vector unit is always complex.

In this paper, we propose a SVA to overcome the disadvantage of a CVA. Instead of using two orthogonal dipoles, the vector unit only includes one dipole with the adjacent unit orthogonal.

The structure of this paper is organized as follows: Section 2 introduces the conventional scalar MUSIC (CSA-MUSIC) and CVA-MUSIC algorithm. The SVA-MUSIC is proposed in Sect. 3. The simulation results in Sect. 4 show the performance of the SVA-MUSIC. The detailed conclusions are stated in Sect. 5.

2 The CSA-MUSIC and CVA-MUSIC Algorithm

As the Fig. 1 shows, we first consider a uniform linear scalar array of N sensors and the distance between two sensors is the half-wavelength.

Assume that far-field waves from M sources (M < N) impinging on the array are narrow-band signals with the center frequency f_0 and the DOA $\boldsymbol{\theta} = [\theta_1, \theta_2, \ldots\ldots \theta_M]^T$, which are supposed to be uncorrelated. The noise with the same power σ^2 in sensor is considered to be uncorrelated as well. Taking the first sensor as a reference, we can obtain the array steering-vector

$$\mathbf{A}(\boldsymbol{\theta}) = [\mathbf{a}(\theta_1), \mathbf{a}(\theta_2), \ldots\ldots, \mathbf{a}(\theta_M)] \tag{1}$$

where $\mathbf{a}(\theta_i) = \left[1, e^{-j\frac{2\pi d \sin\theta_i}{\lambda}}, \ldots\ldots, e^{-j\frac{(N-1)2\pi d \sin\theta_i}{\lambda}}\right]$ is the ith source steering vector. Thus the output of array can be written as

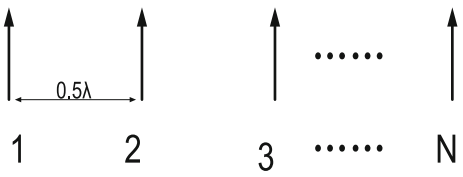

Fig. 1 The conventional scalar array

$$\mathbf{X} = \sum_{i=1}^{K} \mathbf{a}(\theta_i) s_i(n) + \mathbf{n}(n) = \mathbf{AS} + \mathbf{n} \tag{2}$$

where $\mathbf{X} = [x_1(n), x_2(n),\ldots\ldots, x_N(n)]^T$ denotes the receive signal of each sensor, $\mathbf{S} = [s_1(n), s_2(n),\ldots\ldots, s_M(n)]^T$ is the incident signal and $\mathbf{n} = [n_1(n), n_2(n),\ldots\ldots, n_N(n)]$ is the Gauss noise added to different sensors. Then, the covariance matrix of CSA is given by

$$\mathbf{R_{xx}} = E\left[\mathbf{x}\mathbf{x}^H\right] = \mathbf{A}\mathbf{R}_{ss}\mathbf{A}^H + {\sigma_n}^2\mathbf{I} \tag{3}$$

It has been proved that the noise subspace is orthogonal to the array steering vector, that is ${\mathbf{V}_n}^H\mathbf{a}(\theta) = 0$ where $\mathbf{V}_n = [\mathbf{q}_{M+1}, \mathbf{q}_{M+2},\ldots\ldots,\mathbf{q}_N]$ is the noise subspace. The CSA-MUSIC spectrum can be expressed as

$$P_{MU}(\theta) = \frac{1}{\mathbf{a}^H(\theta)\mathbf{V}_n{\mathbf{V}_n}^H\mathbf{a}(\theta)} \tag{4}$$

The CSA-MUSIC is conducted under the condition that the incident signals are not polarized. However the far-field signals contain the polarization information of signals, which requires that the receive sensor must be a vector sensor so that it can estimate the polarization parameters. The vector sensor can record all the components of electric and magnetic field which are always redundant for the estimation. As Fig. 2 shows, the classical vector sensor unit consists of two orthogonal dipoles. In this paper, we consider the x and y components of the electronic field. In the paper [11], a single far-field signal recorded by the unit can be denoted as

$$\begin{aligned} x(n) &= \begin{pmatrix} -\sin\theta & \cos\phi\cos\theta \\ \cos\theta & \cos\phi\sin\theta \end{pmatrix} \begin{pmatrix} \cos\gamma \\ \sin\gamma e^{j\eta} \end{pmatrix} s(n) + n(n) \\ &= \psi(\theta,\phi)\, h(\gamma,\eta) s(n) + n(n) \end{aligned} \tag{5}$$

where $\psi(\theta,\phi)$ corresponds to the x and y axis components, $h(\gamma,\eta)$ contains the polarization information, $0 \le \theta < \frac{\pi}{2}$ is the elevation angle, $0 \le \phi < 2\pi$ is the azimuth angle, $0 \le \gamma < \frac{\pi}{2}$ is the polarization auxiliary angle and $0 < \eta < 2\pi$ is the polarization skewing angle.

Consider that the M narrow-band sources from the far-field with the direction of angles $\boldsymbol{\theta}$ and $\boldsymbol{\varphi}$ and the polarization parameters $\boldsymbol{\gamma}$ and $\boldsymbol{\eta}$, the output of the SVA has the following expression:

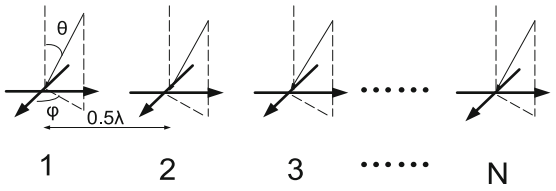

Fig. 2 The uniform liner vector array

$$\begin{aligned} \mathrm{X} &= [\mathrm{x}_1, \mathrm{x}_2, \mathrm{x}_3, \mathrm{x}_4, \ldots\ldots, \mathrm{x}_{2\mathrm{N}\text{-}1}, \mathrm{x}_{2\mathrm{N}}]^{\mathrm{T}} = \sum_{i=1}^{M} \mathbf{a}_i s_i(\mathrm{n}) + \mathbf{n}(\mathrm{n}) \\ &= \mathbf{A}_p \mathbf{S} + \mathbf{n} \end{aligned} \tag{6}$$

where $\mathbf{a}_i$ and $s_i(\mathrm{n})$ denotes the ith source steering vector and incident signal, $\mathbf{A}_p(\boldsymbol{\theta},\boldsymbol{\varphi},\boldsymbol{\gamma},\boldsymbol{\eta}) = [\mathbf{a}_1,\mathbf{a}_2,\ldots\ldots,\mathbf{a}_\mathrm{M}] \in \mathrm{C}^{2\mathrm{N} \times \mathrm{M}}$ is the array steering vector. And the $\mathbf{a}_i$ can be expressed as:

$$\mathbf{a}_{\theta_i,\phi_i,\eta_i,\gamma_i} = \begin{pmatrix} u_1(\theta_i,\varphi_i) \\ \vdots \\ u_N(\theta_i,\varphi_i) \end{pmatrix} \bigotimes \psi(\theta_i,\varphi_i) h(\gamma_i,\eta_i) \tag{7}$$

where $\bigotimes$ denotes the Kronecker product, $\mathbf{u}(\theta_i, \varphi_i) = [\mathrm{u}_1(\theta_i,\varphi_i), \ldots, \mathrm{u}_\mathrm{N}(\theta_i,\varphi_i)]^{\mathrm{T}}$ is spatial steering-vector of the ith source and $\psi(\theta_i,\varphi_i)h(\gamma_i,\eta_i)$ contains its polarization parameters. $\mathbf{S} = [\mathrm{s}_1(\mathrm{n}), \mathrm{s}_2(\mathrm{n}),\ldots\ldots, \mathrm{s}_\mathrm{M}(\mathrm{n})]^{\mathrm{T}}$ is the M impinging sources.

With the $\mathbf{a}(\theta)$ replacing by $\mathbf{a}(\theta,\varphi,\gamma,\eta)$, CVA-MUSIC spectrum can be expressed as:

$$P_{MUp}(\theta,\varphi,\gamma,\eta) = \frac{1}{\mathbf{a}^H(\theta,\varphi,\gamma,\eta)\mathbf{V}_n{\mathbf{V}_n}^H\mathbf{a}(\theta,\varphi,\gamma,\eta)} \tag{8}$$

where $\mathbf{V}_n$ is the noise subspace obtained by the decomposition of $\mathbf{R}_{\mathbf{xx}}$.

3 The SVA-MUSIC Algorithm

The conventional vector unit consists of two orthogonal dipoles which are not always orthogonal since the isolation between the two dipoles is not ideal. The fact that the energy of the electromagnet waves from one dipole can couple to the other dipole brings the model error into the algorithm which decreases the estimation accuracy. Moreover, the design of the vector unit is always complex.

In this section, a SVA is proposed to overcome the disadvantage of CVA. The vector unit only includes one dipole and the adjacent unit is orthogonal to it just as the Fig. 3 shows. Unlike the conventional vector sensor unit, the simple vector sensor unit has the unique channel output. And the single signal received by the unit can be written as

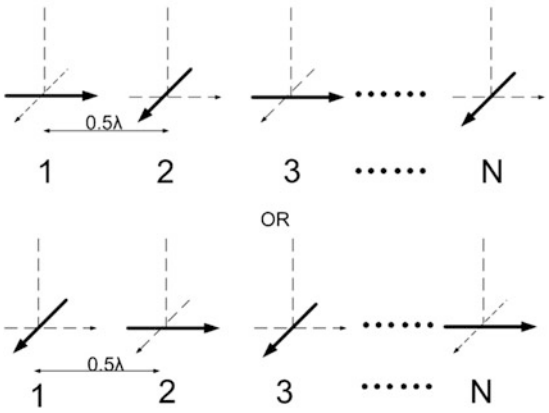

Fig. 3 The simple uniform liner vector array

$$\begin{aligned} x(n) &= C_k \begin{pmatrix} -\sin\theta & \cos\phi\cos\theta \\ \cos\theta & \cos\phi\sin\theta \end{pmatrix} \begin{pmatrix} \cos\gamma \\ \sin\gamma e^{j\eta} \end{pmatrix} s(n) + n(n) \qquad (\mathrm{k}=0,1) \\ &= C_k \psi(\theta,\phi) h(\gamma,\eta) s(n) + n(n) \qquad (\mathrm{k}=0,1) \end{aligned} \tag{9}$$

where $C_1 = [0,1]$ and $C_2 = [1,0]$ denotes the polarization output of x axis and y axis.

Then the SVA-MUSIC spectrum can be written as

$$P'_{MUP}(\theta,\varphi,\gamma,\eta) = \frac{1}{\mathbf{a}'^{H}(\theta,\varphi,\gamma,\eta)\mathbf{V}_n\mathbf{V}_n{}^{H}\mathbf{a}'(\theta,\varphi,\gamma,\eta)} \tag{10}$$

where $\mathbf{a}' = \mathbf{C}\psi(\theta,\phi)h(\gamma,\eta)\mathbf{.}*\mathbf{u}(\theta,\varphi)$ is the steering vector of the SVA. The sign $\mathbf{.}*$ denotes dot product and $\mathbf{C} = [C_1, C_2, \ldots\ldots C_{k_N}]$ states the array sensor polarization information where $k_N = 1$ or 2 depends on the value of N.

4 Simulation Results

In this section, we first discuss the estimation performances of CSA-MUSIC and SVA-MUSIC. The following simulation results are conducted under the assumption that the narrow-band sources are uncorrelated and the noise added in the receive-sensor is gauss white noise. The CSA and SVA are composed of ten identical equally spaced sensors with the distance $\frac{\lambda}{2}$ between two adjacent units. The two adjacent units are orthogonal in the SVA. To simplify the simulation, we lay the uniform liner arrays at the x axis and fix the azimuth and skewing angles of sources respective to 0° and 90°. The sample length is 1024 in all the simulations.

We consider the scenario with two polarized sources impinging on two arrays with Signal Noise Ration(SNR) equaling to 10 dB. First, we consider the elevation

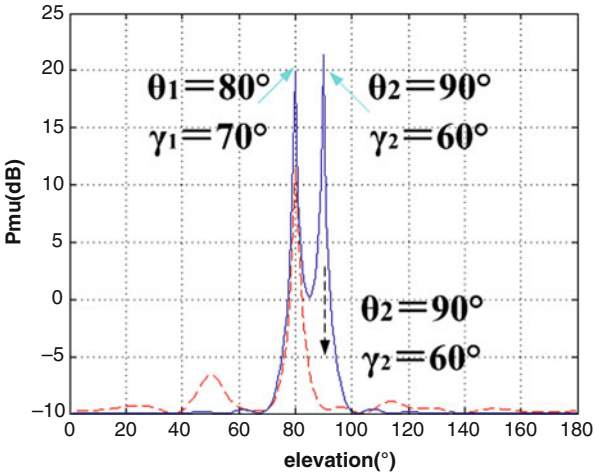

Fig. 4 The estimation of the same elevations but different polarization auxiliary angles using CSA-MUSIC

angles of the sources are $\boldsymbol{\theta} = [80^{\circ},90^{\circ}]$ and the polarization auxiliary angles are $\boldsymbol{\gamma} = [70^{\circ},60^{\circ}]$. Using the CSA-MUSIC, we can estimate the DOA of the signals just as the Fig. 4 solid line shows. Then, we reconsider the sources with the same elevation angles but different polarization auxiliary angles $\boldsymbol{\gamma} = [70^{\circ},7^{\circ}]$. The dot line plotted in the Fig. 4 denotes the failure of estimation of this situation. From the Fig. 4, we can learn that the CSA-MUSIC which ignores the polarization information can estimate the elevation angles of the sources with two closely polarization auxiliary angles successfully but not for all the situations. In a word, the performance of CSA-MUSIC is affected greatly by the polarization parameters of the signals.

In the Fig. 5, we draw the SVA-MUSIC spectrums from which we can learn that the SVA-MUSIC gains the accurate estimations for both situations.

Consider the same polarization auxiliary angles $\boldsymbol{\gamma} = [70^{\circ},30^{\circ}]$, then we study the elevation resolution between the CSA-MUSIC and SVA-MUSIC algorithm.

From the Fig. 6a, we can learn that the CSA-MUSIC fails to discriminate the two sources with the DOA $\boldsymbol{\theta} = [80^{\circ},84^{\circ}]$. However, in the Fig. 6b two peaks are clearly obtained from SVA-MUSIC for the same situation. Comparing Fig. 6a and b, we conclude that the SVA-MUSIC has a better resolution than the CSA-MUSIC under the same assumption.

In summary, the SVA-MUSIC algorithm not only can estimate the direction of arrivals but also the polarization parameters successfully and it has a better performance than the CSA-MUSIC algorithm.

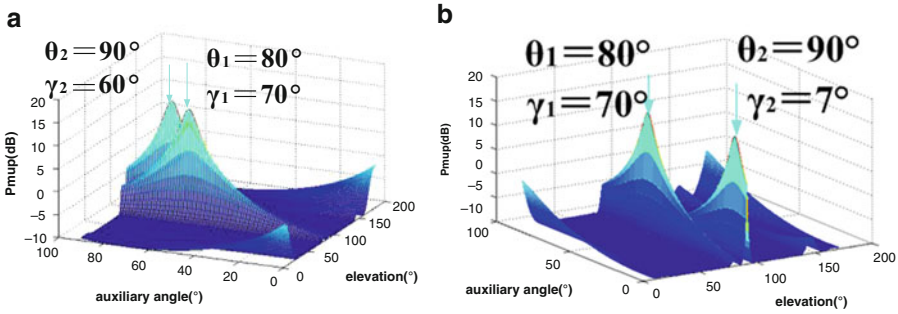

Fig. 5 The estimation using the SVA-MUSIC

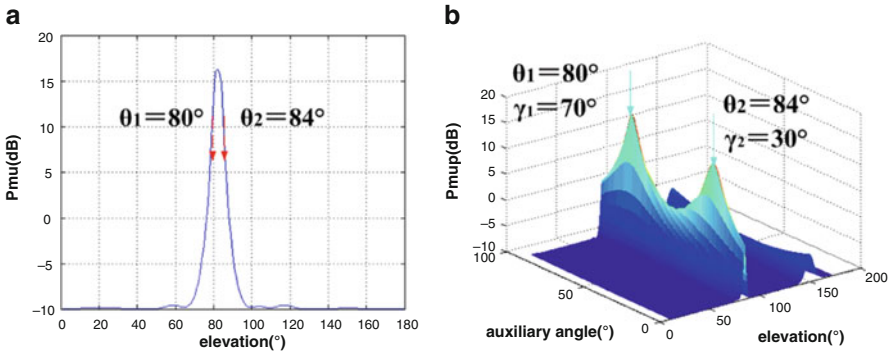

Fig. 6 Elevation resolution between CSA-MUSIC and SVA-MUSIC

5 Conclusion

We first introduce the CSA-MUSIC and CVA-MUSIC algorithm. The CVA-MUSIC based on a CVA can estimate the direction of arrivals and the polarization parameters exactly. Conventional vector unit consists of two orthogonal dipoles which are not completely orthogonal to each other. Moreover, the design of the vector unit is always complex. In this paper, we propose a simple vector array (SVA) which does not require the vector unit consisting of two orthogonal dipoles. The simple vector unit contains only one dipole and the adjacent unit is orthogonal to it. The SVA-MUSIC is also presented in this paper.

The simulation results prove the feasibility of the SVA and SVA-MUSIC algorithm. From the simulation results, we conclude that the SVA-MUSIC has a better resolution and estimation performance than the CSA-MUSIC.

References

1. Krim H, Viberg M (1996) Two decades of array signal processing research. IEEE Signal Process Mag 13(4):67–94
2. Burg JP (1967) Maximum entropy spectral analysis. Proceedings of the 37th meeting of the annual Int. SEG meeting, Oklahoma city, OK
3. Capon J (1969) High-resolution frequency-wavenumber spectrum analysis. Proc IEEE 57 (8):1408–1418
4. Schmidt RO (1981) A signal subspace approach to multiple estimator location and spectral estimation. Ph.D. dissertation, Stanford University, Stanford, CA
5. Schmidt RO (1979) Multiple emitter location and signal parameter estimation. In: Proceedings of RADC spectrum estimation workshop, Rome, Italy, pp 243–258
6. Bienvenu G, Kopp L (1979) Principle delay goniometric passive adaptive. In: Proceedings of 7'eme Colloque, Nice, France, pp 106/1–106/10
7. Roy RH (1987) ESPRIT-Estimation of signal parameters via rotational invariance techniques. Ph.D. dissertation, Stanford University
8. Roy R, Paulraj A, Kailath T (1986) Estimation of signal parameters via rotational invariance techniques—ESPRIT. In: Proceedings of IEEE ICASSP, vol 4, Tokyo, Japan, pp 2495–2498
9. Roy R, Kailath T (1990) ESPRIT—estimation of signal parameters via rotational invariance techniques. Opt Eng 29(4):296–313
10. Weiss AJ, Friedlander B (1991) Performance analysis of diversely polarized antennae arrays. IEEE Trans Signal Process 39(7):1589–1603
11. Nehorai A, Paldi E (1994) Vector-sensor array processing for electromagnetic source localization. IEEE Trans Signal Process 42(2):376–398
12. Miron S, Le Bihan N, Mars J (2005) Vector-MUSIC for polarized seismic sources localization. EURASIP J Appl Signal Process 1:74–84

Automatic Car Tracing Based on Ultrasonic Distance Measurement

Mingcheng Liu, Bin Liang, and Jingrui Sun

Abstract The main content is the electric car pursuit design based on ultrasonic distance measurement circuit. The circuit is designed to calculates the distance around obstacle and the electric car by the ultrasonic distance function, Choose the best path forward, and use optical encoder detects the operation of the car running deviation angle, for the timely correction of the direction of the car in order to achieve self-drive car forward. Experimental results show that the set of simple and reliable design, with good controllability, to meet the design requirements.

Keywords Automatic tracing • Ultrasonic distance measurement • Hotoelectric encoder • The stepper motor • Atmega16L • Incremental PID algorithm

1 Introduction

With microprocessor technology, communication technology, sensor technology, Smart cars will become the development trend of automobile, become a part of people's lives. Sensor technology in the application of intelligent control car do more and more widely used, Such as at night, fog, high pollution and other environmental risk under the road [1]. This paper presents a Atmega16L with AVR microcontroller as the core of the control car, using HY-SRF05 ultrasonic distance measurement circuit detects the surrounding environment, Provided to the electric car distance from surrounding obstacles, according to the monitoring of environmental parameters determine the travel path of the trolley. Article described in detail the working principle and design of intelligent vehicle approach from the hardware and software, The design of the car circuit has advantages of simple circuit design and software control efficient.

M. Liu (✉) • B. Liang • J. Sun
College of Electronic and Communication Engineering, Tianjin Normal University, Tianjin, China
e-mail: 747938791@qq.com

B. Zhang et al. (eds.), *The Proceedings of the Second International Conference on Communications, Signal Processing, and Systems*, Lecture Notes in Electrical Engineering 246, DOI 10.1007/978-3-319-00536-2_138,

2 The Principle of Ultrasonic Distance Measurement

Ultrasonic Ranging is emitting an ultrasonic wave in one direction by ultrasonic transmitter, At the same time the transmitting start timing, Ultrasonic wave propagation in the air, Ultrasonic propagation reflected back immediately on the way when the obstacles encountered, Ultrasonic echoes received by the receiver to stop the clock immediately. Based on the timer of the transmitting and receiving echo measured time difference t, the distance S can be calculated from Emission pitch to obstacle [2]:

$$S = Ct/2 \tag{1}$$

Formula (1), C is an ultrasonic propagation velocity in air, it changes with temperature. The change is as follows:

$$C = 331.5 + 0.6\,T \tag{2}$$

Formula (2), T is the ambient temperature values in Celsius, the temperature values obtained by the temperature sensor.

3 Overall System Design

The smart car two front wheels and a rear wheel mounted on the vehicle body, It uses two stepper motor drive system, two front wheel drive sports car, the car can move forward, backward, turn left, turn right. The use of ultrasonic distance measurement circuit in front of the vehicle, to run the channel information collected in front of the smart car. The Rear axle photoelectric encoder issue trolley offset pulse signal. Upper body in the car, installing another stepper motor drive system, so that the second set of ultrasonic distance measurement circuit can always be rotated 360°, it is always monitoring the situation surrounding obstacles. These signals are conditioned by the microcontroller, they are used to determine the two front wheels of the car running direction, the car speed and the rotation angle for the control of the smart car. These make the car run on the channel automatically, smooth ride [3–5]. They make the car in the shortest possible time and the fastest speed to finish the course. In addition, the smart car overall system block diagram shown in Fig. 1.

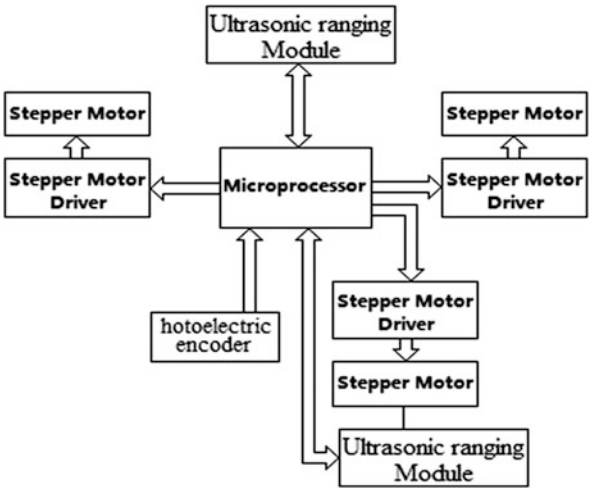

Fig. 1 The smart car overall system block diagram

4 Hardware Design

The hardware design is the use of high-speed 8-bit AVR Microcontroller ATmega16L, it is produced by ATMEL Corporation. As the circuit-core microprocessor, it controls three-way stepper drives and stepper, controls two-way ultrasonic ranging circuit both static and dynamic, between the microcontroller and two ultrasonic distance circuits, conduct bidirectional data **transfer**. And, the optical encoder mounted on the rear of the car, on a vertical shaft driven wheels, which real-time monitoring angle of rotation of the driven wheel, it is the rotation angle of deflection parameters (pulse number and direction) transmitted to the microcontroller. Microcontroller based ultrasonic ranging circuit and optical encoder data to adjust the direction and speed of the trolley.

The circuit uses **17H185**-04A2 of Aix stepper motor, the optical encoder is ZSP3803-003G-1000BZ3-5-24C optical encoder, Rui Puan WAG (Wuxi) Electronic Technology Co., Ltd. Produces. Ultrasonic Ranging circuit using HY-SRF05 Ultrasonic Ranging Module.

The ultrasonic Ranging Module provides 2–450 cm non-contact distance measurement function, in comparison, a high ranging accuracy. its range accuracy up to 3 mm. HY-SRF05 ultrasonic module corresponding timing diagram shown in Fig. 2 below:

5 Software Design and Algorithms

5.1 The Software Design Flow Chart as Shown Below (Fig. 3)

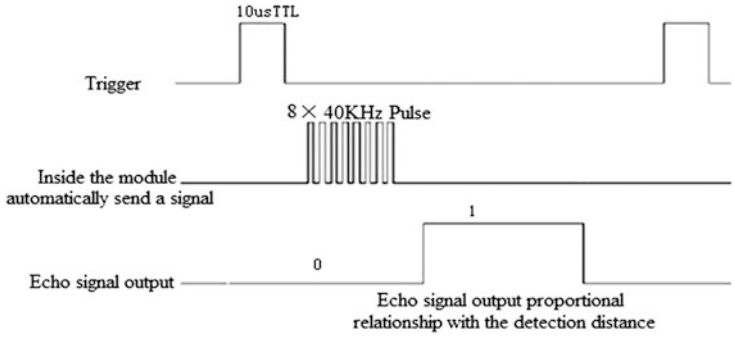

Fig. 2 Ultrasonic timing diagram

5.2 Trolley Algorithm

5.2.1 Car Forward Calculation

Figure 4a in Fig. Let trolley wheel radius is r, stepper further wheels turn each step angle (step angle) is α, if the distance of the car ahead l, then the trolley wheels will turn n ring, turn the wheels of the total angle θ, the number of steps of the stepper to m. Backward and forward like the reverse, drive DIR pin of stepper motor driver can be placed.

$$n = \frac{l}{2\pi \mathrm{r}} \tag{3}$$

$$\theta = 2\pi \mathrm{n} \tag{4}$$

$$m = \frac{\theta}{\alpha} = \frac{2\pi \cdot \frac{1}{2\pi \mathrm{r}}}{\alpha} = \frac{l}{\alpha \mathrm{r}} \tag{5}$$

5.2.2 Calculation of the Car Left

Figure 4b in Fig. Let trolley wheel radius is r, car wheelbase is d, Each step further stepper wheel turn angle (step angle) is α, if the distance traveled by the car completely turn left (i.e., quarter circle arc length) is l, then the car wheels will turn n turn, the wheels total turn angle θ, the stepper stepper number of steps to m, Turn right and left like.

$$l = \frac{1}{4} 2\pi d = 2\pi \mathrm{r} \cdot n \tag{6}$$

$$n = \frac{d}{4r} \tag{7}$$

$$\theta = 2\pi \mathrm{n} = \frac{\pi \mathrm{d}}{2r} \tag{8}$$

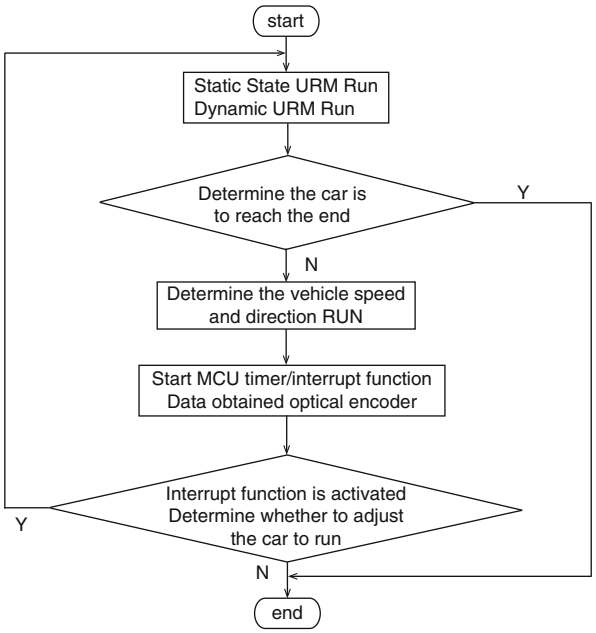

Fig. 3 The software design flow chart

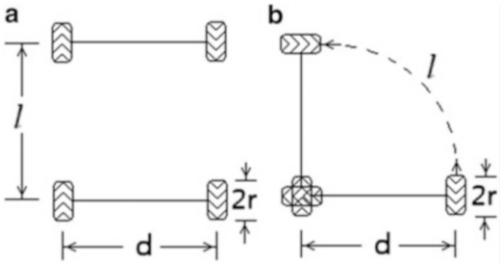

Fig. 4 (**a**) Trolley forward Schematic. (**b**) Trolley left Schematic

$$m = \frac{\theta}{\alpha} = \frac{\frac{\pi d}{2r}}{\alpha} = \frac{\pi d}{2r\alpha} \tag{9}$$

5.3 Incremental PID Control Algorithm of Car When Cornering

PID control algorithm is a control strategy based on the classical control theory. The warranty does not affect system stability under the premise, PID control algorithm can improve the stability of the system and improve the system dynamic

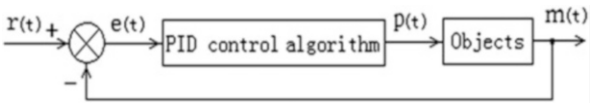

Fig. 5 PID controller block diagram

performance. PID controller block diagram shown in Fig. 5. System is mainly controlled by the PID controller and objects, It is constitutes the control deviation based on setpoint r (t) and the actual output value of m (t). in order for the controlled object, it constitutes a deviation amount of control by linear combination of Proportional, integral and differential[1, 6].

PID graphic expression [6]:

$$u(t) = K_P\left[e(t) + \frac{1}{T_i}\int_0^1 e(t)dt + T_D\frac{de(t)}{dt}\right] \tag{10}$$

Where, T_i is the integration time constant; T_d is the derivative time constant; K_p is a proportional coefficient; e (t) is the error term; u (t) as a control amount.

Discrete control algorithm is:

$$\mathrm{u(KT)} = \mathrm{K_P}\left\{e(KT) + \frac{T}{T_i}\sum_{j=0}^{1}E(jT) + \frac{T_d}{T}[e(t)dt - E(kT-T)]\right\} \tag{11}$$

Formula (11), T is the sampling period, must be small enough to ensure that the system has a certain accuracy; T_i is the integration time of the regulator; T_d for the differential time regulator; K_p is the proportional regulator factor; e (k) the k th sampling bias; u (k) as a control amount.

Using incremental PID control, By

$$\Delta u(KT) = u(KT) - u(KT-T) \tag{12}$$

can be obtained

$$\begin{aligned}\Delta u(KT) = {} & K_P[e(KT) - e(KT-T)] + K_i e(KT) \\ & + K_d[e(KT) - 2e(KT-T) + e(KT-2T)]\end{aligned} \tag{13}$$

Where, e (kT) is the k-th degree of deviation of the center position; e (kT-T), e (kT - 2T) are k - 1, k - 2 times errors.

According to the experimental conditions and site commissioning experience, When the car is generally curved state, the use of incremental PID algorithm, it can adjust the speed according to the actual situation, so that the car has good controllability.

6 Conclusion

The smart car design covers electronics, automatic control and many other disciplines. Its technology can be applied to intelligent robotics, automation platforms and other areas, With strong practicability. The papers combined with practical experience in the design, from smart car hardware design, software design and other aspects discussed intelligent vehicle design. Test proved, With incremental PID algorithm, even in the case of complex road, can better ensure smart car Smooth running along in the right direction.

References

1. Deng P (2013) Design of a smart automatic tracing car based on Renesas MCU. Electron Sci Technol 1:107–109
2. Wei S, Wu QM (2012) Design of servo brushless DC motor driver based on MSP430. Autom Appl 9:64–66
3. Chen SQ (2011) Development of reversing radar system based on AT89S51 MCU. Artif Intell Identification Tech 11:95–97
4. Hou T, Zhao H (2013) Design of the high precision control for flat panel system based on free pendulum. Process Autom Instrum 1:18–20
5. Li CQ, Xu SP (2012) Design and implementation of real-time inverted pendulum system. Comput Eng Des 11:4144–4148
6. Wang RR, Zhang HY (2012) Research of ultrasonic ranging error compensation algorithm. Ind Mine Autom 12:62–65

Improved Spectrum Sensing Method for Cognitive Radio Based on Time Domain Averaging and Correlation

Shenghong Li and Guoan Bi

Abstract Based on the combination of time domain averaging and correlation, we propose an effective time domain averaging and correlation based spectrum sensing (TDA-C-SS) method used in very low SNR environments. With the assumption that the received signal samples from the primary users are deterministic, the proposed TDA-C-SS method processes the received samples by a time averaging operation to improve the SNR. Correlation operation is then performed with a correlation matrix to determine the existence of the primary signal in the received samples. The TDA-C-SS method does not need any prior information on the received samples and the associated noise power to achieve improved sensing performance. Simulation results are presented to show the effectiveness of the proposed TDA-C-SS method.

Keywords Cognitive radio • Spectrum sensing • Time domain averaging • Correlation

1 Introduction

Cognitive radio (CR) networks allow unlicensed (or secondary) users to opportunistically exploit the under-utilized spectrum bandwidth of the licensed (or primary) users. Spectrum sensing is a key operation performed by the CR networks to determine the spectrum holes of the spectrum allocated to a primary

S. Li (✉)
Department of Electronic Engineering, Shanghai Jiao Tong University, Shanghai 200240, China
e-mail: shli@sjtu.edu.cn

G. Bi
Information Engineering School of EEE, Nanyang Technological University, Singapore 639798, Singapore
e-mail: EGBI@ntu.edu.sg

B. Zhang et al. (eds.), *The Proceedings of the Second International Conference on Communications, Signal Processing, and Systems*, Lecture Notes in Electrical Engineering 246, DOI 10.1007/978-3-319-00536-2_139,

user. In the literature, several kinds of typical spectrum sensing methods have been reported, e.g. energy detection methods [1, 2], matched-filter detection methods [3, 4], and cyclostationarity feature detection methods [5]. The energy detection methods need the prior knowledge of noise power and are vulnerable to the noise uncertainty. The matched-filter detection methods need the waveform of the primary user in advance. The cyclostationarity feature detection methods require the information on the cyclic frequencies of the primary user. The prior knowledge requirements of these methods limit their applicability. To avoid these limitations, some new statistical covariance based methods for spectrum sensing in additive i.i.d white noise environments have been proposed [6–8]. These methods do not need the prior information about the signal and the noise power to achieve a sensing performance in a low SNR environment of -22 dB. However, these methods assume that the primary user's signal is a stationary random process and all the received samples contain the primary user's signal if it exists. Most existing spectrum sensing methods require the last assumption. In fact, it is probably that only a part of the received samples in practice contain the signal from the primary user, or a part of or all the received samples are from some signals that are not stationary. For example, the initial transient signal, known as fingerprint of a wireless device [9], from the primary user is not stationary. If such samples are used, the methods reported in [6–8] will lose the supporting prerequisite and become unusable. Even in the cases that these required assumptions are valid, it is difficult for the methods in [6–8] to obtain theoretical sensing performance in lower SNR environments when the number of the received samples available is limited.

To overcome these problems and support more effective sensing in low SNR environments, we propose an effective TDA-C-SS method based on time domain averaging and correlation for spectrum sensing in additive i.i.d white noise environments. Similar to the methods reported in [6–8], the proposed TDA-C-SS method does not need any aforementioned prior information and achieve desirable sensing performance in very low SNR environments. The TDA-C-SS method assumes the signal from the primary user to be deterministic. By making use of time domain averaging, the SNR of the received samples is increased. Then the task of spectrum sensing is obtained by performing the correlation operation. Simulation results from various environments are presented to show the effectiveness of the proposed TDA-C-SS method.

The rest of this paper is organized as follows. Section 2 describes the system model and sampling operations to obtain the input sample sequence. Section 3 gives the proposed TDA-C-SS spectrum sensing method. Simulation results and discussions are presented in Sect. 4. Finally, conclusion is drawn in Sect. 5.

2 System Model and Sampling Description

In a duration, $[t_1,t_2]$, of spectrum sensing, let $z(t)$ be the continuous-time signal received by the secondary user. The process of spectrum sensing is regarded as a two-hypotheses-test problem at a duration, $[t_1,t_2]$, i.e., $\mathcal{H}_0$: the primary signal is absent and $\mathcal{H}_1$: the primary signal is present, described by

$$z_c(t) = \begin{cases} w_c(t) & t\in[t_1,t_2] \quad \mathcal{H}_0 \\ s_c(t) + w_c(t) & t\in[t_1,t_2] \quad \mathcal{H}_1 \end{cases} \tag{1}$$

where for $t_1 \leq t_3$, $t_4 \leq t_2$, $s_c(t) = s_{pri\_c}(t)$ if $t \in [t_3,t_4]$ else $s_c(t) = 0$,and $s_{pri\_c}(t)$ is any received primary signal, and $w_c(t)$ is the i.i.d white noise with a zero mean and a variance represented by δ^2.

Let us be interested in the frequency band with central frequency f_0 and a narrow bandwidth W. $z_c(t)$ defined in (1) is sampled at a frequency $f_s \geq L_{mul}(f_0 + W/2)$, where, L_{mul} is a large constant. The choice of f_s and L_{mul} is for the purpose of time domain averaging, which is to be described in Sect. 3. The two hypotheses in (1) are then expressed as

$$z(n) = \begin{cases} w(n) & n = 1, \cdots, N_0 \quad \mathcal{H}_0 \\ s(n) + w(n) & n = 1, \cdots, N_0 \quad \mathcal{H}_1 \end{cases} \tag{2}$$

where, $z(n) = z_c(n/f_s)$, $s(n) = s_c(n/f_s)$ and $w(n) = w_c(n/f_s)$.

Note that if $f_0 + W/2$ is very high, it is difficult to implement the sampling process because the available high speed samplers can support up to several tens of GHz [10, 11]. Therefore, we should suitably select the value of $f_0 + W/2$ to allow an appropriate large value of L_{mul} possible. It is also possible to use down conversion process [12] to generate the received samples when the value of $f_0 + W/2$ is very high.

3 The Proposed Spectrum Sensing Method

The proposed TDA-C-SS method treats the samples of the primary users to be deterministic. It averages the received data samples in the time domain to increase SNR and obtains the spectrum sensing by correlation operations.

3.1 Sample Time Domain Averaging

Time domain averaging is an effective method to decrease noise power for periodic signal detection [13]. For the obtained sample sequence $\{z(n), n \in [1,N_0]\}$, the time average operation is defined by

$$e(n) = \sum_{j=-M}^{M} z(n \cdot L_{mul} + j)/(2M+1) \qquad n = 1, \cdots, N \tag{3}$$

where M is a small positive integer and $N = [N_0/L_{mul}]$.

If the samples from the primary users are treated as deterministic ones, f_s is L_{mul} times of $f_0 + W/2$ and M is small, it means that

$$s(n \cdot L_{mul}) \approx \sum_{j=-M}^{M} s(n \cdot L_{mul} + j)/(2M+1), \quad n = 1, \cdots, N.$$

With the assumption that $w_c(t)$ is i.i.d white noise, we can easily obtain:

$$e(n) = \begin{cases} \sum_{j=-M}^{M} w(n \cdot L_{mul} + j)/2M + 1 = \bar{\omega}(n) & n = 1, \cdots, N \mathcal{H}_0 \\ \sum_{j=-M}^{M} s(n \cdot L_{mul} + j)/2M + 1 + \sum_{j=-M}^{M} w(n \cdot L_{mul} + j)/2M & \\ +1 \approx s(n \cdot L_{mul}) + \bar{\omega}(n) & n = 1, \cdots, N \mathcal{H}_1 \end{cases} \tag{4}$$

where $\bar{\omega}(n)$ can be considered as the samples of the i.i.d white noise $\bar{\omega}_c(t)$ with a zero mean and a variance $\delta^2/(2M+1)$. Define $SNR = 10\lg\left\{\sum_{n=1}^{N} s^2(nL_{mul})/N\mathrm{Var}[\text{noise}]\right\}$, where $Var[\cdot]$ denotes the variance. It can be proved that the SNR of the sequence produced by the time averaging process is increased by 10 lg(2M + 1) dB. This gain in SNR is very valuable for effective spectrum sensing in the environment of strong noise.

3.2 Correlation Operation and Sensing Decision

Similar to the method in [6], we perform the correlation operation on the input samples and make a decision on the signal presence of the primary user based on a constructed correlation matrix. Different from [6], the correlation used here is to be discussed from the view of deterministic signal samples.

Consider the correlation defined by $r_e(i) = \frac{1}{N}\sum_{n=1}^{N} e(n)e(n-i)$. Under $\mathcal{H}_0$

$$r_e(i) = \frac{1}{N}\sum_{n=1}^{N} \bar{\omega}(n)\bar{\omega}(n-i) \tag{5}$$

Under $\mathcal{H}_1$, we have

$$\begin{aligned} r_e(i) &\approx \frac{1}{N}\sum_{n=1}^{N}[s(nL_{mul}) + \bar{\omega}(n)][s((n-i)L_{mul}) + \bar{\omega}(n-i)] \\ &= \frac{1}{N}\sum_{n=1}^{N} s(nL_{mul})s((n-i)L_{mul}) + \frac{1}{N}\sum_{n=1}^{N} s(nL_{mul})\bar{\omega}(n-i) \\ &+ \frac{1}{N}\sum_{n=1}^{N} s((n-i)L_{mul})\bar{\omega}(n) + \frac{1}{N}\sum_{n=1}^{N} \bar{\omega}(n)\bar{\omega}(n-i) \end{aligned} \tag{6}$$

It is noted that $\bar{\omega}(n)$ are the samples from the i.i.d white noise, $\bar{\omega}_c(t)$, $s(nL_{mul})\bar{\omega}(n-i)$ are the samples from mutually independent random variables with a zero mean and variance $s^2(nL_{mul})\delta^2/(2M+1)$. Therefore, based on the central limit theorem, $\sum_{n=1}^{N} s(nL_{mul})\bar{\omega}(n-i)/N$ in (6) can be treated as a sample sequence of a Gaussian random variable λ when $N \to \infty$. Since $\lim_{n\to\infty} Prob\{|g-0| < \varepsilon\} = 1$ for an arbitrary positive ε, $\frac{1}{N}\sum_{n=1}^{N} s(nL_{mul})\bar{\omega}(n-i) \to 0$ when $N \to \infty$. We conclude that $\frac{1}{N}\sum_{n=1}^{N} s((n-i)L_{mul})\bar{\omega}(n) \to 0$ in (6) when $N \to \infty$. In addition, it is also noted that when $N \to \infty$, (5) or the last term in (6) satisfies $\frac{1}{N}\sum_{n=1}^{N} \bar{\omega}(n)\bar{\omega}(n-i) = E[\bar{\omega}_c(t)\bar{\omega}_c(t-i)] = \delta^2/(2M+1)$ for i = 0 and 0 otherwise, where $E[\cdot]$ is the expectation. Finally, the first term in (6) are usually not identically zero when s(n) is a deterministic sample sequence.

Let us construct an L×L correlation matrix in the same form as that in [6],

$$R_e = \begin{pmatrix} r_e(0) & r_e(1) & \cdots & r_e(L-1) \\ r_e(1) & r_e(0) & \cdots & r_e(L-2) \\ \vdots & \vdots & \ddots & \vdots \\ r_e(L-1) & r_e(L-2) & \cdots & r_e(0) \end{pmatrix}. \tag{7}$$

Based on the previous analysis of $r_e i$), the sensing test statistics and decision policies of the CAV method and the GCBA method in [6] are still applicable for our

method. For simplicity, we use the test statistics and decision policy of the CAV method in [6], i.e.

$$T = \sum_{n=1}^{L} \sum_{m=1}^{L} |r_{nm}| / \sum_{m=1}^{L} |r_{mm}| \tag{8}$$

where r_{nm} is the element of R_e. With a threshold $\lambda > 0$, the sensing decision for the primary signal is made by (i) $T > \lambda$ present, (ii) $T \leq \lambda$ absent.

3.3 The TDA-C-SS Method

Based on the discussion above, we propose an improved spectrum sensing method as follows. Step-1: Sample the received signal at frequency f_s to obtain the discrete samples $z(n)$, $n = 1, \cdot \cdot, N_0$; Stpe-2: For a given value of M, calculate $e(n)$, $n = 1, \cdot \cdot, N$ by (3); Step-3: For a given L, calculate $r_e i)$, i = 0,1,. . .L-1 and construct R_e in (7); Step-4: Calculate T in (8), choose the value of λ for sensing decision.

Same as the approach in [6, 8], we use the computer simulation approach based on P_f, to choose the threshold λ. That is, a P_f is given and white noise is generated as the input, then with a number of simulation results of T in (8), λ is selected to meet the requirement of P_f.

4 Simulations

In this section, simulation results are reported for three signal settings in the AWGN environments to verify the effectiveness of the proposed method. Case I: The signal from the primary user is stationary. During spectrum sensing, all the received samples contain the signal of the primary user. Case II: The signal from the primary user is stationary. During spectrum sensing, a part of the received samples contain the signal of primary user. Case III: The signal from the primary user is not stationary.

For comparison, we also present the simulation results of the CAV method [6] applicable for Case I. λ are chosen by the approach described previously, and 1,000 Monte Carlo runs are carried out to estimate the value of λ.

4.1 Simulation for Case I

We use a wireless microphone signal generated by the method in [14] with the following parameters: central frequency $f_0 = 100$ MHz, bandwidth $W = 36.8$ KHz.

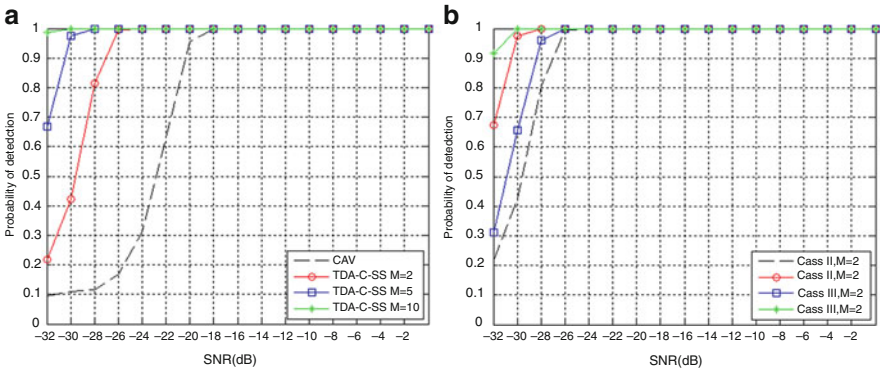

Fig. 1 P_d curves versus SNR. (**a**) Case I, (**b**) Case II and Case III

Based on the discussion in Sect. 2, the sampling frequencies are $f_s = 10.3GHz \geq L_{mul}(f_0 + W/2)$, where, $L_{mul} = 100$, and $f_s = 103MHz \geq f_0 + W/2$.

Figure 1a gives the detection probability, P_d versus SNR, with $P_f = 0.1$, $L = 10$, $N = 50000$, for the proposed TDA-C-SS method, with different values of M, and the CAV method. It can be observed that under the same conditions, the detection performance of the proposed method outperforms that of CAV and can be improved further with increase of M.

4.2 Simulation for Case II and Case III

In case II, the received samples sequence is 45,000 zero-valued signal samples followed by 5,000 wireless microphone signal samples generated in case I. The segment of zero-valued signal samples is included for the frequently observed situation in which the primary user begins to occupy its channel after the secondary user has monitored the channel for certain period of time. The sampling frequency for TDA-C-SS is $f_s = 10.3GHz$. For case III, we use a fingerprint signal, which is generated by the unit-step response of a second-order RLC parallel circuit described by:

$$\frac{d^2 i_l(t)}{dt^2} + 2\sigma \frac{di_l(t)}{dt} + {w_0}^2 i_l(t) = \frac{1}{L_f C_f} i_s(t)$$

$L_f = 10^{-8}, C_f = 10^{-10}, R = 0.08, \sigma = R/2L_f = 4000000, w_0 = \sqrt{1/L_f C_f} = 10^9$. The fingerprint signal has the central frequency $f_0 = 160MHz$ and the bandwidth $W = 8MHz$. The sampling frequency for TDA-C-SS is $f_s = 16.4GHz \geq L_{mul}(f_0 + W/2), L_{mul} = 100$.

It is unreasonable to use the CAV method, because the signals used in case II and III are not stationary. Therefore, we only verify the effectiveness of the TDA-C-SS method. Figure 1b gives the detection probability versus SNRs for the two cases with $P_f = 0.1$, $L = 10$, $N = 50000$.It can be seen that the TDA-C-SS method is still effective because this method does not consider the properties of the received signal. Similarly, the detection performance can be improved further with the increased value of M.

5 Conclusion

In this paper, an improved spectrum sensing method, TDA-C-SS, based on time domain averaging and correlation has been proposed. The time domain averaging process has been typically used to decrease the noise effects and correlation matrix has been constructed to decide the existence of the primary user's signal. Comparing with other reported method, such as CAV method, the proposed one can sense a primary user's signal in the white noise environment in very low SNR environments without requiring any prior knowledge about the signal and noise power. In particular, the proposed method is flexible to effectively sense the signals that are not stationary. Our simulation results have shown the desirable advantages of the proposed methods.

References

1. Cabric D, Mishra SM, Brodersen RW (2004) Implementation issues in spectrum sensing for cognitive radios. In: Proc. Asilomar conf. signals, syst. computers, Pacific Grove, CA, Nov 2004
2. Sahai A, Cabric D (2005) Spectrum sensing: fundamental limits and practical challenges. A tutorial in IEEE int. symp. New Frontiers DySPAN, Baltimore, MD, Nov 2005
3. Cabric D, Tkachenko A, Brodersen RW (2006) Spectrum sensing measurements of pilot, energy, and collaborative detection. In: Proc. military commun. conf. (MILCOM), Washington, DC, Oct 2006
4. Chen H-S, Gao W, Daut DG (2007) Signature based spectrum sensing algorithms for IEEE 802.22 WRAN. In: Proc. IEEE int. conf. communications (ICC), Jun 2007
5. Han N, Shon SH, Joo JO, Kim JM (2006) Spectral correlation based signal detection method for spectrum sensing in IEEE 802.22 WRAN systems. In: Proc. intern. conf. advanced commun. technology, Korea, Feb 2006
6. Zeng Y, Liang Y-C (2009) Spectrum-sensing algorithms for cognitive radio based on statistical covariance. IEEE Trans Veh Technol 58(4):1804–1815
7. Zeng Y, Liang Y-C (2009) Eigenvalue-based spectrum sensing algorithms for cognitive radio. IEEE Trans Commun 57(6):1784–1793
8. Zeng Y, Liang Y-C, Zhang R (2008) Blindly combined energy detection for spectrum sensing in cognitive radio. IEEE Signal Process Lett 15:649–652

9. Xu J-Y, Zhang H-S (2009) Detection to primary user based on radio frequency fingerprint in cognitive radio. In: Proc. intern. cong. image and signal processing (CISP), P.R. China, Oct 2009
10. Lecklider T (2010) Raising the B/W Bar to 32 GHz. Eval Eng 49(6):34
11. Zhao YJ, Hu YH, Wang HJ (2012) Enhanced random equivalent sampling based on compressed sensing. IEEE Trans Instrum Meas 61(3):579–586
12. López-Valcarce R, Vazquez-Vilar G (2009) Wideband spectrum sensing in cognitive radio: joint estimation of noise variance and multiple signal levels. 2009 I.E. international workshop on signal processing advances for wireless communications (SPAWC 2009), Italy, Jun 2009
13. Pini M, Akos D-M (2007) Exploiting GNSS signal structure to enhance observability. IEEE Trans Aerospace Electron Sys 43(4):1553–1565
14. Zeng Y, Liang Y-C (2006) Performance of Eigenvalue based sensing algorithms for detection of DTV and wireless microphone signals. IEEE 802.22-06/186r0, Sept 2006

Index

B. Zhang et al. (eds.), *The Proceedings of the Second International Conference on Communications, Signal Processing, and Systems*, Lecture Notes in Electrical Engineering 246, DOI 10.1007/978-3-319-00536-2,